IntechOpen

Semiconductor Photocatalysis
Materials, Mechanisms and Applications

Edited by Wenbin Cao

SEMICONDUCTOR PHOTOCATALYSIS - MATERIALS, MECHANISMS AND APPLICATIONS

Edited by **Wenbin Cao**

Contributors

Xiangchao Zhang, Duan Huang, Kaiqiang Xu, Difa Xu, Yunlong Li, Shiying Zhang, Alex Tawanda Kuvarega, Bhekie Mamba, Pengyu Dong, Xinguo Xi, Guihua Hou, Ion N. Mihailescu, Oksana Linnik, Nataliia Smirnova, Nicolaie Stefan, Carmen-Georgeta Ristoscu, Gabriel Socol, Marimona Miroiu, Oleksandr Korduban, Anna Eremenko, Nataliia Chorna, Ana Pimentel, Daniela Nunes, Sonia Pereira, Rodrigo Martins, Elvira Fortunato, Xinmei Hou, Song Sun, Fan Zhang, Zhengjun Zhang, Shuang Shuang, Zheng Xie, Hongxing Dai, Kunfeng Zhang, Jiguang Deng, Yuxi Liu, Shaohua Xie, Hamid Reza Rajabi, Joao Henrique Zimnoch Dos Santos, Yolice Patricia Moreno Ruiz, Cicero Escobar, William Da Silva, Damien Lenoble, Guillaume Lamblin, Vincent Rogé, Olga Ishchenko, Claudia Letizia Bianchi, Carlo Pirola, Giuseppina Cerrato, Marta Stucchi, Benedetta Sacchi, Sara Morandi, Alessandra Carletti, Valentino Capucci, Alessandro Di Michele, Fei Huang, Aihua Yan, Hui Zhao, Yuri Zhukovskii, Sergey Piskunov, Oleg Lisovski, Andrei Chesnokov, Dmitry Bocharov, Ewelina Grabowska, Liqun Ye, Ahmad Alshammari, Nimai Mishra, Peter M Czermak, Colin Awungacha Lekelefac, Mahabubur Chowdhury, Ncumisa Mpongwana, Franscious Cummings, Veruscha Fester, Seteno Karabo Obed Ntwampe, Manuel Nuño, Richard J. Ball, Chris R. Bowen, Carlos Velasco-Santos, Ana Laura Martínez-Hernandez, Eduardo Enrique Perez-Ramirez, Miguel De La Luz-Asunción

Notice

Statements and opinions expressed in the chapters are these of the individual contributors and not necessarily those of the editors or publisher. No responsibility is accepted for the accuracy of information contained in the published chapters. The publisher assumes no responsibility for any damage or injury to persons or property arising out of the use of any materials, instructions, methods or ideas contained in the book.

We are IntechOpen,
the world's leading publisher of Open Access books
Built by scientists, for scientists

3,800+
Open access books available

116,000+
International authors and editors

120M+
Downloads

151
Countries delivered to

Our authors are among the
Top 1%
most cited scientists

12.2%
Contributors from top 500 universities

Interested in publishing with us?
Contact book.department@intechopen.com

Numbers displayed above are based on latest data collected.
For more information visit www.intechopen.com

Meet the editor

Dr. Wenbin Cao is a Professor in the School of Materials Science and Engineering at the University of Science and Technology Beijing (USTB). He received his PhD in Materials Science from the USTB in 1998. His current research is directed toward the development of synthesis, property, and industrialization of semiconductor photocatalysis, which is applied in pollutant decomposition, self-cleaning coating, and bacteria inactivation. He worked on the photocatalytic property improvement by metal and nonmetal doping, heterojunction construction with semiconductors, and core-shell structure. Other functional materials, such as thermal-induced phase transition materials and microwave absorbing ceramics, are also well studied in his group. Dr. Wenbin Cao has published more than 100 papers in international journals and has authorized more than 10 patents.

Contents

Preface

In recent years, photocatalysis has attracted increasing attention because it can provide an environmentally friendly approach toward the conversion of light energy into chemical energy at mild reaction environments through photophysical processes and photochemical reactions. Wide potential applications of photocatalysis have been developed in renewable energy production and environmental remediation. It is currently extremely active and continuously growing. Numerous research works and large number of papers have been published each year, which involve new materials systems, new preparation methods, new applications, and so on.

It is well known that titanium dioxide (TiO_2) is one of the most practical photocatalysts due to its photo-stability, non-toxicity, and high photocatalytic activity in pollutant elimination in air and water. Extensive research has been performed during the past decades. So, in the first section, descriptions of the synthesis, characterization, and applications of TiO_2-based photocatalysts are involved. Various methods such as doping, synthesis method modification, and morphology design are discussed, and their effects on photocatalytic property improvement are assessed. Though difficult, the mechanism of the reactions happened in the photocatalysis is explained by both theoretical calculation and experimental proof. A full map of TiO_2-based photocatalytic materials could be addressed with the information in the first section.

At the same time, some novel photocatalytic oxides and non-oxides, except for TiO_2, are attracting research effort due to the limited visible light efficiency absorption of TiO_2. The typical non-TiO_2-based photocatalysts such as WO_3, Ag_3PO_4, BiOX (X = Cl, Br, and I), and indium-containing oxides are introduced in the second section of this book. Some of these newly developed compounds are demonstrating promising photodegradation ability together with properties such as low cost, harmlessness, and stability in acidic and oxidative conditions, contributing to industry potentials. Moreover, complex structures such as metal organic frameworks are also assessed in the second section.

Manipulation of the structure from the very basic physical aspect is an effective method for photocatalytic reactivity improvement. Modification of photocatalysis based on a design of the heterostructure is an effective method to achieve improvement in photocatalytic property. The heterojunction structure could act as an electron scavenger to inhibit the e^-–h^+ from recombination, so the photocatalytic property is enhanced. Researches regarding different heterostructures modified photocatalysts are discussed in the third section.

With the continuous efforts exerted on photocatalysis, its application areas are broadened to environmental and energy challenges, which are ever increasing and emergent. Photocataly-

sis showed promising degradation ability to organic pollutants, heavy metals, and bacteria both in air and in water. The photocatalytic efficiency is maintained with long-time cycles, which contributes to a prospective method for pollutants' removal, self-cleaning, and bacteria elimination and prevention. Although the applications of photocatalysis are too broad to be stated in one section, the most covered aspects are selected in the fourth section.

I am confident that this book provides readers with an in-depth understanding of fundamental aspects and current research progresses of photocatalysis. While the length of this book is limited and the evolution of this topic is everlasting, I hope this book will shed light on the helpful understanding of photocatalysis. The accomplishment of this book is attributed to the collaboration of authors, whose fruitful opinions and beneficial discussions are provided in the individual chapters. And finally, I sincerely appreciate Ms. Dajana Pemac and all the authors for their valuable and dedicated efforts exerted on this book.

Wenbin Cao
University of Science and Technology Beijing,
China

TiO2-based Photocatalysis

TiO$_2$- and ZnO-Based Materials for Photocatalysis: Material Properties, Device Architecture and Emerging Concepts

Olga M. Ishchenko, Vincent Rogé,
Guillaume Lamblin and Damien Lenoble

Additional information is available at the end of the chapter

Abstract

Numerous kinds of photocatalysts such as oxide-, nitride- or sulfide-based semiconductors, conducting polymers or graphene oxide–based materials have emerged since the discovery of water splitting on TiO$_2$ electrodes in 1972. Yet, metal-oxides are still largely the main family of materials promoted into photocatalytic applications.

In this chapter, we focus on the application of supported nanostructures of metal oxides, principally TiO$_2$ and ZnO, for the heterogeneous photocatalysis. We emphasize the benefits of increasing the specific surface area by using the direct growth of metal-oxide nanostructures onto porous templates. Among the numerous strategies to improve the photocatalytic activity, we detail the fabrication of semiconductor metal-oxide heterostructures promoting the charge separation under UV irradiation. We also describe how the use of plasmonic nanostructures allows the shifting of the light absorption in the visible range. Finally, we give an overview on the new strategies to increase the photocatalytic activity with new architectures and materials based on metal-oxides.

Keywords: photocatalysis, TiO$_2$, ZnO, heterostructures, plasmonic nanoparticles

1. Introduction

In the context of major environmental problems such as the lack of fresh water and the global planet warming, the most important expectations about photocatalysis are certainly coming from the perspective of energy storage and water/air depollution. Photocatalysis would allow

the direct transformation of solar energy into chemical energy for water splitting and hydrogen production [1], or water/air remediation of organic pollutants via redox reactions.

The implementation of depollution technologies in Europe has already been initiated. Numerous examples of self-cleaning and/or remediation cements, glass or paints are already commercialized by companies like Siplast (remediation membranes) [2], Calcia (self-cleaning and remediation cements) [3], Saint-Gobain (self-cleaning glass) [4], and Auro (Auro n°328, remediation paints) [5]. Among those commercial solutions a large debate on the real efficiency of those materials still exists [6]. As an example, the photocatalytic reduction of the concentration of NO_x in Leopold II tunnel in Brussels has been shown to be weak in spite of the use of photocatalytic cements. Indeed, the pollutants concentrations as well as the low power irradiation of the UV-visible light and the humidity conditions apparently impair the photocatalytic reaction. Concerning the water depollution or the hydrogen production, current installations do not exceed the scale of pilot demonstrators [7, 8].

A huge number of photocatalysts have already been reported in the literature and can be classified in the family of metal-oxides, metal-sulfides, metal-nitrides and also from metal free compounds like polymers or graphenes. In this chapter, our interest is principally focused on metal-oxides materials which are certainly the most studied when photocatalytic applications are concerned. In a non-exhaustive way, metal oxides like TiO_2, ZnO, Fe_2O_3, SnO_2, ZrO_2, MgO, GeO_2, Sb_2O_3, V_2O_5, WO_3, Cu_2O, In_2O_3, Nb_2O_5 [9, 10], and perovskites are among the most investigated materials for the photocatalysis today. In the 70s, a photocatalytic activity was already known for TiO_2 or ZnO [11]. In the same decade, Fe_2O_3, SnO_2, ZrO_2, MgO, GeO_2, Sb_2O_3, or V_2O_5 were also investigated as photocatalysts, but their activity were considered to be relatively weak compared to the one of TiO_2 [12, 13]. In the same years, Cu_2O was suspected to be involved in the photodegradation of polyethylene plastic [14]. First publications about organic dyes degradation by WO_3 were reported in 1993 [15], whereas In_2O_3 materials were shown to be active for the photodegradation of ethane in 1988 [16], and Nb_2O_5 to strongly increase TiO_2 activity toward the degradation of dichloro-benzene in 1994 [17].

Since the 70s, TiO_2 and in a lesser extent ZnO had continued to attract a particular interest in the research and industry communities. TiO_2 and ZnO present a high photocatalytic activity, good chemical stability, non- or low-toxicity, low cost, and more or less long term photostability. However, one of their important drawbacks is their lack of performances in the visible range of the solar spectrum.

The development of new photocatalysts appeared therefore to be a necessity to push forward the current photocatalytic performances. A lot of researches are currently conducted to find out new materials and/or improve the properties of the current ones. This chapter focuses on the enhancing strategies to boost the photocatalytic efficiency of the two most common photocatalysts, TiO_2 and ZnO.

Biocompatibility and/or durability properties of photocatalyst are rarely taken into consideration. We provide a prospective view of the pure photocatalytic performances or benefits of the cited materials, devices, or architectures. However, it is obvious that, to be selected as a

good candidate for commercial applications, a photocatalyst should not only demonstrate excellent photocatalytic activity but also needs to be biocompatible, low-cost, and durable.

Given that the photocatalysis is a surface based mechanism, one of the simplest ways to increase the activity is to increase the active surface area. Therefore, supported nanomaterials are obvious candidates of choice to reply to this challenge. The first section of this chapter describes nanotextured photocatalysts supported on porous template. In the second section, we focus the reader's attention on the band gap engineering that increase the separation of photo-generated carriers. The third section deals with the introduction of the plasmonic effect to shift in the visible range the light absorption properties of TiO$_2$ and ZnO photocatalysts. Finally, we propose an overview on the emerging new materials and concepts based on metal-oxides.

2. Nanostructured supported photocatalysts

In the earlier ages of photocatalysis, the experiments were conducted from bulk photocatalysts. The emergence of nanomaterials pushed in the late 80s by the development of characterization and visualization techniques stimulated a huge interest for those nanomaterials in the scientific community. Compared to bulk materials, nanomaterials exhibit a higher specific surface area. Two kinds of nanoscale photocatalysts can be distinguished: suspensions of nanostructures in solutions, or supported nanomaterials on appropriated templates. The main advantages of dispersed nanostructures are the simplicity of use and their low cost. Nevertheless, dispersed nanomaterials in solution tend to agglomerate, lowering their exposed specific surface area. Furthermore, a filtration step is needed to remove them from the solution. For this reason, a rising interest occurs on supported nanomaterials. In seek of always increasing the exposed specific surface area of nanotextured photocatalysts, their synthesis at the surface of porous support like membranes has been envisaged for water treatment [18, 19] or water splitting [20, 21]. Currently, membranes are mainly studied for the photocatalytic water treatment as they combine the double advantages of filtration, and photocatalytic degradation of water pollutants (hybrid filtration/photocatalytic membranes).

Stable photocatalytic membranes, can be obtained using inorganic membranes. The main advantages of inorganic membranes are their good chemical and thermal resistance. These allows the use of a wide panel of photocatalyst synthesis processes, like high temperature gas phase chemical vapor deposition (CVD), and hydrothermal growth followed by high temperature annealing. In addition, with those types of synthesis techniques many different photocatalytic structures of semiconductors can be achieved: nanoparticles, nanowires, nanorods, or nanofilms. Hong *et al.* [22] have pointed out the photocatalytic performances of Al$_2$O$_3$–ZrO$_2$ composite membrane coated with TiO$_2$ nanorods (**Figure 1a**) using a sol-gel process followed by an annealing step (510°C). The photocatalytic degradation curves of Methyl orange and Methylene blue (**Figure 1b**) clearly demonstrate an efficient photocatalytic activity of the elaborated membrane.
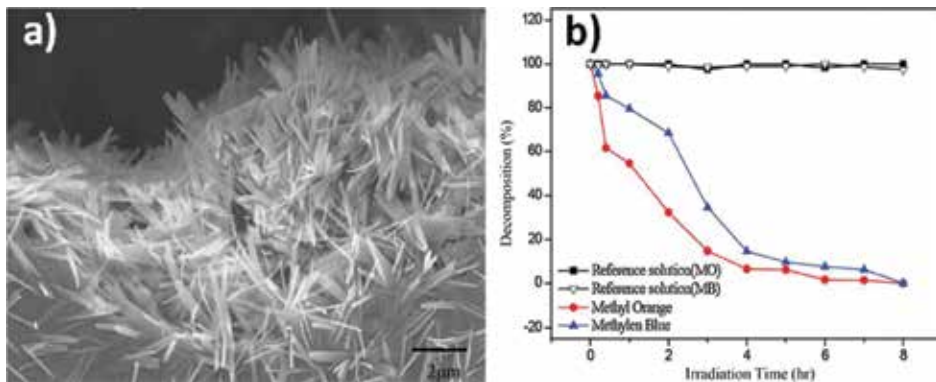
Figure 1. (a) Inside of a pore of a Al_2O_3–ZrO_2 composite membrane coated with TiO_2 nano-rods. (b) Photodegradation curves of Methylene blue and Methyl orange on a micro-channeled Al_2O_3–ZrO_2 composite membrane decorated with TiO_2 nano-rods. Picture reproduced from Hong *et al.* [22].

ZnO-based photocatalytic membranes can also be envisaged. Rogé [10] performed the growth of ZnO nano-wires inside glass fibers membrane with a solvothermal synthesis at low temperature (below 90°C). However, a better crystallinity of the ZnO, leading to better photocatalytic degradation properties can be reached after an annealing process around 200–300°C. The grown ZnO nano-wires on glass fibers are illustrated in **Figure 2**.
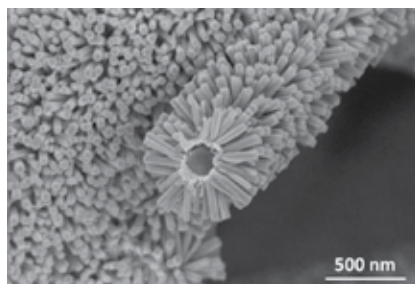
Figure 2. ZnO nanowires grown around glass fibers in a macro-porous glass fibers membrane.

When the pore size in membranes is lower than the micrometer scale, one technique is particularly adapted to the fabrication of photocatalytic porous membranes: atomic layer deposition (ALD). The ALD technique is indeed the most suitable gas phase technique for the growth of conformal metal-oxide nano-films inside porous structure. Rogé *et al.* [23] showed that ZnO nano-films grown by ALD between 150°C and 250°C exhibit good photocatalytic properties for the Methylene blue degradation. The authors highlighted that, for the same specific surface area, the ZnO realized by ALD are more active than other structures of ZnO grown in liquid or vapor phase. In another publication [24], the conformality of the ZnO deposited on nano-structured membranes of anodic aluminum oxide (AAO) has been also attested. **Figure 3** represents the cross-section of a ZnO film grown inside a 200 nm diameter AAO pore. We clearly notice the homogeneous film inside the porous structure.
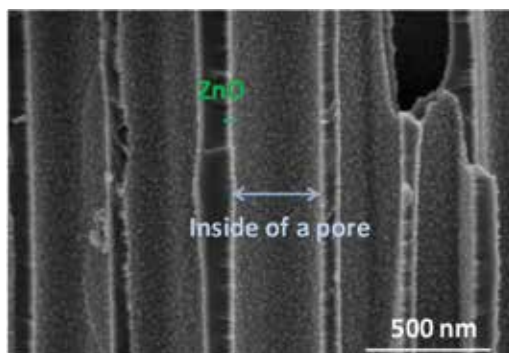
Figure 3. SEM picture of a ZnO nano-film grown in an anodic aluminum oxide membrane.

Similar results have been observed by Lee *et al.* [25]. They realized the synthesis of ZnO and TiO$_2$ nano-films inside bio-template membranes prepared from inner shell membranes of avian eggshells (**Figure 4**). They indicate that low temperature synthesis (100°C) of ZnO and TiO$_2$ leads to a ZnO-based material being more attractive for the photocatalytic activity, whereas at higher temperature synthesis (275°C), the TiO$_2$-based materials show more interesting bactericidal photocatalytic properties. Those results can be explained by the presence of a ZnO hexagonal crystalline structure at low temperature, being favorable to the electron/holes transport in the material. An amorphous structure, like the one of TiO$_2$ grown at low temperature, is less favorable for the charge carriers diffusion.
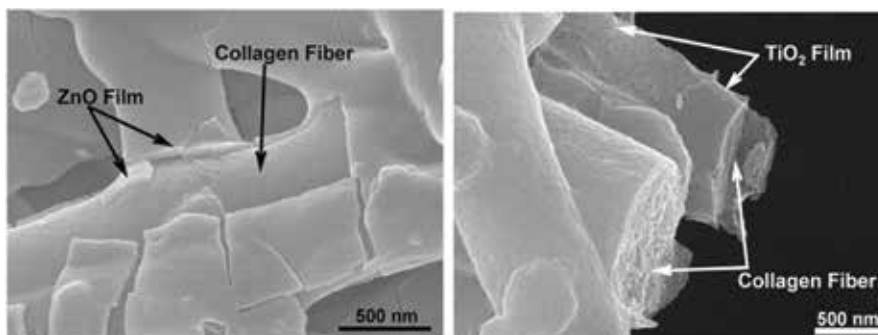
Figure 4. SEM picture of a composite membrane of collagen fibers and ZnO (on the left) and TiO$_2$ (on the right). Picture reproduced from Lee *et al.* [25].

Hybrid filtration/photocatalytic organic membranes can be synthesized by two different methods: deposition of the photocatalyst onto the membrane [26], or dispersion of the photocatalyst into the polymer [27]. The functionalization of organic membranes with TiO$_2$ nanoparticles can be performed by a dip coating [22] process using a TiO$_2$ precursor solution. This kind of membranes seems well adapted as they show improved hydrophilicity perform-ance and photocatalytic properties due to the presence of the TiO$_2$ particles [28]. However, the immobilization of the TiO$_2$ nanoparticles is often not stable. Mansourpanah *et al.* [28] high-

lighted an important loss of TiO_2 nanoparticles from the membrane after a filtration process. To avoid this detrimental loss that may be prejudicial to the surrounding environment, a second approach consists in blending the photocatalyst in the polymer matrix. As an example, Rahimpour *et al.* [29] entrapped TiO_2 nano-particles in PVDF/SPES membranes using phase inversion induced by immersion precipitation process, as shown on the **Figure 5**.
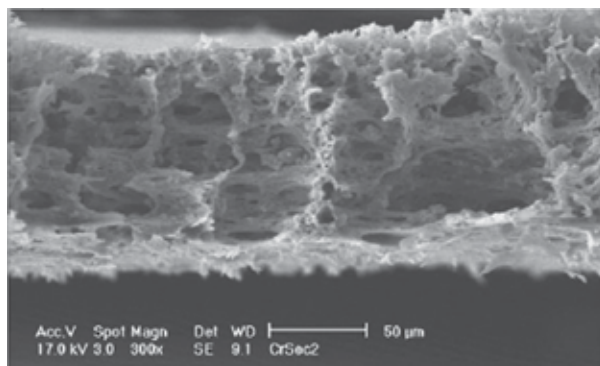
Figure 5. SEM picture of a PVDF/SPES membrane containing 4 wt% TiO_2 nano-particles. Picture reproduced from Rahimpour *et al.* [29].

The main drawback of the blended photocatalytic membranes is their limited photocatalytic performances compared to coated membranes, as the nano-particles are embedded in the polymeric matrix. As a consequence, an important part of photocatalysts does not contribute to the photodegradation mechanisms: either the UV light is trapped by the polymer [30], or either the electrons/holes photogenerated cannot migrate to the reactive surface in contact with pollutants species.

3. Improvement of the photocatalytic activity of photocatalysts by the fabrication of heterostructures

One of the limitations of the photocatalytic efficiency is the fast recombination of the photo-generated electron (e^-) and holes (h^+). Promoting the charge separation in photocatalysts is one strategy that has been proposed to increase the lifetime of the electron-hole pairs. The most common approaches include the development of (1) semiconductor/semiconductor hetero-structures [31], (2) semiconductor/metal heterostructures [31, 32], (3) semiconductor/carbon heterostructure [31], or (4) the surface modification with electron or hole scavengers [33, 34].

Semiconductor/semiconductor heterostructures are defined when two semiconductors with different electronic band structures form a heterojunction. As illustrated in **Figure 6**, three types of heterojunctions can be distinguished based on the relative position of the conduction band and the valence band of the two semiconductors: the type-I or straddling gap, the type-II or staggered gap, and the type III or broken gap.
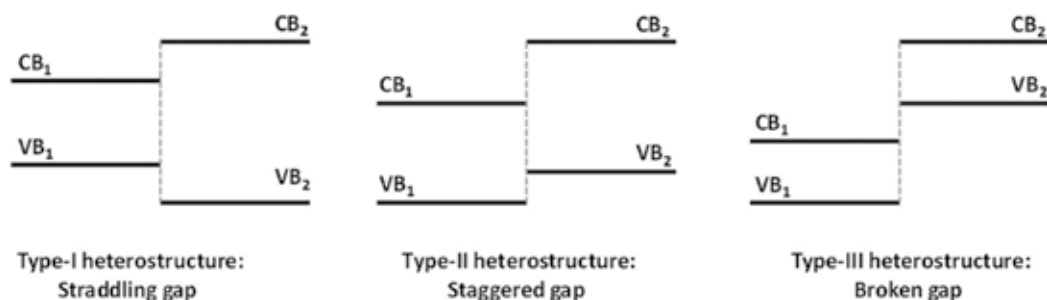
Figure 6. Representation of the three different heterostructures possible between two semi-conductors. CB$_1$ and VB$_1$ represent the conduction band and the valence band respectively of the semi-conductor 1. CB$_2$ and VB$_2$ represent the conduction band and the valence band respectively of the semi-conductor 2.

The type-II heterostructure is the most interesting one in photocatalysis as the energy gradient present at the interface allows the separation of the charge carriers on each part of the heterojunction, as represented in **Figure 7**. For a typical ZnO/SnO$_2$ type-II heterostructure, the electrons photogenerated in the semiconductor with the highest conduction band energy (CB of ZnO) migrate in the conduction band of the semiconductor having the minimum conduction band energy (CB of SnO$_2$). Whereas the holes photogenerated in semiconductor with the lowest valence band energy (VB of SnO$_2$) migrate toward the valence band of the semiconductor having the maximum of valence band energy (VB of ZnO).
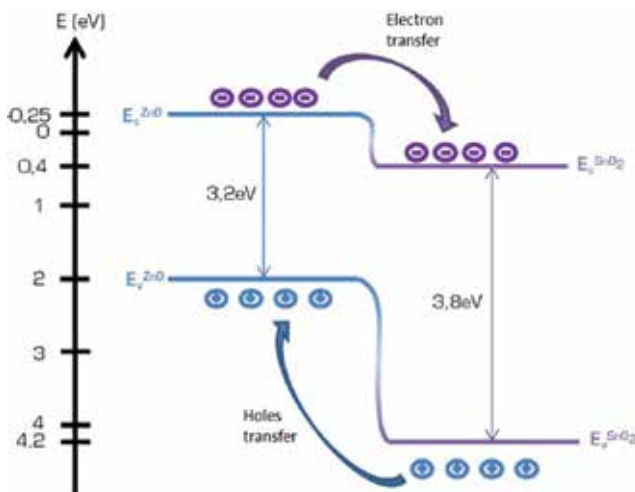
Figure 7. Representation of the type-II heterostructure present in a ZnO/SnO$_2$ heterostructure.

Rogé *et al.* [24] have characterized the bands alignment in the case of a ZnO nano-films/SnO$_2$ nano-particles heterostructure with XPS analysis. The valence band offset (VBO or ΔE_v), as well as the conduction band offset (CBO or ΔE_c) in the heterostructure are determined using the following equation:

$$\Delta Ev = \left(E_{Zn2p} - E_{v_{ZnO}} \right)_{ZnO\,bulk} - \left(E_{Sn3d} - E_{v_{SnO_2}} \right)_{SnO_2\,bulk} - \Delta E_{CL} \tag{1}$$

where E_{Zn2p} corresponds to the binding energy of the Zn2p peak in bulk ZnO, E_{vZnO} to the valence band maximum of bulk ZnO, E_{Sn3d} to the binding energy of the Sn3d peak in bulk SnO_2 and E_{vSnO2} to the valence band maximum in bulk SnO_2. The ΔE_{CL} term can be determined from:

$$\Delta E_{CL} = \left(E_{Zn2p} - E_{Sn3d} \right)_{heterostructure} \tag{2}$$

where E_{Zn2P} corresponds to the position of the Zn2p peak in the heterostructure of ZnO/SnO$_2$ and E_{Sn3d} to the position of the Sn3d peak in the heterostructure of ZnO/SnO$_2$.

The conduction band offset (ΔE_c) can be calculated using:

$$\Delta E_c = \Delta E_v + E_{g_{ZnO}} - E_{g_{SnO_2}} \tag{3}$$

where ΔE_v is the valence band offset previously calculated, E_{gZnO} is the optical band gap of ZnO and E_{gSnO2} is the optical band gap of SnO_2.

As a result, the band alignment at the ZnO/SnO$_2$ interface revealed a valence band offset around 0.67 eV and a conduction band offset around 0.24 eV, confirming the presence of a type-II heterostructure between those two materials.
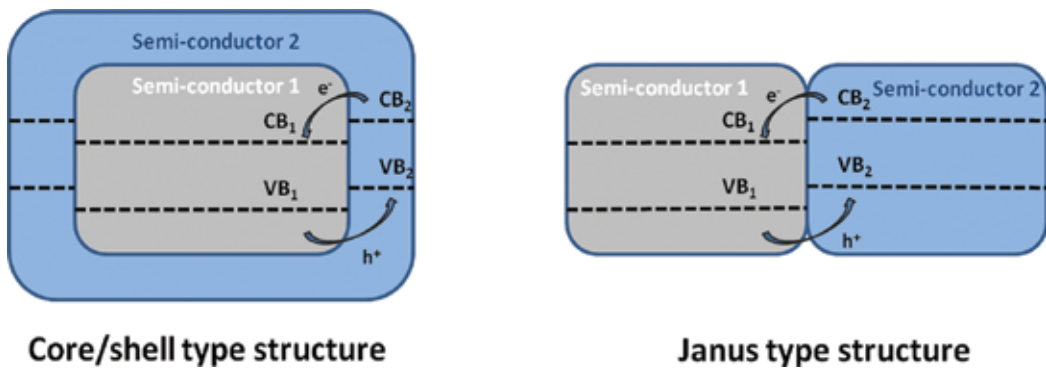
Figure 8. Representation of a core/shell (on the left) and a Janus type (on the right) heterostructure.

Two morphologies can be distinguished for the semiconductor/semiconductor heterostructures: the core/shell structure, and the Janus type structure (**Figure 8**). In a core/shell structure, one semiconductor is completely covered by the second one. Thus, only the charge carriers injected in the external material can undergo oxidative or reductive reactions at the surface.

In the Janus type structure, both materials are exposed to the environment. In this case, the two charge carriers e$^-$ and h$^+$ are potentially available for oxidative or reductive reactions. Consequently, the Janus type morphology is the most studied in photocatalysis, as both e$^-$ and h$^+$ can potentially be exploited. Therefore we focus on Janus type heterostructures.

Many different metal-oxide or metal-sulfide semiconductors are known to form a type-II heterostructure when coupled. Among them, ZnO- and TiO$_2$-based heterostructures are still strongly investigated: ZnO/SnO$_2$ [35–38], TiO$_2$/SnO$_2$ [39–41], TiO$_2$/ZnO [42–45], TiO$_2$/WO$_3$ [46], or ZnO/CuS [47]. ZnO and TiO$_2$ are two metal-oxides with similar properties. They both have a band gap around 3.2 eV, with light absorption properties in the near ultraviolet region. In addition, they have similar conduction and valence bands position. SnO$_2$ is a material with a much higher band gap, around 3.7 eV, absorbing far in the ultraviolet range, but the position of its conduction and valence bands relatively to the ZnO or TiO$_2$ ones makes it a suitable material for the development of a heterostructure with ZnO or TiO$_2$.

In the literature, different Janus type ZnO/SnO$_2$ and TiO$_2$/SnO$_2$ heterostructures have already been reported. Uddin *et al.* [36] have performed the synthesis of SnO$_2$/ZnO nano-particles forming a contact type heterostructure in liquid phase by precipitation/hydrothermal process. They have shown that the heterostructure allowed a two-time faster photocatalytic degradation of a methylene blue solution (10 mg.l^{-1}) under a UV light source (365 nm–125 W) compared to ZnO only. The same behavior has been observed by Cun *et al.* [37] with ZnO/SnO$_2$ nanoparticles prepared also by a co-precipitation process in liquid phase. They highlighted a decolourization speed of a methyl orange solution 100% faster with ZnO/SnO$_2$ nanoparticles instead of ZnO nano-particles only. It is worth mentioning that the specific surface area of both materials (ZnO/SnO$_2$ and ZnO) used was in the same range and cannot explain such a difference in the photocatalytic performance. In their paper, De Mendonça*et al.* [41] synthesized TiO$_2$/SnO$_2$ nano-particles using two different liquid phase techniques: a hydrolytic sol-gel process and a polymeric process. The photocatalytic performance of those nano-particles, tested on Rhodamine B, was found to be 50% faster than commercial TiO$_2$ nano-particles.

ZnO/SnO$_2$ heterostructures composed of ZnO nanowires functionalized by SnO$_2$ particles can be synthesized using gas phase processes on flat surfaces or in porous membranes. Huang *et al.* [38] realized the growth of ZnO nanowires on silicon wafers, using a CVD process at high temperature (600°C) with Zn powder as zinc source and air as oxidant. The growth of SnO$_2$ nano-particles on top of the ZnO was performed also via a CVD process at high temperature (800°C) using SnO powder as tin source. The synthesized materials are presented on **Figure 9a**. The resulting photocatalytic performance showed a twofold improvement compared to ZnO only. Rogé *et al.* proposed an alternative method for the growth of ZnO nanowires covered by SnO$_2$ nano-particles at lower temperatures. ZnO nano-wires were synthesized by a solvothermal process below 90°C in a macro-porous glass fiber membrane (**Figure 9b**). A modified ALD process allowed the growth of SnO$_2$ nano-particles on the ZnO nano-wires at temperatures around 300°C.
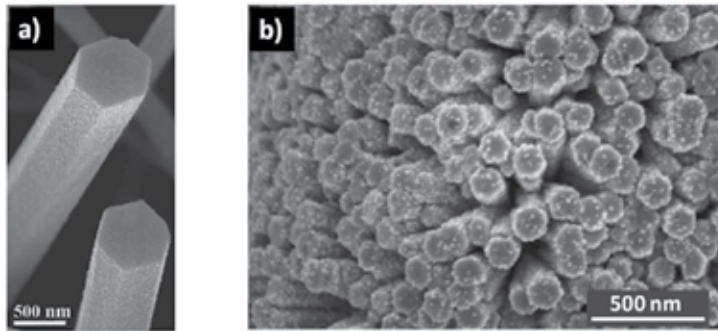
Figure 9. (a) SEM picture of ZnO/SnO$_2$ nano-wires/nano-particles grown by CVD. The picture was taken from Huang *et al*. [26]. (b) ZnO/SnO$_2$ nano-wires/nano-particles grown by hydrothermal/modified ALD processes.

Heterostructures of SnO$_2$/ZnO have been realized by Zhu *et al*. [48] using electrospun SnO$_2$ fibers that have been functionalized by ZnO nano-rods (**Figure 10a**) or nano-sheets (**Figure 10b**). The degradation rate of those ZnO decorated SnO$_2$ fibers is more than 100% faster than bare ZnO. If the authors did not analyze the SnO$_2$/ZnO heterostructure by XPS, they proved the charge separation in the ZnO/SnO$_2$ heterostructure by photo-current measurements. As depicted in **Figure 10c**, the photo-current produced by the ZnO/SnO$_2$ materials (named SZ-10/ZnO NRs and SZ-10/ZnO NSs) when illuminated under a simulated sunlight, shows a threefold intensity improvement compared to the bare ZnO.
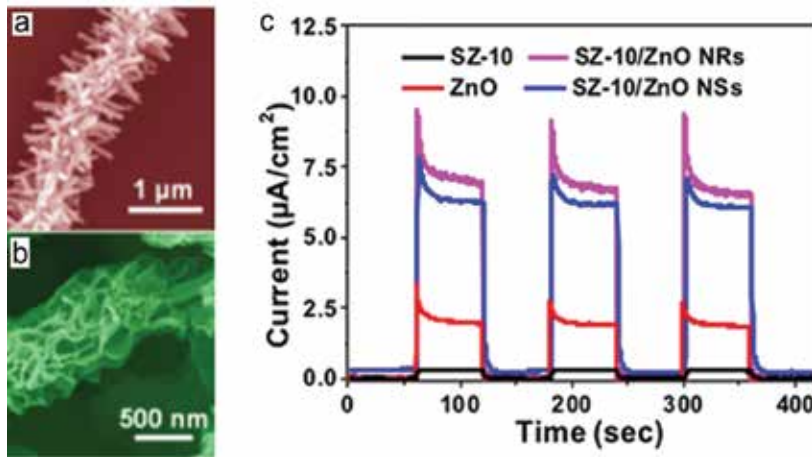
Figure 10. (a) SEM picture of a SnO$_2$ fiber decorated with ZnO nano-rods (SZ-10/ZnO NRs). (b) SEM picture of a SnO$_2$ fiber decorated with ZnO nano-sheets (SZ-10/ZnO NSs). (c) Photo-current responses of SZ-10/ZnO NRs, SZ-10/ZnO NSs and bare ZnO. Results copied from Zhu *et al*. [36].

This photo-current improvement results from the heterostructure formation which promotes an efficient separation of photo-excited electron-hole pairs and thus enhances the photocatalytic performance.

4. Plasmonics for visible light photocatalysis

4.1. How plasmonics work

Plasmonics deal with the core idea of a coherent oscillation of electrons in metals induced by the interaction of an incident electromagnetic radiation with metallic nanostructures.

A clear explanation of this phenomenon was suggested by Jones *et al.* [49]. The authors proposed an analogy with a mechanical oscillator. The displacement of a simple harmonic oscillator from equilibrium results into a continuous sinusoidal motion. An external periodical force applied to the system with an identical frequency ("in phase") fulfills the resonance conditions and can therefore increase the amplitude of the harmonic oscillator. Similarly, in plasmonics, the incident electromagnetic light acts as the external force on the delocalized electrons (electrons cloud) of the conduction band and causes their enhanced displacement. Coulombic forces induced between the delocalized electrons cloud and the nucleus of the metal atoms are opposed to this displacement. The plasmon resonance corresponds to the conditions where the resultant of those two opposite phenomenon leads to the collective oscillation of the delocalized electrons (**Figure 11**).

In the case of metal nanoparticles, where the size is significantly lower than the light wavelength, the resulting collective oscillation of electrons is called *localized surface plasmon resonance (LSPR)*. The oscillation frequency mainly depends on the electrons properties, such as their density and effective mass, and also on the nanoparticles size, shape, and charge distribution [50, 51]. Among the numerous metals showing the LSPR, the noble metals are gaining popularity for their stability at the nanometer scale and the strong LSPR in the visible region of the sun spectrum.
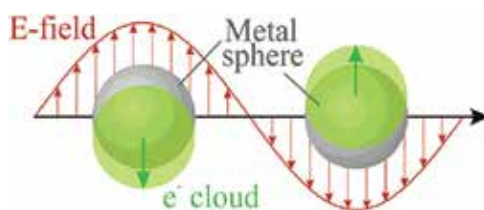
Figure 11. Schematic illustration of surface plasmon resonance. (reprinted with permission from ref. [50]).

The application of plasmonics in metal oxide photocatalysis is particularly interesting since the charge recombination, that reduces the degradation efficiency, and the narrowness of the absorbed sun irradiation (near UV range) is limited.

In the UV-visible range, nanoparticles act as small light concentrators and result in the increase of the electromagnetic field on the semiconductor surface due to the LSPR. Earlier publications, reporting on the enhancement of the photocatalytic activity using plasmonic nanoparticles coupled with semiconductor materials, focused on the ability of nanoparticles to promote the carriers separation. The proposed mechanism considers the interface between the photocata-

lytic semiconductor and the metallic nanoparticle as a Schottky barrier [52–57]. Under a visible range irradiation, the electrons could be injected from the photo-excited metal to the semiconductor (**Figure 12a**). As an example described in **Figure 12a**, this electron transfer modifies the gold into an oxidized state. According to a mechanism proposed by Tian and Tatsuma [54], the oxidized gold could be immediately reduced by an electron donor present in the solution. Furube *et al.* [55] demonstrate in 2007, by femtosecond IR probe, that this electron injection occurs within few hundreds femtoseconds.
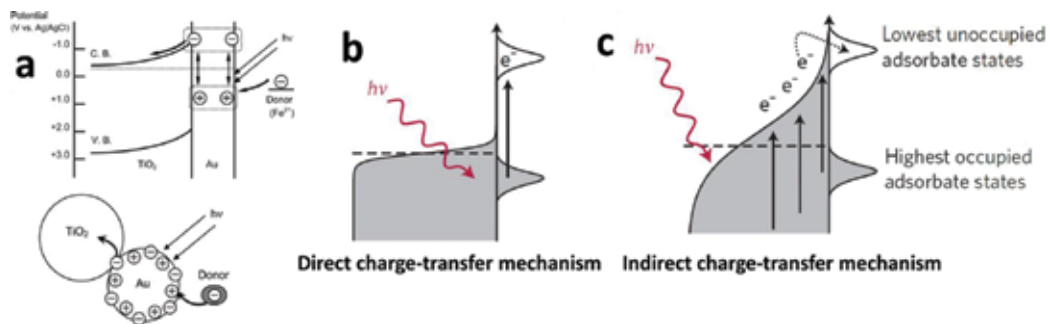
Figure 12. (a, b) Possible mechanism of charge separation (direct charge transfer mechanism). (c) Indirect charge-transfer mechanism (reprinted with permission from refs. [54, 58]).

However, the complete understanding of mechanisms leading to this enhancement is not fully achieved. The mechanism related to the *direct charge injection* found an important support through theoretical and experimental investigations [58–60]. Linic *et al.* consider that the direct electron injection occurs via the direct excitation of an electron to an unoccupied adsorbate state of the semiconductor without the formation of an excited electron distribution in the metal (**Figure 12a** and **b**). However, the authors propose to take into consideration another plausible mechanism – *indirect charge transfer* (**Figure 12c**). The indirect charge-transfer mechanism considers that energetic charge-carriers are formed under the influence of the electric field. The excited charge-carriers interact with orbitals close to Fermi level and the plasmon relaxation results in an electron distribution above the metal Fermi level [58, 61].

Another important fact to be taken into account is the effect of local heating on the plasmonic nanoparticles. This phenomenon happens because of the local electromagnetic field induced by the plasmonic phenomena. This effect has already been used in photothermal therapy in medicine [62] and in photoassisted synthesis [63, 64]. In this evidence, Fasciani and co-workers [65] have estimated that the temperature raising on the surface of a gold nanoparticle exposed to a laser pulse (8 ns at 532 nm, 50 mJ/pulse) could achieve $500 \pm 100°C$.

The literature overview does not provide a clear mechanism of how exactly LSPR effect activates the wide band gap semiconductor in the visible range. However, the main adopted mechanism is the direct carriers transfer from the exited metal nanoparticle into the semiconductor [51, 52, 54, 55, 58, 66–68].

Various combinations of assembly of the conventional photocatalysts material (TiO$_2$, ZnO, CeO, Fe$_2$O$_3$, CdS, etc.) with plasmonic nanoparticles, typically silver, gold, platinum, or mixed alloys are currently reflected in the literature [69].

4.2. Architecture of plasmonic systems

The decoration of the photocatalytic surface by plasmonic nanoparticles shows an enhancement of the photocatalytic activity. Yet, the coverage by more than 15% of metal nanoparticles inhibits the plasmonic enhancement by the reduction of the specific surface area of the semiconductor [57, 70, 71].
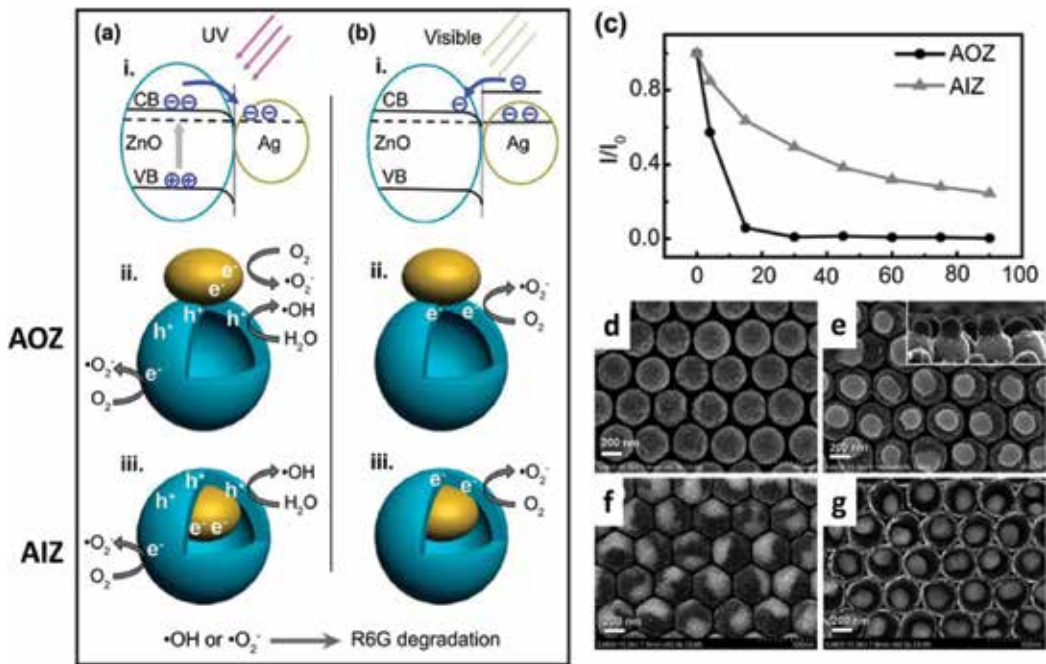
Figure 13. Energy band gap and photocatalytic mechanisms of asymmetric arrays Ag on top of ZnO nanospheres (AOZ) and Ag inside ZnO (AIZ) under (a) UV light and (b) visible light. (c) Photocatalytic degradation plot; SEM images for (d) ZnO nanospheres, (e) AOZ arrays, (f) top view AIZ arrays, and (g) AIZ arrays internal structure (reprinted with permission from ref. [72]).

An important number of publications investigate the possible architectures which would allow getting maximum LSPR effect without depleting the photocatalytic activity. Zang *et al.* [72] have demonstrated that the architecture plays an important role. The authors realized two different asymmetric composite arrays of hollow ZnO nanospheres and silver nanoparticles placed on top and inside ZnO spheres (**Figure 13**). ZnO spheres were supported on Silicon substrates. In both cases the local enhancement of the field has a double impact: improvement of light adsorption on the semiconductor material and charge separation. Comparing the photocatalytic activity of both configurations, placing a nanoparticle inside a nanosphere

reduces the degradation rate. The comparison of asymmetric assembly architectures was also demonstrated by Seh *et al*. [73] using different types of Au-TiO$_2$ nanostructures assembly, such as Janus (**Figure 14a**) and core–shell (**Figure 14b**).
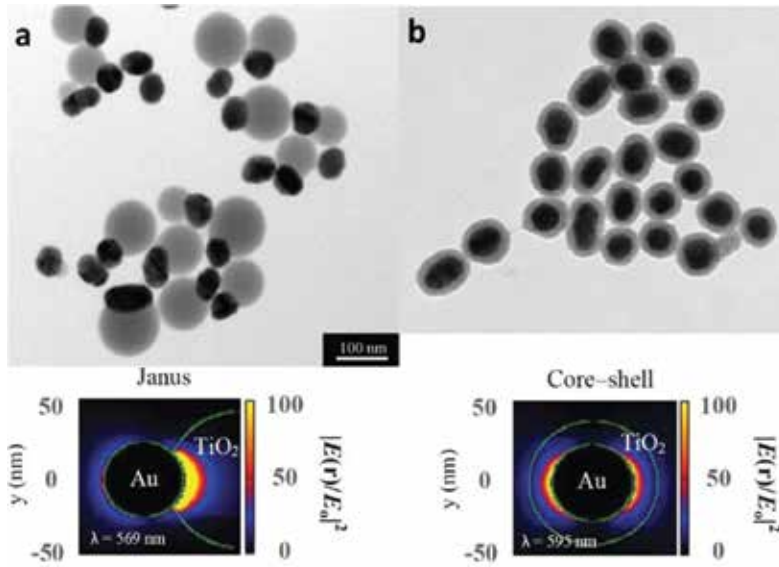
Figure 14. Illustration for Janus (a) and core-shell (b) Au 50 nm-TiO$_2$ nanostructures and their plasmonic near-field maps obtained by DDA simulation (reprinted with permission from ref. [73]).

Discrete dipole approximation (DDA) calculations and experimental investigations on both type of TiO$_2$ assembly with 50 nm gold particles showed an enhancement of the electric near-field intensity due to the high refractive index of TiO$_2$ on the materials interface. In Janus structures the plasmonic near-field is localized on one side of gold nanoparticle (non-symmetric distribution) whereas in core-shell configuration, it provides a symmetric distribution. However, the power of absorbed light on non-symmetric Janus nanostructures was 1.75 times larger than the one of core-shell. It results in an increase of the efficiency of photocatalytic hydrogen production by 1.7 times compared to the core/shell structure and confirms that Janus configuration has more benefits for the photocatalytic enhancement. Actually, in Janus type assembly, the plasmonic near field is localized close to the Au-TiO$_2$ interface and the carrier's generation occurs closer to the TiO$_2$ surface. Therefore, the carrier's recombination is decreased and the carrier injection into the semiconductor is improved. These results confirm that plasmonic nanoparticles on top of the semiconductor material, instead of inside, result in significant improvement of the photocatalytic activity. A different type of core-shell structures was designed by Eom and co-workers [74]. A periodic array of open core-shell Ag-TiO$_2$ nanostructures was realized using nanoimprint lithography (NIL) and UV-sensitive resin. The silver nanowires were formed by thermal evaporation from Ag-target on the patterned substrate and following TiO$_2$ coating was electrodeposited. This type of core-shell structures also demonstrated an important enhancement of the photocatalytic activity in UV and visible

ranges. The degradation of Methylene blue under visible light evidences 9 times improvement of the photocatalytic efficiency when compared to simple TiO$_2$ film.

Studies investigate low cost metals for plasmonic applications such as aluminum. According to finite-difference time domain (FDTD) simulation Al/CdS core-shell system realized by Duan and Xuan. [75], demonstrate a significant enhancement of optical absorption in the visible range. Authors also conclude on the importance of the core/shell ratio (radius ratio) which should be equal to 30/40 nm to achieve the strongest absorption.

Recently, Hao and co-authors [76] reported the enhancement of light absorption on Al/TiO$_2$ structures due to the LSPR effect on aluminum nanostructures. The aluminum nano-void arrays were fabricated by the anodizing process. Typically, the fabrication process of nano-voids includes two steps: an anodization followed by a chemical etching of the grown alumina. The UV-visible spectra of nano-voids demonstrate the presence of the SPR which could be tuned by the size of the aluminum nano-voids. However, the response was restricted to the UV range only (**Figure 15**).
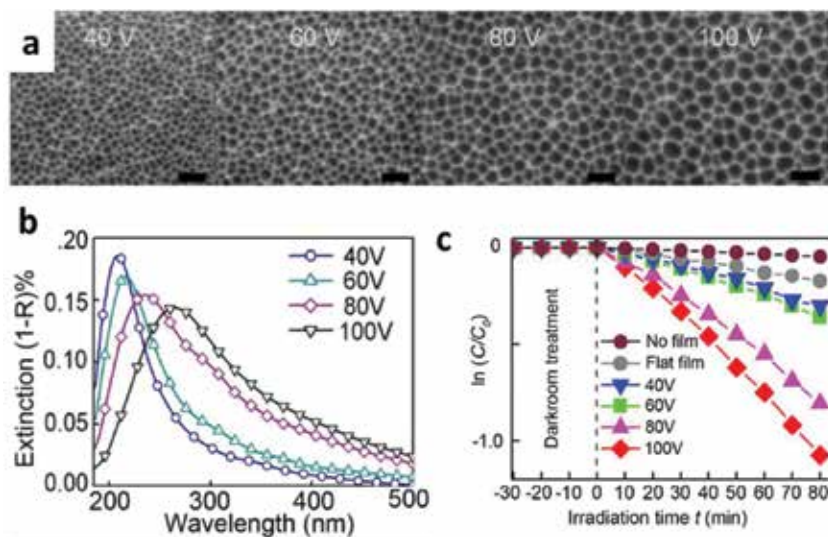
Figure 15. (a) SEM images of the aluminum foils with nano-void arrays (scale bar being 500 nm). (b) UV-visible spectra of nano-voids. (c) Photocatalytic degradation of Rhodamine B under UV-visible irradiation (reprinted with permission from ref. [76]).

Although aluminum nano-voids show the plasmonic enhancement of the light absorption, the samples with TiO$_2$ coating do not manifest significant improvement of the photocatalytic activity in the visible range. However, an increase of the degradation rate in the UV range could still be observed by plasmonic effect [76]**.**

Another interesting approach that is claimed to improve the light absorption in the semiconductors for photovoltaic or photocatalytic application is the assembly of plasmonic nanoparticles into a periodic structure [77]. The well-controlled nanoparticles deposition with precise

size and spacing control can induce advantageous optical effect for the light management. For instance, placing nanoparticles in a close proximity (1 nm) has an important effect on their scattering performance and their near-field due to the local coupling effect [78]. If this inter-particles distance could be well controlled, that would offer the possibility of tailoring the light scattering and the light absorption on the semiconductor (**Figure 16**) [77]. This promising approach attracts a strong interest for the photovoltaic application but could be also success-fully implemented for the photocatalytic devices.
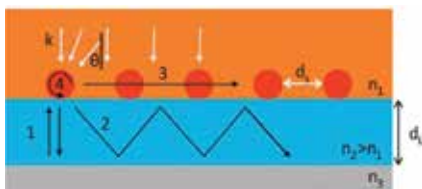
Figure 16. Representation of four common modes for increasing of light absorption: Fabry–Perot resonance (1), guided resonance (2), grating coupling (3), and Whispering gallery modes (4) (reprinted with permission from ref. [77]).

5. Overview on the emerging new materials and concepts

5.1. New materials to design photocatalysts

New emerging materials, strategies, and/or architectures based on metal-oxides allows to push forward the photocatalytic performances. Ideally, those materials and systems should be durable and eco-friendly. As already largely well described in the literature [79–82], several steps need to take place in a photocatalytic phenomenon: the excitation of the photocatalyst that leads to electron-hole pair creation, their migration toward the surface, the adsorption of the reactant, and finally the redox reactions. The enhancement of the photocatalytic efficiency depends on how the photocatalytic materials or architectures can promote at least one of these parameters without deteriorating the others. As the abundance of ideas in the scientific community is high, we could certainly not claim to be exhaustive, but we believe that the reader will find here the most important matter to have a fairly large view on what is currently set about the improvement of the efficiency of photocatalytic systems.

5.1.1. Binary oxides

Few binary metal oxides have been reported to be active in water splitting [83]. Cerium oxide is a fairly recent binary metal oxide material that has been shown to have a water splitting activity when doped by Strontium [84] or more recently as oriented hexagonal nanorods on Titanium substrates with a Na_2S-Na_2SO_3 sacrificial agent [85]. This last material had also been successfully used for the degradation of pollutants. Tang *et al.* [86] demonstrated a photocatalytic degradation of aromatic benzenes by CeO_2 nanotubes in air. The cerium oxides

nanomaterials were grown from hydrothermal synthesis of Ce(OH)CO$_3$ precursors with alkali solution in an aqueous phase.

In a recent review, Miseki *et al.* [83] reported others recent materials that present a water splitting activity : binary oxides like Ga$_2$O$_3$ doped with Zinc and coupled to a cocatalyts, mesostructured crystalline Ta$_2$O$_5$ with a 3% cocatalyst of NiO$_x$ and TiS$_2$.

5.1.2. Ternary and quaternary metal oxides

Most of metal oxides that exhibit an activity in water splitting are ternary or quaternary metal oxides. Boosted by the societal interest of the hydrogen fuel cell production, most of the novel photocatalytic materials have been applied to water splitting [9]. Among them, perovskite materials occupy a place of choice. Recently, metal halide perovskites for photovoltaics have emerged as a contender of the leading photovoltaic materials. Indeed their power to conversion efficiency had grown from 3% to 20% in four years [87]. Those impressive performances raise interests to scrutinize if such performance could be reached in the photocatalytic field.

Perovskite minerals were originally associated to CaTiO$_3$ in homage to Lev Perowski (1792–1856) but are now more generally designating materials with the general chemical formula ABX$_3$ (where A is a rare or alkaline earth metal, B is a transition metal, and X the oxygen generally) and the kind of crystallographic structure illustrated in **Figure 17**.
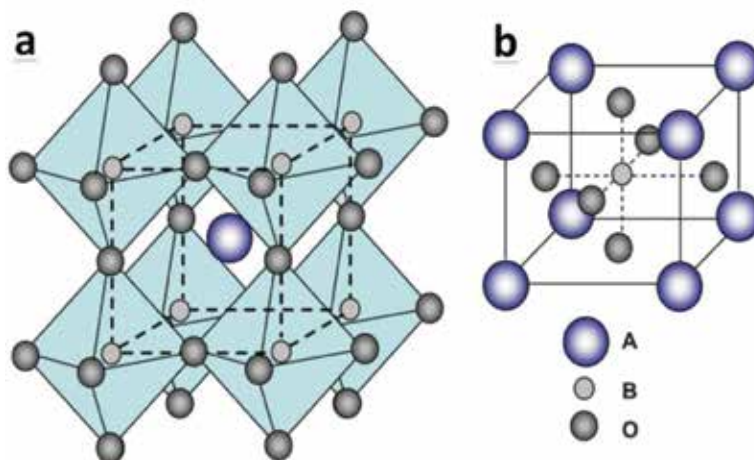
Figure 17. Crystallographic structure of a perovskite lattice. (a) BO$_6$ octahedral view with A site surrounded by 12 co-ordinated interstices. (b) Cubic lattice with B-site cation at the center of the cell (reprinted with permission from ref. [88]).

The most studied compounds revolve around the periodical elements Ta, Ti, Nb, Sn, V, Fe as B sites which found photocatalytic applications related to both hydrogen fuel production or degradation of pollutants. Some interesting results have already been reported: Grewe *et al.* [89] for example recently showed the simple hydrothermal synthesis of NaTaO$_3$ nanoparticles leading to the hydrogen production rate of 94 µmol/h. Yin *et al.* [90] prepared also via hydro-

thermal synthesis octahedral shaped $PbTiO_3$ nanocrystals with well define (111) facets that exhibit interesting performances related to the degradation of Methylene blue. These results have never been reported in conventional perovskite systems (100% degradation of Methylene blue 10^{-5} M after 35 min of irradiation). Perovskite materials present several advantages reviewed by Tanaka and Misono [91]: a large variety of compositions and chemical elements can be used while keeping the basic structure and their valency, stoichiometry, and vacancy concentration can be varied widely. Finally, a lot of information on their physical and solid state chemical properties has been accumulated. Strategies to boost their photocatalytic performance consist frequently in A, B, or X site doping (N_3^- doping of oxygen sites to oxynitrides for example) but also in the development of new synthesis methods or the improvement of the current ones [92].

Jingshan *et al*. [93] unveiled the first water-splitting cell with 12.3% efficiency based on $CH_3NH_3PbI_3$ (see **Figure 18**) and opened the route to the use of such metal halide perovskites in photocatalysis.
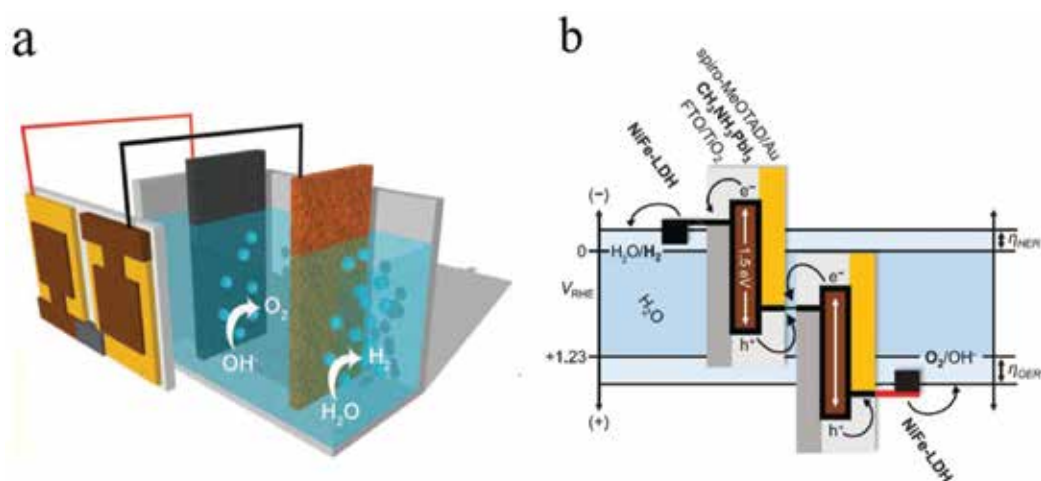
Figure 18. Jinshan water photolysis device. (a) 3D representation. (b) Schematic including the materials used for the cocatalyts and the light sensitive parts as well as the energy levels of water oxidation and reduction (reprinted with permission from ref. [93]).

Pyrochlore metal oxides with the general chemical formula $A_2B_2O_7$ are certainly less known than perovskite but are also investigated [82]. The angle B-O-B close to 180° in those structures is reported to facilitate the migration of the electron-hole pairs and is a good illustration of how the crystallographic structure of a photocatalyst can impact the photocatalytic degradation processes. Vanadium derived compounds based on the general chemical formula $M_3V_2O_8$ were synthetized in 2005 and more recently MVO_4 ones were reported to be active in the degradation of dye waste water under visible light irradiation [94]. Molybdenum or Tungsten derived compounds like $Bi_2Mo_2O_9$, $ZrMo_2O_8$, $NiMoO_4$, Bi_2WO_6, and Bi_2WO_6 are also

known as photocatalysts applied to the degradation of pollutants (Methyl Orange, Rhodamine B, Malachite green).

Finally the layered perovskites, for which photocatalytic activity was already reported in the 90s, continue to be under investigation and give promising results [95]. Aurivillius Layered Perovskites, Bi$_{5-x}$La$_x$Ti$_3$FeO$_{15}$ (x = 1, 2) were demonstrated to be particularly active for the degradation of Rhodamine B (RhB) under sun-light irradiation in mild acidic medium. Supramolecular structures like MOFs (metal organic frameworks) or polyoxometallates have also recently been reviewed as they can exhibit some interesting photocatalytic properties [9].

Generally speaking, the chemical construction of a potentially efficient photocatalyst for water splitting draws from the Mendeleev table metal cations with a d^0 or d^{10} electronic configuration. They are involved in the construction of the crystal and energy structure. Alkali, alkaline earth, and some lanthanide ions do not play a role directly in the band formation but simply contribute to the construction of the crystal structure. **Figure 19** summarizes the key chemical elements that can play a role to design new photocatalytic materials.
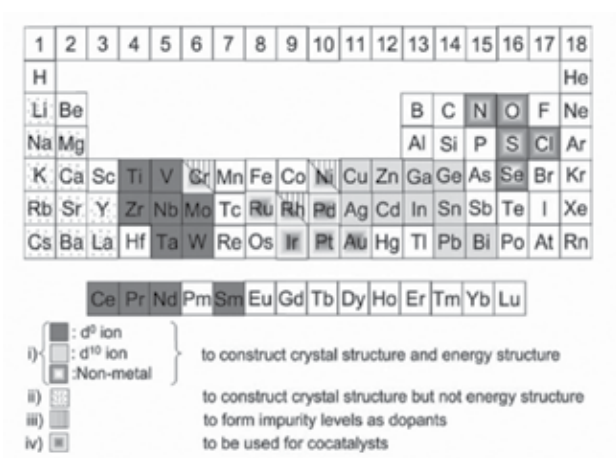
Figure 19. Chemical elements from the Mendeleev table to construct a photocatalyst (reprinted with permission from ref. [83]).

5.2. New strategies to design photocatalysts

The example about new halides perovskites illustrates how photovoltaics research can inspire the one conducted in photocatalysis. The recent 3D TiO$_2$ anatase nanostructures based solar cell developed by Wu *et al.* [96] which reach a power conversion efficiency of 9.09% (to be compared to the 5% one for the same material as simple nanowires of same thickness), could be an interesting candidate for photocatalytic applications (**Figure 20**). In this work, the authors start from TiO$_2$ anatase nanowires grown by hydrothermal methods. Acid thermal reaction was then used to produce on the nanowires, TiO$_2$ nanosheets on which nanorods were finally grown by a last hydrothermal reaction step.
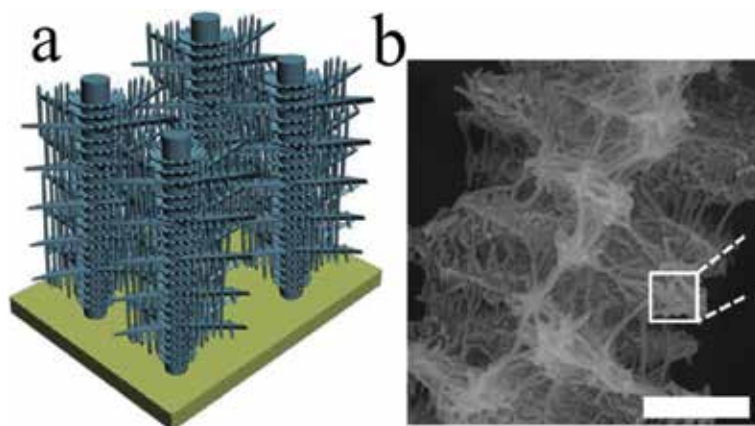
Figure 20. TiO$_2$ hyperbranched nanostructures. (a) 3D representation, (b) SEM image of the interlaced nanowires, nanosheets, and nanorods (scale bar: 500 nm) (reprinted with permission from ref. [96]).

Li *et al.* [97] recently reported the fabrication of TiO$_2$ nanoparticles with sub-10 nm dimensions that exhibit visible light driven photocatalytic hydrogen production. With a 1% platinum cocatalyst deposited on nanoparticles, the photocatalytic hydrogen production performance was 932 μmol.h^{-1}.g^{-1} under visible light (400 nm ‹ λ ‹ 780 nm).

Ultrathin 2D nanomaterials, which are comparable to graphene type materials with sheet-like structures find more and more applications including photocatalysis [98]. Recently Zhou *et al.* [99] successfully separated 2D ultrathin Bi$_2$WO$_6$ monolayers from the same nanocrystal and showed excellent photodegradation of Rhodamine B under visible light with a separation of holes and electrons on two different active sites located at two different layers. An excellent hydrogen production activity under visible light is also reported for this new kind of horizontally designed heterostructures. Similarly, 2D nanosheets of the layered perovskite, Ba$_5$Nb$_4$O$_{15}$, were synthesized by a hydrothermal route. The nanosheets showed much enhanced photocatalytic activity compared to thick nanosheets for the production of H$_2$ from water splitting under UV light illumination. The enhanced activity is predominantly attributed to the larger surface area, higher optical absorption, and charge separation ability of the 2D nanosheet.

6. Conclusion

In this chapter, we highlighted different strategies to improve the photocatalytic performance of TiO$_2$- and ZnO-based nanomaterials. We pointed out the benefits of photocatalytic filtration membranes functionalized with TiO$_2$ and ZnO nanostructures. Due to their high specific surface area and their filtration properties, photocatalytic membranes allow the filtration and the degradation of organic pollutants. In some cases, especially after dip coating synthesis processes, the stability of nanomaterials at the surface of the membranes is not sufficient, resulting in a leakage of the photocatalyst in the environment. In the second section, we

discussed the strategies to improve the photocatalytic properties of ZnO and TiO$_2$ photocatalysts by engineering heterostructures with other metal-oxides, like SnO$_2$. We showed that TiO$_2$/SnO$_2$ and ZnO/SnO$_2$ type-II heterostructures lead to efficient charge carriers (e$^-$ and h$^+$) separation toward each electrode of the heterojunction, resulting in a longer lifetime of both carriers. As a result, improved photocatalytic performance is observed. In the third section, we present a strategy to activate TiO$_2$ and ZnO photocatalysts in the visible range of the sunlight spectrum, using the plasmonic effect in metal-oxides materials decorated with metallic nanoparticles. We describe different mechanisms explaining the impact of the plasmonic effect on the photocatalytic activity in the visible range. In a last section, new promising nanomaterials and nanoarchitectures based on binary, ternary, and quaternary metal-oxides have been reviewed.

Author details

Olga M. Ishchenko, Vincent Rogé, Guillaume Lamblin[*] and Damien Lenoble

*Address all correspondence to: Guillaume.lamblin@list.lu

Luxemburg Institute of Science and Technology, Esch-Sur-Alzette, Luxemburg

References

[1] Pasternak S, Paz Y. On the similarity and dissimilarity between photocatalytic water splitting and photocatalytic degradation of pollutants. ChemPhysChem. 2013;14(10): 2059–70.

[2] Siplast. Available from: http://www.siplast.fr/profil/maitres-ouvrage-maitres-oeuvre/nox-activ-video.

[3] Calcia. Available from: http://fr.i-nova.net/fr/content?articleId=198660.

[4] Saint-Gobain. Available from: http://fr.saint-gobain-glass.com/product/937/sgg-biocleane.

[5] Auro. Available from: http://www.auro.fr/produits_3.php?sub_id=26.

[6] Gallus M, Akylas V, Barmpas F, Beeldens A, Boonen E, Boréave A, et al. Photocatalytic de-pollution in the Leopold II tunnel in Brussels: NOx abatement results. Build Environ. 2015;84(2):125–33.

[7] Guo L. Advances in solar hydrogen technologies. SPIE Newsroom. 2011;10–2. Available from: http://www.spie.org/x48082.xml.

[8] Sowarla GmbH. Available from: http://www.sowarla.de/demonstration-plant.html.

[9]   Hernández-Alonso MD, Fresno F, Suárez S, Coronado JM. Development of alternative photocatalysts to TiO2: Challenges and opportunities. Energy Environ Sci. 2009;2(12): 1231.

[10] Rogé V., PhD Thesis, Etude, Fabrication et Caractérisation de nanostructures catalytiques de type ZnO/SnO2 intégrées à des membranes modèles pour la dépollution de l'eau. Université de Strasbourg. 2015.

[11] Bickley RI. Photo-induced reactivity at oxide surfaces. M W Roberts, J M Thomas editors. Chemical Physics of Solid and their Surfaces. Royal Society of Chemistry 1977, Vol. 7, pp. 118–56.

[12] Formenti M, Juillet F, Meriaudeau P, Teichner SJ, Vergnon P. Preparation in a hydrogen-oxygen flame of ultrafine metal oxide particles. Aerosols Atmos Chem. 1972;1:79-89.

[13] Francois J, Stanislas Teichner MF. Process for the photocatalytic oxidation of hydrocarbons into aldehydes and ketones. United State Patent n°3781194, 1973. pp. 1–7.

[14] Belokoneva GI, Demchenko SS, Red'ko LA, Kachan AA, Chervyatsova LL. Effect of some fillers on the photo- and thermal decomposition of polyethylene. Plast Massy. 1975;(1):57–8.

[15] Bedja I, Hotchandani S, Kamat PV. Photoelectrochemistry of quantized WO3 colloids: Electron storage electrochromic and photoelectrochromic effects. J Phys Chem. 1993;97:11064–70.

[16] Sato S. Photocatalytic activities of indium oxide powder prepared from indium hydroxide. J Photochem Photobiol A Chem. 1988;45(3):361–7.

[17] Cui H, Dwight K, Soled S, Wold A. Surface acidity and photocatalytic activity of Nb2O5/TiO2 photocatalysts. J Sol Sta Chem. 1995; 115:187–91.

[18] Mozia S. Photocatalytic membrane reactors (PMRs) in water and wastewater treatment: A review. Sep Purif Technol. Elsevier B.V. 2010;73(2):71–91.

[19] Buscio V, Brosillon S, Mendret J, Crespi M, Gutiérrez-Bouzán C. Photocatalytic membrane reactor for the removal of CI disperse Red 73. Materials. 2015;8(6):3633–47.

[20] Kakuta N, White JM, Campion A, Bard AJ, Fox MA, Webber SE. Surface analysis of semiconductor incorporated polymer systems. 1. Nafion and cadmium sulfide-Nafion. J Phys Chem. 1985;89:48–52.

[21] Tsydenov DE, Parmon VN, Vorontsov AV. Toward the design of asymmetric photocatalytic membranes for hydrogen production: Preparation of TiO2-based membranes and their properties. Int J Hydrogen Energy. 2012;37(15):11046–60.

[22] Hong HJ, Sarkar SK, Lee BT. Formation of TiO2 nano fibers on a micro-channeled Al2O3-ZrO2/TiO2 porous composite membrane for photocatalytic filtration. J Eur Ceram Soc. 2012;32(3):657–63.

[23] Rogé V, Bahlawane N, Lamblin G, Fechete I, Garin F, Dinia A, et al. Improvement of the photocatalytic degradation property of ZnO atomic layer deposition thin films: Interplay between film properties and functional performances. J Mater Chem A. 2015;3:11453–61.

[24] Rogé V, Georgantzopoulou A, Mehennaoui K. Tailoring the optical properties of ZnO nano-layers and their effect on in vitro biocompatibility. RSC Adv. 2015;97635–47.

[25] Lee SM, Grass G, Kim GM, Dresbach, Zhang,Gösele U, Knez M. Low-temperature ZnO atomic layer deposition on biotemplates: Flexible photocatalytic ZnO structures from eggshell membranes. Phys Chem Chem Phys. 2009;11(19):3607.

[26] Kim SH, Kwak SY, Sohn BH, Park TH. Design of TiO2 nanoparticle self-assembled aromatic polyamide thin-film-composite (TFC) membrane as an approach to solve biofouling problem. J Memb Sci. 2003;211(1):157–65.

[27] Rahimpour A, Madaeni SS, Taheri AH, Mansourpanah Y. Coupling TiO2 nanoparticles with UV irradiation for modification of polyethersulfone ultrafiltration membranes. J Memb Sci. 2008;313(1–2):158–69.

[28] Mansourpanah Y, Madaeni SS, Rahimpour A, Farhadian A, Taheri AH. Formation of appropriate sites on nanofiltration membrane surface for binding TiO2 photo-catalyst: Performance, characterization and fouling-resistant capability. J Memb Sci. 2009;330(1–2):297–306.

[29] Rahimpour A, Jahanshahi M, Rajaeian B, Rahimnejad M. TiO2 entrapped nano-composite PVDF/SPES membranes: Preparation, characterization, antifouling and antibacterial properties. Desalination. 2011;278(1–3):343–53.

[30] Leong S, Razmjou A, Wang K, Hapgood K, Zhang X, Wang H. TiO2 based photocata-lytic membranes: A review. J Memb Sci. 2014;472:167–84.

[31] Wang H, Zhang L, Chen Z, Hu J, Li S, Wang Z, et al. Semiconductor heterojunction photocatalysts: design, construction, and photocatalytic performances. Chem Soc Rev. 2014;43(15):5234–44.

[32] Dutta SK, Mehetor SK, Pradhan N. Metal semiconductor heterostructures for photo-catalytic conversion of light energy. J Phys Chem Lett. 2015;6(6):936–44.

[33] Reynal A, Willkomm J, Muresan NM, Lakadamyali F, Planells M, Reisner E, et al. Distance dependent charge separation and recombination in semiconductor/molecular catalyst systems for water splitting. Chem Commun. Royal Society of Chemistry. 2014;50:12768–71.

[34] Berr MJ, Wagner P, Fischbach S, Vaneski A, Schneider J, Susha AS, et al. Hole scavenger redox potentials determine quantum efficiency and stability of Pt-decorated CdS nanorods for photocatalytic hydrogen generation. Appl Phys Lett. 2012;100(22):2014–7.

[35] Wang C, Wang X, Xu BQ, Zhao J, Mai B, Peng P, et al. Enhanced photocatalytic performance of nanosized coupled ZnO/SnO2 photocatalysts for methyl orange degradation. J Photochem Photobiol A Chem. 2004;168(1–2):47–52.

[36] Uddin T, Nicolas Y, Toupance T, Servant L, Mu MM, Kleebe H, et al. Nanostructured SnO2−ZnO heterojunction photocatalysts showing enhanced photocatalytic activity for the degradation of organic dyes. Inorg Chem. 2012;51(14):7764–73.

[37] Cun W, Jincai Z, Xinming W, Bixian M, Guoying S, Ping'an P, et al. Preparation, characterization and photocatalytic activity of nano-sized ZnO/SnO2 coupled photocatalysts. Appl Catal B Environ. 2002;39(3):269–79.

[38] Huang X, Shang L, Chen S, Xia J, Qi X, Wang X, et al. Type-II ZnO nanorod-SnO2 nanoparticle heterostructures: Characterization of structural, optical and photocatalytic properties. Nanoscale. 2013;5:3828–33.

[39] Liu Z, Sun DD, Guo P, Leckie JO. An efficient bicomponent TiO2/SnO2 nanofiber photocatalyst fabricated by electrospinning with a side-by-side dual spinneret method. Nano Lett. 2007;7(4):1081–5.

[40] Wang C, Shao C, Zhang X, Liu Y. SnO2 nanostructures-TiO$_2$ nanofibers heterostructures: Controlled fabrication and high photocatalytic properties. Inorg Chem. 2009;48(15):7261–8.

[41] De Mendonça VR, Lopes OF, Fregonesi RP, Giraldi TR, Ribeiro C. TiO2-SnO2 heterostructures applied to dye photodegradation: The relationship between variables of synthesis and photocatalytic performance. Appl Surf Sci. 2014;298:182–91.

[42] Lei JF, Li LB, Shen XH, Du K, Ni J, Liu CJ, et al. Fabrication of ordered ZnO/TiO2 heterostructures via a templating technique. Langmuir. 2013;29(45):13975–81.

[43] Tian J, Chen L, Yin Y, Wang X, Dai J, Zhu Z, et al. Photocatalyst of TiO2/ZnO nano composite film: Preparation, characterization, and photodegradation activity of methyl orange. Surf Coatings Technol [Internet]. Elsevier B.V.; 2009;204(1–2):205–14. Available from: http://dx.doi.org/10.1016/j.surfcoat.2009.07.008.

[44] Ceylan H, Ozgit-Akgun C, Erkal TS, Donmez I, Garifullin R, Tekinay AB, et al. Size-controlled conformal nanofabrication of biotemplated three-dimensional TiO$_2$ and ZnO nanonetworks. Sci Rep. 2013;3:2306.

[45] Athauda TJ, Neff JG, Sutherlin L, Butt U, Ozer RR. Systematic study of the structure-property relationships of branched hierarchical TiO2/ZnO nanostructures. ACS Appl Mater Interfaces. 2012;4(12):6917–26.

[46] Chen Z, Zhao J, Yang X, Ye Q, Huang K, Hou C, et al. Fabrication of TiO$_2$/WO$_3$ composite nanofibers by electrospinning and photocatalystic performance of the resultant fabrics. Ind Eng Chem Res. 2016;55(1):80–5.

[47]   Basu M, Garg N, Ganguli AK. A type-II semiconductor (ZnO/CuS heterostructure) for visible light photocatalysis. J Mater Chem A. 2014;2(20):7517–25.

[48]   Zhu L, Hong M, Wei Ho G. Hierarchical assembly of SnO2/ZnO nanostructures for enhanced photocatalytic performance. Sci Rep. Nature Publishing Group; 2015;5:1–11. Article No. 11609.

[49]   Jones MR, Osberg KD, Macfarlane RJ, Langille MR, Mirkin CA. Templated techniques for the synthesis and assembly of plasmonic nanostructures. Chem Rev. 2011, 111(6): 3736–827.

[50]   Kelly KL, Coronado E, Zhao LL, Schatz GC. The optical properties of metal nanoparticles: The influence of size, shape, and dielectric environment. J Phys Chem B. 2003;107(3):668–77.

[51]   Linic S, Christopher P, Ingram DB. Plasmonic-metal nanostructures for efficient conversion of solar to chemical energy. Nature Publishing Group; 2011;10(12):911–21.

[52]   McFarland EW, Tang J. A photovoltaic device structure based on internal electron emission. Nature. 2003;421(6923):616–8.

[53]   Zhao G, Kozuka H, Yoko T. Sol—gel preparation and photoelectrochemical properties of TiO2 films containing Au and Ag metal particles. Thin Solid Films. 1996;277(1–2): 147–54.

[54]   Tian Y, Tatsuma T. Mechanisms and applications of plasmon-induced charge separation at TiO2 films loaded with gold nanoparticles. J Am Chem Soc. 2005;127(20):7632–7.

[55]   Furube A, Du L, Hara K, Katoh R, Tachiya M. Ultrafast plasmon-induced electron transfer from gold nanodots into TiO2 nanoparticles. J Am Chem Soc. 2007;129(48): 14852–3.

[56]   Fang Y, Jiao Y, Xiong K, Ogier R, Yang Z-J, Gao S, et al. Plasmon enhanced internal photoemission in antenna-spacer-mirror based Au/TiO$_2$ nanostructures. Nano Lett. 2015;15:4059–65.

[57]   He Y, Basnet P, Hunyadi Murph SE, Zhao Y. Ag nanoparticle embedded TiO$_2$ composite nanorod arrays fabricated by oblique angle deposition: Toward plasmonic photocatalysis. ACS Appl Mater Interfaces. 2013;5:11818–27.

[58]   Linic S, Aslam U, Boerigter C, Morabito M. Photochemical transformations on plasmonic metal nanoparticles. Nat Mater. 2015;14(6):567–76.

[59]   Liu F, Luber EJ, Huck LA, Olsen BC, Buriak JM. Nanoscale plasmonic stamp lithography on silicon. ACS Nano. 2015;9(2):2184–93.

[60]   Yan J, Jacobsen KW, Thygesen KS. First-principles study of surface plasmons on Ag(111) and H/Ag(111). Phys Rev B. 2011;84:235430-4.

[61] Zhao L-B, Liu X-X, Zhang M, Liu Z-F, Wu D-Y, Tian Z-Q. Surface plasmon catalytic aerobic oxidation of aromatic amines in metal/molecule/metal junctions. J Phys Chem C. 2016;120:944–55.

[62] Wang S, Riedinger A, Li H, Fu C, Liu H, Li L, Liu T, Tan L, Barthel MJ, Pugliese G, De Donato F, Scotto D'Abbusco M, Meng X, Manna L, Meng H, Pellegrino T. Plasmonic copper sulfide nanocrystals exhibiting near-infrared photothermal and photodynamic therapeutic effects. ACS Nano. 2015;9(2):1788–800.

[63] Govorov AO, Richardson HH. Generating heat with metal nanoparticles. Nano Today. 2007;2(1):30–8.

[64] Boyd D, Greengard L, Brongersma M, El-Naggar MY, Goodwin DG. Plasmon-assisted chemical vapor deposition. Nano Lett. 2006;6(11):2592–7.

[65] Fasciani C, Alejo CJB, Grenier M, Netto-Ferreira JC, Scaiano JC. High-temperature organic reactions at room temperature using plasmon exmixed-citation: Decomposition of dicumyl peroxide. Org Lett. 2011;13(2):204–7.

[66] Verbruggen SW, Keulemans M, Filippousi M, Flahaut D, Van Tendeloo G, Lacombe S, et al. Plasmonic gold–silver alloy on TiO2 photocatalysts with tunable visible light activity. Appl Catal B Environ. 2014;156–157:116–21.

[67] Yu K, Tian Y, Tatsuma T. Size effects of gold nanaoparticles on plasmon-induced photocurrents of gold TiO2 nanocomposites. Phys Chem Chem Phys. 2006;8(46):5417.

[68] Boerigter C, Campana R, Morabito M, Linic S. Evidence and implications of direct charge exmixed-citation as the dominant mechanism in plasmon-mediated photocatalysis. Nat Commun. 2016;7:1–9. Article No. 10545.

[69] Kochuveedu ST, Jang YH, Kim DH. A study on the mechanism for the interaction of light with noble metal-metal oxide semiconductor nanostructures for various photophysical applications. Chem Soc Rev. 2013;42(21):8467–93.

[70] Chen Z, Fang L, Dong W, Zheng F, Shena M, Wang J. Inverse opal structured Ag/TiO2 plasmonic photocatalyst prepared by pulsed current deposition and its enhanced visible light photocatalytic activity. J Mater Chem A. 2014;2:824–32.

[71] Zhang Z, Zhang L, Hedhili MN, Zhang H, Wang P. Plasmonic gold nanocrystals coupled with photonic crystal seamlessly on TiO2 nanotube photoelectrodes for efficient visible light photoelectrochemical water splitting. Nano Lett. 2013;13(1):14–20.

[72] Zang Y, Yin J, He X, Yue C, Wu Z, Li J, et al. Plasmonic-enhanced self-cleaning activity on asymmetric Ag/ZnO surface-enhanced Raman scattering substrates under UV and visible light irradiation. J Mater Chem A. 2014;2(21):7747–53.

[73] Seh ZW, Liu S, Low M, Zhang S-Y, Liu Z, Mlayah A, et al. Janus Au-TiO_2 photocatalysts with strong localization of plasmonic near-fields for efficient visible-light hydrogen generation. Adv Mater. 2012;24(17):2310–4.

[74] Eom H, Jung J-Y, Shin Y, Kim S, Choi J-H, Lee E, et al. Strong localized surface plasmon resonance effects of Ag/TiO2 core-shell nanowire arrays in UV and visible light for photocatalytic activity. Nanoscale. 2014;6(1):226–34.

[75] Duan H, Xuan Y. Enhanced optical absorption of the plasmonic nanoshell suspension based on the solar photocatalytic hydrogen production system. Appl Energy. 2014;114:22–9.

[76] Hao Q, Wang C, Huang H, Li W, Du D, Han D, et al. Aluminum plasmonic photoca-talysis. Sci Rep. Nature Publishing Group. 2015;5:1–7. Article No. 15288.

[77] Karg M, König TAF, Retsch M, Stelling C, Reichstein PM, Honold T, et al. Colloidal self-assembly concepts for light management in photovoltaics. Mater Today. 2015;18(4):185–205.

[78] Pastorelli F, Bidault S, Martorell J, Bonod N. Self-assembled plasmonic oligomers for organic photovoltaics. Adv Opt Mater. 2014;2(2):171–5.

[79] Chong MN, Jin B, Chow CWK, Saint C. Recent developments in photocatalytic water treatment technology: A review. Water Res. 2010;44(10):2997–3027.

[80] Linsebigler AL, Linsebigler AL, Yates Jr JT, Lu G, Lu G, Yates JT. Photocatalysis on TiO2 surfaces: principles, mechanisms, and selected results. Chem Rev. 1995;95(3):735–58.

[81] Marschall R. Semiconductor composites: Strategies for enhancing charge carrier separation to improve photocatalytic activity. Adv Funct Mater. 2014;24:2421–40.

[82] Ganguly A, Anjaneyulu O, Ojha K, Ganguli AK. Oxide-based nanostructures for photocatalytic and electrocatalytic applications. CrystEngComm. Royal Society of Chemistry. 2015;17(47):8978–9001.

[83] Kudo A, Miseki Y. Heterogeneous photocatalyst materials for water splitting. Chem Soc Rev. 2009;38(1):253–78.

[84] Kadowaki H, Saito N, Nishiyama H, Inoue Y. RuO2-loaded Sr2+-doped CeO2 with d0 electronic configuration as a new photocatalyst for overall water splitting. Chem Lett. 2007;36:440–441.

[85] Lu X, Zhai T, Cui H, Shi J, Xie S, Huang Y, et al. Redox cycles promoting photocatalytic hydrogen evolution of CeO2 nanorods. J Mater Chem. 2011;21(15):5569.

[86] Tang Z-R, Zhang Y, Xu Y-J. A facile and high-yield approach to synthesize one-dimensional CeO2 nanotubes with well-shaped hollow interior as a photocatalyst for degradation of toxic pollutants. RSC Adv. 2011;1(9): 1772–7.

[87] Stranks SD, Snaith HJ. Metal-halide perovskites for photovoltaic and light-emitting devices. Nat Nanotechnol. Nature Publishing Group. 2015;10(5):391–402.

[88] Zhang K, Sunarso J, Shao Z, Zhou W, Sun C, Wang S, et al. Research progress and materials selection guidelines on mixed conducting perovskite-type ceramic membranes for oxygen production. RSC Adv. 2011;1(9):1661–76.

[89] Grewe T, Tüysüz H. Amorphous and crystalline sodium tantalate composites for photocatalytic water splitting. ACS Appl Mater Interfaces. 2015;7(41):23153–62.

[90] Yin S, Tian H, Ren Z, Wei X, Chao C, Pei J, et al. Octahedral-shaped perovskite nanocrystals and their visible-light photocatalytic activity. Chem Commun. 2014;50(45):6027–30.

[91] Tanaka H, Misono M. Advances in designing perovskite catalysts. Curr Opin Solid State Mater Sci. 2001;5(5):381–7.

[92] Grabowska E. Selected perovskite oxides: Characterization, preparation and photocatalytic properties—a review. Appl Catal B Environ. 2015;186:97–126.

[93] Jingshan L, Jeong-Hyeok I, Mayer MT, Schreier M, Nazeeruddfn MK, Nam-Gyu P, et al. Water photolysis at 12.3% efficiency via perovskite photovoltaics and Earth-abundant catalysts. Science. 2014;345:1593–6.

[94] Chan SHS, Wu TY, Juan JC, Teh CY. Recent developments of metal oxide semiconductors as photocatalysts in advanced oxidation processes (AOPs) for treatment of dye waste-water. J Chem Technol Biotechnol. 2011;86(9):1130–58.

[95] Naresh G, Mandal TK. Excellent sun-light-driven photocatalytic activity by aurivillius layered perovskites, Bi5-xLaxTi3FeO15 (x = 1, 2). ACS Appl Mater Interfaces. 2014;6(23): 21000–10.

[96] Wu W-Q, Feng H-L, Rao H-S, Xu Y-F, Kuang D-B, Su C-Y. Maximizing omnidirectional light harvesting in metal oxide hyperbranched array architectures. Nat Commun. Nature Publishing Group. 2014;5:1–9. Article No. 3968.

[97] Li L, Yan J, Wang T, Zhao Z-J, Zhang J, Gong J, et al. Sub-10 nm rutile titanium dioxide nanoparticles for efficient visible-light-driven photocatalytic hydrogen production. Nat Commun. Nature Publishing Group. 2015;6:1–10. Article No. 5881.

[98] Tan C, Zhang H. Wet-chemical synthesis and applications of non-layer structured two-dimensional nanomaterials. Nat Commun. Nature Publishing Group. 2015;6:1–13.

[99] Zhou Y, Zhang Y, Lin M, Long J, Zhang Z, Lin H, et al. Monolayered Bi2WO6 nanosheets mimicking heterojunction interface with open surfaces for photocatalysis. Nat Commun. Nature Publishing Group. 2015;6,8340:1–8.

Influences of Doping on Photocatalytic Properties of TiO$_2$ Photocatalyst

Fei Huang, Aihua Yan and Hui Zhao

Additional information is available at the end of the chapter

Abstract

As a kind of highly effective, low-cost, and stable photocatalysts, TiO$_2$ has received substantial public and scientific attention. However, it can only be activated under ultraviolet light irradiation due to its wide bandgap, high recombination, and weak separation efficiency of carriers. Doping is an effective method to extend the light absorption to the visible light region. In this chapter, we will address the importance of doping, different doping modes, preparation method, and photocatalytic mechanism in TiO$_2$ photocatalysts. Thereafter, we will concentrate on Ti^{3+} self-doping, nonmetal doping, metal doping, and codoping. Examples of progress can be given for each one of these four doping modes. The influencing factors of preparation method and doping modes on photocatalytic performance (spectrum response, carrier transport, interfacial electron transfer reaction, surface active sites, etc.) are summed up. The main objective is to study the photocatalytic processes, to elucidate the mechanistic models for a better understanding the photocatalytic reactions, and to find a method of enhancing photocatalytic activities.

Keywords: TiO$_2$, doping, photocatalytic properties, mechanism, carrier transfer

1. Background

As the best known photocatalyst, TiO$_2$ has attracted more attention and interest of many researchers due to its exceptional properties, such as high refractive index and ultraviolet (UV) absorption, excellent incident photoelectric conversion efficiency and dielectric constant, good photocatalytic activity, photostability, chemical stability, and long-time corrosion resistance as well as nontoxicity [1–4]. It has been widely used to solve a variety of environmental problems for the water-based solution utilization.

However, there are three key drawbacks for TiO$_2$ materials to limit their practical application. Firstly, one shortcoming is related to their large bandgap (3.0 eV for rutile and 3.2 eV for anatase TiO$_2$, respectively). It is well known that the photon absorption of semiconductors depends greatly on their bandgap energy. The photons can only be absorbed by the photocatalyst if the photon energies are higher than the semiconducting bandgap energy. Consequently, its surface photoactivation can be exclusively done under UV radiation ($\lambda \leq 390$ nm) or it only can respond and generate electron-hole pairs under UV light [5]. However, solar light consists of 5% UV light (300–400 nm), 43% visible light (400–700 nm), and 52% infrared light (700–2500 nm). That is, the UV light only occupies a small portion of the sunlight and a large part of solar energy cannot be utilized. In the future, one of the most urgent tasks is finding or modifying the photocatalysts with proper semiconducting bandgaps to maximize the absorption of solar energy. Secondly, a high recombination rate of electron-hole pairs is another disadvantageous effect on the photocatalytic efficiency for TiO$_2$ photocatalysis, resulting in a low quantum yield rate and a limited photooxidation rate. Thirdly, the weak separation efficiency of photocarries results in low photocatalytic activity. All three limitations induce great influence for a wide practical application.

To overcome above-mentioned problems, many studies have been conducted in the past 5 years based on the idea of extending the wavelength range of the photoactivation of TiO$_2$ photocatalysts towards visible light region and enhancing the utilization efficiency of solar energy. That is, an increased amount of energy from the solar light spectrum is well utilized.

Recently, a path to achieve above-mentioned goal is represented by alien ion doping to improve the adsorption capacity and photocatalytic activity, such as self-doping [6–8], nonmetal doping [9–11], transitional metal doping [12, 13], and rare-earth metal doping [14, 15]. Usually, the doped ions introduce additional energy levels into the band structure, which can be used to trap electrons or holes to separate carriers from the bands, thus allowing more carriers to successfully diffuse to the surface. It has also been suggested that the required red shift of the absorption edge might be done by increasing the impurity ion concentration or increasing the oxygen defects in TiO$_2$. That is, the purpose of doping is relatively straightforward: modifying its large bandgap and electronic structure to optimize its optical properties for visible light harvest, improving each step in the charge kinetics to reduce the massive recombination of photogenerated carriers, and improving the interface and surface characteristics [16]. On the contrary, the photocatalytic activity depends strongly on the exposed crystalline faces [17, 18]. Given that different crystal surfaces have different surface energy levels for the conduction band (CB) and valence band (VB), such differences in the energy levels will drive the electrons and holes to different crystal faces. Obviously, doping can effectively modulate the lattice face structures.

To make clear the original question about the photocatalytic mechanism for doped TiO$_2$, it is important to explain and understand the doping process, doping method, and defect chemistry, especially the physics of the energy levels induced by the incorporation of dopants. This chapter comprises the following four sections to elaborate above concerns and recent progresses:

1. Ti^{3+} self-doping in TiO$_2$ crystals and its photocatalytic mechanism,

2.   Nonmetal doping in TiO$_2$ crystals and its photocatalytic mechanism,

3.   Metal doping in TiO$_2$ crystals and its photocatalytic mechanism, and

4.   Codoping in TiO$_2$ crystals and its photocatalytic mechanism.

2. Self-doping

It is widely accepted that the degradation of pollutants in water proceeds by oxidation either reacting directly with generated holes or indirectly with OH free radicals [19, 20]. Moreover, the photocatalytic activity of TiO$_2$ is often dependent on the nature and density of surface defect sites. Usually, incorporating dopants into TiO$_2$ crystals at the oxygen (O) and/or titanium (Ti) sites can generate midgap states [21]. Furthermore, interactions of photogenerated carriers with impurities in TiO$_2$ can also alter the electric structure and energy band structure, which enhances the photocatalytic performance [22]. Of course, excess doping also increases crystal defects (for example, oxygen vacancies, titanium vacancies, and interstitial titanium), thermal instability, carrier trapping, and carrier recombination centers [23, 24]. In other words, system-charge equilibria and/or geometric structure optimization should be considered during the doping process, especially the doping level or doping concentration and dopant distribution.

Recently, both experimental results and theoretical predictions have demonstrated that Ti^{3+} self-doped TiO$_2$ could obviously increase concomitant intrinsic oxygen vacancies in TiO$_2$ crystals because the surface chemistry of nonstoichiometric TiO$_2$ containing Ti^{3+} differs markedly from that of perfect TiO$_2$. Different from traditional impurity incorporation, Ti^{3+} self-doping has been reported as an effective way to extend the visible light absorption of TiO$_2$, which can avoid the mismatching of atomic diameters with other foreign elements [25–28]. Self-doping can easily modulate and realize the system-charge equilibria just through synthesis method, process control, and raw material selection. Theoretical calculations evidence that interstitial Ti can cause impurity energy levels at 1.23 to 1.56 eV below the CB, whereas vacant Ti just makes impurity energy levels above the VB [29, 30]. Usually, the two defects can result in extra shoulder absorption or a tail absorption, which is the root cause for the enhancement of photocatalytic performance [31, 32].

2.1. Preparation of Ti^{3+} self-doping

The basic process of self-doping includes that the electrons can be trapped and tended to reduce Ti^{4+} cations to Ti^{3+} state [33], the holes oxidize O^{2-} anions for the formation of O$^-$ trapped hole or even O$_2$ gas, and the charge transfer steps are as follows:

$$TiO_2 + hv \rightarrow e^-_{CB} + h^+_{VB} \tag{1}$$

$$e^-_{CB} + Ti^{4+} \rightarrow Ti^{3+} \left(trapped \ electron \right) \tag{2}$$

$$h^+_{VB} + O^{2-} \rightarrow O^- \left(trapped \ hole \right) \tag{3}$$

$$4h^+_{VB} + 2O^{2-} \rightarrow O_2 \tag{4}$$
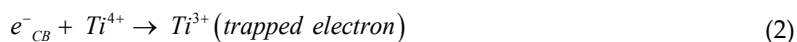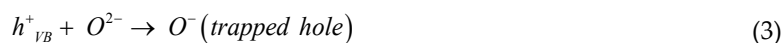
Subsequently, many methods are developed according to the above mechanism, such as hydrothermal method [25, 34–37], solvothermal method [38, 39], metallic reduction method [28, 40], solution-based oxidative method [41, 42], solution-based reduction method [43, 44], ionothermal method [26], vapor-fed aerosol flame synthesis [27], combustion method [33], and evaporation-induced self-assembly (EISA) method [45].

The hydrothermal method is widely used to synthesize Ti^{3+} self-doped TiO_2 compared to other methods. Wang et al. changed hydrothermal conditions to treat a gel precursor and obtained Ti^{3+} self-doped TiO_2 nanoparticles [34]. They found that the contents of Ti^{3+} and oxygen vacancy (O_v) in TiO_2 crystals could be reasonably adjusted. Xin et al. demonstrated that the oxidation-based solvothermal synthesis of Ti^{3+} self-doped anatase TiO_2 was an effective strategy to prepare uniform Ti^{3+} self-doped anatase TiO_2 nanocrystals. Both the concentration and location of the Ti^{3+} defects could be well managed by simply controlling the annealing temperature. This temperature-mediated management of the location and concentration of Ti^{3+} defects was achieved through a Ti^{3+} reversible diffusion mechanism [38]. The metallic reduction method was also used to synthesize Ti^{3+} self-doped TiO_2 with dominant (001) facets, and the presence of Zn obviously caused the formation of Ti^{3+} ions coming from the reduction of Ti^{4+} [40].

Liu et al. successfully synthesized anatase Ti^{3+} self-doped TiO_{2-x} nanoparticles by a simple interface ion diffusion-redox reaction, and the resulting Ti^{3+} self-doped TiO_{2-x} had high crystallinity and showed enhanced visible light-driven photocatalytic oxidation [41]. Tian et al. used $NaBH_4$ as a reduced source and prepared TiO_2 nanobelts, and the theoretical calculations and experimental results indicated that the oxygen vacancies and Ti^{3+} ions were successfully formed by reduction [43].

2.2. Mechanism of enhanced photocatalytic

It is well known that the Fermi level is much closer to the CB tail at a high oxygen vacancy concentration. Therefore, it is reasonably deduced that the higher oxygen vacancies can lead to an enhanced absorption of photon energy below the direct bandgap. The midgap states below the CB edge turn broad at an enhanced oxygen vacancy concentration (**Figure 1**). Meanwhile, the band of defect states resulting from oxygen vacancies is close to the CB edge, allowing photogenerated electrons to easily exchange between two bands. Namely, the electrons from the VB can easily transfer to the oxygen vacancy level under visible light irradiation. In other words, the electron transfer takes place from both VB and oxygen vacancy level localized states to the tailed CB. Consequently, the onset of optical absorption of the TiO_2 nanocrystals is lowered to 900 to 1100 nm [46–48].
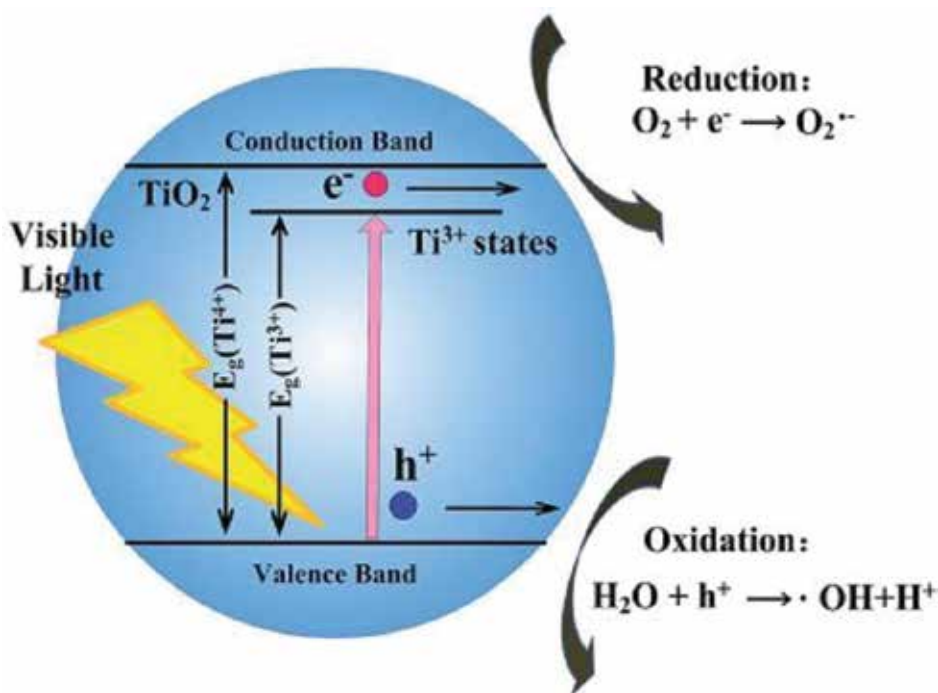
Figure 1. Schematic diagram of a proposed photocatalytic mechanism of Ti^{3+} self-doped TiO$_2$ for the visible-light response [27].

Many theoretical data from calculation and simulation also confirm that the local electrostatic balance is broken when host Ti^{4+} ions are reduced to Ti^{3+} ions, and oxygen vacancies are introduced because of charge compensation [49–51]. Because the effective charge of the oxygen vacancy is positive, the central Ti^{3+} is expected to shift away from the oxygen vacancy, forming a special sublevel electric state. Conversely, the shift Ti^{3+} also forces the four O^{2-} ions to move towards the oxygen vacancy to keep the electrostatic balance. The electrons can be photoexcited to CB under the irradiation of visible light. Meanwhile, the oxygen vacancies can inhibit the photogenerated electron-hole recombination. Furthermore, those Ti^{3+} ions act as hole traps and suppress the recombination of carriers and therefore extend the lifetime of the charges. That is, the higher light absorption in Ti^{3+} self-doping may come from the strong distortion of the outer orbitals of the Ti^{3+} ions.

In other words, Ti^{3+} self-doped TiO$_2$ exhibits a remarkable activity and enhanced performance as a photocatalyst. However, it is difficult to implant Ti^{3+} into TiO$_2$ crystals in practical application because Ti^{3+} species are usually unstable and can be easily oxidized by O. Therefore, it is still challenging to develop a simple and phase-controlled method to synthesize stable Ti^{3+} self-doped TiO$_2$ photocatalysts in the future. Moreover, it is important to have a comprehensive understanding of the methods and the techniques of Ti^{3+} generation and monitoring as well as Ti^{3+} property exploration.

3. Nonmetal doping

Nonmetal elements with high ionization energies and high electronegativity, such as nitrogen (N) [52–54], carbon (C) [55, 56], boron (B) [57–59], sulfur (S) [60, 61], fluorine (F) [62–64], and chlorine (Cl) [65, 66], are an efficient strategy to enhance the visible light photocatalytic activity, which results in higher photocatalytic activity in the visible light region owing to the bandgap narrowing and the shift of absorption edge.

The basic process is that the nonmetal dopants influence the VB through interaction with the O $2p$ electrons. The localized states or p states of nonmetallic dopants generally form the impurity levels and lie above VB, which extends the optical absorption edge of TiO_2. On the contrary, nonmetal dopants within a surface can exist as isolated atoms rather than clusters. Consequently, the distribution of dopant states is above the VB maximum, which has greater potential for realizing visible light photoactivity.

3.1. N doping

Among all nonmetal elements, N element has been proven to be one of the most efficient dopants for visible light-responsive TiO_2 photocatalyst. Since Asahi et al. made a breakthrough work in 2001 and found that doped TiO_2 with N could enhance its photocatalytic activity for the photodegradation of methylene blue under visible light irradiation [67]. Many theoretical calculations and experiments have demonstrated and confirmed that N is one of the most promising dopant candidates for red shift of the absorption edge so far. Some authors suggested a model in which the incorporation of N via O substitution results in bandgap narrowing due to the mixing of the N $2p$ and O $2p$ states, which shows a remarkable red shift of the spectrum onset [68, 69]. In most of the reported studies, only N dopant concentration below 1 at.% are mentioned, and surface photoactivation with visible light is less effective compared to UV [70–72]. In other words, N-doped TiO_2 is a promising candidate photocatalyst for enhanced light harvest in the visible region because it has strongly localized N $2p$ states (0.3–0.5 eV) at the VB maximum [73].

3.1.1. Preparation

The formation mechanism of N-doped catalysts obtained via different preparation methods is usually different. Moreover, N doping plays an important role on the exposed high-energy facets to a certain extent, which is apparently influenced by different preparation methods.

Generally speaking, there are two kinds of processes to prepare N-doped TiO_2. One process can be ascribed as one-step direct incorporation of N atoms into TiO_2 lattice, such as sol-gel method [74–76], chemical vapor deposition (CVD) [77, 78], atomic layer deposition (ALD) [79–81], hydrothermal method [82–84], solvothermal method [85–88], sol-hydrothermal process [89], hydrolysis-precipitation process [90], bioprocess-inspired method [91], electrochemical method [92–94], ion implantation [95, 96], combustion method [97–99], mechanochemical method [100, 101], low-temperature direct nitridization method [102], and microwave-assisted method [103].

Samsudin et al. synthesized undoped and N-doped TiO$_2$ via a sol-gel technique using Ti(IV) isopropoxide and triethylamine as the Ti and N precursors, respectively [74]. N was doped interstitially forming Ti-O-N or Ti-N-O linkages, and induced local states 0.23 to 0.26 eV above the VB, which was responsible for the visible light response between 400 and 550 nm. Gao et al. prepared N-doped TiO$_2$ films by the dielectric barrier discharge enhanced CVD method using Ti tetraisopropoxide and NH$_3$ as Ti precursor and doping gas [77]. It was found that N doping sources changed the growth orientation, affected the surface microstructure, narrowed the bandgap, and improved the photocatalytic activity in the visible light region. Liu et al. conducted an ALD method to fabricate N-doped TiO$_2$ hollow fibers with polysulfone fibers as a template [79]. The results showed that N was successfully inserted into the anatase TiO$_2$ lattice to form impurity levels above the VB top that narrowed the bandgap.

Therein, the hydrothermal method and solvothermal method are most frequently used because of their low cost, perfect crystallinity, and good repeativity. Wang et al. prepared N-doped TiO$_2$ nanoparticles by a facile one-pot hydrothermal treatment in the presence of L-lysine, and the results showed that N-TiO$_2$/C nanocomposites increased absorption in the visible light region and exhibited a higher photocatalytic activity than pure TiO$_2$, commercial P25, and previously reported N-doped TiO$_2$ photocatalysts [82]. Li et al. prepared a series of N-doped anatase TiO$_2$ samples using a solvothermal method in an organic amine/ethanol-water reaction system [85]. Both the degree of N doping and oxygen vacancies made contributions to the visible light absorption of the sample.

Recently, Cheng et al. synthesized N-doped TiO$_2$ nanoparticles through a hydrolysis-precipitation process using ammonia water as the doping species [90]. They found that the light absorbance edge of N-doped TiO$_2$ nanoparticle was obviously red-shifted to visible light region and the separation rates of photogenerated carriers were greatly improved. Further analysis implied that the VB maximum of O 2p was 2.3 eV. Hu et al. also developed a facile low-temperature direct nitridization method to synthesize colloidal N-doped TiO$_2$ nanocrystals in triethylamine solution during the hydrolysis of tetrabutyl titanate followed by acidic peptization at 70°C [102]. The N-doped TiO$_2$ exhibited higher photocatalytic activity both in the UV and visible light regions in contrast to the undoped TiO$_2$ because of the improved light response in the range of 400 to 500 nm, narrowing bandgap, more production of e$^-$-h$^+$ pairs, and inhibiting recombination of the photo-induced carriers.

The other important preparation process of N-doped TiO$_2$ can be ascribed as two-step oxidization of Ti nitride, such as sputtering method [104, 105], thermal annealing [106–108], and plasma-enhanced microarc oxidation [109]. As for two-step methods, there are less research compared to one-step methods due to its higher cost and more complex technique process. Abadias et al. thought that the visible light activity of these materials mainly depended on the location of this impurity states and the microstructure of the N-doped TiO$_2$ materials [104]. They synthesized N-TiO$_2$ films through reactive magnetron sputtering method under a mixture gas of argon (Ar), N, and O. N diffusion was suggested to be responsible for the more complex crystallization and a better photocatalytic activity. Ha et al. prepared a new type of N-doped TiO$_2$ mesoporous inverse opal structure via heat treatment in the presence of an N-rich precursor, and the N doping with 9.4 wt.% concentration narrowed the bandgap from 3.2

to 2.4 eV, which corresponded to light absorption at wavelengths as long as 520 nm [106]. Jiang et al. developed a novel plasma-enhanced microarc oxidation process for preparing a high concentration substitutional N-doped TiO_2, compared to the traditional thermal annealing, and the process provides a possibility to increase the N doping concentration up to 3.21 at.% in $TiO_{2-x}N_x$, which exhibits a significant red shift in the bandgap transition and narrows bandgap to 2.6 eV [109].

3.1.2. Photocatalytic mechanism of N-doped TiO_2

The mechanism, especially the origin of visible light photoactivity for N-doped TiO_2, is still in debate up to now. Valentin et al. [111] and Gao et al. [101] studied substitutional and interstitial N impurities in bulk anatase TiO_2 lattice (**Figure 2**). They thought that the N atom replaced lattice O in TiO_2 for the substitutional case and showed positive oxidation state ranging from hyponitrite species (NO^-), nitrite (NO_2^-), to nitrate species (NO_3^-). The visible light responses for substitutional N-doped anatase TiO_2 came from occupied N $2p$ localized states, which were slightly above the VB maximum. The N-O bond showed localized π-bond states. The two bonding states were found in deep energy level and lay below the top of the O $2p$ band. The other two antibonding states were found located over the O $2p$ band. In other words, the localized states were responsible for the excellent optical adsorption when the N atom was located at the substitutional site. On the contrary, interstitial site for N doping had some disadvantageous effects on the photocatalytic reaction because of the hole trapping.
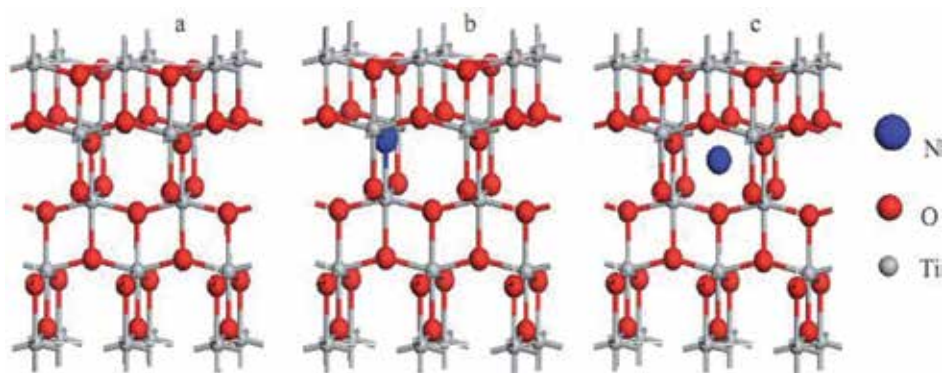
Figure 2. Supercells of (a) pure, (b) substitutional, and (c) interstitial TiO_2 [111].

Energy bandgap models also predict that substitutional (interstitial) N generates shallow (deep) midgap states above the top of the VB due to the mixing of N $2p$ and Ti $3d$ orbitals (**Figure 3**). Usually, N doping is associated with the formation of oxygen vacancies and electrons to maintain lattice neutrality. From this perspective, it has been suggested that the presence of extra oxygen vacancies might be the key factor allowing for better photocatalytic performances to be achieved, which causes a red shift of the absorption band edge due to a positive shift of VB and improves electron injection [112–114]. Under visible light irradiation, electrons of the localized N $2p$ states can be excited up to the individual CB, leaving holes on

the localized states. The energy barrier between midgap states would suppress electron transfer. This can also inhibit the recombination of photoelectrons and holes to some extent [115]. In other words, the efficient separation of photo-induced carriers under visible light excitations enables N-doped TiO$_2$ to have higher photocatalytic activity in a wide wavelength ranging from UV to the visible region.
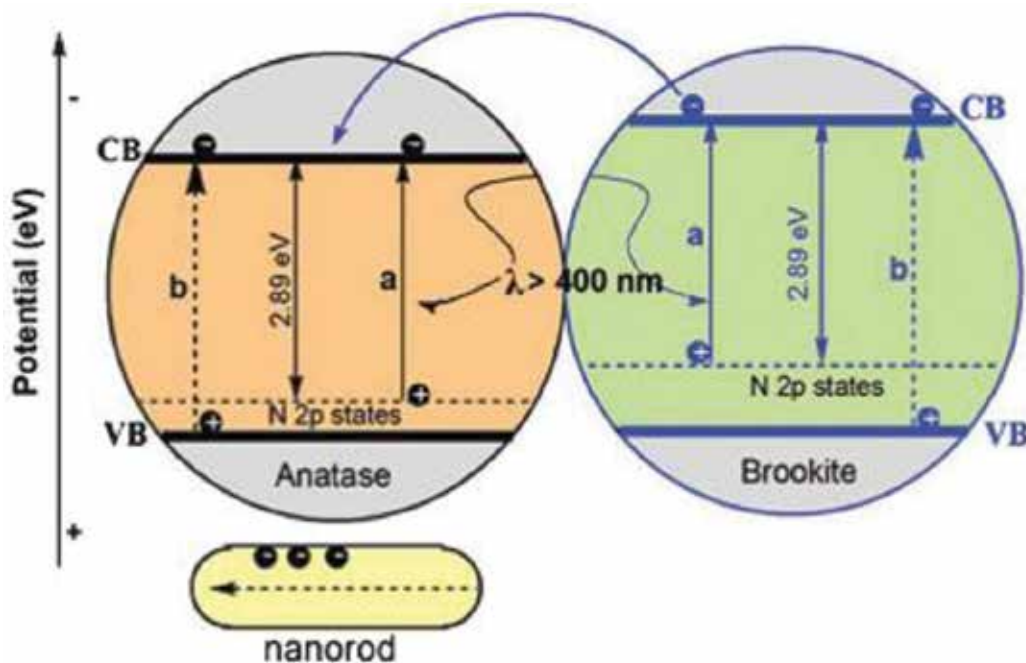
Figure 3. Schematic illustration of electron migration in anatase/brookite structures: under visible light irradiation (path a) and under UV light illumination (path b) [114].

3.2. C doping

Among the nonmetal elements, C doping has also been proposed as one of the best candidates [116]. The origin of C doping is mainly incorporated interstitially, narrowed bandgap and resulted in a red shift in the UV-visible (UV-vis) spectrum, resulting in an increase in adsorption of near-infrared (NIR) spectrum [117, 118]. Khan et al. first reported that C-doped TiO$_2$ was visible light active, and found that that the three kinds of C species could influence the photocatalytic activity, namely, elemental C, carbonate species (C-O bond) as interstitial dopant, and C substituted for O (Ti-C bond) in TiO$_2$ lattice [119].

Subsequently, a lot of researches were conducted to synthesize C-doped TiO$_2$ photocatalysts [120–124]. Shi et al. prepared nanometer-sized C-doped TiO$_2$ nanoplates with exposed {001} facets via the hydrothermal treatment of TiC powder in an HF-HNO$_3$ mixed aqueous solution and found that C doping also obviously presented red shift absorption edge towards visible

light [120]. Further analysis found that the electrons in the localized C states could be excited to the CB under visible light irradiation and effectively scavenged by molecular O to produce the superoxide radical anion ($\bullet O_2^-$) and hydrogen peroxide (H_2O_2), which could interact to produce hydroxyl radicals ($\bullet OH$). Recently, Shao et al. prepared amorphous C-doped TiO_2 with visible light photocatalytic activity by a facile sol-gel route for the first time. The results also indicated that the most active sample with oxygenic groups had a narrower bandgap and lower recombination of electron hole, significantly broadening its potential for many practical applications [122].

About the mechanism of photocatalytic activity for C-doped TiO_2 catalysts, it is similar to N-doped TiO_2 catalysts, except some little differences. Liu et al. investigated that C doping in the TiO_2 lattice had graphite- and carbonate-like species at interstitial positions [125]. They thought that the two C states could narrow the bandgap of anatase TiO_2, serving as a photosensitizer to absorb visible light and promote the charge carrier separation, which enhanced the visible light photocatalytic activity remarkably. Zhang et al. insisted that the substitutional C (C_s) at O sites modified the electronic band structure of TiO_2 by mixing C $2p$ orbitals with O $2p$ orbitals, resulting in bandgap narrowing [123]. Under visible light irradiation, electrons can be excited directly into the CB and transferred to the adsorbed O molecule to produce $\bullet O_2^-$ and subsequently $\bullet OH$ with strong oxidation power. Recently, Sun and Zhang investigated the C doping of anatase TiO_2 in detail using density functional theory (DFT) calculation [126]. They found that C_{Ti} and C_i with a shallow donor had no effect on the bandgap, whereas the $(CO)_{2O}$, C_O-V_O, and $(C_2)_{2O}$ defect reduced the bandgap to about 1.1, 1.7, and 1.4 eV, respectively. Based on the electronic structure analysis of the C defects, they excluded the possibility of C occupying Ti sites or interstitial sites to be responsible for the enhancement of photoactivity in the visible light region.

3.3. S doping

S doping in TiO_2 structure also shows bandgap narrowing effects [127]. However, its large ionic radius makes it difficult to incorporate into TiO_2 crystals due to the large formation energy. Therefore, the key issues are to find a facile, low-cost, and stable process to synthesize S-doped TiO_2.

Goswami and Ganguli developed a novel approach to synthesize sulfated TiO_2 nanoparticles using 15% Ti trichloride and thiophene in the presence and absence of oxalic acid [128]. They found that S-doped samples had higher surface area, smaller crystallite size, greater thermal stability, and better photocatalytic performance. Li et al. demonstrated a facile nonhydrolytic thermolysis route for monodisperse S-doped TiO_2 nanocatalysts in hot boiling organic solvents of oleic/oleyl-amine/1-octadecene [129]. Compared to the undoped TiO_2 nanocatalysts, S-doped TiO_2 nanocatalysts presented obviously enhanced visible light activation for the degradation of rhodamine B and methylene blue dyes under the artificial visible light irradiation. Recently, Ramacharyulu et al. synthesized S-doped TiO_2 catalysts by a sol-gel process followed by hydrothermal treatment at low temperature and tested for catalytic activity by natural sunlight photocatalytic degradation of a toxic chemical warfare agent [130]. It was observed that S-doped TiO_2 exhibited superior photocatalytic activity under sunlight irradia-

tion. Further analysis indicated that the superior photocatalytic activity could be attributed to the presence of S^{4+}/S^{6+} or N$^-$ impurity levels. Lin et al. [131] and Sharotri and Sud [131, 132] further found the importance of S^{6+} for S-doped TiO$_2$ photocatalysts, which could form h$^+$/e$^-$ trapping centers, delay the phase transition from anatase to rutile, promote photocatalytic activity, and prevent h$^+$/e$^-$ recombination.

3.4. Halogen doping

Halogen doping in TiO$_2$ crystals is another important approach to improve photocatalytic performance, such as F doping [133–135], Cl doping [136–138], and iodine (I) doping [139–141]. Pan et al. developed an effective bottom-up synthesis strategy to prepare monodisperse F-doped TiO$_2$ mesoporous spheres by integrating sol-gel and solvothermal processes [133]. The photocatalytic experiments showed that the formation of surface fluorination was helpful to improve and enhance light harvesting in the UV-vis range. Fang et al. also synthesized F-doped rutile TiO$_2$ with tunable solar absorption via one-pot hydrothermal method [142]. They found that the optical bandgap of the catalyst could be easily manipulated from 3.05 to 2.58 eV through altering the initial F:Ti molar ratio.

The origin of the visible light activity of F-doped TiO$_2$ has been systematically investigated by many researchers via comprehensive theoretical and experimental studies [134, 143–145]. It is widely accepted that the three-coordinated surface F atoms with higher 1s binding energy are identified to be the origin of the visible light activity. The surface group can also trap the CB electrons by tightly holding electrons due to the strongest electronegativity of F. The calculated results using DFT principle show that F implantation resulted in Ti^{3+} self-doping and contributes to the enhancement photocatalytic activity. Moreover, the strong electron-withdrawing ability of the surface three-coordinated surface F also reduces the recombination of photogenerated electrons and holes.

Similarly, Cl doping has the same role in TiO$_2$ crystals with F doping. Wang et al. prepared Cl-doped TiO$_2$ nanocrystalline via a simple single-step method by sonicating a solution of tetraisopropyl titanate and sodium chloride in water/ethanol at 70°C and found that the Cl doping of TiO$_2$ shifts the absorption edge toward a higher wavelength [136]. The photodegradation rates of butyl benzyl phthalate reached 92% under visible light irradiation for 240 min, which was much higher than undoped TiO$_2$.

Doping with I element in TiO$_2$ crystals also can enhance light absorption and decrease recombination [146–149]. Lin et al. synthesized I-modified TiO$_2$ nanocrystallites through a combination of sol-gel process and solvothermal process in the presence of HI solution [146]. The results showed that the I in the form of I$_2$ was responsible for the visible light response. Liu et al. developed a new strategy for homogeneous doping of I molecules (I$_2$) to achieve bandgap narrowing of TiO$_2$ nanosheets and investigated the extension of the intrinsic absorption edge into the visible light region through a shifting of the VB maximum [149]. Importantly, the geometric structure of the host retained its integrity. The experiment together with first-principles calculations revealed the molecular nature of adsorbed I atoms and implied that the mechanism of electronic structure modulation in the TiO$_2$ layers changed depending on the concentration of I$_2$ molecules.

3.5. Other doping

B^{3+} is incorporated both substitutionally and interstitially in TiO_2 crystals. Usually, the replacement of B^{3+} for Ti^{4+} generates one hole in O 2*p* orbital, which can also be accompanied by a blue shift of the UV‐vis absorption spectrum and an increase in oxygen vacancies [150, 151]. Xu et al. developed a new method allowing a clean one‐step synthesis to obtain B-doped TiO_2 for the first time [150]. B doping resulted in a shift of the absorption edge up to 460 nm with a concomitant reduction of the bandgap energy. The narrowing bands were attributed to ionized oxygen vacancies and defect states in anatase for the presence of interstitial B tricoordinate and tetracoordinate to O.

Another concerned nonmetal dopant is phosphorus (P). Many papers indicated that P dopant could also improve the photocatalytic activity [152, 153]. Zheng et al. synthesized a novel thermally stable P‐doped TiO_2 by liquid hydrolysis of $TiCl_4$ using hypophosphorus acid as the precursor of the dopant [152]. They found that increased surface P content led to a linear enhancement of the specific adsorption capacity of methylene blue because of the Coulombic attractive force between the cationic dye and the negatively charged P‐doped TiO_2 surface.

4. Metal dopants

It is well known that the photoexcitation of TiO_2 catalysts involves excitation, diffusion, and surface transfer of photogenerated carriers. Therefore, the carrier's lifetime is vital in determining the photoactivity during the photodegradation process. Usually, the surface properties of TiO_2 intrinsically could be influenced by the preparation method, process, and doping, which determines the surface separation and transfer of charge carriers by generating surface states where electrons and holes are spatially trapped and transferred for subsequent redox reactions.

Compared to nonmetal dopant, substitution of metal ions can introduce an intraband state close to CB edge, which results in an obvious red shift in bandgap adsorption due to sub-band gap energies, such as transition metal doping [154–156], rare-earth metal doping [157–159], and other metal doping [160–162].

However, the diffusion of metal atoms is difficult in solid materials under low temperature. Consequently, it leads to inhomogeneous distributions of dopants and limited depth near a subsurface region. To obtain metal-doped TiO_2 nanoparticles with good homogeneity, sintering has to be conducted at a high temperature, which leads to particle agglomeration. Moreover, the metal dopants also provide more trapping sites for electrons and holes compared to nonmetal dopants. Furthermore, electron trapping occurs at a much faster process compared to hole trapping. In other words, trapping an electron or a hole is always ineffective for carrier separation because immobilized charge species rapidly recombine with its mobile counterparts. Last, metal doping has also some other drawbacks, especially thermal instability, which reduces the repeativity of TiO_2 photocatalysts. That is to say, it has a detrimental effect if the process is not under the control. Therefore, many researchers focused on the resolution of the above four problems in recent several years.

4.1. Transition metal element doping

Various properties of transition metal with 3d or 4d electron structure are influenced by many factors, such as the number of d-electrons on transition metal ions, crystalline structures, oxygen defects, and preparation methods [163–165]. Usually, the bandgap energy and band positions, Fermi level, and d-electron configuration of the electronic structure in TiO$_2$ can be effectively modulated when transition metal ions were introduced into TiO$_2$ lattice. Subsequently, it forms a wide range of new energy levels below CB arising from their partially filled d-orbitals, which results in an obvious red shift in bandgap and increases its visible light harvest [166, 167]. In addition, transition metal ions alter the carrier equilibrium concentration by serving as electron-hole trapping, suppress the recombination rate of electron-hole pairs, and enhance the degradation rates. That is, the photocatalytic performance for TiO$_2$ can be effectively improved through transition metal doping.

However, transition metal ions-doped TiO$_2$ appears to be a complex function of dopant concentration, energy level of dopant within the lattice, the d electron configuration, distribution of dopants, electron donor density, and incident light intensity. Every transition metal ion has different d electron configurations and its own characteristics. Therefore, it is important to further elaborate the process for every transition metal ion.

4.1.1. Iron (Fe) doping

Fe-doped TiO$_2$ shows superior activity due to its unique half-filled electronic configuration and shallow trapping compared to other metal dopants with closed shell electronic configuration, which can be more effective to influence the photoactivity [168–176]. Theoretical and experimental studies show that Fe doping can effectively reduce the trapping density and charge recombination, resulting in drastically improved adsorption.

Manu and Khadar synthesized Fe-doped TiO$_2$ nanocrystals at different atomic ratios through the hydrothermal method [168]. They found that the concentration of Fe dopants was more near the grain boundary because the dopant atoms were incorporated into the lattice at substitutional positions. The energy level associated with the peak at 2.63 eV was the deepest defect level. Consequently, the photocatalytic activity was enhanced greatly. Yan et al. developed a facile fast hydrolysis route to prepare a three-dimensional flow-like Fe-doped rutile TiO$_2$ nanostructure and investigated the relation between Fe doping and crystal planes [169]. Because the ionic radius of Fe was smaller than that of Ti, and the corresponding interplanar spacing distance of TiO$_2$ (110) was reduced with the replacement of Ti atoms by Fe atoms, as reflected by the shift of the (110) diffraction peak, which was similar with Liu and Zhang's result [170]. With Fe species doping into both the bulk phase and the surface, the bandgap narrowing of rutile TiO$_2$ was realized and the dissociative adsorption of water on the surface was promoted, which accordingly led to greatly enhanced activity in visible light-driven water oxidation.

4.1.2. Chromium (Cr) doping

Cr doping of TiO_2 also leads to a clear red shift in the UV-vis absorption spectrum, evidencing a decrease in bandgap and VB shift. Moreover, the Fermi level is also shifted to a higher energy by ~0 to 1 eV. With the change of preparation method and doped concentration, Cr-O anti-bond orbitals located slightly below the CBM in the region of ~3.0 to 2.2 eV and the unsaturated nonbonding d orbitals located in the middle of the gap region of ~2.5 to 1 eV. It also is suggested that Cr^{3+} doping is attributed to the increase of conductivity due to more free charges [177–180].

Li et al. synthesized Cr-doped TiO_2 via a hydrothermal method and found that Cr^{3+} ions could replace the Ti atoms in the lattice with oxygen vacancy compensation [177]. It was interesting that Cr doping also could prolong the lifetime of photogenerated carriers because the doped Cr^{3+} ions might act as the recombination centers of carriers.

4.1.3. Niobium (Nb) doping

Over the past few years, Nb-doped TiO_2 has received special attention due to its excellent electrical conductivity at room temperature. The ionic radius of Nb^{5+} of 0.064 nm is slightly larger than Ti^{4+} of 0.0605 nm. Therefore, Nb^{5+} works as an n-type dopant in TiO_2 lattice and generates additional carriers in its CB, which can notably increase photocatalytic performance [181–186].

Joshi et al. successfully prepared Nb-doped TiO_2 transparent films on glass substrates using a nonaqueous sol-gel spin coating technique [181]. Photocatalytic experiments showed that the films with 12 at.% Nb doping had excellent photocatalytic activity with 97.3% degradation of methylene blue after 2 h of UV irradiation. Archana et al. reported the high electron mobility and optical transparency of Nb-doped TiO_2, giving rise to the enhancement in charge transport behavior after 2 at.% Nb doping, which could assist the speedy initial reaction of the organic decomposition process and enhance the overall photocatalytic activity [182].

4.1.4. Other transition metal doping

Except above transition metal dopants, other transition metal atoms, including tungsten (W) [187–191], silver (Ag) [192–197], copper (Cu) [198, 199], cobalt (Co) [200–202], tantalum (Ta) [203–205], molybdenum (Mo) [206–208], zinc (Zn) [209–213], manganese (Mn) [214, 215], nickel (Ni) [216, 217], and vanadium (V) [218, 219], are also investigated by many researchers.

Recently, considerable enhancements of photocatalytic activity with W-doped TiO_2 in aqueous systems for the degradation of organic compounds have also been reported [187–191]. Liu et al. synthesized ordered mesoporous crystalline TiO_2 with various W doping level using SBA-15 as a hard template [187]. The existence of W ions expanded the range of useful excitation light to the visible spectra, greatly inhibited the recombination of electron-hole pairs on mesoporous TiO_2, and played an important role in improving the photocatalytic activity in the visible light region. The enhanced photocatalytic activity for W-doped TiO_2 could also be especially attributed to the presence of much higher Lewis surface acidity of a W-doped TiO_2 surface with a higher affinity for chemical species having unpaired electrons than pure TiO_2.

Ag is another important dopant in TiO$_2$ crystals and Ag doping can also cause an obvious shift towards narrowing the bandgap. Zhang et al. successfully synthesized Ag-doped TiO$_2$ with a novel hierarchical architecture via a combination of an electrospinning method and a hydrothermal process [192]. They found that Ag doping played a great role in the photocatalytic activity. Electron transfer to the Ag sites reduced the carrier recombination rate and allowed a more effective reaction between the surface trapped holes and electrons. However, excessive Ag dopant could also cause a decrease in the activity of TiO$_2$ because they occupied the active sites on the surface of the TiO$_2$. Moreover, the photogenerated electrons on the Ag sites attracted holes and recombined together.

Cu, as a kind of transition metal, is also found to be an effective dopant for TiO$_2$ to enhance the photocatalytic activity. Sajjad et al successfully prepared mesoporous Cu-doped TiO$_2$ via a sol-gel method at low temperature using water-immiscible room-temperature ionic liquid organic materials as a template and an effective additional solvent [198]. The results showed that Cu-doped TiO$_2$ samples exhibited superior visible light photocatalytic activities compared to undoped TiO$_2$ and P-25 [199, 200]. Further characterization indicated that Cu$^+$/Cu^{2+} sites as interfacial Ti-O-Cu surface linkages reduced bandgap energy as well as efficient charge separation due to the formation of Ti-O-Cu bonding at the surface and the associated appearance of oxygen vacancies, resulting in higher degradation rate.

Usually, Co dopant concentrations show weak influence on photocatalytic performance, whereas the oxygen vacancy concentration and distribution in the system show much stronger influence on the optical performance due to the shift of Fermi level up by ~0.75 eV [201]. Cai et al. presented a controllable and reliable method to synthesize Co-doped TiO$_2$ nanowires through a combining versatile solution phase chemistry and rapid flame annealing process [202]. They found an enhanced catalytic activity in Co-doped TiO$_2$ crystals. However, Co doping was also shown to drastically deteriorate performance at high doping concentration due to the formation of sub-band gap states that act as recombination centers.

Sengele et al. obtained Ta-doped TiO$_2$ via a sol-gel route and found that the Ta doping could induce significant modifications on the structural, morphological, surface, electronic, and optical properties of TiO$_2$ [203]. Total diethylsulfide elimination could be reached for 100 min under continuous contaminant flux before deactivation and the conversion maintained to 80% of degradation after 200 min, which was higher than undoped TiO$_2$ catalysts [204–208].

Recently, many researchers found that transition metal could effectively modulate the crystal face, which could improve photocatalytic performance [209–213]. Saad et al. synthesized Zn-doped TiO$_2$ nanowall with a (001) facet and porous structure [209]. They found that the samples with a (001) facet exhibited enhanced photocatalytic activity and Zn-doped TiO$_2$ had better degradation rates compared to other samples.

4.2. Rare-earth metal doping

Another path to achieve the abovementioned goal is represented by rare-earth doping [214–219]. Compared to transition metals, rare-earth metals with 4f, 5d, and 6s^2 states are considered as the ideal dopants to modify the crystal structure, electronic structure, and optical properties

of TiO_2, which can effectively influence the positions, widths, and density of states of CB and VB [220, 221]. Furthermore, rare-earth metals can form complexes with various Lewis-based organic compounds through interaction of the functional groups with their f orbital, thereby improving the photoactivity. Last, the functional integration of upconversion luminescent rare-earth ions with photocatalyst provides a potential for wavelength conversion and efficient utilization of solar energy for this purpose [222, 223]. This approach appears to be a completely new alternative for enhancing the efficiency of the photocatalytic process. In other words, the applications of the upconversion process by phosphor-like systems can optimize the photo-catalytic performance of traditional UV active photocatalysts.

Therein, lanthanide (La) has been widely used and investigated in the field of optical application (LED light, laser, photocatalytic, solar cell, etc.). Particularly, the ability of these nanomaterials to release high-energy photons after NIR laser-light stimulation allows deep tissue imaging and luminescent nanoparticles [224, 225]. Du et al. prepared pure and La-doped TiO_2 thin films via a sol-gel method using tetrabutyl titanate as Ti precursors [224]. The results showed that the content of La was the key factor for hydrophilic and photocatalytic activity. $LaTiO_3$ could be formed in La-doped TiO_2 thin films, which caused the TiO_2 lattice distortion and restrained the transition from anatase to rutile. By adding 0.3 wt.% La to the TiO_2 thin films, 92.02% methylene blue was finally degraded.

Cerium (Ce), as a typical rare-earth metal, is widely used to dope TiO_2 because of its unique electronic structure. The main feature of Ce ion doping is the different electronic structures of $4f$ states, such as Ce^{3+} with $4f^15d^0$ and Ce^{4+} with $4f^05d^0$. The visible light photoactivity of Ce-doped TiO_2 nanoparticles is mainly due to the presence of $4f$ level in the mid-bandgap of TiO_2 crystals, which leads to the optical absorption between 400 and 500 nm. The possible transition of d and f orbital electrons can also reduce the recombination rate of electron-hole pairs, thereby making TiO_2 more feasible for photocatalytic response under visible light [226–229]. Maddila et al. prepared Ce-doped TiO_2 catalysts using a wet impregnation method [226]. The results indicated that Ce-doped TiO_2 exhibited an obvious red shift, reducing the bandgap and improving the photocatalytic efficiency. Photocatalyzed ozonation with 1at.% Ce/TiO_2 yielded 100% degradation in 2 h under basic pH conditions.

Among various upconverting nanomaterials, erbium (Er) can be excited by NIR or visible light [230–232]. Obregon and Colon synthesized Er-doped TiO_2 through a surfactant free hydro-thermal method, which exhibited good photoactivities under sun-like excitation for the degradation of phenol [231]. The presence of Er^{3+} did not affect the structural and morpho-logical features of the TiO_2 significantly, whereas photocatalytic experiments clearly evidenced that Er introduction into TiO_2 matrix would promote the profiting of NIR photons, enhancing the photoactivity of the catalyst.

Gadolinium (Gd) doping raises VB maximum with respect to the Fermi level and thus turns the intrinsic virgin phase into a p-type semiconductor. Choi et al. synthesized three-dimen-sional Gd-doped TiO_2 nanofibers using a simple electrospinning technique [233]. The pristine Gd-doped TiO_2 nanofibers showed a higher photocatalytic activity than the TiO_2 nanoparticles, which could be attributed to the fast electron transport. In addition, Gd-doped TiO_2 nanofibers

showed nearly five-fold enhancement in the photocatalytic degradation rate due to synergistically higher electron transport.

Europium (Eu) is also a good candidate for upconversion materials and is widely used in the field of photocatalyst, laser, solar cell, etc. Recently, many researchers also attempted to dope Eu into TiO$_2$ lattice [234–236]. Leroy et al. prepared periodic mesoporous Eu-doped TiO$_2$ through the EISA process [234]. They found that strong fluctuations existed in the intensity of the $^5D_0 \rightarrow {}^7F_2$ transition under UV light exposure. Correlation of the emission with the photocatalytic activity of the semiconductor for the photodegradation of an organic molecule could also be firmed.

Yttrium (Y) doping usually shows weak influence on bandgap energy and does not alter the Fermi level. However, it can increase hole mobility to generate p-type TiO$_2$, which is helpful for the carrier transport. Wu et al. prepared a novel mesoporous Y-doped TiO$_2$ nanosheet array via a low-cost, facile, and template-free solvothermal method by employing waste tricolor fluorescent powder (WTFP) as a dopant Y source and acetic acid as a mesopore template [237]. The 2.5 and 5 wt.% Y-doped TiO$_2$ films showed higher photocatalytic activity for the methyl orange, with 82.6% and 81.3% reduction within 6 h irradiation, respectively. The enhanced photocatalytic activity of Y-doped TiO$_2$ film was attributed to the large surface area and the low electron-hole recombination rate as well as enhanced absorption of organic pollutants on the semiconductor surface. Li et al. also confirmed that ytterbium (Yb) doping was also a kind of route to improve the NIR photocatalytic degradation of rhodamine B [238].

4.3. Other metal dopants

Recently, many researchers found that lithium (Li) doping plays an important role in the inhibition of activity in the TiO$_2$ network acting as an electron trapping or hole trapping [239–241]. Bouattour et al. reported Li-doped TiO$_2$ nanoparticles through a sol-gel process and investigated their potential application as a photocatalyst for degradation of different organic compounds [240]. Results showed that an inhibition of activity is presented in the Li doping network. However, the surface accumulation of Li$^+$ on TiO$_2$ particles could favor better interfacial charge transfer.

Long et al. calculated the electronic structures of silicon (Si)-, germanium (Ge)-, tin (Sn)-, and lead (Pb)-doped anatase and rutile TiO$_2$ systematically using DFT calculations [242]. Doping with Si, Ge, Sn, and Pb elements also narrowed the bandgap of rutile TiO$_2$ due to a shift far away from the CB minimum. The reduction of the bandgap is 0.20 and 0.15 eV in Si- and Ge-doped anatase TiO$_2$, respectively. However, there were enlargements of 0.06 and 0.02 eV in the bandgap of Sn- and Pb-doped anatase TiO$_2$, respectively. They predicted that Ge-doped TiO$_2$ was efficient for the overall water splitting using visible light irradiation.

Doping with bismuth (Bi) ions can also decrease the bandgap of TiO$_2$ and thereby extend its absorption into the visible light region, enhancing its photocatalytic efficiency [243–245]. The impurity energy level from the hybrid of Bi 6s, O 2p, and Ti 3d orbitals is the cause of the red shift of the absorption edge. Therefore, Bi-doped TiO$_2$ systems are more effective for the photodegradation of organic pollutants under visible light irradiation, such as methyl blue

and methyl orange. Wu et al. developed a facile method to prepare Bi-doped TiO_2 through hydrothermal synthesis followed by thermal annealing treatment [243]. Bi doping caused the formation of Bi_xTiO_y and reduced bandgap widths. Moreover, some special structural defects created by the migration of Bi^{3+} ions were also responsible for the high photoactivity. Bi-doped TiO_2 catalysts with high doping concentration (such as 5 and 10 mol%) showed the highest activity for the catalyzed photodegradation of methyl orange under visible light irradiation.

Sn doping is another important supplementary form to improve photocatalytic performance [246, 247]. Oropeza et al. investigated the influence of Sn doping on the anatase to rutile phase transition, as well as the photocatalytic performance [246]. They found that Sn-doped TiO_2 exhibited enhanced visible light region photocatalytic activity compared to undoped TiO_2 in dye degradation experiments, even it was higher than that of N-doped TiO_2. This was attributed to the narrowing of the bulk bandgap at low doping levels. The Sn surface states laid above the VB top and could therefore act as trapping sites for holes.

5. Codoping

Although the monodoped nonmetal or metal atoms can obviously enhance photocatalytic performance, they always act as the recombination centers because of the partially occupied impurity bands. It has been recognized theoretically that codoping using two or more foreign atoms can passivate the impurity bands and decrease the formation of recombination centers by increasing the solubility limit of dopants. Furthermore, codoping can also modulate the charge equilibrium. Consequently, codoping can effectively enhance the photocatalytic activity. Based on the research of doping effects, two or more elements are introduced into TiO_2 lattice to check the changes of electronic structure and bandgap energy, including nonmetal and nonmetal atoms [248–250], nonmetal and metal atoms [251–253], and metal and metal atoms [254–256].

Regardless of whether doping is based on single heteroatoms or coupled heteroatoms, the spectral distribution and localized states in the bandgap essentially determine the visible light absorbance and redox potential of the photo-induced charge carriers. Therefore, it is a challenge and hot topic to introduce different dopants, which can realize substantial synergistic effects.

5.1. Nonmetal-nonmetal doping

5.1.1. N-nonmetal codoping

To improve the photocatalytic performance of N-doped TiO_2 catalysts, the modification strategy has been extensively adopted and investigated by many researchers, such as N-nonmetal codoping, C-nonmetal codoping, and other nonmetal-nonmetal codoping. The modified N-doped TiO_2 usually showed favorable effects for improving the photocatalytic activity in the range of visible light compared to N-doped TiO_2.

Therein, the (N, S) codoping TiO$_2$ can play a vital role in significantly improving photocatalytic activity because of the strong synergistic interaction between S and N, in which the surface separation of photoexcited electron-hole pairs is promoted [257–259]. Consequently, the VB of TiO$_2$ shifts to a positive direction, which leads to higher oxidative ability and degradation ability towards pollutant under visible light irradiation. Etacheri et al. further proved that the formation of isolated S 3p, N 2p, and π* N-O states between the VB and CB was responsible for the visible light absorption [260].

Chung et al. synthesized the (N, S) codoped TiO$_2$ with an anatase phase using a simple solvothermal treatment and investigated their visible light photocatalytic activity associated with the thermal behavior [257]. They found that the (N, S) codoped TiO$_2$ had better visible light photocatalytic activity and adsorptivity than the commercially available P25. The S dopants effectively assisted the surface reaction by adsorbing cations of organic dyes on the codoped TiO$_2$ surface. The N dopants formed a delocalized state in the bandgap, which led to the enhanced solution bulk reaction by increasing visible light absorbance (**Figure 4**).
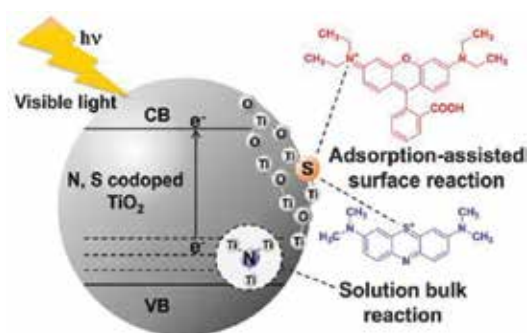
Figure 4. Schematic illustration of the suggested effects of N and S dopants on the enhanced visible light photocatalytic activity of TiO$_2$ [257].

It is noteworthy that (N, S) codoping can also effectively modulate the preferential growth plane of TiO$_2$ crystals. Xiang et al. prepared (N, S) codoped TiO$_2$ nanosheets with exposed {001} facets by a simple mixing-calcination method using the hydrothermally prepared TiO$_2$ nanosheets as a precursor and thiourea as a dopants [261]. The first-principles DFT proved that the electrons could be easily excited in the impurity states and then migrated between VB and intermediate. These resulted in stronger absorption with a red shift in the bandgap transition.

Recently, Samsudin et al. used (N, F) codoping to improve the intrinsic properties of the TiO$_2$ catalyst and found that the (N, F) codoping not only introduced activity in the visible light region but also improved the performances of intrinsic TiO$_2$ itself. The high activity could be attributed to the presence of N and F, which resulted in the change in the morphology and increasing presence of {001} facets [262]. Subsequently, a great number of experiments and theoretical calculations were carried out to further discuss (N, F) codoping in TiO$_2$ crystals [263–267]. Rahul and Sandhyarani synthesized three-dimensionally ordered (N, F) codoped

TiO$_2$ by templating with polystyrene colloidal photonic crystals using nitric acid and trifluoro-acetic acid as raw materials and found an obvious red shift due to (N, F) codoping [263]. Further investigation showed that the enhancement of photocatalytic activity could be attributed to the bandgap scattering effect and the slow photon effect, leading to a significant improvement in solar light harvesting.

(N, B) codoped TiO$_2$ is also an effective approach to improve photocatalytic activity [268–270]. Usually, N and B atoms are interstitial species connected to the same O lattice. The energy level of the [NOB] species is located close to edge of the VB and lies below the corresponding level of [N$_i$O]• because of the electrostatic stabilization. In other words, the photocatalytic activities are influenced not by [NOB] center but by [NOB]• center located at higher energy level. Moreover, the presence of N and B species can effectively narrow the bandgap and inhibit the transformation of anatase TiO$_2$ to rutile phase [269].

Other N-nonmetal codoping includes (N, C) codoping [271, 272] and (N, H) codoping [273, 274]. Liu et al. exploited (N, C) codoped porous TiO$_2$ nanofibers by a combination of electro-spinning and controlled calcination technologies [271]. The codoping of N and C in TiO$_2$ not only led to a shift of the absorption edge to lower energy by inducing new band levels but also created a large amount of single electron-trapped oxygen vacancies. Recently, Wei et al. demonstrated a new chemical approach to prepare black anatase TiO$_{2-x}$ and yellow anatase TiO$_2$ nanoparticles by doping with N and H [273]. The substitutional nonmetal doping of N and H, especially the *p* states of N, contributed to the bandgap narrowing by mixing with O 2*p* states and formed the new VB. Theoretical work suggested that the adequately high concentration of Ti^{3+} could induce a continuous oxygen vacancy of electronic states just below the CB edge of TiO$_2$, which strongly enhanced visible light absorption and the photocatalytic performance of the catalysts under visible light. The bandgap energy of the samples also decreased substantially, which was narrowed to about 2.0 eV.

5.1.2. C-nonmetal codoping

C-nonmetal codoping is also a kind of common approach to improve photocatalytic activity, such as (C, B) codoping [275, 276], (C, F) codoping [277], and (C, S) codoping [278].

Yu et al. investigated the geometry structures, formation energies, and electronic properties of the C, B and (C, B)-doped anatase TiO$_2$ using DFT calculations [275]. The results implied that (C, B)-codoped anatase TiO$_2$ could markedly influence the photocatalytic activity and light adsorption due to the change of the energy gaps (E_g) and Fermi levels (E_F). Moreover, the separation efficiency of carriers could be improved because of the existence of Ti^{3+} ions. Lin et al. systematically investigated the electronic and optical properties of several possible (C, B) codoped models of anatase and rutile TiO$_2$ using DFT calculations [276]. The further calculation indicated that B 2*p* and C 2*p* decreased the bandgap by about 0.8 eV and the couples of the two hybridized states could also result in a downward red shift for spectrum response.

Deng et al. prepared F-modified C-doped TiO$_2$ composites via a simple sol-gel method using NaF as the F source followed by heat treatment at 700°C in N atmosphere [277]. The C atoms and F species interacted in the TiO$_2$ lattice and resulted in the narrowed bandgap (2.50 eV),

which could inhibited the recombination of photo-induced irradiation and resulted in a superior photocatalytic activity.

5.1.3. Other nonmetal-nonmetal codoping

Except for the above N-nonmetal codoping and C-nonmetal codoping, other nonmetal atoms, including (B, P) codoping [279], (B, F) codoping [280], and tridoping [281–284], are also investigated by many researchers. Yu et al. prepared a series of TiO$_2$ hollow sphere catalysts with or without nonmetal (B, P) dopants through a sol-gel process with styrene-methyl methacrylate copolymer microspheres as the template [279]. They found that both B and P dopants could also narrow the bandgap of the TiO$_2$ catalyst.

Recently, many researchers found that tridoping in TiO$_2$ crystals is an effectively supplemental tool. Ramanathan and Bansal synthesized (N, C, F) tridoped rutile TiO$_2$ nanorods that not only displayed enhanced photocatalytic performance in UV light but also allowed a significant level of visible light photocatalytic activity [281]. In visible light, pure TiO$_2$ only got 6% photodegradation of Congo red over 30 min, whereas (N, C, F) tridoped TiO$_2$ caused 56% dye degradation.

5.2. Metal-metal codoping

Although monometal doping can improve the bandgap structure, the serious recombination centers also deteriorate carrier transport due to its partially occupied impurity bands. Hence, many researchers want to improve carrier transport through codoping with two different metal elements, such as (Ti, Ni) codoping [285], (Ti, Fe) codoping [286], (Ag, W) codoping [287], (Ag, Zr) codoping [288], (Zn, Mn) codoping [289], (Cu, V) codoping [290], and (Fe, Ce) codoping [291].

Zhang et al. developed a novel Ni^{2+} and Ti^{3+} codoped porous anatase TiO$_2$ via a facile sol-gel technique combined with an *in situ* solid-state chemical reduction approach followed by mild calcinations (350°C) in Ar atmosphere [285]. The results showed that the doping of Ti^{3+} and Ni^{2+} species for TiO$_2$ could result in the tail states and significantly narrowed the bandgap of

Figure 5. Schematic diagram of the photocatalytic process for Ni^{2+} and Ti^{3+} codoped TiO$_2$ under visible light irradiation [285].

anatase TiO_2 due to the formation of midgap states. Namely, Ti^{3+} state below CB minimum and Ni^{2+} state above VB maximum would be helpful in light adsorption and slowed the carrier recombination (**Figure 5**). In other words, (Ti, Ni) codoped porous black anatase TiO_2 resulted higher photocatalytic performance for methyl orange and rhodamine B.

Chen et al. found that Fe^{3+}/Ti^{3+} codoping was also a good way to further improve Ti^{3+} self-doping TiO_2 photocatalyst [286]. Fe^{3+} doping could result in a blue shift for the VB edge by 1.0 eV. The synergistic effects between Ti^{3+} and Fe^{3+} dopants in the samples significantly narrowed the bandgap, leading to efficient photocatalytic performance in the visible light range.

Khan et al. synthesized (Ag, W) codoped TiO_2 with different W doping concentrations using the hydrothermal method [287]. The codoped TiO_2 displayed pure anatase phase with strong absorption in visible light region. Among all the codoped samples, the one with W doping concentration of 3.5 at.% possessed the best photocatalytic activity, which was attributed to the synergistic effect between the dopants and optimal doping concentration.

Benjwal and Kar investigated (Zn, Mn) codoped TiO_2 photocatalysts through varying dopant concentrations and found that the highest photocatalytic degradation of methyl blue was obtained with 1.0 at.% (Zn, Mn) codoped TiO_2 [289]. Further analysis showed that the incorporation of Zn^{2+} and Mn^{2+} ions into TiO_2 lattice caused a decrease of the energy bandgap due to the formation of impurity levels below VB, which resulted in an enhancement of light absorbance in the UV region. With further increasing codoping concentration, the density of new energy levels also increased, which ultimately enhanced the recombination possibilities of electron and holes because they could be easily trapped on these recombination centers.

Christoforidis and Fernández-García prepared two series of Cu^{2+} and V^{4+} codoped anatase TiO_2 samples using the microemulsion synthetic route by varying the metal/Ti ratio [290]. They found that isolated and highly dispersed Cu^{2+} and V^{4+} species favored the hole formation while at the same time decreased the amount of Ti^{3+} centers under irradiation. Therefore, it could be deduced that (Cu, V) codoping contributed to the better photocatalytic performance due to the faster carrier separation.

Visible light-sensitive Fe^{3+} and Ce^{4+} codoped nano-TiO_2 photocatalyst was also investigated by Jaimy et al. [291]. They concluded that Fe doping and Ce doping could improve the light adsorption through trapping carriers and bending the VB and CB, respectively. In other words, the recombination of photoexcited electrons and holes was obviously prevented. Consequently, the codoped TiO_2 compositions exhibited higher photocatalytic activity than that of pure TiO_2 and commercial Degussa P25 under visible light.

5.3. Nonmetal-metal doping

5.3.1. N-metal doping

Recently, many researches about metal and N comodified TiO_2 indicate that metal assist N doping into the lattice TiO_2 and enhanced the shift of absorption edge to the visible light range, such as La, Ti, Zn, W, Cu, Fe, Ni, V, Cr, Ce, and Mn. Usually, N doping can form new states lying just above the VB, whereas the metal ion incorporated into the lattice TiO_2 or dispersed

on the surface of TiO$_2$ can enhance the separation rate of photogenerated charges. Under visible light irradiation, the electron can be excited from the N impurity level to the metal ion impurity level or from the N impurity level to the CB or from the VB to the metal ion impurity level. This strategy has been extensively adopted to design visible-active photocatalysts with high efficiency.

Sun et al. [292] and Yu et al. [293] investigated the interaction between substitutional N and implanted La at the (101) and {001} facets of TiO$_2$ using first-principles DFT calculations and analyzed the origin of enhanced visible light photocatalytic activity of (N, La) codoped TiO$_2$. They found that substitutional probability of N atom obviously decreased due to La implantation. However, oxygen vacancies were greatly enhanced because of the synergistic effects of La doping and N doping. For the substitutional La/N codoped surface, the charge compensation between the substitutional La and substitutional N led to the formation of two isolated occupied N(s)-O π^* impurity levels in the gap, forming the acceptor-donor-acceptor compensation pair and providing a reasonable mechanism for the enhanced visible light photocatalytic activity of (N, La) codoped TiO$_2$ anatase.

Li et al. developed a facile solvothermal strategy to simultaneously realize N doping and Ti^{3+} self-doping in TiO$_2$ crystals [294]. N doping and concomitant Ti^{3+} incorporation accounted for the reduction of the bandgap and realized photocatalytic activity in the visible light region. In other words, the introduced Ti^{3+} ions could form a new sublevel state below the CB and thus generate more electrons and holes, which combined with the midgap state induced by N doping, synergistically reduced the bandgap to a lower level and finally improved the response to visible light. Consequently, (N, Ti) codoped hierarchical anatase TiO$_2$ catalysts manifested an excellent photocatalytic activity, deriving from its superior light harvesting ability, narrowing bandgap from the codoping strategy, enhancing adsorption capacity, and accelerating carrier transport rate.

A new type of (N, Zn) codoped TiO$_2$ photocatalyst was prepared by Wang et al. via a simple sol-gel technique, which exhibited a higher photocatalytic activity than pure TiO$_2$, N-doped TiO$_2$, and Sn-doped TiO$_2$ under both visible and UV light irradiation [295]. This implied that (N, Zn) codoping was a more efficient way to improve the photocatalytic activity than doping with just one type of ion. Hu et al. further confirmed the above results through nitridation and hydrogenation of a zinc titanium precursor [296].

(N, W) codoping is also an efficient way to improve the recombination of photogenerated carriers [297, 298]. Lai and Wu prepared (N, W) codoped TiO$_2$ nanobelt through a facile and low-temperature route followed by a subsequent calcination [297]. The achieved nanobelt film possessed a reduced bandgap of approximately 2.3 eV at approximately 2.6 at.% W and 3.1 at. % N. Moreover, the single N-doped, W-doped, and (N, W) codoped TiO$_2$ induced photodegradations of 88%, 73%, and 95% rhodamine B molecules, respectively. The higher activity of the (N, W) codoped TiO$_2$ further supported the positively synergetic effects arising from the codoping.

Recently, some researchers develop a novel (N, Cu) codoped TiO$_2$ photocatalysts and also find that the photocatalytic effect was good. For example, Wang et al. found that 7.7% of methyl

blue were adsorbed on the surface of (N, Cu) codoped TiO_2 nanosheet when the adsorption reached equilibrium in the dark, whereas 5.9% of methyl blue were adsorbed on the control sample [299]. The relatively low adsorption of methyl blue might be attributed to the low surface area of the N-doped TiO_2 nanosheet, and the slightly enhanced adsorption for (N, Cu) codoped TiO_2 nanosheet might be attributed to its modified surface by the Cu doping.

Zhang et al. prepared TiO_2 nanotubes codoped with Fe and N using a one-step hydrothermal method [300]. Compared to the commercial TiO_2 powders and pure TiO_2 nanotubes, (N, Fe) codoped TiO_2 nanotubes exhibited a stronger visible light absorption capability and an enhanced photocatalytic activity under visible light irradiation. The increase in photocatalytic activity could be ascribed to the narrowing of the bandgap and the promoted separation of the photogenerated electrons and holes. Fe^{3+} ions were thought to occupy the active sites on the surface of (N, Fe) codoped TiO_2 as recombination centers for the electrons and holes.

Other N and metal codoping also includes (N, Ni) codoping [301], (N, Bi) codoping [302], (N, V) codoping [303], and (N, Mo) codoping [304]. Liu et al. reported the facile synthesis of reduced (N, Ni) codoped TiO_2 nanotubes and their photocatalytic activity application [301]. The narrowed bandgap of TiO_2 due to the doping of N and Ni elements could enhance the light absorption effectively. The electrochemical characterization revealed that photo-induced carriers were more efficient charge separation and transportation in reduced (N, Ni) codoped TiO_2 nanotubes photoanodes.

5.3.2. S-metal codoping

Recently, S-metal codoping has also been widely researched, such as (S, Fe) codoping [305], (S, Mo) codoping [306], and (S, Cu) codoping [307]. He et al. found that S and Fe could be easily implanted into the lattice of TiO_2 via a precipitation method [305]. Compared to undoped TiO_2, (S, Fe) codoped TiO_2 showed a higher photocatalytic activity under both UV and visible light irradiation, and the optimal methyl blue degradation level was 96.92%.

Zhang also developed for the first time a one-step hydrothermal process to synthesize (S, Mo) codoped TiO_2 mesoporous nanospheres [306]. The photodegradation ability towards rhodamine B was 3.8 times higher than that of the only S-doped samples.

5.3.3. Other nonmetal-metal doping

(F, Ca) codoped TiO_2 also caused several beneficial effects, including the enhancement of surface acidity, creation of oxygen vacancies, and increase of active sites as well as an impurity energy state (2.0 eV) below the CB of TiO_2, which could shorten the excitation path of electrons and reduce the apparent bandgap [308]. The smaller crystal size caused by doping with Ca could exhibit more powerful redox ability and the efficient separation of photogenerated electron-hole pairs. This implied that (F, Ca) codoping might be a kind of efficient way to improve the photocatalytic activity of TiO_2.

(B,Co) codoped TiO_2 was also investigated by Jaiswal et al. via DFT calculations [309]. They found that B occupied the interstitial site at low concentration (1 at.%), whereas it occupied

substitutional O position as the concentration increased (2 and 3 at.%). Both these B-doped TiO$_2$ showed improved photocatalytic activity due to the formation of shallow energy level, whereas higher visible light absorption was achieved owing to the presence of two deep energy levels in the bandgap according to DFT calculations.

Recently, a series of tridoped has also been developed [310, 311]. For example, Li et al. prepared (Cu, Ce, B) tridoped TiO$_2$ nanotubes via a hydrothermal method assisted by cetyl trimethyl ammonium bromide [310]. They found that Cu, Ce, and B could be intercalated into the interlayer spacing of the nanotubes besides the substitution for the Ti^{4+} or O$_2^-$. The synergetic effect of narrowing the bandgap of (Cu, Ce, B) tridoping exhibited the highest photocatalytic activity, which greatly inhibited the recombination of electrons and holes and enhanced the concentration of photogenerated carriers.

Acknowledgements

Author details

Fei Huang[1,2,*], Aihua Yan[1,2] and Hui Zhao[2]

*Address all correspondence to: huangfei7804@163.com

1 Low Carbon Energy Institute, China University of Mining and Technology, Xuzhou, China

2 School of Materials Science and Engineering, China University of Mining and Technology, Xuzhou, China

References

[1] F. Spadavecchia, M. Ceotto, L. L. Presti, C. Aieta, I. Biraghi, D. Meroni, S. Ardizzone, G. Cappelletti. Second generation nitrogen doped titania nanoparticles: A comprehensive electronic and microstructural picture. Chin. J. Chem., 2014, 32, 1195–1213.

[2] N. Yamada, M. Suzumura, F. Koiwa, N. Negishi. Differences in elimination efficiencies of *Escherichia coli* in freshwater and seawater as a result of TiO_2 photocatalysis. Water Res., 2013, 47, 2770–2776.

[3] F. D. Angelis, C. D. Valentin, S. Fantacci, A. Vittadini, A. Selloni. Theoretical studies on anatase and less common TiO_2 phases: Bulk, surfaces, and nanomaterials. Chem. Rev., 2014, 114(19), 9708–9753.

[4] Z. Zheng, J. Zhao, Y. Yuan, H. Liu, D. Yang, S. Sarina, H. Zhang, E. R. Waclawika, H. Zhu. Tuning the surface structure of nitrogen-doped TiO_2 nanofibres—An effective method to enhance photocatalytic activities of visible-light-driven green synthesis and degradation. Chem. Eur. J., 2013, 19, 5731–5741.

[5] B. Zheng, Q. Guo, D. Wang, H. Zhang, Y. Zhu, S. Zhou. Energy-transfer modulation for enhanced photocatalytic activity of near-infrared upconversion photocatalyst. J. Am. Ceram. Soc., 2015, 98(1), 136–140.

[6] L. Liu, X. B. Chen. Titanium dioxide nanomaterials: Self-structural modifications. Chem. Rev., 2014, 114, 9890–9918.

[7] F. Zuo, K. Bozhilov, R. J. Dillon, L. Wang, P. Smith, X. Zhao, C. Bardeen, P. Y. Feng. Active facets on titanium (III)-doped TiO_2: An effective strategy to improve the visible-light photocatalytic activity. Angew. Chem. Int. Ed., 2012, 124, 6327–6330.

[8] M. Xing, X. Li, J. Zhang. Synergistic effect on the visible light activity of Ti^{3+} doped TiO_2 nanorods/boron doped graphene composite. Sci. Rep., 2014, 4, 5493–5499.

[9] S. X. Liu, J. L. Liu, X. S. Li, X. Zhu, A. M. Zhu. Gliding arc plasma synthesis of visible-light active C-doped titania photocatalysts. Plasma Process. Polym., 2015, 12, 422–430.

[10] R. Marschall, L. Wang. Non-metal doping of transition metal oxides for visible-light photocatalysis. Catal. Today, 2014, 225(15), 111–135.

[11] M. Li, S. Zhang, Y. Peng, L. Lv, B. Pan. Enhanced visible light responsive photocatalytic activity of TiO_2-based nanocrystallites: Impact of doping sequence. RSC Adv., 2015, 5, 7363–7369.

[12] K. Song, X. Han, G. Shao. Electronic properties of rutile TiO_2 doped with $4d$ transition metals: First-principles study. J. Alloy Compd., 2013, 551, 118–124.

[13] X. Yu, T. Hou, X. Sun, Y. Li. The influence of defects on Mo-doped TiO_2 by first-principles studies. Chem. Phys. Chem., 2012, 13, 1514–1521.

[14] F. D. Angelis, S. Fantacci, A. Selloni, M. Grätzel, M. K. Nazeeruddin. Influence of the sensitizer adsorption mode on the open-circuit potential of dye-sensitized solar cells. Nano Lett., 2007, 7, 3189–3195.

[15] M. Borlaf, M. T. Colomer, A. de Andrés, F. Cabello, R. Serna, R. Moreno. TiO_2/Eu^{3+} thin films with high photoluminescence emission prepared by electrophoretic deposition from nanoparticulate sols. Eur. J. Inorg. Chem., 2014, 5152–5159.

[16] N. Umezawa, J. Ye. Role of complex defects in photocatalytic activities of nitrogen-doped anatase TiO$_2$. Phys. Chem. Chem. Phys., 2012, 14, 5924–5934.

[17] H. Lin, L. Li, M. Zhao, X. Huang, X. Chen, G. Li, R. Yu. Synthesis of high-quality brookite TiO$_2$ single-crystalline nanosheets with specific facets exposed: Tuning catalysts from inert to highly reactive. J. Am. Chem. Soc., 2012, 134, 8328–8331.

[18] M. Zhao, H. Xu, H. Chen, S. Ouyang, N. Umezawa, D. Wang, J. Ye. Photocatalytic reactivity of {121} and {211} facets of brookite TiO$_2$ crystals. J. Mater. Chem. A, 2015, 3, 2331–2337.

[19] C. C. Mao, H. S. Weng. Effect of heat treatment on photocatalytic activity of titania incorporated with carbon black for degradation of methyl orange. Environ. Prog. Sustain. Energ., 2012, 31(2), 306–317.

[20] M. L. Satuf, R. J. Brandi, A. E. Cassano, O. M. Alfano. Photocatalytic degradation of 4-chlorophenol: A kinetic study. Appl. Catal. B Environ., 2008, 82(1), 37–49.

[21] X. Jiang, Y. Zhang, J. Jiang, Y. Rong, Y. Wang, Y. Wu, C. Pan. Characterization of oxygen vacancy associates within hydrogenated TiO$_2$: A positron annihilation study. J. Phys. Chem. C, 2012, 116, 22619–22624.

[22] A. Eslami, M. M. Amini, A. R. Yazdanbakhshc, A. Mohseni-Bandpei, A. A. Safari, A. Asadi. N, S co-doped TiO$_2$ nanoparticles and nanosheets in simulated solar light for photocatalytic degradation of non-steroidal anti-inflammatory drugs in water: A comparative study. J. Chem. Technol. Biot., 2016, doi: 10.1002/jctb.4877.

[23] I. N. Martyanov, S. Uma, S. Rodrigues, K. J. Klabunde. Structural defects cause TiO$_2$-based photocatalysts to be active in visible light. Chem. Commun., 2004, 21, 2476–2477.

[24] A. Naldoni, M. Allieta, S. Santangelo, M. Marelli, F. Fabbri, S. Cappelli, C. L. Bianchi, R. Psaro, V. D. Santo. Effect of nature and location of defects on bandgap narrowing in black TiO$_2$ nanoparticles. J. Am. Chem. Soc., 2012, 134, 7600–7603.

[25] J. Cai, Z. Huang, K. Lv, J. Sun, K. Deng. Ti powder-assisted synthesis of Ti^{3+} self-doped TiO$_2$ nanosheets with enhanced visible-light photoactivity. RSC Adv., 2014, 4, 19588–19593.

[26] G. Li, Z. Lian, X. Li, Y. Xu, W. Wang, D. Zhang, F. Tian, H. Li. Ionothermal synthesis of black Ti^{3+}-doped single-crystal TiO$_2$ as an active photocatalyst for pollutant degradation and H$_2$ generation. J. Mater. Chem. A, 2015, 3, 3748–3756.

[27] J. Huo, Y. Hu, H. Jiang, C. Li. *In situ* surface hydrogenation synthesis of Ti^{3+} self-doped TiO$_2$ with enhanced visible light photoactivity. Nanoscale, 2014, 6, 9078–9084.

[28] Z. Zheng, B. Huang, X. Meng, J. Wang, S. Wang, Z. Lou, Z. Wang, X. Qin, X. Zhang, Y. Dai. Metallic zinc-assisted synthesis of Ti^{3+} self-doped TiO$_2$ with tunable phase composition and visible-light photocatalytic activity. Chem. Commun., 2013, 49, 868–870.

[29] I. Justicia, P. Ordejon, G. Canto, J. L. Mozos, J. Fraxedas, G. A. Battiston, R. Gerbasi, A. Figueras. Designed self-doped titanium oxide thin films for efficient visible-light potocatalysis. Adv. Mater., 2002, 14, 1399–1402.

[30] F. Zuo, L. Wang, T. Wu, Z. Zhang, D. Borchardt, P. Feng. Self-doped Ti^{3+} enhanced photocatalytic for hydrogen production under visible light. J. Am. Chem. Soc., 2010, 132(34), 11856–11857.

[31] G. Lu, A. Linsebigler, J. T. Yates. Ti^{3+} defect sites on TiO_2(110): Production and chemical detection of active sites. J. Phys. Chem., 1994, 98(45), 11733–11738.

[32] G. D. Bromiley, A. A. Shiryaev. Neutron irradiation and post-irradiation annealing of rutile (TiO_{2-x}): Effect on hydrogen incorporation and optical absorption. Phys. Chem. Miner., 2006, 33(6), 426–434.

[33] X. Q. Chen, H. B. Liu, G. B. Gu. Preparation of nanometer crystalline TiO_2 with high photocatalytic activity by pyrolysis of titanyl organic compounds and photocatalytic mechanism. Mater. Chem. Phys., 2005, 91(2–3), 317–324.

[34] X. Wang, Y. Li, X. Liu, S. Gao, B. Huang, Y. Dai. Preparation of Ti^{3+} self-doped TiO_2 nanoparticles and their visible light photocatalytic activity. Chin. J. Catal., 2015, 36, 389–399.

[35] B. Qiu, Y. Zhou, Y. Ma, X. Yang, W. Sheng, M. Xing, J. Zhang. Facile synthesis of the Ti^{3+} self-doped TiO_2-graphene nanosheet composites with enhanced photocatalysis. Sci. Rep., 2015, 5, 8591.

[36] R. Fu, S. Gao, H. Xu, Q. Wang, Z. Wang, B. Huang, Y. Dai. Fabrication of Ti^{3+} self-doped TiO_2(A) nanoparticle/TiO_2(R) nanorod heterojunctions with enhanced visible-light-driven photocatalytic properties. RSC Adv., 2014, 4, 37061–37069.

[37] X. Liu, S. Gao, H. Xu, Z. Lou, W. Wang, B. Huang, Y. Dai. Green synthetic approach for Ti^{3+} self-doped TiO_{2-x} nanoparticles with efficient visible light photocatalytic activity. Nanoscale, 2013, 5, 1870–1875.

[38] X. Xin, T. Xu, J. Yin, L. Wang, C. Wang. Management on the location and concentration of Ti^{3+} in anatase TiO_2 for defects-induced visible-light photocatalysis. Appl. Catal. B Environ., 2015, 176–177, 354–362.

[39] A. Sirisuk, E. Klansorn, P. Praserthdam. Effects of reaction medium and crystallite size on Ti^{3+} surface defects in titanium dioxide nanoparticles prepared by solvothermal method. Catal. Commun., 2008, 9(9), 1810–1814.

[40] L. Si, Z. Huang, K. Lv, D. Tang, C. Yang. Facile preparation of Ti^{3+} self-doped TiO_2 nanosheets with dominant {001} facets using zinc powder as reductant. J. Alloy Compd., 2014, 601, 88–93.

[41] X. Liu, H. Xu, L. R. Grabstanowicz, S. Gao, Z. Lou, W. Wang, B. Huang, Y. Dai, T. Xu. Ti^{3+} self-doped TiO$_{2-x}$ anatase nanoparticles via oxidation of TiH$_2$ in H$_2$O$_2$. Catal. Today, 2014, 225, 80–89.

[42] L. R. Grabstanowicz, S. Gao, T. Li, R. M. Rickard, T. Rajh, D. J. Liu, T. Xu. Facile oxidative conversion of TiH$_2$ to high-concentration Ti^{3+}-self-doped rutile TiO$_2$ with visible-light photoactivity. Inorg. Chem., 2013, 52(7), 3884–3890.

[43] J. Tian, X. Hu, H. Yang, Y. Zhou, H. Cui, H. Liu. High yield production of reduced TiO$_2$ with enhanced photocatalytic activity. Appl. Surf. Sci., 2016, 360, 768–743.

[44] C. Mao, F. Zuo, Y. Hou, X. Bu, P. Feng. *In situ* preparation of a Ti^{3+} self-doped TiO$_2$ film with enhanced activity as photoanode by N$_2$H$_4$ reduction. Angew. Chem. Int. Ed., 2014, 53, 10485–10489.

[45] M. Wen, S. Zhang, W. Dai, G. Li, D. Zhang. *In situ* synthesis of Ti^{3+} self-doped meso-porous TiO$_2$ as a durable photocatalyst for environmental remediation. Chin. J. Catal., 2015, 36(12), 2095–2102.

[46] Z. He, W. Que, H. Xie, J. Chen, Y. Yuan, P. Sun. Facile synthesis of self-sensitized TiO$_2$ photocatalysts and their higher photocatalytic activity. J. Am. Ceram. Soc., 2012, 95(12), 3941–3946.

[47] Q. Guo, C. Zhou, Z. Ma, Z. Ren, H. Fan, X. Yang. Elementary photocatalytic chemistry on TiO$_2$ surfaces. Chem. Soc. Rev., 2016, DOI: 10.1039/c5cs00448a.

[48] S. Wang, X. Yang, Y. Wang, L. Liu, Y. Guo, H. Guo. Morphology-controlled synthesis of Ti^{3+} self-doped yolk–shell structure titanium oxide with superior photocatalytic activity under visible light. J. Solid State Chem., 2014, 213, 98–103.

[49] T. C. Lu, S. Y. Wu, L. B. Lin, W. C. Zheng. Defects in the reduced rutile single crystal. Physica B, 2001, 304(1–4), 147–151.

[50] W. A. Weyl, T. Forland. Photochemistry of rutile. Ind. Eng. Chem., 1950, 42(2), 257–263.

[51] L. B. Xiong, J. L. Li, B. Yang, Y. Yu. Ti^{3+} in the surface of titanium dioxide: Generation, properties and photocatalytic application. J. Nanomater., 2012, 2012, 1–13.

[52] A. S. Bolokang, D. E. Motaung, C. J. Arendse, T. F. G. Muller. Morphology and structural development of reduced anatase-TiO$_2$ by pure Ti powder upon annealing and nitrida-tion: Synthesis of TiO$_x$ and TiO$_x$N$_y$ powders. Mater. Charact., 2015, 100, 41–49.

[53] J. Zhang, W. Fu, J. Xi, H. He, S. Zhao, H. Lu, Z. Ji. N-doped rutile TiO$_2$ nano-rods show tunable photocatalytic selectivity. J. Alloy Compd., 2013, 575, 40–47.

[54] J. Lynch, C. Giannini, J. K. Cooper, A. Loiudice, I. D. Sharp, R. Buonsanti. Substitutional or interstitial site-selective nitrogen doping in TiO$_2$ nanostructures. J. Phys. Chem. C, 2015, 119(13), 7443–7452.

[55] S. M. El-Sheikh, G. Zhang, H. M. El-Hosainy, A. A. Ismail, K. E. O'Shea, P. Falaras, A. G. Kontos, D. D. Dionysiou. High performance sulfur, nitrogen and carbon doped

mesoporous anatase-brookite TiO_2 photocatalyst for the removal of microcystin-LR under visible light irradiation. J. Hazard. Mater., 2014, 280, 723–733.

[56] J. Yu, G. Dai, Q. Xiang, M. Jaroniec. Fabrication and enhanced visible-light photocatalytic activity of carbon self-doped TiO_2 sheets with exposed {001} facets. J. Mater. Chem., 2011, 21(4), 1049–1057.

[57] V. Štengl, V. Houšková, S. Bakardjieva, N. Murafa. Photocatalytic activity of boron-modified titania under UV and visible-light illumination. ACS Appl. Mater. Inter., 2010, 2(2), 575–580.

[58] X. Wang, M. Blackford, K. Prince, R. A. Caruso. Preparation of boron-doped porous titania networks containing gold nanoparticles with enhanced visible-light photocatalytic activity. ACS Appl. Mater. Inter., 2012, 4(1), 476–482.

[59] N. Patel, A. Dashora, R. Jaiswal, R. Fernandes, M. Yadav, D. C. Kothari, B. L. Ahuja, A. Miotello. Experimental and theoretical investigations on the activity and stability of substitutional and interstitial boron in TiO_2 photocatalyst. J. Phys. Chem. C, 2015, 119(32), 18581–18590.

[60] Z. Li, R. Wnetrzak, W. Kwapinski, J. J. Leahy. Synthesis and characterization of sulfated TiO_2 nanorods and ZrO_2/TiO_2 nanocomposites for the esterification of biobased organic acid. ACS Appl. Mater. Inter., 2012, 4, 4499–4505.

[61] D. Tipayarom, K. Wantala, N. Grisdanurak. Optimization of alachlor degradation on S-doped TiO_2 by sonophotocatalytic activity under visible light. Fresen. Environ. Bull., 2011, 20(6), 1425–1431.

[62] M. Senna, V. Šepelák, J. Shi, B. Bauer, A. Feldhoff, V. Laporte, K. D. Becker. Introduction of oxygen vacancies and fluorine into TiO_2 nanoparticles by co-milling with PTFE. J. Solid State Chem., 2012, 187, 51–57.

[63] A. Kafizas, N. Noor, P. Carmichael, D. O. Scanlon, C. J. Carmalt, I. P. Parkin. Combinatorial atmospheric pressure chemical vapor deposition of $F:TiO_2$: The relationship between photocatalysis and transparent conducting oxide properties. Adv. Funct. Mater., 2014, 24, 1758–1771.

[64] Z. Qiao, S. S. Brown, J. Adcock, G. M. Veith, J. C. Bauer, E. A. Payzant, R. R. Unocic, S. Dai. A topotactic synthetic methodology for highly fluorine-doped mesoporous metal oxides. Angew. Chem. Int. Ed., 2012, 51, 2888–2893.

[65] P. L. Ji, X. Z. Kong, J. G. Wang, X. L. Zhu. Characterization and photocatalytic properties of silver and silver chloride doped TiO_2 hollow nanoparticles. Chin. Chem. Lett., 2012, 23(12), 1399–1402.

[66] H. Xu, Z. Zheng, L. Zhang, H. Zhang, F. Deng. Hierarchical chlorine-doped rutile TiO_2 spherical clusters of nanorods: Large-scale synthesis and high photocatalytic activity. J. Solid State Chem., 2008, 181(9), 2516–2522.

[67] R. Asahi, T. Morikawa, T. Ohwaki, K. Aoki, Y. Taga. Visible-light photocatalysis in nitrogen-doped titanium oxides. Science, 2001, 293, 269–271.

[68] B. Viswanathan, K. R. Krishanmurthy. Nitrogen incorporation in TiO$_2$: Does it make a visible light photo-active material? Int. J. Photoenergy, 2012, 2012, 1–10.

[69] M. Khan, S. R. Gul, J. Li, W. Cao. Variations in the structural, electronic and optical properties of N-doped TiO$_2$ with increasing N doping concentration. Mod. Phys. Lett. B, 2015, 29, 1550022.

[70] A. Manole, V. Dₒsčaleanu, M. Dobromir, D. Luca. Combining degradation and contact angle data in assessing the photocatalytic TiO$_2$:N surface. Surf. Interface Anal., 2010, 42(6–7), 947–954.

[71] J. Zhang, Y. Wu, M. Xing, S. Leghari, S. Sajjad. Development of modified N doped TiO$_2$ photocatalyst with metals, nonmetals and metal oxides. Energ. Environ. Sci., 2010, 3(6), 715–726.

[72] J. Xu, Y. Ao, M. Chen, D. Fu. Photoelectrochemical property and photocatalytic activity of N-doped TiO$_2$ nanotube arrays. Appl. Surf. Sci., 2010, 256(13), 4397–401.

[73] Z. Lin, A. Orlov, R. M. Lambert, M. C. Payne. New insights into the origin of visible light photocatalytic activity of nitrogen-doped and oxygen-deficient anatase TiO$_2$. J. Phys. Chem. B, 2005, 109, 20948–20952.

[74] E. M. Samsudin, S. B. A. Hamid, J. C. Juan, W. J. Basirun, A. E. Kandjani, S. K. Bhargava. Controlled nitrogen insertion in titanium dioxide for optimal photocatalytic degrada-tion of atrazine. RSC Adv., 2015, 5, 44041–44052.

[75] H. Y. Ai, J. W. Shi, R. X. Duan, J. W. Chen, H. J. Cui, M. L. Fu. Sol-gel to prepare nitrogen doped TiO$_2$ nanocrystals with exposed {001} facets and high visible-light photocatalytic performance. Int. J. Photoenergy, 2014, 2014, 1–9.

[76] J. Shi, S. Chen, S. Wang, Z. Ye. Sol-gel preparation and visible light photocatalytic activity of nitrogen doped titania. Procedia Eng., 2012, 27, 564–569.

[77] Q. Gao, Z. Li, M. Li, Y. Liu, C. Song, G. Han. Microstructure and properties of N-doped TiO$_2$ films grown by dielectric barrier discharge enhanced chemical vapor deposition. J. Mater. Sci. Eng., 2012, 30(1), 93–97.

[78] C. Sarantopoulos, A. N. Gleizes, F. Maury. Chemical vapor deposition and character-ization of nitrogen doped TiO$_2$ thin films on glass substrates. Thin Solid Films, 2009, 518(4), 1299–1303.

[79] K. I. Liu, C. Y. Su, T. P. Perng. Highly porous N-doped TiO$_2$ hollow fibers with internal three-dimensional interconnected nanotubes for photocatalytic hydrogen production. RSC Adv., 2015, 5, 88367–88374.

[80] H. E. Cheng, Y. R. Chen, W. T. Wu, C. M. Hsu. Effect of nitrogen doping concentration on the properties of TiO$_2$ films grown by atomic layer deposition. Mater. Sci. Eng. B, 2011, 176(7), 596–599.

[81] L. Tian, A. Soum-Glaude, F. Volpi, L. Salvo, G. Berthomé, S. Coindeau, A. Mantoux, R. Boichot, S. Lay, V. Brizé, E. Blanquet, G. Giusti, D. Bellet. Undoped TiO$_2$ and nitrogen-doped TiO$_2$ thin films deposited by atomic layer deposition on planar and architectured surfaces for photovoltaic applications. J. Vac. Sci. Technol. A, 2015, 33, 01A141.

[82] D. H. Wang, L. Jia, X. L. Wu, L. Q. Lu, A. W. Xu. One-step hydrothermal synthesis of N-doped TiO$_2$/C nanocomposites with high visible light photocatalytic activity. Nanoscale, 2012, 4, 576–584.

[83] B. Buchholcz, H. Haspel, Á. Kukovecz, Z. Kónya. Low-temperature conversion of titanate nanotubes into nitrogen-doped TiO$_2$ nanoparticles. CrystEngComm, 2014, 16, 7486–7492.

[84] X. Zhang, X. Cui. Facile synthesis of flowery N-doped titanates with enhanced adsorption and photocatalytic performances. RSC Adv., 2014, 4, 60907–60913.

[85] Z. Li, Z. Ren, Y. Qu, S. Du, J. Wu, L. Kong, G. Tian, W. Zhou, H. Fu. Hierarchical N-doped TiO$_2$ microspheres with exposed (001) facets for enhanced visible light catalysis. Eur. J. Inorg. Chem., 2014, 2146–2152.

[86] J. H. Pan, G. Han, R. Zhou, X. S. Zhao. Hierarchical N-doped TiO$_2$ hollow microspheres consisting of nanothorns with exposed anatase {101} facets. Chem. Commun., 2011, 47, 6942–6944.

[87] Q. Xiang, J. Yu, W. Wang, M. Jaroniec. Nitrogen self-doped nanosized TiO$_2$ sheets with exposed {001} facets for enhanced visible-light photocatalytic activity. Chem. Commun., 2011, 47, 6906–6908.

[88] X. Zhou, F. Peng, H. Wang, H. Yu, Y. Fang. A simple preparation of nitrogen doped titanium dioxide nanocrystals with exposed (001) facets with high visible light activity. Chem. Commun., 2012, 48, 600–602.

[89] Y. Luan, L. Jing, M. Xie, X. Shi, X. Fan, Y. Cao, Y. Feng. Synthesis of efficient N-containing TiO$_2$ photocatalysts with high anatase thermal stability and the effects of the nitrogen residue on the photoinduced charge separation. Phys. Chem. Chem. Phys., 2012, 14, 1352–1359.

[90] X. Cheng, X. Yu, Z. Xing. Characterization and mechanism analysis of N doped TiO$_2$ with visible light response and its enhanced visible activity. Appl. Surf. Sci., 2012, 258, 3244–3248.

[91] H. Zeng, J. Xie, H. Xie, B. L. Su, M. Wang, H. Ping, W. Wang, H. Wang, Z. Fu. Bioprocess-inspired synthesis of hierarchically porous nitrogen-doped TiO$_2$ with high visible-light photocatalytic activity. J. Mater. Chem. A, 2015, 3, 19588–19596.

[92] K. Siuzdak, M. Szkoda, M. Sawczaka, A. Lisowska-Oleksiak. Novel nitrogen precursors for electrochemically driven doping of titania nanotubes exhibiting enhanced photo-activity. N. J. Chem., 2015, 39, 2741–2751.

[93] S. Li, S. Lin, J. Liao, N. Pan, D. Li, J. Li. Nitrogen-doped TiO$_2$ nanotube arrays with enhanced photoelectrochemical property. Int. J. Photoenergy, 2012, 2012, 1–7.

[94] I. Hanzu, T. Djenizian, P. Knauth. Electrical and point defect properties of TiO$_2$ nanotubes fabricated by electrochemical anodization. J. Phys. Chem. C, 2011, 115(13), 5989–5996.

[95] H. Feng, P. Z. Si, Y. C. Shi, C. H. Jin, X. L. Zhang, J. J. Liu, S. J. Yu, G. H. Zhang, H. L. Ge. Structure and photocatalytic properties of N-doped TiO$_{2-x}$ films prepared by N-ion implantation. Surf. Rev. Lett., 2013, 20, 1350059.

[96] P. Sudhagar, K. Asokan, E. Ito, Y. S. Kang. N-ion-implanted TiO$_2$ photoanodes in quantum dot-sensitized solar cells. Nanoscale, 2012, 4(7), 2416–2422.

[97] K. Sivaranjani, C. S. Gopinath. Porosity driven photocatalytic activity of wormhole mesoporous TiO$_{2-x}$N$_x$ in direct sunlight. J. Mater. Chem., 2011, 21, 2639–2647.

[98] J. Huo, Y. Hu, H. Jiang, X. Hou, C. Li. Continuous flame synthesis of near surface nitrogen doped TiO$_2$ for dye-sensitized solar cells. Chem. Eng. J., 2014, 258, 163–170.

[99] R. A. R. Monteiro, S. M. Miranda, V. J. P. Vilar, L. M. Pastrana-Martínez, P. B. Tavares, R. A. R. Boaventura, J. L. Faria, E. Pinto, A. M. T. Silva. N-modified TiO$_2$ photocatalytic activity towards diphenhydramine degradation and *Escherichia coli* inactivation in aqueous solutions. Appl. Catal. B Environ., 2015, 162, 66–74.

[100] Y. C. Tang, X. H. Huang, H. Q. Yu, L. H. Tang. Nitrogen-doped photocatalyst prepared by mechanochemical method: Doping mechanisms and visible photoactivity of pollutant degradation. Int. J. Photoenergy, 2012, 2012, 1–10.

[101] R. Rattanakam, S. Supothina. Visible-light-sensitive N-doped TiO$_2$ photocatalysts prepared by a mechanochemical method: Effect of a nitrogen source. Res. Chem. Intermediat., 2009, 35(3), 263–269.

[102] L. Hu, J. Wang, J. Zhang, Q. Zhang, Z. Liu. An N-doped anatase/rutile TiO$_2$ hybrid from low-temperature direct nitridization: Enhanced photoactivity under UV-/visible-light. RSC Adv., 2014, 4, 420–427.

[103] H. H. H. Lin, A. Y. C. Lin, C. L. Hung. Photocatalytic oxidation of cytostatic drugs by microwave-treated N-doped TiO$_2$ under visible light. J. Chem. Technol. Biotechnol., 2015, 90, 1345–1354.

[104] G. Abadias, F. Paumier, D. Eyidi, P. Gúerin, T. Girardeau. Structure and properties of nitrogen-doped titanium dioxide thin films produced by reactive magnetron sputter-ing. Surf. Interface Anal., 2010, 42, 970–973.

[105] S. Cao, B. Liu, L. Fan, Z. Yue, B. Liu, B. Cao. Highly antibacterial activity of N-doped TiO$_2$ thin films coated on stainless steel brackets under visible light irradiation. Appl. Surf. Sci., 2014, 309, 119–127.

[106] S. J. Ha, D. H. Kim, J. H. Moon. N-doped mesoporous inverse opal structures for visible-light photocatalysts. RSC Adv., 2015, 5, 77716–77722.

[107] Y. Chen, X. Cao, B. Lin, B. Gao. Origin of the visible-light photoactivity of NH$_3$-treated TiO$_2$: Effect of nitrogen doping and oxygen vacancies. Appl. Surf. Sci., 2013, 264, 845–852.

[108] G. Wang, X. Xiao, W. Li, Z. Lin, Z. Zhao, C. Chen, C. Wang, Y. Li, X. Huang, L. Miao, C. Jiang, Y. Huang, X. Duan. Significantly enhanced visible light photoelectrochemical activity in TiO$_2$ nanowire arrays by nitrogen implantation. Nano Lett., 2015, 15(7), 4692–4698.

[109] X. Jiang, Y. Wang, C. Pan. High concentration substitutional N-doped TiO$_2$ film: Preparation, characterization, and photocatalytic property. J. Am. Ceram. Soc., 2011, 94(11), 4078–4083.

[110] C. D. Valentin, G. Pacchioni, A. Selloni, S. Livraghi, E. Giamello. Characterization of paramagnetic species in N-doped TiO$_2$ powders by EPR spectroscopy and DFT calculations. J. Phys. Chem. B, 2005, 109, 11414–11419.

[111] H. Gao, J. Zhou, D. Dai, Y. Qu. Photocatalytic activity and electronic structure analysis of N-doped anatase TiO$_2$: A combined experimental and theoretical study. Chem. Eng. Technol., 2009, 32(6), 867–872.

[112] A. V. Emeline, V. N. Kuznetsov, V. K. Rybchuk, N. Serpone. Visible-light-active titania photocatalysts: The case of N-doped TiO$_2$—Properties and some fundamental issues. Int. J. Photoenergy, 2008, 2008, 258394.

[113] H. M. Yates, M. G. Nolan, D. W. Sheel, M. E. J. Pemble. The role of nitrogen doping on the development of visible light-induced photocatalytic activity in thin TiO$_2$ films grown on glass by chemical vapour deposition. J. Photochem. Photobiol. A, 2006, 179, 213–223.

[114] L. Gai, X. Duan, H. Jiang, Q. Mei, G. Zhou, Y. Tian, H. Liu. One-pot synthesis of nitrogen-doped TiO$_2$ nanorods with anatase/brookite structures and enhanced photocatalytic activity. CrystEngComm, 2012, 14, 7662–7671.

[115] H. Irie, Y. Watanabe, K. Hashimoto. Nitrogen dependence on photocatalytic activity of TiO$_{2-x}$N$_x$ powders. J. Phys. Chem. B, 2003, 107, 5483–5486.

[116] Y. T. Lin, C. H. Weng, Y. H. Lin, C. C. Shiesh, F. Y. Chen. Effect of C content and calcination temperature on the photocatalytic activity of C-doped TiO$_2$ catalyst. Sep. Purif. Technol., 2013, 116, 114–123.

[117] V. Etacheri, G. Michlits, M. K. Seery, S. J. Hinder, S. C. Pillai. A highly efficient TiO$_{2-x}$C$_x$ nano-heterojunction photocatalyst for visible light induced antibacterial applications. ACS Appl. Mater. Inter., 2013, 5(5), 1663–1672.

[118] F. Cuomo, F. Venditti, A. Ceglie, A. D. Leonardis, V. Macciola, F. Lopez. Cleaning of olive mill wastewaters by visible light activated carbon doped titanium dioxide. RSC Adv., 2015, 5, 85586–85591.

[119] S. U. Khan, M. Al-Shahry, W. B. Ingler. Efficient photochemical water splitting by a chemically modified n-TiO$_2$. Science 2002, 297, 2243–2245.

[120] J. W. Shi, C. Liu, C. He, J. Li, C. Xie, S. Yang, J. W. Chen, S. Li, C. Niu. Carbon-doped titania nanoplates with exposed {001} facets: Facile synthesis, characterization and visible-light photocatalytic performance. RSC Adv., 2015, 5, 17667–17675.

[121] Y. Zhang, Z. Zhao, J. Chen, L. Cheng, J. Chang, W. Sheng, C. Hu, S. Cao. C-doped hollow TiO$_2$ spheres: *In situ* synthesis, controlled shell thickness, and superior visible-light photocatalytic activity. Appl. Catal. B Environ., 2015, 165, 715–722.

[122] P. Shao, J. Tian, Z. Zhao, W. Shi, S. Gao, F. Cui. Amorphous TiO$_2$ doped with carbon for visible light photodegradation of rhodamine B and 4-chlorophenol. Appl. Surf. Sci., 2015, 324, 35–43.

[123] L. Zhang, M. S. Tse, O. K. Tan, Y. X. Wang, M. Han. Facile fabrication and characterization of multi-type carbon-doped TiO$_2$ for visible light-activated photocatalytic mineralization of gaseous toluene. J. Mater. Chem. A, 2013, 1, 4497–4507.

[124] Y. Yang, D. Ni, Y. Yao, Y. Zhong, Y. Ma, J. Yao. High photocatalytic activity of carbon doped TiO$_2$ prepared by fast combustion of organic capping ligands. RSC Adv., 2015, 5, 93635–93643.

[125] J. Liu, Q. Zhang, J. Yang, H. Ma, M. O. Tade, S. Wang, J. Liu. Facile synthesis of carbon-doped mesoporous anatase TiO$_2$ for the enhanced visible-light driven photocatalysis. Chem. Commun., 2014, 50, 13971–13974.

[126] Y. Y. Sun, S. Zhang. Kinetics stabilized doping: Computational optimization of carbon-doped anatase TiO$_2$ for visible-light driven water splitting. Phys. Chem. Chem. Phys., 2016, 18(4), 2776–2783.

[127] G. Liu, C. Sun, S. C. Smith, L. Wang, G. Q. Lu, H. M. Cheng. Sulfur doped anatase TiO$_2$ single crystals with a high percentage of {001} facets. J. Colloid Interf. Sci., 2010, 349(2), 477–483.

[128] P. Goswami, J. N. Ganguli. A novel synthetic approach for the preparation of sulfated titania with enhanced photocatalytic activity. RSC Adv., 2013, 3, 8878–8888.

[129] N. Li, X. Zhang, W. Zhou, Z. Liu, G. Xie, Y. Wang, Y. Du. High quality sulfur-doped titanium dioxide nanocatalysts with visible light photocatalytic activity from non-hydrolytic thermolysis synthesis. Inorg. Chem. Front., 2014, 1, 521–525.

[130] P. V. R. K. Ramacharyulu, D. B. Nimbalkar, J. P. Kumar, G. K. Prasad, S. C. Ke. N-doped, S-doped TiO$_2$ nanocatalysts: Synthesis, characterization and photocatalytic activity in the presence of sunlight. RSC Adv., 2015, 5, 37096–37101.

[131] Y. H. Lin, S. H. Chou, H. Chu. A kinetic study for the degradation of 1,2-dichloroethane by S-doped TiO$_2$ under visible light. J. Nanopart. Res., 2014, 16(8), 1016–1030.

[132] N. Sharotri, D. Sud. A greener approach to synthesize visible light responsive nano-porous S-doped TiO$_2$ with enhanced photocatalytic activity. N. J. Chem., 2015, 39, 2217–2223.

[133] J. H. Pan, Z. Cai, Y. Yu, X. S. Zhao. Controllable synthesis of mesoporous F-TiO$_2$ spheres for effective photocatalysis. J. Mater. Chem., 2011, 21, 11430–11438.

[134] D. Lozano, J. M. Hernández-López, P. Esbrit, M. A. Arenas, E. Gómez-Barrena, J. de Damborenea, J. Esteban, C. Pérez-Jorge, R. Pérez-Tanoira, A. Conde. Influence of the nanostructure of F-doped TiO$_2$ films on osteoblast growth and function. Soc. Biomater., 2014, 1985–1990.

[135] K. Lv, B. Cheng, J. Yu, G. Liu. Fluorine ions-mediated morphology control of anatase TiO$_2$ with enhanced photocatalytic activity. Phys. Chem. Chem. Phys., 2012, 14, 5349–5362.

[136] X. K. Wang, C. Wang, W. Q. Jiang, W. L. Guo, J. G. Wang. Sonochemical synthesis and characterization of Cl-doped TiO$_2$ and its application in the photodegradation of phthalate ester under visible light irradiation. Chem. Eng. J., 2012, 189–190, 288–294.

[137] J. Guo, L. Mao, J. Zhang, C. Feng. Role of Cl$^-$ ions in photooxidation of propylene on TiO$_2$ surface. Appl. Surf. Sci., 2010, 256(7), 2132–2137.

[138] R. Yuan, T. Chen, E. Fei, J. Lin, Z. Ding, J. Long, Z. Zhang, X. Fu, P. Liu, L. Wu, X. Wang. Surface chlorination of TiO$_2$-based photocatalysts: A way to remarkably improve photocatalytic activity in both UV and visible region. ACS Catal., 2011, 1(3), 200–206.

[139] H. Lin, W. Deng, T. Zhou, S. Ning, J. Long, X. Wang. Iodine-modified nanocrystalline titania for photocatalytic antibacterial application under visible light illumination. Appl. Catal. B Environ., 2015, 176, 36–43.

[140] D. Wang, X. Li, J. Chen, X. Tao. Enhanced visible-light photoelectrocatalytic degradation of organic contaminants at iodine-doped titanium dioxide film electrode. Ind. Eng. Chem. Res., 2012, 51(1), 218–224.

[141] L. Zhang, J. Zhou, J. Li, G. Liu, X. Lin, B. Mao, R. Liu, S. Zhang, J. Q. Wang. Surface structural reconstruction for optical response in iodine-modified TiO$_2$ photocatalyst system. J. Phys. Chem. C, 2014, 118(25), 13726–13732.

[142] W. Q. Fang, X. L. Wang, H. Zhang, Y. Jia, Z. Huo, Z. Li, H. Zhao, H. G. Yang, X. Yao. Manipulating solar absorption and electron transport properties of rutile TiO$_2$ photocatalysts via highly n-type F-doping. J. Mater. Chem. A, 2014, 2, 3513–3520.

[143] R. Rahimi, S. Saadati, E. H. Fard. Fluorine-doped TiO$_2$ nanoparticles sensitized by tetra(4-carboxyphenyl)porphyrin and zinc tetra(4-carboxyphenyl)porphyrin: Preparation, characterization, and evaluation of photocatalytic activity. Environ. Prog. Sustain. Energ., 2015, 34(5), 1341–1348.

[144] M. V. Dozzi, C. D'Andrea, B. Ohtani, G. Valentini, E. Selli. Fluorine-doped TiO$_2$ materials: Photocatalytic activity vs time-resolved photoluminescence. J. Phys. Chem. C, 2013, 117(48), 25586–25595.

[145] Y. Wang, H. Zhang, P. Liu, T. Sun, Y. Li, H. Yang, X. Yao, H. Zhao. Nature of visible-light responsive fluorinated titanium dioxides. J. Mater. Chem. A, 2013, 1, 12948–12953.

[146] H. Lin, W. Deng, T. Zhou, S. Ning, J. Long, X. Wang. Iodine-modified nanocrystalline titania for photo-catalytic antibacterial application under visible light illumination. Appl. Catal. B Environ., 2015, 176–177, 36–43.

[147] K. Siuzdak, M. Szkoda, M. Sawczak, A. Lisowska-Oleksiak, J. Karczewski, J. Ryl. Enhanced photoelectrochemical and photocatalytic performance of iodine-doped titania nanotube arrays. RSC Adv., 2015, 5, 50379–50391.

[148] Z. He, L. Xie, J. Tu, S. Song, W. Liu. Visible light-induced degradation of phenol over iodine-doped titanium dioxide modified with platinum: Role of platinum and the reaction mechanism. J. Phys. Chem. C, 2010, 114(1), 526–532.

[149] G. Liu, C. Sun, L. Wang, S. C. Smith, G. Q. Lu, H. M. Cheng. Bandgap narrowing of titanium oxide nanosheets: Homogeneous doping of molecular iodine for improved photoreactivity. J. Mater. Chem., 2011, 21, 14672–14679.

[150] H. Xu, R. A. Picca, L. D. Marco, C. Carlucci, A. Scrascia, P. Papadia, B. F. Scremin, E. Carlino, C. Giannini, C. Malitesta, M. Mazzeo, G. Gigli, G. Ciccarella. Nonhydrolytic route to boron-doped TiO$_2$ nanocrystals. Eur. J. Inorg. Chem., 2013, (3), 364–374.

[151] T. T. Wu, Y. P. Xie, L. C. Yin, G. Liu, H. M. Cheng. Switching photocatalytic H$_2$ and O$_2$ generation preferences of rutile TiO$_2$ microspheres with dominant reactive facets by boron doping. J. Phys. Chem. C, 2015, 119(1), 84–89.

[152] R. Zheng, Y. Guo, C. Jin, J. Xie, Y. Zhu, Y. Xie. Novel thermally stable phosphorus-doped TiO$_2$ photocatalyst synthesized by hydrolysis of TiCl$_4$. J. Mol. Catal. A, 2010, 319(1–2), 46–51.

[153] Y. Xia, Y. Jiang, F. Li, M. Xia, B. Xue, Y. Li. Effect of calcined atmosphere on the photocatalytic activity of P-doped TiO$_2$. Appl. Surf. Sci., 2014, 289, 306–315.

[154] W. Q. Fan, H. Y. Bai, G. H. Zhang, Y. S. Yan, C. B. Liu, W. D. Shi. Titanium dioxide macroporous materials doped with iron: Synthesis and photo-catalytic properties. CrystEngComm, 2014, 16, 116–122.

[155] S. M. Chang, W. S. Liu. The roles of surface-doped metal ions (V, Mn, Fe, Cu, Ce, and W) in the interfacial behavior of TiO_2 photocatalysts. Appl. Catal. B Environ., 2014, 156–157, 466–475.

[156] R. Hahn, M. Stark, M. S. Killian, P. Schmuki. Photocatalytic properties of *in situ* doped TiO_2-nanotubes grown by rapid breakdown anodization. Catal. Sci. Technol., 2013, 3, 1765–1770.

[157] M. Ishii, B. Towlson, S. Harako, X. W. Zhao, S. Komuro, B. Hamilton. Roles of electrons and holes in the luminescence of rare-earth-doped semiconductors. Electr. Commun. Jpn., 2013, 96(11), 1–7.

[158] D. M. Tobaldi, R. C. Pullar, A. F. Gualtieri, M. P. Seabra, J. A. Labrincha. Sol-gel synthesis, characterisation and photocatalytic activity of pure, W-, Ag- and W/Ag co-doped TiO_2 nanopowders. Chem. Eng. J., 2013, 214, 364–375.

[159] J. F. de Lima, M. H. Harunsani, D. J. Martin, D. Kong, P. W. Dunne, D. Gianolio, R. J. Kashtiban, J. Sloan, O. A. Serra, J. Tang, R. I. Walton. Control of chemical state of cerium in doped anatase TiO_2 by solvothermal synthesis and its application in photocatalytic water reduction. J. Mater. Chem. A, 2015, 3, 9890–9898.

[160] H. Li, J. Liu, J. Qian, Q. Li, J. Yang. Preparation of Bi-doped TiO_2 nanoparticles and their visible light photocatalytic performance. Chin. J. Catal., 2014, 35, 1578–1589.

[161] R. Klaysri, S. Wichaidit, T. Tubchareon, S. Nokjan, S. Piticharoenphun, O. Mekasu-wandumrong, P. Praserthdam. Impact of calcination atmospheres on the physiochemical and photocatalytic properties of nanocrystalline TiO_2 and Si-doped TiO_2. Ceram. Int., 2015, 41(9), 11409–11417.

[162] Y. Zhao, J. Liu, L. Shi, S. Yuan, J. Fang, Z. Wang, M. Zhang. Solvothermal preparation of Sn^{4+} doped anatase TiO_2 nanocrystals from peroxo-metal-complex and their photocatalytic activity. Appl. Catal. B Environ., 2011, 103(3–4), 436–443.

[163] Y. Zhang, D. S. Kilin. Computational modeling of wet TiO_2 (001) anatase surfaces functionalized by transition metal doping. Int. J. Quantum Chem., 2012, 112(24), 3867–3873.

[164] J. Choi, H. Park, M. R. Hoffmann. Effects of single metal-ion doping on the visible-light photoreactivity of TiO_2. J. Phys. Chem. C, 2010, 114, 783–792.

[165] Y. Ni, Y. Zhu, X. Ma. A simple solution combustion route for the preparation of metal-doped TiO_2 nanoparticles and their photocatalytic degradation properties. Dalton Trans., 2011, 40, 3689–3694.

[166] Q. Meng, T. Wang, E. Liu, X. Ma, Q. Geac, J. Gong. Understanding electronic and optical properties of anatase TiO_2 photocatalysts co-doped with nitrogen and transition metals. Phys. Chem. Chem. Phys., 2013, 15(24), 9549–9561.

[167] Y. F. Zhao, C. Li, S. Lu, L. J. Yan, Y. Y. Gong, L. Y. Niu, X. J. Liu. Effects of oxygen vacancy on $3d$ transition-metal doped anatase TiO$_2$: First principles calculations. Chem. Phys. Lett., 2016, 647, 36–41.

[168] S. Manu, M. A. Khadar. Non-uniform distribution of dopant iron ions in TiO$_2$ nano-crystals probed by X-ray diffraction, Raman scattering, photoluminescence and photocatalysis. J. Mater. Chem. C, 2015, 3, 1846–1853.

[169] J. Yan, Y. Zhang, S. Liu, G. Wu, L. Li, N. Guan. Facile synthesis of an iron doped rutile TiO$_2$ photocatalyst for enhanced visible-light-driven water oxidation. J. Mater. Chem. A, 2015, 3, 21434–21438.

[170] T. Liu, H. Zhang. Novel Fe-doped anatase TiO$_2$ nanosheet hierarchical spheres with 94% {001} facets for efficient visible light photodegradation of organic dye. RSC Adv., 2013, 3, 16255–16258.

[171] R. M. Ramli, F. K. Chong, A. A. Omar, T. Murugesan. Performance of surfactant assisted synthesis of Fe/TiO$_2$ on the photodegradation of diisopropanolamine. Clean Soil Air Water, 2015, 43 (5), 690–697.

[172] Y. Su, Z. Wu, Y. Wu, J. Yu, L. Sun, C. Lin. Acid orange II degradation through a heterogeneous Fenton-like reaction using Fe-TiO$_2$ nanotube arrays as a photocatalyst. J. Mater. Chem. A, 2015, 3, 8537–8544.

[173] G. K. Dinesh, S. Anandan, T. Sivasankar. Sonophotocatalytic treatment of Bismarck Brown G dye and real textile effluent using synthesized novel Fe(0)-doped TiO$_2$ catalyst. RSC Adv., 2015, 5, 10440–10451.

[174] D. Flak, E. Coy, G. Nowaczyk, L. Yate, S. Jurga. Tuning the photodynamic efficiency of TiO$_2$ nanotubes against HeLa cancer cells by Fe-doping. RSC Adv., 2015, 5, 85139–85152.

[175] R. Su, R. Bechstein, J. Kibsgaard, R. T. Vang, F. Besenbacher. High-quality Fe-doped TiO$_2$ films with superior visible-light performance. J. Mater. Chem., 2012, 22, 23755–23758.

[176] S. Wang, J. S. Lian, W. T. Zheng, Q. Jiang. Photocatalytic property of Fe doped anatase and rutile TiO$_2$ nanocrystal particles prepared by sol-gel technique. Appl. Surf. Sci., 2012, 263(15), 260–265.

[177] X. Li, Z. Guo, T. He. The doping mechanism of Cr into TiO$_2$ and its influence on the photocatalytic performance. Phys. Chem. Chem. Phys., 2013, 15, 20037–20045.

[178] J. M. Herrmann. Detrimental cationic doping of titania in photocatalysis: Why chromium Cr^{3+}-doping is a catastrophe for photocatalysis, both under UV- and visible irradiations. N. J. Chem., 2012, 36, 883–890.

[179] S. Ould-Chikh, O. Proux, P. Afanasiev, L. Khrouz, M. N. Hedhili, D. H. Anjum, M. Harb, C. Geantet, J. M. Basset, E. Puzenat. Photocatalysis with chromium-doped TiO_2: Bulk and surface doping. ChemSusChem, 2014, 7(5), 1361–1371.

[180] C. Diaz-Uribe, W. Vallejo, W. Ramos. Methylene blue photocatalytic mineralization under visible irradiation on TiO_2 thin films doped with chromium. Appl. Surf. Sci., 2014, 319, 121–127.

[181] B. N. Joshi, H. Yoon, M. F. A. M. van Hest, S. S. Yoon. Niobium-doped titania photocatalyst film prepared via a nonaqueous sol-gel method. J. Am. Ceram. Soc., 2013, 96(8), 2623–2627.

[182] P. S. Archana, R. Jose, T. M. Jin, C. Vijila, M. M. Yusoff, S. Ramakrishna. Structural and electrical properties of Nb-doped anatase TiO_2 nanowires by electrospinning. J. Am. Ceram. Soc., 2010, 93(12), 4096–4102.

[183] P. S. Archana, R. Jose, M. M. Yusoff, S. Ramakrishna. Near band-edge electron diffusion in electrospun Nb-doped anatase TiO_2 nanofibers probed by electrochemical impedance spectroscopy. Appl. Phys. Lett., 2011, 98(15), 152103.

[184] J. Yang, X. Zhang, C. Wang, P. Sun, L. Wang, B. Xia, Y. Liu. Solar photocatalytic activities of porous Nb-doped TiO_2 microspheres prepared by ultrasonic spray pyrolysis. Solid State Sci., 2012, 14(1), 139–144.

[185] J. Liu, X. Zhao, L. Duan, M. Cao, H. Sun, J. Shao, S. Chen, H. Xie, X. Chang, C. Chen. Influence of annealing process on conductive properties of Nb-doped TiO_2 polycrystalline films prepared by sol-gel method. Appl. Surf. Sci., 2011, 257(23), 10156–10160.

[186] S. Wang, X. Zhang, D. Ma, Z. Yu, X. Wang, Y. Niu. Photocatalysis performance of Nb-doped TiO_2 film *in situ* growth prepared by a micro plasma method. Rare Metal Mater. Eng., 2014, 43(7), 1549–1552.

[187] S. Liu, E. Guo, L. Yin. Tailored visible-light driven anatase TiO_2 photocatalysts based on controllable metal ion doping and ordered mesoporous structure. J. Mater. Chem., 2012, 22, 5031–5041.

[188] E. O. Oseghe, P. G. Ndungu, S. B. Jonnalagadda. Photocatalytic degradation of 4-chloro-2-methylphenoxyacetic acid using W-doped TiO_2. J. Photochem. Photobiol. A, 2015, 312, 96–106.

[189] W. Sangkhun, L. Laokiat, V. Tanboonchuy, P. Khamdahsag, N. Grisdanurak. Photocatalytic degradation of BTEX using W-doped TiO_2 immobilized on fiber glass cloth under visible light. Superlattice Microst., 2012, 52, 632–642.

[190] A. Mayoufi, M. F. Nsib, A. Houas. Doping level effect on visible-light irradiation W-doped TiO_2-anatase photocatalysts for Congo red photodegradation. C. R. Chimie, 2014, 17(7–8), 818–823.

[191] E. Grabowska, J. W. Sobczak, M. Gazda, A. Zaleska. Surface properties and visible light activity of W-TiO$_2$ photocatalysts prepared by surface impregnation and sol-gel method. Appl. Catal. B Environ., 2012, 117–118, 351–359.

[192] F. Zhang, Z. Cheng, L. Kang, L. Cui, W. Liu, X. Xu, G. Hou, H. Yang. A novel preparation of Ag-doped TiO$_2$ nanofibers with enhanced stability of photocatalytic activity. RSC Adv., 2015, 5, 32088–32091.

[193] L. M. Santos, W. A. Machado, M. D. França, K. A. Borges, R. M. Paniago, A. O. T. Patrocinio, A. E. H. Machado. Structural characterization of Ag-doped TiO$_2$ with enhanced photocatalytic activity. RSC Adv., 2015, 5, 103752–103759.

[194] A. M. A. Abdel-Wahab, O. S. Mohamed, S. A. Ahmed, M. F. Mostafa. Ag-doped TiO$_2$ enhanced photocatalytic oxidation of 1,2-cyclohexanediol. J. Phys. Org. Chem., 2012, 25, 1418–1421.

[195] A. López Ortiz, M. Meléndez Zaragoza, J. Salinas Gutiérrez, M. M. da Silva Paula, V. Collins-Martínez. Silver oxidation state effect on the photocatalytic properties of Ag doped TiO$_2$ for hydrogen production under visible light. Int. J. Hydrogen Energ., 2015, 40(48), 17308–17315.

[196] R. Nainan, P. Thakur, M. Chaskar. Synthesis of silver doped TiO$_2$ nanoparticles for the improved photocatalytic degradation of methyl orange. J. Mater. Sci. Technol., 2012, 1, 52–58.

[197] K. Gupta, R. P. Singh, A. Pandey, P. Anjana. Photocatalytic antibacterial performance of TiO$_2$ and Ag-doped TiO$_2$ against *S. aureus. P. aeruginosa* and *E. coli*. Beilstein J. Nanotechnol., 2013, 4, 345–351.

[198] S. Sajjad, S. A. K. Leghari, J. Zhang. Copper impregnated ionic liquid assisted meso-porous titania: Visible light photocatalyst. RSC Adv., 2013, 3, 12678–12687.

[199] X. J. Yang, S. Wang, H. M. Sun, X. B. Wang, J. S. Lian. Preparation and photocatalytic performance of Cu-doped TiO$_2$ nanoparticles. Trans. Nonferrous Met. Soc. China, 2015, 25, 504–509.

[200] C. Zhao, X. Shu, D. C. Zhu, S. H. Wei, Y. X. Wang, M. J. Tu, W. Gao. High visible light photocatalytic property of Co^{2+}-doped TiO$_2$ nanoparticles with mixed phases. Super-lattice Microst., 2015, 88, 32–42.

[201] I. Ganesh, A. K. Gupta, P. P. Kumar, P. S. C. Sekhar, K. Radha, G. Padmanabham, G. Sundararajan. Preparation and characterization of Co-doped TiO$_2$ materials for solar light induced current and photocatalytic applications. Mater. Chem. Phys., 2012, 135(1), 220–234.

[202] L. Cai, I. S. Cho, M. Logar, A. Mehta, J. He, C. H. Lee, P. M. Rao, Y. Feng, J. Wilcox, F. B. Prinz, X. Zheng. Sol-flame synthesis of cobalt-doped TiO$_2$ nanowires with enhanced electrocatalytic activity for oxygen evolution reaction. Phys. Chem. Chem. Phys., 2014, 16, 12299–12306.

[203] A. Sengele, D. Robert, N. Keller, V. Keller, A. Herissan, C. Colbeau-Justin. Ta-doped TiO$_2$ as photocatalyst for UV: A activated elimination of chemical warfare agent simulant. J. Catal., 2016, 334, 129–141.

[204] S. M. Bawaked, S. Sathasivam, D. S. Bhachu, N. Chadwick, A. Y. Obaid, S. Al-Thabaiti, S. N. Basahel, C. J. Carmalt, I. P. Parkin. Aerosol assisted chemical vapor deposition of conductive and photocatalytically active tantalum doped titanium dioxide films. J. Mater. Chem. A, 2014, 2, 12849–12856.

[205] L. R. Sheppard, J. Holik, R. Liu, S. Macartney, R. Wuhrer. Tantalum enrichment in tantalum-doped titanium dioxide. J. Am. Ceram. Soc., 2014, 97(12), 3793–3799.

[206] J. Majeed, C. Nayak, S. N. Jha, K. Bhattacharyya, D. Bhattacharyy, A. K. Tripathi. Correlation of Mo dopant and photocatalytic properties of Mo incorporated TiO$_2$: An EXAFS and photocatalytic study. RSC Adv., 2015, 5, 90932–90940.

[207] J. Q. Li, D. F. Wang, H. Liu, Z. F. Zhu. Multilayered Mo-doped TiO$_2$ nanofibers and enhanced photocatalytic activity. Mater. Manuf. Process., 2012, 27(6), 631–635.

[208] S. Wang, L. N. Bai, H. M. Sun, Q. Jiang, J. S. Lian. Structure and photocatalytic property of Mo-doped TiO$_2$ nanoparticles. Powder Technol., 2013, 244, 9–15.

[209] S. K. M. Saad, A. A. Umar, H. Q. Nguyen, C. F. Dee, M. M. Salleh, M. Oyama. Porous (001)-faceted Zn-doped anatase TiO$_2$ nanowalls and their heterogeneous photocatalytic characterization. RSC Adv., 2014, 4, 57054–57063.

[210] M. Sanchez-Dominguez, G. Morales-Mendoza, M. J. Rodriguez-Vargas, C. C. Ibarra-Malo, A. A. Rodriguez-Rodriguez, A. V. Vela-Gonzalez, S. A. Perez-Garcia, R. Gomez. Synthesis of Zn-doped TiO$_2$ anoparticles by the novel oil-in-water (O/W) microemulsion method and their use for the photocatalytic degradation of phenol. J. Environ. Chem. Eng., 2015, 3(4), 3037–3047.

[211] Y. Wang, X. Xue, H. Yang. Modification of the antibacterial activity of Zn/TiO$_2$ nanomaterials through different anions doped. Vacuum, 2014, 101, 193–199.

[212] H. Hu, W. Zhang, Y. Qiao, X. Jiang, X. Liu, C. Ding. Antibacterial activity and increased bone marrow stem cell functions of Zn-incorporated TiO$_2$ coatings on titanium. Acta Biomater., 2012, 8, 904–915.

[213] C. M. Malengreaux, S. L. Pirard, J. R. Bartlett, B. Heinrichs. Kinetic study of 4-nitrophenol photocatalytic degradation over a Zn^{2+} doped TiO$_2$ catalyst prepared through an environmentally friendly aqueous sol-gel process. Chem. Eng. J., 2014, 245, 180–190.

[214] V. D. Binasa, K. Sambani, T. Maggosc, A. Katsanaki, G. Kiriakidis. Synthesis and photocatalytic activity of Mn-doped TiO$_2$ nanostructured powders under UV and visible light. Appl. Catal. B Environ., 2012, 113–114, 79–86.

[215] V. C. Papadimitriou, V. G. Stefanopoulos, M. N. Romanias, P. Papagiannakopoulos, K. Sambani, V. Tudose, G. Kiriakidis. Determination of photo-catalytic activity of un-

doped and Mn-doped TiO$_2$ anatase powders on acetaldehyde under UV and visible light. Thin Solid Films, 2011, 520, 1195–1201.

[216] M. E. Olya, A. Pirkarami, M. Soleimani, M. Bahmaei. Photoelectrocatalytic degradation of acid dye using Ni-TiO$_2$ with the energy supplied by solar cell: Mechanism and economical studies. J. Environ. Manage., 2013, 121, 210–219.

[217] C. Y. Chen, L. J. Hsu. Kinetic study of self-assembly of Ni(II)-doped TiO$_2$ nanocatalysts for the photodegradation of azo pollutants. RSC Adv., 2015, 5(107), 88266–88271.

[218] R. Vasilić, S. Stojadinović, N. Radić, P. Stefanov, Z. Dohčević-Mitrović, B. Grbić. One-step preparation and photocatalytic performance of vanadium doped TiO$_2$ coatings. Mater. Chem. Phys., 2015, 151, 337–344.

[219] M. Khan, Y. Song, N. Chen, W. Cao. Effect of V doping concentration on the electronic structure, optical and photocatalytic properties of nano-sized V-doped anatase TiO$_2$. Mater. Chem. Phys., 2013, 142(1), 148–153.

[220] W. Li. Influence of electronic structures of doped TiO$_2$ on their photocatalysis. Phys. Status Solidi R, 2014, 1–18.

[221] E. L. Boulbar, E. Millon, C. Boulmer-Leborgne, C. Cachoncinlle, B. Hakim, E. Ntsoen-zok. Optical properties of rare earth-doped TiO$_2$ anatase and rutile thin films grown by pulsed-laser deposition. Thin Solid Films, 2014, 553, 13–16.

[222] Y. T. Ma, S. D. Li. Photocatalytic activity of TiO$_2$ nanofibers with doped La prepared by electrospinning method. J. Chin. Chem. Soc., 2015, 62, 380–384.

[223] M. Borlaf, M. T. Colomer, A. de Andrés, F. Cabello, R. Serna, R. Moreno. TiO$_2$/Eu^{3+} thin films with high photoluminescence emission prepared by electrophoretic deposition from nanoparticulate sols. Eur. J. Inorg. Chem., 2014, 5152–5159.

[224] J. Du, B. Li, J. Huang, W. Zhang, H. Peng, J. Zou. Hydrophilic and photocatalytic performances of lanthanum doped titanium dioxide thin films. J. Rare Earth, 2013, 31(10), 992–996.

[225] S. Han, R. Deng, X. Xie, X. Liu. Enhancing luminescence in lanthanide-doped upconversion nanoparticles. Angew. Chem. Int. Ed., 2014, 53, 11702–11715.

[226] S. Maddila, E. O. Oseghe, S. B. Jonnalagadda. Photocatalyzed ozonation by Ce doped TiO$_2$ catalyst degradation of pesticide Dicamba in water. J. Chem. Technol. Biotechnol., 2016, 91(2), 385–393.

[227] J. Santiago-Morales, A. Agüera, M. del Mar Gómez, A. R. Fernández-Alba, J. Giménez, S. Esplugas, R. Rosal. Transformation products and reaction kinetics in simulated solar light photocatalytic degradation of propranolol using Ce-doped TiO$_2$. Appl. Catal. B Environ., 2013, 129, 13–29.

[228] B. Choudhury, B. Borah, A. Choudhury. Extending photocatalytic activity of TiO$_2$ nanoparticles to visible region of illumination by doping of cerium. Photochem. Photobiol., 2012, 88, 257–264.

[229] Z. Shi, M. Zhou, D. Zheng, H. Liu, S. Yao. Preparation of Ce-doped TiO$_2$ hollow fibers and their photocatalytic degradation properties for dye compound. J. Chin. Chem. Soc., 2013, 60, 1156–1162.

[230] W. Luo, C. Fu, R. Li, Y. Liu, H. Zhu, X. Chen. Er^{3+}-doped anatase TiO$_2$ nanocrystals: Crystal-field levels, excited-state dynamics, upconversion, and defect luminescence. Small, 2011, 7(21), 3046–3056.

[231] S. Obregon, G. Colon. Evidence of upconversion luminescence contribution to the improved photoactivity of erbium doped TiO$_2$ systems. Chem. Commun., 2012, 48, 7865–7867.

[232] Y. Zheng, W. Wang. Electrospun nanofibers of Er^{3+}-doped TiO$_2$ with photocatalytic activity beyond the absorption edge. J. Solid State Chem., 2014, 210, 206–212.

[233] J. Choi, P. Sudhagar, P. Lakshmipathiraj, J. W. Lee, A. Devadoss, S. Lee, T. Song, S. Hong, S. Eito, C. Terashima, T. H. Han, J. K. Kang, A. Fujishima, Y. S. Kang, U. Paik. Three-dimensional Gd-doped TiO$_2$ fibrous photoelectrodes for efficient visible light-driven photocatalytic performance. RSC Adv., 2014, 4, 11750–11757.

[234] C. M. Leroy, H. F. Wang, A. Fargues, T. Cardinal, V. Jubera, M. Treguer-Delapierre, C. Boissière, D. Grosso, C. Sanchez, B. Viana, F. Pelle. Emission-photoactivity cross-processing of mesoporous interfacial charge transfer in Eu^{3+} doped titania. Phys. Chem. Chem. Phys., 2011, 13, 11878–11884.

[235] A. Mezzi, S. Kaciulis, I. Cacciotti, A. Bianco, G. Gusmano, F. R. Lamastra, M. E. Fragal. Structure and composition of electrospun titania nanofibres doped with Eu. Surf. Interface Anal., 2010, 42, 572–575.

[236] H. Zhang, Y. Sheng, K. Zheng, X. Zhou, Z. Shi, X. Xu, H. Zou. Hydrothermal fabrication and luminescence properties of one-dimensional TiO$_2$: Eu^{3+} spindlelike nanorods. Eur. J. Inorg. Chem., 2014, 3305–3311.

[237] Y. Wu, Q. Zhang, X. Yin, H. Cheng. Template-free synthesis of mesoporous anatase yttrium-doped TiO$_2$ nanosheet-array films from waste tricolor fluorescent powder with high photocatalytic activity. RSC Adv., 2013, 3, 9670–9676.

[238] Z. X. Li, F. B. Shi, T. Zhang, H. S. Wu, L. D. Sun, C. H. Yan. Ytterbium stabilized ordered mesoporous titania for near-infrared photocatalysis. Chem. Commun., 2011, 47, 8109–8111.

[239] C. Spreafico, J. V. Vondele. Excess electrons and interstitial Li atoms in TiO$_2$ anatase: Properties of the (101) interface. J. Phys. Chem. C, 2015, 119(27), 15009–15018.

[240] S. Bouattour, W. Kallel, A. B. do Rego, L. F. V. Ferreira, I. F. Machado, S. Boufi. Li-doped nanosized TiO$_2$ powder with enhanced photocatalytic activity under sunlight irradiation. Appl. Organometal. Chem., 2010, 24, 692–699.

[241] W. Yue, C. Randorn, P. S. Attidekou, Z. Su, J. T. S. Irvine, W. Zhou. Syntheses, Li insertion, and photoactivity of mesoporous crystalline TiO$_2$. Adv. Funct. Mater., 2009, 19, 2826–2833.

[242] R. Long, Y. Dai, G. Meng, B. B. Huang. Energetic and electronic properties of X-(Si, Ge, Sn, Pb) doped TiO$_2$ from first-principles. Phys. Chem. Chem. Phys., 2009, 11, 8165–8172.

[243] M. C. Wu, J. S. Chih, W. K. Huang. Bismuth doping effect on TiO$_2$ nanofibres for morphological change and photocatalytic performance. CrystEngComm, 2014, 16, 10692–10699.

[244] W. Zhao, X. Wang, H. Sang, K. Wang. Synthesis of Bi-doped TiO$_2$ nanotubes and enhanced photocatalytic activity for hydrogen evolution from glycerol solution. Chin. J. Chem., 2013, 31, 415–420.

[245] S. Murcia-López, M. C. Hidalgo, J. A. Navío. Synthesis, characterization and photocatalytic activity of Bi-doped TiO$_2$ photocatalysts under simulated solar irradiation. Appl. Catal. A Gen., 2011, 404(1–2), 59–67.

[246] F. E. Oropeza, B. Davies, R. G. Palgrave, R. G. Egdell. Electronic basis of visible region activity in high area Sn-doped rutile TiO$_2$ photocatalysts. Phys. Chem. Chem. Phys., 2011, 13, 7882–7891.

[247] J. Du, G. Zhao, H. Pang, Y. Qian, H. Liu, D. J. Kang. A template method for synthesis of porous Sn-doped TiO$_2$ monolith and its enhanced photocatalytic activity. Mater. Lett., 2013, 93, 419–422.

[248] J. A. Rengifo-Herrera, K. Pierzchała, A. Sienkiewicz, L. Forró, J. Kiwi, J. E. Moser, C. Pulgarin. Synthesis, characterization, and photocatalytic activities of nanoparticulate N, S-codoped TiO$_2$ having different surface-to-volume ratios. J. Phys. Chem. C, 2010, 114, 2717–2723.

[249] C. Yu, D. Cai, K. Yang, J. C. Yu, Y. Zhou, C. Fan. Sol-gel derived S, I-codoped mesoporous TiO$_2$ photocatalyst with high visible-light photocatalytic activity. J. Phys. Chem. Solids, 2010, 71, 1337–1343.

[250] Q. C. Xu, D. V. Wellia, S. Yan, D. W. Liao, T. M. Lim, T. T. Y. Tan. Enhanced photocatalytic activity of C-N-codoped TiO$_2$ films prepared via an organic-free approach. J. Hazard. Mater., 2011, 188, 172–180.

[251] J. Zhang, C. Pan, P. Fang, J. Wei, R. Xiong. Mo plus C codoped TiO$_2$ using thermal oxidation for enhancing photocatalytic activity. ACS Appl. Mater. Inter., 2010, 2(4), 1173–1176.

[252] Y. Zhang, C. Li, C. Pan. N plus Ni codoped anatase TiO_2 nano-crystals with exposed {001} facets through two-step hydrothermal route. J. Am. Ceram. Soc., 2012, 95(9), 2951–2956.

[253] X. Li, Y. Liu, P. Yang, Y. Shi. Visible light-driven photocatalysis of W, N co-doped TiO_2. Particuology, 2013, 11, 732–736.

[254] F. Li, L. X. Guan, M. L. Dai, J. J. Feng, M. M. Yao. Effects of V and Zn codoping on the microstructures and photocatalytic activities of nanocrystalline TiO_2 films. Ceram. Int., 2013, 39(7), 7395–7400.

[255] W. F. Chen, P. Koshy, C. C. Sorrell. Effect of intervalence charge transfer on photocatalytic performance of cobalt- and vanadium-codoped TiO_2 thin films. Int. J. Hydrogen Energ., 2015, 40(46), 16215–16229.

[256] Y. Wang, Y. Zhang, F. Yu, C. Jin, X. Liu, J. Ma, Y. Wang, Y. Huang, J. Wang. Correlation investigation on the visible-light-driven photocatalytic activity and coordination structure of rutile Sn-Fe-TiO_2 nanocrystallites for methylene blue degradation. Catal. Today, 2015, 258, 112–119.

[257] J. Chung, J. W. Chung, S. Y. Kwak. Adsorption-assisted photocatalytic activity of nitrogen and sulfur codoped TiO_2 under visible light irradiation. Phys. Chem. Chem. Phys., 2015, 17, 17279–17287.

[258] S. Pany, K. M. Parida. Sulfate-anchored hierarchical meso-macroporous N-doped TiO_2: A novel photocatalyst for visible light H_2 evolution. ACS Sustain. Chem. Eng., 2014, 2(6), 1429–1438.

[259] Z. Li, Y. Zhu, F. Pang, H. Liu, X. Gao, W. Ou, J. Liu, X. Wang, X. Cheng, Y. Zhang. Synthesis of N doped and N, S co-doped 3D TiO_2 hollow spheres with enhanced photocatalytic efficiency under nature sunlight. Ceram. Int., 2015, 41(8), 10063–10069.

[260] V. Etacheri, M. K. Seery, S. J. Hinder, S. C. Pillai. Nanostructured $Ti_{1-x}S_xO_{2-y}N_y$ heterojunctions for efficient visible-light-induced photocatalysis. Inorg. Chem., 2012, 51(13), 7164–7173.

[261] Q. Xiang, J. Yu, M. Jaroniec. Nitrogen and sulfur co-doped TiO_2 nanosheets with exposed {001} facets: Synthesis, characterization and visible-light photocatalytic activity. Phys. Chem. Chem. Phys., 2011, 13, 4853–4861.

[262] E. M. Samsudin, S. B. A. Hamid, J. C. Juan, W. J. Basirun, G. Centi. Enhancement of the intrinsic photocatalytic activity of TiO_2 in the degradation of 1,3,5-triazine herbicides by doping with N, F. Chem. Eng. J., 2015, 280, 330–343.

[263] T. K. Rahul, N. Sandhyarani. Nitrogen-fluorine co-doped titania inverse opals for enhanced solar light driven photocatalysis. Nanoscale, 2015, 7, 18259–18270.

[264] X. Wang, X. Wang, J. Zhao, J. Chen, J. Zhang, J. Song, J. Huang. Bioframe synthesis of NF-TiO$_2$/straw charcoal composites for enhanced adsorption-visible light photocatalytic degradation of RhB. RSC Adv., 2015, 5, 66611–66620.

[265] A. E. Giannakas, E. Seristatidou, Y. Deligiannakis, I. Konstantinou. Photocatalytic activity of N-doped and N-F co-doped TiO$_2$ and reduction of chromium(VI) in aqueous solution: An EPR study. Appl. Catal. B Environ., 2013, 132–133, 460–468.

[266] X. Zong, Z. Xing, H. Yu, Z. Chen, F. Tang, J. Zou, G. Q. Lu, L. Wang. Photocatalytic water oxidation on F, N co-doped TiO$_2$ with dominant exposed {001} facets under visible light. Chem. Commun., 2011, 47, 11742–11744.

[267] A. G. Kontos, M. Pelaez, V. Likodimos, N. Vaenas, D. D. Dionysiou, P. Falaras. Visible light induced wetting of nanostructured N-F co-doped titania films. Photochem. Photobiol. Sci., 2011, 10, 350–354.

[268] A. M. Czoska, S. Livraghi, M. C. Paganini, E. Giamello, C. Di Valentin, G. Pacchioni. The nitrogen-boron paramagnetic center in visible light sensitized N-B co-doped TiO$_2$: Experimental and theoretical characterization. Phys. Chem. Chem. Phys., 2011, 13, 136–143.

[269] X. Wang, W. Wang, X. Wang, J. Zhang, Z. Gu, L. Zhou, J. Zhao. Enhanced visible light photocatalytic activity of a floating photocatalyst based on B-N-codoped TiO$_2$ grafted on expanded perlite. RSC Adv., 2015, 5, 41385–41392.

[270] K. Zhang, X. Wang, T. He, X. Guo, Y. Feng. Preparation and photocatalytic activity of B-N co-doped mesoporous TiO$_2$. Powder Technol., 2014, 253, 608–613.

[271] X. Liu, Y. Chen, C. Cao, J. Xu, Q. Qian, Y. Luo, H. Xue, L. Xiao, Y. Chenac, Q. Chen. Electrospun nitrogen and carbon co-doped porous TiO$_2$ nanofibers with high visible light photocatalytic activity. N. J. Chem., 2015, 39, 6944–6950.

[272] L. Li, J. Shi, G. Li, Y. Yuan, Y. Li, W. Zhao, J. Shi. One-pot pyrolytic synthesis of C-N-codoped mesoporous anatase TiO$_2$ and its highly efficient photo-degradation properties. N. J. Chem., 2013, 37, 451–457.

[273] S. Wei, R. Wu, J. Jian, F. Chen, Y. Sun. Black and yellow anatase titania formed by (H, N)-doping: Strong visible-light absorption and enhanced visible-light photocatalysis. Dalton Trans., 2015, 44, 1534–1538.

[274] H. Pan, Y. W. Zhang, V. B. Shenoy, H. Gao. Effects of H-, N-, and (H, N)-doping on the photocatalytic activity of TiO$_2$. J. Phys. Chem. C, 2011, 115(24), 12224–12231.

[275] J. Yu, P. Zhou, Q. Li. New insight into the enhanced visible-light photocatalytic activities of B-, C- and B/C-doped anatase TiO$_2$ by first-principles. Phys. Chem. Chem. Phys., 2013, 15, 12040–12047.

[276] Y. Lin, Z. Jiang, C. Zhu, X. Hu, X. Zhang, H. Zhu, J. Fand, S. H. Lin. C/B codoping effect on band gap narrowing and optical performance of TiO$_2$ photocatalyst: A spin-polarized DFT study. J. Mater. Chem. A, 2013, 1, 4516–4524.

[277] Q. Deng, Y. Liu, K. Mu, Y. Zeng, G. Yang, F. Shen, S. Deng, X. Zhang, Y. Zhang. Preparation and characterization of F-modified C-TiO$_2$ and its photocatalytic properties. Phys. Status Solidi A, 2015, 212(3), 691–697.

[278] P. Xu, T. Xu, J. Lu, S. Gao, N. S. Hosmane, B. Huang, Y. Dai, Y. Wang. Visible-light-driven photocatalytic S- and C- codoped meso/nanoporous TiO$_2$. Energ. Environ. Sci., 2010, 3, 1128–1134.

[279] S. Yu, B. Li, Y. Luo, L. Dong, M. Fan, F. Zhang. Preparation of Ag-modified (B, P)-codoped TiO$_2$ hollow spheres with enhanced photocatalytic activity. Eur. J. Inorg. Chem., 2014, 1142–1149.

[280] H. Li, J. Xing, Z. Xia, J. Chen. Preparation of extremely smooth and boron-fluorine co-doped TiO$_2$ nanotube arrays with enhanced photoelectrochemical and photocatalytic performance. Electrochim. Acta, 2014, 139, 331–336.

[281] R. Ramanathan, V. Bansal. Ionic liquid mediated synthesis of nitrogen, carbon and fluorine-codoped rutile TiO$_2$ nanorods for improved UV and visible light photocatalysis. RSC Adv., 2015, 5, 1424–1429.

[282] A. E. Giannakas, M. Antonopoulou, C. Daikopoulos, Y. Deligiannakis, I. Konstantinou. Characterization and catalytic performance of B-doped, B-N co-doped and B-N-F tri-doped TiO$_2$ towards simultaneous Cr(VI) reduction and benzoic acid oxidation. Appl. Catal. B Environ., 2016, 184, 44–54.

[283] J. Yu, Q. Li, S. Liu, M. Jaroniec. Ionic-liquid-assisted synthesis of uniform fluorinated B/C-codoped TiO$_2$ nanocrystals and their enhanced visible-light photocatalytic activity. Chem. Eur. J., 2013, 19, 2433–2441.

[284] G. Zhang, Y. C. Zhang, M. Nadagouda, C. Han, K. O'Shea, S. M. El-Sheikh, A. A. Ismail, D. D. Dionysiou. Visible light-sensitized S, N and C co-doped polymorphic TiO$_2$ for photocatalytic destruction of microcystin-LR. Appl. Catal. B Environ., 2014, 144, 614–621.

[285] H. Zhang, Z. Xing, Y. Zhang, Z. Li, X. Wu, C. Liu, Q. Zhu, W. Zhou. Ni^{2+} and Ti^{3+} co-doped porous black anatase TiO$_2$ with unprecedented-high visible-light-driven photocatalytic degradation performance. RSC Adv., 2015, 5, 107150–107157.

[286] B. Chen, A. J. Haring, J. A. Beach, M. Li, G. S. Doucette, A. J. Morris, R. B. Moore, S. Priya. Visible light induced photocatalytic activity of Fe^{3+}/Ti^{3+} co-doped TiO$_2$ nanostructures. RSC Adv., 2014, 4, 18033–18037.

[287] M. Khan, S. R. Gul, J. Li, W. Cao. Tungsten concentration influence on the structural, electronic, optical and photocatalytic properties of tungsten-silver codoped titanium dioxide. Ceram. Int., 2015, 41(4), 6051–6054.

[288] H. F. Moafi, A. F. Shojaie, M. A. Zanjanchi. Photoactive behavior of polyacrylonitrile fibers based on silver and zirconium co-doped titania nanocomposites: Synthesis, characterization, and comparative study of solid-phase photocatalytic self-cleaning. J. Appl. Polym. Sci., 2013, 3778–3789.

[289] P. Benjwal, K. K. Kar. Removal of methylene blue from wastewater under a low power irradiation source by Zn, Mn co-doped TiO$_2$ photocatalysts. RSC Adv., 2015, 5, 98166–98176.

[290] K. C. Christoforidis, M. Fernández-García. Photoactivity and charge trapping sites in copper and vanadium doped anatase TiO$_2$ nano-materials. Catal. Sci. Technol., 2016, 6, 1094–1105.

[291] K. B. Jaimy, V. P. Safeena, S. Ghosh, N. Y. Hebalkar, K. G. K. Warrier. Photocatalytic activity enhancement in doped titanium dioxide by crystal defects. Dalton Trans., 2012, 41, 4824–4832.

[292] L. M. Sun, X. Zhao, X. F. Cheng, H. G. Sun, Y. L. Li, P. Li, W. L. Fan. Synergistic effects in La/N codoped TiO$_2$ anatase (101) surface correlated with enhanced visible-light photocatalytic activity. Langmuir, 2012, 28, 5882–5891.

[293] L. Yu, X. Yang, J. He, Y. He, D. Wang. One-step hydrothermal method to prepare nitrogen and lanthanum co-doped TiO$_2$ nanocrystals with exposed {001} facets and study on their photocatalytic activities in visible light. J. Alloy Compd., 2015, 637, 308–314.

[294] G. Li, J. Li, G. Li, G. Jiang. N and Ti^{3+} co-doped 3D anatase TiO$_2$ superstructures composed of ultrathin nanosheets with enhanced visible light photocatalytic activity. J. Mater. Chem. A, 2015, 3, 22073–22080.

[295] E. Wang, T. He, L. Zhao, Y. Chen, Y. Cao. Improved visible light photocatalytic activity of titania doped with tin and nitrogen. J. Mater. Chem., 2011, 21, 144–150.

[296] Y. Hu, G. Chen, C. Li, Y. Yu, J. Sun, H. Dong. Improved light absorption and photocatalytic activity of Zn, N-TiO$_{2-x}$ rich in oxygen vacancies synthesized by nitridation and hydrogenation. N. J. Chem., 2015, 39, 2417–2420.

[297] L. L. Lai, J. M. Wu. A facile solution approach to W, N co-doped TiO$_2$ nanobelt thin films with high photocatalytic activity. J. Mater. Chem. A, 2015, 3, 15863–15868.

[298] T. Mishra, M. Mahato, Noor Aman, J. N. Patel, R. K. Sahu. A mesoporous WN co-doped titania nanomaterial with enhanced photocatalytic aqueous nitrate removal activity under visible light. Catal. Sci. Technol., 2011, 1, 609–615.

[299] X. Wang, Y. Yan, B. Hao, G. Chen. Biomimetic layer-by-layer deposition assisted synthesis of Cu, N co-doped TiO$_2$ nanosheets with enhanced visible light photocatalytic performance. Dalton Trans., 2014, 43, 14054–14060.

[300] Y. Zhang, W. Zhu, X. Cui, W. Yao, T. Duan. One-step hydrothermal synthesis of iron and nitrogen co-doped TiO_2 nanotubes with enhanced visible-light photocatalytic activity. CrystEngComm, 2015, 17, 8368–8376.

[301] Q. Liu, D. Ding, C. Ning, X. Wang. Reduced N/Ni-doped TiO_2 nanotubes photoanodes for photoelectrochemical water splitting. RSC Adv., 2015, 5, 95478–95487.

[302] J. Zhang, X. Wang, X. Wang, J. Song, J. Huang, B. Louangsouphom, J. Zhao. Floating photocatalysts based on loading Bi/N-doped TiO_2 on expanded graphite C/C (EGC) composites for the visible light degradation of Diesel. RSC Adv., 2015, 5, 71922–71931.

[303] J. Xu, C. Chen, X. Xiao, L. Liao, L. Miao, W. Wu, F. Mei, A. L. Stepanov, G. Cai, Y. Liu, Z. Dai, F. Ren, C. Jiang, J. Liu. Synergistic effect of V/N codoping by ion implantation on the electronic and optical properties of TiO_2. J. Appl. Phys., 2014, 115(14), 143106.

[304] J. Zhang, J. Xi, Z. Ji. (Mo, N)-codoped TiO_2 sheets with dominant {001} facets for enhancing visible-light photocatalytic activity. J. Mater. Chem., 2012, 22, 17700–17708.

[305] W. He, Z. Fang, K. Zhang, X. Li, D. Ji, X. Jiang, C. Qiu, K. Guo. Continuous synthesis of a co-doped TiO_2 photocatalyst and its enhanced visible light catalytic activity using a photocatalysis microreactor. RSC Adv., 2015, 5, 54853–54860.

[306] Y. Zhang, H. Zhang, L. Cheng, Y. Miao, L. Hu, G. Ding, Z. Jiao, L. Bian, M. Nguyen, G. Zheng. Vacuum-treated Mo, S-doped TiO_2:Gd mesoporous nanospheres: An improved visible-light photocatalyst. Eur. J. Inorg. Chem., 2015, 2895–2900.

[307] C. Yan, W. Yi, H. Yuan, X. Wu, F. Li. A highly photoactive S, Cu-codoped nano-TiO_2 photocatalyst: Synthesis and characterization for enhanced photocatalytic degradation of neutral red. Environ. Prog. Sustain. Energ., 2014, 33(2), 419–429.

[308] W. Fu, S. Ding, Y. Wang, L. Wu, D. Zhang, Z. Pan, R. Wang, Z. Zhang, S. Qiu. F, Ca co-doped TiO_2 nanocrystals with enhanced photocatalytic activity. Dalton Trans., 2014, 43, 16160–16163.

[309] R. Jaiswal, N. Patel, A. Dashora, R. Fernandes, M. Yadav, R. Edla, R. S. Varma, D. C. Kothari, B. L. Ahuja, A. Miotello. Efficient Co-B-codoped TiO_2 photocatalyst for degradation of organic water pollutant under visible light. Appl. Catal. B Environ., 2016, 183, 242–253.

[310] R. Li, G. Dong, G. Chen. Synthesis, characterization and performance of ternary doped Cu-Ce-B/TiO_2 nanotubes on the photocatalytic removal of nitrogen oxides. N. J. Chem., 2015, 39, 6854–6863.

[311] J. M. Wu, M. L. Tang. One-pot synthesis of N-F-Cr-doped anatase TiO_2 microspheres with nearly all-(001) surface for enhanced solar absorption. Nanoscale, 2011, 3, 3915–3922.

Photocatalytic Activity of TiO$_2$ Nanostructured Arrays Prepared by Microwave-Assisted Solvothermal Method

Ana Pimentel, Daniela Nunes, Sónia Pereira,
Rodrigo Martins and Elvira Fortunato

Additional information is available at the end of the chapter

Abstract

The use of metal-oxide-semiconductor nanostructures as photocatalytic materials has been an area of intense research over the last decade, and in this field, titanium dioxide (TiO$_2$) receives much attention. TiO$_2$ is an attractive material since it is stable, insoluble, non-toxic, resistant to corrosion and relatively inexpensive. In this chapter, we will demonstrate the influence of different solvents on the synthesis of TiO$_2$ nanostructures considering a solvothermal method assisted by microwave radiation and their photocatalytic behaviour. The TiO$_2$ nanostructured arrays were synthesized on seeded polyethylene naphthalate (PEN) substrates with different solvents: water, 2 – propanol, ethanol and methanol. TiO$_2$ thin films deposited by spin-coating were used as seed layer for the nanostructures growth. Structural characterization of the microwave synthesized materials has been carried out by scanning electron microscopy (SEM) and X-Ray diffraction (XRD). The optical properties have also been investigated. The TiO$_2$ nanostructures arrays were tested as photocatalytic agents in the degradation of pollutant dyes like methylene blue (MB) in the presence of UV radiation. Expressive differences between the different solvents were detected, in which methanol demonstrated higher MB degradation for the conditions tested.

Keywords: titanium dioxide, nanostructures, microwave radiation, solvents, photocatalysis

1. Introduction

Titanium dioxide (TiO$_2$) is a n-type semiconductor material that has attracted considerable attention in several applications, such as sensor devices [1], dye-solar cells [2], photocatalysis

INTECH
open science | open minds

[3], among others. Lately, the growing interest in this material is mainly associated to its long-term photostability, non-toxicity, low cost availability [4] and for being a semiconductor material, with a band gap of approximately 3 eV. Moreover, this material is sensitive to UV radiation, with notable transmittance in the visible region (superior to 80%), high refractive index (between 2.5 and 2.7) and chemical stability [5].

1.1. TiO$_2$ as a photocatalyst material

Titanium dioxide is non-toxic, chemically stable, earth-abundant and inexpensive, being considered attractive as a photocatalytic material [6]. TiO$_2$ photocatalytic activity is directly related to size, specific surface area, impurities on crystalline phase, and the exposed surface facets [7], thus several TiO$_2$ nano/micro structures were reported in order to improve its final performance [7].

One-dimensional nanostructures, such as nanowires and nanorods, offer a higher surface to volume ratio, when compared to other type of morphologies, which turn them interesting to photocatalytic application. Nevertheless, when these nanostructures are used in the powder form, the separation of the catalyst from solution becomes a problem, which makes the use of films highly appealing. Moreover, when included the option of using flexible substrates, such as polyethylene naphthalate (PEN) on these nanostructured films, opens to a broad range of possibilities and low cost strategies.
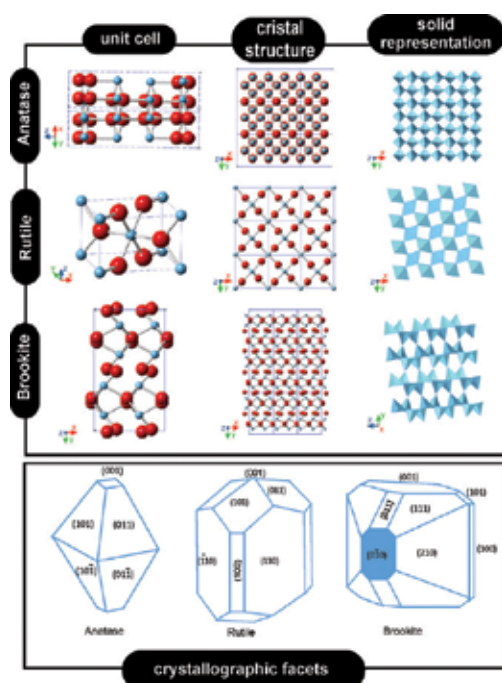

Figure 1. Crystallographic structures of different TiO$_2$ crystals: anatase, rutile and brookite.

TiO$_2$ used as a photocatalytic material for decomposition of organic pollutants and its photo-catalytic activity has been reported in several different studies [3, 8, 9]. Rutile and anatase structures are the most important phases for TiO$_2$. TiO$_2$ can exist in amorphous form or in three crystalline phases: rutile (a tetragonal structure, P4$_{2/mmm}$), anatase (also a tetragonal structure, I4$_{1/amd}$) and brookite (an orthorhombic structure, Pbca), at ambient temperature [10], as shown on **Figure 1**. Among these three different phases, rutile is the one with the most stable phase. The optical band gap of titanium dioxide is slightly above 3 eV (rutile: 3.0 eV, anatase: 3.4 eV and brookite: 3.3 eV) [10].

TiO$_2$ in the form of anatase is the most used as a photocatalyst under UV radiation [11]. Rutile has a smaller electron effective mass, higher density and higher refractive index [5]. Anatase contains more defects in the lattice, producing more oxygen vacancies and capturing the electrons [12]. Moreover, the later possesses a shallow donor level, high electron mobility and trap controlled electronic conduction [13]. Considering such properties, the anatase form is preferred to be used in most optoelectronic and photocatalyst applications. Anatase and rutile are generally regarded to be used in photocatalytic applications, while brookite is not.

An n-type semiconductor has a filled valence band (VB) and an empty conduction band (CB). The absorption of a photon (with an energy at least equal to the bandgap) by TiO$_2$ nanoparticles will result in the promotion of an electron, e$^-$, from the valence band to the conduction band, leaving behind a "hole", h$^+$, (an electron vacancy) in the VB [14]. For anatase and rutile, as mentioned above, the bandgaps values are 3.2 and 3.0 eV (corresponding to wavelengths of 385 and 410 nm), respectively. Ultraviolet light is necessary for the material photoexcitation. The electron-hole pairs can recombine or participate in chemical reactions with the surface adsorbed species.
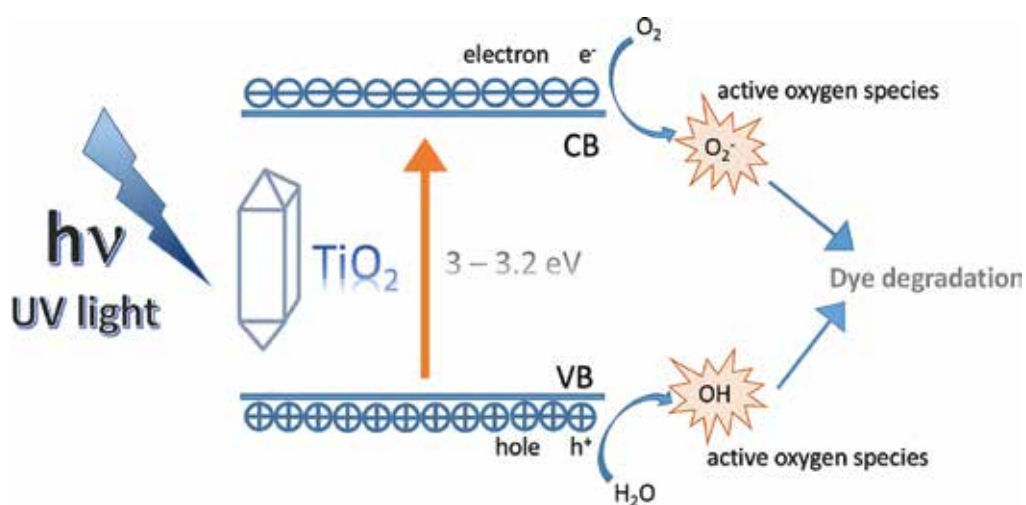

Figure 2. Schematic of the titanium dioxide band levels in the presence of UV radiation.

The electron-hole, h$^+$, in the valence band provides a site where the adsorbed hydroxyl ions (OH$^-$) and disassociated water (H$_2$O) can lose an electron forming a hydroxyl radical (OH·). Hydroxyl radicals are electrically neutral but highly reactive. The CB electrons (e$^-$) can react with molecular oxygen (O$_2$) and form the superoxide radical-anion, O_2^-, which will also be involved in reaction of dye degradation [15]. In addition, the hole h$^+$ and the electron e$^-$ can react directly with adsorbed pollutants (see **Figure 2**).The excitation of valence band electrons to the conduction band allowing for the formation of hydroxyl radicals is what makes TiO$_2$ a catalyst.

The catalysts materials at the nanoscale have the advantage of presenting large surface area and, therefore, larger number of active sites per volume to promote the photocatalytic reaction. Smaller particle sizes imply shorter distances for photogenerated charge carriers to migrate before reaching surface reaction sites [16].

As photocatalytic redox reactions take place on the crystal surface, the surface reactivity of TiO$_2$ strongly influences the material photocatalytic activity [17]. The effect of particle shape on the photochemistry also plays an important role. It has been demonstrated that some crystal orientation are much more reactive than others, so the overall reactivity could be related to the particle shape [16].

The TiO$_2$ nanocrystal growth is based on the minimization of surface energy, which will lead to the disappearance of the most reactive facets [18]. In general surfaces with higher surface energy disappear rapidly during the crystal growth process in order to minimize the total surface energy.

The equilibrium shape of anatase crystal consists of a truncated tetragonal bipyramidal structure constructed by eight {101} facets and two top squared {001} facets [19] (see **Figure 1**). For rutile, the equilibrium shape consists of a tetragonal prism bounced by a {110} facet and terminated by two tetragonal pyramids bounded by {011} facets [20]. In the case of brookite, the equilibrium crystal possesses seven different facets [20]. The equilibrium shape of the latter materials will vary according to the growth conditions employed and the different facets will present different properties.

The photocatalytic oxidation and reduction sites of rutile were reported as being present on the {011} and {110} facets, respectively. In the case of anatase, it was mainly present in {001} and {011} facets, respectively [20, 21] (see **Figure 3**). Brookite has not attracted much attention for photocatalytic applications due to its lack of photocatalytic activity. In contrast to this latter, anatase has the {101} surface facet, for which only 50% of the Ti atoms are five-coordinated (Ti$_{5c}$), both the {001} and {100} surfaces facets consist of 100% Ti$_{5c}$ atoms [17]. These atoms act as active sites in the photocatalytic experiments, so by this reason, the facets {001} and {100} should be more active than {101} facets.

The origin of the higher reactivity of these facets can be associated to the increased density of undercoordinated Ti atoms at the surface and to the surface atom arrangement [22].
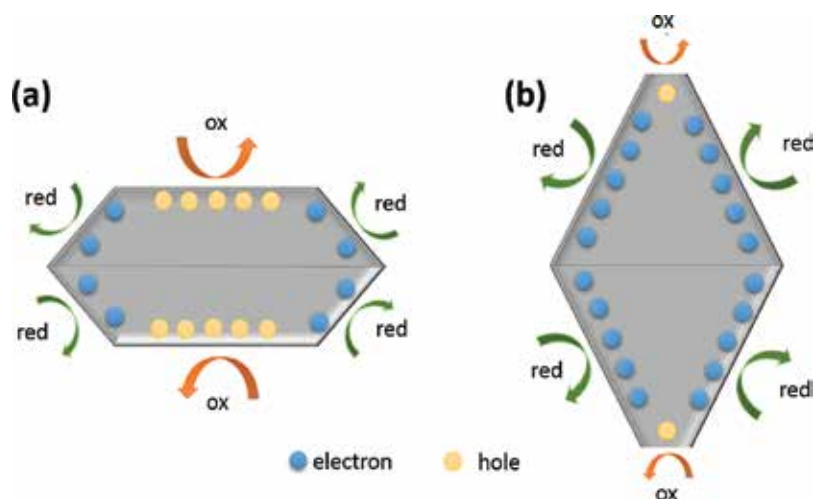
Figure 3. Schematic images of spatial separation of redox sites on titanium dioxide structures with a specific exposed crystal facets: (a) larger surface area of oxidation sites (holes) and small surface area of reduction sites (electrons), and (b) smaller surface area of oxidation sites and larger surface area of reduction sites.

1.2. Solvothermal method assisted by microwave radiation

The structural, optical and electrical properties of titanium dioxide nanostructures strongly depend on the growth method. Several chemical, electrochemical and physical techniques have been employed to grow different TiO$_2$ nanostructures [3, 23–26] with different properties, like thermal evaporation [27], potentiostatic anodization [28], electrospinning [29], precipitation [30], solvothermal and hydrothermal synthesis, whether by conventional heating [31] or microwave radiation [3]. The use of this latter synthesis technique has been growing lately for different types of nanostructured semiconductors [3, 32–36].

The greatest advantage of using microwave radiation synthesis is related to the opportunity to complete reactions in a short period of time, when compared with conventional heating. Microwave radiation transfers the energy directly to the reactive species of the solutions favoring some transformations that are unobtainable with conventional heating [37]. By coupling directly with the molecules dipoles, the microwaves promote a rapid increase of temperature, originating a localized superheating of the molecules, which thus influences the solution [37].

So, the heating with microwave process occurs by two distinct mechanisms: through dipole rotation and/or ionic conduction, by the reversals of dipoles and displacement of charged ions present in the solution (solute and solvent) [38].

The heating caused by dipole rotation movement is due to an energy transfer between molecules when their dipoles try to align with the electric field changing of the electromagnetic radiation (see **Figure 4**). The coupling efficiency of dipoles with the electric field is related with the solution molecules polarity [37].

The heating due to ionic conduction movement results from the free ions or ionic species movement present in the solution. The friction between this species results in the increase of solution temperature [37].

So, microwave heating is mainly characterized by energy transfer between molecules, while conventional heating is characterized by energy transfer through convection, thermal conduction or radiation between the vessels external materials to the solution. Microwave radiation will interact with the solution molecules, converting the electromagnetic energy into thermal energy [40].
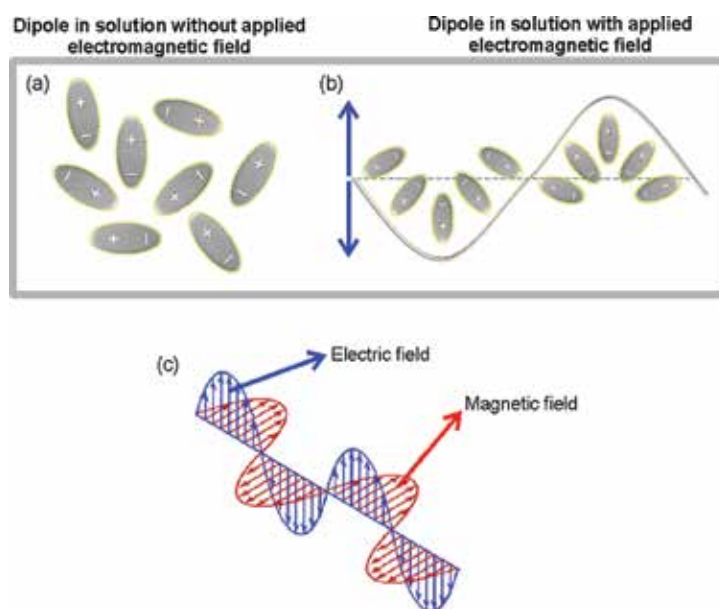
Figure 4. (a) Dipoles in the solution with no applied field; (b) dipoles alignment with the applied field; (c) Schematic representation of an applied electromagnetic field.

By this reason, it can be concluded that the use of different solvents will be relevant in organic synthesis. The polarity of a solvent is one of the most important parameters to be considered in microwave synthesis. The ability of a molecule to couple with microwave energy increases with the increase of solution polarity and thus the heating is more efficient.

The interaction between a polar molecule and microwave radiation can be estimated by the Loss Tangent (tan δ, see Equation 1), that determines the ability that a solvent possesses in absorbing microwave radiation and convert the electric energy into heat. This parameter give us the efficiency of microwave heating of a certain solvent [39, 41]:

$$\tan \delta = \frac{\varepsilon''}{\varepsilon'}$$

where ε″ is the loss factor that determines the efficiency of converting absorbed microwave energy into heat; ε′ is the dielectric constant that measure the ability of a molecule to store electrical potential energy with an applied electric field.

Thus, the higher the Loss Tangent (tan δ) is, the better will be the solvent in absorbing the microwave radiation and converting it into heat [37, 39].

Table 1 shows the loss tangents, dielectric constant, boiling point and viscosity of different types of solvents, including water, ethanol, 2 - propanol and methanol [37, 42, 43].

The solvents with higher values of dielectric loss are considered higher absorbers, which leads to the fast heating of the solution with the presence of microwave radiation. The solvents that are considered medium absorbers, also heat the solution efficiently but require more time to reach the synthesis temperature. The low absorbers solvents can heat to temperatures high above the solution boiling point, but longer times or higher microwave power is necessary.

	Solvent	Tan δ	Dielectric Constant	Boiling point (°C)	Viscosity (cP) at 25 °C
High	Ethylene glycol	1.17	38.0	197.3	35.7
(tan δ > 0.5)	**Ethanol**	**0.94**	**24.6**	**78.4**	**0.983**
	2 – propanol	**0.80**	**20.2**	**82.6**	**2.040**
	Methanol	**0.66**	**33.0**	**64.7**	**0.507**
	1 – butanol	0.57	17.8	117.6	2.573
Medium	2 – butanol	0.45	15.8	98.0	3.100
(0.1 < tan δ < 0.5)	Dichlorobenzene	0.28	9.9	180.5	1.320
	Acetic acid	0.17	6.1	118.0	1.060
	Dichloroethane	0.13	10.7	84.0	0.780
	Water	**0.12**	**80.0**	**100.0**	**0.890**
Low	Chloroform	0.091	4.8	61.2	0.510
(tan δ < 0.1)	Ethyl Acetate	0.059	6.0	77.0	0.420
	Acetone	0.054	21.0	56.0	0.300
	Toluene	0.040	2.4	111.0	0.560
	2 - ethoxyethanol	0.039	3.3	135.0	2.100

Table 1. Loss tangents, dielectric constant, boiling point and viscosity of solvents.

The viscosity of a solvent is also an important factor, as it will affect its ability to absorb microwave energy since it will affect the molecular rotation. In a high viscous medium, molecular mobility is reduced, thus making it difficult for the molecules to align with the electromagnetic radiation. By this reason, the heat produced by dipole rotation decreases [38].

As mentioned above, the use of different solvents could strongly affect the crystalline phase and microstructure of TiO$_2$ structures and its facets, due to the different boiling points, chain

lengths and structure, possible complexes and polarity of the solvents used [44–47]. For this case, the selection of the solvent should consider the high extracting power and strong interaction with electromagnetic field. Polar molecules and ionic solutions strongly absorb microwave energy due to the permanent dipole moment. Non-polar solvents will not heat up.

2. Methods used

2.1. Seed layer and synthesis of TiO_2 nanostructured arrays

The TiO_2 thin film to serve as a seed was deposited on a flexible PEN (Polyethylene naphthalate) substrate using the spin-coating method. A coating solution have been prepared from titanium isopropoxide ($Ti[OCH(CH_3)_2]_4$; 97%, CAS: 546-68-9), ethanolamine, MEA (C_2H_7NO; 99%, CAS: 141-43-5) and 2-methoxyethanol ($C_3H_8O_2$, 99.8%, CAS: 109-86-4), all from Sigma-Aldrich, that were used without further purification. In a typical experiment, the spin-coating solution was prepared by dissolving the $Ti[OCH(CH_3)_2]_4$ in 2-methoxyethanol and adding the ethanolamine. The concentration of the solution was chosen to be 0.35 M, in a proportion of 1:1 of titanium isopropoxide and ethanolamine. The resulting solution was then stirred for 2 hours at 60°C. The mixed solution was filtered to yield a clear and homogeneous solution and then used for preparing films by spin-coating method. Before deposition, the substrates (with 20 × 20 mm side) were successively cleaned with ethanol, and deionized water in an ultrasonic bath. The prepared solution was then spin coated on the substrate at 3000 rpm for 35 seconds at room temperature. After deposition, the films were dried at 180°C for 10 minutes in a hot plate in order to remove the solvent. After repeating the coating – drying cycles 4 times, the substrates were annealed for 1 hour at a temperature of 180°C.

After uniformly coating the PEN substrates with TiO_2 thin films, TiO_2 nanostructured arrays were synthesized by solvothermal method assisted by microwave radiation. The solution has been prepared from titanium isopropoxide ($Ti[OCH(CH_3)_2]_4$; 97%, CAS: 546-68-9), hydrochloric acid (HCl; 37% CAS: 7647-01-0) and as solvent it was used double distilled water, isopropyl alcohol (or 2 – propanol, $(CH_3)_2CHOH$, 99.5%, CAS: 67-63-0), ethanol (CH_3CH_2OH, 99.5%, CAS: 64-17-5) and methanol (CH_3OH, 99.8%, CAS: 67-56-1). In a typical reaction, 15 ml of HCl was added to 45 ml of each solvent. To each of these mixtures were added 2 ml of titanium isopropoxide. The solutions were stirred for 10 minutes.

The synthesis of TiO_2 nanostructures were performed by solvothermal method assisted by microwave radiation using a CEM Focused Microwave Synthesis System Discover SP. The TiO_2 seeded PEN substrates (20 × 20 mm) were placed at an angle against the vessel, with the seed layer facing down (see **Figure 5**) and filled with 20 ml of the prepared solution [3]. Time, power and maximum pressure (limited pressure) have been set at 120 min, 100 W and 250 Psi, respectively. The vessels were kept sealed by the constraining surrounding pressure. The temperature was kept at 110°C due to the use of flexible substrates.
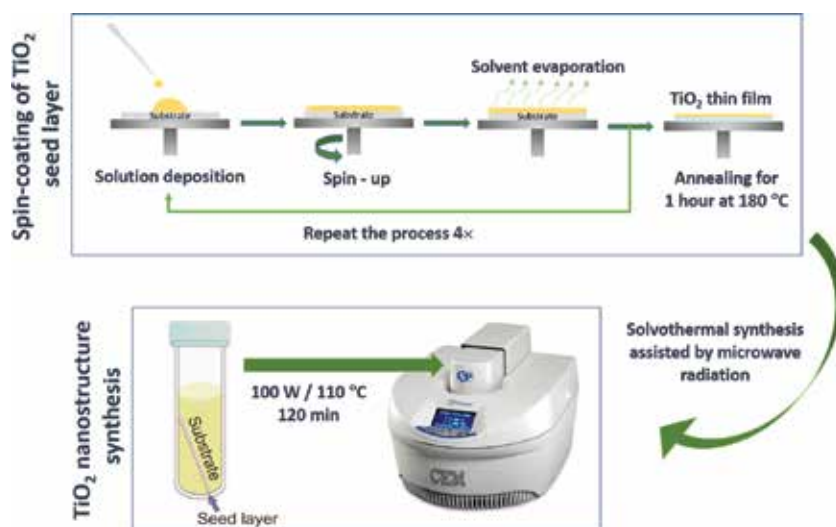
Figure 5. Scheme of the TiO$_2$ seed layer production using the spin-coating method, followed by TiO$_2$ nanostructured synthesis by solvothermal method assisted by microwave radiation.

2.2. Characterization techniques

The surface morphology and cross-section observations of TiO$_2$ nanocrystals has been characterized by scanning electron microscopy (SEM) with a Carl Zeiss AURIGA equipment coupled with an X-ray Energy Dispersive Spectrometer (EDS). X-ray diffraction measurements were carried out using a PANalytical's X'Pert PRO MRD, with a monochromatic CuKα radiation source (wavelength 1.540598 Å) and from 30° to 75° (2θ), in a parallel beam config-uration for grazing-incident experiments. The grazing XRD data were recorded with the detector rotated to a 0D configuration and at grazing-incident angles of 0.75, 1.0 and 1.25° with a step size of 0.1°. For comparison, rutile, anatase, brookite power diffractograms have been simulated with PowderCell [48] using crystallographic data from [49].

Optical transmittance and band gap measurements of the TiO$_2$ nanorods films were performed at room temperature (RT) using a Perkin Elmer lambda 950 UV/VIS/NIR spectrophotometer. The transmittance spectra were recorded between 250 to 850 nm.

2.3. Characterization of TiO$_2$ nanostructured arrays as photocatalytic agent

TiO$_2$ nanostructures arrays have been used in photocatalytic degradation of organic pollutants due to their non-toxic and higher photocatalytic efficiency with good sensing behaviour. The ultra violet (UV) photocatalytic activities of TiO$_2$ nanostructures were evaluated at RT from the degradation of methylene blue, MB, (C$_{16}$H$_{18}$ClN$_3$S·3H$_2$O, CAS: 61-73-4) from Scharlau. The experiments were carried out following the International standard ISO 10678. The MB concentration used was 4 mg/l, in which a PEN substrate with the TiO$_2$ nanostructured array produced with each solvent was immersed in 50 ml of this solution for each experiment. Prior

to UV exposure, the sample was placed in the dark for 30 min to establish absorption-desorption equilibrium.

For UV exposure, a deuterium lamp model L11798 was used, from Hamamatsu, with an emission wavelength of 160 nm. In each measurement, 4 ml of MB solution were collected regular intervals (from 15 min up to a total time of 120 min). At each time, it was tested by a UV-Vis spectrophotometry, using the same Perkin Elmer lambda 950 UV/VIS/NIR spectro-photometer. The absorbance (A) was obtained between 250 to 800 nm.

3. Results and discussion

Figure 6 shows a real image of the materials produced after microwave radiation. As it can be seen, the substrates are fully covered demonstrating that the seed layer is efficient for the TiO$_2$ nanostructured arrays growth (the edges are seed/arrays free, due to the use of kapton tape for support). Moreover, this also demonstrates that microwave synthesis using flexible substrates is a valid option for low cost applications. Regarding the solvents tested, several solvents were used; however only the ones presented on this study resulted in a homogeneous growth of TiO$_2$ nanostructures covering completely the PEN substrate.

Figure 6. Photograph of TiO$_2$ nanostructured arrays on PEN substrates. All solvents produced similar samples, such as the one presented in this image.

3.1. Behaviour of solvents under microwave radiation

To infer the solvent behaviour under microwave radiation, the temperature and pressure profile of each solvent during TiO$_2$ synthesis was recorded and is presented on **Figure 7**. Pressure and temperature are two important parameters that will influence the nanoparticle morphology [50]. So, in a typical microwave assisted synthesis, in which the temperature is controlled, the path will involve ramping up to the desired temperature and holding the

desired temperature for a specific period of time, while the power fluctuates in order to maintain the parameters of the reaction (temperature and pressure). Once the holding time is complete, the reaction is quenched by a stream of nitrogen in order to cold down the vessel and the solution.
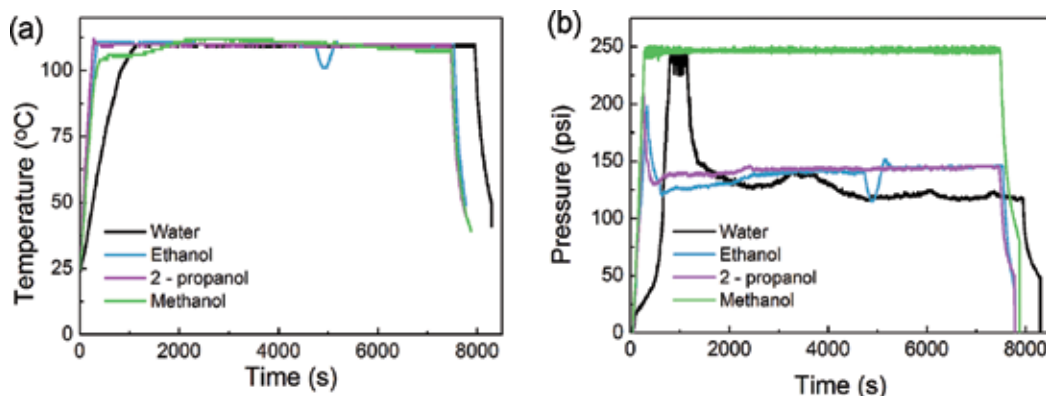

Figure 7. Profile of (a) temperature and (b) pressure obtained during TiO$_2$ nanostructured synthesis with different solvents, water, ethanol, 2 – propanol and methanol, when subject to microwave radiation of 100 W for 120 minutes and a pressure limit of 250 Psi.

As expected and in accordance to the values presented in **Table 1** (*Tan δ)*, in the case of water (a medium absorber), it took a longer period of time to reach the synthesis temperature when compared to the other solvents (all considered higher absorbers), see **Figure 7.a**).

The other parameter that is imperative to control in microwave assisted synthesis is the pressure inside the vessel. A pressurized environment can bring some advantages. As the temperature of a solvent increase above its boiling point, more pressure builds inside the reaction vessel [37]. From **Figure 7**, it is possible to observe that methanol (the solvent with a lower boiling point) originated a higher pressure value inside the reaction vessel.

3.2. SEM analysis

It is well known that for preparing uniform nanoparticles, it is necessary to induce a single nucleation event and thus preventing additional nucleation during the subsequent growth process [51]. Nevertheless, the presence of inorganic and organic anionic species in the starting solution will affect parameters such as nucleation, crystal growth and morphology of nanoparticles [52]. Moreover, synthesis employing different solvents, such as the ones used in this work, is highly expected to affect the crystalline phase, microstructure and optoelectronic properties of the produced nanoparticles, mainly due to the difference in the boiling point, chain lengths and structure, coordination numbers and polarity [5].

As it has been shown previously, the heating and pressure inside the reaction vessels will greatly depend on the solvents and precursors used. By this reason, it is clear that the temperature of reaction and the heating method will strongly influence the nucleation and crystal

growth, which will produce effect on size, shape, morphology and crystal structure (crystal facets) of the final synthesized nanoparticle.

Figure 8 shows the morphology of TiO_2 nanostructures formed with the different solvents under 100 W for 120 minutes with limited temperature and pressure of 110°C and 250 Psi, respectively. The microwave synthesis with water as solvent resulted in agglomerates with higher packing density of TiO_2 nanorods, forming compact structures (see **Figure 8.a**) and displaying average width of ~20 nm and length ranging from 1 to 1.5 μm. These results are in agreement to [3], where thin and long nanorods were observed using the same proportion of water/acid. Ethanol, on the other hand, resulted in TiO_2 nanorods with approximately 20 nm in width, however smaller in length (see **Figure 8.b**). The length varied from 800 to 1000 nm. When using 2 – propanol, the array structures varied and turned to be a mixture of nanorods and nanoparticles without a defined shape. These mixed nanostructures appeared as agglomerates of flower-like TiO_2 nanostructures (see **Figure 8.c**). The agglomerate sizes varied from 800 to 1100 nm. Methanol resulted in TiO_2 nanowires (~20 nm in width) grouped in agglomerates (see **Figure 8.d**). The compact structure observed with water was not observed, where the nanorods appeared to be well separated. Two sources of structures could be detected on the cross-section image, forming a dense layer of TiO_2 nanorods at the bottom with nanorod agglomerates on top. The total length of these structures together varied from 800 to 1000 nm. From the cross-section images, it could be identified that the arrays were grown with similar thickness, despite the disparities on the structures observed.

In solvothermal synthesis reactions, the temperature has been reported as one of the most important parameters to control the morphology of nanoparticles [52, 53]. In this present study, the synthesis temperature was limited to 110°C, due to the use of a low temperature polymeric substrate, so it will be the pressure inside the vessel that is going to play an important role in the TiO_2 nanostructure synthesis.

The use of water, with a higher boiling point but lower $tan\ \delta$, and thus with a small microwave coupling efficiency [37], induces a lower heating rate and lower pressure inside the reaction vessel. The produced nanorods are longer in length (slower reaction rate induces large particle size). On the other hand, the nanorods produced with ethanol are smaller in length, and this can be associated to the fact that ethanol displays a higher value of $tan\ \delta$, and a lower boiling point (when compared with water) and in consequence with higher microwave coupling efficiency and thus higher heating rate resulting in slightly higher pressure inside the vessel (faster reaction rate induces smaller particle size) [54].

In the case of 2 – propanol, as this solvent presents a medium value of $tan\ \delta$ (see **Table 1**) it is one of the most efficient in terms of coupling with microwave radiation. In this case, it is expected to be promoted a rapid growth of TiO_2 nanostructures. On the other hand, this is the solvent that presents higher value of viscosity which will reduce the dipole movement on the solution. The diffusion of ions in the solvent decrease with increasing viscosity [55].These characteristics are expected to be responsible for the undefined structures observed for this solvent.

Due to the very low boiling point of methanol, the pressure inside the reaction vessel increases rapidly, reaching the imposed limit. The synthesis of TiO$_2$ nanoparticles in such high pressure condition induces the growth of very thin TiO$_2$ nanowires, as reported by Wen et al., [56] that states the formation of ultra-long nanowires which may arise from the slow nucleation rate and very fast growth rate.
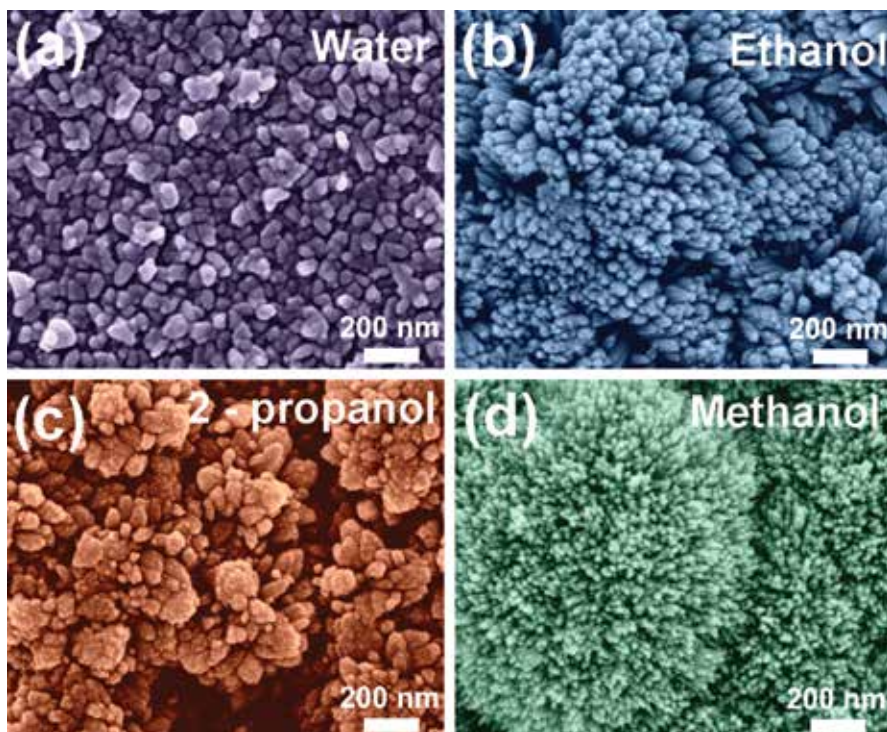
Figure 8. SEM images of TiO$_2$ nanostructures synthesized by solvothermal method, assisted by microwave radiation, using a microwave power of 100 W for 120 minutes and a temperature of 100°C for the solvents tested: (a) water, (b) ethanol, (c) 2 – propanol and (d) methanol. The insets show the cross-section of the produced TiO$_2$ nanostructures.

3.3. XRD analysis

Due to the intense XRD peak of PEN substrate at 2θ = 26°, GIXRD experiments were carried out for the TiO$_2$ nanostructures obtained with all the solvents tested. The results are presented on **Figure 9**, where it is possible to observe the experimental diffractograms for the different materials, together with the simulated diffractograms for anatase, rutile and brookite.

For all the materials synthesized, the XRD peaks could be assigned to either rutile or anatase. The nanorod arrays produced with water presented a predominant rutile phase, and the presence of anatase is not clear. This result is expected as the proportion of water/acid used during synthesis under microwave radiation has been reported to form essentially rutile [3]. For the materials synthesized with ethanol, as for the water arrays, just the rutile phase could

be assigned. The 2 – propanol solvent, on the other hand, can be expected to contain minor amounts of anatase, together with rutile. Methanol, just like the 2 – propanol arrays, is expected to have mainly the anatase phase and rutile. The appearance of the peak of PEN at ~48° is expected to be related to the thinner array thickness of the materials. Water formed thicker arrays, and the PEN peak is not evident.

Figure 9. Grazing incident XRD diffractograms of TiO_2 nanostructured arrays produced with different solvents: water, ethanol, 2 – propan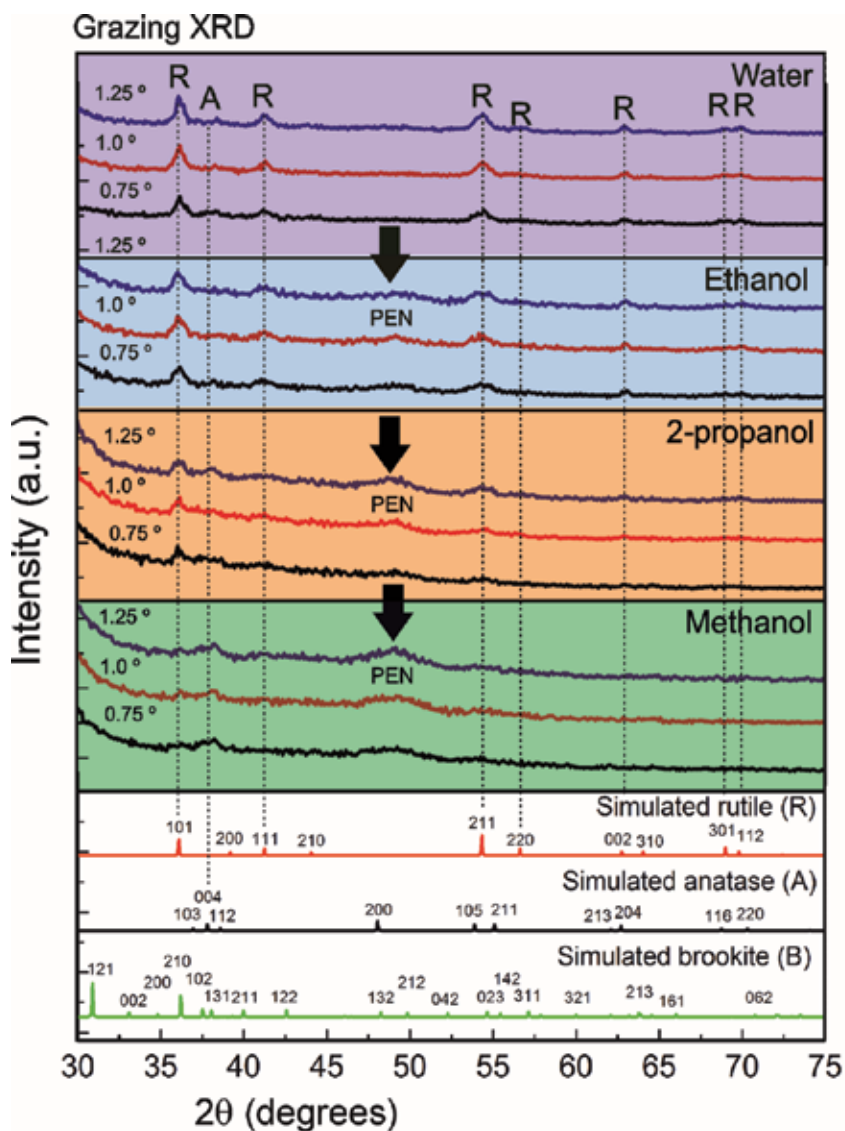ol and methanol. The grazing incident angles tested were 0.75, 1.0 and 1.25 °. The simulated rutile, anatase and brookite diffractograms are presented for comparison.

The coordination number of different types of alcohol can affect the final non-covalent bonding between molecules (oligomers) and the final structure of building blocks of a material. So, by using different types of solvents, it is possible to obtain a fivefold coordinated titanium and twofold coordinated oxygen in (1 0 1) plane of anatase phase of TiO$_2$ nanostructures instead of a fivefold coordinated titanium and two and threefold coordinated oxygen in (1 0 0) plane of rutile phase [5].

As reported by Yoon et al., [57], the TiO$_2$ crystal structure of the as-synthesized nanostructures, may change from anatase to rutile or brookite, with the number of carbon atoms to the solvent used for synthesis. The reaction between the precursor and the alcohol solvents become less vigorous with the increase in the number of carbon atoms.

3.4. Optical characterization

The bandgap of the TiO$_2$ nanostructured arrays were estimated from transmittance data through Tauc plots. Transmittance studies were carried out for the TiO$_2$ nanostructures produced with the different solvents tested. The optical bandgap (E_g) on the semiconductor is related to the optical transmittance coefficient (α) and the incident photon energy [58]. The relation can be given as:

$$\alpha\left(h\nu\right) = A(h\nu - E_g)^n$$

where α is the linear absorption coefficient of the material, $h\nu$ is the photon energy impinging on the material, A is a proportionality constant of the matrix density states and n is a constant exponent, that for the case of TiO$_2$ (a direct band gap semiconductor), presents the value, n = ½.

The following relation is obtained:

$$[\alpha(h\nu)]^2 = A(h\nu - E_g)$$

The bandgap can be estimated by plotting $[\alpha(h\nu)]^2$ against $h\nu$, and extracting the intersection of the extrapolation of the linear portion with zero in the photon energy axis, when no bandtails are considered [58]. The results are shown on **Figure 10**. Similar values were obtained for synthesis with water, ethanol and 2 – propanol, with a bandgap value of 3.2 eV. For methanol it was observed at a slight lower bandgap value of 3.16 eV. As most of the materials presented the rutile phase, and as the bandgap of a TiO$_2$ nanostructure is strongly dependent on the grain size and crystallographic phase, the presence of anatase (with a higher bandgap value) on TiO$_2$ nanostructured arrays could have influenced the bandgap values. Nevertheless, these values are within the values range reported in the literature for different crystallographic structures of TiO$_2$.
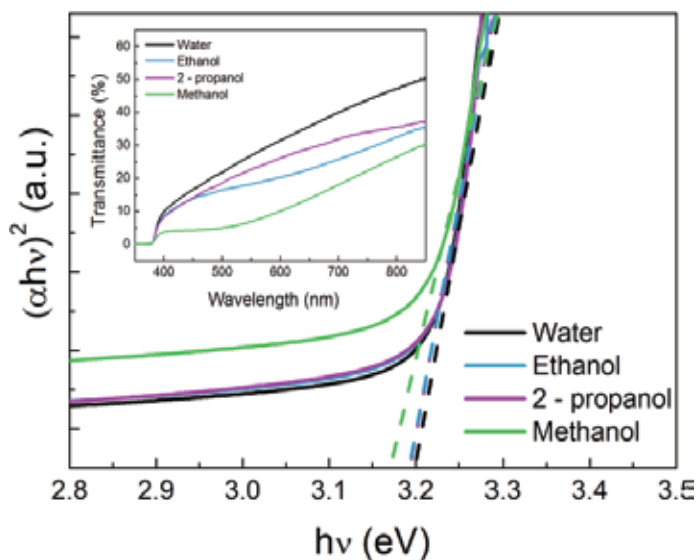
Figure 10. $[\alpha(h\nu)]^2$ variation versus photon energy hν. The inset shows the optical transmittance of TiO$_2$ nanostructured arrays on PEN substrate.

3.5. TiO$_2$ nanostructures arrays photocatalytic activity

Although it has been reported by several authors that the photocatalytic efficiency of anatase is higher than rutile or brookite, it has been recognized in the last few years that the simultaneous presence of all or some polymorphic phases may also be beneficial in photocatalytic applications [59].

The photocatalytic activity of TiO$_2$ nanostructures is related to the surface-phase structure and depends on different properties such as bandgap, crystallite size, specific surface are and active facets [60]. The TiO$_2$ active facets are {001} for anatase [22], {110} > {001} > {100} for rutile [11] and {210} for brookite [9].

The photocatalytic behaviour of different TiO$_2$ nanostructures arrays produced with the different solvents was evaluated by observing their efficiency on degrading the MB under UV radiation. **Figure 11** shows the photocatalytic results for the MB degradation with different TiO$_2$ nanostructures produced with each solvent tested. It is possible to observe that a gradual MB degradation occur under UV radiation, for all TiO$_2$ nanostructures produced, reaching values of 77% for water, 84% for ethanol, 79% for 2-propanol and 90% for methanol, after 120 min of exposure.

The higher MB degradation obtained for samples produced with methanol can be attributed to different factors, such as having a higher specific surface area (thin nanorods, relatively separated, when compared to the other morphologies) or by containing a greater amount of anatase as TiO$_2$ crystallographic phases, being directly related to the different exposed facets [3].
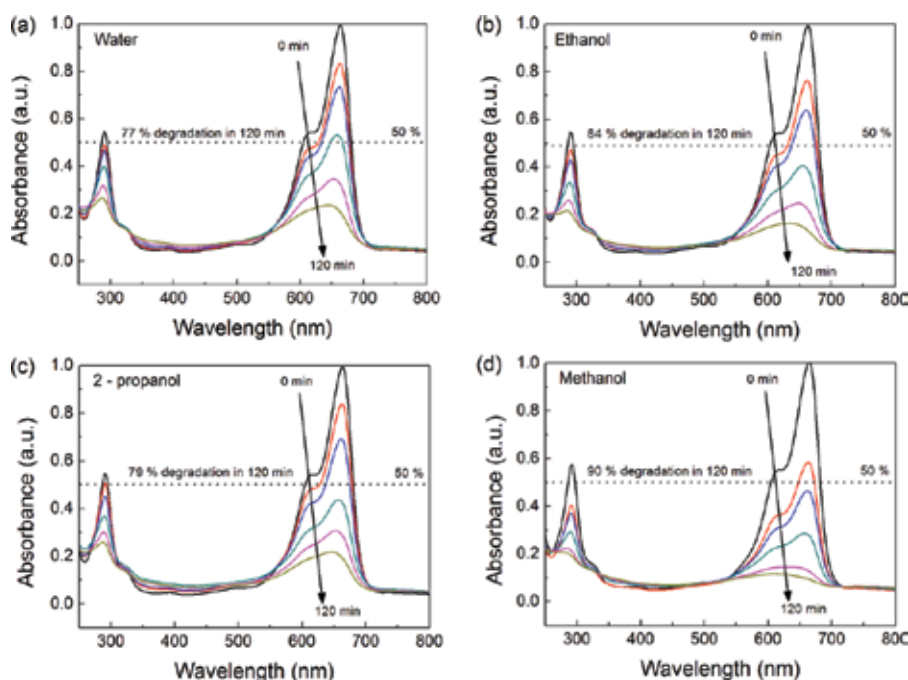
Figure 11. Normalized absorbance spectra of MB degradation under UV radiation as a function of exposure time in the presence of each TiO₂ nanostructured arrays synthesized with (a) water, (b) ethanol, (c) 2 - propanol and (d) methanol at room temperature and under an UV radiation of 160 nm, for 120 minutes.
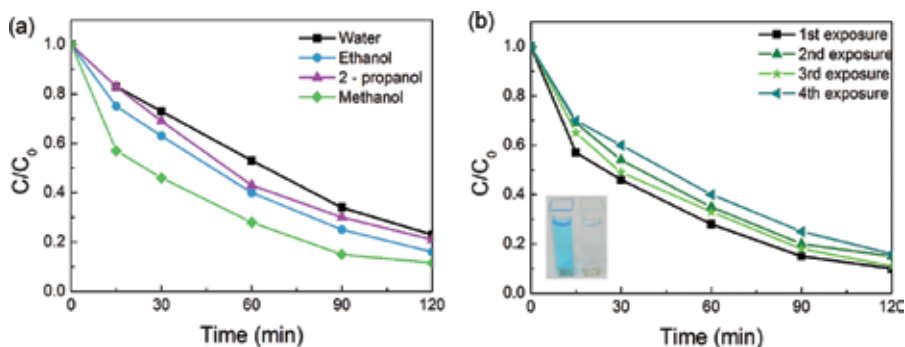
Figure 12. (a) MB concentration versus exposure time for the different photocatalysts produced with each solvent tested; (b) MB degradation ratio (C/C_0) *vs.* UV exposure time for the TiO₂ synthesized with methanol, after several UV exposure experiments. On the inset is possible to observe the colour difference in MB before and after the degradation experiment.

Figure 12.a presents the degradation ratio (C/C_0) as a function of UV exposure time, where C is the absorbance of the MB solution at each exposure time and C_0 is the absorbance of the initial solution [61]. By analyzing the obtained results, the methanol presents an initial higher efficiency on MB degradation; nevertheless for all the arrays produced, the MB degradation

appears to be continuous over time, with methanol always showing higher degradation for all UV exposure times. The efficiency of the TiO_2 nanostructured arrays synthesized with methanol under microwave radiation was confirmed and is presented in **Figure 12.b**. It is clear that the material presents remarkable stability and reusability after several UV exposures.

4. Conclusion

On the present chapter, we have shown the influence of using different solvents on the synthesis of TiO_2 nanostructured arrays under microwave radiation. The solvents played a crucial role on the final TiO_2 structure, which influenced directly their photocatalytic behaviour. Different TiO_2 nanostructures morphologies were obtained with an evident effect on the nanostructure sizes. The produced TiO_2 nanostructures arrays were essentially from rutile phase; nevertheless in some conditions they presented a mixture of crystallographic phases (rutile and anatase) which may enhance the photocatalytic activity of the nanostructured arrays. The optical bandgap of the materials were measured to be 3.16 and 3.2 eV, consistent with the theoretical values of the TiO_2 phases.

Regarding the photocatalytic degradation of methylene blue in the presence of TiO_2 nanostructured arrays, the ones synthesized with methanol presented a higher photocatalytic activity (90% over 120 min) probably due to its higher surface area, and taking the advantage of having higher amounts of the anatase phase. Some experiments were carried out to infer the stability and reproducibility for MB photodegradation with arrays synthesized with methanol, which demonstrated enhanced and comparable results after several exposure experiences.

Acknowledgements

Author details

Ana Pimentel[*], Daniela Nunes, Sónia Pereira, Rodrigo Martins and Elvira Fortunato[*]

*Address all correspondence to: acgp@campus.fct.unl.pt, emf@fct.unl.pt

CENIMAT/I3N, Department of Materials Science, Faculty of Science and Technology, NOVA University of Lisbon, FCT-UNL,Lisbon, Portugal

References

[1] Lee W.S., Park Y. S., Chou Y. K. Hierarchically Structured Suspended TiO$_2$ Nanofibers for Use in pH Sensor Devices. ACS Applied Materials Interfaces. 2014;6(12189–12195) DOI: http://dx.doi.org/10.1021/am501563v

[2] Roy P., Kim D., Lee K., Spiecker E., Schmuki P. TiO$_2$ nanotubes and their application in dye-sensitized solar cells. Nanoscale. 2010;2(45–49) DOI: 10.1039/b9nr00131j

[3] Nunes D., Pimentel A., Pinto J. V., Calmeiro T. R., Nandy S., Barquinha P., et al. Photocatalytic behavior of TiO$_2$ films synthesized by microwave irradiation. Catalysis Today. 2015; DOI: 10.1016/j.cattod.2015.10.038

[4] Ohno T., Lee S. Y., Yang Y. Fabrication of morphology-controlled TiO$_2$ photocatalyst nanoparticles and improvement of photocatalytic activities by modification of Fe compounds. Rare Metals. 2015;34(291–300) DOI: 10.1007/s12598-015-0483-8

[5] Golobostanfard M. R., Abdizadeh H. Effect of mixed solvent on structural, morphological, and optoelectrical properties of spin-coated TiO$_2$ thin films. Ceramics International. 2012;38(5843–5851) DOI: 10.1016/j.ceramint.2012.04.034

[6] Zhao L., Xia M., Liu Y., Zheng B., Jiang Q., Lian J. Structure and photocatalysis of TiO$_2$/ZnO double-layer film prepared by pulsed laser deposition. Materials Transactions. 2012;53(463–468) DOI: 10.2320/matertrans.M2011345

[7] Nakata K., Fujishima A. TiO$_2$ photocatalysis: Design and applications. Journal of Photochemistry and Photobiology C: Photochemistry Reviews. 2012;13(169–189) DOI: 10.1016/j.jphotochemrev.2012.06.001

[8] Lin H., Huang C., Li W. Ni C. Shah S., Tseng Y. Size dependency of nanocrystalline TiO$_2$ on its optical property and photocatalytic reactivity exemplified by 2-chlorophenol. Applied Catalysis B: Environmental. 2006;68(1–11) DOI: 10.1016/j.apcatb.2006.07.018

[9] Di Paola A., Bellardita M., Palmisano L. Brookite, the Least Known TiO$_2$ Photocatalyst. Catalysts. 2013;3(36–73) DOI: 10.3390/catal3010036

[10] Landmann M., Rauls E., Schmidt, W. G. The electronic structure and optical response of rutile, anatase and brookite TiO$_2$. Journal of physics. Condensed matter: an Institute of Physics journal. 2012;24(195503) DOI: 10.1088/0953-8984/24/19/195503

[11] Fujishima A., Rao T. N. Tryk D. A. Titanium dioxide photocatalysis. Journal of Photochemistry and Photobiology C: Photochemistry Reviews. 2000;1(1-21) DOI: 10.1016/S1389-5567(00)00002-2

[12] Sun W., Liu H., Hu J., Li,J. Controllable synthesis and morphology-dependent photocatalytic performance of anatase TiO$_2$ nanoplates. RSC Advances. 2015;5(513-520) DOI: 10.1039/C4RA13596B

[13] Tang H., Prasad K., Sanjinès R., Schmid P. E., Lévy F. Electrical and optical properties of TiO_2 anatase thin films. Journal of Applied Physics. 1994;75(2042) DOI: 10.1063/1.356306

[14] Daude N., Gout C., Jouanin C. Electronic band structure of titanium dioxide. Physical Review B. 1977;15(3229-3235) DOI: 10.1103/PhysRevB.15.3229

[15] Agrios A. G., Pichat P. State of the art and perspectives on materials and applications of photocatalysis over TiO_2. Journal of Applied Electrochemistry. 2005;35(7-8):(655-663) DOI: 10.1007/s10800-005-1627-6

[16] Li L., Salvador P. A., Rohrer G. S. Photocatalysts with internal electric fields. Nanoscale. 2014;6(1):(24-42) DOI: 10.1039/c3nr03998f

[17] Xu H., Ouyang S., Liu L., Reunchan P., Umezawa N., Ye J. Recent advances in TiO_2-based photocatalysis. Journal of Materials Chemistry A. 2014;2(32):(12642). DOI: 10.1039/C4TA00941J

[18] Pan L., Zou J. J., Wang S., Liu X. Y., Zhang X., Wang L. Morphology evolution of TiO_2 facets and vital influences on photocatalytic activity. ACS applied materials & interfaces. 2012;4(3):(1650-1655) DOI: 10.1021/am201800j

[19] Li J., Xu D. Tetragonal faceted-nanorods of anatase TiO_2 single crystals with a large percentage of active {100} facets. Chemical communications (Cambridge, England). 2010;46(13):(2301-2303) DOI: 10.1039/b923755k

[20] Kobayashi M., Kato H., Kakihana M. Synthesis of Titanium Dioxide Nanocrystals with Controlled Crystal- and Micro-structures from Titanium Complexes. Nanomaterials and Nanotechnology. 2013;3(1-10) DOI: 10.5772/57533

[21] Ohno T., Sarukawa K., Matsumura M. Crystal faces of rutile and anatase TiO_2 particles and their roles in photocatalytic reactions. New Journal of Chemistry. 2002;26(9): 1167-1170. DOI: 10.1039/b202140d

[22] Dozzi M., Selli E. Specific facets-dominated anatase TiO_2: fluorine-mediated synthesis and photoactivity. Catalysts. 2013;3(2):455-485. DOI: 10.3390/catal3020455

[23] Wang S., Qian H., Hu Y., Dai W., Zhong Y., Chen J., et al. Facile one-pot synthesis of uniform TiO_2 −Ag hybrid hollow spheres with enhanced photocatalytic activity. Dalton Trans. 2013;42(4):1122-1128. DOI: 10.1039/C2DT32040A

[24] Sodano H. A., Koka A., Guskey C. R., Michael Seigler T., Bailey S. C. C. Introducing perturbations into turbulent wall-bounded flow with arrays of long TiO_2 nanowires. Journal of Fluids Engineering. 2014;137(2):024501. DOI: 10.1115/1.4027432

[25] Bauer S., Park J., Faltenbacher J., Berger S., von der Mark K., Schmuki P. Size selective behavior of mesenchymal stem cells on ZrO(2) and TiO(2) nanotube arrays. Integrative biology: quantitative biosciences from nano to macro. 2009;1(8-9):525-32. DOI: 10.1039/b908196h

[26] Lui G., Liao J.-Y., Duan A., Zhang Z., Fowler M., Yu A. Graphene-wrapped hierarchical TiO$_2$ nanoflower composites with enhanced photocatalytic performance. Journal of Materials Chemistry A. 2013;1(30):12255. DOI: 10.1039/c3ta12329d

[27] Lee J.-C., Park K.-S., Kim T.-G., Choi H.-J., Sung Y.-M. Controlled growth of high-quality TiO$_2$ nanowires on sapphire and silica. Nanotechnology. 2006;17(17):4317-4321. DOI: 10.1088/0957-4484/17/17/006

[28] Paulose M., Shankar K., Yoriya S., Prakasam H. E., Varghese O. K., Mor G. K., et al. Anodic growth of highly ordered TiO$_2$ nanotube arrays to 134 microm in length. The journal of physical chemistry. B. 2006;110(33):16179-84. DOI: 10.1021/jp064020k

[29] Song M. Y., Kim D. K., Ihn K. J., Jo S. M., Kim D. Y. Electrospun TiO$_2$ electrodes for dye-sensitized solar cells. Nanotechnology. 2004;15(12):1861-1865. DOI: 10.1088/0957-4484/15/12/030

[30] Kim S.-J., Lee E. G., Park S. D., Jeon C. J., Cho Y. H., Rhee C. K., et al. Hotocatalytic effects of rutile phase tio2 ultrafine powder with high specific surface area obtained by a homogeneous precipitation process at low temperatures. Journal of Sol-Gel Science and Technology. 2001;22(1-2):63-74. DOI: 10.1023/A:1011264320138

[31] Liu B., Aydil E. S. Growth of oriented single-crystalline rutile TiO(2) nanorods on transparent conducting substrates for dye-sensitized solar cells. Journal of the American Chemical Society. 2009;131(11):3985-90. DOI: 10.1021/ja8078972

[32] Nunes D., Pimentel A., Barquinha P., Carvalho,P. A., Fortunato E., Martins R. Cu$_2$O polyhedral nanowires produced by microwave irradiation. Journal of Materials Chemistry C. 2014;2(30):6097. DOI: 10.1039/C4TC00747F

[33] Pimentel A., Rodrigues J., Duarte P., Nunes D., Costa F. M., Monteiro T., et al. Effect of solvents on ZnO nanostructures synthesized by solvothermal method assisted by microwave radiation: a photocatalytic study. Journal of Materials Science2015. 2015;50(17):5777-5787. DOI: 10.1007/s10853-015-9125-7

[34] Pimentel A., Nunes D., Duarte P., Rodrigues J., Costa F. M., Monteiro T., et al. Synthesis of long ZnO nanorods under microwave irradiation or conventional heating. The Journal of Physical Chemistry C. 2014;118(26):14629-14639. DOI: 10.1021/jp5027509

[35] Gonçalves A., Resende J., Marques A. C., Pinto J. V., Nunes D., Marie A., et al. Smart optically active VO$_2$ nanostructured layers applied in roof-type ceramic tiles for energy efficiency. Solar Energy Materials and Solar Cells. 2015;150:1-9. DOI: 10.1016/j.solmat.2016.02.001

[36] Marques A. C., Santos L., Costa M. N., Dantas J. M., Duarte P., Gonçalves A., et al. Office paper platform for bioelectrochromic detection of electrochemically active bacteria using tungsten trioxide nanoprobes. Scientific reports. 2015;5:9910. DOI: 10.1038/srep09910

[37] Hays B. L. Microwave Synthesis: Chemistry at the Speed of Light. 1st ed. Michigan University: CEM Publishing; 2002. 295 p. DOI: ISBN-0-9722229-0-1

[38] Veggi, P., Martinez J., Meireles A. Microwave-assisted extraction for bioactive compounds. In: Chemat F., Cravotto G., editors. Food Engineering Series. 1st ed. Boston: Springer US; 2013. p. 15–52. DOI: 10.1007/978-1-4614-4830-3

[39] Lidström P., Tierney J., Wathey B., Westman J. Microwave assisted organic synthesis —a review. Tetrahedron. 2001;57(45):9225-9283. DOI: 10.1016/S0040-4020(01)00906-1

[40] Thostenson E. T., Chou T.-W. Microwave processing: fundamentals and applications. Composites Part A: Applied Science and Manufacturing. 1999;30(9):1055-1071. DOI: 10.1016/S1359-835X(99)00020-2

[41] Gabriel C., Gabriel S., Grant E. H., Halstead S.J., Mingos B.M.D. Dielectric parameters relevant to microwave dielectric heating. Chemical Society Reviews. 1998;27(3):213. DOI: 10.1039/a827213z

[42] Nemmaniwar B. G., Kalyankar N. V., Kadam P. L. Dielectric behaviour of binary mixture of 2-chloroaniline with 2-methoxyethanol and 2-ethoxyethanol. Orbital - The Electronic Journal of Chemistry. 2013;5(1):1-6. DOI: ISSN 1984-6428

[43] Kappe C. O. How to measure reaction temperature in microwave-heated transformations. Chemical Society reviews. 2013;42(12):4977-90. DOI: 10.1039/c3cs00010a

[44] Karpovich N. F., Pugachevskii M. A., Shtarev D. S. Influence of synthesis conditions on the shape and size characteristics of TiO_2 nanocrystals. Nanotechnologies in Russia. 2013;8(11-12):751-755. DOI: 10.1134/S1995078013060086

[45] Wu Z., Gu Z., Zhao W. Wang H. Photocatalytic oxidation of gaseous benzene over nanosized TiO_2 prepared by solvothermal method. Chinese Science Bulletin. 2007;52(22):3061-3067. DOI: 10.1007/s11434-007-0456-x

[46] Zhou, Y., Wu H., Zhong X., Liu C. Effects of non-polar solvent on the morphology and property of three-dimensional hierarchical TiO_2 nanostructures by one-step solvothermal route. Journal of Nanoparticle Research. 2014;16(7):2466. DOI: 10.1007/s11051-014-2466-3

[47] Wu Y.-C., Tai Y.-C. Effects of alcohol solvents on anatase TiO_2 nanocrystals prepared by microwave-assisted solvothermal method. Journal of Nanoparticle Research. 2013;15(6):1686. DOI: 10.1007/s11051-013-1686-2

[48] Kraus W., Nolzeb G. POWDER CELL – a program for the representation and manipulation of crystal structures and calculation of the resulting X-ray powder patterns. Journal of Applied Crystallography. 1996;29(3):301-303. DOI: 10.1107/S0021889895014920

[49] Pearson W. B., Villars P., Calvert L. D. Pearson's Handbook of CrystallographicData for Intermetallic Phases. 1st ed. Ohio, USA: ASM International; 1985. 2886 p. DOI: ISBN 10: 0871702177

[50] Saxena V. K., Chandra U. Microwave synthasis: a physical concept. In: Chandra U., editors. Microwave Heating. 1st ed. India: InTech; 2011. p. 3-22. DOI: 10.5772/22888

[51] Bilecka I., Niederberger M. Microwave chemistry for inorganic nanomaterials synthesis. Nanoscale. 2010;2(8):1358. DOI: 10.1039/b9nr00377k

[52] Wu Z., Yang S., Wu W. Shape control of inorganic nanoparticles from solution. Nanoscale. 2016;8(3):1237-59. DOI: 10.1039/c5nr07681a

[53] Polsongkram D., Chamninok P., Pukird S., Chow L., Lupan O., Cha, G., et al. Effect of synthesis conditions on the growth of ZnO nanorods via hydrothermal method. Physica B: Condensed Matter. 2008;403(19-20):3713-3717. DOI: 10.1016/j.physb.2008.06.020

[54] Cao G. Nanostructures & Nanomaterials: Synthesis, Properties & Applications. 1st ed. London: Imperial College Press; 2004. 433 p. DOI: 1860944809

[55] Hu Z., Oskam G., Searson P. C. Influence of solvent on the growth of ZnO nanoparticles. Journal of Colloid and Interface Science. 2003;263(2):454-460. DOI: 10.1016/S0021-9797(03)00205-4

[56] Wen B.-M., Liu C.-Y., Liu Y. Solvothermal synthesis of ultralong single-crystalline TiO$_2$ nanowires. New Journal of Chemistry. 2005;29(7):969. DOI: 10.1039/b502604k

[57] Yoon S., Lee E.-S., Manthiram A. Microwave-solvothermal synthesis of various polymorphs of nanostructured TiO$_2$ in different alcohol media and their lithium ion storage properties. Inorganic chemistry. 2012;51(6):3505-12. DOI: 10.1021/ic202239n

[58] Pankove J.I. Optical Processes in Semiconductors. 1st ed. New Jersey: Dover Publications, Inc.; 1971. 422 p. DOI: 0486602753

[59] Zeng H. C. Preparation and integration of nanostructured titanium dioxide. Current Opinion in Chemical Engineering. 2011;1(1):11-17. DOI: 10.1016/j.coche.2011.07.002

[60] Guo Y., Li H., Chen J., Wu X., Zhou L. TiO$_2$ mesocrystals built of nanocrystals with exposed {001} facets: facile synthesis and superior photocatalytic ability. J. Mater. Chem. A. 2014;2(46):19589-19593. DOI: 10.1039/C4TA05068A

[61] Zhou N., Polavarapu L., Gao N., Pan Y., Yuan P., Wang Q., et al. TiO$_2$ coated Au/Ag nanorods with enhanced photocatalytic activity under visible light irradiation. Nanoscale. 2013;5(10):4236-41. DOI: 10.1039/c3nr00517h

First Principle Evaluation of Photocatalytic Suitability for TiO₂-Based Nanotubes

Yuri F. Zhukovskii, Sergey Piskunov, Oleg Lisovski,
Andrei Chesnokov and Dmitry Bocharov

Additional information is available at the end of the chapter

Abstract

Water splitting under the influence of solar light on semiconducting electrodes Immersed in aqueous electrolyte is a potentially clean and renewable source for hydrogen fuel production. Its efficiency depends on relative position of the band gap edges (the visible light interval between infrared and ultraviolet (UV) ranges of electromagnetic spectrum corresponds to gap widths 1.5–2.8 eV) accompanied by a proper band alignment relative to both reduction (H^+/H_2) and oxidation (O_2/H_2O) potentials (−4.44 eV and −5.67 eV on energy scale for vacuum, respectively) which must be positioned inside the band gap. Its width for TiO_2 anatase-structured bulk is experimentally found to be 3.2 eV, which corresponds to photocatalytic activity under UV light possessing only ~1% efficiency of sunlight energy conversion. Noticeable growth of this efficiency can be achieved by by adjusting the band gap edges for titania bulk through nanoscale transformation of its morphology to anatase-type nanotubes (NTs) (formed by folding of (001) or (101) nanothin TiO_2 sheets consisting of 9 or 6 atomic layers and possessing either $(n,0)$ or $(−n,n)$ chiralities, respectively) accompanied by partial substitution of pristine atoms by C_O, Fe_{Ti}, N_O and S_O single dopants as well as N_O+S_O codopants. In the latter case, the band gap can be reduced down to 2.2 eV while the efficiency is achieved up to ~15%. The energy differences between the edges of band gap (VB and CB), the highest occupied and lowest unoccupied impurity levels inside the band gap (HOIL and LUIL, respectively) induced in doped NTs, while preserving the proper disposition of these levels relatively to the redox potentials, so that $\varepsilon_{VB} < \varepsilon_{HOIL} < \varepsilon_{O_2/H_2O} < \varepsilon_{H^+/H_2} < \varepsilon_{LUIL} < \varepsilon_{CB}$, thus reducing the photon energy required for dissociation of H_2O molecule. In this chapter, we analyze applicability of large-scale first principle calculations on the doped single-wall titania NTs of different morphologies with the aim of establishment of their suitability for photocatalytic water splitting.

---

1. Introduction

Finding alternative energy sources is one of the most urgent research problems since traditional fuels run out at an extreme rate as their depleting rate surpasses the rate of restoration. Photocatalytic dissociation of H_2O molecules under the influence of solar light on a semiconductor electrode is a very promising process for production of hydrogen fuel, which is an environmentally friendly energy source. Indeed, the only combustion product of H_2 is water, while traditional hydrogen production technologies (e.g., steam reforming) are accompanied by CO_2 release and/or other undesirable side products. Another advantage of hydrogen as energy carrier is its high energy density ~237 kJ/mol [1]. On the other hand, among different energy sources surrounding people, the Sun is the most abundant – approximately 3.0×10^{24} J of its emitted energy reaches the Earth every year. In turn, the humanity consumes around 4.0×10^{20} J [2], so advances in technology are required to converse, use and store the solar energy with high efficiency. Moreover, photocatalysis is often considered as artificial photosynthesis and as such is an attractive and challenging research topic in the fields of contemporary chemistry and renewable energetics [3, 4].

In this chapter, we systematize, analyze and verify, systematize and analyze the results obtained using first principle calculations on the atomic and electronic structure of pristine and doped by C_O, Fe_{Ti}, N_O and S_O substitutes TiO_2 anatase-structured single-wall nanotubes (SW NTs). Their chirality vectors are perpendicular to (001) and (101) nanosheets consisting of 9 or 6 layers, respectively, while chirality indexes have been chosen among $(n,0)$ vs. $(-n,n)$ sets, respectively. Evaluation of photocatalytic suitability of all titania NTs simulated by us has been performed taking into account their correspondence to band gaps, widths of which are smaller than photon energies in visible light interval while redox levels H^+/H_2 and O_2/H_2O (−4.44 and −5.67 eV, respectively) are positioned inside these band gaps. This chapter is based on results of our own studies [5–9] as well as theoretical and experimental data available in the literature.

2. Literature review

2.1. Fundamentals of water photocatalytic splitting

In the first publication on water photocatalytic splitting, Honda and Fujishima managed to split water into oxygen and hydrogen using rutile-structured TiO_2 anode and platinum cathode [10], both immersed into water electrolyte solution. Since titania bulk samples were

found to be suited for solar energy conversion, they attracted a great attention in electrochemical technologies. **Figure 1** clearly illustrates the mechanism of photocatalytic splitting.
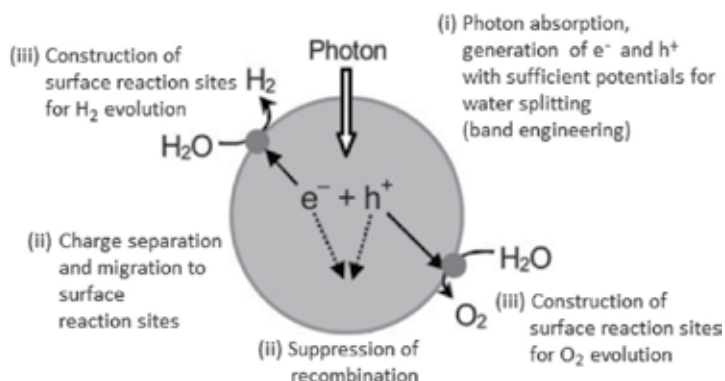
Figure 1. Elemental stages of photocatalytic water splitting [4].

In the first stage, a photon is absorbed by a semiconductor electrode (anode) which leads to generation of excitons – pairs of excited electrons and electron holes (second stage). Electrons being excited migrate to a conduction band (CB), and electron holes stay in a valence band (VB). The third stage includes charge separation and migration to reaction centers on a catalyst's or cocatalyst's surface. Usually cocatalyst is used because in that case photoanode and cathode, i.e., areas where hydrogen and oxygen are generated, are divided, and the backward reaction between the gases cannot happen. Another important aspect is that the kinetics of electron transfer on a semiconductor surface may cause a necessity of the cocatalyst presence (such as Pt, NiO or RuO$_2$), which can suppress charge recombination (fourth stage) occurring mainly due to the presence of irregularities in the semiconductor crystalline structure. The fifth stage results in the appearance of reaction centers on the electrode substrate. A better understanding of the whole water-splitting process can be gained from **Figure 2**.
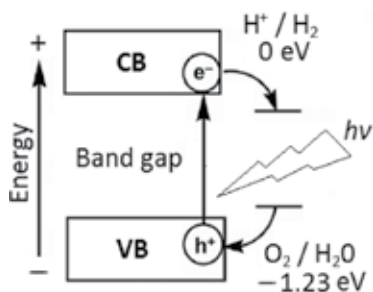
Figure 2. The model of photocatalytic activity of semiconducting electrode [4].

Fundamental requirement to an electrode is to be a semiconductor possessing band gap in the energy spectrum which cannot be passed by the compound's electrons. Normally, they are

localized at the ground states below the top of the band gap. But, when an electron receives additional portion of energy from an external source (for example, due to rising temperature or light photon absorption), which is sufficient to overcome the band gap – the electron turns into an excited state, above the bottom of CB (**Figure 2**), while an electron hole (positive charge carrier) is left in a VB. An electron cannot exist in an excited (metastable) state for a long time – it is not energetically beneficial. This is why electrons transferred to a CB tend to get rid of energy surplus (e.g., by irradiating it) and to return back into their ground state in a VB.

The next requirement is connected with the positions of the CB and the VB on energy scale. The bottom of the CB must be situated slightly higher than the standard hydrogen electrode (SHE) level (0 V, or −4.44 eV, in compliance with vacuum level) as shown in **Figure 2**, so the following reaction is energetically favorable in electrolyte contacting the electrode [1]:

$$2H^+ \text{ (aq)} + 2e^- \rightarrow H^2 \text{ (g)} \tag{1}$$

The position of the $\varepsilon(H^+/H_2)$ level relative to the vacuum level on the energy scale has been calculated earlier using a Born–Haber thermochemical cycle [11]. Obviously, the electrons lose a part of their energy while migrating to a reaction center (**Figure 1**). And the top of the VB ought to be slightly below the oxidation energy level (**Figure 2**) at which hydroxyl groups are oxidized (−1.23 V, or −5.67 V, in compliance with the vacuum level):

$$\left(OH\right)^- + 2h^+ \rightarrow H_2O + \frac{1}{2}O_2\left(g\right) \tag{2}$$

It should be also noted that the band structure imaged in **Figure 2** does not take into account the influence of the electrolytic environment to catalyst. When electrodes are put into water or aqueous electrolyte solution, the band levels and potentials can bend according to different scenarios, e.g., that suggested by Grätzel (**Figure 3**).
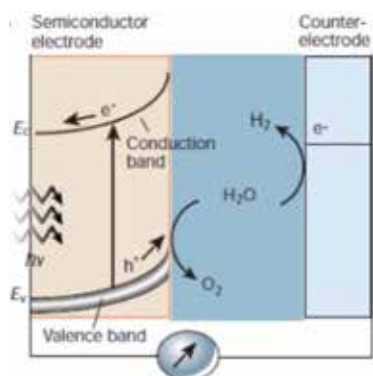

Figure 3. The band structure bending of *n*-type semiconductor in the presence of electrolyte [12].

Changes in the band potentials depend on charge surplus or shortage in the semiconductor. In other words, is it a *p*-type or *n*-type semiconductor? **Figure 3** illustrates *n*-type semicon-ductor, while for *p*-type direction of bending is opposite. Bending degree depends on several factors, e.g., on pH of electrolyte. Obviously, traditional first principle methods of *ab initio* simulations cannot describe the bending effect in principle and we do not consider it in this chapter. An important aspect of photocatalytic suitability is also a width of the band gap.

The energy threshold between SHE level and the level at which hydroxyl groups are oxidized is found to be 1.23 eV [1]. Taking the aforementioned requirements about the positions of the bands into account, it is easy to understand that the band gap width has to be larger than 1.23 eV (optimally, it should exceed 1.5 eV), which corresponds to ranges of visible light and near-infrared (IR) light. Also, the band gap must be narrower than 2.8 eV in order to allow a catalyst to employ energy of visible light and near-ultraviolet (UV) light, excluding UV range. UV light constitutes only few percents out of total Sun's irradiation (4–5% [4, 10, 13]), whereas the visible light constitutes 43–46% [13, 14]. Obviously, the band gap must correspond to the range of visible light in order to provide high efficiency of semiconductor photocatalysts.

Titania is considered to be prospective material for solving the problem due to a wide range of its properties [14]. Those include chemical stability, insolubility in water, nontoxicity, low price and sustainability against photocorrosion. Its position at the bottom of CB, formed by empty 3*d* atomic orbitals of titanium, is very beneficial – slightly above the SHE level, in respect to the requirement. However, the top of the VB, formed by 2*p* atomic orbitals of O atoms, is essentially below the level at which hydroxyl groups are oxidized. And the band gap is too wide – 3.2 eV in anatase- and brookite-structured phases, vs. 3.0 eV in rutile phase. In general, most metal oxides have band gaps larger than 3.0 eV [1].

Theoretical maximum of solar energy conversion degree for a titania catalyst with 3.2 eV wide band gap is approximately 1%. In turn, it is 15% for a catalyst with a 2.2 eV band gap (as for Fe$_2$O$_3$ bulk). A band gap of 2.0–2.2 eV width is generally considered to be optimum [15]. Still, according to another study, total energy losses are evaluated to be around 0.8 eV, which implies an optimal band gap of roughly 2.0 eV [16]. Photocatalytic water splitting efficiency must reach at least 10% conversion to be competitive against solar-cell-driven water electrolysis and to be economically profitable [15]. Obviously, photocatalytic properties of pristine TiO$_2$ bulk are not good enough to maintain the process effectively, so there is a need to modify the electronic structure of the material either by defect engineering (e.g., doping) or nanoscale transformation of its morphology. Our theoretical simulations show that pristine anatase-structured titania SWNTs rolled up from both (001) and (101) nanothin sheets possess the band gaps noticeably larger than those of TiO$_2$ bulk (by several tenths eV) [5, 7, 9]. On the other hand, the band gaps of doped titania NTs are essentially reduced, down to 2.2 eV in the case of N$_O$+S$_O$ codoping of TiO$_2$ (001) NT [7].

2.2. Advances in experimental studies of TiO$_2$ photocatalysts

Numerous experiments focused on titania doping by different metal ions have already been performed. Among effective dopants one can find V, Ni, Cr, Mo, Fe, Sn, Mn and other cations [13]. In 1982, Borgarello et al. [17] discovered that Cr^{5+} doped TiO$_2$ could generate hydrogen

and oxygen in the process of water splitting under visible light irradiation (wavelength interval 400–550 nm). Klosek and Raftery [18] demonstrated that visible light absorption in titania doped with V^{4+} is a result of the electron transfer from the V $3d$ electron-induced energy level to the CB. Their research became a key to more effective ways of ethanol photooxidation under visible light, another route to hydrogen generation. Fe^{3+} doped TiO_2 also exhibits enhanced photocatalytic activity. Moreover, Fe^{3+} $3d$ electrons induce additional levels in the TiO_2 CB [19]. Doping of titania photocatalysts by Cr, Mg and Fe cations can improve their efficiency, for example, magnesium can reduce energy barrier for interphase transfer of electrons [20]. At the same time, the newly induced electronic states can behave as recombination centers, e.g., shift the impurity levels lower than the reduction SHE level.

TiO_2 doped by nonmetal ions exhibits a red shift of the absorption spectrum and possesses a higher photocatalytic activity than pure TiO_2, especially in the visible part of the solar irradiation spectrum [12]. Unlike metal ions, nonmetallic dopants usually do not induce new energy levels but squeeze the band gap directly by shifting the top of the VB upward [12], still it is not always the case. Nevertheless, Chen et al. [21] used X-ray photoelectron spectroscopy to show that in the electronic structure of C-, N- or S-doped TiO_2 the extra mid-gap states between the VB and the CB induced by dopants can appear. For example, titania doped by nitrogen exhibits high photocatalytic activity in water/methanol solution [22]. On the other hand, the S dopants substituting host oxygens or host titans can improve its photocatalytic activity too [23, 24]. Moreover, sulfur-doped titania exhibits higher photocatalytic activity with respect to the nitrogen-doped system [25]. The C-doped TiO_2 compounds were synthesized too [26], which exhibit a quite narrow forbidden gap and an enhanced photocatalytic activity than pure TiO_2 with mixed rutile and anatase domains. C-doped TiO_2 NTs also possess better photocatalytic activity [27]. Levels induced in the band gap were shown to broaden the activity of C-doped TiO_2 NTs from the visible to the IR region.

Limited amount of information on codoping of titania photocatalysts is available for nonmetallic dopants so far. Yan et al. [28] reported about the study on N- and S-codoping applied to TiO_2 NT array films by treatment with thiourea and calcination under vacuum and high temperature. The codoped NTs exhibit essentially broadened absorption spectrum and enhanced photocatalytic activity in methylene blue degradation process. Alternatively, Lv et al. [29] studied N+S codoped TiO_2/fly ash beads composite material and its photocatalytic activity in visible light range. Besides doped photocatalysts, appearance of vacancies as point defects can lead to rise in electrical conductivity and to changes in band gap structures [30].

2.3. Progress in *ab initio* modelling of TiO_2 photocatalytic efficiency

In spite of all the aforementioned efforts, the current understanding of fundamental changes in the electronic structure with atomic composition of doped semiconducting NTs is not sufficient for rational design of the atomic composition of these new compounds. To guide the search, a theoretical procedure is necessary in order to prudently predict the electronic structure and the charge redistribution in catalyst materials. Theoretical simulations performed up to date deal mainly with doped and codoped photocatalytic bulk materials [31–33], their low-index surfaces [34, 35] as well as nanoparticles and nanowires (NWs) [36, 37].

There are two critical issues that are important for photocatalysis but not yet well treated in the conventional density functional theory (DFT) and other packages: (a) the lack of resources, essential for simulations of the strong polarization on the charged electrode surfaces in aqueous electrolyte; (b) the inaccuracy of current DFT functionals in describing the redox levels of oxides (i.e., the band gap and positions of its edges relative to the H$^+$/H$_2$ and H$_2$O/O$_2$ levels) [38]. The great challenges still exist for the computation of photocatalytic reaction kinetics as it is driven by excess holes/electrons accumulated on the catalyst surfaces.

For titania bulk structure, spin-polarized DFT calculations predict that (2N, W) codoped TiO$_2$ can be considered as an efficient visible-light photocatalyst [31]. Using the projected augmented wave (PAW) method for *ab initio* calculations, Nolan found that small iron oxide clusters can be stable at the TiO$_2$ surface [34] and their presence squeeze the band gap towards the frequency range of visible light arising from the presence of iron oxide states lying above the VB of titania. The W-doped anatase (101) surface was also simulated using DFT PAW calculations [35]. C-, N- and S-doped (TiO$_2$)$_n$ nanoclusters were studied by Shevlin and Woodley using both DFT and time-dependent DFT calculations [36]. Asahi et al. [32] studied the band structure of the C-, N-, F-, P- and S-doped anatase structure of titania bulk using the same FP LAPW method. The substitution of O by N (which led to mixing of N(2p) and O(2p) states) produces the best conditions for photocatalytic applications since such structural modification results in upward shift of the top of the VB, thus reducing the width of the band gap.

A number of doped materials exhibit a large mismatch between the length scales over which the photon absorption takes place (up to micrometers), while at the relatively short distances within the limit of few tens nanometers, at which electrons can be extracted, electron–hole recombination was observed [16]. Reliable approach for solving this problem was found to be the synthesis of nanostructured electrodes with the orthogonalized directions of photon and electrons propagations, which is caused by markedly increased surface-to-volume ratios [39, 40]. Hollow NTs synthesized from the wide gap materials exhibit not only large surface area, but also high mechanical stability and integrity leading to both charge transport and electron–hole separation [41, 42]. TiO$_2$ (6,6) NTs built as regularly distributed bundles consisting of rutile (110) monolayers were calculated recently using DFT method [37]. Reported electronic structure of such a materials is predicted to be close to that of TiO$_2$ bulk. The electronic structures of the C, N, V and Cr doped as well as C/V, C/Cr, N/V and N/Cr codoped titania NWs were calculated too, in the case of C/Cr and C/V codoping a visible-light driven photoresponse was found to be the most enhanced [37].

On the whole, rather scarce number of publications focused on the computer simulations of defective NTs and NWs, including their photocatalytic properties, can be explained by a lack of methodical solutions for their construction in a variety of existing *ab initio* codes, which makes their comprehensive study very time-consuming and expensive. Meanwhile, the last versions of CRYSTAL code based on DFT-LCAO formalism, allow users either to exploit periodic rototranslation symmetry of 1D NTs, or to generate differently structured 1D NWs, setting the properly chosen Miller indexes of their lateral facets and simultaneously defining their crystallographic orientations, both for efficient ground-state calculations on their structural and electronic properties [43].

3. Theoretical background

3.1. Computational details

We have performed first-principle ground-state calculations on the SW anatase-structured TiO_2 (001) and (101) NTs, with fixed number of atomic layers as well as chiral indexes (n,0) vs. ($-n,n$), respectively, doped by C, N, S, or Fe atoms and codoped by pair of N and S atoms. We have simulated periodic and cluster models of doped NTs, for which either CRYSTAL code [43] or NWChem code [44] has been applied, respectively. For both types of DFT-LCAO calculations, we have used the formalism of the localized Gaussian-type functions (GTFs), which form the basis set (BS) of atomic orbitals for each chemical element as implemented in CRYSTAL and NWChem codes using crystalline and molecular orbitals constructed within either CO LCAO or MO LCAO approaches.

To avoid shortcomings of the traditional DFT methodology, especially underestimate of band gap widths, we have gone beyond this approach, applying the hybrid DFT-HF method for the electronic structure calculations. The hybrid functionals incorporate traditional Hartree-Fock (HF) approach determining the exchange energy E_x^{HF} [45]. Practical justification for this approach is the fact that errors of HF and DFT calculations often have opposite signs. For example, the former overestimates the values of band gaps while the latter underestimates them. The exchange-correlation energy in hybrid DFT-HF methods is expressed as linear combination of two quasi-independent contributions [43]:

$$E_{xc}^{DFT+HF} = \alpha_{DFT} E_{xc}^{DFT} + \alpha_{HF} E_x^{HF} \tag{3}$$

where coefficients determine hybrid functional parameters. It is very important to find such a functional which can be used for qualitative description of a large number of systems without additional parameters involved during calculation.

Values	α_{HF} = 14%	α_{HF} = 20%	Exp[*]
ε_{CB}, eV	−4.3	−4.2	−4.3
ε_{VB}, eV	−7.4	−7.8	−7.3
$\Delta\varepsilon$, eV	3.1	3.6	3.2

[*]Experimental values are taken from Ref. [4].

Table 1. Edges of the CB bottom (ε_{CB}), the VB top (ε_{VB}) and the band gaps ($\Delta\varepsilon$, eV) calculated for 20-layer TiO_2 (101) slab using the hybrid B3LYP functional vs. varied α_{HF}.

To perform all calculations on the pristine and doped titania NTs considered in this chapter, a modified B3LYP hybrid exchange-correlation functional [46] has been adopted by us since it provides the better reproduction for parameters of their atomic and electronic structure obtained earlier in experiments and theoretical simulations. To achieve a quantitative agree-

ment with the experimentally observed band gap for bulk anatase-structured TiO$_2$ ($\Delta \varepsilon$ = 3.18 eV) and the positions of band edges (**Table 1**), the admixture of nonlocal HF exchange in the B3LYP functional defined by α_{DFT} in Eq. (3) has been reduced from the standard 20% [43] to 14% [5].

The following configurations of localized GTF functions describing atoms of doped titania NTs are adopted by us for further first principle calculations:

(i) For Ti atoms in TiO$_2$, the basis set (BS) has been chosen in the form 411sp–311d, using the efficient core potentials (ECPs) implemented by Hay and Wadt [47].

(ii) Full-electron basis sets have been adopted for all other atoms, except Ti, which are contained in doped titania NTs, i.e., O: 8s–411sp–1d; C: 6s–411sp–11d; N: 6s–31p–1d, S: 8s–63111sp–11d and Fe: 8s–6411sp–41d [43].

The most comprehensive simulations have been performed by us for periodic models of NTs, for which the formalism of periodic rototranslation symmetry [43] has been exploited. This approach has been successfully applied by us earlier for simulations of perfect SW TiO$_2$ NTs of either anatase or fluorite phases [48, 49] as well as [001]- and [110]-oriented titania NWs of rutile phase [50, 51]. Reciprocal space integration over the direct and reciprocal lattices of NTs has been done by sampling the Brillouin zone of 2×2 supercells with 6×1×1 Pack–Monkhorst k-mesh [52] in order to ensure an equable summation over the direct and reciprocal lattices of NTs [45]. The outcome is 4 evenly distributed k-points within the segment of the irreducible Brillouin zone. Further increase of k-mesh results in much more expensive calculations yielding at the same time a negligible change in the total energy ($\sim 10^{-7}$ au). Self-consisted field calculations are considered as converged when the total energy differs by less than 10^{-7} au in two successive SCF cycles. For Fe- and N-doped NTs of both types as well as for the S+N codoped TiO$_2$ NT, spin-polarized calculations have been performed (as shown in Section 4.1 by the presence of doubly-generated DOS) since numbers of electrons per unit cell with opposite spins do not coincide, unlike pristine NTs and that doped by C and S atoms where these numbers are equal.

Hybrid DFT-HF calculations on cluster and periodic models of pristine and doped titania (001) NTs have been simultaneously performed by us using hybrid B3LYP functional as implemented in NWChem [44] and CRYSTAL [43] codes, respectively. Other computational parameters have been chosen similar in both codes. The obtained results have been comprehensively analyzed and compared [8]

3.2. Definition and verification of calculated properties

For reliable first-principle calculations of TiO$_2$ anatase-structured NTs, verification of bulk titania properties is a necessary step. Moreover, variation of α_{HF} when using B3LYP exchange-correlation functional has been performed as described in Section 3.1, to reproduce parameters of titania band structure with maximum precision (Table 1). Obviously, we have to check whether it is also true for structural parameters of anatase bulk crystal (**Figure 4**). Its lattice is characterized by tetragonal space group $I4_1/amd$ (space group Nr 141) [43, 49] with two formula units in the primitive cell. Two lattice parameters a and c measured experimentally (3.78 and

9.51 Å, respectively) are well correlated with those values calculated using hybrid DFT-LCAO B3LYP method (3.80 and 9.65 Å). Dimensionless parameter u of anatase lattice exactly reproduces its experimentally observed value (0.208 [45]). Thus, verification of obtained results gives us grounds to predict reliability of computational parameters for large-scale calculations on pristine and doped titania NTs possessing either (001) or (101) rectangular morphologies as well as (n,0) vs. ($-n,n$) chiralities, respectively.
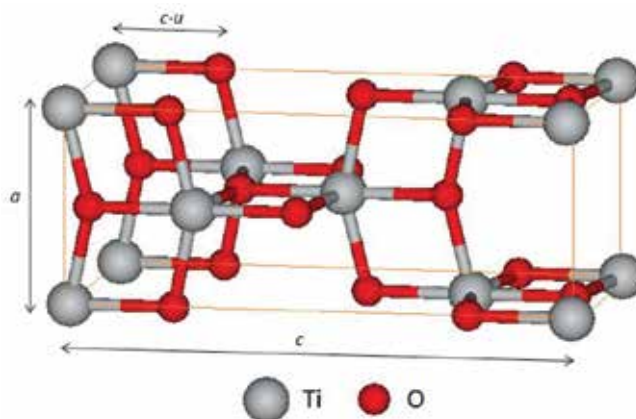
Figure 4. Unit cell of anatase-type titania lattice possessing tetragonal space symmetry.

To estimate the ability of forming single substitutional dopant in a substrate, e.g., NT, one has to calculate the corresponding formation energy:

$$E_{A_h}^{form} = E_{A_h/NT}^{tot} + E_h^{tot} - E_{A_h}^{tot} - E_{NT}^{tot} \qquad (4)$$

where $E_{A_h/NT}^{tot}$ is the calculated total energy of a NT containing substitutional A_h atom, E_h^{tot} is the total energy of the host (h) atom, which is removed from the NT and $E_{A_h}^{tot}$ is the total energy calculated for the impurity atom while E_{NT}^{tot} stands for the total energy calculated for the perfect NT. Obviously, comparative analysis of formation energies for different dopants and sites of their location within various substrates allows one to determine energetically most favorable configurations of titania NTs for photocatalytic applications although conclusion on their suitability can be done when analyzing band structures.

Defective NTs are often characterized by the presence of defect levels inside the band gaps. In this case, the energy balance for possible water splitting under influence of visible light photons is changed. The differences between the highest occupied and lowest unoccupied impurity levels inside the band gap (HOIL and LUIL, respectively) are reduced in doped NTs, while preserving the proper disposition of these levels relatively to the redox potentials, so that [7]

$$\varepsilon_{\text{VB}} < \varepsilon_{\text{HOIL}} < \varepsilon_{\text{O}_2/\text{H}_2\text{O}} < \varepsilon_{\text{H}^+/\text{H}_2} < \varepsilon_{\text{LUIL}}\varepsilon_{\text{CB}} < \varepsilon_{\text{CB}} \tag{5}$$

thus, reducing the photon energy required for dissociation of H$_2$O molecule. Should a stand-alone electrode be unable to fulfill these requirements, other steps may be undertaken, e.g., application of external bias voltage or fabrication of a system consisting of two (or more) materials which are capable to ensure the required exciton generation as well as charge separation and migration when acting jointly. The redox potentials displayed in **Figure 2** are related to standard conditions and aqueous medium with pH = 0; further increase in pH value results in shifting both redox levels towards the vacuum level (**Figure 3**) [42].

3.3. Models and properties of (001) and (101) TiO$_2$ anatase slabs

Before folding of titania anatase-structured nanothin films to TiO$_2$ NTs, we have to understand their structure and main properties. **Figure 5** shows two slab models with the highest and lowest surface energy among anatase structures, i.e., (001) (0.90 J/m^2) and (101) (0.44 J/m^2), respectively [53].
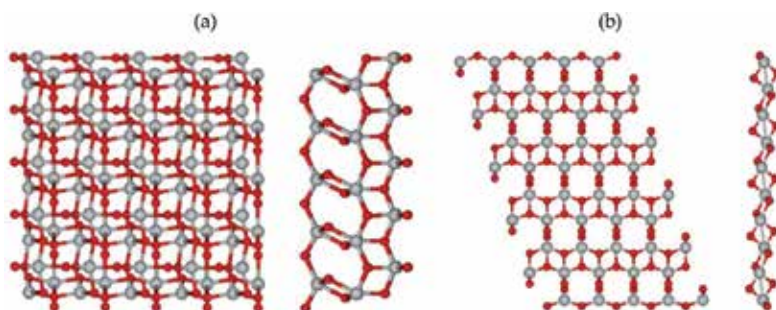
Figure 5. Atop and across views of 9-layer (001) (a) and 6-layer (101) (b) nanosheets of anatase-type titania [5]. Ti atoms are shown in gray, while O atoms are in red (dark gray) [5].

Obviously, (101) surfaces, normally the majority of the external surface of anatase titania (more than 94%, according to the Wulff's construction), are thermodynamically stable with a low surface energy, which determines its low reactivity [54]. On the contrary, (001) surface is characterized by the highest reactivity, e.g., towards adsorption of various species. To improve titania's reactivity, the preparation of shape-controlled TiO$_2$ nanocrystals with specific reactive facets exposed is a greatly desired, and the minority (001) surfaces with a higher surface energy attract extensive interest [55]. From the other side, an interesting effect was observed by Herman et al. who discovered reconstruction of (001) titania surface under ultrahigh-vacuum (UHV). This reconstruction significantly stabilizes the high-energy surface, but at the same time reduces its reactivity [56]. Therefore, investigation of possible facet reconstruction is important, and developing novel synthesis routes is necessary to prevent the reconstruction. Reactivity of the NTs under consideration is another important aspect.

3.4. Models of pristine and doped titania NTs

First, we have studied photocatalytic efficiency of pristine anatase (001) NTs (**Figure 6**) folded from 9-layer (001) slab (**Figure 5**). Range of NT diameters has been varied from 0.6 to 4.0 nm [5]. Optimized model of TiO$_2$ NT (**Figure 6**) has been used for simulation of different properties as described in Section 4.1 (formation energies, widths of band gaps and positions of their edges at the top of the VB and the bottom of the CB as well as mid-gap levels induced by dopants).
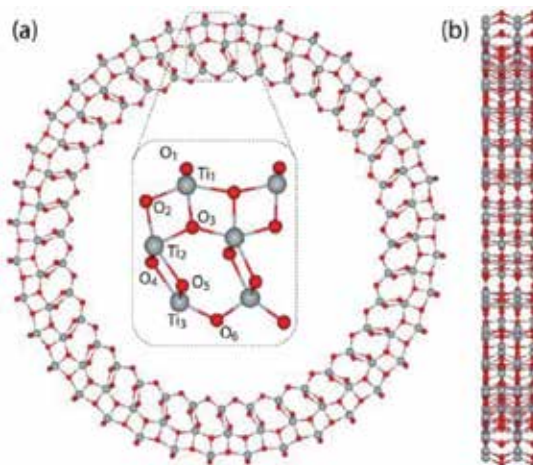

Figure 6. Schematic images of a unit cell monoperiodically repeated along a (36,0) TiO$_2$ (001) NT (d$_{NT}$=4.81 nm) having the substitutional point defects: (a) nanotube's top view; (b) nanotube's side view. Ti atoms are shown in gray, while O atoms are in red (dark gray). At the inset drawn in (a) the basic unit cell of the TiO$_2$ NT is repeated by 18 symmetry rototranslational operators. The numbered titan and oxygen atoms of the inset show the substitutional sites for impurity defect atoms (A$_h$, where "h" is for "host" atom) [7].

We have chosen the 2×2 supercell of the (001) nanosheet prototype (**Figure 5a**), when constructing pristine 9-layer TiO$_2$ (36,0) NT with an internal diameter of 3.47 nm and walls of thickness 0.67 nm (**Figure 6**) for further doping. Such a NT contains 648 atoms per NT unit cell. In our study, C, N and S impurities substitute the host oxygens in six possible positions (shown in the inset of **Figure 6**), while three possible dopant positions have been considered for Fe$_{Ti}$ substitute. We define the defect concentration as the number of dopant atoms relative to the number of atoms per supercell of a periodic structure which can be substituted by the dopant. Since the extended periodically repeated 2×2 supercell possesses 12 TiO$_2$ formula units, incorporation of the doping impurity leads to the 8% defect concentration in the titania NT for the Ti site and ~4% for the O site. Modelling nitrogen and sulfur codoping at the titania NT with similar defect concentration, we have substituted oxygens in O$_1$ and O$_2$ sites by S- and N-dopants as shown in **Figure 6**. We note that reduction of defect concentration results in larger supercell and leads to expensive calculations beyond our current computer facilities. For the same reason, charge compensation defects for anionic dopants are not considered in this study at all.

Figure 7. Cluster models of TiO$_2$ (001) NTs: (a) ring fragment and (b) arc segment of ring.

For cluster models of TiO$_2$ (001) NTs, we use either several rings cut from periodic NT models (**Figure 7a**), lengths of which correspond to the period of 1D NT, or even arc fragments of rings (**Figure 7b**), which can be transformed to the whole rings using rototranslational symmetry. Important part of cluster models is their boundary conditions around broken edges which substitute the absence of periodicity in 0D models by hydrogen atom termination of all broken bonds [8].

Initial internal morphology of cluster corresponds to analogous NT structure. Cluster models have been used for simulation of (001)-oriented TiO$_2$ NTs only. In Section 4.2, we perform comparative analysis of photocatalytic properties of doped anatase-structured NTs obtained in cluster and periodic models.
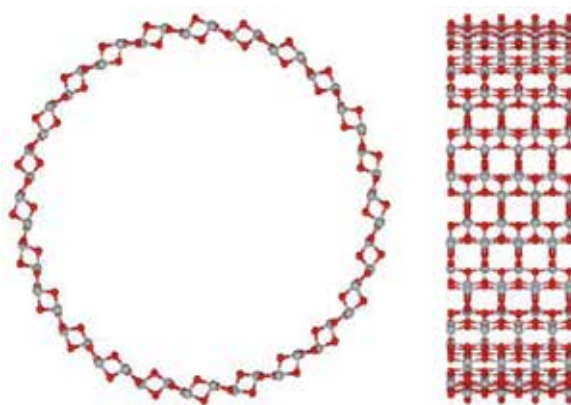
Figure 8. 6-layer TiO2(101) NT with chirality indexes (−12,12): front view (left panel) and aside view (right panel). Large Ti atoms are shown in gray, while O atoms are in red [9].

A number of pristine 6-layered anatase (101) NTs with chirality indexes (n,n) and ($−n,n$) have been modelled. TiO$_2$ (101) NT with chirality indexes (−12,12) has been chosen (**Figure 8**) as optimal for further doping. This choice is a result of compromise between the minimal formation energy estimated according to Eq. (4) and a number of atoms in the NT unit cell. Such a NT consists of 432 atoms per unit cell. Here, we consider NTs 1×3 and 2×3 periodically repeated "basic" unit cells containing 36 and 72 atoms, respectively, giving dopant concentration of 2.78% (12 dopant atoms per NT unit cell) and 1.39% (6 dopant atoms per NT unit

cell), respectively. Suitability of these (101) titania NTs for photocatalytic applications is discussed in Section 4.3.

4. Photocatalytic efficiency of doped titania NTs

4.1. Periodic model of doped (001)-oriented NTs

The energy balance between the band gap edges (e.g., mid-gap levels induced by defects) and the redox levels described in Eq. (5) is considered as a criterion for efficiency of photocatalytic water splitting [1, 4, 38]. **Figure 9** includes a pair of vertical lines denoting the reduction and oxidation levels fixed in the plots of the densities of states calculated for pristine and doped TiO_2 NTs. The band gap edges of the titania anatase-structured (101) slabs are compared with the corresponding experimental values presented in Table 1 (Section 3.1).

We note that the band gap edge positions presented in Table 1 differ not more than 0.1–0.2 eV from those experimentally observed, which gives us a reason to believe that predictions made by us on the electronic structure of doped TiO_2 NTs are at least qualitatively and possibly semiquantitatively reliable.

n	C_{On}	N_{On}	S_{On}	Fe_{Tin}
1	**1.16****	3.79	**2.61****	5.58
2	3.23	**3.56****	3.6	5.42
3	2.99	3.95	4.34	**5.37****
4	3.13	3.88	5.33	–
5	3.31	4.08	5.65	–
6	3.78	4.11	3.37	–
Bulk***	4.12	3.22	5.36	4.44

*Host atoms A_h substituted by impurities (h) are labeled in **Figure 8**.
**The lowest formation energies for each dopant are shown in bold.
***The last row contains $E_{A_h}^{form}$ values calculated for doped anatase bulk using 2×2 supercell.

Table 2. Defect formation energies ($E_{A_h}^{form}$, eV) in doped TiO_2 NTs calculated using Eq. (4)*. n is index number of $O_{(n)}$ or $Ti_{(n)}$ atoms imaged in **Figure 6** (inset).

In our study, impurity atoms have substituted each possible irreducible host O or Ti atom in the NTs with rototranslationally and periodically repeated cells as shown in **Figure 6** (Section 3.4). Therefore, one of the six types of O atoms and one of the three types of Ti atoms have

been consequently substituted by C$_O$, N$_O$, S$_O$ and Fe$_{Ti}$. According to our calculations, the carbon and sulfur dopants would prefer to be positioned at the site of the outermost oxygen, while nitrogen would prefer the second oxygen layer counting from the outer side (**Table 2**).

Obviously, the smallest formation energy of anion dopants has been found for C$_O$ (1.16 eV). For S$_O$-doped TiO$_2$NT, $E_{A_h}^{form}$ = 2.61 eV, while 3.56 eV is required for N$_O$ dopant. The most energetically favorable position for the host Ti atom to be substituted by iron atom ($E_{A_h}^{form}$ = 5.37 eV) to be located in the Ti layer closest to the inner wall of the titania NT (inset of **Figure 6** and Table 2). When calculating the band structure of the doped NTs, only the NTs with the smallest defect formation energies have been taken into account. The formation energy of the nitrogen–sulfur pair has been obtained to be 5.64 eV, which fulfils the relation 2E^{form}(S$_O$) < E^{form}(S$_O$+N$_O$) < 2E^{form}(N$_O$) (in accordance with Table 2), thus confirming the approximate additivity of estimated dopant formation energies, when these contain different numbers of impurity atoms, irrespective of their chemical nature. Substitutional point defects in TiO$_2$ NTs reveal a tendency to form defect-induced levels inside the optical band gap. In the case of the C$_{O_1}$/TiO$_2$ NT, the filled band is positioned ~2.2 eV above the top of the VB (**Figure 9b**), while in the case of the N$_{O_2}$/ TiO$_2$ NT impurity (**Figure 9c**), the induced mid-gap state is found to be 0.9 eV above the top of the VB. The mid-gap states computed for the S$_{O_1}$/TiO$_2$ NT (**Figure 9d**) forms the top of the VB (for the S-doped bulk, the defect level lies ~0.2 eV above the top of the VB), and in the case of Fe$_{Ti_3}$/TiO$_2$ NT, the vacancy-induced level is positioned in the middle of the band gap (**Figure 9f**). The top of the VB of the perfect titania NT is formed by O 2p orbitals, while the bottom of the CB is formed by Ti 3d states.

The projected DOS computed for the nitrogen and sulfur codoped TiO$_2$ NT is shown in **Figure 9e**. For the nitrogen and sulfur codoped TiO$_2$ NT, the N-dominated mid-gap levels shift by 0.3 eV downward, formed the occupied gap level below the O$_2$/H$_2$O redox potential. By the presence of the sulfur codopant, the bottom of the CB shifts downward with an energy gap of about 2.2 eV, thus reducing the photon energy required for water splitting reaction. The nitrogen and sulfur codoped structure exhibits a gap state below the top of the VB because of defect–defect interactions. For this system the top of the VB and the bottom of the CB shift downward relative to the nitrogen-doped structure. Relative to the bottom of the CB of the sulfur-doped structure, the CB shifts back toward the CB position of the pristine structure. Codoping thus gives rise to visible-light-driven excitation from the mid-gap states of 2.3 eV, which is just slightly smaller than for the nitrogen-doped NT. This allows one to predict that nitrogen and sulfur codoped TiO$_2$ NTs can be suggested as a good candidate for the visible-light-driven photocatalytic water splitting [30].

On the basis of the standard thermodynamic conditions of an active photocatalyst for H$_2$O splitting, we discuss and evaluate the influence of the incorporated cation and anion species on the photocatalytic activity of TiO$_2$ NTs. We have calculated the total and projected DOS for C-, N-, S- and Fe-doped NTs, as compared with that of pristine TiO$_2$ NT (**Figure 9**). The schematic representation of the band gap edges and mid-gap states of all these NTs is shown in **Figure 10**.
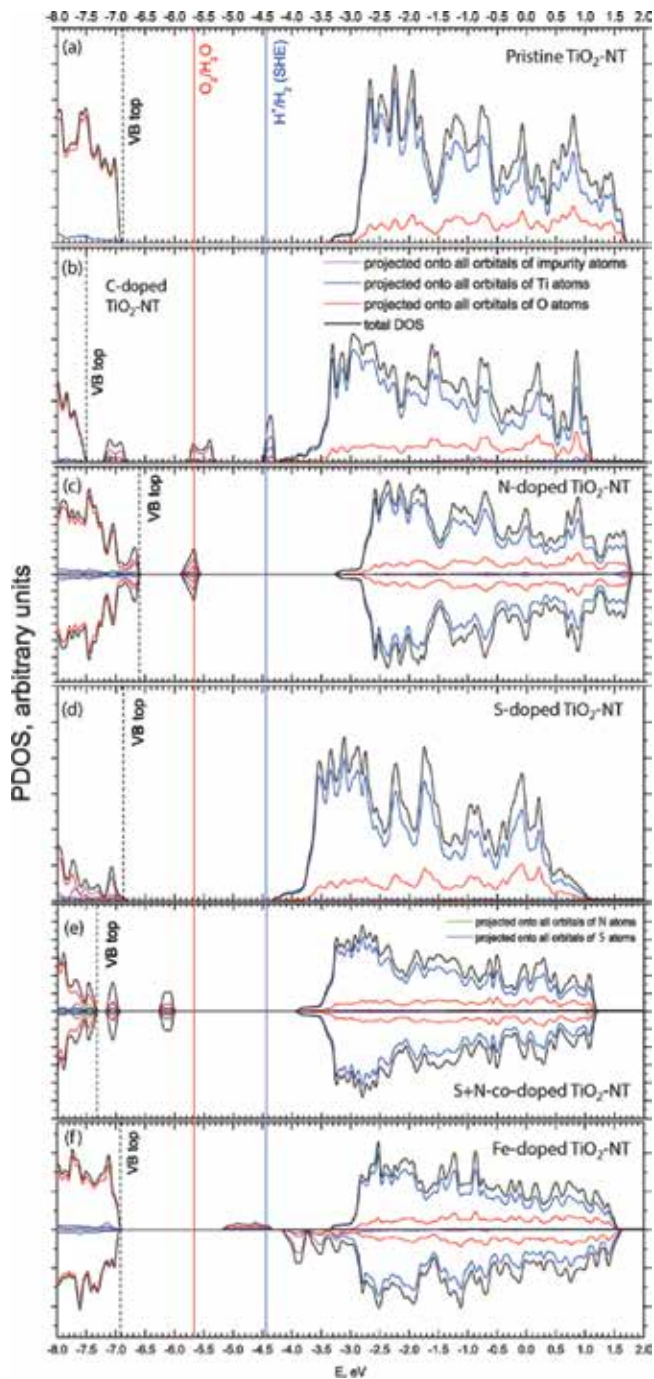
Figure 9. Total and projected densities of states calculated for perfect and doped titania nanotubes: (a) pristine, (b) C-doped, (c) N-doped, (d) S-doped, (e) N+S codoped and (f) Fe-doped. Vertical lines stand for ε_{O_2/H_2O} and ε_{H^+/H_2} potentials. Zero of the energy scale corresponds to the vacuum level [7].
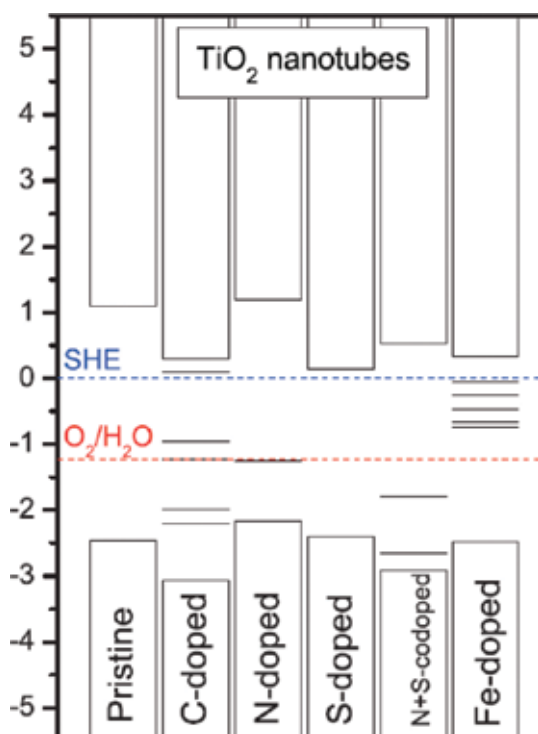
Figure 10. Schematic representation of the band edges and mid-gap states of pristine and doped TiO$_2$ nanotubes. The blue and red horizontal dashed lines correspond to the redox ε_{O_2/H_2O} and ε_{H^+/H_2} potentials, respectively. Zero of the energy scale corresponds to the standard hydrogen electrode (SHE) [7].

As can be seen from Table 2, the most energetically favorable positions for anion dopant on titania NT are the outer host oxygen atoms, while Fe prefers to substitute the inner titan atoms. For pristine TiO$_2$ (001) NT, the bottom of the CB is ~1.0 eV above the H$^+$/H$_2$ potential, whereas the top of its VB is ~1.2 eV below the O$_2$/H$_2$O potential (**Figures 9a** and **10**). A carbon substitutional impurity in a TiO$_2$ NT induces an occupied defect level ~0.2 eV above the oxidation potential (**Figures 9b** and **10**). This leads to an unsuitable VB position for the oxygen evolution reaction. The N-doped TiO$_2$ NT possesses an occupied impurity level practically at the O$_2$/H$_2$O potential (**Figures 9c** and **10**), while the bottom of the CB relative to the perfect NT is almost unchanged. For the sulfur-doped titania NT, we predict that the bottom of the CB is located almost at the level of reduction potential, while the top of the VB corresponds to that of the ideal NT being practically unchanged (**Figures 9d** and **10**). The iron-doped titania NT exhibits defect-induced mid-gap states about 0.5 eV lower than the ε_{H^+/H_2} level (**Figures 9f** and **10**), which results in the recombination of electrons and holes. On the whole, considering the possible configurations of the doped titania NT, we predict that the most efficient nanophotocatalyst for the visible-light-driven H$_2$O splitting could be N and S codoped titania NTs (cf. **Figures 9e** and **10**).

4.2. Cluster models of doped (001)-oriented NTs

To verify the periodic model of doped SW nine-layer (36,0) TiO_2 (001) NT (**Figure 6**) and results obtained in its DFT-LCAO calculations, we have performed time-dependent TD DFT-LCAO calculations, using NWChem code [44], on 2×2, 3×3 and 4x4 arc-segment models of TiO_2 NT (**Figure 7**), reproducing the morphology of periodic NT and providing adequate boundary conditions around each cluster model as shortly described in Section 3.4 [8]. Positions of N_O and S_O (as the most preferable dopants) are also reproduced from the periodic model of doped titania NT (**Figure 6**).

To perform simultaneously 1D NT and 0D cluster calculations within the same theoretical approach described in Section 3.1, we have used a modified B3LYP hybrid exchange-correlation functional [46] adopted earlier to perform periodic calculations on the doped titania NTs [5–7].
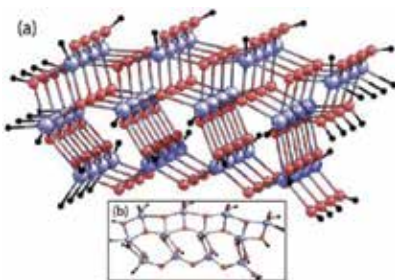
Figure 11. (a) Schematic representation of the 0D 4 × 4 fragment of TiO_2 NT (chosen as its cluster model) with dangling bonds saturated by hydrogen atoms (black). (b) Front view [8].

We have studied 0D cluster models of the 1D periodic NTs intending to perform TD-DFT calculations, which unfortunately are still not possible using the periodic first principle codes. Meanwhile, it is possible to run these calculations within cluster approach, e.g., using NWChem code [44]. On the other hand, this code does not admit performance of periodic 1D calculations, which also should take into account the symmetry of system allowing growth of size for model with correspondingly arranged atoms. To reduce the total number of atoms, while preserving geometry and stoichiometry, we have generated a number of 0D clusters by slicing the NT (**Figure 11**). Since it is possible to perform both 1D and 0D calculations at the same level of theory with the same set of parameters, the results calculated for the 1D NTs can serve as a performance benchmark for the 0D cluster models. We have sliced the NT into different arc-segments $n×n×d$ (**Figure 7**), where d is the NT's thickness (a constant, and therefore omitted from the clusters' shorthand notation $n×n$), while n has been chosen to be 2, 3 and 4. During calculations, positions of atoms in clusters have been kept fixed to avoid relaxation and to preserve the curvature of the NT.

We have simulated stoichiometric segment-like 0D clusters with varying parameter n and with different terminations of the bonds that were broken while cutting the NT. In such models, a common practice is to saturate broken bonds with hydrogen atoms [57]. However, in order to

reproduce a partial charge on the outermost Ti atoms, we explored several saturation modes other than H. Hydrogen is less electronegative than oxygen, and when slicing the NT, we disconnect titanium from oxygen and pair Ti with H, effectively altering metal's partial charge. To compensate for that, we have tried also to terminate our clusters with hydroxyl groups OH and with halogens F and Cl. However, our results indicate that these substituents not only introduce a number of electronic levels, polluting the gap between the highest occupied molecular orbital and the lowest unoccupied molecular orbital (HOMO/LUMO), but they also shift the energies of these orbitals by 1–2 eV. Hydrogens do that as well (**Figure 12**), but their effect on the HOMO/LUMO energies is less pronounced.
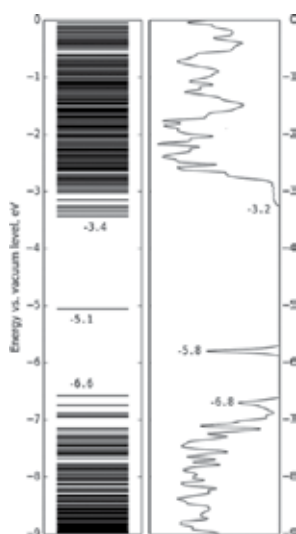
Figure 12. Left: MO levels of the 4 × 4 0D cluster model for the N-doped TiO$_2$ NT. Right: The total density of states for the 1D NT model of the analogous N-doped titania nanotube [8].

Arrangement of H-saturated atoms is another important issue. A change between relaxed and unrelaxed geometry (effectively, a difference of ca. 0.1 Å in Ti–H bond length) translates into 0.5 eV large shift of the band edges. We have achieved the best agreement between 0D and 1D models (in terms of band edges' energies and HOMO/LUMO energies, respectively) for H-terminated 0D clusters. Coordinates of terminating atoms in them have been relaxed relative to the TiO$_2$ backbone (which has been kept rigid during the optimization to preserve the geometry of the NT). To sum up, in all our calculations that we shall discuss further, clusters are arc-segments of the NT, that preserve stoichiometry and curvature of the NT, with any dangling bonds saturated by hydrogen atoms. Positions of these atoms relative to fixed coordinates of Ti and O atoms are relaxed in order to minimize the total energy of the object. To avoid a gap pollution, we have decided not to analyze any states dominated by energies arising due to hydrogen atoms. We have achieved this by excluding all the states in which hydrogen orbitals contribute to the electron density more than 2.25%.

The 0D cluster models have been investigated with the goal of using NWChem's implementation of the TD-DFT method [44] to perform nonadiabatic simulations of the relaxation on both NT and its environment following absorption of a photon. For direct verification of cluster calculations using results obtained for periodic NT, we have considered 4×4 cluster model of N-doped TiO_2 (001) NT (**Figure 11**). However, due to size restrictions, this model does not allow us to simulate N+S codoped NT. To compare with results of periodic model calculations, we construct MO level distribution in cluster models vs. total DOS for TiO_2 NT (**Figure 12**) as well as schematic representation of the band edges and mid-gap states of pristine and doped TiO_2 NTs imaged for periodic and three cluster models: 2×2, 3×3 and 4x4, where the extension numbers denote the number of elementary cells along and perpendicular to the NT axis, respectively (**Figure 13**). Within our notation, the top of the VB and the bottom of the CB have been defined as, respectively, the highest occupied level and the lowest unoccupied level the contribution to which from dopant atom orbitals is relatively small. **Figure 13** displays the band edges within this set of definitions. It also shows a converging trend: while for the undoped 2×2 clusters the disagreement with the pristine 1D NT model is quite noticeable, while it becomes less significant for the 3×3 clusters and even more so for the 4×4 clusters. Unsurprisingly, 0D models reproduce the top of the VB more accurately than the bottom of the CB. What is surprising is that the relative positions of the defect-induced mid-gap states with respect to the band edges between the 1D and 0D models are similar, even though they possess very different defect concentrations. For example, the left side of **Figure 12** shows the single level at the gap between the LUMO and HOMO levels which is dominantly composed of N $2p_x$ states (along the NT axis). The band edges of 0D and 1D models become closer while the 0D cluster size increases, yet the position of the defect-level does not show any convergence. At −5.1 eV, it is significantly higher for the 4×4 0D cluster than the value of −5.8 eV for the 1D NT.
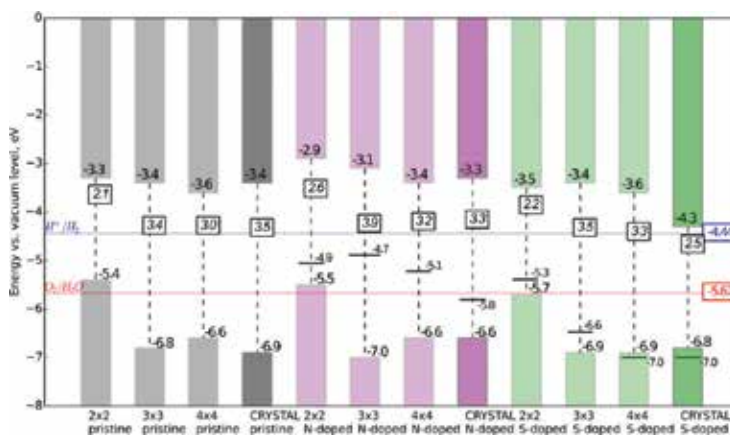

Figure 13. Comparison of band edges and gaps obtained for 0D and 1D NT models. All values are given in terms of electron volt vs. vacuum level; ε_{H^+/H_2} and ε_{O_2/H_2O} potentials are given for reference. CRYSTAL data refer to 1D models while 0D results are obtained using NWChem code [8].

Noncoincidence of the dopant-induced levels in both 0D and 1D NT models may be a consequence of the effectively larger defect concentration in the latter, which is 1 dopant per 24 O atoms in the periodically repeated unit cell (≈4%), versus 1 dopant per 96 O atoms (≈1%) in the 4×4 0D cluster. For S-doping, size of the cluster heavily affects position of the defect level. Moreover, for 2×2 and 3×3 models, the positions of S-induced levels are qualitatively different from those of 4×4 and NT models: the former are in-gap while the latter are located below the top of the VB.

To conclude, we observe that the 0D model qualitatively corresponds to the 1D model as far as the band edges are concerned. Positions of the dopant-induced states, however, strongly depend on the size of the cluster and, therefore, differ from those calculated for the NT. In N-doped cluster, where this effect is the most emphasized, it can be partially attributed to the spin polarization of the system, although the relatively naïve definition of the cluster model could have affected it just as much. More elaborate schemes exist, for example, polarizable polar background embedding [58], but these schemes are beyond the scope of our study.

4.3. Periodic models of doped (101)-oriented NTs

For energetically more stable but possessing lower reactivity (101) types of TiO$_2$ NTs with anatase morphology, we have considered only N and S dopants as well as N+S codoping since C- and Fe-substitutes have been found to be ineffective for photocatalytic applications of (001)-oriented TiO$_2$ NTs (Section 4.1). Calculations on these NTs have been performed using the same DFT-LCAO method with the hybrid exchange-correlation functional B3LYP [46] as used earlier having 14% of nonlocal Fock exchange as implemented in CRYSTAL code [43].
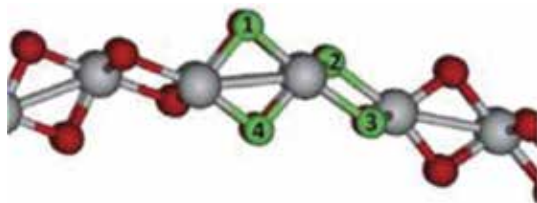
Figure 14. Nonequivalent S or N dopant positions in the segment of 6-layer wall of (−12,12) TiO$_2$ (101) nanotube (**Figure 4**) [9].

As mentioned in Section 3.4, the pristine titania NT with chirality indexes (−12,12) (**Figure 8**) has been chosen as the most suitable for our simulations on the doped TiO$_2$ (101) NTs. We consider four possible dopant sites to substitute the nonequivalent oxygen atoms (**Figure 14**). We denote the outermost O site as position 1, while the innermost O site is position 4. The S1 site is found to be the most energetically favorable – it requires the lowest formation energy per unit cell/dopant, 2.47 eV for both concentrations (**Table 3**). As it has been found in all cases the S dopant shows a tendency to be displaced from its initial position. The displacement direction is orthogonal to the tangent line passing through the initial S atom position, and the S atom is protruding out the NT wall. Obviously, it is easier to follow such displacement from

initial positions S1 and S4, which explains that the dopant formation energies are lower for these cases. Formation energies of S dopants presented in **Table 3** almost do not depend on their concentration, unlike N dopants for which this dependence is noticeable, excluding external N1 site.

	Concentration of defects			
Site	1.39%		2.78%	
	S_O	N_O	S_O	N_O
1	**2.47**[*]	**3.39**[*]	**2.47**[*]	**3.39**[*]
2	2.89	3.49	2.90	4.10
3	3.43	3.51	3.47	4.15
4	2.62	3.51	2.62	3.39

[*]The lowest energies are shown in bold.

Table 3. Defect formation energy (in eV) of S and N dopants at 2.78% and 1.39% defect concentrations as calculated using Eq. (4).

For the two sulfur dopant sites lying closer to the outer surface, sites S1 and S2 (**Figure 14**), there is a negative shift in energy for both the bottom of CB and the top of the VB. In fact, there is no difference between CB/VB positions of the pristine NT and the NTs containing S dopants at the positions S3 and S4. Doping at positions S1 and S4 promotes the highest photocatalytic enhancement, reducing the gap between the lowest unoccupied state and the highest occupied state, from 4.19 eV to 3.14 eV (3.12 eV) vs. 3.08 eV (3.07 eV) for 1.39% (2.78%) defect concentrations, respectively. It means that sulfur atoms themselves do not provide sufficient rise of photocatalytic activity. S-induced occupied levels have been found to be lower at 1.39% concentration. Unlike S-doped NTs, N dopants do not induce any visible shift in positions of the VB top and the CB bottom, levels are almost the same as in the case of the pristine structure. N dopants, however, induce empty states inside the band gap. For 2.78% defect concentration these empty states are not always higher than the highest occupied state. For N2 case, the empty state is located below an occupied state and is very close to the VB top, which means that in reality it will be easily occupied by electrons with similar energies.

Suitability of N_O+S_O codoped TiO_2 (101) NTs is likely noticeably higher than S and N mono-doped ones. Indeed, in the latter, there are only four nonequivalent dopant positions (**Figure 14**). However, after one dopant is already introduced, a number of options for different combinations of codopant positions appear. Due to limited computational resources, we have decided to put S dopant in its preferable position, S1 (**Figure 14** and Table 3). Therefore, in every modelled codoped structure the S atom is fixed in position 1, while N dopants can be inserted in different surrounding positions. Possible dimer-type sites for S+N codopants are assigned by additional indexes for identification (**Figure 15**: "*FR*" stands for "front", "*B*" for "between", "*N*" for "near" and "*UND*" for "under").
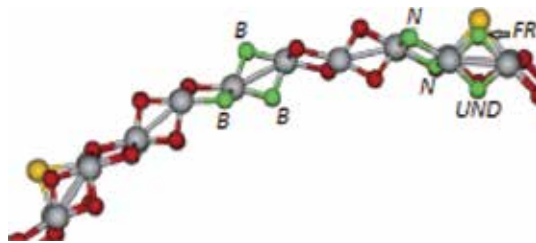
Figure 15. Possible sites for N dopant if S atom is located in position S1 (**Figure 14**), in the segment of 6-layer wall of (−12,12) TiO$_2$ (101) nanotube [9].

Electronic diagram of six studied N$_O$+S$_O$ codoped TiO$_2$ NT configurations with defect concentration of 2.78% is shown in **Figure 16**. Obviously, (N3-S1)*B* and (N3-S1)*N* are identical (**Figure 15**), and one of them (the latter) must be excluded from further consideration. The general observation is that the enhancement of the photocatalytical efficiency of the simulated structures may be expected. In four cases out of six, the lowest empty state is induced slightly below the ε_{O_2/H_2O} level (oxygen potential), and the highest occupied state is located between the empty state and the VB top. The distances between the empty and the occupied induced states are the smallest for (N1-S1)$_B$ or (N4-S1)$_B$ configurations, which means that it might be relatively easy for electrons to transfer to the empty state and, consequently, to overcome the $\varepsilon_{H^+/H_2}−\varepsilon_{O_2/H_2O}$ interval between redox potentials (**Figure 16**). The general observation is that in most cases S and N atoms have a tendency to be found closer to each other.
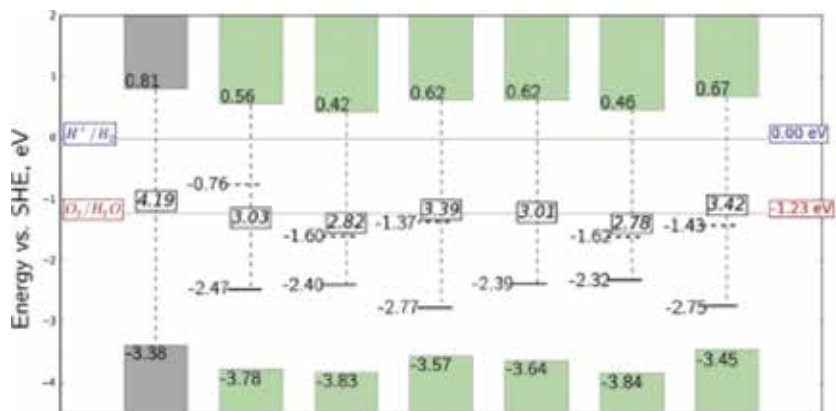
Figure 16. Energy diagram for the band gap edges and mid-gap states of pristine and N+S codoped TiO$_2$(101) NTs. Gray column correspond to pristine (−12,12) NTs while green columns from the second to the sixth from the left correspond to (N1-S1)*FR*, (N1-S1)*B*, (N2-S1)*N*, (N3-S1)*B*, (N4-S1)*B* and (N4-S1)*UND* codopants imaged in **Figures 14** and **15** [9].

Based on the results of our calculations, we predict that S or N dopants alone introduced into the 6-layer TiO$_2$ (−12,12) NT cannot result in a significant rise of photocatalytic response. For instance, the N doping may induce empty mid-gap states that can disrupt the photocatalytic

process. We found that defect concentration does not have a big impact on the electronic structure of NTs under study; our results show that rise in defect concentration from 1.39% to 2.78% (of doping atoms per unit cell) practically does not shift the band gap edges and mid-gap states induced by these defects. We show that the S+N codoping of titania NT can result in enhancement of photocatalytic efficiency, at least qualitatively. At the same time, we have to conclude that changes of titania NT electronic structure induced by codoping depend on defect concentration.

5. Summary

1. In a series of recent papers [5–9], we have formulated main goals of our studies:

    a. To evaluate photocatalytic suitability of inorganic nanostructures, as a first step we have considered SW titania anatase-structured (101) and (001) NTs, both pristine and doped.

    b. To justify application of computational methods of ground state *ab initio* DFT-LCAO calculations, e.g., CRYSTAL code (periodic structures of different dimensionalities) and TD DFT NWChem code (0D cluster structures), reliability of both models as well as reliable choice of hybrid Hamiltonian.

    c. To calculate the structural and electronic properties of nanomaterials under study in order to estimate their mechanical durability and homogeneity, electronic structure and photocatalytic efficiency.

    d. To search for novel nanomaterials suitable for photocatalytic applications.

2. Main results obtained in our large-scale computer simulations:

    a. Both SW (001) and (101) titania NTs are suitable for photocatalytic applications: although the latter is more stable energetically, the former possesses noticeably higher chemical reactivity.

    b. The necessary condition to achieve suitability of doped nanostructures for photocatalytic application is a proper disposition of band gap edges and impurity levels relative to the redox potentials: $\varepsilon_{VB} < \varepsilon_{HOIL} < \varepsilon_{O_2/H_2O} < \varepsilon_{H^+/H_2} < \varepsilon_{LUIL} < \varepsilon_{CB}$ where HOIL and LUIL are the highest occupied and the lowest unoccupied impurity levels, respectively.

    c. The next condition for such a suitability is the absence of the impurity levels between oxidation and reduction levels ε_{O_2/H_2O} and ε_{H^+/H_2}, respectively, in order to exclude electron–hole recombination.

    d. The best candidates for doping of titania NTs have been found to be N_O and S_O substitutes, however, $N_O + S_O$ codoping of TiO_2 NTs is certainly the best choice.

3. Further activities in the field of theoretical simulations in order to evaluate photocatalytic suitability of nanoelectrodes:

   a. To look for the best nanomaterials, both NTs and NWs, we have already studied SrTiO$_3$ NWs [59] and continue comprehensive simulations on ZnO NWs including their doping.

   b. To look for new types of defective structures of studied nanomaterials suitable for photocatalytic applications, e.g., vacancies and cation dopants.

   c. For better understanding of photocatalytic processes upon nanoelectrodes we are beginning TD DFT calculations on their charged and excited states.

   d. To study the charge transfer at the surface of doped nanoelectrodes immersed in aqueous electrolyte we intend to perform large-scale nonadiabatic molecular dynamics (MD) calculations.

Author details

Yuri F. Zhukovskii[*], Sergey Piskunov, Oleg Lisovski, Andrei Chesnokov and Dmitry Bocharov

*Address all correspondence to: quantzh@latnet.lv

Institute of Solid State Physics, University of Latvia, Riga, Latvia

References

[1] C.R.A. Catlow, Z.X. Guo, M. Miskufova, S.A. Shevlin, A.G.H. Smith, A.A. Sokol, A. Walsh, D.J. Wilson, and S.M. Woodley. Advances in computational studies of energy materials. Philos. Trans. Royal Soc. A, 2010, 368, p. 3379–3456.

[2] M. Kitano and M. Hara. Heterogeneous photocatalytic cleavage of water. J. Mater. Chem., 2010, 20, p. 627–641.

[3] N.S. Lewis. Toward cost-effective solar energy use. Science, 2007, 315, p. 798–801.

[4] A. Kudo and Y. Miseki. Heterogeneous photocatalyst materials for water splitting. Chem. Soc. Rev., 2009, 38, p. 253–278.

[5]   O. Lisovski, S. Piskunov, Yu.F. Zhukovskii, and J. Ozolins. *Ab initio* modeling of sulphur doped TiO_2 nanotubular photocatalyst for water-splitting hydrogen generation. IOP Conf. Ser.: Mater. Sci. Eng., 2012, 38, 012057 (p. 1–5).

[6]   Yu.F. Zhukovskii, S. Piskunov, J. Begens, J. Kazerovskis, and O. Lisovski. First-principles calculations of point defects in inorganic nanotubes. Phys. Status Solidi B, 2013, 250, p. 793–800.

[7]   S. Piskunov, O. Lisovski, J. Begens, D. Bocharov, Yu.F. Zhukovskii, M. Wessel, and E. Spohr. C-, N-, S-, and Fe-doped TiO_2 and $SrTiO_3$ nanotubes for visible-light-driven photocatalytic water splitting: Prediction from first principles. J. Phys. Chem. C, 2015, 119, p. 18686–18696.

[8]   A. Chesnokov, O. Lisovski, D. Bocharov, S. Piskunov, Yu.F. Zhukovskii, M. Wessel, and E. Spohr. *Ab initio* simulations on N and S co-doped titania nanotubes for photocatalytic applications. Phys. Scr., 2015, 90, 094013 (p. 1–7).

[9]   O. Lisovski, A. Chesnokov, S. Piskunov, D. Bocharov, Yu.F. Zhukovskii, M. Wessel, and E. Spohr. *Ab initio* calculations of doped TiO_2 anatase (101) nanotubes for photocatalytical water splitting applications. Mater. Sci. Semicond. Process., 2016, 42, p. 138–141.

[10] A. Fujishima and K. Honda. Electrochemical photolysis of water at a semiconductor electrode. Nature, 1972, 238, p. 37–38.

[11] Memming, R. Semiconductor Electrochemistry (Wiley-VCH Verlag: Weinheim), 2001.

[12] M. Grätzel. Photoelectrochemical cells. Nature, 2001, 414, p. 338–344.

[13] X. Chen, S. Shen, L. Guo, and S. S. Mao. Semiconductor-based photocatalytic hydrogen generation. Chem. Rev., 2010, 110, p. 6503–6570.

[14] S.G. Kumar and L.G. Devi. Review on modified TiO_2 photocatalysis under UV/visible light: Selected results and related mechanisms on interfacial charge carrier transfer dynamics. J. Phys. Chem. A, 2011, 115, p. 13211–13241.

[15] E. Thimsen, S. Biswas, C.S. Lo, and P. Biswas. Predicting the band structure of mixed transition metal oxides: Theory and experiment. J. Phys. Chem. C, 2009, 113, p. 2014–2021.

[16] T. Bak, J. Nowotny, M. Rekas, and C.C. Sorrell. Photo-electrochemical hydrogen generation from water using solar energy: Materials-related aspects. Int. J. Hydrogen Energy, 2010, 27, p. 991–1022.

[17] E. Borgarello, J. Kiwi, M. Grätzel, E. Pelizzetti, and M. Visca. Visible light induced water cleavage in colloidal solutions of chromium-doped titanium dioxide particles. J. Am. Chem. Soc., 1982, 104, p. 2996–3002.

[18] S. Klosek and D. Raftery. Visible light driven V-doped TiO_2 photocatalyst and its photooxidation of ethanol. J. Phys. Chem. B, 2001, 105, p. 2815–2819.

[19] M. Khan, S. Woo, and O. Yang. Hydrothermally stabilized Fe(III) doped titania active under visible light for water splitting reaction. Int. J. Hydrogen Energy, 2008, 33, p. 5345–5351.

[20] L.G. Devi, N. Kottam, S.G. Kumar, and K.S.A. Raju. Mechanism of charge transfer in the transition metal ion doped TiO$_2$ with bicrystalline framework of anatase and rutile: Photocatalytic and photoelectrocatalytic activity. Catal. Lett., 2009, 131, p. 612–617.

[21] X. Chen and C. Burda. The electronic origin of the visible-light absorption properties of C-, N- and S-doped TiO$_2$ nanomaterials. J. Am. Chem. Soc., 2008, 130, p. 5018–5019.

[22] W. Lin, W. Yang, I. Huang, T. Wu, and Z. Chung. Hydrogen production from methanol/water photocatalytic decomposition using Pt/TiO$_2$-xNx catalyst. Energy Fuel, 2009, 23, p. 2192–2196.

[23] T. Umebayashi, T. Yamaki, H. Itoh, and K. Asai. Band gap narrowing of titanium dioxide by sulfur doping. Appl. Phys. Lett., 2002, 81, p. 454–456.

[24] J.C. Yu, W. Ho, J. Yu, H. Yip, P.K. Wong, and J. Zhao. Efficient visible-light-induced photocatalytic disinfection on sulfur-doped nanocrystalline titania. Environ. Sci. Technol., 2005, 39, p. 1175–1179.

[25] K. Nishijima, T. Kamai, N. Murakami, T. Tsubota, and T. Ohno. Photocatalytic hydrogen or oxygen evolution from water over S- or N-doped TiO$_2$ under visible light. Int. J. Photoenergy, 2008, 2008, p. 1–7.

[26] S.U.M. Khan, M. Al-Shahry, and W.B. Ingler. Efficient photochemical water splitting by a chemically modified n-TiO$_2$. Science, 2002, 297, p. 2243–2245.

[27] C. Xu, Y.A. Shaban, W.B. Ingler, and S.U.M. Khan. Nanotube enhanced photoresponse of carbon modified (CM)-n-TiO$_2$ for efficient water splitting. Energy Mater. Sol. Cells, 2007, 91, p. 938–943.

[28] G. Yan, M. Zhang, J. Hou, and J. Yang. Photoelectrochemical and photocatalytic properties of N+S co-doped TiO$_2$ nanotube array films under visible light irradiation. Mater. Chem. Phys., 2011, 129, p. 553–557.

[29] J. Lv, T. Sheng, L. Su, G. Xu, D. Wang, Z. Zheng, and Y. Wu. N, S co-doped-TiO$_2$/fly ash beads composite material and visible light photocatalytic activity. Appl. Surf. Sci., 2013, 284, p. 229–234.

[30] G. Wang, Y. Ling, and Y. Li. Oxygen-deficient metal oxide nanostructures for photo-electrochemical water oxidation and other applications. Nanoscale, 2012, 4, p. 6682–6691.

[31] M. Li, J. Zhang, and Y. Zhang. First-principles calculation of compensated (2N, W) co-doping impacts on band gap engineering in anatase TiO$_2$. Chem. Phys. Lett., 2012, 527, p. 63–66.

[32] R. Asahi, T. Morikawa, T. Ohwaki, K. Aoki, and Y. Taga. Visible-light photocatalysis in nitrogen-doped titanium oxides. Science, 2001, 293, p. 269–271.

[33] D. Zhang and M. Yang. Band structure engineering of TiO_2 nanowires by *n-p* co-doping for enhanced visible-light photoelectrochemical water-splitting. Phys. Chem. Chem. Phys., 2013, 15, p. 18523–18529.

[34] M. Nolan. Electronic coupling in iron oxide-modified TiO_2 leads to a reduced band gap and charge separation for visible light active photocatalysis. Phys. Chem. Chem. Phys., 2011, 13, p. 18194–18199.

[35] A.M. Márquez, J. Plata, Y. Ortega, and J.F. Sanz. Structural defects in W-doped TiO_2 (101) anatase surface: DFT study. J. Phys. Chem. C, 2011, 115, p. 16970–16976.

[36] S.A. Shevlin and S.M. Woodley. Electronic and optical properties of doped and undoped $(TiO_2)n$ nanoparticles. J. Phys. Chem. C, 2010, 114, p. 17333–17343.

[37] Q. Meng, J. Wang, Q. Xie, H. Dong, and X. Li. Water splitting on TiO_2 nanotube arrays. Catal. Today, 2011, 165, p. 145–149.

[38] W.N. Zhao and Z.P. Liu. Mechanism and active site of photocatalytic water splitting on titania in aqueous surroundings. Chem. Sci., 2014, 5, p. 2256–2264.

[39] S.W. Boettcher, J.M. Spurgeon, M.C. Putnam, E.L. Warren, D.B. Turner-Evans, M.D. Kelzenberg, J.R. Maiolo, H.A. Atwater, and N.S. Lewis. Energy-conversion properties of vapor–liquid-solid-grown silicon wire-array photocathodes. Science, 2010, 327, p. 185–187.

[40] N. Beermann, L. Vayssieres, S.-E. Lindquist, and A. Hagfeldt. Photoelectrochemical studies of oriented nanorod thin films of hematite. J. Electrochem. Soc., 2000, 147, p. 2456–2461.

[41] J.M. Macak, M. Zlamal, J. Krysa, and P. Schmuki. Self-organized TiO_2 nanotube layers as highly efficient photocatalysts. Small, 2007, 3, p. 300–304.

[42] M.A. Khan, H. Jung, and O. Yang. Synthesis and characterization of ultrahigh crystalline TiO_2 nanotubes. J. Phys. Chem. B, 2006, 110, p. 6626–6630.

[43] R. Dovesi, V.R. Saunders, C. Roetti, R. Orlando, C.M. Zicovich-Wilson, F. Pascale, B. Civalleri, K. Doll, N.M. Harrison, I.J. Bush, P. D'Arco, M. Llunell, M. Causà, Y. Noël. CRYSTAL14 User's Manual, (University of Torino, 2014). http://www.crystal.unito.it/.

[44] M. Valiev, E.J. Bylaska, N. Govind, K. Kowalski, T.P. Straatsma, H.J.J. Van Dam, D. Wang, J. Nieplocha, E. Apra, T.L. Windus, and W.A. de Jong. NWChem: A comprehensive and scalable open-source solution for large scale molecular simulations. Comput. Phys. Commun., 2010, 181, p. 1477–1489.

[45] R.A. Evarestov. Theoretical Modeling of Inorganic Nanostructures. Symmetry and *Ab initio* Calculations of Nanolayers, Nanotubes and Nanowires, 2015 (Series: Nano-Science and Technology; Springer-Verlag, Berlin-Heidelberg).

[46] A.D. Becke. Density-functional thermochemistry. III. The role of exact exchange. J. Chem. Phys., 1993, 98, p. 5648–5652.

[47] P.J. Hay and W.R. Wadt. *Ab initio* effective core potentials for molecular calculations. Potentials for K to Au including the outermost core orbitals. J. Chem. Phys., 1985, 82, 299–310.

[48] R.A. Evarestov, A.V. Bandura, M.V. Losev, S. Piskunov, and Yu.F. Zhukovskii. Titania nanotubes modeled from 3- and 6-layered (101) anatase sheets: Line group symmetry and comparative *ab initio* LCAO calculations. Phys. E, 2010, 43, p. 266–278.

[49] R.A. Evarestov, Yu.F. Zhukovskii, A.V. Bandura, and S. Piskunov. Symmetry and models of single-wall TiO$_2$ nanotubes with rectangular morphology. Cent. Eur. J. Phys., 2011, 9, p. 492–501.

[50] R.A. Evarestov, D.B. Migas, and Yu.F. Zhukovskii. Symmetry and stability of the rutile-based TiO$_2$ nanowires: Models and comparative LCAO plane wave DFT calculations. J. Phys. Chem. C, 2012, 116, p. 13395–13402.

[51] R.A. Evarestov and Yu.F. Zhukovskii. Four-faceted nanowires generated from densely-packed TiO$_2$ rutile surfaces: *Ab initio* calculations. Surf. Sci., 2013, 608, p. 226–240.

[52] H.J. Monkhorst and J.D. Pack. Special points for Brillouin-zone integrations. Phys. Rev. B, 1976, 13, p. 5188–5192.

[53] U. Diebold. The surface science of titanium dioxide. Surf. Sci. Rep., 2003, 48, p. 53–229.

[54] C.Z. Wen, H.B. Jiang, S.Z. Qiao, H.G. Yang, and G.Q. Lu. Synthesis of high-reactive facets dominated in anatase TiO$_2$. Chem. Commun., 2011, 21, p. 7052–7061.

[55] M. Lazzeri, A. Vittadini and A. Selloni. Structure and energetics of stoichiometric TiO$_2$ anatase surfaces. Phys. Rev. B, 2001, 63, 155409 (p. 1–9).

[56] A.M. Ferrari, D. Szieberth, C.M. Zicovich-Wilson, and R. Demichelis. Anatase (001) 3 ML nanotubes, the first TiO$_2$ nanotube with negative strain energies: A DFT prediction. J. Phys. Chem. Lett., 2010, 1, p. 2854–2857.

[57] J. Sauer. Molecular models in *ab initio* studies of solids and surfaces: From ionic crystals and semiconductors to catalysts. Chem. Rev., 1989, 89, p. 199–255.

[58] D. Berger, A.J. Logsdail, H. Oberhofer, M.R. Farrow, C.R.A. Catlow, P. Sherwood, A.A. Sokol, V. Blum, and K. Reuter. Embedded-cluster calculations in a numeric atomic orbital density-functional theory framework. J. Chem. Phys., 2014, 141, 024105.

[59] A.V. Bandura, R.A. Evarestov, and Yu.F. Zhukovskii. Energetic stability and photocatalytic activity of SrTiO$_3$ nanowires: Ab initio simulations. Royal Soc. Chem. Advances, 2015, 5, p. 24115–24125.

Pulsed Laser-Deposited TiO$_2$-based Films: Synthesis, Electronic Structure and Photocatalytic Activity

Oksana Linnik, Nataliia Chorna, Nataliia Smirnova,
Anna Eremenko, Oleksandr Korduban,
Nicolaie Stefan, Carmen Ristoscu, Gabriel Socol,
Marimona Miroiu and Ion N. Mihailescu

Additional information is available at the end of the chapter

Abstract

Active under visible light, photocatalysts based on doped titania were obtained via pulsed laser deposition (PLD) method. To find out the crystalline structure, optical properties, and electronic structure, the following techniques such as X-ray diffraction, electronic spectroscopy, electrical conductivity measurements, and X-ray photoelectron spectroscopy (XPS) are used. Photocatalytic activity is monitored by applying the photoreduction of dichromate ions under UV and visible light. The influence of zirconium ions and its content and synthesis conditions on the efficiency of nitrogen incorporation into titania structure that, in turn, determines the electronic structure and photocatalytic ability of the semiconductive materials are discussed. A substitutional nitrogen (Ti–N) rather than an interstitial one (Ti–O–N) is mainly responsible for the observed photoactivity. It is pointed that substitutional nitrogen is responsible for bandgap narrowing or formation of intragap localized states within semiconductor bandgap. The bandgap energy values are sharply decreased, while the relative intensity of substitutional nitrogen XPS peaks is increased. Pulsed laser synthesis of TiO$_2$ films in N$_2$/CH$_4$ atmosphere not only leads to nitrogen incorporation but also to the formation of defects including oxygen vacancies and Ti^{3+} states which are all contributing to light absorption. An appropriate ratio of gas mixture, optimum zirconia content, suitable pressure, and temperature during synthesis was found for the synthesis of highly active semiconductive films. The highest photocatalytic conversion yields are obtained for nitrogen-doped 10% ZrO$_2$/TiO$_2$ synthesized in N$_2$:CH$_4$ = 5:1 at 100 Pa and at 450°C under both UV and visible light.

---

1. Introduction

Among the ways leading to the intensive climate change, the widespread contamination of air, soil, and water sources are to be considered. Titania is recognized as the most prospective photocatalyst used in air purification, surface self-cleaning, and wastewater treatment [1–7]. Since solar radiation includes light of wavelengths from 280 to 4000 nm, the use of titania that absorbs the edge (3–5%) of solar energy is not efficient. Many studies are performed to design and develop photocatalysts based on titania to allow for their use under visible-light irradiation [8, 9]. Nitrogen, the most promising among nonmetal dopants, facilitates visible light absorption by nanomaterials based on TiO_2 as a result of its incorporation into titania matrix due to its comparable atomic size with oxygen, small ionization energy, and high stability. Another approach to change the physical, optical, structural, and photocatalytic properties of titania includes employment of d-block metal ions (*e.g.,* zinc, zirconium, iron, chromium, nickel, vanadium, or copper).

An incorporation of zirconium ions in TiO_2 lattice was reported to enhance the specific surface area and the surface acidity and to modify the photo-electrochemical properties, leading to the improvement of the photocatalytic activity [10]. $Ti_{1-x}Zr_xO_2$ solid solution containing anatase led to the increase of bandgap energy with the anodic shift of the upper edge of the valence band position accelerating photocatalytic processes due to the improvement of charge separation. It was found an optimum content of ZrO_2 in TiO_2 that increased the quantity of the surface active sites such as OH-groups [11]. In the case of zinc-containing nanocomposites, their crystallinity slightly increased with Zn content and $ZnTiO_3$ perowskite phase is formed. The films with low Zn content (1–5 wt%) exhibited superhydrophilicity. Direct photo-electrochemical measurements showed the cathodic shift of the flat band potential position and the increase of the photocurrent quantum yield for TiO_2/ZnO in comparison with un-modified TiO_2 electrodes that coincided with the increase of their photocatalytic activity [11]. More effective degradation was observed for Zn^{2+}-doped samples with homogeneously distributed noble metal nanoparticles as a result of synergetic effect of new formed $Zn_2Ti_3O_8$ phase and the charge separation promoted by the noble metal nanoparticles. It was found that a higher dispersion of noble metal crystallization centers did occur near zinc ions in titania matrix [12, 13]. Nanostructured iron titanate and ruthenium-modified titania thin films are reported to catalyze the photocatalytic dinitrogen reduction that is the second, after photosynthesis, most important chemical process in nature. A detailed mechanism investigation clarified the role of metal ions in all complicated steps of this process [14, 15]. However, d-block metals may also act as recombination sites for the photo-induced charge carriers lowering the activity of the semiconductors. Despite the fact that a decrease in bandgap energy was achieved by metal doping, photocatalytic activity has not been remarkably enhanced [16].

Since Sato [17] reported the visible-light activity of N-doped titania in the oxidation of carbon monoxide and ethane, and later, Asahi [18] explored the visible-light activity of N-doped TiO$_2$, there have been many efforts dealing with nitrogen doping of TiO$_2$. Numerous physical techniques such as sputtering [19, 20] and ion implantation [21], atomic layer deposition [22], pulse laser deposition [23], gas phase reaction [24], and the sol–gel method [16] have been successfully applied to obtain nitrogen-modified TiO$_2$.

It is reported [18] that the doping of nonmetals could narrow the bandgap and might drive the response to visible light due to the similar energies of oxygen and nitrogen resulting in the hybridization of N 2p with O 2p states in anatase TiO$_2$. On the other hand, it is stated [25] that isolated impurity energy levels above the valence band are formed as a result of oxygen atoms substitution by nitrogen ones. Irradiation with UV light excites electrons in both the valence band (VB) and the impurity energy levels, but illumination with visible light only excites electrons in the impurity energy level. An alternative point of view, where the visible-light activation of anion-doped TiO$_2$ originates from the defects associated with oxygen vacancies, was also reported. As a result, the color centers appeared displaying these absorption bands, and not to a narrowing of the bandgap of TiO$_2$ [26]. Whereas surface oxygen vacancies were reduced considerably after reheating at 400°C, the activity of N-doped TiO$_2$ was enhanced fourfold suggesting no oxygen vacancies influence on visible-light activity [27]. In addition, nitrogen-modified titania powder obtained by mixing a commercially manufactured titania powder and the different nitrogen containing organic substances were applied for photomineralization of formic acid under visible light. It is concluded that neither nitridic nor NO$_x$ species nor defect states are responsible for the visible-light photocatalytic activity of modified titania prepared from urea, but higher melamine condensation products acting as visible-light sensitizers [28].

The main technique proving the nitrogen incorporation into a semiconductor structure as substitutional nitrogen atom (N$_s$), where nitrogen substitutes oxygen lattice ions or interstitial one (N$_i$), and N binds to O lattice ions, is X-ray photoelectron spectroscopy (XPS). There is no definite opinion about the XPS measurements of N1s binding energy (BE). The peak at 395.7 eV is assignable to N^{3-} bonded to three Ti atoms because the measured binding energy is very close to that of titanium nitrides (ca. 396.0 eV) [29, 30]; the values of 396–397 eV are assigned to the N–Ti–N [31] or O–Ti–N bonds [32]. The formation of N–N or N–C, N–O groups or chemisorbed dinitrogen was suggested for higher energies of (400–402 eV) [33]. Note that N1s binding energies of 399.1 and 400.5 eV measured for modified by urea commercially available TiO$_2$ powder were assigned to carbon nitrides (399–400 eV, C=N–C), graphite-like phases (400.6 eV, N-Csp^2), and to polycyanogen (399.0, 400.5 eV (–C=N–)$_x$) [34]. XPS and electron paramagnetic resonance (EPR) measurements showed that the interstitial nitrogen atoms corresponded to BE of 400–401 eV are the photoactive species and can be prepared from discharge in molecular nitrogen in the presence of pure anatase [35]. However, the intensity of 400 eV peak belonged to the nitrogen atom from ammonium ions is reduced after rinsing as provided by XPS and solid-state nuclear magnetic resonance (NMR) [36].

The geometric structures of diamagnetic (**Scheme 1, i**) and paramagnetic (**Scheme 1, ii–vi**) nitrogen species incorporated into titania suggested from the literature were summarized in

Ref. [29]. Nitrogen species with a binding energy of ca. 396 eV represent TiN species (nitridation of titania) described as structure i, where N^{3-} species are directly bonded to three Ti^{3+} cations [29]. The N contained species corresponding to structure ii are related to a binding energy in the range of 397–399 eV [30, 37]. The formation of O–Ti–N–Ti during the synthesis could take place (structures iii and iv), when nitrogen substituted the lattice oxygen atom of O–Ti–O–Ti [38]. The structure v where the nitrogen atom connected with two oxygen of the TiO_2 lattice depicted as imino-type species and may be formed as a result of the incomplete reaction of ammonia with surface oxygen atoms [39]. It is believed [40] that the imino-type species undergoes to nitrate-type species (structure vi) where the last is the photoactive nitrogen species.
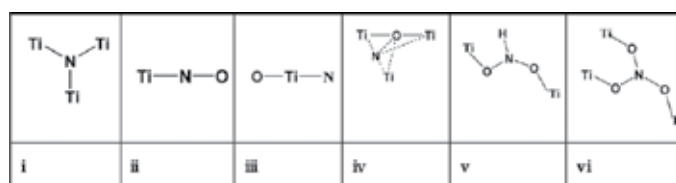
Scheme 1. Proposed structures of N species incorporated into titania as summarized in Ref. [29]. Reproduced with permission.

In light of numerous literature investigations, the applied synthesis conditions and the source of nitrogen are the turning points for the level of nitrogen doping and its states that change optical, electronic, and photocatalytic properties of a semiconductor.

The main principles of heterogeneous photocatalysis are presented as follows (**Figure 1**): (i) A semiconductor is characterized by an electronic band structure in which the highest occupied energy valence band (VB) and the lowest empty conduction band (CB) are separated by bandgap; (ii) only a photon of energy higher or equal to the bandgap energy (≥3.2 eV for anatase) promotes to a charge separation resulting in an electron (e^-) transferring from the VB to the CB with simultaneous generation of a hole (h^+) in the VB (pathway 1); (iii) an electron and a hole can be trapped in surface states and react with donor (D) and acceptor (A) species, respectively, adsorbed or close to the surface of the particle resulting in the simultaneous oxidation and reduction (pathways 1.1 and 1.2); or (iv) a photoformed electron–hole pair can be recombined (pathway 2) on the surface or in the bulk of the particle in a few nanoseconds. The energy level at the bottom of the CB is actually the reduction potential of photoelectrons and the energy level at the top of the VB determines the oxidizing ability of photoformed holes. The flat-band potential presents the energy of both charge carriers at the semiconductor–electrolyte interface and depends on the nature of the material and the system equilibrium.

From a thermodynamic point of view, the trapped electron reduces an electron acceptor only if its redox potential is more positive than the flat-band potential of the CB, while the trapped hole oxidizes the adsorbed species having the redox potential more negative than the flat-band potential of the VB. The visible-light photoactivity of metal-ions-doped TiO_2 can be explained by a new energy level produced in the bandgap where an electron can be excited from the
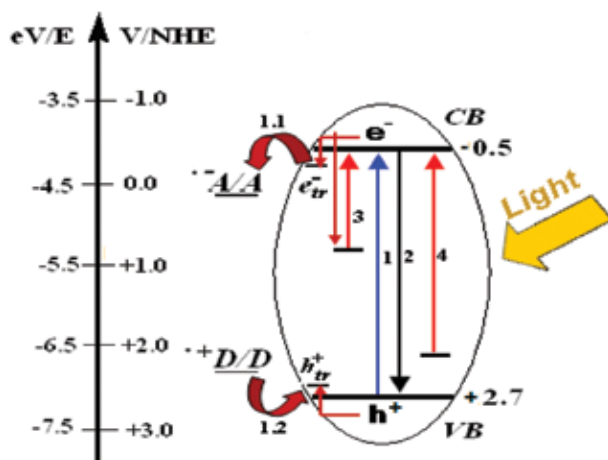
Figure 1. Schematic presentation of possible pathways after light absorption by doped titania particle.

defect state to the TiO$_2$ conduction band by photon with the lower energy (pathway 3). Inhibition of charge carrier recombination rate resulting in enhanced photoactivity is attributed to the transition metal ions doping of TiO$_2$. Visible-light illumination can generate a hole in the mid-gap level above the top of the VB for the N-doped TiO$_2$ (pathway 4).

The nitrogen-modified TiO$_2$ thin films exhibited photocurrents in the visible up to 700 nm as a result of occupied nitrogen-centered surface states above the valence band edge as noted in Ref. [41]. Moreover, the observed photocurrent under visible-light irradiation of N-doped TiO$_2$ in the presence of reducing agent strongly depend on the reaction mechanism of oxidation rather than on the redox potential of the whole acceptors [42]. Photo-electrochemical measurements showed that the visible-light photogenerated holes in TiO$_2$ modified by urea are able to oxidize formic acid comparing with ammonia modified one. An enhanced stabilization of the photogenerated hole against recombination with conduction band electrons for the former sample is explained [43]. In addition to the electrochemical investigations, preliminary computer simulations based on innovative cluster approaches demonstrated that nitrogen doping narrowed the optical bandgap of TiO$_2$ generating N(2p) states [44]. Density functional theory (DFT) was employed to demonstrate the interstitial nitrogen character within anatase TiO$_2$. No significant shift in the CB or VB of the TiO$_2$ was recognized. The energy bonding states associated below the valence band and anti-bonding states present above the valence band. The anti-bonding nitrogen orbital between the TiO$_2$ VB and CB is suggested to be responsible for the visible light absorption by acting as a stepping stone for excited electrons between conduction and valence bands [45].

Our investigation was directed to the synthesis of nitrogen-doped photocatalysts based on titania and/or mixed semiconductive oxides films and understanding the relationship between synthesis conditions, electronic structures, and photocatalytic activity. The influence of zirconium ions and its content as well as pulsed laser synthesis conditions on the efficiency of

nitrogen incorporation into titania structure that, in turn, determines the photocatalytic ability of the semiconductive materials are obtained.

2. Correlation of electronic structure, optical, structural, and photocatalytic properties of TiO$_2$-doped films

Pulsed laser deposition method used for the film synthesis allows obtaining high purity thin films of single or multicomponent materials [46]. **PLD** or **laser ablation** is a physical vapor deposition process based on the vaporization of condensed matter by means of photons [46–50]. A highly intense short-pulsed high-power laser beam (usually a ns UV one) is focused under vacuum or a working gas atmosphere on a piece of material (on a material specimen) called "target." If the laser fluence exceeds a specific threshold, one after one, each tiny quantity of ablated material by a laser pulse, is directed forward, in form of a plume, towards the deposition substrate, where the growing film is formed by recondensation [47–50]. Due to the high energetic species arriving on the substrate, the synthesized films are very adherent. The plasma plume plays a significant piston-like role, pushing and carrying the removed matter from the target to the substrate [49]. In the most common setup geometry, "on axis," the collector is placed parallel to the target, at a distance of some centimeters and, after being focused and transmitted by suitable optics, the laser pulses hit the target under 45°. The target is normally rotated in order to get a uniform ablation of its surface, avoiding drilling, thus obtaining a homogenous film. The collector, which is named usually "substrate," may be heated if a high degree of crystallinity or even epitaxy is of interest for the obtained coating. A schematic of PLD setup is given in **Figure 2**.
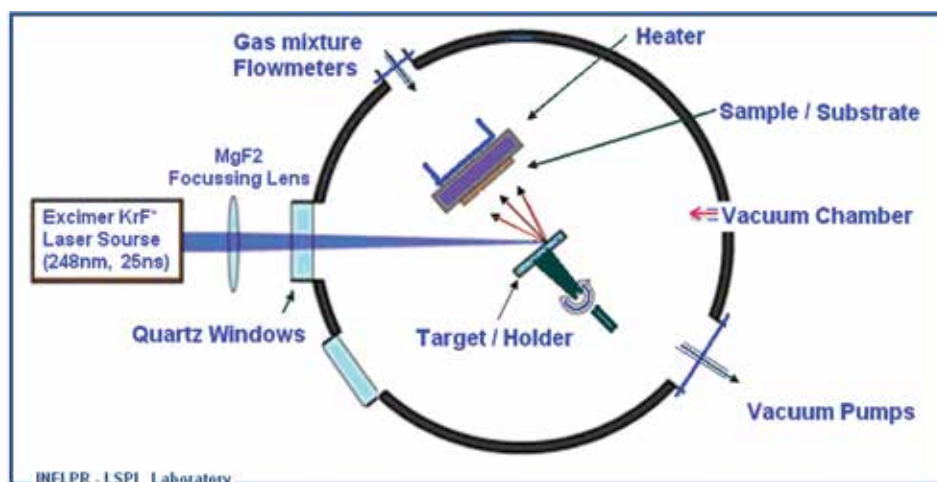

Figure 2. Schematic setup of a PLD system: The laser source is outside the deposition chamber, which is coupled to a vacuum system. Inside chamber, a classical "on axis" geometry is presented.

The PLD presents a series of advantages [47–50], among which we mention: almost any material or materials' combination may be congruently transferred as thin film on a suitable substrate after the identification of a selected deposition regime, a fine control of thickness is obtained by the number of the applied laser pulses (and the appropriate setting of various parameters), it is a clean, non-contaminating method, also allowing for an easy doping or multilayer structures. These and others made PLD a tool of remarkable performance, versatility, and simplicity for the growth of various types of thin films: complex oxides, high-temperature superconducting, protective or ultrahard coatings, polymer or organic thin films [50–52].

ZrO$_2$% in TiO$_2$	Ratio of gases	Sample code	P, Pa	t, °C	E$_{bg}$, eV
0	O$_2$	**TiO/20**	20	450	3.3
0	N$_2$:O$_2$ = 1:1	**TiNO/10**	10	450	2.8
0	N$_2$	**TiN/20**	20	450	2.6
0	CH$_4$	**TiC/5**	5	450	–
0	N$_2$:CH$_4$ = 5:1	**TiN5C1/100**	100	450	3.3
0	N$_2$:CH$_4$ = 5:1	**TiN5C1/3**	3	450	–
2.5	O$_2$	**2.5ZrTiO/100**	100	450	3.3
5	O$_2$	**5ZrTiO/100**	100	450	3.4
10	O$_2$	**10ZrTiO/100**	100	450	3.5
2.5	N$_2$:CH$_4$ = 9:1	**2.5ZrTiN9C1/100**	100	450	3.0
5	N$_2$:CH$_4$ = 9:1	**5ZrTiN9C1/100**	100	450	2.9
2.5	N$_2$:CH$_4$ = 5:1	**2.5ZrTiN5C1/100**	100	450	3.4
5	N$_2$:CH$_4$ = 5:1	**5ZrTiN5C1/100**	100	450	3.3
10	N$_2$:CH$_4$ = 5:1	**10ZrTiN5C1/100**	100	450	3.1
50	N$_2$:O$_2$ = 1:1	**50ZrTiN1O1/5**	5	600	3.5
50	O$_2$	**50ZrTiO/10**	10	600	3.7
50	N$_2$	**50ZrTiN/10**	10	600	3.0
50	CH$_4$	**50ZrTiC/10**	10	600	3.2
50	N$_2$:CH$_4$ = 10:1	**50ZrTiN10C1/3**	3	600	–
50	CH$_4$	**50ZrTiC/5**	5	600	–
50	N$_2$:CH$_4$ = 5:1	**50ZrTiN5C1/10**	10	600	3.6

Table 1. PLD conditions and bandgap values of TiO$_2$-based films.

PLD experiments were performed using a KrF* laser source (COMPexPro 205 Coherent, τ_{FWHM} ≤ 25 ns). Pristine TiO_2 or ZrO_2-mixed TiO_2 targets with different content of zirconium oxide were laser ablated to grow coatings on glass plates. The films were synthesized at substrate temperatures of 450 or 600°C. The samples were deposited at different pressure of pure oxygen, nitrogen, methane, and mixed N_2:CH_4 atmosphere with 1:1, 5:1, 9:1, and 10:1 ratios.

Photocatalytic activity of the films was assessed via dichromate ions reduction reaction. The film was immersed in 15 ml of an aqueous solution of potassium dichromate (in all experiments, the initial concentration of dichromate ions was $2*10^{-4}$ M) and the reducing agent (disodium salt of ethylenediaminetetraacetic acid) in the molar ratio 1:1 adjusted to pH ≥ 2 by perchloric acid. The mass of the films was found to be 0.40 ± 0.02 mg (the concentration of the catalyst in aqueous solution of redox couple was 2.7×10^{-2} g/L, 37 times lower than usually used suspension 1 g/L). The reaction temperature was kept constant (25°C) during the experimental procedure. The change of Cr(VI) ions concentration was monitored with a Lambda 35 UV–Vis spectrophotometer (PerkinElmer) every 20 min. The film was immersed in the solution until complete adsorption in the dark occurred and then irradiated by 1000 W middle-pressure mercury lamp for 120 min. The distance lamp reactor was set at 90 cm. Two blank experiments were carried out: the catalytic reduction of dichromate ions (dark condition) and photoreduction reaction (a bare glass was used instead of film). The conversion percentage of every photocatalytic run is given after subtraction of the corresponding value of the last blank. For testing the visible-light sensitivity, a filter transmitting light with $\lambda > 380$ nm was introduced in the photocatalytic setup.

The sample codes that will appear over the chapter can be easily understand as *x(Zr)TiYy(Zz)/P*, where *x* is the ZrO_2 percentage, *(Zr)Ti* is a target composition, *Y* and *Z* mean gas atmosphere (*O* is O_2, *N* is N_2, *C* is CH_4), *y* and *z* are the ratio of *Y* and *Z*, *P* is the gas pressure during PLD procedure. The synthesis conditions and the measured value of bandgap energy (E_{bg}) are collected in **Table 1**.

2.1. Nitrogen-doped TiO_2 films

Pulsed laser synthesis of TiO_2 films in oxygen, nitrogen, methane and their mixtures was performed (**Table 1**) [53]. Excluding the UV part of spectrum by cut-of-filter, the films obtained at different atmospheres exhibited the visible light absorption (**Figure 3**). Compared to bare TiO_2, nonmetal-doped films show a change in optical absorption that was originally associated to a bandgap narrowing. Comparing the values of bandgap energy calculated by extrapolating the linear parts of the $(\alpha h\nu)^{1/2} \sim f(h\nu)$ curves, that is assuming an indirect electronic transition (Table 1), the decrease in its values for the doped samples is obvious proving that the electronic structure of a photocatalyst affects its optical absorption. The sharp decrease of E_{bg} was demonstrated when pure dinitrogen or the mixture of dinitrogen and oxygen has been applied.
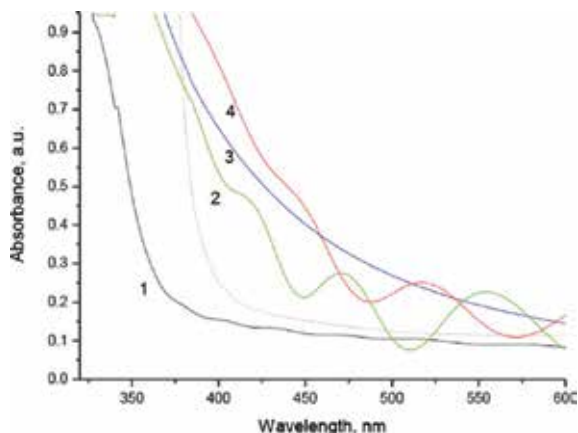
Figure 3. Absorption spectra of TiO (1), TiN (2), TiN5C1 (3), TiNO (4), and cut-of-filter (dashed line).

As revealed by X-ray diffraction (XRD) spectra (**Figure 4**), anatase phase formation has been obtained for all films excepting TiC/5. Moreover, the samples TiNO/10 and TiO/20 present a preferential texture along the <004> plane. On the other hand, the peaks at 37.80°, 43.30°, and 62.80° visible in the diffractogram of the TiO₂ film deposited in CH₄ (TiC/5 film) could be related to <004>, <002>, and <202> planes of TiO phase indicating the formation of a sub-stoichiometric compound [53] or even Ti crystalline phase [29, 54, 55]. It is obvious that pure methane used in PLD prevents anatase formation providing oxygen atoms deficiency.
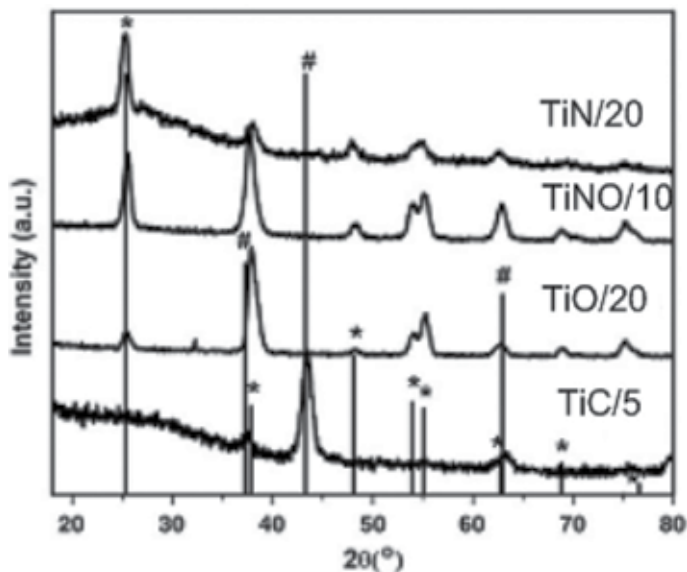
Figure 4. XRD spectra of TiO₂ films deposited at 450°C in oxygen, nitrogen, methane, and mixture of nitrogen and oxygen (*—anatase phase and #—TiO or Ti phase). Reproduced with permission from [53].

Intensity belonging to substitutional Ns (N–Ti) lines at 395.2 and 395.8 eV for **TiYy(Zz)/P** is varied as clearly seen from **Figure 5** and **Table 1**. In addition, the appearance of the line at 397.8 and 398.1 eV accompanied by characteristic lines in the O$1s$ and Ti$2p$ spectra (not shown here) reveals a more complex structure of nitrogen in the doped TiO$_2$ films. The peak at $BE \sim$ 457.5 eV in the Ti$2p$ XPS spectrum of this film can be attributed to either the Ti atoms in the N–Ti–O linkages or Ti species interacting with V_O, whose formation is highly favored in the oxygen-poor conditions (**Table 2**) [57].
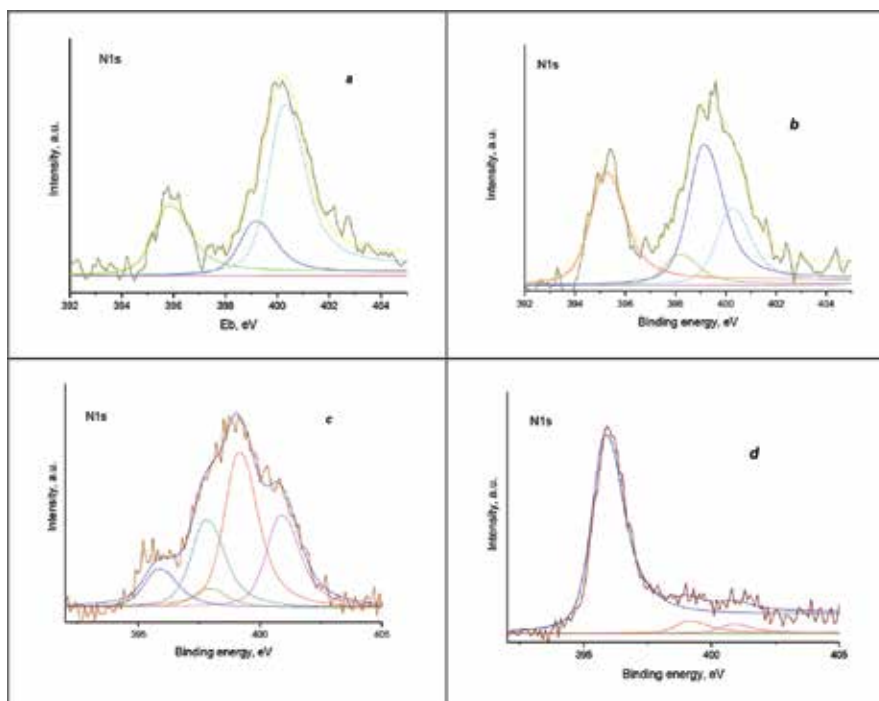
Figure 5. XPS spectra of N1s binding energy for samples **TiNO/10** (a) and **TiN/20** (b) adopted from [9] and **TiN5C1/100** (c) and **TiN5C1/3** (d). Adapted with permission from [56].

Replacing dinitrogen or the mixture of dinitrogen/oxygen by the mixture of dinitrogen/ methane leads to the change not only the line intensities but also some peaks position. Quite surprisingly, the intensity of N1s peak of N$_s$ is sharply raised and reached ca. 90% for **TiN5C1/3**. It points that no other nitrogen contained species are present in the lattice structure of titania for this materials. A new additional peak of Ti2p$_{3/2}$ region at lower BE (456.3 eV) is observed for **TiN5C1/3**. Similarly, the Ti2p$_{3/2}$ lines corresponded to 455.6 and 456.9 eV appeared with increasing nitridation temperature leading to the formation of TiN phase as proven by XRD [29]. Taking into account that the peak at 456.3 eV is assigned by the published literature to TiN phase [30], it could be suggested the deeper nitrogen doping into titania at the low pressure (N–Ti–N and the dative-bonded N atoms). Thus, the deposition atmosphere and pressure have strong influence on the efficiency of N$_s$ and N$_i$ atoms incorporation.

BE, eV	TiNO/10	TiN/20	TiN5C1/100	TiN5C1/3
	I, %			
N1s				
395.2	–	26.4	–	–
395.8	25.2	–	9.7	90.1
397.8	–	–	27.4	–
398.1	–	7.3	–	–
399.1	12.9	33.2	39.6	5.6
400.3	61.9	18.0	–	–
400.8	–	–	23.3	4.3
409.2	–	15.1	–	–
Ti2p$_{3/2}$				
456.3	–	–	–	15.3
457.5	2.6	16.8	24.4	20.3
458.1	–	–	60.6	48.1
458.3	62.9	67.9	–	–
458.8	34.5	15.3	15.0	16.3

Table 2. N1s and Ti2p$_{3/2}$ binding energy values and their relative intensity.

Comparing the bandgap energy values of *TiN/20* (2.6 eV), *TiNO/10* (2.8 eV), and *TiN5C1/100* (3.3 eV) with their intensity of N$_s$ peak 26.4, 25.2, and 9.7, respectively, the bandgap narrowing of anatase could result in the incorporation of substituted nitrogen.

Sample	UV, %	vis, %
TiC/5	15	3
TiO/20	24	3
TiNO/10	–	3
TiN/20	–	9
TiN5C1/100	25	9
TiN5C1/3	–	1

Table 3. Conversion percentage of dichromate ions after 120 min under UV and visible light.

The catalytic response under UV light exposure was observed for *TiC/5*, *TiO/20,* and *TiN5C1/100* samples (**Table 3**). *TiNO/10* and *TiN/20* films were completely inactive under UV light, while the activity of *TiN5C1/100* is comparable with pure TiO$_2$ (*TiO/20*). The low activity of former N-doped materials could be explained by the nitrogen-induced levels formation in

the banggap of TiO_2, acting as recombination centers for charge carriers under irradiation with UV light. *TiN/20* and *TiN5C1/100* exhibited an identical level of photocatalytic conversion under visible light, while the relative intensities of N_s (26.4 and 9.7 for TiN/20 and TiN5C1/100, respectively) and N_i (7.3 and 27.4 for TiN/20 and TiN5C1/100, respectively) are different for these samples. No photocatalytic activity in the presence of TiN5C1/3 is observed.

2.2. Nitrogen-doped ZrO_2/TiO_2 films

2.2.1. Low content of ZrO_2 in the target

Incorporation of transition metal oxides into titania improved the photocatalytic activity due to the mutual action of metal ions and anatase resulting in increased specific surface area, surface acidity, and changed photo-electrochemical properties. Coupling of two semiconductors is useful to achieve a more efficient separation of photogenerated electron–hole pair that led to the improvement of the photoactivity. It is found that the photocatalytic activity depends on the phase composition and crystalline size that modify the TiO_2 bandgap [11]. Zirconium incorporation into TiO_2 lattice by sol–gel synthesis was achieved with the formation of $Ti_{1-x}Zr_xO_2$ solid solution for the film with a Zr content up to 10 mol% as evidenced by XRD and XPS. It was demonstrated that the formation of Zr–O–Ti bonds has an influence on the thermal stability during sintering of the mesoporous structure of the films, surface texture, and optical properties as well as in the changes of number of surface active sites for nanocomposite films [10, 58].

Pulsed laser-deposited (2.5, 5, and 10%) ZrO_2/TiO_2 thin films were synthesized under various gas atmospheres (see Table 1). We inferred the characteristic E_{bg} values for pure titania and zirconia of 3.3 and 4.2 eV. All nonmetal-doped films showed more intensive absorption extending into the visible-light region comparing *xZrTiO/100*. A shift to the longer wavelength from lower to higher contents of ZrO_2 results in decrease of bandgap energy, as oppositely observed for the samples synthesized in O_2. The bandgap values of the films synthesized in a gas atmosphere with a higher ratio of N_2 to CH_4 (9:1) are lowered when increasing zirconia content.

For films synthesized at 3 Pa, the calculation of E_{bg} was impossible because of the strong absorption in the visible region (**Figure 6** inset) [56]. Similar broad absorption was reported for N-doped TiO_2 after the nitridation by ammonia at 650°C or above and explained by the metallic property of samples as indicated by the XRD and transmission electron microscopy (TEM) result [29].

The N1s line at 395.8 eV attributed to N_s is present for all nonmetal-doped samples. The XPS spectra of *2.5ZrTiN9C1/100* and *2.5ZrTiN5C1/100* films showed almost the same relative intensity of N_s lines as *TiN5C1/100* (**Figures 5c** and **7b**, **d**) and **Tables 2** and **4**). On the other hand, the increased intensity of N_s lines is fixed for the samples containing 5% ZrO_2, especially for the film synthesized at higher ratio of N_2 to CH_4 (*5ZrTiN9C1/100*). It shows that the higher the dinitrogen content in the gas mixture, the more substitutional nitrogen is incorporated in the semiconductive structure. Comparing the intensity of N1s line at 395.8 eV of all samples

synthesized at 100 Pa, it is evident that highest peak intensity (~43%) corresponds to the sample with the largest content (10%) of zirconia, while the lowest intensity at 397.8 eV is observed.

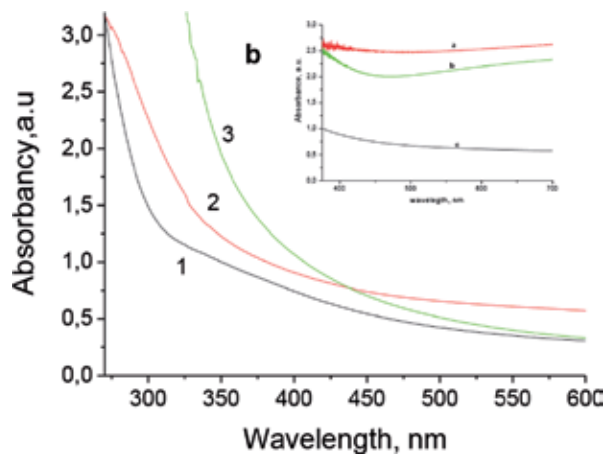**Figure 6.** Absorption spectra of *2.5ZrTiN5C1/100* (1), *5ZrTiN5C1/100* (2), and *10ZrTiN5C1/100* (3). Inset: samples *5ZrTiN5C1/3*—a, *5ZrTiN9C1/3*—b, *5ZrTiN5C1/100*—c. Reproduced with permission from [56].
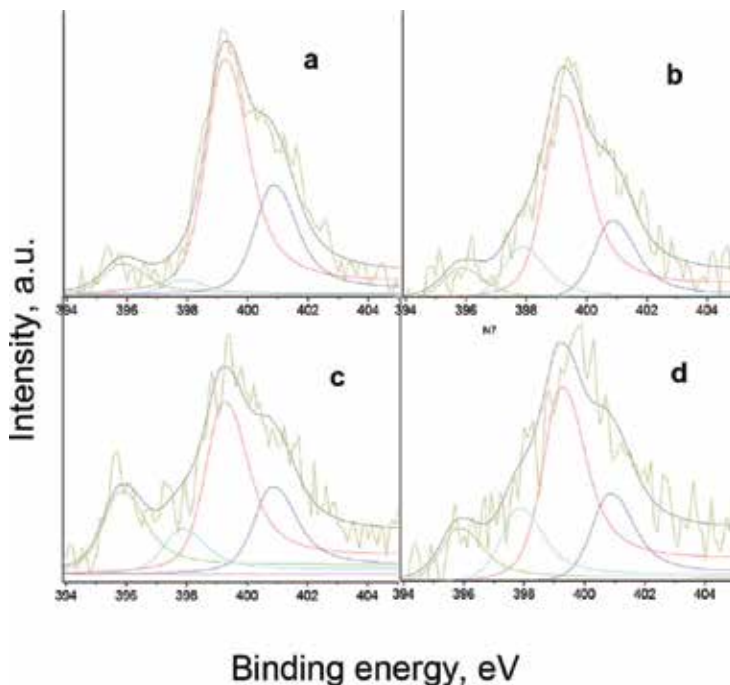
Figure 7. XPS spectra of N1s binding energy for *2.5ZrTiN9C1/100* (a), *2.5ZrTiN5C1/100* (b), *5ZrTiN9C1/100* (c), and *5ZrTiN5C1/100* (d) samples. Reproduced with permission from [56].

BE, eV	2.5ZrTiN9C1/100	2.5ZrTiN5C1/100	5ZrTiN9C1/100	5ZrTiN5C1/100
	I, %			
N1s				
395.8				
397.8	3.8	14.4	11.6	18.1
399.2	60.3	55.5	44.5	47.0
400.8	27.9	21.4	22.5	21.5
$Ti2p_{3/2}$				
457.5	3.2	7.2	11.2	5.1
458.3	68.3	57.4	72.9	63.5
458.8	28.5	35.4	15.9	31.4

Table 4. N1s and $Ti2p_{3/2}$ binding energy values and their relative intensity.

Analogous to *TiN5C1/3*, N_s peak for *10ZrTiN5C1/3* films contains the single high-intensity N1s line at 395.7 eV. No other deconvoluted peaks were found (**Figure 8**; **Table 5**). Thus, an incorporation of substitutional nitrogen ions without any other forms can be achieved by carrying the synthesis at 3 Pa pressure.
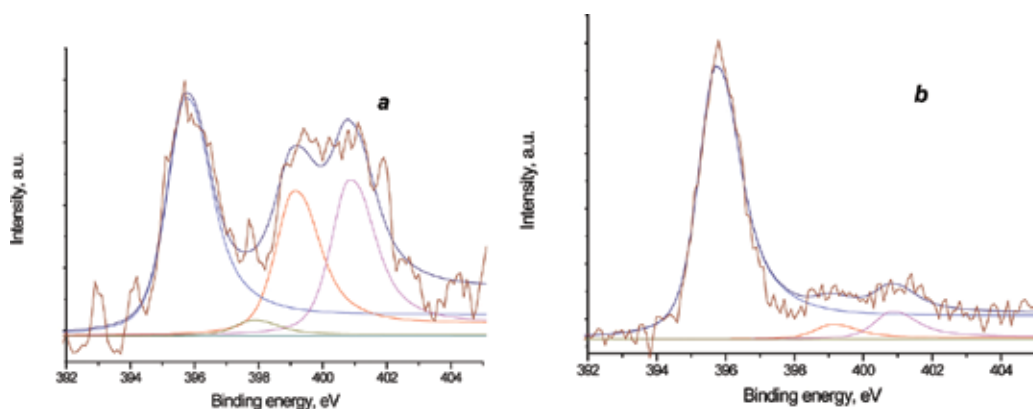
Figure 8. XPS spectra of N1s binding energy for *10ZrTiN5C1/100* (a) and *10ZrTiN5C1/3* samples (b).

Such effective nitrogen incorporation in oxide matrix can be the effect of an interaction between carbon (and/or hydrogen) and laser ablated oxygen atoms forming CO_2 during PLD that leads to the oxygen deficiency and the formation of nonstoichiometric $TiO_{2-x}N_x$ structure. This can be confirmed by the lower ratio (1.6) of $O_{Ti}1s/Ti2p$ for samples synthesized at 3 Pa in comparison with pristine TiO_2 where this ratio equals 2 [56].

BE, eV	10ZrTiN5C1/100	10ZrTiN5C1/3
	(a)	(b)
	I, %	
N1s		
395.7	43.2	86.8
397.8	2.8	–
399.1	26.2	4.6
400.8	27.9	8.7
Ti2p$_{3/2}$		
456.3	–	8.1
457.5	21.0	37.2
458.1	72.80	47.1
458.8	6.24	7.6

Table 5. Relative intensity of N1s and Ti2p$_{3/2}$ binding energy.

A significant intensity of peak at 457.5 eV assigned to the Ti–N bonds was observed for **10ZrTiN5C1/100** and **10ZrTiN5C1/3**, assuming also the presence of Ti^{3+} states. According to the literature [59], such titanium species have oxidation states between +3 and +4. Moreover, the appearance of additional Ti2p$_{3/2}$ peaks with lower BE similar to **TiN5C1/3** (Section 2.1) is assigned to the change of surrounding titanium, where more oxygen atoms are substituted by nitrogen. The Zr3$_{d5/2}$ line (E$_{bg}$ = 182.3 eV) was recorded for all zirconia-containing samples, meaning the formation of Zr^{4+} ions surrounded by O^{2-} ions [10]. No signal pointing on the formation of Ti–O–Zr bonds was obtained (not shown here).

Additionally, the ratio of N1s line at 395.8 eV to Ti2p$_{3/2}$ line at 457.5 eV corresponds as 1:2 and 2:1 for **TiN5C1/100** and **10ZrTiN5C1/100**, respectively. It is supposed that the distortion of Ti^{4+}O$_2$ lattice with the advent of Ti^{3+} states occurs due to larger size of zirconium ions (R$_{Zr4+}$ = 0.720 Å vs. R$_{Ti4+}$ = 0.650 Å). The relatively high stability of Ti^{3+} states of the tested samples is associated to the presence of Zr^{4+} ions. Note that the non-equilibrium character of the PLD process is favorable to the generation of strains in the lattice. XPS data pointed to the correlation between zirconium contents and ratio of number of nitrogen atoms linked in Ti–N bonds to the number of Ti^{3+} states as well as the relative contents of N1s at 395.8 eV. This can be indicative for the formation of Ti–N fragments in the coordination sphere of Ti^{3+} ions. In other words, the N$_s$ states (395.8 eV) responsible for photocatalytic activity of doped samples could be also connected with Ti^{3+} states of Ti^{4+}O$_2$ lattice.

Certainly, the non-doped ZrO$_2$/TiO$_2$ films (columns 7, 8, and 9 in **Figure 9**) exhibit much lower activity under both UV and visible light compared to nitrogen-doped synthesized at 100 Pa. The highest yield under both UV (51% reduced ions) and visible light (14%) was demonstrated by **10ZrTiN5C1/100**. The activity of this film is twice higher than **TiO/20** and **TiN5C1/100** under UV light and 1.5 times higher comparing with **TiN/20** and **TiN5C1/100** under visible light. We

have shown that the conversion percentage under UV light is strongly correlated with the contribution of N1s at 395.8 eV which in turn depends on the zirconia content (Tables 4 and 5). Hence, the photocatalytic activity strongly depends on the efficiency of substitutional nitrogen incorporation inside titania matrix that is, in turn, affected by zirconia content and the gas ratio used during PLD synthesis.
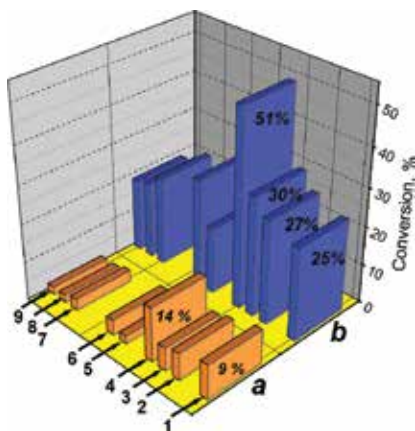
Figure 9. Conversion of dichromate ions after 120 min under visible (a) and UV (b) light: 1—*TiN5C1/100*; 2—*2.5ZrTiN5C1/100*; 3—*5ZrTiN5C1/100*; 4—*10ZrTiN5C1/100*; 5—*2.5ZrTiN9C1/100*; 6—*5ZrTiN9C1/100*; 7—*2.5ZrTi/100*; 8—*5ZrTi/100*; 9—*10ZrTi/100*.

It must be emphasized that all films obtained at lowest pressure are completely inactive under both UV and visible-light irradiation (not shown here). In order to understand in depth this
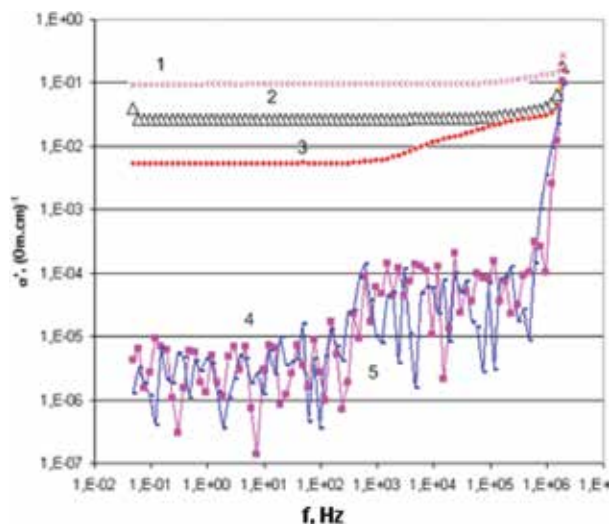
Figure 10. Electrical conductivity of *10ZrTiN5C1/X*: 3 (1), 6 (2), 10 (3), 50 (4), and 100 Pa (5).

phenomenon, the electrical conductivity (**Figure 10**) measurements were performed. The samples obtained in the range of (3–10) Pa are black colored (**Figure 11**) and exhibit the electrical conductivity pointing on the appearance of oxygen vacancies, which results in metallic character of these materials. The formation of nonstoichiometric TiO$_{2-x}$N$_x$ containing in excess of Ti–N bonds exhibiting a low semiconductive behavior is concluded.

Moreover, no electrical conductivity (**Figure 10**, curves 4 and 5) was observed for the samples obtained at 50 and 100 Pa providing their semiconductive behavior. This indicates that anatase in conjunction with a certain numbers of Ti–N bonds is beneficial on the effective photocatalytic transformations.
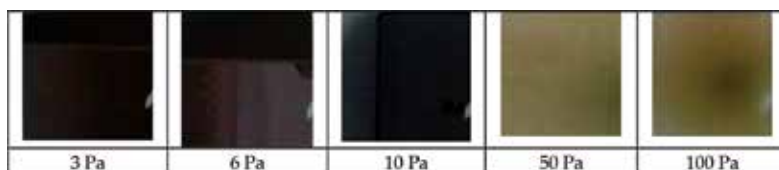
Figure 11. Images of *10ZrTiN5C1/X* obtained under different gas pressures.

As seen from **Figure 11**, the level of nitrogen incorporation strongly affects the optical properties of the films which turned from black to dark yellow color.

2.2.2. High weight content of ZrO$_2$ in the sample

The next series of the films used in our investigation was based on the mixed titania–zirconia films with the component ratio 50:50 wt%. The synthesis conditions are detailed in **Table 1**.
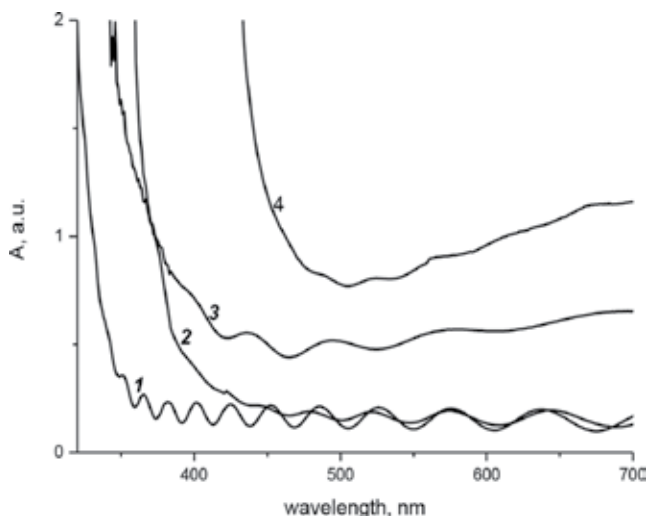
Figure 12. Absorption spectra of *50ZrTiO/10* (1), *50ZrTiN1O1/5* (2), *50ZrTiN5C1/10* (3), and *50ZrTiN/10* (4) films.

TiO$_2$/ZrO$_2$ films prepared in ambient N$_2$ and/or CH$_4$ atmosphere had different absorption spectra. The shift of the absorption band edge to the red region of the spectra with the increase of N$_2$ content in the gas mixtures was observed (**Figure 12**). The influence of the doping agent nature and its content was observed in the variation of bandgap energy values (**Table 1**).

Similar to the bandgap values of low zirconia content films (Section 2.2.1), E_{bg} values correlate with dinitrogen content in the gas mixture and applied pressure. For non-doped ZrO$_2$/TiO$_2$ (*50ZrTiO/10*), the bandgap energy value is higher (3.7 eV) than for anatase, pointing on the presence of wide bandgap semiconductor as zirconia. In particular, the E_{bg} values are decreased with the increase of dinitrogen content in a gas mixture, reaching 3.0 eV for *50ZrTiN/ 10*. On the other hand, for the doped composite samples *50ZrTiN10C1/3* and *50ZrTiC/5*, the calculation of E_{bg} was impossible because of the strong absorption in the visible region.

Unexpectedly, no crystallization of titania but incipient crystallization corresponding to the (101) line of ZrO$_2$ were confirmed by XRD investigation (not shown here) [60]. It can be explained by the existence of undetectable very small TiO$_2$ particles or by the excess of ZrO$_2$ in the film matrix inhibiting the titania crystallization.
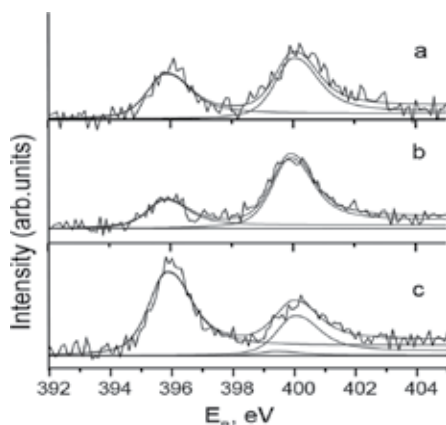
Figure 13. XPS spectra of N1s energy for the samples *50ZrTiN/10* (a), *50ZrTiN5C1/10* (b), *50ZrTiN10C1/3* (c).

The sample synthesized at the high content of N$_2$ in the gas mixture (*50ZrTiN10C1/3*) contains the most prominent peaks of Ti2p$_{3/2}$ at 457.5 eV and N1s at 395.8 eV (**Figure 13**; **Table 6**), indicating the effective N_s incorporation at low pressure similar to low zirconia content films (Section 2.2.1). Existence of other nitrogen species (400 eV) could be explained by high content of zirconia that caused the distortion of the crystalline lattice and easier incorporation of other N species. Almost equal intensity of the peaks at 395.8 and 400.0 eV was observed for sample deposited in pure N$_2$. The Ti2p$_{3/2}$ signal at 457.5 eV was weaker for sample obtained in pure N$_2$ than in 5:1 N$_2$:CH$_4$ at 10 Pa. The binding energy of Zr3d$_{5/2}$ peak for all samples (182.3 eV) corresponded to Zr^{4+} species in ZrO$_2$.

BE, eV	50ZrTiN/10 (a)	50ZrTiC/5 (b)	50ZrTiN5C1/10 (c)	50ZrTiN10C1/3 (d)
	I,%			
N1s				
395.8	42.5	–	27.6	67.6
400.0	57.5	100	68.5	32.4
Ti2p$_{3/2}$				
457.5	7.5	–	8.1	23.5
458.3	36.9	9.0	31.7	27.8
	55.6	91.0	60.2	

Table 6. Relative intensity of N1s and Ti2p$_{3/2}$ binding energy from Figure 13.

All the films were inert under UV and visible-light irradiation showing an activity similar to that of blank sample. The photocatalytic performance of *50ZrTiN10C1/3* film was comparable to TiO$_2$ one under UV light. The highest activity for this series of films was reached for the structure with the largest number of N$_s$ [60]. As clearly seen, no favorable effect of half doping level of ZrO$_2$ in titania was recognized as a result of the low crystallization degree of anatase, while the synthesis conditions for the effective nitrogen substitution were chosen.

3. Conclusions

In summary, an appropriate selection of gas mixture, pressure, and temperature during PLD synthesis is identified for the optimum photocatalytic activity of semiconductive materials. The highest photocatalytic conversion yields in the dichromate ions reduction are obtained for nitrogen-doped 10% ZrO$_2$/TiO$_2$ synthesized in N$_2$:CH$_4$ = 5:1 at 100 Pa and at 450°C under both UV and visible light. This is the result of effective nitrogen atom substitution into titania lattice as confirmed by N1s XPS line at 395.8 eV. When the films were synthesized at low pressure of 3 Pa, the only Ns peak with the binding energy 395.8 eV was observed and photocatalytically inactive nonstoichiometric TiO$_{2-x}$N$_x$ structures were deposited. The absence of semiconductive properties of the films obtained at the low pressures is a direct evidence of no anatase formation and, respectively, their photocatalytic performance remained at the level of blank experiments. It can be suggested that carbon and hydrogen radicals/atoms forming as a result of laser action react with oxygen species causing the subsequent oxygen substitution by nitrogen atoms. This mechanism is supported by the XPS evidence, according to which the intensity of N–Ti peak at 395.9 eV is lower for the samples synthesized in a pure N$_2$ atmosphere. Thus, the effective incorporation of substitutional nitrogen in oxide matrix can be caused by a direct interaction of carbon or hydrogen atom with oxygen species during PLD resulting in an oxygen deficient lattice, taking into account that pure methane used in PLD prevents anatase formation providing oxygen atoms deficiency. At high pressure, a number of collisions between C or H species and ablated oxygen atoms are less probable owing to the screening effect of other atoms/species (**Figure 14**a). When pressure is decreased, the deposition rate is enhanced in

addition to much higher probability for carbon/oxygen and hydrogen/oxygen interactions (**Figure 14**b). This can result in the higher efficiency of Ti–N as compared with Ti–O fragments formation.
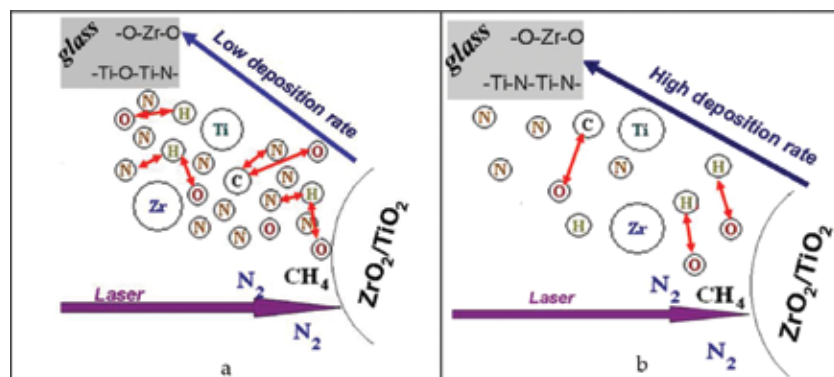
Figure 14. Schematic representation of pulse laser deposition in a mixture of N_2/CH_4 at 100 Pa (a) and 3 Pa (b).

As seen from **Figure 15**, the percentage of reduced dichromate ions under UV light is correlated with the contributions of N1s at 395.8 eV which is in turn dependent on the zirconia content. The ratio of line intensities of N1s at 395.8 eV to $Ti2p_{3/2}$ at 457.5 eV is pointing to the large number of O–Ti^{3+}–N bonds with the increase of ZrO_2 contents. It is obvious that photocatalytic activity under UV light strongly depends on the efficiency of substitutional nitrogen incorporation inside titania matrix. The high ZrO_2 content (50%) induces the deceleration of anatase crystallization rate leading to the activity decrease, while a much lower zirconia amount (2.5 and 5%) is still not enough to stimulate an appropriate quantity of substituted nitrogen embedded in titania matrix. The correlation between the zirconia content and the efficiency of substitutional N incorporation is established. The distortion of $Ti^{4+}O_2$ lattice with the advent
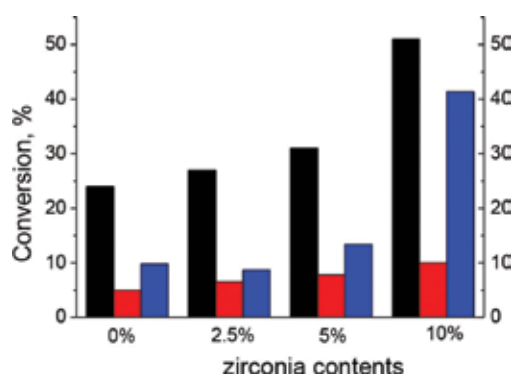
Figure 15. Influence of zirconia contents in *(xZr)TiN5C1/100* films on the photocatalytic conversion under UV (black column), ratio of N1s at 395.8 eV to Ti2p at 457.5 eV (red column) and N1s at 395.8 eV to total N1s (blue column). Reproduced with permission from [56].

of Ti^{3+} states occurred due to the larger radius of zirconium ions (R$_{Zr4+}$ = 0.720 Å vs. R$_{Ti4+}$ = 0.650 Å). The relative high stability of Ti^{3+} states is assigned to the presence of Zr^{4+} ions.
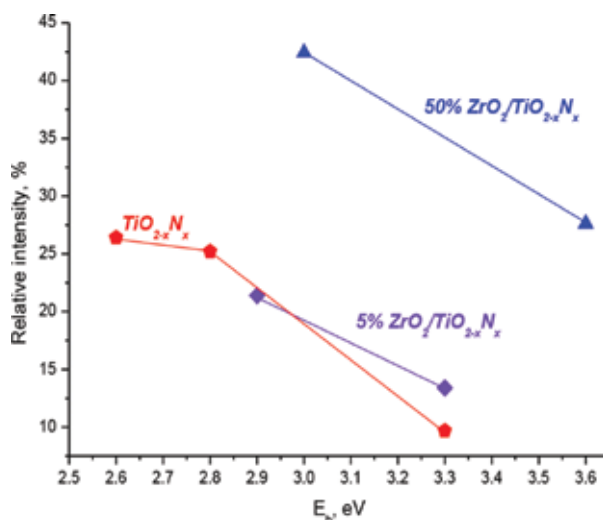
Figure 16. Dependence of bandgap energy of the semiconductive materials with the relative intensity of N1s XPS signal at 395.2–395.8 eV.

In general, the low photocatalytic efficiency is explained by the limited photo-excitation of electrons in the intragap localized states, the very low mobility of photogenerated holes [2], and the high recombination rate due to the creation of oxygen vacancies by doping [61]. Hence, the photoreactivity of doped TiO$_2$ appeared to be a complex function of the doping agent concentration, the energy level of doping agent within the TiO$_2$ lattice, their d electronic configurations, the distribution of doping agent, the electron donor concentrations, and light intensity.

The debates concerning the preferred N substitutional or interstitial sites which induce the highest photocatalytic action is still alive in the literature [62–64]. Our investigation suggests that the substitutional nitrogen (Ti–N) that belongs to XPS lines at 395.2–395.8 eV is basically responsible for the observed photoactivity. Additionally, it can be proved by the next two observations. (i) The peak at 397.8 eV has the negligible relative intensity (2.8%) for most active **10ZrTiN5C1/100,** and (ii) the peaks in the range of 398–401 eV are observed for the other samples with low reactivity. We also underline that N$_s$ species with 395.2–395.8 eV binding energy are responsible for bandgap narrowing or formation of intragap localized states of the doping agent within bandgap (**Fig. 16**). It is pointed that the bandgap energy values are sharply declined when the relative intensity of this XPS peaks is increased, while no dependence between 397.8 or 398–401 eV peaks and E$_{bg}$ is observed. PLD synthesis of TiO$_2$ films in N$_2$/CH$_4$ atmosphere not only leads to nitrogen incorporation but also to the formation of defects including oxygen vacancies and Ti^{3+} states which are all contributing to light absorption.

Acknowledgements

Author details

Oksana Linnik[1], Nataliia Chorna[1], Nataliia Smirnova[1], Anna Eremenko[1], Oleksandr Korduban[2], Nicolaie Stefan[3], Carmen Ristoscu[3], Gabriel Socol[3], Marimona Miroiu[3] and Ion N. Mihailescu[3*]

*Address all correspondence to: ion.mihailescu@inflpr.ro

1 Chuiko Institute of Surface Chemistry, National Academy of Science of Ukraine, Kyiv, Ukraine

2 Kurdyumov Institute of Metallophysics, National Academy of Sciences of Ukraine, Kyiv, Ukraine

3 National Institute for Lasers, Plasma and Radiation Physics, Magurele, Ilfov, Romania

References

[1] Fujishima A., Rao TN, Tryk DA., Titanium dioxide photocatalysis. *J. Photochem. Photobiol. C: Photochem. Rev*. 2000; 1(1): 1–21.

[2] Hashimoto K., Irie H., Fujishima A., TiO_2 photocatalysis: a historical overview and future prospects. *Jpn. J. Appl. Phys*. 2005; 44: 8269–8285.

[3] Thompson TL, Yates JTJr, Surface science studies of the photoactivation of TiO_2 new photochemical processes. *Chem. Rev*. 2006; 106: 4428–4453.

[4] Fujishima A., Honda K., Electrochemical photolysis of water at a semiconductor electrode. *Nature*. 1972; 238(5358): 37–38.

[5] Frank SN, Bard AJ, Heterogeneous photocatalytic oxidation of cyanide ion in aqueous solutions at titanium dioxide powder. *J. Am. Chem. Soc*. 1977; 99(1): 303–304.

[6] Wang R., Hashimoto K., Fujishima A., Chikuni M., Kojima E., Kitamura A., Shimohi-goshi M., Watanabe T., Light-induced amphiphilic surfaces. *Nature*. 1997; 388: 431–432.

[7]   O'Regan B., Gratzel M., Low-cost, high-efficiency solar cell based on dye-sensitized colloidal TiO$_2$ films. *Nature* 1991; 353: 737–739.

[8]   Fujishima A., Zhang X., Tryk D.A., TiO$_2$ photocatalysis and related surface phenomena. *Surf. Sci. Rep*. 2008; 63 (12): 515–582.

[9]   Sakthivel S., Kisch H., Daylight photocatalysis by carbon-modified titanium dioxide. *Angew. Chem. Int. Ed*. 2003; 42 (40): 4908–4911.

[10] Gnatyuk Y., Smirnova N., Eremenko A., Ilyinl V., Design and photocatalytic activity of mesoporous TiO$_2$/Zr O$_2$ thin films, *Adsorp. Sci. Technol*. 2005; 23(6); 497–408.

[11] Smirnova N., Gnatyuk Y., Vityuk N., Linnik O., Eremenko A., Vorobets V., Kolbasov G., Nanosized TiO$_2$-based mixed oxide films: sol–gel synthesis, structure, electrochemical characteristics and photocatalytic activity. *Int. J. Mater. Eng*. 2013; 3(6): 124–135.

[12] Smirnova N., Vorobets V., Linnik O., Manuilov E., Kolbasov G., Photoelectrochemical and photocatalytic properties of mesoporous TiO$_2$ films modified with silver and gold nanoparticles. *Surf. Interface. Anal*. 2010; 42: 1205–1208.

[13] Linnik O., Smirnova N., Korduban O., Eremenko A., Gold nanoparticles into Ti$_{1-x}$Zn$_x$O$_2$ films: synthesis, structure and application. *Mater. Chem. Phys*. 2013; 142 (1): 318–324.

[14] Linnik O., Kisch H., On the mechanism of nitrogen photofixation at nanostructured iron titanate films. *Photochem. Photobiol. Sci*. 2006; 5: 938–942.

[15] Linnik O., Kisch H., Dinitrogen photofixation at ruthenium-modified titania films. *Mendeleev Commun*. 2008; 18(1): 10–11.

[16] Shestopal N., Linnik O., Smirnova N., Influence of metal and non-metal ions doping on the structural and photocatalytic properties of titania films. *Chem. Phys. Technol. Surf*. 2015; 6(2): 203–210.

[17] Sato S., Photocatalytic activity of NO$_x$-doped TiO$_2$ in the visible light region, *Chem. Phys. Lett*. 1986; 123: 126–128.

[18] Asahi R., Morikawa T., Ohwaki T., Aoki K., Taga Y., Visible-light photocatalysis in nitrogen-doped titanium dioxide. *Science*. 2001; 293: 269–271.

[19] Abadias G., Paumier F., Eyidi D., Guerin P., Girardeau T., Structure and properties of nitrogen-doped titanium dioxide thin films produced by reactive magnetron sputtering. *Surf. Interface. Anal*. 2010; 42: 970–973.

[20] Nakano Y., Morikawa T., Ohwaki T., Yaga Y., Deep-level optical spectroscopy investigation of N-doped TiO$_2$ films. *Appl. Phys. Lett*. 2005; 86: 132104.

[21] Li Jinlong, Xinxin M., Mingren S., Li X., Zhenlun S., Fabrication of nitrogen-doped mesoporous TiO$_2$ layer with higher visible photocatalytic activity by plasma-based ion implantation. *Thin. Solid. Films*. 2010; 519 (1): 101–105.

[22] Pore V., Heikkila M., Ritala M., Leskela M., Arev S., Atomic layer deposition of TiO$_{2-x}$N$_x$ thin films for photocatalytic applications. *J. Photochem. Photobiol. A Chem.* 2006; 177 (1); 68–75.

[23] Zhao L., Jiang Q., Lian J., Visible-light photocatalytic activity of nitrogen-doped TiO$_2$ thin film prepared by pulsed laser deposition. *Appl. Surf. Sci.* 2008; 254 (15): 4620–4625.

[24] Kafizas A., Crick C., Parkin IP, The combinatorial atmospheric pressure chemical vapour deposition (c APCVD) of a gradating substitutional/interstitial N-doped anatase TiO$_2$ thin-film; UVA and visible light photocatalytic activities. *J. Photochem. Photobiol. A: Chem.* 2010; 216 (2–3): 156–166.

[25] Irie H., Watanabe Y., Hashimoto K., Nitrogen-concentration dependence on photocatalytic activity of TiO$_{2-x}$N$_x$ powders. *J. Phys. Chem. B* 2003; 107(23): 5483–5486.

[26] Serpone N., Is the band gap of pristine Tio$_2$ narrowed by anion- and cation-doping of titanium dioxide in second-generation photocatalysts? *J. Phys. Chem. B* 2006; 110 (48): 24287–24293.

[27] Chen X., Wang X., Hou Y., Huang J., Wu L., Fu X., The effect of postnitridation annealing on the surface property and photocatalytic performance of N-doped Ti O$_2$ under visible light irradiation. *J. Catal.* 2008; 255 (1): 59–67.

[28] Mitoraj D., Kisch H., The nature of nitrogen-modified titanium dioxide photocatalysts active in visible light. *Angew. Chem. Int. Ed.* 2008; 47(51): 9975–9978.

[29] Zhang Z., Wang X., Long J., Gu Q., Ding Z., Fu X., Nitrogen-doped titanium dioxide visible light photocatalyst: spectroscopic identification of photoactive centers. *J. Catal.* 2010; 276 (2): 201–214.

[30] Saha NC, Tompkins HG, Titanium nitride oxidation chemistry: an x-ray photoelectron spectroscopy study. *J. Appl. Phys.* 1992; 72: 3072–3079.

[31] Nosaka Y., Matsushita M., Nishino J., Nosaka AY, Nitrogen-doped titanium dioxide photocatalysts for visible response prepared by using organic compounds. *Sci. Technol. Adv. Mater.* 2005; 6(2): 143–148.

[32] Cong Y., Zhang J., Chen F., Anpo M., Synthesis and characterization of nitrogen-doped TiO$_2$ nanophotocatalyst with high visible light activity. *J. Phys. Chem. C* 2007; 111 (19): 6976–6982.

[33] Beranek R., Kisch H., Tuning the optical and photoelectrochemical properties of surface-modified TiO$_2$. *Photochem. Photobiol. Sci.* 2008; 7: 40–48.

[34] Mitoraj D., Kisch H., On the mechanism of urea-induced titania modification. *Chem. Eur. J.* 2010; 16: 261–269.

[35] Napoli F., Chiesa M., Livraghi S., Giamello E., Agnoli S., Granozzi G., Pacchioni G., Di Valentin C., The nitrogen photoactive centre in N-doped titanium dioxide formed via

interaction of N atoms with the solid. Nature and energy level of the species. *Chem. Phys. Lett.* 2009; 477 (1–3): 135–138.

[36] Livraghi S., Giamello MRCE, Magnacca G., Paganini MC, Cappelletti G., Bianchi CL, Nitrogen-doped titanium dioxide active in photocatalytic reactions with visible light: a multi-technique characterization of differently prepared materials. *J. Phys. Chem. C* 2008; 112 (44): 17244–17252.

[37] György E., Pérez del Pino A., Serra P., Morenza JL, Depth profiling characterisation of the surface layer obtained by pulsed Nd:YAG laser irradiation of titanium in nitrogen. *Surf. Coat. Technol.* 2003; 173 (2–3): 265–270.

[38] Chen X., Burda C., Photoelectron spectroscopic investigation of nitrogen-doped titania nanoparticles. *J. Phys. Chem. B* 2004; 108 (40): 15446–15449.

[39] Diwald O., Thompson TL, Zubkov T., Goralski EGO, Walck SD, Yates JT, Photochemical activity of nitrogen-doped rutile TiO$_2$(110) in visible light. *J. Phys. Chem. B* 2004; 108 (19): 6004–6008.

[40] Reyes-Garcia EA, Sun Y., Reyes-Gil K., Raftery D., 15N solid state NMR and EPR characterization of N-doped TiO$_2$ photocatalysts. *J. Phys. Chem. C* 2007; 111 (6): 2738–2748.

[41] Beranek R., Kisch H., Surface-modified anodic TiO$_2$ films for visible light photocurrent response. *Electrochem. Commun.* 2007; 9 (4): 761–766.

[42] Nakamura R., Tanaka T., Nakato Y., Mechanism for visible light responses in anodic photocurrents at N-doped TiO$_2$ film electrodes. *J. Phys. Chem. B* 2004; 108 (30): 10617–10620.

[43] Mitoraj D., Berranek R., Kisch H., Mechanism of aerobic visible light formic acid oxidation catalyzed by poly(tri-s-triazine) modified titania. *Photochem. Photobiol. Sci.* 2010; 9: 31–38.

[44] Melhem H., Simon P., Wang J., Di Bin C., Ratier B., Leconte Y., Herlin-Boime N., Makowska-Janusik M., Kassiba A., BoucléJ., Direct photocurrent generation from nitrogen doped TiO$_2$ electrodes in solid-state dye-sensitized solar cells: towards optically-active metal oxides for PV applications. *Solar Energy Mater. Solar Cells*. 2012; 117: 624–631.

[45] Di Valentin C., Finazzi E., Pacchioni G., Selloni A., Livraghi S., Paganini MC, Giamello E., N-doped TiO$_2$: theory and experiment. *Chem. Phys.* 2007; 339 (1–3): 44–56.

[46] Mihailescu IN, Ristoscu C., Bigi A., Mayer I., Advanced biomimetic implants based on nanostructured coatings synthesized by pulsed laser technologies, Chapter 10. In: *Laser-Surface Interactions for New Materials Production Tailoring Structure and Properties*, Series: Springer Series in Materials Science, Vol. 130, Miotello A.; Ossi P.M. (Eds.), 2010, pp. 235–260.

[47] Schneider CW, Lippert T., Laser ablation and thin film deposition, Chapter 5. In: *Laser Processing of Materials Fundamentals, Applications and Developments*, Schaaf P. (Ed.), Springer Series in Materials Science 139, Berlin, 2010, pp. 89–112.

[48] Bauerle D., *Laser Processing and Chemistry*, Springer-Verlag, Berlin Heidelberg, 3rd ed., 2000.

[49] Mihailescu IN, Gyorgy E., Pulsed laser deposition: an overview. In: *International Trends in Optics and Photonics*, Asakura T. (Ed.), Heidelberg, Springer, 1999, pp. 201–2014.

[50] Eason R. (Ed.), *Pulsed Laser Deposition of Thin Films: Applications-led Growth of Functional Materials*, Wiley & Sons, 2007.

[51] Craciun D., Bourne G., Zhang J., Siebein K., Socol G., Dorcioman G., Craciun V. Thin and hard ZrC/TiN multilayers grown by pulsed laser deposition. *Surf. Coat. Technol.*, 2011; 205 (23–24): 5493–549.

[52] Ristoscu C., Mihailescu IN, Biomimetic coatings by pulsed laser deposition, Chapter 7. In: *Laser Technology in Biomimetics*, Schmidt V., Belegratis M.R. (Eds.), 2013, Basics and Applications, Series: Biological and Medical Physics, Biomedical Engineering, Springer-Verlag, Heidelberg, New York, Dordrecht, London, pp. 163–191.

[53] Socol G., Gnatyuk Y., Stefan N., Smirnova N., Sutan C., Malinovski V., Stanculescu A., Korduban O., Mihailescu I.N., Photocatalytic activity of pulsed laser deposited TiO_2 thin films in N_2, O_2 and CH_4. *Thin Solid Films* 2010; 518: 4648–4653.

[54] Oh S., Moon K.-S., Moon J.-H., Bae Ji-M., Jin S., Visible light irradiation-mediated drug elution activity of nitrogen-doped Ti O_2 nanotubes. *J. Nanomater.* 2013; 2013: Article ID 802318.

[55] Wang H., Hu Y., The photocatalytic property of nitrogen-doped TiO_2 nanoball film. *Int. J. Photoenergy* 2013; 2013: Article ID 179427.

[56] Linnik O., Shestopal N., Smirnova N., Eremenko A., Korduban O., Kandyba V., Kryshchuk T., Socol G., Stefan N., Popescu-Pelin G., Ristoscu C., Mihailescu IN, Correlation between electronic structure and photocatalytic properties of non-metal doped TiO_2/ZrO_2 thin films obtained by pulsed laser deposition method. *Vacuum.* 2015; 115: 166–171.

[57] Nakano Y., Morikawa T., Ohwaki T., Taga Y., Origin of visible-light sensitivity in N-doped TiO_2 films. *Chem. Phys.* 2007; 339: 20–26.

[58] Gnatuk Y., Smirnova N., Korduban O., Eremenko A., Effect of zirconium incorporation on the stabilization of TiO_2 mesoporous structure. *Surf. Interface Anal.* 2010; 42: 1276–1280.

[59] Chen H., Nambu A., Wen W., Graciani J., Zhong Z., Hanson JC, Fujita E., Rodriguez JA, Reaction of NH3 with titania: N-doping of the oxide and TiN formation. *J. Phys. Chem. C* 2007; 111 (3): 1366–1372.

[60] Linnik O., Petrik I., Smirnova N., Kandyba V., Korduban O., Eremenko A., Socol G., Stefan N., Ristoscu C., Mihailescu I. N., Sutan C., Malinovski V., Djokic V., Janakovic D., TiO$_2$/ZrO$_2$ thin films synthesized by PLD in low pressure N-, C- and/or O-containing gases: structural, optical and photocatalytic properties. *Digest J. Nanomater. Biostruct.* 2012; 7(3): 1343–1352.

[61] Katoh R., Furube A., Yamanaka K.-i, Morikawa T., Charge separation and trapping in N-doped TiO$_2$ photocatalysts: a time-resolved microwave conductivity study. *J. Phys. Chem. Lett.* 2010; 1 (22): 3261–3265.

[62] Dunnill CWH, Aiken ZA, Pratten J., Wilson M., Morgan DJ, Parkin IP, Enhanced photocatalytic activity under visible light in N-doped TiO$_2$ thin films produced by APCVD preparations using t-butylamine as a nitrogen source and their potential for antibacterial films. *J. Photochem. Photobiol. A: Chem.* 2009; 207 (2–3): 244–253.

[63] Oropeza FE, Harmer J., Egdell RG, Palgrave RG, A critical evaluation of the mode of incorporation of nitrogen in doped anatase photocatalysts. *Phys. Chem. Chem. Phys.* 2010; 12: 960–969.

[64] Braun A., Akurati KK, Fortunato G., Reifler FA, Ritter A., Harvey AS, Vital A., Graule T., Nitrogen doping of TiO$_2$ photocatalyst forms a second eg state in the oxygen 1s NEXAFS pre-edge. *J. Phys. Chem. C* 2010; 114 (1): 516–519.

Enhanced Visible Light Photocatalytic Performance by Nanostructured Semiconductors with Glancing Angle Deposition Method

Shuang Shuang, Zheng Xie and Zhengjun Zhang

Additional information is available at the end of the chapter

Abstract

The glancing angle deposition (GLAD) method in physical vapor deposition is proved to be a versatile tool to fabricate nanostructured TiO_2 as the photocatalyst on specific substrates to form self-standing structures, which are much easier to be recycled. And novel designs of doping, decorating photocatalytic active substance, are brought in to make TiO_2 respond to visible light. In this chapter, we introduce our previous works such as TiO_2 nanorods with CdS quantum dots, noble metallic nanoparticles, coating TiO_2 via atomic layer deposition (ALD), and so on.

Keywords: Nanostructured, TiO_2, GLAD, visible light, degradation

1. Introduction

As we all know, population growth and rapid industrial development lead to global energy and environment crisis. However, sufficient utilization of solar energy could alleviate these issues, as the solar energy irradiating the surface of the Earth exceeds the current global human energy consumption by nearly four orders of magnitude. Thus, there has been keen interests in developing photocatalysts like semiconductors that can produce chemical energy from light. Semiconductor photocatalysis, which is regarded as a good candidate to convert renewable photon energy into chemical energy and decompose organic pollutants, has drawn much attention of researchers.

Since the first report of photocatalytic splitting over water taking use of TiO_2 photoanode by Fujisima and Honda in 1972 [1], TiO_2 has been widely studied and considered as one of the

superior candidates to settle the environmental concerns owing to its chemical inertness, low cost, photostability, nontoxicity and strong photocatalytic activity [2]. However, the industrial applications of it are also limited due to its large band gap (*ca.* 3.2 eV and 3.0 eV for anatase and rutile, respectively), which makes it to become active only under ultraviolet (UV) light (accounting for ~5% of the solar energy) [3]. And many efforts are made to enhance the photocatalytic performance of TiO_2 under visible lights range. So far, there are three main strategies to improve the photocatalytic efficiency and visible light utilization of TiO_2: (1) coupling with different semiconductors (e.g., TiO_2/Cu_2O [4] and TiO_2/WO_3 [5]), (2) combining with noble metals (e.g., Au/TiO_2 [6], Pt/TiO_2 [7] and Ag/TiO_2 [8, 9]), and (3) introducing dopants (e.g., oxygen defects [10], and sulfur [11], nitrogen [12]). Here, we will introduce these three methods in detail.

From previous studies, there are many methods to fabricate nanostructured materials. Among them, the glancing angle deposition (GLAD) technique is regarded as one simple but highly repeatable physical vapor deposition technology to prepare 1-dimensional and 2-dimensional nanomaterials, such as slanted posts, spirals, zigzag columns, nanopillars, etc. [13]. This method takes advantage of atomic shadowing and adatom diffusion to grow nanostructure materials. And these specific shaped nanostructures can be applied in many areas such as catalyst, optical element and magnetic storage media, etc. For instance, HfO_2 nanocolumn arrays can be applied as antireflection coating [14]. And altering GLAD fabrication conditions could also adjust relating the property parameter. Ag nanorod arrays (NRAs) could serve as surface-enhanced Raman scattering substrates. The limit Rhodamine 6G concentration of 10^{-14} mol/L can even be perceived using such kind of array structure. [15]

2. Doping

Traditional strategies in previous researches to broaden the solar spectral response of TiO_2 include surface sensitization by organic dyes and doping with transition metals. However, the commonly used dyes are in high price and the long-term stability of many dyes is also uncertain. Doping with transition metals makes the absorption shift to the visible region, even including all the solar spectra. While the metal ions could form recombination centers in the TiO_2 [16], which will reduce the efficiency of its photocatalytic activity.

Doping non-metal ion into TiO_2 may be a promising way to avoid the deterioration of the thermal stability of oxide lattice [17]. Many researchers reported doping experiments with various substances, such as nitrogen [18], sulfur [19] and fluoride [20] elements. Asahi et al. [21] reported that the band gap narrowed by N-doping, which improves the photocatalytic activity of TiO_2 under visible light irradiation. Since this work, such type of doping has been considered as one of the most effective approaches to shift the optical response of TiO_2 from the UV to the visible spectral range. There are mainly two major ways to prepare the N-doped TiO_2. One of them is using incorporation of N into TiO_2 lattice by ion-implantation technique, or other techniques, such as magnetron sputtering, hydrothermal method, etc. Another way, described in this work, relies upon the oxidation process of TiN_x like powders and films prepared by these techniques.

2.1. Fabrication of N-doped TiO$_2$ NRAs

The TiN NRAs were deposited on F-doped SnO$_2$ (FTO) and quartz substrates through GLAD method. The substrate temperature was controlled at *ca*. −20°C by using liquid nitrogen to maintain the temperature. The N-doped TiO$_2$ NRAs were obtained by oxidizing the as-prepared TiN NRAs in a tube furnace under atmosphere at 330°C, and the N contents in TiO$_2$ NRAs were controlled by varying the annealing time (i.e., 5, 15, 30, 60 and 120 min). For the sake of convenience, one mark the TiN NRAs annealed for 5, 15, 30, 60 and 120 min as 5N-TiO$_2$, 15N-TiO$_2$, 30N-TiO$_2$, 60N-TiO$_2$ and 120N-TiO$_2$, respectively.
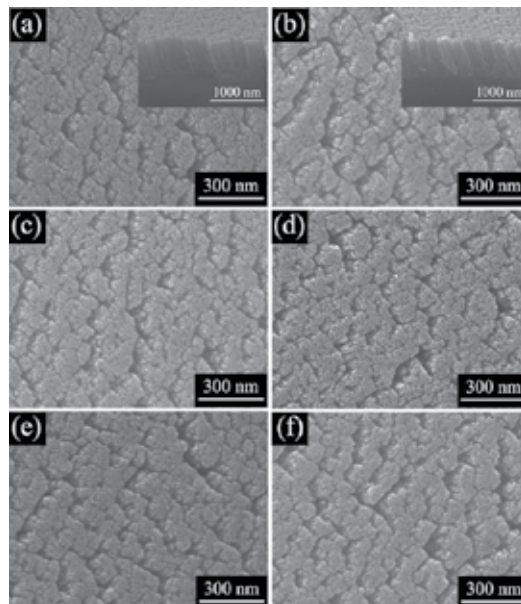
Figure 1. SEM images of the as-deposited TiN NRAs (a) 5N-TiO$_2$ NRAs (b), 15N-TiO$_2$ NRAs (c), 30N-TiO$_2$ NRAs (d), 60N-TiO$_2$ NRAs (e) and 120N-TiO$_2$ NRAs (f). The insets in (a) and (b) are the corresponding SEM images with a tilt angle of 45°.

Figure 1 is the scanning electron microscope (SEM) images of samples with various annealing time. Top-view image from **Figure 2(a)** shows that the as-prepared TiN NRAs exhibits porous structure. These nanorods (NRs) are found to be quite uniform with the length of ~600 nm, which are separated by voids as exhibited specially in the inset of **Figure 1(a)**. Moreover, it can be seen that the NRs are tilted with an angle of ~30° in the case of the substrate normal because of high angle of the incident adatom plume related to the substrate (α = 85°) [22]. The porous structure was also formed during the deposition process due to the self-shadowing effects and the limited mobility of the deposited atoms. The morphologies of the TiN NRAs annealed at 330°C for 5, 15, 30, 60 and 120 min do not change mainly and is corresponding with that of the as-deposited NRAs as exhibited in **Figures 1(b)–(f)**.

To study the microstructures of the as-prepared TiN NRAs and annealed samples furthermore, transmission electron microscope (TEM) is performed. **Figure 2(a)** shows the low-resolution TEM image of the TiN NRAs. It can be seen that the NR is of length ~600 nm and diameter of ~80 nm, which is in agreement with the SEM results. These pine needle structure NRs lead to an important enhancement in the total surface area, which is much higher than that of NRs with smooth surface. This microstructure can promote the performance of photoelectrochemistry because of the 1D structure with high specific surface area. **Figure 2(b)** exhibits the high-resolution TEM (HRTEM) image of the as-prepared TiN NRAs. The TiN crystalline grains can be observed clearly with interplanar lattice spacing of 0.212 nm, corresponding to (200) plane. TiN can be converted into TiO_2 by a complete oxidation at medium temperature in air condition. The oxidation occurs from the surface to the inner of NRs with diffusion of O_2. And the annealing time is also the critical parameter to decide the final oxidation degree. 15N-TiO_2 NRAs that annealed for 15 min at 330°C have huge amount of amorphous state, and only trace amount of TiO_2 crystalline grains with lattice spacing of 0.354 nm existed as shown in **Figure 2(c)**. Prolonging the annealing time to 120 min, huge amount of TiO_2 crystalline grains appeared and no TiN crystalline is found as shown in **Figure 2(d)**.
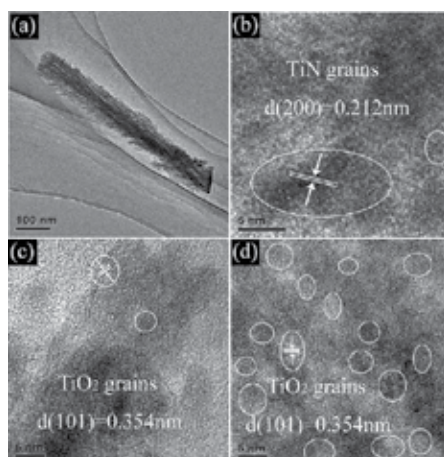
Figure 2. (a) Low-resolution cross-sectional TEM images of the as-prepared TiN NRAs; (b) HRTEM images of (a); (c) and (d) are the HR-TEM of the images of the 5N-TiO_2 NRAs and 120N-TiO_2, respectively.

Figure 3(a) exhibits the UV-visible light transmittance spectra of the TiN NRAs sample annealed during different time at 330°C. The as-prepared TiN films were assumed to be opaque with thickness of several tens of nanometers in previous report [23]; however, the transmittance of the as-prepared TiN NRAs actually in this study is ~25% under visible light test. With the increase in annealing time, the transmittance increases step by step at the wavelength of 300 to 600 nm, may due to the discrepancy in the degree of oxidation of the films from TiN to TiO_2. The spectra are studied by a high regularity of the interference fringes and a systematic increase in wavelength in which the film practically is no longer transparent in the visible range. This behavior has been previously found in TiO_2 doped with metals [24]. The optical

gap (E_g) of the semiconductor with large band gap can be calculated from the absorption coefficient α. The absorption coefficient can be expressed by, if scattering effect is neglected:

$$\left(\alpha E_g\right)^n = A\left(Eg - \hbar\upsilon\right), \tag{1}$$

where $n = 1/2$ is for an indirect transmission [25]. It could be assumed that the film contained both TiO_2 and TiN is the indirect semiconductor, similar with TiO_2. The Tauc plot of $(\alpha E)^{1/2}$ vs photon energy ($E = h\upsilon$) is shown in **Figure 3(b)**. Usually, the band gap can be gained by extrapolating the linear region to $(\alpha E)^{1/2}=0$. The band gap of the as-deposited TiN NRAs is *ca.* 1.49 eV. The band gap of the 120N-TiO_2 NRAs is 3.19 eV, which is very close to that of reported anatase TiO_2 (3.2 eV). It confirms that the TiN is turned to TiO_2 completely by annealing. The band gap varies from 1.49 to 3.19 eV with prolongation of annealing time. This result is pretty interesting from the photocatalysis viewpoint since it is possible to tune the onset of the absorption to the required visible wavelength range.
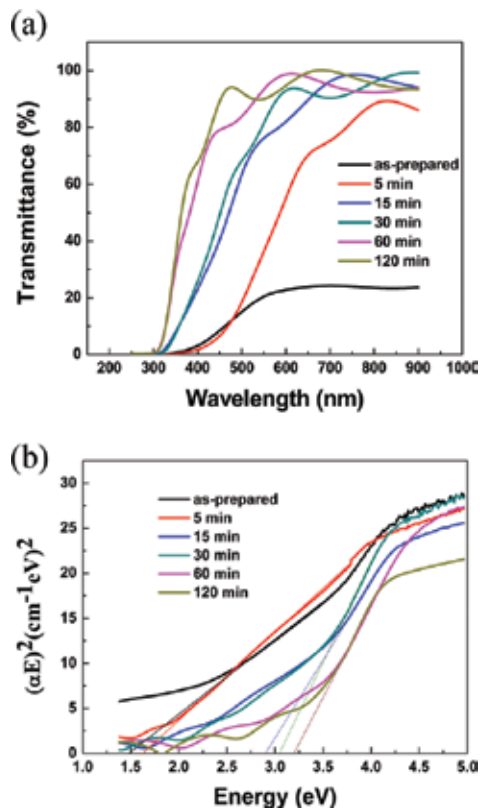

Figure 3. (a) Transmittance spectra of the doped samples annealed in different time; (b) Tauc plot of $(\alpha E)^{1/2}$ vs photon energy ($E = h\upsilon$) for the doped samples annealed for different time.

3. Coupling with other semiconductors

PbS [26], CdSe [27], ZnS [28] and CdS [29, 30] are semiconductors which own narrow band gap. They can be used as a sensitizer combined with TiO_2 to enhance the photocatalytic property. Especially, the band gap of CdS is about 2.4 eV which is of great advantage in photoelectrochemisty and photocatalysis [32]. Researchers have reported many works on growing CdS nanoparticles (NPs) on TiO_2 directly by chemical bath deposition (CBD) [34], electrodeposition [33] and successive ion layer adsorption and reaction (SILAR) [35, 36]. Improving electron-hole separation efficiency is beneficial for the photocatalytic performance [37]. Nano-sized TiO_2 is also good for reduction on recombining with photo-generated electrons [38]. What is more, nanostructured TiO_2 always shows various characteristics on property enhancement according to huge surface areas, high optical absorption degree and low reflectivity [39].

3.1. Decoration CdS NPs on TiO_2 NRAs

3.1.1. Fabrication of TiO_2 NRAs

Choosing FTO and Si as substrates to deposit Ti NRAs using GLAD technique, in which the morphology of nanostructure was investigated by SEM. Firstly, clean the substrates sequentially in acetone, alcohol and deionized water by ultrasonic, respectively, and each for 5 min. Then, the as-prepared samples were oxidized from Ti NRAs to TiO_2 NRAs using tube furnace of 450°C for 2 hrs with a rate of 5°C min^{-1} in air.

3.1.2. CdS NPs deposition on TiO_2 substrates

CdS NPs deposited TiO_2 NRAs by SILAR method have been reported previously [30, 46]. TiO_2 NRAs substrates were alternatively dipped in $Cd(Ac)_2$ and Na_2S solutions each for 30 s to react with CdS nanostructure for each time. They were also rinsed in deionized water between every solutions for 30 s. The SILAR process was repeated until it reached the satisfied cycle numbers.

Top-view SEM image of Ti NRAs is showed in **Figure 4(a)** and the insert picture exhibits tilted angle-view SEM image of the samples. And the Ti NRs are uniformed with ~70 nm in diameter, ~220 nm in length. The top-view SEM image of oxide sample was exhibited in **Figure 4(b)** which kept the similar dimensions and sample compared to Ti NRAs. **Figure 4(c–f)** are the top-view SEM images of CdS deposition samples with 5, 10, 15 and 20 SILAR cycles. SILAR method has been used in previous research and it is thought as an effective way to synthesis of CdS [47]. Large CdS particles were formed after 15 cycles, and after 20 cycles CdS particles even aggregated with each other.
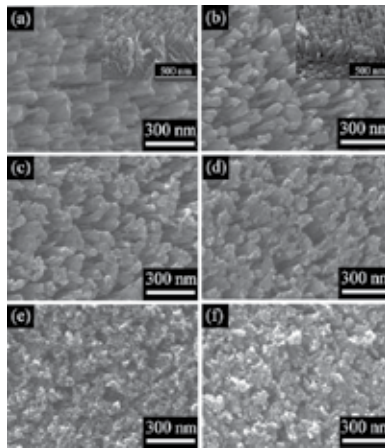
Figure 4. SEM images of the as-prepared samples: (a) Ti NRAs; (b) TiO$_2$ NRAs sample, the insets in (a) and (b) are the images recorded at a tilt angle of 45°; CdS deposition with cycle number of (c) 5, (d) 10, (e) 15, and (f) 20 SILAR.

Different cycle numbers of CdS SILAR coating on TiO$_2$ NRs were observed by HRTEM technology. The morphology of TiO$_2$ NRs are exhibited in **Figure 5(a–b)**. It can be seen that TiO$_2$ NRs are polycrystalline which contain two phases (anatase and the rutile). And the heterojunction of these two phases could block recombination of electrons and holes [48]. HRTEM images of 15 cycles CdS NPs decoration are shown in **Figure 5(c–d)**. And we can see that the average diameter of CdS NPs is ~5 nm, which attach to TiO$_2$ NRs forming heterojunctions of TiO$_2$ and CdS. And large amount of CdS wraps up TiO$_2$ NRs when cycle number reaches to 25.
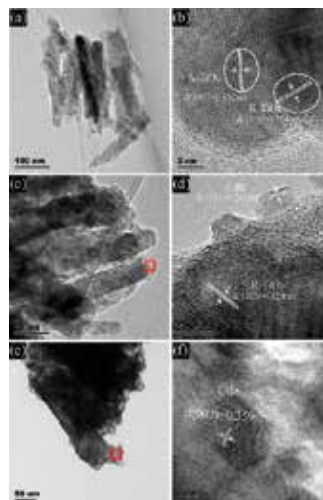
Figure 5. TEM images and HRTEM images: (a, b) TiO$_2$ NRAs; (c, d) 15 SILAR cycles TiO$_2$ NRAs/ CdS NPs; (e, f) 25 SILAR cycles TiO$_2$ NRAs/CdS NPs.

Discoloration of methyl orange (MO) under visible light of different SILAR cycle numbers is measured to test its photocatalytic performance. As we all know, the absorbance peak intensity of the λ = 462 nm is proportional to the concentration of MO solution [49]. And the reaction rate η can be computed by

$$\eta = 1 - \frac{A(t)}{A_0},\tag{2}$$

where A_o and $A(t)$ are absorbance intensity values at the 0 and t reaction time, respectively.

Discoloration rate of prepared samples with the irradiation time is exhibited in **Figure 6**. It can be seen that discoloration rate of pure TiO$_2$ NRAs was only 3.2% just due to photobleaching process [50]. Then with the increase in SILAR cycle number, the discoloration rate improved first and then reduced. Specially, when cycle number is 20, it showed the best photocatalytic performance which reached to 42.0% after 150 min irradiation.
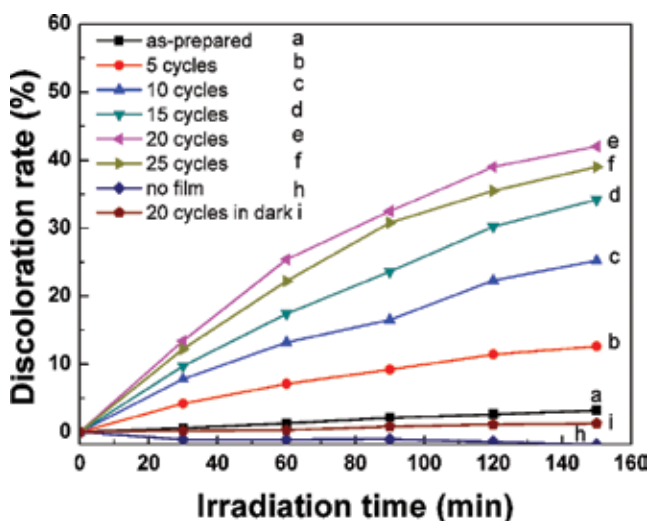
Figure 6. Visible light ($\lambda \geq 420$ nm) discoloration of MO of samples.

When visible light irradiate on materials, the CdS reacted due to the narrow band gap and produce electrons and holes. What is more, CdS decorated with TiO$_2$ NRAs also reduced the happening of recombination because of band gap matching, thus improving the photocatalytic performance. The electrons accumulated at the conduction band (CB) of semiconductors change to active oxygen species (*e.g.*, $\cdot O_2^-$) with oxygen, which could also participate in discoloration [51]. Meantime, the formed hydroxyl radicals ($\cdot$OH) could also help break down organic molecule. Holes produced in the valence band of CdS often take part in decomposition to let the dye turn to intermediates or mineralized products [52]. Thus, the addition of CdS is

beneficial to the enhancement of MO discoloration in a degree. The whole reaction process is shown in **Figure 7**.
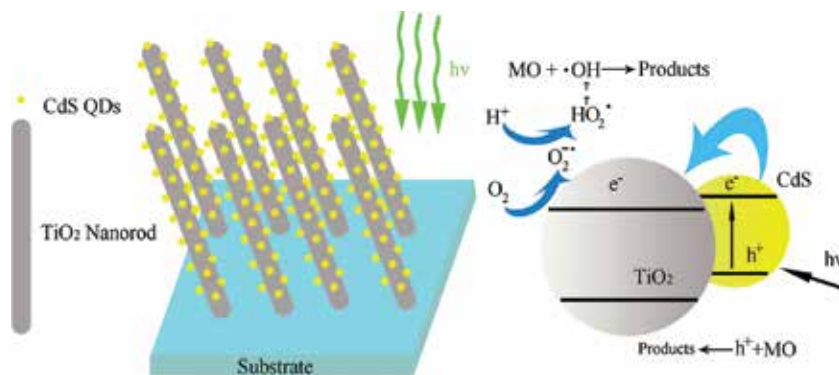
Figure 7. Schematic of degradation process of MO process for TiO_2 NRAs/CdS NPs.

3.2. TiO_2 NRAs/CdS quantum dots by coating TiO_2 *via* atomic layer deposition (ALD)

One big disadvantage of CdS QDs is that the excited electrons and holes of CdS QDs will be trapped by the surface states in ambient conditions. This problem causes the degradation of photostability and photocatalytic efficiency. Hence, it is crucial to reduce the recombination of electrons and holes, in order to improve the photostability of CdS and enhance the photo-catalytic efficiency [53]. One effective way to decrease the surface recombination velocity is to fabricate a surface coating on CdS QDs. ALD is a kind of coating technique to deposit a very thin film that could passivate the surface states and then reduce the surface recombination velocity. The layer-by-layer deposition allows highly conformal coating even on the dense and rough surface of certain nanostructures. In previous study, ALD technique has had success in preventing anodic corrosion on other nanostructured materials [54].

Here, a TiO_2 NRAs/CdS QDs/ALD-TiO_2 composite material is investigated. The TiO_2 NRAs were also made by GLAD method, while the CdS QDs and the ultra-thin TiO_2 film were coated alternatively by SILAR and ALD technique, respectively. Outstanding photocatalytic property and stability were achieved in this kind of structure, which predicts huge potency on solar energy conversion.

3.2.1. Fabrication ALD on TiO_2 NRAs

The substrate temperature of ALD was controlled at 150°C during the coating process. Four dimethylamino titanium, the precursor, was maintained at 110°C and water at 40°C. N_2 was assumed as purge and carrier gas. To guarantee enough penetration of the precursors into the whole NRs, a soak step was taken, which is very similar to that adopted in previous study [55, 56]. First, four dimethylamino titanium was pulsed for 250 ms and kept for additional 5 s, and then the chamber was evacuated. After that H_2O was pulsed in for 5 ms and allowed to soak

for another 3 s, followed by a 20 s purge step. This process was repeated until the demanded deposition of TiO_2 was complicated.

The typical top-view SEM image of 5 SILAR cycles CdS QDs decoration was showed in **Figure 8(a)**, and the inset image of the NRs with a tilt angle of 45°. The uniform NRAs are about ~70 nm in diameter, and ~220 nm in length, while the CdS QDs deposited on TiO_2 NRAs are rather small with size below 20 nm. **Figure 8(b–f)** show the top-view SEM images of the TiO_2 NRAs/CdS QDs coated with TiO_2 layers by 20, 40, 60, 80 and 160 ALD cycles, respectively. Specially, there is no obvious change in morphology when the ALD cycles are less than 80.
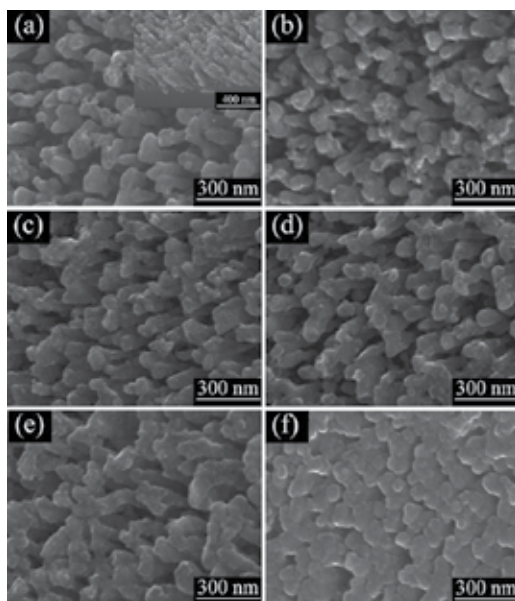
Figure 8. SEM images of the samples: (a) TiO_2 NRAs/CdS QDs, inset is the image with a tilt angle of 45°; TiO_2 NRAs/CdS QDs coated with ALD TiO_2 with different cycles: (b) 20 cycles; (c) 40 cycles; (d) 60 cycles; (e) 80 cycles; (f) 160 cycles.

The TiO_2 layers deposited on TiO_2 NRAs/CdS QDs by ALD were studied in detail by HRTEM technique. **Figure 9(a–b)** are the images of TiO_2 NRAs/CdS QDs before coating with TiO_2 layer. The TiO_2 NRs are in polycrystalline state with the length of ~220 nm and diameter of ~50 nm, which is corresponding with SEM results. Ultrafine CdS QDs with diameter of ~3 nm are coated on TiO_2 NRs, making up the CdS/TiO_2 heterojunction. **Figure 9(c–d)** are the HRTEM images of TiO_2 NRAs/CdS QDs decorated with 60 ALD cycles TiO_2 layer (i.e., TiO_2 NRAs/CdS QDs/ 60c-ALD-TiO_2). It is obvious that an ultrathin amorphous TiO_2 layer (~2 nm thick) was deposited completely and uniformly on the TiO_2 NRAs/CdS QDs, forming another CdS/TiO_2 heterojunction. Furthermore, **Figure 9(e–f)** exhibit the TEM images of TiO_2 NRAs/CdS QDs/ 80c-ALD-TiO_2, and the thickness of the amorphous TiO_2 layer is ~2.8 nm which can be seen clearly in the HRTEM image corresponding to **Figure 9(f)**.
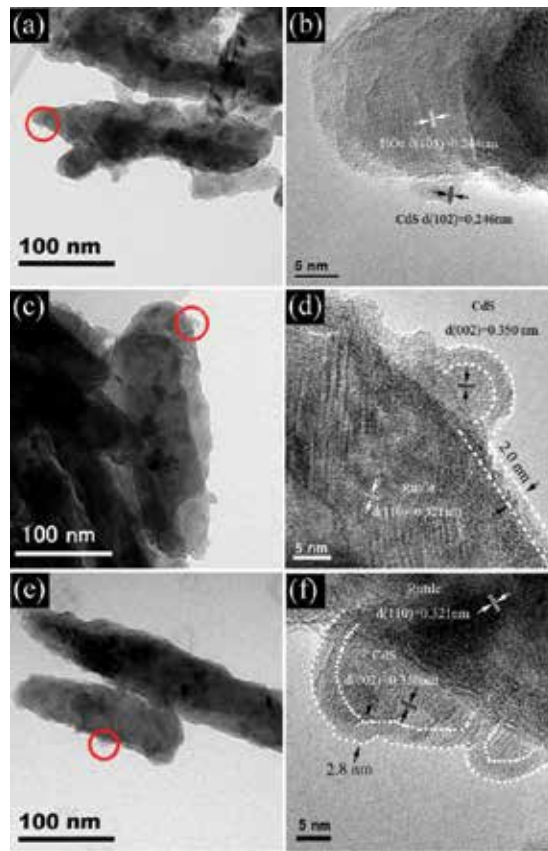
Figure 9. TEM images and HRTEM images: (a, b) TiO$_2$ NRAs/CdS QDs; TiO$_2$ NRAs/CdS QDs coated with ALD TiO$_2$ with various cycles: (c, d) for 60 and (e, f) for 80 cycles.

We also test the photocatalytic performance of composite materials by the photodegradation experiments of MO under visible light irradiation. It is also following the Beer's law as introduced previously [49]. **Figure 10** shows the degradation rate of MO after 1 h irradiation under visible light range, choosing TiO$_2$ NRAs/CdS QDs/ALD-TiO$_2$ as the photocatalyst. The degradation rate is only 2.92% when choosing TiO$_2$ NRAs/CdS QDs without coating ALD TiO$_2$. And enhancement of degradation rate occurred when taking TiO$_2$ NRAs/CdS QDs/ALD-TiO$_2$ as the photocatalyst.

For instance, the degradation rate was 4.16% for TiO$_2$ NRAs/CdS QDs/20c-ALD-TiO$_2$, and it promoted 7.47% for TiO$_2$ NRAs/CdS QDs/60c-ALD-TiO$_2$, in which the rate improved 156% compared to that of TiO$_2$ NRAs/CdS QDs in the absence of coating. However, it is also obvious that when taking the TiO$_2$ NRAs/CdS QDs/80c-ALD-TiO$_2$ and TiO$_2$ NRAs/CdS QDs/160c-ALD-TiO$_2$ as photocatalysts, the degradation rate of both decreases greatly. The annealed samples exhibit similar catalytic performance without obvious variation of degradation between the annealed and the original samples.
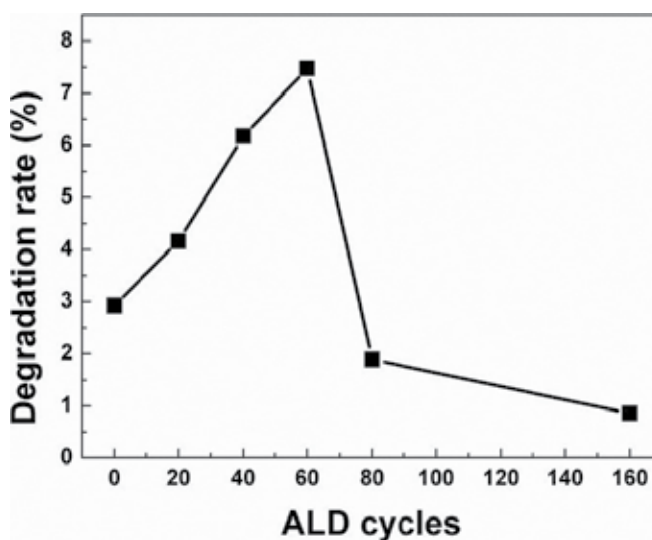
Figure 10. Visible light ($\lambda \geq 420$ nm) degradation behavior of MO using TiO$_2$ NRAs/CdS QDs/ALD-TiO$_2$ as catalyst.

4. Coupling with noble metal

Combining with metal is a promising method to develop highly efficient visible light photocatalyst. On one hand, the deposition of the metal on TiO$_2$ can greatly improve its photoefficiency through the Schottky barrier CB electron trapping and consequent longer electron-hole pair lifetime [57]. Hu et al. [58] reported a highly efficient Pt-doped TiO$_2$ which have enhanced photocatalytic activity for NO$_x$ oxidation both under UV and visible light irradiation. Ingram et al. managed to reduce the high rate of charge-carrier recombination by combining a semiconductor photocatalyst with tailored plasmonic-metal nanostructures [59]. The presence of Pt deposited on TiO$_2$ is believed to retard the rapid charge-pair recombination by serving as an electron sink and facilitating interfacial electron transfer to dioxygen or other electron acceptors. Pt can also trap electrons on the CB, which are subsequently transferred to electron acceptors [60]. On the other hand, some noble metal NPs, such as Ag and Au, exhibit strong UV-vis absorption due to their plasmon resonance, produced by the collective oscillations of surface electrons. Pu et al. demonstrated those Au NPs, Au NRs and a mixture of Au NPs and NRs on the surface of TiO$_2$ nanowire arrays could be prepared for effective photocatalysis and the activities were enhanced in both the UV and the visible regions [61].

Despite these promising studies, combining the plasmonic effect of Au and electron sink effect of Pt has not been reported so far to our knowledge. Furthermore, photocatalysts in previous reports were usually in the form of powders and in an amorphous state, which was hard to handle and restricted its practical applications. In the present work, we designed a plasmonic photocatalyst consisting of bimetallic Au-Pt/TiO$_2$ supported on specific SiO$_2$ substrates. Firstly, the vertically aligned TiO$_2$ NRAs were fixed on specific SiO$_2$ substrates by GLAD technique.

Then, the Au and Pt NPs were deposited on TiO_2 by using SILAR method. Excellent photocatalytic property and stability were achieved and the fabrication of TiO_2 self-standing structures, which will be easier for recycling and thus facilitating their potential applications in solar energy-driven photocatalysis.

4.1. Metallic NPs deposition on TiO_2 NRAs

Au/Pt NPs were deposited on TiO_2 NRs through SILAR method with slight modification as previously reported [30]. Briefly, the TiO_2 NRAs substrates were successively exposed to $HAuCl_4$ (or HPt_2Cl_6) and $NaBH_4$ solutions to deposit nanocrystallites. The TiO_2 NRAs were immersed in 0.1 mg/mL $HAuCl_4$ (or 0.1 mg/mL HPt_2Cl_6) solution for 60 s, followed by rinsing with DI water and then immersed in $NaBH_4$ solution (1 mg/mL) for another 60 s, after which the resultant was rinsed with DI water for several times. This SILAR process was repeated for several cycles until the desired quantity of metallic nanocrystallites was achieved. Here, Au/Pt-TiO_2 sample was alternately coated with Au and Pt NPs, respectively, for 5 times.

Figure 11 presents the X-ray diffraction (XRD) patterns of different samples. All samples exhibited diffraction peaks at 25.2° and 27.3° corresponding to the (101) crystal planes of the anatase phase (JCPDS No. 21–1272) and (110) crystal planes of the rutile phase (JPCDS No. 21–1276). Besides this, the diffraction peaks (38.2°, 41.4°) assigned to Au (JCPDS No. 04–0784) and the peak at 39.7° assigned to Pt (JCPDS No. 04–0802) were displayed in Au-TiO_2 and Pt-TiO_2, respectively. These three peaks were also observed in Au/Pt-TiO_2 sample.
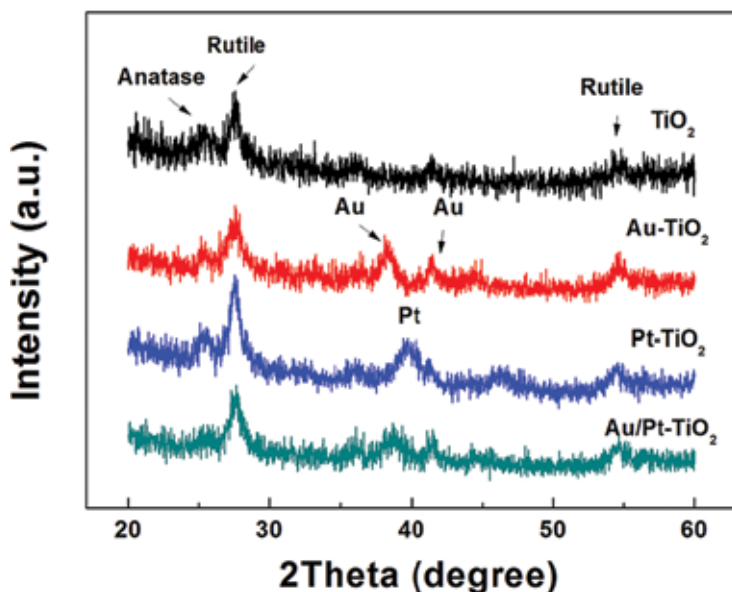
Figure 11. XRD patterns of the Au/TiO_2 NRAs coated with 10 cycles, Pt/TiO_2 NRAs coated with 10 cycles and Au/Pt/TiO_2 NRAs.

Figure 12 shows the SEM images of the pure TiO_2 film and those coated with Au, Pt and Au/Pt NPs with 10 cycles, respectively. As-annealed film consists of vertically aligned TiO_2 NRs with a diameter of ~50 nm and a length of ~200 nm (**Figure 12(a)**). Au and Pt NPs distribute uniformly on the TiO_2 NRAs surface (**Figure 12(d) and 12(c)**).
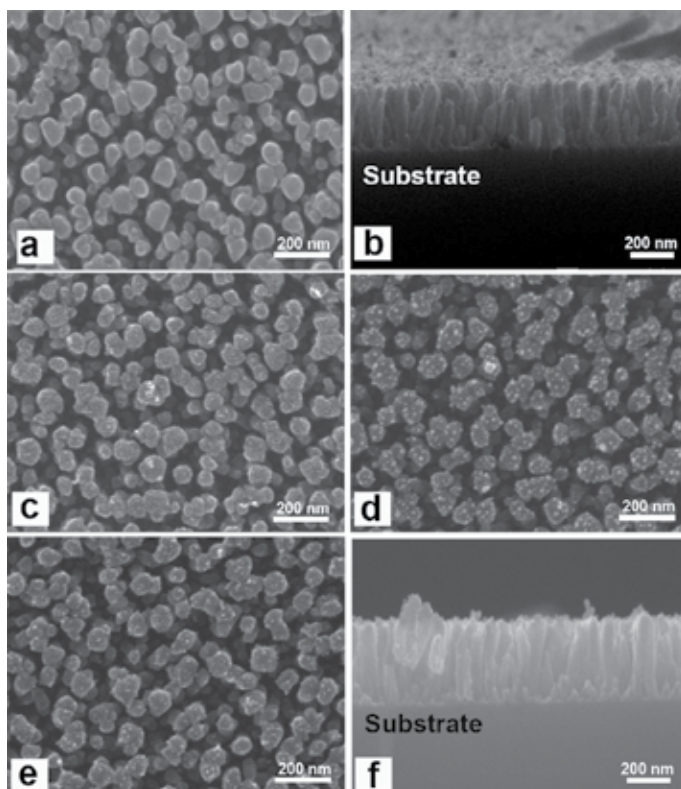
Figure 12. SEM images of the different samples: (a) TiO_2 NRAs; (b) cross-section of TiO_2 NRAs; (c) Pt-TiO_2 NRAs coated with 10 cycles; (d) Au-TiO_2 NRAs coated with 10 cycles; (e) Au/Pt-TiO_2 NRAs; (f) cross-section of sample Au/Pt-TiO_2 NRAs.

Furthermore, TEM images in **Figure 13** show that Au and Pt were uniformly dispersed on the surface of TiO_2. Their average sizes were about ~4 nm, and in a regular cubic shape. According to the measurement of lattice fringes, $d = 0.23$, 0.24, 0.34 and 0.32 nm match very well with the crystallographic planes of Pt (111), Au (111), anatase (101) and rutile (110), respectively. This result indicated that Au, Pt and TiO_2 were effectively interfaced. The formation of metal-semiconductor nanojunctions, including Au-TiO_2 and Pt-TiO_2, could be favorable for interfacial charge transfer among the three components, enhancing photocatalytic activities of the composites. In addition, the existence of anatase-rutile heterojunction in the NRs may help the rutile particles to efficiently collect photon-induced electrons from the anatase particles to reduce the carrier recombination [48].
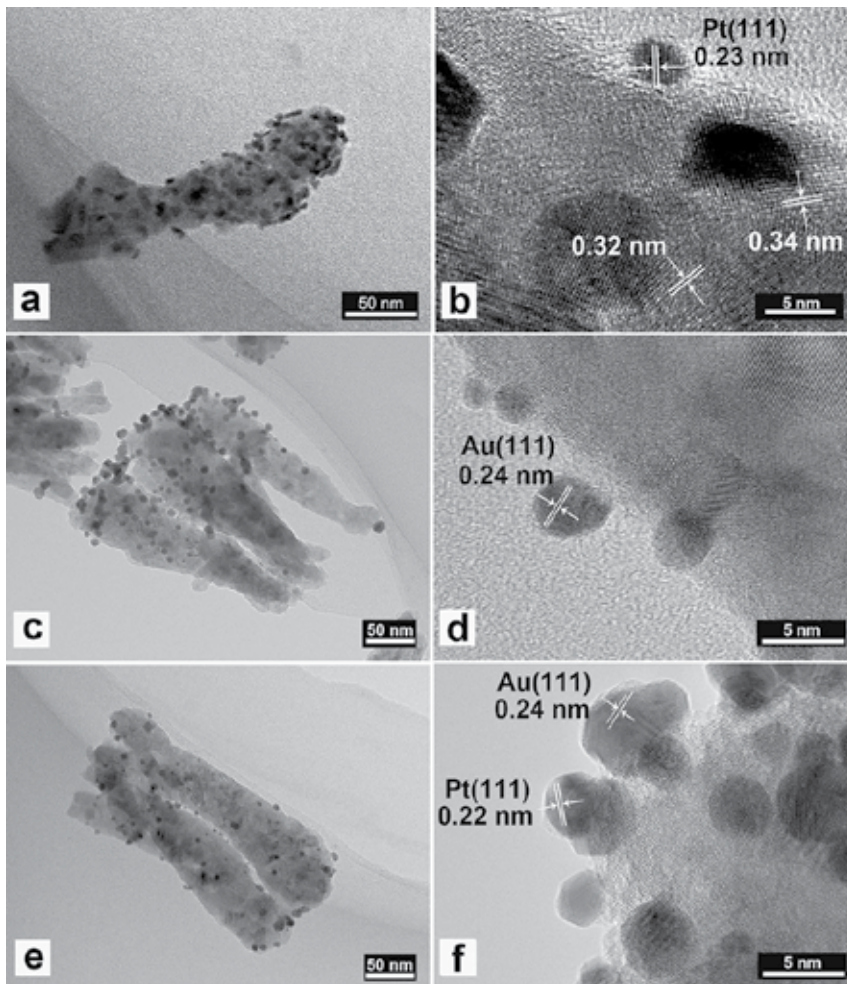
Figure 13. TEM images and HRTEM images of (a–b) Pt/TiO$_2$ NRAs coated with 10 cycles; (c–d) Au/TiO$_2$ NRAs coated with 10 cycles; (e–f) Au/Pt/TiO$_2$ NRAs.

To evaluate the effect of bimetal Au-Pt on the photocatalytic activity of TiO$_2$, the photodegradation of MO was carried out under visible irradiation. As a comparison, MO degradation were also performed in Pt/TiO$_2$, Au/TiO$_2$ and TiO$_2$. As shown in **Figure 14**, neither TiO$_2$ nor Pt-TiO$_2$ showed any activity for the MO degradation, while 20% MO was degraded by Au-TiO$_2$ after 120 illumination under otherwise condition. In the range of wavelength $\lambda > 420$ nm, only Au NPs have light absorption, and the degradation of MO in Au-TiO$_2$ is from the plasmon-induced Au NPs. Moreover, the rate of MO photodegradation on Au/Pt-TiO$_2$ was 1.36 times faster than that on Au-TiO$_2$. Therefore, Pt NPs also played an important role in the enhanced activity of Au-Pt/TiO$_2$. Compared with the photocurrent of Au-TiO$_2$, which of Au-Pt/TiO$_2$ was remarkably enhanced, indicating that the latter sample exhibited higher charge separation efficiency.
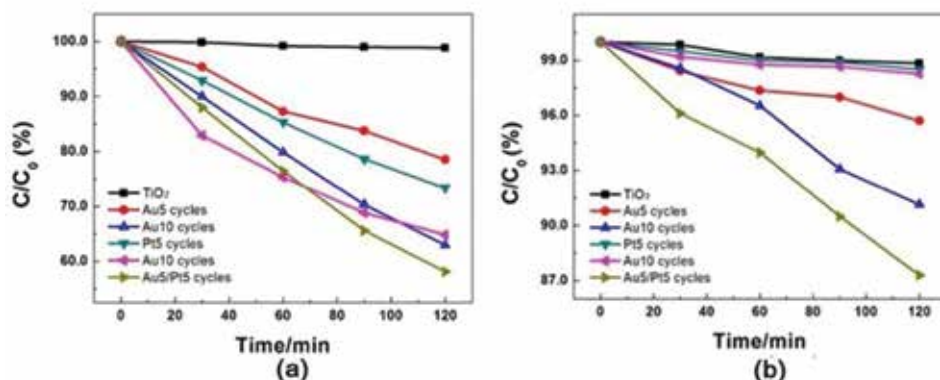
Figure 14. UV-vis light discoloration of (a) MO and (b) current versus time measurements; visible light ($\lambda \circledcirc 420$ nm) discoloration of (c) MO and (d) current versus time measurements.

Surface plasmon resonance (SPR) peak wavelength of Au NPs in visible light region is ~520 nm. And the incident photons are absorbed by Au NPs through SPR excitation [62]. Soon afterwards, hot electrons move from the plasmon-excited Au to the CB of TiO_2 [63]. And then electrons transfer from CB to Pt due to the work function of Pt larger than Au. Here, Pt NPs take part in the process as cocatalyst at which electrons could react with electron acceptors (O_2 absorbed on the surface of Ti^{3+} or dissolved in water) to create superoxide radicals ($O_2^{\bullet-}$). At the meantime, the resultant electron-deficient Au particles can oxidize the organic molecule or react with OH^- to form hydroxyl radicals, $OH\bullet$, which are highly oxidizing species. The process is shown in **Figure 15**. And co-decoration of Au/Pt not only improves the efficiency of charge separation, improving its photocatalytic efficiency, but also expands the active range of TiO_2 to visible light region. What is more, it was also verified that active radicals produced from UV-photoexcited TiO_2 create electron-hole pairs reacting with adsorbed oxygen/H_2O [65]. As a result, the highly efficient degradation of dyes came from both photoexcited TiO_2 and plasmon-excited Au NPs under UV irradiation.
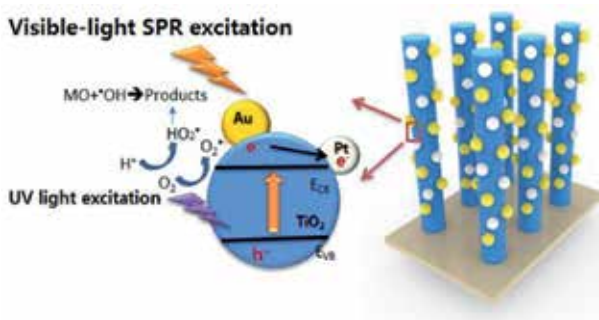
Figure 15. The photocatalytic process for Au/Pt/TiO_2 NRAs under UV-vis lights.

5. Summary

In this chapter is introduced three main methods of coupling with different semiconductors, combining with noble metals and introducing dopants to make TiO_2 be active in visible light region. Our studies demonstrate that through rational design of composite nanostructures, one can achieve on utilizing a high-energy photon under sunlight. And combining different materials together, which matches their bands with each other and with various nanostructures, could both eventually realize higher efficiency of solar spectrum.

Author details

Shuang Shuang[1], Zheng Xie[1,3] and Zhengjun Zhang[2*]

*Address all correspondence to: zjzhang@tsinghua.edu.cn

1 State Key Laboratory of New Ceramics and Fine Processing, School of Materials Science and Engineering, Tsinghua University, Beijing, China

2 Key Laboratory of Advanced Materials (MOE), School of Materials Science and Engineering, Tsinghua University, Beijing, China

3 High-Tech Institute of Xi'an, Xi'an, China

References

[1] Fujishima A, Honda K. Electrochemical photolysis of water at a semiconductor electrode. Nature. 1972;238(5358):37–38. DOI: 10.1038/238037a0

[2] Yuan RS, Chen T, Fei EH, Lin JL, Ding ZX, Long JL, et al. Surface chlorination of TiO2-based photocatalysts: a way to remarkably improve photocatalytic activity in both UV and visible region. Acs Catal. 2011;1(3):200–206. DOI: 10.1021/cs100122v

[3] Barborini E, Conti AM, Kholmanov I, Piseri P, Podesta A, Milani P, et al. Nanostructured TiO2 films with 2 eV optical gapsDOI. Adv Mater. 2005;17(15):1842–1846. DOI: 10.1002/adma.200401169

[4] Zhang JY, Zhu HL, Zheng SK, Pan F, Wang TM. TiO2 Film/Cu2O microgrid heterojunction with photocatalytic activity under solar light irradiation. Acs Appl Mater Inter. 2009;1(10):4207–4209 . DOI: 10.1063/1.1426256

[5] Higashimoto S, Sakiyama M, Azuma M. Photoelectrochemical properties of hybrid WO3/TiO2 electrode. Effect of structures of WO3 on charge separation behavior. Thin Solid Films. 2006;503(1–2):201–206. DOI: 10.1016/j.tsf.2005.11.110

[6]   Tian Y, Tatsuma T. Mechanisms and applications of plasmon-induced charge separation at TiO2 films loaded with gold nanoparticles. J Am Chem Soc. 2005;127(20):7632–7633. DOI: 10.1021/ja042192u

[7]   Low CTJ, de Leon CP, Walsh FC. The reduction of hydrogen peroxide at an Au-coated nanotubular TiO2 array. J Appl Electrochem. 2014;44(1):169–177. DOI: 10.1007/s10800-013-0623-5

[8]   Hirakawa T, Kamat PV. Photoinduced electron storage and surface plasmon modulation in Ag@TiO2 clusters. Langmuir. 2004;20(14):5645–5647. DOI: 10.1021/la048874c

[9]   Akhavan O. Lasting antibacterial activities of Ag-TiO2/Ag/a-TiO2 nanocomposite thin film photocatalysts under solar light irradiation. J Colloid Interf Sci. 2009;336(1):117–124. DOI: 10.1016/j.jcis.2009.03.018

[10] Ihara T, Miyoshi M, Ando M, Sugihara S, Iriyama Y. Preparation of a visible-light-active TiO2 photocatalyst by RF plasma treatment. J Mater Sci. 2001;36(17):4201–4207. DOI: 10.1023/A:1017929207882

[11] Umebayashi T, Yamaki T, Itoh H, Asai K. Band gap narrowing of titanium dioxide by sulfur doping. Appl Phys Lett. 2002;81(3):454–456. DOI: 10.1063/1.1493647

[12] Miyauchi M, Ikezawa A, Tobimatsu H, Irie H, Hashimoto K. Zeta potential and photocatalytic activity of nitrogen doped TiO2 thin films. Phys Chem Chem Phys. 2004;6(4):865–870. DOI: 10.1039/b314692h

[13] Qin Z, Zhengcao L, Jie N, Zhengjun Z. A simple model to describe the rule of glancing angle deposition. Mater Transac 2011;52(3):469–473. DOI: 10.2320/matertrans.M2010342

[14] Jie N, Yu Z, Qin Z, Zhengjun Z. Morphology in-design deposition of HfO2 thin films. 2008;91:3458–3460. DOI: 10.1111/j.1551-2916.2008.02654.x

[15] Chaney SB, Shanmukh S, Dluhy RA, Zhao YP. Aligned silver nanorod arrays produce high sensitivity surface-enhanced Raman spectroscopy substrates. 2005;87(3): DOI: 10.1063/1.1988980

[16] Herrmann JM, Disdier J, Pichat P. Effect of chromium doping on the electrical and catalytic properties of powder titania under UV and visible illumination. Chem Phys Lett. 1984;108(6):618–622. DOI: 10.1016/0009-2614(84)85067-8

[17] Yin S, Aita Y, Komatsu M, Sato T. Visible-light-induced photocatalytic activity of TiO2-xNy prepared by solvothermal process in urea-alcohol system. J Eur Ceram Soc. 2006;26(13):2735–2742. DOI: 10.1016/j.jeurceramsoc.2005.05.012

[18] Shieh DL, Lin YS, Yeh JH, Chen SC, Lin BC, Lin JL. N-doped, porous TiO2 with rutile phase and visible light sensitive photocatalytic activity. Chem Commun. 2012;48(19):2528–2530. DOI: 10.1039/c2cc16960f

[19] Ohno T, Akiyoshi M, Umebayashi T, Asai K, Mitsui T. Preparation of S-doped TiO2 photocatalysts and their photocatalytic activities under visible light. Appl Catal a-Gen. 2004;265(1):115–121. DOI: 10.1016/j.apcata.2004.01.007

[20] Ho W, Yu JC, Lee S. Synthesis of hierarchical nanoporous F-doped TiO2 spheres with visible light photocatalytic activity. Chem Commun. 2006;10:1115–1117. DOI: 10.1039/b515513d

[21] Asahi R, Morikawa T, Ohwaki T, Aoki K, Taga Y. Visible-light photocatalysis in nitrogen-doped titanium oxides. Science. 2001;293(5528):269–271. DOI: 10.1126/science.1061051

[22] Wolcott A, Smith WA, Kuykendall TR, Zhao YP, Zhang JZ. Photoelectrochemical water splitting using dense and aligned TiO2 nanorod arrays. Small. 2009;5(1):104–111. DOI: 10.1002/smll.200800902

[23] Van Bui H, Groenland AW, Aarnink AAI, Wolters RAM, Schmitz J, Kovalgin AY. Growth kinetics and oxidation mechanism of ALD TiN thin films monitored by in situ spectroscopic ellipsometry. J Electrochem Soc. 2011;158(3):H214–H220. DOI: 10.1149/1.3530090

[24] Pereira ALJ, Gracia L, Beltran A, Lisboa PN, da Silva JHD, Andres J. Structural and electronic effects of incorporating Mn in TiO2 films grown by sputtering: anatase versus rutile. J Phys Chem C. 2012;116(15):8753–8762. DOI: 10.1021/jp210682d

[25] Miyata N, Akiyoshi S. Preparation and electrochromic properties of Rf-sputtered molybdenum oxide-films. J Appl Phys. 1985;58(4):1651–1655. DOI: 10.1063/1.336307

[26] Lee H, Leventis HC, Moon SJ, Chen P, Ito S, Haque SA, et al. PbS and CdS quantum dot-sensitized solid-state solar cells: old concepts, new results. Adv Func Mater. 2009;19(17):2735–2742. DOI: 10.1021/la900247r

[27] Lee HJ, Bang J, Park J, Kim S, Park S-M. Multilayered semiconductor (CdS/CdSe/ZnS)-sensitized TiO2 mesoporous solar cells: all prepared by successive ionic layer adsorption and reaction processes. Chem Mater. 2010;22(19):5636–5643. DOI: 10.1021/cm102024s

[28] Guijarro N, Campiña JM, Shen Q, Toyoda T, Lana-Villarreal T, Gómez R. Uncovering the role of the ZnS treatment in the performance of quantum dot sensitized solar cells. Phys Chem Chem Phys. 2011;13(25):12024–12032. DOI: 10.1039/c1cp20290a

[29] Li G-S, Zhang D-Q, Yu JC. A new visible-light photocatalyst: CdS quantum dots embedded mesoporous TiO2. Environ Sci Technol. 2004;43(18):7079–7085. DOI: 10.1039/c3nr34253k

[30] Baker DR, Kamat PV. Photosensitization of TiO2 nanostructures with CdS quantum dots: particulate versus tubular support architectures. Adv Func Mater. 2009;19(5):805–811. DOI: 10.1002/adfm.200801173

[31] Das K, De S. Optical properties of the type-II core-shell TiO2@ CdS nanorods for photovoltaic applications. J Phys Chem C. 113(9):3494–501. DOI: 10.1039/c4ra01769b

[32] Liu Y, Zhou H, Zhou B, Li J, Chen H, Wang J, et al. Highly stable CdS-modified short TiO$_2$ nanotube array electrode for efficient visible-light hydrogen generation. Int J Hydrogen Energy. 2011;36(1):167–174. DOI: 10.1016/j.ijhydene.2010.09.089

[33] Wang C, Sun L, Yun H, Li J, Lai Y, Lin C. Sonoelectrochemical synthesis of highly photoelectrochemically active TiO2 nanotubes by incorporating CdS nanoparticles. Nanotechnology. 2009;20(29):295601. DOI: 10.1088/0957-4484/20/29/295601

[34] Lin S-C, Lee Y-L, Chang C-H, Shen Y-J, Yang Y-M. Quantum-dot-sensitized solar cells: assembly of CdS-quantum-dots coupling techniques of self-assembled monolayer and chemical bath deposition. Appl Phys Lett. 2007;90(14):143517–143530. DOI: 10.1063/1.2721373

[35] Luo J, Ma L, He T, Ng CF, Wang S, Sun H, et al. TiO2/(CdS, CdSe, CdSeS) nanorod heterostructures and photoelectrochemical properties. J Phys Chem C. 2012;116(22): 11956–11963. DOI: 10.1021/jp3031754

[36] Cheng S, Fu W, Yang H, Zhang L, Ma J, Zhao H, et al. Photoelectrochemical performance of multiple semiconductors (CdS/CdSe/ZnS) cosensitized TiO2 photoelectrodes. J Phys Chem C. 2012;116(3):2615–2621. DOI: 10.1021/jp209258r

[37] Shaislamov U, Yang BL. CdS-sensitized single-crystalline TiO2 nanorods and polycrystalline nanotubes for solar hydrogen generation. J Mater Res. 2013;1(1):1–6. DOI: 10.1557/jmr.2012.373

[38] Salvador P. Hole diffusion length in n-TiO 2 single crystals and sintered electrodes: photoelectrochemical determination and comparative analysis. J Appl Phys. 1984;55(8): 2977–2985. DOI: 10.1063/1.333358

[39] Zhou H, Qu Y, Zeid T, Duan X. Towards highly efficient photocatalysts using semiconductor nanoarchitectures. Energy Environ Sci. 2012;5(5):6732–6743. DOI: 10.1039/c2ee03447f

[40] Pradhan SK, Reucroft PJ, Yang F, Dozier A. Growth of TiO$_2$ nanorods by metalorganic chemical vapor deposition. J Crystal Growth. 2003;256(1):83–88. DOI: 10.1016/S0022-0248(03)01339-3

[41] Nian J-N, Teng H. Hydrothermal synthesis of single-crystalline anatase TiO2 nanorods with nanotubes as the precursor. J Phys Chem B. 2006;110(9):4193–4198. DOI: 10.1021/jp0567321

[42] González-García L, González-Valls I, Lira-Cantu M, Barranco A, González-Elipe AR. Aligned TiO2 nanocolumnar layers prepared by PVD-GLAD for transparent dye sensitized solar cells. Energy Environ Sci. 2011;4(9):3426–3435. DOI: 10.1039/c0ee00489h

[43] He Y, Zhang Z, Zhao Y. Optical and photocatalytic properties of oblique angle deposited TiO2 nanorod array. J Vacuum Sci Technol B: Microelectronics Nanometer Struct. 2008;26(4):1350–1358. DOI: 10.1116/1.2949111

[44] Wolcott A, Smith WA, Kuykendall TR, Zhao Y, Zhang JZ. Photoelectrochemical water splitting using dense and aligned TiO2 nanorod arrays. Small. 2009;5(1):104–111. DOI: 10.1002/smll.200800902

[45] Krause KM, Taschuk MT, Harris KD, Rider DA, Wakefield NG, Sit JC, et al. Surface area characterization of obliquely deposited metal oxide nanostructured thin films. Langmuir. 2009;26(6):4368–4376. DOI: 10.1021/la903444e

[46] Lee HJ, Chen P, Moon SJ, Sauvage F, Sivula K, Bessho T, et al. Regenerative PbS and CdS quantum dot sensitized solar cells with a cobalt complex as hole mediator. Langmuir. 2009;25(13):7602–7608. DOI: 10.1021/la900247r

[47] Zewdu T, Clifford JN, Hernandez JP, Palomares E. Photo-induced charge transfer dynamics in efficient TiO2/CdS/CdSe sensitized solar cells. Energy Environ Sci. 2011;4(11):4633–4638. DOI: 10.1021/la900247r

[48] Sun PP, Zhang XT, Wang CH, Wei YA, Wang LL, Liu YC. Rutile TiO2 nanowire array infiltrated with anatase nanoparticles as photoanode for dye-sensitized solar cells: enhanced cell performance via the rutile-anatase heterojunction. J Mater Chem A. 2013;1(10):3309–3314. DOI: 10.1021/la900247r

[49] Li ZC, Zhu Y, Zhou Q, Ni J, Zhang ZJ. Photocatalytic properties of TiO2 thin films obtained by glancing angle deposition. Appl Surf Sci. 2012;258(7):2766–2770. DOI: 10.1016/j.apsusc.2011.10.129

[50] Cheng P, Deng C, Gu M, Shangguan W. Visible-light responsive zinc ferrite doped titania photocatalyst for methyl orange degradation. J Mater Sci. 2007;42(22):9239–9244. DOI: 10.1007/s10853-007-1902-5

[51] Jin SF, Li YZ, Xie H, Chen X, Tian TT, Zhao XJ. Highly selective photocatalytic and sensing properties of 2D-ordered dome films of nano titania and nano Ag2+ doped titania. J Mater Chem. 2012;22(4):1469–1476. DOI: 10.1039/c1jm14216j

[52] Xie Y, Ali G, Yoo SH, Cho SO. Sonication-assisted synthesis of CdS quantum-dot-sensitized TiO2 nanotube arrays with enhanced photoelectrochemical and photocatalytic activity. Acs Appl Mater Inter.2(10):2910–2914. DOI: 10.1021/am100605a

[53] Tang WZ, Huang CP. Photocatalyzed oxidation pathways of 2,4-dichlorophenol by Cds in basic and acidic aqueous-solutions. Water Res. 1995;29(3):745–756. DOI: 10.1016/0043-1354(94)00151-V

[54] Yu K, Lin X, Lu GH, Wen ZH, Yuan C, Chen JH. Optimized CdS quantum dot-sensitized solar cell performance through atomic layer deposition of ultrathin TiO2 coating. Rsc Adv. 2012;2(20):7843–7848. DOI: 10.1039/c2ra20979a

[55] Roelofs KE, Brennan TP, Dominguez JC, Bailie CD, Margulis GY, Hoke ET, et al. Effect of Al2O3 recombination barrier layers deposited by atomic layer deposition in solid-state CdS quantum dot-sensitized solar cells. J Phys Chem C. 2013;117(11):5584–5592. DOI: 10.1021/jp311846r

[56] Kang Q, Cao JY, Zhang YJ, Liu LQ, Xu H, Ye JH. Reduced TiO2 nanotube arrays for photoelectrochemical water splitting. J Mater Chem A. 2013;1(18):5766–5774. DOI: 10.1039/c3ta10689f

[57] Kang Q, Cao J, Zhang Y, Liu L, Xu H, Ye J. Reduced TiO 2 nanotube arrays for photo-electrochemical water splitting. J Mater Chem A. 2013;1(18):5766–5774. DOI: 10.1039/c3ta10689f

[58] Hu Y, Song X, Jiang SM, Wei CH. Enhanced photocatalytic activity of Pt-doped TiO2 for NOx oxidation both under UV and visible light irradiation: A synergistic effect of lattice Pt4+ and surface PtO. Chem Eng J. 2015;274:102–112. DOI: 10.1016/j.cej.2015.03.135

[59] Ingram DB, Linic S. Water splitting on composite plasmonic-metal/semiconductor photoelectrodes: evidence for selective plasmon-induced formation of charge carriers near the semiconductor surface. J Am Chem Soc. 2011;133(14):5202–5205. DOI: 10.1021/ja200086g

[60] Meng ZD, Zhu L, Choi JG, Chen ML, Oh WC. Effect of Pt treated fullerene/TiO2 on the photocatalytic degradation of MO under visible light. J Mater Chem. 2011;21(12):7596–7603. DOI: 10.1039/c1jm10301f

[61] Pu YC, Wang GM, Chang KD, Ling YC, Lin YK, Fitzmorris BC, et al. Au Nanostructure-decorated TiO2 nanowires exhibiting photoactivity across entire UV-visible region for photoelectrochemical water splitting. Nano Lett. 2013;13(8):3817–3823. DOI: 10.1021/nl4018385

[62] Kominami H, Tanaka A, Hashimoto K. Mineralization of organic acids in aqueous suspensions of gold nanoparticles supported on cerium(IV) oxide powder under visible light irradiation. Chem Commun. 2010;46(8):1287–1289. DOI: 10.1039/b919598j

[63] Szabo Z, Furo I, Csoregh I. Combinatorial multinuclear NMR and X-ray diffraction studies of uranium(VI)-nucleotide complexes. J Am Chem Soc. 2005;127(43):15236–15247. DOI: 10.1021/ja0550273

[64] Trasatti S. Work function, electronegativity, and electrochemical behaviour of metals. 2. Potentials of zero charge and electrochemical work functions. J Electroanal Chem. 1971;33(2):351. DOI: 10.1016/0368-1874(71)80045-X

[65] Di Valentin C, Selloni A. Bulk and surface polarons in photoexcited anatase TiO2. J Phys Chem Lett. 2011;2(17):2223–2228 . DOI: 10.1021/jz2009874

Insights into the Mechanism of Photocatalytic Degradation of Volatile Organic Compounds on TiO₂ by Using In-situ DRIFTS

Song Sun and Fan Zhang

Additional information is available at the end of the chapter

Abstract

Photocatalytic degradation is a cost-effective technology for the removal of volatile organic compounds. However, the mechanism of photocatalytic degradation of volatile organic compounds on TiO_2 is still a challenging issue. Fortunately, infrared spectroscopy is a powerful technique, able to provide information about adsorption/desorption, intermediates/products, and interfacial reaction. The aim of this chapter is to review several aspects of our current understanding of the role of TiO_2 in the degradation of volatile organic compounds, by using in situ diffuse reflectance infrared Fourier transform spectroscopy. We firstly review the state of photocatalytic degradation of volatile organic compounds briefly. This is followed by a summary of in situ infrared techniques. The interaction of TiO_2 surfaces with vapor organic molecules and other species is then reviewed with the representative works in recent years. It ends with a brief future outlook on the mechanism of photocatalytic air purification of TiO_2.

Keywords: infrared spectroscopy, photocatalysis, volatile organic compounds, TiO_2, DRIFTS, air purification

1. Introduction

Volatile organic compounds (VOCs), such as toluene, formaldehyde, and benzene, emitted from decoration materials, paint and cementing compound, are the major pollutants in indoor air [1]. There is evidence that most of the VOCs significantly impact human health. In general, they can irritate the mucous membranes of eyes and respiratory tract, and even damage the nervous system [2,3]. Compared with adsorption by activated carbon, biofiltration, or thermal cataly-

sis, photocatalytic degradation is a cost-effective technology for removal of VOCs, because the pollutants can be oxidized to mineral salts, CO_2, and H_2O under mild operating conditions [4,5]. In a typical process, a semiconductor is irradiated with light whose energy is higher than the band gap energy of the semiconductor, generating an electron (e^-) from the valence band to the conduction band and leaving a hole (h^+) in the valence band. Some electron–hole charge carriers can in turn undergo recombination and dissipate the excess energy, while the other carriers can migrate to the surface of the semiconductor and initiate redox reactions with the surface-adsorbed organic compounds.

One of the most widely used semiconductor photocatalysts at present is TiO_2, due to its good chemical and thermal stabilities, low cost, innocuousness, and relatively high photocatalytic activity [7–9]. As evidenced by a wide number of publications that have appeared in the past 20 years, the photocatalytic degradation of VOCs on TiO_2 mainly involves three aspects:

i. Given that TiO_2 possesses the relatively large band gap (3.2 eV) so that only UV radiation can activate it, many modification methods, including ion doping and semiconductors coupling, are developed on TiO_2 to use low-energy photons available in the visible spectral region. In the meantime, efforts have been made to enhance its photocatalytic performance by increasing the electron–hole pair separation and/or specific surface area.

ii. Photocatalytic reactor development, as an engineering approach to enhance the efficiency of degradation of VOCs, involves updating existing fixed and flow bed reactors, and designing new reactors.

iii. Various researchers were dedicated to interpreting the mechanism and kinetics of photocatalytic degradation of VOCs. Since the photocatalytic degradation of VOCs is a complicated process and critically depends on the temperature, humidity level, pressure, and the composition of the reaction's gaseous environment, it is desirable to identify the mechanism to help researchers rational design new photocatalysts and reactors for better photocatalytic activities of degradation of VOCs.

Until now, the use of infrared (IR) spectroscopy has become one of the most powerful techniques to study the photocatalytic mechanism of degradation of VOCs with the advent of in situ accessories [10,11]. A greater variety of important information about the nature of adsorbed molecules and reaction intermediates can be obtained by using IR. In many cases, it has been possible to establish relationships between surface properties of photocatalysts, interactions of interfacial species, and the changes of these species and the photocatalytic activities. The improved understanding obtained from such in situ IR characterizations has led to the developments of new photocatalysts and better understanding of photocatalytic processes. We have also noticed that some reviews and books had highlighted the representative examples in this field [12,13]. Given that the mechanism of photocatalytic degradation of VOCs on TiO_2 is still a challenging issue, herein, we review several aspects of our current understanding of the role of TiO_2 in the degradation of VOCs by using in situ diffuse reflectance infrared Fourier transform spectroscopy (DRIFTS). Special interest is taken in describing the interaction of TiO_2 surfaces with vapor organic molecules and other species, considering that

the target pollutants, humidity level and oxygen play an important role in TiO$_2$ photocatalysis in gaseous. A summary of the remaining challenges and prospects of in situ IR for photocatalytic air purification investigation is also given.

2. In situ DRIFTS technique and related accessories

IR is the vibrational technique based on the interaction of electromagnetic radiation with species that possess a permanent or induced dipole moment and the excitation of different vibrational states [14]. The test forms of IR mainly include transmission/absorption spectroscopy, internal reflection spectroscopy (IRS) which is well known for attenuated total reflection (ATR), and DRIFTS. In principle, DRIFTS is most suitable for in situ measurements of gas–solid interface reaction, especially for photocatalytic degradation of VOCs on solid photocatalysts, because it can collect and analyze the surface-reflected electromagnetic radiation carrying surface and interfacial information. As shown in **Figure 1**, the regular and specular reflection from the photocatalyst powders with infrared beam incidence can be obtained by using a particular reflection light collector. Moreover, this collection mode allows the introduction of gaseous species to the surface of the photocatalysts so that the in situ experimental condition can be achieved [10,15].
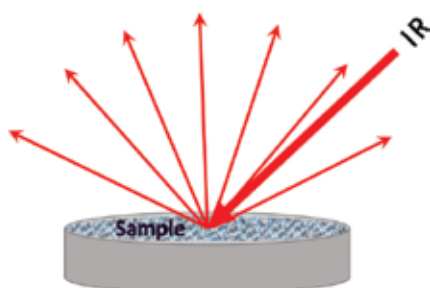
Figure 1. Basic scheme of DRIFTS technique.

Generally, an in situ DRIFTS experimental apparatus consists of one reaction cell, one diffuse reflectance accessory, and one gas-dosing system. A typical design of the diffuse reflectance accessory with on-axis geometry (**Figure 2**) has a higher optical efficiency than the other designs, off-axis accessory and integrating spheres [16]. However, one major drawback of on-axis geometry is that much of the front-surface reflection is collected along with the diffusely reflected reflection that has penetrated into the sample before reemerging from its top surface. It means that bands become distorted, and the ratio of the absorption coefficient and the scattering coefficient versus concentration becomes nonlinear at low concentration [16]. All specularly reflected radiation can be eliminated by accessories with off-axis design (**Figure 3a**). In this case, it should be pointed out that band shapes are more symmetrical, apart from the contribution of compensation by the Kubelka–Munk transform,

$$f(R) = (1 - R)^2/2R = 2.3ac/s,$$

where R is absolute reflectivity, a is absorbance, c is concentration, and s is scattering coefficient.
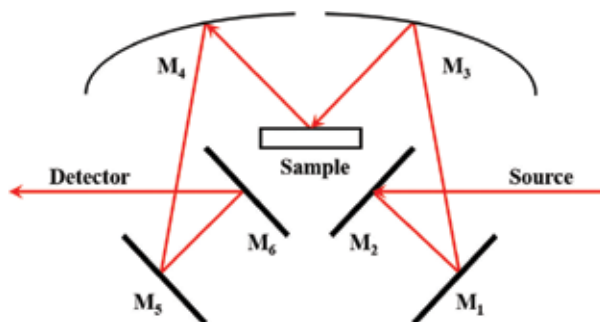
Figure 2. The principle of DRIFTS accessory with on-axis optical geometry. M_1, M_2, M_5, and M_6 are plane mirrors, while M_3 and M_4 are opposed ellipsoids (©2007 John Wiley & Sony Inc. [16]).

Commercial DRIFTS accessories usually consist of the reaction cell covered by a dome with three windows (**Figure 3b,c**) for solid–gas interfacial investigation in photocatalysis. Two of them are IR-transparent windows for the spectrometer infrared beam to enter and exit the cell, while the third one allows for observation or irradiation by excitation light source on photo-catalysts. IR-transparent windows can be made of KBr, ZnSe, and CaF_2 for mid-infrared test, and polyethylene (PE), Ge, and Si for far-infrared test, respectively. Quartz is the common material for viewing window.
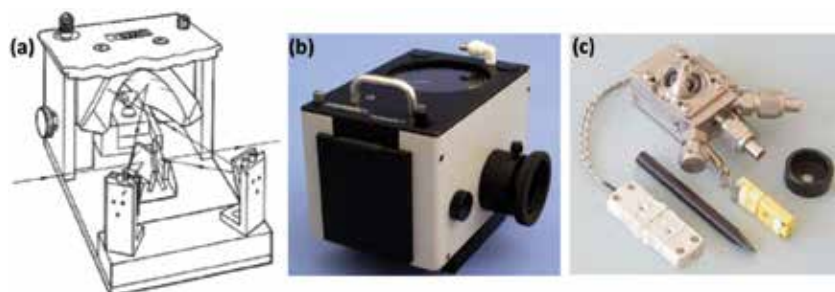
Figure 3. (a) Interior view of Harrick Scientific's Praying Mantis DRIFTS accessory with off-axis design, and images of (b) Harrick Scientific's DRIFTS accessory product, and (c) reaction cell enclosed with a dome with three windows. The cell enables a reaction gas to be introduced and reacted with the sample so that the reaction can be studied in situ.

In situ experimental conditions can be achieved by coupling the gas-dosing system with DRIFTS accessory and its cell. Photocatalytic air purification, compared with degradation in aqueous, water splitting and CO_2 reduction, seldom uses commercial gas-dosing systems to meet the requirement of DRIFTS investigation, because the gas-dosing system should offer each reaction gas with different concentrations, flow rates and humidity levels in a wide range,

and different residual gas absorbers for different VOCs. Therefore, the gas-dosing system was always built by independent groups. **Figure 4** shows the schematic diagram of the gas-dosing system for photocatalytic air purification and in situ DRIFTS measurements by Zhang et al. [17,18]. Take toluene for example; mass flow controllers were used to control the 20 vol% O$_2$/N$_2$ compressed air which carried toluene vapor from the saturator containing toluene. The water vapor was supplied to the cell via a bypass line. Argon (Ar) was used as purging gas. In the experiment, the accurate concentration of toluene was analyzed by gas chromatography. The relative humidity (RH%) in the cell was determined using an electronic hygrometer fixed in the bypass line. The whole system operating interface has been renovated based on the previous study for convenience and user-friendliness (**Figure 5**).
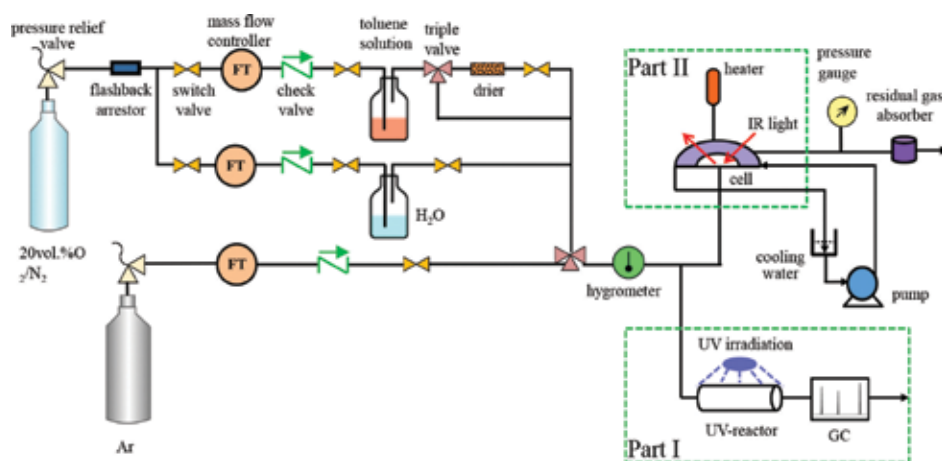
Figure 4. Schematic diagram of the gas-dosing system for (Part I) the photocatalytic activity and (Part II) in situ DRIFTS (©2015 Elsevier [17]).

Figure 5. Images of the operating interface of reaction gas-dosing system for in situ DRIFTS test (©2014 Springer [18]).

The setup reported by Deveau et al. [23–25]. But describing in situ IR cells and gas-dosing system in DRIFTS investigation in photocatalysis is the scope of the present view. It can be concluded that although DRIFTS provides a useful means for gathering information concerning the photocatalytic air purification, it is still on the initial stage, both for in situ cells and gas-dosing systems.

3. In situ DRIFTS investigation of photocatalytic degradation of VOCs on TiO$_2$

Although many studies have focused on photocatalytic degradation of VOCs on TiO$_2$, the reaction mechanism and a comprehensive picture of the adsorption structure and degradation route are unclear or remain controversial. In principle, the photogenerated e$^-$ and h$^+$ can directly initiate redox reaction with surface-adsorbed molecules of VOCs: electron donors (D$_{ads}$) and acceptor (A$_{ads}$) on TiO$_2$, respectively. If multiple kinds of electron donors (D$_{ads}$) and/or acceptor (A$_{ads}$) are present on the surface, however, the e$^-$ and h$^+$ may be trapped to form secondary radicals which further react with the target VOCs. For pure TiO$_2$, its surface coordinatively unsaturated Ti^{4+} and O^{2-} species allow dissociative chemisorption of molecular water to satisfy the coordination of Ti^{4+} and O^{2-} sites, making the surface of TiO$_2$ hydroxylated [31–33], making the air purification complex. Here, some representative works in recent years and several examples from our group are discussed.

3.1. Degradation of toluene

Reports have shown that surface hydroxyl groups formed by water vapor interacting with TiO$_2$ surface can easily affect the adsorption and photocatalytic processes of toluene degradation. Augugliaro and coworkers [34] carried out the toluene and toluene/water adsorption experiments on TiO$_2$ samples. The corresponding IR spectra are shown in **Figure 6**. Curve a is the spectrum of the TiO$_2$ powder pre-outgassed at room temperature, exhibiting a peak at 3665 cm^{-1} and a very broad adsorption in the high wavenumber region. These components can be assigned to the stretching mode of free hydroxyl groups, hydrogen-bonded OH groups, and water molecules coordinated to surface Ti^{4+}. In contact with toluene, the band at 3665 cm^{-1}, due to the free hydroxyl groups, completely disappeared, indicating that free hydroxyl groups are effective Lewis acid adsorption sites for toluene, and a new broad and complex band appeared at lower wavenumber region, the shift resulting from the interaction between the OH groups and the π electrons of the aromatic molecules. In addition, peaks due to adsorbed toluene appeared in the 3100–2800 cm^{-1} (CH stretching) and 1610–1360 cm^{-1} (ring stretching, CH deformation) ranges. After short outgassing at room temperature, the bands of the adsorbed toluene disappeared, and the characteristic bands of the free OH species were completely restored (curve c), indicating that the interaction between aromatic molecules and hydroxyl group is quite weak and fully reversible.
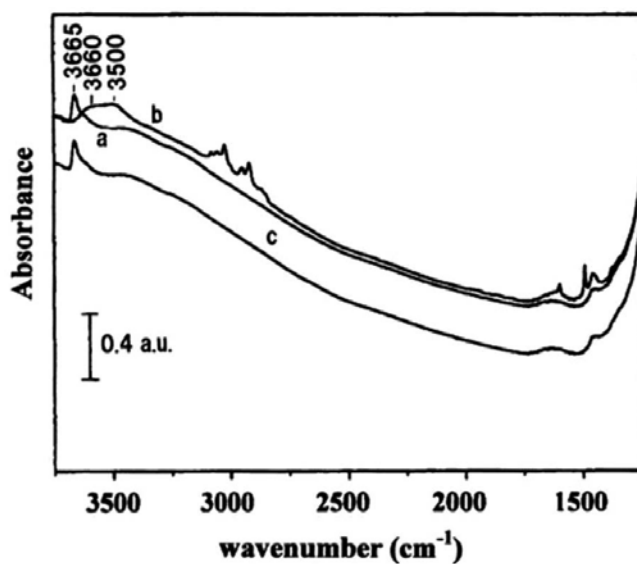
Figure 6. IR spectra of TiO$_2$: (a) outgassed at room temperature for 45 min; (b) in contact with 3 Torr toluene; (c) after 5 min re-outgassing at room temperature (©2015 Elsevier [34]).
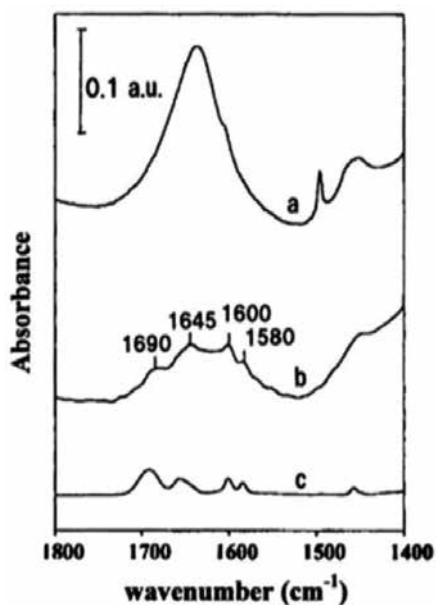
Figure 7. IR results for the photo-oxidation of toluene on the TiO$_2$ pre-outgassed at room temperature. IR spectra of TiO$_2$: (a) in the presence of the toluene/H$_2$O/O$_2$ mixture, (b) after 10 min UV irradiation and subsequent outgassing at room temperature for 45 min, (c) in the presence of benzaldehyde (©2015 Elsevier [34]).

Then they investigated toluene photocatalytic oxidation on two TiO$_2$ samples with different surface hydration states: one pre-outgassed at room temperature and the other pre-outgassed at 873 K without the occurrence of the anatase–rutile phase transition. **Figure 7** shows the results of the toluene photocatalytic oxidation experiment obtained in the case of TiO$_2$ pre-outgassed at room temperature. After exposing TiO$_2$ to the toluene/H$_2$O/O$_2$ mixture, bands due to adsorbed water (peak at 1640 cm^{-1}) and aromatic molecules (signals at 1600, 1496, and 1460 cm^{-1}) were observed (**Figure 7a**). After irradiation, a slight decrease in the toluene bands at 1496 and 1460 cm^{-1} was observed, while new bands appeared (**Figure 7b**). This suggested that a fraction of toluene transformed to a new species under UV irradiation. Finally, they found that the main oxidation product of toluene was benzaldehyde. In the case of the dehydroxylated TiO$_2$, the admission of the toluene/H$_2$O/O$_2$ mixture onto the TiO$_2$ produced bands due to physically adsorbed water and toluene molecules (**Figure 8a**). Nevertheless, after UV irradiation, traces of bands due to benzaldehyde were hardly recognizable in the spectrum (**Figure 8c**). Compared with the fully hydroxylated TiO$_2$, the dehydroxylated one exhibited strongly reduced photocatalytic activity, confirming that surface OH groups play an important role in the photocatalytic oxidative process.
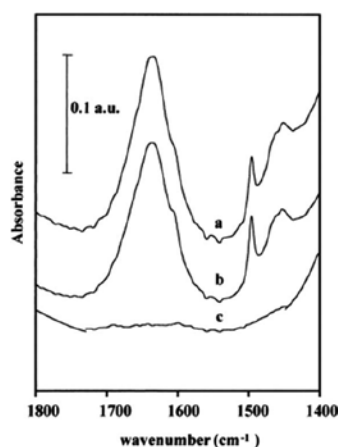
Figure 8. IR results for the photo-oxidation of toluene on the TiO$_2$ pre-outgassed at 873 K. IR spectra of TiO$_2$: (a) in the presence of the toluene/H$_2$O/O$_2$ mixture, (b) after exposure to the UV light for 10 min, (c) after subsequent outgassing at room temperature for 45 min (©2015 Elsevier [34]).

Maira et al. [35] studied the photocatalytic activities of TiO$_2$ which are prepared by thermal and hydrothermal methods, respectively, for the gas-phase photocatalytic oxidation of toluene. A comparative IR study of the surface structure of the samples was also conducted. **Figure 9** shows the results of photocatalytic oxidation of toluene on the TiO$_2$ prepared by thermal method. Upon adsorption of toluene, the bands (3630, 3674, and 3687 cm^{-1}) of the isolated hydroxyl groups were replaced by a broad band centered at 3550 cm^{-1} (**Figure 9c**), indicating that toluene was mainly adsorbed on the isolated hydroxyl groups at the TiO$_2$ prepared by thermal method. The irradiation of TiO$_2$ under H$_2$O/O$_2$ condition (**Figure 9d**) caused a slight decrease of the bands due to the adsorbed toluene (3085, 3066, 3027, 3927, and

2872 cm^{-1}) and the formation of several small bands due to benzaldehyde in the 1900–1100 cm^{-1} range. The band at 1682 cm^{-1} was attributed to the carbonyl vibration of the aldehyde group, and the bands at 1641, 1595, and 1580 cm^{-1} may arise from the different vibrational modes of the aromatic ring. After a subsequent outgassing at room temperature (**Figure 9e**), the 3550 cm^{-1} band and the bands due to adsorbed toluene practically disappeared, and the bands of isolated hydroxyls were partially recovered. This indicated that toluene was weakly adsorbed on the hydroxyls. In addition, the decrease of the bands due to benzaldehyde indicated that a small amount of benzaldehyde was also desorbed. After exposing the treated sample to water vapor and subsequent irradiation, the bands due to benzaldehyde reduced but did not disappear. Toluene adsorption on the TiO$_2$ prepared by hydrothermal method resulted in several changes. Toluene was adsorbed not only on the isolated hydroxyls, but also on the H-bonded hydroxyls. The irradiation of TiO$_2$ under H$_2$O/O$_2$ condition caused decrease of toluene and hydroxyl species, and formation of benzaldehyde. A subsequent outgassing of the sample resulted in the disappearance of the bands related to toluene adsorption and a slight decrease of the adsorbed benzaldehyde bands. By considering the photocatalytic activity of these two samples and the IR results, they concluded that the interaction of toluene with the hydroxyl groups of isolated types mainly leads to the formation of benzaldehyde, while the interaction with H-bonded hydroxyls leads to nearly complete degradation. Both types of hydroxyl groups are lost during the reaction, which produces a decrease in the photocatalytic degradation of toluene. The photocatalytic degradation of toluene adsorbed on H-bonded hydroxyls can be regenerated in the presence of water vapor.
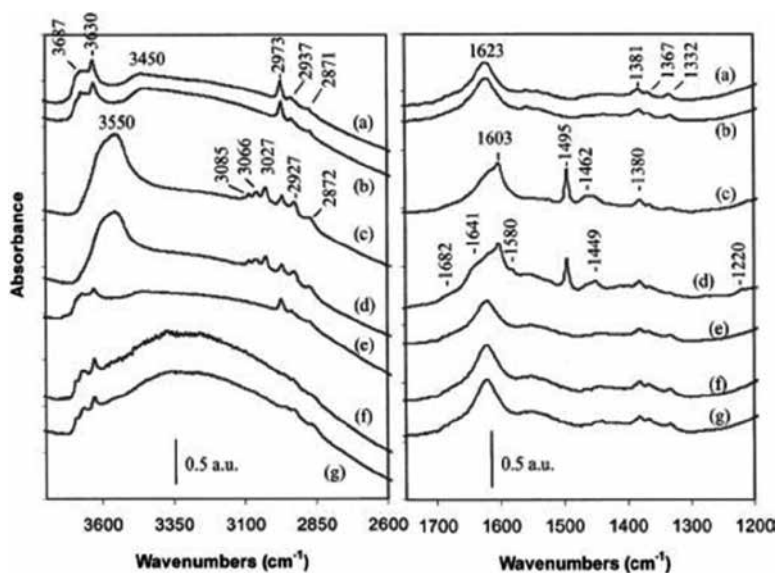
Figure 9. IR spectra of TiO$_2$ prepared by thermal method after the following treatments performed at room temperature: (a) evacuation for 15 min, (b) evacuation for 2 h, (c) introduction of 5 Torr of toluene into IR cell and subsequent introduction of 50 Torr of oxygen, (d) irradiation for 30 min, (e) evacuation of the sample for 15 min, (f) introduction of 5 Torr of H$_2$O into the cell, and (g) irradiation for 30 min (©2001 Elsevier [35]).
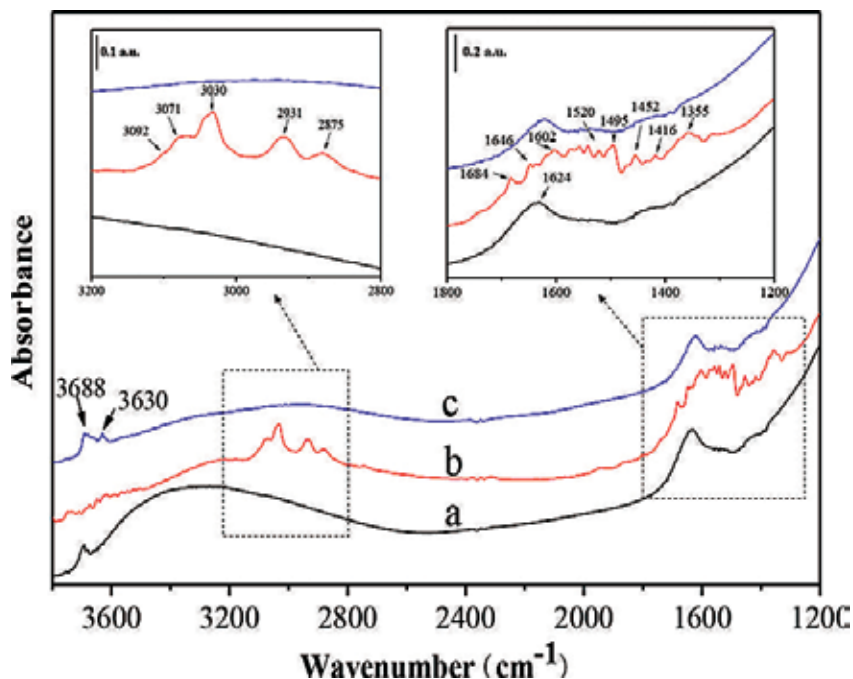
Figure 10. In situ DRIFTS spectra of (a) fresh Fe–TiO₂, (b) Fe–TiO₂ used for 20 consecutive reaction runs, and (c) Fe–TiO₂ after heat-treatment at 653 K for 3 h (©2012 Elsevier [40]).

Ibusuki et al. [37–39]. Our group has also carried out some research on the photocatalytic degradation of toluene by using in situ DRIFTS. Sun et al. [40] found that the Fe–TiO₂ photocatalyst was partially deactivated after 20 consecutive reaction runs. A DRIFTS experiment was then performed to investigate the deactivation mechanism, and the results are shown in **Figure 10**. From **Figure 10a**, the surface of a fresh photocatalyst was relatively clean. After 20 consecutive reaction runs, many new bands appeared (**Figure 10b**). The bands at 3092, 3071, 3030, 2931, 2875, 1646, 1602, 1495, 1452, and 1355 cm^{-1} were due to the adsorbed toluene on the surface of the photocatalyst. The band at 1684 cm^{-1} was attributed to the carbonyl vibration of the aldehyde group, and the bands at 1520 and 1416 cm^{-1} may arise from the asymmetric and symmetric vibrations of the COO$^-$ group. This result indicated that the intermediates benzaldehyde and benzoic acid were formed during the photocatalytic degradation of toluene. After heat treatment at 653 K for 3 h in air, the bands of benzaldehyde and benzoic acid disappeared completely (**Figure 10c**). From this experiment, the reason for deactivation was attributed to the formation of stable intermediates, such as benzaldehyde and benzoic acid, which occupied the active sites on the surface of the photocatalyst. These intermediates can be removed with heat treatment at 653 K for 3 h, and the deactivated photocatalyst can be regenerated completely.
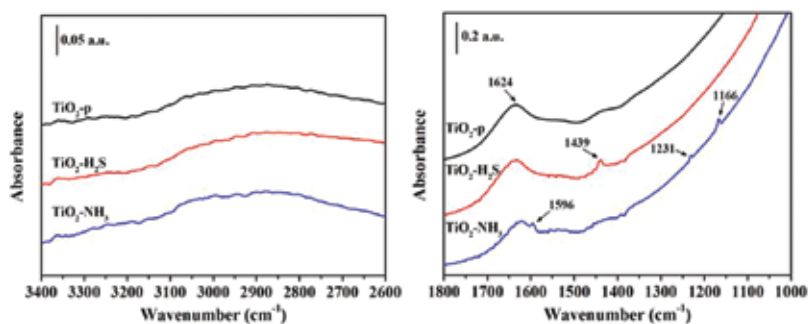
Figure 11. DRIFTS spectra of TiO$_2$–p, TiO$_2$ modified with H$_2$S, and TiO$_2$ modified with NH$_3$ (©2015 Elsevier [17]).
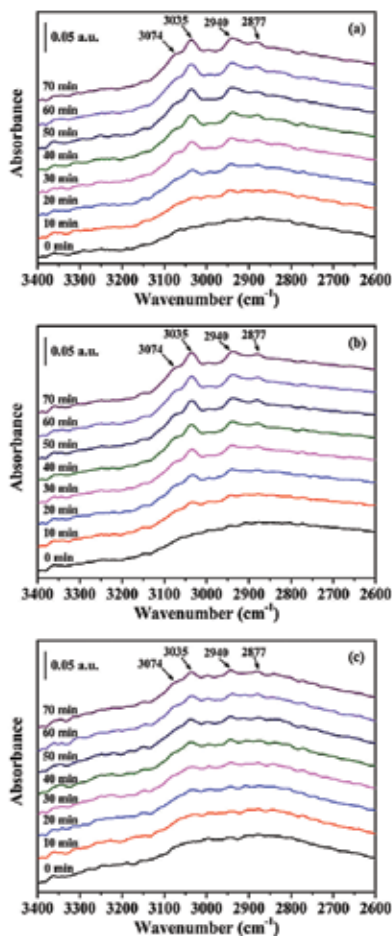
Figure 12. In situ DRIFTS spectra of toluene adsorption on (a) TiO$_2$–p, (b) TiO$_2$–H$_2$S, and (c) TiO$_2$–NH$_3$ photocatalysts (©2015 Elsevier [17]).

In order to understand the influences of H_2S/NH_3 species on the photocatalytic degradation of toluene on TiO_2, Zhang et al. [17] investigated the adsorption and photocatalytic degradation of gaseous toluene on TiO_2 surface modified with H_2S and NH_3 species. **Figure 11** shows the DRIFTS spectra of the samples. The surface of fresh TiO_2 (TiO_2-p) was relatively clean. A small band attributed to the bending vibration of δ(H–S) was observed at 1439 cm^{-1} (curve TiO_2–H_2S), suggesting the presence of sulfhydryl on the TiO_2–H_2S surface. In the curve TiO_2–NH_3, the band at 1596 cm^{-1} was attributed to the coordinated NH_3, and the bands at 1231 and 1166 cm^{-1} were due to the symmetric deformation of NH_3. **Figure 12** shows the DRIFTS spectra of toluene adsorbed on the samples. After toluene was introduced, the characteristic bands of toluene (3074, 3035, 2940, and 2877 cm^{-1}) appeared. The intensities of these bands on TiO_2–NH_3 were obviously weaker than those on TiO_2–H_2S and TiO_2–p after 70 min of adsorption, indicating that the adsorption capacity of TiO_2–NH_3 for toluene is smaller than those of TiO_2–p and TiO_2–H_2S. After the adsorption of toluene reached equilibrium, the samples were irradiated by UV light (**Figure 13**). In the high wavenumber region, the characteristic bands of toluene decreased in different degrees for all the samples, indicating that adsorbed toluene was decomposed. In the low wavenumber region, many bands of benzaldehyde and benzoic acid appeared, and these bands on TiO_2–H_2S were significantly strengthened, suggesting that there were more intermediates on TiO_2–H_2S. Combined with the results of photocatalytic activity and other characterizations of the samples, it is concluded that surface modification with H_2S enhanced the adsorption of toluene and promoted the degradation rate at the start of photocatalytic degradation, while that with NH_3 inhibited the adsorption of toluene but enhanced the photocatalytic activity for the degradation of toluene. For TiO_2–H_2S, the sulfhydryl group formed from the dissociation of H_2S molecules was favorable for toluene adsorption. The low photocatalytic activity may be caused by the inhibition of the regeneration of surface hydroxyl groups, poor generation of $O^{2-}\bullet$ radicals, and accumulation of highly stable intermediates. For TiO_2–NH_3, steric hindrance interfered with the adsorption of toluene, while the abundant surface hydroxyl groups were likely to contribute to the degradation of toluene.
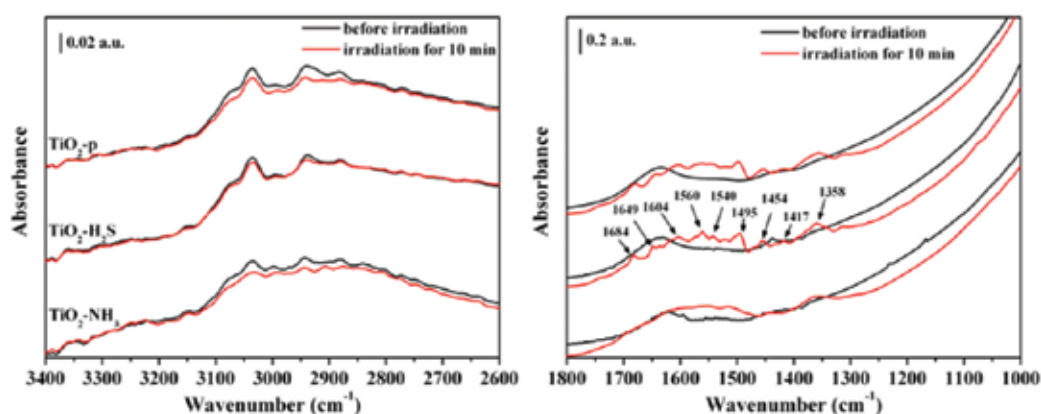
Figure 13. In situ DRIFTS spectra of toluene oxidation on (a) TiO_2–p, (b) TiO_2–H_2S, and (c) TiO_2–NH_3 photocatalysts with UV irradiation (©2012 Elsevier [17]).
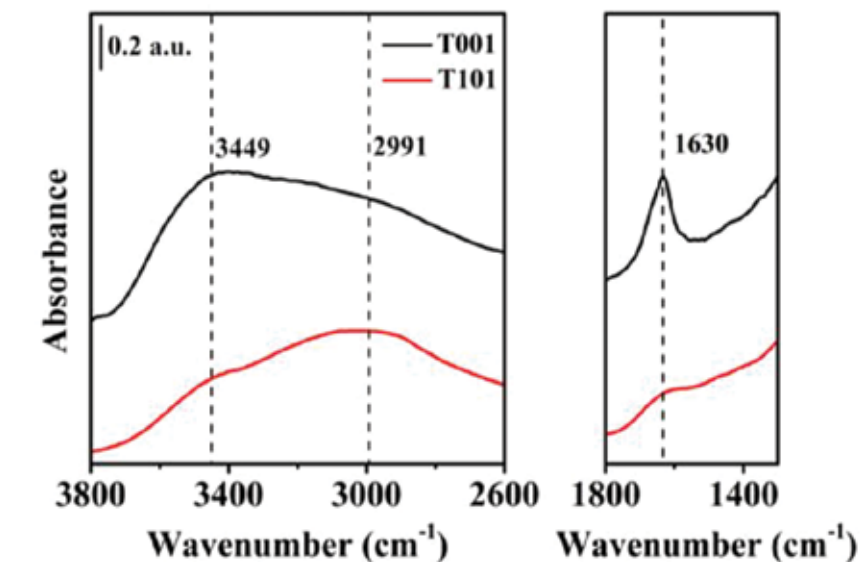
Figure 14. DRIFTS spectra of pure T001 and T101 (©2015 American Chemical Society [41]).

Wang et al. [41] identified the facet-dependent adsorption of toluene on TiO_2 by using an in situ DRIFTS apparatus. **Figure 14** shows the DRIFTS spectra of TiO_2 with dominant {001} facets (T001) and TiO_2 with dominant {001} facets (T101) before toluene adsorption. The bands at 3449, 2991, and 1630 cm^{-1} were assigned to O–H stretching mode of the terminal Ti–OH, adsorbed water Ti–OH_2 species, and H–O–H bending mode of free molecularly adsorbed water, respectively. The intensities of these bands suggested that the hydroxyl groups tend to be formed as terminal Ti–OH on the {001} facets and the {101} facets favor the formation of adsorbed water Ti–OH_2 species. Additionally, there is a large amount of free water on the {001} facets. **Figure 15** shows the in situ DRIFTS spectra of toluene adsorbed on T001 and T101. After toluene was introduced, the characteristic bands of toluene appeared. The positions of these bands on T101 were red-shifted slightly, compared to that on T001, which may be attributed to the different Ti^{4+} adsorption sites on {001} and {101} facets for toluene adsorption. The toluene adsorption increased more rapidly on {001} facets and the adsorption process was typically in accordance with Langmuir−Hinshelwood model of first-order reaction, while the adsorption process on {101} facets was in accordance with the two-step kinetic equation. The distinction of the adsorption capability was probably due to the different number of unsaturated 5c-Ti, capable of forming the main active adsorption sites (terminal Ti−OH species). During the photocatalytic degradation of toluene, TiO_2 with dominant {001} facets showed a significantly high photocatalytic activity. This outstanding performance was mainly attributed to the high adsorption ability and the preservation of the free molecularly adsorbed water, which can be dissociated to form hydroxyls and further promote the degradation.
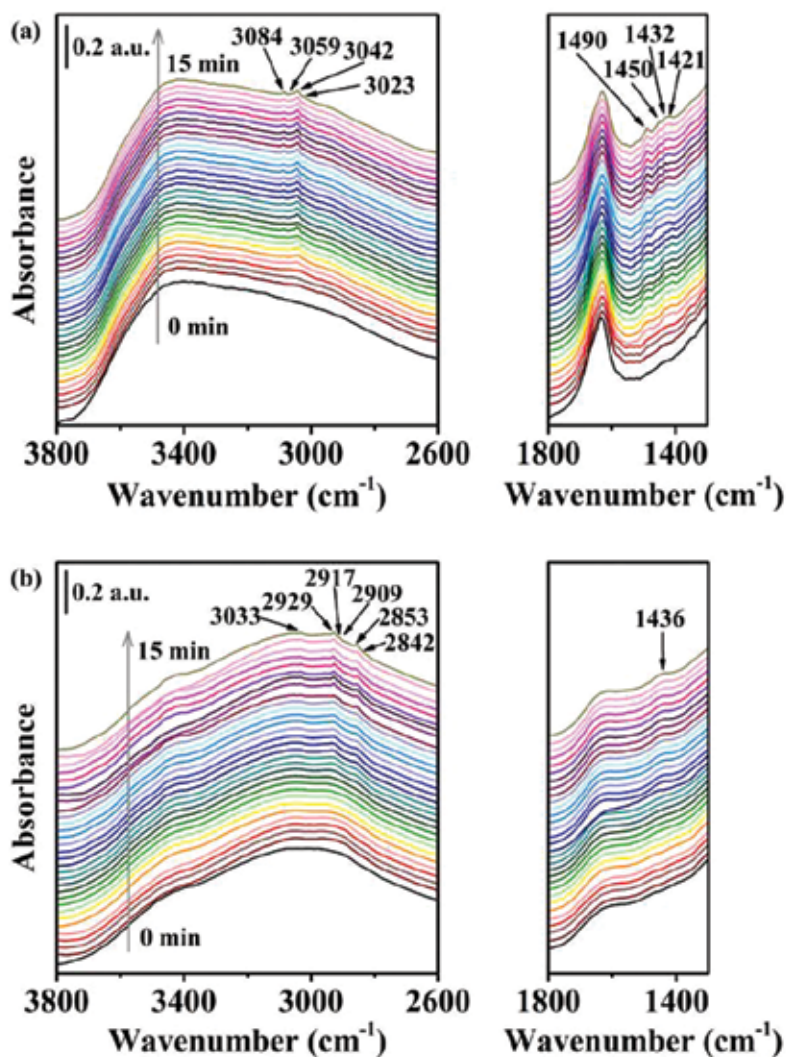
Figure 15. In situ DRIFTS spectra of toluene adsorption on (a) T001 and (b) T101 (©2015 American Chemical Society [41]).

3.2. Degradation of formaldehyde

The adsorption and photocatalytic oxidation of formaldehyde have been frequently studied on TiO_2 with metal co-catalyst. The related mechanisms have also been investigated by in situ IR. In these cases, it was noteworthy that the formate species did not appear on pure TiO_2 without UV irradiation, indicating that the noble metal addition promoted the formation of formate species [42,43]. However, a few literature paid attention to the photocatalytic degradation process of formaldehyde on TiO_2. In the adsorption process, the interaction between

formaldehyde and the hydroxyl groups depends on hydrogen bonding. As shown in **Figure 16** [44], when water vapor was introduced, a large part of weakly adsorbed water can be detected from the broad band in the 3600–3050 cm^{-1} range and the band at 1652 cm^{-1}. However, no obvious difference about formaldehyde adsorption appears, because even in the dry condition, TiO$_2$ can provide the hydroxyl sites from dissociative chemisorption of water onto the Ti^{4+} sites.
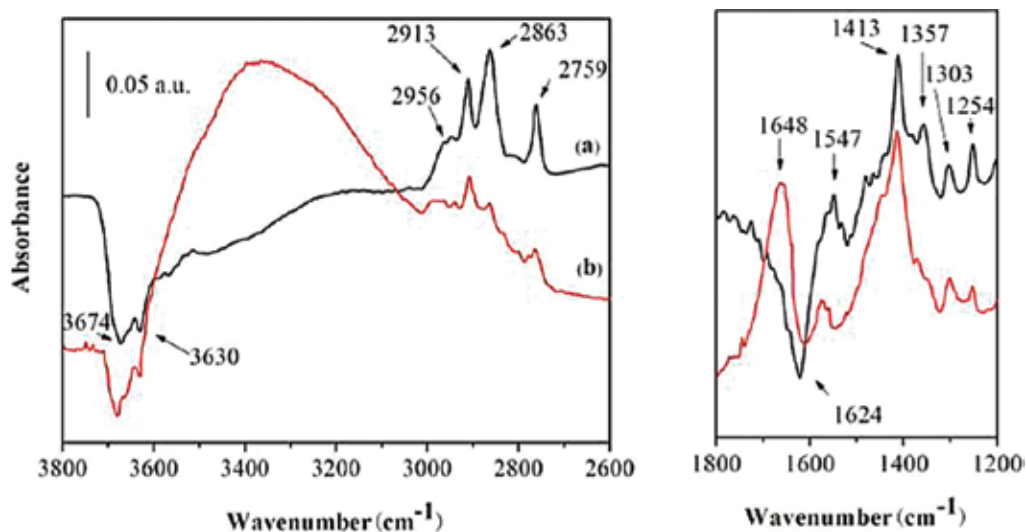
Figure 16. Differential spectra of TiO$_2$ after 30 min adsorption in (a) dry and (b) humidity condition (©2010 Springer [44]).

It yields significant difference after introduction of UV irradiation (**Figure 17**). In the dry condition, the bands at 2956, 2913, 2759 cm^{-1} decreased, and almost disappeared after UV irradiation for 30 min, while the bands at 2863 cm^{-1} decreased slowly relatively. All of these bands can be assigned to the C–H stretching mode υ(C–H) of formaldehyde. The small bands at low frequency (1551, 1413, 1357, 1303, and 1254 cm^{-1}) were also decreased. Meanwhile, two strong bands at 1572 and 1361 cm^{-1} appeared and reached a steady level after 30 min. The two bands could be assigned to asymmetric and symmetric υ(COO) on TiO$_2$ sites, respectively. These spectra suggest that the adsorbed formaldehyde converts to formate species on TiO$_2$. In the humidity condition, according to the changes of the integrated areas of the bands as a function of time for TiO$_2$ under UV irradiation, the characteristic bands of formaldehyde decrease more quickly along with quick increasing of formate species. In other words, the introduction of water promotes the conversion of adsorbed formaldehyde to formate species. It can be attributed to the fact that oxidation of water and hydroxyl groups by the photogenerated holes produces very active OH• radicals that take part in the redox reactions and improve significantly the mineralization rate of formaldehyde.
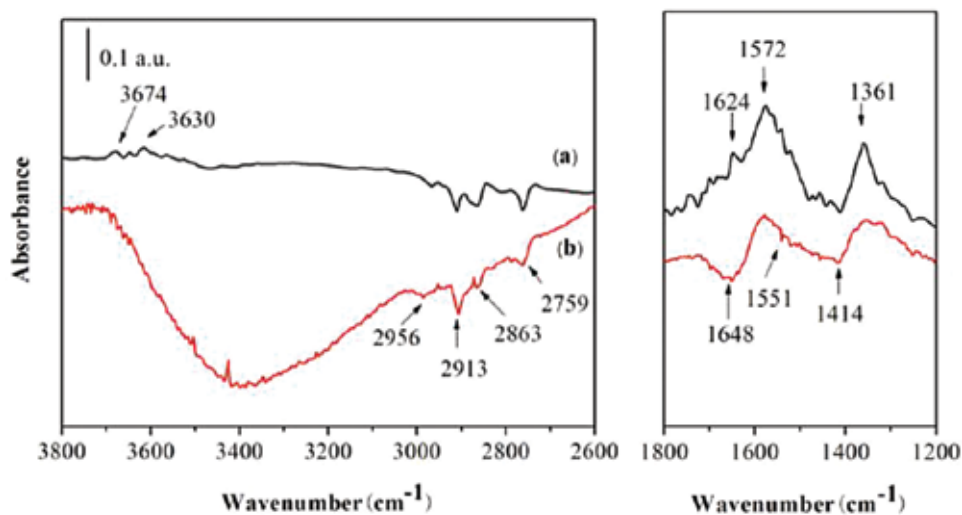
Figure 17. Differential spectra of TiO_2 without UV irradiation to the spectra under 30 min UV irradiation for (a) dry and (b) humidity condition (©2010 Springer [44]).

It should be pointed out that water produced during the photocatalytic process can redistribute on the surface in the form of different hydroxyl groups and further contribute to the degradation of formaldehyde. But, excessively high concentration of water vapor negatively affects the degradation efficiency because of the competitive adsorption between water and formaldehyde [46–48].

3.3. Degradation of other VOCs

The adsorption and photocatalytic oxidation of ethanol and acetone vapor on TiO_2 have been studied by Coronado et al. [49] using in situ DRIFTS. The in situ DRIFTS spectra obtained during the photocatalytic oxidation of ethanol and acetone vapor over TiO_2 powder are shown in **Figures 18** and **19**, respectively.

They found that ethanol was adsorbed on the TiO_2 surface either molecularly or in the form of ethoxide complexes. Acetates (the bands at 1540 and 1440 cm^{-1} can be assigned to the asymmetric and symmetric $\upsilon(COO)$, respectively, of acetate complexes) and formates (the band at 1360 cm^{-1} can be attributed to the symmetric $\upsilon(COO)$ mode of formate species) were intermediates during the photocatalytic oxidation of ethanol. In the case of acetone, it was suggested to be adsorbed exclusively in a molecular form on TiO_2. Acetates and formates were detected as the major intermediates and secondary intermediates, respectively. Adsorbed acetaldehyde (the peak at 1715 cm^{-1} can be assigned to the $\upsilon(C=O)$ vibration mode of aldehyde, and the band at 2870 cm^{-1} is characteristic of the $\upsilon(C–H)$ vibration of aldehyde molecules) and formic acid (the shoulder at 1745 cm^{-1} can be ascribed to the dimeric form of formic acid) were also observed. They suggested that the hydroxyl groups on the TiO_2 surface play a key role in the photocatalytic degradation of ethanol and acetone. However, Mattsson et al. [50] found

that the bidentate bridged formate and carbonate were the main intermediates during the photocatalytic degradation of acetone on TiO$_2$.
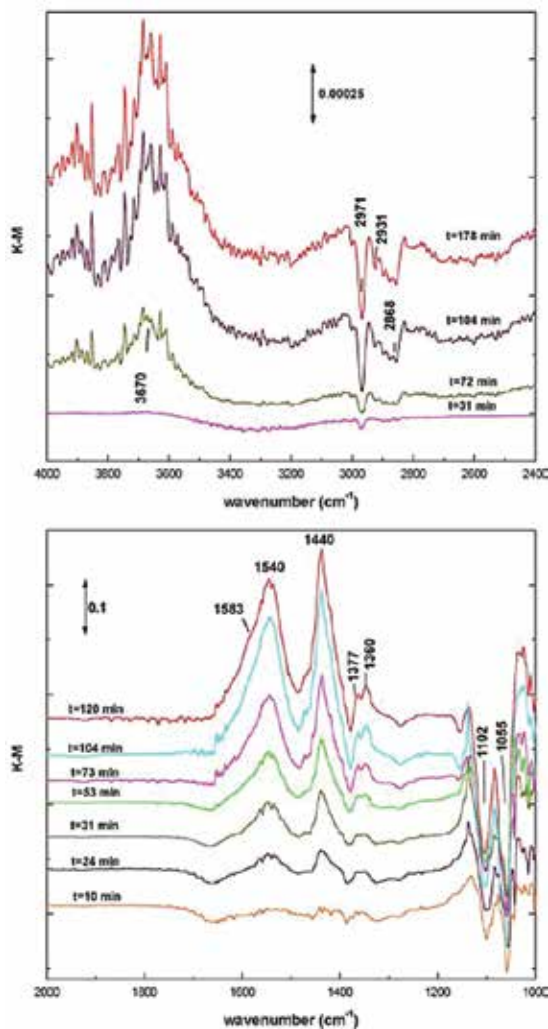
Figure 18. In situ DRIFTS spectra obtained during the photocatalytic oxidation of ethanol vapor over TiO$_2$ powder (© 2003 Elsevier [49]).

The illuminated TiO$_2$ surfaces, in the presence of methanol, were studied using in situ DRIFTS by Balcerski [51]. It was found that the irradiation of TiO$_2$ in the presence of methanol and O$_2$ produced H$_2$O, CO$_2$, and surface-bound formic acid.

An in situ DRIFTS study of acetic acid adsorption and photocatalytic oxidation on TiO$_2$ by Backes et al. [52] suggested that acetic acid adsorbed both molecularly and dissociatively as acetate on TiO$_2$. Molecularly adsorbed acetic acid was oxidized by first generation acetate.

During the photocatalytic oxidation of acetic acid on TiO_2, the α-carbon in acetate directly formed CO_2, whereas the β-carbon formed CO_2 through intermediates, such as methoxy, formaldehyde, and formate.
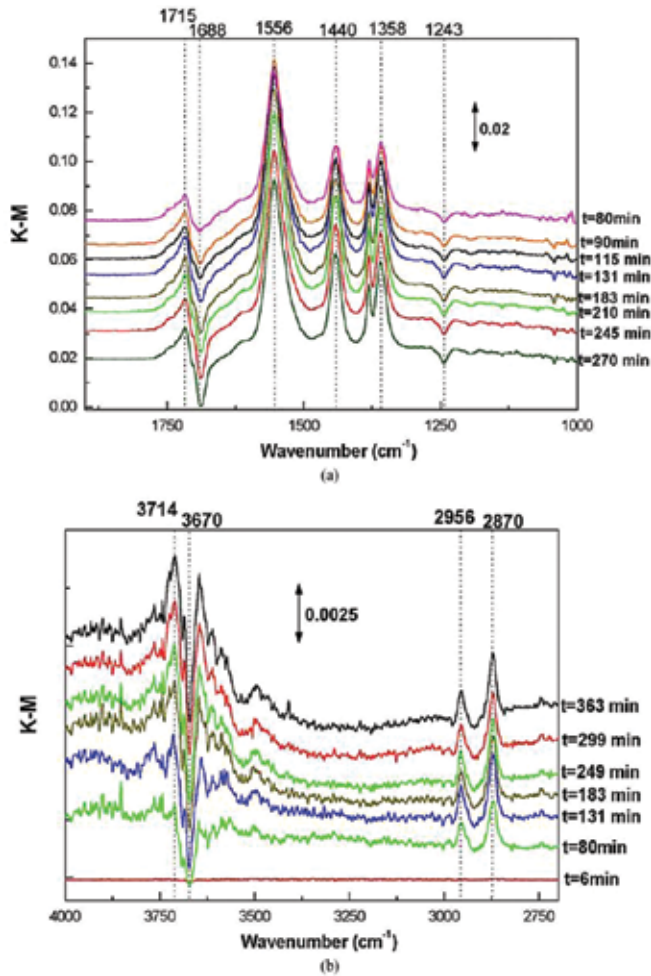
Figure 19. In situ DRIFTS spectra obtained during the photocatalytic oxidation of acetone vapor over TiO_2 powder (© 2003 Elsevier [49]).

A comparative study of the photocatalytic degradation of trichloroethylene on titanate and TiO_2 nanostructures was reported by Hernández-Alonso et al. [53]. In this study, in situ DRIFTS approach was adopted for surface analysis. They found that at least three different carboxylate species with different kinds of coordination symmetry (e.g., bridged dichloroacetate, bidentate formate, etc.) were present on the surface of the samples. The main difference between TiO_2 and nanotubes was suggested to be the larger proportion of formate species for the nanotubes. Moreover, the nanotube samples showed selective removal of some specific hydroxyl groups,

which may be due to the accumulation of carboxylate complexes (mainly dichloroacetate and formate) and/or chloride on the surface.

4. Summary and outlook

It has been demonstrated that VOCs can be efficiently photocatalytic-mineralized on TiO_2. This chapter reviewed a series of studies investigating the mechanism of photocatalytic degradation of VOCs on TiO_2 by using in situ DRIFTS. It involves in situ infrared techniques with the development of reaction cells, in situ accessories and gas-dosing systems, representative examples of spectral analyses, and special understanding of the adsorption and degradation processes. The nature of toluene, formaldehyde, and acetone, adsorbed and decomposed on TiO_2, has been obtained from in situ DRIFTS under simulated operating photocatalytic conditions. In general, surface hydroxyl groups are considered to be the major active species that the adsorption is taking place. Photogenerated charge carriers most likely react with these species to generate extremely powerful radicals which can further react with surface-adsorbed molecules of VOCs. Therefore, it drives the rising of some surface modification strategies, such as NH_3/H_2S treatment and facet engineering, to promote the performance of TiO_2. Considering that other factors, such as the oxygen adsorption, operating temperature, the initial concentration of VOCs, etc. also influence the adsorption and degradation, much work is needed to perform experiments in such conditions.

Although in situ DRIFTS is very useful to investigate the photocatalytic air purification, it should be recognized that the development of reaction cells and accessories lags behind the experimental demands. We noticed that exploiting the related accessories and gas-dosing systems is only facing limited consumer groups; therefore, it may be worthwhile expanding the success from the independent scientific group. Furthermore, coupling in situ DRIFTS with other characterization techniques, for example, gas chromatography and mass spectroscopy, is essential to obtain more kinetic information. It can be expected that further insights of in situ DRIFTS in photocatalytic air purification will be fruitful with huge amount of effort on the extension of the concept and development of instruments.

Author details

Song Sun[1*] and Fan Zhang[2]

*Address all correspondence to: suns@ustc.edu.cn

1 National Synchrotron Radiation Laboratory & Collaborative Innovation Center of Chemistry for Energy Materials, University of Science and Technology of China, Hefei, Anhui, China

2 Hefei Normal University, Hefei, Anhui, China

References

[1] Vilcekova S, Meciarova L, International Multidisciplinary Scientific Geoconference Surveying Geology and Mining Ecology Management. 2015;1:945–952.

[2] Sarigiannis DA, Karakitsios SP, Gotti A, Liakos IL, Katsoyiannis A, Environment International. 2011;37:743–765.

[3] Guo H, Lee SC, Chan LY, Li WM, Environmental Research. 2004;94:57–66.

[4] Wang S, Ang HM, Tade MO, Environment International. 2007;33:694–705.

[5] Lin L, Chai Y, Zhao B, Wei W, He D, He B, Tang Q, Open Journal of Inorganic Chemistry. 2013;3:14–25.

[6] Fujishima A, Rao TN, Tryk DA, Journal of Photochemistry and Photobiology C: Photochemistry Reviews. 2000;1:1–21.

[7] Dhada I, Nagar PK, Sharma M, Industrial & Engineering Chemistry Research. 2015;54:5381–5387.

[8] Chen H, Nanayakkara CE, Grassian VH, Chemical Reviews. 2012;112:5919–5948.

[9] Pelaez M, Nolan NT, Pillai SC, Seery MK, Falaras P, Kontos AG, Dunlop PSM, Hamilton JWJ, Byrne JA, O'Shea K, Entezari MH, Dionysioua DD, Applied Catalysis B: Environmental. 2012;125:331–349.

[10] Ryczkowski J, Catalysis Today. 2001;68:263–381.

[11] Lukaski AC, Muggli DS, Journal of Catalysis. 2004;223:250–261.

[12] Pichat P, Catalysis Today. 2014;224:251–257.

[13] Dolamic I, Bürgi T, Journal of Catalysis. 2007;248:268–276.

[14] Hunger M, Weitkamp J, Angewandte Chemie International Edition. 2001;40:2954–2971.

[15] Cao L, Gao Z, Suib SL, Obee TN, Hay SO, Freihaut JD, Journal of Catalysis. 2000;196:253–261.

[16] Griffiths PR, de Haseth JA, Fourier Transform Infrared Spectroscopy. 2nd ed. A John Wiley & Sony Inc. Publication; 2007.

[17] Zhang F, Wang M, Zhu X, Hong B, Wang W, Qi Z, Xie W, Ding J, Bao J, Sun S, Gao C, Applied Catalysis B: Environmental. 2015;170:215–224.

[18] Zhang F, Zhu X, Ding J, Qi Z, Wang M, Sun S, Bao J, Gao Ch, Catalysis Letters. 2014;144:995–1000.

[19] Deveau PA, Arsac F, Thivel PX, Ferronato C, Fe Delpech, Chovelon JM, Kaluzny P, CMonnet, Journal of Hazardous Materials. 2007;144:692–697.

[20] Kozlov DV, Paukshtis EA, Savinov EN, Applied Catalysis B: Environmental. 2000;24:L7–L12.

[21] Zheng C, Li X, Zhao Q, Qu Z, Quan X, Separation and Purification Technology. 2009;67:326–330.

[22] Hauchecorne B, Tytgat T, Terrens D, Vanpachtenbeke F, Lenaerts S, Infrared Physics & Technology. 2010;53:469–473.

[23] Xu J, Chen Q, Ji H, Progress in Chemistry. 2008;20:811–820.

[24] Wood J, Alldrick MJ, Winterbottom JM, Stitt EH, Bailey S, Catalysis Today. 2007;128:52–62.

[25] Zhang M, Zhang W, Xie W, Qi Z, Wu G, Lv M, Sun S, Bao J, Journal of Molecular Catalysis A: Chemical. 2014;395:269–275.

[26] Turchi CS, Ollis DF, Journal of Catalysis. 1990;122:178–192.

[27] Henderson MA, Surface Science Reports. 2011;66:185–297.

[28] Andreozzi R, Caprio V, Insola A, Marotta R, Catalysis Today. 1999;53:51–59.

[29] Quici N, Vera ML, Choi H, Puma GL, Dionysiou DD, Litter MI, Destaillats H, Applied Catalysis B: Environmental. 2010;95:312–319.

[30] Lee SL, Scott J, Chiang K, Amal R, Journal of Nanoparticle Research. 2009;11:209–219.

[31] Davit P, Martra G, Coluccia S, Journal of the Japan Petroleum Institute. 2004;47:359–376.

[32] Farfan-Arribas E, Madix RJ, Journal of Physical Chemistry B. 2003;107:3225–3233.

[33] Hadjiivanov KI, Klissurski DG, Chemical Society Reviews. 1996;25:61–69.

[34] Augugliaro V, Coluccia S, Loddo V, Marchese L, Martra G, Palmisano L, Schiavello M, Applied Catalysis B: Environmental. 1999;20:15–27.

[35] Maira AJ, Coronado JM, Augugliaro V, Yeung KL, Conesa JC, Soria J, Journal of Catalysis. 2001;202:413–420.

[36] Ibusuki T, Takeuchi K, Atmospheric Environment. 1986;20:1711–1715.

[37] Zhao J, Yang XD, Building and Environment. 2003;38:645–654.

[38] Li X, Zou X, Qu Z, Zhao Q, Wang L, Chemosphere. 2011;83:674–679.

[39] Méndez-Román R, Cardona-Martínez N, Catalysis Today. 1998;40:353–365.

[40] Sun S, Ding J, Bao J, Gao C, Qi Z, Yang X, He B, Li C, Applied Surface Science. 2012;258:5031–5037.

[41] Wang M, Zhang F, Zhu X, Qi Z, Hong B, Ding J, Bao J, Sun S, Gao C, Langmuir. 2015;31:1730–1736.

[42] Zhang C, He H, Tanaka K, Applied Catalysis B: Environmental. 2006;65:37–43.

[43] RaskóJ, Kecskés T, Kiss J, Journal of Catalysis. 2004;224:261–268.

[44] Sun S, Ding J, Bao J, Gao C, Qi Z, Li C, Catalysis Letters. 2010;137:239–246.

[45] Obee TN, Brown RT, Environmental Science and Technology. 1995;29:1223–1231.

[46] Martra G, Coluccia S, Marchese L, Augugliaro V, Loddo V, Palmisano L, Schiavello M, Catalysis Today. 1999;53:695–702.

[47] Ao CH, Lee SC, Yu JZ, Xu JH, Applied Catalysis B: Environmental. 2004;54:41–50.

[48] Yang J, Li D, Zhang Z, Li Q, Wang H, Journal of Photochemistry and Photobiology A: Chemistry. 2000;137:197–202.

[49] Coronado JM, Kataoka S, Tejedor-Tejedor I, Anderson MA, Journal of Catalysis. 2003;219:219–230.

[50] Mattsson A, Leideborg M, Larsson K, Westin G, Österlund L, Journal of Physical Chemistry B. 2006;110:1210–1220.

[51] Balcerski W, SY Ryu, MR Hoffmann, International Journal of Photoenergy. 2008;2008:964721.

[52] Backes MJ, Lukaski AC, Muggli DS, Applied Catalysis B: Environmental. 2005;61:21–35.

[53] Hernández-Alonso MD, García-Rodríguez S, Suárez S, Portela R, Sánchez B, Coronado JM, Catalysis Today. 2013;206:32–39.

Non-TiO2-based Photocatalysis

Typical Non–TiO$_2$-Based Visible-Light Photocatalysts

Pengyu Dong, Xinguo Xi and Guihua Hou

Additional information is available at the end of the chapter

Abstract

Photocatalysis has received much attention as a potential solution to the worldwide energy shortage and for counteracting environmental degradation. However, the traditional photocatalyst, TiO$_2$, cannot make use of visible light that accounts for 45% of solar spectrum because of a large bandgap (3.2 eV). Therefore, it is urgent to develop visible-light-driven photocatalysts. On the one hand, some modification technologies were explored to extend the light absorption of TiO$_2$ to visible-light region, such as doping of metal and non-metal elements, dye sensitization, and so on. On the other hand, much effort has been directed toward the development of new visible-light photocatalysts. The good news is, some novel and efficient non-TiO$_2$-based photocatalysts have been discovered, such as WO$_3$, Ag$_3$PO$_4$, BiVO$_4$, g-C$_3$N$_4$. In this chapter, these four typical visible light–driven semiconductor photocatalysts were highlighted. WO$_3$ is a visible light–responsive photocatalyst that absorbs light up to ca. 480 nm. Besides that, WO$_3$ has some advantages, such as low cost, harmlessness, and stability in acidic and oxidative conditions. Preparation of WO$_3$ films with the deposition of noble metal is considered to be a promising approach for the photocatalytic applications. In addition, the characteristic morphology and improved photocatalytic performance of Ag$_3$PO$_4$-based and BiVO$_4$-based have been raised up. New methods for fabrication Ag$_3$PO$_4$ with exposed high-energy facets and novel heterogeneous Ag$_3$PO$_4$ co-catalysts have been developed. Monoclinic BiVO$_4$ is a promising photo-anode material for photocatalytic water splitting to produce hydrogen. Co-catalysts loaded on BiVO$_4$ could improve the surface charge transfer efficiency. Furthermore, g-C$_3$N$_4$ is a promising visible-light photocatalyst due to its unique electronic structure. To date, g-C$_3$N$_4$-based photocatalysis has become a very hot research topic. The synthesis, bandgap engineering, and semiconductor composites of g-C$_3$N$_4$-based photocatalysts are highlighted.

Keywords: visible-light-driven photocatalysts, WO$_3$, Ag$_3$PO$_4$, BiVO$_4$, g-C$_3$N$_4$, structures, morphologies, heterojunction

1. Introduction

In the past decades, the development of photocatalysis has been the focus of considerable attention with photocatalysis being used in a variety of products across a broad range of research areas, including especially environmental and energy-related fields [1]. The pioneering discovery from the water splitting reported by Fujishima and Honda in 1972 [2] is considered to be unlock the doors of the photocatalysis research. This is because they found that the photocatalytic properties of certain materials could convert solar energy into chemical energy to oxidize or reduce materials to obtain useful materials including hydrogen [3, 4] and hydrocarbons [5] and to remove pollutants and bacteria [6] on wall surfaces and in air and water [7]. Among the various photocatalysts developed, TiO_2 is undoubtedly the most popular and widely used photocatalyst since it is of low cost, high photocatalytic activity, chemical, and photochemical stability [8]. However, due to the wide bandgap of TiO_2, it could absorb and utilize ultraviolet (UV) light, which accounts for a small fraction of solar light (3–5%). Hence, it is necessary to develop a particular photocatalyst, which is sensitive to sunlight. The range of optical absorption of TiO_2 could be extended from UV to visible light, which is a good way to utilize of solar energy effectively in photocatalytic reactions. In the past decades, researchers spent a great deal of time and resources developing visible light–active photocatalysts [9]. In order to design visible-light response photocatalysts, two strategies have been proposed. One approach is the modification of the wide bandgap photocatalysts (such as TiO_2, ZnO) by doping or by producing between them and other materials. The other approach is the exploration and development of novel semiconductor materials capable of absorbing visible light.

From the view point of using solar light, the first step in the development of a technology that makes efficient use of solar energy is the discovery of a photocatalyst that becomes highly active under visible light ($\lambda > 400$ nm). Since the optical absorption properties of a photocatalyst is determined by the energy bandgap of semiconductor photocatalyst, it is necessary to choose a narrow band of semiconductor as photocatalyst. Hence, the energy band engineering is a fundamental aspect of the design and fabrication of visible-light–driven photocatalysts. Considering the optical absorption, direct, and narrow bandgap semiconductors are more likely to exhibit high absorbance and be suitable for the efficient harvesting of low-energy photons. However, it is a pity that the recombination probability for photo-excited electron–hole pairs is rather high in direct and narrow bandgap semiconductors, and the band-edge positions are frequently incompatible with the electrochemical potential that is necessary to trigger specific redox reactions [10]. Therefore, the energy band structure of a photocatalyst plays a significant role in the light absorption property and in determining the redox potentials. In order to effectively utilize the solar energy, design and adjustment of band structure are an effective approach to obtain visible-light response photocatalyst with excellent performance. Through unremitting efforts, researchers have developed some typical and excellent visible-light-driven semiconductor photocatalysts, such as WO_3, Ag_3PO_4, $BiVO_4$, g-C_3N_4-based photocatalysts, which possess suitable energy band configurations. In this chapter, we would like to focus on these four typical visible-light-driven semiconductor photocatalysts and summarize the recent progress of enhanced visible-light efficiency.

Furthermore, we also highlight the crucial issues that should be addressed in future re-search activities.

2. WO$_3$-based photocatalysts

2.1. Structures and morphologies of WO$_3$

The crystal structures of WO$_3$ are described below: WO$_3$ crystals are generally formed by corner and edge sharing of WO$_6$ octahedra. The following phases are obtained by corner sharing: monoclinic II (ε-WO$_3$), triclinic (δ-WO$_3$), monoclinic I (γ-WO$_3$), orthorhombic (β-WO$_3$), tetragonal (α-WO$_3$), and cubic WO$_3$ [11]. However, cubic WO$_3$ is not commonly observed experimentally. Szilágyi et al. [12] found that the monoclinic WO$_3$ always shows the best photocatalytic activity among these crystal phases.

The electronic band structure of WO$_3$ can be described as follows: WO$_3$ is an n-type semicon-ductor, with an electronic bandgap (Eg), corresponding to the difference between the energy levels of the valence band (VB), formed by filled O 2p orbitals and the conduction band (CB) formed by empty W 5d orbitals [13]. It is known that the cubic phase is the ideal crystal phase of WO$_3$, and the crystal phase changes with the distortion degree from the ideal phase, which is accompanied by a change in Eg since the occupied levels of the W 5d states change [14]. As a photocatalytic material, stoichiometric WO$_3$ has a CB edge, which is positioned slightly more positive (versus NHE (normal hydrogen electrode)) than the H$_2$/H$_2$O reduction potential [15] and a VB edge much more positive than the H$_2$O/O$_2$ oxidation potential, which makes WO$_3$ capable of efficiently photo-oxidizing a wide range of organic compounds [16] such as textile dyes and bacterial pollutants. When compared to TiO$_2$, another advantage of WO$_3$ is that it can be irradiated by the blue region of the visible solar spectrum. Furthermore, WO$_3$ has a remarkable stability in acidic environments, making it a promising candidate for treatment of water contaminated by organic acids [17].

The preparation of nanometer-sized crystalline WO$_3$ particles and control of their morphology is important to improve photocatalytic activity. Zhao and Miyauchi [18] developed a facile and economical method to produce high-purity tungstic acid hydrate nanotubes and nano-porous-walled WO$_3$ nanotubes on a large scale. They found that the WO$_3$ nanotubes loaded with Pt nanoparticles show larger surface area and higher visible-light-driven photocatalytic activity compared to Pt-nanoparticle-loaded commercial WO$_3$. Recently, attention has been focused on three-dimensionally ordered macroporous (3DOM) materials with pores sizes in the sub-micrometer range, because of the potential of photocatalysis application. Generally, the 3DOM materials can be prepared by three steps. Firstly, some mono-disperse polymer spheres such as poly(methyl methacrylate) (PMMA), and polystyrene (PS) were selected as a colloidal crystal template. Secondly, the colloidal crystal template was immersed into the material precursors. Thirdly, the polymer colloidal crystal template was removed by the calcination removed to form an ordered porous structure. The ordered ("inverse opal") structures prepared by this method consist of a skeleton surrounding and a uniform close-

packed macropores. For instance, Sadakane et al. [19] prepared 3DOM WO_3 using a colloidal crystal template of PMMA spheres.

2.2. WO_3 films and photocatalytic applications

Generally, WO_3 exhibits low photocatalytic activity for decomposing organic compounds compared with traditional TiO_2 photocatalyst under UV light irradiation. However, WO_3 could show high photocatalytic activity for the decomposition of organic compounds under visible light when the surface is modified with noble metal nanoparticles, such as platinum (Pt), palladium (Pd), and so on. For instance, Abe et al. demonstrated that WO_3 deposited with Pt nanoparticles exhibits good photocatalytic activity for the decomposition of liquid and gaseous organics. It was an impressive performance that the photocatalytic activity of Pt/WO_3 was almost close to that of TiO_2 under UV light irradiation and much higher than that of N-doped TiO_2 under visible irradiation [20]. In the Pt/WO_3 system, the electrons were excited to the CB from the VB of WO_3 and then were injected into Pt nanoparticles, which act as electron pools to participate in two or four electron reductions of the adsorbed oxygen molecules. Hence, the particle size of the Pt nanoparticles plays a very important role in the multi-electron reduction process. On the other side, the metal surface of Pt induces the photocatalyst is more hydrophobic compared with a metal oxide surface. These findings were widely concerned in the past years and were considered to open up a research upsurge of WO_3 photocatalyst.

Large area uniformity, low production cost, and excellent durability of WO_3 thin films can play a very important role in the fabrication of electrochromic devices and photocatalytic materials. In the past years, the electrodeposition, sol–gel processing, one-pot direct hydrothermal growth, chemical vapor deposition, sputtering, and vacuum evaporation methods were used to prepare WO_3 thin films. In particular, Miyauchi M synthesized WO_3 films with underlying Pt nanoparticles ($WO_3/Pt/substrate$) and those with overlying Pt nanoparticles ($Pt/WO_3/substrate$) by sputtering and sol–gel methods [21]. **Figure 1** shows the SEM images of different Pt layer surfaces. Moreover, it is found that underlying Pt nanoparticles greatly enhanced the photocatalytic oxidation activity of WO_3 without decreasing the photo-induced hydrophilic conversion between these films. The optimum structure for high performance in both photocatalysis and photo-induced hydrophilicity was WO_3 (50 nm)/Pt(1.5 nm)/substrate, and this film exhibited a significant self-cleaning property even under visible-light irradiation.

3. Ag_3PO_4-based photocatalysts

In 2010, a breakthrough on visible-light-driven photocatalysts was made by Ye's research team, who reported the use of Ag_3PO_4 as an active visible-light-driven photocatalyst for the oxidation of water and photodecomposition of organic compounds [22]. Ye's research team demonstrated that Ag_3PO_4 photocatalyst could achieve high quantum efficiency under visible-light irradiation. The quantum efficiency of this novel photocatalyst could up to 90% which is significantly superior to others such as $BiVO_4$ or N-doped TiO_2. However, it should be noted that there are still some limitations in the Ag_3PO_4 photocatalytic system. Firstly, the particle

size of Ag$_3$PO$_4$ is relatively large (0.5–2 μm) that limits the photocatalytic performance. To enhance photocatalytic activity of this new material, it is desirable to synthesize nanosized Ag$_3$PO$_4$ particles with higher surface area which is beneficial to the photocatalytic reaction. Secondly, the Ag$_3$PO$_4$ photocatalyst suffers from serious stability issue which is the main hindrance for the practical application of Ag$_3$PO$_4$ as a recyclable and highly efficient photocatalyst. This is because the CB potential of Ag$_3$PO$_4$ is more positive than that of the hydrogen potential (0 V). As shown in **Figure 2**, the CB and VB potentials of Ag$_3$PO$_4$ are +0.45, +2.9 V vs. NHE, respectively [23]. Thus, under visible-light irradiation, electrons and holes were generated in the CB and VB of Ag$_3$PO$_4$, and then, the photogenerated electrons could reduce
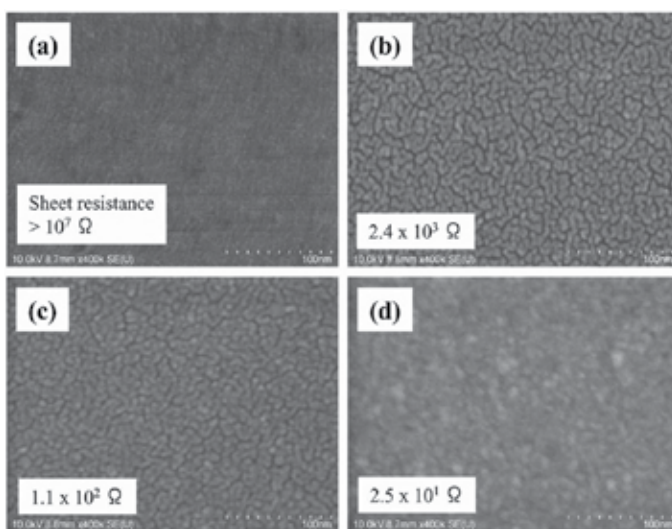
Figure 1. SEM images of different Pt layer surfaces: (a) 0.5 nm, (b) 1.5 nm, (c) 3 nm, and (d) 10 nm thick. The inset words describe the sheet resistance of the film surfaces measured by a four-pin probe method (reproduced with permission from [21]).
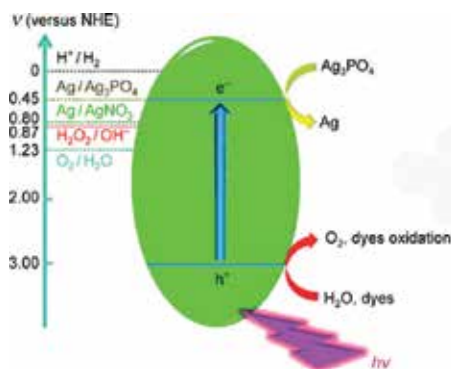
Figure 2. Schematic drawing of redox potentials of Ag$_3$PO$_4$ (reproduced with permission from [23]).

the interstitial silver ions (Ag^+) to form the silver atoms (Ag), resulting in the photocorrosion of Ag_3PO_4 without a sacrificial reagent. The formed Ag nanoparticles would adhere to the surface of the Ag_3PO_4 photocatalyst and suspend in the photocatalytic reaction systems, giving rise to the prevention of absorption of visible light and the decrease of photocatalytic activity [24]. Hence, it is necessary to enhance the photocatalytic activity and stability of Ag_3PO_4.

3.1. Morphology-controlled syntheses of Ag_3PO_4

The morphology control of photocatalysts has been considered to be one of the most promising avenues to improve the photocatalytic properties. This is because photocatalytic reactions are typically surface-based processes, and thus, the photocatalytic efficiency is closely related to the morphology and microstructure of a photocatalyst. Accordingly, further studies on Ag_3PO_4 crystals with new morphologies and structures will be of great value.

To investigate the effects of the shapes and facets of particular photocatalysts on their photo-catalytic properties, single-crystals of Ag_3PO_4 were synthesized in two forms by Ye's research team [25], firstly with rhombic dodecahedron shapes and exposed {110} facets, and secondly cubes bounded by {100} facets. Ye's research team found that rhombic dodecahedral Ag_3PO_4 crystals could be prepared using CH_3COOAg as the silver ion precursors, while cubic Ag_3PO_4 crystals could be prepared using $[Ag(NH_3)_2]^+$ as the silver ion precursors. The Ag_3PO_4 dodecahedrons were formed by 12 well-defined {110} planes with cubic crystal symmetry (**Figure 3a**), whereas the Ag_3PO_4 cubes showed sharp corners, edges, and smooth
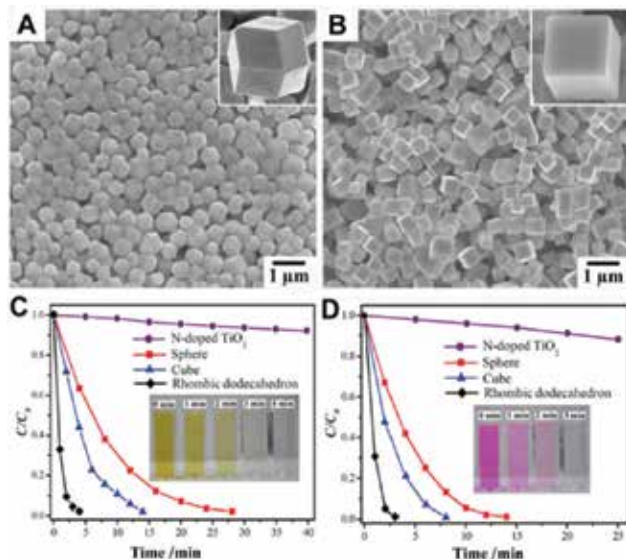
Figure 3. SEM images of Ag_3PO_4 sub-microcrystals with different morphologies: (A) rhombic dodecahedrons and (B) cubes. The photocatalytic activities of Ag_3PO_4 rhombic dodecahedrons, cubes, spheres, and N-doped TiO_2 are shown for the degradation of (C) MO and (D) RhB under visible-light irradiation ($\lambda > 400$ nm) (reproduced with permission from [25]).

surfaces (**Figure 3b**). The results of photocatalytic degradation of methyl orange (MO) and RhB dyes indicated that the rhombic dodecahedral Ag$_3$PO$_4$ exposed {110} facet showed higher photocatalytic activity than the cubic Ag$_3$PO$_4$ exposed {100} facet (**Figure 3c**, **d**) under visible-light irradiation, which is in accordance with the higher surface energy of 1.31 J/m^2 for the {110} facet compared to 1.12 J/m^2 for the {100} facet.

Very recently, some morphologies of Ag$_3$PO$_4$ have been reported by other research teams. For examples, Liu and co-workers [26] reported Ag$_3$PO$_4$ crystals with porous structure. Guo and co-workers synthesized tetrahedral Ag$_3$PO$_4$ crystals with exposed {111} facets and tetrapod-shaped Ag$_3$PO$_4$ microcrystals with exposed {110} facets [23, 27]. Teng and co-workers [28] synthesized Ag$_3$PO$_4$ crystals with tetrapod morphology by a hydrothermal method. Liang et al. [29] synthesized hierarchical Ag$_3$PO$_4$ porous microcubes with enhanced photocatalytic properties. However, these reported various morphologies of Ag$_3$PO$_4$ crystals were obtained by adjusting internal experimental conditions such as raw materials, solvents, pH values, and additives. Our research team found that the Ag$_3$PO$_4$ products with various new morphologies such as branch, tetrapod, nanorod, and triangular prism were prepared via a facile and efficient synthesis process [30], as shown in **Figure 4**. It is demonstrated that the morphology of Ag$_3$PO$_4$ crystals can be controlled by simply adjusting external experimental conditions such as static and ultrasonic conditions. When the product was prepared under static conditions for 0 h, branched Ag$_3$PO$_4$ was achieved. Increasing the static time led to the formation of
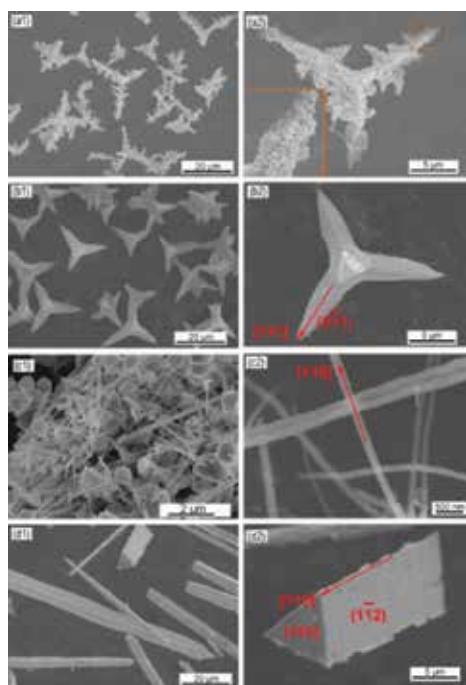
Figure 4. SEM images of branched (a), tetrapod (b), nanorod-shaped (c), and triangular-prism-shaped (d) Ag$_3$PO$_4$ crystals (reproduced with permission from [30]).

tetrapod morphology. When the synthesis process was completed under ultrasonic conditions within 2 h, nanorod-shaped Ag_3PO_4 was obtained. Prolonging the ultrasonic time could result in the formation of triangular-prism-shaped Ag_3PO_4. The photocatalytic results indicate that the branched Ag_3PO_4 sample shows greatly enhanced photocatalytic activity compared with other as-prepared Ag_3PO_4 samples.

3.2. Theoretical study of the electronic structure of Ag_3PO_4

To elucidate its mechanism of the extremely high photo-oxidative activity under visible-light irradiation of Ag_3PO_4, theoretical works have been carried out using first-principle method. So far, theoretical investigations are mainly focused on the energy band configuration because photo-excited carriers are generated when the incident photon energy is higher than the bandgap of Ag_3PO_4. Besides that, the alignment between the band edges and the redox potentials of the target molecules should also be considered. This is because the photogenerated electrons can be transferred to the adsorbed oxygen molecules only when there is a sufficiently large negative offset of the conduction band minimum (CBM), and the photogenerated holes could combine with water molecules when there is a sufficiently large positive offset of the valence band maximum (VBM) according to the redox potentials [31].

To obtain insight into the high photo-oxidative activity of Ag_3PO_4, *ab initio* density functional theory (DFT) calculations have also been carried out by Ye's research team [22]. It is found that Ag_3PO_4 is an indirect bandgap semiconductor, and the bottoms of the CB are mainly composed of hybridized Ag 5s5p as well as a small quantity of P 3s orbitals, whereas the tops of the VB are composed of hybridized Ag 4d and O2p orbitals. Moreover, Ye's research team further studied the electronic structures of three different Ag-based oxides Ag_3PO_4, Ag_2O, and $AgNbO_3$ to understand the high photocatalytic performance of Ag_3PO_4 [32]. The total and local DOS results were shown in **Figure 5**. The calculated DOS results revealed that the CBM of Ag_3PO_4 is made up of Ag s states due to the formation of the rigid tetrahedral units PO_4, which decrease and increase the strength of Ag–O and Ag–Ag bonds, respectively. This induces to a very dispersive electronic structure at the CBM, resulting in a highly delocalized and isotropic distribution of wave function. Therefore, they conclude that the excellent photocatalytic performance of Ag_3PO_4 is attributed partly to the highly dispersive band structure of the CBM, resulting from Ag s–Ag s hybridization without localized d states.

In addition, Ma et al. [33] used first-principles density functional theory incorporating the LDA + U formalism to investigate the origin of photocatalytic activation of Ag_3PO_4. They found that Ag_3PO_4 has a great distribution of CB and the inductive effect of PO_4^{3-}, which is benefit for the separation of photogenerated electron–hole pairs. It is theoretically demonstrated that Ag vacancies in Ag_3PO_4 with high concentration have an evident influence on the separation of electron–hole pairs and the optical absorbance of visible light, which presents a rational interpretation of the experimental results of high photocatalytic activity of Ag_3PO_4.

3.3. Ag$_3$PO$_4$-based composites

To harvest photons in visible region, many narrow bandgap metal oxides or chalcogenides have been coupled with TiO$_2$ to fabricate visible-light photocatalysts, which exhibit visible-light photocatalytic activity to a certain extent. Such a strategy is also applied to modify Ag$_3$PO$_4$ photocatalyst to enhance its photocatalytic activity and/or improve its stability.

Recent reports indicated that the insoluble AgX (X = Cl, Br, I) nanoshells on the surface of Ag$_3$PO$_4$ could improve its photocatalytic activity and stability [24]. In addition, various coupled systems, such as Ag$_3$PO$_4$/TiO$_2$ [34], Ag$_3$PO$_4$/Ag [35] composites have been developed to improve the photocatalytic activity and/or stability of Ag$_3$PO$_4$. Our research team found that Ag$_3$PO$_4$ and reduced graphite oxide sheets (RGOs) nanocomposites show the enhanced photocatalytic activity and structural stability [36]. We also found that, when Ag$_3$PO$_4$ and TiOF$_2$ were compounded, the stability of composite photocatalysts was highly enhanced but the photocatalytic activity was not improved. In the case of Ag$_3$PO$_4$/TiOF$_2$ composite, Ag$_3$PO$_4$ and TiOF$_2$ have different conduction bands (Ec), valence bands (Ev), and Fermi levels (Ef) (the detail analysis of level energies was shown in the Supplementary data). When the mixed Ag$_3$PO$_4$/TiOF$_2$ composite is formed, the Fermi energies of these two phases have to be the same in the boundary between the Ag$_3$PO$_4$ and TiOF$_2$ phases. This leads to both of the Ec and Ev of Ag$_3$PO$_4$ lie above that of TiOF$_2$, as shown in **Figure 6**. Under visible-light irradiation, a larger number of electrons are excited to the Ec from the Ev of Ag$_3$PO$_4$ and then transferred to the Ec of TiOF$_2$, while the holes left on the VB of Ag$_3$PO$_4$. Thus, the enriched electrons on the surface of TiOF$_2$ could facilitate their participation in a multiple-electron reduction reaction of oxygen ($O_2 + 2H^+ + 2e^- \rightarrow H_2O_2$), which effectively protects Ag$_3$PO$_4$ semiconductors to avoid its self-corrosion by a single-electron reduction reaction ($Ag^+ + e^- \rightarrow Ag$). Therefore, the Ag$_3PO_4$/
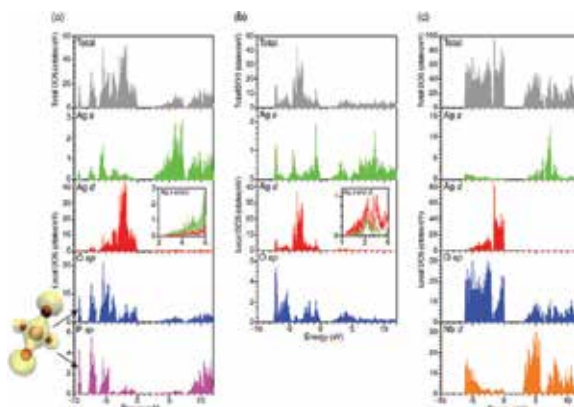
Figure 5. (Color) Total and local DOS for (a) Ag$_3$PO$_4$, (b) Ag$_2$O, and (c) AgNbO$_3$. For the local DOS, we use spheres of radii 1.503, 0.82, 1.233, and 1.503 Å for Ag, O, P, and Nb, respectively. The VBM represents the zero energy. The insets in (a) and (b) display the extended plots of DOS for Ag s and d at the energy range near the CBM. The partial charge density corresponding to one of the P-O bonding states is illustrated in the leftmost area in (a). The mauve and red spheres denote the positions of P and O atoms, and the isosurface (yellow surface) is at 0.03 e/Å^3, respectively (reproduced with permission from [32]).

TiOF$_2$ composite photocatalyst exhibits enhanced photocatalytic stability compared with that of pure Ag$_3$PO$_4$. It is thought that TiOF$_2$ was used as an electron acceptor and protected Ag$_3$PO$_4$ particles to avoid the self-corrosion of Ag$_3$PO$_4$. On the other hand, the left holes on the VB of Ag$_3$PO$_4$ could migrate to the surface of photocatalysts and participate in the photo-oxidative reaction and then decompose the methylene blue (MB) molecules.
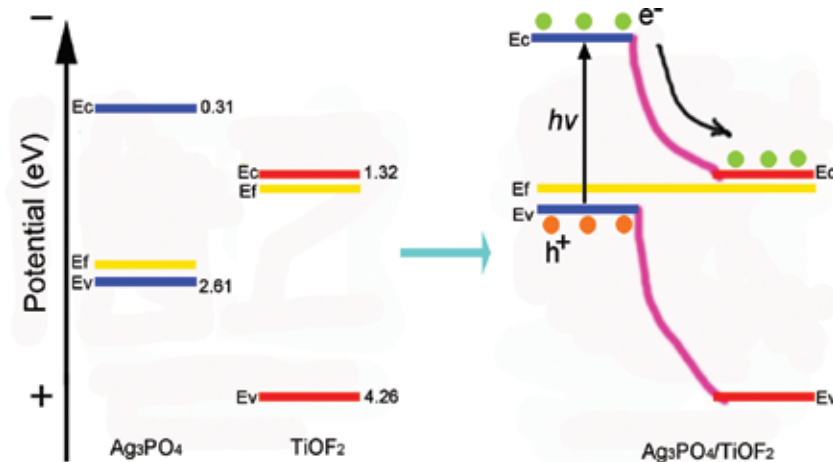
Figure 6. Schematic diagram for the CB, VB, and Fermi level of Ag$_3$PO$_4$ as well as TiOF$_2$, and the electron–hole separation and energy band matching of Ag$_3$PO$_4$/TiOF$_2$ composite under visible-light irradiation (reproduced with permission from [37]).

4. BiVO$_4$-based photocatalysts

BiVO$_4$ is one of the typical complex oxides with narrow bandgap, which possess excellent visible-light photocatalytic properties. As an n-type semiconductor with a direct bandgap of 2.4 eV, BiVO$_4$ could absorb ample visible light and is stable in neutral electrolyte, nontoxic, and relatively cheap [38]. BiVO$_4$ has three crystal systems of zircon-tetragonal, scheelite tetragonal, and scheelite-monoclinic. However, only the scheelite-monoclinic phase is reportedly active in the photocatalytic oxygen evolution [39]. In addition, the scheelite-monoclinic can be obtained from the irreversible phase transformation of the zircon-tetragonal structure at the temperature of 400–500°C [40].

4.1. Syntheses of BiVO$_4$ with different morphologies

BiVO$_4$ could be synthesized by various methods, such as solid-state reaction, metal organic decomposition, hydrothermal treatment, and coprecipitation.

BiVO$_4$ prepared via a solid-state reaction always shows big particle size and low surface area, which resulted in poor photocatalytic activity. So, it is encouraged to synthesize BiVO$_4$ by new methods.

Zhang et al. [41] reported BiVO$_4$ nanosheets were hydrothermally synthesized by a simple one-step route in the presence of sodium dodecyl benzene sulfonate (SDBS) as a morphology-directing template. The BiVO$_4$ nanosheets had a monoclinic structure, were ca. 10–40 nm thick, and showed a preferred (010) surface orientation.

Single-crystalline BiVO$_4$ microtubes with square cross sections and flower-like morphology was prepared by a facile reflux method at 80°C [42]. In the synthesis process, no surfactants or templates were involved. The prepared microtubes show the monoclinic structure with a growth direction of [010], and the side length is about 800 nm as well as the wall thickness is around 100 nm.

Li et al. [43] describes a nanocasting synthesis of ordered mesoporous BiVO$_4$ photocatalyst with the help of a template of silica (KIT-6) using ammonia metavanadate and bismuth nitrate hydrate as vanadium and bismuth sources, respectively. Monoclinic scheelite BiVO$_4$ crystals were formed inside the mesopores of hard template (silica) by a mild thermal process, and mesoporous BiVO$_4$ was obtained after the removal of silica by NaOH treatment. The prepared mesoporous BiVO$_4$ showed not only the activity for photocatalytic O$_2$ evolution but also the photocatalytic oxidation of NO gas in air under visible-light irradiation.

In particular, Li's research team prepared BiVO$_4$ crystals exposed with {010} and {110} crystal facets, as shown in **Figure 7**. They found that the reduction reaction with photogenerated electrons occurs separately on the {010} facet under visible-light irradiation, while the oxidation reaction with photogenerated holes takes place on the {110} facet. Therefore, a conclusion that efficient charge separation can be achieved on different crystal facets was given. Based on this finding, they further demonstrated that the reduction and oxidation co-catalysts could be selectively deposited on the {010} and {110} facets, respectively, giving rise to a much higher photocatalytic and photo-electrocatalytic activity for water oxidation reactions than the photocatalyst with randomly distributed co-catalysts. Overall, these results indicate that the photogenerated electrons and holes can be separated between the different facets of semiconductors.
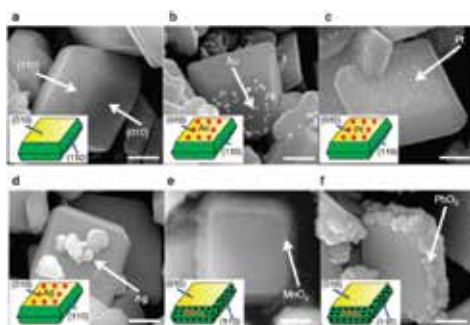
Figure 7. SEM images of BiVO$_4$ (a), Au/BiVO$_4$ (b), Pt/BiVO$_4$ (c), Ag/BiVO$_4$ (d), MnOx/BiVO$_4$ (e), and PbO$_2$/BiVO$_4$ (f). The deposited contents of the metals/metal oxides are all 5 wt%. The scale bar is all 500 nm (reproduced with permission from [44]).

4.2. Modification of BiVO$_4$ with enhanced photocatalytic performance

Heterostructure formation is widely utilized to improve the properties of a semiconductor by combining with other functional materials. It has a large scope of materials as well as applications including photocatalysis, photovoltaics, light-emitting devices, and optoelectronics [45]. Combination of two semiconductors (n/n or p/n) with proper band positions can make cascade electron transfer from CB of upper potential to CB of lower potential. Successful heterojunction formation of BiVO$_4$ has been reported with WO$_3$, SnO$_2$, Fe$_2$O$_3$, CuWO$_4$, and CdS, in which the WO$_3$/BiVO$_4$ has been the most common. WO$_3$ (Eg = 2.6–2.8 eV) is one of the most active metal oxide photocatalyst with CB at 0.42 V$_{RHE}$ (RHE: reversible hydrogen electrode) and VB at 3.12 V$_{RHE}$ [46]. With such band configurations presented at **Figure 8a**, the photo-induced electrons transfer from BiVO$_4$ to WO$_3$, whereas holes cannot. This prevents electron/hole recombination in BiVO$_4$. Since WO$_3$ has better mobility and longer diffusion length than BiVO$_4$, the photo-induced electrons collected in WO$_3$ can be more efficiently converted to photocurrents with much reduced recombination compared to the case when the photo-induced electrons are locked in BiVO$_4$. Since BiVO$_4$ has a smaller bandgap and wider pH stability, BiVO$_4$/WO$_3$ heterojunction can absorb larger portion of solar light and has better neutral stability compared with pure WO$_3$. The improved charge transfer characteristics of BiVO$_4$/WO$_3$ heterojunction was confirmed by electrochemical impedance spectroscopy (EIS) that showed that resistance of the heterojunction is reduced almost to that of WO$_3$. Moreover, nanostructured WO$_3$ was found to be more effective. As shown in **Figure 8b**, WO$_3$ prepared in one-dimensional (1D) nanorods or nanowires makes the BiVO$_4$/WO$_3$ heterojunction more effective [47]. The particular geometry reduces the distance that the photo-induced holes have to travel in radial direction to reach the surface of WO$_3$ photocatalyst. On the other hand, the photo-induced electrons have to flow along the axial direction making a vectorial flow. Another successful heterojunction is BiVO$_4$/SnO$_2$, as shown in **Figure 8c**. SnO$_2$ has a large bandgap of 3.5 eV and potentials of CB (0.27 V$_{RHE}$) and VB (3.77 V$_{RHE}$), which are favorable for cascade the photo-induced electron transferred from BiVO$_4$ [48]. In addition, SnO$_2$ has a passivation effect of FTO glass. Thus, a large number of interfacial defects and the potential
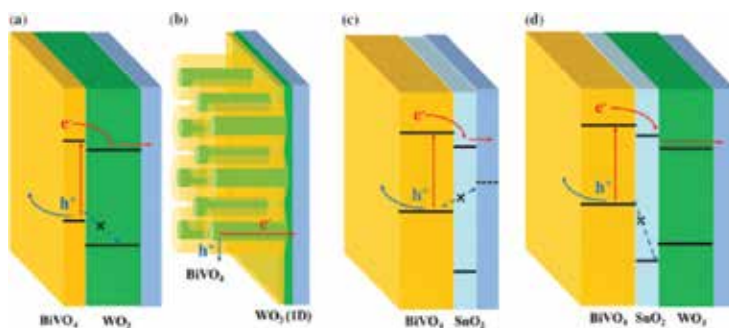
Figure 8. Schemes of BiVO$_4$-based heterojunction: (a) BiVO$_4$/WO$_3$ [46], (b) BiVO$_4$/WO$_3$ 1D nanostructure [47], (c) BiVO$_4$/SnO$_2$ (hole mirror) [49, 50], and (d) BiVO$_4$/SnO$_2$/WO$_3$ dual-hole mirror [48] (reproduced with permission from [46–50]).

electron trap states of FTO can be passivated by a thin SnO$_2$ layer, improving charge transfer at BiVO$_4$/FTO interface [49]. Also very positive VB of SnO$_2$ prevents a backward hole transfer through SnO$_2$ layer forming a "hole mirror." As CB potential of BiVO$_4$, SnO$_2$, and WO$_3$ is aligned in cascade (0.02/0.27/0.41 V$_{RHE}$), ternary composite of BiVO$_4$/SnO$_2$/WO$_3$ could be prepared as an effective heterojunction, as shown in **Figure 8d** [48].

5. g-C$_3$N$_4$-based photocatalysts

Since the pioneering work in 2009 on graphitic carbon nitride (g-C$_3$N$_4$) for visible-light photocatalytic water splitting [51], g-C$_3$N$_4$-based photocatalysis has become a very hot research topic. Unlike TiO$_2$, which is only active in the UV region, g-C$_3$N$_4$ has a bandgap of ca. 2.7 eV, with the CB and VB positions at ca. −1.1 and ca. +1.6 eV vs. NHE, respectively. This electronic structural character suggests the g-C$_3$N$_4$ could be a visible-light active photocatalyst. g-C$_3$N$_4$ is not only the most stable allotrope of carbon nitrides at ambient atmosphere, but it also has rich surface properties that are attractive for catalysis application due to the presence of basic surface sites. The ideal g-C$_3$N$_4$ consists solely of an assembly of C–N bonds without electron localization in the π state (this material is a π-conjugated polymer).

5.1. Syntheses of pristine g-C$_3$N$_4$

The most common precursors used for chemical synthesis of g-C$_3$N$_4$ are reactive nitrogen-rich and oxygen-free compounds containing prebonded C–N core structures, such as triazine and heptazine derivatives, but most of them is unstable and difficult to obtain and/or highly explosive. The synthesis of single-phase sp^3-hybridized carbon nitrides is a challenging task due to their low thermodynamic stability. Generally, the defect materials are much more valuable than the ideal one, in particular for catalysis, which requires surface defects. Thus, the synthesis of g-C$_3$N$_4$ with defects is an interesting topic, when the material is going to be used in catalysis.

Pure g-C$_3$N$_4$ can be obtained at ca. 500°C when the precursor cyanamide is pretreated with a basic solution (like aqueous NaOH) [52]. It is found that the presence of hydroxyl ions facilitates the transformation of cyanamide to g-C$_3$N$_4$, probably due to the hydroxyl ions that promote the condensation process, by reacting with the hydrogen atoms on the edges of the intermediate.

Generally, porous photocatalysts are very fascinating, because the porous structure can provide a large surface area and a lot of channels, which is benefit for the diffusion of con-taminant molecules, as well as charge migration and separation. Researchers always synthe-size the porous g-C$_3$N$_4$ photocatalyst using hard and soft templates because the porous structure of g-C$_3$N$_4$ can be tuned by choosing different templates. Recently, porous g-C$_3$N$_4$ can also be synthesized using surfactants (e.g., Triton X-100, P123, Brij 58) or ionic liquids as soft templates through a self-polymerization reaction [53].

1D nanostructured photocatalysts such as nanorods, nanowires, nanobelts, and nanotubes continue to attract special attention. This is because unique chemical, optical, and electronic

properties can be achieved by tuning their length, diameter, and aspect ratio, which is beneficial for optimizing their photocatalytic activity. For example, g-C_3N_4 nanorod networks were fabricated by a solvothermal method using cyanuric chloride and melamine in a sub-critical acetonitrile solvent [54]. It needs only a temperature of 180°C, which is much lower than that of traditional solid-state synthesis method (normally 500–600°C). The as-prepared sample mainly consists of regularly nanorods (accounts for 90%). The average diameter of these nanorods is 50–60 nm, and the length is about several micrometers.

5.2. Bandgap engineering of g-C_3N_4

Bandgap engineering of g-C_3N_4 to control its light-absorption ability and redox potential plays an important role in enhancing its photocatalytic performance. The main strategies to adjust the band structure of g-C_3N_4 are operated at the atomic level (such as elemental doping) and the molecular level (such as copolymerization).

On one hand, elemental doping plays an essential role in tuning the electronic structure of g-C_3N_4. Non-metal doping occurs via substitution of the C or N atoms, which affects the corresponding CB and VB, while metal doping occurs via insertion into the framework of g-C_3N_4. In most cases, a decreased bandgap can be obtained, resulting in extending the light absorption ability. This is quite a flexible strategy that enables the bandgap engineering of g-C_3N_4 by choosing specific doping elements and their amounts, depending on the desired band positions. On the other hand, molecular doping is a unique way for modifying the bandgap of g-C_3N_4 but is usually not available for inorganic semiconductors. Anchoring a very small amount of structure matching organic groups at the edges of g-C_3N_4 nanosheets can significantly affect its bandgap and light-harvesting ability. The doping amount of organic additives can be changed to obtain g-C_3N_4 with the desired bandgap. To illustrate the bandgap engineering of g-C_3N_4 by both elemental doping and molecular doping, the band structures of some typical samples of modified g-C_3N_4 are summarized in **Figure 9** [55].

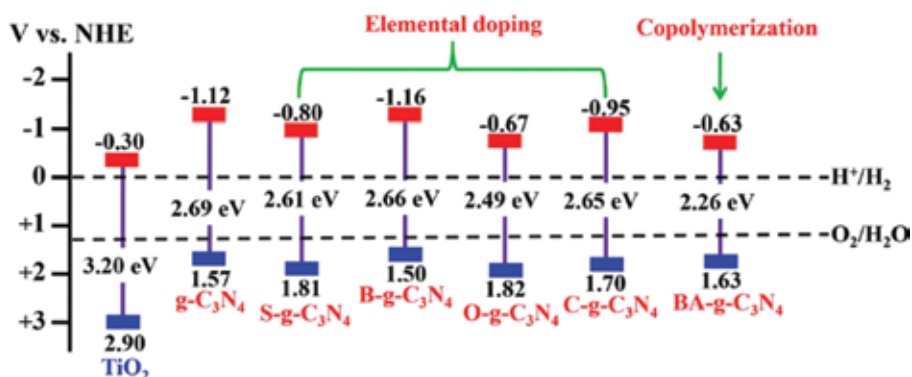**Figure 9.** Schematic illustration of the band structures of typical samples of g-C_3N_4 in comparison with TiO_2 (reproduced with permission from [55]).

5.3. g-C₃N₄-based semiconductor composites

To develop effective g-C_3N_4-based nanocomposites with enhanced photocatalytic perform-ance, several main requirements must be considered. Firstly, the composite semiconductor should absorb efficient sunlight. Secondly, the photogenerated charges should be separated effectively and the transfer process should be accelerated. Thirdly, the composite semicon-ductor must have sufficient redox potential for the desired photochemical reactions. Finally, the composite semiconductor should be stable during the photocatalytic reaction process [56]. Of course, it is difficult to meet all these requirements for a single-material system, while the composite photocatalysts may have the potential to achieve these goals.

So far, a large number of semiconductors have been coupled with g-C_3N_4 to form semicon-ductor–semiconductor heterojunctions. Among them, two types of heterojunctions have been mainly investigated: traditional type-II heterojunctions and all-solid-state Z-scheme hetero-junctions.

A g-C_3N_4-based traditional type-II heterojunction is constructed using g-C_3N_4 and another semiconductor, in which both the CB and VB positions of the g-C_3N_4 are higher or lower than those of another semiconductor. Due to the difference of chemical potential between the two semiconductor units, the band at the contact interface of the heterojunction could bend. This band bending induces to a built-in electric field, resulting in an opposite migration of photo-generated electrons and holes (**Figure 10a**) [57]. For example, g-C_3N_4/In_2O_3 heterojunctions were prepared by in situ growth of In_2O_3 nanocrystals on the surface of g-C_3N_4 via dimethyl sulfoxide (DMSO)-assisted solvothermal method [58]. The traditional type-II heterojunction has been proved to be an efficient method for spatial charge separation. However, the major shortcoming of this heterojunction is the weaker redox ability of the photogenerated electrons and holes originated from the less-negative CB of semiconductor II and the less-positive VB of semiconductor I. Hence, it is difficult to achieve both of the outstanding charge separation efficiency and a strong redox ability for the traditional type-II heterojunction. Fortunately, a new type of all-solid-state Z-scheme heterojunction has been developed recently [59], which could overcome these shortcomings. There are two main types of all-solid-state Z-scheme heterojunctions: semiconductor–semiconductor (S–S) Z-scheme heterojunctions (**Figure 10b**) and semiconductor–conductor–semiconductor (S–C–S) Z-scheme heterojunctions (**Figure 10c**). Such a heterojunction allows for the utilization of semiconductor pairs with narrow bandgap without losing the strong redox ability of the photo-induced electrons and holes. In the S–S Z-scheme heterojunction, the photogenerated electrons from semiconductor II with less-negative CB tend to transfer to semiconductor I with less-positive VB via the contact interface and are further excited to the CB of semiconductor I to participate in the reduction reaction, leaving holes in the VB of semiconductor II to involve into the oxidation reaction. For example, Kumar et al. [60] reported the synthesis of N-doped ZnO/g-C_3N_4 hybrid core–shell nanoplates via a dispersion–evaporation method. By investigating the reactive species of the photocatalytic degradation of rhodamine B in the presence of N-doped ZnO/g-C_3N_4 core–shell structures, a mechanism for S–S Z-scheme heterojunction was proposed. In the case of the S–C–S Z-scheme heterojunction, the conductor material between the two semiconductors serves as an electron mediator to enable the migration of photo-induced electrons from semiconduc-

tor II to semiconductor I. For example, Katsumata et al. [61] obtained a similar S–C–S Z-scheme heterojunction composed of Ag_3PO_4, Ag, and g-C_3N_4 for the efficient photocatalytic decolorization of methyl orange.
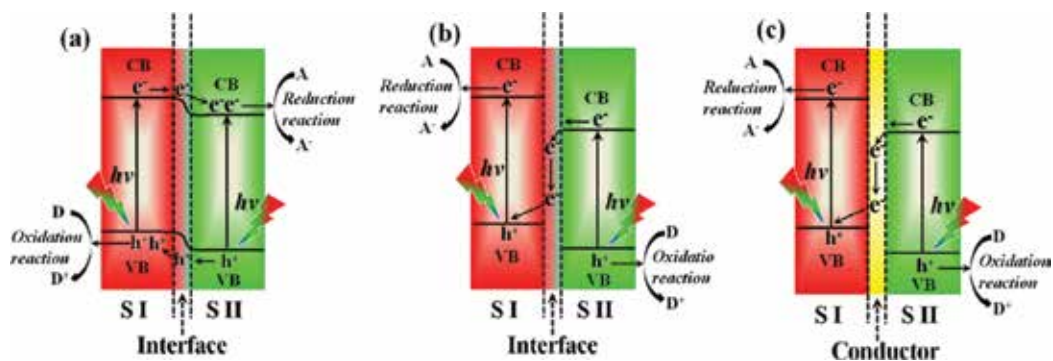
Figure 10. Proposed transfer pathways of photo-induced carriers for different semiconductor heterojunctions: traditional type II heterojunction (a), all solid-state S–S Z-scheme heterojunction (b), all-solid-state S–C–S Z-scheme heterojunction (c). The abbreviations of A, D, S I, and S II denote the electron acceptor, electron donor, semiconductor I, and semiconductor II, respectively (reproduced with permission from [59]).

5.4. Photocatalytic applications of g-C_3N_4

g-C_3N_4 can be used for various photocatalytic applications, such as water splitting, CO_2 reduction, pollutant degradation, organic syntheses, and bacteria disinfection. Remarkable accomplishments have been already achieved in the area of the g-C_3N_4-based photocatalytic hydrogen evolution by dye sensitization, hybridization with carbon materials, and introduction of non-noble-metal co-catalysts. Also, g-C_3N_4/carbon composites and g-C_3N_4-based all-solid-state Z-scheme heterojunctions have been shown to be superior for the photocatalytic degradation of organic pollutants. However, visible-light photocatalytic efficiency of g-C_3N_4 is still relatively low and far from the requirements of practical applications. Therefore, it is required to develop higher performance g-C_3N_4-based photocatalysts in the future.

Acknowledgements

Author details

Pengyu Dong[*], Xinguo Xi and Guihua Hou

*Address all correspondence to: dongpy11@gmail.com

Key Laboratory for Advanced Technology in Environmental Protection of Jiangsu Province/
Jiangsu Collaborative Innovation Center for Ecological Building Materials and Environmental
Protection Equipments/Yancheng Institute of Technology, Yancheng, Jiangsu Province, China

References

[1] K. Nakata, A. Fujishima. TiO$_2$ photocatalysis: design and applications. J. Photochem. Photobiol., C, 13 (2012) 169–189.

[2] A. Fujishima, K. Honda. Photolysis-decomposition of water at the surface of an irradiated semiconductor. Nature., 238 (1972) 37–38.

[3] A. Kudo, Y. Miseki. Heterogeneous photocatalyst materials for water splitting. Chem. Soc. Rev., 38 (2009) 253–278.

[4] K. Maeda. Photocatalytic water splitting using semiconductor particles: history and recent developments. J. Photochem. Photobiol., C, 12 (2011) 237–268.

[5] T. Inoue, A. Fujishima, S. Konishi, K. Honda. Photoelectrocatalytic reduction of carbon dioxide in aqueous suspensions of semiconductor powders. Nature., 277 (1979) 637–638.

[6] K. Sunada, T. Watanabe, K. Hashimoto. Bactericidal activity of copper-deposited TiO$_2$ thin film under weak UV light illumination. Environ. Sci. Technol., 37 (2003) 4785–4789.

[7] S. Yin, Y. Aita, M. Komatsu, J. Wang, Q. Tang, T. Sato. Synthesis of excellent visible-light responsive TiO$_{2-x}$N$_y$ photocatalyst by a homogeneous precipitation-solvothermal process. J. Mater. Chem., 15 (2005) 674–682.

[8] K. Hashimoto, H. Irie, A. Fujishima. TiO$_2$ photocatalysis: a historical overview and future prospects. Jpn. J. Appl. Phys., 44 (2005) 8269.

[9] P. Dong, B. Liu, Y. Wang, H. Pei, S. Yin. Enhanced photocatalytic activity of (Mo, C)-codoped anatase TiO$_2$ nanoparticles for degradation of methyl orange under simulated solar irradiation. J. Mater. Res., 25 (2010) 2392–2400

[10] H. Tong, S. Ouyang, Y. Bi, N. Umezawa, M. Oshikiri, J. Ye. Nano-photocatalytic materials: possibilities and challenges. Adv. Mater., 24 (2012) 229–251.

[11] H. Zheng, J.Z. Ou, M.S. Strano, R.B. Kaner, A. Mitchell, K. Kalantar-zadeh. Nanostructured tungsten oxide—properties, synthesis, and applications. Adv. Funct. Mater., 21 (2011) 2175–2196.

[12] I.M. Szilágyi, B. Fórizs, O. Rosseler, Á. Szegedi, P. Németh, P. Király, G. Tárkányi, B. Vajna, K. Varga-Josepovits, K. László. WO_3 photocatalysts: influence of structure and composition. J. Catal., 294 (2012) 119–127.

[13] S. Gullapalli, R. Vemuri, C. Ramana. Structural transformation induced changes in the optical properties of nanocrystalline tungsten oxide thin films. Appl. Phys. Lett., 96 (2010) 1903.

[14] M. Gillet, K. Aguir, C. Lemire, E. Gillet, K. Schierbaum. The structure and electrical conductivity of vacuum-annealed WO_3 thin films. Thin. Solid. Films., 467 (2004) 239–246.

[15] M. Grätzel. Photoelectrochemical cells. Nature., 414 (2001) 338–344.

[16] H. Zhang, G. Chen, D.W. Bahnemann. Photoelectrocatalytic materials for environmental applications. J. Mater. Chem., 19 (2009) 5089–5121.

[17] D. Monllor-Satoca, L. Borja, A. Rodes, R. Gómez, P. Salvador. Photoelectrochemical behavior of nanostructured WO_3 thin-film electrodes: the oxidation of formic acid. ChemPhysChem., 7 (2006) 2540–2551.

[18] Z.-G. Zhao, M. Miyauchi. Nanoporous-walled tungsten oxide nanotubes as highly active visible-light-driven photocatalysts. Angew. Chem., 120 (2008) 7159–7163.

[19] M. Sadakane, K. Sasaki, H. Kunioku, B. Ohtani, R. Abe, W. Ueda. Preparation of 3-D ordered macroporous tungsten oxides and nano-crystalline particulate tungsten oxides using a colloidal crystal template method, and their structural characterization and application as photocatalysts under visible light irradiation. J. Mater. Chem., 20 (2010) 1811–1818.

[20] R. Abe, H. Takami, N. Murakami, B. Ohtani. Pristine simple oxides as visible light driven photocatalysts: highly efficient decomposition of organic compounds over platinum-loaded tungsten oxide. J. Am. Chem. Soc., 130 (2008) 7780–7781.

[21] M. Miyauchi, Photocatalysis and photoinduced hydrophilicity of WO_3 thin films with underlying Pt nanoparticles. Phys. Chem. Chem. Phys., 10 (2008) 6258–6265.

[22] Z. Yi, J. Ye, N. Kikugawa, T. Kako, S. Ouyang, H. Stuart-Williams, H. Yang, J. Cao, W. Luo, Z. Li. An orthophosphate semiconductor with photooxidation properties under visible-lightirradiation. Nat. Mater., 9 (2010) 559–564.

[23] H. Wang, Y. Bai, J. Yang, X. Lang, J. Li, L. Guo. A facile way to rejuvenate Ag_3PO_4 as a recyclable highly efficient photocatalyst. Chem. A Eur. J., 18 (2012) 5524–5529.

[24] Y. Bi, S. Ouyang, J. Cao, J. Ye. Facile synthesis of rhombic dodecahedral AgX/Ag$_3$PO$_4$ (X = Cl, Br, I) heterocrystals with enhanced photocatalytic properties and stabilities. Phys. Chem. Chem. Phys., 13 (2011) 10071–10075.

[25] Y. Bi, S. Ouyang, N. Umezawa, J. Cao, J. Ye. Facet effect of single-crystalline Ag$_3$PO$_4$ sub-microcrystals on photocatalytic properties. J. Am. Chem. Soc., 133 (2011) 6490–6492.

[26] J.-K. Liu, C.-X. Luo, J.-D. Wang, X.-H. Yang, X.-H. Zhong. Controlled synthesis of silver phosphate crystals with high photocatalytic activity and bacteriostatic activity. CrystEngComm., 14 (2012) 8714–8721.

[27] H. Wang, L. He, L. Wang, P. Hu, L. Guo, X. Han, J. Li. Facile synthesis of Ag$_3$PO$_4$ tetrapod microcrystals with an increased percentage of exposed {110} facets and highly efficient photocatalytic properties. CrystEngComm., 14 (2012) 8342–8344.

[28] W. Jun, F. Teng, M. Chen. Facile synthesis of novel Ag$_3$PO$_4$ tetrapods and the {110} facets-dominated photocatalytic activity. CrystEngComm., 15 (2013) 39–42.

[29] Q. Liang, W. Ma, Y. Shi, Z. Li, X. Yang. Hierarchical Ag$_3$PO$_4$ porous microcubes with enhanced photocatalytic properties synthesized with the assistance of trisodium citrate. CrystEngComm., 14 (2012) 2966–2973.

[30] P. Dong, Y. Wang, H. Li, H. Li, X. Ma, L. Han. Shape-controllable synthesis and morphology-dependent photocatalytic properties of Ag$_3$PO$_4$ crystals. J. Mater. Chem. A, 1 (2013) 4651–4656.

[31] G.-F. Huang, Z.-L. Ma, W.-Q. Huang, Y. Tian, C. Jiao, Z.-M. Yang, Z. Wan, A. Pan. Ag$_3$PO$_4$ semiconductor photocatalyst: possibilities and challenges. J. Nanomater., 2013 (2013) 1.

[32] N. Umezawa, O. Shuxin, J. Ye. Theoretical study of high photocatalytic performance of Ag$_3$PO$_4$. Phys. Rev. B, 83 (2011) 035202.

[33] X. Ma, B. Lu, D. Li, R. Shi, C. Pan, Y. Zhu. Origin of photocatalytic activation of silver orthophosphate from first-principles. J. Phys. Chem. C, 115 (2011) 4680–4687.

[34] W. Yao, B. Zhang, C. Huang, C. Ma, X. Song, Q. Xu. Synthesis and characterization of high efficiency and stable Ag$_3$PO$_4$/TiO$_2$ visible light photocatalyst for the degradation of methylene blue and rhodamine B solutions. J. Mater. Chem., 22 (2012) 4050–4055.

[35] Y. Liu, L. Fang, H. Lu, Y. Li, C. Hu, H. Yu. One-pot pyridine-assisted synthesis of visible-light-driven photocatalyst Ag/Ag$_3$PO$_4$. Appl. Catal. B, 115–116 (2012) 245–252.

[36] P. Dong, Y. Wang, B. Cao, S. Xin, L. Guo, J. Zhang, F. Li. Ag$_3$PO$_4$/reduced graphite oxide sheets nanocomposites with highly enhanced visible light photocatalytic activity and stability. Appl. Catal. B, 132–133 (2013) 45–53.

[37] P. Dong, E. Cui, G. Hou, R. Guan, Q. Zhang. Synthesis and photocatalytic activity of Ag$_3$PO$_4$/TiOF$_2$ composites with enhanced stability. Mater. Lett., 143 (2015) 20–23.

[38] J.H. Kim, J.S. Lee. BiVO$_4$-based heterostructured photocatalysts for solar water splitting: a review. Energy. Environ. Focus, 3 (2014) 339–353.

[39] A. Kudo, K. Omori, H. Kato. A novel aqueous process for preparation of crystal form-controlled and highly crystalline BiVO$_4$ powder from layered vanadates at room temperature and its photocatalytic and photophysical properties. J. Am. Chem. Soc., 121 (1999) 11459–11467.

[40] S. Tokunaga, H. Kato, A. Kudo. Selective preparation of monoclinic and tetragonal BiVO$_4$ with scheelite structure and their photocatalytic properties. Chem. Mater., 13 (2001) 4624–4628.

[41] L. Zhang, D. Chen, X. Jiao. Monoclinic structured BiVO$_4$ nanosheets: hydrothermal preparation, formation mechanism, and coloristic and photocatalytic properties. J. Phys. Chem. B, 110 (2006) 2668–2673.

[42] L. Zhou, W. Wang, L. Zhang, H. Xu, W. Zhu. Single-crystalline BiVO$_4$ microtubes with square cross-sections: microstructure, growth mechanism, and photocatalytic property. J. Phys. Chem. C, 111 (2007) 13659–13664.

[43] G. Li, D. Zhang, J.C. Yu. Ordered mesoporous BiVO$_4$ through nanocasting: a superior visible light-driven photocatalyst. Chem. Mater., 20 (2008) 3983–3992.

[44] R. Li, F. Zhang, D. Wang, J. Yang, M. Li, J. Zhu, X. Zhou, H. Han, C. Li. Spatial separation of photogenerated electrons and holes among {010} and {110} crystal facets of BiVO$_4$. Nat. Commun., 4 (2013) 1432.

[45] B. Liu, Y. Fang, Z. Li, S. Xu. Visible-light nanostructured photocatalysts—a review. J. Nanosci. Nanotechnol., 15 (2015) 889–920.

[46] S.J. Hong, S. Lee, J.S. Jang, J.S. Lee. Heterojunction BiVO$_4$/WO$_3$ electrodes for enhanced photoactivity of water oxidation. Energy Environ. Sci., 4 (2011) 1781–1787.

[47] J. Su, L. Guo, N. Bao, C.A. Grimes. Nanostructured WO$_3$/BiVO$_4$ heterojunction films for efficient photoelectrochemical water splitting. Nano Lett., 11 (2011) 1928–1933.

[48] R. Saito, Y. Miseki, K. Sayama. Highly efficient photoelectrochemical water splitting using a thin film photoanode of BiVO$_4$/SnO$_2$/WO$_3$ multi-composite in a carbonate electrolyte. Chem. Commun., 48 (2012) 3833–3835.

[49] F.F. Abdi, T.J. Savenije, M.M. May, B. Dam, R. van de Krol. The origin of slow carrier transport in BiVO$_4$ thin film photoanodes: a time-resolved microwave conductivity Study. J. Phys. Chem. Lett., 4 (2013) 2752–2757.

[50] P. Chatchai, Y. Murakami, S.-Y. Kishioka, A. Nosaka, Y. Nosaka. FTO/SnO$_2$/BiVO$_4$ composite photoelectrode for water oxidation under visible light irradiation. Electrochem. Solid State Lett., 11 (2008) H160–H163.

[51] X. Wang, K. Maeda, A. Thomas, K. Takanabe, G. Xin, J.M. Carlsson, K. Domen, M. Antonietti. A metal-free polymeric photocatalyst for hydrogen production from water under visible light. Nat. Mater., 8 (2009) 76–80.

[52] A. Thomas, A. Fischer, F. Goettmann, M. Antonietti, J.-O. Müller, R. Schlögl, J.M. Carlsson. Graphitic carbon nitride materials: variation of structure and morphology and their use as metal-free catalysts. J. Mater. Chem., 18 (2008) 4893–4908.

[53] W. Shen, L. Ren, H. Zhou, S. Zhang, W. Fan. Facile one-pot synthesis of bimodal mesoporous carbon nitride and its function as a lipase immobilization support. J. Mater. Chem., 21 (2011) 3890–3894.

[54] Y. Cui, Z. Ding, X. Fu, X. Wang. Construction of conjugated carbon nitride nanoarchitectures in solution at low temperatures for photoredox catalysis. Angew. Chem. Int. Ed., 51 (2012) 11814–11818.

[55] S. Cao, J. Low, J. Yu, M. Jaroniec. Polymeric photocatalysts based on graphitic carbon nitride. Adv. Mater., 27 (2015) 2150–2176.

[56] Z. Zhao, Y. Sun, F. Dong. Graphitic carbon nitride based nanocomposites: a review. Nanoscale, 7 (2015) 15–37.

[57] Y. Wang, Q. Wang, X. Zhan, F. Wang, M. Safdar, J. He. Visible light driven type II heterostructures and their enhanced photocatalysis properties: a review. Nanoscale, 5 (2013) 8326–8339.

[58] S.-W. Cao, X.-F. Liu, Y.-P. Yuan, Z.-Y. Zhang, Y.-S. Liao, J. Fang, S.C.J. Loo, T.C. Sum, C. Xue. Solar-to-fuels conversion over In$_2$O$_3$/gC$_3$N$_4$ hybrid photocatalysts. Appl. Catal. B, 147 (2014) 940–946.

[59] P. Zhou, J. Yu, M. Jaroniec. All-solid-state Z-scheme photocatalytic systems. Adv. Mater., 26 (2014) 4920–4935.

[60] S. Kumar, A. Baruah, S. Tonda, B. Kumar, V. Shanker, B. Sreedhar. Cost-effective and eco-friendly synthesis of novel and stable N-doped ZnO/gC$_3$N$_4$ core–shell nanoplates with excellent visible-light responsive photocatalysis. Nanoscale, 6 (2014) 4830–4842.

[61] H. Katsumata, T. Sakai, T. Suzuki, S. Kaneco. Highly efficient photocatalytic activity of g-C$_3$N$_4$/Ag$_3$PO$_4$ hybrid photocatalysts through Z-scheme photocatalytic mechanism under visible light. Ind. Eng. Chem. Res., 53 (2014) 8018–8025.

Some Unitary, Binary, and Ternary Non-TiO$_2$ Photocatalysts

Martyna Marchelek, Magdalena Diak,
Magda Kozak, Adriana Zaleska-Medynska and
Ewelina Grabowska

Additional information is available at the end of the chapter

Abstract

Among all kinds of green earth and renewable energy projects underway, semiconductor photocatalysis has received wide interest because it provides an easy way to directly utilize the energy of either natural sunlight or artificial indoor illumination. TiO$_2$, the most widely used photocatalyst, due to its wide band gap, can only be activated under UV irradiation, and thus, the development of novel semiconductor photocatalysts makes a significant advancement in photocatalytic functional materials. One of the effective strategies to overcome this shortcoming is photosensitizing these wide band gap semiconductors with narrow band gap semiconductors which have proper energy levels. This method can not only improve the photocatalytic activity, due to increasing visible-light-harvesting efficiency, but also can decrease the recombination of the charge carriers, because the formation of n–n or n–p heterojunctions between the combined semiconductors can induce internal electric fields between them. In this regard, this review presents some unitary, binary, and ternary non-TiO$_2$ photocatalysts used for the degradation for organic pollutants and for water splitting.

Keywords: semiconductor photocatalysis, non-TiO$_2$ photocatalysts, composite photocatalysts, pollutant degradation, photoactivity under UV–Vis or visible light

1. Introduction

Among the various Advanced Oxidation Process methods, semiconductor-mediated photocatalysis has been accorded a great significance in recent times due to its potential to mineralize

a wide range of organic pollutants at ambient temperature and pressures into harmless substances, to produce hydrogen in photocatalytic water-splitting process, and to apply in dye-sensitized solar cells [1–3].

From the simple oxides (e.g., TiO_2, ZnO, WO_3, Fe_2O_3), anatase–TiO_2 is a dominant structure employed for sunlight applications mostly due to its charge carrier handling properties. However, the TiO_2-based photocatalyst cannot effectively absorb visible solar light due to a rather large band gap (>3.2 eV), rendering it of little practical significance for solar energy harvesting. Additionally, pure TiO_2 used during photocatalytic processes has few disadvantages, such as low quantum yield due to a high recombination rate between photogenerated electron–hole pairs, or the need of high-energy photons to activate the semiconductors in the UV region.

Qu et al. [4] pointed that designing of an efficient and stable photocatalysts must follow several critical requirements: (*i*) Semiconductor must have band gap large enough to provide energetic electrons and smaller enough to allow for efficient absorption overlap with the solar spectrum (1.23 eV $\ll E_g \ll$ 3.0 eV, typically >2.0 eV); (*ii*) there must be a mechanism to efficiently drive charge separation and the transportation process; and (*iii*) there must be a mechanism to efficiently drive charge separation and the transportation process.

Because, in most cases, single semiconductors are unlikely to satisfy all these requirements, one of the important issues in the photocatalysis fields is to exploit new combining of some semiconductors to form composites which can improve the efficiency of a photocatalytic system. This fact provides an excellent opportunity to continue developing new materials with higher photocatalytic activity and capable to use the sunlight as a green energy source.

The current review is focused on non-TiO_2 materials with particular emphasis placed on application of these photocatalysts in heterogeneous photocatalysis and insight into explanation the photocatalytic mechanism of the composite photocatalyst. This review is organized into four sections: (1) single-semiconductor photocatalysts for pollutant degradation, (2) single-semiconductor photocatalysts for water splitting, (3) semiconductor composite photocatalysts, and (4) conclusions and perspectives.

2. Single-semiconductor photocatalysts for pollutant degradation

In general, fundamental principles of photodegradation mechanism was based on oxidation and reduction reactions of induced charged carriers. Ultimately, in both reactions from water oxidation and dissociation of H_2O_2, hydroxyl radical could be produced, which are highly powerful and nonselective oxidizing agent. During the past few years, numerous efforts have been made for the discovery of new visible-light-responding semiconductors. Among the created groups of photocatalysts, the biggest part in the literature belongs to ferrates, halides, oxides, tungstates, sulfides, and vanadates. All the groups utilized recently in heterogeneous photocatalysis are listed in **Table 1**, while band gap values for selected groups of photocatalyst are shown in **Figure 1**.

Recently, metal sulfides received much attention because their promising properties. CdS is one of the intensively investigated semiconductors owing to the narrow band gap (2.1–2.5 eV) in comparison with TiO$_2$ which may extend the utilization of visible light. For instance, Eskandari et al. [99] synthesized CdS by simple chemical precipitation method using mercaptoethylamine hydrochloride (MEA) as a capping agent. CdS showed higher photocatalytic activity than P25-TiO$_2$ in the photodegradation of methylene blue under blue LED and solar light irradiation. Reusability of the photocatalyst was checked five times; during the first three times, the activity decreased gradually, but in the last two cycles, they observed very sharp drop in photoactivity. Chen et al. [100] also observed higher activity of CdS in comparison with P25-TiO$_2$, after 60 min of UV irradiation nearly 95% of rhodamine B (RhB) was degraded. The band gap (2.24 eV) was calculated according to the UV–Vis absorption spectra [100]. Another very often mentioned material is ZnS. Chen et al. used ZnS rods as photocatalysts for the degradation of methyl orange (95% of MO was degraded after 20 min) and 2,4-dinitrophenol (54% of 2,4-NP was degraded after 20 min) under UV irradiation [105]. ZnS with a band gap equals to 3.84 eV exceeded activity of commercial P25-TiO$_2$. Chen et al. also proposed photocatalytic degradation mechanism of OM and 2,4-NP over ZnS under UV light. For this reason, EDTA-Na$_2$ and potassium iodide (KI) were introduced as the scavengers for h$^+$, isopropanol, and ethanol were used for $^\bullet$OH, and 1,4-benzoquinone for $^\bullet$O$_2^-$, respectively. They confirmed that the photocatalytic process proceeds analogously like for TiO$_2$, and thus, h$^+$ and $^\bullet$O$_2^-$ are the crucial in the degradation pathway under UV irradiation [105]. Chen et al. [115] applied simple wet chemical method for obtaining Bi$_2$S$_3$. The photocatalytic activity was measured by methyl orange degradation in the presence of UV light. After 4 h of irradiation, 97% of methyl orange was decolorized in the presence of Bi$_2$S$_3$ photocatalyst with specific surface area about 20 m^2 g^{-1} [115]. Luo et al. [116] performed Bi$_2$S$_3$ nanorods which exhibited superior activity than P25-TiO$_2$ in rhodamine B degradation under visible light ($\lambda > 420$ nm).

Another extensively examined groups are wide band gap oxides such as ZnO, WO$_3$, Nb$_2$O$_5$, and Bi$_2$O$_3$. Nanosized ZnO photocatalysts were synthesized by Liu et al. Obtained samples exhibited high activity in methyl orange degradation under UV light. After 30 min irradiation, the efficiency was nearly 100%. ZnO was proved to be very stable during 4 cycles. In many publications, some of the photocatalysts are perceived as a narrow band gap semiconductor such as Bi$_2$O$_3$, CeO$_2$, Fe$_2$O$_3$, and WO$_3$. This dispersion in the values of the band gap is inter alia due to different preparation method. Zheng et al. [166] synthesized WO$_3$ nanorod arrays by hydrothermal method, and the results showed that the pH value of the precursor solutions plays crucial role in the formation of the as-prepared structures, which leads to different band gap values. Ameen et al. [50] synthesized ZnO flower-like photocatalysts (E$_g$ = 3.24 eV) which showed very high efficiency for crystal violet degradation under UV light irradiation. After 80 min of irradiation, about 96% was degraded. Mahmodiet al. [51] investigated the photocatalytic activity of ZnO on stainless steel support. The activity measurements were concerned with photoreduction of carbon dioxide in the presence of H$_2$, H$_2$O, and CH$_4$. It was noticed that TiO$_2$ has better photoreduction activity while the highest result for ZnO was achieved in the presence of CH$_4$ [51]. Li et al. [52] tested ZnO nanoparticles in the degradation reaction of methyl orange under UV light illumination. ZnO exhibited excellent degradation efficiency of methyl orange reached 97.84% after 30 min. Moreover, ZnO showed no significant loss of

photocatalytic activity during four repeated cycles [52]. Bismuth oxide with optical band gap value of 2.7 eV could be utilized as a visible-light-driven photocatalyst [79]. Iyyapushpam et al. prepared Bi_2O_3 by sol–gel method. Samples were calcined at two different temperatures (600 and 700°C), and the highest degradation efficiency was attained by semiconductor with higher crystallinity and specific surface area (sample calcined at 600 ◦C). The degradation percentage of methyl orange was found to be 76% [79].
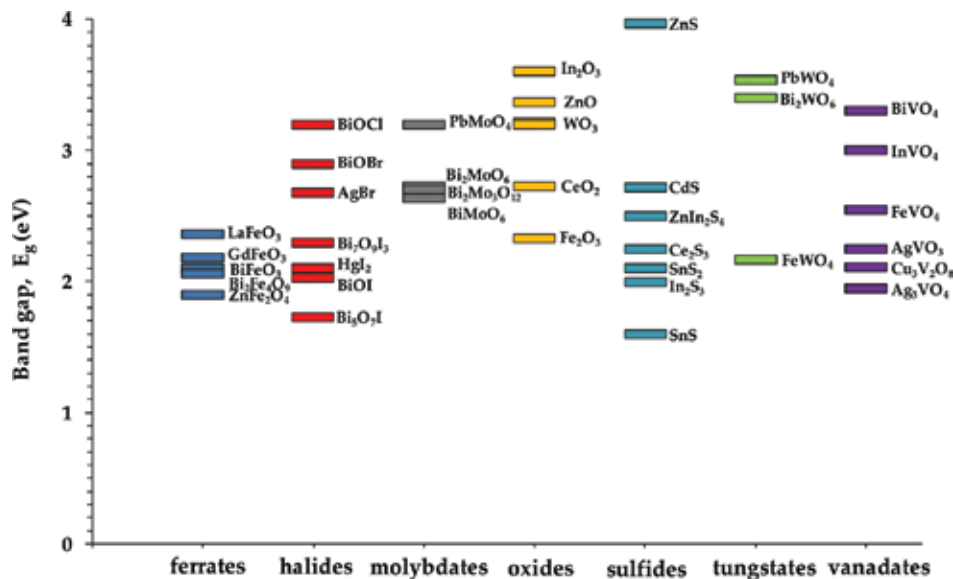
Figure 1. Band gap values for selected groups of photocatalyst collected based on the literature review.

Tungsten-based materials with a low band gap seemed to be promising candidate for the degradation of organic compound under visible light. For instance, Phattharanit et al. [128] obtained multi-layered flower-like Bi_2WO_6 by hydrothermal method and estimated activity of the powder in the degradation of rhodamine B under visible light. The results shown that after 360 min of irradiation, 88% of rhodamine B was degraded, which could be related to photo-sensibilization of semiconductor by dyes. In comparison, Saison et al. [129] synthesized Bi_2WO_6 with the band gap equals 2.9 eV and measured photocatalytic efficiency for Bi_2WO_6 and TiO_2. They observed relatively low activity of Bi_2WO_6 during rhodamine B and stearic acid degradation process under visible light. After calculation of the band diagram, Saison et al. explained that bismuth tungstate has inadequate band positions resulted in rapid recombination of excited pairs because electrons are not able to react with dioxygen.

Among the vanadates, $BiVO_4$ paid much attention because of the stability, nontoxicity, and relative high activity under the visible irradiation. In the most of the published papers, the photocatalytic activity of $BiVO_4$ was measured on model reaction of rhodamine B degradation [145–152]. Lin et al. [145] synthesized $BiVO_4$ (E_g = 2.36 eV) by simple hydrothermal

method. After 180 min of visible light illumination, 100% of rhodamine B (λ >420 nm) was degraded. The stability was evaluated during four cycles, which indicated no significant decrease in photocatalytic activity [145]. Tan et al. [148] synthesized BiVO$_4$ powders by hydrothermal method. By the manipulation of reaction condition, different hierarchical structures such as octahedron, decahedron, spherical, and polyhedral were obtained [148]. The influence of pH values on the crystalline phase and morphology of the BiVO$_4$ powders was examined. The highest visible light photocatalytic activity for the rhodamine B degradation was achieved by sample prepared at pH 7.81 with specific surface area equals 5.15 m^2 g^{-1}. Lin et al. [145] also observed high activity of fishbone-like BiVO$_4$ for RhB degradation. The band gap around 2.36 eV was estimated from UV–Vis spectra. After 180 min irradiation, 100% of dye was removed.

Recently, encountered research about silver halides provides information about excellent activity, however, suffers by very low stability of AgX, which radically limited potentially reuse and application [38]. On the other hand, majority of the bismuth oxyhalides described in literature are perceived as a wide band gap semiconductor with high stability. Guan et al. [21] compared properties of two different kinds BiOCl nanoplates and ultrathin nanosheets. They indicated that these powders varied in band gap value, for BiOCl nanoplates E$_g$ reached 3.25 eV while for nanosheets 3 eV. The higher photocatalytic activity for the degradation of RhB was observed in the case of ultrathin BiOCl. This phenomenon was explained by the creation of different defects which are formed after reducing the thickness of the nanosheets to the atomic scale [21]. Xiao et al. [35] prepared Bi$_7$O$_9$I$_3$ microsheets using simple microwave heating route. The degradation of bisphenol A induced *via* visible light irradiation was investigated. After 60 min of irradiation, almost 100% of bisphenol A was degraded. The reaction rate constant of the optimal sample was over 16 times greater than that of TiO$_2$-P25. Bi$_7$O$_9$I$_3$ microsheets revealed high mineralization capacity of bisphenol A and good stability during the recycle tests, implying a promising forecast in the industrial application of the photodegradation of organic pollutants. The mechanism analyses conducted by LC–MS suggested that the degradation of bisphenol A under visible light irradiation occurred predominantly by direct holes, and the main detected intermediates were hydroquinone and methyl 4-hydroxybenzoate [35].

Ferrates can be specified as a semiconductor with narrow band gap. There are several synthesis methods described in the literature used for ferrate preparation such as hydrothermal [11, 13, 14, 17], microwave hydrothermal [15], microwave [16], solid-state reactions [12], and solution combustion method [18]. These photocatalysts possess superior properties, and therefore, they seemed to allow their use in environmental purification. Due to magnetic properties of ferrates, they can be easily separated from reaction suspension. Shahid et al. reported high photocatalytic activity of MgFe$_2$O$_4$ in the degradation of methylene blue under UV (350 nm) and visible light (λ > 420 nm). In comparison with ferrate, TiO$_2$-P25 exhibited poor photocatalytic activity under visible light; after 50 min of irradiation, only 10% of dye was decomposed, whereas in the presence of MgFe$_2$O$_4$ even 95% of MB was degraded [12]. Tang et al. indicated that LaFeO$_3$ with band gap equals 2.36 eV and strong visible light absorption exhibited much higher activity in the MB degradation than

TiO_2-P25 [16]. Li et al. [11] have examined activity of $GdFeO_3$ in the degradation of 4-chlorophenol under visible light irradiation ($\lambda > 420$ nm). After 5 h of illumination, only 20% of 4-chlorophenol was removed by TiO_2-P25, while almost 85% was degraded over $GdFeO_3$. That obtained $GdFeO_3$ microspheres have characterized by broad absorption in visible light region and quite well photocatalytic stability after fifth run [11].

According to the literature data, many other groups of semiconductors are also used in heterogeneous photocatalysis, such as tantalates, titanates, molybdates, niobates, selenides, phosphates, stannate, carbonate, germanate, and cobaltites. Most of tantalate- and titanate-based materials can be activated only *via* UV light due to generally wide band gap, which can reached even 5.05 eV [167–169]. Nevertheless, it has been reported that these photocatalysts exhibited high activity which may be attributed to crystal structure of perovskites. Liang et al. [47–49]. Microcrystalline $AgNbO_3$ was synthesized by Wu et al. [47] by sol–gel method. The photocatalyst has proved to be stable for all recycle experiments. However, $AgNbO_3$ has shown high activity only for the decomposition of methylene blue and rhodamine B, and for 4-chlorophenol and methyl orange, there was no obvious drop of contaminants concentration. Bismuth niobate prepared by a facile hydrothermal route showed very good visible-light-induced performance for the removal of nitrogen monoxide [48]. It has been shown that the activity results of bismuth niobate are better than that for C-doped TiO_2, $InVO_4$, and BiOBr nanoplates [48]. Promising properties have been noticed also for molybdate-containing materials such as Bi_2MoO_6 with interesting layered perovskite structure [40]. Sun et al. [40] tested Bi_2MoO_6 with nanoplate like morphology prepared *via* hydrothermal method. The photocatalytic performance was evaluated by the degradation of rhodamine B and phenol under environment-friendly blue light emitting diode ($\lambda = 465$ nm) irradiation. They have found that after 30 min of illumination, almost 100% of rhodamine B was degraded, while in the presence of TiO_2-P25, only several percent of dye was removed even with addition of H_2O_2. Phenol was chosen as another model substance in order to exclude the influence of photosensitization. They have examined synergistic effect of photocatalysts and H_2O_2 for the phenol degradation. After 2 h of irradiation, the amount of phenol decreased up to 8% in over Bi_2MoO_6. They have concluded that Bi_2MoO_6 with narrow energy gap is able to respond directly to blue light emitting diode in contrast to TiO_2-P25 [40]. Bi et al. [41] have investigated the stability of Bi_2MoO_6, and during five-cycle experiments, they have not observed any obvious decrease in photocatalytic activity for rhodamine B degradation. Hipolito et al. [46] prepared bismuth molybdate photocatalysts using co-precipitation method. The activity of so obtained $Bi_2Mo_3O_{12}$ was further investigated for the removal of nitric oxide under UVA light irradiation. In comparison with Bi_2MoO_6 with a band gap equals 2.44 eV, the $Bi_2Mo_3O_{12}$ ($E_g = 2.7$ eV) turned out to be more active reaching around 30% more of NO removal. This dispersion of results could be attributed to higher surface area of $Bi_2Mo_3O_{12}$ and its abundant adsorption sites for NO adsorption [46].

Summarizing, it is possible to find several photocatalysts which provide better light-harvesting performance than TiO_2, and it is assumed that they can be good replacement of TiO_2. Unfortunately, there is still lack of precise research related to possibility of reuse the powders. It is

needed to search new materials which will be environmental friendly, resistant to photocorrosion, and will not dissolve in water; otherwise, toxic metals and compounds such as Cd, Pb, or semiconductor sulfides will be useless for practical application. Most of the current research based on degradation of dyes, which can act as an organic semiconductor and participate in charge transition into CB under visible light irradiation. Therefore, the use of dye-photocatalysts system should be taken into consideration in the process of sewage treatment. Also, it should be noticed that the examination of activity in the degradation compounds such as 4-chlorophenol under UV light must be consider due to sensitivity to photolysis. Furthermore, results from the photolysis should be always placed with actual photocatalytic activity in order to make a reasonably comparison. There is still need for the standardization of photocatalytic measurements by utilizing the identical test equipment, photocatalysts dosage, kind and concentration of model compound, and other experiments condition, which allow making proper worldwide comparison of photocatalytic results.

Group	Semiconductor, Eg (eV)	Model pollutant	Irradiation range	Ref.
Antimonate	GaSbO$_4$ (3.7)	Acetone, salicylic acid	UV	[5]
	AgSbO$_3$ (2.6)	Rhodamine B	Vis	[6]
Carbonate	Ag$_2$CO$_3$ (2.46)	Rhodamine B, methyl orange, methylene blue	Vis	[7]
	(BiO)$_2$CO$_3$ (3.09–2.67)	Rhodamine B	UV	[8]
Cobaltites	LaCoO$_3$ (n/a)	Methyl orange	Vis	[9]
	La1–xBaxCoO$_3$ (2.80–2.21)	Formalachite green	Vis	[10]
Ferrate	GdFeO$_3$ (1.97–2.18)	4-Chlorophenol	Vis	[11]
	MgFe$_2$O$_4$ (n/a)	Methylene blue	Vis	[12]
	BiFeO$_3$ (2.1)	Rhodamine B	Vis	[13]
	Bi$_2$Fe$_4$O$_9$ (1.94–2.06)	Methyl orange	Vis	[14, 15]
	LaFeO$_3$ (2.36)	Methylene blue	Vis	[16]
	ZnFe$_2$O$_4$ (1.9)	Rhodamine B	Vis	[17, 18]
Germanate	CeGeO$_4$ (3.1)	Terephthalic acid	UV	[19]
	ZnGa$_2$O$_4$ (4.5)	Ethylbenzene, methyl orange, rhodamine B, methylene blue benzene, toluene	UV-Vis	[20]
Halides	BiOCl (2.87–3.2)	17 Alpha-ethinyl estradiol (EE2) and estriol, methyl orange, methylene green, rhodamine B, tetracycline hydrochloride	UV, Vis	[21–29]
	BiOBr (2.45–2.9)	Methyl orange, rhodamine B, tetracycline hydrochloride	UV, Vis	[22–24, 28, 30, 31]

Group	Semiconductor, Eg (eV)	Model pollutant	Irradiation range	Ref.
	BiOI (1.43–2.03)	Methyl orange, rhodamine B, tetracycline hydrochloride, 17 alpha-ethinyl estradiol (EE2), estriol	UV, Vis	[22–24, 32–34]
	$Bi_7O_9I_3$ (2.23–2.30)	Bisphenol-A	Vis	[35]
	Bi_5O_7I (1.73)	Rhodamine B	Vis	[36]
	HgI_2 (2.10)	Rhodamine B	Vis	[37]
	AgBr (2.58–2.68)	Methylene blue, methyl orange	Vis	[38, 39]
Molybdate	Bi_2MoO_6 (2.51–2.73)	Phenol, rhodamine B	Vis	[40, 41]
	$BiMoO_6$ (2.64)	Phenol, ibuprofen, rhodamine B	Vis	[42, 43]
	$PbMoO_4$ (3.1–3.2)	Methyl orange, rhodamine B, indigo carmine, orange G	UV, Vis	[44, 45]
	$Bi_2Mo_3O_{12}$ (2.73–2.70)	Nitric oxide	UV	[46]
Niobate	$AgNbO_3$ (2.9)	4-Chlorophenol, methyl blue, methyl orange, rhodamine B	Vis	[47]
	Bi_3NbO_7 (2.89)	Nitrogen monoxide	Vis	[48]
	$SnNb_2O_6$ (2.3–2.6)	Rhodamine B, methyl orange, malachite green	UV, Vis	[49]
Oxides	ZnO (2–3.37)	4-Chlorophenol, alizarin red S, CO2 reduction, hexane, methylene blue, reactive brilliant red K-2BP, methyl orange, rhodamine B, thionine, estrone, H2O2 generation, yellow 15	UV, UV-Vis	[50–70]
	ZrO_2 (n/a)	Direct Red 81 victoria Blue	UV-Vis	[71]
	WO_3 (2.4–3.21)	CO_2, CR, methyl blue, methylene blue, Orange II, rhodamine B	UV, Vis	[72–77]
	In_2O_3 (3.6)	Perfluorooctanoic acid	UV	[70]
	$a\text{-}Fe_2O_3$ (2.33)	Methylene blue	Vis	[78]
	Bi_2O_3 (1.3–2.73)	Cr(VI), aldehydes, congo red, rhodamine B, methyl orange	UV, Vis	[79–82]

Group	Semiconductor, Eg (eV)	Model pollutant	Irradiation range	Ref.
	CeO$_2$ (2.81–3.2)	4-Nitrophenol, indigo carmine, AO7, methylene blue, rhodamine B	UV, Vis	[83–86]
	Cu$_2$O (n/a)	Methyl orange	Vis	[87]
	Ga$_2$O$_3$ (n/a)	Methyl orange, rhodamine B	UV	[88]
	Nb$_2$O$_5$	Rhodamine B	UV, Vis	[89]
Phosphates	Ag$_3$PO$_4$ (2.35–2.47)	Bisphenol A, rhodamine B	Vis	[90–92]
	BiPO$_4$ (3.35–4.4)	Benzene, rhodamine B	UV	[93, 94]
selenides	ZnSe (2.9)	Methylene blue	Vis	[95]
Stannates	CdSnO$_3$ (4.4)	Benzene	UV	[96]
	Zn$_2$SnO$_4$ (n/a)	Reactive Red 141	Sunlight	[97]
	ZnSnO$_3$ (3.34)	Methylene blue	UV-Vis	[98]
Sulfides	CdS (2.1–2.5)	Methyl orange, methylene blue, methylene blue, rhodamine B	UV, Vis	[99–104]
	ZnS (3.37–3.97)	2, 4-Dinitrophenol, dinitrobenzene methylene green, rhodamine B, methyl orange	UV	[105–108]
	SnS$_2$ (2.1–2.25)	Methyl orange phenol, rhodamine B	Vis	[109–111]
	In$_2$S$_3$ (1.89–2.0)	DNA purine bases, formic acid, hydrogenation of 4-nitroaniline	UV, Vis	[112, 113]
	SnS (1.6–1.3)	Methylene blue	Vis	[114]
	Bi$_2$S$_3$ (n/a)	Methyl orange rhodamine B	UV, Vis	[115, 116]
	Ce$_2$S$_3$ (2.1)	Nitrobenzene reduction	UV, Vis	[117]
	ZnIn$_2$S$_4$ (2.72–1.92)	Benzyl alcohol	Vis	[118]
	CdIn$_2$S$_4$(n/a)	Inactivation of *Escherichia coli*	Vis	[119]
	ZnIn$_2$S$_4$ (n/a)	Methyl orange	Vis	[120]

Group	Semiconductor, Eg (eV)	Model pollutant	Irradiation range	Ref.
	$CdIn_2S_4$(n/a)	Methyl orange	Vis	[121]
Tantalates	$Sr_{0.25}H_{1.5}$ Ta_2O_6 H_2O (4.9)	Benzene oxidation	UV	[122]
	β-$BiTaO_4$ (2.45–2.65)	Methylene blue	Vis	[123]
	$Ba_4Ta_2O_9$ (5.05)	Methyl orange	UV	[124]
Titanate	$K_2Ti_6O_{13}$ (3.06–3.48)	Methyl orange	UV	[125]
	$FeTiO_3$ (2.54–2.58)	Rhodamine B	Vis	[126]
	$BaTiO_3$ (n/a)	Rhodamine B	Vis	[127]
Tungstates	Bi_2WO_6 (2.48–3.4)	2,4-Dichlorophenoxyacetic acid, methylene blue, rhodamine 6G, rhodamine B, tetracycline	UV, Vis	[128–139]
	$FeWO_4$ (2.17 eV)	Methyl orange	UV-Vis	[140]
	$SrWO_4$ (n/a)	Rhodamine B, rhodamine 6G	UV	[141]
	$Na_4W_{10}O_{32}$ (n/a)	Coumarin propan-2-ol	UV	[142]
	$NiWO_4$ (n/a)	Methylene blue	Vis	[143]
	$PbWO_4$ (3.54)	Acid orange II	UV	[144]
Vanadates	$BiVO_4$ (1.85–3.3)	Blue, ciprofloxacin, methylene phenol, rhodamine B	UV, Vis	[145–158]
	$AgVO_3$ (2.11–2.25)	Bisphenol A, rhodamine B	Vis	[159]
	Ag_3VO_4 (1.95)	Rhodamine B	Vis	[160]
	$InVO_4$ (2.4–3.0)	Ciprofloxacin, methylene blue, rhodamine B	Vis	[161–163]
	$FeVO_4$ (2.02–2.55)	Phenol	UV-Vis	[164]
	$Cu_3V_2O_8$ (2.11–2.05)	Methyl orange	Vis	[165]

Table 1. Selected representative photocatalysts and model substances used for activity measurements.

3. Single-semiconductor photocatalysts for water splitting

Photocatalytic water splitting, which is a process of decomposition of water into hydrogen and oxygen, is a promising method for obtaining clean and renewable energy. When light with an energy equivalent or greater than band gap of the semiconductor photocatalysts is irradiated,

the electrons in the valence band are excited into the conduction band. The excitation of electrons creates holes in the valence band. These photogenerated electrons and holes trigger the redox reaction [170]. There are three main steps of photocatalytic water splitting: (1) The photocatalyst absorbs photon energy and electron–hole pairs are generated in the bulk; (2) the photo-excited charge carriers should separate and migrate to the surface with minimal recombination; and finally, (3) the free charge carriers triggers the oxidation and reduction reaction respectively at the surface, that is, the electron reduces H$_2$O to H$_2$ and the hole oxidized H$_2$O to O$_2$, respectively.

The production of hydrogen using a particulate photocatalyst has been examined by various research groups since 1972 and since that time scientists are trying to obtain the most efficient combination of semiconductors which will give payable level of hydrogen recovery [171]. In recent years, many various types of homogeneous and heterogeneous photocatalysts have been developed and intensively analyzed. Summary of studied heterogeneous photocatalysts used for water-splitting process are presented in **Table 2**. In fact, heterogeneous photocatalysis received lately more attention because of wider application scale. There is no single photocatalyst which can meet all the requirements to proceed efficient water-splitting process for H$_2$ production. The success is not only in careful selection of semiconductor photocatalysts but also their optimal surface structures. Additionally, a suitable band gap, matching energy band for H$_2$ and O$_2$ evolution, high quantum efficiency and stability are also important. The main task of scientists is to develop the composition of semiconductor materials, which will carry out suitable optical absorption, reduction, and oxidation abilities and increase efficiency in solar energy conversion [197]. It is thought that co-catalyst components such as Pt, Ni, Rh, and Ru can promote H$_2$ evolution because of their lower over potentials, while they are also active for the oxygen reduction reaction (ORR), which corresponds to the reverse of the water-splitting reaction [36]. Positive water splitting was also observed in the presence of co-catalysts such as Pt, Pd, and Rh or a metal oxide such as NiO, RuO$_2$, and Cr$_2$O$_3$, which are loaded onto the photocatalyst surface to produce active sites for water reduction reaction [171]. Following the assumption of water-splitting process for hydrogen production, we chose these examples, which demonstrate the best perspectives.

Following the idea of development of better photocatalysts for water splitting in visible light spectrum, we chose the most promising examples by comparing energy band gaps and hydrogen production rate, not considering TiO$_2$ photocatalysts. The apparent quantum yield (AQY) for the production of hydrogen and oxygen gas can be estimated by the following Equation (1):

$$AQY(\%) = \frac{\text{number of reacted electrones}}{\text{number of incident photons}} \times 100 \tag{1}$$

Liao et al. [180] conducted water-splitting process using cobalt oxide particles. The photocatalysts were obtained from nonactive CoO micropowders with two distinct methods —femtosecond laser ablation and mechanical ball-milling. Water-splitting experiments were performed in air-tight flasks with CoO nanoparticles suspended in neutral water. Generation

of hydrogen and oxygen was measured by a gas chromatograph (GC) equipped with a thermal conduction detector (Gow-Mac). High photocatalytic activity of the nanoparticles was analyzed by electrochemical impedance spectroscopy (SRS residue gas analyser, RGA200), which comes from a significant shift in the position of the band edge of the material with regard to water redox potential. The conduction band of CoO micropowder is located below the hydrogen—evolution potential what leads to inactivity in water splitting process. A mass spectrometer was also used to identify isotope gas species from water splitting. Received CoO nanoparticles can decompose pure water under visible light irradiation without any co-catalysts or sacrificial reagents with the hydrogen production assessed for 71,429 µmol/h g^{-1} [180].

Twinned Cd$_{0.5}$Zn$_{0.5}$S anisotropic nanocrystals (called nanorods) with controllable aspect ratios and a high proportion of long-range ordered twin planes were investigated by Liu et al. [195]. Between the planes in the crystal, the zinc–blende (ZB) and wurtzite (WZ) were generated. The TEM image revealed that nanorods consisted of a high density of stacking faults with parallel distribution, which were coherent twin boundaries. During the process between the segments of ZB and WZ, the type II staggered band was created which in particular dimension cause the generation of myriad homojunctions. This formation leads to photocatalytic hydrogen production with a remarkable QE of 62% and 25,800 µmol/h g^{-1}. Different combinations of the same elements were investigated by Li et al. [194], where the solid solution of Zn$_{1-x}$Cd$_x$S was analyzed. Obtained structures characterized with a small crystallite size and precise band structure. The photocatalytic hydrogen production experiment was performed at ambient temperature and atmospheric pressure, using 350 W xenon arc lamp through a UV cut-off filter ($\lambda > 400$ nm). Study revealed that sample containing Zn$_{0.5}$Cd$_{0.5}$S is the most promising in terms of hydrogen production with the rate of 7420 µmol/h g^{-1}, which is much more than amounts produced with the pure CdS or ZnS samples.

Group	Semiconductor, Eg (eV)	Irradiation range(nm)	H$_2$ production rate (µmol/h g^{-1})	O$_2$ production rate (µmol/h g^{-1})	Apparent quantum yield (%)	Ref.
Sulfides	CdS (2.4)	$\lambda > 420$	25	n/a	n/a	[172]
	CaIn$_2$S$_4$(1.84–168)	$\lambda > 420$	2.64	n/a	n/a	[173]
	Sb$_2$TiS$_5$ (1.87)	UV	10.4	n/a	n/a	[174]
	(CuAg)$_{0.15}$In$_{0.3}$ Zn$_{1.4}$S$_2$ (2.72–1.92)	$\lambda > 420$	1750	n/a	12.8	[175]
	ZnIn$_{2.3}$S$_{4+y}$ (4.894)	$\lambda > 420$	363	n/a	n/a	[176]
	Cu$_3$SnS$_4$(1.38)	$\lambda > 420$	1100	n/a	3.9	[177]
	Mn$_{0.24}$Cd$_{0.76}$ S(2.28)	$\lambda > 420$	10,900	n/a	9.5	[178]
Oxides	Ta$_2$O$_5$ (3.9)	$\lambda > 420$	7100	n/a	n/a	[179]

Group	Semiconductor, Eg (eV)	Irradiation range(nm)	H$_2$ production rate (μmol/h g^{-1})	O$_2$ production rate (μmol/h g^{-1})	Apparent quantum yield (%)	Ref.
	CoO (2.6)	λ>420	71,429	35 714	5	[180]
	Fe$_2$O$_3$ (2.3)	λ>420	n/a	3	n/a	[181]
Vanadates	InVO$_4$(3.0)	λ>420	14.16	n/a	n/a	[182]
	Ag$_2$Sr(VO$_3$)$_4$(2.4)	λ>420	n/a	8,1	n/a	[183]
	Sr(VO$_3$)$_2$ (2.7)	λ>420	n/a	12	n/a	[183]
Halides	LaOF (4.7)	UV	27	n/a	n/a	[184]
Tantalites	NaTaO$_3$ (4.1)	UV	3106	n/a	n/a	[185]
	Cd$_2$Ta$_2$O$_7$ (3.35)	UV	173	86.3	n/a	[186]
Ferrates	GaFeO$_3$ (2.02-2.18)	λ>395	289	n/a	n/a	[187]
	LaFeO$_3$ (2.07)	λ>420	3315	n/a	n/a	[188]
	ZnRh$_2$O$_4$(1.2-2.2)	UV, Vis	500	n/a	27	[189]
	NiFe$_2$O$_4$ (1.7)	λ>420	1.97	n/a	0.07	[190]
	Ta$_3$N$_5$ (2.08)	λ>420	410	n/a	–	[191]
	ZnIn$_2$S$_4$(2.59-2.83)	λ>420	220.45	n/a	13.16	[192]
	Bi$_{0.5}$Na$_{0.5}$TiO$_3$ (2.82-2.92)	UV-Vis	324.5	n/a	3	[193]
	Zn$_{0.5}$Cd$_{0.5}$S (2.45)	λ>420	7420	n/a	9.6	[194]
	Cd$_{0.5}$Zn$_{0.5}$S (2.62)	λ>420	25,800	n/a	62	[195]
	K$_{0.5}$La$_{0.5}$Bi2 Ta$_2$O$_9$/ K$_{0.5}$La$_{0.5}$ Bi$_2$Nb$_2$O$_9$ (3.22-3.9)	UV	5.9–531	3.4 – 182	n/a	[196]

Table 2. Non-TiO$_2$ single photocatalysts for water splitting in UV/visible light spectrum.

Solid solutions of Mn$_{1-x}$Cd$_x$S were fabricated by hydrothermal route in low temperature (130°C) by Liu et al. [178]. The H$_2$ evolution from water was performed under 300 W Xe lamp. 0.025 g of powder photocatalyst was dispersed in a pyrex cell with aqueous solution of 0.1 M Na$_2$S and 0.5 M Na$_2$SO$_3$. The characterization of samples revealed that with growing value of x, the rate of hydrogen increases. The highest value of H$_2$ production presented Mn$_{0.24}$Cd$_{0.76}$S which in fact exceeds rate for pure CdS. The procedure was continued, and after third turn, the amount of H$_2$ decreased, what can be the result of consumption of the sacrificial agents—Na$_2$S and Na$_2$SO$_3$. The examined solution shows good photocatalytic stability and anti-

photocorrosion capability during water-splitting reaction what can be a promising discovery for the future. There are some examples of semiconductors which generate smaller amount of hydrogen than compounds described above; however, it still have potential for further studies in water-splitting area. $ZnRh_2O_4$ with rate of hydrogen production of 500 μmol/h g^{-1} was studied by Takimoto et al. [189]. The measurements were conducted under monochromatic light and full Xe light lamp in wide range of wavelengths (400 < λ ≤ 770 nm) with an intensity of 10 μW/cm^2. The amount of hydrogen produced is much less than in case of other presented semiconductors, but it is extraordinary because of a high efficiency yield (12%) at a wavelength of λ = 770 nm. The study revealed that this photocatalyst should be deeper investigated mainly because of possible usage in a wide range of light spectrum both visible and infrared light what is quite unique [189].

The overall compilation of already conducted experiments shows that there is a big potential for hydrogen production in photocatalytic water splitting in visible light range. The values of energy band gap indicate that non-TiO_2 single photocatalysts should be good candidates used in hydrogen production process without light limitations. The most promising results were obtained for different combinations of Cd composite what can lead to further studies in this particular area. Unfortunately, it is clear that single photocatalysts are not as efficient as should be expected. This is the reason why attention of researchers has been moved to more promising topics as the binary and ternary compounds or doping processes. Moreover, the demonstration of the simultaneous evolution of H_2 and O_2 is extremely difficult in the two-step water-splitting system because backward reactions easily proceed over each photocatalyst.

4. Binary composite photocatalysts

There are number of different types of photocatalytic materials, which are inefficient or not active during the light-mediated process of pollutants degradation. Various methods are used to improve the oxidation ability of photocatalysts in purification systems, such as doping with nonmetal ions, rare-earth metals, noble metals and transition metal ions, surface modification, dye sensitizing [198]. Among them, enhancing the photocatalytic activity can be achieved by coupling single semiconductors in composites.

Synthesis of new 3D semiconductor composites creates the opportunity to use materials with lower energy activation as a photocatalysts. Furthermore, application of the composite structures can lead to photocatalysts activated by low powered and low cost irradiation sources (such as LEDs or black fluorescent UV lamps) and can be used both in air and water purification systems. Therefore, it is important to develop convenient, low-cost, and environmental-friendly methods to synthesize high-quality photocatalysts.

Nowadays promising idea based on combining wide band gap semiconductors with narrow band gap materials. The narrow band gap photocatalyst can be excited in visible light region. The photogenerated holes and electrons can be transported to the wide band gap semiconductor and photo-excited with lower energy transfer. Furthermore, the nanocomposites materials exhibit improved quantum efficiency. Therefore, composites with narrower band

gap semiconductors have been developed to extend the photo-absorption range, facilitate the separation of the photo-induced carriers, and extend the activity into the visible light region. A composite of two photocatalysts with surface contact formed a heterojunction which limits the electron transfer. There are three main processes which may lead to consumption of the photo-induced electrons: (*i*) volume recombination (recombination with produced holes inside the photocatalyst), (*ii*) surface recombination (reaction with spices on surface of the particle, and (*iii*) the H$_2$ production as a result of reaction with protons.

4.1. Photo-excitation mechanisms of binary composites

In general, there are three different mechanisms of binary composite photo-excitation under ultraviolet and visible light. Most of the current research is focused on efficiently suppression of the recombination processes. Summary of studied composites and possible mechanisms of photo-excitation (named mechanism A, B, and C) are presented in **Table 3**. During the irradiation, both photocatalysts can be excited with photogenerated charge carriers depending on the band gap energy (E$_g$). Usually under visible light irradiation, the electrons produced in narrow band gap semiconductor (named semiconductor A) with less positive conduction band (CB) can be transferred quickly to the more positive CB of the photocatalyst with the wider band gap (semiconductor B). In the other hand, the photo-excited holes from semiconductor B could be shifted easily into the valence band (VB) of the semiconductor A. The each position of conduction and valence band in photocatalysts according to the mechanism A is presented in **Figure 2a**. The Ag$_3$PO$_4$/ZnFe$_2$O$_4$ composite was synthesized by Chen et al. *via* a solvothermal-liquid phase deposition method [230]. The photocatalytic activity test was performed as a 2,4-dichlorophenol degradation under visible light irradiation. During the process using Ag$_3$PO$_4$/ZnFe$_2$O$_4$ with mass ratio 9:1, 95% of the pollutant was decomposed after 70 min of irradiation (two and three times higher than result for single photocatalyst). It was found that the conduction and valence band of ZnFe$_2$O$_4$ is more negative than CB and VB of Ag$_3$PO$_4$. Structure formation of Ag$_3$PO$_4$/ZnFe$_2$O$_4$ material resulted in expanding the spectral responsive range of Ag$_3$PO$_4$. High-effective photocatalyst under Vis light was obtained by combining the single BiVO$_4$ with FeVO$_4$ [222]. The heterojunction composite photocatalysts was stable in photocatalytic removal of metronidazole in aqueous phase. Moreover, enhanced oxidation properties resulted from the fast transfer of photogenerated charge carriers. The optimal weight ratio in Ag$_3$PO$_4$/BiOBr composite was equal to 0.7. The process of energy bias generation at heterojunction plays significant role in electron and hole pair transfer. The rate of removal rhodamine B under visible light was maintained at 95% after 6 recycling processes [224].

In view of the internal field between semiconductors, in some composites used for photodegradation under visible light, only electron transfer exists without hole migration in the valence band (the process is named mechanism B, see **Figure 2b**) [199, 213, 214, 218, 219]. Xu et al. [213] synthesized CdS/MoS$_2$ composite active under visible irradiation range. The favorable heterojunction between CdS and MoS$_2$ extended lifetime of the charge carriers [213, 214]. The same type of mechanism was observed for CdS/SnO$_2$ photocatalyst where electrons shift from cadmium sulfides conduction band to the thin oxides band [199]. Consequently, the charge carriers in junction between semiconductors were effectively separated *via* one-step process.

All types of described mechanisms (mechanism A, B, and C) are caused by the presence of heterojunctions among different semiconductors that enhance the separation of the photo-generated electron–hole pairs, hindering their recombination.

Whereas, under the ultraviolet light illumination, both semiconductors simultaneously or the semiconductor with wider band gap in the composite could be excited. The mechanism of photo-excitation in binary composites was investigated by Hamrouni et al. Two photocatalysts: $ZnO/ZnWO_4$ and ZnO/SnO_2 prepared by a facile sol–gel method were examined in the photocatalytic decomposition of 4-nitrophenol under ultraviolet light range [200]. It was found that the local heterojunction between the photocatalysts pair facilitates the separation of the photogenerated e^-/h^+ pairs (mechanism C, see **Figure 2c**). A photocatalysts with enhanced electron–hole separation and excellent photocatalytic performance was investigated by Duo et al. [215, 217]. The methyl orange solution and Rhodamine B were used as a model substance in degradation under simulated sunlight. Both composites $BiPO_4/BiOCl$ and $BiPO_4/BiOBr$ exhibited significantly higher activity in dyes elimination than single semiconductors [216, 217].
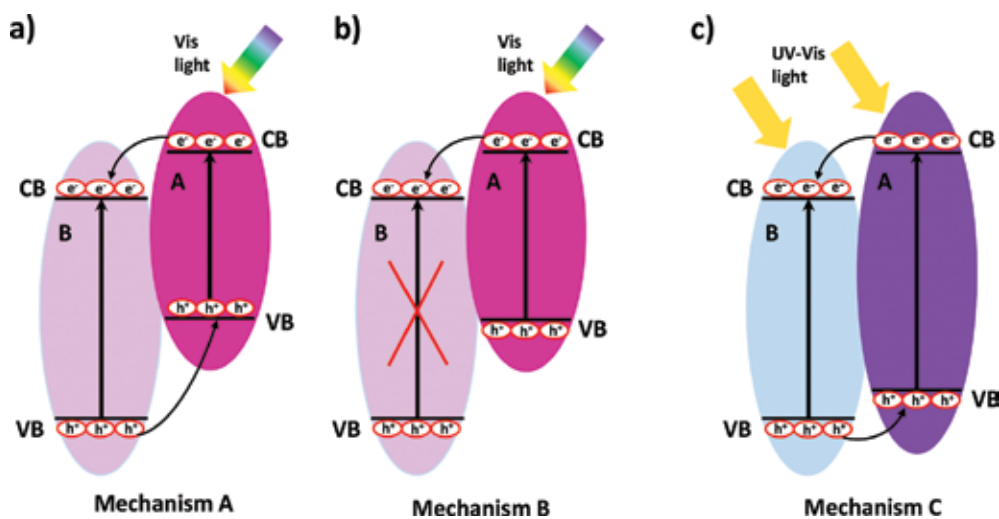
Figure 2. Possible mechanism of semiconductors composite photo-excitation: (a) Mechanism A under UV–Vis light, (b) Mechanism B under Vis light, and (c) Mechanism C under Vis light.

Semiconductor A	Semiconductor B	Irradiation range	Excitation mechanism	Ref.
CdS (2.17)	SnO_2 (3.3; 3.55)	Vis	Mechanism C	[199]
ZnO_2 (3.2)		UV	Mechanism A	[200]
ZnO_2 (3.2)	$ZnWO_4$ (3.14)	UV	Mechanism A	[200]
ZnO_2 (3.2)	Bi_2O_3 (2.8; 2.38; 2.75; 2.89)	UV	Mechanism A	[201]
$NaBiO_3$ (2.36)		Vis	Mechanism B	[202, 203]

Semiconductor A	Semiconductor B	Irradiation range	Excitation mechanism	Ref.
BaTiO$_3$ (3.18)		UV	Mechanism A	[204]
NaBi(MoO$_4$)$_2$ (3.08)		Vis	Mechanism B	[205]
Bi$_5$O$_7$I (3.13)		Vis	Mechanism B	[206, 207]
Bi$_2$O$_3$ (2.9)	Bi$_2$WO$_6$ (2.8; 3.1; 2.97)	Vis	Mechanism B	[208]
ZnWO$_4$ (3.75)		UV-Vis	Mechanism A	[209]
CeO$_2$ (2.58)		UV-Vis	Mechanism A	[210]
Bi$_{12}$TiO$_{20}$ (2.57		UV-Vis	Mechanism A	[211]
CdS (2.22)	Bi$_2$MoO$_6$ (2.8)	Vis	Mechanism B	[212]
CdS (2.25)	MoS$_2$ (1.75)	Vis	Mechanism C	[213, 214]
BiOBr (2.62)	BiPO$_4$ (4.16; 3.83; 4.11)	Sunlight, Vis	Mechanism A, Mechanism C	[215, 216]
BiOCl (3.12)		Sunlight	Mechanism A	[217]
Bi$_2$MoO$_6$ (2.53)		Vis	Mechanism C	[218]
Bi$_2$MoO$_6$ (2.71)	BiIO$_4$ (3.02)	Vis	Mechanism C	[219]
Cu$_2$O (2.5)	BiVO4 (2.0; 2.47)	Vis	Mechanism B	[220, 221]
FeVO$_4$ (2.05)		Vis	Mechanism B	[222]
BiVO$_4$ (2.49)	Bi$_4$V$_2$O$_{11}$ (2.22)	Vis	Mechanism B	[223]
Ag$_3$PO$_4$ (2.36)	BiOBr (2.74; 3.13; 2.76; 2.81)	Vis	Mechanism B	[224]
BiOI (2.45; 1.74; 1.72)		Vis	Mechanism B	[225–227]
BiOI (1.90)	WO$_3$ (2.60)	Vis	Mechanism B	[228]
WO$_3$ (2.68)	H$_2$WO$_4$ (2.45)	Vis	Mechanism B	[229]
ZnFe$_2$O$_4$ (1.88)	Ag$_3$PO$_4$ (2.44)	Vis	Mechanism B	[230]
Ag$_3$VO$_4$ (2.05)	Co$_3$O$_4$ (2.07)	Vis	Mechanism B	[231]
	ZnFe$_2$O$_4$ (1.90)	Vis	Mechanism B	[232]
Ag$_4$P$_2$O$_7$ (2.63)	AgBr (2.6)	Vis	Mechanism B	[233]
AgBr (2.64)	ZnO (3.0; 3.22; 3.3; 3.37; 3.26)	Vis	Mechanism C	[234–237]
Ag$_2$S (1.0)		Sunlight	Mechanism A	[238]
AgI (−)		Vis	Mechanism C	[239]
AgI (2.51)	Ag$_2$CO$_3$ (2.30)	Vis	Mechanism B	[240]
SmCrO$_3$ (2.7)	Sm$_2$Ti$_2$O$_7$ (3.2)	Sunlight	Mechanism A	[241]
In$_2$O$_3$ (2.90)	α-Fe$_2$O$_3$ (2.03)	Vis	Mechanism B	[242]

Table 3. Summary of studied composites and possible mechanisms of photo-excitation.

4.2. Ternary composite photocatalysts

Based on the literature data, it could be expected that ternary semiconductor composites provide an opportunity for multi(two)-photons excitation of photoactive materials with lower energy photons and utilization of heterojunction to drive electronic processes in the desired direction. Consequently, the selective photo-excitation of localized electronic states to gain better selectivity should be achieved [243].

The composite of $KTaO_3$–CdS–MoS_2 with different molar ratio was synthesized by Bajorowicz et al. [244] *via* hydrothermal method. The micromaterials were prepared under strictly controlled conditions of temperature and pressure depending on the material type. Hydrothermal method does not require a calcination step and is easy to carry out technological conditions. Various structures of the photocatalysts such as cubic, hexagonal, nanoleaf, and microspheres were obtained. Calcination at 500°C for 3 h and hydro/solvothermal mixed solutions method were used to combine single semiconductors. The highest phenol photodegradation (80% under UV–Vis and 42% under Vis light) was observed for the $KTaO_3$–CdS–MoS_2 at the 10:5:1 molar ratio. In the toluene oxidation process under ultraviolet light, the powder exhibit very good stability and efficiency during four measurement cycles (activity reached about 50%) [244]. A comparatively to SnO_2/ZnO/$ZnWO_4$ composites in this case probably a two-photon excitation occurs under UV–Vis irradiation [200, 244]. The $KTaO_3$/CdS/WO_3, $KTaO_3$/CdS/MoS_2, $KTaO_3$/$CdSe$/$SrTiO_3$ composites preparing by various route with different molar ratio were compare in photocatalytic degradation of gaseous toluene under ultraviolet light. The results suggest that the structure, morphology, and photoactivity depend on the type and molar content of additional semiconductors as well as on the preparation method. Samples prepared by one-pot hydrothermal synthesis had higher surface area. Unfortunately, the morphology was not well developed and crystal structures of each single semiconductor were not formed. In four subsequent cycles, the photoactivity using the $KTaO_3$/CdS/MoS_2 (10:5:1) ranged 60% after 60 min of irradiation [245]. Hong et al. found that highly enhanced photocatalytic activity is due to synergistic effects of heterostructured ZnS/CuS/CdS material which can improve light absorption and charge carriers flow. The photocatalyst was stable under applied conditions (under solar irradiation 1 kW/m², AM 1.5 G) in H_2-production from a water splitting. The optimum ratio of loading the Cu equal to 0.81 wt% and Cd equal to 14.7 wt% was selected. The authors believed that the solar light causes electron excitation and separation in CdS (because of relatively narrow band gap), and consequently, efficient separated carriers flow to CuS conduction band during the holes from the ZnS were transferred to the valence band of CdS. Additionally, enhancing the H_2 production may result from the interfacial charge transfer between valence band of ZnS and CuS and partial reduction of CuS to Cu_2S [246]. It was observed that for some composites (i.e., ZnO/$AgBr$/Ag_2CrO_4), two semiconductors are excited and act as electron donors for wider photocatalyst. Reduction processes of the pollutant occur in the conduction band of the electron acceptor, whereas the electron donors will responsible for the oxidation reactions on valence band [247]. On the other hand, other mechanism, where ZnO plays a role of electron donor, was observed for SnO_2/ZnO/$ZnWO_4$ composite [200]. The SnO_2/ZnO/$ZnWO_4$ composite was examined under UV irradiation in 4-nitrophenol degradation process. Generated

electrons in the conduction band of ZnO are shifted to those of SnO_2 and $ZnWO_4$; meanwhile, holes may be transferred from the valence band of SnO_2 and $ZnWO_4$ to that of ZnO. It was established that the elimination efficiency of a pollutant depends on adsorption level on the photocatalytic surface and ability to react with the photogenerated charge carriers. The amount of each semiconductors in the photocatalytic material determined the photocatalytic activity [200]. Enhanced photocatalytic activity in rhodamine B degradation process was observed for In_2O_3/AgBr/Bi_2WO_6 ternary composite (see structure on **Figure 3a**) [248]. Photocatalyst has exhibited higher activity under UV, visible, and simultaneous sunlight in comparison to single Bi_2WO_6 semiconductor, binary AgBr/Bi_2WO_6 material and pure P25. Proposed mechanism based on electrons transfer from In_2O_3 with the widest band gap to AgBr and consequently transition e^- from AgBr to Bi_2WO_6, which is semiconductor with the least negative CB in composite. The generated O_2^{*-} radicals in the conduction band plays a role in oxidation processes of pollutant. The produced holes (h^+) in the VB of semiconductors can oxidize the water molecules on the photocatalyst surface and leads to produce hydroxyl radicals (*OH) which are able to degrade dyes into CO_2 and H_2O (see **Figure 3b**.) [248]. A various materials are tested in different model photocatalytic reactions and under various conditions. Therefore, it is intricate to summarize and compare properties and photoactivity of new 3D structures. Some already investigated combinations of ternary composites are presented in **Table 4**.

Semiconductor I, Eg (eV)	Semiconductor II, Eg (eV)	Semiconductor III, Eg (eV)	Irradiation range	Ref.
ZnO (3.2)	AgBr (2.6)	Ag_2CrO_4 (1.8)	Vis	[247]
ZnO (−)	Ag_3VO_4 (2.1)	Fe_3O_4 (−)	Vis	[249]
ZnO (3.2)	AgI (2.8)	Fe_3O_4 (0.1)	Vis	[250]
ZnO	Ag_1	Ag_2CrO_4	Vis	[251]
SnO_2 (3.2)	ZnO (3.55)	$ZnWO_4$ (3.14)	UV	[200]
CdS (2.25)	PbS (1.2–1.5)	ZnO (3.36)	Vis	[252]
ZnS	CuS	CdS	Sunlight	[246]
Fe_3O_4 (−)	AgBr (−)	ZnO (3.2)	Vis	[253]
Fe_3O_4 (0.1)	SiO_2 (8.9)	Bi_2MoO_6 (2.71)	Vis	[254]
BiOBr (2.72)	SiO_2 (−)	Fe_3O_4 (−)	UV-Vis, Vis	[255]
Bi_2S_3	Bi_2O_3	$Bi_2O_2CO_3$	Vis	[256]
In_2O_3 (3.75)	AgBr (2.6)	Bi_2WO_6 (2.76)	UV, Vis, sunlight	[248]
Ag_2O	Ag_3VO_4	$Ag_4V_2O_7$	Vis	[257]
PdS (−)	CdS (−)	NiS (−)	Vis	[258]

Table 4. Compilation of ternary composites and photo-excitation irradiation range.

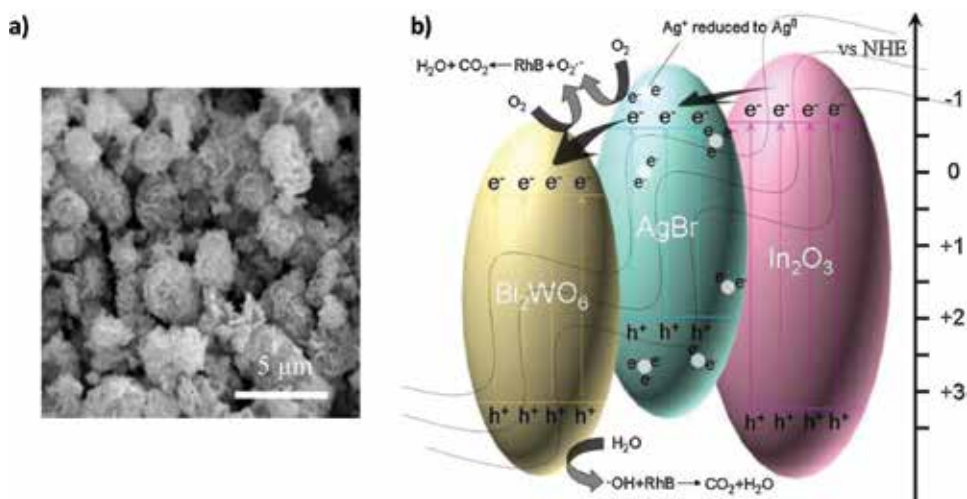**Figure 3.** Ternary $In_2O_3/AgBr/Bi_2WO_6$ photocatalyst (a) Scanning Electron Microscope image, (b) Possible mechanism of photo-excitation in composite structure. Adapted with permission from Ref. [248].

Concluding the mechanism of photo-excitation of ternary composites, it is still not well understood. According to Serpone theory, photo-excitation of components A and B would be very efficient because the two nanomaterials are activated through their fundamental absorption band [243, 259]. There are some interactions which probably occur, while the irradiation excites photocatalyst. The process could be sophisticated and need further investigation.

5. Conclusions

Semiconductor photocatalysis affords a potential solution to the problems of energy shortages and environmental pollution. However, photo-efficiency of the most single semiconductors is limited because of the rapid electron–hole recombination. Therefore, the development of efficient visible-light-driven photocatalysts is a major challenge in this field. The photocatalytic activity of semiconductor photocatalysts depends on its physical and chemical properties, and additionally, depends on the recombination of photo-excited electrons and holes occurs at crystal lattice defects. Fortunately, the coupling of two or three semiconductors with different band gap values could improve the stability, necessary for practical applications and could extend the energy range used for excitation. Especially, the fabrication of a *p–n* junction is believed to be the most effective because of the existence of an internal electric field. Moreover, the hybrid photocatalyst can benefit from the synergistic effects such as enhanced light-harvesting ability, efficient photogenerated electron–hole separation, and improved photo-stability, and thus, the photoactivity is remarkably improved. However, it should be noted that the reason for the improvement of composite photocatalyst is not only due to the effects described above but also due to enhancement of surface acidity or alkalinity and the surface

population of OH groups, which can promote the adsorption of reaction substrates and facilities the generation of hydroxyl radicals (•OH), respectively.

Based on the literature data, it can be concluded that most of the photocatalytic investigations are focused on dyes oxidation (such as methyl orange, rhodamine B, methylene blue, and malachite green) as the model degradation process of pollutants. According to Ohtani recommendation, the use of organic dyes as a model compound for photocatalytic decomposition reaction, enabling the feasible determination of photocatalytic activity, especially using spectrophotometric analysis [260]. He indicated at least three reasons for its inappropriateness. One is that the dye molecules absorb photons, especially in the visible light range, and thus photo-excited electrons may be injected into photocatalyst particles as has been suggested by the action spectrum similar to the absorption spectrum of the dye. Another reason is that the absolute molar amount of dye contained in the reaction system can be much smaller than that of a solid photocatalyst. Since the photo-absorption coefficient of dyes is generally large, for example, $>10^5$ mol^{-1} L cm^{-1}, the concentration can be 10^{-5} mol L^{-1} and the absolute molar amount can be 10^{-6} mol when the volume of the solution is 100 mL. The third reason is that the mechanism of dye degradation is so complicated that efficiency of the photocatalytic reaction cannot be measured.

In this point of view, there are still few works investigated on the photoactivity of composite photocatalyst shows enhanced photocatalytic activity for water splitting and organic degradation except dyes. Additionally, to better understand the properties of semiconductor composites and their role in photocatalysis processes, novel preparation methods need to be developed. Moreover, photocatalytic mechanisms and relationships among the structures forming the composites, surface, and crystal properties and photocatalytic activity should be thoroughly investigated and clarified.

Acknowledgements

Author details

Martyna Marchelek, Magdalena Diak, Magda Kozak, Adriana Zaleska-Medynska and Ewelina Grabowska*

*Address all correspondence to: ewelina.grabowska@ug.edu.pl

Department of Environmental Technology, Faculty of Chemistry, University of Gdansk, Gdansk, Poland

References

[1]   Chen C, Ma W, Zhao J. Semiconductor-mediated photodegradation of pollutants under visible-light irradiation. Chemical Society Reviews. 2010;39(11):4206–4219.

[2]   Li K, An X, Park KH, Khraisheh M, Tang J. A critical review of CO_2 photoconversion: Catalysts and reactors. Catalysis Today. 2014;224:3–12.

[3]   Ahmad H, Kamarudin S, Minggu L, Kassim M. Hydrogen from photo-catalytic water splitting process: A review. Renewable and Sustainable Energy Reviews. 2015;43:599–610.

[4]   Qu Y, Duan X. Progress, challenge and perspective of heterogeneous photocatalysts. Chemical Society Reviews. 2013;42(7):2568–2580.

[5]   Fu Y, Xue H, Qin M, Liu P, Fu X, Li Z. Nanocrystalline $GaSbO_4$ with high surface area prepared via a facile hydrothermal method and its photocatalytic activity study. Journal of Alloys and Compounds. 2012;522:144–148.

[6]   Liu W, Liu X, Fu Y, You Q, Huang R, Liu P, et al. Nanocrystalline pyrochlore $AgSbO_3$: Hydrothermal synthesis, photocatalytic activity and self-stable mechanism study. Applied Catalysis B: Environmental. 2012;123:78–83.

[7]   Dong H, Chen G, Sun J, Li C, Yu Y, Chen D. A novel high-efficiency visible-light sensitive Ag_2CO_3 photocatalyst with universal photodegradation performances: Simple synthesis, reaction mechanism and first-principles study. Applied Catalysis B: Environmental. 2013;134:46–54.

[8]   Tang J, Zhao H, Li G, Lu Z, Xiao S, Chen R. Citrate/urea/solvent mediated self-assembly of $(BiO)_2CO_3$ hierarchical nanostructures and their associated photocatalytic performance. Industrial & Engineering Chemistry Research. 2013;52(35):12604–12612.

[9]   Jung WY, Hong S-S. Synthesis of $LaCoO_3$ nanoparticles by microwave process and their photocatalytic activity under visible light irradiation. Journal of Industrial and Engineering Chemistry. 2013;19(1):157–160.

[10] Zhang C, He H, Wang N, Chen H, Kong D. Visible-light sensitive $La_{1-x}Ba_xCoO_3$ photocatalyst for malachite green degradation. Ceramics International. 2013;39(4):3685–3689.

[11] Li X, Duan Z-Q. Synthesis of $GdFeO_3$ microspheres assembled by nanoparticles as magnetically recoverable and visible-light-driven photocatalysts. Materials Letters. 2012;89:262–265.

[12] Shahid M, Jingling L, Ali Z, Shakir I, Warsi MF, Parveen R, et al. Photocatalytic degradation of methylene blue on magnetically separable $MgFe_2O_4$ under visible light irradiation. Materials Chemistry and Physics. 2013;139(2):566–571.

[13] Wei J, Zhang C, Xu Z. Low-temperature hydrothermal synthesis of BiFeO$_3$ microcrystals and their visible-light photocatalytic activity. Materials Research Bulletin. 2012;47(11):3513–3517.

[14] Liu Y, Zuo R. Morphology and optical absorption of Bi$_2$Fe$_4$O$_9$ crystals via mineralizer-assisted hydrothermal synthesis. Particuology. 2013;11(5):581–587.

[15] Liu Z, Wu B, Zhu Y. Microwave hydrothermal synthesis of Bi$_2$Fe$_4$O$_9$ crystals with visible light photocatalytic activity. Materials Chemistry and Physics. 2012;135(2):474–478.

[16] Tang P, Tong Y, Chen H, Cao F, Pan G. Microwave-assisted synthesis of nanoparticulate perovskite LaFeO$_3$ as a high active visible-light photocatalyst. Current Applied Physics. 2013;13(2):340–343.

[17] Sun Y, Wang W, Zhang L, Sun S, Gao E. Magnetic ZnFe$_2$O$_4$ octahedra: Synthesis and visible light induced photocatalytic activities. Materials Letters. 2013;98:124–127.

[18] Sun S, Yang X, Zhang Y, Zhang F, Ding J, Bao J, et al. Enhanced photocatalytic activity of sponge-like ZnFe$_2$O$_4$ synthesized by solution combustion method. Progress in Natural Science: Materials International. 2012;22(6):639–643.

[19] Xing J, Yang C, Li WK, Gong XQ, Yang HG. Soft chemistry synthesis of high-crystalline orthogermanate CeGeO$_4$: A new photocatalyst. Journal of Solid State Chemistry. 2013;197:204–208.

[20] Sun M, Li D, Zhang W, Chen Z, Huang H, Li W, et al. Rapid microwave hydrothermal synthesis of ZnGa$_2$O$_4$ with high photocatalytic activity toward aromatic compounds in air and dyes in liquid water. Journal of Solid State Chemistry. 2012;190:135–142.

[21] Guan M, Xiao C, Zhang J, Fan S, An R, Cheng Q, et al. Vacancy associates promoting solar-driven photocatalytic activity of ultrathin bismuth oxychloride nanosheets. Journal of the American Chemical Society. 2013;135(28):10411–10417.

[22] Li G, Qin F, Wang R, Xiao S, Sun H, Chen R. BiOX (X = Cl, Br, I) nanostructures: Mannitol-mediated microwave synthesis, visible light photocatalytic performance, and Cr(VI) removal capacity. Journal of Colloid and Interface Science. 2013;409:43–51.

[23] Qin X, Cheng H, Wang W, Huang B, Zhang X, Dai Y. Three dimensional BiOX (X = Cl, Br and I) hierarchical architectures: Facile ionic liquid-assisted solvothermal synthesis and photocatalysis towards organic dye degradation. Materials Letters. 2013;100:285–288.

[24] Zhang W, Zhang Q, Dong F. Visible-light photocatalytic removal of NO in air over BiOX (X = Cl, Br, I) single-crystal nanoplates prepared at room temperature. Industrial & Engineering Chemistry Research. 2013;52(20):6740–6746.

[25] Chen L, Yin S-F, Huang R, Zhou Y, Luo S-L, Au C-T. Facile synthesis of BiOCl nanoflowers of narrow band gap and their visible-light-induced photocatalytic property. Catalysis Communications. 2012;23:54–57.

[26] Ahern JC, Fairchild R, Thomas JS, Carr J, Patterson HH. Characterization of BiOX compounds as photocatalysts for the degradation of pharmaceuticals in water. Applied Catalysis B: Environmental. 2015;179:229–238.

[27] Zhang X, Wang X-B, Wang L-W, Wang W-K, Long LL, Li W-W, et al. Synthesis of a highly efficient BiOCl single-crystal nanodisk photocatalyst with exposing {001} facets. ACS Applied Materials & Interfaces. 2014;6(10):7766–7772.

[28] Cheng H, Huang B, Dai Y. Engineering BiOX (X = Cl, Br, I) nanostructures for highly efficient photocatalytic applications. Nanoscale. 2014;6(4):2009–2026.

[29] Pare B, Sarwan B, Jonnalagadda S. The characteristics and photocatalytic activities of BiOCl as highly efficient photocatalyst. Journal of Molecular Structure. 2012;1007:196–202.

[30] Huo Y, Zhang J, Miao M, Jin Y. Solvothermal synthesis of flower-like BiOBr microspheres with highly visible-light photocatalytic performances. Applied Catalysis B: Environmental. 2012;111:334–341.

[31] Liu Z, Wu B, Xiang D, Zhu Y. Effect of solvents on morphology and photocatalytic activity of BiOBr synthesized by solvothermal method. Materials Research Bulletin. 2012;47(11):3753–3757.

[32] Cao J, Zhou C, Lin H, Xu B, Chen S. Direct hydrolysis preparation of plate-like BiOI and their visible light photocatalytic activity for contaminant removal. Materials Letters. 2013;109:74–77.

[33] Shi X, Chen X, Chen X, Zhou S, Lou S. Solvothermal synthesis of BiOI hierarchical spheres with homogeneous sizes and their high photocatalytic performance. Materials Letters. 2012;68:296–299.

[34] Hao R, Xiao X, Zuo X, Nan J, Zhang W. Efficient adsorption and visible-light photocatalytic degradation of tetracycline hydrochloride using mesoporous BiOI microspheres. Journal of hazardous materials. 2012;209:137–145.

[35] Xiao X, Hao R, Zuo X, Nan J, Li L, Zhang W. Microwave-assisted synthesis of hierarchical $Bi_7O_9I_3$ microsheets for efficient photocatalytic degradation of bisphenol-A under visible light irradiation. Chemical Engineering Journal. 2012;209:293–300.

[36] Cao J, Li X, Lin H, Xu B, Luo B, Chen S. Low temperature synthesis of novel rodlike Bi_5O_7I with visible light photocatalytic performance. Materials Letters. 2012;76:181–183.

[37] Tang J, Li D, Feng Z, Long C. HgI_2: A novel photocatalyst with high performance in degradation of rhodamine B dyes under visible-light irradiation. Journal of Alloys and Compounds. 2015;653:310–314.

[38] Dai K, Lu L, Liu Z, Liu Q, Chen Z. A scalable synthesis technique of novel AgBr microcrystal and its visible light photocatalytic performance. Materials Letters. 2012;87:94–96.

[39] Liu L, Xu H, Li H, Xu Y, Xia J, Yin S. Synthesis and characterization of the efficient visible-light-induced photocatalyst AgBr and its photodegradation activity. Journal of Physics and Chemistry of Solids. 2012;73(4):523–529.

[40] Sun Y, Wang W, Zhang L, Sun S. The photocatalysis of Bi$_2$MoO$_6$ under the irradiation of blue LED. Materials Research Bulletin. 2013;48(10):4357–4361.

[41] Bi J, Che J, Wu L, Liu M. Effects of the solvent on the structure, morphology and photocatalytic properties of Bi$_2$MoO$_6$ in the solvothermal process. Materials Research Bulletin. 2013;48(6):2071–2075.

[42] Zhang Z, Wang W, Ren J, Xu J. Highly efficient photocatalyst Bi$_2$MoO$_6$ induced by blue light-emitting diode. Applied Catalysis B: Environmental. 2012;123:89–93.

[43] Zhang M, Shao C, Zhang P, Su C, Zhang X, Liang P, et al. Bi$_2$MoO$_6$ microtubes: Controlled fabrication by using electrospun polyacrylonitrile microfibers as template and their enhanced visible light photocatalytic activity. Journal of Hazardous Materials. 2012;225:155–163.

[44] Hernández-Uresti D, Martínez-de la Cruz A, Aguilar-Garib J. Photocatalytic activity of PbMoO$_4$ molybdate synthesized by microwave method. Catalysis Today. 2013;212:70–74.

[45] Hashim M, Hu C, Wang X, Li X, Guo D. Synthesis and photocatalytic property of lead molybdate dendrites with exposed (001) facet. Applied Surface Science. 2012;258(15):5858–5862.

[46] Luévano-Hipólito E, Martínez-de la Cruz A, Yu Q, Brouwers H. Photocatalytic removal of nitric oxide by Bi$_2$Mo$_3$O$_{12}$ prepared by co-precipitation method. Applied Catalysis A: General. 2013;468:322–326.

[47] Wu W, Liang S, Chen Y, Shen L, Yuan R, Wu L. Mechanism and improvement of the visible light photocatalysis of organic pollutants over microcrystalline AgNbO$_3$ prepared by a sol–gel method. Materials Research Bulletin. 2013;48(4):1618–1626.

[48] Ai Z, Ho W, Lee S. A stable single-crystal Bi$_3$NbO$_7$ nanoplates superstructure for effective visible-light-driven photocatalytic removal of nitric oxide. Applied Surface Science. 2012;263:266–272.

[49] Liang S, Liang R, Wen L, Yuan R, Wu L, Fu X. Molecular recognitive photocatalytic degradation of various cationic pollutants by the selective adsorption on visible light-driven SnNb$_2$O$_6$ nanosheet photocatalyst. Applied Catalysis B: Environmental. 2012;125:103–110.

[50] Ameen S, Akhtar MS, Nazim M, Shin H-S. Rapid photocatalytic degradation of crystal violet dye over ZnO flower nanomaterials. Materials Letters. 2013;96:228–232.

[51] Mahmodi G, Sharifnia S, Madani M, Vatanpour V. Photoreduction of carbon dioxide in the presence of H_2, H_2O and CH_4 over TiO_2 and ZnO photocatalysts. Solar Energy. 2013;97:186–194.

[52] Li G, Liu Y. Photocatalytic degradation of methyl orange and gas-sensing performance of nanosized ZnO. Materials Science in Semiconductor Processing. 2013;16(3):792–796.

[53] Kansal SK, Lamba R, Mehta S, Umar A. Photocatalytic degradation of Alizarin Red S using simply synthesized ZnO nanoparticles. Materials Letters. 2013;106:385–389.

[54] Kumar R, Kumar G, Umar A. ZnO nano-mushrooms for photocatalytic degradation of methyl orange. Materials Letters. 2013;97:100–103.

[55] Lv Y, Pan C, Ma X, Zong R, Bai X, Zhu Y. Production of visible activity and UV performance enhancement of ZnO photocatalyst via vacuum deoxidation. Applied Catalysis B: Environmental. 2013;138:26–32.

[56] Muthirulan P, Meenakshisundararam M, Kannan N. Beneficial role of ZnO photocatalyst supported with porous activated carbon for the mineralization of alizarin cyanin green dye in aqueous solution. Journal of Advanced Research. 2013;4(6):479–484.

[57] Pei Z, Ding L, Hu J, Weng S, Zheng Z, Huang M, et al. Defect and its dominance in ZnO films: A new insight into the role of defect over photocatalytic activity. Applied Catalysis B: Environmental. 2013;142:736–743.

[58] Rahman QI, Ahmad M, Misra SK, Lohani MB. Hexagonal ZnO nanorods assembled flowers for photocatalytic dye degradation: Growth, structural and optical properties. Superlattices and Microstructures. 2013;64:495–506.

[59] Vu TT, del Río L, Valdés-Solís T, Marbán G. Fabrication of wire mesh-supported ZnO photocatalysts protected against photocorrosion. Applied Catalysis B: Environmental. 2013;140:189–198.

[60] Li J, Lu G, Wang Y, Guo Y, Guo Y. A high activity photocatalyst of hierarchical 3D flowerlike ZnO microspheres: Synthesis, characterization and catalytic activity. Journal of Colloid and Interface Science. 2012;377(1):191–196.

[61] Liu Y, Lv H, Li S, Xing X, Xi G. Preparation and photocatalytic property of hexagonal cylinder-like bipods ZnO microcrystal photocatalyst. Dyes and Pigments. 2012;95(3): 443–449.

[62] Xu F, Chen J, Guo L, Lei S, Ni Y. In situ electrochemically etching-derived ZnO nanotube arrays for highly efficient and facilely recyclable photocatalyst. Applied Surface Science. 2012;258(20):8160–8165.

[63] Khayyat SA, Akhtar M, Umar A. ZnO nanocapsules for photocatalytic degradation of thionine. Materials Letters. 2012;81:239–241.

[64] Jongnavakit P, Amornpitoksuk P, Suwanboon S, Ratana T. Surface and photocatalytic properties of ZnO thin film prepared by sol–gel method. Thin Solid Films. 2012;520(17): 5561–5567.

[65] Wang H, Dong S, Chang Y, Zhou X, Hu X. Microstructures and photocatalytic properties of porous ZnO films synthesized by chemical bath deposition method. Applied Surface Science. 2012;258(10):4288–4293.

[66] Hafez HS. Highly active ZnO rod-like nanomaterials: Synthesis, characterization and photocatalytic activity for dye removal. Physica E: Low-dimensional Systems and Nanostructures. 2012;44(7):1522–1527.

[67] Lee SD, Nam S-H, Kim M-H, Boo J-H. Synthesis and photocatalytic property of ZnO nanoparticles prepared by spray-pyrolysis method. Physics Procedia. 2012;32:320–326.

[68] Umar A, Akhtar M, Al-Hajry A, Al-Assiri M, Almehbad NY. Hydrothermally grown ZnO nanoflowers for environmental remediation and clean energy applications. Materials Research Bulletin. 2012;47(9):2407–2414.

[69] Anas S, Rahul S, Babitha K, Mangalaraja R, Ananthakumar S. Microwave accelerated synthesis of zinc oxide nanoplates and their enhanced photocatalytic activity under UV and solar illuminations. Applied Surface Science. 2015;355:98–103.

[70] Li Z, Zhang P, Shao T, Li X. In$_2$O$_3$ nanoporous nanosphere: A highly efficient photocatalyst for decomposition of perfluorooctanoic acid. Applied Catalysis B: Environmental. 2012;125:350–357.

[71] Bansal P, Chaudhary GR, Mehta S. Comparative study of catalytic activity of ZrO$_2$ nanoparticles for sonocatalytic and photocatalytic degradation of cationic and anionic dyes. Chemical Engineering Journal. 2015;280:475–485.

[72] Gao X, Su X, Yang C, Xiao F, Wang J, Cao X, et al. Hydrothermal synthesis of WO$_3$ nanoplates as highly sensitive cyclohexene sensor and high-efficiency MB photocatalyst. Sensors and Actuators B: Chemical. 2013;181:537–543.

[73] Huang J, Xiao L, Yang X. WO$_3$ nanoplates, hierarchical flower-like assemblies and their photocatalytic properties. Materials Research Bulletin. 2013;48(8):2782–2785.

[74] Ou JZ, Rani RA, Balendhran S, Zoolfakar AS, Field MR, Zhuiykov S, et al. Anodic formation of a thick three-dimensional nanoporous WO$_3$ film and its photocatalytic property. Electrochemistry Communications. 2013;27:128–132.

[75] Yamazaki S, Yamate T, Adachi K. Photocatalytic activity of aqueous WO$_3$ sol for the degradation of Orange II and 4-chlorophenol. Applied Catalysis A: General. 2013;454:30–36.

[76] Szilágyi IM, Fórizs B, Rosseler O, Szegedi Á, Németh P, Király P, et al. WO$_3$ photocatalysts: Influence of structure and composition. Journal of Catalysis. 2012;294:119–127.

[77] Kumar SG, Rao KK. Tungsten-based nanomaterials (WO$_3$ & Bi$_2$WO$_6$): Modifications related to charge carrier transfer mechanisms and photocatalytic applications. Applied Surface Science. 2015;355:939–958.

[78] Zhang G-Y, Feng Y, Xu Y-Y, Gao D-Z, Sun Y-Q. Controlled synthesis of mesoporous α-Fe$_2$O$_3$ nanorods and visible light photocatalytic property. Materials Research Bulletin. 2012;47(3):625–630.

[79] Iyyapushpam S, Nishanthi S, Padiyan DP. Photocatalytic degradation of methyl orange using α-Bi$_2$O$_3$ prepared without surfactant. Journal of Alloys and Compounds. 2013;563:104–107.

[80] Iyyapushpam S, Nishanthi S, Padiyan DP. Synthesis of room temperature bismuth oxide and its photocatalytic activity. Materials Letters. 2012;86:25–27.

[81] Riente P, Matas Adams A, Albero J, Palomares E, Pericàs MA. Light-driven organocatalysis using inexpensive, nontoxic Bi$_2$O$_3$ as the photocatalyst. Angewandte Chemie. 2014;126(36):9767–9770.

[82] Qin F, Zhao H, Li G, Yang H, Li J, Wang R, et al. Size-tunable fabrication of multifunctional Bi$_2$O$_3$ porous nanospheres for photocatalysis, bacteria inactivation and template-synthesis. Nanoscale. 2014;6(10):5402–5409.

[83] Qian J, Chen F, Wang F, Zhao X, Chen Z. Daylight photocatalysis performance of biomorphic CeO$_2$ hollow fibers prepared with lens cleaning paper as biotemplate. Materials Research Bulletin. 2012;47(8):1845–1848.

[84] Feng T, Wang X, Feng G. Synthesis of novel CeO$_2$ microspheres with enhanced solar light photocatalyic properties. Materials Letters. 2013;100:36–39.

[85] Ansari SA, Khan MM, Ansari MO, Kalathil S, Lee J, Cho MH. Band gap engineering of CeO$_2$ nanostructure using an electrochemically active biofilm for visible light applications. RSC Advances. 2014;4(32):16782–16791.

[86] Liyanage AD, Perera SD, Tan K, Chabal Y, Balkus KJ, Jr. Synthesis, characterization, and photocatalytic activity of Y-Doped CeO2 nanorods. ACS Catalysis. 2014;4(2):577–584.

[87] Li L, Zhang W, Feng C, Luan X, Jiang J, Zhang M. Preparation of nanocrystalline Cu$_2$O by a modified solid-state reaction method and its photocatalytic activity. Materials Letters. 2013;107:123–125.

[88] Li X, Zhen X, Meng S, Xian J, Shao Y, Fu X, et al. Structuring β-Ga$_2$O$_3$ photonic crystal photocatalyst for efficient degradation of organic pollutants. Environmental Science & Technology. 2013;47(17):9911–9917.

[89] Lopes OF, Paris EC, Ribeiro C. Synthesis of Nb$_2$O$_5$ nanoparticles through the oxidant peroxide method applied to organic pollutant photodegradation: A mechanistic study. Applied Catalysis B: Environmental. 2014;144:800–808.

[90] Katsumata H, Taniguchi M, Kaneco S, Suzuki T. Photocatalytic degradation of bisphe-
nol A by Ag_3PO_4 under visible light. Catalysis Communications. 2013;34:30–34.

[91] Vu TA, Dao CD, Hoang TT, Nguyen KT, Le GH, Dang PT, et al. Highly photocatalytic
activity of novel nano-sized Ag_3PO_4 for rhodamine B degradation under visible light
irradiation. Materials Letters. 2013;92:57–60.

[92] Wan J, Sun L, Fan J, Liu E, Hu X, Tang C, et al. Facile synthesis of porous Ag_3PO_4
nanotubes for enhanced photocatalytic activity under visible light. Applied Surface
Science. 2015;355:615–622.

[93] Pan C, Xu J, Chen Y, Zhu Y. Influence of OH-related defects on the performances of
$BiPO_4$ photocatalyst for the degradation of rhodamine B. Applied Catalysis B: Envi-
ronmental. 2012;115:314–319.

[94] Long B, Huang J, Wang X. Photocatalytic degradation of benzene in gas phase by
nanostructured $BiPO_4$ catalysts. Progress in Natural Science: Materials International.
2012;22(6):644–653.

[95] Wang X, Li L, Lin Y, Zhu J. EDTA-assisted template-free synthesis and improved
photocatalytic activity of homogeneous ZnSe hollow microspheres. Ceramics Interna-
tional. 2013;39(5):5213–5218.

[96] Chen Y, Li D, Chen J, Wang J, Meng S, Xian J, et al. A promising new photocatalyst
$CdSnO_3 \cdot 3H_2O$ for air purification under ambient condition. Applied Catalysis B:
Environmental. 2013;129:403–408.

[97] Foletto EL, Battiston S, Simões JM, Bassaco MM, Pereira LSF, de Moraes FloresÉM, et
al. Synthesis of $ZnAl_2O_4$ nanoparticles by different routes and the effect of its pore size
on the photocatalytic process. Microporous and Mesoporous Materials. 2012;163:29–
33.

[98] Borhade AV, Baste YR. Study of photocatalytic asset of the $ZnSnO_3$ synthesized by
green chemistry. Arabian Journal of Chemistry. 2012.

[99] Eskandari P, Kazemi F, Azizian-Kalandaragh Y. Convenient preparation of CdS
nanostructures as a highly efficient photocatalyst under blue LED and solar light
irradiation. Separation and Purification Technology. 2013;120:180–185.

[100] Chen F, Cao Y, Jia D, Niu X. Facile synthesis of CdS nanoparticles photocatalyst with
high performance. Ceramics International. 2013;39(2):1511–1517.

[101] Li X, Xi Y, Hu C, Wang X. Water induced size and structure phase transition of CdS
crystals and their photocatalytic property. Materials Research Bulletin. 2013;48(2):295–
299.

[102] Deng C, Tian X. Facile microwave-assisted aqueous synthesis of CdS nanocrystals with
their photocatalytic activities under visible lighting. Materials Research Bulletin.
2013;48(10):4344–4350.

[103] Patel JD, Mighri F, Ajji A, Chaudhuri TK. Fatty acid-assisted synthesis of CdS microspheres: Physicochemical properties and photocatalytic activity. Materials Letters. 2013;110:94–97.

[104] Chen F, Jia D, Cao Y, Jin X, Liu A. Facile synthesis of CdS nanorods with enhanced photocatalytic activity. Ceramics International. 2015;41(10):14604–14609.

[105] Chen F, Cao Y, Jia D. A facile route for the synthesis of ZnS rods with excellent photocatalytic activity. Chemical Engineering Journal. 2013;234:223–231.

[106] Dong F, Guo Y, Zhang J, Li Y, Yang L, Fang Q, et al. Size-controllable hydrothermal synthesis of ZnS nanospheres and the application in photocatalytic degradation of organic dyes. Materials Letters. 2013;97:59–63.

[107] Emin S, Lisjak D, Pitcher M, Valant M. Structural and morphological transformations of textural porous zinc sulfide microspheres. Microporous and Mesoporous Materials. 2013;165:185–192.

[108] Pal B, Pal B. Tuning the optical and photocatalytic properties of anisotropic ZnS nanostructures for the selective reduction of nitroaromatics. Chemical Engineering Journal. 2015;263:200–208.

[109] Liu H, Su Y, Chen P, Wang Y. Microwave-assisted solvothermal synthesis of 3D carnation-like SnS_2 nanostructures with high visible light photocatalytic activity. Journal of Molecular Catalysis A: Chemical. 2013;378:285–292.

[110] Umar A, Akhtar M, Dar G, Abaker M, Al-Hajry A, Baskoutas S. Visible-light-driven photocatalytic and chemical sensing properties of SnS_2 nanoflakes. Talanta. 2013;114:183–190.

[111] Park S, Park J, Selvaraj R, Kim Y. Facile microwave-assisted synthesis of SnS_2 nanoparticles for visible-light responsive photocatalyst. Journal of Industrial and Engineering Chemistry. 2015;31:269–275.

[112] Ferancova A, Rengaraj S, Kim Y, Vijayalakshmi S, Labuda J, Bobacka J, et al. Electrochemical study of novel nanostructured In_2S_3 and its effect on oxidative damage to DNA purine bases. Electrochimica Acta. 2013;92:124–131.

[113] Wu W, Lin R, Shen L, Liang R, Yuan R, Wu L. Visible-light-induced photocatalytic hydrogenation of 4-nitroaniline over In_2S_3 photocatalyst in water. Catalysis Communications. 2013;40:1–4.

[114] Biacchi AJ, Vaughn DD, Schaak RE. Synthesis and crystallographic analysis of shape-controlled SnS nanocrystal photocatalysts: Evidence for a pseudotetragonal structural modification. Journal of the American Chemical Society. 2013;135(31):11634–11644.

[115] Chen F, Cao Y, Jia D. Facile synthesis of Bi_2S_3 hierarchical nanostructure with enhanced photocatalytic activity. Journal of Colloid and Interface Science. 2013;404:110–116.

[116] Luo Y, Chen H, Li X, Gong Z, Wang X, Peng X, et al. Wet chemical synthesis of Bi$_2$S$_3$ nanorods for efficient photocatalysis. Materials Letters. 2013;105:12–15.

[117] Chen S, Zhang H, Fu X, Hu Y. Preparation, characterization, and photocatalytic performance of Ce$_2$S$_3$ for nitrobenzene reduction. Applied Surface Science. 2013;275:335–341.

[118] Chen Z, Xu J, Ren Z, He Y, Xiao G. Low temperature synthesis of ZnIn$_2$S$_4$ microspheres as a visible light photocatalyst for selective oxidation. Catalysis Communications. 2013;41:83–86.

[119] Wang W, Ng TW, Ho WK, Huang J, Liang S, An T, et al. CdIn$_2$S$_4$ microsphere as an efficient visible-light-driven photocatalyst for bacterial inactivation: Synthesis, charac-terizations and photocatalytic inactivation mechanisms. Applied Catalysis B: Environ-mental. 2013;129:482–490.

[120] Chen Z, Li D, Xiao G, He Y, Xu Y-J. Microwave-assisted hydrothermal synthesis of marigold-like ZnIn$_2$ S 4 microspheres and their visible light photocatalytic activity. Journal of Solid State Chemistry. 2012;186:247–254.

[121] Mu J, Wei Q, Yao P, Zhao X, Kang S-Z, Li X. Facile preparation and visible light photocatalytic activity of CdIn$_2$S$_4$ monodispersed spherical particles. Journal of Alloys and Compounds. 2012;513:506–509.

[122] Liang S, Lin Q, Zhu S, Wu L. PVP-assisted synthesis of porous strontium tantalate hydrate nanosphere and enhanced photocatalytic properties. Materials Letters. 2013;113:138–141.

[123] Maia D, Pepe I, da Silva AF, Silva L. Visible-light-driven photocatalytic hydrogen production over dye-sensitized β-BiTaO$_4$. Journal of Photochemistry and Photobiology A: Chemistry. 2012;243:61–64.

[124] Androš L, Jurić M, Popović J, Šantić A, Lazić P, Benčina M, et al. Ba$_4$Ta$_2$O$_9$ Oxide prepared from an oxalate-based molecular precursor—characterization and properties. Inorganic Chemistry. 2013;52(24):14299–14308.

[125] Siddiqui MA, Chandel VS, Azam A. Comparative study of potassium hexatitanate (K$_2$Ti$_6$O$_{13}$) whiskers prepared by sol–gel and solid state reaction routes. Applied Surface Science. 2012;258(19):7354–7358.

[126] Zhang X, Li T, Gong Z, Zhao H, Wang L, Wan J, et al. Shape controlled FeTiO$_3$ nanostructures: Crystal facet and photocatalytic property. Journal of Alloys and Compounds. 2015;653:619–623.

[127] Cui Y, Briscoe J, Dunn S. Effect of ferroelectricity on solar-light-driven photocatalytic activity of BaTiO$_3$ influence on the carrier separation and Stern layer formation. Chemistry of Materials. 2013;25(21):4215–4223.

[128] Dumrongrojthanath P, Thongtem T, Phuruangrat A, Thongtem S. Hydrothermal synthesis of Bi_2WO_6 hierarchical flowers with their photonic and photocatalytic properties. Superlattices and Microstructures. 2013;54:71–77.

[129] Saison T, Gras P, Chemin N, Chanéac C, Durupthy O, Brezova V, et al. New insights into Bi_2WO_6 properties as a visible-light photocatalyst. The Journal of Physical Chemistry C. 2013;117(44):22656–22666.

[130] Pei CC, Chu W. The photocatalyic degradation and modeling of 2,4-dichlorophenoxy-acetic acid by bismuth tungstate/peroxide. Chemical Engineering Journal. 2013;223:665–669.

[131] Duan F, Zhang Q, Shi D, Chen M. Enhanced visible light photocatalytic activity of Bi_2WO_6 via modification with polypyrrole. Applied Surface Science. 2013;268:129–135.

[132] Liu Y, Li Z, Lv H, Tang H, Xing X. Synthesis of hierarchical Bi_2WO_6 microspheres with high visible-light-driven photocatalytic activities by sol–gel-hydrothermal route. Materials Letters. 2013;108:84–87.

[133] Hu S-P, Xu C-Y, Zhen L. Solvothermal synthesis of Bi_2WO_6 hollow structures with excellent visible-light photocatalytic properties. Materials Letters. 2013;95:117–120.

[134] Yan Y, Wu Y, Yan Y, Guan W, Shi W. Inorganic-salt-assisted morphological evolution and visible-light-driven photocatalytic performance of Bi_2WO_6 nanostructures. The Journal of Physical Chemistry C. 2013;117(39):20017–20028.

[135] Zhang F-J, Xie F-Z, Liu J, Zhao W, Zhang K. Rapid sonochemical synthesis of irregular nanolaminar-like Bi_2WO_6 as efficient visible-light-active photocatalysts. Ultrasonics Sonochemistry. 2013;20(1):209–215.

[136] Zhao G, Liu S, Lu Q, Xu F, Sun H. Fabrication of electrospun Bi_2WO_6 microbelts with enhanced visible photocatalytic degradation activity. Journal of Alloys and Compounds. 2013;578:12–16.

[137] Zhuo Y, Huang J, Cao L, Ouyang H, Wu J. Photocatalytic activity of snow-like Bi_2WO_6 microcrystalline for decomposition of rhodamine B under natural sunlight irradiation. Materials Letters. 2013;90:107–110.

[138] Huang H, Chen H, Xia Y, Tao X, Gan Y, Weng X, et al. Controllable synthesis and visible-light-responsive photocatalytic activity of Bi_2WO_6 fluffy microsphere with hierarchical architecture. Journal of Colloid and Interface Science. 2012;370(1):132–138.

[139] He J, Wang W, Long F, Zou Z, Fu Z, Xu Z. Hydrothermal synthesis of hierarchical rose-like Bi_2WO_6 microspheres with high photocatalytic activities under visible-light irradiation. Materials Science and Engineering: B. 2012;177(12):967–974.

[140] Guo J, Zhou X, Lu Y, Zhang X, Kuang S, Hou W. Monodisperse spindle-like $FeWO_4$ nanoparticles: Controlled hydrothermal synthesis and enhanced optical properties. Journal of Solid State Chemistry. 2012;196:550–556.

[141] Cavalcante L, Sczancoski J, Batista N, Longo E, Varela JA, Orlandi M. Growth mechanism and photocatalytic properties of SrWO$_4$ microcrystals synthesized by injection of ions into a hot aqueous solution. Advanced Powder Technology. 2013;24(1):344–353.

[142] Molinari A, Argazzi R, Maldotti A. Photocatalysis with Na$_4$W$_{10}$O$_{32}$ in water system: Formation and reactivity of OH radicals. Journal of Molecular Catalysis A: Chemical. 2013;372:23–28.

[143] Karthiga R, Kavitha B, Rajarajan M, Suganthi A. Photocatalytic and antimicrobial activity of NiWO$_4$ nanoparticles stabilized by the plant extract. Materials Science in Semiconductor Processing. 2015;40:123–129.

[144] Yu C, Cao F, Li X, Li G, Xie Y, Jimmy CY, et al. Hydrothermal synthesis and characterization of novel PbWO$_4$ microspheres with hierarchical nanostructures and enhanced photocatalytic performance in dye degradation. Chemical Engineering Journal. 2013;219:86–95.

[145] Lin X, Li H, Yu L, Zhao H, Yan Y, Liu C, et al. Efficient removal rhodamine B over hydrothermally synthesized fishbone like BiVO$_4$. Materials Research Bulletin. 2013;48(10):4424–4429.

[146] Obregón S, Colón G. On the different photocatalytic performance of BiVO$_4$ catalysts for methylene blue and rhodamine B degradation. Journal of Molecular Catalysis A: Chemical. 2013;376:40–47.

[147] Sun J, Chen G, Wu J, Dong H, Xiong G. Bismuth vanadate hollow spheres: Bubble template synthesis and enhanced photocatalytic properties for photodegradation. Applied Catalysis B: Environmental. 2013;132:304–314.

[148] Tan G, Zhang L, Ren H, Wei S, Huang J, Xia A. Effects of pH on the hierarchical structures and photocatalytic performance of BiVO$_4$ powders prepared via the microwave hydrothermal method. ACS Applied Materials & Interfaces. 2013;5(11):5186–5193.

[149] Yao M, Liu M, Gan L, Zhao F, Fan X, Zhu D, et al. Monoclinic mesoporous BiVO$_4$: Synthesis and visible-light-driven photocatalytic property. Colloids and Surfaces A: Physicochemical and Engineering Aspects. 2013;433:132–138.

[150] Zhang Y, Li G, Yang X, Yang H, Lu Z, Chen R. Monoclinic BiVO$_4$ micro-/nanostructures: Microwave and ultrasonic wave combined synthesis and their visible-light photocatalytic activities. Journal of Alloys and Compounds. 2013;551:544–550.

[151] Lei B-X, Zhang P, Wang S-N, Li Y, Huang G-L, Sun Z-F. Additive-free hydrothermal synthesis of novel bismuth vanadium oxide dendritic structures as highly efficient visible-light photocatalysts. Materials Science in Semiconductor Processing. 2015;30:429–434.

[152]   Wang X, Li G, Ding J, Peng H, Chen K. Facile synthesis and photocatalytic activity of monoclinic $BiVO_4$ micro/nanostructures with controllable morphologies. Materials Research Bulletin. 2012;47(11):3814–3818.

[153]   Shi W, Yan Y, Yan X. Microwave-assisted synthesis of nano-scale $BiVO_4$ photocatalysts and their excellent visible-light-driven photocatalytic activity for the degradation of ciprofloxacin. Chemical Engineering Journal. 2013;215:740–746.

[154]   Zhang J, Cui H, Wang B, Li C, Zhai J, Li Q. Fly ash cenospheres supported visible-light-driven $BiVO_4$ photocatalyst: Synthesis, characterization and photocatalytic application. Chemical Engineering Journal. 2013;223:737–746.

[155]   Ressnig D, Kontic R, Patzke GR. Morphology control of $BiVO_4$ photocatalysts: pH optimization vs. self-organization. Materials Chemistry and Physics. 2012;135(2):457–466.

[156]   Jiang H, Meng X, Dai H, Deng J, Liu Y, Zhang L, et al. High-performance porous spherical or octapod-like single-crystalline $BiVO_4$ photocatalysts for the removal of phenol and methylene blue under visible-light illumination. Journal of Hazardous Materials. 2012;217:92–99.

[157]   Abdullah AH, Moey HJM, Yusof NA. Response surface methodology analysis of the photocatalytic removal of Methylene Blue using bismuth vanadate prepared via polyol route. Journal of Environmental Sciences. 2012;24(9):1694–1701.

[158]   Chen L, Wang J, Meng D, Xing Y, Tian X, Yu X, et al. Effects of citric acid and urea on the structural and morphological characteristics of $BiVO_4$ synthesized by the sol–gel combustion method. Journal of Sol-Gel Science and Technology. 2015;76(3):562–571.

[159]   Ju P, Fan H, Zhang B, Shang K, Liu T, Ai S, et al. Enhanced photocatalytic activity of β-$AgVO_3$ nanowires loaded with Ag nanoparticles under visible light irradiation. Separation and Purification Technology. 2013;109:107–110.

[160]   Belver C, Adán C, García-Rodríguez S, Fernández-García M. Photocatalytic behavior of silver vanadates: Microemulsion synthesis and post-reaction characterization. Chemical Engineering Journal. 2013;224:24–31.

[161]   Wang Y, Dai H, Deng J, Liu Y, Zhao Z, Li X, et al. Three-dimensionally ordered macroporous $InVO_4$: fabrication and excellent visible-light-driven photocatalytic performance for methylene blue degradation. Chemical Engineering Journal. 2013;226:87–94.

[162]   Yan Y, Liu X, Fan W, Lv P, Shi W. $InVO_4$ microspheres: Preparation, characterization and visible-light-driven photocatalytic activities. Chemical Engineering Journal. 2012;200:310–316.

[163]   Noh TH, Kim DW, Seo SW, Cho IS, Kim DH, Han HS, et al. Facile hydrothermal synthesis of $InVO_4$ microspheres and their visible-light photocatalytic activities. Materials Letters. 2012;72:98–100.

[164] Ozturk B, Soylu GSP. Synthesis of surfactant-assisted FeVO$_4$ nanostructure: Characterization and photocatalytic degradation of phenol. Journal of Molecular Catalysis A: Chemical. 2015;398:65–71.

[165] Zhang S, Sun Y, Li C, Ci L. Cu$_3$V$_2$O$_8$ hollow spheres in photocatalysis and primary lithium batteries. Solid State Sciences. 2013;25:15–21.

[166] Zheng F, Zhang M, Guo M. Controllable preparation of WO$_3$ nanorod arrays by hydrothermal method. Thin Solid Films. 2013;534:45–53.

[167] Grabowska E. Selected perovskite oxides: Characterization, preparation and photocatalytic properties—A review. Applied Catalysis B: Environmental. 2016;186:97–126.

[168] Dahl M, Liu Y, Yin Y. Composite titanium dioxide nanomaterials. Chemical Reviews. 2014;114(19):9853–9889.

[169] Tian J, Zhao Z, Kumar A, Boughton RI, Liu H. Recent progress in design, synthesis, and applications of one-dimensional TiO$_2$ nanostructured surface heterostructures: A review. Chemical Society Reviews. 2014;43(20):6920–6937.

[170] J. McKone and N. Lewis, in Photoelectrochemical Water Splitting: Materials, Processes and Architectures, The Royal Society of Chemistry, 2013, pp. 52–82 Editor(s): Hans-Joachim Lewerenz, Laurie Peter.

[171] Martha S, Sahoo PC, Parida KM. An overview on visible light responsive metal oxide based photocatalysts for hydrogen energy production. Rsc Advances. 2015;5(76): 61535–61553.

[172] Zhang S, Chen Q, Wang Y, Guo L. Synthesis and photoactivity of CdS photocatalysts modified by polypyrrole. International Journal of Hydrogen Energy. 2012;37(17): 13030–13036.

[173] Ding J, Sun S, Yan W, Bao J, Gao C. Photocatalytic H-2 evolution on a novel CaIn$_2$S$_4$ photocatalyst under visible light irradiation. International Journal of Hydrogen Energy. 2013;38(30):13153–13158.

[174] Kim J, Sohn Y, Kang M. New fan blade-like core-shell Sb$_2$Ti$_x$S$_y$ photocatalytic nanorod for hydrogen production from methanol/water photolysis. International Journal of Hydrogen Energy. 2013;38(5):2136–2143.

[175] Zhang X, Yang M, Zhao J, Guo L. Photocatalytic hydrogen evolution with simultaneous degradation of organics over (CuIn)$_{(0.2)}$Zn$_{1.6}$S$_2$ solid solution. International Journal of Hydrogen Energy. 2013;38(36):15985–15991.

[176] Song K, Zhu R, Tian F, Cao G, Ouyang F. Effects of indium contents on photocatalytic performance of ZnIn2S4 for hydrogen evolution under visible light. Journal of Solid State Chemistry. 2015;232:138–143.

[177] Chen F, Zai J, Xu M, Qian X. 3D-hierarchical Cu_3SnS_4 flowerlike microspheres: Controlled synthesis, formation mechanism and photocatalytic activity for H-2 evolution from water. Journal of Materials Chemistry A. 2013;1(13):4316–4323.

[178] Liu M, Zhang L, He X, Zhang B, Song H, Li S, et al. L-Cystine-assisted hydrothermal synthesis of $Mn_{1-x}Cd_xS$ solid solutions with hexagonal wurtzite structure for efficient photocatalytic hydrogen evolution under visible light irradiation. Journal of Materials Chemistry A. 2014;2(13):4619–4626.

[179] Lin S, Shi L, Yoshida H, Li MR, Zou XD. Synthesis of hollow spherical tantalum oxide nanoparticles and their photocatalytic activity for hydrogen production. Journal of Solid State Chemistry. 2013;199:15–20.

[180] Liao LB, Zhang QH, Su ZH, Zhao ZZ, Wang YN, Li Y, et al. Efficient solar water-splitting using a nanocrystalline CoO photocatalyst. Nature Nanotechnology. 2014;9(1):69–73.

[181] GurudayalChiam SY, Kumar MH, Bassi PS, Seng HL, Barber J, et al. Improving the efficiency of hematite nanorods for photoelectrochemical water splitting by doping with manganese. Acs Applied Materials & Interfaces. 2014;6(8):5852–5859.

[182] Yan Y, Cai F, Song Y, Shi W. $InVO_4$ nanocrystal photocatalysts: Microwave-assisted synthesis and size-dependent activities of hydrogen production from water splitting under visible light. Chemical Engineering Journal. 2013;233:1–7.

[183] Li P, Umezawa N, Abe H, Ye J. Novel visible-light sensitive vanadate photocatalysts for water oxidation: Implications from density functional theory calculations. Journal of Materials Chemistry A. 2015;3(20):10720–10723.

[184] Xie Q, Wang Y, Pan B, Wang H, Su W, Wang X. A novel photocatalyst LaOF: Facile fabrication and photocatalytic hydrogen production. Catalysis Communications. 2012;27:21–25.

[185] Jiang W, Jiao XL, Chen DR. Photocatalytic water splitting of surfactant-free fabricated high surface area NaTaO3 nanocrystals. International Journal of Hydrogen Energy. 2013;38(29):12739–12746.

[186] Yang H, Liu X, Zhou Z, Guo L. Preparation of a novel $Cd_2Ta_2O_7$ photocatalyst and its photocatalytic activity in water splitting. Catalysis Communications. 2013;31:71–75.

[187] Dhanasekaran P, Gupta NM. Factors affecting the production of H_2 by water splitting over a novel visible-light-driven photocatalyst GaFeO3. International Journal of Hydrogen Energy. 2012;37(6):4897–4907.

[188] Tijare SN, Joshi MV, Padole PS, Mangrulkar PA, Rayalu SS, Labhsetwar NK. Photocatalytic hydrogen generation through water splitting on nano-crystalline $LaFeO_3$ perovskite. International Journal of Hydrogen Energy. 2012;37(13):10451–10456.

[189] Takimoto Y, Kitta T, Irie H. Visible-light sensitive hydrogen evolution photocatalyst ZnRh2O4. International Journal of Hydrogen Energy. 2012;37(1):134–138.

[190] Peng T, Zhang X, Lv H, Zan L. Preparation of $NiFe_2O_4$ nanoparticles and its visible-light-driven photoactivity for hydrogen production. Catalysis Communications. 2012;28:116–119.

[191] Wang Z, Wang JT, Hou JG, Huang K, Jiao SQ, Zhu HM. Facile synthesis of efficient photocatalytic tantalum nitride nanoparticles. Materials Research Bulletin. 2012;47(11): 3605–3611.

[192] Shen J, Zai J, Yuan Y, Qian X. 3D hierarchical ZnIn2S4: The preparation and photocatalytic properties on water splitting. International Journal of Hydrogen Energy. 2012;37(22):16986–16993.

[193] Wang L, Wang W. Photocatalytic hydrogen production from aqueous solutions over novel Bi0.5Na0.5TiO3 microspheres. International Journal of Hydrogen Energy. 2012;37(4):3041–3047.

[194] Li Q, Meng H, Zhou P, Zheng Y, Wang J, Yu J, et al. $Zn_{1-x}Cd_xS$ solid solutions with controlled bandgap and enhanced visible-light photocatalytic H-2-production activity. Acs Catalysis. 2013;3(5):882–889.

[195] Liu M, Jing D, Zhou Z, Guo L. Twin-induced one-dimensional homojunctions yield high quantum efficiency for solar hydrogen generation. Nature Communications. 2013;4.

[196] Chen W, Li C, Gao H, Yuan J, Shangguan W, Su J, et al. Photocatalytic water splitting on protonated form of layered perovskites $K_{0.5}La_{0.5}Bi_2M_2O_9$ (M = Ta; Nb) by ion-exchange. International Journal of Hydrogen Energy. 2012;37(17):12846–12851.

[197] Li X, Yu J, Low J, Fang Y, Xiao J, Chen X. Engineering heterogeneous semiconductors for solar water splitting. Journal of Materials Chemistry A. 2015;3(6):2485–2534.

[198] Zaleska A. Doped-TiO₂: A review. Recent Patents on Engineering. 2008;2(3):157–164.

[199] Ghugal SG, Umare SS, Sasikala R. A stable, efficient and reusable CdS–SnO₂ hetero-structured photocatalyst for the mineralization of acid Violet 7 dye. Applied Catalysis A: General. 2015;496:25–31.

[200] Hamrouni A, Moussa N, Di Paola A, Palmisano L, Houas A, Parrino F. Photocatalytic activity of binary and ternary $SnO_2–ZnO–ZnWO_4$ nanocomposites. Journal of Photochemistry and Photobiology A: Chemistry. 2015;309:47–54.

[201] Balachandran S, Swaminathan M. Facile fabrication of heterostructured $Bi_2O_3–ZnO$ photocatalyst and its enhanced photocatalytic activity. The Journal of Physical Chemistry C. 2012;116(50):26306–26312.

[202] Cheng L, Kang Y. Synthesis and characterization of $Bi_2O_3/NaBiO_3$ composite visible light-driven photocatalyst. Materials Letters. 2013;97:125–128.

[203] Cheng L, Kang Y. Synthesis of $NaBiO_3/Bi_2O_3$ heterojunction-structured photocatalyst and its photocatalytic mechanism. Materials Letters. 2014;117:94–97.

[204] Fan H, Li H, Liu B, Lu Y, Xie T, Wang D. Photoinduced charge transfer properties and photocatalytic activity in $Bi_2O_3/BaTiO_3$ composite photocatalyst. ACS Applied Materials & Interfaces. 2012;4(9):4853–4857.

[205] Liu J, Wei R, Hu J, Li L, Li J. Novel $Bi_2O_3/NaBi(MoO_4)_2$ heterojunction with enhanced photocatalytic activity under visible light irradiation. Journal of Alloys and Compounds. 2013;580:475–480.

[206] Cheng L, Liu X, Kang Y. Bi_5O_7I/Bi_2O_3: A novel heterojunction-structured visible light-driven photocatalyst. Materials Letters. 2014;134:218–221.

[207] Cheng L, Kang Y. Bi_5O_7I/Bi_2O_3 composite photocatalyst with enhanced visible light photocatalytic activity. Catalysis Communications. 2015;72:16–19.

[208] Li X, Huang R, Hu Y, Chen Y, Liu W, Yuan R, et al. A templated method to Bi_2WO_6 hollow microspheres and their conversion to double-shell Bi2O3/Bi2WO6 hollow microspheres with improved photocatalytic performance. Inorganic Chemistry. 2012;51(11):6245–6250.

[209] Hojamberdiev M, Katsumata K-I, Morita K, Bilmes SA, Matsushita N, Okada K. One-step hydrothermal synthesis and photocatalytic performance of $ZnWO_4/Bi_2WO_6$ composite photocatalysts for efficient degradation of acetaldehyde under UV light irradiation. Applied Catalysis A: General. 2013;457:12–20.

[210] Issarapanacheewin S, Wetchakun K, Phanichphant S, Kangwansupamonkon W, Wetchakun N. A novel CeO_2/Bi_2WO_6 composite with highly enhanced photocatalytic activity. Materials Letters. 2015;156:28–31.

[211] Zhang X, Zhang L, Hu J-S, Pan C-L, Hou C-M. Facile hydrothermal synthesis of novel $Bi_{12}TiO_{20}$-Bi_2WO_6 heterostructure photocatalyst with enhanced photocatalytic activity. Applied Surface Science. 2015;346:33–40.

[212] Feng Y, Yan X, Liu C, Hong Y, Zhu L, Zhou M, et al. Hydrothermal synthesis of CdS/Bi_2MoO_6 heterojunction photocatalysts with excellent visible-light-driven photocatalytic performance. Applied Surface Science. 2015;353:87–94.

[213] Xu J, Cao X. Characterization and mechanism of MoS_2/CdS composite photocatalyst used for hydrogen production from water splitting under visible light. Chemical Engineering Journal. 2015;260:642–648.

[214] Chen G, Li D, Li F, Fan Y, Zhao H, Luo Y, et al. Ball-milling combined calcination synthesis of MoS_2/CdS photocatalysts for high photocatalytic H 2 evolution activity under visible light irradiation. Applied Catalysis A: General. 2012;443:138–144.

[215] Duo F, Fan C, Wang Y, Cao Y, Zhang X. One-pot hydrothermal synthesis of a novel BiPO$_4$/BiOBr composite with enhanced visible light photocatalytic activities. Materials Science in Semiconductor Processing. 2015;38:157–164.

[216] Liu ZS, Wu BT, Niu JN, Feng PZ, Zhu YB. BiPO$_4$/BiOBr p–n junction photocatalysts: One-pot synthesis and dramatic visible light photocatalytic activity. Materials Research Bulletin. 2015;63:187–193.

[217] Duo F, Wang Y, Mao X, Zhang X, Wang Y, Fan C. A BiPO$_4$/BiOCl heterojunction photocatalyst with enhanced electron-hole separation and excellent photocatalytic performance. Applied Surface Science. 2015;340:35–42.

[218] Lin X, Liu D, Guo X, Sun N, Zhao S, Chang L, et al. Fabrication and efficient visible light-induced photocatalytic activity of Bi$_2$MoO$_6$/BiPO$_4$ composite. Journal of Physics and Chemistry of Solids. 2015;76:170–177.

[219] Huang H, Liu L, Zhang Y, Tian N. One pot hydrothermal synthesis of a novel BiIO$_4$/Bi$_2$MoO$_6$ heterojunction photocatalyst with enhanced visible-light-driven photocatalytic activity for rhodamine B degradation and photocurrent generation. Journal of Alloys and Compounds. 2015;619:807–811.

[220] Wang W, Huang X, Wu S, Zhou Y, Wang L, Shi H, et al. Preparation of p–n junction Cu$_2$O/BiVO$_4$ heterogeneous nanostructures with enhanced visible-light photocatalytic activity. Applied Catalysis B: Environmental. 2013;134:293–301.

[221] Min S, Wang F, Jin Z, Xu J. Cu$_2$O nanoparticles decorated BiVO$_4$ as an effective visible-light-driven pn heterojunction photocatalyst for methylene blue degradation. Superlattices and Microstructures. 2014;74:294–307.

[222] Li J, Zhao W, Guo Y, Wei Z, Han M, He H, et al. Facile synthesis and high activity of novel BiVO$_4$/FeVO$_4$ heterojunction photocatalys for degradation of metronidazole. Applied Surface Science. 2015.

[223] Lv C, Chen G, Sun J, Zhou Y, Fan S, Zhang C. Realizing nanosized interfacial contact via constructing BiVO$_4$/Bi$_4$V$_2$O$_{11}$ element-copied heterojunction nanofibres for superior photocatalytic properties. Applied Catalysis B: Environmental. 2015;179:54–60.

[224] Mehraj O, Mir NA, Pirzada BM, Sabir S. Fabrication of novel Ag$_3$PO$_4$/BiOBr heterojunction with high stability and enhanced visible-light-driven photocatalytic activity. Applied Surface Science. 2015;332:419–429.

[225] Lin L, Huang M, Long L, Sun Z, Zheng W, Chen D. Fabrication of a three-dimensional BiOBr/BiOI photocatalyst with enhanced visible light photocatalytic performance. Ceramics International. 2014;40(8):11493–11501.

[226] Lin H, Ye H, Li X, Cao J, Chen S. Facile anion-exchange synthesis of BiOI/BiOBr composite with enhanced photoelectrochemical and photocatalytic properties. Ceramics International. 2014;40(7):9743–9750.

[227] Liu Z, Ran H, Wu B, Feng P, Zhu Y. Synthesis and characterization of BiOI/BiOBr heterostructure films with enhanced visible light photocatalytic activity. Colloids and Surfaces A: Physicochemical and Engineering Aspects. 2014;452:109–114.

[228] Luo J, Zhou X, Ma L, Xu X. Enhanced visible-light-driven photocatalytic activity of WO_3/BiOI heterojunction photocatalysts. Journal of Molecular Catalysis A: Chemical. 2015;410:168–176.

[229] Cao J, Luo B, Lin H, Xu B, Chen S. Thermodecomposition synthesis of WO_3/H_2WO_4 heterostructures with enhanced visible light photocatalytic properties. Applied Catalysis B: Environmental. 2012;111:288–296.

[230] Chen X, Dai Y, Huang W. Novel Ag_3PO_4/$ZnFe_2O_4$ composite photocatalyst with enhanced visible light photocatalytic activity. Materials Letters. 2015;145:125–128.

[231] Zhang L, He Y, Ye P, Qin W, Wu Y, Wu T. Enhanced photodegradation activity of Rhodamine B by Co_3O_4/Ag_3VO_4 under visible light irradiation. Materials Science and Engineering: B. 2013;178(1):45–52.

[232] Zhang L, He Y, Ye P, Wu Y, Wu T. Visible light photocatalytic activities of $ZnFe_2O_4$ loaded by Ag_3VO_4 heterojunction composites. Journal of Alloys and Compounds. 2013;549:105–113.

[233] Song L, Li Y, Tian H, Wu X, Fang S, Zhang S. Synthesis of AgBr/$Ag_4P_2O_7$ composite photocatalyst and enhanced photocatalytic performance. Materials Science and Engineering: B. 2014;189:70–75.

[234] Krishnakumar B, Subash B, Swaminathan M. AgBr–ZnO–An efficient nano-photocatalyst for the mineralization of acid Black 1 with UV light. Separation and Purification Technology. 2012;85:35–44.

[235] Pirhashemi M, Habibi-Yangjeh A. Simple and large scale one-pot method for preparation of AgBr–ZnO nanocomposites as highly efficient visible light photocatalyst. Applied Surface Science. 2013;283:1080–1088.

[236] Shi L, Liang L, Ma J, Sun J. Improved photocatalytic performance over AgBr/ZnO under visible light. Superlattices and Microstructures. 2013;62:128–139.

[237] Wu C, Shen L, Zhang YC, Huang Q. Synthesis of AgBr/ZnO nanocomposite with visible light-driven photocatalytic activity. Materials Letters. 2012;66(1):83–85.

[238] Subash B, Krishnakumar B, Pandiyan V, Swaminathan M, Shanthi M. An efficient nanostructured Ag_2S–ZnO for degradation of Acid Black 1 dye under day light illumination. Separation and Purification Technology. 2012;96:204–213.

[239] Shaker-Agjekandy S, Habibi-Yangjeh A. Facile one-pot method for preparation of AgI/ZnO nanocomposites as visible-light-driven photocatalysts with enhanced activities. Materials Science in Semiconductor Processing. 2015;34:74–81.

[240] Yu C, Wei L, Zhou W, Chen J, Fan Q, Liu H. Enhancement of the visible light activity and stability of Ag_2CO_3 by formation of AgI/Ag 2 CO 3 heterojunction. Applied Surface Science. 2014;319:312–318.

[241] Nashim A, Parida K. Novel $Sm_2Ti_2O_7$/SmCrO₃ heterojunction based composite photo‐catalyst for degradation of rhodamine 6G dye. Chemical Engineering Journal. 2013;215:608–615.

[242] Zhang F, Li X, Zhao Q, Zhang Q, Tadé M, Liu S. Fabrication of α-Fe_2O_3/In_2O_3 composite hollow microspheres: A novel hybrid photocatalyst for toluene degradation under visible light. Journal of Colloid and Interface Science. 2015;457:18–26.

[243] Serpone N, Emeline A. Semiconductor photocatalysis—past, present, and future outlook. The Journal of Physical Chemistry Letters. 2012;3(5):673–677.

[244] Bajorowicz B, Cybula A, Winiarski MJ, Klimczuk T, Zaleska A. Surface properties and photocatalytic activity of $KTaO_3$, CdS, MoS_2 semiconductors and their binary and ternary semiconductor composites. Molecules. 2014;19(9):15339–15360.

[245] Marchelek M, Bajorowicz B, Mazierski P, Cybula A, Klimczuk T, Winiarski M, et al. $KTaO_3$ based nanocomposites for air treatment., Catalysis Today 252 (2014) 47-53.

[246] Hong E, Kim D, Kim JH. Heterostructured metal sulfide (ZnS–CuS–CdS) photocatalyst for high electron utilization in hydrogen production from solar water splitting. Journal of Industrial and Engineering Chemistry. 2014;20(5):3869–3874.

[247] Pirhashemi M, Habibi-Yangjeh A. Ternary ZnO/AgBr/Ag_2CrO_4 nanocomposites with tandem n–n heterojunctions as novel visible-light-driven photocatalysts with excellent activity. Ceramics International. 2015;41(10):14383–14393.

[248] Chen X, Li L, Zhang W, Li Y, Song Q, Zhang J, et al. Multi-pathway photoelectron migration in globular flower-like In_2O_3/AgBr/Bi_2WO_6 synthesized by microwave-assisted method with enhanced photocatalytic activity. Journal of Molecular Catalysis A: Chemical. 2016;414:27–36.

[249] Shekofteh-Gohari M, Habibi-Yangjeh A. Ternary ZnO/Ag_3VO_4/Fe_3O_4 nanocomposites: Novel magnetically separable photocatalyst for efficiently degradation of dye pollu‐tants under visible-light irradiation. Solid State Sciences. 2015;48:177–185.

[250] Shekofteh-Gohari M, Habibi-Yangjeh A. Ultrasonic-assisted preparation of novel ternary ZnO/AgI/Fe_3O_4 nanocomposites as magnetically separable visible-light-driven photocatalysts with excellent activity. Journal of colloid and interface science. 2016;461:144–153.

[251] Shaker-Agjekandy S, Habibi-Yangjeh A. Ultrasonic-assisted preparation of novel ternary ZnO/AgI/Ag_2CrO_4 nanocomposites as visible-light-driven photocatalysts with excellent activity. Materials Science in Semiconductor Processing. 2016;44:48–56.

[252] Liu C, Liu Z, Li Y, Liu Z, Wang Y, Lei E, et al. Enhanced visible-light-responsive photocatalytic property of CdS and PbS sensitized ZnO nanocomposite photocatalysts. Materials Science and Engineering: B. 2012;177(8):570–574.

[253] Shekofteh-Gohari M, Habibi-Yangjeh A. Facile preparation of $Fe_3O_4@$ AgBr–ZnO nanocomposites as novel magnetically separable visible-light-driven photocatalysts. Ceramics International. 2015;41(1):1467–1476.

[254] Hou X, Tian Y, Zhang X, Dou S, Pan L, Wang W, et al. Preparation and characterization of $Fe_3O_4/SiO_2/Bi_2MoO_6$ composite as magnetically separable photocatalyst. Journal of Alloys and Compounds. 2015;638:214–220.

[255] Zhang L, Wang W, Sun S, Sun Y, Gao E, Zhang Z. Elimination of BPA endocrine disruptor by magnetic BiOBr@ $SiO_2@$ Fe_3O_4 photocatalyst. Applied Catalysis B: Environmental. 2014;148:164–169.

[256] Huang Y, Fan W, Long B, Li H, Zhao F, Liu Z, et al. Visible light $Bi_2S_3/Bi_2O_3/Bi_2O_2CO_3$ photocatalyst for effective degradation of organic pollutions. Applied Catalysis B: Environmental. 2016;185:68–76.

[257] Ran R, McEvoy JG, Zhang Z. $Ag_2O/Ag_3VO_4/Ag_4V_2O_7$ heterogeneous photocatalyst prepared by a facile hydrothermal synthesis with enhanced photocatalytic performance under visible light irradiation. Materials Research Bulletin. 2016;74:140–150.

[258] Meng J, Yu Z, Li Y, Li Y. PdS-modified CdS/NiS composite as an efficient photocatalyst for H_2 evolution in visible light. Catalysis Today. 2014;225:136–141.

[259] Emeline A, Kuznetsov V, Ryabchuk V, Serpone N. On the way to the creation of next generation photoactive materials. Environmental Science and Pollution Research. 2012;19(9):3666–3675.

[260] Reszczyńska J, Grzyb T, Sobczak JW, Lisowski W, Gazda M, Ohtani B, et al. Visible light activity of rare earth metal doped (Er^{3+}, Yb^{3+} or Er^{3+}/Yb^{3+}) titania photocatalysts. Applied Catalysis B: Environmental. 2015;163:40–49.

BiOX (X = Cl, Br, and I) Photocatalysts

Liqun Ye

Additional information is available at the end of the chapter

Abstract

Photocatalysis technology has been wildly used to remove the most pollutants for environmental remediation under light irradiation. This chapter summarized the applications of BiOX (X = Cl, Br, and I) photocatalysts, including synthesis, photocatalytic performance without modification, enhanced VLD photocatalytic activity with the modification, and photocatalytic stability. Photocatalytic degradation (PCD) removal of volatile organic compounds (VOCs), contaminated chemicals, organic pollutants, and biological substances were introduced in this chapter. On the other hand, the morphologies, bismuth-rich effects, facet effects, and photocatalytic mechanisms of BiOX were discussed to provide effective methods for designing highly visible-light-driven (VLD) photocatalytic activity BiOX photocatalysts. The unsatisfactory points and future research directions also were briefly discussed at the end.

Keywords: BiOX, photocatalysis, environmental, bismuth-rich, facet effect

1. Introduction

Twenty-first century, with the urbanization and the industrialization increasing dramatically, the contamination caused by solid waste, gases, contaminated chemicals, organic pollutants, and biological substances has become a severe problem [1–3]. At present, many organic pollutants are in very low concentration and are high toxic. Therefore, it is required an effective and "green" method to transform them into non-hazardous compounds without secondary pollution [4–6]. In the past years, physical treatment methods (adsorption, ultrafiltration, coagulation, etc.) and chemical degradation methods (include ozone/UV radiation/H_2O_2 oxidation, semiconductor photocatalysis technique, advanced oxidation, photo-fenton reaction, and photo-electrochemical method) were the main ways to eliminate the environmental contaminants [7, 8]. Among the above methods, semiconductor photocatalysis technique can

degrade the contaminants completely, environmental friendly, rapidly, and cheaply. It has been suggested as one of the most effective and "green" ways to eliminate the environmental contaminants [9–12].

Photocatalyst is the body of photocatalysis technique. Therefore, the development of high-performance photocatalysts has attracted great interest. To date, there are two main synthesis strategies that have been investigated for the preparation of high-activity photocatalysts. The first one is to extend the modification of conventional photocatalysts (simple oxides, sulfides) by doping, coupling, and sensitization. The other strategy is to develop new photocatalysts. The former has been obtained many achievements, but it still cannot satisfy the requirement for practical application. So, more and more researchers changed to explore new high-efficiency photocatalysts, such as complex oxides, AgX (X = Cl, Br, I), and polymer [13–17]. BiOX (X = Cl, Br, I) are important V–VI–VII ternary semiconductor compounds because of their optical properties. All BiOX are tetragonal matlockite structure with [Bi_2O_2] slabs interleaved by double halogen atom slabs (**Figure 1**). In the past reports, BiOX were usually applied as thermal-induced catalysts [18, 19], ferroelectric materials [20], energy storage materials [21], and pigments [22]. Recently, BiOX were reported as photocatalysts to degrade pollutants for environmental remediation and solar fuel production. And more and more workers study the photocatalytic performance of BiOX under sunlight irradiation.
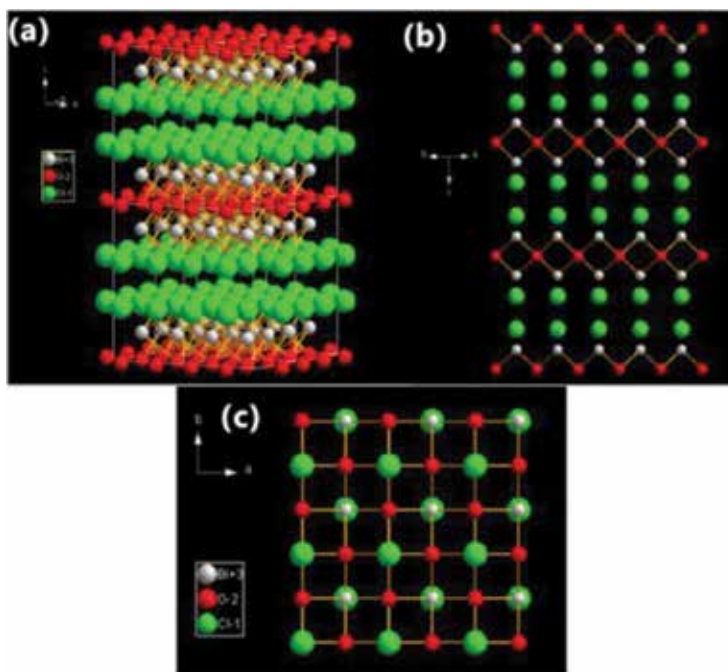

Figure 1 The 3 × 3 lattices model of BiOCl crystals (3 × 3 lattices): (a) three-dimensional projection; (b) [110] direction; and (c) [001] direction.

Structure determines the features. For BiOX, their open crystalline structure resulted the outstanding photocatalytic activity. The open-layered structure means enough space to polarize the related atoms and orbitals and then to induce the presence of internal static electric fields which are perpendicular to {001} facets of BiOX [23–28]. On the other hand, it has reported that the excited electron should travel a certain k-space distance to be emitted to the valence band (VB) due to the indirect-transition bandgap [23–28]. Therefore, BiOX displayed low recombination probability of the excited electrons and the holes, and the outstanding photocatalytic activity was obtained. Among BiOCl, BiOBr, and BiOI, BiOCl exhibited the best UV light–induced photocatalytic activity and even displayed higher activity than TiO_2 (P25, Degussa) for photocatalytic degradation (PCD) of dyes. BiOI exhibited the best photocatalytic activity for PCD of organic pollutants under the visible light irradiation attributed to its smallest bandgap. BiOBr has the appropriate bandgap (2.7–2.9 eV), which results in the best photocatalytic activity under full light spectrum irradiation.

In this chapter, we summarize the recent advances on BiOX. It may give us insight into the trend in the development of BiOX for environmental protection. At present, PCD of gas-phase and liquid-phase substrates over BiOX are researched widely. But PCD of solid-phase substrates was researched very few due to the long research cycle [29–33]. For example, all organic compounds, bacteria and heavy metals can be removed by BiOX via liquid-phase photocatalysis under light irradiation. VOCs and NO_x can be decomposed by BiOX via gas-phase photocatalysis. Polyvinyl chloride (PVC) can be decomposed by BiOI via solid-phase photocatalysis [29]. The detailed pollutant degradation pathways and the intermediates of mainly pollutants also were shown. In addition, we also emphasize on the modification, facet effect, bismuth-rich effect, and the photocatalytic mechanisms of BiOX for efficient photocatalytic applications in this review, which can provide effective methods develop much higher photocatalytic activity BiOX photocatalysts for environment photocatalysis. At end, the unsatisfactory points and future research directions are simply discussed.

2. Synthesis

2.1. Methods

The size, surface area, and morphology of photocatalysts can be changed with different synthesis method using. And the cheap and "green" methods were also necessary for the industrialized applications [34–37]. The bismuth sources include $Bi(NO_3)_3 \bullet 5H_2O$, Na-$BiO_3 \bullet 2H_2O$, Bi_2O_3, Bi, $BiCl_3$, and BiI_3. And CTAX (X = Cl, Br, or I) KX (X = Cl, Br, or I), NaX (X = Cl, Br, or I), HX (X = Cl, Br, or I), and ionic liquid with halogen element were usually used as halogen source [38–66]. At present, the main BiOX synthesis methods included precipitation, solvothermal, reverse microemulsions route, molecular precursor route, calcination, microwave irradiation process, ionic liquid modified, etc. Furthermore, the pH value, reaction temperature, and reaction time also can affect the synthesis of BiOX.

The reported morphology indicated that BiOX were single-crystal nanosheets or 3D hierarchical structures with nanosheets. In addition, BiOI quantum dot was reported by Liu [42]. The

size of BiOI quantum dot can be controlled <5 nm. As-synthesized RGO/BiOI nanocomposites showed very high photocatalytic activity under visible light irradiation. Except for BiOX quantum dot, one-dimension nanobelts also was synthesized with reaction temperature at 160–180°C and pH value at 8. But the exposed dominant facet of BiOX nanobelts also were {001} facet which is in agreement with two dimension BiOCl nanosheet [67]. It is indicated that BiOX generally exposed {001} facets, and the synthesis methods cannot change the dominant facet easily.

2.2. Synthesis mechanisms

Synthesis mechanisms were the key roles to suggest us perfecting the synthesis factors. For BiOX, the main-based morphology was 2D nanosheets. In liquid reaction, the formation of 2D structure was due to the low surface energy of {001} facets and layer structure of BiOX. In solid reaction, the BiOX 2D structure can be obtained via chemical transport. For example, our group synthesized BiOI nanosheets with very high symmetry with thermal treatment of BiI_3 [60]. **Figure 2** showed the possible synthesis mechanisms. BiI_3 reacted with O_2 to produce BiOI and iodine vapor when the temperature higher than 350°C. At the same time, BiI_3 also can be sublimated. The freed off iodine and BiI_3 vapors spilling over from bulk BiI_3, the pressure resulted the BiOI nanosheets shelling from BiI_3.
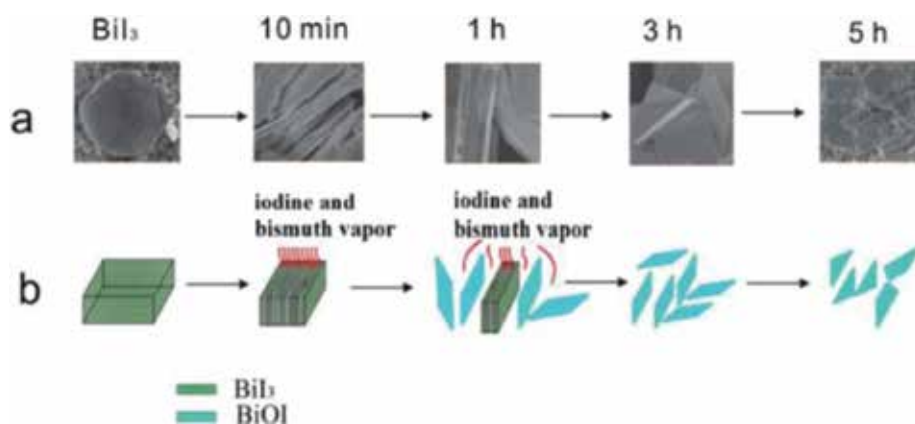

Figure. 2 Illustration of formation mechanism of BiOI SCNs: (a) original formation process; (b) simulation formation process [60]. Reprinted with permission from Royal Society of Chemistry.

3. Photocatalytic performance of pure BiOX

3.1. Photocatalytic activity

Since Huang reported BiOCl for photocatalytic dye degradation at 2006 [23], BiOX were widely studied as photocatalysts. In general, BiOCl displayed high photocatalytic activity for dyes (RhB, MO, MB, etc.) and phenols degradation under UV, visible, or UV–Vis light irradiation

via excitation of BiOCl or dye sensitization pathway [68]. BiOI can absorb more visible light (ca. 650 nm) than BiOCl (ca. 360 nm) and BiOBr (ca. 430 nm). Therefore, BiOI showed higher photocatalytic activity than BiOCl and BiOBr under visible light irradiation. For example, Zhang reported that the BiOI displayed higher photocatalytic activity than BiOBr and BiOCl for methyl orange degradation [38]. Lei synthesized BiOI flower-like hierarchical structures with higher photocatalytic activities for dyes and phenol degradation under visible light irradiation than the BiOI platelets [59]. Due to the most appropriate bandgap (2.8 eV), BiOBr showed the best photocatalytic oxidation and reduction activity under full light spectrum irradiation. So, it can be used to remove more organic pollutants, especially for bacterium and microcystin-LR [49–53, 69–71]. Until now, only BiOBr usually was reported to photo-degrade biological substances. For instances, Yu found that hierarchical BiOBr microspheres can effectively kill Micrococcus lylae, a positive bacterium, in water under fluorescent light irradiation [50]. Wong also reported the facets effect of BiOBr for *Escherichia coli* photocatalytic inactivation [70]. Fang firstly reported Microcystin-LR degradation over BiOBr under visible light irradiation [71].

3.2. Photocatalytic selectivity

Catalytic data included many parts, and selectivity was a very important factor. In TiO_2 system, selective photocatalytic degradation of alcohols and azo dyes has been paid more attention [72–76]. However, TiO_2 without surface modification showed very poor photocatalytic selectivity due to the low adsorption selectivity. In order to obtaining high photocatalytic selectivity, TiO_2 was usually modified by surfactant to enhance the adsorption selectivity. For BiOX system, the atoms structural (**Figure 1**) showed that the dominant {001} facets of BiOX covered with 100% terminal oxygen atoms. So, {001} facets of BiOX should be more negatively charged than other facets. And, BiOX nanosheets with dominant exposed {001} facets can show very high adsorption selectivity for cationic dyes and result in high photocatalytic degradation selectivity.

Recently, our group reported the photocatalytic selectivity of BiOI. By analyzing the UV–Vis absorption spectra during the photocatalytic degradation of RhB with BiOI, we found that the characteristic absorption peak of RhB exhibited obvious blue shift (from 554 to 500 nm). This phenomenon indicated that the mainly PCD path of the RhB was deacetylation process. On the other hand, once RhB molecules were adsorbed on the surface of BiOI, a new N1s XPS peak appeared at 401.1 eV, and the shift was about 1.8 eV compare to the pure RhB due to the interaction between the {001} facets of BiOI and the N^+ group of RhB. So, it can be suggested that adsorption selectivity of BiOI for RhB and resulted in high photocatalytic degradation selectivity. Furthermore, the photocatalytic results showed that the degradation rates of MB were much faster than those of MO for BiOI TF, and the selective photocatalytic ability R (R = k_{MB}/k_{MO}) is 6.9 which are six times higher than TiO_2 TF. It implied that BiOI displayed high selective photocatalysis.

3.3. Photocatalytic stability

Except for photocatalytic selectivity, photocatalytic stability was another important factor for the practical application. It has been reported that the affect factors of photocatalytic stability included intrinsic structure and solubility product constant of photocatalyst, pH value, and properties of substrate. As g-C_3N_4, the interaction force between layers of BiOX also was van der Waals force, but covalently bonded layers also appeared in BiOX layer structure. So, BiOX are more stable than other layer photocatalysts such as g-C_3N_4 whose interaction force between layers is van der Waals force. It had been reported that the solubility product constant of BiOCl is very low with 1.8×10^{-31}, which indicated that BiOX cannot easily dissolve or transform under normal circumstances. However, the pH value and properties of substrate can affect the stability of BiOX. For example, BiOX can dissolve under acid environment [68] and can react with S_2^- to transform to Bi_2S_3 [66].

For BiOCl, Huang firstly evaluated the photocatalytic stability of BiOCl [28]. The stable XRD pattern and cycles reaction of BiOCl revealed the stability for the PCD of dyes, and this conclusion was also proved by Sarwan [68]. For BiOBr, Huo researched the photocatalytic stability by comparing the photocatalytic activity, crystallization and morphology after six photocatalytic cycles [69]. The photocatalytic stability of BiOI also was proved as stability VLD photocatalyst by our group and Zhang' group [59]. However, the photocorrosion of BiOX was not considered. The releasing traces of Bi via photocorrosion of BiOX are critical for environment. So, in future work, the photocorrosion of BiOX should be taken into account.

3.4. Degradation pathways and intermediates of pollutant over BiOX

In reported works, the main study of BiOX photocatalysts focuses on enhancing the photocatalytic activity for environmental remediation. But the degradation pathways of pollutant were researched very few. For gas-phase substrate photocatalytic degradation, Zhang reported the degradation pathways and intermediates of NO [54]. The amount of NO_3^- increased with prolonged illumination, but the amount of NO_2^- kept almost constant at 0.08 μmol with reaction time. It implied that NO to NO_3^- was the major the oxidation pathway for NO over BiOBr microspheres. Furthermore, it had been reported that the NO_3^- and NO_2^- came from the reaction between NO_x and $O_2^{\bullet-}$ and •OH, respectively. Therefore, $O_2^{\bullet-}$ was the major reactive oxygen species (ROS) for NO remove over BiOBr.

For liquid-phase substrate photocatalytic degradation, dyes (such as MO, MB, and RhB) and phenols were the most used substrates. The degradation pathways and intermediates of dye molecules had been studied deeply. So, in this chapter, we did not discuss it. On the contrary, the degradation pathways of phenols were complex, and it is meaningful to investigate the degradation pathways and intermediates of phenols. In BiOX/UV–Vis systems, Chen [76] proved that hydroxyl adducts such as catechol and hydroquinone were the main intermediates for phenol degradation. Meng showed that the degradation of tetrabromobisphenol A started with hydroxylation and debromination. As shown in **Figure 3**, •OH was the major reactive oxygen species [51].
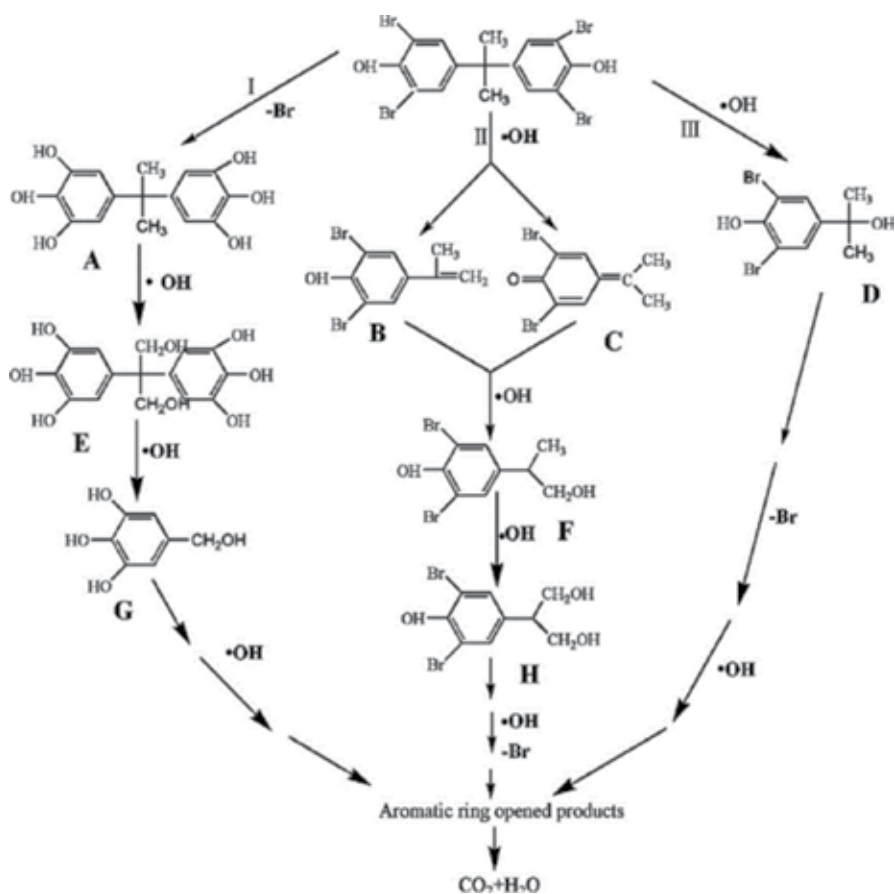
Figure. 3 Proposed TBBPA degradation pathway [51]. Reprinted with permission from Elsevier.

In addition, microcystins-LR is a very hazardous pollutant. It can cause sickness in life body, and World Health Organization has identified it as strongly hepatotoxic. Recently, Huang reported the degradation pathways and intermediates of microcystins-LR in BiOBr/vis systems [70]. Isotope labeling technique proved the decarboxylation process over BiOBr. Furthermore, •OH and hole were the active species for MC-LR remove.

4. Modification for enhanced VLD photocatalytic activity

In general, there are three key steps (light harvesting, photo-induced carriers separation, and the photocatalytic reduction and oxidation reactions) for photocatalytic processes. At present, although BiOX had excellent photocatalytic activity for environmental contaminants degradation, the photocatalytic activity of BiOX were still very low and cannot be used for practical application under sunlight irradiation. For improving the VLD photocatalytic activity of BiOX, many modification strategies had been applied to enhance the solar light harvesting and photo-

induced carriers separation. These strategies included cocatalyst using, element doping, semiconductor coupling, dye sensitization, surface plasmon resonance, defect making, bismuth-rich effect, and so on [77–150]. And the above methods successfully improved the VLD photocatalytic activity of BiOX.

4.1. Cocatalyst

Cocatalysts of photocatalysts can act as reaction sites and active sites. It also provided photogenerated charges trapping sites to promote the photo-induced carriers separation. Then, enhanced photocatalytic activity was displayed [82, 152]. Therefore, at presently, cocatalyst wildly used to enhance the photocatalytic activity of photocatalysts for environmental pollutants degradation and solar fuels generation. Recently, cocatalysts were divided into deriving-electron types (Ag, Pt, Au) and deriving-hole-types (PbO_2, MnO_x) [82, 152]. Our group reported that deriving-hole types cocatalyst (MnO_x) enhanced the separation efficiency of the photo-induced carriers better than that of deriving-electron types (Pt) over BiOI, and then improve the photocatalytic activity for PCD of dye (**Figure 4**) [78–81]. Analyzing the reason, it must be pointed out that almost all of works suggested holes as the main active species over BiOX photocatalysts for degrading pollutants. Therefore, deriving-hole-type cocatalysts showed more effective for enhancing the photocatalytic activity of BiOX.
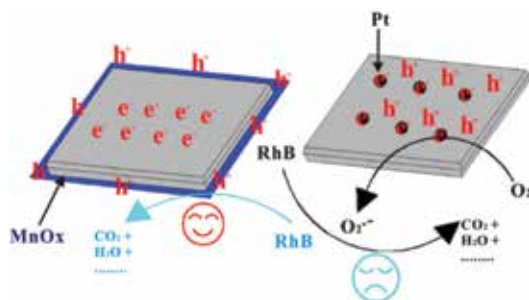

Figure 4 The mechanism of cocatalyst selectivity of BiOI under visible light irradiation ($\lambda \geq 420$ nm) [82]. Reprinted with permission from Royal Society of Chemistry.

4.2. Element doping

Element doping had been wildly used to enhance the photocatalytic activity in TiO_2 system. The defect energy level decreased bandgap enhanced visible light harvesting and defect sites improved trapping of electrons to inhibit electron–hole recombination. Recently, it has been reported that C, I, N, and Mn-doped BiOCl with an obvious red shift compared to the pure BiOCl and resulted in excellent photocatalytic activity under visible light [84–87]. It indicated that the element doping can effectively expand the light adsorption region. In order to surface photovoltage spectroscopy (SPS) and transient photovoltage (TPV), measurements were used to prove the visible light harvesting ability and separate efficiency of photo-induced electron–hole of self-doping BiOX. The increased SPS signal intensity implied that the generation of

electron–hole pairs can be enhanced on $BiOI_{1.5}$due to its good visible light harvesting ability. The increased TPV signal intensity indicated that the photo-induced electron–hole pairs of $BiOI_{1.5}$ were separated more easily than that of BiOI. Therefore, self-doping $BiOI_{1.5}$ displayed higher VLD photocatalytic activity than pure BiOI [83]. On the other hand, the facets-dependent C-doping mechanism of BiOCl also was studied as shown in **Figure 5**. The impurity energy level of carbon caused the absorption edge shifting to higher wavelength and increasing the lifetime of charge carries. Thus, the photocatalytic activity of BiOCl was enhanced by both the effective usage of light source and the inhibition of recombination of photo-induced charge carriers [85].
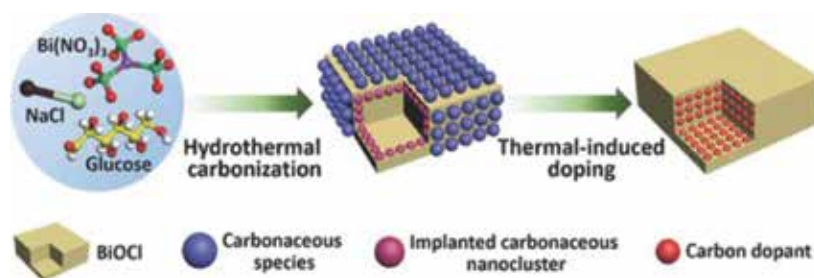
Figure 5 Schematic illustration of homogeneous carbon doping strategy comprised of bottom-up hydrothermal processing and subsequent thermal treatment with taking carbon doped BiOCl as the example [85]. Reprinted with permission from Wiley.

4.3. Semiconductor coupling

Semiconductor coupling photocatalysts constructed a heterojunction interface between two type semiconductor photocatalysts with matching energy bandgaps. It has been becoming the most important method to enhance the photocatalytic efficiency by improving the photo-induced carriers separation and expanding the energy range of photoexcitation for the system, thus achieving better photocatalytic activity for dye degradation. In generally, two photocatalysts coupling do not show selectivity [90–130]. In our recent work, we found that the interaction between BiOBr and $g\text{-}C_3N_4$ was facet (2D/2D) coupling between BiOBr-{001} and $g\text{-}C_3N_4$-{002}. The facets coupling resulted in photo-induced charges transfer between BiOBr and $g\text{-}C_3N_4$ and improve the VLD photocatalytic activity for environmental remediation. This research offered a possible explanation for the 2D/2D heterojunction of inorganic–organic composite photocatalysts [103].

4.4. Graphene

Because graphene's superior physical and chemical properties, it has stimulated great interests for preparing many functional composite materials with outstanding applications [20]. For BiOX photocatalysts, modification with graphene also was researched strongly. Our group and Zeng's group suggested the C–Bi chemical coupling improved photo-induced charges separation [131, 132]. Based on this advantage, graphene-BiOCl exhibited enhanced photoca-

talytic activity. The similar photocatalytic results of graphene-BiOBr also were reported by Li, Zhang, Ai, and Bai [133–136]. They proved that the enhanced photocatalytic activity come from the strong C–Bi chemical bonding, rather than their higher surface area and light absorption extension in the visible region between BiOBr and graphene. For graphene-BiOI, RGO/BiOI nanocomposites showed improved photocatalytic activity for dye degradation under visible light. But C–Bi chemical coupling did not found in graphene-BiOI system, and Fang suggested that the improved light absorption and efficient charge separation and transportation induced the improved photocatalytic activity under visible light irradiation [42].

4.5. Dye sensitization

Chemisorbed or physisorbed photosensitizers (dye molecules or quantum dots) can expand the spectrum range from UV light to the full spectrum. The excited-state electrons of sensitizer can transfer to the photocatalysts, and then the photocatalysis reaction occurred at the conduction band (CB) of photocatalysts. Organometallic complex were the most using sensitizers Copper complexes, ruthenium complexes (N719, C101, C102, and $[Ru(bpy)_3]^{2+}$), and zinc complexes were all used as photosensitizers [153–157]. For example, simultaneous over all water splitting and RhB degradation reaction occurred on copper phthalocyanine (CuPc) sensitized BiOCl composite under simulated solar light irradiation [150]. However, we known that ruthenium complexes are difficult to synthesize and very expensive. Copper and zinc complexes displayed very low efficiencies. So, it is very important to develop some new sensitizers.

In our recent work, $Bi_n(Tu)_xCl_{3n}$ bismuth complexes were used as new sensitizers. $Bi_n(Tu)_xCl_{3n}$ inner sensitized BiOCl displayed very high photocatalytic activity under visible light ($\lambda > 420$ nm) (**Figure 6**) [150]. At present, there were few reports about inner sensitized photocatalysts system. Most photosensitizers were absorbed on the surface of photocatalysts. Obviously, the inner sensitization displayed many advantages. Firstly, the stability of inner sensitized photocatalysts system was enhanced. This sensitized type avoided the sensitizer consumption during the photocatalytic process. Secondly, it expanded the applied condition of the sensitizers. For example, water soluble photosensitizers can be used in the in-aqueous solution by inner sensitization.
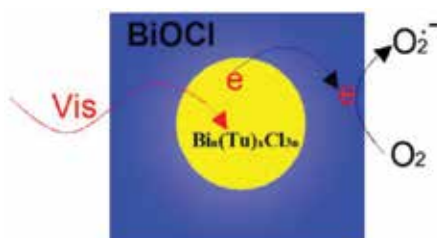

Figure 6 $Bi_n(Tu)_xCl_{3n}$ sensitized the BiOCl and resulted in unusual high visible light pholocatalytic activity [150]. Reprinted with permission from Royal Society of Chemistry.

4.6. Surface plasmon resonance

Surface plasmon resonance (SPR) can be improved the visible light absorption dramatically and offered new way to develop new VLD photocatalysts. Among noble metals, Ag was suggested as the best SPR effects. Therefore, more interests have been paid to Ag–TiO_2, Ag–ZnO, Ag/AgX (X = Cl, Br, I), Ag/$AgPO_4$, Ag/AgBr/TiO_2, Ag/AgBr/Bi_2WO_6, and Ag/AgBr/WO_3 three composite photocatalysts to enhance the VLD photocatalytic activities [162–173]. For BiOX system, Ag/AgCl/BiOCl and Ag/AgBr/BiOBr showed much higher VLD photocatalytic activity for pollutants degradation than Ag/AgX and pure BiOX [137–144]. Furthermore, superoxide radical quantification and active species trapping experiments showed that metallic Ag played different role for Ag/AgX/BiOX VLD photocatalysts. SPR for Ag/AgCl/BiOCl, and the Z-scheme bridge for Ag/AgBr/BiOBr [144]. As shown in **Figure 7**, the photo-induced electrons transferred from metallic Ag to the CB of AgCl and further transferred to the CB of BiOCl. Then, the electrons reacted with O_2 to produce $O_2{}^{\bullet-}$ for RhB degradation. And the photogenerated holes transfer to the VB of AgCl and BiOCl to oxidize Cl^- ions with Cl· radicals producing. The Cl radical can degrade RhB, and hence, Cl·was reduced to Cl^- ions again [144]. Based on the photocatalytic mechanism analysis, we deemed that metallic Ag had very important role in SPR.
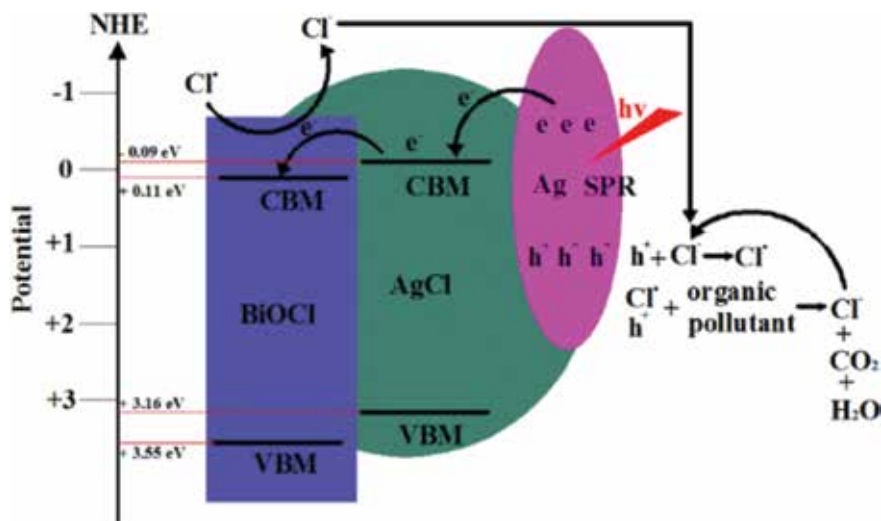

Figure 7 Photocatalytic mechanism scheme of Ag/AgCl/BiOCl under visible light irradiation ($\lambda \geq 400$ nm) [144]. Reprinted with permission from American Chemical Society.

4.7. Defects

In previous reports, it had been proved that the oxygen vacancies occurred under UV light irradiation due to the low-bond energy and long-bond length of the Bi–O bond [47]. Furthermore, our group prepared black BiOCl with oxygen vacancies 20 times higher VLD photocatalytic activity than pure BiOCl for RhB degradation [148]. Recently, Xie found the defects

change from isolated defects $V_{Bi'''}$ to triple vacancy associates $V_{Bi'''} V_O^{\bullet\bullet} V_{Bi'''}$ with the thickness of BiOCl nanosheets reducing to 3 nm [149]. And the ultrathin BiOCl nanosheets showed five times higher VLD photocatalytic activity than bulk BiOCl nanoplates (30 nm) for RhB degradation.

4.8. Solid solutions

It has been reported that the absorption edges of $BiOCl_{(1-x)}Br_x$, $BiOBr_{(1-x)}I_x$, and $BiOCl_{(1-x)}I_x$ solid solutions changed as a function of x, and they all displayed enhanced VLD photocatalytic activities than pure BiOX [145–147]. The reasons of the good VLD photocatalytic activity of BiOX solid solutions may be the enhanced internal electric field and the deeply valence band edge position [146, 147]. Alternatively, by DFT calculations, Huang considered that the trapping of photogenerated carriers in BiOX solid solutions arises the most likely from the cation vacancy V_{Bi} [145].

4.9. Bismuth-rich effect

BiOX photocatalyst also has its drawbacks. The conduction band positions of BiOX are too positive, limiting its ability of activating molecular oxygen, degradation of pollutants, and other applications. For improving its photocatalytic activity, the CB position must be decreased. It has been proved that the CB of bismuth-based photocatalyst mainly included Bi 6p orbits. Therefore, the increase bismuth content may decrease the CB potential, and then, the bismuth-rich $Bi_xO_yX_z$ (X = Cl, Br, I) showed very high photocatalytic reduction activity. For example, Huang found that the increments of the content of bismuth in bismuth titanate can improve the position of CBM [178]. Since Huang' group first reported Bi_3O_4Cl photocatalyst in 2006 [179], several other $Bi_xO_yX_z$ photocatalysts such as Bi_3O_4Cl, Bi_3O_4Br, $Bi_4O_5I_2$, $Bi_4O_5Br_2$, $Bi_{24}O_{31}Cl_{10}$, $Bi_{24}O_{31}Br_{10}$, Bi_5O_7I, Bi_5O_7Br, $Bi_7O_9I_3$ were reported and showed higher activity than their corresponding BiOX [179–190].

5. Facet effect

Different crystal surface of nanomaterials showed different electronic and geometric structures and also exhibited different surface physical, chemical properties, and photoreactivity. Therefore, the facet-dependent photocatalytic properties have aroused much research interest [191–197]. Since Yang firstly reported {001} facet-dependent photocatalytic properties of anatase TiO_2 properties [198, 199], anatase TiO_2 has been intensively investigated with different facet exposure [200–217]. Except for TiO_2, the facet-dependent photocatalytic properties of many other photocatalysts, such as ZnO [219–221], $BiVO_4$ [152, 194], AgBr [195], and $AgPO_4$ [197, 222], also were studied. For BiOX, the layer structure resulted that the mainly exposed facets were {001}, and other facets ({100} or {010} facets) of BiOX were very difficult to expose. So, until 2011, the facet-dependent photocatalytic properties of BiOX were reported by our group for the first time. Our group and Zhang's group have detailedly researched the facets effect of BiOCl [44, 60, 223, 224]. And then, the facets effects of BiOBr and BiOI were reported

[225–228]. But, the relevant studies about facet-dependent photocatalytic properties of BiOX were still very limited.
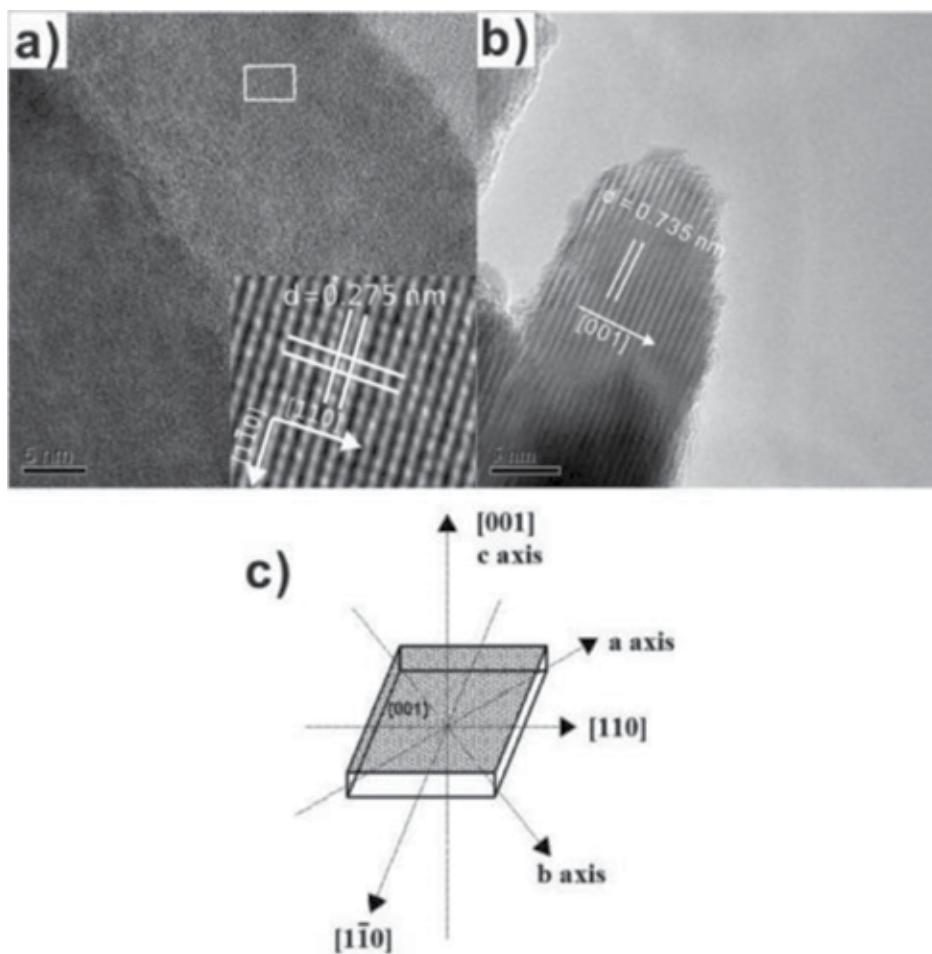
5.1. {001} facet

Figure 8 (a) Top view HRTEM images of BiOCl NS-3; (b) side view HRTEM images of BiOCl NS-3; and (c) simulation structure of single BiOCl NS [44]. Reprinted with permission from Royal Society of Chemistry.

BiOCl: Our group synthesized the BiOCl nanosheets with different {001} facets (71–87%) percentage through a molecular precursor ($Bi_n(Tu)_xCl_{3n}$ (Tu = thiourea)) route (**Figure 8**) [44]. With the {001} facets percentage increase, the photocatalytic activity increasing strongly. The electron paramagnetic resonance (EPR) and PL techniques were used to study the reason of the high photoactivity of {001} facets. We firstly observed the EPR signal intensity arising from UV light-induced oxygen vacancy and a new PL signal intensity also increased with {001} facets percentage increasing. It was suggested that 100% oxygen atom density in {001} facets was the

fundamental cause for the UV-induced oxygen vacancies generated in the crystal lattice. And then, high UV light photocatalytic activity of BiOCl appeared.

Recently, atomic thickness BiOCl nanosheets were reported [225, 229, 230]. And the researcher found that the high density of oxygen atoms of exposed {001} facets not only are useful for the cationic dye adsorption but also can improve the photo-induced electrons injected via dye excitation. And these photo-induced electrons were captured by O_2 to create reactive oxygen species, which displayed strong photooxidative ability to remove pollutants.

BiOBr: Wu synthesized BiOBr nanosheets with {001} facets exposure by adjusting solvent and reaction temperature [227]. The VLD photocatalytic efficiency for RhB degradation enhanced with the {001} facets percentage increasing from 83 to 94% of BiOBr. Furthermore, the as-synthesized BiOBr nanosheets exhibited selective VLD photocatalytic activity with RhB is much higher than that MO or MB degradation due to the 100% oxygen terminated atoms of {001} facets.

BiOI: Our group prepared the BiOI single-crystal nanosheets (BiOI SCNs) with highly symmetry and dominant exposed {001} facets (up to 95%) via annealing BiI_3 [60]. The synthesis mechanism with thermal decomposition process of BiI_3 was studied. And it was found that the reactive facets of BiOI were {001} facets. The photocatalytic results showed that BiOI SCNs exhibited higher VLD photocatalytic activity for RhB degradation than irregular BiOI. The improved separation efficiency of photo-induced carriers resulted the {001} facet-dependent photocatalytic activity of BiOI. Recently, our group also synthesized BiOI-001 ultrathin nanosheets for CO_2 reduction [231].
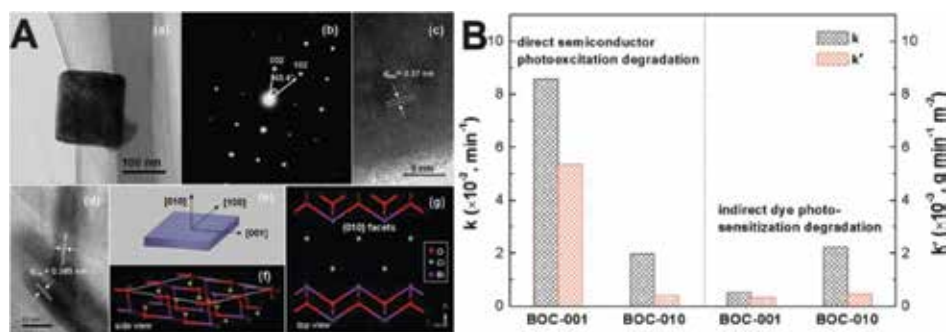
5.2. {010} facet

Figure 9 (A): (a) TEM image, (b) SAED pattern, and (c, d) HRTEM images of the BOC-010 SCNSs. (e) Schematic illustration of the crystal orientation of the nanosheet. (f, g) Atomic structure of the {010} facets: (f) side view; (g) top view. (B): Comparison of the apparent reaction rate constants for photocatalytic degradation of MO over the BOC SCNSs under (left) UV (λ = 254 nm) and (right) visible-light (λ > 420 nm) irradiation [210]. Reprinted with permission from American Chemical Society.

BiOCl:In general, the side surface of BiOX nanosheets was {010} facets are and it was difficult to expose due to its high surface energy. So, special synthetic methods should be used to expose {010} facets of BiOX. Recently, Zhang firstly reported the facet controllable synthesis of BiOCl

single-crystalline nanosheets (BOC SCNSs) by adjusting the pH value of the solution with adding NaOH (**Figure 9a**) to exposed {010} or {001} facets [223]. And this method offered to hope to research the facet effect of all BiOX photocatalysts. Based on the surface atomic structure and internal electric fields direction, BiOCl-001 had higher direct photocatalytic activity under UV light. However, BiOCl-010 had superior activity for indirect dye sensitization degradation under visible light due to the open channel characteristic and larger surface area (**Figure 9b**).

BiOBr: Following Zhang's work, Wong also used the same method to synthesize BiOBr single-crystalline nanosheets with {010} facets [70]. The photocatalytic activity results showed the BiOBr-001 exhibited much higher photocatalytic activity for *Escherichia coli* inactivation under visible light. The above same pH controlled method for {010} exposure of BiOCl and BiOBr proved the universality. But, it can be used to exposure {010} facets of BiOI?

BiOI: It was a pity that pH controlled method cannot be used to exposure {010} facets of BiOI. And these results have been proved by many research groups. Fortunately, our group prepared BiOI-010 sample via reaction time method recently [228]. When reaction time was 2 h, the sample was BiOI-010, and BiOI-001 was obtained when the reaction time more than 12 h. The photocatalytic activity data showed BiOI-001 still displayed higher activity than BiOI-010 for CO_2 reduction under UV–Vis light.

5.3. Advice on facets confirmation of BiOX

The basic premise of the facet effect research was the confirming the dominant exposed facet, transmission electron microscope (TEM) images and the corresponding selected-area electron diffraction (SAED) pattern, or high resolution TEM and the corresponding fast-Fourier transform (FFT) pattern were needed. However, the facets confirmation of BiOX was very difficult due to the theoretical value of the angle between the (102) and (002) facets is very close to that of between the (200) and (110) facets. Based on the symmetries of tetragonal BiOX and the above observation, the dominant exposed facets of BiOX samples should be identified discreetly. And our group give some proposals [232].

	a = b (nm)			110	200	102	002
BiOCl	0.3883	0.7347	d value	0.275 nm	0.194 nm	0.267 nm	0.367 nm
			Angle	45.0°		43.4°	
BiOBr	0.3915	0.8076	d value	0.277 nm	0.196 nm	0.281 nm	0.404 nm
			Angle	45.0°		45.9°	
BiOI	0.3984	0.9128	d value	0.282 nm	0.199 nm	0.300 nm	0.456 nm
			Angle	45.0°		48.7°	

Table 1. Theoretical d value of the theoretical angles of relevant diffraction spots.

Table 1 shows the theoretical angles of (110)/(200) and (102)/(200) and the theoretical d value of (110), (200), (102), and (200) of BiOX. We found the theoretical angles of (110)/(200) which very close to that of (102)/(200), especially for BiOBr. But, the theoretical d values of (110), (200), (102), and (200) of BiOX were different. The $d_{(001)}$ of BiOX were much higher than that of (110), (200), and (102). So, if the SAED or FFT pattern had scaleplate, the d values of the diffraction spots can be indexed and the exposed facets can be confirmed.

6. Summary and future perspectives

This chapter summarized the recent studies about BiOX for efficient photocatalytic degradation removal of gas, liquid, and solid pollutants. Firstly, advanced synthesis methods resulted high surface area and {001} facets exposure of BiOX with excellent photocatalytic performances. Secondly, after the modification with cocatalyst using, element doping, semiconductor coupling, dye sensitization, surface plasmon resonance, defect making, bismuth-rich effect BiOX displayed excellent photocatalytic activity for environmental remediation under visible light. At end, we give some proposals to confirm facet exposure for studying facet-dependent photocatalytic properties of BiOX. Although there are many achievements about BiOX photocatalysis, there still many fields were needed to research, such as photocatalytic H_2 generation, photocatalytic CO_2 reduction, photocatalytic N_2 fixation, good synthesis methods for active facets exposure, and more deeply photocatalytic mechanism studies. The corporate efforts of experimental studies and theory computations should be used to resolve the above questions. The unsatisfactory points and future research directions include the following:

(1) In general, BiOX were 2D nanosheets with {001} facets exposing. Other morphologies, such as 1D nanorods and 3D nanocube, and other high index facets exposing were reported few. New synthesis ways should be employed to expose the high index facet of BiOX. In addation, BiOX immobilization should be studied to perfect the practical application.

(2) To date, most reports about BiOX photocatalysts were focused on the PCD of liquid organic pollutants. BiOX photocatalysis in atmospheric and solid-phase contaminants should be enhanced. Furthermore, except for our group, BiOX were rarely used in energy photocatalysis field, such as water splitting and CO_2 photoreduction. It should be expanded the energy photocatalysis field for BiOX.

(3) As the layered crystal structure of BiOX interlacing of [Bi_2O_2] slabs with double halogen slabs, the strong ionic feature could result in ion exchange reactions between BiOX and incoming species. For instances, Bi_2S_3 disk-like networks [233], and Bi_2WO_6 hollow microspheres [234] were prepared by this strategy. It indicated that BiOX had wide applications, not only can be used as photocatalysts but also can be used as hard template to synthesize other photocatalysts with different nanostructures.

Acknowledgements

Author details

Liqun Ye

Address all correspondence to: yeliquny@163.com

1 College of Chemistry and Pharmaceutical Engineering, Nanyang Normal University, Nanyang, China

2 School of Oil and Natural Gas Engineering, Southwest Petroleum University, Chengdu, China

References

[1] Chen H., Nanayakkara C. E., Grassian V. H., Chem. Rev., 2012, 112, 5919–5948.

[2] Chen C., Ma W., Zhao J., Chem. Soc. Rev., 2010, 39, 4206–4219.

[3] Konstantinou I. K., Albanis T. A., Appl. Catal. B, 2004, 49, 1–14.

[4] Kubacka A., Fernández-García M., Colón G., Chem. Rev., 2012, 112, 1555–1614.

[5] Wang Y., Wang X., Antonietti M., Angew. Chem. Int. Ed., 2011, 50, 2–24.

[6] Chen X., Shen S., Guo L., Mao S. S., Chem. Rev., 2010, 110, 6503–6570.

[7] Khin M. M., Nair A. S., Babu V. J., Murugan R., Ramakrishna S., Energy. Environ. Sci., 2013, 5, 8075–8109.

[8] Andreozzi R., Caprio V., Ermellino I., Tufano A. I., Ind. Eng. Chem. Res., 1996, 35, 1467–1471.

[9] Linsebigler A. L., Lu G., Yates J. T., Chem. Rev., 1995, 95, 735–758.

[10] Dalrymple O. K., Stefanakos E., Trotz M. A., Goswami D. Y., Appl. Catal. B, 2010, 98, 27–38.

[11] Thompson T. L., Yates J. T., Chem. Rev., 2006, 106, 4428–4453.

[12] Serpone N., Emeline A. V., J. Phys. Chem. Lett., 2012, 3, 673–677.

[13] Hoffmann M. R., Martin S. T., Choi W., Bahnemannt D. W., Chem. Rev., 1995, 95, 69–96.

[14] Linic S., Christopher P., Ingram D. B., Nat. Mater., 2011, 10, 911–921.

[15] Xiang Q., Yu J., Jaroniec M., Chem. Soc. Rev., 2012, 41, 782–796

[16] Liu S., Yu J., Cheng B., Jaroniec M., Adv. Colloid. Interface. Sci., 2012, 173, 35–53.

[17] Reed J., Ceder G., Chem. Rev., 2004, 104, 4513–4534.

[18] Burch R., Chalker S., Loader P., Thomas J. M., Ueda W., Appl. Catal. A, 1992, 82, 77–90.

[19] Kijima N., Matano K., Saito M., Oikawa T., Konishi T., Yasuda H., Sato T., Yoshimura Y., Appl. Catal. A., 2001, 206, 237–244.

[20] Kusainova A. M., Lightfoot P., Zhou W., Stefanovich S. Y., Mosunov A. V., Dolgikh V. A., Chem. Mater., 2001, 13, 4731–4737.

[21] Ye L., Wang L., Xie H., Su Y., Jin X., Zhang C., Energy. Technol., 2015, 3, 1115–1120.

[22] Maile F. J., Pfaff G., Reynders P., Prog. Org. Coat., 2005, 54, 150–163.

[23] Zhang K. L., Liu C. M., Huang F. Q., Zheng C., Wang W. D., Appl. Catal. B., 2006, 68, 125–129.

[24] Huang W., Zhu Q., Comput. Mater. Sci., 2008, 43, 1101–1108.

[25] Zhang H., Liu L., Zhou Z., RSC Adv., 2012, 2, 9224–9229.

[26] Wang W., Yang W., Chen R., Duan X., Tian Y., Zeng D., Shan B., Phys. Chem. Chem. Phys., 2012, 14, 2450–2454.

[27] Zhang X., Fan C., Wang Y., Wang Y., Liang Z., Han P., Comput. Mater. Sci., 2013, 71, 135–145.

[28] Zhao L., Zhang X., Fan C., Liang Z., Han P., Phys. B., 2012, 407, 3364–3370.

[29] Yang C., Deng K., Peng T., Zan L., Chem. Eng. Technol., 2011, 34, 1–8.

[30] Zhao X., Li Z., Chen Y., Shi L., Zhu Y., Mol J.. Catal. A., 2007, 268, 101–106.

[31] Zan L., Fang W., Wang S., Environ. Sci. Technol., 2006, 40, 1681–1685.

[32] Yang C., Gong C., Peng T., Deng K., Zan L., J. Hazard. Mater., 2010, 178, 152–156.

[33] Fa W., Zan L., Gong C., Zhong J., Deng K., Appl. Catal. B., 2008, 79, 216–223.

[34] Huang M. H., Lin P. H., Adv. Funct. Mater., 2012, 22, 14–24.

[35] Tong H., Ouyang S., Bi Y., Umezawa N., Oshikiri M., Ye J., Adv. Mater., 2012, 24, 229–251.

[36] Jiang Z. Y., Kuang Q., Xie Z. X., Zheng L. S., Adv. Funct. Mater., 2010, 20, 3634–3645.

[37] Liu G., Yu J. C., Lu G. Q., Cheng H. M., Chem. Commun., 2011, 47, 6763–6783.

[38] Zhang X., Ai Z., Jia F., Zhang L., J. Phys. Chem. C., 2008, 112, 747–753.

[39] Chang X., Huang J., Cheng C., Sui Q., Sha W., Ji G., Deng S., Yu G., Catal. Commun., 2010, 11, 460–464.

[40] An H., Du Y., Wang T., Wang C., Hao W., Zhang J., Rare. Metals., 2008, 27, 243–250.

[41] Deng Z., Chen D., Peng B., Tang F., Cryst. Growth. Des., 2008, 8, 2995–3003.

[42] Liu Z., Xu W., Fang J., Xu X., Wu S., Zhu X., Chen Z., Appl. Surf. Sci., 2012, 259, 441–447.

[43] Peng S., Li L., Zhu P., Wu Y., Srinivasan M., Mhaisalkar S. G., Ramakrishna S., Yan Q., Chem. Asian J., 2013, 8, 258–268

[44] Ye L., Zan L., Tian L., Peng T., Zhang J., Chem. Commun., 2011, 47, 6951–6953.

[45] Peng H., Chan C. K., Meister S., Zhang X. F., Cui Y., Chem. Mater., 2009, 21, 247–252.

[46] Song J. M., Mao C. J., Niu H. L., Shen Y. H., Zhang S. Y., Cryst Eng Comm., 2010, 12, 3875–3881.

[47] Shao C., Liu Y., Micro. Nano. Lett., 2012, 7, 152–154.

[48] Xiong J., Cheng G., Li G. F., Qin F., Chen R., RSC Adv., 2011, 1, 1542–1552.

[49] Zhang L., Cao X. F., Chen X. T., Xue Z. L., J. Colloid. Interface. Sci., 2011, 354, 630–636.

[50] Zhang D., Wen M., Jiang B., Li G., Yu J. C., J. Hazard. Mater., 2012, 212, 104–111.

[51] Xu J., Meng W., Zhang Y., Li L., Guo C., Appl. Catal. B., 2011, 107, 355–362.

[52] Feng Y., Li L., Li J., Wang J., Liu L., J. Hazard. Mater., 2011, 192, 538–544.

[53] Cheng H., Huang B., Wang Z., Qin X., Zhang X., Dai Y., Chem. Eur. J., 2011, 17, 8039–8043.

[54] Ai Z., Ho W., Lee S., Zhang L., Environ. Sci. Technol., 2009, 43, 4143–4150.

[55] Jiang Z., Yang F., Yang G., Kong L., Jones M. O., Xiao T., Edwards P. P., J. Photochem. Photobiol. A., 2010, 212, 8–13.

[56] Wang Y., Deng K., Zhang L., J. Phys. Chem. C., 2011, 115, 14300–14308.

[57] Xia J., Yin S., Li H., Xu H., Yan Y. G., Zhang Q., Langmuir., 2011, 27(3), 1200–1206.

[58] Li Y., Wang J., Yao H., Dang L., Li Z., J. Mol. Catal. A., 2011, 334, 116–122.

[59] Xiao X., Zhang W. D., J. Mater. Chem., 2010, 20, 5866–5870.

[60] Ye L., Tian L., Peng T., Zan L., J. Mater. Chem., 2011, 21, 12479–12484.

[61] Shang M., Wang W., Zhang L., J. Hazard. Mater., 2009, 167, 803–809.

[62] Li Y., Liu J., Jiang J., Yu J., Dalton Trans., 2011, 40, 6632–6634.

[63] Wu S., Fang J., Hong X., K Hui, Y. Cen, Dalton Trans., 2014, 43, 2611–2619.

[64] Hahn N. T., Hoang S., Self J. L., Mullins C. B., ACS Nano., 2012, 6(9), 7712–7722.

[65] Liu M., Zhang L., Wang K., Zheng Z., Cryst Eng Comm., 2011, 13, 5460–5466.

[66] Liu Z., Fang J., Xu W., Xu X., Wu S., X. Zhu. Mater. Lett., 2012, 88, 82–85.

[67] Deng H., Wang J., Peng Q., Wang X., Li Y., Chem. Eur. J., 2005, 11, 6519–6524.

[68] Pare B., Sarwan B., Jonnalagadda S. B., J. Mol. Struct., 2012, 1001, 196–202.

[69] Huo Y., Zhang J., Miao M., Jin Y., Appl. Catal. B., 2012, 111–112, 334–341.

[70] Wu D., Wang B., Wang W., An T., Li G., Ng T. W., Yip H. Y., Xiong C., Lee H. K., Wong P. K., J. Mater. Chem. A., 2015, 3, 15148–15155.

[71] Fang Y. F., Ma W. H., Huang Y. P., Cheng G. W., Chem. Eur. J., 2013, 19, 3224–3229.

[72] Zhang M., Chen C., Ma W., Zhao J., Angew. Chem. Int. Ed., 2008, 47, 9730–9733.

[73] Zhang M., Wang Q., Chen C., Zang L., Ma W., Zhao J., Angew. Chem., 2009, 121, 6197–6200.

[74] Liu S., Yu J., Jaroniec M., J. Am. Chem. Soc., 2010, 132, 11914–11916.

[75] Xiang Q., Yu J., Jaroniec M., Chem. Commun., 2011, 47, 4532–4534.

[76] Chen F., Liu H., Bagwasi S., Shen X., Zhang J., J. Photochem. Photobiol. A., 2010, 215, 76–80.

[77] Weng S., Chen B., Xie L., Zheng Z., Liu P., J. Mater. Chem. A., 2013, 1, 3068–3075.

[78] Li H., Zhang L., Nanoscale., 2014, 6, 7805–7810.

[79] Li H., Shi J., Zhao K., Zhang L., Nanoscale., 2014, 6, 14168–14173.

[80] Liu H., Cao W., Su Y., Wang Y., Wang X., Appl. Catal. B., 2012, 111–112, 271–279.

[81] Yu C., Yu J. C., Fan C., Wen H., Hu S., Mater. Sci. Eng. B., 2010, 166, 213–219.

[82] Ye L., Liu X., Zhao Q., Xie H., Zan L., J. Mater. Chem. A., 2013, 1, 8978–8983.

[83] Zhang X., Zhang L., J. Phys. Chem. C., 2010, 114, 18198–18206.

[84] Zhang K., Zhang D., Liu J., Ren K., Luo H., Peng Y., Li G., Yu X., Cryst Eng Comm., 2012, 14, 700–707.

[85] Li J., Zhao K., Yu Y., Zhang L., Adv. Funct. Mater., 2015, 25, 2189–2201.

[86] Wang P. Q., Bai Y., Liu J. Y., Fan Z., Hu Y. Q., Micro. Nano. Lett., 2012, 7, 876–879.

[87] Pare B., Sarwan B., Jonnalagadda S. B., Appl. Surf. Sci., 2011, 258, 247–253.

[88] Jiang G., Wang X., Wei Z., Li X., Xi X., Hu R., Tang B., Wang R., Wang S., Wang T., Chen W., J. Mater. Chem. A., 2013, 1, 2406–2410.

[89] Wang R., Jiang G., Wang X., Hu R., Xi X., Bao S., Zhou Y., Tong T., Wang S., Wang T., Chen W., Powder. Technol., 2012, 228, 258–263.

[90] Cheng H., Huang B., Qin X., Zhang X., Dai Y., Chem. Commun., 2012, 48, 97–99.

[91] Cao J., Xu B., Lin H., Luo B., Chen S., Catal. Commun., 2012, 26, 204–208.

[92] Chang X., Yu G., Huang J., Li Z., Zhu S., Yu P., Cheng C., Deng S., Ji G., Catal. Today., 2010, 153, 193–199.

[93] Zhang L., Wang W., Zhou L., Shang M., Sun S., Appl. Catal. B., 2009, 90, 458–462.

[94] Chai S. Y., Kim Y. J., Jung M. H., Chakraborty A. K., Jung D., Lee W. I., J. Catal., 2009, 262, 144–149.

[95] Cao J., Zhou C., Lin H., Xu B., Chen S., Appl. Surf. Sci., 2013, 284, 263–269.

[96] Shamaila S., Khan A., Sajjad L., Chen F., Zhang J., Colloid Interface J.. Sci., 2011, 356, 465–472.

[97] Gao B., Chakraborty A. K., Yang J. M., Lee W. I., Bull. Korean. Chem. Soc., 2010, 31, 1941–1944.

[98] Shenawi-Khalil S., Uvarov V., Menes E., Popov I., Sasson Y., Appl. Catal. A. Gen., 2012, 413–414, 1–9.

[99] Wang Q., Hui J., Li J., Cai Y., Yina S., Wang F., Su B., Appl. Surf. Sci., 2013, 283, 577–583.

[100] Kong L., Jiang Z., Xiao T., Lu L., Jones M. O., Edwards P. P., Chem. Commun., 2011, 47, 5512–5514.

[101] Li Y., Liu Y., Wang J., Uchaker E., Zhang Q., Sun S., Huang Y., Li J., Cao G., J. Mater. Chem. A., 2013, 1, 7949–7956.

[102] Fu J., Tian Y., Chang B., Xi F., Dong X., J. Mater. Chem., 2012, 22, 21159–21166.

[103] Ye L., Liu J., Jiang Z., Peng T., Zan L., Appl. Catal. B, 2013, 142–143, 1–7.

[104] Di J., Xia J., Yin S., Xu H., He M., Li H., Xu L., Jiang Y., RSC Adv., 2013, 3, 19624–19631.

[105] Cheng C., Ni Y., Ma X., Hong J., Mater. Lett., 2012, 79, 273–276.

[106] Kong L., Jiang Z., Lai H. H., Nicholls R. J., Xiao T., Jones M. O., Edwards P. P., J. Catal., 2012, 293, 116–125.

[107] Cao J., Xu B., Lin H., Luo B., Chen S., Dalton. Trans., 2012, 41, 11482–11490.

[108] Cui Z., Si M., Zheng Z., Mi L., Fa W., Jia H., Catal. Commun., 2013, 42, 121–124.

[109] Jiang D., Chen L., Zhu J., Chen M., Shi W., Xie J., Dalton Trans., 2013, 42, 15726–15734.

[110] Hou D., Hu X., Hu P., Zhang W., Zhang M., Huang Y., Nanoscale., 2013, 5, 9764–9772.

[111] Li P., Zhao X., Jia C., Sun H., Sun L., Cheng X., Liu L., Fan W., J. Mater. Chem. A., 2013, 1, 3421–3429.

[112] Cao J., Li X., Lin H., Chen S., Fu X., J. Hazard. Mater., 2012, 239–240, 316–324.

[113] Li H., Cui Y., Hong W., Appl. Surf. Sci., 2013, 264, 581–588.

[114] Cao J., Xu B., Lin H., Chen S., Chem. Eng. J., 2013, 228, 482–488.

[115] Li Y., Wang J., Yao H., Dang L., Li Z., Catal. Commun., 2011, 12, 660–664.

[116] Jiang J., Zhang X., Sun P., Zhang L., J. Phys. Chem. C., 2011, 115, 20555–20564.

[117] Li H., Cui Y. , Hong W., Xu B., Chem. Eng. J., 2013, 228, 1110–1120.

[118] Zhang X., Zhang L., Xie T., Wang D., J. Phys. Chem. C., 2009, 113, 7371–7378.

[119] Dai G., Yu J., Liu G., J. Phys. Chem. C., 2011, 115, 7339–7346.

[120] Cheng H., Huang B., Dai Y., Qin X., Zhang X., Langmuir., 2010, 26(9), 6618–6624.

[121] Chen L., Jiang D., He T., Wu Z., Chen M., Cryst Eng Comm., 2013, 15, 7556–7563.

[122] Cheng H., Wang W., Huang B., Wang Z., Zhan J., Qin X., Zhang X., Dai Y., J. Mater. Chem. A., 2013, 1, 7131–7136.

[123] Lv Y., Liu H., Zhang W., Ran S., Chi F., Yang B., Xia A., J. Environ. Chem. Eng., 2013, 1, 526–533.

[124] Li T. B., Chen G., Zhou C., Shen Z. Y., Jin R. C., Sun J. X., Dalton. Trans., 2011, 40, 6751–6758.

[125] Xiao X., Hao R., Liang M., Zuo X., Nan J., Li L., Zhang W., J. Hazard. Mater., 2012, 233–234, 122–130.

[126] Dong F., Sun Y., Fu M., Wu Z., Lee S. C., J. Hazard. Mater., 2012, 219–220, 26–34.

[127] Cao J., Xu B., Luo B., Lin H., Chen S., Catal. Commun., 2011, 13, 63–68.

[128] Cao J., Xu B., Lin H., Luo B., Chen S., Chem. Eng. J., 2012, 185–186, 91–99.

[129] Zhang J., Xia J., Yin S., Li H., Xu H., He M., Huang L., Zhang Q., Colloids Surf. A., 2013, 420, 89–95.

[130] Reddy K. H., Martha S., Parida K. M., Inorg. Chem., 2013, 52, 6390–6401.

[131] Gao F., Zeng D., Huang Q., Tian S., Xie C., Phys. Chem. Chem. Phys., 2012, 14, 10572–10578.

[132] Tian L., Liu J., Gong C., Ye L., Zan L., J. Nano. Res., 2013, 15(9), 1–11.

[133] Tu X., Luo S., Chen G., Li J., Chem. Eur. J., 2012, 18, 14359–14366.

[134] Ai Z., Ho W., Lee S., J. Phys. Chem. C., 2011, 115(51), 25330–25337.

[135] Liu J. Y., Bai Y., Luo P. Y., Wang P. Q., Catal. Commun., 2013, 42, 58–61.

[136] Zhang X., Chang X., Gondal M. A., Zhang B., Liu Y., Ji G., Appl. Surf. Sci., 2012, 258, 7826–7832.

[137] Lei Y., Wang G., Guo P., Song H., Appl. Surf. Sci., 2013, 279, 374–379.

[138] Xiong W., Zhao Q., Li X., Zhang D., Catal. Commun., 2011, 16, 229–233.

[139] Cheng H., Huang B., Wang P., Wang Z., Lou Z., Wang J., Qin X., Zhang X., Dai Y., Chem. Commun., 2011, 47, 7054–7056.

[140] Yan T., Yan X., Guo R., Zhang W., Li W., You J., Catal. Commun., 2013, 42, 30–34.

[141] Li T., Luo S., Yang L., J. Solid. State. Chem., 2013, 206, 308–316.

[142] Cao J., Zhao Y., Lin H., Xu B., Chen S., J. Solid. State. Chem., 2013, 206, 38–44.

[143] Li T., Luo S., Yang L., Mater. Lett., 2013, 109, 247–252.

[144] Ye L., Liu J., Gong C., Tian L., Peng T., Zan L., ACS Catal., 2012, 2, 1677–1683.

[145] Liu Y., Son W. J., Lu J., Huang B., Dai Y., Whangbo M. H., Chem. Eur. J., 2011, 17, 9342–9349.

[146] Wang W., Huang F., Lin X., Yang J. A., Catal. Commun., 2008, 9, 8–12.

[147] Ren K., Liu J., Liang J., Zhang K., Zheng X., Luo H., Huang Y., Liu P., Yu X., Dalton. Trans., 2013, 42, 9706–9712.

[148] Ye L., Deng K., Xu F., Tian L., Peng T., Zan L., Phys. Chem. Chem. Phys., 2012, 14, 82–85.

[149] Guan M., Xiao C., Zhang J., Fan S., An R., Cheng Q., Xie J., Zhou M., Ye B., Xie Y., J. Am. Chem. Soc., 2013, 135, 10411–10417.

[150] Ye L., Gong C., Liu J., Tian L., Peng T., Deng K., Zan L., J. Mater. Chem., 2012, 22, 8354–8360.

[151] Zhang L., Wang W., Sun S., Sun Y., Gao E., Xu J., Appl. Catal. B., 2013, 132–133, 315–320.

[152] Li R., Zhang F., Wang D., Yang J., Li M., Zhu J., Zhou X., Han H., Li C., Nat. Commun., 2013, 4, 1432.

[153] Jensen R. A., Ryswyk H. V., She C., Szarko J. M., Chen L. X., Hupp J. T., Langmuir., 2010, 26, 1401–1404.

[154] Angelis F. D., Fantacci S., Selloni A., Nazeeruddin M. K., Gratzel M., J. Am. Chem. Soc., 2007, 129, 14156–14157.

[155] Gao F., Wang Y., Shi D., Zhang J., Wang M., Jing X., Humphry-Baker R., Wang P., Zakeeruddin S. M., Gratzel M., J. Am. Chem. Soc., 2008, 130, 10720–10728.

[156] Youngblood W. J., Lee S. A., Maeda K., Mallouk T. E., Acc. Chem. Res., 2009, 42, 1966–1973.

[157] Zhang X., Veikko U., Mao J., Cai P., Peng T., Chem. Eur. J., 2012, 18, 12103–12111.

[158] Pan L., Zou J. J., Zhang X. W., Wang L., J. Am. Chem. Soc., 2011, 133, 10000–10003.

[159] Ji P. F., Zhang J. L., Chen F., Anpo M., Appl. Catal. B, 2009, 85, 148–154.

[160] Chang X., Gondal M. A., Al-Saadi A. A., Ali M. A., Shen H., Zhou Q., Zhang J., Du M., Liu Y., Ji G., J. Colloid. Interface. Sci., 2012, 377, 291–298.

[161] Gondal M. A., Chang X., Ali M. A., Yamani Z. H., Zhou Q., Ji G., Appl. Catal. A., 2011, 397, 192–200.

[162] Zhang L., Wong K. H., Chen Z., Yu J. C., Zhao J., Hu C., Chan C. Y., Wong P. K., Appl. Catal. A., 2009, 363, 221–229.

[163] Zhang Y., Tang Z. R., Fu X., Xu Y. J., Appl. Catal. B., 2011, 106, 445–452.

[164] Wang P., Huang B., Qin X., Zhang X., Dai Y., Wei J., Whangbo M. H., Angew. Chem. Int. Ed., 2008, 47, 7931–7933.

[165] Wang P., Huang B., Lou Z., Zhang X., Qin X., Dai Y., Zheng Z., Wang X., Chem. Eur. J., 2010, 16, 538–544.

[166] Wang P., Huang B., Zhang X., Qin X., Jin H., Dai Y., Wang Z., Wei J., Zhan J., Wang S., Wang J., Whangbo M. H., Chem. Eur. J., 2009, 15, 1821–1824.

[167] An C., Peng S., Sun Y., Adv. Mater., 2010, 22, 2570–2574.

[168] Zhu M., Chen P., Liu M., ACS Nano., 2011, 5, 4529–4536.

[169] Xu H., Li H., Xia J., Yin S., Luo Z., Liu L., Xu L., ACS Appl. Mater. Interfaces., 2011, 3, 22–29.

[170] Li Y., Ding Y., J. Phys. Chem. C., 2010, 114, 3175–3179.

[171] Tian G., Chen Y., Bao H. L., Meng X., Pan K., Zhou W., Tian C., Wang J. Q., Fu H., J. Mater. Chem., 2012, 22, 2081–2088.

[172] Elahifard M. R., Rahimnejad S., Haghighi S., Gholami M. R., J. Am. Chem. Soc., 2007, 129, 9552–9553.

[173] Zhang L. S., Wong K. H., Yip H. Y., Hu C., Yu J. C., Chan C. Y., Wong P. K., Environ. Sci. Technol., 2010, 44, 1392–1398.

[174] Nakamura I., Negishi N., Kutsuna S., Ihara T., Sugihara S., Takeuchi K., J. Mol. Catal. A. Chem., 2000, 161, 205–212.

[175] Ihara T., Miyoshi M., Iriyama Y., Matsumoto O., Sugihara S., Appl. Catal. B., 2003, 42, 403–409.

[176] Chen X., Liu L., Yu P. Y., Mao S. S., Science., 2011, 331, 746–750.

[177] Maeda K., Teramura K., Lu D. L., Takata T., Saito N., Inoue Y., Domen K., Nature., 2006, 440, 295–295.

[178] Wei W., Dai Y., Huang B., J. Phys. Chem. C., 2009, 113, 5658–5663.

[179] Lin X., Huang T., Huang F. Q., Wang W. D., Shi J. L., J. Phys. Chem. B., 2006, 110, 24629–24634.

[180] Li J., Zhang L., Li Y., Yu Y., Nanoscale., 2014, 167–171.

[181] Wang J., Yu Y., Zhang L., Appl. Catal. B., 2013, 136, 112–121.

[182] Xiao X., Xing C. L., He G. P., Zuo X. X., Nan J. M., Wang L. S., Appl. Catal. B., 2014, 148, 154–163.

[183] Di J., Xia J. X., Ji M. X., Yin S., Li H. P., Xu H., Zhang Q., Li H. M., J. Mater. Chem. A., 2015, 3, 15108–15118.

[184] Jin X., Ye L., Wang H., Su Y., Xie H., Zhong Z., Zhang H., Appl. Catal. B. Environ., 2015, 165, 668–675.

[185] Ye L., Jin X., Liu C., Ding C., Xie H., Chu K. H., Wong P. K., Appl. Catal. B Environ., 2016, doi:10.1016/j.apcatb.2016.01.044.

[186] Xiao X., Hu R. P., Liu C., Xing C. L., Zuo X. X., Nan J. M., Wang L. S., Chem. Eng. J., 2013, 225, 790–797.

[187] Xiao X., Hao R., Zuo X. X., Nan J. M., Li L. S., Zhang W. D., Chem. Eng. J., 2012, 209, 293–300.

[188] Sun S. M., Wang W. Z., Zhang L., Zhou L., Yin W. Z., Shang M., Environ. Sci. Technol., 2009, 43, 2005–2010.

[189] Su Y., Wang H., Ye L., Jin X., Xie H., He C., Bao K., RSC Adv., 2014, 4, 65056–65064.

[190] Ye L., Su Y., Jin X., Xie H., Cao F., Guo Z., Appl. Surf. Sci., 2014, 311, 858–863.

[191] Cho S., Jang J. W., Lee J. S., Lee K. H., Langmuir., 2010, 26, 14255–14262.

[192] Fan W., Wang X., Cui M., Zhang D., Zhang Y., Yu T., Guo L., Environ. Sci. Technol., 2012, 46, 10255–10262.

[193] Leng M., Liu M., Zhang Y., Wang Z., Yu C., Yang X., Zhang H., Wang C., J. Am. Chem. Soc., 2010, 132, 17084–17087.

[194] Wang D., Jiang H., Zong X., Xu Q., Ma Y., Li G., Li C., Chem. Eur. J., 2011, 17, 1275–1282.

[195] Wang H., Yang J., Li X., Zhang H., Li J., Guo L., Small., 2012, 8, 2802–2806.

[196] Yi Z., Ye J., Kikugawa N., Kako T., Ouyang S., Stuart-Williams H., Yang H., Cao J., Luo W., Li Z., Liu Y., Withers R. L., Nat. Mater., 2010, 9, 559–564.

[197] Bi Y., Ouyang S., Umezawa N., Cao J., Ye J., J. Am. Chem. Soc., 2011, 133, 6490–6492.

[198] Selloni A., Nat. Mater., 2008, 7, 613–615.

[199] Yang H. G., Sun C. H., Qiao S. Z., Zou J., Liu G., Smith S. C., Cheng H. M., Lu G. Q., Nature., 2008, 453, 638–641.

[200] Yang H. G., Liu G., Qiao S. Z., Sun C. H., Jin Y. G., Smith S. C., Zou J., Cheng H. M., Lu G. Q., J. Am. Chem. Soc., 2009, 131, 4078–4083.

[201] Han X., Kuang Q., Jin M., Xie Z., Zheng L., J. Am. Chem. Soc., 2009, 131, 3152–3153.

[202] Pan J., Liu G., Lu G. Q., Cheng H. M., Angew. Chem. Int. Ed., 2011, 50, 2133–2137.

[203] Zhao X., Jin W., Cai J., Ye J., Li Z., Ma Y., Xie J., Qi L., Adv. Funct. Mater., 2011, 21, 3554–3563.

[204] Wu X., Chen Z., Lu G. Q., Wang L., Adv. Funct. Mater., 2011, 21, 4167–4172.

[205] Yu H., Tian B., Zhang J., Chem. Eur. J., 2011, 17, 5499–5502.

[206] Ye L., Liu J., Jiang Z., Peng T., Zan L., Nanoscale., 2013, 5, 9391–9396.

[207] Ye L., Liu J., Tian L., Peng T., Zan L., Appl. Catal. B, 2013, 134–135, 60–65.

[208] Gordon T. R., Cargnello M., Paik T., Mangolini F., Weber R. T., Fornasiero P., Murray C. B., J. Am. Chem. Soc., 2012, 134, 6751–6761.

[209] Murakami N., Kurihara Y., Tsubota T., Ohno T., J. Phys. Chem. C., 2009, 113, 3062–3069.

[210] Ohno T., Sarukawa K., Matsumura M., New. J. Chem., 2002, 26, 1167–1170.

[211] Tachikawa T., Yamashita S., Majima T., J. Am. Chem. Soc., 2011, 133, 7197–7204.

[212] Tachikawa T., Wang N., Yamashita S., Cui S., Majima T., Angew. Chem., 2010, 122, 8775–8779.

[213] Maitani M. M., Tanaka K., Mochizuki D., Wada Y., J. Phys. Chem. Lett., 2011, 2, 2655–2659.

[214] Arienzo M. D., Carbajo J., Bahamonde A., Crippa M., Polizzi S., Scotti R., Wahba L., Morazzoni F., J. Am. Chem. Soc., 2011, 133, 17652–17661.

[215] Zheng Z., Huang B., Lu J., Qin X., Zhang X., Dai Y., Chem. Eur. J., 2011, 17, 15032–15038.

[216] Xiang Q., Lv K., Yu J., Appl. Catal. B, 2010, 96, 557–564.

[217] Ye L., Mao J., Liu J., Jiang Z., Peng T., Zan L., J. Mater. Chem. A., 2013, 1, 10532–10537.

[218] Han X. G., He H. Z., Kuang Q., Zhou X., Zhang X. H., Xu T., Xie Z. X., Zheng L. S., J. Phys. Chem. C., 2009, 113, 584–589.

[219] Zheng Z., Huang B., Wang Z., Guo M., Qin X., Zhang X., Wang P., Dai Y., J. Phys. Chem. C., 2009, 113, 14448–14453.

[220] Zhang Y., Deng B., Zhang T., Gao D., Xu A. W., J. Phys. Chem. C., 2010, 114, 5073–5079.

[221] Huang W. C., Lyu L. M., Yang Y. C., Huang M. H., J. Am. Chem. Soc., 2012, 134, 1261–1267.

[222] Wang J., Teng F., Chen M., Xu J., Song Y., Zhou X., Cryst Eng Comm., 2013, 15, 39–42.

[223] Jiang J., Zhao K., Xiao X., Zhang L., J. Am. Chem. Soc., 2012, 134, 4473–4476.

[224] Ye L., Chen J., Liu J., Peng T., Deng K., Zan L., Appl. Catal. B, 2013, 130–131, 1–7.

[225] Wang D. H., Gao G. Q., Zhang Y. W., Zhou L. S., Xu A. W., Chen W., Nanoscale., 2012, 4, 7780–7785.

[226] Wang C., Zhang X., Yuan B., Shao C., Liu Y., Micro. Nano. Lett., 2012, 7, 152–154.

[227] Zhang D., Li J., Wang Q., Wu Q., J. Mater. Chem. A., 2013, 1, 8622–8629.

[228] Ye L., Jin X., Ji X., Liu C., Su Y., Xie H., Liu C., Chem. Eng. J., 2016, 291, 39–46.

[229] Ye L., Jin X., Leng Y., Su Y., Xie H., Liu C., J. Power. Sources., 2015, 293, 409–415.

[230] Guan M., Xiao C., Zhang J., Fan S., An R., Cheng Q., Xie J., Zhou M., Ye B., Xie Y., Am J.. Chem. Soc., 2013, 135(28), 10411–10417.

[231] Ye L., Wang H., Jin X., Su Y., Wang D., Xie H., Liu X., Liu X., Sol. Energy. Mater. Sol. C., 2016, 144, 732–739.

[232] Ye L., Su Y., Jin X., Xie H., Zhang C., Environ. Sci. Nano, 2014, 1, 90–112.

[233] Chen J. I. L., von Freymann G., Kitaev V., Ozin G. A., J. Am. Chem. Soc., 2007, 129, 1196–1202.

[234] Cheng H. F., Huang B. B., Liu Y. Y., Wang Z. Y., Qin X. Y., Zhang X. Y., Dai Y., Chem. Commun., 2012, 48, 9729–9731.

Metal Organic Frameworks as Emerging Photocatalysts

Ahmad Alshammari, Zheng Jiang and
Kyle E. Cordova

Additional information is available at the end of the chapter

http://dx.doi.org/10.5772/63489

Abstract

Increasing number of metal-organic frameworks (MOFs) have recently been recognised as a new generation of emerging porous photocatalysts in photocatalysis and photoelectrocatalysis, since their intrinsic coordination structure between the metal cluster and organic ligands offers MOFs great flexibility to tune their semiconducting property for enhanced light harvesting. In order to improve their performance substantially and achieve widespread application of MOF photocatalysts, it is necessary to develop effective synthesis strategies and understand their semiconducting crystal structure, photocatalytic mechanism in depth. This chapter firstly provides a brief introduction of the MOF materials; this chapter addresses the crystallinity, porosity and electronic semiconducting structures that are essential in solar energy conversion. Established and innovative syntheses strategies of MOFs are then categorised and illustrated, followed by various characterisations techniques applied to investigate their structural and semiconducting properties (band structure and charge transfer), including X-ray Diffraction XRD, small angle X-ray Diffraction SAXRD, adsorption/desorption, UV-Vis, nuclear magnetic resonance (NMR), extended fine Auger structures (EXFAS), inelastic neutron scattering (INS) spectroscopy, high-resolution transmission electron microscopy (HR)TEM and electrochemical measurements. The photocatalytic and photoelectrocatalytic application of MOFs are introduced addressing their unique photocatalytic mechanism. The perspectives of MOF photocatalysts are finally presented to encourage the future development. The content of this chapter suits the users including beginners, postgraduates and professionals.

Keywords: metal organic framework, photocatalysis, light harvesting, photocatalysis, water splitting, photocatalytic CO_2 reduction

1. Introduction

1.1. General introduction

In the late 1990s, the discovery of a new type of porous compounds has appealed great attention due to the potential these materials exhibited in advanced technological applications. These compounds, termed porous coordination polymers (PCPs) or more commonly, metal-organic frameworks (MOFs), result from the combination of two distinct disciplines, organic and inorganic chemistry, which form open frameworks. MOFs are well known to possess large surface areas due to ultrahigh porosity with the size of their pores ranging from the micro- to mesoporous regime. As shown in **Figure 1**, the structures of MOFs are composed of organic ligands (referred to as linkers) and metal clusters that serve as connecters. Due to a high degree of variability for both the inorganic and organic components, there is a large library of aesthetically pleasing structures that have been shown to be of potential use in applications such as clean energy storage (methane and hydrogen) [1], CO_2 capture and sequestration and various separation processes [2–5]. Furthermore, MOFs use in thin film devices [6, 7], biomedical imaging, light harvesting, optical luminescence [8, 9] and catalysis [10, 11] is also gaining importance.
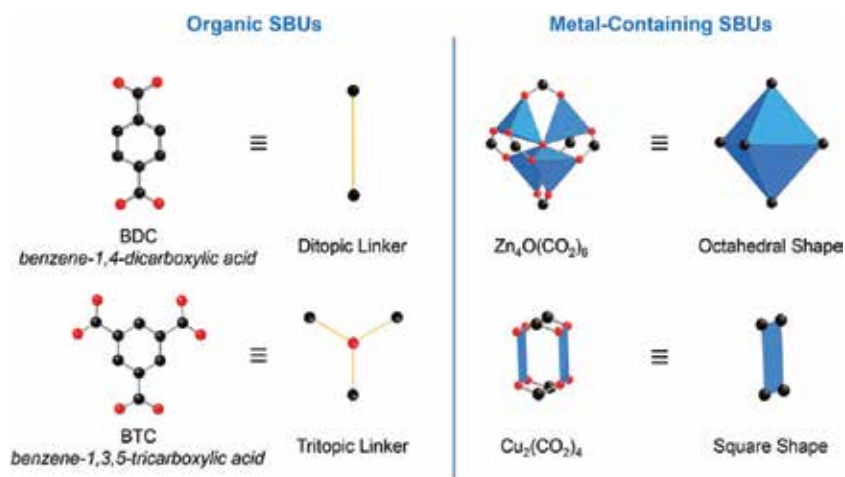

Figure 1. The chemical formula and names are provided for each MOF. Atom colours in molecular drawings: C, black; O, red; N, green; Zn, blue polyhedral; Cu, blue squares. Hydrogen atoms are omitted for clarity.

By definition, two secondary building units (SBUs) are involved in the formation of a crystalline MOF structure. The first SBU is the organic linker, which may be ditopic (having two types of coordinative functionalities), tritopic (three types) or polytopic (more than three types). The second SBU is a metal atom, a finite polyatomic inorganic cluster with two or more metal atoms, or an infinite inorganic unit such as an infinite periodic rod of metal atoms. Metal-containing SBUs are generated in situ and can be predesigned as a result of the judicious choice of reaction conditions (solvent system, temperature, molar concentration, pH). The shapes of SBUs are

defined by their points of extension (connectivity with organic linker SBU) and can be described as a polyhedron, polygon or infinite rod. By contrast, organic linkers are preformed to a custom shape. The aesthetic chemistry of MOFs depends on combination of given metal secondary building unit with variety of organic SBUs. In particular, the organic linker may have the same topology, but a different metric, and may yield an isoreticular series of structures with the same basic net. As organic compounds are quite flexible, it is important to properly identify all vertices and edges along with the point of extension. The components of MOFs are linked by coordination bonds and some other weak interactions (pi-electron, H-bond or Van der Waals interaction), which provide more flexibility to crystalline material and add to the usefulness of MOFs among porous materials.
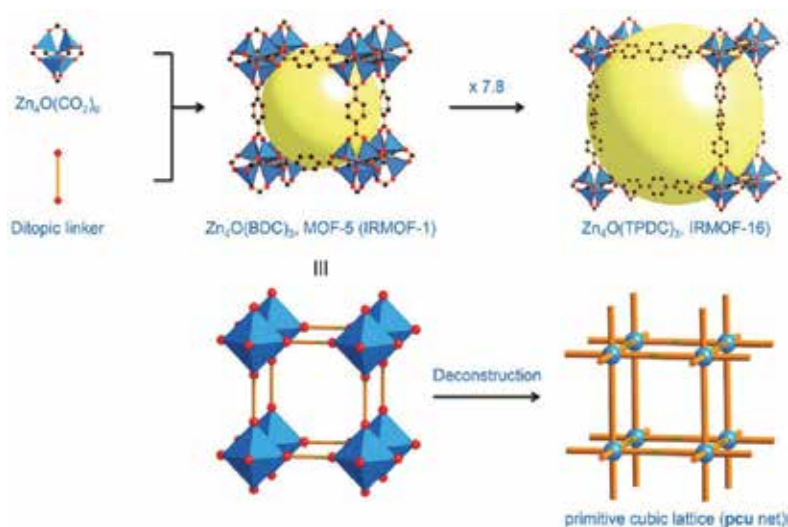

Figure 2. The chemical formula and names are provided for each MOF. Atom colours: C, black; O, red; N, green; Zn, blue polyhedral. Hydrogen atoms are omitted for clarity.

Modelling of a targeted structure with desirable properties and functions represents the eternal goal for material chemists. Therefore, first point is to comprehend the underlying geometric principles involved in MOFs crystal formation. The reverse engineering approach is used by some researchers by which crystal structure of MOFs are deconstructed into core topological nets, and helps in laying a foundation for subsequent description and designing of crystal structure of other MOFs [12]. The advancement in synthetic techniques now allows researchers to design novel and flexible porous crystalline materials by utilising the compounds and structural topologies.

1.2. Historical developments

Coordination polymers represent a group of compounds with extended entities that arise through the linking of metal ions by coordinate bonds to either organic or inorganic ligands. Coordination polymers give rise to structures which can take the form of one (1D)-, two (2D)-

or three (3D)-dimensional networks. Cu, Zn, Ag and Cd—the late transition metals—typically form such kind of network (**Figure 3**), and it was only with the advent of single-crystal X-ray diffraction (SCXRD) that coordination polymer structures could be determined. Coined as early as 1916 [13], 'coordination polymer' is not a novel concept, although it was originally not possible to verify the nature of the continuous framework in the absence of X-ray crystallography. With the discovery of the Prussian blue compounds in 1936, however, it became apparent that 3D coordination frameworks with a cyanide bridging group existed. At present, the term PCP or MOF is used to denote porous coordination polymers, given the broad use and ambiguity of the more historical term, coordination polymer [14]. According to the nature of the compound represented, distinct terminology is utilised and efforts to distinguish between their definitions can be found in the literature [15, 16], partly with respect to composition; solid compounds with considerable inorganic clusters linked by short organic ligands are distinct from those with isolated cations located within an extensive organic structure. The term MOF is typically applied to solid compounds that encompass tightly bonding, linking units of a highly crystalline and well-defined geometric composition, and which can be altered post-treatment. It should be noted that there are several key factors that can be used to explain the chemistry of these compounds. These factors are briefly discussed in following sections.

1.2.1. Coordination framework

Of the one-, two- or three-dimensional forms in which coordination polymers can be found, Hofmann and Kuspert [17] initially described layered two-dimensional structural entities, termed Hofmann compounds. The development of SCXRD method led to the elucidation of the first structure in 1949 [18]. Although such structure does not fully described until the work of Iwamoto et al. in 1967 [19], the Prussian blue complexes were discovered in 1936 and represented the first of the three-dimensional compounds.

1.2.2. Organic-inorganic hybrid materials

Given the incorporation of a CN^- ion as a bridging element within the coordination framework, the structural diversity among the established Prussian blue and Hofmann compounds remains limited. By contrast, adaptability of design and framework functionality can be attributed to the use of organic linkers. In 1959, the metal organic structure of $Cu[NC(CH_2)_4CN]_2 NO_3$ was determined using SCXRD [20], and a broad spectrum of compounds have since been synthesised and characterised by the same means. In 1995, these types of coordination compounds were designated as coordination compounds by Yaghi et al. [21], while coordination polymers in which the nitrate ion is present in the cavity of $Cu[NC(CH_2)_4CN]_2 NO_3$ are termed clathrates and are not regarded as porous compounds. A wide variety of clathrate type coordination compounds were described in the late 1990s.

1.2.3. Ultrahigh porosity of MOFs

The characteristic of existing as a porous material, containing an amount of small holes through which, for example, air and water can pass, is considered porosity, and it is frequently misinterpreted by researchers who use it to describe the crystallographic structures of MOFs

which contain guest molecules in their cavities. The description is therefore not applicable to frameworks in which the solvent molecules cannot be removed or exchanged, when describing novel MOFs which have been characterised by X-ray crystallography alone. Materials which incorporate significantly disordered, free solvent molecules which flow uninterrupted through the empty spaces of the framework can be considered as open frameworks, although the ease with which these molecules can flow out of the structure must first be determined. An evaluation of the host structure prior to and after the elimination of guest molecules is frequently used to determine the stability of MOF. In addition, the ability of a compound to retain its porosity in the absence of guest incorporation was observed in 1997 using a gas sorption procedure under ambient conditions. The novel porous compounds that MOFs represented were shown to have reversible gas storage properties and rapidly garnered a significant degree of interest. The depth of existing literature on MOFs is testament to the research which has since been carried out on these compounds, and indicates the considerable potential and new approaches that have been implemented in the design of novel and valuable MOF materials.
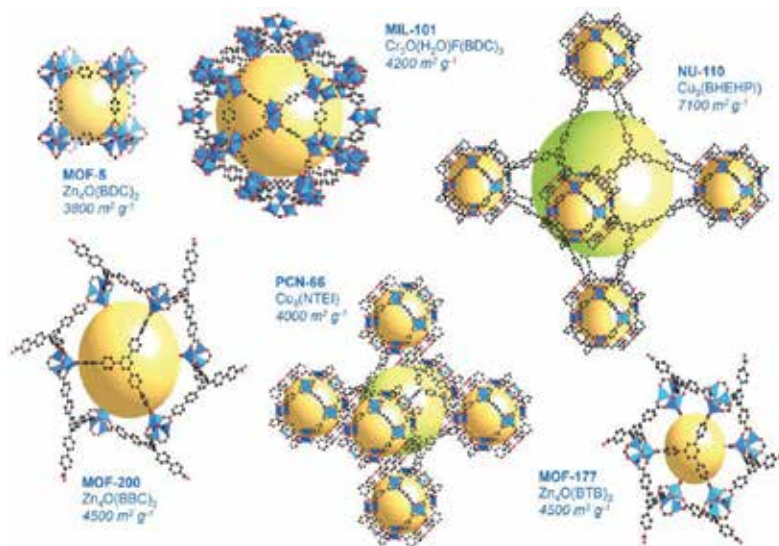

Figure 3. Crystal structure of selected MOFs with high Brunauer-Emmett-Teller (BET) surface area. The chemical formula and BET surface areas are provided for each MOF. Orange and green spheres indicate the free space in the framework. Atom colours: C, black; O, red; N, green; Zn or Cr metal, blue polyhedral; Cu, blue squares. Hydrogen atoms are omitted for clarity.

1.3. Ultrahigh surface area MOFs

Extensive surface area, the result of low density and a porous structure, is a characteristic of MOFs. A three-dimensional (cubic), porous MOF was synthesised from Zn_4O clusters linked with terephthalate [Zn_4O (terephthalate)$_3$] (MOF-5) in 1999 [22], and BET was used to calculate the surface area of the resulting compound, 3800 m^2g^{-1} [23]. The compound subsequently

formed a structural motif template for the preparation of a number of other porous compounds, a strategy which was further expanded to the design of essential frameworks. Other similar frameworks of high porosity are $[Zn_4O(btb)_2]$ (MOF-177) and $[Zn_4O(bbc)_2]$ (MOF-200) {where btb = 1,3,5-benzenetribenzoate, bbc = 4,4′,4″-[benzene-1,3,5-triyltris(benzene-4,1-diyl)]tribenzoate)}; the surface areas attributed to these compounds are 4746 and 6260 m^2g^{-1}, respectively, as determined by BET [24, 25]. Network interpenetration during the self-assembly process represents a significant limitation to structural expansion, restricting a large surface area; this issue can be circumvented using small modifications of network topology design. However, as long as the porosity of single network goes over 50%, 3D networks show more susceptibility to interpenetration, which can be eliminated, however, by using an approach in which a small side group is incorporated into a single network, thus decreasing porosity. Interpenetration can therefore be avoided through partial inhibition of the coordination network, while retaining the porosity of the final crystal. Pillared-layer-type MOF structures, for example, are largely considered non-interpenetrated as one of the three dimensions is inhibited by considerably dense layers. MOFs of adequate porosity pore size and surface can be synthesised by pillar ligands by using an appropriately layered structure format that includes coordinatively unsaturated sites. The stratification of unsaturated metal sites throughout the layer determines the pillar ligand layout. Informal pillared-layer structures (PLS), in which short pillars are used to constrain two of the three dimensions, are a class of porous MOF synthesised from porous layers with short pillars. Comparatively long bipyridyl ligands in $[M_2(bdc)_2(bpy)]$ frameworks with unsymmetrical pcu topologies, for instance, can lead to interpenetration; however, interpenetration does not take place if the pillar ligand is sufficiently small, even where the dicarboxylate ligand is overly long [26, 27]. That the 3D structure arises from layer formation in the first step and their subsequent interconnection by pillars is suggested by the term 'pillared-layer'; as the entire process (from self-assembly to crystallisation) takes place in a single pot reaction, it is therefore difficult to study. The potential exists for an individual single-layered structure to be formed through a more judicious choice of non-bridged ligand over pillared ligand. A unique incidence of the isolation of a hypothetical monolayer and pillared double layer through the preparation of pillared-layer MOFs has been reported [28].

The application of mixed ligand systems to generate porous frameworks can often be a more appropriate strategy for the design of compounds with large surface areas. Zn_4O clusters linked to a pair of separate ligands, for instance, comprise the $Zn_4O(t_2dc)(btb)_{4/3}$ (UMCM-2) (t_2dc = thieno-3,2-bithiophene-2,5-dicarboxylate) compound [29], in which micro pores were shown to be tightly dispersed at 1.4–1.6 and at 1.6–1.8 nm with a mesopore at 2.4–3.0 nm and BET surface area of 5200 m^2g^{-1}. The Zn_4O cluster is replaced with chromium in an alternative framework, and connected with a terephthalate ligand $[Cr_3F(H_2O)O(bdc)_3]$ (MIL-101) to produce a trimer composed of three chromium cations and μ_3O oxygen anions [30]. A pair of cages, 1.2 and 1.45 nm in diameter, give rise to the pores, and the compound exhibits a BET surface area of 4100 m^2g^{-1}. Increased aqueous (and other chemical) stability is observed for this structure compared with those incorporating Zn_4O clusters, and its stability and adaptability allow it to be implemented post-synthesis and for hybridisation with other materials [31].

The paddle-wheel-type dimetal cluster is a frequently used component of framework synthesis and incorporates a range of transition metals, giving rise to a square grid extended framework. A Cu^{+2} paddle wheel cluster has been synthesised along with 4,4′,4″-nitrilotris(benzene-4,1-diyl)tris(ethyne-2,1-diyl)triisopthalate (ntei), $[Cu(H_2O)]_3$(ntei) (PCN-66), and gave a BET surface area of 4000 m^2g^{-1} [32]. A number of alternative isostructures have also been synthesised, with the aim of generating an even greater surface area through the use of hexatopic carboxylate.

1.4. MOFs with Lewis acid frameworks

Of significant importance are frameworks featuring guest interaction sites, particularly those with unsaturated metal sites due to their application in the storage of CO_2, H_2 and other gases. HKUST-1 $[Cu_3(btc)_2.n(H_2O)]$ MOF, consisting of Cu_2 paddle wheel units connected with benzene-1,3,5-tricarboxylic acid, represents one of the earliest examples of this type of framework containing unsaturated metal sites, as shown in **Figure 4** [33]. The resulting three-dimensional network displays thermal stable materials with 1 nm pore size. Applicable in gas storage and heterogeneous catalysis, the axial sites of Cu^{2+} are accountable for incorporating guest molecules [34, 35]. Comparable motif and chromium analogues arise when metals (e.g., W, Fe) are alternatively used, displaying oxygen adsorption with type 1 isotherm at an ambient temperature at which adsorption takes place at low pressures [36–38]. Reversible chemisorption with inconsequential nitrogen uptake is similarly exhibited by the redox-active Cr centres.

In a comparable manner, a further category of frameworks with unsaturated metal cores are represented by M_2(dhtp) (H_4dhtp = 2,5-dihydroxyterephthalic acid, M = Mg, Mn, Zn, Co) [39, 40]. Mg_2(dhtp), one member of this category, displays a significant uptake of CO_2 (almost 35.2
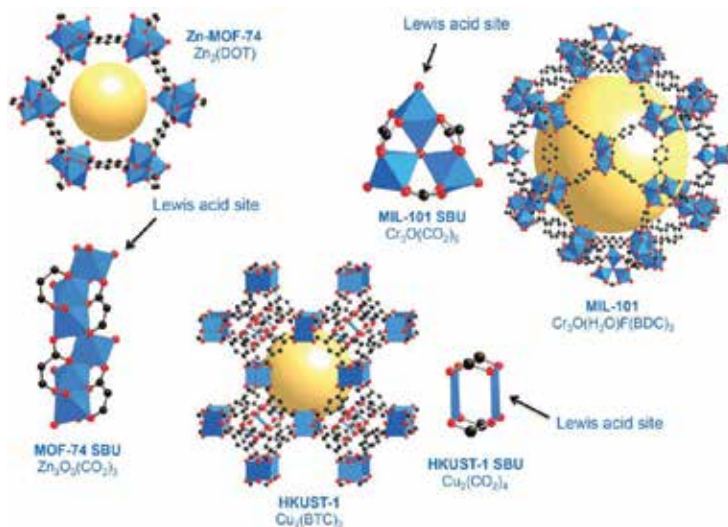

Figure 4. Orange spheres indicate the free space in the framework. Atom colours: C, black; O, red; N, green; Zn or Cr metal, blue polyhedral; Cu, blue squares. Hydrogen atoms are omitted for clarity.

wt%, at 1 atm and 298 K) which is attributable to the strong interaction of oxygen with metal and the low weight of the framework [41]. Exhibiting a high degree of hydrophilicity and acceptable stability, the compound is a biocompatible material and can be used to trap not only CO_2 but also other gases such as NO [42].

Applicable as a catalyst and featuring unsaturated Cr^{+3} centres, $[Cr_3F(H_2O)O(bdc)_3]$ (MIL-101), the aforementioned MOF with high porosity, has the additive benefit of large pores which facilitate effective substrate diffusion during heterogeneous catalysis [43, 44]. Following complete expulsion of the coordinating guest, the unsaturated sites are replenished and an organic linker can be further included into the unsaturated metal cores [45]. The addition of strong Lewis sites to the framework is challenging when using a self-assembly approach, although high design flexibility may provide a template for multifunctional catalysts. The implementation of post-synthetic procedures is a valuable approach for incorporating unsaturated metal sites into the framework and may also be applied to the addition of functional groups to MOFs with satisfactory outcomes for catalysis or other purposes.

1.5. Soft porous MOFs with flexible framework

With respect to structural flexibility and dynamic attributes, the soft properties of MOFs are described in the existing literature to date. Where porous compounds forfeit their porous structure following guest expulsion, porous compounds which can incorporate guest material can nonetheless be determined. These compounds are classed as soft porous materials and display some important and unique characteristics [46–48], although their adsorption isotherm is frequently variable as a result of dynamic guest accommodation properties and therefore cannot be determined using the standard International Union of Pure and Applied Chemistry (IUPAC) classification [49]. A gate-opening behaviour, in case no initial uptake of guest molecules to a specific concentration is observed, is a feature of soft porous materials; upon attaining the threshold concentration, a sudden increase in adsorption behaviour is observed which is linked with the structural change from the non-porous to the porous phase. Compound softness is extremely sensitive to the gas species to be incorporated, a characteristic of value in gas separation. 2D materials can usually be transformed in a straightforward manner upon guest accommodation, and a distinguishing composition of soft porous materials featuring gate type sorption has been reported [50]. 2D materials with interdigitated layers are specifically relevant, given that interlayer relationships can be modified by careful adjustment of the groups to be interdigitated. Upon guest incorporation, numerous chemical compounds displaying this behaviour have been described, all featuring a characteristic transformation [51].

A category of coordination polymers with interdigitated structures which incorporate zinc $[Zn(bpy)(C_5H_6O_4)]$ (CID-1) and further illustrate the nature of these materials have been described [52, 53]. V-shaped dicarboxylate, 4,4′-bipyridyl and dipositive metal units comprise the 2D layer, and the gate-type sorption function is significantly modulated by the effect of interactions between various carboxylate ligands and the subsequent layers. CO_2 gas, the partitioning of which from the CO_2-CH_4 mixture is partly facilitated by the flexible nature of

the structure, can be easily emitted with low energy consumption, given that the separation of CO_2 requires only structural flexibility without the need for strong interactions. The process can therefore be considered to differ significantly from standard separation strategies that use strong binding energies.

This flexibility is not only being attributable to the 2D structures as 3D porous frameworks also feature intrinsic flexibility. [Al(bdc)(OH)] (MIL-53), displaying diamond shaped 1D channels, is an example of this type of framework [54]. Al-OH-Al units are used to link one of the axes, and the Al-O-Al bond angle can be modified by guest sorption. Material softness can be attributed to elements such as rotatable single bonds, bond reorientation and weak supramolecular interactions, and a significant effect on the general properties of the porous structure can arise from even a minor variation in bond angle/distance. Flexible frameworks also discard a long range ordered arrangement so that amorphous or quasi amorphous phases develop. Al(bdc-OH)x exhibits selective adsorption of p-xylene isomers and in drug delivery applications as a result of its guest-mediated flexibility [55, 56]. Rearrangement of network topologies and orientation in local bonds contribute in parallel to the flexibility of MOFs. Interpenetrated frameworks, with respect to network rearrangement, can sometimes display soft material properties as a result of adjacent network rearrangement. [Zn_2(bdc)$_2$(bpy)] (MOF-508), which is found in both open and closed forms according to the relative network position, is an example of a compound with twofold symmetry [57]. The type of guest molecule determines the change from the closed to the open form, a trait of value in the separation of pentane and hexane branched and linear isomers. The characterisation of guest molecules can be facilitated by the sensitivity displayed by this type of flexible MOF, the application of which in industrial gas separation is the subject of additional research.

2. Potential applications of MOFs

The highly periodic and crystalline nature of MOFs can be readily revealed by their crystal structures, a useful evaluation when determining structure-property relationships. When incorporating guest molecules into the framework, however, their subsequent removal may lead to structural collapse as a result of weak coordination bonds, unlike the stronger covalent bonds observed in standard adsorbent compounds. MOF structure becomes distorted upon exposure to heat and guest removal, suggesting that the compound do not exhibit true crystallinity. Given that a rigid, highly thermostable framework is considered of functional value [58], several MOFs with stability up to 300 or 400°C (and even 500°C) have been developed, rendering them suitable for the majority of applications. Although heat resistant, these compounds have other limitations including chemical instability in the presence of moisture, as exhibited by carboxylate-based MOFs. Azolate-based frameworks (metal-azolate framework, MAFs), on the other hand, display suitably strong coordination bonding between the metal-azolate system and therefore show a greater degree of stability when exposed to heat or chemicals. MOFs can thus be considered suitable for novel practical applications as a result of these varied and singular structural characteristics.

2.1. Gas storage

The extensive surface area and significantly greater pore volume, compared with activated carbon, zeolites and other standard adsorbents, are notable features of MOFs that contribute to their value in gas storage. An adaptable and modifiable synthesis process in which various permutations of metal nodes and organic linkers give rise to multiple original compounds with affinities specific to different gases. A particularly high incorporation of gas has been observed in MOFs, which resulted in very large BET surface areas (up to 6000 m^2/g) that have been formulated to date [59]. As a result of dispersive and repulsive interactions between gas molecules and framework atoms, MOFs can exhibit surface gas sorption. Modulation of the interactions of gas molecules with the surface of MOFs with the intent of optimising gas storage is the focus of much research, and can be achieved by incorporating unsaturated metal sites into the nodes [60–62], by catenation of the framework [63–67] or by substitution of different functional groups of the organic linkers [68, 69]. It is only when the adsorption capacity is significantly greater than that of the empty container that the adsorbent is of value, and several MOFs that have a large pore volume adsorb substantial quantities of nitrogen at 77 K. Given that a greater volume of liquid nitrogen can be kept in empty container at the same temperature, these compounds are not of particular use. MOFs can also effectively adsorb CO_2, although the readiness of CO_2 to liquefy also renders this property of little value. The storage of gases such as hydrogen, methane and acetylene, which are hard to be compressed, is thus a suitable application for MOFs.

2.2. Hydrogen storage

Given its high gravimetric energy density, low toxicity and formation of water upon oxidation, hydrogen is considered a valuable, more clean and high-energy fuel. Its extremely low boiling point and volumetric density of just 0.089 kg/m^3, however, present major challenges to its storage. Although multiple approaches to this have been evaluated, none have proved suitable for practical purposes. Chemical absorption, one frequently implemented approach, is capable of high storage capacity; the process is not reversible, however, meaning that hydrogen release is significantly reduced. Porous MOFs, on the other hand, absorb hydrogen strongly [70, 71], and some with ultrahigh surface area and porosity are capable of approaching the requirement of the department of energy (DOE) in the USA for H_2 storage which about 6.5 wt% and 45 g/L. However, as the enthalpy for physical adsorption is insufficiently low, these requirements are attainable only at relatively low temperatures (e.g., 77 K). Modulation of pore size, a key determinant of affinity, is one of several methods to increase the adsorption affinity of MOFs, despite the incompatibility of extremely small pore sizes with extensive surface areas in practical use. Application of unsaturated metal to the pore surfaces can significantly increase physical adsorption, but framework density is subsequently affected by such an increase in metal concentration.

2.3. Methane storage

An advantage of methane, an important fuel source and major component of natural gas, is that it burns in more clean manner compared to gasoline and exhibits a greater H_2/C ratio

compared to other non-renewable hydrocarbon [72]. Gasoline, however, has a volumetric energy density three times that of methane. Compounds capable of increasing the volumetric density of methane may therefore be beneficial in the transport of natural gas. Given its significantly higher boiling point compared with hydrogen, methane is readily absorbed by porous materials. By establishing a storage specification of 180 v/v (which certain highly porous MOFs are capable of attaining), the DOE encourages the research activities for developing new and unique materials for gas storage, particularly methane. An efficacious and porous framework, $Cu_2(adip)$, adip =5,50-(9,10-anthracenediyl)di-isophthalate, which is known as PCN-14, with a large Langmuir surface area approaching 2100 m^2g^{-1} was first introduced by Zhou et al. [73]. A CH_4 uptake of 230 v/v at 290 K and 35 bar is achieved by this network as a result of its 0.8 cm^3g^{-1} pore volume and nanocage-type pores, as well as large aromatic rings on the pore surface. In addition to uptake, storage can be considered as the elimination or expulsion of gas, despite the primary research focus of raising the adsorption affinity of MOFs in order to optimise gas storage capacity. Adsorption levels measured between a pair of temperature or pressure coordinates, instead of at a single point, can be considered the effective storage capacity, and desorption can present challenges under conditions of elevated adsorption enthalpy. The peak storage value is known to occur at an adsorption enthalpy of 15.1 kJ mol^{-1} [74], under standard type-1 hydrogen isotherm storage conditions between 1.5 and 35 bar and 298 K. The sudden decline in type-1 isotherms observed under low pressure conditions correlates to a significant level of adsorbate which cannot be desorbed. A high uptake of 48.3 gL^{-1} was observed for highly porous MOF-177, at 1.5 bar as well as not only at 70 atm, suggesting an effective storage capacity of 40 gL^{-1} [75].

2.4. Acetylene storage

Given its widespread application as an essential until in organic chemistry, the global pro-duction of acetylene approaches half a million tonnes annually [76]. Its transportation presents challenges, however, given its considerable instability and inability to be compressed above an explosive threshold of 2 bar, unlike hydrogen and methane. Furthermore, products such as benzene or vinylacetylene can be formed at higher concentrations of acetylene. A need therefore exists to formulate a comparably high surface area material without the correspond-ing high pressure requirements, and research into huge BET surface area adsorbents for low pressure acetylene desorption has thus been reported in the literature [77–79]. Zeolites, MOFs and other microporous compounds absorb relatively large amounts of acetylene, although their excessive desorption affinity limits desorption to below 1 bar. Type III and V isotherms exhibit superior storage capacity than type I, which typically retains an excess of guest molecules; these isotherms display a low adsorption capacity and affinity, however. By designing an appropriate pore surface structure and flexible framework, MOFs can be developed which exhibit lower affinity and optimum uptake difference at working tempera-tures [78]. For example, Zhang and Chen [78] reported that a metal azolate framework shows an increase of acetylene volumetric storage at 1 atm using 40-fold, while an analogue of MOF-505 exhibited exceptional storage capacity under ambient conditions [79]. Enhancing the capacity storage of acetylene (230 v/v and 1 atm) for a Co analogue was demonstrated by Xiang et al., who synthesised a series of isostructural $[M_2(DHTP)]$ MOFs, where M = Co, Mn, Mg or

Zn and DHTP = 2,5-dihydroxyterephthalate, compounds known as M-MOF-74 [80], CPO-27-M [81] and M/DOBC [41] using open metal sites [77]. Within the same MOF, the authors contrasted the acetylene binding energies at Mg, Mn, Zn and Co metal sites and reported that acetylene exhibited the greatest affinity for the Co analogue, with a binding energy of 18.5 $kJmol^{-1}$ that followed by 17.3, 16.9 and 16.5 $kJmol^{-1}$, respectively.

3. Synthesis of MOFs

When implementing the range of strategies that can be used to generate MOFs, specific parameters must be taken into account in parallel with the geometric specifications of MOF design. One such parameter is building block integrity, which must not be compromised. To date, emphasis has been placed on developing new and original organic connections and the conditions most appropriate for sustaining group functionality and conformation, while remaining sufficiently reactive to form metal-organic bonds. Conditions must facilitate the conservation of linking units for synthesis which requires the in situ preparation of SBU, a process which can be achieved through precipitation of the product from the solution. This potential drawback can be circumvented by implementing a solvothermal strategy, given that solubility is an essential property of SBU. As the preparation of single crystals appropriate for single crystal analysis was originally the primary objective of MOF synthesis, earlier studies were therefore exploratory prior to the development of an adequate knowledge base. MOF design is typically influenced by intermolecular forces that limit predictability, as well as synthetic conditions which warrant optimisation to allow building units to be amassed in a specific manner. Minor adjustments in pH, solvent polarity, concentration or temperature have widely been associated with inferior quality crystals and even the formation of an entirely different phase. Crystals of optimum quality and maximum yield can be achieved under a low energy expenditure and acceptable time frame, with adequate comprehension of the optimised conditions.

3.1. Solvothermal synthesis

MOF can be successfully prepared using solvothermal and hydrothermal strategies, uncomplicated and well-established approaches which were adapted from zeolite synthesis and therefore remain in use today [82]. The process usually requires metal salt and carboxylic acid to be combined in an appropriate solvent, stoppered and incubated until the reaction is complete, after which the product crystallises out from the original solution. Given its extensive range of solubility, high boiling point and ability to serve as a weak base to deprotonate carboxylic acid, DMF is frequently designated the most suitable solvent for this purpose. Some benefits of using the solvothermal method over other, less simple approaches include the production of large crystals, ready scalability of synthesis and the capacity to use high throughput methods, and reaction efficiency can also be improved using microwave applications. However, this approach is limited by low product yield, extensive reaction times, and the need for high temperatures and toxic solvents such as Dimethylformamide (DMF) [83].

3.2. Microwave assisted synthesis

This approach harnesses the interaction of electromagnetic waves with charged molecules of polar solvent molecules which hence facilitating a quicker reaction rate as well as improved particle size reduction, phase selectivity and controlling the morphology. The synthesis of MIL-101(Fe) was described by Lin et al. using DMF at 150°C, and a yield of 20% with particle size approaching 200 nm was reported [84]. Cr-MIL-101, an additional MOF of interest, has also been prepared using microwave heating at 210°C [85]. By raising the concentration of water or the pH value, crystal size can be reduced, as illustrated by research into reaction parameters which demonstrated that uniform crystals of 50 nm can be synthesised efficiently when optimised conditions are used. Using an analogous approach, Cr-MIL-101 of 100 nm in size was synthesised by Zhao et al. and applied to the adsorption of benzene up to 16.5 mmolg^{-1} at 288 K and 56 mbar [86]. Microwave helps to synthesise the materials at 95°C, and a reduced duration of 9 min has also been used to produce MOF-5 [87]; the p-XRD pattern of which, apart from a smaller size of 5–25 μm, was similar to that produced using a solvothermal approach (where a size of almost 500 μm is typically obtained). Increased research focus on Zr-based MOFs is apparent as a result of their significant thermal and chemical stability [88], a property which can be attributed to strong coordination interactions of high charge density zirconium (Zr(IV)) ions with oxygen component of organic linkers. A microwave-assisted solvothermal approach to prepare phase pure MIL-140 was described by Liang et al. in 2013 [89], resulting in a superior compound with reduced preparation time than that required for conventional electric heating approaches. The generation of highly crystalline, prototype, octahedral-shaped crystals of UiO-66 with 1.26 wt.% H_2 storage capacity was developed by Ren et al. using a process which required as little as 5 min to complete [90].

3.3. Vapour diffusion

A relatively straightforward approach for the preparation of MOF is vapour diffusion, requiring salt and acid ligand to be dissolved in a solvent like DMF and transferred to an open vessel surrounded by a volatile base such as triethylamine. This volatile base gradually diffuses into the reaction mixture where MOF synthesis is promoted by acid deprotonation, which causes the concentration of conjugate base of acidic ligand to increase. Given the prolonged diffusion rate and reaction time of this process, large crystals can be produced at ambient temperatures [91]. This approach was adopted by Wu et al. to produce [Pb(1,4-NDC)(DMF)] [91] by dissolving $Pb(NO_3)_2$ and H_2-1,4-NDC (naphthalene dicarboxylate) in DMF in one vessel, situated within a second vessel in which triethylamine was also dissolved in DMF. Steady growth of MOF crystals resulted from the prolonged diffusion of triethylamine from the outer to the inner container.

3.4. Gel crystallisation

Gel crystallisation, an advantageous approach to the synthesis of MOF, requires a gelling agent to be added to the reaction mixture, thus decreasing the rate of diffusion and subsequently the rate of framework formation by increasing the viscosity of the solution. Using this strategy, Tuikka et al. [92] synthesised [$Ba_2(O_3P(CH_2)_3PO_3)$].$_3H_2O$ MOF by initially dissolving the metal

salt, barium(II) chloride, in water and a gelling agent (tetramethoxysilane). The mixture was thoroughly mixed before being used to produce a gel, upon which layers of ethanediphos-phonic acid in aqueous solution were prepared and incubated for a period of 3 weeks. Although this process requires a considerable amount of time, with additional separation stages necessary to purify the product, crystals of a reasonably large size can be produced using this method.

3.5. Solventless synthesis

MOF preparation requires the use of relatively toxic solvents, an important issue which is the focus of several studies. A suitable approach is the use of solventless synthesis which, as the name implies, reduces solvent toxicity by eliminating it from reaction. Mechanosynthesis (or milling) represents a rapid, scalable and non-toxic strategy for producing MOFs, as reported by James et al. [93], in which ball bearings are placed into a stainless steel vessel with the reagents and a stoichiometric quantity of solvent. MOF synthesis proceeds following complete closure of the vessel and pulverisation of the reagents by thorough mixing. Given the nano-to microcrystalline nature of the resulting product, rapidly synthesised at room temperature (a standard liquid-assisted grinding reaction running at 30 Hz requires only 20 min), this approach can be considered relatively efficient [93].

3.6. Sonochemical

A straightforward and productive approach, the sonochemical synthesis of MOFs can be performed by subjecting the reaction mixture to ultrasound waves at an intensity of 20 kHz to 10 MHz. Some benefits of this strategy include the lack of extra heat needed, a rapid reaction time and the generation of a monodispersed crystalline product, which is of value in membrane coating applications [94, 95]. Given that crystals are instantly produced within local solvent cavity regions of short life time (ms) and size in the range of ten of microns, sonochemical synthesis can be considered an appropriate method for the generation of nanoscale crystals [96]. Under a phenomenon termed cavitation, a region within which bubbles develop expands and collapses, the effective temperature can rise to as much as 5000 K with 1000 bar pressure [96]. Several examples of MOFs synthesised by a sonochemical approach at room temperature are MOF-5, MOF-177 and HKUST-1 [97, 98]. Fard et al. showed the synthesis of a 2D MOF $[Pb_2(N_3)(NO_3)L_2]$, (L = 8-hydroxy quinolate) in aqueous solution using a sonochemical strategy, after which the nanocrystals produced can be calcinated to 400 °C to generate nanosized PbO [99].

3.7. Electrochemical synthesis

Although unsuitable for implementation on an industrial scale, electrochemical synthesis offers a different approach to the sonochemical process without the need for an external heat source. This strategy also does not require a base for deprotonation of acid, given that ions are produced by the reagents in solution. MOF membranes of high standard can be synthesised using this approach due to the well-dispersed coverage of scaffold it entails. Using direct nucleation on an anode surface with an EtOH-H$_2$O solution and a copper mesh, which reacted

with anions and thus did not require metal salt with calculable linker depletion, the synthesis of HKUST-1 was described by Joaristi et al. [100]. Process continuity and speed at ambient temperature are advantages of the direct nucleation approach, which is limited however by the disassociation of copper from the anodic scaffold and loss of film at the scaffold extremities [100]. Implementing an electrochemical process whereby 1,3,5-benzenetricarboxylic acid (H_3BTC) was dissolved in a 2:1 mix of ethanol and Milli-Q water under high temperature and pressure in an electrochemical cell, MIL-100(Fe) was first produced by Campagnol et al. in 2013 [101]. Both in the form of crystals and as deposits on pure iron substrates, MIL-100(Fe) was synthesised at temperatures ranging between 110 and 190°C and current densities of 2–20 mAm cm^{-2} using an Fe anode. With respect to HKUST-1, the HT-HP cell was shown to be applicable for the alteration of MOF crystal morphology. Research by Stassen et al. [102], in which synthesis was initiated by heating a solution of BDC:HNO$_3$:H$_2$O:AA:DMF = 1:2:4:5/10/50:130 to 383 K, resulted in UiO-66 anodic/cathodic electrochemical film deposition on zirconium foil through the application of 80 mA at 383 K. Although a benefit of cathodic deposition includes broad substrate flexibility, better MOF adhesion on zirconium substrate was reported for anodic deposition.

4. MOFs as photocatalysts

With ever-increasing demands of energy and with fossil fuels becoming ever more diminished, solar energy represents an attractive alternative solution and a large body of research describes the harnessing and sequestering of energy from the sun. Several approaches to transform and store solar energy as chemical bonds have been proposed, including photochemical procedures such as the reduction of CO_2 and H_2O splitting. The inherent ability of plants to trap sunlight and transform water and CO_2 to carbohydrates (a process termed photosynthesis) is the source of much inspiration for researchers in the field. The development of techniques to facilitate photochemical transformation has also been the subject of significant focus. Despite certain materials exhibiting the ability to split water by harnessing UV light [103–106], some restrictions on the use of the solar spectrum exist. It nonetheless remains of primary importance to formulate a stable, efficient and cost-effective approach that can convert solar energy by capitalising on the maximum solar spectrum.

The absorption of light by certain photoactive organic molecules causes them to undergo changes which normally cannot be facilitated under standard thermally activated conditions. Given that the large part of the spectrum is not used by organic compounds, which only absorb UV photons, their efficiency is suboptimal. Limitations related to solar spectrum absorption can be mitigated by the use of molecular dyes which can absorb low energy photons, giving rise to new photocatalytic reactions under visible light [107–111]. Three stages comprise the conversion of solar energy into useful chemical energy: the generation of charge-separated excited states by using a photosensitiser to absorb sunlight, the creation of redox equivalent and subsequent transfer to reactive sites and the presence of oxidation and reduction half reactions at catalytic centres. With the objective of merging photosensitiser and catalytic components into covalent bonded dimers, supramolecular structures or polymers [112–114],

several types of compounds have been generated; this approach has a high degree of complexity, however, in that the process is laborious and requires many steps, thus limiting it applicability.

As a novel category of organic-inorganic hybrid supramolecular structures, MOFs can function as photocatalysts for the main reason that they incorporate photosensitiser and catalytic functionality within one structure. The aforementioned three stages of photocatalysis are thus facilitated within one solid compound [115]. Through substitution of the standard photocatalyst which typically includes heavy metals, photoactive MOFs can function as superior photocatalysts by minimising contamination and can readily be recovered and reused due to their solid form, thus conferring fiscal benefits.

4.1. Hydrogen generation by MOFs

Given their significant potential for harvesting solar energy, research efforts in the past 10 years have been devoted to the production of compounds that can serve as photocatalysts for the production of H_2 from H_2O, with several candidates having been described to this end. Catalytic activity has thus been reported for UiO-66, a simple MOF [116] with a photocatalytic water-splitting capacity which has been verified in a water-methanol system. The photocatalytic activity of this compound was shown to be increased by the introduction of platinum nanoparticles as a co-catalyst [117], and the location of an amino group within the MOF structure was shown to create intense absorption (between 300 and 400 nm) with a marginal increase in catalytic activity [118]. Lin et al. described an MOF for hydrogen evolution comprising molecular phosphor as a structural unit in addition to platinum nanoparticles [119]. Given the reported success of using iridium-based photosensitisers, an iridium-based MOF was synthesised using bis(4-phenyl-2-pyridine)(5,5′-dicarboxylate)-2,2′-bipyridine)-Ir(III) chloride or bis(4-phenyl-2-pyridine)(5,5′-di(4-phenylcarboxylate)-2,2′-bipyridine)-iridium(III) chloride structural units with $Zr_6(O)_4(OH)_4$ SBUs. The resulting MOF exhibited superior stability in aqueous solution, and Pt nanoparticles were incorporated within the MOF spaces using in situ photoreduction of the Pt precursor. This type of MOF exhibits extremely high photocatalytic activity, probably attributable to readiness of electrons to transfer between platinum nanoparticles and Ir complexes.

4.2. Photocatalytic reduction of carbon dioxide on MOFs

Given its capacity for CO_2 reduction from the environment without the need to utilise solar energy, significant research focus has been turned to catalytic reduction of carbon dioxide. Several compounds such as semiconductors and metal-based zeolites have been recently described for the photocatalytic reduction of CO_2 [120–123]. Lin et al. reported in 2011 the production of an MOF catalyst $Zr_6(\mu_3\text{-}O)_4(\mu_3\text{-}OH)_4(bpdc)_{5.83}(L_8)_{0.17}$ (where bpdc = 5,5′-biphenyldicarboxylate and $H_2L_8 = Re(CO)_3(5,5'\text{-}dcbpy)Cl)$ through the introduction of $Re(CO)_3(5,5'\text{-}dcbpy)Cl)$ into the UiO-67 backbone [124]. A well-characterised catalyst for CO_2 reduction, the insertion of $Re(CO)_3(5,5'\text{-}dcbpy)Cl)$ into UiO-67 demonstrated that catalyst addition did not influence the pXRD pattern, an effect most likely attributable to the comparable ligand lengths of $Re(CO)_3(5,5'\text{-}dcbpy)Cl)$ and bpdc. Following an evaluation of photocatalytic behaviour in

CO_2-saturated acetonitrile in the presence of triethyl amine as a sacrificial reducing agent, high efficiency in the photocatalytic reduction of CO_2, represented by a turnover number of 10.9 over 12 h for selective reduction of CO_2 to CO, was demonstrated by the resulting MOF. This elevated catalytic activity, which inhibits the bimolecular catalytic decomposition pathway, can be attributed to site segregation in the $Re(CO)_3(5,5'$-dcbpy)Cl) catalyst. The incorporation of $Fe_2(dcbdt)(CO)_6$ into the UiO-66 framework by way of a post-synthetic exchange process was recently described by Ott et al. [125]. This process was evaluated by Energy-dispersive X-ray spectroscopy (EDX) and found to exhibit 14% incorporation, with the emergent MOF significantly more efficient compared to the analogous ligand for photochemical reduction using ascorbic acid which represents the sacrificial electron donor. The stabilisation of catalyst within the framework was used to explain the elevated activity levels observed.

5. Photocatalytic applications of MOFs

Over the past 10 years, MOFs have been successfully established as a new, promising class of heterogeneous photocatalytic materials. The use of MOFs in the photocatalytically driven degradation of organic pollutants and NO_x, antibacterial activity and generation of solar fuels and photoelectrochemical (PEC) energy highlights the impressive potential these materials possess [126–128]. Furthermore, there are several reported MOFs that have also been employed in the photocatalytic production of high-value chemicals under mild conditions. In these reports, the feasibility of fine tuning the MOF's energy band structure and surface functional group was proven. It is interesting to note that, although MOFs now stand on their own as a unique class of photocatalytic materials, they have been shown to be used as sacrificial precursors in the precisely controlled fabrication (phase, shape, morphology and porosity) of traditional semiconductor photocatalysts with greatly enhanced photocatalytic activity.

There are several excellent reviews that address the advances of MOFs in photodegradation of organic pollutants in wastewater [126, 129], water splitting [126, 128] and photoreduction of CO_2 [126, 128], where these materials' stability and light absorption properties are critically discussed. However, these reviews are limited in terms of delineating the design principle/ criteria and the photocatalytic working mechanism, both of which are central to the development of new MOF photocatalysts having desirable properties for realisation in future practical applications. Accordingly, this section seeks to (1) present the primary processes involved in general photocatalytic reactions as they relate to the specific electronic band structures of MOFs, and (2) exemplify the photocatalytic applications of MOFs that were designed to address these fundamental photocatalytic processes.

5.1. Fundamental processes of photocatalysis as related to MOFs

Similar to classic photocatalysis theory developed for traditional semiconductor photocatalytic materials (**Figure 5**), MOF-based photocatalysis involves four fundamental processes of operation with additional distinct characteristics that can be intrinsically derived from their
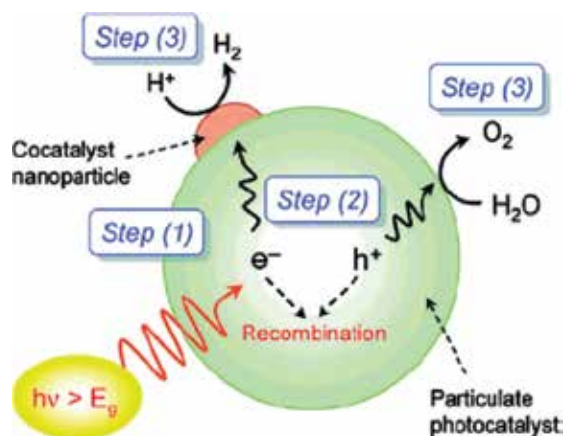
Figure 5. The major processes in classic photocatalysis system [136].

crystalline structure. These fundamental processes of operation, as they relate to MOF-based photocatalysis, are

1. Photoexcitation: In MOF-based photocatalysts, light absorption may occur either through the inorganic SBU or through the organic linker. MOFs typically have few absorption bands (broad bands are often seen) in the UV-Vis region depending on the chemical nature of the chromophore centres that arise from the inorganic SBUs or organic linkers. These absorption bands can often be ascribed to distinct π-π^* transitions of the aromatic units in the organic linker or to metal-to-ligand (MLCT) or ligand-to-metal (LMCT) charge transfer transitions. Therefore, the band theory of semiconductors is not effective in describing the light absorption and subsequent transitions observed in MOF materials. On the other hand, it is more suitable to use molecular orbital theory, in which the peak of occupied molecular orbitals (HOMO) and the lowest unoccupied molecule orbital (LUMO) determine the so-called 'band gaps' of MOF photocatalysts [130]. As a result of the inorganic SBUs and organic linkers possessing distinct molecular orbitals, MOF photocatalysts often exhibit several discrete absorbance bands and the band with the lowest energy (longest wavelength) is used to define the band gaps. It is noted that LMCT effects are especially important for those MOFs that contain chromophore units originating at the organic linkers. Aside from determining the band gap energy, the energy positions of the HOMO and LUMO orbitals are critical for understanding the pathways and reaction products in photocatalytic reactions involving MOFs. This is critical as the photo-generated holes and electrons possess the same energetic levels as the HOMO and LUMO orbitals of MOFs, respectively.

2. Charge separation, transfer and transport processes: These processes, initiated and sustained through the absorption of excessive light energy, lead to positively and negatively charged excitons being separated and then transferred from the bulk to the surface of the photocatalyst. The efficiency of these processes decidedly relies on the type

of material, the material's crystallinity, as well as its particle size. For instance, high charge mobility is commonly associated with highly crystalline semiconductor materials, in which oriented charge mobility is observed. Structural deficiency in inorganic photocatalysts lies in the presence of chromophore centres, which may also serve as recombination centres where charge carriers are trapped and quenched leading to significant energy loss through realised heat. Semiconductor nanocrystals with small particle sizes generally possess satisfactory charge transfer performance; however, if particles are too small, then recombination may occur due to improved surface defects.

3. Surface reaction: Photo-generated charge carriers travel to the surface of the photocatalyst, in which they can be induced to participate in certain related chemical reactions or be collected by photoelectrodes in order to be passed to an external circuit. It is noted that the surface chemical reaction rate also influences the charge transition and transfer.

    The first step in a typical photocatalytic reaction is surface adsorption followed by the photocatalytic redox of the adsorbents. Taking into consideration the structural uniqueness of MOFs (functionalisable), remarkable surface properties by MOF photocatalysts are expected and, in fact, have been demonstrated [131–133]. Indeed, Natarajan, et al. investigated the adsorption and the catalytical photodegradation behaviour of different dyes on three Cd-containing MOFs, namely $Cd_2(4,4'\text{-bpy})_3(S_2O_3)_2$, $Cd_2(4,4'\text{-bpy})_{2.5}(S_2O_3)_2$ and $[Cd(4,4'\text{-bpy})(H_2O)_2(S_2O_3)]\cdot2H_2O$ [134]. In this report, the anionic (orange G, methyl orange) and cationic dyes (methylene blue, methyl violet and brilliant blue R) exhibited distinct surface adsorption capacity and photocatalytic activity. By analyzing the adsorption data using the Langmuir adsorption model, the authors reported that the anionic dyes (e.g., sulphonated) were significantly more adsorbed by $Cd_2(4,4'\text{-bpy})_3(S_2O_3)_2$, $Cd_2(4,4'\text{-bpy})_{2.5}(S_2O_3)_2$ and $[Cd(4,4'\text{-bpy})(H_2O)_2(S_2O_3)]\cdot2H_2O$ in the dark with no apparent adsorption occurring for the non-cationic dyes. Furthermore, it was determined that the dye molecule adsorption did not lead to any structural changes in the cadmium thiosulfphte MOF materials, but rather weak electronic interactions were observed. The hydroxyl radicals play crucial roles in breaking down the anthraquinonic anionic dyes while surface-controlled N-de-ethylation reaction mechanism was proposed to explain the stepwise decomposition of cationic dyes through serials intermediates, where MLCT arisen from HOMO of filled d^{10} orbitals of Cd and ligand-associated LUMO plays dominant roles. [135].

4. Charge carrier recombination: Charge carrier recombination is a process in which photo-generated electrons and holes will recombine and, as a result, release energy that was gained during excitation in the form of fluorescence or heat. The energy emitted during recombination can be captured and interpreted using photoluminescence (PL) spectroscopy. The recombination of charge carriers accounts for the largest energy loss in most photocatalytic and PEC systems and remains as one of the greatest challenges necessary to tackle. In general, the recombination of charge carriers occurs in both the bulk and surface of the photocatalyst; therefore, it is very important to study the bulk and surface recombination when sorting recombination. The recombination can be largely suppressed by decreasing the photocatalyst particle size or by applying an external energy bias. These

methods have proven effective for both classical semiconductors as well as in MOF photocatalysts. It is noted that surface metallisation using noble metals has also been reported useful [131, 136–138].

5.2. Extensive application of MOFs in photocatalysis

5.2.1. Photocatalytic decomposition of organic pollutants

The semiconducting behaviour was first proposed and observed on MOF-5 which displayed comparable specific activity (phenol decomposition per metal atom) to TiO_2-P25 and ZnO in photodegration of phenol under UV illumination (125 W medium pressure Hg lamp) but the apparent mass photoactivity was weaker than TiO_2 and ZnO [139]. The photocatalytic phenol decomposition was proposed to follow the LMCT mechanism, in which photoexcited holes oxidise phenol to form phenol cation or phenol is oxidised by active oxygen species generated from photo-generated CB electrons inject to dissolved oxygen. Encouraged by the promising photocatalysis on MOF-5, a variety of UV-responsive MOFs have been developed and examined for photocatalytic decomposition of organic pollutants in water [129]. In these semiconducting MOFs, d-block and f-block metals, including Mn, Fe, Co, Ni, Zn, Cd, Ti, Zr and Gd, are frequently applied, while the organic linkers are found determining their bandgap and photocatalytic activity due to the LMCT mechanism. Another important factor influencing the photocatalytic activity is the selective adsorption of organic pollutant compounds owing to the static electrical interaction or shape selectivity.
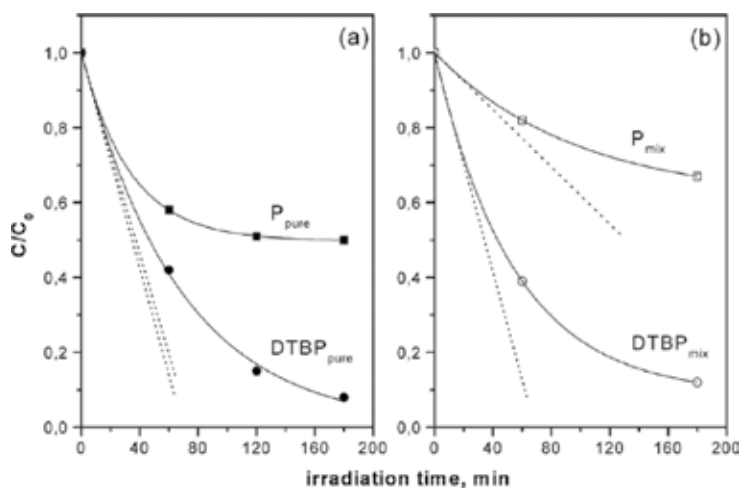

Figure 6. UV-driven photodegradation curves of phenol (P) and 2,6-di-*tert*-butylphenol (DTBP), obtained using MOF-5 as a photocatalyst. (a) Curves correspond to photodegradation of 40 mg L^{-1} of the pure species, (b) curves correspond to competitive photodegradation (irradiation of a mixture of 20 mg L^{-1} of both molecules). Solid lines are the best fit to the experimental data obtained with a first-order exponential decay. Dotted straight lines show the initial degradation rates [136].

The microporous MOF-5 showed (**Figure 6**) an interesting reverse shape selectivity in photo-catalytic decomposition of mixed solution of 2,6-di-*tert*-butylphenol (DTBP) and phenol(P). Under UV irradiation, the large DTBP molecule underwent faster photodegradation than small phenol molecule in the mixed solution, which was attributed to the phenol diffusing into the interior channels of MOF-5 and less exposure to light than DTBP which cannot diffuse into the MOF-5's micropores [140].

The adsorption and photocatalytical degradation of different types of dyes on the MOFs containing similar Cd cluster vary along with the organic linkers. It was found the sulphonated anionic dyes were significantly adsorbed by $Cd_2(4,4'-bpy)_3(S_2O_3)_2$, $Cd_2(4,4'-bpy)_{2.5}(S_2O_3)_2$ and $[Cd(4,4'-bpy)(H_2O)_2(S_2O_3)]·2H_2O$ in the dark, but the photodegradation performance was not examined. Despite these MOFs almost did not adsorb non-sulphonated cationic dyes (e.g., methylene blue, MB) [134], they showed comparable activity to TiO_2 in the UV-driven photodegradation of non-sulphate dyes because of the complex photocatalysis mechanism involving active oxygen species arisen from bandgap excitation and dye photosensitisation. The same mechanism was also proposed in the X3B photodegradation on $[Mn_3(btc)_2(bimb)_2]·4H_2O$ and $[Co_3(btc)_2(bimb)_2]·4H_2O$ [141], and rhodamine B photodegrada-tion on $[Ag(bipy)(UO_2)(bdc)_{1.5}]$ (bipy=2,2'-bipyridyl, bdc=1,4-benzenedicarboxylate) and $[Ag_2(phen)_2UO_2(btec)]$ (phen=1,10-phenanthroline, btec=1,2,4,5-benzenetetracarboxylate)[17]. It is worth noting the $[Co_3(btc)_2(bimb)_2]·4H_2O$ exhibited better photoactivity than the $[Mn_3(btc)_2(bimb)_2]·4H_2O$ despite the Co-based MOF (~4.04 eV) possessed larger bandgap than the Mn-based MOF (~3.72 eV). The reverse activity order to the bandgap is because Co-based MOF possesses two additional d-d spin-allowed LMCT transition of Co^{2+} within 400–800 nm band region, besides the aforementioned complex mechanism (dye-sensitising and active oxygen species, **Figure 7**) [142].
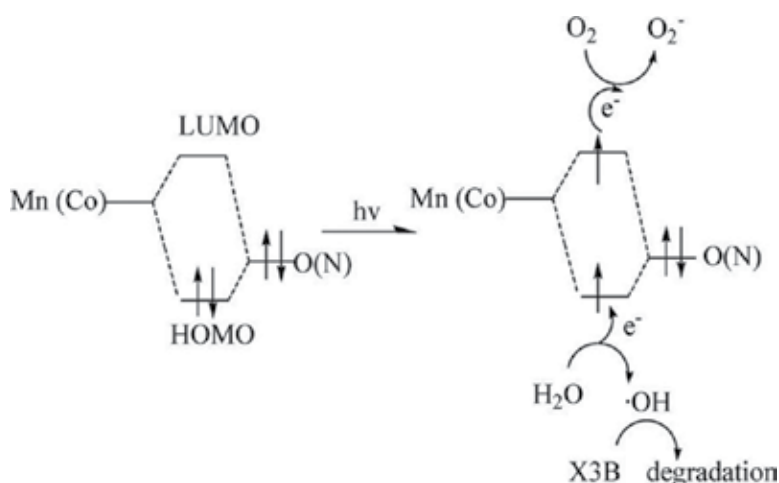

Figure 7. A simplified model of photocatalytic reaction mechanism of $[Mn_3(btc)_2(bimb)_2]·4H_2O$ and $[Co_3(btc)_2(bimb)_2]·4H_2O$ [143].

In order to maximise the visible-light harvesting in solar spectrum, intensive efforts have been made to develop visible-light-responsive MOFs via various strategies, such as modifying metal nodes, functionalising organic linkers, using hybrid linkers as well as constructing composite photocatalysts [143]. Although the light absorption of MOF-5 may be extended to 400 nm, its visible-light-driven photocatalysis is negligible due to the large bandgap (~3.4 eV) but its bandgap may be reduced largely once the bdc linker is functionalised [144, 145]. Diverse visible-light-responsive and stable MOFs have recently been tested in photocatalytic reactions, particularly in dye decomposition.

The present investigated visible-light-responsive MOFs may be roughly categorised as follows [126–129, 146, 147]:

1. Simple MOFs, sMIL-88A, MIL (TM) (TM=Fe, Cr), NTU-9, Fe_2(bhbdh),

2. MOFs with hybrid organic linkers: $[Zn_4(O)(tdc)_3(4,4'-bimb)_4]\cdot5.25H_2O\cdot CH_3OH$, $Cu^{II}(salimcy)](Cu^{I}I)_2\cdot DMF$, $Cu(Br-ip)(bitmb)(H_2O)$, etc.

3. Linker-functionalised. Amino-group functionalised NH_2-MIL-125[Ti] and MOF-5, etc.

4. Node-substituted MOFs. For example, X_4Y–MOF-5 (X = Zn, Cd, Be, Mg, Ca, Sr, Ba; Y = O, S, Se, Te), etc.

5. Metal-substituted or ion exchanged zeolitic MOFs. Cu/ZIF-67.

6. Heterojunctions. For instance, Fe_3O_4@MIL-100(Fe), Bi_2WO_6/UiO-66, C_3N_4/MOF-5, Fe3O4@HKUST-1, UiO-66/CdS [148], Ag_2O/MOF, etc.

7. Polyoxometalate-based MOFs, for example $[Cu_8(1,3-btp)_8[Mo_{12}O_{46}(AsPh)_4]_2]\cdot3H_2O$, $[CoCl_{0.5}(H_2O)_{0.5}(Hdppzc)_2](PW_{12}O_{40})_{0.5}\cdot3.5H_2O$, $[Cu(II)_2Cu(I)_3(OH)_4(H_2O)_2(tpt)_4]$ $(PW_{12}O_{40})$, etc.

8. Photosensitised MOFs. Photosensitisation is widely observed in various MOFs once dye is involved in the photocatalytic reaction. It is interesting that the photosensitisation effect may coexist within a complex MOF, such as CuPW and CuPM.

9. Surface metalised MOFs. The plasmonic effect of the nanosized metal particle sit on the MOF surface may endow visible light response to the host MOF. For example, Au@UiO-66(NH_2)[10] and Ag/AgCl@ZIF-8 [149].

5.2.2. Photocatalytic selective redox in organic synthesis

Normally, photocatalytic oxidation is a non-selective reaction on conventional inorganic photocatalyst because the photo-generated redox radical is non-selective. However, due to the tuneable HUMO and LUMO energy levels, LMCT effect, shape-selective adsorption and orientation of organic linkers, given proper design of structure and components of the MOF photocatalysts, they may enable selective oxidation of organic substrates under ambient conditions. Under UV irradiation and existence of a unique porous MOF having 3D structure, obtained from tin(IV)–porphyrin struts connected to Zn atoms and formats linking Sn^{IV} centres [150], 1,5-dihydroxynaphthalene can be oxidised into 5-hydroxynaphthalene-1,4-

dione, while different organic sulphides into organic sulphoxides rather than sulphones, respectively. In the both cases, the yield and selectivity are nearly 100%. In this MOF photocatalyst, the anchored tin(IV)-porphyrin serves as photoactive site and the tin(IV)-porphyrin itself is a proven photocatalyst for such reactions yet suffers from fast deactivation. However, the heterogeneous MOF showed remarkably higher product yield, selectivity and stability than the tin(IV)–porphyrin in homogeneous system.

Entry	–R	Conversion (%)		Selectivity (%)
		NH$_2$-MIL-125(Ti)	Ni-doped NH$_2$-MIL-125(Ti)	
1	–NO$_2$	8.2	10.5	>99
2	–Cl	11.8	20.6	>99
3	–H	12.5	21.5	>99
4	–CH$_3$	25.8	43.2	>99
5	–OCH$_3$	42.5	47.4	>99

[a]Reaction conditions: 50 mg of catalyst and 0.3 mmol of aromatic alcohol in 6 ml of BTF at room temperature for 10 h.

Table 1. Aerobic photocatalytic oxidation of aromatic alcohols over NH$_2$-MIL-125(Ti) and Ni-doped NH$_2$-MIL-125(Ti) upon visible light irradiation[a] [152].

Upon visible light irradiation, the oxidation of aerobic amines was obtained using NH$_2$-MIL-125(Ti) as active photocatalysts and the photocatalyst was evidenced as stable catalyst in such photocatalytic reaction [132]. Photo-generated Ti^{3+} and .O^{2-} are supposed to be involved in the reaction of amines transformation through a five-step redox mechanism. As shown in the schematic mechanism (**Figure 8**), there are five steps for the photocatalytic oxidation of amines using NH$_2$-MIL-125(Ti) as photocatalyst. The first step shows the transformation of electron to Ti-O oxo-cluster to create Ti^{3+} moiety. This step occurs upon the irradiation of the aminoterephthalic acid (ATA) ligand. In the second step, the obtained Ti^{3+} would react with O$_2$ to create ·O$_2^-$ while Ti^{3+} was oxidised back to Ti^{4+}. It should be noted that amines in the third step will able to provide electron followed by a deprotonation process to form the carbon-centered radical. In the fourth step, the aldehyde will be obtained by the interaction between the photo-generated carbon cantered radical and the ·O$_2^-$. Finally (step 5), the nucleophilic attack on aldehydes through the unreacted amines will therefore yield the corresponding imines via dehydration step. Some other by-product such benzaldoximeis can

be observed which occurs due to the reaction between carbon-centred radical and O_2 which then followed by a dehydration step [132].

Similarly, the NH_2-MIL-125(Ti) and Ni-doped NH_2-MIL-125(Ti) photocatalysts can also transform aromatic alcohols to their corresponding aldehydes with almost absolute selectivity using O_2 as the oxidant under visible light irradiation [151]. As shown in **Table 1**, Compared with the parent catalyst NH_2-MIL-125(Ti), Ni-doped NH_2-MIL-125(Ti) significantly enhances the photocatalytic activity for the selective oxidation of aromatic alcohols. The photoelectrochemical characterisation results suggest that the doping of Ni nanoparticles into NH_2-MIL-125(Ti) can improve the visible-light harvesting, charge separation and electron transport of the resultant catalyst, which lead to the enhanced photocatalytic activity.

Figure 8. Suggested photocatalytic mechanism of the amines oxidation using NH_2-MIL-125(Ti).

5.2.3. Photoelectrochemical application

It has recently evidenced that MOFs may be promising materials in photoelectrochemical catalysis or photoelectrochemical cells for enhanced solar energy conversion. The intrinsic properties of the MOFs, peculiarly the linkers, would endow interesting properties to the pure or hybridised MOFs.

As shown in **Figure 9(a)**, a metal oxide semiconductor supported on MOF core/shell heterostructure (e.g., ZnO@ZIF-8 nanorod) was ever effectively synthesised via a simple self-template method [151]. In such producer, ZnO nanorods do not act only as template but they provide Zn^{2+} ions in order to obtain ZIF-8 [150]. In such method, the reaction temperature and the solvent compaction were found to play a significant role in order make ZnO@ZIF-8 heterostructures. It has observed that such obtained materials show a diverse photoelectrochemical response stewards these hole scavengers to hole scavengers. The reason behind such phenomena is the limitation of the aperture of the ZIF-8 shell, as shown **Figure 9(b)**, which is

different from ZnO nanorod arrays. Such interesting properties enable the composite electrode to be successfully used for the H_2O_2 detection, as shown in **Figure 9(c)**.
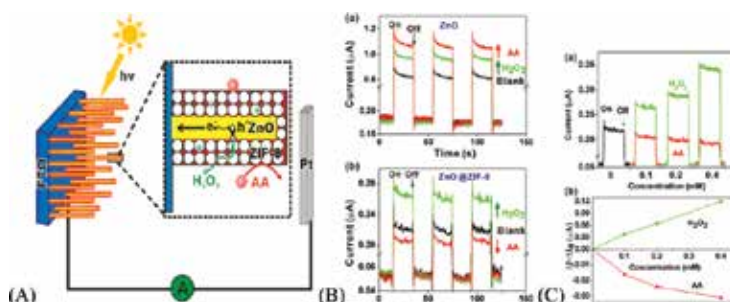

Figure 9. (a) schematic configuration of an photoelectrodes of ZnO@ZIF-8 nanorod array; (b) Photocurrent response of ZnO nanorod and ZnO@ZIF-8 nanorod arrays against H_2O_2 (0.1 mM) and AA (0.1 mM); (c) Photocurrent responses of the ZnO@ZIF-8 nanorod array in the presence of H_2O_2 and AA with different concentrations. (b) $\Delta I - \Delta I0$ curves in the presence of H_2O_2 and AA with the concentrations as function.

Lee et al. fabricated Cu-based copper(II) benzene-1,3,5-tricarboxylate layer using a layer-by-layer (LBL) method, and applied as a light-absorbing layer in TiO_2-based solar cells [152]. The TiO_2-based solar cell fabricated was the first report using iodine-doped Cu-MOFs which act as active layer. The reported confirmed that the cell performance with J_{sc} = 1.25 mA cm^{-2} and Eff = 0.26% using illumination of 1 sun radiation was obtained. On the other hand, the cell contains undoped MOF layer showed J_{sc} = 0.05 mA cm^{-2} and Eff = 0.008%. The results showed that the iodine doping considerably reduces the charge-transfer resistance through the
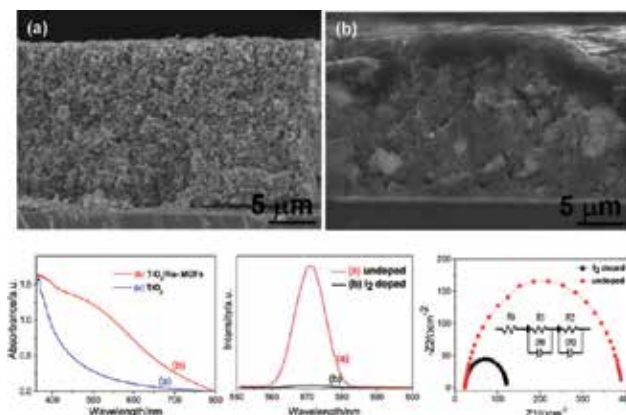

Figure 10. SEM cross-sectional views of doctor blade TiO_2 film using FTO glass (a) before and (b) after, deposition of Ru-MOFs for 10 LbL cycles; UV-visible spectrum of doctor blade TiO_2 film on FTO glass (a) before and (b) after, deposition of Ru-MOFs for 10 LbL cycles; emission spectrum of TiO_2/Ru-MOFs film (a) before and (b) after, doping MOFs with iodine. Excitation at wavelength ~535 nm. Nyquist plots of Ru-MOF-sensitized cell under open circuit and 1 sun illumination conditions. Iodine doping of MOFs is showing the facilitation of charge transfer process. Dots are experimental data and the solid lines are the fitted curves using an equivalent circuit shown in set [155].

TiO_2/MOF/electrolyte interface, as confirmed by electrochemical impedance spectroscopy. The similar LBL was also applied by the same group to fabricate Ru-based MOFs photoelectrode for solar cell application [153]. They observed the similar phenomena as the Cu-MOF solar cell, confirming the I-doped Ru-MOF possesses enhanced light absorption, reduced charge recombination and higher charge conductivity which contribute to enhanced solar energy efficiency (**Figure 10**).

5.2.4. Photocatalytic oxidation of nitric oxide (NO) and antibacterial activity

It was reported that one-pot microwave synthesised $Ag@NH_2$-MOP(Ti) exhibited excellent activity in visible-light-driven photocatalytic NO oxidisation, much higher than NH_2-MOP(Ti) and twofold than on *N*-doped TiO_2, as shown in **Figure 11(a)**. The NH_2-MOP(Ti) absorbed visible lights to generate photoelectrons and holes, accompanied by producing HO• and O_2^- active species for the subsequent NO oxidation into NO_3^-. The supported Ag nanoparticles allowed assembly of NH_2-MOP(Ti) polymer, favoured light absorbance via multiple reflections and facilitated photoelectrons transfer with inhibited recombination of photo-generated charge transporters, which lead to enhance the photocatalytic activity for NO oxidation. Besides the high activity, the $Ag@NH_2$-MOP(Ti) also showed strong durability and could be used repetitively without significant decrease in activity (**Figure 11(b)**). No obvious changes on the physicochemical properties and morphology of the samples after the cycled reaction were observed. The slight decrease of activity could be mainly attributed to the adsorption of HNO_3 product onto the photocatalyst. The $Ag@NH_2$-MOP(Ti) was claimed to be able to photocatalytically inactivate bacteria, whereas it remains unclear if the bactericidal effects were induced by Ag or the MOF because Ag has intrinsic antibacterial function and the photocatalytically antibacterial activity was not examined. The research verifies the feasibility to apply pristine and composite MOFs for photocatalytic removal of gaseous pollutants which has not been well explored.
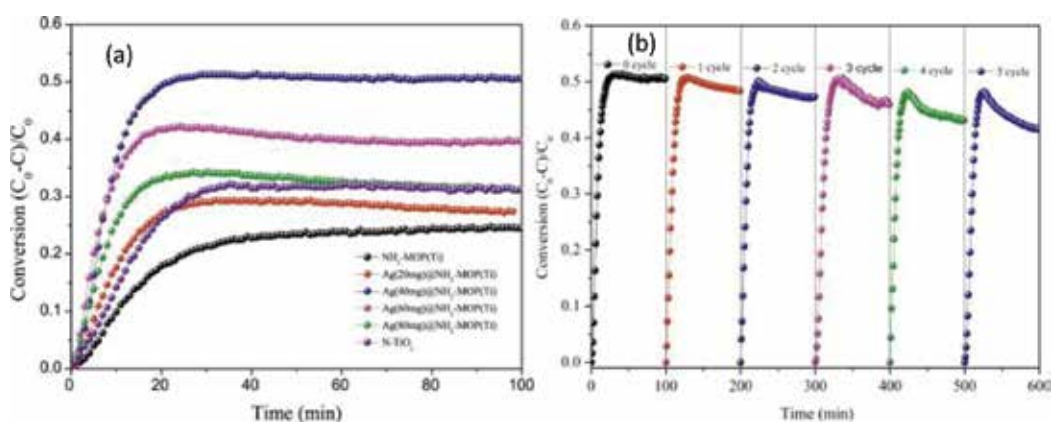

Figure 11. (a) Photocatalytic NO oxidation profiles on N-TiO_2, NH_2-MOP(Ti) and $Ag@NH_2$-MOP(Ti); (b) recycling photocatalytic NO oxidation tests on $Ag@NH_2$-MOP(Ti) under visible light ($\lambda \geq 420$ nm).

5.2.5. Photocatalytic reduction of metal cations for metal recovery or detoxcity

Shi et al. confirmed that due to the direct excitation of Fe_3-μ_3-oxo clusters in the MIL-88B (Fe) MOFs, this material is a good candidate for the photocatalytic reduction of Cr(VI) using visible light irradiation [154]. It is clear that the amine-functionalised MIL-88B (Fe) MOFs display a better photocatalytic efficiency for the reduction of Cr(VI) under visible-light irradiation compared to MIL-88B (Fe). As proposed in **Figure 12**, the direct excitation of Fe_3-μ_3-oxo clusters lead to excite the amine functionality in NH_2-MIL-88B (Fe). In such phenomena, the electron will be then transferred to Fe_3-μ_3-oxo clusters, which is considered to be responsible for the enhancement of the reduction of Cr(VI) photocatalytically.

With proper design, a stable and active MOF as photocatalyst can be prepared. For example, Shen et al. synthesised Pd@UiO-66(NH_2) nanocomposite, on which highly dispersed Pd nanoparticles having a diameter size between 3 and 6 nm were immobilised into UiO-66(NH_2) using hydrothermal preparation method. Obtained Pd nanoparticles supported on UiO66 show an excellent photocatalytic activity for the reduction of Cr(VI) compared to unsupported Pd nanoparticles. The reason of such good activities can be attributed to the fact that the Pd nanoparticles were well dispersed in the surface of UiO66-NH_2, which leads to improve the light harvesting and better efficient separation of the photo-generated electron-hole pairs [155]. Furthermore, Pd nanoparticles supported on UiO66-NH_2 could also be applied to photodegrade other types of organic pollutants such methylene blue (MB) and methyl orange (MO) with enhanced activity in the binary system. The synergetic effect between photocatalytic oxidation and reduction can be individually consumed photo-generated holes and electrons [156].
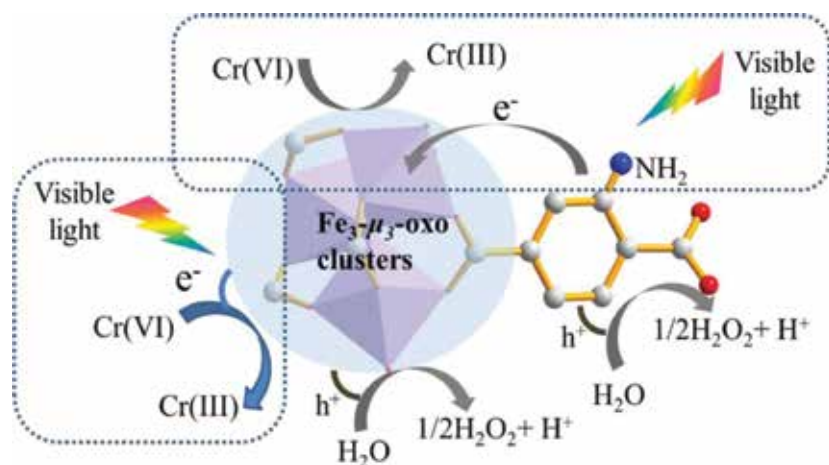

Figure 12. Suggestion dual excitation ways mechanism for photocatalytic reduction of Cr(VI) on NH_2–MIL-88B (Fe) [154].

6. Perspectives

As emerging photocatalytic materials, semiconducting MOFs exhibited promising future and have attracted extensive research interest, whereas they face significant challenges for widespread application. In order to tackle these issues, great research efforts are necessary to put on:

1. Design the energy bandgap and band positions through tuning the metal or metal cluster nodes as well as target-directed design of the ligands.

2. The incorporation of inorganic semiconductors, polymer semiconductors and surface metallisation may enrich the family of the MOFs photocatalysts with desirable performance because of their ability in fine tuning the energy alignment of the materials as well as the charge carrier transportation.

3. Extend the photocatalytic application fields of MOF-based photocatalysts. Recovery of noble metals from metallurgy industries and heavy metal cations from wastewater or soil, the bactericidal applications and photocatalytic cleanup of indoor air are highly demanding and can be strong spur for the extended applications of MOFs. Artificial photosynthesis, including water splitting and photoreduction of CO_2, represents an emerging and ever-fast increasing application of MOFs. The direct capture and photoreduction of CO_2 from air might be realisable in terms of the selective adsorption and the separated redox active sites of the MOFs, which enable the designed MOFs to mimic natural plants, for conducting light oxidation reaction on the external surface or shallow pores of MOFs yet reductive 'dark' reaction within the MOFs' channels. The photocatalytic selective redox in production of value-added advanced chemicals or pharmaceutical intermediates would open new and sustainable pace for MOFs' applications.

4. Develop MOF-based photocatalysis devices, for example, MOF solar cells and photocatalytic-based sensors, where photoelectrochemical signals may be used to diagnose the specific chemical substrates.

5. Develop and apply spectral and photoelectrochemical characterisation techniques, in particular transient characterisations, for precisely exploring the exact photocatalytic and photoelectrochemical catalysis mechanism.

6. Demonstrate the potentials of MOF-based photocatalysts at pilot scale. There are a large number of evidences to confirm the potentials of the photocatalytic applications of MOFs at laboratory-scale tests while the large-scale applications still are not convinced due to the high cost of MOFs and the suspicious stability of such complex inorganic-organic networks. The involvement of industrial partners and diverse stakeholders would be more persuasive to commercialise MOFs in the utilisation of planet-saving solar energy photocatalysis technologies.

    The ever-increasing expansion and enormous progress of MOFs have been observed since the discovery of first MOFs. It is undoubted the MOFs would be an important class of alternative photocatalysts relative to the conventional inorganic semiconductor photoca-

talysts, despite that various strategies still are under development and are verifying to tackle the present challenges associated with MOFs.

Author details

Ahmad Alshammari[1*], Zheng Jiang[2*] and Kyle E. Cordova[3]

*Address all correspondence to: aalshammari@kacst.edu.sa and z.jiang@soton.ac.uk

1 Materials Science Research Institute (MSRI), King Abdulaziz City for Science and Technology (KACST), Riyadh, Saudi Arabia

2 Faculty of Engineering and the Environment, University of Southampton, Southampton, UK

3 Department of Chemistry, University of California-Berkeley, Berkeley, California, USA

References

[1] Ma S, Zhou H-C. Gas storage in porous metal–organic frameworks for clean energy applications. Chem. Commun. 2010; 46:44–53. DOI: 10.1039/B916295J.

[2] Li J-R, Sculley J, Zhou H-C. Metal-organic frameworks and porous polymer networks for carbon capture. Chem. Rev. 2012; 112:869–932.

[3] Makal TA, Li J-R, Lu W, Zhou H-C. Fine-tuning the balance between crystallization and gelation and enhancement of CO2 uptake on functionalized calcium based MOFs and metallogels. Chem. Soc. Rev. 2012; 41:7761–7779.

[4] Liu C, Li F, Ma L-P, Cheng H-M. Advanced materials for energy storage. Adv. Mater. 2010; 22:E28–E62.

[5] Li J-R, Kuppler RJ, Zhou H-C. Selective gas adsorption and separation in metal-organic frameworks. Chem. Soc. Rev. 2009; 38:1477–1504.

[6] Zacher D, Shekhah O, Woll C, Fischer RA. Thin films of metal-organic frameworks. Chem. Soc. Rev. 2009; 38:1418–1429.

[7] Bradshaw D, Garai A, Huo J. Metal–organic framework growth at functional interfaces: thin films and composites for diverse applications. Chem. Soc. Rev. 2012; 41:2344–2381.

[8] Cui Y, Yue Y, Qian G, Chen B. Confinement of pyridinium hemicyanine dye within an anionic metal-organic framework for two-photon-pumped lasing. Chem. Rev. 2012; 112:1126–1162.

[9] Chen L, Tan K, Lan Y-Q, Li S-L, Shao K-Z, Su ZM. Self-assembly versus stepwise synthesis: heterometal-organic frameworks based on metalloligands with tunable luminescence properties. Chem. Commun. 2012; 48:5919–5921.

[10] Lee JY, Farha OK, Roberts J, Scheidt KA, Nguyen ST, Hupp JT. Metal-organic framework materials as catalysts. Chem. Soc. Rev. 2009; 38:1450–1459.

[11] Ma L, Abney C, Lin W. Enantioselective catalysis with homochiral metal-organic frameworks. Chem. Soc. Rev. 2009; 38:1248–1256.

[12] O'Keeffe M, Yaghi OM. Deconstructing the crystal structures of metal-organic frameworks and related materials into their underlying nets. Chem. Rev. 2012; 112:675–702. DOI: dx.doi.org/10.1021/cr200205j

[13] Shibata YJ. Coll. Sci., Imp. Univ. Tokyo. 1916; 37:1–31.

[14] Keggin JF, Miles FD. Structures and formulae of the Prussian blues and related compounds. Nature. 1936; 137:577–578. DOI:10.1038/137577a0

[15] Ferey G. Microporous solids: from organically templated inorganic skeletons to hybrid frameworks…ecumenism in chemistry. Chem. Mater. 2001; 13:3084–3098.

[16] Janiak C. Engineering coordination polymers towards applications. Dalton Trans. 2003; 2781–2804. DOI:10.1039/B305705B

[17] Hofmann KA, Kuspert FA. Z. Compounds of hydrocarbons with metal salts. Anorg. Allg. Chem. 1897; 15:204–207. DOI:10.1002/zaac.18970150118

[18] Powell HM, Rayner JH. Clathrate compound formed by benzene with an ammonia–nickel cyanide complex. Nature. 1949; 163:566–567. DOI:10.1038/163566a0

[19] Iwamoto T, Miyoshi T, Miyamoto T, Sasaki Y, Fujiwara S. The metal ammine cyanide aromatics clathrates. I. The preparation and stoichiometry of the diamminemetal(II) tetracyano-niccolate(II) dibenzene and dianiline. Bull. Chem. Soc. Jpn. 1967; 40:1174–1178. DOI:10.1246/bcsj.40.1174

[20] Kinoshita Y, Matsubara I, Higuchi T, Saito Y. The crystal structure of Bis(adiponitrile)copper(I) Nitrate. Bull. Chem. Soc. Jpn. 1959; 32:1221–1226. DOI: http://doi.org/10.1246/bcsj.32.1221

[21] Yaghi OM, Li GM, Li HL. Selective binding and removal of guests in a microporous metal–organic framework. Nature. 1995; 378:703–706. DOI:10.1038/378703a0

[22] Li H, Eddaoudi M, O'Keeffe M, Yaghi OM. Design and synthesis of an exceptionally stable and highly porous metal-organic framework. Nature. 1999; 402:276–279. DOI: 10.1038/46248

[23] Kaye SS, Dailly A, Yaghi OM, Long JR. Impact of preparation and handling on the hydrogen storage properties of Zn4O(1,4-benzenedicarboxylate)3 (MOF-5). J. Am. Chem. Soc. 2007; 129:14176–14177. DOI:10.1021/ja076877g

[24] Chae HK, Siberio-Perez DY, Kim J, Go Y, Eddaoudi M, Matzger AJ, O'Keeffe M, Yaghi OM. A route to high surface area, porosity and inclusion of large molecules in crystals. Nature. 2004; 427:523–527. DOI:10.1038/nature02311

[25] Furukawa H, Ko N, Go YB, Aratani N, Choi SB, Choi E, Yazaydin AO, Snurr RQ, O'Keeffe M, Kim J, Yaghi OM. Ultrahigh porosity in metal-organic frameworks. Science. 2010; 329:424–428. DOI:10.1126/science.1192160

[26] Chen BL, Liang CD, Yang J, Contreras DS, Clancy YL, Lobkovsky EB, Yaghi OM, Dai S. A microporous metal-organic framework for gas-chromatography separation of alkane. Angew. Chem. Int. Ed. 2006; 45:1390–1393. DOI:10.1002/anie.200502844

[27] Lee JY, Pan L, Huang XY, Emge TJ, Li J. A systematic approach to building highly porous, noninterpenetrating metal–organic frameworks with a large capacity for adsorbing H2 and CH4. Adv. Funct. Mater. 2011; 21:993–998. DOI:10.1002/adfm. 201001790

[28] Wang XF, Wang Y, Zhang YB, Xue W, Zhang JP, Chen XM. Layer-by-layer evolution and a hysteretic single-crystal to single-crystal transformation cycle of a flexible pillared-layer open framework. Chem. Commun. 2012; 48:133–135. DOI:10.1039/ C1CC15891K 29. Koh K, Wong-Foy AG, Matzger AJ. A porous coordination copoly-mer with over 5000 m2/g BET surface area. J. Am. Chem. Soc. 2009; 131:4184–4185. DOI:10.1021/ja809985t

[29] Ferey G, Mellot-Draznieks C, Serre C, Millange F, Dutour J, Surble S, Margiolaki I. A chromium terephthalate-based solid with unusually large pore volumes and surface area. Science. 2005; 309:2040–2042. DOI:10.1126/science.1116275

[30] Hong DY, Hwang YK, Serre C, Ferey G, Chang JS. Porous chromium terephthalate MIL-101 with coordinatively unsaturated sites: surface functionalization, encapsula-tion, sorption and catalysis. Adv. Funct. Mater. 2009; 19:1537–1552. DOI:10.1002/ adfm.200801130

[31] Zhao D, Yuan DQ, Sun DF, Zhou HC. Stabilization of metal-organic frameworks with high surface areas by the incorporation of meso cavities with micro windows. J. Am. Chem. Soc. 2009; 131:9186–9187. DOI:10.1021/ja901109t

[32] Chui SSY, Lo SMF, Charmant JPH, Orpen AG, Williams ID. A chemically functiona-lizable nanoporous material. Science. 1999; 283:1148–1150. DOI:10.1126/science. 283.5405.1148

[33] Schlichte K, Kratzke T, Kaskel S. Improved synthesis, thermal stability and catalytic properties of the metal-organic framework compound Cu3(BTC)2. Micropor. Mesopor. Mater. 2004; 73:81–88. DOI:10.1016/j.micromeso.2003.12.027

[34] Alaerts L, Seguin E, Poelman H, Thibault-Starzyk F, Jacobs PA, De Vos DE. Probing the Lewis acidity and catalytic activity of the metal-organic framework [Cu-3(btc)(2)] (BTC = benzene-1,3,5-tricarboxylate) Chem. Eur. J. 2006; 12:7353–7363. DOI:1854/5954

[35] Kramer M, Ulrich SB, Kaskel S. Synthesis and properties of the metal-organic framework Mo3(BTC)2(TUDMOF-1). J. Mater. Chem. 2006; 16:2245–2248. DOI:10.1039/ B601811D

[36] Xie LH, Liu SX, Gao CY, Cao RG, Cao JF, Sun CY, Su ZM. Mixed-valence Iron(II, III) trimesates with open frameworks modulated by solvents. Inorg. Chem. 2007; 46:7782– 7788. DOI:10.1021/ic062273m

[37] Murray LJ, Dinca M, Yano J, Chavan S, Bordiga S, Brown CM, Long JR. Highly-selective and reversible O2 binding in Cr3(1,3,5-benzenetricarboxylate)2. J. Am. Chem. Soc. 2010; 132:7856–7857. DOI:10.1021/ja1027925

[38] Dietzel PDC, Morita Y, Blom R, Fjellvag H. An in situ high-temperature single-crystal investigation of a dehydrated metal–organic framework compound and field-induced magnetization of one-dimensional metal–oxygen chains. Angew. Chem. Int. Ed. 2005; 44:6354–6358. DOI:10.1002/anie.200501508

[39] Rowsell JLC, Yaghi OM. Effect of functionalization, catenation, and variation of the metal oxide and organic linking units on the low-pressure hydrogen adsorption properties of metal–organic frameworks. J. Am. Chem. Soc. 2006; 128:1304–1315. DOI: 10.1021/ja056639q

[40] Caskey SR, Wong-Foy AG, Matzger AJ. Dramatic tuning of carbon dioxide uptake via metal substitution in a coordination polymer with cylindrical pores. J. Am. Chem. Soc. 2008; 130:10870–10871. DOI:10.1021/ja8036096

[41] McKinlay AC, Xiao B, Wragg DS, Wheatley PS, Megson IL, Morris RE. Exceptional behavior over the whole adsorption–storage–delivery cycle for no in porous metal organic frameworks. J. Am. Chem. Soc. 2008; 130:10440–10444. DOI:10.1021/ja801997r

[42] Henschel A, Gedrich K, Kraehnert R, Kaskel S. Catalytic properties of MIL-101. Chem. Commun. 2008; 4192–4194. DOI:10.1039/B718371B

[43] Kim J, Bhattacharjee S, Jeong KE, Jeong SY, Ahn WS. Selective oxidation of tetralin over a chromium terephthalate metal organic framework, MIL-101. Chem. Commun. 2009; 3904–3906. DOI:10.1039/B902699A

[44] Kitaura R, Onoyama G, Sakamoto H, Matsuda R, Noro S, Kitagawa S. Immobilization of a metallo schiff base into a microporous coordination polymer. Angew. Chem. Int. Ed. 2004; 43:2684–2687. DOI:10.1002/anie.200352596

[45] Fletcher AJ, Thomas KM, Rosseinsky MJ. Flexibility in metal-organic framework materials: impact on sorption properties. J. Solid State Chem. 2005; 178:2491–2510. DOI:10.1016/j.jssc.2005.05.019

[46] Kitagawa S, Uemura K. Dynamic porous properties of coordination polymers inspired by hydrogen bonds. Chem. Soc. Rev. 2005; 34:109119. DOI:10.1039/B313997M

[47] Horike S, Shimomura S, Kitagawa S. Soft porous crystals. Nat. Chem. 2009; 1:695–704. DOI:10.1038/nchem.444

[48] Sing KSW, Everett DH, Haul RAW, Moscou L, Pierotti RA, Rouquerol J, Siemieniewska T. Reporting physiosorption data for gas/solid systems with special reference to determination of surface area and porosity. Pure Appl. Chem. 1985; 57:603–619. DOI:http://dx.doi.org/10.1351/pac198557040603.

[49] Li D, Kaneko K. Hydrogen bond-regulated microporous nature of copper complex-assembled microcrystals. Chem. Phys. Lett. 2001; 335:50–56. DOI:10.1016/S0009-2614(00)01419-6

[50] Kitaura R, Seki K, Akiyama G, Kitagawa S. Porous coordination-polymer crystals with gated channels specific for supercritical gases. Angew. Chem. Int. Ed. 2003; 42:428–431. DOI:10.1002/anie.200390130

[51] Horike S, Tanaka D, Nakagawa K, Kitagawa S. Selective guest sorption in an interdigitated porous framework with hydrophobic pore surfaces. Chem. Commun. 2007; 3395–3397. DOI:10.1039/B703502K

[52] Nakagawa K, Tanaka D, Horike S, Shimomura S, Higuchi M, Kitagawa S. Enhanced selectivity of CO2 from a ternary gas mixture in an interdigitated porous framework. Chem. Commun. 2010; 46:4258–4260. DOI:10.1039/C0CC00027B

[53] Loiseau T, Serre C, Huguenard C, Fink G, Taulelle F, Henry M, Bataille T, Ferey G. A rationale for the large breathing of the porous aluminum terephthalate (MIL-53) upon hydration. Chem. Eur. J. 2004; 10:1373–1382. DOI:10.1002/chem.200305413

[54] Horcajada P, Serre C, Maurin G, Ramsahye NA, Balas F, Vallet-Regi M, Sebban M, Taulelle F, Ferey G. Flexible porous metal-organic frameworks for a controlled drug delivery. J. Am. Chem. Soc. 2008; 130:6774–6780. DOI:10.1021/ja710973k

[55] Finsy V, Kirschhock CEA, Vedts G, Maes M, Alaerts L, De Vos DE, Baron GV, Denayer JFM. Framework breathing in the vapour-phase adsorption and separation of xylene isomers with the metal–organic framework MIL-53. Chem. Eur. J. 2009; 15:7724–7731. DOI:10.1002/chem.200802672

[56] Barcia PS, Zapata F, Silva JAC, Rodrigues AE, Chen BL. Kinetic separation of hexane isomers by fixed-bed adsorption with a microporous metal–organic framework. J. Phys. Chem. B. 2007; 111:6101–6103. DOI:10.1021/jp0721898

[57] Kitagawa S, Kitaura R, Noro S. Functional porous coordination polymers. Angew. Chem. Int. Ed. 2004; 43:2334–2375. DOI:10.1002/anie.200300610

[58] Farha OK, Yazaydin AO, Eryazici I, Malliakas CD, Hauser BG, Kanatzidis MG, Nguyen ST, Snurr RQ, Hupp JT. De novo synthesis of a metal–organic framework material

featuring ultrahigh surface area and gas storage capacities. Nat. Chem. 2010; 2:944–948. DOI:10.1038/nchem.834

[59]   Dinca M, Dailly A, Liu Y, Brown CM, Neumann DA, Long JR. Hydrogen storage in a microporous metal–organic framework with exposed Mn2+ coordination sites. J. Am. Chem. Soc. 2006; 128:16876–16883. DOI:10.1021/ja0656853

[60]   Dinca M, Long JR. Hydrogen storage in microporous metal-organic frameworks with exposed metal sites. Angew. Chem. Int. Ed. 2008; 47:6766–6779. DOI:10.1002/anie. 200801163

[61]   Chen B, Ockwig NW, Millward AR, Contreras DS, Yaghi OM. High H2 adsorption in a microporous metal–organic framework with open metal sites. Angew. Chem., Int. Ed. 2005; 44:4745–4749. DOI:10.1002/anie.200462787

[62]   Rowsell JLC, Yaghi OM. Strategies for hydrogen storage in metal-organic frameworks. Angew. Chem. Int. Ed. 2005; 44:4670–4679. DOI:10.1002/anie.200462786

[63]   Jung DH, Kim D, Lee TB, Choi SB, Yoon JH, Kim J, Choi K, Choi SHJ. Grand canonical Monte Carlo simulation study on the catenation effect on hydrogen adsorption onto the interpenetrating metal–organic frameworks. Phys. Chem. B. 2006; 110:22987–22990. DOI:10.1021/jp065819z

[64]   Ma S, Sun D, Ambrogio M, Fillinger JA, Parkin S, Zhou HC. Framework-catenation isomerism in metal–organic frameworks and its impact on hydrogen uptake. J. Am. Chem. Soc. 2007; 129:1858–1859. DOI:10.1021/ja067435s

[65]   Ryan P, Broadbelt LJ, Snurr RQ. Is catenation beneficial for hydrogen storage in metal–organicframeworks? Chem. Commun. 2008; 4132–4134. DOI:10.1039/B804343D

[66]   Han SS, Mendoza-Cortes JL, Goddard WA III. Recent advances on simulation and theory of hydrogen storage in metal–organic frameworks and covalent organic frameworks. Chem. Soc. Rev. 2009; 38:1460–1476. DOI:10.1039/B802430H

[67]   Mulfort KL, Farha OK, Stern CL, Sarjeant AA, Hupp JT. Post-synthesis alkoxide formation within metal–organic framework materials: a strategy for incorporating highly coordinatively unsaturated metal ions. J. Am. Chem. Soc. 2009; 131:3866–3868. DOI:10.1021/ja809954r

[68]   Himsl D, Wallacher D, Hartmann M. Improving the hydrogen-adsorption properties of a hydroxy-modified MIL-53(Al) structural analogue by lithium doping. Angew. Chem. Int. Ed. 2009; 48:4639–4642. DOI:10.1002/anie.200806203

[69]   Murray LJ, Dinca M, Long JR. Hydrogen storage in metal–organic frameworks. Chem. Soc. Rev. 2009; 38:1294–1314. DOI:10.1039/B802256A

[70]   Suh MP, Park HJ, Prasad TK, Lim DW. Hydrogen storage in metal–organic frameworks. Chem. Rev. 2012; 112:782–835. DOI:10.1021/cr200274s

[71] Burchell, T.; Rogers, M. Low pressure storage of natural gas for vehicular applications. SAE Tech. Pap. Ser. 2000; 2000-01-2205. DOI:10.4271/2000-01-2205

[72] Ma SQ, Sun DF, Simmons JM, Collier CD, Yuan DQ, Zhou HC. Metal-organic framework from an anthracene derivative containing nanoscopic cages exhibiting high methane uptake. J. Am. Chem. Soc. 2008; 130:1012–1016. DOI:10.1021/ja0771639

[73] Bhatia SK, Myers AL. Optimium conditions for adsorptive storage. Langmuir. 2006; 22:1688–1700. DOI:10.1021/la0523816

[74] Furukawa H, Miller MA, Yaghi OM. Independent verification of the saturation hydrogen uptake in MOF-177 and establishment of a benchmark for hydrogen adsorption in metal–organic frameworks. J. Mater. Chem. 2007; 17:3197–3204. DOI: 10.1039/B703608F

[75] P€assler P, Hefner W, Buckl K, Meinass H, Meiswinkel A, Wernicke, H-J, Ebersberg G, M€uller R, B€assler J, Behringer H, Mayer D. Acetylene; Wiley-VCH Verlag GmbH & Co. KGaA: New York, 2000.

[76] Xiang SC, Zhou W, Zhang ZJ, Green MA, Liu Y, Chen BL. Open metal sites within isostructural metal-organic frameworks for differential recognition of acetylene and extraordinarily high acetylene storage capacity at room temperature. Angew. Chem., Int. Ed. 2010; 49:4615–4618. DOI:10.1002/anie.201000094

[77] Zhang JP, Chen XM. Optimized acetylene/carbon dioxide sorption in a dynamic porous crystal. J. Am. Chem. Soc. 2009; 131:5516–5521. DOI:10.1021/ja8089872

[78] Hu YX, Xiang SC, Zhang WW, ZhangZX, Wang L, Bai JF, Chen BL. A new MOF-505 analog exhibiting high acetylene storage. Chem. Commun. 2009; 7551–7553. DOI: 10.1039/B917046D

[79] Rosi N, Kim J, Eddaouddi M, Chen B, O'Keeffe M, Yaghi OM. Rod packings and metal−organic frameworks constructed from rod-shaped secondary building units. J. Am. Chem. Soc. 2005; 127:1504–1518. DOI:10.1021/ja045123o

[80] Dietzel PDC, Besikiotis V, Blom R. Application of metal–organic frameworks with coordinatively unsaturated metal sites in storage and separation of methane and carbon dioxide. J. Mater. Chem. 2009; 19:7362–7370. DOI:10.1039/B911242A

[81] Cundy CS, Cox PA. The hydrothermal synthesis of zeolites: history and development from the earliest days to the present time. Chem. Rev. 2003; 103:663–702. DOI: 10.1021/cr020060i

[82] Stock N, Biswas S. Synthesis of metal-organic frameworks (MOFs): routes to various MOF topologies, morphologies, and composites. Chem. Rev. 2012; 112:933–969. DOI: 10.1021/cr200304e

[83] Bauer S, Serre C, Devic T, Horcajada P, Marrot J, Férey G, Stock N. High-throughput assisted rationalization of the formation of metal organic frameworks in the iron(III)

aminoterephthalate solvothermal system. Inorg. Chem. 2008; 47:7568–7576. DOI: 10.1021/ic800538r

[84] Khan NA, Kang IJ, Seok HY, Jhung SH. Facile synthesis of nano-sized metal-organic frameworks, chromium-benzenedicarboxylate, MIL-101. Chem. Eng. J. 2011; 166:1152–1157. DOI:10.1016/j.cej.2010.11.098

[85] Zhao Z, Li X, Huang S, Xia Q, Li Z. Adsorption and diffusion of benzene on chromium-based metal organic framework MIL-101 synthesized by microwave irradiation. Ind. Eng. Chem. Res. 2011; 50:2254–2261. DOI:10.1021/ie101414n

[86] Choi JY, Kim J, Jhung SH, Kim HK, Chang J-S, Chae HK. Microwave synthesis of a porous metal-organic framework, zinc terephthalate MOF-5. Bull. Korean Chem. Soc. 2006; 27:1523–1524. DOI:10.5012/bkcs.2006.27.10.1523

[87] Ren J, Langmi HW, North BC, Mathe M, Bessarabov D. Modulated synthesis of zirconium-metal organic framework (Zr-MOF) for hydrogen storage applications. Int. J. Hydrogen Energy. 2014; 39:890–895. DOI:10.1016/j.ijhydene.2013.10.087

[88] Liang W, D'Alessandro DM. Microwave-assisted solvothermal synthesis of zirconium oxide based metal-organic frameworks. Chem. Commun. 2013; 49:3706–3708. DOI:10.1039/c3cc40368h.

[89] Ren J, Segakweng T, Langmi H, Musyoka N, North B, Mathe M, Bessarabov D. Microwave-assisted modulated synthesis of zirconium-based metal–organic framework (Zr-MOF) for hydrogen storage applications. Int. J. Mater. Res. 2014;105:516–519. DOI:10.3139/146.111047

[90] Wu RF, Zhang TL, Qiao XJ, Zhang JG, Liu YH. Synthesis, crystal structure and thermal stability of a novel 3D coordination polymer Pb(1,4-napdc)(DMF). Chin. J. Inorg. Chem. 2006; 22:1340–1344. ISSN: 1001-4861; 22(7).

[91] Tuikka M, Haukka M, Ahlgrén M. Three barium diphosphonates with 3-D structures. Solid State Sci. 2007; 9:535–541. DOI:10.1016/j.solidstatesciences.2007.04.006

[92] Yuan W, O'Connor J, James SL. Mechanochemical synthesis of homo- and hetero-rare-earth(III) metal–organic frameworks by ball milling. CrystEngComm. 2010; 12:3515–3517. DOI:10.1039/C0CE00216J

[93] Seoane B, Zamaro JM, Tellez C, Coronas J. Sonocrystallization of zeolitic imidazolate frameworks (ZIF-7, ZIF-8, ZIF-11 and ZIF-20). CrystEngComm. 2012; 14:3103–3107. DOI:10.1039/C2CE06382D

[94] Thompson JA, Chapman KW, Koros WJ, Jones CW, Nair S. Sonication-induced Ostwald ripening of ZIF-8 nanoparticles and formation of ZIF-8/polymer composite membranes. Microporous Mesoporous Mater. 2012; 158:292–299. DOI:10.1016/j.micromeso.2012.03.052

[95]   Bang JH, Suslick KS. Applications of ultrasound to the synthesis of nanostructured materials. Adv. Mater. 2010; 22:1039–1059. DOI:10.1002/adma.200904093

[96]   Tranchemontagne DJ, Hunt JR, Yaghi OM. Room temperature synthesis of metal-organic frameworks: MOF-5, MOF-74, MOF-177, MOF-199, and IR MOF-0. Tetrahedron. 2008; 64:8553–8557. DOI:10.1016/j.tet.2008.06.036

[97]   Schlesinger M, Schulze S, Hietschold M, Mehring M. Evaluation of synthetic methods for microporous metal–organic frameworks exemplified by the competitive formation of [Cu2(btc)3(H2O)3] and [Cu2(btc)(OH)(H2O)]. Microporous Mesoporous Mater. 2010; 132:121–127. DOI:10.1016/j.micromeso.2010.02.008

[98]   Fard MJS, Rastaghi F, Ghanbari N. Sonochemical synthesis of new nano-two-dimensional lead(II) coordination polymer: as precursor for preparation of PbO nanostructure. J. Mol. Struct. 2013; 1032:133–137. DOI:10.1016/j.molstruc.2012.07.020

[99]   Martinez Joaristi A, Juan-Alcaniz J, Serra-Crespo P, Kapteijn F, Gascon J. Electrochemical synthesis of some archetypical Zn2+, Cu2+, and Al3+ metal organic framework. Cryst. Growth Des. 2012; 12:3489–3498. DOI:10.1021/cg300552w

[100] Campagnol N, Van Assche T, Boudewijns T, Denayer J, Binnemans K, De Vos D, Fransaer J. High pressure, high temperature electrochemical synthesis of metal–organic frameworks: films of MIL-100 (Fe) and HKUST-1 in different morphologies. J. Mater. Chem. A. 2013; 1:5827–5830. DOI:10.1039/C3TA10419B

[101] Stassen I, Styles M, Van Assche T, Campagnol N, Fransaer J, Denayer J, Tan J-C, Falcaro P, De Vos D, Ameloot R. Electrochemical film deposition of the zirconium metal–organic framework UiO-66 and application in a miniaturized sorbent trap. Chem. Mater. 2015; 27:1801–1807. DOI:10.1021/cm504806p

[102] Youngblood WJ, Lee SA, Kobayashi Y, Hernandez-Pagan E, Hoertz PG, Moore TA, Moore AL, Gust D, Mallouk TE. Photoassisted overall water splitting in a visible light-absorbing dye-sensitized photoelectrochemical cell. J. Am. Chem. Soc. 2009; 131:926–927. DOI:10.1021/ja809108y

[103] Reece SY, Hamel JA, Sung K, Jarvi TD, Esswein AJ, Pijpers JJH, Nocera DG. Wireless solar water splitting using silicon-based semiconductors and earth-abundant catalysts. Science. 2011; 334:645–648. DOI:10.1126/science.1209816

[104] Ohno T, Bai L, Hisatomi T, Maeda K, Domen K. Photocatalytic water splitting using modified GaN:ZnO solid solution under visible light: long-time operation and regeneration of activity. J. Am. Chem. Soc. 2012; 134:8254–8259. DOI:10.1021/ja302479f

[105] Wang X, Xu Q, Li M, Shen S, Wang X, Wang Y, Feng Z, Shi J, Han H, Li C. Photocatalytic overall water splitting promoted by an phase junction on Ga2O3. Angew. Chem. Int. Ed. 2012; 51:13089–13092. DOI:10.1002/anie.201207554

[106] Nicewicz DA, MacMillan DWC. Merging photo redox catalysis with organo catalysis: the direct asymmetric alkylation of aldehydes. Science. 2008; 322:77–80. DOI:10.1126/science.1161976

[107] Nagib DA, Scott ME, MacMillan DWC. Enantioselective α-trifluoromethylation of aldehydes via photoredox organo catalysis. J. Am. Chem. Soc. 2009; 131:10875–10877. DOI:10.1021/ja9053338

[108] Du J, Yoon TP. Crossed intermolecular [2+2] cycloadditions of acyclic enones via visible light photocatalysis. J. Am. Chem. Soc. 2009; 131:14604–14605.

[109] Condie AG, Gonza´lez-Go´mez JC, Stephenson CRJ. Visible-light photoredox catalysis: Aza-Henry reactions via C-H functionalization. J. Am. Chem. Soc. 2010; 132:1464–1465.

[110] Lang X, Ji H, Chen C, Ma W, Zhao J. Selective formation of imines by aerobic photo-catalytic oxidation of amines on TiO2. Angew. Chem. Int. Ed. 2011; 50:3934–3937

[111] Chen W, Rein FN, Rocha RC. Homogeneous photocatalytic oxidation of alcohols by a chromophore-catalyst dyad of ruthenium complexes. Angew. Chem. Int. Ed. 2009; 48:9672–9675. DOI:10.1002/anie.200904756

[112] Li F, Jiang Y, Zhang B, Huang F, Gao Y, Sun L. Towards a solar fuel device: light-driven water oxidation catalyzed by a supramolecular assembly. Angew. Chem. Int. Ed. 2012; 51:2417–2420. DOI:10.1002/anie.201108051

[113] Windle CD, Perutz RN. Advances in molecular photocatalytic and electrocatalytic CO2 reduction. Coord. Chem. Rev. 2012; 256:2562–2570. DOI:10.1016/j.ccr.2012.03.010

[114] Yoon M, Srirambalaji R, Kim K. Homochiral metal–organic frameworks for asymmetric heterogeneous catalysis. Chem. Rev. 2012; 112:1196–1231. DOI:10.1021/cr2003147

[115] Cavka JH, Jakobsen S, Olsbye U, Guillou N, Lamberti C, Bordiga S, Lillerud KP. A new zirconium inorganic building brick forming metal organic frameworks with exceptional stability. J. Am. Chem. Soc. 2008; 130:13850–13851. DOI:10.1021/ja8057953

[116] Gomes Silva C, Luz I, Llabre´s i Xamena FX, Corma A, Garcı´a H. Water stable Zr–benzenedicarboxylate metal–organic frameworks as photocatalysts for hydrogen generation. Chem. Eur. J. 2010; 16:11133–11138. DOI:10.1002/chem.200903526

[117] Sun D, Fu Y, Liu W, Ye L, Wang D, Yang L, Fu X, Li Z. Studies on photocatalytic CO2 reduction over NH2-Uio-66(Zr) and its derivatives: towards a better understanding of photocatalysis on metal–organic frameworks. Chem. Eur. J. 2013; 19:14279–14285. DOI:10.1002/chem.201301728

[118] Wang C, deKrafft KE, Lin W. Pt nanoparticles@photoactive metal-organic frameworks: efficient hydrogen evolution via synergistic photoexcitation and electron injection. J. Am. Chem. Soc. 2012; 134:7211–7214. DOI:10.1021/ja300539p

[119] Hawecker J, Lehn J, Ziessel R. Efficient photochemical reduction of CO2 to CO by visible light irradiation of systems containing Re(bipy)(CO)3X or Ru(bipy)32+-Co2+ combi-

nations as homogeneous catalysts. J. Chem. Soc. Chem. Commun. 1983; 0:536–538. DOI:10.1039/C39830000536

[120] Lin W, Frei H. Photochemical CO2 splitting by metal-to-metal charge-transfer excitation in mesoporous ZrCu(I)-MCM-41 silicate sieve. J. Am. Chem. Soc. 2005; 127:1610–1611.

[121] Liu Q, Zhou Y, Kou J, Chen X, Tian Z, Gao J, Yan S, Zou Z. High-yield synthesis of ultra-long and ultrathin Zn2GeO4 nanoribbons toward improved photocatalytic reduction of CO2 into renewable hydrocarbon fuel. J. Am. Chem. Soc. 2010; 132:14385–14387.

[122] Yan S, Ouyang S, Gao J, Yang M, Feng J, Fan X, Wan L, Li Z, Ye J, Zhou Y, Zou Z. A room-temperature reactive-template route to mesoporous ZnGa2O4 with improved photocatalytic activity in reduction of CO2. Angew. Chem. Int. Ed. 2010; 49:6400–6404

[123] Wang C, Xie Z, DeKrafft KE, Lin W. Doping metal–organic frameworks for water oxidation, carbon dioxide reduction, and organic photocatalysis. J. Am. Chem. Soc. 2011; 133:13445–13454. DOI:10.1021/ja203564w

[124] Pullen S, Fei H, Orthaber A, Cohen SM, Ott S. Enhanced photochemical hydrogen production by a molecular diiron catalyst incorporated into a metal–organic framework. J. Am. Chem. Soc. 2013; 135:16997–17003. DOI:10.1021/ja407176p

[125] Wang JL, Wang C, Lin W. Metal-organic frameworks for light harvesting and photocatalysis. ACS Catalysis 2012; 2, 2630–2640, DOI:10.1021/cs3005874

[126] Navarro Amador R, Carboni M, Meyer D. Photosensitive titanium and zirconium metal organic frameworks: current research and future possibilities. Mater. Lett. 2015. DOI:10.1016/j.matlet.2015.12.023

[127] Horiuchi Y, Toyao T, Takeuchi M, Matsuoka M, Anpo M. Recent advances in visible-light-responsive photocatalysts for hydrogen production and solar energy conversion-from semiconducting TiO2 to MOF/PCP photocatalysts. Phys. Chem. Chem. Phys. 2013; 15:13243–13253. DOI:10.1039/c3cp51427g

[128] Wang C-C, Li J-R, Lv X-L, Zhang Y-Q, Guo G. Photocatalytic organic pollutants degradation in metal-organic frameworks. Energy Environ. Sci. 2014; 7:2831–2867. DOI:10.1039/C4EE01299B

[129] Mahata P, Madras G, Natarajan S. Novel photocatalysts for the decomposition of organic dyes based on metal-organic framework compounds. J. Phys. Chem. B 2006; 110:13759–13768. DOI:10.1021/jp0622381

[130] Wang Y. et al. Controlled fabrication and enhanced visible-light photocatalytic hydrogen production of Au at CdS/MIL-101 heterostructure. Appl. Catalysis B Environ. 2016; 185:307–314. DOI:10.1016/j.apcatb.2015.12.020

[131] Sun D, Ye L, Li Z. Visible-light-assisted aerobic photocatalytic oxidation of amines to imines over NH2-MIL-125(Ti). Appl. Catalysis B Environ. 2015; 164:428–432. DOI: 10.1016/j.apcatb.2014.09.054

[132] Ke F, Wang L, Zhu J. Facile fabrication of CdS-metal-organic framework nanocomposites with enhanced visible-light photocatalytic activity for organic transformation. Nano Res. 2015; 8:1834–1846. DOI:10.1007/s12274-014-0690-x

[133] Kumar Paul A, Madras G, Natarajan S. Adsorption-desorption and photocatalytic properties of inorganic-organic hybrid cadmium thiosulfate compounds. Phys. Chem. Chem. Phys. 2009; 11:11285–11296. DOI:10.1039/B913407G

[134] Maeda K, Domen K. New non-oxide photocatalysts designed for overall water splitting under visible light. J. Phys. Chem. C 2007; 111:7851–7861. DOI:10.1021/jp070911w

[135] Gu Z. et al. Synthesis of Au@UiO-66(NH2) structures by small molecule-assisted nucleation for plasmon-enhanced photocatalytic activity. Chem. Commun. 2016; 52:116–119. DOI:10.1039/c5cc07042b

[136] Sun D, et al. Noble metals can have different effects on photocatalysis over metal-organic frameworks (MOFs): a case study on M/NH2-MIL-125(Ti) (M=Pt and Au). Chem. Eur. J. 2014; 20:4780–4788. DOI:10.1002/chem.201304067

[137] Liang R, et al. A simple strategy for fabrication of Pd@MIL-100(Fe) nanocomposite as a visible-light-driven photocatalyst for the treatment of pharmaceuticals and personal care products (PPCPs). Appl. Catalysis B Environ. 2015; 176–177, 240–248. DOI: 10.1016/j.apcatb.2015.04.009

[138] Tilgner D, Friedrich M, Hermannsdörfer J, Kempe R. Titanium dioxide reinforced metal-organic framework Pd catalysts: activity and reusability enhancement in alcohol dehydrogenation reactions and improved photocatalytic performance. ChemCatChem 2015; 7:3916–3922. DOI:10.1002/cctc.201500747

[139] Alvaro M, Carbonell E, Ferrer B, Llabrés i Xamena FX, Garcia H. Semiconductor behavior of a metal-organic framework (MOF). Chem. Eur. J. 2007; 13:5106–5112. DOI:10.1002/chem.200601003

[140] Llabrés i Xamena FX, Corma A, Garcia H. Applications for metal-organic frameworks (MOFs) as quantum dot semiconductors. J. Phys. Chem. C 2007; 111:80–85. DOI:10.1021/jp063600e

[141] Wen L-L, et al. Structures, photoluminescence, and photocatalytic properties of six new metal–organic frameworks based on aromatic polycarboxylate acids and rigid imidazole-based synthons. Crystal Growth Des. 2009; 9:3581–3589. DOI:10.1021/cg900317d

[142] Yu Z-T, Liao Z-L, Jiang Y-S, Li G-H, Chen J-S. Water-insoluble Ag–U–organic assemblies with photocatalytic activity. Chem. Eur. J. 2005; 11:2642–2650. DOI:10.1002/chem.200401189

[143]   Yang LM, Pushpa R. Tuning electronic and optical properties of a new class of covalent organic frameworks. J. Mater. Chem. C 2014; 2:2404–2416. DOI:10.1039/c3tc32252a

[144]   Yang L-M, Fang G-Y, Ma J, Ganz E, Han SS. Band gap engineering of paradigm MOF-5. Crystal Growth Des. 2014; 14:2532–2541. DOI:10.1021/cg500243s

[145]   Zhang H, Zhou Y, Song X. Advanced functional materials derived from metal-organic frameworks. Prog. Chem. 2015; 27:174–191. DOI:10.7536/PC140925

[146]   Odoh SO, Cramer CJ, Truhlar DG, Gagliardi L. Quantum-chemical characterization of the properties and reactivities of metal–organic frameworks. Chem. Rev. 2015; 115:6051–6111. DOI:10.1021/cr500551h

[147]   Shen L, et al. Noble-metal-free MoS2 co-catalyst decorated UiO-66/CdS hybrids for efficient photocatalytic H2 production. Appl. Catalysis B Environ. 2015; 166–167, 445–453. DOI:10.1016/j.apcatb.2014.11.056

[148]   Gao ST, et al. Integration of a plasmonic semiconductor with a metal-organic framework: a case of Ag/AgCl@ZIF-8 with enhanced visible light photocatalytic activity. RSC Adv. 2014; 4:61736–61742. DOI:10.1039/c4ra11364k

[149]   Xie MH, Yang XL, Zou C, Wu CD. A Sn IV-porphyrin-based metal-organic framework for the selective photo-oxygenation of phenol and sulfides. Inorg. Chem. 2011; 50:5318–5320, DOI:10.1021/ic200295h

[150]   Zhan W-w, et al. Semiconductor@Metal–organic framework core–shell heterostructures: a case of ZnO@ZIF-8 nanorods with selective photoelectrochemical response. J. Am. Chem. Soc. 2013; 135:1926–1933. DOI:10.1021/ja311085e

[151]   Lee DY. Cu-based metal–organic frameworks for photovoltaic application. J. Phys. Chem. C 2014; 118:16328–16334. DOI:10.1021/jp4079663

[152]   Lee DY. Layer-by-layer deposition and photovoltaic property of Ru-based metal-organic frameworks. RSC Adv. 2014; 4:12037–12042. DOI:10.1039/C4RA00397G

[153]   Shi L. An amine-functionalized iron(III) metal–organic framework as efficient visible-light photocatalyst for Cr(VI) reduction. Adv. Sci. 2015; 2:n/a–n/a. DOI:10.1002/advs.201500006

[154]   Shen L, Wu W, Liang R, Lin R, Wu L. Highly dispersed palladium nanoparticles anchored on UiO-66(NH2) metal-organic framework as a reusable and dual functional visible-light-driven photocatalyst. Nanoscale 2013; 5:9374–9382. DOI:10.1039/c3nr03153e

[155]   Shen L, Wu W, Liang R, Lin R, Wu L. Highly dispersed palladium nanoparticles anchored on UiO-66(NH2) metal-organic framework as a reusable and dual functional visible-light-driven photocatalyst. Nanoscale. 2013; 5(19):9374–82. DOI:10.1039/c3nr03153e

Indium-Containing Visible-Light-Driven (VLD) Photocatalysts for Solar Energy Conversion and Environment Remediation

Xiangchao Zhang, Duan Huang, Kaiqiang Xu, Difa Xu, Fang Liu and Shiying Zhang

Additional information is available at the end of the chapter

Abstract

Indium-containing visible-light-driven (VLD) photocatalysts including indium-containing oxides, indium-containing sulfides, indium-containing hydroxides, and other categories have attracted more attention due to their high catalytic activities for oxidation and reduction ability under visible light irradiation. This chapter will therefore concentrate on indium-containing nano-structured materials that demonstrate useful activity under solar excitation in fields concerned with the elimination of pollutants, partial oxidation and the vaporization of chemical compounds, water splitting, and CO_2 reduction processes. The indium-containing photocatalysts can extend the light absorption range and improve the photocatalytic activity by doping, heterogeneous structures, load promoter, and morphology regulation. A number of synthetic and modification techniques for adjusting the band structure to harvest visible light and improve the charge separation in photocatalysis are discussed. In this chapter, preparation, properties, and potential applications of indium-containing nano-structured materials used as photocatalysis will be systematically summarized, which is beneficial for understanding the mechanism and developing the potential applications.

Keywords: photocatalysis, visible-light-driven (VLD), indium-containing, solar energy conversion, environment remediation

1. Introduction

The current rapid industrial development causes the serious energy and environmental crises. Since Fujishima [1] reported the photocatalytic activity of TiO_2, the research enthusiasm has not diminished. Semiconductor photocatalysis has received much attention as a potential solution to the worldwide energy shortage and for counteracting environmental degradation. Photocatalysis is a light-driven chemical process over the surface of photocatalyst that can produce hydrogen from water, convert solar energy into electric energy, degrade organic pollutants, and reduce CO_2 into organic fuels [2]. Photocatalyts provide a potential strategy to solve these problems because these materials not only convert solar energy directly into usable or storable energy resources, but can also decompose organic pollutants under solar-light irradiation [3–9].

Over the past several years, researchers have made considerable effort to increase the visible-light-driven (VLD) photocatalytic activity of the photocatalysts [10, 11]. There are two strategies employed in the design of the VLD photocatalysts. One is the chemical modifications on a UV-active photocatalyst, including doping of foreign elements or coupling with a narrow band gap semiconductor. In order to extend the absorption of light into the visible region, three approaches have been widely used on semiconductors: (I) modification of the VB, (II) adjustment of the CB, and (III) continuous modulation of the VB and/or CB (see **Figure 1**) [12]. The other is to develop novel photocatalysts with VLD photocatalytic activity. The development of photocatalysts under visible light irradiation is one of the major goals for enhancing the efficient utilization of solar energy and realizing practical industrialization.
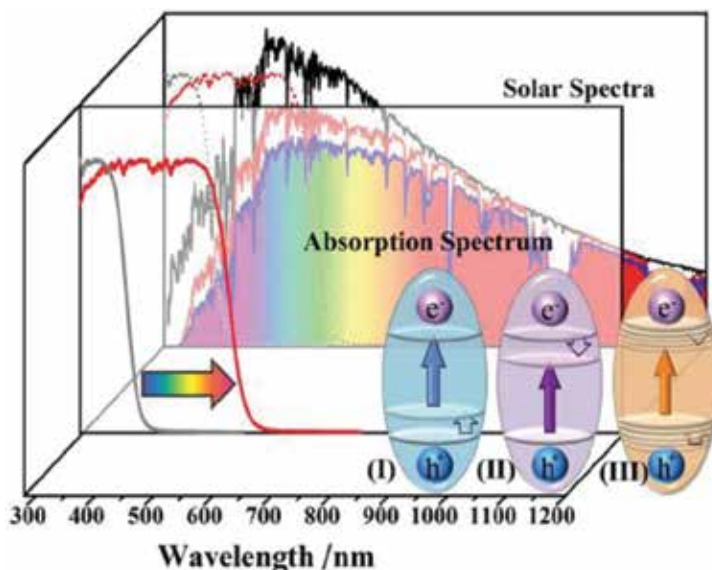

Figure 1. Three strategies to narrow the band gap of semiconductor photocatalysts to match the solar spectrum [12].

Recently, photocatalysis driven by visible light has gained great attention, as the visible light occupies most part of the solar spectrum such as: bismuth compounds (Bi_2WO_6 [13], Bi_2MoO_6 [14], $BiVO_4$ [15], $BiOBr$ [16]), silver compounds($AgAlO_2$ [17], Ag_2CrO_4 [18], Ag_2CO_3 [19], $AgVO_3$ [20], Ag_3PO_4 [21]), and indium compounds(In_2O_3 [22], $CaIn_2O_4$ [23], $InVO_4$ [24], In_2S_3 [25]). Up to now, much attention has been given to a series of visible light active indium compound. The In 5s orbital in the valence band of the semiconductor may hybrid with O 2p or S 2p orbital to form a new energy level, which could narrow the band gap of the indium compound and enhance the photocatalytic activity with the visible light irradiations [26]. Many novel indium-containing VLD photocatalysts were reported. Herein we review the fundamental challenges and recent progress on indium-containing VLD photocatalysts.

Starting with a brief introduction, we will give an overview on the development of high-efficiency, indium-containing VLD photocatalysts. Section 2 covers indium-containing oxides including single-metal oxide (In_2O_3), double-metal containing indium oxides $A_xB_yO_z$ (A site containing indium compounds $InMO_4$ (M=V, Nb, Ta), B site containing indium compounds $AInO_2$ (A=Ag, Na, Li), MIn_2O_4 (M = Ca, Sr, Ba). Section 3 describes systems involving indium based sulfides such as single-metal sulphide (In_2S_3), double-metal containing indium sulfides AIn_xS_y (A=Na, Cu, Ag, Cd, Zn), and containing indium solid solution ZnS-CuInS_2-AgInS_2, $(CuIn)_xZn_{2(1-x)}S_2$. Indium-containing hydroxides will be discussed in section 4. A number of synthetic and modification techniques for adjusting the band structure to harvest visible light and improve the charge separation in photocatalysis are discussed. A comparative analysis of the systems discussed and their future projection as environmentally friendly photocatalytic systems will conclude the review. Finally, some feasible ways to design and improve the visible-light responding photocatalysts are concluded, and the development of indium-containing oxides semiconductor photocatalysts is also proposed.

The application of indium-containing VLD photocatalysts for solar energy conversion and environment remediation as an important challenge will be listed. We aim to put together the research effort having been made so far, with a view of providing a good reference and inspiring new ideas for tackling this important challenge. In this chapter, preparation, properties, and potential applications of indium-containing nano-structured materials used as photocatalysts will be systematically summarized, which is beneficial for mechanism understanding and developing potential applications.

2. Indium-containing oxides

2.1. Indium oxide

Recently, the reported research has investigated In_2O_3 in an attempt to develop novel photocatalysts for water splitting. In_2O_3 fulfils some important requirements for the direct photo electrolysis of water such that the position of the conduction and valence band edges bracket the radix potentials of water, and In_2O_3 has an excellent conductivity and stability. In_2O_3 generally exists in two forms: cubic (C-In_2O_3) and hexagonal (H-In_2O_3). Currently, there are reports on the morphology of In_2O_3 mostly in the cubic structure of C-In_2O_3 and a few hexagonal structure of H-In_2O_3. So far, researchers have successfully synthesized the In_2O_3

with various morphology such as particles [27], fibers [28], porous particles [29], and cubes of nanostructures [30]. **Figure 2** shows the SEM images of In_2O_3 nanostructures with different morphologies.
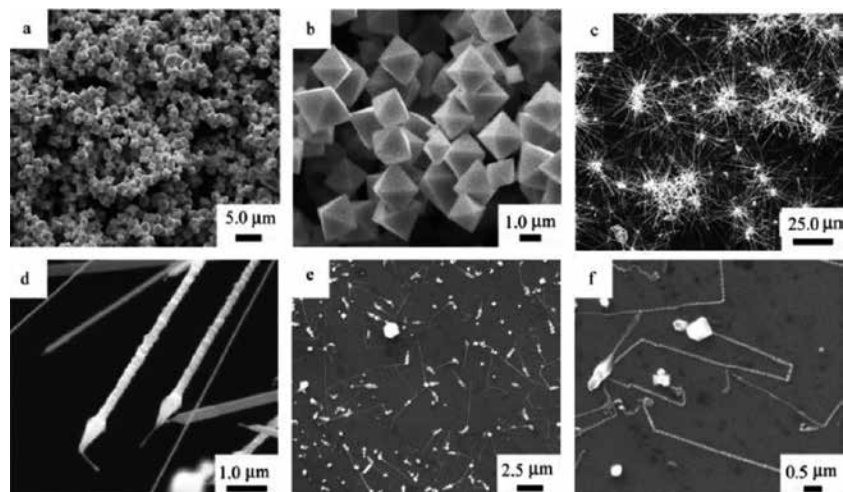

Figure 2. SEM images of In_2O_3 nanostructures with different morphologies synthesized at 800℃ for 1 h: a, b-octahedrons; c, d-nanobelts and dentate nanowires; e, f-nanocrystal chains [31].

In_2O_3 is transparent to visible light because of its wide band gap (E_g=3.55-3.75 eV) [31], which decreases its potential efficiency for water splitting under solar illumination. In_2O_3 was modified by various methods. The results showed that the modified In_2O_3 have better response in the visible light region and have higher photocatalytic activity than In_2O_3. For example, Karla et al. [32] reported that N-doped In_2O_3 were prepared and found that the rate of decomposition of water under visible light has improved compared with pure In_2O_3. Compared to ion doping methods, constructing compound semiconductor heterojunction broaden the optical response range and effectively, the separation of electrons and holes. Li et al. [33] successfully synthesized heterojunction CuO/In_2O_3 composite photocatalysts by hydrothermal method. Under visible light, Rhodamine B as the target pollutants examined the catalytic properties of the composite photocatalysts and found its catalytic activity much higher than pure In_2O_3. The enhanced photocatalytic activity is due to the CuO and In_2O_3 forming heterogeneous structures, which can effectively improve the separation efficiency of the light-generated charge and extend the light absorption range. For solid solutions consisting of Ga_2O_3 and In_2O_3, $Ga_{1.14}In_{0.86}O_3$ showed the highest photocatalytic activity for H_2 evolution from aqueous methanol solutions and for O_2 evolution from aqueous silver nitrate solutions. In comparison, the solid solutions of Y_2O_3 and In_2O_3, $Y_{1.3}In_{0.7}O_3$, showed the highest photocatalytic activity for the overall water splitting when combined with RuO_2 as a promoter.

So far, the preparation methods of In_2O_3 mainly are thermal evaporation (TE) [34], chemical vapour deposition (CVD) [35], laser ablation (PLD) [36], metal organic chemical vapour deposition (MOCVD) [37], and a variety of wet chemical methods [38–40]. Among them, the

characteristic of wet chemical method is the lowest preparation temperature, but their degree of crystallinity is poor; their morphology is mainly nanowire hexagonal structure, nanoparticles, and squares. In addition to the main method as described above, preparation cubic In_2O_3 by processing the precursor material is also suffering much attention [41–43].

2.2. Double-metal containing indium oxides

Double-metal containing indium oxides $(A_xB_yO_z)$ due to the different site of element In position (A or B bits), can be divided into two categories: A site containing indium compounds $InMO_4$(M=V, Nb, Ta), B site containing indium compounds $AInO_2$ (A=Ag, K, Na, Li), MIn_2O_4 (M = Ca, Sr, Ba).

2.2.1. A site containing indium oxides

$InMO_4$ (M = V, Nb, Ta) compounds belong to ABO_4 compound, where In is in A bit. Their crystal structures were: $InNbO_4$ ($InTaO_4$) belong to monoclinic system with octahedral InO_6 and NbO_6 (TaO_6); $InVO_4$ belongs to orthorhombic system with octahedral InO_6 and tetrahedral VO_4. $InTaO_4$ was 5d compound (E_g = 2.6 eV), $InNbO_4$ was 4d compound (E_g = 2.5 eV), and $InVO_4$ was 3d compound (E_g = 2.0 eV), bandgap of the $InMO_4$ compound with M from 5d Ta to 4d Nb to 3d V reduced [44]. Song et al. [45] prepared one-dimensional $InVO_4$ nanofibers with width of 30-100 nm under visible light illuminated through 6 h, wherein the nitrobenzene degradation reached 69%. Zou [46] prepared $InMO_4$ (M = Nb^{5+}, Ta^{5+}) by high-temperature solid phase method. Under visible light (λ > 420 nm) irradiation, the hydrogen production rate of $InMO_4$ (M = Nb^{5+}, Ta^{5+}) is that of P25, 4.0 and 3.5 times, respectively. Meanwhile, the $InMO_4$ (M = V, Nb, Ta) photocatalysts were modified by doping heterogeneous structures method. The results showed that visible light absorption and photocatalytic activity of $InVO_4$ after modification had been enhanced [47, 48]. Zhang et al. [49] prepared graphene (Gr)/ $InNbO_4$ composite photocatalysts by hydrothermal method from which the apparent rate constant of (0.0346 min^{-1}) degradation MB is higher than pure $InNbO_4$ (0.0185 min^{-1}) under visible light illumination.

$InVO_4$, due to suitable conduction band can be a promising photocatalyst for H_2 production under visible light irradiation. In addition, there are many reports indicating that the desired morphology and size of photocatalysts could regulate the position of the energy band to achieve higher radix ability. Yan et al. [50] reported that the nanosized $InVO_4$ nanoparticles with the size of 20 nm showed higher photocatalytic activity of H_2 production than $InVO_4$ microspheres. Hu et al. [51] synthesized g-C_3N_4/nano-$InVO_4$ heterojunction-type photocatalysts by in situ growth of $InVO_4$ nanoparticles onto the surface of g-C_3N_4 sheets via hydrothermal process. The formation of interfaces could promote the charge transfer and inhibit recombination of charge-hole pairs, which significantly improved the photocatalytic activity of H_2 evolution of 212 µmol/g·h from water-splitting. **Figure 3** is a schematic illustration of g-C_3N_4/$InVO_4$ composite under visible light irradiation.

Currently, these are the following methods for synthetic $InVO_4$: solid-phase synthesis [52], which is difficult to obtain a large surface area, pore volume, and a high mesoporous materi-

als; mesoporous $InVO_4$ obtained by sol-gel method [53] are disorderly, has wide pore size distribution, pore walls were generally amorphous, and with poor thermal stability; surfactant templating method [54] can obtain larger surface area mesoporous $InVO_4$, but the manufacturing process requires high temperatures and the morphology is irregular.
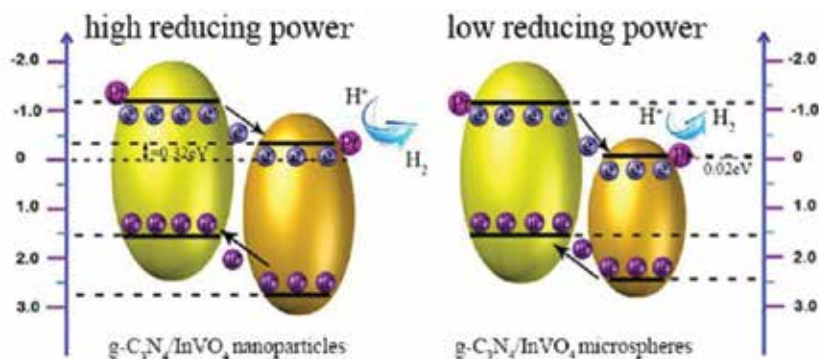

Figure 3. Schematic illustration of g-C$_3$N$_4$/InVO$_4$composite under visible light irradiation [51].

2.2.2. B site containing indium oxides

Photochemical dye degradation has been limited by the efficiency of the catalyst materials with respect to photon absorption. An ideal catalyst would be capable of using as much of the solar spectrum as possible, in particular the visible region. As we know, delafossites structure of materials have the potential to provide this photoactivity. These materials have the general formula ABO_2 and are based on the mineral $CuFeO_2$, also known as delafossite. $AInO_2$ (A = Ag, K, Na, Li) belong to ternary oxide ABO_2, where In is in B bit. Crystal structure of $AgInO_2$, $LiInO_2$ and $NaInO_2$ are delafossite, α-$LiFeO_2$ and α-$NaFeO_2$, respectively. The band gap values of $AgInO_2$, $LiInO_2$ and $NaInO_2$ are 2.0eV, 3.7eV and 3.9eV, respectively. These materials share the ability to alter the band structure by using chemical substitution. In particular, substitution on the B-site in these materials can be used to tune the physical properties of delafossites for specific applications. $AgInO_2$ is a narrow bandgap semiconductor material which responds in the visible light range. Wang et al. [55] reported 0.5 wt% Pt/$NaInO_2$ can completely degrade MB in 1h. Jonathan et al. [56] reported the effect of electronic structure changes in $NaInO_2$ and $NaIn_{0.9}Fe_{0.1}O_2$ on the photo reduction of Methylene Blue. **Figure 4** shows the (A) crystal structure, (B) diffuse reflectance spectroscopy, and (C) energy level diagram of the $NaInO_2$ and $NaIn_{0.9}Fe_{0.1}O_2$, respectively. Diffuse reflectance spectroscopy was used to determine the band gap values of 3.9 eV and 2.8 eV for $NaInO_2$ and $NaIn_{0.9}Fe_{0.1}O_2$, respectively. Energy level diagram describing the flat band (EFB; dashed line), conduction band (ECB), and valence band (EVB) potentials of TiO_2, $NaInO_2$, and $NaIn_{0.9}Fe_{0.1}O_2$ in relation to some relevant electrochemical radix couples; potentials are in the reversible hydrogen electrode (RHE) scale (b). The spread in CB and VB potentials represents the experimental uncertainty in band edge determination.
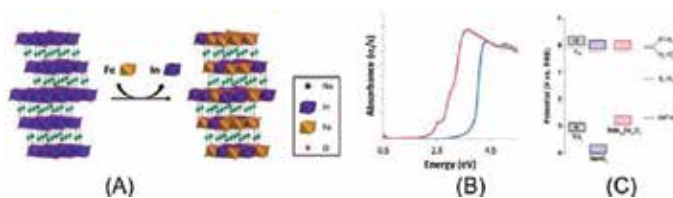
Figure 4. (A) Rhombohedral crystal structure,(B) Diffuse reflectance spectroscopy, and (C) Energy level diagram of the $NaInO_2$ and $NaIn_{0.9}Fe_{0.1}O_2$ [56].

MIn_2O_4 (M = Ca, Sr, Ba) belongs to the family of ternary oxide AB_2O_4, where In is in B bit. Their crystal structures are: $CaIn_2O_4$ and $SrIn_2O_4$ having the same octahedral InO_6 network structure, and $BaIn_2O_4$ having a more complex polyhedron InO_x structure. Sato and Tang team synthesized a series of photocatalysts MIn_2O_4 (M = Ca, Sr, Ba) and studied the crystal and electronic structure of the photocatalysts relationship with their visible light photocatalytic activity. Sato group [57] found that different crystal structures of MIn_2O_4 (M = Ca, Sr, Ba) have an impact on their photocatalytic activity. The crystal structures of $CaIn_2O_4$ and $SrIn_2O_4$ are orthorhombic and $BaIn_2O_4$ was monoclinic. The order of catalytic activity of water splitting in the xenon lamp irradiation were: $CaIn_2O_4 > SrIn_2O_4 > BaIn_2O_4$. Tang et al. [58] prepared MIn_2O_4 (M = Ca, Sr, Ba) by solid phase methods. They fall in the visible order solution MB catalytic activity were: $CaIn_2O_4 > SrIn_2O_4 > BaIn_2O_4$, wherein $CaIn_2O_4$ showed the highest activity (**Figure 5**). The reason of the order activity is that mesh structure of $CaIn_2O_4$ and $SrIn_2O_4$ helps photogenerated electron transfer. Inoue et al. [59] investigated the photocatalytic properties for water decomposition of alkali metal, alkaline earth metal, and lanthanum indates with an octahedrally coordinated In^{3+} d10 configuration ion. The photocatalytic activity for water decomposition under UV irradiation was considerably large for RuO_2-dispersed $CaIn_2O_4$, $SrIn_2O_4$, and $Sr_{0.93}Ba_{0.07}In_2O_4$ but very poor for RuO_2-dispersed $AInO_2$ (A = Li, Na) and $LnInO_3$ (Ln = La, Nd). The geometric structures of the InO_6 octahedral units for these indate were compared. As shown, the photo-catalytic active indates possessed distorted InO_6 octahedral with dipole moments. The internal fields that arose due to the dipole moment promoted the charge separation in the initial process of photo-excitation.
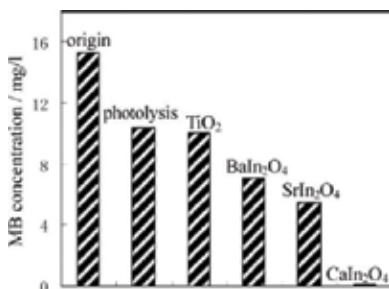

Figure 5. MB original concentration, MB photolysis and its concentration variation after 120 min visible light irradiation ($\lambda > 420$ nm) on the different oxides [58].

3. Indium-containing sulfide

Indium based sulphides include single-metal sulfide (In_2S_3), double-metal containing indium sulfides AIn_xS_y (A = Na, Cu, Ag, Cd, Zn), and containing indium solid solution ZnS-$CuInS_2$-$AgInS_2$, $(CuIn)_xZn_{2(1-x)}S_2$. Compared with indium-containing oxides, Indium based sulphides has narrow band gap which can make good use of visible light and have been extensively studied. But its low stability, prone to light decay, and other shortcomings limit its further application.

3.1. Indium sulfide

In_2S_3 have three different forms of structural defects: α-In_2S_3(defect cube), β-In_2S_3(defect spinel, cubic, or tetragonal structure), and γ-In_2S_3 (layered hexagonal). The band gap of In_2S_3 is E_g=1.9-2.3 eV [60], and it belongs to the n-type narrow band gap semiconductor. Researchers mostly used solvothermal or hydrothermal methods to prepare excellent performance of visible light photocatalyst In_2S_3. Liu et al. [61] prepared tetragonal β-In_2S_3 nanotube by solvothermal method. The nanotube with diameter of about 10-20 nm, pipe wall thickness of 2 nm, tube length 1μm, and under simulated sunlight degraded Rhodamine with high rate. In addition, the researchers have further explored In_2S_3, such as the following: (1) the relationship between crystal or precious metal co-catalyst species and the catalytic activity and selectivity of light catalysis: Xing et al. [62] prepared a heterogeneous structure photocatalyst In_2S_3/g-C_3N_4 by hydrothermal method and they found 40 wt% In_2S_3/g-C_3N_4 degradation RhB rate in 30 min, can be 96% under visible light ($\lambda > 420$ nm) irradiation, far higher than the 50% of pure In_2S_3; (2) the relationship between crystal or precious metal co-catalyst species: Fu et al. [63] reported the preparation of the tetragonal and cubic phases In_2S_3 by hydrothermal method, both of their photocatalytic hydrogen production under visible light were investigated (**Figure 6**). The results showed that ordered tetragonal In_2S_3 has no hydrogen production activity, while disordered cubic structure In_2S_3 showed stable photocatalytic hydrogen production activity. At the same time, the authors also investigated the effect of precious metal as co-catalyst on the order photocatalytic activity of In_2S_3 and results are: Pd>Pt>Ru>Au; (3) the catalytic activity and selectivity of light catalysis: Xie et al. [64] used the microspheres In_2S_3 prepared by hydrothermal method, with selective degradation using 41.4% benzyl alcohol in 4 h invisible light.

Currently, researchers have explored a variety of ways for preparing In_2S_3 with different morphology. For example: Afzaal et al. [65] used high temperature vapour deposition to get In_2S_3 nanorods on a glass substrate. Liu et al. [66] used indium nitrate as an indium source, dodecyl mercaptan as a sulfur source to synthesis β-In_2S_3 nanotube structure with nanotube length of 1-10 μm, and width less than 15 nm by pyridine solvent thermal reaction method. Son et al. [67] reported the use of $InCl_3 \cdot 4H_2O$ and elemental sulfur as a precursor with a certain proportion of the oleylamine oil, then obtained hexagonal indium sulfide nanosheets with thickness of 0.76 nm. In addition, the researchers also used the hot water or solvent hot methods for preparing a variety of three-dimensional structures In_2S_3, such as flower microspheres [68], hollow microspheres [69], and dendrites [70].
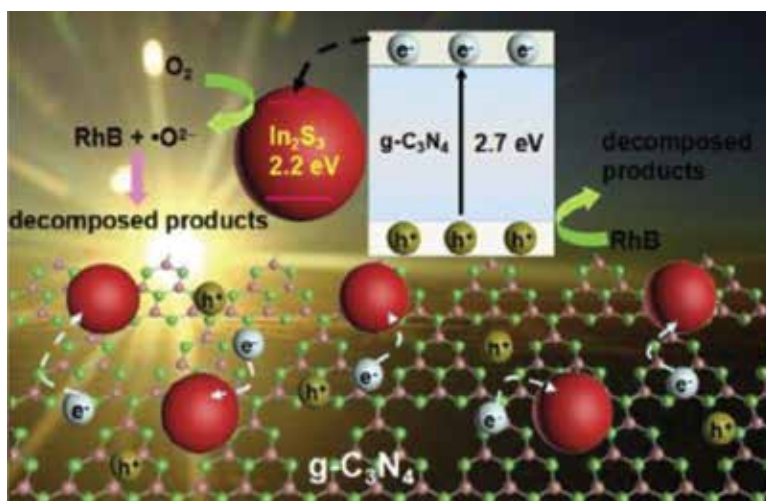
Figure 6. Schematic illustration of the $In_2S_3/g-C_3N_4$ photocatalytic reaction process under visible light irradiation [62].

3.2. Double-metal containing indium sulfide

The band gap of double-metal containing indium sulphides AIn_xS_y (A = Na, Cu, Ag, Zn) range from 1.87 to 2.5eV which have light response in the visible light. In recent years, the AIn_xS_y as visible light catalyst have been extensively studied with focus mainly on $ZnIn_2S_4$.

$ZnIn_2S_4$ is a II-III-VI family ternary metal sulfides with hexagonal and cubic spinel structure and have narrow band gap (E_g = 2.1-2.4 eV). $ZnIn_2S_4$ has strong light absorption in the visible region which is worth studying as a visible light catalyst. Li et al. [71] were first using $ZnIn_2S_4$ on visible light catalytic hydrogen. Hexagonal $ZnIn_2S_4$ (space group P3m1) is a typical layered compound and the band gap is about 2.4 eV (CB: –0.29 eV vs NHE; VB: 2.11 eV vs NHE) which have a strong and appropriate response on visible light. Li et al. [72] prepared cubic $ZnIn_2S_4$ nanoparticles and hexagonal phase $ZnIn_2S_4$ microspheres by changing the indium precursor and then investigated two crystal phases $ZnIn_2S_4$ degrade methyl orange in visible light. The results showed cubic phase $ZnIn_2S_4$ having activity just at the beginning, while the hexagonal phase has shown a high catalytic activity.

Researchers modified $ZnIn_2S_4$ to further improve its photocatalytic activity by means of ion doping and semiconductor composite. Wen-Hui Yuan group [73] first reported that doping N can improve visible light photocatalytic activity of $ZnIn_2S_4$ degradation of MB. Shen et al. [74] reported composite photocatalysts $Cu-ZnIn_2S_4$ have higher visible light catalytic activity than pure $ZnIn_2S_4$ (**Figure 7**).

So far, the preparation methods of $ZnIn_2S_4$ mainly are: chemical precipitation method [75], precursor route [76], hydrothermal method [77], microwave-hydrothermal method [78], solid phase method [79], the template [80], and so on. Among them, the hydrothermal method is the typical preparation method, which is more beneficial to controlling the different morphologies of $ZnIn_2S_4$.
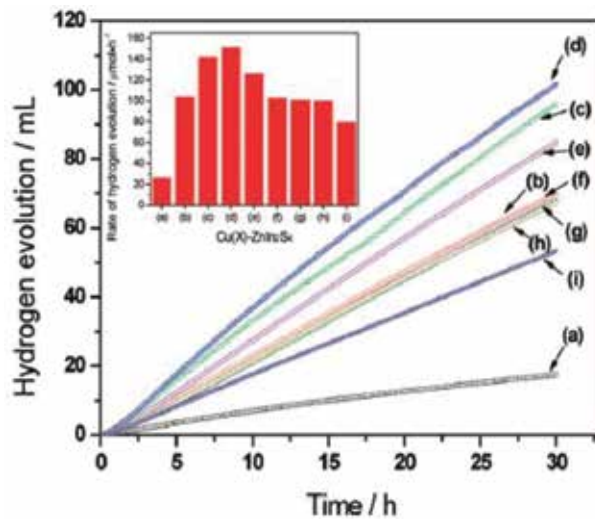
Figure 7. Hydrogen production under visible-light irradiation over Cu(X)-ZnIn$_2$S$_4$; the values of X were (a) 0.0 wt%, (b) 0.1 wt%,(c) 0.3 wt%, (d) 0.5 wt%, (e) 0.7 wt%, (f) 0.9 wt%, (g) 1.2 wt%, (h)1.6 wt%, (i) 2.0 wt%[74].

CdIn$_2$S$_4$ also is a kind of II-II-VI family ternary metal sulphides, its band gap E$_g$=2.12-2.29 eV [81]. Researchers prepared different morphologies CdIn$_2$S$_4$ by different methods and studied their visible light photocatalytic activity. Bhirud et al. [81] prepared different morphologies CdIn$_2$S$_4$. When not added, the active agent was flower shape; adding a surfactant polyvinyl-pyrrolidone was double cone; adding a surfactant CTAB was hollow spheres. Three differ-ent morphologies CdIn$_2$S$_4$ catalysed water splitting under visible light have shown different catalytic activity and double cone is the highest (3238 μmol. (g.h)$^{-1}$). Mu et al. [82] prepared spherical particles CdIn$_2$S$_4$ with average size of 236 nm from which degradation rate for methyl orange is 98% in the visible light illumination.

=2.12-2.29 eV [56AgIn$_x$S$_y$ include AgInS$_2$ and AgIn$_5$S$_8$. AgInS$_2$ has chalcopyrite (t-AgInS$_2$) and orthogonal (o-AgInS$_2$) two crystal phases and the band gap values respectively were 1.87 and 1.98 eV [83, 84]; AgIn$_5$S$_8$ is cubic crystalline phase (c-AgIn$_5$S$_8$) and its the band gap value is 1.7-2.0 eV [85]. Both of the degrading organic substances under visible light irradiation exhibited good photocatalytic properties [86, 87]. NaInS$_2$ belongs to a narrow band gap semiconductor material (E$_g$ = 2.3 eV) [88]. Researchers applied hydrogen production and degradation of organic pollutants under visible light [88, 89].

3.3. Solid solution containing indium sulfide

Solid solution containing indium adjust the content of the different components of the solid solution to achieve the band gap of a solid solution of regulation. For now, there are reports of solid solution system ZnS-CuInS$_2$, ZnS-AgInS$_2$, and ZnS-AgInS$_2$-CuInS$_2$. In this regard, Kudo teams have done a lot of research. Tsuji group [90, 91] used ZnS and narrow bandgap CuInS$_2$ or AgInS$_2$ by calculating to form a visible light catalyst (CuIn)$_x$Zn$_{2(1-x)}$S$_2$, (AgIn)$_x$Zn$_{2(1-x)}$S$_2$, and ZnS-CuInS$_2$-AgInS$_2$. Guo [92, 93] prepared (CuIn)$_x$Zn$_{2(1-x)}$S$_2$ (x = 0.01–0.5) solid solution

using CTAB as surfactant by hydrothermal method. Compared with the method used by Kudo group, their method has no calcination and the products have smaller particle size. Studies have shown that with the increase of x value, the absorption band edge of $(CuIn)_xZn_{2(1-x)}S_2$ became obvious red shift and the composition of the solid solution have great influence on hydrogen production performance (**Figure 8**).
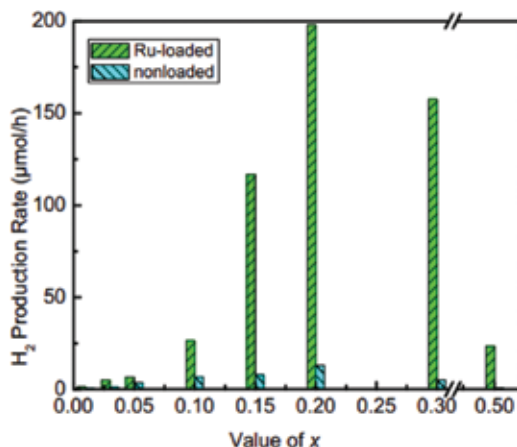

Figure 8. The photocatalytic hydrogen production activities of $(CuIn)_xZn_{2(1-x)}S_2$ solid solutions under visible-light irradiation [92].

In recent years, containing indium solid solution has made great progress in China. Guijun Ma [94] who belongs to CAS Dalian Institute of Physical Chemistry used solvothermal method to synthesize $CuInS_2$-ZnS solid solution. Compared with the results of Kudo, their products have smaller particle size (average particle size 30-50 nm) and exhibit stable photocatalytic hydrogen production. Chen et al. [95, 96] from Harbin Institute of Technology synthesized nano-porous solid solution photocatalysts ZnS-In_2S_3-Ag_2S and ZnS-In_2S_3-CuS by self-assembled solvothermal method. Under visible light, the photocatalysts exhibit excellent photocatalytic hydrogen performance and the apparent quantum yield is 19.8% and 22.6%, respectively.

Kudo et al. [97] synthesized $(AgIn)_xZn_{2(1-x)}S_2$(x = 0.17–0.5) solid solutions. The band gaps can be tuned from 2.40 to 1.95 eV, which lie between that of ZnS and $AgInS_2$ (**Figure 9A**). The intensive absorption bands with steep edges of the doped ZnS photocatalysts indicate that the visible light absorption was due to the band transition instead of the transition from impurity levels to the conduction band of ZnS. DFT calculations revealed that the valence band of it is mainly composed of hybrid orbitals of S 3p and Ag 4d, and the conduction band is composed of hybrid orbitals of In 5s5p +Zn 4s4p in $(AgIn)_xZn_{2(1-x)}S_2$ solid solution, which is located between those of ZnS and $AgInS_2$ (**Figure 9B**). The photocatalytic activity is greatly dependent on the composition and the Pt (3 wt%) loaded. $(AgIn)_{0.22}Zn_{1.56}S_2$ photocatalyst exhibited the highest activity for H_2 evolution in the presence of sacrificial reagent under visible light irradiation (λ > 420 nm); the quantum yield of the samples was as high as 20% at 420 nm.
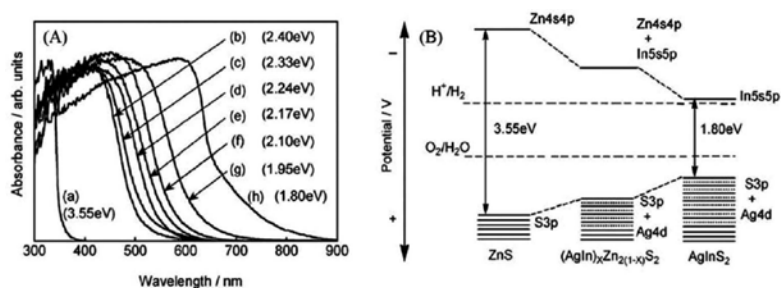
Figure 9. (A) Diffuse reflection spectra of $(AgIn)_xZn_{2(1-x)}S_2$ solid solutions; the values of x are (a) 0, (b) 0.17, (c) 0.22, (d) 0.29, (e) 0.33, (f) 0.40, (g) 0.5, and (h) 1. (B) Band structures of $(AgIn)_xZn_{2(1-x)}S_2$ solid solutions, ZnS and $AgInS_2$[97].

4. Indium-containing hydroxides

Indium-containing hydroxides include $In(OH)_3$ and $InOOH$. The band gap values were 5.15 eV and 3.70 eV respectively [98], and they belongs to the wide band gap semiconductor photocatalyst.

$In(OH)_3$ is a very important n-type photocatalyst and its crystal structure is: per In^{3+} ions with six OH^- ions constituting the octahedral structure and $In(OH)_3$ belongs to wide-band gap light catalyst which does not respond in the visible light range. The researchers modified it to try to expand its range of light absorption by a variety of methods. For example, Lei et al. [99] synthesized photocatalyst $In(OH)_yS_z$ by hydrothermal method. The result is that the absorption edge of $In(OH)_3$ followed S^{2-} substituted with OH^- moved from 240 nm to 570 nm (**Figure 10**).
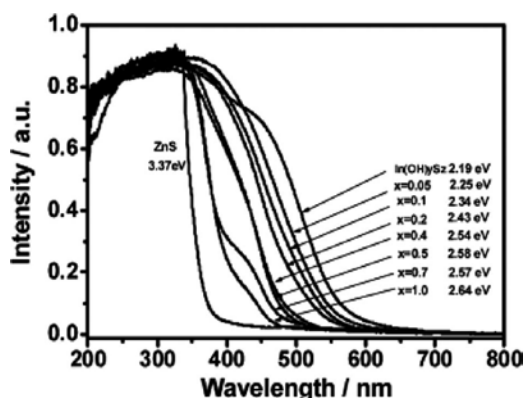

Figure 10. DRS of ZnS, $In(OH)_yS_z$ and $In(OH)_yS_z$:Zn catalysts with different X value (X denotes the atomic ratio of Zn/In in the synthesis solution). The $In(OH)_yS_z$ and $In(OH)_yS_z$:Zn were obtained with atomic ratio of S/In = 2.0 [99].

InOOH is orthorhombic crystal, compared with the crystal structure of $In(OH)_3$, InOOH can be seen as distorted octahedral InO_6 co-built by the edge of the way. Researchers, through the composite doping methods such as wide band gap photocatalyst InOOH modified to the scope and the absorption of visible light photocatalytic activity. Song et al. [100] prepared porous carbon spheres/InOOH composite photocatalyst by in-situ reaction. Compared with the pure InOOH, the composite photocatalyst of optical absorption edge had undergone a drastic red shift and improved the visible light photocatalytic activity. Ge et al. [101] reported that N, C doping InOOH has a response in the visible light range due to the doping, and narrowing of the band gap of InOOH (**Figure 11**).
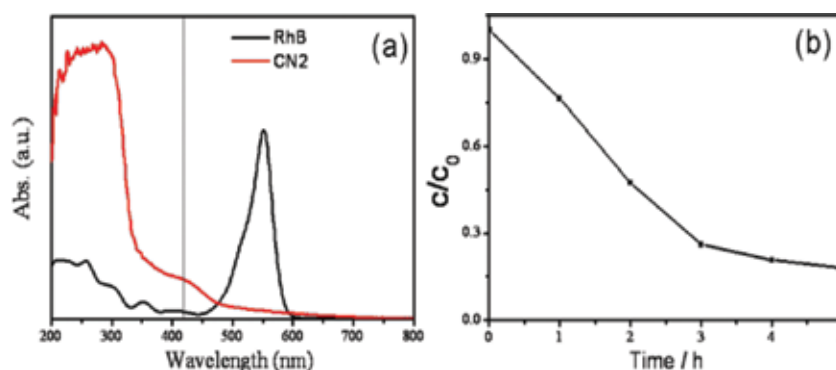

Figure 11. Comparison of UV-vis diffuse reflectance spectral of CN_2 and RhB (a) and the photo degradation efficiencies of RhB by 0.1 g of CN_2 under monochromatic light source (λ= 420 nm) (b). C_0 and C are the initial concentration after the adsorption equilibrium and temporal concentration of RhB at different times, respectively [101].

5. Conclusion and prospective

The use of semiconductor materials photocatalytic degradation organic pollutants and producing hydrogen has very important significance for environmental management, and energy depletion. However, the low visible light catalytic efficiency has hampered the development of photocatalytic technology. There is an urgent task in developing new and efficient visible light catalytic system.

In summary, the indium-based photocatalytic materials have good visible response and strong visible light photocatalytic activity and possess broad prospects on photocatalytic water environment, capacity, and other degradation of organic pollutants. The current findings indicate that photocatalytic activity of indium-based photocatalysts is affected by its size, morphology, and crystal structure; doping, heterogeneous structures, load promoter, and morphology regulation methods can extend the light absorption range and improve the photocatalytic activity. Indium-based photocatalysts also have the following problems which needs to do further exploration and research:

1. At the moment, researches of indium-based photocatalysts mainly focus on degradation of organic compounds and hydrogen production with little research for CO_2 reduction, which may be the weakness of reducing capacity. Using widely the photocatalysts on CO_2 reduction by various channels to improve their reducing ability is needed.

2. Indium-based photocatalyst of electron transfer mechanism, carrier generation and recombination, free radical generation and detection, and photocatalytic mechanism of research reports is little and this may require deeper and more systematic research and inspection.

3. So far, the reports on some narrow band gap and good photoelectric properties of indium-based photocatalysts application on the visible light catalysis have not appeared yet. For example, InN ($E_g = 0.7$ eV) [102].

4. Finally, the high cost for all indium-based compound limited its large-scale application. Therefore, how to significantly reduce its production cost is an issue to consider.

Acknowledgements

Author details

Xiangchao Zhang[1*], Duan Huang[1,2], Kaiqiang Xu[1,2], Difa Xu[1], Fang Liu[1,2] and Shiying Zhang[1,2*]

*Address all correspondence to: xczhang@ccsu.edu.cn; cszhangsy@ccsu.edu.cn

1 Hunan Province Key Laboratory of Applied Environmental Photocatalysis, Changsha University, Changsha, Hunan, PR China

2 College of Material Science and Engineering, Hunan University, Hunan, PR China

References

[1] Fujishima A, Honda K. Electrochemical photolysis of water at a semiconductor electrode. Nature, 1972, 238(5358):37–38.

[2] Carey J H, Lawrence J, Tosine H M. Photodechlorination of PCB's in the presence of titanium dioxide in aqueous suspensions. Bulletin of Environmental Contamination & Toxicology, 1976, 16(6):697–701.

[3] Matsunaga T, Tomoda R, Nakajima T, et al. Photoelectrochemical sterilization of microbial cells by semiconductor powders. Fems Microbiology Letters, 1985, 29(1–2): 211–214.

[4] Fujishima A, Rao T N, Tryk D A. Titanium dioxide photocatalysis. Journal of Photochemistry & Photobiology C Photochemistry Reviews, 2000, 1(1):1–21.

[5] Farrauto R J, Heck R M. Environmental catalysis into the 21st century. Catalysis Today, 2000, 55:179–187.

[6] Muneer M, Philip R, Das S. Photocatalytic degradation of waste water pollutants. Titanium dioxidemediated oxidation of a textile dye, Acid Blue 40. Research on Chemical Intermediates, 1997, 23(3):233–246.

[7] Asahi R, Morikawa T, Ohwaki T, et al. Visible-light photocatalysis in nitrogen-doped titanium oxides. Science, 2001, 293(5528):269–271.

[8] Li D, Haneda H, Hishita S, et al. Visible-light-driven nitrogen-doped TiO_2 photocatalysts: effect of nitrogen precursors on their photocatalysis for decomposition of gas-phase organic pollutants. Materials Science & Engineering B, 2005, 117:67–75.

[9] Li S, Liao J J, Lin S W, et al. Researches progress on fabrication and doping as well as modification of titania nanotubes. Journal of the Chinese Society, 2011, 39(6):1034–1044. (In Chinese)

[10] Zhao Z Z, Xie Y D, Zhang B, et al. Advances on doped TiO_2 visible light driven photocatalysts. Bulletin of the Chinese Ceramic Society, 2012, 31(1):92–95.

[11] Zhuo W Y, Cao Q Y, Tang S Q, et al. Progress in improving visible light photocatalytic activity of nano-titanium dioxide. Journal of the Chinese Society, 2006, 34(7):861–867. (In Chinese)

[12] Tong H, Ouyang S, Bi Y, et al. Nano-photocatalytic materials: possibilities and challenges. Advanced Materials, 2012, 24(2):229–251.

[13] Ju W, Fang D, Yan Z, et al. Synthesis of Bi_2WO_6 nanoplate-built hierarchical nest-like structures with visible-light-induced photocatalytic activity. Journal of Physical Chemistry C, 2007, 111(34):12866–12871.

[14] Tian G, Chen Y, Zhou W, et al. Facile solvothermal synthesis of hierarchical flower-like Bi_2MoO_6 hollow spheres as high performance visible-light driven photocatalysts. Journal of Materials Chemistry, 2010, 3(3):887–892.

[15] Jiang H, Meng X, Dai H, et al. High-performance porous spherical or octapod-like single-crystalline $BiVO_4$ photocatalysts for the removal of phenol and methylene blue

under visible-light illumination. Journal of Hazardous Materials, 2012, 217–218(6):92–99.

[16] Zhang J, Shi F, Lin J, et al. Self-assembled 3-D architectures of BiOBr as a visible light-driven photocatalyst. Chemistry of Materials, 2008, 20(9):2937–2941.

[17] Shu X O, Hai T Z, Dun F L, et al. Electronic structure and photocatalytic characterization of a novel photocatalyst $AgAlO_2$. Journal of Physical Chemistry B, 2006, 110(24): 11677–11682.

[18] Xu D, Cao S, Zhang J, et al. Effects of the preparation method on the structure and the visible-light photocatalytic activity of Ag_2CrO_4. Beilstein Journal of Nanotechnology, 2014, 5(5):658–666.

[19] Xu C, Liu Y, Huang B, et al. Preparation, characterization, and photocatalytic properties of silver carbonate. Applied Surface Science, 2011, 257(20):8732–8736.

[20] Peng J, Fan H, Zhang B, et al. Enhanced photocatalytic activity of β-$AgVO_3$ nanowires loaded with Ag nanoparticles under visible light irradiation. Separation & Purification Technology, 2013, 109(109):107–110.

[21] Zhiguo Y, Jinhua Y, Naoki K, et al. An orthophosphate semiconductor with photooxidation properties under visible-light irradiation. Nature Materials, 2010, 9(7):559–564.

[22] Lu X, Yu Q, Wang K, et al. Synthesis, characterization and gas sensing properties of flowerlike In_2O_3 composed of microrods. Crystal Research & Technology, 2010, 45(5): 557–561.

[23] Tang J, Zou Z, Yin J, et al. Photocatalytic degradation of methylene blue on $CaIn_2O_4$ under visible light irradiation. Chemical Physics Letters, 2003, 382:175–179.

[24] Ye J, Zou Z, Oshikiri M, et al. A novel hydrogen-evolving photocatalyst $InVO_4$ active under visible light irradiation. Chemical Physics Letters, 2002, 356(3):221–226.

[25] Fu X, Wang X, Chen Z, et al. Photocatalytic performance of tetragonal and cubic β-In_2S_3 for the water splitting under visible light irradiation. Applied Catalysis B Environmental, 2010, 95(3):393–399.

[26] Yan S C, Luo W J, Li Z S, et al. Progress in research of novel photocatalytic materials. Online Journal, 2010, 29(1):1–9. (In Chinese)

[27] Epifani M, Siciliano P, Gurlo A, et al. Ambient pressure synthesis of corundum-type In_2O_3. Journal of the American Chemical Society, 2004, 126:4078–4079.

[28] Yu D, Wang D, Qian Y. Synthesis of metastable hexagonal In_2O_3 nanocrystals by a precursor-dehydration route under ambient pressure. Journal of Solid State Chemistry, 2004, 177(4–5):1230–1234.

[29] Huang J, Gao L. Synthesis and characterization of porous single-crystal-like In_2O_3 nanostructures via a solvothermal-annealing route. Journal of the American Ceramic Society, 2006, 89(2):724–727.

[30] Lee C H, Kim M, Kim T, et al. Ambient pressure syntheses of size-controlled corundum-type In_2O_3 nanocubes. Journal of the American Chemical Society, 2006, 24(2):105–112.

[31] Dong H X, Yang H Q, Yin W Y, et al. Controlled synthesis of octahedrons, nanobelts, dentate nanowires and nanocrystal chains of In_2O_3. Acta Chimica Sinica, 2007, 65(22): 2611–2617. (In Chinese)

[32] Reyes-Gil K R, Reyes-García E A, Raftery D. Nitrogen-doped In_2O_3 thin film electrodes for photocatalytic water splitting. Journal of Physical Chemistry, 2007, 111(39): 14579–14588.

[33] Li X, Lv N, Liang S, et al. Synthesis of In_2O_3/CuO heterojunctions and their photocatalytic activity under visible light irradiation. Chinese Journal of Luminescence, 2014, 35(6):695–700. (In Chinese)

[34] Chakraborty A K, Masudur R M, Emran H M, et al. Preparation of WO_3/TiO_2/In_2O_3 composite structures and their enhanced photocatalytic activity under visible light irradiation. Reaction Kinetics Mechanisms & Catalysis, 2014, 111(1):371–382.

[35] Wang Z L, Pan Z W, Dai Z R. Structures of oxide nanobelts and nanowires. Microscopy & Microanalysis the Official Journal of Microscopy Society of America Microbeam Analysis Society Microscopical Society of Canada, 2002, 8(6):467–474.

[36] Yang H F, Shi Q H, Tian B Z, et al. One-step nanocasting synthesis of highly ordered single crystalline indium oxide nanowire arrays from mesostructured frameworks. Journal of the American Chemical Society, 2003, 125(16):4724–4725.

[37] Li C, Zhang D, Han S, et al. Diameter-controlled growth of single-crystalline In_2O_3 nanowires and their electronic properties. Advanced Materials, 2003, 15(2):143–146.

[38] Kim H W, Kim N H, Lee C. An MOCVD route to In_2O_3 one-dimensional materials with novel morphologies. Applied Physics A, 2005, 81(6):1135–1138.

[39] Liu Q, Lu W, Ma A, et al. Study of quasi-monodisperse In_2O_3 nanocrystals: synthesis and optical determination. Journal of the American Chemical Society, 2005, 127(15): 5276–5277.

[40] Lu X, Yu Q, Wang K, et al. Synthesis, characterization and gas sensing properties of flowerlike In_2O_3 composed of microrods. Crystal Research & Technology, 2010, 45(5): 557–561.

[41] Yong L, Chim W K. Highly ordered arrays of metal/semiconductor core–shell nanoparticles with tunable nanostructures and photoluminescence. Journal of the American Chemical Society, 2005, 36(18):1487–1492.

[42] Wang C, Chen D, Jiao X, et al. Lotus-root-like In_2O_3nanostructures: fabrication, characterization, and photoluminescence properties. Journal of Physical Chemistry C, 2007, 111(36):13398–13403.

[43] Jun Y, Cui K L, Zhen L W, et al. $In(OH)_3$ and In_2O_3 nanorod bundles and spheres: microemulsion-mediated hydrothermal synthesis and luminescence properties. Inorganic Chemistry, 2006, 45(22):8973–8979.

[44] Yan Y, Cai F, Song Y, et al. $InVO_4$ nanocrystal photocatalysts: microwave-assisted synthesis and size-dependent activities of hydrogen production from water splitting under visible light. Chemical Engineering Journal, 2013, 233(11):1–7.

[45] Song L, Liu S, Lu Q, et al. Fabrication and characterization of electrospun orthorhombic $InVO_4$ nanofibers. Applied Surface Science, 2012, 258(8):3789–3794.

[46] Zou Z, Ye J, Arakawa H. Photophysical and photocatalytic properties of $InMO_4$ ($M=Nb^{5+}$, Ta^{5+}) under visible light irradiation. Materials Research Bulletin, 2001, 36(7): 1185–1193.

[47] Yan M, Yan Y, Wang C, et al. Ni^{2+} doped $InVO_4$ nanocrystals: one-pot microwave-assisted synthesis and enhanced photocatalytic O_2 production activity under visible-light. Materials Letters, 2014, 121(15):215–218.

[48] Shi W, Guo F, Chen J, et al. Hydrothermal synthesis of $InVO_4$/graphitic carbon nitride heterojunctions and excellent visible-light-driven photocatalytic performance for Rhodamine B. Journal of Alloys and Compounds, 2014, 612:143–148.

[49] Zhang X, Quan X, Chen S, et al. Constructing graphene/$InNbO_4$ composite with excellent absorptivity and charge separation performance for enhanced visible-light-driven photocatalytic ability. Applied Catalysis B Environmental, 2011, 105(105):237–242.

[50] Yan Y, Cai F, Song Y, Shi W. $InVO_4$ nanocrystal photocatalysts: microwave-assisted synthesis and size-dependent activities of hydrogen production from water splitting under visible light. Chemical Engineering Journal, 2013, 233(11):1–7.

[51] Hu B, Cai F, Chen T, et al. Hydrothermal synthesis g-C_3N_4/nano-$InVO_4$nanocomposites and enhanced photocatalytic activity for hydrogen production under visible light irradiation. ACS Applied Materials & Interfaces, 2015, 7(33):18247–18256.

[52] Ye J, Zou Z, Oshikiri M, et al. A novel hydrogen-evolving photocatalyst $InVO_4$ active under visible light irradiation. Chemical Physics Letters, 2002, 356(3):221–226.

[53] Xiao G, Wang X, Li D, et al. $InVO_4$-sensitized TiO_2 photocatalysts for efficient air purification with visible light. Journal of Photochemistry & Photobiology A Chemistry, 2008, 193(2):213–221.

[54] Xu L, Sang L, Ma C, et al. Preparation of mesoporous $InVO_4$ photocatalyst and its photocatalytic performance for water splitting. Chinese Journal of Catalysis, 2006, 27(2):100–102. (In Chinese)

[55] Wang J, Nonami T. Photocatalytic activity for methylene blue decomposition of $NaInO_2$ with a layered structure. Journal of Materials Science, 2004, 39(20):6367–6370.

[56] Lekse J W, Haycock B J, Lewis J P, et al. The effect of electronic structure changes in $NaInO_2$ and $NaIn_{0.9}Fe_{0.1}O_2$ on the photo reduction of methylene blue. Journal of Materials Chemistry A, 2014, 24(24):9331–9337.

[57] Sato J, Saito N, Nishiyama H, et al. New photocatalyst group for water decomposition of RuO_2 loaded p-block metal (In, Sn, and Sb) oxides with d10 configuration. Journal of Physical Chemistry B, 2001, 105(26):6061–6063.

[58] Tang J, Zou Z, Katagiri M, et al. Photocatalytic degradation of MB on MIn_2O_4 (M=alkali earth metal) under visible light: effects of crystal and electronic structure on the photocatalytic activity. Catalysis Today, 2004, 93–95:885–889.

[59] Chen X, Shen S, Guo L, et al. Semiconductor-based photocatalytic hydrogen generation. Chemical Reviews, 2010, 110:6503–6570.

[60] Selvaraj R, Selvaraj V, Cheuk W T, et al. Self-assembled mesoporous hierarchical-like In_2S_3 hollow microspheres composed of nanofibers and nanosheets and their photocatalytic activity. Langmuir, 2011, 27(9):5534–5541.

[61] Liu G, Jiao X, Qin Z, et al. Solvothermal preparation and visible photocatalytic activity of polycrystalline β-In_2S_3 nanotubes. Crystengcomm, 2010, 1:182–187.

[62] Xing C, Wu Z, Jiang D, et al. Hydrothermal synthesis of In_2S_3/g-C_3N_4 heterojunctions with enhanced photocatalytic activity. Journal of Colloid & Interface Science, 2014, 433(11):9–15.

[63] Fu X, Wang X, Chen Z, et al. Photocatalytic performance of tetragonal and cubic β-In_2S_3 for the water splitting under visible light irradiation. Applied Catalysis B Environmental, 2010, 95(3):393–399.

[64] Xie M, Dai X, Meng S, et al. Selective oxidation of aromatic alcohols to corresponding aromatic aldehydes using In_2S_3 microsphere catalyst under visible light irradiation. Chemical Engineering Journal, 2014, 245(6):107–116.

[65] Afzaal M, Malik M A, O'Brien P. Indium sulfide nanorods from single-source precursor. Chemical Communications, 2004, 3(3):334–335.

[66] Liu G, Jiao X, Qin Z, Chen D. Solvothermal preparation and visible photocatalytic activity of polycrystalline β-In_2S_3 nanotubes. Crystengcomm, 2010, 1:182–187.

[67] Hyun P K, Kwonho J, Uk S S. Synthesis, optical properties, and self-assembly of ultrathin hexagonal In_2S_3 nanoplates. Angewandte Chemie, 2006, 45(28):4608–4612.

[68] Chen L, Zhang Z, Wang W. Self-assembled porous 3D flowerlike β-In$_2$S$_3$ structures: synthesis, characterization, and optical properties. Journal of Physical Chemistry C, 2008, 112(11):4117–4123.

[69] Zhao P, Huang T, Huang K. Fabrication of indium sulfide hollow spheres and their conversion to indium oxide hollow spheres consisting of multipore nanoflakes. Journal of Physical Chemistry C, 2007, 111(35):12890–12897.

[70] Datta A, Gorai S, Ganguli D, et al. Surfactant assisted synthesis of In$_2$S$_3$ dendrites and their characterization. Materials Chemistry & Physics, 2007, 102(2):195–200.

[71] Lei Z, You W, Liu M, et al. Photocatalytic water reduction under visible light on a novel ZnIn$_2$S$_4$ catalyst synthesized by hydrothermal method. Chemical Communications, 2003, 17(17):2142–2143.

[72] Yong J C, Shun W H, Wen J L, et al. Controlled syntheses of cubic and hexagonal ZnIn$_2$S$_4$ nanostructures with different visible-light photocatalytic performance. Dalton Transactions, 2011, 40(11):2607–2613.

[73] Yuan W H, Xia Z L, Li L, et al. Preparation and photocatalytic performance of N-doped ZnIn$_2$S$_4$ photocatalysts under visible light illumination. Journal of Functional Materials, 2014, 45(12):12117–12121. (In Chinese)

[74] Shen S, Zhao L, Zhou Z, et al. Enhanced photocatalytic hydrogen evolution over Cu-doped ZnIn$_2$S$_4$ under visible light irradiation. Journal of Physical Chemistry C, 2008, 112(41):16148–16155.

[75] Sriram M A, McMichael P H, Waghray A, et al. Chemical synthesis of the high-pressure cubic-spinel phase of ZnIn$_2$S$_4$. Journal of Materials Science, 1998, 33(17):4333–4339.

[76] Fang F, Chen L, Chen Y, et al. Synthesis and photocatalysis of ZnIn$_2$S$_4$ nano/micropeony. Journal of Physical Chemistry C, 2010, 114(6):2393–2397.

[77] Lei Z, You W, Liu M, et al. Photocatalytic water reduction under visible light on a novel ZnIn$_2$S$_4$ catalyst synthesized by hydrothermal method. Chemical Communications, 2003, 17(17):2142–2143.

[78] Shen S, Zhao L, Guan X, et al. Improving visible-light photocatalytic activity for hydrogen evolution over ZnIn$_2$S$_4$: a case study of alkaline-earth metal doping. Journal of Physics & Chemistry of Solids, 2012, 73(1):79–83.

[79] Lappe F, Niggli A, Nitsche R, et al. The crystal structure of In$_2$ZnS$_4$. Zeitschrift für Kristallographie - Crystalline Materials. DOI: 10.1524/zkri.1962.117.16.146, 1962, 117:146–152.

[80] Liang S, Peiqun Y, Yumei D. Synthesis and photocatalytic performance of ZnIn$_2$S$_4$ nanotubes and nanowires. Langmuir, 2013, 29(41):12818–12822.

[81] Bhirud A, Chaudhari N, Nikam L, et al. Surfactant tunable hierarchical nanostructures of $CdIn_2S_4$ and their photohydrogen production under solar light. International Journal of Hydrogen Energy, 2011, 36(18):11628–11639.

[82] Mu J, Wei Q, Yao P, et al. Facile preparation and visible light photocatalytic activity of $CdIn_2S_4$ monodispersed spherical particles. Journal of Alloys & Compounds, 2012, 513(6):506–509.

[83] Aguilera M L A, Hernández J R A, Trujillo M A G, et al. Photoluminescence studies of p-type chalcopyrite $AgInS_2$:Sn. Solar Energy Materials & Solar Cells, 2007, 91(s 15–16): 1483–1487.

[84] Aguilera M L A, Ortega-López M, Resendiz V M S, et al. Some physical properties of chalcopyrite and orthorhombic $AgInS_2$ thin films prepared by spray pyrolysis. Materials Science & Engineering B, 2003, 102(s 1–3):380–384.

[85] Li X, Wang L, Wei D, et al. One-pot synthesis and visible light photocatalytic activity of monodispersed $AgIn_5S_8$ microspheres. Materials Research Bulletin, 2013, 48(2):286–289.

[86] Zhang W, Li D, Chen Z, et al. Microwave hydrothermal synthesis of $AgInS_2$ with visible light photocatalytic activity. Materials Research Bulletin, 2011, 46(7):975–982.

[87] Zhang W, Li D, Sun M, et al. Microwave hydrothermal synthesis and photocatalytic activity of $AgIn_5S_8$ for the degradation of dye. Journal of Solid State Chemistry, 2010, 183(10):2466–2474.

[88] Kudo A, Nagane A, Tsuji I, et al. H_2 evolution from aqueous potassium sulfite solutions under visible light irradiation over a novel sulfide photocatalyst $NaInS_2$ with a layered Structure. Chemistry Letters, 2002, 31:882–883.

[89] Gao Y, Zhai X, Zhang Y, et al. Self-assembled cabbage-like $NaInS_2$ microstructures with efficient visible light photocatalytic performance. Journal of Solid State Chemistry France, 2013, 203(7):44–50.

[90] Tsuji I, Kato H, Prof A K. Visible-light-induced H_2 evolution from an aqueous solution containing sulfide and sulfite over a ZnS-$CuInS_2$-$AgInS_2$ solid-solution photocatalyst. Angewandte Chemie, 2005, 44(34):3565–3568.

[91] Tsuji I, Kato H, Kudo A. Photocatalytic hydrogen evolution on ZnS–$CuInS_2$–$AgInS_2$ solid solution photocatalysts with wide visible light absorption bands. Chemistry of Materials, 2006, 18(7):1969–1975.

[92] Zhang X, Du Y, Zhou Z, et al. A simplified method for synthesis of band-structure-controlled $(CuIn)_xZn_{2(1-x)}S_2$ solid solution photocatalysts with high activity of photocatalytic H_2 evolution under visible-light irradiation. International Journal of Hydrogen Energy, 2010, 35(8):3313–3321.

[93] Shen S, Zhao L, Zhou Z, et al. Enhanced photocatalytic hydrogen evolution over Cu-doped $ZnIn_2S_4$ under visible light irradiation. Journal of Physical Chemistry C, 2008, 112(41):16148–16155.

[94] Ma G J, Lei Z B, Yan H J, et al. Photocatalytic hydrogen production on $CuInS_2$-ZnS solid solution prepared by solvothermal method. Chinese Journal of Catalysis, 2009, 30(1): 73–77. (In Chinese)

[95] Li Y, Chen G, Zhou C, et al. A simple template-free synthesis of nanoporous ZnS–In_2S_3–Ag_2S solid solutions for highly efficient photocatalytic H_2 evolution under visible light. Chemical Communications, 2009, 15:2020–2022.

[96] Li Y X, Chen G, Wang Q, et al. Hierarchical ZnS-In_2S_3-CuS nanospheres with nanoporous structure: facile synthesis, growth mechanism, and excellent photocatalytic activity. Advanced Functional Materials, 2010, 20(19):3390–3398.

[97] Tsuji T, Kato H, Kobyashi H, et al. Photocatalytic H_2 evolution reaction from aqueous solutions over band structure-controlled $(AgIn)_xZn_{2(1-x)}S_2$ solid solution photocatalysts with visible-light response and their surface nanostructures. Journal of the American Chemical Society, 2004, 126(41):13406–13413.

[98] Zhang K, Jing D W, Xing C J, et al. Research on the preparation of $(CuAg)_xIn_{2x}Zn_{2(1-2x)}S_2$ solid solution photocatalysts. International Symposium on Multiphase Flow, 2010, 1207:1066–1069.

[99] Lei Z, Liu M, You W, et al. Sulfur-substituted and zinc-doped $In(OH)_3$: a new class of catalyst for photocatalytic H_2 production from water under visible light illumination. Journal of Catalysis, 2008, 237(2):322–329.

[100] Song Y, Xu L, Shi W, et al. A facile in situ fabrication and visible-light-response photocatalytic properties of porous carbon sphere/InOOH nanocomposites. Journal of Nanoparticle Research, 2014, 2295(3):452–457.

[101] Ge S, Wang B, Lin J, et al. C, N-co doped InOOH microspheres: one-pot synthesis, growth mechanism and visible light photocatalysis. Crystengcomm, 2012, 4(4):721–728.

[102] Matsuoka T, Nakao M. Mysterious material InN in nitride semiconductors – what's the bandgap energy and its application? 2007 IEEE 19th International Conference on Indium Phosphide & Related Materials, 2007:372–375.

Nanoheterostructures Photocatalysis

β-FeOOH/TiO₂ Heterojunction for Visible Light-Driven Photocatalytic Inactivation of *E. coli*

Mahabubur Chowdhury, Ncumisa Mpongwana,
Franscious Cummings, Veruscha Fester and
Seteno Ntwampe

Additional information is available at the end of the chapter

Abstract

In this work, we report on the photocatalytic properties of β-FeOOH/TiO₂ heterojunction material for the inactivation of *Escherischia coli*. XRD, HRTEM, EELS, ELNEFS were used to characterize the as-prepared material. A log reduction of the initial bacterial population was achieved after 45 min of irradiation in the presence of 0.1 mL of hydrogen peroxide. The enhanced photocatalytic activity was due to the effective charge transfer between Ti^{4+}, Fe^{3+}, and O^{2+} as shown from the EELS analysis of the heterojunction structure. The role of various reactive species formed due to the photocatalytic reaction was also investigated. Presence of •OH radicals in the bulk solution was the key factor in the photocatalytic inactivation of *E. coli*.

Keywords: photocatalysis, heterojunction structure, microbial inactivation, *E. coli* , charge transfer

1. Introduction

Risk associated with waterborne diseases such as typhoid, hepatitis A and E, polio, diarrhoea, and cholera are increasing in developing countries due to shortages of clean and safe drinking water [1]. Various chemical and physical treatment processes have been used to disinfect drinking water. Chlorination is a widely used method to disinfect water. However, chlorination can be problematic as it reacts with naturally occurring organic compounds in water to produce carcinogenic by-products such as trihalomethanes (THMs) and haloacetic acids (HAAs)

[2]. Ozonation is another method that is used to disinfect water [1]. On the other hand, ozonation is an energy intensive technique which can be proved to be costly in many developing countries. Physical separation process like thermal destruction at elevated temperatures and membrane filtration of pathogens is effective but not economically feasible. Water disinfection by UV radiation can also be utilized. Conversely, the use of direct and intensive UV radiation possesses health hazards. Hence, its application is limited within the special medical and laboratory purposes only [3, 4]. Therefore, new techniques are required to control the spread of microorganisms in water due to the complications related to different water disinfection processes [4]. Photocatalysis is a promising method that can be used to disinfect water cheaply, as the energy required to activate photocatalytic reaction can be obtained freely from the sun. In the presence of light, electron (e^-) - hole (h^+) pairs are generated due to band gap photoexcitation of photocatalyst (semiconductors) [5]. The photo generated (e^-)-(h^+) pairs are capable of oxidising organic matter either directly or indirectly by reacting with solvents or additives to generate highly nonselective reactive species, hydroxide radicals ($\bullet OH$) [5–7]. Photocatalysis is an environmentally benign process as the ultimate by-product of the treatment process is carbon dioxide and water.

Since the discovery of water splitting by Fujishima and Honda using TiO_2, there has been an explosion of various studies on TiO_2 as a photocatalyst [8]. TiO_2 is generally considered as nontoxic, photocorrosion resistant, and inexpensive photocatalyst [5]. One of the biggest drawback of TiO_2 as photocatalyst is that it can only utilise photon from near UV light range to generate electron (e^-) - hole (h^+) pairs due to its very large band gap (3.2 eV) [6, 9]. The UV region is only 4% in the solar spectrum. Hence, a large amount of sunlight is unexploited in TiO_2 photocatalysis processes. Because of this, designing of efficient visible-light driven (VLD), TiO_2-based photocatalyst is of importance from energy, environment, and economic point of view. Various TiO_2-based VLD photocatalyst has been developed up to date [9–14]. Most of the developed catalyst has been tested for the degradation of organic pollutants. There is a scarcity of literature in the application of VLD photocatalyst for the inactivation of microorganisms in water. A great deal of effort should be given in improving the efficiency of photocatalytic inactivation of microorganisms to prevent the outbreak of waterborne diseases and to cope with the future energy and environmental challenges [4].

The efficacy of the VLD photocatalyst depends on the efficient separation of charge carriers. Formation of heterojunction between TiO_2 and other oxide materials have has been proven to be an effective way of enhancing the efficiency of photocatalysis process under visible light [6, 9, 10, 15]. Besides the band potential matching of the semiconductors, ability to conduct ($e-$) – (h^+) pairs in the respective electron and hole accepting semiconductors are very important in the formation of a heterojunction structure [6, 10]. In our previous work [6], we have prepared β-FeOOH/TiO_2 heterojunction for photocatalytic degradation of textile effluent. However, the photocatalytic efficiency of the heterojunction for microorganism inactivation has not been evaluated, despite a strong correlation between antimicrobial effect and organic compounds degradation effect [4, 16]. Within this view, we report on the photocatalytic inactivation of microorganisms by using β-FeOOH/TiO_2 heterojunction as a VLD photocatalyst. *Escherischia coli* was used as a target microorganism. Hydrogen peroxide was used as a

green electron scavenger to increase the photocatalytic inactivation efficiency of the VLD photocatalyst.

2. Materials and Methods

Analytical grade reagents, without any further purifications, were used in all preparation methods. FeCl$_3$.6H$_2$O, NH$_4$OH, EtOH, hydrogen peroxide (30% V/V), isopropanol, sodium oxalate, Cr(VI), and Degussa-P25 were purchased from Sigma Aldrich South Africa.

2.1. Catalyst preparation

Nanorod-shaped β-FeOOH particles were synthesised according to the previously reported method [17, 18]. Typical synthesis process consists of adding certain amount of FeCl$_3$.6H$_2$O in a solution of equal amount of water and EtOH (V/V). The final pH of the solution was kept at ~2. 200 mL of the solution was placed in a Teflon lined autoclave. The autoclave was slowly heated to 100°C and was kept at that temperature for 2 h; then followed by washing and centrifuging of the precipitated sample once the autoclave cooled down naturally. The sample were dried in a desiccator.

The method of heterojunction formation between TiO$_2$ and P25 was adopted from previously reported study [6, 19, 20]. Maleic acid was used as an organic binder to form a chemically bonded interface between TiO$_2$ and β-FeOOH. The role of maleic acid was, to anchor the TiO$_2$ on the surface of β-FeOOH through its dicarboxylic functional group [21]. In a typical synthesis procedure, an appropriate amount of β-FeOOH nanorods were dispersed in 30 mL of EtOH. In a separate beaker, a gram of P25 powder was dispersed in 30 ml of EtOH. Maleic acid of 0.1 M concentration (10 mL) was added to the β-FeOOH suspension. Both solutions were stirred for 4 h. After 4 h, the TiO$_2$ suspension was added to the β-FeOOH suspension and stirred for 12 h. The mixture was washed and centrifuged several times. The samples were dried in an oven at 60°C. The dried samples were calcined at 300°C. The calcined samples were further treated by UV irradiation for 4 h.

2.2. *E. coli* cell preparation

Single colony of *E. coli* bacterial cells was taken from the stock and incubated in 10% nutrient broth solution at 37°C for 18 h with shaking. Certain amount of culture was washed with saline and centrifuged at 2000 rpm for 5 minute. The supernatant solution was discarded, and the bacterial pellet was re-suspended in sterile saline solution.

2.3. Photocatalytic inactivation of *E. coli*

The photocatalytic inactivation of *E. coli* was carried in a homemade jacketed glass reactor. A catalyst load of 0.02 g was added to 100 mL of deionised water and placed in the reactor. A 300 W halogen tungsten lamp was used as a visible light source. The halogen tungsten lamp was placed inside a cooling jacket. The circulating water in the cooling jacket placed around

the halogen tungsten lamp minimised the heat generation due to infrared light emitted from the halogen lamp and also acted as a UV filter. The lamp with the cooling jacket was submerged in the 100 mL catalyst suspension placed in the glass reactor under stirring. The solution temperature was always found to be ~30°C. Hydrogen peroxide (0.1 mL) was Used as a green electron scavenger. A Li-CORE LI-250A light metrer coupled with quantum photosynthetically active radiation PAR (PARphotosynthetically active radiation) sensor was used to measure the photosynthetic photon flux density (PPFD) emitted from the halogen tungsten lamp. The PPFD emitted from the halogen tungsten light source was measured to be $1 \text{ X} \times 10^4$ μmols^{-1}. It was assumed that the number of incident photons reaching the catalyst surface will be constant throughout the reactor because of homogeneous suspension around lamp. A working cell suspension was obtained by serially diluting the stock microbial solution and adding 1 mL of the solution to the 100 mL catalyst suspension. An initial concentration of ~300 CFU/mL of *E. coli* was used for all the experiments reported in this study. Sample from the reactor was withdrawn at regular interval and centrifuged to separate the solid catalyst. The supernatant solution was diluted with sterilized solution. An appropriate amount of diluted sample was spread in agar solution and incubated at 37°C for 24 h. The number of viable cells was determined by counting the number of the colonies formed. All experiments were conducted in triplicates.

2.4. Characterization of the material

A Phillips PW 3830/40 Generator with Cu-Kα radiation was used to determine the X-ray diffraction patterns of the heterojunction structure for phase identification purposes. High resolution transmission electron microscopy (HR-TEM) was performed using a Tecnai F20 FEG-TEM, equipped with a Gatan Image Filter (GIF2001) for morphology evaluation and also electron energy loss spectroscopy (EELS) and energy-filtered TEM (EFTEM) analysis. Plural scattering and the contribution from low low-energy plasmon losses were eliminated by applying a power law background -shape to each spectrum.

3. Results and discussion

3.1. β-FeOOH/TiO$_2$ heterojunction characterization

Degusa P25, a mixture of anatase and rutile, was used as TiO$_2$ material. Hence, both anatase (JCPDS card no: 71–1167) and rutile (JCPDS card no: 75–1748) peaks could be observed from the XRD patterns of TiO$_2$ (Data not shown). **Figure 1a** presents TEM Micrographs of TiO$_2$. Selected area electron diffraction pattern (**Figure 1b**) shows that the TiO$_2$ is predominantly anatase as the first four diffracting planes indicates. High-resolution TEM micrograph viewed along the [001] direction (Inset **Figure 1a**), allowed for direct measurement of the lattice constants and found to be value of $a = b = 0.378$ nm, as determined for the tetragonal crystal structure. A value of 0.944 nm was calculated for lattice constant c from the SAED pattern (1b). TEM image of the pristine β-FeOOH nanorods (JCPDS No. 42–1315) is presented in **Figure 1c**. TEM image of the β-FeOOH/TiO$_2$ heterojunction material is presented in **Figure 1e**. It can be

seen from **Figure 1e** that tight contacts between particles have been formed. Interestingly no rod-shaped β-FeOOH/TiO₂ particles were found in the heterojunction structure. Transformation of rod shaped β-FeOOH to pseudo spherical particles in chemically bonded interface between β-FeOOH and TiO₂ has been well documented in our earlier work [6]. **Figure 1d** presents the EDS of the heterojunction structure. The presence of Fe and Ti signal in the EDS is a signature of the formation of a composite structure. Further evaluation of heterojunction formation between β-FeOOH and TiO₂ was done by electron energy loss-filtered transmission electron microscopy (EFTEM). Formation of interface between β-FeOOH and TiO₂ in the composite material can be clearly seen from the EFTEM images EFTEM images (**Figure 1 f–h**).
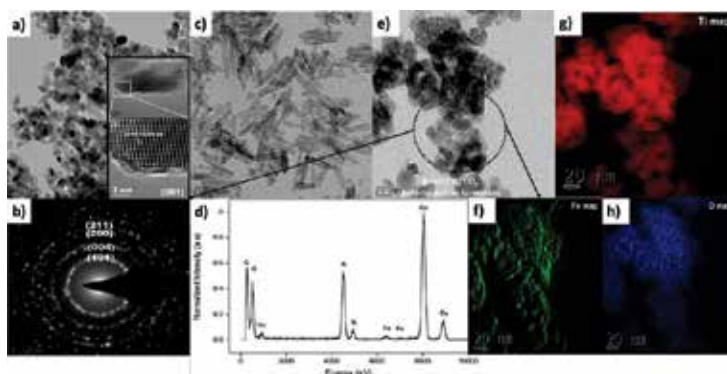

Figure 1. (a) TEM image of pristine P25 material, (b) SAED pattern of the pristine P25 material, (c) TEM image of pristine β-FeOOH nanorods, (d & and, e) TEM image and corresponding EDS of the β-FeOOH/TiO₂ heterojunction structure, and (f, g, –h) elemental X-ray mapping of the composite structure.

Anatase and rutile both have Ti⁴⁺ valency as well as a tetragonal crystal structure. However, rutile contains six atoms per unit cell whereas anatase has twelve. In either polymorph, each Ti atom is coordinated to six O atoms, whereas each O atom is coordinated to three Ti atoms, thereby forming a perfect TiO₆ octahedron. These octahedra are slightly slanted in both anatase and rutile, with two Ti-O distances being 0.1 Å greater in length compared to the other four bond lengths. This is accompanied by a deviation from 90° of the O-Ti-O angles. Subsequently, the local point-group symmetry is lowered around the Ti atom from O_h to D_{2h} in rutile and D_{2d} in anatase. Anatase and rutile differ as a result of secondary coordination during which the TiO₆ octahedra are joined together by sharing two edges in rutile and four in anatase [22, 23]. A study of the molecular orbital (MO) energy level diagram of rutile [24] shows that the two lowest unoccupied orbitals separate into a threefold t_{2g} and twofold e_g orbital, commonly known as the crystal-field orbitals. In ideal O_h symmetry, they consist of two distinct levels; however, with the lowering of the symmetry in rutile, t_{2g} orbital splits into b_{3g}, a_g, and b_{2g} suborbitals, whereas the e_g orbital morphs into b_{1g} and a_g sub-levels. Tight-binding theory [25] shows that the electronic band structure for rutile exhibits $L_{2,3}$ ionization edges in the conduction band, which are basically t_{2g} and e_g levels, their maxima separated by about 4.5 eV; for anatase, the L_2 and L_3 bands are slightly closer at 3.8 eV. From **Figure 2a**, it can be seen that the $L_{2,3}$ obtained during electron energy loss maxima is separated by 5.17 eV (465.31 and 470.48

eV), with the crystal-field splitting of the L_2 and L_3 lineshapes into the respective t_{2g} and e_g sub-bands clearly visible, as indicated by the arrows in the inset. As determined from the SAED pattern of **Figure 1b**, the P25 particles are predominantly anatase; however, the separation of the L_3 and L_2 ionization edges of 5.17 eV suggests the presence of rutile.

Figure 2b shows the $L_{2,3}$ ionization edge of the β-FeOOH nanorods. In all iron-oxides, this lineshape is characterized by Fe $2p \rightarrow 3d$ and 4s transitions. However, a lower probability of transition to the s orbitals exist, and hence, the Fe $L_{2,3}$ edges are comprised of mainly excitation to Fe 3d orbitals. This spin–orbit interaction separates the Fe L_3 ($2p_{3/2}$) and L_2 ($2p_{1/2}$) edges by about 13 eV. The unoccupied states in the 3d bands of the Fe atom are related to the white-line intensities. EELS of β-FeOOH shows an ionization edge onset at 708 eV, peaking at 716.58 eV for L_3, and 729.63 eV for the L_2 edge. A deconvolution of the L_3 peak shows the characteristic crystal field splitting into the t_{2g} and e_g bands. This is shown in the inset of **Figure 2b**. The L_3/L_2 ratio of 2.29 is recorded for these nanostructures.

The EELS spectrum of the composite material is shown in **Figure 2c** and compared to that of the P25 and as-synthesized β-FeOOH nanorods samples. A study of the $L_{3,2}$ ionization edge of
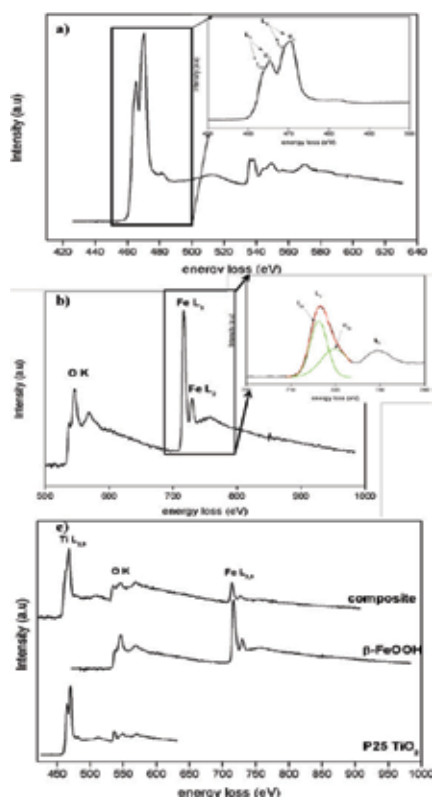

Figure 2. (a) EELS of pristine P25, (b) EELS of the Fe $L_{3,2}$ and oxygen K edges of the β-FeOOH nanorods, and (c) comparison of EELS between P25, β-FeOOH nanorods and β-FeOOH/TiO$_2$ heterojunction structure.

Ti and Fe in **Figure 2c** shows a lack of evidence of the crystal-field splitting in the Ti $L_{3,2}$ lineshape, which is accompanied by a rearrangement of the L_3/L_2 ratio of Fe to 1.65. Investigation of the O K edge shows a similar decrease in the splitting. This suggested the presence of charge transfer/bonding between the Ti^{4+}, Fe^{3+}, and O^{2+} ions during the composite synthesis.

3.2. Evaluation of photocatalytic inactivation of *E. coli*

Figure 3a presents the photocatalytic activity of the heterojunction structure under visible light. A common microorganism; i.e. that is *E. coli* was used to evaluate the inactivation efficiency of the *E. coli*. In the absence of light, the photocatalyst did not show any antimicrobial activity, implying that the heterojunction material is not toxic. It is known that UV ray can inactivate microorganisms. A halogen tungsten lamp with a water filter was used to simulate the solar irradiation. In the absence of catalyst, there was no decrease in bacterial population after 45 minutes of irradiation. Hence, the role of UV-induced disinfection of the bacterial cells can be ignored. In the presence of the catalyst and light only, no significant reduction of bacterial population was observed. The efficiency of a photocatalyst depends on the successful separation of photogenerated $e-- h^+$. Hydrogen peroxide have been used in many studies as a green electron scavenger [26–28]. Hydrogen peroxide (in the presence of light only) was used to evaluate the role of hydrogen peroxide in the inactivation of *E. coli*. In the absence of catalyst (in the presence of light and hydrogen peroxide), only 0.2 log reduction of bacterial population was achieved after 45 minutes of irradiation. However, in the presence of light, catalyst and hydrogen peroxide 1 log reduction of bacterial population was achieved. This composition showed a synergistic catalytic inactivation of *E. coli*. Three different catalyst load, i.e. that is 0.01, 0.02, and 0.04 g/L, was evaluated to optimise the photocatalytic inactivation of *E. coli*. 0.5 log reduction of bacterial population was achieved in the case of 0.01 and 0.04 g/L catalyst load. A catalyst load of 0.02 g/L showed the highest photocatalytic inactivation (1 log reduction). It is well known that the presence of excessive amount of catalyst creates the screening effect which reduces the photocatalytic activity of the catalyst in a given system.
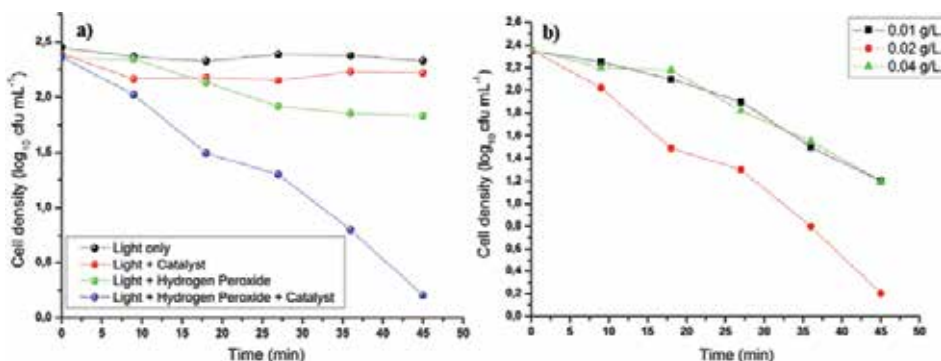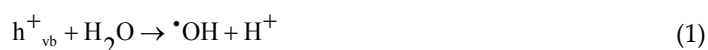

Figure 3. (a) Catalytic activity of the heterojunction structure, (b) Effect of catalyst load on photocatalytic inactivation of *E. coli*.

3.3. Photocatalytic inactivation mechanism of *E. coli*

In our previous study [6], we have showed the existence of an inter semiconductor e^-- h^+ transport mechanism in the β-FeOOH/TiO$_2$ heterojunction structure. This phenomenon was responsible for the enhanced photocatalytic performance of the structure. Various reactive species are, e.g. for example, •OH and O$_2$ $^{•-}$; are generated during the photocatalytic reaction [(Equations. (1)–(4)]. However, the roles of photogenerated reactive species, whether they remain bound to the surface or diffuse into the bulk solution, Were not investigated in the case of β-FeOOH/TiO$_2$ heterojunction structure.

$$h^+_{vb} + H_2O \rightarrow {}^{\bullet}OH + H^+ \tag{1}$$

$$H_2O_2 + e^- \rightarrow {}^{\bullet}OH + OH^- \tag{2}$$

$$H_2O_2 \xrightarrow{h\nu} {}^{\bullet}OH \tag{3}$$

$$O_2 + e^- \rightarrow O_2{}^{\bullet-} \tag{4}$$

As discussed previously, in the absence of the hydrogen peroxide, no significant reduction in bacterial population was observed. This was due to the rapid recombination of e^-- h^+ pairs. Hydrogen peroxide itself in the presence of UV (emitted from halogen tungsten lamp) generates •OH [(Equation. (3)] via photolysis. To evaluate the role of bacterial inactivation due to valence band hole, 40 μmol L^{-1}, Cr (VI) was used as an electron scavenger [4] to isolate the role of photolysis (**Figure 4**). It can be seen from **Figure 4a** that 87% of the bacterial colony was reduced. This highlights the possibility photocatalytic inactivation of *E. coli* by either •OH [(Eq.uation (1)] or O$_2{}^{\bullet-}$ [(Equation. (4)]. Sodium oxalate of 20 μmol L^{-1} concentration, a hole scavenger [4], was used to explore the role of O$_2{}^{\bullet-}$ for bacterial inactivation purpose. It can be seen from **Figure 4** that no significant reduction of bacterial population occurred in the absence of valence band hole. Hence, the contribution of O$_2{}^{\bullet-}$ was postulated to be minimal. So, it can be postulated that the photocatalytic inactivation of *E. coli* is mainly due to the presence •OH. To evaluate the significant •OH generation process [(between Equation (1), and 2+(3)] and its role in *E. coli* inactivation, sodium oxalate and hydrogen peroxide were added simultaneously in the solution. This was done to suppress the formation of •OH due to Equation (1). Hence, the effect of Equations (2) and (3) could be observed directly. It can be seen from **Figure 4** that the reduction in bacterial population was lower compared to when Cr(VI) was used as an electron scavenger. This demonstration postulated that there is a synergistic effect between photocatalysis and photolysis in the generation of •OH for *E. Coli coli* inactivation. Isopropanol was used as a radical quenching agent to isolate the effect of catalyst surface bound •OH or those diffusing in the solution. Isopropanol is easily oxidised by •OH and exhibits low affinity towards semiconductor surface in aqueous media as reported in previous literature [4,

29, 30]. Isopropanol of 15 mol L^{-1} isopropanol was used as a •OH quenching agent in the presence of hydrogen peroxide. The photocatalytic inactivation was completely inhibited in the presence of isopropanol highlighting the role of •OH in bulk solution. From the control experiments, it was established that the catalyst and the scavengers (the amount used) had no significant effect on the inactivation of *E. coli*.
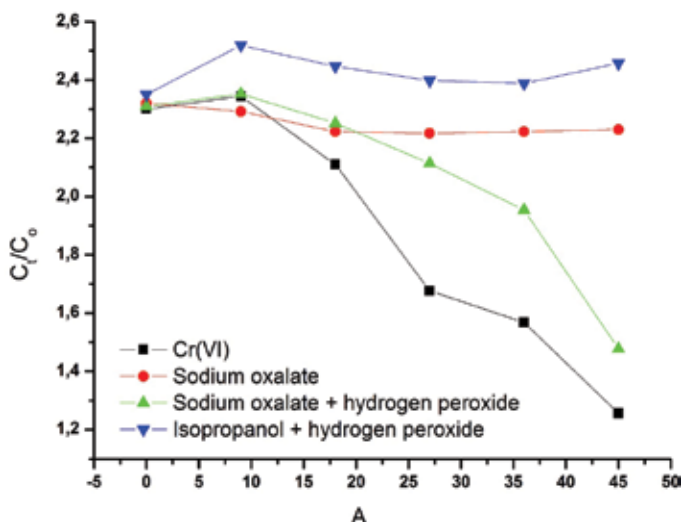

Figure 4. Role of reactive species on the photocatalytic inactivation of *E. coli*.

4. Conclusion

β-FeOOH/TiO₂ heterojunction prepared via organic linker mediated route was used for photocatalytic inactivation of *E. coli*. Controlled experiments showed that the as as-prepared catalyst had no antimicrobial properties in the absence of light. The catalyst showed good photocatalytic properties in the presence of simulated solar light and 0.1 mL of hydrogen peroxide. Hydrogen peroxide acted as a green electron scavenger to inhibit the e^-- h^+ recombination rate. Different scavenger was used to identify the role of exact reactive species in the photocatalytic disinfection of *E. Coli*. Generation of •OH via photocatalysis and photolysis and its presence in the bulk solution was the main driver behind the inactivation of *E. coli*.

Acknowledgements

Author details

Mahabubur Chowdhury[1*], Ncumisa Mpongwana[2], Franscious Cummings[3],
Veruscha Fester[1] and Seteno Ntwampe[2*]

*Address all correspondence to: chowdhurym@cput.ac.za and ntwampes@cput.ac.za

1 Flow Process and Rheology Centre, Cape Peninsula University of Technology, Cape Town, South Africa

2 Bioresource Engineering Research Group, Cape Peninsula University of Technology, Cape Town, South Africa

3 Electron Microscopy Unit, University of the Western Cape, Bellville, South Africa

References

[1] M. Vijay, K. Ramachandran, P.V. Ananthapadmanabhan, B. Nalini, B.C. Pillai, F. Bondioli, A. Manivannan, R.T. Narendhirakannan. Photocatalytic inactivation of Gram-positive and Gram-negative bacteria by reactive plasma processed nanocrystalline TiO_2 powder. Current Applied Physics, 13 (2013) 510–516.

[2] L. Liang, P.C. Singer. Factors influencing the formation and relative distribution of haloacetic acids and trihalomethanes in drinking water. Environmental Science & Technology, 37 (2003) 2920–2928.

[3] M.A. Shannon, P.W. Bohn, M. Elimelech, J.G. Georgiadis, B.J. Marinas, A.M. Mayes. Science and technology for water purification in the coming decades. Nature, 452 (2008) 301–310.

[4] L.-S. Zhang, K.-H. Wong, H.-Y. Yip, C. Hu, J.C. Yu, C.-Y. Chan, P.-K. Wong. Effective photocatalytic disinfection of *E. coli* K-12 using $AgBr$-Ag-Bi_2WO_6 nanojunction system irradiated by visible light: the role of diffusing hydroxyl radicals. Environmental Science & Technology, 44 (2010) 1392–1398.

[5] R. Comparelli, E. Fanizza, M.L. Curri, P.D. Cozzoli, G. Mascolo, R. Passino, A. Agostiano. Photocatalytic degradation of azo dyes by organic-capped anatase TiO_2 nanocrystals immobilized onto substrates. Applied Catalysis B: Environmental, 55 (2005) 81–91.

[6] M. Chowdhury, M. Ntiribinyange, K. Nyamayaro, V. Fester. Photocatalytic activities of ultra-small β-$FeOOH$ and TiO_2 heterojunction structure under simulated solar irradiation. Materials Research Bulletin, 68 (2015) 133–141.

[7] A.K. Chakraborty, M.A. Kebede. Preparation and characterization of WO₃/Bi₃O₄Cl nanocomposite and its photocatalytic behavior under visible light irradiation. Reaction Kinetics, Mechanisms and Catalysis, 106 (2012) 83–98.

[8] A. Fujishima, K. Honda. Electrochemical photolysis of water at a semiconductor electrode. Nature, 238 (1972) 37–38.

[9] S.B. Rawal, S. Bera, D. Lee, D.-J. Jang, W.I. Lee. Design of visible-light photocatalysts by coupling of narrow bandgap semiconductors and TiO₂: effect of their relative energy band positions on the photocatalytic efficiency. Catalysis Science & Technology, 3 (2013) 1822–1830.

[10] S.B. Rawal, A.K. Chakraborty, Y.J. Kim, H.J. Kim, W.I. Lee. Double-heterojunction structure of SbxSn$_{1-x}$O₂/TiO₂/CdSe for efficient decomposition of gaseous 2-propanol under visible-light irradiation. RSC Advances, 2 (2012) 622–630.

[11] B. Pal, M. Sharon, G. Nogami. Preparation and characterization of TiO₂/Fe₂O₃ binary mixed oxides and its photocatalytic properties. Materials Chemistry and Physics, 59 (1999) 254–261.

[12] J. Tokarský, P. Čapková. Structure compatibility of TiO₂ and SiO₂ surfaces. Applied Surface Science, 284 (2013) 155–164.

[13] Y. Bessekhouad, D. Robert, J.V. Weber. Bi₂S₃/TiO₂ and CdS/TiO₂ heterojunctions as an available configuration for photocatalytic degradation of organic pollutant. Journal of Photochemistry and Photobiology A: Chemistry, 163 (2004) 569–580.

[14] Y. Bessekhouad, D. Robert, J.V. Weber. Photocatalytic activity of Cu₂O/TiO₂, Bi₂O₃/TiO₂ and ZnMn₂O₄/TiO₂ heterojunctions. Catalysis Today, 101 (2005) 315–321.

[15] S.B. Rawal, A.K. Chakraborty, W.I. Lee. Heterojunction of FeOOH and TiO₂ for the formation of visible light photocatalyst. Bulletin of the Korean Chemical Society, 30 (2009) 2613–2616.

[16] F. Chen, X. Yang, Q. Wu. Photocatalytic oxidation of *Escherischia coli*, *Aspergillus niger*, and formaldehyde under different ultraviolet irradiation conditions. Environmental Science & Technology, 43 (2009) 4606–4611.

[17] M. Chowdhury, V. Fester, G. Kale. Growth kinetics evaluation of hydrothermally synthesized β-FeOOH nanorods. Journal of Crystal Growth, 387 (2014) 57–65.

[18] M. Chowdhury, V. Fester, G. Kale, O. Cespedes. Hydrothermal precipitation of β-FeOOH nanostructure(s) in mixed solvent: study of their morphological and structural evolution. Journal of Nanoparticle Research, 16 (2014) 1–11.

[19] O. Oghenochuko, M. Chowdhury, N. Kudzanai, F. Cummings, V. Fester, O.S. Fatoki. Novel β-FeOOH/NiO composite material as a potential catalyst for catalytic ozonation degradation of 4-chlorophenol. RSC Advances, 5 (2015) 59513–59521.

[20] A.K. Chakraborty, M.E. Hossain, M.M. Rhaman, K.M.A. Sobahan, Fabrication of Bi2O3/ TiO2 nanocomposites and their applications to the degradation of pollutants in air and water under visible-light, Journal of Environmental Sciences, 26 (2014) 458–465.

[21] Y.J. Kim, B. Gao, S.Y. Han, M.H. Jung, A.K. Chakraborty, T. Ko, C. Lee, W.I. Lee. Heterojunction of $FeTiO_3$ nanodisc and TiO_2 nanoparticle for a novel visible light photocatalyst. The Journal of Physical Chemistry C, 113 (2009) 5.

[22] R. Brydson, H. Sauer, W. Engel, J.M. Thomass, E. Zeitler, N. Kosugi, H. Kuroda. Electron energy loss and X-ray absorption spectroscopy of rutile and anatase: a test of structural sensitivity. Journal of Physics: Condensed Matter, 1 (1989) 797.

[23] F.R. Cummings, T.F.G. Muller, G.F. Malgas, C.J. Arendse. Investigation of the growth and local stoichiometric point group symmetry of titania nanotubes during potentiostatic anodization of titanium in phosphate electrolytes. Journal of Physics and Chemistry of Solids, 85 (2015) 278–286.

[24] L.A. Grunes. Study of the K edges of $3d$ transition metals in pure and oxide form by X-ray-absorption spectroscopy. Physical Review B, 27 (1983) 2111–2131.

[25] L.A. Grunes, R.D. Leapman, C.N. Wilker, R. Hoffmann, A.B. Kunz. Oxygen K near-edge fine structure: an electron-energy-loss investigation with comparisons to new theory for selected $3d$ transition-metal oxides. Physical Review B, 25 (1982) 7157–7173.

[26] J. Li, F. Sun, K. Gu, T. Wu, W. Zhai, W. Li, S. Huang. Preparation of spindly CuO microparticles for photodegradation of dye pollutants under a halogen tungsten lamp. Applied Catalysis A: General, 406 (2011) 51–58.

[27] W. Zhai, F. Sun, W. Chen, Z. Pan, L. Zhang, S. Li, S. Feng, Y. Liao, W. Li. Photodegradation of p-nitrophenol using octahedral Cu_2O particles immobilized on a solid support under a tungsten halogen lamp. Applied Catalysis A: General, 454 (2013) 59–65.

[28] W. Zhai, F. Sun, W. Chen, L. Zhang, Z. Min, W. Li. Applications of Cu_2O octahedral particles on ITO glass in photocatalytic degradation of dye pollutants under a halogen tungsten lamp. Materials Research Bulletin, 48 (2013) 4953–4959.

[29] Y. Chen, S. Yang, K. Wang, L. Lou. Role of primary active species and TiO_2 surface characteristic in UV-illuminated photodegradation of Acid Orange 7. Journal of Photochemistry and Photobiology A: Chemistry, 172 (2005) 47–54.

[30] A. Amine-Khodja, A. Boulkamh, C. Richard. Phototransformation of metobromuron in the presence of TiO_2. Applied Catalysis B: Environmental, 59 (2005) 147–154.

Alternative Approaches in Development of Heterogeneous Titania-Based Photocatalyst

Yolice P. Moreno, Cicero C. Escobar,
William L. da Silva and João H. Z. dos Santos

Additional information is available at the end of the chapter

Abstract

Three alternative approaches for the development of heterogeneous photocatalysts are comparatively evaluated, namely (i) the use of molecular imprinting concept for the development of heterogeneous catalysts employing rhodamine B as template and sol–gel as synthesis route; (ii) the impregnation of $TiCl_4$ on mixed nano- and micro-metric silicas, followed by calcination; (iii) the use of industrial and academic chemical residues as source of potential photocatalyst species impregnated on supports. All tests were carried on with rhodamine B as target molecule. For comparative reasons, photocatalytic tests were carried out with commercial titania (P25). The solids were characterized by nitrogen porosimetry, small-angle X-ray scattering (SAXS), zeta potential (ZP), diffuse reflectance spectroscopy in the ultraviolet region (DRS-UV), diffuse reflectance infrared Fourier transmission spectroscopy (DRIFTS), and Rutherford backscattering spectrometry (RBS). The supported catalysts resulting from silica nanoparticles and residue of the petrochemical industry achieved higher percentage of the dye degradation under ultraviolet (68.0 and 66.8%, respectively) radiation. The industrial waste reached the highest photocatalytic activity under visible (61%) radiation, while the commercial P25 achieved 82.0 and 12.3% for ultraviolet and visible radiation, respectively. The textural and structural characteristics of the supported catalyst prepared with fumed silica and petrochemical waste (SiPe), namely the low-energy bandgap (1.8 eV), large surface area (280 $m^2 g^{-1}$), high pore volume (1.9 $cm^3 g^{-1}$), and high zeta potential value (−36.4 mV), may have been responsible for their high activity.

Keywords: supported photocatalyst, Rhodamine B, titania, silicas, residue, molecular imprinting

1. Introduction

Advanced oxidation processes (AOPs) are environmentally friendly technologies for the removal of organic pollutants in water and waste water. AOPs generate powerful oxidizing species, such as hydroxyl radicals ($^{\bullet}$OH, E^0 = 2.80 V) which can fragment, destroy, and degrade contaminants into small molecules (1, 2). The oxidation processes (i.e., mineralization) involve the production of CO_2, H_2O, and, eventually, inorganic ions as end products (3). The effectiveness of an AOP is proportional to its ability to generate hydroxyl radicals. This is dependent on: (i) the chemical and physical mechanisms of this technology; (ii) the nature and concentration of target contaminant; (iii) background water quality; (iv) reactor contact time; and (v) reactor configuration (3, 4).

Among the AOPs, heterogeneous photocatalysis is one of the most promising to degrade emerging contaminants and it is based on the use of bandgap semiconductors metal oxide as catalyst (3, 4). When these materials are being exposed to light with energy equal or superior than their bandgap they tend to generate electron-hole pairs which increase the number of free carriers and hence the conductivity. The ideal characteristics of a catalyst are: low raw material cost, relatively simple processing, useful temperature range, very high reaction, photochemical stability, and ability to adsorb reactants on the particle surface (3). Moreover, this method shows clear advantages, such as low cost, low toxicity, and chemical stability (5). However, once it is affected by photogenerated holes and hydroxyl radicals with a strong oxidation potential, a serious shortcoming in heterogeneous photocatalytic oxidation is the low selectivity for the most hazardous contaminants (6).

The lack of selectivity is a disadvantage, as mixtures derived from effluent streams may contain hazardous contaminants and low toxicity contaminants. In many cases, the former is present in lower concentrations, and the latter is the majority (6), but it is desirable to preferentially degrade the most toxic materials. Other drawbacks include the necessity of improving the contact between pollutant molecules and the catalyst. Regarding to this issue, the low surface area commercial catalysts, which in addition demand UV-light for the oxidative process, and UV-light in natural sunlight represents only 5–8% of the solar spectrum (7). Considering these drawbacks, alternative approaches in development of heterogeneous titania-based photocatalyst are an important issue in the topic of photocatalysis. **Table 1** illustrates recent attempts and designs of heterogeneous photocatalysts and the target molecule to which they have been tested.

As shown in **Table 1**, most of the reported systems involve the use of TiO_2 as the photocatalyst. On the other hand, the use of supports has been varied encompassing inorganic materials (silica), organic supports, ashes and, derivate from wastes. From the heterogenization point of view, sol–gel seems to be the most widely employed method, probably due to its easiness of manipulation, versatility, and broad range of potential experimental variations. The use of approaches which provide nanostructured systems has also been reported. Phenol, drugs, pesticides, and dyes have been investigated as the target pollutant.

Catalyst system	Preparative method	Target molecule	Comments[a]	References
MI-coated photocalaysts (P25 as precursor)	Organic polimerization	2,4-Dinitro phenol	SF ranging from 1.59–3.29 for similar chlorophenols. CF ranging from 1.47 to 1.74 for similar chlorophenols. SF and CF were estimated from Kinetic experiments	(8)
MI TiO_2/WO_3 nanocomposites	Sol–gel	2-nitrophenol and 4-nitro phenol	Tetrabutyl Orthotitanate as precursor. SF ranging from 2.5 to 3.95. SF was estimated from adsorption experiments	(9)
MI based on fly-ash ceno sphere	Organic polimerization	Tetracycline	CF in ternary antibiotic solution ranging from 1.25 to 1.67. CF was estimated from Kinetic experiments	(10)
TiO_2/coconut shell powder	Acid-catalyzed sol–gel method	Carbamazepine, clofibric acid, and tri closan	Pharmaceuticals and personal care products (PPCPs) pollutants. Photocatalytic activity of the novel TiO_2–coconut shell powder (TCNSP) composite for the photodegradation of three PPCPs pollutants is investigated under UVC and black light blue UVA irradiation. Under the UVC/TCNP combination, 99% removal was achieved compared to 30% for P25	(11)
TiO_2/waste material (BEW)	Impregnation $Ti(OCH(CH_3)_2)_4$ solution was added to BEW solution	Atrazine	Synthesis of the TiO_2 nanoparticles was performed by using BEW without a reducing agent and the photocatalytic activity of the catalyst was investigated for the degradation of atrazine with UV irradiation. TiO_2 with waste material can be recycled and reused four times for the removal of atrazine. Degradation 85% after 70 min reaction	(12)
TiO_2/almond shell activated carbon	Metal organic chemical vapor deposition and impregnation	Industrial phosphoric acid solution	Load TiO_2 on the surface of active carbon by using two techniques. These photocatalysts were employed not only for the adsorption of total organic carbon (TOC) from industrial phosphoric acid solution. The catalysts showed performance higher than P25 with 90% degradation of the solution after 300 min	(13)
TiO_2/perlite granules	Metal organic chemical vapor deposition and impregnation	Ammonia	Investigate the photocatalytical activity improvement of TiO_2 (P25) powder as a photocatalyst which immobilized on perlite granules to remove ammonia from synthetic wastewater under UV irradiation	(14)
TiO_2/sand or fumed silica	Sol–gel	Nitrogen monoxide (NO)	Modification of sand and fumed silica with titania in order to obtain a photocatalytic active material for the degradation of pollutants. The sample of sand showed a high photonic	(15)

Catalyst system	Preparative method	Target molecule	Comments[a]	References
			efficiency (0.41%) comparable to that of P25 (0.40%). The coated silica fumed containing the most titania content (28 wt%) showed the best photonic efficiency (0.56%) in the degradation of NO	
TiO$_2$/hydroxylated fly ash ceno spheres (FACs)	Sol–gel and photoreduction method	Methylene blue (MB)	TiO$_2$ was coated on the surface of FACs by the sol–gel method. Platinum was then deposited on these TiO$_2$/FAC particles by a photoreduction method. The photocatalytic activity for the degradation of MB under visible light irradiation. Photocatalytic experiments indicated that 3 g L^{-1} of the photocatalyst (calcinated 450°C with a Pt/TiO$_2$ mass ratio of 1.5%) exhibited the best photocatalytic activity, as a 95% degradation of methylene blue after 8 h	(16)
TiO$_2$/carbon composites	Self-assembly of carbon precursors and titanium isopropoxide	Rhodamine B	Pluronic F127 was employed as a soft template. The presence of titania nanoparticles uniformly dispersed in the carbon mesostructure. Synthesis of ordered mesoporous titania–carbon composites. Under UV radiation decomposition of RhB with TiO$_2$/composites was (90–86%) and P25 was 50%	(17)
SnO$_2$/carbon nanocomposites	Solvothermal method	Rhodamine B glyphosate	Photocatalytic activity on the degradation under simulated sunlight irradiation. Uniform distribution of SnO$_2$ nanoparticles on the graphite-like carbon surface.	(18)
Au/TiO$_2$ nanocomposite	Inverse miniemulsion by sol–gel	Rhodamine B	Visible-light photocatalytic activity in the degradation of the organic dye. The Au content in the nanocomposite particles could be conveniently tuned by the amount of HAuCl$_4$ dissolved	(19)
TiO$_2$/catalyst residue from a Ziegler–Natta catalyst petrochemical plant	Impregnation	Drugs	Drugs, namely, atorvastatin calcium, diclofenac sodium, fluoxetine, ketoconazole, ibuprofen, dexamethasone, tioconazole, naphazoline hydrochloride, valsartan, guaifenesin, and paracetamol. The highest drug degradation was observed under UV (48.6%) and visible (45.2%) radiation with the synthesized photocatalyst	(20)

[a]Selectivity factor (SF) for single component; competitivity factor (CF) for mixture
[b]MI: molecularly imprinted

**Table 1.** Solid photocatalysts typically used for degradation processes.

In parallel, some alternative approaches in the development of potential heterogeneous photocatalyst, namely (i) the use of industrial wastes as source of photocatalyst systems which were impregnated on commercial supports (20–22); (ii) the use of the concept of molecular imprinting (MI) to afford selectivity to the adsorption and photocatalyst degradation of target molecules (23–25), and (iii) combination of nano- and micro-particles as supports (26–28) for the impregnation of titania active species were explored. Regarding to the former, the rationale was that several photocatalyst systems imply the use of metal doping to guarantee a better photocatalyst activity or to shift the spectrum of actuation toward the visible spectrum region. The employed residues (industrial petrochemical chemistry, galvanic bath residuals, silver-containing residual solutions from photography classes, metal-containing residual solutions from academic analytical chemistry classes) contained several metals (Zn, Ag, Cr, Cu Mg, including Ti) which could exhibit photocatalyst activity (29), as shown in Scheme 1.
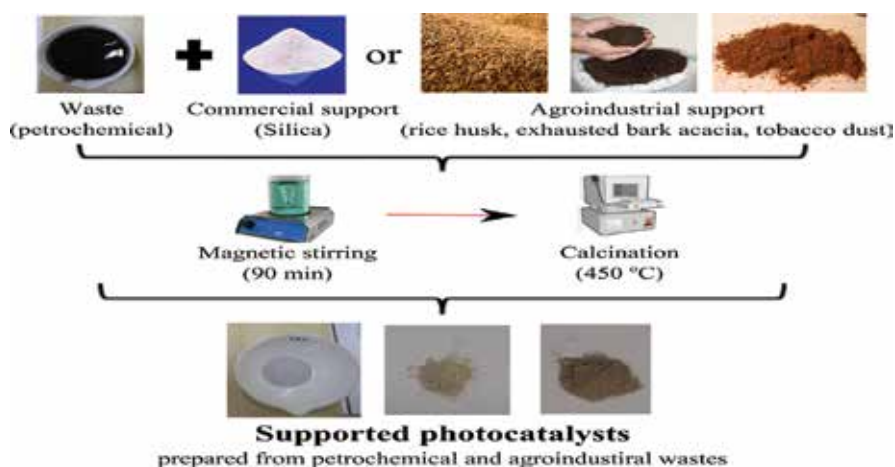
Scheme 1. Representation for the preparation of the supported photocatalysts from petrochemical and agroindustrial wastes.

In the case of MI systems, template-shaped cavities are designed using polymer matrices with memory of the template molecules that can be applied in molecular recognition (30, 31). As reported in the literature (32, 33), matrices prepared by the sol–gel method offer certain advantages compared to conventional organic polymerization methods, such as rigidity, thermal stability, tailored porosity, and flexibility in processing conditions. MI process can be roughly described in Scheme 2. At first stage, a template–functional monomer complex is assembled via appropriate interactions. A cross-linking monomer is then used to form the solid MIP matrix. Finally, the removal of the template molecule liberates an imprint cavity of a defined size and shape.

The aim of such approach is to provide a selectivity factor for heterogeneous photocatalysts, considering that the target molecule would be employed in the synthesis of the solid material. The presence of the cavities in the shape of a given pollutant would favor its adsorption and photocatalytical decomposition viz-a-viz to the other species present in the milieu.
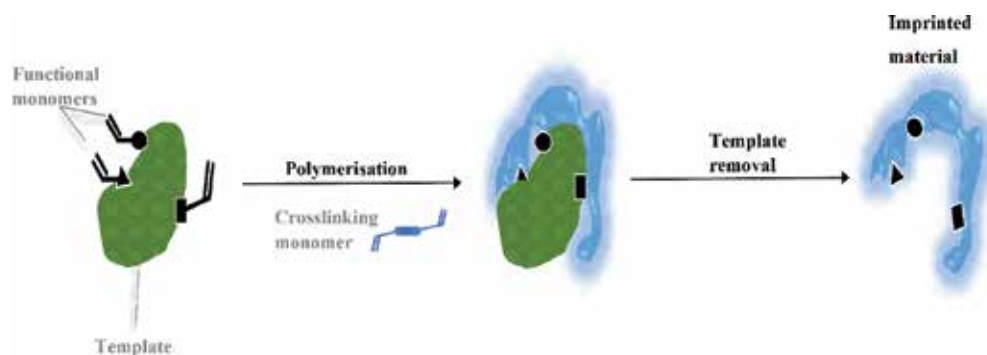
Scheme 2. Schematic representation of the imprinting process.

Concerning the third approach, nanosilicas are the materials of large surface area, bearing uniform and tunable pores, and small particle size and mechanical strength. These are important characteristics that may affect the photocatalytic activity and enhance the thermal stability of the photocatalyst. During the last decade, several mesoporous materials with different compositions of metal nanoparticles and complex nanostructured hybrid systems using SiO_2 supports have been explored for degradation of RhB by photocatalysis. For instance, core@dual–shell SiO_2–TiO_2 composite fibers (34), TiO_2/Au/SiO_2 (~50 nm) (35), Fe_3O_4@SiO_2@TiO_2@Pt (~420 nm) (36), Pt@SiO_2@TiO_2 core–shell composites (~120 nm) (37), etc. But these catalyst systems do not exhibit very large surface areas, and they may present limitations in catalyst reuse due to their size. The proposed strategy here consists in combining silica nanoparticles (7.8–12.3 nm) produced by the sol–gel method with commercial microsilica as support for $TiCl_4$ impregnation, which would be further calcinated to TiO_2 (21, 24) as shown in Scheme 3. This system offers considerable potential as solid nano-/microstructured supports for the immobilization of heterogeneous photocatalysts overcoming the size problem in the reuse, generating catalyst species both on the surface of the nanoparticle moieties, as well as on the micrometric particle (silica bulk), which improve the adsorption and the contact between the pollutant molecules and the catalyst.
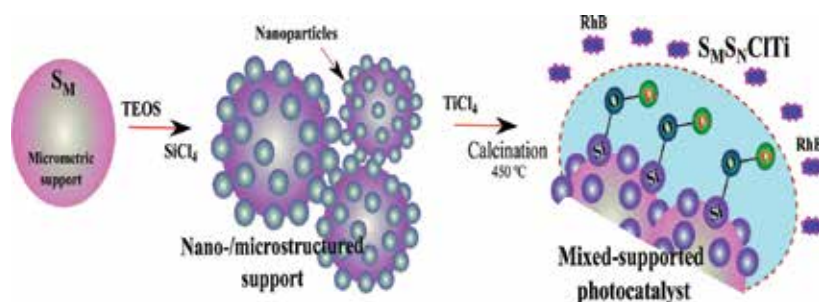
Scheme 3. Representation for preparation of mixed-supported heterogeneous photocatalyst.

The aim of the present manuscript is to compare the photocatalyst activity of these three above-cited approaches, operating under the same reactor conditions and with the same target molecule (Rhodamine B). For comparative reasons, commercial TiO$_2$ (Degussa P25) was also evaluated.

2. Experimental

2.1. Materials

Silica solutions were prepared using tetraethoxysilane (TEOS, >98%, Sigma-Aldrich) and ethanol (99.5%, Nuclear) as the solvent. Hydrochloric acid (HCl, Nuclear, 38%) and ammonium hydroxide (29%, Nuclear) solution were used as catalysts by the sol–gel method. Silicon tetrachloride (SiCl$_4$, 99%, Sigma Aldrich) was used to chemically modify the silica solutions. Sylopol-948 (Grace) was used as the micrometric silica reference. In addition, fumed silica (Wacker HDKN20), zeolite NaY (Zeolyst Internatial), and agroindustrial waste (rice husk) were used as the support for the photocatalysts. TiCl$_4$ (Merck), metal-containing residual solutions from academic analytical chemistry classes and residual Ziegler–Natta catalyst slurry (Ti-based polymerization catalyst) from a petrochemical plant were employed for the preparation of the supported titania photocatalyst. Rhodamine B (C$_{28}$H$_{31}$N$_2$O$_3$Cl, PrótonQuímica, P.A) was used as the dye probe for the degradation tests. Double-distilled deionized water was used for the preparation of solutions used in the catalytic tests. For comparative purposes, Degussa P25 (denoted as TiO$_2$) was also employed as received.

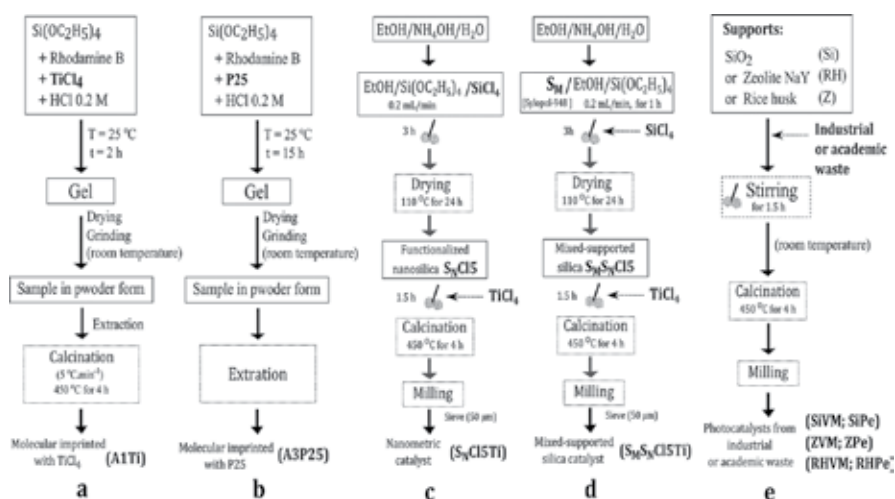### 2.2. Preparation of supported photocatalysts

The molecular imprinting (MI) materials were prepared using the sol–gel process by acid route and TEOS as the raw material. Three different protocols were investigated: acid-catalyzed route 1 using TiCl$_4$ as TiO$_2$ precursor followed by a fast calcination (A1Ti), acid-catalyzed route 2 followed by a slow calcination (A2Ti), and acid-catalyzed route 3 using P25 as TiO$_2$ precursor (A3P25). All samples were prepared with 0.2 M of hydrochloric acid at a 1:2 (HCl–TEOS) ratio. For each sample, RhB was fixed at 150 mg. RhB was added to a solution of TEOS followed by addition of TiCl$_4$, and then the catalyst was added. For template removal, ultrasound-assisted (Branson-Sonifer®, Model 250) extraction was employed using methanol as the solvent (approximately 70 mL). These samples were labeled as molecularly imprinted (MI). Equivalent sample was prepared without the addition of RhB, that is, non-imprinted (NI) system (ATi). Both systems were submitted to a calcination process (450°C for 4 h at a rate of 5°C/min). In the case of system containing P25 (A3P25), this was added 2½ h after the beginning of the synthesis reaction. For comparison, the same material was synthesized without P25 (AWP25). There was no need for calcination in these systems. More details are reported elsewhere (23, 24, 38).

In the case of supported photocatalysts prepared using waste materials, 3 mL of residue was added to 1.0 g of fumed silica or zeolite NaY or rice husk. These materials were maintained

under stirring for 90 min. Then, the solution was placed in a muffle furnace for 4 h for calcination (450°C). More details are reported elsewhere (20–22).

Functionalized nanosilicas were prepared by the hydrolysis of TEOS using a standard procedure described in the literature (21, 27). Thereafter, $SiCl_4$ was added to the nanoparticles in solution. The silica nanoparticles were prepared using TEOS/$SiCl_4$ in a molar ratio of 5.0–8.0. Hereafter, the resulting nanoparticles (powder) are labeled according to the TEOS/$SiCl_4$ molar ratio employed in the synthesis. For example, S_NCl5 refers to nanosilicas prepared with a TEOS/$SiCl_4$ molar ratio equal to 5.0. Mixed-supported silicas were obtained by mixing the silica nanoparticles (previously synthesized) with 0.2 g of a Sylopol-948 (commercial micrometric silica (S_M)) and stirred for 3 h. Mixed silicas were labeled as S_MS_NCl, indicating the presence of Sylopol-948 (S_M) combined with synthesized nanosilicas (S_NCl) from the preparation with $SiCl_4$. Further details are reported elsewhere (27). 3.0 mL of $TiCl_4$ was added to 1.0 g of synthesized silica particles and stirred for 90 min. After, the samples were then placed in a muffle furnace for 4 h for calcination (450°C). Two different nanometric supports were used in the production of nanometric catalysts (labeled S_NCl5Ti to S_NCl8Ti), and mixed silicas were used in the production of two mixed support catalysts (S_MS_NCl5Ti to S_MS_NCl8Ti).

Scheme 4 depicts the steps involved in the preparation of each supported photocatalyst as well as the corresponding labels. Preparation of MI materials is illustrated in Scheme 4a, b. Synthesis of functionalized nanosilicas catalysts and mixed-supported silicas ones is shown in Scheme 4e, d. Scheme 4e displays the preparation of catalysts using industrial and academics waste as the source of photocatalysts as well as the corresponding employed labels.

Scheme 4. Steps employed for preparation of the supported titania photocatalysts from MI materials (a, b), nanosilicas (c), mixed silicas (d), and fumed silicas or zeolite or rice husk (e).

Table 2 presents the set of photocatalyst compared in the present study, as well as the corresponding label.

Method	System	Label
	Degussa P25	**P25**
	Photolysis	**PHOTO**
Molecular imprinted (MI)	$TiCl_4$ + RhB	**A1Ti**
	$TiCl_4$ + RhB	**A2Ti**
	P25 + RhB	**A3P25**
	RhB	**A4WP25**
	$TiCl_4$	**ATi**
Nanoparticles and mixed silicas	$TiCl_4$ + S_M	**S_MTi**
	$TiCl_4$ + S_NCl5	**S_NCl5Ti**
	$TiCl_4$ + S_NCl8	**S_NCl8Ti**
	$TiCl_4$ + $S_M S_N$Cl5	**$S_M S_N$Cl5Ti**
	$TiCl_4$ + $S_M S_N$Cl8	**$S_M S_N$Cl8Ti**
Industrial and academic wastes	Various metals + SiO_2	**SiVM**
	Petrochemical + SiO_2	**SiPe**
	Various metals + Zeolite NaY	**ZVM**
	Petrochemical + Zeolite NaY	**ZPe**
	Various metals + Rice husk	**RHVM**
	Petrochemical + Rice husk	**RHPe**

Table 2. Supported photocatalysts prepared from MI materials, synthesized silica particles, and chemical waste.

2.3. Characterization of the supported titania photocatalysts

The specific surface area (S_{BET}), the pore diameter (Dp_{BJH}), and pore volume (Vp_{BJH}) were calculated by the Brunauer-Emmett-Teller method (BET) (39) and Barrett-Joyner-Halenda (BJH) algorithm (40), respectively. Measurements were taken using a Micromeretics TriStar II 3020 in the partial pressure range of $0.01 < P P_0^{-1} < 0.95$. Small-angle X-ray scattering (SAXS) measurements were performed at the SAXS1 beamline at the National Synchrotron Light Laboratory (LNLS), Campinas, Brazil. The scattered X-ray beam presenting a wavelength (λ) of 1.488 Å was detected on a Pilatus 300 k detector (27). I(q) vs. q scattering profiles were fit by multi-level of structural organization using the Beaucage model (41–43) in the Irena routine (44). The zeta potential of the nanoparticles and mixed supports (approximately 250 mg) was measured using Zetamaster equipment (Malvern Instrument). Metal content in the catalysts was determined by Rutherford backscattering spectrometry (RBS) using a He^{2+} beam of 2.0 MeV incident on the homogeneous tablets of the compressed (12 MPa) catalyst powder. SEM images were collected at the Center for Nanoscience and Nanotechnology (CNANO, UFRGS) in an EVO-50 (Carl Zeiss, Inc.) field emission scanning electron microscope equipped with a secondary electron detector Everhart-Thornley (ETSE) at 0.2–30 kV and with a working distance of 14 mm. UV–vis spectra of the supported photocatalysts in powder form were

recorded using a Varian Cary 100 Scan Spectrophotometer with an accessory DRA-CA-301 (Labsphere) in the diffuse reflectance mode by co-adding 32 scans in the 200–800 nm range. The energy bandgap was determined by means of the Kubelka–Munk function. Scans ranged from 200 to 800 nm. Scanning electron microscopy (SEM) and energy dispersive X-ray (EDX) were performed using a JSM5800 (JEOL) microscope, operating between 5 and 20 kV. The samples were coated with a thin layer of conductive carbon by a sputtering technique. Diffuse reflectance infrared Fourier transmission spectroscopy (DRIFTS) was carried out at room temperature in a Bomem MB-102 spectrometer equipped with a diffuse reflectance accessory. Analyses at the absorbance modes were performed by co-adding 32 scans with 4 cm^{-1} of resolution. The spectral characteristic bands of the harmonic vibration of the silica materials network [$\nu_{as(Si-O(-Si))}$] [$\nu_{as(Si-O(-Si))}$] were studied by the FT-IR spectra in the region of 1300–1000 cm^{-1} (45–47). The broadband between 1300–1000 cm^{-1} was deconvoluted via Gaussian functions into four independent components: two (TO_4 and TO_6) associated with the transverse-optic (TO) modes and two (LO_4 and LO_6) with the longitudinal-optic (LO) modes of Si-O-Si using a nonlinear least-squares fitting method [39]. The percentage of sixfold rings (SiO_6) in the silica network (Q_6) was estimated using the following ratio of fitted areas (27, 48, 49):

$$\%(SiO_6) = \frac{[A(LO_6) + A(TO_6)]}{[A(LO_6) + A(TO_6) + A(LO_4) + A(TO_4)]} \times 100 \tag{1}$$

2.4. Statistical analysis

The SPSS Statistical software (SPSS for Windows, version 19, IBM®) was used to analyze the relationships among the data. All statistical tests were performed at the $P < 0.05$ level of significance. The Spearman correlation coefficient (r_{Sp}) was used as a nonparametric measure of statistical dependence between two variables.

2.5. Photocatalyst tests

For tests with the Rhodamine B, 0.0175 g of catalyst was added to 25 mL of the test molecule (20 mg L^{-1}) at pH of the reaction medium (pH $\cong$ 4.3). The solution was then transferred to the reactor, and after adjusting the temperature (at 30°C), the lamp was switched on to start the irradiation. During each experiment, circulation of suspension was maintained to keep it homogenous and to have uniform temperature. Samples (5 mL) were taken at regular time intervals (0, 5, 15, 30, and 60 min) and then centrifuged (Cientec CT-5000R) for 20 min at 5000 rpm in order to separate the catalyst particles from the samples. To determine the concentration of RhB, solution absorbance was read in a Varian Cary 100 UV–vis spectrophotometer at the wavelength of maximum absorbance of target molecule (553 nm for RhB), and the absorbance was related to the concentration of the RhB through a calibration curve: Abs = 0.2053 C (mg L^{-1}) (R^2 = 0.9911; N = 7). All photocatalytic tests were performed in duplicate (error value lower than 5%). Photolysis tests were also performed to determine the percentage of dye degradation due to UV light exposure without the presence of a photocatalyst.

3. Results and discussion

According to the RBS results, the metal concentration is low in terms of the Ti/Si ratio. Systems S_MS_NClTi showed a Ti average composition of 0.45 wt%/SiO$_2$, whereas the S_NClTi obtained 1.33 wt%/SiO$_2$. Therefore, the S_N5ClTi achieved a higher metal content. According to the SEM-EDX results, the average atomic percentage of Ti was 16.04 ± 3.05 at.%. As shown in **Table 3**, Si was present in all the samples. Depending on the photocatalysts from wastes, Cu, Zn, Al, Ti, Cr, or Mg were also present.

System	C/Si	Cu/Si	Zn/Si	Al/Si	Ti/Si	Cr/Si	Mg/Si
SiVM	1.03	0.05	0.01	0.13	0.01	0.01	–
SiTi	4.55	0.04	–	–	0.52	–	2.11
ZVM	–	0.01	0.01	0.67	0.01	0.01	–
ZPe	–	0.02	–	0.67	0.35	–	0.08
RHVM	7.60	0.01	0.01	–	0.02	0.01	0.01
RHPe	7.60	0.01	–	–	0.04	–	0.04

Table 3. The chemical composition of the catalysts in terms of atomic ratio determined by SEM-EDX, considering Si as internal standard.

Photocatalyst activity in the degradation of rhodamine B was comparatively evaluated by the three supported catalyst systems, under UV and visible irradiation, as shown in **Table 4**.

As shown in **Table 4**, the efficiency of the photolysis degradation was <8%. The P25 showed an excellent performance in the UV (82%), but poor performance in the visible (12.3%). All of the supported titania photocatalysts exhibited better photocatalyst activity (25.4–61.6%) for RhB degradation than commercial P25 under visible radiation. The S_NCl5Ti catalyst showed the best photocatalyst activity under UV (68%) irradiation, followed by SiPe (66.8%).

The approach of nanometric photocatalysts showed better performance (59–68%) than the nano-micrometer systems (33.6–42.7%) under UV and visible radiation. This is due to the incorporation of higher amount of titanium on the surface of nano-catalysts, as shown in the results of RBS. However, both approaches are valid for the degradation of organic pollu-tants from supports such as silicas synthesized by sol–gel, because nano-micrometer photo-catalysts (25.4–30.1%) also were better than the P25 under visible radiation. The advantage of a nano-micrometric system resides in the possibility of reusing the catalyst several times as have already studied (27, 28, 50), which is a current limitation of nanoscale catalysts.

All the supported photocatalysts from industrial waste exhibited photocatalyst activity in dye degradation, although with catalyst activity lower than that of Degussa P25 under UV radiation. On the other hand, all the catalysts from industrial and academic wastes exhibited activity higher than that of Degussa P25 under visible radiation, suggesting a potential

application of such photocatalysts under sun irradiation. Among them, the SiPe catalyst showed the best photocatalyst activity under UV (66.8) and visible (61.6%) irradiation. The higher efficiency in the photocatalytic activity of the SiPe sample compared with the other samples may be because the SiPe sample has the lowest Eg value, the largest ZP value (in the module), and the highest S_{BET} (available surface area of the active sites) and Vp values.

Method	System	Degradation RhB (%) radiation	
		UV	Visible
	P25[a]	82.0	12.3
	P25[b]	44.3	n.d.
	Photo	5.5	n.d.
Molecular imprinted (MI)	A1Ti	32.2	n.d.
	A2Ti	37.8	n.d.
	A3P25	50.9	n.d.
	A4WP25	20.0	n.d.
	ATi (NI)	12.7	n.d.
Nanoparticles and mixed silicas	S_MTi	n.d	n.d.
	S_NCl5Ti	68.0	45.1
	$S_M S_N$Cl5Ti	42.7	30.1
	S_NCl8Ti	59.0	35.6
	$S_M S_N$Cl8Ti	33.6	25.4
Photocatalysts from wastes	SiVM	41.1	48.2
	SiPe	66.8	61.6
	ZVM	31.7	30.7
	ZPe	53.0	46.3
	RHVM	27.8	11.2
	RHPe	30.9	30.6

[a]Experimental WL; catalyst = 0.7 g L^{-1}, CRhB = 20 mg L^{-1}, T = 30°C, natural pH = 4.3, UV radiation of 30 W m^{-2}, and visible of 202 W m^{-2} error of 5%.
[b]Experimental conditions: catalyst = 0.55 g L^{-1}, CRhB = 20 mg L^{-1}, T= 30°C, natural pH, UV radiation of 30 W m^{-2}, and error of 5%.

Table 4. Percentage degradation of RhB under visible (a) and UV (b) irradiation after 60 min of reaction.

We have shown that our MI systems showed selectivity and competitiveness up to 1.9 and 3.5, respectively, toward RhB. Also, compared to the commercial sample (P25), selectivity (up to 180%) and competitiveness (up to 290%) were obtained (24). However, the average of activities under UV radiation was lower than the average values obtained by nano-silica (1.44-fold

lower) and industrial wastes routes (1.16-fold lower). On the other hand, the lowest value of activity achieved within the MI systems containing TiO_2 (32.2%) was comparable to the S_MS_NC18Ti (33.6%) and higher than RHVM (27.8%), which showed the lowest activities within nanosilica and industrial wastes routes, respectively. Despite their lower activities, one of the main advantages of MI approach is the possibility to achieve better selectivity removal compared to the commercial samples and also reusability (51), which are recognized drawbacks in heterogeneous photocatalysis (6). **Figure 1** shows the results of RhB photocatalyst decomposition under visible and UV radiation by selected photocatalysts from each of the three approaches.
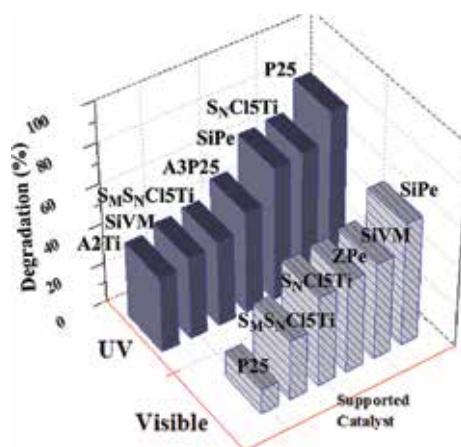
Figure 1. Percentage of degradation of RhB under visible (a) and UV (b) irradiation after 60 min of reaction by better photocatalysts each approaches.

As shown in **Figure 1**, comparing among all the supported photocatalysts, the performance of P25 is inverted under visible radiation, becoming the lowest among all. The catalysts from industrial waste dominate over nanosilicasand mixed silicas supports.

In order to understand the differences concerning each alternative route, these systems were characterized by a series of complementary techniques aiming at accessing some informa-tion concerning textural, structural, and morphological aspects of these supported catalysts.

3.1. Textural characteristics of photocatalysts

The catalytic activity of the particle samples is proportional to their specific surface area because it requires the adsorption of reactants and also the transfer of photoexcited electrons into the adsorbed molecules, which is directly related to the diffusion of the RhB to the catalyst center (52). The specific surface area (S_{BET}), the specific pore volume (Vp_{BJH}), pore diameter (Dp_{BJH}) are presented in **Table 5**.

Method	System	S_{BET} (m² g⁻¹)	Vp_{BJH} (cm³ g⁻¹)	Dp_{BJH} (nm)	Rg (nm)	P	ZP (mV)	Eg (eV)	SiO₆ ᵉ (%)
	P25	56.0	0.22	2.6	1.4	4.0	−3.6	3.3	n.d.
Molecular imprinted (MI)	**A1Ti**	634.5	0.47	3.1	9.8	3.4	−22.9	2.1	48.7
	A2Ti	750.6	0.40	2.9	9.8	3.6	−10.9	2.0	54.9
	A3P25	516.4	0.25	2.7	7.5	3.3	−21.9	2.8	60.0
	A4WP25	837.8	0.42	2.3	1.0	3.7	−10.6	n.d.	52.0
	ATi (NI)	463.4	0.30	2.9	4.3ᶜ	3.3ᵈ	−29.3	2.2	41.0
Nanoparticles and mixed silicas	**S_MTi**	240.9	0.10	3.0	4.2	4.0	−8.4	3.8	37.2
	S_NCl5Ti	123.6	0.01	2.9	6.8	2.5	−29.5	2.8	50.3
	S_MS_NCl5Ti	155.8	0.09	4.3	12.3	2.0	−21.9	3.1	31.4
	S_NCl8Ti	107.1	0.16	9.1	7.8	3.6	−26.5	3.0	88.7
	S_MS_NCl8Ti	109.8	0.17	8.4	8.6	3.6	−10.8	3.7	74.7
Photocatalysts from wastes	**SiVM**	277.0	0.4	12.1	6.2	3.9	−22.3	2.7	n.d.
	SiPe	280.0	1.9	20.1	2.7	3.9	−36.4	1.8	n.d.
	ZVM	156.0	0.3	0.6	2.4	4.0	−26.4	2.9	n.d.
	ZPe	272.0	0.3	0.7	2.6	4.0	−27.6	2.3	n.d.
	RHVM	118.0	0.5	1.3	3.1	4.0	−20.3	3.2	n.d.
	RHPe	182.0	0.5	8.0	0.6	4.0	−28.6	2.9	n.d.

ᵃExtracted from high-q region (SAXS);
ᵇPower-law decay (P) extracted from low-q region (SAXS);
ᶜ,ᵈThese systems showed a structure that consists of two organizational levels;
ᵉ%(SiO)₆ was determined by Eq. (1).

Table 5. BET isotherm parameters, radius of gyration of particles (Rg), and the linear Power-law decay (P) obtained through unified fit on the SAXS profiles, zeta potential (ZP), bandgap energy (Eg), and percentage of sixfold rings (SiO₆) for the photocatalysts.

According to **Table 5**, all systems prepared are mesoporous materials as classified by the International Union of Pure and Applied Chemistry (IUPAC) (53, 54). It can be seen that all systems have shown values of surface area higher than the commercial sample. Also, the mean value achieved for the MI systems is ca. 4.6-fold and 3.1-fold higher than the mean values found for nanometric and photochemical residue, respectively. Moreover, the supported photocatalysts with $TiCl_4$ showed a reduction in the final surface area in relation to the nanometric and mixed supports, which also are observed in photocatalysts prepared with petrochemical residue and solution of various metals supported on zeolite NaY (ZVM and

ZPe) and the system with molecular imprinted in which P25 was added (A3P25). This fact can be due to the high calcination temperature providing the agglomeration of the catalytic metal particles, thus decreasing the available surface area (55, 56) and the degree of structural organization and internal pores between nanoparticles, mixed silicas, and zeolite NaY (27, 56). Considering the resulting heterogeneous photocatalysts from $TiCl_4$ or wastes impregnation, the SiPe reached the highest specific surface area and pore volume. This increase can be associated with action of the waste or $TiCl_4$ on the respective support rendering difficult the contact between the particles and avoiding the agglomeration of the catalytic particles.

3.2. Multi-scale organization of the photocatalysts analyzed by SAXS

The photocatalysts were further analyzed by SAXS, which provides structural information, that is, a broader and clearer view of catalysts formation and aggregation (57). The multi-hierarchical organization of these materials, their gyration radius (Rg), and fractal structure (P) were investigated through the Unified approach (41–43) in the Guinier and Power-law regions. Table 5 shown radius of gyration of particles (Rg) and the linear Power-law decay (P), obtained through Unified fit on SAXS profiles of photocatalysts.

As shown in Table 5, photocatalysts are organized into three levels, excepting ATI and P25 which show two levels. Rg results show that the primary particle size ranges from 0.6 to 12.3 nm, according to the preparation method. Catalysts $S_M S_N Cl5Ti$ was the largest particle, due to the combination of nanoparticles incorporated into the surface of a micrometric support as (S_M), resulting in bigger aggregated mixed silica catalyst ($S_M S_N ClTi$).

Comparing fractal structure (P) results, P25 is a completely spherical particle, as well as the photocatalyst from industrial wastes (P = 4), which corresponds to spherical and dense clusters of approximately smooth surface according to Beaucage (42, 43). On the other hand, all MI systems showed fractal surface (3.3 < P < 3.7), whereas that nano- and micronano-photocatalysts mass fractals (2.0 < P < 2.5) to surface fractals aggregates (P = 3.6).

3.3. Zeta potential (ZP) measurements

Zeta potential (ZP) measurements were used to verify the stability of the suspensions of the studied systems, to determine its influence on the RhB dye adsorption of the supported photocatalysts and to correlate the electric potential information with the results obtained by SAXS. Table 5 shown the ZP and E_g values. **Figure 2** shows the relationship among S_{BET}, Rg and ZP of the best catalysts for each strategy discussed in this article.

The supported catalysts using the MI approach present ZP between −10.6 and −22.9 mV and in the case of synthesized nanoparticles and mixed silicas, ZP lies between −10.8 and −29.5 mV. For the impregnated with industrial and academic wastes ZP was between −20.3 and −36.4 mV (as shown in Table 5).
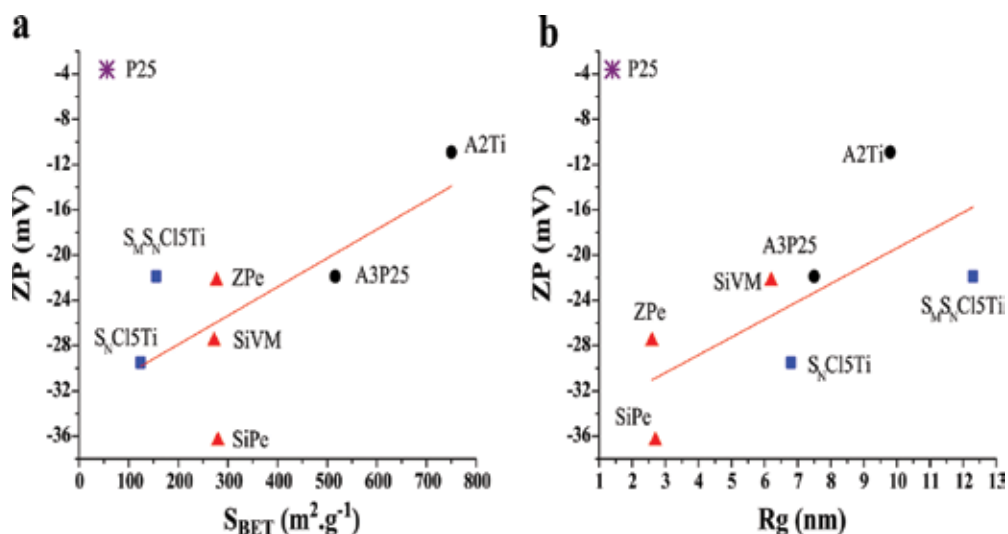
Figure 2. The zeta potential of better photocatalyst dispersions as a function of (a) S_{BET} and Rg by SAXS. Spearman's correlations: $r_{Sp} > 0.705$ for (a) and $r_{Sp} > 0.757$ for (b).

According to **Figure 2a**, there is a direct correlation ($r_{Sp} > 0.705$) between electronic (ZP) and textural properties (SBET) of photocatalysts. Among all the photocatalysts, SiPe showed the highest ZP (−36.4 mV) (in module) and all systems bear a negative charge on their surfaces. The negative charge density on the surface is greater in the smaller photocatalyst, most likely due to the smaller particle size (2.4–6.8 nm). It is worth noting that high surface area supports are desirable for photocatalysis because it can promote the adsorption of the dye RhB to be degraded on the catalyst/support surface (21). Such behavior is in accordance with the results of Ribeiro et al. (58) and Gaya and Abdullah (59), who reported that the performance of a photocatalyst is dependent on the surface textural characteristics (size, surface area, and pore volume) because the local morphology strongly influences the number of striking photons and the rate of the photocatalytic reaction.

Conversely, it was possible to observe a strong direct correlation ($r_{Sp} > 0.757$) between the zeta potential and the particle radius supported catalysts, as shown in **Figure 2b**. A smaller particle size corresponds to a higher negative surface charge: The nanometric photocatalyst (SiPe, ZP = −36.4 mV and Rg = 2.7 nm) exhibited this trend. The preparation of photocatalyst by impregnation with industrial and academic waste showed two effects: (i) increase the particle radius (Rp) and (ii) enhance the negative zeta potential. In this study, better photocatalyst showed an increase in zeta potential as the particle radius increased (−10.9 to −36.4 mV). The trend is consistent with the fact that the van der Waals forces are dominant over the electrostatic repulsive ones: the electrical double-layer thickness decreases, thereby promoting the agglomeration of primary particles, which in turn affords the particle growth size, as shown in the SAXS analyses.
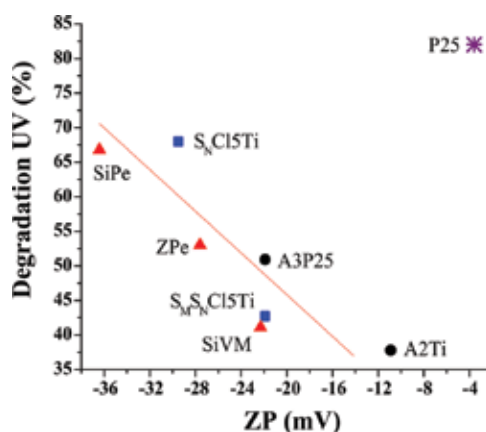
Figure 3. Correlation between degradation RhB under UV radiation and ZP of the better photocatalysts. Spearman's correlations: $r_{Sp} > -0.827$.

According to **Figure 3**, the performance of heterogeneous photocatalysts under UV radiation is related to the zeta potential showing a strong correlation ($r_{Sp} > -0.827$). In the present case, RhB is characterized by its cationic nature, and its compatibility with the photocatalyst surface potential (negative charge) may potentially improve the photocatalyst activity (59). On the other hand, all the photocatalysts exhibited activity higher than that of Degussa P25 under visible radiation, suggesting a potential application of such photocatalysts under sun irradiation. It is important to highlight that S_NCl5Ti is synthesized from silicas nanoparticles, whereas SiPe is prepared from petrochemical waste. Both strategies are viable for the degradation of organic pollutants. Based on the ZP results, we established that photocatalyst dispersions are stable and that the BET and SAXS analyses are in agreement and interrelated with the discussion about the electronic properties of these photocatalysts.

3.4. Energy bandgap (Eg) by DRS

The energy bandgap (E_g) is a relevant parameter for the photocatalytic process because lower values of E_g correspond to less radiation energy required to activate the process, which may reduce the required radiation into the visible light range (60). To determine the photoabsorbance properties, UV-DRS was employed in the wavelength range of 200–800 nm. Table 5 shows E_g of photocatalysts. For comparative reasons data from commercial photocatalyst (P25) were also included.

It was possible to observe strong correlations ($r_{Sp} > -0.749$ and $r_{Sp} > -0.788$) between the energy bandgap (Eg) with pore volume (Vp_{BJH}) and surface area (S_{BET}). Thus, the higher the pore volume, the higher the surface charge (in module), which may promote diffusion of the dye from the solution to the catalyst centers. On the other hand, the higher the surface charge (in module), the lower the energy to promote the electron from the valence band to the conduction band. Comparing the E_g values between the prepared photocatalysts, as shown in Table 5, the E_g of the catalysts ranged from 1.8 to 3.7 eV. Notably, the SiPe sample exhibited the lowest

E_g value among the prepared titania photocatalysts. These results illustrate the role played by E_g on the photocatalytic process and the effects of textural (surface area and pore volume) and electronic (ZP) characteristics.

3.5. Four- and six-membered Silica

Comparing MI systems with nanoparticles and mixed silicas, one can see that systems containing $TiCl_4$ (A1Ti, A2Ti and ATi) and the systems with lower TEOS:$SiCl_4$ ratio (S_NCl5Ti and S_MS_NCl5Ti) afford the lowest $\%(SiO)_6$ content (below than 55%). Thus, these materials tend to present more rigid structure of silica represented by four-membered silica ($(SiO)_4$). In the other words, both the presence of P25 and higher TEOS:$SiCl_4$ ratio result in more hydrophilic materials. As a general trend, hydrophilic materials seem to be more easily achieved by a protocol using the synthesis of silica nanoparticles than the MI materials. Although $\%(SiO)_6$ was not correlated with degradation of RhB, it is interesting to note that materials with the highest $\%(SiO)_6$ content (A3P25 and $S_NCl18Ti$) afforded better degradation under UV radiation.

3.6. Morphological characteristics obtained using SEM

Scanning electron microscopy (SEM) was used to evaluate the particle morphologies of supports. The low- and high-magnification images of the nanoparticles are shown in **Figure 4**.
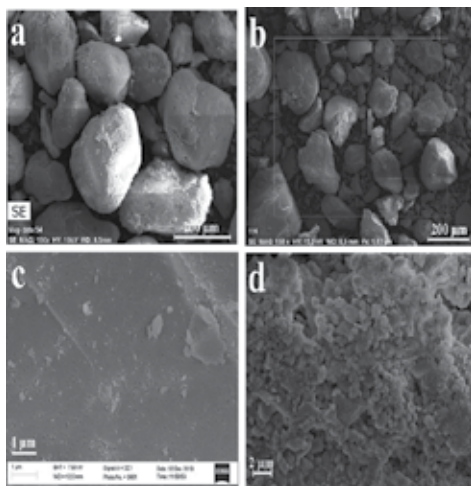

Figure 4. SEM images of (a) SPe, (b) ZPe, (c) of MI materials, (d) S_MS_N5ClTi.

According to **Figure 4a, b** supports SPe and ZPe are larger particles and approximately rounded, whereas synthesized silica supports (S_MS_NCl5Ti) are smaller, amorphous, and aggregate particles (**Figure 4d**). In the case of MI materials, as observed in **Figure 4c**, a large number porous and some particle agglomerates are present on the surface of system. In the

case of MI materials, as observed in **Figure 4c**, a large number porous and some particle agglomerates are present on the surface of system.

4. Conclusions

This work presented three alternative approaches for the degradation of organic pollutants such as RhB. Imprinting molecular materials, synthesized silica particles as catalytic supports from $TiCl_4$ and photocatalysts from industrial and academic waste demonstrated activity for degradation of RhB dye under visible (61.6%) and UV (68%) radiation and are better than the commercial TiO_2 (12.3%) under visible radiation. The textural and structural characteristics of the supported catalyst prepared with fumed silica and petrochemical waste (SiPe), namely the low-energy bandgap (1.8 eV), large surface area (280 $m^2 g^{-1}$), high pore volume (1.9 $cm^3 g^{-1}$), and high zeta potential value (−36.4 mV), may have been responsible for their high activity.

Our alternative approaches herein studied could help to overcome the main drawbacks involved in heterogeneous photocatalyst, such as the lack of selectivity, the low surface area, and UV-limited spectrum for commercial samples.

Acknowledgements

Author details

Yolice P. Moreno[1], Cicero C. Escobar[1], William L. da Silva[1] and João H. Z. dos Santos[2*]

*Address all correspondence to: jhzds@iq.ufrgs.br

1 Department of Chemical Engineering - Federal University of Rio Grande do Sul, Rua Engenheiro Luis Englert, CEP Porto Alegre, RS, Brazil

2 Institute of Chemistry - Federal University of Rio Grande do Sul, Av. Bento Gonçalves, CEP Porto Alegre, RS, Brazil

References

[1] Chen J, Liu M, Zhang J, Ying X, Jin L. Photocatalytic degradation of organic wastes by electrochemically assisted TiO$_2$ photocatalytic system. Journal of Environmental Management. 2004; 70(1): 43–7.

[2] Parolin F, Nascimento UM, Azevedo EB. Microwave-enhanced UV/H$_2$O$_2$ degradation of an azo dye (tartrazine): optimization, colour removal, mineralization and ecotoxicity. Environmental Technology. 2013; 34(10): 1247–53.

[3] Ribeiro AR, Nunes OC, Pereira MFR, Silva AMT. An overview on the advanced oxidation processes applied for the treatment of water pollutants defined in the recently launched Directive 2013/39/EU. Environment International. 2015; 75: 33–51.

[4] Andreozzi R, Caprio V, Insola A, Marotta R. Advanced oxidation processes (AOP) for water purification and recovery. Catalysis Today. 1999; 53(1): 51–9.

[5] Nakata K, Fujishima A. TiO$_2$ photocatalysis: design and applications. Journal of Photochemistry and Photobiology C: Photochemistry Reviews. 2012; 13(3): 169–89.

[6] Shaham-Waldmann N, Paz Y. Modified Photocatalysts. Photocatalysis and Water Purification. Wiley-VCH Verlag GmbH & Co. KGaA; 2013. pp. 103–43.

[7] Ibhadon AO, Fitzpatrick P. Heterogeneous photocatalysis: recent advances and applications. Catalysts. 2013; 3(1): 189–218.

[8] Huang C, Tu Z, Shen X. Molecularly imprinted photocatalyst with a structural analogue of template and its application. Journal of Hazardous Materials. 2013; 248–249(0): 379–86.

[9] Luo X, Deng F, Min L, Luo S, Guo B, Zeng G, et al. Facile one-step synthesis of inorganic-framework molecularly imprinted TiO$_2$/WO$_3$ nanocomposite and its molecular recognitive photocatalytic degradation of target contaminant. Environmental Science & Technology. 2013; 47(13): 7404–12.

[10] Lu Z, Huo P, Luo Y, Liu X, Wu D, Gao X, et al. Performance of molecularly imprinted photocatalysts based on fly-ash cenospheres for selective photodegradation of single and ternary antibiotics solution. Journal of Molecular Catalysis A: Chemical. 2013; 378(0): 91–8.

[11] Khraisheh M, Kim J, Campos L, Al-Muhtaseb AaH, Al-Hawari A, Al Ghouti M, et al. Removal of pharmaceutical and personal care products (PPCPs) pollutants from water by novel TiO$_2$–Coconut Shell Powder (TCNSP) composite. Journal of Industrial and Engineering Chemistry. 2014; 20(3): 979–87.

[12] Yola ML, Eren T, Atar N. A novel efficient photocatalyst based on TiO$_2$ nanoparticles involved boron enrichment waste for photocatalytic degradation of atrazine. Chemical Engineering Journal. 2014; 250(0): 288–94.

[13] Omri A, Lambert SD, Geens J, Bennour F, Benzina M. Synthesis, surface characterization and photocatalytic activity of TiO$_2$ supported on almond shell activated carbon. Journal of Materials Science & Technology. 2014; 30(9): 894–902.

[14] Shavisi Y, Sharifnia S, Hosseini SN, Khadivi MA. Application of TiO$_2$/perlite photocatalysis for degradation of ammonia in wastewater. Journal of Industrial and Engineering Chemistry. 2014; 20(1): 278–83.

[15] Kamaruddin S, Stephan D. Sol–gel mediated coating and characterization of photocatalytic sand and fumed silica for environmental remediation. Water, Air, & Soil Pollution. 2014; 225(5): 1–11.

[16] Wang B, Yang Z, An H, Zhai J, Li Q, Cui H. Photocatalytic activity of Pt–TiO$_2$ films supported on hydroxylated fly ash cenospheres under visible light. Applied Surface Science. 2015; 324(0): 817–24.

[17] Wickramaratne NP, Jaroniec M. Ordered mesoporous carbon–titania composites and their enhanced photocatalytic properties. Journal of Colloid and Interface Science. 2015; 449(0): 297–303.

[18] Chen X, Liu F, Liu B, Tian L, Hu W, Xia Q. A novel route to graphite-like carbon supporting SnO$_2$ with high electron transfer and photocatalytic activity. Journal of Hazardous Materials. 2015; 287(0): 126–32.

[19] Cao Z, Yang L, Chen H, Xu C, Qi D, Zhu S, et al. Preparation of Au/TiO$_2$ nanocomposite particles with high visible-light photocatalytic activity in inverse miniemulsions. Colloid and Polymer Science. 2015; 293(1): 277–88.

[20] da Silva WL, Lansarin MA, Livotto PR, dos Santos JHZ. Photocatalytic degradation of drugs by supported titania-based catalysts produced from petrochemical plant residue. Powder Technology. 2015; 279(0): 166–72.

[21] da Silva WL, Lansarin MA, Stedile FC, dos Santos JHZ. The potential of chemical industrial and academic wastes as a source of supported photocatalysts. Journal of Molecular Catalysis A: Chemical. 2014; 393: 125–33.

[22] da Silva WL, Lansarin MA, dos Santos JHZ. Industrial and agroindustrial wastes: an echotechnological approach to the production of supported photocatalysts. Water Science and Technology. 2016; 73(1): 28–38.

[23] de Escobar CC, Fisch A, dos Santos JHZ. Effect of a sol–gel route on the preparation of silica-based sorbent materials synthesized by molecular imprinting for the adsorption of dyes. Industrial & Engineering Chemistry Research. 2015; 54(1): 254–62.

[24] de Escobar CC, Dallegrave A, Lasarin MA, Zimnoch dos Santos JH. The sol–gel route effect on the preparation of molecularly imprinted silica-based materials for selective and competitive photocatalysis. Colloids and Surfaces A: Physicochemical and Engineering Aspects. 2015; 486: 96–105.

[25] de Escobar CC, Lansarin MA, Zimnoch dos Santos JH. Synthesis of molecularly imprinted photocatalysts containing low TiO_2 loading: evaluation for the degradation of pharmaceuticals. Journal of Hazardous Materials. 2016; 306: 359–66.

[26] de Franco MAE, da Silva WL, Bagnara M, Lansarin MA, dos Santos JHZ. Photocatalytic degradation of nicotine in an aqueous solution using unconventional supported catalysts and commercial ZnO/TiO_2 under ultraviolet radiation. Science of the Total Environment. 2014; 494–495(0): 97–103.

[27] Moreno YP, Cardoso MB, Moncada EA, dos Santos JHZ. Correlating the morphological properties and structural organization of monodisperse spherical silica nanoparticles grown on a commercial silica surface. ChemPhysChem. 2015; 16(14): 2981–94.

[28] Ruiz YPM, Silva WLd, Lansarin MA, Stedile FC, Moncada EA, dos Santos JHZ. Nanoparticles and mixed silicas as supports for the preparation of heterogeneous titania photocatalysts for application in the degradation of rhodamine B dye. In: 18th Brazilian Congress on Catalysis (CBCat); 13–17 September 2015; Porto Seguro. Brazil: CBCat (AJ6H); 2015. p. 1–6.

[29] Fan H-J, Lu C-S, Lee W-LW, Chiou M-R, Chen C-C. Mechanistic pathways differences between $P25-TiO_2$ and $Pt-TiO_2$ mediated CV photodegradation. Journal of Hazardous Materials. 2011; 185(1): 227–35.

[30] Whitcombe MJ, Kirsch N, Nicholls IA. Molecular imprinting science and technology: a survey of the literature for the years 2004–2011. Journal of Molecular Recognition. 2014; 27(6): 297–401.

[31] Lofgreen JE, Ozin GA. Controlling morphology and porosity to improve performance of molecularly imprinted sol–gel silica. Chemical Society Reviews. 2014; 43(3): 911–33.

[32] Díaz-García ME, Laínño RB. Molecular imprinting in sol–gel materials: recent developments and applications. Microchimica Acta. 2005; 149(1–2): 19–36.

[33] Walcarius A, Collinson MM. Analytical chemistry with silica sol–gels: traditional routes to new materials for chemical analysis. Annual review of analytical chemistry. 2009; 2: 121–43.

[34] Chen W, Ma Z, Pan X, Hu Z, Dong G, Zhou S, et al. Core@dual–Shell nanoporous SiO_2–TiO_2 composite fibers with high flexibility and its photocatalytic activity. Journal of the American Ceramic Society. 2014; 97(6): 1944–51.

[35] Wang M, Han J, Xiong H, Guo R, Yin Y. Nanostructured hybrid shells of r-GO/AuNP/m-TiO_2 as highly active photocatalysts. ACS Applied Materials & Interfaces. 2015; 7(12): 6909–18.

[36] Li X, Liu D, Song S, Zhang H. Fe_3O_4@SiO_2@TiO_2@Pt hierarchical core–shell microspheres: controlled synthesis, enhanced degradation system, and rapid magnetic separation to recycle. Crystal Growth & Design. 2014; 14(11): 5506–11.

[37] Zhang F, Liu W, Liu Y, Wang J, Ji G. Fabrication and enhanced photocatalytic properties of Pt@SiO$_2$@TiO$_2$ composites by surface plasma resonance from Pt nanoparticles. Journal of Nanoparticle Research. 2015; 17(2): 1–9.

[38] de Coelho Escobar C, dos Santos JHZ. Effect of the sol–gel route on the textural characteristics of silica imprinted with Rhodamine B. Journal of Separation Science. 2014; 37(7): 868–75.

[39] Brunauer S, Emmett PH, Teller E. Adsorption of gases in multimolecular layers. Journal of the American Chemical Society. 1938; 60(2): 309–19.

[40] Barrett EP, Joyner LG, Halenda PP. The determination of pore volume and area distributions in porous substances. I. Computations from nitrogen isotherms. Journal of the American Chemical Society. 1951; 73(1): 373–80.

[41] Beaucage G. Approximations leading to a unified exponential/power-law approach to small-angle scattering. Journal of Applied Crystallography. 1995; 28(6): 717–28.

[42] Beaucage G. Small-angle scattering from polymeric mass fractals of arbitrary mass-fractal dimension. Journal of Applied Crystallography. 1996; 29(2): 134–46.

[43] Beaucage G, Kammler HK, Pratsinis SE. Particle size distributions from small-angle scattering using global scattering functions. Journal of Applied Crystallography. 2004; 37(4): 523–35.

[44] Kammler HK, Beaucage G, Kohls DJ, Agashe N, Ilavsky J. Monitoring simultaneously the growth of nanoparticles and aggregates by in situ ultra-small-angle X-ray scattering. Journal of Applied Physics. 2005; 97(5): 054309.

[45] Fidalgo A, Ilharco LM. Chemical tailoring of porous silica xerogels: local structure by vibrational spectroscopy. Chemistry-A European Journal. 2004; 10(2): 392–8.

[46] Fidalgo A, Ciriminna R, Ilharco LM, Pagliaro M. Role of the alkyl-alkoxide precursor on the structure and catalytic properties of hybrid sol–gel catalysts. Chemistry of Materials. 2005; 17(26): 6686–94.

[47] Fidalgo A, Ciriminna R, Lopes L, Pandarus V, Béland F, Ilharco LM, et al. The sol–gel entrapment of noble metals in hybrid silicas: a molecular insight. Chemistry Central Journal. 2013; 7(1): 161.

[48] Fidalgo A, Ilharco LM. Chemical tailoring of porous silica xerogels: local structure by vibrational spectroscopy. Chemistry—A European Journal. 2004; 10(2): 392–8.

[49] Fidalgo A, Ciriminna R, Ilharco LM, Pagliaro M. Role of the alkyl–alkoxide precursor on the structure and catalytic properties of hybrid sol–gel catalysts. Chemistry of Materials. 2005; 17(26): 6686–94.

[50] Zhou W, Fu H. Mesoporous TiO$_2$: preparation, doping, and as a composite for photocatalysis. ChemCatChem. 2013; 5(4): 885–94.

[51] Ranade VV, Bhandari VM. Industrial wastewater treatment, recycling, and reuse: an overview. Industrial Wastewater Treatment, Recycling and Reuse. 2014; 1–80.

[52] Bayal N, Jeevanandam P. Sol–gel synthesis of SnO_2–MgO nanoparticles and their photocatalytic activity towards methylene blue degradation. Materials Research Bulletin. 2013; 48(10): 3790–9.

[53] Wang M, Song G, Li J, Miao L, Zhang B. Direct hydrothermal synthesis and magnetic property of titanate nanotubes doped magnetic metal ions. Journal of University of Science and Technology Beijing, Mineral, Metallurgy, Material. 2008; 15(5): 644–8.

[54] Sing KSW, Everett DH, Haul RAW, Moscou L, Pierotti RA, Rouquerol J, et al. Reporting physisorption data for gas/solid systems with special reference to the determination of surface area and porosity (Recommendations 1984). Pure and Applied Chemistry. 1985; 57(4): 603–19.

[55] Brinker CJ, Scherer GW. Sol–gel science: the physics and chemistry of sol–gel processing: Access Online via Elsevier; 1990.

[56] Brinker CJ, Frye GC, Hurd AJ, Ashley CS. Fundamentals of sol–gel dip coating. Thin Solid Films. 1991; 201(1): 97–108.

[57] Stoeckel D, Wallacher D, Zickler GA, Perlich J, Tallarek U, Smarsly BM. Coherent analysis of disordered mesoporous adsorbents using small angle X-ray scattering and physisorption experiments. Physical Chemistry Chemical Physics. 2014; 16(14): 6583–92.

[58] Ribeiro PC, Kiminami R, Costa A. Nanosilica synthesized by the Pechini method for potential application as a catalytic support. Ceramics International. 2014; 40(1): 2035–9.

[59] Gaya UI, Abdullah AH. Heterogeneous photocatalytic degradation of organic contaminants over titanium dioxide: a review of fundamentals, progress and problems. Journal of Photochemistry and Photobiology C: Photochemistry Reviews. 2008; 9(1): 1–12.

[60] Gamage McEvoy J, Cui W, Zhang Z. Degradative and disinfective properties of carbon-doped anatase–rutile TiO_2 mixtures under visible light irradiation. Catalysis Today. 2013; 207(0): 191–9.

Metal–Semiconductor Hybrid Nano-Heterostructures for Photocatalysis Application

Nimai Mishra

Additional information is available at the end of the chapter

http://dx.doi.org/10.5772/62636

Abstract

This chapter will address the development of colloidal synthesis of hybrid metal–semiconductor nanocrystals and their application in the field of photocatalysis. Despite the plethora of examples of different-shaped metal–semiconductor nanostructures that have been reported, metal-tipped semiconductor nanorods are perhaps the most intensively studied, and their use as a photocatalyst will be the focus of the chapter. First, we will discuss different wet-chemical synthesis techniques to control the synthesis of these metal–semiconductor hybrid structures. Afterward, we will discuss their unique physicochemical properties that are a combination of semiconductor and metal properties. Finally, we will showcase several examples from the literature demonstrating the possible application of these unique hybrid structures in photocatalysis.

Keywords: semiconductor nanocrystals, metal–semiconductor, hybrid structures, charge separation, photocatalysis

1. Introduction

There has recently been great interest in metal-hybrid semiconductor nanoparticles. This is largely due to the fact that they can exhibit the physical and chemical characteristics of both the individual metal and semiconductor or display unique properties not seen in either component [1]. These hybrid materials can potentially be exploited for a number of applications which cannot be addressed by semiconductor-only particles, for example, the directed assembly of gold-tipped semiconductor nanorods where the gold tip acts as both a means to initiate directed assembly as well as serve as electrical contacts [2]. Most importantly, metal-tipped semicon-

ductors were found to be good photocatalysis, as shown by Costi et al., where redox-based reactions were enhanced by the fact that photogenerated charges in the semiconductor component could be transferred to the metal tip [3]. Such hybrid nanostructures combine different material components into a single nanoparticle and provide a powerful strategy for modifying the properties of nanoparticles. Colloidal metal-tipped semiconductor hybrid nanomaterials were first realized by Banin's group in 2004, where they demonstrated that gold nanocrystals preferentially nucleate and grow at the tips of CdSe nanorods rather than at the sides of the nanorods (**Figure 1**) [4, 5]. These synthetic techniques opened up new possibilities for designing hybrid structures via epitaxial growth between a noble metal and semiconductors in colloidal solution. This can be seen in **Figure 2**, where TEM images are shown for a few hybrid structures, including Au–CdSe [6, 7], Au–ZnSe [8], Au–Bi_2S_3 [9], Au–SnS [10], and Au–CZTS [11].
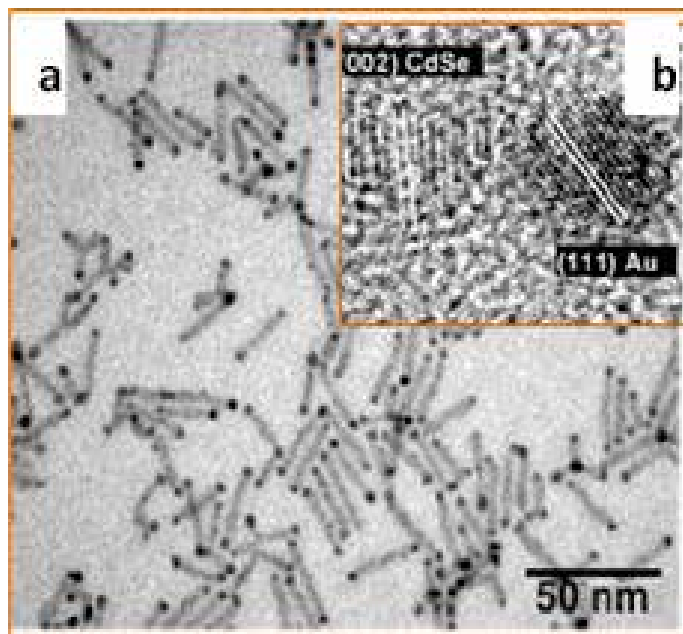
Figure 1. (a) CdSe nanorods after Au treatment using $AuCl_3$; Au tips are visible. (b) Inset shows HRTEM images of a single Au-tipped CdSe nanorod. The CdSe lattice for the rod in the center and Au tips at the rod edges can be identified, as marked. Adapted with permission [3].

Photocatalysis is a phenomenon in which photons are used for catalytically activating chemical reactions on the surface of photosensitized catalysts. Photocatalysis has been the hottest topic of research in the field of solar energy harvesting [9, 13–17]. In these processes, the photocatalyst generates charge carriers upon excitation from a suitable light source. These photoexcited charges are then transferred to reaction medium to initiate the chemical reaction. Over the decades, lots of progress has been made in photocatalysis research where researchers are using optically tuned semiconducting nanomaterials [18–21] and plasmonic noble metals [22–

24] as the photocatalyst. These materials have tunable absorption across the solar spectrum and can generate photoelectrons for use in a variety of chemical reactions. However, recent research efforts focused on using metal–semiconductor hybrid materials as a photocatalyst for harvesting solar energy show better results and will potentially opens up new avenues for photocatalysis [4, 11, 12, 25–31].
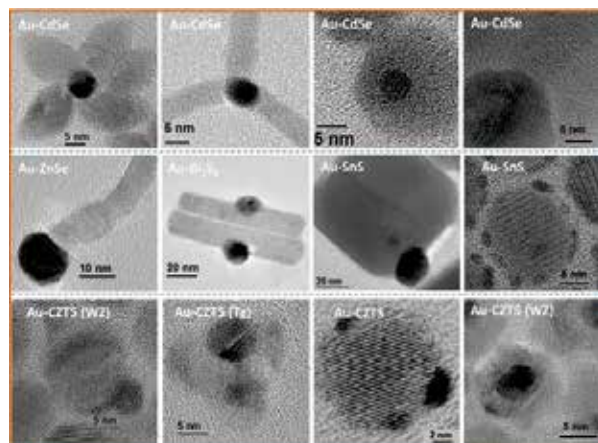

Figure 2. Representative HRTEM images of various nano-heterostructures. Reprinted with permission [12].

These metal–semiconductor hybrid materials can exhibit the properties of the individual materials or generate new properties when they combined together in the same nanostructures. In an ideal scenario, photogenerated charges could be quickly transferred to one component of the hybrid to the other due to band alignments, thus reducing the possibility of radiative recombination processes and enabling the opportunity for their use in chemical reactions [1, 4, 11, 27, 30]. In addition to that, these hybrid structures, because they can be engineered to have many different facets on their surface, have a higher probability for absorbing the targeted molecule of interest for photocatalytic conversion [1, 32]. In light of these unique properties, these metal–semiconductor hybrid structures have gained more attention for their use as photocatalysts as compared with the individual components.

The metal–semiconductor hybrid-based photocatalytic materials can be classified into three categories. In the first scenario, one of the components of the hybrid structure is the photoactive material, whereupon photo-excitation, the charge created transfers to the other component to start the catalytic process. An example of this category is the Au–TiO$_2$ hybrid structure, where gold act as a plasmonic antenna that absorbs light and generates charges, and the photo-excited plasmonic charges are then transferred to the higher bandgap TiO$_2$ [22, 26, 33–35]. This phenomenon can be illustrated in **Figure 3a**, where electrons from the surface plasmon state of Au are transferred to the higher bandgap material [36, 37]. In the second scenario, photo-excited electrons generated in low bandgap semiconductor nanoparticles transfer to the metal that it is attached to. Au–CdSe, Au–CdS, Au–PbS fall in this category, and a schematic is shown in **Figure 3b** [1, 32, 38, 39]. In the third scenario, as shown in **Figure 3c**, the coupling occurs

between excitons in the semiconductor and plasmons in gold [38, 40]. The excited state electronic coupling between two materials generates a greater number of charges and thus could be more effective for photocatalysis as compared with other two cases.
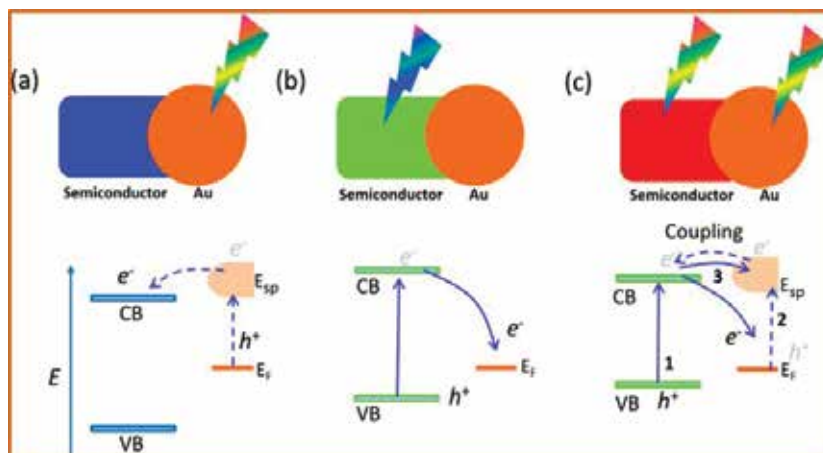

Figure 3. Schematic presentation of the electron transfer processes in Au-semiconductor heterostructures. For Au-semiconductor heterostructure where (a) only Au is excited, (b) only semiconductor is excited, and (c) there are simultaneous excitations of both Au and semiconductor. The electron transfer path 1 refers for semiconductor excitation followed by electron transfer to Au, path 2 follows just the reverse process, and path 3 shows the coupling of exciton of the semiconductor and plasmon of Au. Here, E_{sp} refers to the Au surface plasmon state and EF refers to the Au Fermi level. Adapted with permission [12].

This chapter will address the development of colloidal syntheses of hybrid metal–semiconductor nanocrystals and their application in the field of photocatalysis. Despite the plethora of examples of different-shaped metal–semiconductor nanostructures reported, metal-tipped semiconductor nanorods are perhaps the most intensively studied, and their uses as a photocatalyst will be the focus of the chapter. First, we will discuss different wet-chemical synthetic techniques to control the synthesis of these kinds of metal–semiconductor hybrid structures. Afterward, we will discuss their unique physicochemical properties that are a combination of both semiconductor and metal properties. And finally, we will showcase several examples from the literature, and how a researcher would use this unique hybrid structure for photocatalysis. The control over the synthesis of hybrid materials is among the hottest topic in the area of colloidal semiconductor nanocrystals or quantum dots (QDs) research. The metal–semiconductor hybrid materials are garnering lots of attention within the scientific community due to their unique properties primarily because these materials show size-dependent optical properties along with plasmonic properties of metals. In this chapter, we will highlight the following topics in detail:

1.   Controlled synthesis of advanced metal–semiconductor hybrid materials.

2.   Synergistic properties of metal–semiconductor hybrid materials.

3.   Photocatalysis with metal–semiconductor hybrid materials.

2. Control synthesis of these advanced metal–semiconductor hybrid materials

After the first report of colloidal metal–semiconductor hybrid materials in 2004, the synthesis of these hybrid materials continues to develop rapidly. The synthesis process could be categorized in following ways. In Section 2.1, we will briefly discuss selective metal deposition onto semiconductors with the help of its different facets reactivity. In Section 2.2, we will see the synthesis of more complex genus particles, where two different metals are grown onto a single semiconductor nanostructure.

2.1. Selective metal deposition onto the semiconductor component

Selective metal deposition onto semiconductor components has gained lots of interest among synthetic routes. This synthetic process occurs due to heterogeneous nucleation of secondary metal particles on host semiconductor nanocrystals. This process is very practical as the heterogeneous nucleation energy barrier is lower compared with homogeneous self-nucleation and leads to the formation of crystalline-phase metallic particles while retaining the crystallinity of the host semiconductor.

Moreover, selective metal deposition onto the host semiconductor be dictated by the crystal morphology, and surface capping provides different chemical reactivities for different facets of the semiconductor nanocrystal. This leads to selective metal deposition onto the semiconductor where a higher reactive facet allows the first nucleation, which is followed by a less reactive facet. One example is anisotropic CdSe/CdS; CdS nanorods have different reactivates for each of its ends facets, and thus, by carefully controlling the Au precursor concentration, one could produce one tip, two tip, and finally everywhere Au–CdS nanorod hybrid structures as can be seen in **Figure 4a–c** [41]. Analogously, following a similar selective Au deposition onto PbS, spherical nanocrystals have been reported as well [44]. Another possible way to achieve selective metal deposition is via defect-mediated growth, since defects have higher energy, this allowing feasible secondary nucleation [45, 46]. Electrochemical Ostwald ripening processes have been found to be another alternate way to achieve selective one-tip metal deposition onto semiconductor nanocrystals [5]. This electrochemical Ostwald ripening process occurs via similar principles as Ostwald ripening, where a small island of particles dissolves to fuel the growth of a larger island. In addition to that, here, the electrochemical ripening requires oxidation/reduction of the metal components. The post-synthesis intraparticle Ostwald ripening due to thermal annealing has also been found to be useful to achieve selective metal deposition, as it is shown in the case of CdSe nanorods [6].

So far, the literature regarding site-selective deposition has been demonstrated on CdSe, CdS, and CdSe/CdS core/shell nanorods with the deposition of various metals, including Au [3, 5, 41, 45, 47], Pt [42, 48, 49], PtCo [42], PtNi [42], Pd, Ag_2S [41], Co [50], PdO, and Pd_4S [51]. Thermal- or photochemical-assisted metal deposition can lead to the formation of different metallic patterns on to the semiconductor surface. This mainly depends on various factors, such as the selection of surface ligands, metal precursor concentration, and reaction temperature. For example, high temperature leads to the formation of facet selective Pt deposition on

CdS nanorods (**Figure 4e**) [42], whereas photodeposition of Pt onto CdS favors no selectivity [48]. On the contrary, hierarchical one tip, two tip, and everywhere Au deposition onto CdSe/CdS nanorod was demonstrated to depend on Au precursor concentration [41]. Similarly, selective photodeposition of Pd nanoparticles onto $CdS_{0.4}Se_{0.6}$ nanorods were also reported [52]. The selective metal deposition onto semiconductor branched structures such as CdSe/CdS tetrapods was difficult to achieve due to the similar reactivity of all four arm tips. Recently, we overcome this problem by controlling the surface morphology of the CdSe/CdS tetrapods with the use of surface capping groups. The selective metal deposition was demonstrated in the cone-like tapered CdSe/CdS tetrapod which has increased selectivity towards single Au tipped (**Figure 4g**) [43]. The rectangular-shaped tetrapods do not show (Figure 4h) any such selectivity, and gold deposition occurs everywhere onto the CdS surface [43]. This unusual metal deposition was attributed to the intraparticle electrochemical Ostwald ripening process.
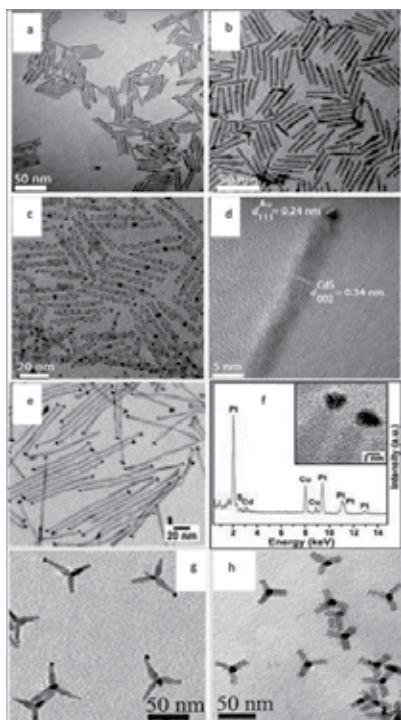

Figure 4 TEM images of CdSe-seeded CdS nano-heterostructures with controlled, varying degrees of Au deposition: CdSe/CdS nanorods exposed to increasing concentrations of Au precursor, resulting in Au deposited at (a) one end, (b) both ends, and (c) throughout the rod, respectively; (d) HRTEM image showing a gold nanoparticle at the apex of the nanorod. The measured d-spacing values from the visible lattice fringes 0.24 and 0.34 nm are assigned to Au (111) and CdS (002), respectively. (e) CdS with small single Pt tips (4.3 nm). (f) Selected area EDS spectrum of a single Pt tip, with inset HRTEM image of two Pt–CdS hybrids. (g, h) TEM images of tetrapods exposed to high concentrations of Au precursor. All of the reactions were done at room temperature for a fixed reaction time of 1.5 h. Adapted with permission [41–43].

2.2. Genus hybrid nanoparticles (semiconductor–dual metal) via selective deposition

Incorporating more than one metal particle onto semiconductor nanocrystals could produce genus type of hybrid material with new chemical and physical properties. This could be achieved via core/shell structures where one metal acts as core for another metal or through interfacial alloying. It was reported previously that bimetallic nanocrystals could enhance the photocatalytic performance [53]. In the case of Pt/Ni and Pt/Ru/Ni alloy nanoparticles, it was found that they show improved catalytic performance compared with pure Pt nanoparticles [54].
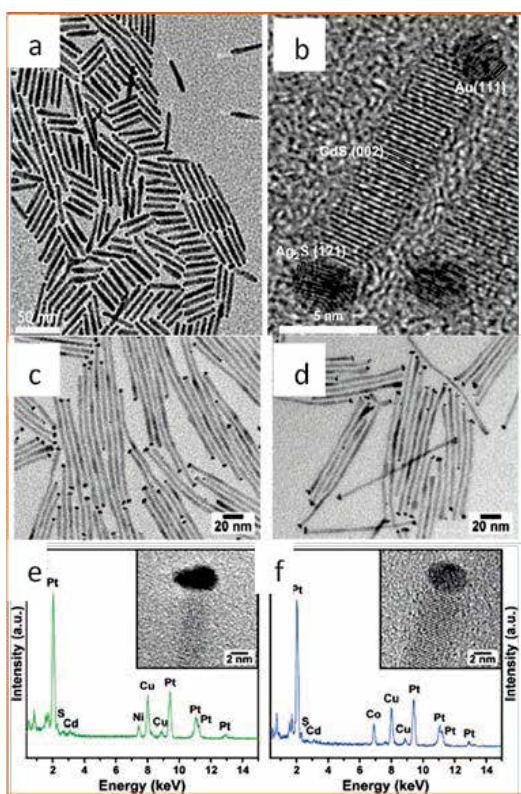
Figure 5. (a) TEM image of seeded CdSe/CdS nanorods with Au nanoparticles at one end and Ag₂S nanoparticles at the other end. (b) HRTEM image showing the visible lattice fringes of the Ag₂S {1¯21} and Au {111} planes with measured d-spacings of 0.26 and 0.24 nm, respectively. (c, d) TEM images of binary-CdS heterostructure nanoparticles with different sizes and ompositions: (c) PtNi–CdS (4.7 nm), (d) PtCo–CdS (5.2 nm), prepared with increased metal concentration showing a loss of selectivity, (e) selected area EDS spectrum taken on the tip of a PtNi–CdS hybrid structure, (f) selected area EDS spectrum of a PtCo–CdS heterostructure. Adapted with permission [41, 42].

In the recent work, using two different metal precursors in the growth solution, Habas et al. [42] reported the synthesis of genus hybrid materials such as CdS–PtNi and CdS–PtCo, in which metals formed an interfacial alloy (**Figure 5c, d**). Afterward, Chakrabortty et al. [41] reported Au–CdSe/CdS–Ag₂S types of genus particles with selective metal deposition using

the difference of reactivity between the two tips of CdSe/CdS rods (**Figure 5a, b**). Moreover, our recent work shows the one Au-tipped CdSe/CdS tetrapods could be useful for further growth of a second metal (Ag in this case) onto the other three CdS tips, as described by schematic in **Figure 6a** [43]. The TEM image in the **Figure 6b** shows the genus structures where one tip of the tetrapod structures has Au and other three have Ag_2S. Further confirmation was done with the HRTEM analysis of single particle which confirms lattice fringes of both Au and Ag_2S (**Figure 6d, e**). Another approach used was light-induced deposition of a secondary metal onto CdSe/CdS–Au hybrid nanorods [55]. UV irradiation causes the exciton to be formed in the CdSe/CdS semiconductor nanorod, and charge separation does occur due to the presence of the Au tip which serves as an electron sink. These electrons reach the Au tips and then act as reduction point for the second metal ions, such as Pd or Fe, and form hybrid genus particles with alloyed Pd/Au tips or Au/Fe_xO_y hollow core/shell structures, which can be seen in **Figure 7a, b** [55]. With the help of kinetically controlled syntheses, Hill et al. reported selective deposition of Co and Co_xO_y on Pt-tipped CdSe/CdS core/shell nanorods (**Figure 7c–h**) [56].
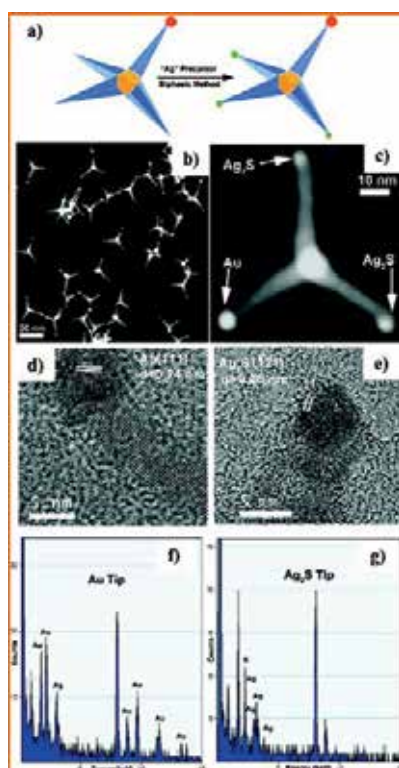

Figure 6. (a) Reaction schematic to obtain hierarchically complex CdSe-seeded CdS tetrapods with Au at precisely one tip and Ag_2S at the other three. (b) Representative HAADF-STEM image of tetrapods with cone-like arms fabricated according to the strategy shown in a. (c) Magnified view of one of the tetrapods in b, with the different tips labeled. (d, e) HRTEM images of the different tetrapod arm tips showing the visible lattice fringes of the Ag_2S (1⊙21) and Au (111)

planes with measured d-spacings of 0.26 and 0.24 nm, respectively. Further confirmation of the (f) Au and (g) Ag₂S tip elemental composition by EDX, respectively. Adapted with permission [43].
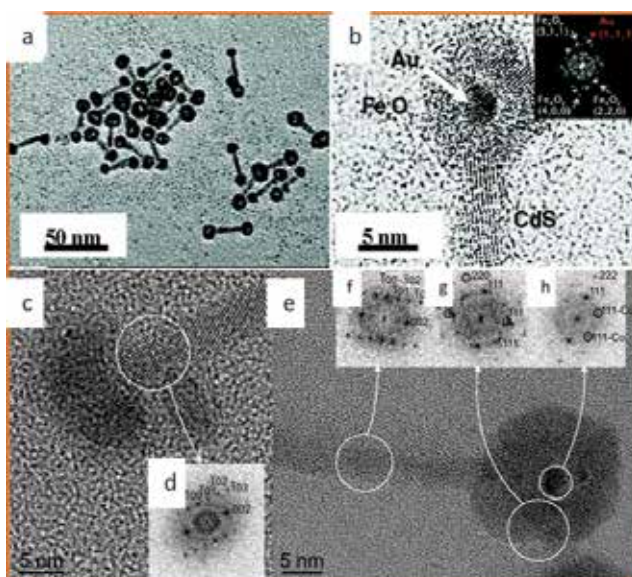

Figure 7. (a) TEM image of ~2.8 nm diameter core Au nanoparticles with a ~3.3 nm thick hollow shell of FexOy exclusively at the Tips of 29 nm long CdSe-seeded CdS semiconductor nanorods. (b) HRTEM image of part of the core-shell-tipped rod. The inset is an FFT image of the spherical tip region. HRTEM and power spectrum analysis used to determine the crystalline phases in (core@shell) (c, d) Pt@Co-tipped and (e, f) Pt@CoO-tipped nanorods. Nanorod dimensions: L = 40 nm, cobalt diameter: D = 12 nm. Adapted with permission [55, 56].

3. Synergistic properties of metal–semiconductor hybrid materials

Metal–semiconductor hybrid materials show some unique properties that arise from the combination of the two different materials on a single particle. Next, we will discuss these properties of hybrid materials, starting with the optical properties (Section 3.1), followed by charge separation in these structures (Section 3.2).

3.1. Optical properties

Metal-tipped semiconductor and core/shell metal–semiconductor hybrid structures show absorption spectra exhibiting combined coupling effects that cannot be replicated with a simple physical mixture of both components. In these hybrid structures, strong coupling occurs between the electronic states of metal and semiconductor, which leads to broadening and shifts in the plasmonic peak of the metal [57] and the excitonic absorption peak of the semiconductor [47]. This could be as a result of the formation of new electronic states in the semiconductor–metal interface. The electrodynamic effect could be another possible reason for the formation of new features in the absorption spectra [58]. The spectra in **Figure 8a, b**

show similar changes in the plasmonic shift occurring in Au–CZTS and Au–Bi$_2$S$_3$ hybrid nanostructures [9, 10]. Due to the coupling of Au plasmons with semiconductor excitons, a strong optical field is generated at the interface of Au. This coupling could be the key factor for the suppression of the exciton, which is facilitated by the efficient transfer of the electrons for triggering photocatalytic chemical reactions. Figure 8c shows Au–CdS hybrid structures, which exhibit both the characteristic excitonic and continuous absorption of the CdS nanorods below 475 nm and an additional broad absorption centered around 532 nm due to the plasmonic Au [38].
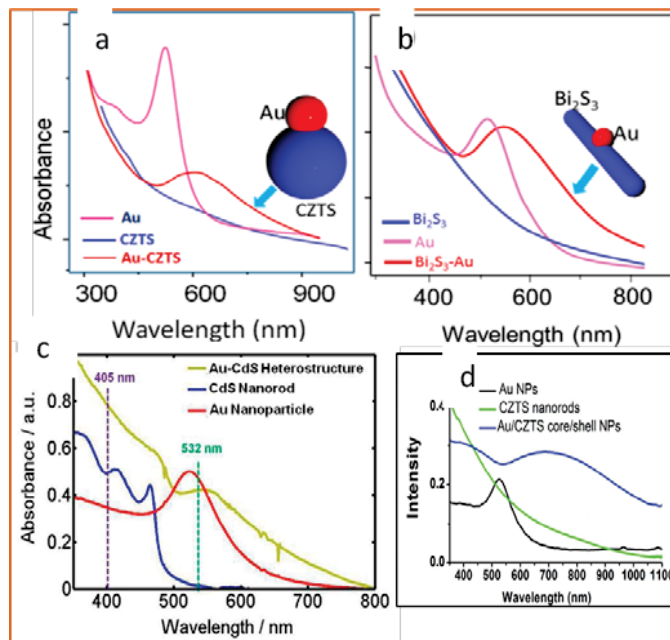

Figure 8. Absorption spectra of (a) Au, CZTS, and coupled Au–CZTS heterostructure and of [10]. (b) Au, Bi$_2$S$_3$, and Au–Bi$_2$S$_3$ heterostructure [9]. (c) UV–Vis absorption spectra of pure CdS nanorods (blue curve), Au nanoparticles (red curve), and high Au–CdS heterostructures (10.8 wt%, yellow curve). The green- and purple-dotted lines indicate the excitation source of a 532 nm laser and a 405 nm laser, respectively [38]. (d) UV–Vis spectra of Au NPs (black), CZTS NPs (green), and Au/CZTS core/shell NPs (blue). Adapted with permission [31].

Figure 8d shows UV–Vis spectra of Au NPs, CZTS NPs, and Au/CZTS core/shell NPs [31]. The thick CZTS shell surrounding the Au cores causes the shift of the plasmonic peak of bare Au particles from 525 to 685 nm. The high dielectric constant of low bandgap CZTS to the composite materials could be the possible reason behind it. The core/shell Au/CZTS hybrid structures also exhibited a broadened peak between 570 and 1100 nm that is a result of the perturbation of energy states by the plasmonic field.

Additionally, these metal–semiconductor hybrids either enhance [59–61] or quench [41, 62] the fluorescence of the semiconductor. Enhancement of the semiconductor emission occurs due to plasmonic effects of metallic portion, but it is strongly dependent on the distance

between the metal and fluorescent semiconductor [63]. Direct growth of the metallic particle onto the semiconductor nanocrystals often exhibits quenching. The charge transfer from the excited semiconductor to the metal is the main cause behind fluorescence quenching thus reduced the radiative life time. This observation is common and can be seen in ZnO–Ag [64], CdS–Au [47], CdSe–Au [3], and CdTe–Au nanoparticles [65]. On the other hand, fluorescence enhancement is generally obtained when a spacer material is introduced in between the metal and semiconductor. One kind of this example is CdSe/ZnS nanoparticles adsorbed on an Ag/SiO_2 core/shell structure. By controlling the thickness of the SiO_2 shell, fluorescence enhancement has been observed with increased SiO_2 shell thickness and attributed to an excitation enhancement effect [66].

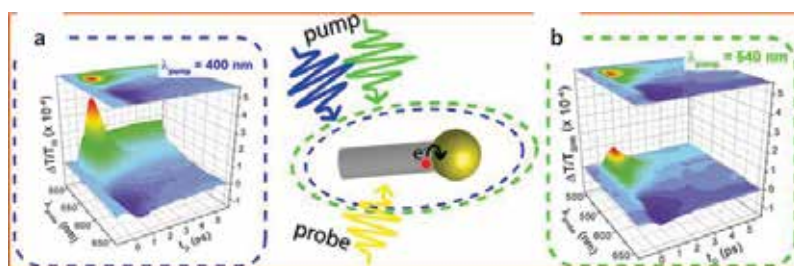### 3.2. Photo-induced charge separation

Figure 9. Ultrafast response of semiconductor–metal nanohybrids: Probing the Au nanoparticle spectral region. Time and spectrally resolved transmission change ΔT/T(tDprobe, λprobe) measured in CdS–Au nanomatchsticks solution for a pump wavelength (a) λpump = 400 nm [below the CdS bandgap and gold interband transition threshold: ΔT/TIB (b) λpump = 540 nm (close to the surface plasmon resonance of gold nanoparticles: ΔT/TSPR) and]. Adapted with permission [67].

Previous work reported the growth of metallic nanoparticles onto a semiconductor facilitates rapid charge transfer from the semiconductor to the metal particle upon light excitation, leading to charge separation [4, 9]. Due to the band alignment at the semiconductor/metal interface, the Fermi level of the metal component is located within the bandgap of the semiconductor, and electronic states promote the transfer of the excited electrons in the semiconductor conduction band into the metal energy levels. On the other hand, holes may remain localized to surface defect states in the semiconductor, or to confined levels, as may be in cases in type-II and quasi type-II core/shell structures. Mongin et al. [67] reported a study of the ultrafast photo-induced charge separation in single-tipped CdS–Au nanorods.

In this work, pump–probe measurements (schematic shown in **Figure 9**) were performed on the semiconductor and the metal domains separately, measuring the contribution of the photo-induced charge transfer. The spectral and amplitude changes between pump, having wavelength corresponding to the plasmonic of metal region, (Figure 9) and pump, having wavelength corresponding to the semiconductor absorption region, (Figure 9) are attributed to charge transfer. Reported transient absorption measurements on other hybrid materials including CdS–Pt [68, 69] and ZnSe/CdS–Pt [68] were interpreted as exhibiting longer charge

separation times such as 3–4 and 14 ps, respectively. The understanding of charge separation and exciton dynamics in these hybrid structures is the key factors for their application in photocatalysis, which is discussed in next section.

4. Photocatalysis with metal–semiconductor hybrid materials

One of the most interesting applications of these metal–semiconductor hybrid structures is photocatalysis. The combined properties make these hybrid structures efficient for photocatalysis. These types of colloidally synthesized hybrid materials work as heterogeneous photocatalysis. Efficient light energy conversion occurs which could be used for photodegradation of organic pollutants in water [70], in photo-electrochemical cells for energy storage [71], and for photo-induced water-splitting hydrogen generation [72]. With a judicious choice of two different components in a semiconductor–metal hybrid, one can tune the band alignment accordingly to match the reduction potential of the target system for photocatalysis. For example, semiconductor core/shell structures with type-II band alignment facilies the charge separation with long-lived excitons. Thus, a metal tip onto these type-II structures could easily extract the charge and act as reservoir of electrons. In addition to that, high crystalline quality in these hybrid structures is required for two reasons: (1) Surface defects localize the charges and reduce the photocatalytic efficiency, and (2) a less defective surface will also enhance the mobility [72]. Photocatalysis using these hybrid structures can be categorized in the following sub topics.

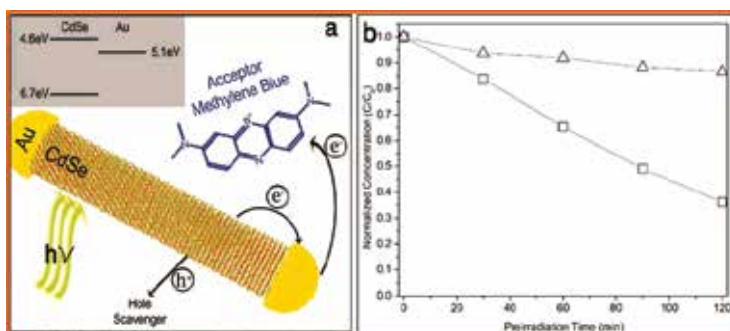### 4.1. Photocatalytic redox reactions

Figure 10. (a) Scheme of a light-induced charge separation mechanism in a nanodumbbell in which the photogenerated electron–hole pair separates so that the electron resides at the gold tip and the hole at the CdSe nanorod. The scheme also depicts the transfer of the hole to the scavenger and the reduction of the MB molecule upon electron transfer from the gold tip. The inset shows the energy band alignment between CdSe (4 nm dots) and Au. (b) Normalized concentration of MB dye reduced by CdSe nanorods gold nanoparticles mixture (open blue triangles) and by hybrid CdSe–Au nanodumbbells solution (open black squares) vs. pre-irradiation time. High efficiency of the charge retention in NDBs is demonstrated, leading to activity toward MB reduction. Adapted with permission [4].

Since the pioneering work by the Banin group using Au-tipped-CdSe rods for the reduction of the organic dye Methylene blue (MB) [4], several research groups demonstrated photocatalysis with different hybrid structures. In the work by the Banin group, they demonstrated proof of concept of charge separation due to the band alignment (see **Figure 10a**) between CdSe and Au. **Figure 10b** shows the degradation of the MB dye with CdSe–Au as a catalyst has more efficiency as compared with the Au particle/CdSe nanorod physical mixture [4]. Similar studies were found in the case of CdS–Au [38].
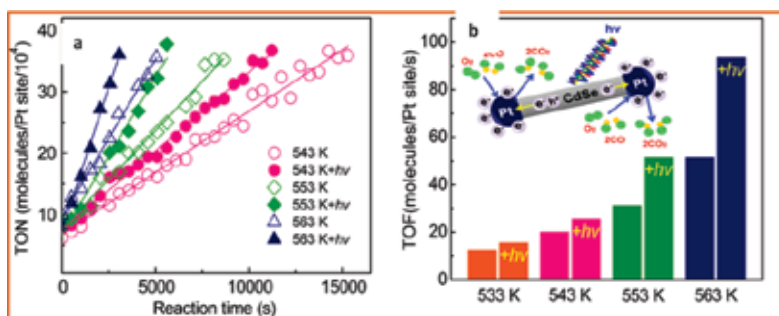

Figure 11. (a) Turnover number (TON) for CO oxidation on Pt–CdSe–Pt nanodumbbells with and without light at three different temperatures and (b) TOF for CO oxidation on Pt–CdSe–Pt nanodumbbells with and without light at four different temperatures. During CO oxidation, the TON was measured after a certain amount of time to allow for product molecules to accumulate. Time zero is the point when we started collecting data, not the start of the reaction. Adapted with permission [73].

Soon after, the first reports several research group work onto this hybrid system for photocatalysis application. Kim et al demonstrated [73] that hot carriers generated upon photon absorption in Pt–CdSe–Pt nanodumbbells significantly impact the catalytic activity of CO oxidation. They found that this hybrid structure exhibits a higher turnover frequency by a factor of 2 during irradiation by light with energy higher than the bandgap of CdSe
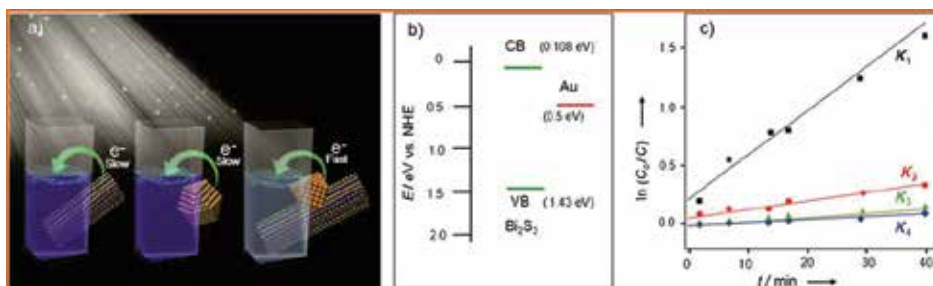

Figure 12. (a) Schematic representation of conditions for the favorable photoreduction of methylene blue. (b) Band alignment of Bi_2S_3 and Au (CB = conduction band, VB = valence band). (c) Rate of dye degradation with irradiation progress under different conditions. The samples were irradiated using Xe lamp with a wavelength of 500 nm. K1 (0.037 min_1), K2 (0.007 min_1), K3 (0.004 min_1), and K4 (0.002 min_1) are the dye degradation rate constants with Au–Bi_2S_3, a mixture of Au and Bi_2S_3, Bi_2S_3, and Au, respectively. Adapted with permission [9].

(**Figure 11a**), while the turnover rate on bare Pt nanoparticles did not depend on light irradiation. The Figure 11b shows enhanced catalytic activity as is demonstrated for the turnover frequency (TOF) under light irradiation at four different temperatures.

More recently, the Pradhan group demonstrated hybrid Au–Bi$_2$S$_3$ heterostructures exhibit photo-catalytic activity which is similar to CdS and CdSe systems [9]. The rate of MB reduction using Au-Bi$_2$S$_3$ is shown in **Figure 12c**. Au–SnS is another new hybrid material developed by same group, and it also shows enhancement of the rate of catalytic activities in the reduction of the dye MB compared with only SnS nanocrystals [10].

4.2. Photocatalytic water splitting

Photocatalytic water splitting for hydrogen generation using these hybrid structures has also gained lot of attention [11, 31]. In this process, the photo-excited electron reduces the H$^+$ ions to molecular H$_2$. Amirav et al. [74] demonstrated that in the case for CdSe/CdS–Pt nanorods,
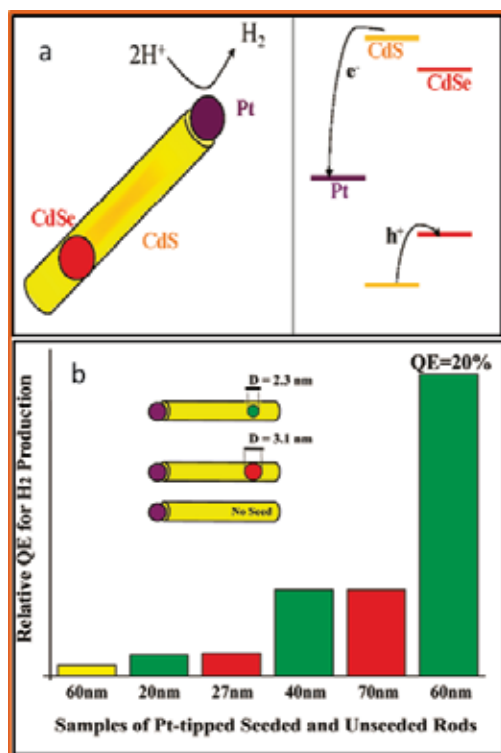

Figure 13. (left top corner) An illustration of the multicomponent nano-heterostructure, composed of a Pt-tipped CdS rod with an embedded CdSe seed. (Top middle) An illustration of the energy band diagram indicating that holes are confined to the CdSe, while electrons are transferred to the Pt and are thus separated from the holes (B) relative quantum efficiency for hydrogen production, obtained from platinum-tipped unseeded CdS rods (yellow), and five different samples of platinum-tipped seeded rods, with seed diameters of 3.1 (red) or 2.3 nm (green). Underneath each bar is the corresponding average sample length. Adapted with Permission [74].

the longer rods provided higher hydrogen production due to better spatial charge separation along the rod length and reduced back-recombination. **Figure 13b** shows the length dependence and effect of core/shell nanorods on the hydrogen production yield. The long arm core/shell CdSe/CdS–Pt hybrid structures have the highest production yield. Additionally, between the two different core/shell CdSe/CdS–Pt hybrid structures, the smaller CdSe core shows higher hydrogen production, because the smaller CdSe core forms quasi type-II band alignment upon growing the CdS rod-like shell over it and thus facilitates charge separation.

Another recent example by Ha et al. shows core/shell hybrid structures with Au core and CZTS shell (**Figure 14a**) could be useful for water splitting (**Figure 14b**) [31]. The CZTS band alignment with respect to Au Fermi level facilities the faster transfer of the photogenerated charge carriers. The S^{2-}/SO_3^{2-} solution acts as a hole scavenger during the photocatalytic process while core/shell structures are more efficient than other shapes of CZTS nanostructures. In this particular example, Au is located at the core, it is expected that upon photo-excitation, and both the electron and hole are transferred to the conduction and valence bands of CZTZ. Therefore, this structure is superior in terms of charge separation for photocatalytic water splitting.
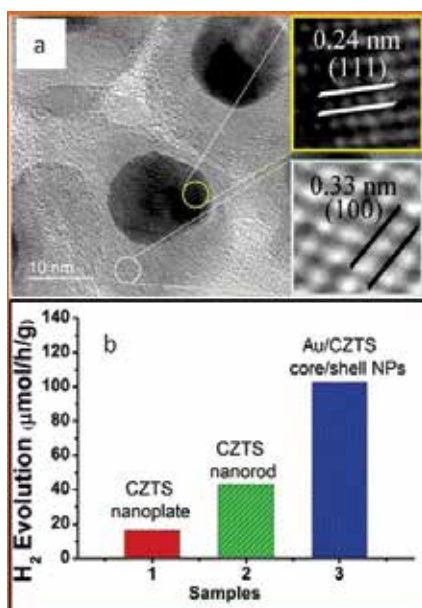

Figure 14. (a) Typical TEM and high-resolution TEM image of as-prepared Au/CZTS core/shell NPs. (b) A Plot comparing the photocatalytic H_2 evolution among CZTS nanoplates (red), CZTS nanorods (green), and Au/CZTS core/shell NPs (blue). Adapted with permission [31].

Another example is demonstrated by Cabot et al. [11] where they examined the activity of CZTS, CZTS–Au, and CZTS–Pt toward photocatalytic hydrogen evolution from water splitting. Interestingly, they found Pt-tipped CZTS is better as compared with Au tipped (**Figure 15c**), where both the hybrid structures are dramatically better than CZTS alone. Here,

the authors used Na_2S and Na_2SO_3 were used as hole scavengers. According to their observa-tion, CZTS–Pt provided the highest H_2 evolution rate (1.02 mmol/g h), which was eightfold higher than that of bare CZTS (0.13 mmol/g·h) and 1.25 times than CZTS–Au. The reasons for high efficiency in the case of CZTS–Pt were not explained well by the authors.
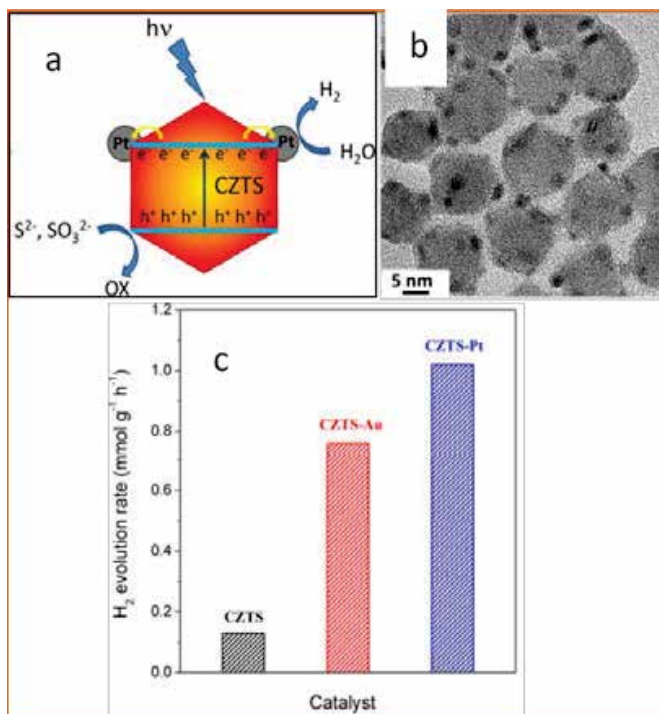

Figure 15. (a) Illustration of the possible mechanism of enhancement of the H_2 evolution rate in CZTS–Pt. (b) HR TEM image of CZTS–Pt heterostructured nanoparticles. (c) Hydrogen evolution rate of CZTS, CZTS–Au, and CZTS–Pt nanomaterials during a 4 h test. Adapted with permission [11].

5. Conclusion

In the last decade, substantial advancements have been made with selective metal deposi-tion onto different-shaped semiconductor nanocrystals. The control synthesis has been demonstrated from binary to ternary hybrid materials with more than one metal onto semiconductor having multiple functionalities. The degree of control was achieved in terms of selective metal deposition onto branched semiconductor structures. An effort has been made in order to understand the fundamentals of the synergistic properties of these special materials related to nonconventional material combinations. Furthermore, few studies were done of light-induced charge separation at the semiconductor–metal interface, which serves as a basis for the implementation of these hybrid structures in photocatalysis applications. In coming

years, further understanding of photo-induced charge separation at the metal semiconductor interface is also expected to develop. Thus, the path for unique applications of these hybrid systems in the field of photocatalysis will further develop in coming years. Future syntheses of metal/semiconductor hybrid structures will yield a wide range of materials for different applications, including practical application in photocatalysis and electronic devices.

Author details

Nimai Mishra

Address all correspondence to: nimaiiitm@gmail.com

CINT—Center for Integrated Nanotechnologies, Los Alamos National Laboratory, Los Alamos, USA

References

[1] Costi, R.; Saunders, AE; Banin, U. Colloidal Hybrid Nanostructures: A New Type of Functional Materials. *Angew. Chem. Int. Ed.* 2010, *49* (29), 4878–4897.

[2] Zhao, N.; Liu, K.; Greener, J.; Nie, Z.; Kumacheva, E. Close-Packed Superlattices of Side-by-Side Assembled Au-Cd Se Nanorods. *Nano Lett.* 2009, *9* (8), 3077–3081.

[3] Mokari, T.; Rothenberg, E.; Popov, I.; Costi, R.; Banin, U. Selective Growth of Metal Tips onto Semiconductor Quantum Rods and Tetrapods. *Science* 2004, *304* (5678), 1787–1790.

[4] Costi, R.; Saunders, AE; Elmalem, E.; Salant, A.; Banin, U. Visible Light-Induced Charge Retention and Photocatalysis with Hybrid CdSe–Au Nanodumbbells. *Nano Lett.* 2008, *8* (2), 637–641.

[5] Mokari, T.; Sztrum, CG; Salant, A.; Rabani, E.; Banin, U. Formation of Asymmetric One-Sided Metal-Tipped Semiconductor Nanocrystal Dots and Rods. *Nat. Mater.* 2005, *4* (11), 855–863.

[6] Figuerola, A.; van Huis, M.; Zanella, M.; Genovese, A.; Marras, S.; Falqui, A.; Zandbergen, HW; Cingolani, R.; Manna, L. Epitaxial CdSe–Au Nanocrystal Heterostructures by Thermal Annealing. *Nano Lett.* 2010, *10* (8), 3028–3036.

[7] Haldar, KK; Pradhan, N.; Patra, A. Formation of Heteroepitaxy in Different Shapes of Au–CdSe Metal–Semiconductor Hybrid Nanostructures. *Small.* 2013, *9* (20), 3424–3432.

[8] Bose, R.; Wasey, AHMA; Das, GP; Pradhan, N. Heteroepitaxial Junction in Au–ZnSe Nanostructure: Experiment Versus First-Principle Simulation. *J. Phys. Chem. Lett.* 2014, *5* (11), 1892–1898.

[9]   Manna, G.; Bose, R.; Pradhan, N. Photocatalytic Au–Bi$_2$S$_3$ Heteronanostructures. *Angew. Chem.* 2014, *126* (26), 6861–6864.

[10] Patra, BK; Guria, AK; Dutta, A.; Shit, A.; Pradhan, N. Au-SnS Hetero Nanostructures: Size of Au Matters. *Chem. Mater.* 2014, *26* (24), 7194–7200.

[11] Yu, X.; Shavel, A.; An, X.; Luo, Z.; Ibáñez, M.; Cabot, A. Cu$_2$ZnSnS$_4$-Pt and Cu$_2$ZnSnS$_4$-Au Heterostructured Nanoparticles for Photocatalytic Water Splitting and Pollutant Degradation. *J. Am. Chem. Soc.* 2014, *136* (26), 9236–9239.

[12] Dutta, SK; Mehetor, SK; Pradhan, N. Metal Semiconductor Heterostructures for Photocatalytic Conversion of Light Energy. *J. Phys. Chem. Lett.* 2015, *6* (6), 936–944.

[13] Maeda, K.; Domen, K. Photocatalytic Water Splitting: Recent Progress and Future Challenges. *J. Phys. Chem. Lett.* 2010, *1* (18), 2655–2661.

[14] Zhao, J.; Osterloh, FE Photochemical Charge Separation in Nanocrystal Photocatalyst Films: Insights from Surface Photovoltage Spectroscopy. *J. Phys. Chem. Lett.* 2014, *5* (5), 782–786.

[15] Liao, L.; Zhang, Q.; Su, Z.; Zhao, Z.; Wang, Y.; Li, Y.; Lu, X.; Wei, D.; Feng, G.; Yu, Q.; Cai, X.; Zhao, J.; Ren, Z.; Fang, H.; Robles-Hernandez, F.; Baldelli, S.; Bao, J. Efficient Solar Water-Splitting Using a Nanocrystalline CoO Photocatalyst. *Nat. Nanotechnol.* 2014, *9* (1), 69–73.

[16] Khon, E.; Lambright, K.; Khnayzer, RS; Moroz, P.; Perera, D.; Butaeva, E.; Lambright, S.; Castellano, FN; Zamkov, M. Improving the Catalytic Activity of Semiconductor Nanocrystals Through Selective Domain Etching. *Nano. Lett.* 2013, *13* (5), 2016–2023.

[17] Kamat, PV Manipulation of Charge Transfer Across Semiconductor Interface. A Criterion That Cannot Be Ignored in Photocatalyst Design. *J. Phys. Chem. Lett.* 2012, *3* (5), 663–672.

[18] Trotochaud, L.; Mills, TJ; Boettcher, SW An Optocatalytic Model for Semiconductor–Catalyst Water-Splitting Photoelectrodes Based on In Situ Optical Measurements on Operational Catalysts. *J. Phys. Chem. Lett.* 2013, *4* (6), 931–935.

[19] Ma, SSK; Hisatomi, T.; Maeda, K.; Moriya, Y.; Domen, K. Enhanced Water Oxidation on Ta$_3$N$_5$ Photocatalysts by Modification with Alkaline Metal Salts. *J. Am. Chem. Soc.* 2012, *134* (49), 19993–19996.

[20] Maeda, KZ-Scheme Water Splitting Using Two Different Semiconductor Photocatalysts. *ACS Catal.* 2013, *3* (7), 1486–1503.

[21] Martin, DJ; Qiu, K.; Shevlin, SA; Handoko, AD; Chen, X.; Guo, Z.; Tang, J. Highly Efficient Photocatalytic H2 Evolution from Water Using Visible Light and Structure-Controlled Graphitic Carbon Nitride. *Angew. Chem. Int. Ed.* 2014, *53* (35), 9240–9245.

[22] Linic, S.; Christopher, P.; Ingram, DB Plasmonic-Metal Nanostructures for Efficient Conversion of Solar to Chemical Energy. *Nat. Mater.* 2011, *10* (12), 911–921.

[23] Zheng, Z.; Tachikawa, T.; Majima, T. Single-Particle Study of Pt-Modified Au Nanorods for Plasmon-Enhanced Hydrogen Generation in Visible to Near-Infrared Region. *J. Am. Chem. Soc.* 2014, *136* (19), 6870–6873.

[24] Zhang, L.; Kim, HY; Henkelman, G. CO Oxidation at the Au–Cu Interface of Bimetallic Nanoclusters Supported on CeO2(111). *J. Phys. Chem. Lett.* 2013, *4* (17), 2943–2947.

[25] Ingram, DB; Linic, S. Water Splitting on Composite Plasmonic-Metal/Semiconductor Photoelectrodes: Evidence for Selective Plasmon-Induced Formation of Charge Carriers near the Semiconductor Surface. *J. Am. Chem. Soc.* 2011, *133* (14), 5202–5205.

[26] DuChene, JS; Sweeny, BC; Johnston-Peck, AC; Su, D.; Stach, EA; Wei, WD Prolonged Hot Electron Dynamics in Plasmonic-Metal/Semiconductor Heterostructures with Implications for Solar Photocatalysis. *Angew. Chem. Int. Ed.* 2014, *53* (30), 7887–7891.

[27] Jakob, M.; Levanon, H.; Kamat, PV Charge Distribution between UV-Irradiated TiO2 and Gold Nanoparticles: Determination of Shift in the Fermi Level. *Nano. Lett.* 2003, *3* (3), 353–358.

[28] Li, J.; Cushing, SK; Zheng, P.; Senty, T.; Meng, F.; Bristow, AD; Manivannan, A.; Wu, N. Solar Hydrogen Generation by a CdS–Au–TiO2 Sandwich Nanorod Array Enhanced with Au Nanoparticle as Electron Relay and Plasmonic Photosensitizer. *J. Am. Chem. Soc.* 2014, *136* (23), 8438–8449.

[29] Subramanian, V.; Wolf, E.; Kamat, PV Semiconductor–Metal Composite Nanostructures. To What Extent Do Metal Nanoparticles Improve the Photocatalytic Activity of TiO2 Films? *J. Phys. Chem. B* 2001, *105* (46), 11439–11446.

[30] Banin, U.; Ben-Shahar, Y.; Vinokurov, K. Hybrid Semiconductor–Metal Nanoparticles: From Architecture to Function. *Chem. Mater.* 2014, *26* (1), 97–110.

[31] Ha, E.; Lee, LYS; Wang, J.; Li, F.; Wong, K-Y; Tsang, SCE Significant Enhancement in Photocatalytic Reduction of Water to Hydrogen by Au/Cu₂ZnSnS₄ Nanostructure. *Adv. Mater.* 2014, *26* (21), 3496–3500.

[32] Sheldon, MT; Trudeau, P-E; Mokari, T.; Wang, L-W; Alivisatos, AP Enhanced Semiconductor Nanocrystal Conductance via Solution Grown Contacts. *Nano Lett.* 2009, *9* (11), 3676–3682.

[33] Xing, M-Y; Yang, B-X; Yu, H.; Tian, B-Z; Bagwasi, S.; Zhang, J-L; Gong, X-Q Enhanced Photocatalysis by Au Nanoparticle Loading on TiO2 Single-Crystal (001) and (110) Facets. *J. Phys. Chem. Lett.* 2013, *4* (22), 3910–3917.

[34] Subramanian, V.; Wolf, EE; Kamat, PV Catalysis with TiO2/gold Nanocomposites. Effect of Metal Particle Size on the Fermi Level Equilibration. *J. Am. Chem. Soc.* 2004, *126* (15), 4943–4950.

[35] Farnesi Camellone, M.; Marx, D. On the Impact of Solvation on a Au/TiO2 Nanocatalyst in Contact with Water. *J. Phys. Chem. Lett.* 2013, *4* (3), 514–518.

[36] Furube, A.; Du, L.; Hara, K.; Katoh, R.; Tachiya, M. Ultrafast Plasmon-Induced Electron Transfer from Gold Nanodots into TiO2 Nanoparticles. *J. Am. Chem. Soc.* 2007, *129* (48), 14852–14853.

[37] Seh, ZW; Liu, S.; Low, M.; Zhang, S-Y; Liu, Z.; Mlayah, A.; Han, M-Y Janus Au-TiO2 Photocatalysts with Strong Localization of Plasmonic Near-Fields for Efficient Visible-Light Hydrogen Generation. *Adv. Mater.* 2012, *24* (17), 2310–2314.

[38] Ha, JW; Ruberu, TPA; Han, R.; Dong, B.; Vela, J.; Fang, N. Super-Resolution Mapping of Photogenerated Electron and Hole Separation in Single Metal–Semiconductor Nanocatalysts. *J. Am. Chem. Soc.* 2014, *136* (4), 1398–1408.

[39] Lee, J-S; Shevchenko, EV; Talapin, DV Au–PbS Core–Shell Nanocrystals: Plasmonic Absorption Enhancement and Electrical Doping via Intra-Particle Charge Transfer. *J. Am. Chem. Soc.* 2008, *130* (30), 9673–9675.

[40] Wu, K.; Rodríguez-Córdoba, WE; Yang, Y.; Lian, T. Plasmon-Induced Hot Electron Transfer from the Au Tip to CdS Rod in CdS-Au Nanoheterostructures. *Nano Lett.* 2013, *13* (11), 5255–5263.

[41] Chakrabortty, S.; Yang, JA; Tan, YM; Mishra, N.; Chan, Y. Asymmetric Dumbbells from Selective Deposition of Metals on Seeded Semiconductor Nanorods. *Angew. Chem. Int. Ed.* 2010, *49* (16), 2888–2892.

[42] Habas, SE; Yang, P.; Mokari, T. Selective Growth of Metal and Binary Metal Tips on CdS Nanorods. *J. Am. Chem. Soc.* 2008, *130* (11), 3294–3295.

[43] Mishra, N.; Lian, J.; Chakrabortty, S.; Lin, M.; Chan, Y. Unusual Selectivity of Metal Deposition on Tapered Semiconductor Nanostructures. *Chem. Mater.* 2012, *24* (11), 2040–2046.

[44] Yang, J.; Elim, HI; Zhang, Q.; Lee, JY; Ji, W. Rational Synthesis, Self-Assembly, and Optical Properties of PbS–Au Heterogeneous Nanostructures via Preferential Deposition. *J. Am. Chem. Soc.* 2006, *128* (36), 11921–11926.

[45] Menagen, G.; Mocatta, D.; Salant, A.; Popov, I.; Dorfs, D.; Banin, U. Selective Gold Growth on CdSe Seeded CdS Nanorods. *Chem. Mater.* 2008, *20* (22), 6900–6902.

[46] Carbone, L.; Jakab, A.; Khalavka, Y.; Sönnichsen, C. Light-Controlled One-Sided Growth of Large Plasmonic Gold Domains on Quantum Rods Observed on the Single Particle Level. *Nano Lett.* 2009, *9* (11), 3710–3714.

[47] Saunders, AE; Popov, I.; Banin, U. Synthesis of Hybrid CdS–Au Colloidal Nanostructures†. *J. Phys. Chem. B* 2006, *110* (50), 25421–25429.

[48] Dukovic, G.; Merkle, MG; Nelson, JH; Hughes, SM; Alivisatos, AP Photodeposition of Pt on Colloidal CdS and CdSe/CdS Semiconductor Nanostructures. *Adv. Mater.* 2008, *20* (22), 4306–4311.

[49] Elmalem, E.; Saunders, AE; Costi, R.; Salant, A.; Banin, U. Growth of Photocatalytic CdSe–Pt Nanorods and Nanonets. *Adv. Mater.* 2008, *20* (22), 4312–4317.

[50] Maynadié, J.; Salant, A.; Falqui, A.; Respaud, M.; Shaviv, E.; Banin, U.; Soulantica, K.; Chaudret, B. Cobalt Growth on the Tips of CdSe Nanorods. *Angew. Chem. Int. Ed.* 2009, *48* (10), 1814–1817.

[51] Shemesh, Y.; Macdonald, JE; Menagen, G.; Banin, U. Synthesis and Photocatalytic Properties of a Family of CdS-PdX Hybrid Nanoparticles. *Angew. Chem. Int. Ed.* 2011, *50* (5), 1185–1189.

[52] Alemseghed, MG; Ruberu, TPA; Vela, J. Controlled Fabrication of Colloidal Semiconductor–Metal Hybrid Heterostructures: Site Selective Metal Photo Deposition. *Chem. Mater.* 2011, *23* (15), 3571–3579.

[53] Xia, Y.; Xiong, Y.; Lim, B.; Skrabalak, SE Shape-Controlled Synthesis of Metal Nanocrystals: Simple Chemistry Meets Complex Physics? *Angew. Chem. Int. Ed. Engl.* 2009, *48* (1), 60–103.

[54] Park, K-W; Choi, J-H; Kwon, B-K; Lee, S-A; Sung, Y-E; Ha, H-Y; Hong, S-A; Kim, H.; Wieckowski, A. Chemical and Electronic Effects of Ni in Pt/Ni and Pt/Ru/Ni Alloy Nanoparticles in Methanol Electrooxidation. *J. Phys. Chem. B* 2002, *106* (8), 1869–1877.

[55] Li, X.; Lian, J.; Lin, M.; Chan, Y. Light-Induced Selective Deposition of Metals on Gold-Tipped CdSe-Seeded CdS Nanorods. *J. Am. Chem. Soc.* 2011, *133* (4), 672–675.

[56] Hill, L. J.; Bull, M. M.; Sung, Y.; Simmonds, A. G.; Dirlam, PT; Richey, NE; DeRosa, SE; Shim, I-B; Guin, D.; Costanzo, PJ.; Pinna, N.; Willinger, M-G; Vogel, W.; Char, K.; Pyun, J. Directing the Deposition of Ferromagnetic Cobalt onto Pt-Tipped CdSe@CdS Nanorods: Synthetic and Mechanistic Insights. *ACS Nano.* 2012, *6* (10), 8632–8645.

[57] Sun, Z.; Yang, Z.; Zhou, J.; Yeung, MH; Ni, W.; Wu, H.; Wang, J. A General Approach to the Synthesis of Gold–Metal Sulfide Core–Shell and Heterostructures. *Angew. Chem. Int. Ed.* 2009, *48* (16), 2881–2885.

[58] Shaviv, E.; Schubert, O.; Alves-Santos, M.; Goldoni, G.; Di Felice, R.; Vallée, F.; Del Fatti, N.; Banin, U.; Sönnichsen, C. Absorption Properties of Metal–Semiconductor Hybrid Nanoparticles. *ACS Nano.* 2011, *5* (6), 4712–4719.

[59] Kulakovich, O.; Strekal, N.; Yaroshevich, A.; Maskevich, S.; Gaponenko, S.; Nabiev, I.; Woggon, U.; Artemyev, M. Enhanced Luminescence of CdSe Quantum Dots on Gold Colloids. *Nano. Lett.* 2002, *2* (12), 1449–1452.

[60] Lee, J.; Govorov, AO; Dulka, J.; Kotov, NA Bioconjugates of CdTe Nanowires and Au Nanoparticles: Plasmon–Exciton Interactions, Luminescence Enhancement, and Collective Effects. *Nano. Lett.* 2004, *4* (12), 2323–2330.

[61] Viste, P.; Plain, J.; Jaffiol, R.; Vial, A.; Adam, PM; Royer, P. Enhancement and Quenching Regimes in Metal–Semiconductor Hybrid Optical Nanosources. *ACS Nano.* 2010, *4* (2), 759–764.

[62] Chakrabortty, S.; Xing, G.; Xu, Y.; Ngiam, SW.; Mishra, N.; Sum, TC.; Chan, Y. Engineering Fluorescence in Au-Tipped, CdSe-Seeded CdS Nanoheterostructures. *Small.* 2011, *7* (20), 2847–2852.

[63] Cheng, D.; Xu, Q-H Separation Distance Dependent Fluorescence Enhancement of Fluorescein Isothiocyanate by Silver Nanoparticles. *Chem. Commun.* 2007, No. 3, 248–250.

[64] Pacholski, C.; Kornowski, A.; Weller, H. Site-Specific Photodeposition of Silver on ZnO Nanorods. *Angew. Chem. Int. Ed.* 2004, *43* (36), 4774–4777.

[65] Haldar, KK; Sen, T.; Mandal, S.; Patra, A. Photophysical Properties of Au-CdTe Hybrid Nanostructures of Varying Sizes and Shapes. *Chemphyschem. Eur. J. Chem. Phys. Phys. Chem.* 2012, *13* (17), 3989–3996.

[66] Naiki, H.; Masuhara, A.; Masuo, S.; Onodera, T.; Kasai, H.; Oikawa, H. Highly Controlled Plasmonic Emission Enhancement from Metal–Semiconductor Quantum Dot Complex Nanostructures. *J. Phys. Chem. C* 2013, *117* (6), 2455–2459.

[67] Mongin, D.; Shaviv, E.; Maioli, P.; Crut, A.; Banin, U.; Del Fatti, N.; Vallée, F. Ultrafast Photoinduced Charge Separation in Metal–Semiconductor Nanohybrids. *ACS Nano.* 2012, *6* (8), 7034–7043.

[68] O'Connor, T.; Panov, MS; Mereshchenko, A.; Tarnovsky, AN; Lorek, R.; Perera, D.; Diederich, G.; Lambright, S.; Moroz, P.; Zamkov, M. The Effect of the Charge-Separating Interface on Exciton Dynamics in Photocatalytic Colloidal Heteronanocrystals. *ACS Nano.* 2012, *6* (9), 8156–8165.

[69] Wu, K.; Zhu, H.; Liu, Z.; Rodríguez-Córdoba, W.; Lian, T. Ultrafast Charge Separation and Long-Lived Charge Separated State in Photocatalytic CdS–Pt Nanorod Heterostructures. *J. Am. Chem. Soc.* 2012, *134* (25), 10337–10340.

[70] Mills, A.; Davies, RH; Worsley, D. Water Purification by Semiconductor Photocatalysis. *Chem. Soc. Rev.* 1993, *22* (6), 417–425.

[71] Grätzel, M. Photoelectrochemical Cells. *Nature.* 2001, *414* (6861), 338–344.

[72] Kudo, A.; Miseki, Y. Heterogeneous Photocatalyst Materials for Water Splitting. *Chem. Soc. Rev.* 2008, *38* (1), 253–278.

[73] Kim, SM; Lee, SJ; Kim, SH; Kwon, S.; Yee, KJ; Song, H.; Somorjai, GA; Park, JY Hot Carrier-Driven Catalytic Reactions on Pt–CdSe–Pt Nanodumbbells and Pt/GaN under Light Irradiation. *Nano. Lett.* 2013, *13* (3), 1352–1358.

[74] Amirav, L.; Alivisatos, AP Photocatalytic Hydrogen Production with Tunable Nanorod Heterostructures. *J. Phys. Chem. Lett.* 2010, *1* (7), 1051–1054.

Applications of Photocatalysis

Fabrication of Semiconductor with Modified Microstructure for Efficient Photocatalytic Hydrogen Evolution Under Visible Light

Tao Yang, Xinmei Hou, Junhong Chen and
Kuo-Chih Chou

Additional information is available at the end of the chapter

Abstract

Since sustainable energy and environment emerging as one of the top issues and challenges for humanity, the photocatalytic hydrogen evolution under visible light has attracted increasing attention. Basically the separation and transmission of photogenerated charge carriers are the two main steps of a photocatalytic reaction. They should be key aspects in the design of efficient photocatalysts for solar energy conversion.

3C-SiC is an important semiconductor with suitable band gap (2.3-3.3 eV) and excellent properties, especially the environmentally-friendly property. Titanium nitride (TiN) has a narrow energy band gap (0.80 eV) and good electrical conductivity. However, they as photocatalysts both do not draw wide attention due to the high recombination rate of photogenerated electron-hole pairs.

Herein B-doped 3C-SiC nanowires with finned microstructure were prepared through carbonthermal reduction combining the ion doping and morphology modification. It shows an outstanding activity toward H2 production as high as 108.4 $\mu mol \bullet h^{-1} \bullet g^{-1}$, which is 2.6 times of the value reported in the literature for SiC. TiOxNy/TiN heterojunction composite with tunable chamber structures were prepared through reduction and nitridation of organotitania. It demonstrates an outstanding photocatalytic activity as high as 34.9 $\mu mol \bullet h^{-1} \bullet g^{-1}$, which is about 1.5 times higher than the highest value reported in the literature for TiN.

Keywords: semiconductors, modified microstructure, plane-wave-density function theory, photocatalytic, hydrogen production

1. Background

In recent years, energy shortage and environmental pollution have become the focus of world attention. Overuse of fossil fuels is the main reason of these problems. Strong dependence on fossil fuels has also made our economy susceptible to price spikes and intensifying air pollution and global warming. Thus, developing a clean, renewable alternative to fossil fuels is a matter of utmost urgency.

The San Francisco earthquake with magnitude 7.8 in 1906 released an estimated 10^{17} joules of energy, the amount the Sun delivers to Earth in one second. So earth can get a staggering amount of energy, which was provided by the Sun. This energy can power the great oceanic and atmospheric currents, the cycle of evaporation and condensation of water, and the typhoons, hurricanes, and tornadoes. The 4.6×10^{20} joules, that humans use annually, is equal to the amount of energy that Earth get from the sun in one hour. The 1.2×10^{5} terawatts, which Earth gets from the Sun, is far above every other energy source [1]. And solar energy is one of the cleanest energy resources that does not compromise or add to the global warming [2]. It is often called "alternative energy" to fossil fuel energy sources such as oil and coal.

The impressive supply of solar energy is complemented by its versatility, as illustrated in **Figure 1**. Solar energy applications are divided into three main categories: yield of electricity by exciting electrons in a solar cell, yield of chemical fuel through natural photosynthesis in green plants or artificial photosynthesis in human-engineered systems, and production of heat using concentrated or unconcentrated sunlight for direct use or further conversion to electricity.
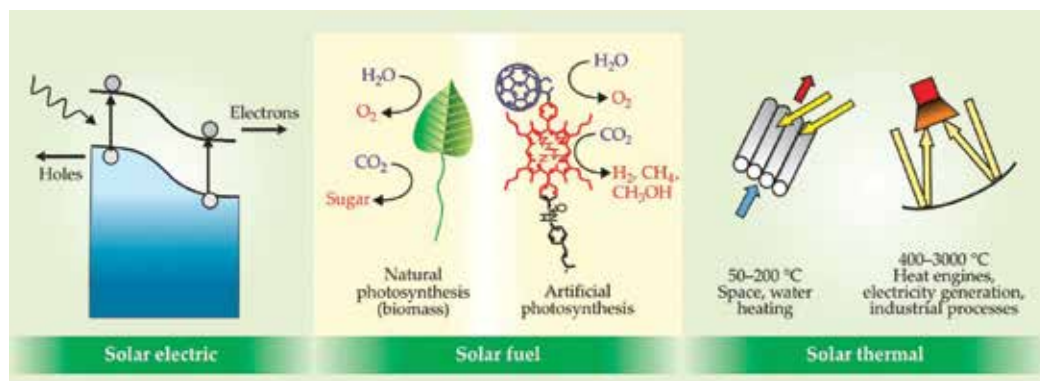

Figure 1. Solar photons convert naturally into three forms of energy – electricity, chemical fuel, and heat – that link seamlessly with existing energy chains [1].

Despite the abundance and versatility of solar energy, we use very little of it to directly power human activities. The reasons are these three main categories have their shortcoming, storage problems for solar electric, emission of greenhouse gases (mainly CO_2) for solar fuel and inefficient for solar thermal energies. So we must find ways to store the large quantities of electricity and heat when conversion on a large scale is achieved. Otherwise, solar energy is

an interrupted energy, which caused by natural cycles of cloudy-sunny and day-night variation, and energy demands are often out of phase with solar energy. Solar fuel production can store energy in chemical bonds. However, it is much more difficult to store electricity and heat. The task, that storing electricity or heat cost effectively for 24 h, is well beyond present technology. So we need a cleaner, more effective, and achieved storage method under present technology.
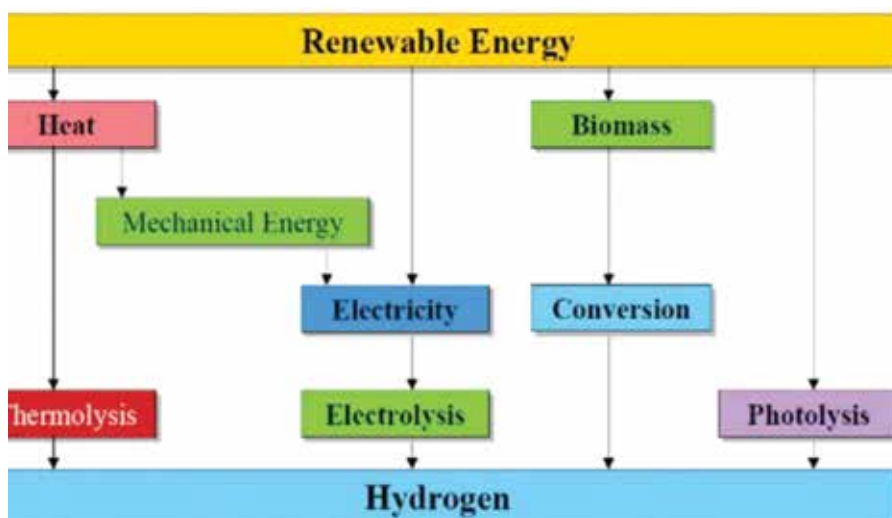

Figure 2. Sustainable pathways for hydrogen production from renewable energy, such as solar energy [10]. Copyright 2014 with permission from The American Association for the Advancement of Science.

Hydrogen is potentially an ideal energy carrier, as it is nonpolluting and gives up both its electrons upon oxidation to form only water. It may enable a secure and clean energy future, which uses hydrogen as the energy carrier connecting energy source to diverse end uses. Hydrogen is only an energy carrier for storing and transporting energy, which is different with oil and natural gas. Before we can use hydrogen, we have to produce it since hydrogen does not exist naturally. Every year, more than 500 billion cubic meters are produced [3, 4]. Most of this hydrogen is used for industrial purposes, such as refining petroleum and producing ammonia for fertilizers and other chemicals. In a hydrogen energy system, hydrogen containing compounds such as fossil fuels and water are potential sources of hydrogen [5, 6]. When hydrogen is derived from hydrocarbons, CO_2 capture and sequestration are requirements in a low greenhouse gas scenario [7, 8]. However, hydrogen produced from water does not present the challenge of unwanted emissions, but it does require an external resource [9]. If this energy can be obtained from a renewable energy source such as solar energy, hydrogen can then be considered a green energy alternative capable of powering everything. Otherwise, the storage problems of solar energy can be solved by hydrogen. Therefore, achievement of solar hydrogen production from water has been explored vigorously. Several ways for solar hydrogen production are applied (**Figure 2**) [10].

i.   Electrolysis of water using a hydroelectric power generation, a solar cell, etc.

ii.   Reforming of biomass.

iii.   Photoelectrochemical or photocatalytic water splitting.

Since water electrolysis needs a large number of infrastructure constructions for clean power, the practical widespread application of this technique is constrained by its high cost. However, direct solar-to-hydrogen conversion based on photochemical and photoelectrochemical water splitting is a promising scheme for sustainable hydrogen production. Currently, direct solar-to-hydrogen conversion is in the conceptualization stage still, but ongoing technological progress will ultimately make this approach enter the stage of actual application in the future.

1.1. Fundamental mechanism of photocatalytic hydrogen generation [11]

Photocatalytic water splitting by solar irradiation is appealing and has been intensively studied in the last four decades [12, 13]. In Fujishima and Honda's pioneering work, they constructed an electrochemical cell for the decomposition of water into hydrogen and oxygen [14]. When the TiO_2 electrode was irradiated by light, oxygen evolution occurred at the TiO_2 electrode. Concomitant reduction led to hydrogen evolution at the platinum black electrode. After the photocatalyst absorbs photon from light source such as sun, the electrons in the valence band of the photocatalyst are excited to the conduction band, while the holes are left in the valence band (called the negative-electron (e^-) and positive-hole (h^+) pairs). The "band gap" is the energy difference between the valence band and the conduction band. And the light can be effectively absorbed by the photocatalyst, while the wavelength of it corresponds to the "band gap". After the excited electrons and holes are generated in photocatalyst, they separate and migrate to the surface. Here, they act as reducing agent and oxidizing agent to produce H_2 and O_2 in the photocatalytic water-splitting reaction. A schematic representation of the principle of the photocatalytic system for water is depicted in **Figure 3**.
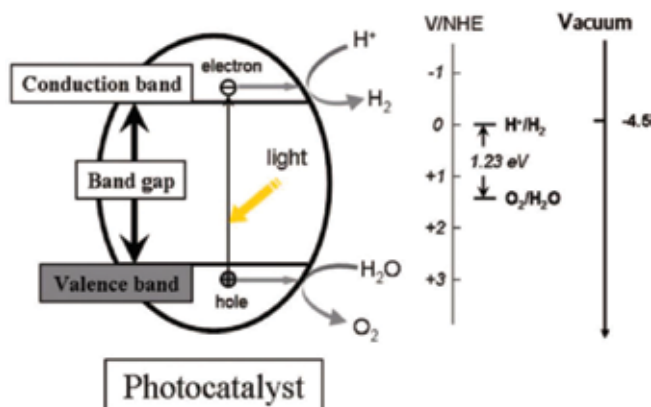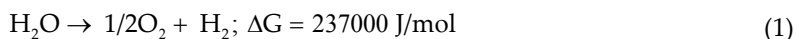

Figure 3. Fundamental principle of semiconductor-based photocatalytic water splitting for hydrogen generation [11].

Water splitting into H_2 and O_2 is an uphill reaction. It needs the standard Gibbs free energy change ΔG^0 of 237 kJ/mol or 1.23 eV, as shown in **equation 1**.

$$H_2O \rightarrow 1/2O_2 + H_2; \ \Delta G = 237000 \ J/mol \tag{1}$$

Therefore, to achieve water splitting, the band gap energy of the photocatalyst should be>1.23 eV (<1000 nm) and it should be <3.0 eV (>400 nm) to use visible light.

The proper band gap and the potentials of the conduction and valence bands are important to facilitate both the reduction and oxidation of H_2O. The top level of the valence band has to be more positive than the oxidation potential of O_2/H_2O (1.23 V), and the bottom level of the conduction band has to be more negative than the reduction potential of H^+/H_2 (0 V vs NHE).

1.2. The processes of photocatalytic hydrogen evolution

Figure 4 shows the processes in the photocatalytic generation of hydrogen [15]. They in-clude the absorption of light by the photocatalyst, generation of excited charges (electrons and holes), separation of excited charges, recombination of the excited charges, and transfer of excited charges to water or other molecules. The final generation of hydrogen from the semiconductor photocatalyst system can be affected by all of these processes.

The amount of excited electrons in the water/photocatalyst interface mainly determines the total amount of hydrogen generated in reducing water. Obviously, for maximizing the efficiency of the hydrogen generation of the photocatalyst system, any other processes that consume excited electrons should be avoided. Thus, for the charge-generation process, the reflection or scattering of light by the photocatalyst should be minimized, and the semicon-ductor photocatalyst should have a low band gap to absorb as much light as possible. Then, the semiconductor photocatalyst should generate excited charges using the absorbed pho-tons, instead of generating phonons or heat.
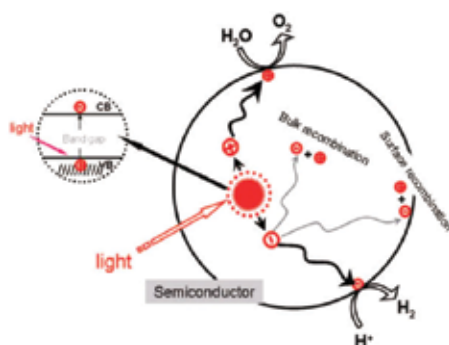

Figure 4. Processes in photocatalytic water splitting. Reprinted with permission from ref [15]. Copyright 1995 Ameri-can Chemical Society.

After excited charges are created in the semiconductor photocatalyst, charge separation/ migration and recombination processes are two important competitive processes [15]. The separation of excited electrons and holes may need to overcome an energy barrier. Charge is separated and migrated to the surface of photocatalyst ready for the desired chemical reaction. These processes are beneficial for hydrogen generation through water splitting. However, charge recombination will reduce the efficiency of water splitting since it reduces the amount of charge. It is important for photocatalytic hydrogen generation through water splitting to include efficient charge separation and fast charge transport for avoiding any bulk/surface charge recombination. Any method beneficial to the charge separation and transport should be applied such as design of heterojunction and use of high performance semiconductor materials (photoconductive).

So two keys should be considered to develop a suitable efficiency semiconductor for the visible-light-driven photocatalytic splitting of water into H_2 and/or O_2. Firstly, for harvest visible light and possess the correct band structure, a photocatalyst should have a sufficiently narrow band gap (1.23 eV< Eg < 3.0 eV). Secondly, to avoid bulk/surface electron/hole recombination, photoinduced charges in the photocatalyst should be separated efficiently. In addition, the electron/hole must migrate to the photocatalyst surface for hydrogen and/or oxygen evolution. In summary, the proper photocatalyst with correct band structure and with economical and highly efficient photocatalytic systems for light-to-hydrogen energy conversion should be constructed.

1.3. Modifying the electronic band structure for visible-light harvesting

To develop photocatalyst using visible-light irradiation, prophase studies were carried out on some narrow band gap semiconductors such as CdS [16] and WO_3[17, 18]. However, the serious photocorrosion of CdS [19] and the relatively positive conduction band of WO_3 proved dissatisfactory for hydrogen production [20] and created major impediments for visible-light-driven water splitting. Some studies were carried out to improve the photocatalytic stability of CdS, [21–24] and others used WO_3 as the photoelectrode in the photoelectrochemical cell for water splitting [25–27]. To overcome these disadvantages, many efforts have been made to develop new visible-light-driven photocatalysts with high water-splitting activities [21–27]. Several common approaches have been adopted in order to enhance the performance of visible-light active of photocatalysts for water splitting, which based on numerous experimental results from the past 20 years. These approaches were shown as follows: (1) developing novel single-phase Vis-active photocatalysts through band gap engineering; (2) dye sensitization to make UV-light-active photocatalysts harvest visible light; (3) developing solid solutions to control the band structure; and (4) metal or/and nonmetal ions doping for band gap narrowing.

In the method of metal or/and nonmetal ions doping for band gap narrowing, one of the most effective ways to develop visible-light driven photocatalysts is to create impurity levels in the forbidden band through nonmetal ion doping. It has been widely used to narrow the band gap and improve the visible-light-driven photocatalytic activity. Nonmetal-ion dopants are less likely to form donor levels just like metal-ion dopants in the forbidden band but instead shift

the valence band edge upward. **Figure 5** shows a narrowing of band gap. The technology of nonmetal-ion doping has been widely used to modify some UV-light-active oxide photocatalysts, such as Ti-based oxides [28–30], Ta-based oxides [31–34], Zr-based oxides [35, 36], and Nb-based oxides [37, 38]. The boron doping has been used to modify 3C-SiC nanowires for effective visible-light-driven photocatalytic activity in our recent work (B-doped 3C-SiC nanowires) [39].
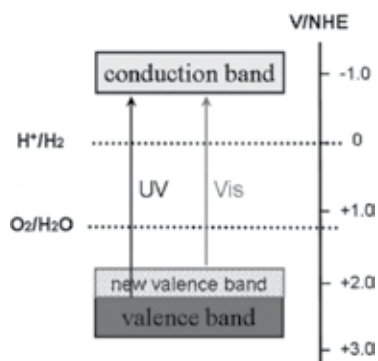

Figure 5. New valence band formation by doping of nonmetal ions [11].

Another promising method for controlling photocatalyst band structure is the formation of solid solutions between wide and narrow band gap semiconductors such as doping. According to this method, varying the ratio of the compositions can control the band gap and position. **Figure 6** shows the controllable band formation by making a solid solution. This method contain (oxy)sulfide solid solutions [40–42], oxide solid solutions [43, 44], and oxynitride solid solutions [45–48]. The way of oxynitride solid solutions were used in our recent work (TiOxNy/TiN) [49].
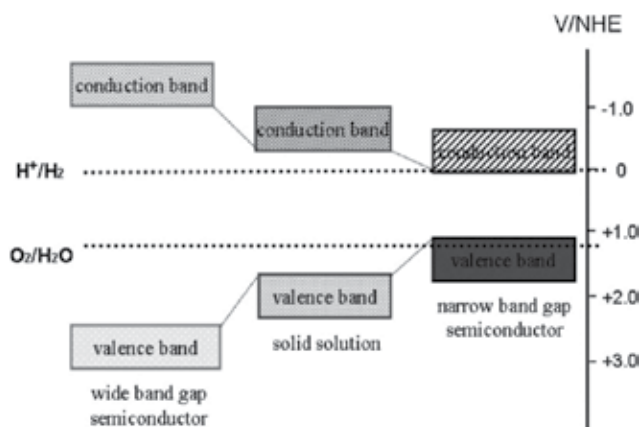

Figure 6. Band structure controlled by making a solid solution [11].

1.4. Efficient photogenerated charge separation

When visible-light-driven photocatalysts with proper band structures are synthesized and charges are excited, the photogenerated charge separation is another key factor strongly affecting the efficiency of the photocatalytic water-splitting process. Clearly, to avoid bulk/ surface charge recombination and transfer to the separated active sites on the surface of the photocatalysts, the utilization rate of the photogenerated charges can be improved and high photocatalytic water-splitting activities can be obtained. On the basis of numerous experimental results and theoretical research results from the past decades, several common approaches have been adopted in order to make efficient photogenerated charge separation: (1) cocatalyst loading; (2) semiconductor combinations; (3) modification of crystal structure and morphology.

Transition metals, especially the noble metals, are widely used as effective cocatalysts for photocatalytic water splitting. Taking Pt as an example, **Figure 7** shows the processes of charge transfer between cocatalyst and host photocatalyst. Since the Fermi energy level of noble metal is always lower than that of the semiconductor photocatalyst, the photogenerated electrons migrate to the surface of the host photocatalyst and are entrapped by the noble metal cocatalyst after the surface of the photocatalyst is loaded with the noble metal. Meanwhile, the photogenerated holes migrate to the surface of host photocatalyst. So the photogenerated electrons and holes can be separated efficiently. Subsequently, in the photocatalytic reaction, the separated electrons and holes are involved in the reaction as the reducer and oxidizer, respectively. Overall, the cocatalysts are extremely important. It improves the overall photocatalytic activity of the water splitting because it helps to promote charge separation, which in return reduces both bulk and surface electron/hole recombination. It also accelerates the surface chemical reaction by inhibiting backward reaction. As one of the noble metals, Pt has been widely used as the cocatalyst in photocatalytic water splitting over many different kinds of semiconductors: oxides [50–52], (oxy)sulfides [53–56], and (oxy)nitrides [57–59]. All have been shown to greatly enhance the photocatalytic activity for hydrogen evolution.

The semiconductor combination approach has been shown to be another effective method for improving photocatalytic activity through better photogenerated charge separation with a formation of a heterojunction structure. As shown in **Figure 8**, the staggered band gap type is the most suitable for photocatalytic applications. In this type, the two semiconductors construct a heterostructure on the basis of the matching band potentials. Holes will transfer to the VB of semiconductor-A from semiconductor-B, in which the VB level of semiconductor-A is higher than semiconductor-B. Electrons will transfer to the CB of semiconductor-B from semiconductor-A, in which the CB level of semiconductor-A is higher than semiconductor-B. So the internal field can promote the separation and migration of photogenerated carriers and reduce the recombination of electron–hole. As a result, a mass of holes accumulate on the surface of semiconductor-A and a mass of electrons accumulate on the surface of semiconductor-B. These carriers will participate in photoredox reaction and thus the reaction can be enhanced greatly.
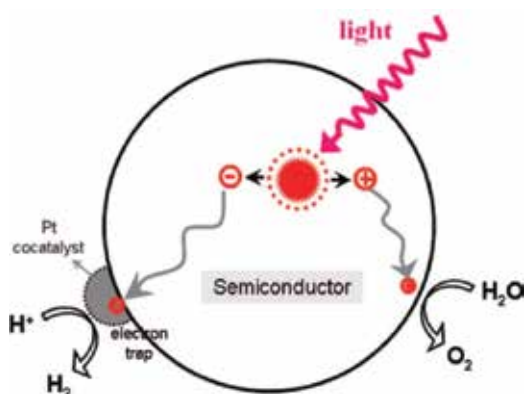
Figure 7. Processes of charge transfer between host photocatalyst and cocatalyst, taking Pt as the example of cocatalyst [11].
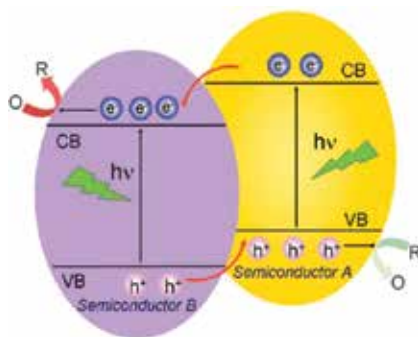

Figure 8. Schematic diagram showing the energy band structure and electron-hole pair separation in the heterojunction [60].

In general, the crystal structural features of the materials, such as crystallinity, defects, and any crystal structure distortion, can strongly affect the charge separation and transfer of photogenerated electrons and holes. Additionally, the morphology of the materials is also important. For example, it includes particle size, surface area, surface structure, and active reaction sites. Thus, on the basis of numerous experimental results and theoretical research results from the past decades, both the modification of crystal structure and morphology of the photocatalysts have been adopted in order to improve efficient charge separation. This has had great success in the enhancement of photocatalytic activity for water splitting.

For crystal structure, it has been well demonstrated that the crystal structure of TiO_2 plays a significant role in photocatalysis. In photocatalysis, for pure-phase TiO_2, the anatase phase was considered to be more active than the rutile phase [61, 62].

It is well-known that particle size is a crucial factor in the dynamics of electron/hole recombination (including bulk recombination and surface recombination) processes, especially in

semiconductor nanomaterials, and that the movement of electrons and holes is primarily governed by the well-known quantum confinement [63]. Generally, when the particle size of photocatalysts decreases, its efficiency will increase in photocatalysis [64–67]. Moreover, reduction in particle size could also lead to a larger surface area and increase the available surface active sites [68, 69]. Lee *et al.* reported that the smaller particle size and higher surface area of $NaTaO_3$ led to higher photocatalytic performance in water splitting [69]. Sathish *et al.* [70] found that CdS nanoparticles showed a higher efficiency of photocatalysis compared to bulk CdS. This result indicated the fact that smaller particle size can increase the performance of a photocatalyst. However, when particle size of the nanocrystalline semiconductor becomes extremely small, this in return can offset the benefits of the ultrahigh surface area of the nanocrystalline particles [71, 72]. So for higher efficiency, the photocatalyst should have the proper size.

Two-dimensional (2D) nanostructures such as nanobelts [73, 74], nanosheets [75, 76], and nanoplates [77, 78] also favor the transfer of electrons and holes generated inside the crystal to the surface and promote charge separation [79–81]. Under identical conditions, Sun *et al.* found that ZnO nanobelt arrays was better than that found for ZnO film or the rod-/comb-like ZnO nanostructures for the photocatalytic properties [73]. Self-assembly of nanoscale building blocks into three dimensional (3D) complex structures is another research hot spot in photocatalysis [82–85]. Song and Gao found that hollow NiO microspheres showed a significantly more enhanced photocatalytic activity than NiO rods [86].

There are two main approaches to enhance the visible-light-driven activity of photocatalysts for developing more efficient that. One is the promotion of the photogenerated charge separation. The other is to narrow the band gaps to harvest visible light in the longer-wavelength regions. Therefore many factors which determine the photocatalytic activity are needed to be applied in one material, such as morphology, structure and crystallinity, chemical composition, surface states, and electronic properties.

Titanium nitride (TiN) is an Fm3m cubic crystal containing both covalent and metallic bonds. It has a narrow energy band gap (0.80 eV) and good electrical conductivity, which are beneficial to photocatalytic H_2 production. However, since the rapid recombination between photoelectrons and holes, its application as a photocatalyst is limited. The inherently high defect density of TiN and unfavorable band position for hydrogen reduction led to the rapid recombination of photoelectrons and holes. 3C-SiC is an important semiconductor with suitable band gap (2.3–3.3 eV) and excellent properties, such as high thermal conductivity, high mechanical strength, and high chemical stability, especially the environmentally friendly property. However, SiC as a photocatalyst does not draw wide attention due to the high recombination rate of photogenerated electron-hole pairs as well as its surface evolution during 3C-SiC nanoparticles or nanocrystal contacting with water. In our recent work, three methods including ion doping, combination with other semiconductor to form heterojunction, and 3D complex structures are adopted to improve the photocatalytic activity of 3C-SiC and TiN from both theoretical and experimental viewpoint, aiming to extend the application of 3C-SiC and TiN as functional material.

2. Theoretical calculations

Band gap engineering is a significant and new approach, which can modify the band struc-
ture of semiconductor. In band gap engineering, solid solution, semiconductor sensitization,
and ion doping are the most common ways. What's more, theoretical calculation based on first-
principle calculations can provide an efficient way to identify a candidate and suggest useful
processing and production conditions.

Plane-wave pseudo-potential with Cambridge Serial Total Energy Package (CASTEP) code is
adopted in the first-principle calculations. The geometry structure is optimized by using the
Broyden-Fletcher-Goldfarb-Shanno (BFGS) [87]. **Table 1** lists all the calculation conditions. The
self-consistent field is set to 1×10^{-6} eV/ atom. In the calculation for the DFT exchange-correla-
tion function, the generalized gradient approximation (GGA) [88, 89]is adopted, as specified
by Perdew and Wang [90]. The density mixing option is chosen in the electronic minimiza-
tion method [91].

Task: Geometry optimization			Energy
Functional	GGA PW91		LDA CA-PZ [92, 93]
Minimizer	Fine quality		-
	Energy:	1.0e-5 eV/atom	-
	Max force:	0.03 eV/	-
	Max stress:	0.05 GPa	-
	Max displacement:	0.001 Å	-
Algorithm	BFGS:	Use line search	-
Stress	0 for all		-
Energy cutoff	700 eV		700 eV
SCF tolerance	1.0×10^{-6}eV/atom		1.0×10^{-6}eV/atom
Pseudopotentials	Ultrasoft [94]		Norm-conserving [95]
FFT grid density	Fine quality		Standard
Finite basis correction	Smart		Smart
Electronic minimizer	Density mixing		Density mixing
Orbital occupancy	Fixed		Fixed
k point quality	Fine quality		Fine quality
Band structure	Unchecked		Checked Fine quality k point set
Density of states	Unchecked		Checked Medium quality k point set

Table 1. Calculation conditions for geometry optimization and energy task.

2.1. B-doped 3C-SiC nanowires with finned microstructure

3C-SiC with zinc blende structure is shown in **Figure 9(a)**, and its lattice constant is a=b=c=0.4341 nm. The optimized models are shown in **Figure 9(a)–(d)**, where Si in the symmetrical positions has been substituted by B [96, 97]. The k-point set mesh parameters are chosen to be fine quality in the Brillouin zone for B-doped 3C-SiC ($Si_{31}BC_{32}$, $Si_{15}BC_{16}$, and Si_7BC_8) corresponding to B concentration about 14.3 at%, 6.7 at%, and 3.2 at% respectively.
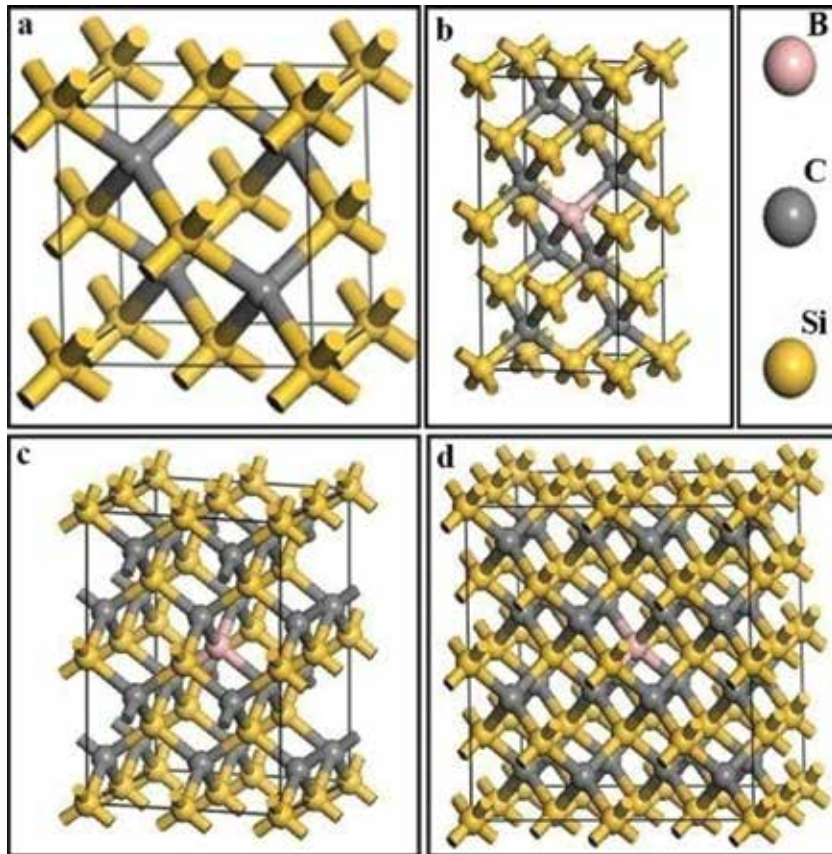

Figure 9. Structures of calculation models for SiC and $Si_{n-1}BC_n$ (n=8, 16, 32).

Figure 10 plots the projected density of states (PDOS) of B-doped 3C-SiC with the ratio of B/Si ranging from 0 to 0.143. According to **Figure 10a**, 3C-SiC is indirect semi-conductor, which is in agreement with the reported result [97]. It is changed to direct semiconductor with B being doped (**Figure 10(b–d)**). As shown in **Figure 10e**, the band gaps decrease continuously from 2.341 eV to 1.935 eV with the molar ratio of B/Si increasing from 0 to 0.143. It is well known that material with much smaller band gap tends to lead to photo-corrosion. Dong *et al.* [96] reported B-doped SiC powder for photocatalytic hydrogen evolution under visible light. In their work, when the B/Si molar ratio is 0.05 in B-doped 3C-SiC, it exhibits the highest hydrogen

evolution rate of 7.41 $\mu mol \mu g^{-1} h^{-1}$. Therefore in the experiment, the molar ratio of B/Si is selected as 0.067, i.e. $Si_{15}BC_{16}$.

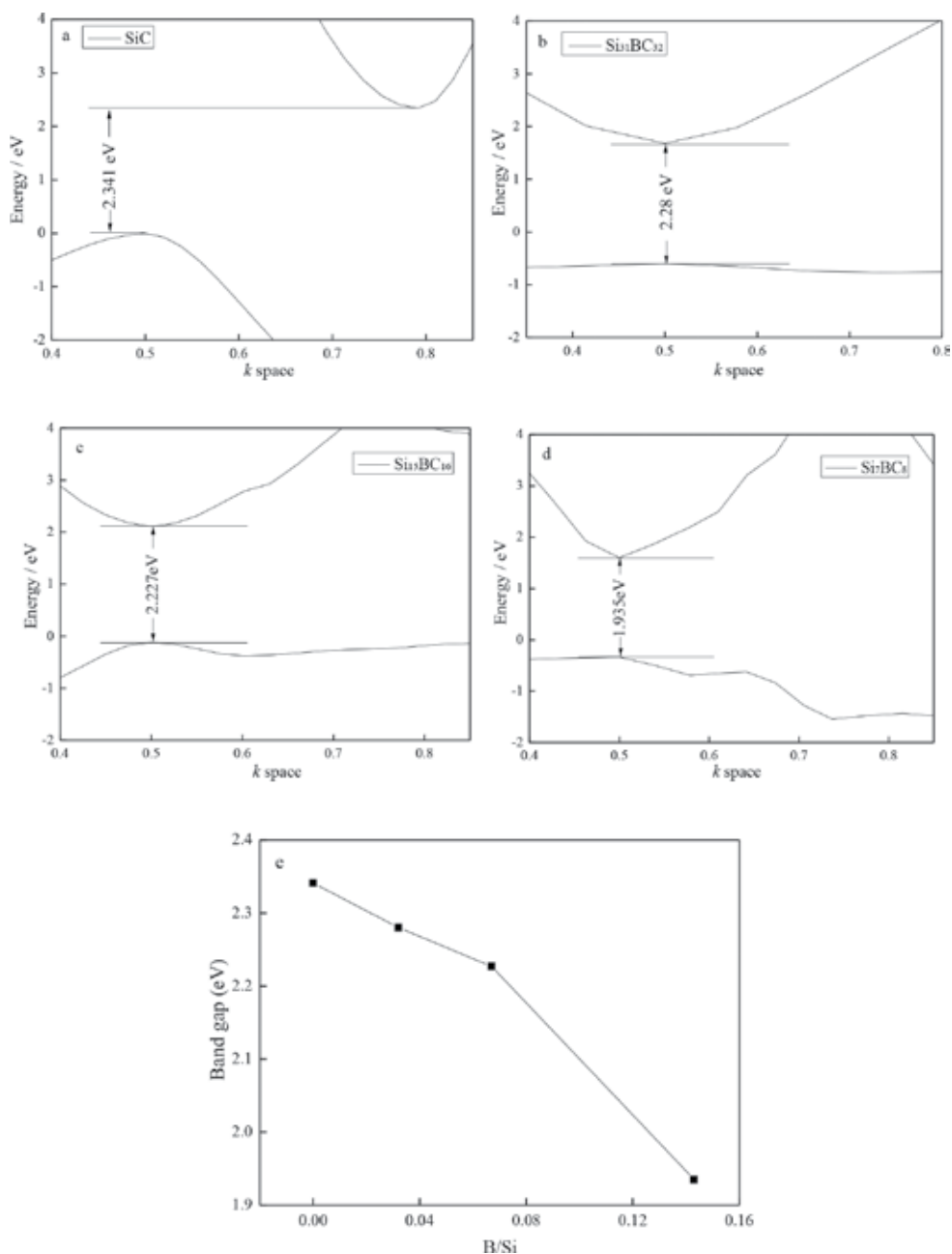**Figure 10.** (a)–(d) Calculated PDOS of 3C-SiC and B-doped 3C-SiC including $Si_{31}BC_{32}$, $Si_{15}BC_{16}$ and Si_7BC_8, (e) is the band gap of $Si_{n-1}BC_n$ (n=8, 16, 32).

2.2. TiO$_x$N$_y$/TiN heterojunction composite

As for TiN, TiO$_x$N$_y$ is selected as a sensitizer to enhance the photoactivity of TiN. The electronic structures of TiN and TiO$_x$N$_y$ can be calculated by plane-wave-density function theory (DFT) using the Cambridge Serial Total Energy Package (CASTEP) program package. **Figure 11** shows the optimized simple crystal structures of TiN, Ti$_2$O$_4$, and TiO$_x$N$_y$ with N doping concentration in the range of 0 to 33 mol% (Ti$_{16}$O$_{31}$N, Ti$_8$O$_{15}$N, Ti$_4$O$_7$N, Ti$_2$O$_3$N, and Ti$_2$O$_2$N$_2$). O in the symmetrical positions of rutile titanium dioxide (TiO$_2$) crystal cell has been substituted by N. TiN has a narrow energy band gap (0.80 eV) in **Figure 12a**, which is in consistent with Li's *et al*. work [98]. The calculated band gaps of TiO$_x$N$_y$ decrease from 3.084 to 0.009 eV with N doping concentration increasing from 0 to 33 mol% (**Figure 12e**).
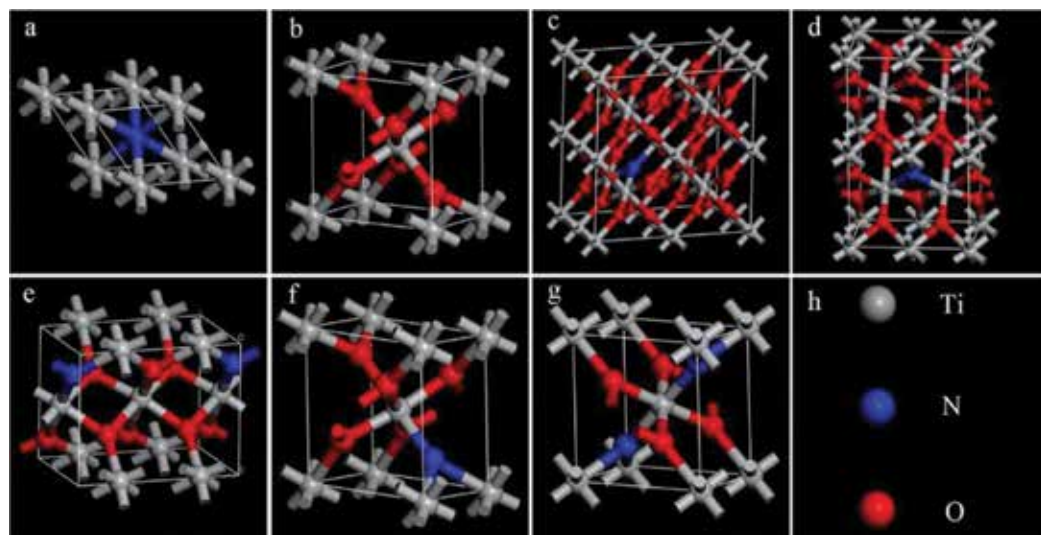

Figure 11. Structures of calculation models for TiO$_x$N$_y$.

It can be seen that the band gap of TiO$_x$N$_y$ is more than 0.8 eV when the doping concentration of N is less than 17 mol% (**Figure 12d** (Ti$_2$O$_3$N, 0.918 eV)). Since N introduce new energy band, band gaps of TiO$_x$N$_y$ changed with N doping concentration. There is a newly formed energy band introduced by the 2p states of doping N in **Figure 12(c–d)**. From above calculation, TiN combining with TiO$_x$N$_y$ with proper N doping concentration is expected to form favorable band-edge position, which may be a potential candidate for visible-light responsive photocatalyst.

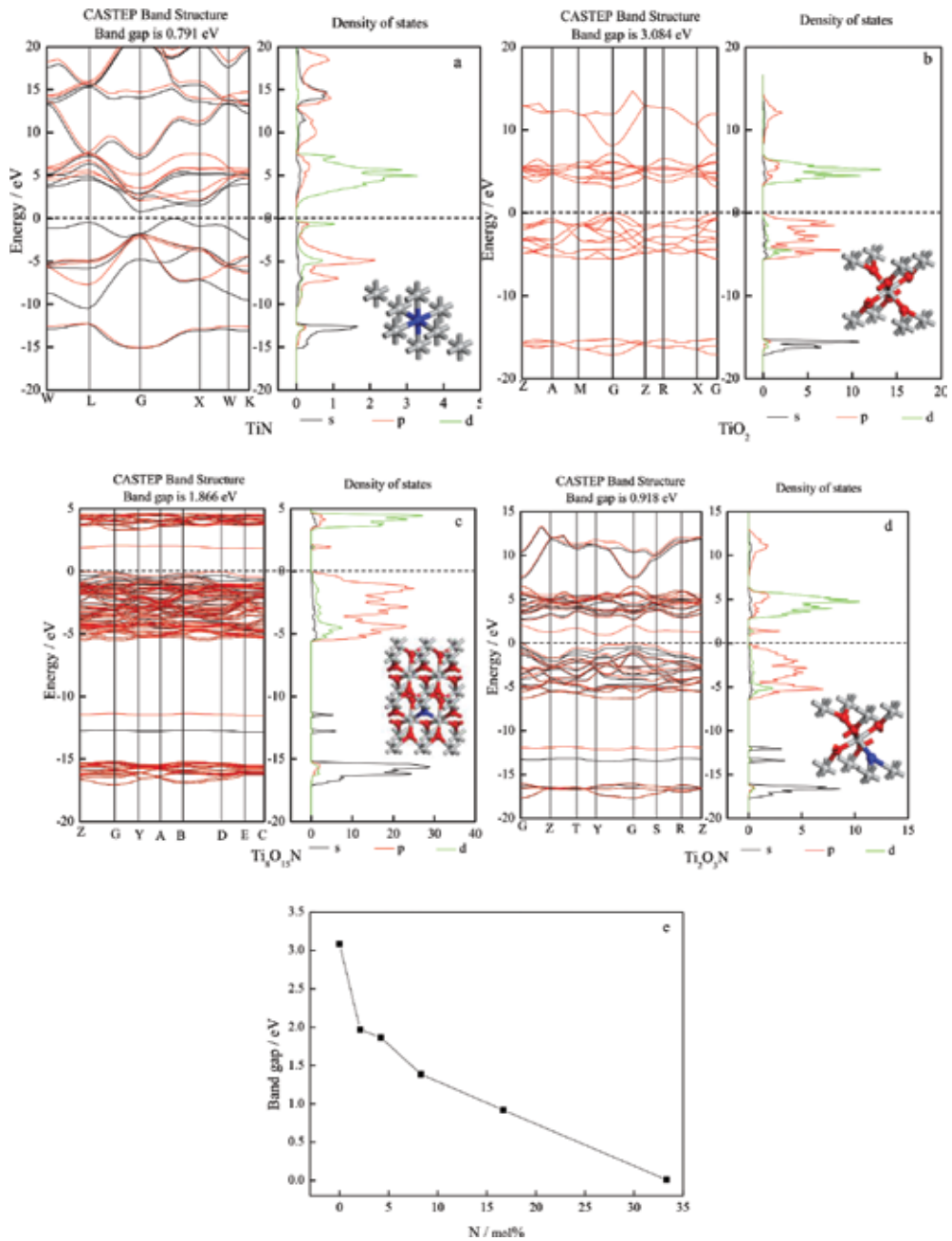**Figure 12.** The calculated energy band and density of states of TiN (a), TiO_2 (b), TiO_xN_y (c and d) and the end of band gaps (e). Inset of the crystal structure by the ball-and-stick mode (gray: Ti; red: O; and blue: N).

3. Experimental method for water splitting

3.1. B-doped 3C-SiC nanowires with finned microstructure

Herein a simple synthesis route, i.e. carbonthermal reduction combining the ion doping and morphology modification is adopted in the present work. By controlling the amount of boron doping and the reaction temperature, B-doped 3C-SiC nanowires (NWs) with finned microstructure are obtained. It shows an outstanding activity toward H_2 production as high as 108.4 μmol•h^{-1}, which is about 20 times higher than that of the 3C-SiC nanowires and 2.6 times of the value reported in the literature [99].

3.2. TiO_xN_y/TiN heterojunction composite

TiO_xN_y/TiN heterojunction composite with tunable chamber structures were prepared through reduction and nitridation of organotitania obtained through solvothermal alcoholysis at 900°C for 4 h in partial cracked NH_3. Owing to the low synthesis temperature, TiO_xN_y/TiN duplicates the original structure of the organotitania. It demonstrates an outstanding photocatalytic activity as high as 34.9 μmol•h^{-1}•g^{-1}, which is about 1.5 times higher than the highest value reported in the literature for TiN [98].

4. Results and discussion

4.1. B-doped 3C-SiC nanowires with finned microstructure

4.1.1. Characterization of B-doped 3C-SiC NWs

Figure 13 shows the pattern of X-ray diffraction (XRD) of the B-doped SiC NWs. For comparison, 3C-SiC NWs obtained in our experiment is also investigated. In the two sample, three diffraction peaks at 2θ =35.8°, 60°, and 72° corresponding to cubic SiC (JCPDS card no. 73-1665) both appear suggesting B doping does not change the phase structure of 3C-SiC. However, the characteristic peak of B-doped 3C-SiC shifts towards higher 2θ angle according to the magnification of diffraction peak (111). This change is possibly caused by the substitution of smaller B (0.095 nm) at Si (0.134 nm) [97]. The stacking defects (SF) of SiC were studied by Tateyama *et al.* [100]. The estimation formula was proposed as follows:

$$d_{SF} = \frac{I_{SF}}{I_{(200)}}$$

In the formula, $I_{(200)}$ is the intensity values of (200) peak (41.4°) and I_{SF} is the intensity values of SF peak (33.6°). The density of SF in SiC is represented by the ratio value (d_{SF}). As shown in **Figure 13**, the SF peak (red circles) is too weak to calculate the density, which indicates that there are only a few defects in SiC whiskers.
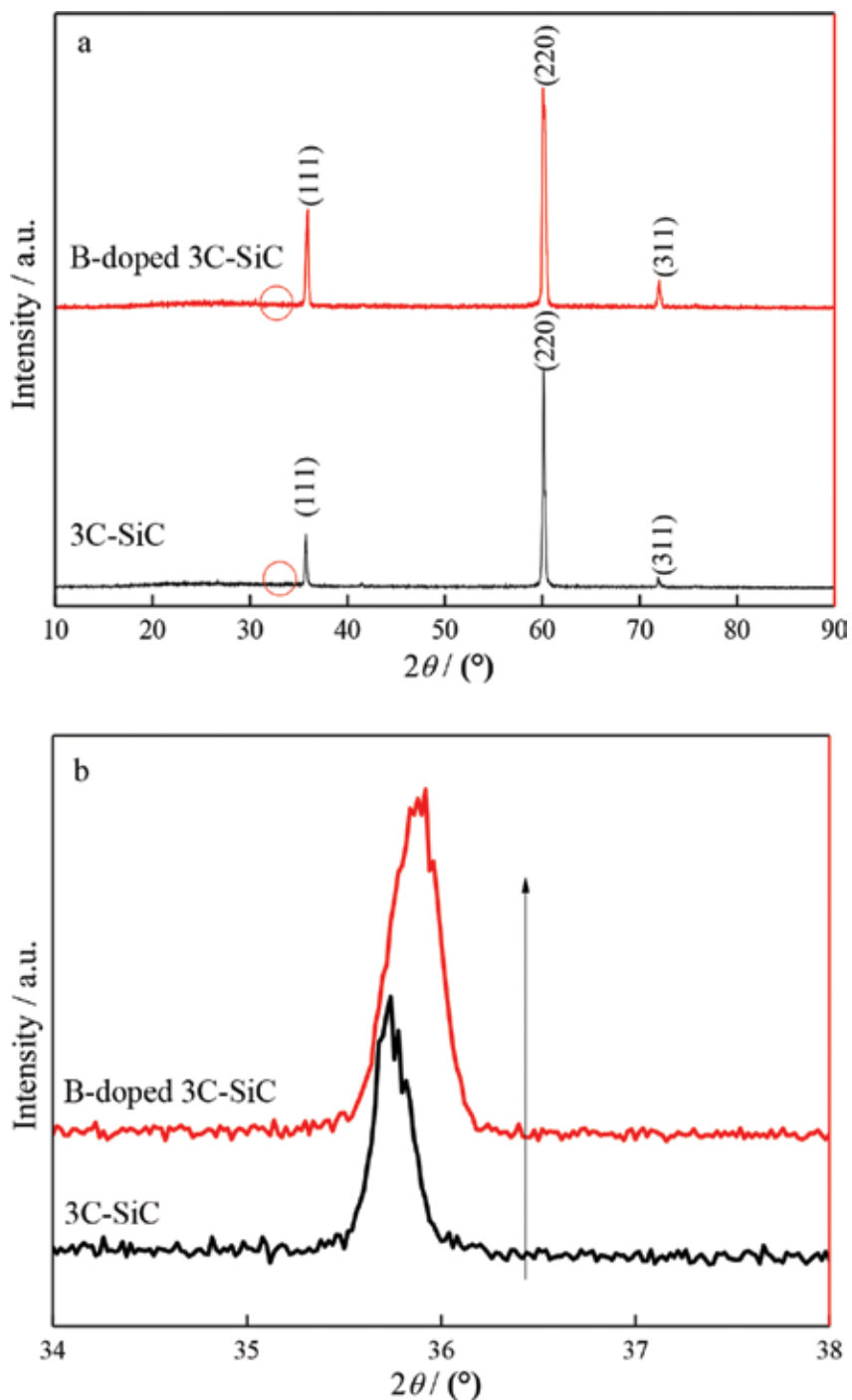
Figure 13. XRD patterns of the as-prepared (a) and the magnification of the diffraction peak (111) (b).
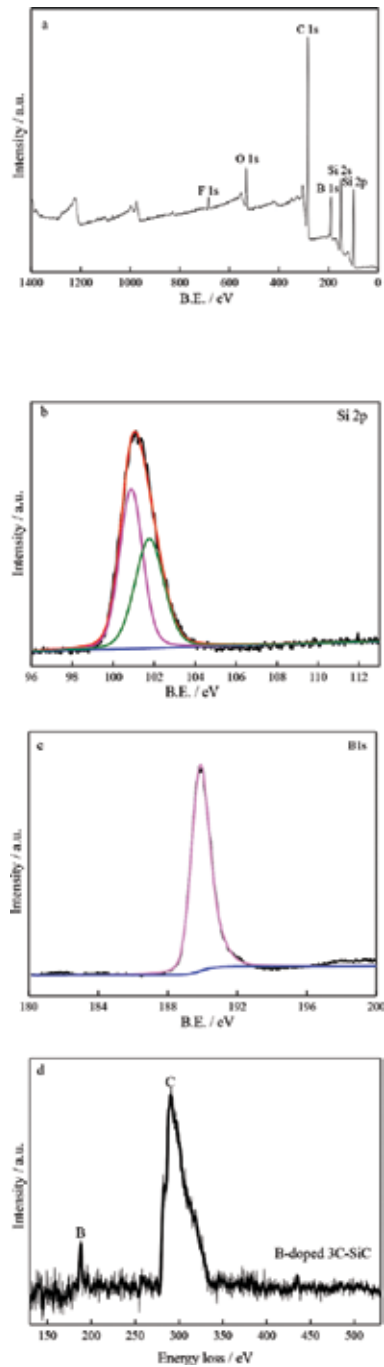
Figure 14. The full spectrum of XPS of B-doped 3C-SiC (a), XPS spectra of (b) Si 2p, (c) B 1s, (d) Electron energy loss spectroscopy (EELS) of B-doped 3C-SiC.

X-ray photoelectron spectroscopy (XPS) is used to characterize B-doped 3C-SiC NWs. The full spectrum of XPS shows the existence of Si, C, B, F, and O in **Figure 14**. Since HF is adopted to treat the surface of sample, F possibly comes from it. **Figure 14b** shows Si 2p fine XPS spectra of the B-doped 3C-SiC NWs sample. From the XPS spectra of Si 2p of B-doped 3C-SiC (**Figure 14b**), the peak centered at 100.7 eV corresponds to Si-C bond in SiC. The peak at 101.8 eV can be assigned to SiOxCy [101]. Two reasons are attributed to the formation of SiOxCy. First is the surface of sample tends to absorb oxygen after treated by HF. Second is SiCxOy is the intermediate product of SiC [101] that is left on the sample. However, the content of SiOxCy is too low to be detected by XRD analysis. **Figure 14c** show B 1s fine XPS spectra of the B-doped 3C-SiC NWs sample.

XPS signals of B 1s can be assigned to the B-C bond in SiC, which are observed at 189.8 eV [101]. The peak at 187.4 eV corresponds to the B-Si bond in SiC and the peak at 193.1 eV corresponds to B-O bond for B_2O_3[102]. In this work, these peaks are not found. This indicates that B atoms incorporate into SiC lattice and substitute Si sites, which are consistent with the reported results [96, 97]. The B/Si molar ratio, as determined by XPS, is 0.066, which is close to the theoretical content of $Si_{15}BC_{16}$. Electron energy loss spectroscopy (EELS) was carried out to further investigate the existence of B element in B-doped 3C-SiC. The peak at 284 eV corresponds to C element and the peak centered at 188 eV corresponds to B element (**Figure 14d**). This further indicates that B-doped 3C-SiC is synthesized in the experiment.
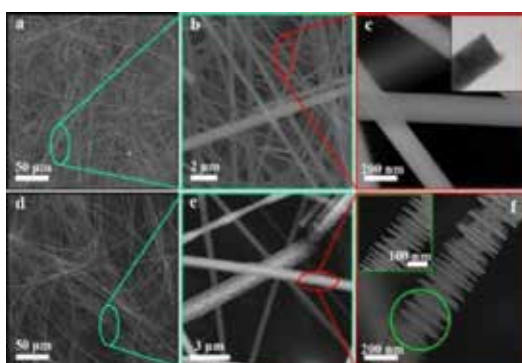
Figure 15. SEM images of the as-prepared 3C-SiC (a–c) and B-doped 3C-SiC (b–d).

SEM and TEM techniques are used to reveal the morphology and microstructure of the as-prepared samples. **Figure 15** show SEM images of the synthesized 3C-SiC NWs. **Figure 15a** and d show the overall looks of the 3C-SiC NWs and B-doped 3C-SiC NWs at low magnification, which indicate that the majority of the nanowires can be described as long and straight filaments with the length up to several mm. As shown in SEM at higher magnification (**Figure 15b**), the typical morphology of 3C-SiC NWs possess smooth surface and the average diameter is about 80 nm. The whisker has a homogeneous crystalline structure with fringes spacing at 2.51 Å as shown in **Figure 16b**, which is characteristic of 3C-SiC. By comparison, the morphology of B-doped 3C-SiC NWs changes a lot. The typical morphology of the B-

doped 3C-SiC NWs is finned nanowires as shown in the magnified images (**Figure 15e** and **f**). It is composed of inner core stems and outer fins. **Figure 16c** and d show TEM images of typical finned like B-doped 3C-SiC NWs. The thickness of the fins is 10–20 nm. The diameter of the inner core stems is about 80 nm and the fins is about 100–200 nm. The lattice spacing of a fin is 2.50 Å as shown in **Figure 16e**. From SAED pattern of the fin (the inset of **Figure 16e**), it is single crystal. The HRTEM image reveals that the lattice spacing of the nanowire is also 2.50 Å in **Figure 16f**. It is caused by substitution of smaller B (0.095 nm) at Si (0.134 nm) and leads to the distortion of the lattice.
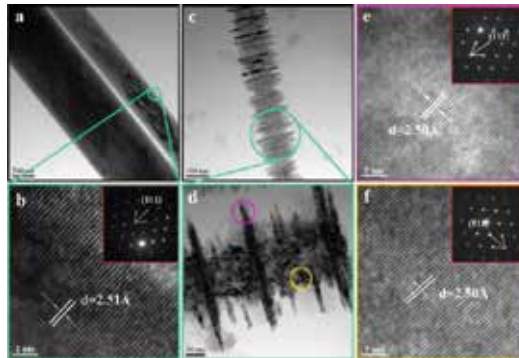
Figure 16. TEM images of the as-prepared 3C-SiC (a–b) and B-doped 3C-SiC (c–f).

For the formation of hierarchical nanostructures, two growth mechanisms are put forward [103–105]. Self-assembly of nanobuilding blocks is one formation mechanism, wherein blocks include balls, wires, and platelets [105]. Inner 1D core structures and then the epitaxial growth of secondary branches is another formation mechanism [103, 104]. As shown in **Figure 17a**, some SiC NWs possessing rough and uneven surface are found in this work. Therefore the formation of finned 3C-SiC NWs cloud be the two-step epitaxial growth process.

Figure 17. (a). The rough and uneven surface of SiC core stem caused by the stacking faults. (b). Schematic illustration of a possible SiC nanoarchitecture growth process.

In the experiment, the possible reactions take place as following:

$$SiO_2(s) + C(s) \rightarrow SiO(g) + CO(g) \tag{1}$$

$$B_2O_3(g) \rightarrow 2B(s) + 3/2O_2(g) \tag{2}$$

$$15SiO(g) + B(s) + 47CO(g) \rightarrow Si_{15}BC_{16}(s) + 31CO_2(g) \tag{3}$$
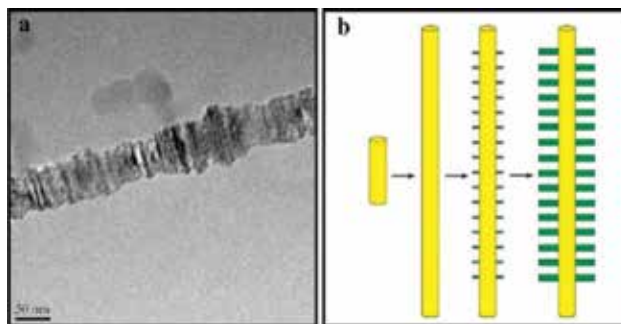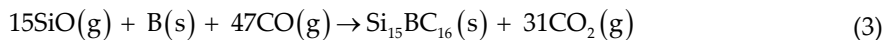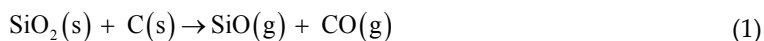
$$C(s) + CO_2(g) \rightarrow 2CO(g) \tag{4}$$

SiO vapor plays an important role during the synthesis of 3C-SiC whiskers [105]. The formation of B according to **Equation (2)** makes B doping possible and thus is a key step. The standard reaction Gibbs energies of **Equation (2)** are 767412.5 J•mol^{-1}using the database of FactSage 6.4. In our experiment, the partial pressure of O_2 is controlled to be 2.6×10^{-12} Pa, which is verified by mass spectrometry. The vapor pressure of B_2O_3 is 152 Pa at 1500°C according to the Speiser's [106] result as following:

$$\lg p_{B_2O_3}(\text{atm.}) = -(77600/4.575\ T) + 6.742$$

Therefore, the reaction Gibbs energy of **Equation (2)** can be calculated as follows:

$$\Delta rG_{1773} = \Delta rG^\theta + RTlnJ$$

$$= 767412.5 + 8.314 \times 1773 \ln \frac{P_{O_2}^{\frac{3}{2}}}{P_{B_2O_3}}$$

$$= 767412.5 + 8.314 \times 1773 \ln \frac{(2.57 \times 10^{-17})^{\frac{3}{2}}}{1.52 \times 10^{-3}}$$

$$= 58715.5\ \text{J·mol}^{-1}$$

where J is the reaction constant of **Equation (2)** at 1500°C. Therefore the reaction Gibbs energy of **Equation (2)** is calculated to be −58715.5 J/mol, indicating that the reaction can take place under the experimental condition.

Owing to the high temperature, the formation of inner 1D core stem is the first step in a two-step epitaxial growth process. When reaction between CO, B, and SiO occurs, the B-doped SiC($Si_{15}BC_{16}$) will be formed (**Equation (3)**). CO_2 reacts with C to form CO according to **Equation (4)**, which causes CO to remain at a supersaturated level and thus **Equation (3)** continues to proceed. This leads B-doped SiC($Si_{15}BC_{16}$) to precipitate as nuclei and grow along the (111) direction due to the lowest surface energy to form the core stem B-doped SiC ($Si_{15}BC_{16}$) nanowires. Since SiC NWs have more defects after B doping, the nanowires possess

rough and uneven surface (as shown in **Figure 17a**). When the temperature is decreased and the amount of SiO becomes less, the growth rate of B-doped SiC will become lower. Since the energy for nucleating SiC on B-doped SiC core stems is far lower than that on the other places, the newly formed B-doped SiC tends to grow on that. Therefore, the fins are formed on the core stems. With time prolonging, B-doped SiC nanowire with finned structure are produced.
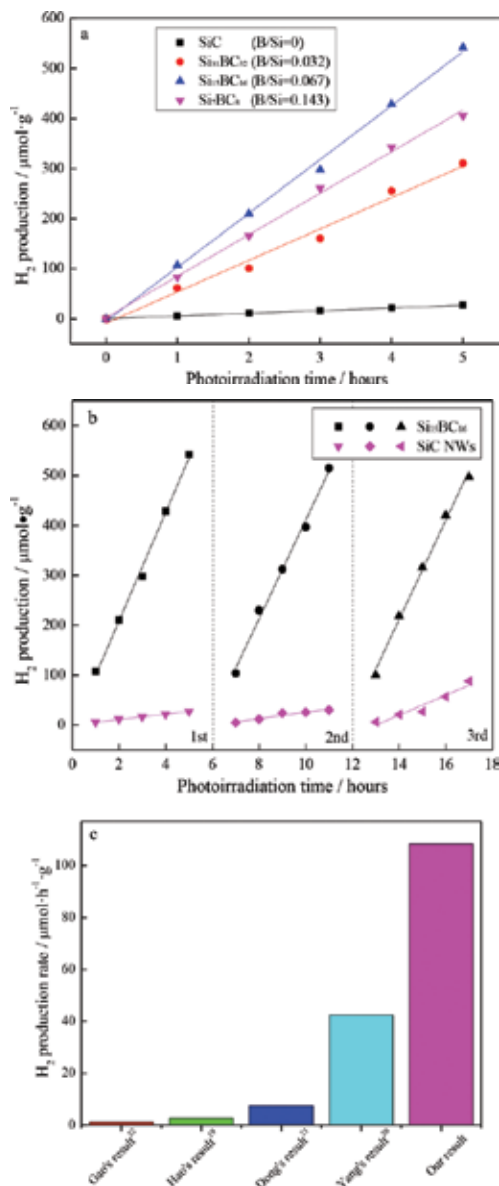

Figure 18. (a). Photocatalytic hydrogen evolution performance over BxSiC. (b). Hydrogen production rates of as-prepared the 3C-SiC NWs and B-doped 3C-SiC NWs. (c). The comparison of Hydrogen production rates.

4.1.2. Water splitting for hydrogen

The 3C-SiC NWs and B-doped 3C-SiC NWs are evaluated under visible-light irradiation for their photocatalytic activities for H_2-production in aqueous suspensions with Na_2S and Na_2SO_3 as sacrificial agents (electron donor). Photocatalytic activities of B-doped SiC with different B/ Si ratios are compared in **Figure 18**. B doping significantly affects the photocatalytic activity as shown in Figure 18. The photocatalytic H_2-production rate of sample from high to low is $Si_{15}BC_{16}$ (108.4 $\mu mol \bullet h^{-1} \bullet g^{-1}$), Si_7BC_8 (81.0 $\mu mol \bullet h^{-1} \bullet g^{-1}$), $Si_{31}BC_{32}$ (62.1 $\mu mol \bullet h^{-1} \bullet g^{-1}$), and pure 3C-SiC (5.46 $\mu mol \bullet h^{-1} \bullet g^{-1}$).The recycling reaction experiments were carried out to investigate the stability of photocatalytic hydrogen production of 3C-SiC NWs and B-doped 3C-SiC NWs ($Si_{15}BC_{16}$) under visible light irradiation. No decrease in catalytic activity is observed in the recycling reactions as shown in **Figure 18b**. The H_2 production rate for the B-doped 3C-SiC NWs exceeds that of 3C-SiC NWs by more than 20 times. It also exhibits enhanced activity toward H_2 production compared with the recent work as shown in **Figure 18c**. Wang's work group reported SiC fine powder, which can achieve at a value of 1.11 $\mu mol \bullet h^{-1} \bullet g^{-1}$[107]. Guo's work group reported modified SiC nanowires, which can achieve at a value of 2.68 $\mu mol \bullet h^{-1} \bullet g^{-1}$[108]. And Dong's work group reported boron-doped SiC powder, which can achieve at a value of 7.41 $\mu mol \bullet h^{-1} \bullet g^{-1}$[96]. Among these work, the reduced grapheme oxide/SiC showed the larger visible-light-driven photocatalytic hydrogen produc-tion done by Yuan's work group to be 42.4 $\mu mol \bullet h^{-1} \bullet g^{-1}$[99]. Our result is 108.4 $\mu mol \bullet h^{-1} \bullet g^{-1}$, which is 2.6 times higher than that of the reported reduced grapheme oxide/SiC.

In view of the photocatalytic hydrogen production mechanism of B-doped 3C-SiC NWs, first is attributed to the smaller band gaps with B doping as shown in **Figure 10**. It is well know that the positions of the valence band maximum (VBM) and the conduction band minimum (CBM) are critical variables in determining the feasibility of visible-light-driven photocatalyt-ic hydrogen production. As shown in **Figure 19**, it can be seen that the CB and VB potentials (E_{CB} and E_{VB}) of 3C-SiC are E_{CB}=0 eV and E_{VB}= 2.341 eV (**Figure 19a** and **b**). After B doping, the CB and VB potentials (E_{CB} and E_{VB}) are decreased to E_{CB}=−0.4 eV and E_{VB}= 1.827 eV (**Figure 19c** and **d**). Since the mixing of Si 3p and B 2p orbital, the CBM of B-doping 3C-SiC decrease. And since the mixing of C 2s, Si 3s, and B 2p orbital, the VBM decrease. As a result, the CB edge potential of B-doped 3C-SiC is more negative than normal hydrogen electrode (NHE), indicating that photoinduced electrons can easily transfer from B-doped 3C-SiC NWs to H^+ and generate hydrogen. This can also be confirmed by the UV-vis diffusion reflectance spectra (**Figure 20a**). The UV-vis spectra of 3C-SiC NWs shows a strong ultraviolet absorp-tion from 200 to 500 nm (the black line of **Figure 20a**). The red line of **Figure 20a** is the UV-vis spectra of B-doped 3C-SiC NWs, which the absorption edge extends to the visible region (about 800 nm) and the absorption intensity is also enhanced. The band gap of the SiC is calculated using the Kubelka-Munk function [109]. As shown in **Figure 20b**, an intercept value of 2.34 eV for 3C-SiC NWs (the black line) is close to that of the bulk 3C-SiC (2.35 eV). An intercept value of 2.216 eV for B-doped 3C-SiC NWs (the red line) is close to that of the calculated value using DFT.
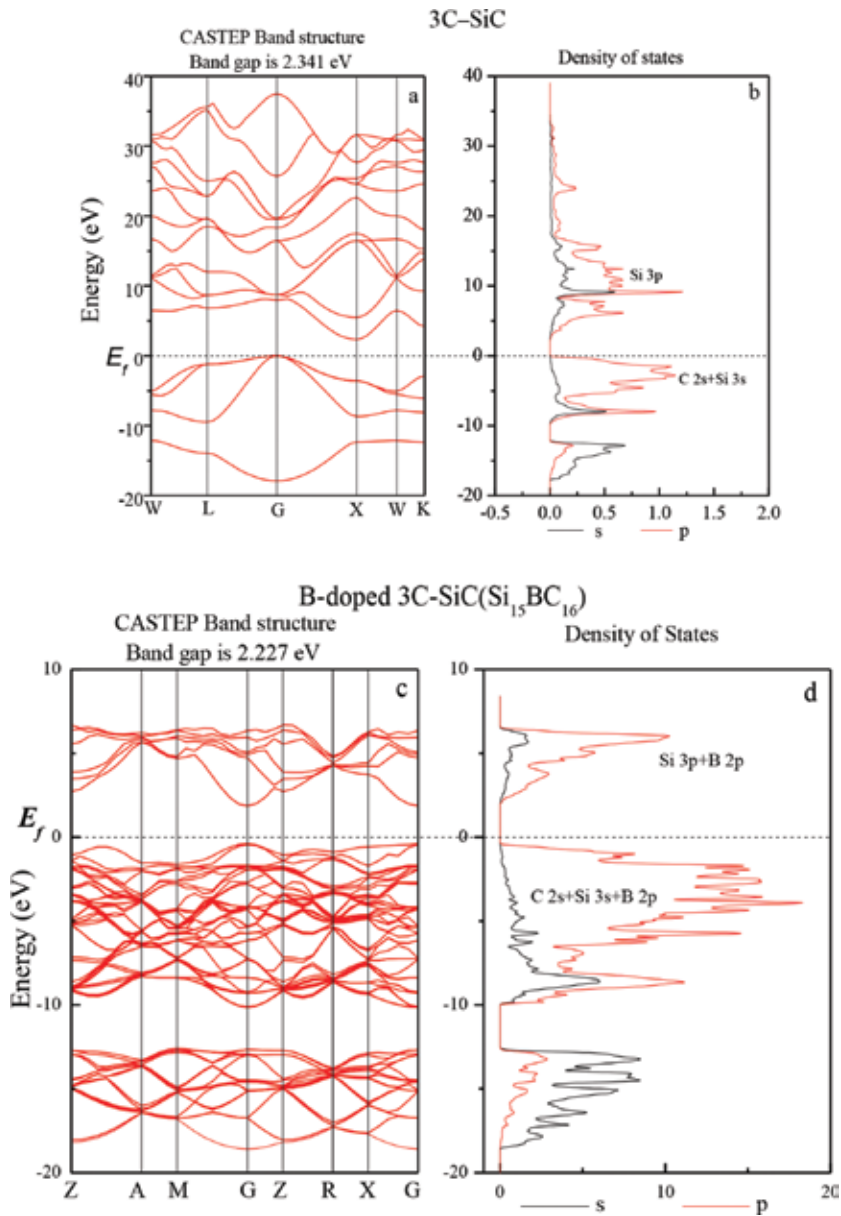
Figure 19. The calculated energy band and density of states (DOS) of pure 3C-SiC (a and b) and B-doped 3C-SiC (c and d).

During the photocatalytic process, the photo generated electron recombination is mainly responsible for the low photocatalysis efficiency. Charge transfer effect can be characterized by PL quenching effect within the sample. After B doping, the PL intensity of 3C-SiC decreases obviously (**Figure 21**). PL is mainly caused by the transitions of electrons to release photons. In this work, electron is transferred instead of transitioning to lower energy level in the B

doping 3C-SiC NWs. Otherwise, as shown in **Figure 13a**, less stacking defects and the special finned like single crystalline nanowires are beneficial to enhance transfer of electron. This makes the charge pathway much smoother. Since the multiple light reflects within the fins of nanowires (inset **Figure 22**) and increases the contacting area with aqueous suspensions, the special finned like morphology also contributes to higher photocatalytic hydrogen production.

Figure 20. (a) UV-Vis diffusion reflectance spectra. (b) The plots of $(\alpha h\nu)^{1/2}$ versus $h\nu$. The band gap of the samples.

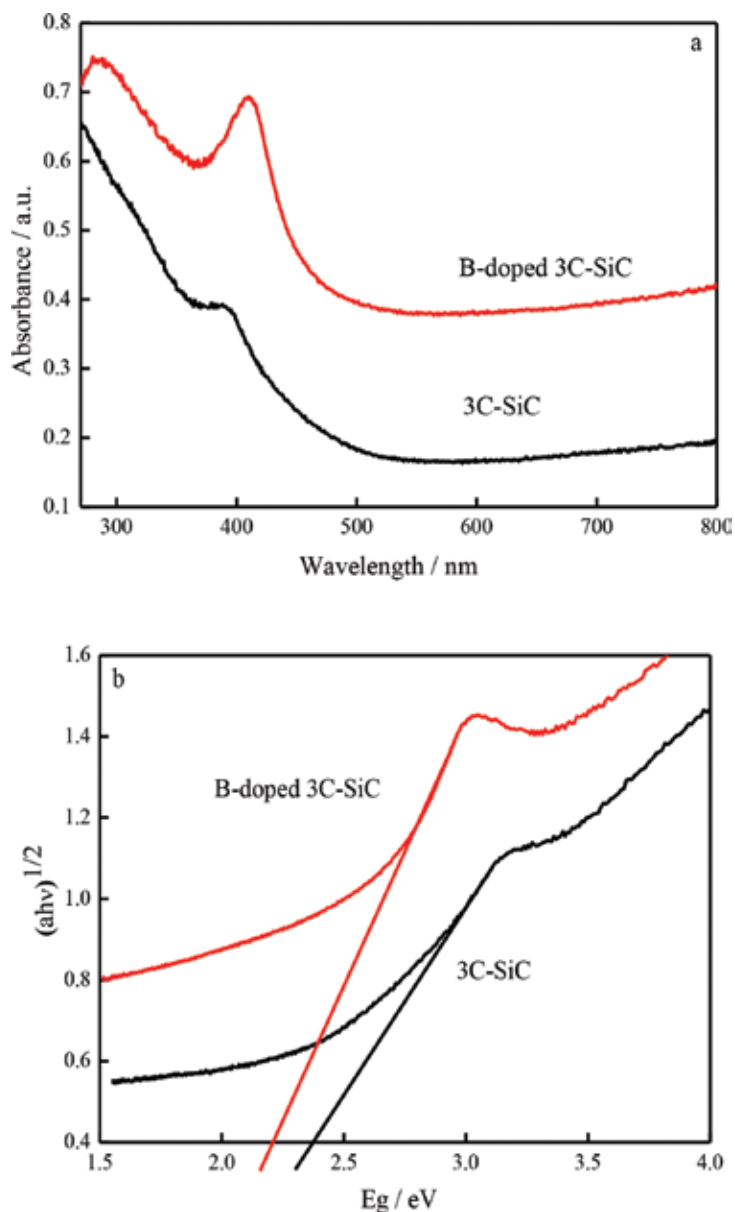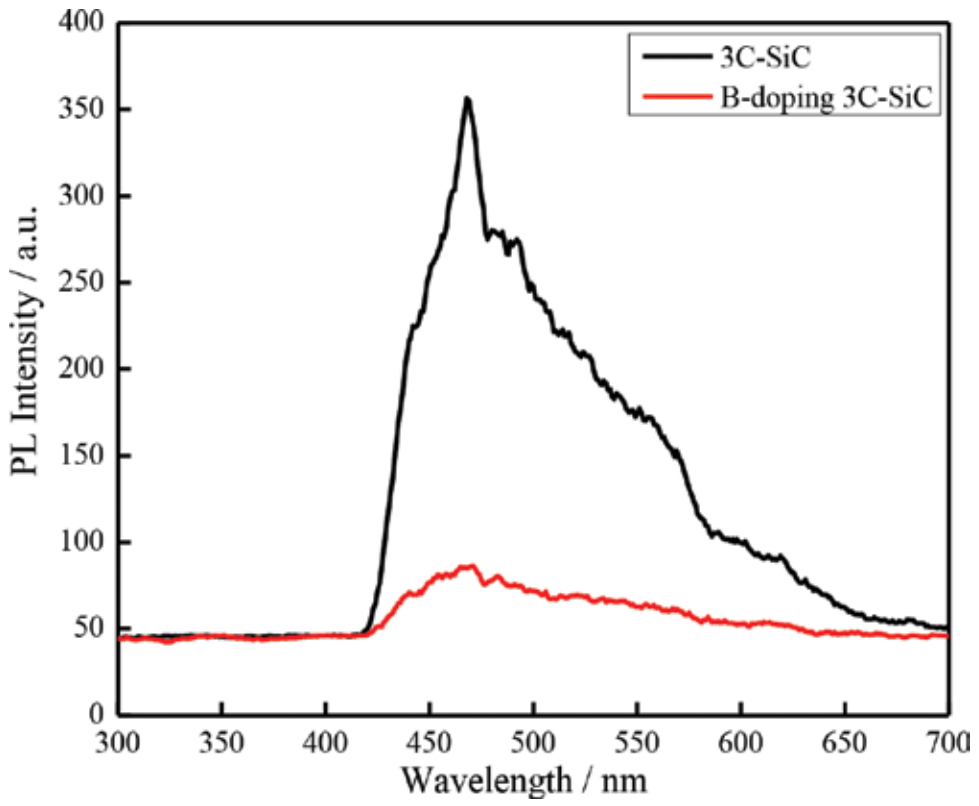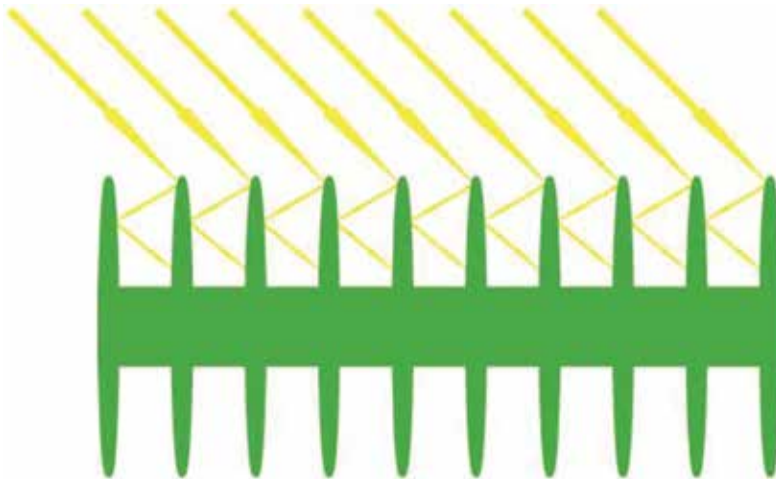**Figure 21.** Photoluminescence spectra of 3C-SiC and B-doped 3C-SiC.

Figure 22. Light reflection models in the B-doped 3C-SiC nanowires.

From above results, using a facile and simple carbothermal reduction of a mixture of low-cost boric oxide powder, gangue and carbon black, finned nanostructure B-doped 3C-SiC NWs were synthesized. The growth process belongs to a two-step epitaxial growth mechanism. Combining the theoretical calculation and experimental result, B substitutes Si during the doping process and possesses smaller band gaps. B-doped 3C-SiC NWs demonstrates an enhanced and stable activity for H_2 production as high as 108.4 $\mu mol \bullet h^{-1}$, which is about 20 times of that of 3C-SiC and 2.6 times of the value reported in the literature. It appears that the combined effect of such factors as the single crystal, electronic structures, and the finned like morphology is attributed to the enhanced photocatalytic hydrogen production. This work presents an applicable method to develop various semiconductors with controllable morphology applied in solar energy conversion, gas sensors, and photoluminescence.

4.2. TiO_xN_y/TiN heterojunction composite

4.2.1. Crystal phase analyses

In all the samples, five diffraction peaks at 2θ = 36.90°, 42.86°, 62.24°, 74.61°, and 78.48° corresponding to TiN (PDF 38-1420).As shown in **Figure 23a**, with increasing nitridation temperature, the crystallization degree and purity of TiN increase. The constant a increases from 4.216 (800°C) to 4.241 Å (900°C) according to the data of refinement XRD (**Table 2**). And the theoretical value of TiO is 4.180 Å and that of TiO is 4.180 Å [110]. The value of sample is between TiO and TiN, indicating the existence of TiO_xN_y. When the temperature reaches up to 950–1000°C, the constant a is calculated to be 4.241Å, which is in consistent with the standard value of TiN (PDF 38-1420 (a=4.241Å)) [111].

Temperature (°C)	800	850	900	950	1000	JCPDS card 38-1420
a (nm)	0.4216	0.4228	0.4237	0.4241	0.4241	0.4241
Grain size (nm)	35.5±1.5	36.1±1.9	37.0±1.6	37.9±1.7	38.5±2.4	

Table 2 .The lattice parameter and grain size of the nitridation products at different temperature with 3 h.

In view of the effect of reaction time, **Figure 23b** shows the XRD patterns of the samples obtained at 900°C for different reaction time at partial cracked NH_3 atmosphere. When the reaction time is 3 h, some small diffraction peaks of TiO_2 still exist. All the characteristic peaks are indexed to be that of TiN with the nitridation time is extended to 4–5 h. **Table 3** shows the refinement of XRD data at 900°C for different time. The constant a increases with the reaction time prolonging. When the nitridation time is 4 h, the constant a (4.238 Å) is between the theoretical value of TiO (4.180 Å) and TiN (4.241 Å), indicating the existence of TiO_xN_y. From above experiments, the synthesis condition of TiO_xN_y/TiN composite is selected as 900°C and 4 h. Pure TiN can be produced at 1000°C for 3 h.
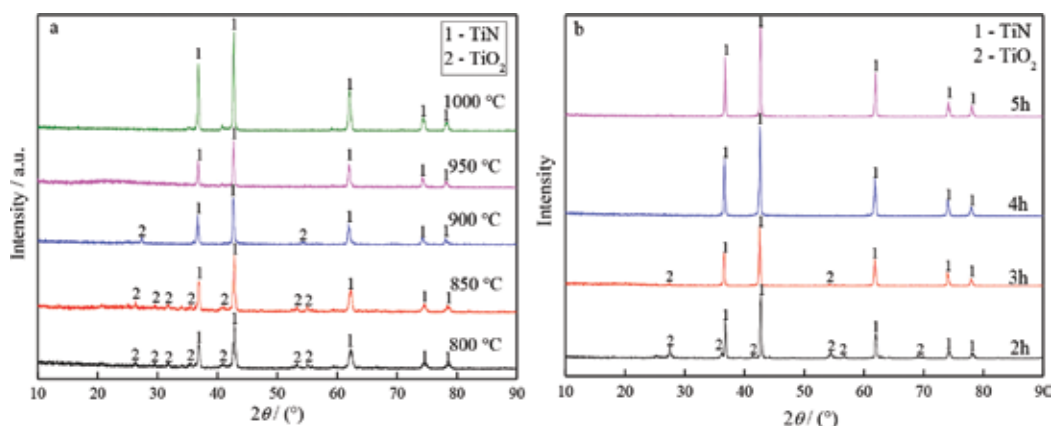
Figure 23. XRD patterns of the obtained yolk-shell TiO_xN_y/TiN composites (a) different temperature for 3 h (b) different time at 900°C.

Time (h)	2	3	4	5	JCPDS card 38-1420
a (nm)	0.4233	0.4236	0.4238	0.4241	0.4241
Grain size (nm)	35.2±1.3	36.8±2.2	37.2±1.4	38.3±0.7	

Table 3. The lattice parameter and grain size of the nitridation products with different time at 900°C.

XPS is adopted to further characterize TiO_xN_y/TiN composite. **Figure 24(a)** shows the full XPS spectrum of the samples obtained at 900°C for 4 h, which indicate the existence of C, N, Ti, and O. **Figure 24(b–d)** show fine XPS spectra of Ti 2p, N 1s, and O 1s. The Ti 2p bands have three groups of peaks, i.e. the typical peaks for TiN (455.3 eV, 457.5 eV, 460.9 eV, and 463.0 eV), the peaks for TiO_xN_y (456.1 eV and 461.7 eV), and the peaks for TiO_2 (459.1 eV and 464.7 eV) (**Figure 24b**) [110–113]. The existence of TiO_2 is attributed to the reaction of TiN and TiO_xN_y particles with oxygen from air atmosphere. From the XPS spectra of N 1s (**Figure 24c**), the peak at 396.3 eV can be assigned to TiO_xN_y [110, 111, 114]. The peak centered at 397.3 eV corresponds to Ti-N bond in TiN and peak at 399.2 eV corresponds to C=N bond [110]. The absorption of C from the atmosphere led to the existence of C=N. From the XPS spectra of N 1s, the molar content of N in TiO_xN_y is about 6.8 mol%. XPS signals of O 1s (**Figure 24d**) are observed at around 530.4 eV and 532.0 eV, which can be assigned to Ti-O bond in TiO_2 and TiO_xN_y respectively [110, 111], indicating that the samples are composed of TiN and TiO_xN_y. The molar ratio of TiO_xN_y/TiN is determined by XPS to be 15.64, corresponding to the mass content of TiN to be 95 mass%. Since the content of TiO_xN_y was too low to be detected by XRD, these are not the diffraction peaks of TiO_xN_y XRD patterns.

4.2.2. Microstructure analyses

SEM images of TiN/TiO_xN_y obtained at 900°C for 4 h in partial cracked NH_3 are shown in **Figure 25**. It can be seen that the microstructure of TiO_xN_y/TiN nanoparticles duplicate the

original structure of the precursors. The average diameter of TiO_xN_y/TiN composite with solid microstructure is about 1–2 μm (**Figure 25b**). As shown in **Figure 25d**, yolk-shell TiO_xN_y/TiN are composed of a thin shell with an average thickness around 20 nm and a small yolk with an average diameter around 500 nm. As shown in **Figure 25f**, a thin shell with an average diameter around 1–2 μm and an average thickness around 20 nm combine the hollow microspheres.

TEM images of TiO_xN_y/TiN composite are shown in **Figure 26**. The low-magnification TEM images (**Figure 26a** and **b**) show that TiO_xN_y/TiN composite is composed of regular aggregated particles. As shown in **Figure 26c**, two particles firmly stick together, in which one lattice spacing is 0.40 nm and the other is 0.25 nm. The lattice spacing of two particles is consistent with the (111) planes of TiO_xN_y and the (111) planes of cubic TiN.
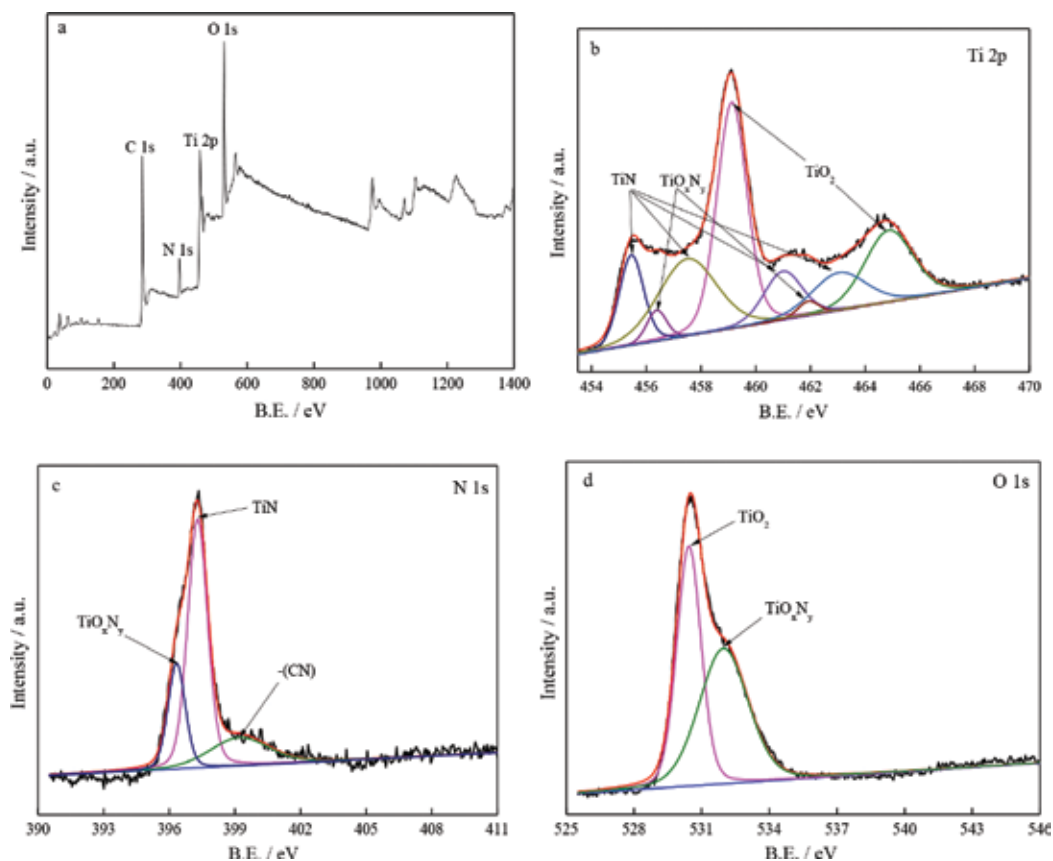
Figure 24. The full spectrum of XPS of the samples obtained at 900°C with 4 h (a), XPS spectra of (b) Ti 2p, (c) N 1s, (d) O 1s.
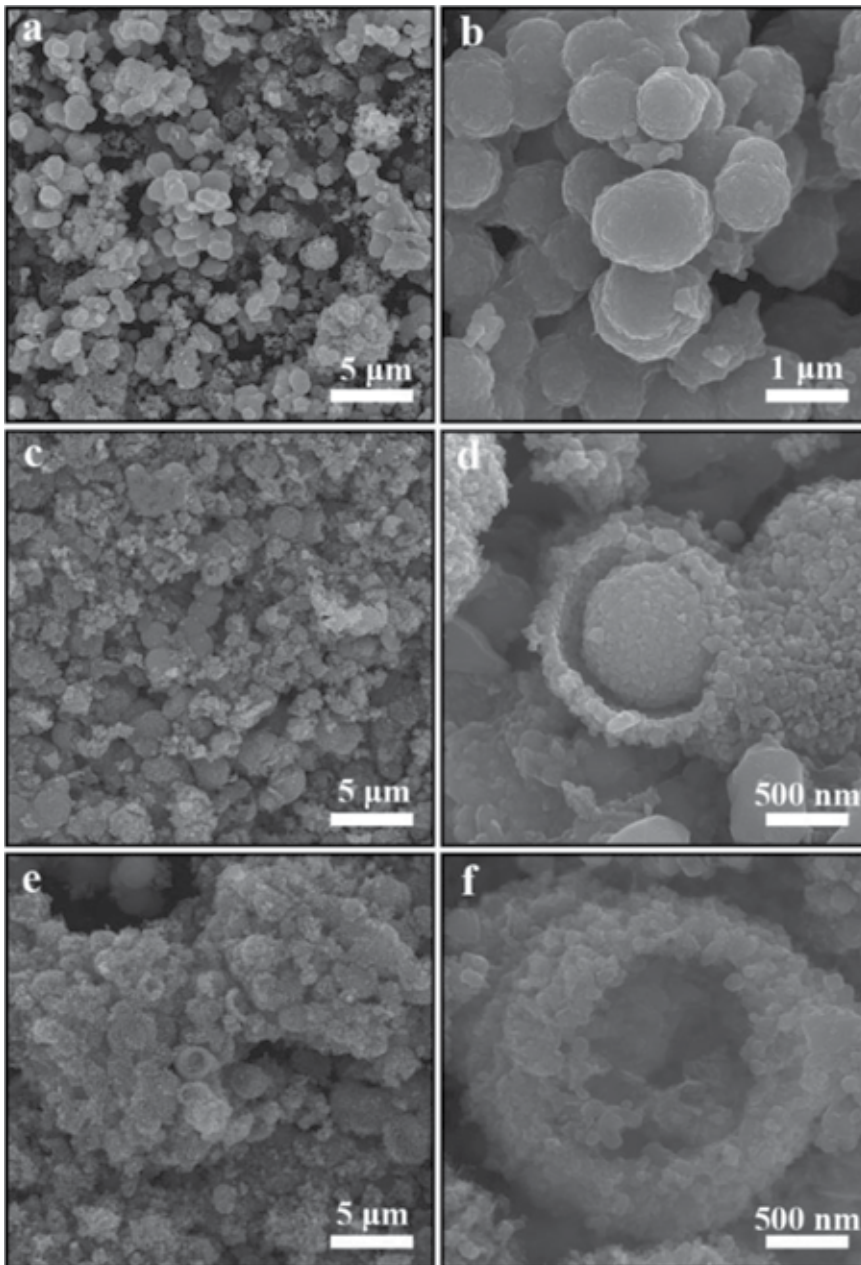
Figure 25. SEM photographs of TiO_xN_y/TiN composites: (a), (b) solid, (c), (d) yolk-shell, (e), (f) hollow.

In addition, it can be seen that TiN crystal is in close contact with TiO_xN_y crystal to form a heterojunction, which is believed to promote the transfer of photogenerated electrons and holes between TiN and TiO_xN_y, suppresses their recombination, and thus enhances the photocatalytic activity [115–117].
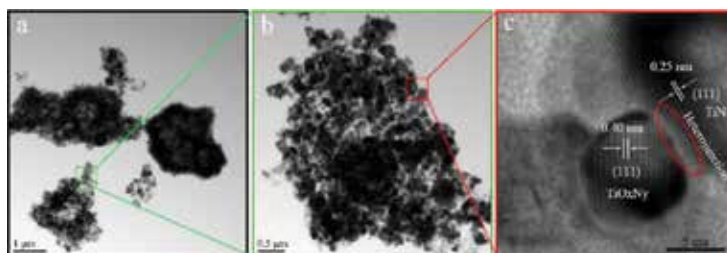
Figure 26. TEM photographs of TiO_xN_y/TiN composite.

4.2.3. Photocatalytic activities

The water splitting of H_2O to H_2 performance of solid TiO_xN_y/TiN, yolk-shell TiO_xN_y/TiN and hollow TiO_xN_y/TiN samples under light irradiation was examined in the presence of Na_2S and Na_2SO_3 as an hole acceptor. For comparison, the photocatalytic H_2 production of TiN and TiOxNy(N/Ti=2) is also carried out respectively. TiN was synthesized at 1000°C for 3 h in flowing partial cracked NH_3. TiOxNy (N/Ti=2) were synthesized through a microemulsion-hydrothermal method using triethylamine, urea, thiourea, and hydrazine as organic compounds [118]. The mixture is put in Teflon-lined stainless steel autoclave and heated at 120°C for 12 h. The results are shown in **Figure 27**. By comparison, the as-prepared TiO_xN_y/TiN heterojunction with yolk-shell and hollow structures exhibit better photocatalytic H_2 production activities, while the maximum H_2 production rate is achieved for yolk-shell TiO_xN_y/TiN with 35 μmol•h^{-1}•g^{-1}. The yolk-shell TiN synthesized at 800°C for 20 h was reported by Li's *et al.* group, which showed the larger visible-light-driven photocatalytic hydrogen production to be 22.8 μmol•h^{-1}•g^{-1}[98]. Our result is 1.5 times of that value. The recycling reaction experiments were carried out to investigate the stability of photocatalytic hydrogen production of yolk-shell TiO_xN_y/TiN under visible light irradiation. No decrease in catalytic activity is observed in the recycling reactions as shown in **Figure 27b**.
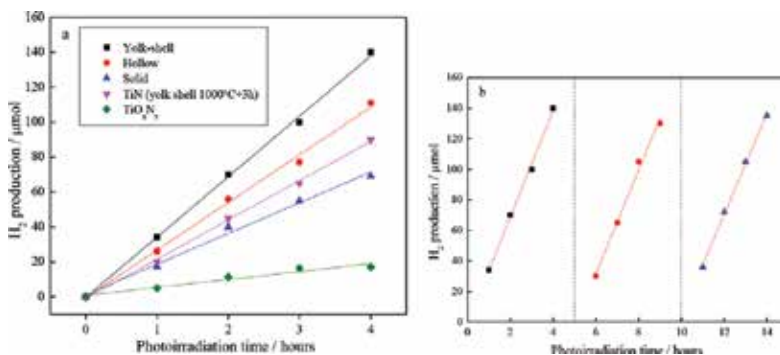
Figure 27. (a). Comparison of H_2 production rates of TiN, TiO_xN_y and TiO_xN_y/TiN heterojunction with different nano-structure. (b). Recycling test of the yolk-shell TiO_xN_y/TiN in the photocatalytic H_2 evolution.

The enhanced photocatalytic hydrogen production performance of the yolk-shell TiO_xN_y/TiN heterojunction is attributed to the formation of heterojunction by TiN and TiO_xN_y with the proper electronic structures and its special nanostructures. From the theoretical calculation as shown in **Figure 12**, TiN combining with TiO_xN_y with proper N doping concentration is expected to form favorable band-edge position, which may be a potential candidate for visible-light responsive photocatalyst. From XPS spectra, the molar content of N in TiO_xN_y is about 6.8 mol%, corresponding to the band gap of 1.56 eV. When TiN and TiO_xN_y is combined together, the band gap should be in the range of 0.8 and 1.56 eV. UV-Vis diffuse reflection spectra (**Figure 28**) is also carried out. The absorption band-edge for yolk-shell TiO_xN_y/TiN are at about 850 nm, corresponding to band gap energy to be 1.4 eV, verifying the theoretical calculation.
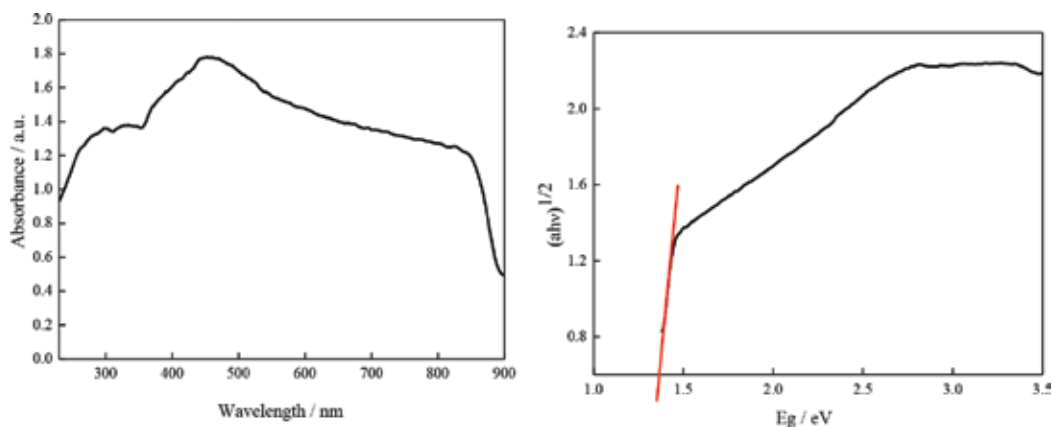
Figure 28. (a) UV-Vis diffuse reflection spectra of yolk-shell TiO_xN_y/TiN. (b) The plots of $(\alpha h\nu)^{1/2}$ versus $h\nu$. The band gap of yolk–shell TiO_xN_y/TiN.

Under visible-light irradiation, the photogenerated electrons are excited from the valence bands (VBs) to the conduction bands (CBs) of TiN and TiO_xN_y in the TiO_xN_y/TiN composite, creating positive holes in VB of TiN and TiO_xN_y (**Figure 29a**). Since CB (−0.6 eV)[12] level of TiN is lower than that of TiO_xN_y (CB: −0.4 eV) [119], electrons in CB of TiN can be transferred to that of TiO_xN_y. The VB (0.2 eV) [98] level of TiN is lower than that of TiO_xN_y (VB 0.6–1.1 eV) [119], holes in VB of TiO_xN_y can be transferred to that of TiN. Therefore, the probability of electron–hole recombination can be reduced, which can be confirmed by the photolumines-cence spectra (**Figure 29b**). It is found that TiO_xN_y/TiN exhibits a fluorescence decrease (or quenching) as compared with TiN and TiO_xN_y [118], indicating that the photogenerated carrier recombination is inhibited greatly. These results should be derived from the imitate contacts between TiN and TiO_xN_y. Finally, the sacrificial reagents oxidized by the positive holes in the surface of TiN and the photo-excited electrons in the surface of TiO_xN_y can generate hydro-gen, and thus the photocatalytic reaction can be enhanced greatly [60].
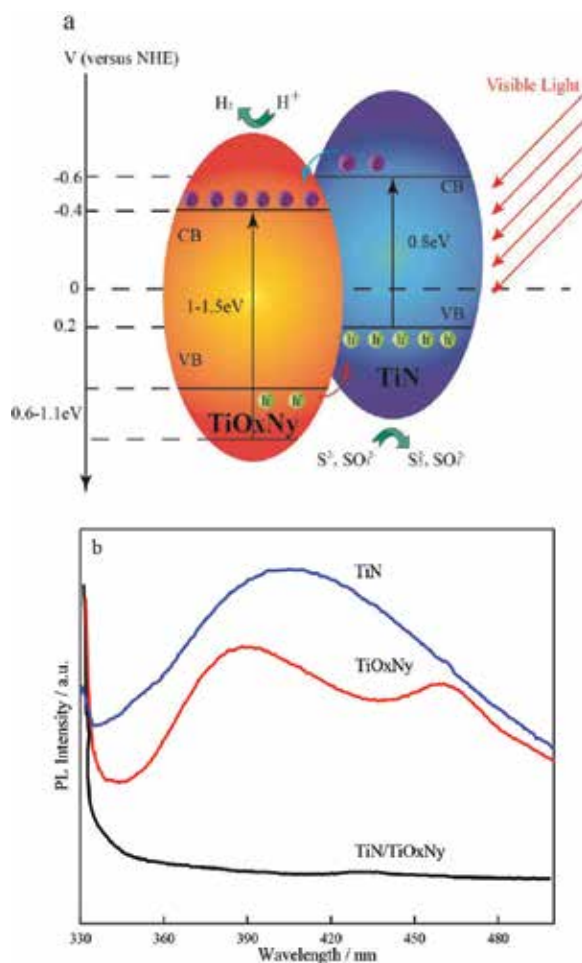
Figure 29. (a) Schematic diagram of photocatalytic mechanism for TiO_xN_y/TiN. (b) Photoluminescence spectra of TiO_xN_y/TiN.

Another important factor for the enhancement of the photocatalytic activities is the special yolk-shell nanostructures. First, the specific surface area of yolk-shell nanostructure is increased significantly, which increase the aqueous suspension contact area. Second, since the resulting yolk-shell nanostructures, there are the multiple light reflections within the chamber, which leads to efficient photocatalytic and photoelectro-chemical performances.

Therefore from above results, TiO_xN_y/TiN heterojunction composite with solid, yolk-shell, and hollow microspheres were prepared through reduction and nitridation of organotitania obtained through solvothermal alcoholysis. Especially, the yolk-shell TiO_xN_y/TiN heterojunction demonstrated an outstanding activity toward H_2 production as high as 34.9 μmol•h^{-1}•g^{-1}, which was about 1.5 times of the value reported in the literature. The electronic structure of heterojunction and the yolk-shell morphology are beneficial to enhance the H_2 production activity.

5. Summary and prospects

In our work including B-doped 3C-SiC nanowires and TiOxNy/TiN heterojunction composite, the electronic band structure, the crystallinity and crystal structure, surface structure, and morphology of photocatalysts on a nanometric scale had been investigated systematically and modified to optimize the preparation methods and refine the materials for maximizing efficiency. B-doped 3C-SiC NWs demonstrates an enhanced and stable activity for H_2 production as high as 108.4 $\mu mol \bullet h^{-1}$, which is about 20 times of that of 3C-SiC, and 2.6 times of the value reported in the literature [99]. And the yolk-shell TiOxNy/TiN heterojunction demonstrated an outstanding activity toward H_2 production as high as 34.9 $\mu mol \bullet h^{-1} \bullet g^{-1}$, which was about 1.5 times of the value reported in the literature [98]. However, these improvements are not enough for industrial applications. Since the low photocatalytic efficiency and the lack of extensive studies for a successful scale-up of the laboratory setup into an industrially relevant scale. Therefore in the viewpoint of material and reactor design, reduction of cost will have to be given special priority before the final utilization of semiconductor-based photocatalytic hydrogen generation [120].

Acknowledgements

Author details

Tao Yang[1], Xinmei Hou[1*], Junhong Chen[2] and Kuo-Chih Chou[1]

*Address all correspondence to: houxinmei@ustb.edu.cn

1 State Key Laboratory of Advanced Metallurgy, University of Science and Technology Beijing, Beijing, China

2 School of Material Science and Engineering, University of Science and Technology Beijing, Beijing, China

References

[1] Crabtree, G.W. and N.S. Lewis, Solar energy conversion. Physics today, 2007. 60(3): pp. 37-42.

[2] Solangi, K.H., et al., A review on global solar energy policy. Renewable and Sustainable Energy Reviews, 2011. 15(4): pp. 2149-2163.

[3] Balat, M., Potential importance of hydrogen as a future solution to environmental and transportation problems. International Journal of Hydrogen Energy, 2008. 33(15): pp. 4013-4029.

[4] Wang, M., et al., The intensification technologies to water electrolysis for hydrogen production–A review. Renewable and Sustainable Energy Reviews, 2014. 29: pp. 573-588.

[5] Lu, Y.J., et al., Hydrogen production by biomass gasification in supercritical water: a parametric study. International Journal of Hydrogen Energy, 2006. 31(7): pp. 822-831.

[6] Navarro, R.M., M.A. Penaand and J. Fierro, Hydrogen production reactions from carbon feedstocks: fossil fuels and biomass. Chemical Reviews, 2007. 107(10): pp. 3952-3991.

[7] Cormos, C., et al., Innovative concepts for hydrogen production processes based on coal gasification with CO_2 capture. International Journal of Hydrogen Energy, 2008. 33(4): pp. 1286-1294.

[8] Cobden, P.D., et al., Sorption-enhanced hydrogen production for pre-combustion CO_2 capture: thermodynamic analysis and experimental results. International Journal of Greenhouse Gas Control, 2007. 1(2): pp. 170-179.

[9] Zhou, H., et al., The development of a new type of rechargeable batteries based on hybrid electrolytes. ChemSusChem, 2010. 3(9): pp. 1009-1019.

[10] Turner, J.A., A realizable renewable energy future. Science, 1999. 285(5428): pp. 687-689.

[11] Chen, X., et al., Semiconductor-based photocatalytic hydrogen generation. Chemical Reviews, 2010. 110(11): pp. 6503-6570.

[12] Esswein, A.J. and D.G. Nocera, Hydrogen production by molecular photocatalysis. Chemical Reviews, 2007. 107(10): pp. 4022-4047.

[13] Balzani, V., A. Credi and M. Venturi, Photochemical conversion of solar energy. ChemSusChem, 2008. 1(1-2): pp. 26-58.

[14] Fujishima, A. and K. Honda, Photolysis-decomposition of water at the surface of an irradiated semiconductor. Nature, 1972. 238(5385): pp. 37-38.

[15] Linsebigler, A.L., G. Lu and J.T. Yates Jr, Photocatalysis on TiO_2 surfaces: principles, mechanisms, and selected results. Chemical Reviews, 1995. 95(3): pp. 735-758.

[16] Reber, J.F. and M. Rusek, Photochemical hydrogen production with platinized suspensions of cadmium sulfide and cadmium zinc sulfide modified by silver sulfide. The Journal of Physical Chemistry, 1986. 90(5): pp. 824-834.

[17] Miseki, Y., et al., Cs-modified WO_3 photocatalyst showing efficient solar energy conversion for O_2 production and Fe (III) ion reduction under visible light. The Journal of Physical Chemistry Letters, 2010. 1(8): pp. 1196-1200.

[18] Erbs, W., et al., Visible-light-induced oxygen generation from aqueous dispersions of tungsten (VI) oxide. The Journal of Physical Chemistry, 1984. 88(18): pp. 4001-4006.

[19] Meissner, D., R. Memming and B. Kastening, Photoelectrochemistry of cadmium sulfide. 1. Reanalysis of photocorrosion and flat-band potential. The Journal of Physical Chemistry, 1988. 92(12): pp. 3476-3483.

[20] Erbs, W., et al., Visible-light-induced oxygen generation from aqueous dispersions of tungsten (VI) oxide. The Journal of Physical Chemistry, 1984. 88(18): pp. 4001-4006.

[21] Kalyanasundaram, K., et al., Cleavage of water by visible-light irradiation of colloidal CdS solutions; inhibition of photocorrosion by RuO_2. Angewandte Chemie International Edition in English, 1981. 20(11): pp. 987-988.

[22] Zhang, H. and Y. Zhu, Significant visible photoactivity and antiphotocorrosion performance of CdS photocatalysts after monolayer polyaniline hybridization. The Journal of Physical Chemistry C, 2010. 114(13): pp. 5822-5826.

[23] Yan, X., et al., Antiphotocorrosive photocatalysts containing CdS nanoparticles and exfoliated TiO_2 nanosheets. Journal of Materials Research, 2010. 25(01): pp. 182-188.

[24] Torimoto, T., et al., Photochemical shape control of cadmium sulfide nanorods coated with an amorphous silica thin layer. Journal of Nanoscience and Nanotechnology, 2009. 9(1): pp. 506-513.

[25] Solarska, R., et al., Tailoring the morphology of WO_3 films with substitutional cation doping: effect on the photoelectrochemical properties. Electrochimica Acta, 2010. 55(26): pp. 7780-7787.

[26] Gaillard, N., et al., Improved current collection in WO_3: Mo/WO_3 bilayer photoelectrodes. Journal of Materials Research, 2010. 25(01): pp. 45-51.

[27] Bär, M., et al., Mo incorporation in WO^3 thin film photoanodes: Tailoring the electronic structure for photoelectrochemical hydrogen production. Applied Physics Letters, 2010. 96(3): pp. 032107.

[28] Zaleska, A., et al., Photocatalytic activity of boron-modified TiO_2 under visible light: the effect of boron content, calcination temperature and TiO_2 matrix. Applied Catalysis B: Environmental, 2009. 89(3): pp. 469-475.

[29] Le Paven-Thivet, C., et al., Photoelectrochemical properties of crystalline perovskite lanthanum titanium oxynitride films under visible light. The Journal of Physical Chemistry C, 2009. 113(15): pp. 6156-6162.

[30] Yan, J., et al., Nitrogen-doped $SrTiO_3/TiO_2$ composite photocatalysts for hydrogen production under visible light irradiation. Journal of Alloys and Compounds, 2009. 472(1): pp. 429-433.

[31] Ravindranathan Thampi, K., Highly active meso–microporous TaON photocatalyst driven by visible light. Chemical Communications, 2005(2): pp. 268-270.

[32] Yashima, M., Y. Lee and K. Domen, Crystal structure and electron density of tantalum oxynitride, a visible light responsive photocatalyst. Chemistry of Materials, 2007. 19(3): pp. 588-593.

[33] Liu, M., et al., Water reduction and oxidation on $Pt–Ru/Y_2Ta_2O_5N_2$ catalyst under visible light irradiation. Chemical Communications, 2004(19): pp. 2192-2193.

[34] Higashi, M., et al., Two step water splitting into H_2 and O_2 under visible light by $ATaO_2N$ (A= Ca, Sr, Ba) and WO_3 with shuttle redox mediator. Chemical Physics Letters, 2008. 452(1): pp. 120-123.

[35] Qiu, X., Y. Zhao and C. Burda, Synthesis and characterization of nitrogen-doped group IVB visible-light-photoactive metal oxide nanoparticles. Advanced Materials-Deerfield Beach Then Weinheim-, 2007. 19(22): p. 3995.

[36] Kanade, K.G., et al., Rose-red color oxynitride $Nb_2Zr_6O_{17-x}N_x$: a visible light photocatalyst to hydrogen production. International Journal of Hydrogen Energy, 2007. 32(18): pp. 4678-4684.

[37] Matsumoto, Y., et al., N doping of oxide nanosheets. Journal of the American Chemical Society, 2009. 131(19): pp. 6644-6645.

[38] Shi, H., et al., 2-Propanol photodegradation over nitrogen-doped $NaNbO_3$ powders under visible-light irradiation. Journal of Physics and Chemistry of Solids, 2009. 70(6): pp. 931-935.

[39] Yang, T., et al., B-doped 3C-SiC nanowires with a finned microstructure for efficient visible light-driven photocatalytic hydrogen production. Nanoscale, 2015. 7(19): pp. 8955-8961.

[40] Li, W., et al., High-efficient degradation of dyes by $Zn_xCd_{1-x}S$ solid solutions under visible light irradiation. The Journal of Physical Chemistry C, 2008. 112(38): pp. 14943-14947.

[41] Wang, W., W. Zhu and H. Xu, Monodisperse, mesoporous $Zn_xCd_{1-x}S$ nanoparticles as stable visible-light-driven photocatalysts. The Journal of Physical Chemistry C, 2008. 112(43): pp. 16754-16758.

[42] Li, M., J. Jiang and L. Guo, Synthesis, characterization, and photoelectrochemical study of $Cd_{1-x}Zn_xS$ solid solution thin films deposited by spray pyrolysis for water splitting. International Journal of Hydrogen Energy, 2010. 35(13): pp. 7036-7042.

[43] Li, G., et al., Composition dependence of the photophysical and photocatalytic properties of (AgNbO$_3$) 1- x (NaNbO$_3$) x solid solutions. Journal of Solid State Chemistry, 2007. 180(10): pp. 2845-2850.

[44] Muktha, B., G. Madras and T.G. Row, A novel scheelite-like structure of BaBi$_2$Mo$_4$O$_{16}$: Photocatalysis and investigation of the solid solution, BaBi$_2$Mo$_{4-x}$W$_x$O$_{16}$(0.25≤ x≤ 1). Journal of Photochemistry and Photobiology A: Chemistry, 2007. 187(2): pp. 177-185.

[45] Maeda, K., et al., GaN: ZnO solid solution as a photocatalyst for visible-light-driven overall water splitting. Journal of the American Chemical Society, 2005. 127(23): pp. 8286-8287.

[46] Maeda, K., et al., Photocatalyst releasing hydrogen from water. Nature, 2006. 440(7082): pp. 295-295.

[47] Maeda, K., et al., Photocatalytic activity of (Ga$_{1-x}$Zn$_x$)(N$_{1-x}$O$_x$) for visible-light-driven H$_2$ and O$_2$ evolution in the presence of sacrificial reagents. The Journal of Physical Chemistry C, 2008. 112(9): pp. 3447-3452.

[48] Maeda, K. and K. Domen, Solid solution of GaN and ZnO as a stable photocatalyst for overall water splitting under visible light†. Chemistry of Materials, 2009. 22(3): pp. 612-623.

[49] Yang, T., et al., Preparation of TiO$_x$N$_y$/TiN composites for photocatalytic hydrogen evolution under visible light. Physical Chemistry Chemical Physics, 2015. 17(43): pp. 28782-28788.

[50] Jing, D., Y. Zhang and L. Guo, Study on the synthesis of Ni doped mesoporous TiO$_2$ and its photocatalytic activity for hydrogen evolution in aqueous methanol solution. Chemical Physics Letters, 2005. 415(1): pp. 74-78.

[51] Ebina, Y., et al., Restacked perovskite nanosheets and their Pt-loaded materials as photocatalysts. Chemistry of Materials, 2002. 14(10): pp. 4390-4395.

[52] Ikuma, Y. and H. Bessho, Effect of Pt concentration on the production of hydrogen by a TiO$_2$ photocatalyst. International Journal of Hydrogen Energy, 2007. 32(14): pp. 2689-2692.

[53] Ogisu, K., et al., Lanthanum-indium oxysulfide as a visible light driven photocatalyst for water splitting. Chemistry Letters, 2007. 36(7): pp. 854-855.

[54] Ogisu, K., et al., Electronic band structures and photochemical properties of La- Ga-based oxysulfides. The Journal of Physical Chemistry C, 2008. 112(31): pp. 11978-11984.

[55] Jang, J.S., U.A. Joshi and J.S. Lee, Solvothermal synthesis of CdS nanowires for photocatalytic hydrogen and electricity production. The Journal of Physical Chemistry C, 2007. 111(35): pp. 13280-13287.

[56] Bao, N., et al., Highly ordered Pt-loaded CdS nanowire arrays for photocatalytic hydrogen production under visible light. Chemistry Letters, 2006. 35(3): pp. 318-319.

[57] Yuan, J., et al., Preparations and photocatalytic hydrogen evolution of N-doped TiO_2 from urea and titanium tetrachloride. International Journal of Hydrogen Energy, 2006. 31(10): pp. 1326-1331.

[58] Hitoki, G., et al., An oxynitride, TaON, as an efficient water oxidation photocatalyst under visible light irradiation ($\lambda \leq 500$ nm). Chemical Communications, 2002(16): pp. 1698-1699.

[59] Xiao, W., et al., TiN film with (111) preferred orientation as a visible-light-driven photocatalyst for hydrogen evolution from water decomposition. Materials Chemistry and Physics, 2007. 105(1): pp. 6-9.

[60] Wang, H., et al., Semiconductor heterojunction photocatalysts: design, construction, and photocatalytic performances. Chemical Society Reviews, 2014. 43(15): pp. 5234-44.

[61] Spanhel, L., H. Weller and A. Henglein, Photochemistry of semiconductor colloids. 22. Electron ejection from illuminated cadmium sulfide into attached titanium and zinc oxide particles. Journal of the American Chemical Society, 1987. 109(22): pp. 6632-6635.

[62] Bickley, R.I., et al., A structural investigation of titanium dioxide photocatalysts. Journal of Solid State Chemistry, 1991. 92(1): pp. 178-190.

[63] Chen, X. and S.S. Mao, Titanium dioxide nanomaterials: synthesis, properties, modifications, and applications. Chemical Reviews, 2007. 107(7): pp. 2891-2959.

[64] Hidalgo, M.C., et al., Hydrothermal preparation of highly photoactive TiO_2 nanoparticles. Catalysis Today, 2007. 129(1): pp. 50-58.

[65] Testino, A., et al., Optimizing the photocatalytic properties of hydrothermal TiO_2 by the control of phase composition and particle morphology: a systematic approach. Journal of the American Chemical Society, 2007. 129(12): pp. 3564-3575.

[66] Datta, A., et al., Temperature tunability of size in CdS nanoparticles and size dependent photocatalytic degradation of nitroaromatics. Journal of Colloid and Interface Science, 2008. 322(1): pp. 128-135.

[67] GuiáYang, H., Nanosized anatase TiO_2 single crystals for enhanced photocatalytic activity. Chemical Communications, 2010. 46(5): pp. 755-757.

[68] Sun, W., et al., Studies on the enhanced photocatalytic hydrogen evolution over Pt/PEG-modified TiO_2 photocatalysts. International Journal of Hydrogen Energy, 2008. 33(4): pp. 1112-1117.

[69] Lee, Y., et al., Hydrothermal synthesis of fine $NaTaO_3$ powder as a highly efficient photocatalyst for overall water splitting. Bulletin of the Chemical Society of Japan, 2007. 80(2): pp. 423-428.

[70] Sathish, M., B. Viswanathan and R.P. Viswanath, Alternate synthetic strategy for the preparation of CdS nanoparticles and its exploitation for water splitting. International Journal of Hydrogen Energy, 2006. 31(7): pp. 891-898.

[71] Zhang, Z., et al., Role of particle size in nanocrystalline TiO_2-based photocatalysts. The Journal of Physical Chemistry B, 1998. 102(52): pp. 10871-10878.

[72] Serpone, N., et al., Subnanosecond relaxation dynamics in TiO_2 colloidal Sols (particle sizes Rp= 1.0-13.4 nm). relevance to heterogeneous photocatalysis. The Journal of Physical Chemistry, 1995. 99(45): pp. 16655-16661.

[73] Sun, T., J. Qiu and C. Liang, Controllable fabrication and photocatalytic activity of ZnO nanobelt arrays. The Journal of Physical Chemistry C, 2008. 112(3): pp. 715-721.

[74] Wang, W.W., Y.J. Zhu and L.X. Yang, ZnO–SnO_2 hollow spheres and hierarchical nanosheets: hydrothermal preparation, formation mechanism, and photocatalytic properties. Advanced Functional Materials, 2007. 17(1): pp. 59-64.

[75] Xu, T., et al., Monomolecular-layer $Ba_5Ta_4O_{15}$ nanosheets: synthesis and investigation of photocatalytic properties. Advanced Functional Materials, 2006. 16(12): p. 1599.

[76] Matsumoto, Y., S. Ida and T. Inoue, Photodeposition of metal and metal oxide at the TiO_x nanosheet to observe the photocatalytic active site. The Journal of Physical Chemistry C, 2008. 112(31): pp. 11614-11616.

[77] Ye, C., et al., Thickness-dependent photocatalytic performance of ZnO nanoplatelets. The Journal of Physical Chemistry B, 2006. 110(31): pp. 15146-15151.

[78] Zhang, C. and Y. Zhu, Synthesis of square Bi_2WO_6 nanoplates as high-activity visible-light-driven photocatalysts. Chemistry of Materials, 2005. 17(13): pp. 3537-3545.

[79] Harada, M., et al., Preparation and characterizations of Fe-or Ni-substituted titania nanosheets as photocatalysts. Journal of Photochemistry and Photobiology A: Chemistry, 2002. 148(1): pp. 273-276.

[80] Zhang, L., D. Chen and X. Jiao, Monoclinic structured $BiVO_4$ nanosheets: hydrothermal preparation, formation mechanism, and coloristic and photocatalytic properties. The Journal of Physical Chemistry B, 2006. 110(6): pp. 2668-2673.

[81] Sarahan, M.C., et al., $K_4Nb_6O_{17}$-derived photocatalysts for hydrogen evolution from water: nanoscrolls versus nanosheets. Journal of Solid State Chemistry, 2008. 181(7): pp. 1678-1683.

[82] Song, X. and L. Gao, Facile synthesis and hierarchical assembly of hollow nickel oxide architectures bearing enhanced photocatalytic properties. The Journal of Physical Chemistry C, 2008. 112(39): pp. 15299-15305.

[83] Lu, F., W. Cai and Y. Zhang, ZnO hierarchical micro/nanoarchitectures: solvothermal synthesis and structurally enhanced photocatalytic performance. Advanced Functional Materials, 2008. 18(7): pp. 1047-1056.

[84] Kale, B.B., et al., $CdIn_2S_4$ nanotubes and "Marigold" nanostructures: a visible-light photocatalyst. Advanced Functional Materials, 2006. 16(10): pp. 1349-1354.

[85] Zhang, J., et al., Self-assembled 3-D architectures of BiOBr as a visible light-driven photocatalyst. Chemistry of Materials, 2008. 20(9): pp. 2937-2941.

[86] Song, X. and L. Gao, Facile synthesis and hierarchical assembly of hollow nickel oxide architectures bearing enhanced photocatalytic properties. The Journal of Physical Chemistry C, 2008. 112(39): pp. 15299-15305.

[87] Fischer, T.H. and J. Almlof, General methods for geometry and wave function optimization. The Journal of Physical Chemistry, 1992. 96(24): pp. 9768-9774.

[88] Langreth, D.C. and M.J. Mehl, Beyond the local-density approximation in calculations of ground-state electronic properties. Physical Review B, 1983. 28(4): p. 1809.

[89] Becke, A.D., Density-functional exchange-energy approximation with correct asymptotic behavior. Physical review A, 1988. 38(6): p. 3098.

[90] Wang, Y. and J.P. Perdew, Correlation hole of the spin-polarized electron gas, with exact small-wave-vector and high-density scaling. Physical Review B, 1991. 44(24): p. 13298.

[91] Kressse, G. and J. Furthmüller, Efficient iterative schemes for ab initio total-energy calculations using a plane–wave basis set. Physical Review B, 1996. 54(16): pp. 11169-11186.

[92] Ceperley, D.M. and B.J. Alder, Ground state of the electron gas by a stochastic method. Physical Review Letters, 1980. 45(7): p. 566.

[93] Perdew, J.P. and A. Zunger, Self-interaction correction to density-functional approximations for many-electron systems. Physical Review B, 1981. 23(10): p. 5048.

[94] Vanderbilt, D., Soft self-consistent pseudopotentials in a generalized eigenvalue formalism. Physical Review B, 1990. 41(11): p. 7892.

[95] Hamann, D.R., M. Schlüter and C. Chiang, Norm-conserving pseudopotentials. Physical Review Letters, 1979. 43(20): p. 1494.

[96] DONG, L., et al., Synthesis and characterization of boron-doped SiC for visible light driven hydrogen production. Acta Physico-Chimica Sinica, 2014. 30(1): pp. 135-140.

[97] Agathopoulos, S., Influence of synthesis process on the dielectric properties of B-doped SiC powders. Ceramics International, 2012. 38(4): pp. 3309-3315.

[98] Li, G., et al., Mesoporous TiN microspheres with hierarchical chambers and enhanced visible light-driven hydrogen evolution. ChemSusChem, 2013. 6(8): pp. 1461-1466.

[99] Yang, J., et al., Photocatalytic water splitting to hydrogen production of reduced graphene oxide/SiC under visible light. Applied Physics Letters, 2013. 102(8): p. 083101.

[100] Tateyama, H., N. Sutoh and N. Murakawa, Quantitative-analysisofstacking-faultsin-thestructureofsicbyx-ray-powderprofile refinementmethod. Nippon Seramikkusu

Kyokai Gakujutsu Ronbunshi-Journal of the Ceramic Society of Japan, 1988. 96(10): pp. 1003-1011.

[101] Shimoda, K., et al., Influence of surface structure of SiC nano-sized powder analyzed by X-ray photoelectron spectroscopy on basic powder characteristics. Applied Surface Science, 2007. 253(24): pp. 9450-9456.

[102] Oswald, S. and H. Wirth, Core-level shifts at B- and Al-doped 6H-SiC studied by XPS. Surface and Interface Analysis, 1999. 27(3): pp. 136-141.

[103] Lu, W., et al., Bismuth telluride hexagonal nanoplatelets and their two-step epitaxial growth. Journal of the American Chemical Society, 2005. 127(28): pp. 10112-10116.

[104] Zhu, Y.C., Y. Bando and L.W. Yin, Design and fabrication of BN-sheathed ZnS nanoarchitectures. Advanced Materials, 2004. 16(4): pp. 331-334.

[105] Yin, L.W., et al., Growth and field emission of hierarchical single-crystalline wurtzite AlN nanoarchitectures. Advanced Materials, 2005. 17(1): pp. 110-114.

[106] Speiser, R., S. Naiditch and H.L. Johnston, The vapor pressure of inorganic substances. II. B2O31. Journal of the American Chemical Society, 1950. 72(6): pp. 2578-2580.

[107] Gao, Y., Y. Wang and Y. Wang, Photocatalytic hydrogen evolution from water on SiC under visible light irradiation. Reaction Kinetics and Catalysis Letters, 2007. 91(1): pp. 13-19.

[108] Hao, J., et al., Photocatalytic hydrogen production over modified SiC nanowires under visible light irradiation. International Journal of Hydrogen Energy, 2012. 37(20): pp. 15038-15044.

[109] Chen, J., et al., Band gap characterization and photoluminescence properties of SiC nanowires. Applied Physics A, 2011. 102(1): pp. 213-217.

[110] Drygas, M., et al., Two-stage aerosol synthesis of titanium nitride TiN and titanium oxynitride TiO_xN_y nanopowders of spherical particle morphology. Chemistry of Materials, 2006. 18(13): pp. 3122-3129.

[111] Zukalova, M., et al., Facile conversion of electrospun TiO_2 into titanium nitride/oxynitride fibers. Chemistry of Materials, 2010. 22(13): pp. 4045-4055.

[112] Prabakar, K., et al., Effect of nitrogen on the photocatalytic activity of TiO_xN_y thin films. Journal of Vacuum Science and Technology A, 2006. 24(4): pp. 1156-1160.

[113] Trenczek-Zajac, A., et al., Structural and electrical properties of magnetron sputtered Ti (ON) thin films: the case of TiN doped in situ with oxygen. Journal of Power Sources, 2009. 194(1): pp. 93-103.

[114] Di Valentin, C., et al., N-doped TiO_2: theory and experiment. Chemical Physics, 2007. 339(1): pp. 44-56.

[115] Mondal, C., et al., Preformed ZnS nanoflower prompted evolution of CuS/ZnS p–n heterojunctions for exceptional visible-light driven photocatalytic activity. New Journal of Chemistry, 2015. 39(7): pp. 5628-5635.

[116] Yu, J., J. Zhang and S. Liu, Ion-exchange synthesis and enhanced visible-light photoactivity of CuS/ZnS nanocomposite hollow spheres. The Journal of Physical Chemistry C, 2010. 114(32): pp. 13642-13649.

[117] Yu, J. and B. Wang, Effect of calcination temperature on morphology and photoelectrochemical properties of anodized titanium dioxide nanotube arrays. Applied Catalysis B: Environmental, 2010. 94(3): pp. 295-302.

[118] Cong, Y., et al., Synthesis and characterization of nitrogen-doped TiO_2 nanophotocatalyst with high visible light activity. The Journal of Physical Chemistry C, 2007. 111(19): pp. 6976-6982.

[119] Wang, W., O. Savadogo and Z. Ma, Preparation of new titanium oxy nitride based electro catalysts using an anhydrous sol-gel method for water electrolysis in acid medium. International Journal of Hydrogen Energy, 2012. 37(9): pp. 7405-7417.

[120] Jing, D., et al., Efficient solar hydrogen production by photocatalytic water splitting: from fundamental study to pilot demonstration. International Journal of Hydrogen Energy, 2010. 35(13): pp. 7087-7097.

Photocatalytic Activity of Quantum Dots

Hamid Reza Rajabi

Additional information is available at the end of the chapter

Abstract

In recent years, nanoscale semiconductors have attracted great interest due to their unique structural, optical and electronic properties, which arise due to their large surface-to-volume ratio and quantum confinement effect. Quantum dots (QDs) as zero-dimensional semiconductor nanomaterials, which are confined to a size of 2–8 nm in three dimensions, are defined as particles with physical dimensions smaller than the exciton Bohr radius. One of the attractive research fields in recent years is the synthesis of various sizes and shapes of semiconductor material nanoparticles as doped with different dopants. The aim of this chapter is to focus on the photocatalytic activity of QDs as new, green and efficient nanophotocatalysts.

Keywords: quantum dots, nanophotocatalyst, pollutants, band gap, semiconductors

1. Introduction

Nowadays, nanotechnology is a field of applied science and technology whose theme is the control of matter and the fabrication of devices or materials on the atomic and molecular scale, generally between 1 and 100 nm. This is a highly multidisciplinary field, benefiting from the efforts and developments in many fields, including applied physics, materials science, interface and colloid science, supramolecular chemistry, chemical engineering, mechanical engineering, biological engineering and electrical engineering. Since the birth of cluster science and the invention of the scanning tunneling microscope in 1980s, nanotechnology has been prosperously developed with the ability to measure and visualize the novel phenomena and to manipulate and manufacture the materials and devices with nanostructures of 100 nm or smaller. In a subfield of nanotechnology, researchers study and develop nanomaterials which are reduced to the nanoscale dimension showing very different properties compared to what they exhibit

on a macroscale. For example, as the size of the system decreases, the "quantum size effect" becomes pronounced where the electronic properties of solids are altered. Meanwhile, the increase of surface area-to-volume ratio changes the mechanical, optical, chemical, thermal and catalytic properties of materials significantly. The distinct properties enable unique applications of nanomaterials [1].

Especially, the semiconductor nanocrystals, the so-called quantum dots (QDs), are a newly emerging nanomaterial, which have attracted many interests. Having excitons confined in all three spatial dimensions, quantum dots have properties that are between those of bulk semiconductors and those of discrete molecules. After excitation of the QDs, the emitted energy by QDs can be adjusted by controlling the composition and the particle size of QDs, due to the well-known effect of quantum size confinement effect. [2].

In the past decades there has been a growing interest in photo-assisted catalysis using semiconductors as an advanced oxidation process for the elimination of many organic pollutants in wastewater systems. Among various physical, chemical and biological techniques, photocatalyst-based degradation process has been considered as an alternative technique for water treatment due to its advantages over the traditional techniques, such as simplicity, quick oxidation, high efficiency and no formation of polycyclic products. Photocatalytic decolorization of pollutants using semiconductors as metal oxides and sulfides, such as TiO_2, ZnO, Fe_2O_3, WS_2, ZrO_2, WO_3, V_2O_5 and CeO_2, has received much attention because of possible practical applications [3]. Among the most extensively studied catalysts, zero-dimensional semiconductor nanomaterials (i.e., quantum dots), as well-known multifunctional materials, have received considerable attentions for degradation of pollutants. Moreover, QDs get more and more attention because their confinement by the excited electrons and holes leads to optical and electronic properties different from those in bulk semiconductors [4]. Moreover, QDs as new semiconductor particles in the nanosized scales possess a higher surface area-to-volume ratio than their bulk counterparts, and thus allows for greater photon absorption on the photocatalyst surface. Furthermore, recombination of the electron–hole pair within the semiconductor particle drastically reduces as particle size decreases. Therefore, the nanoscale semiconductor is expected to have higher photocatalytic activity than its bulk [5].

This material has been proved as a better photocatalyst due to rapid generation of electron–hole pairs with photoexcitation as it is a direct wide band gap semiconductor material [6]. Furthermore, it possesses high negative reduction potential of excited electrons due to its higher conduction band (CB) position in aqueous solution as compared to other extensively studied photocatalysts [7]. It has also been used in UV detectors due to its high resistivity at ambient conditions and fast switching time upon UV light illumination, thus exhibiting the highest potential for a UV-light detector.

On the other hand, surface modification of QDs can change their optical, chemical and photocatalytic properties. Surface modification possibility and capability of the band gap of QDs are the potential advantages of the colloidal QDs. It can also cause an improvement in the photostability of QDs, the generation of new traps on the surface of the QD leading to the appearance and efficiency of light-induced reactions occurring on the surface of QDs [8].

2. Semiconductor quantum dots

Luminescent QDs are zero-dimensional semiconductors that may be used in a wide array of fields and which will, along with rod and tetrapod nanoparticle semiconductors, see use in applications such as electrooptical devices, spectral bar coding, light filtering and computing applications. QDs are nanometer-scale semiconductor crystals composed of groups II–VI or III–V elements and are defined as particles with physical dimensions smaller than the exciton Bohr radius [9]. A typical QD has a diameter ranging from 2 to 20 nm containing roughly 200–10,000 atoms, with size comparable to a large protein. Quantum dots, rods and tetrapods have diameters that fall below the material's Bohr-exciton radius. When a photon hits such a semiconductor, some of their electrons are excited into higher energy states. When they return to their ground state, a photon of a frequency characteristic of that material is emitted [10].

Quantum confinement is the phenomenon which is the widening of the band gap energy of the semiconductor material when its size has been shrunken to nanoscale. The band gap of a material is the energy required to create an electron and a hole with zero kinetic energy at a distance far enough apart that their Columbic attraction could be ignored. A bound electron-hole pair, termed exciton, would be generated if one carrier approaches the other. This exciton behaves like a hydrogen atom, except that a hole, which is not a proton, forms the nucleus. The distance between the electron and hole defined as the exciton Bohr radius (r_B), which can be expressed by:

$$r_B = \frac{\hbar^2 \varepsilon}{e^2}\left(\frac{1}{m_e} + \frac{1}{m_h}\right) \tag{1}$$

where m_e and m_h are the effective masses of electrons and holes, and ε, $\hbar$ and e are the dielectric constant, reduced Planck constant and the charge of an electron, respectively. If the radius (R) of a quantum dot shrinks to r_B, especially when $R < r_B$, the motion of the electrons and holes is strongly confined spatially to the dimension of the quantum dot. Consequently, the excitonic transition energy and the band gap energy will increase, which results in the blue shift of the emission of the quantum dot [11].

If excitons in a solid are confined to a two-dimensional thin layer of the order of the exciton Bohr radius, one needs to treat the excitons as particles in a quantum well. Such a quantum well can be made using two different semiconductors, where a nanometer scale thin layer of semiconductor is sandwiched between two identical semiconductors which have a higher band gap compared to that of the thin layer. Also, the valence band edge and conduction band edge of the thin layer (the quantum well) must fall between the valence band edge and the conduction band edge of the second semiconductor (the barrier). This type of structure is known as a 2D nanostructure because excitons are restricted to move only along a 2D plane. Further confinement can be achieved if the excitons are confined along one more direction so that excitons are able to move only in the other direction. This structure is called a 1D nano-structure or quantum wire. This structure consists of nm^2 cross-section and long tube of the

lower band gap semiconductor surrounded by larger gap semiconductor. In a 0D nanostructure or quantum dot, excitons are confined in all directions. Here the quantum dots are made using lower band gap semiconductor surrounded by higher band gap semiconductor. The electronic and optical properties of these nanostructures are significantly different from the bulk semiconductor material. A schematic representation of these nanostructures is shown in **Figure 1** [12].
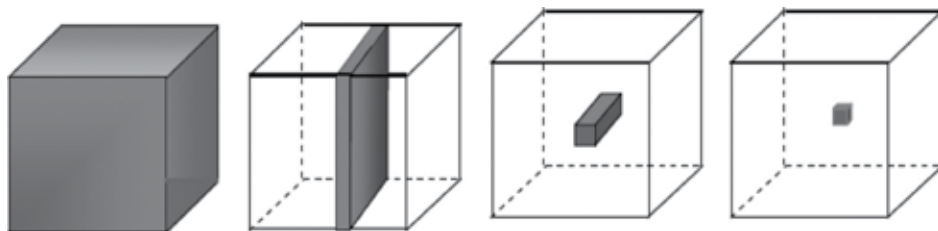
Figure 1. A schematic of bulk, quantum well, quantum wire and quantum dot (from left to right).

The separation between the valence band maximum and the conduction band minimum becomes smaller when the QD size increases. Consequently, one important advantage of semiconductor QDs is the tunability of the emission wavelength, simply by changing the QD size. The origin of the energy gap of QDs is described primarily as a perturbation that results from the Columbic interaction between the electron and the hole and the confinement of this exciton. Therefore, quantum confinement effects of quantum dots can be described as:

$$E \sim E_g + \frac{\hbar^2 \pi^2}{2R^2}\left(\frac{1}{m_e} + \frac{1}{m_h}\right) - \frac{1.8e^2}{\varepsilon R} \tag{2}$$

where E is the band gap energy of QDs, E_g is the bulk band gap and R is the radius of QDs. The quantum confinement terms follow R2 and shift E to higher energy as the radius decreases; oppositely, the Coulomb term shifts E to lower energy as R decreases. In this equation, the correlation between electron and hole positions induced by the Coulomb interaction is not strong, and the major effect is the electron and hole confinement energy. Therefore, the QD energy gap increases as the particle size is reduced [13].

2.1. Optical properties of QDs

As it has already been stated, due to quantum size confinement, decreasing the particle size results in a hypsochromic (blue-) shift of the absorption onset [14, 15]. While its position depends on the band gap and, consequently, on the particle size, its form and width are strongly influenced by the distribution in size, as well as the form and stoichiometry of the nanocrystals [16]. In **Figure 2**, the absorption and photoluminescence spectra of a series of CdSe nanocrystals differing in size are depicted.
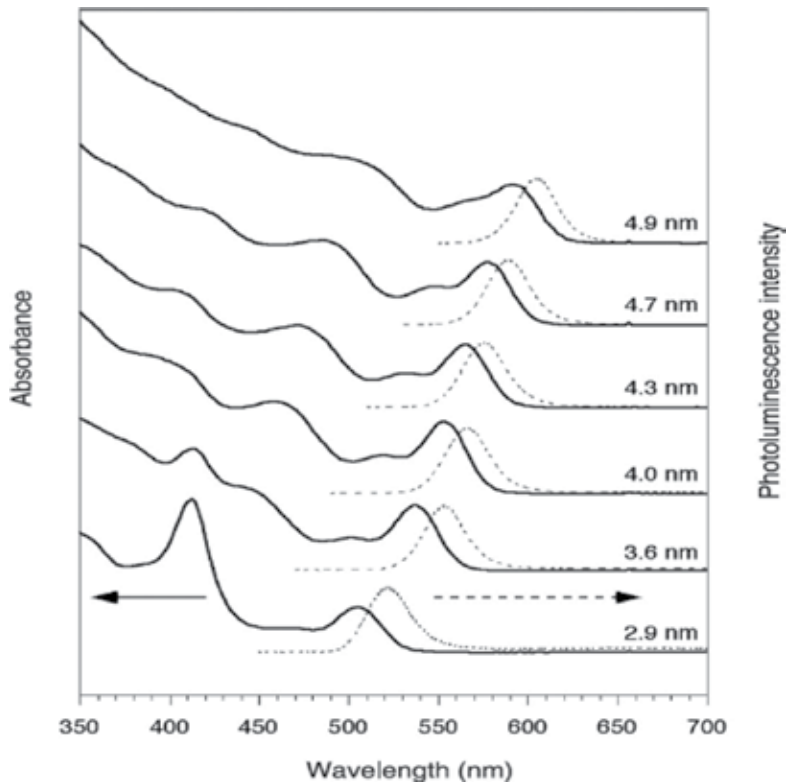
Figure 2. Absorption and normalized photoluminescence spectra of a series of CdSe NCs differing in size.

From the position of the absorption edge the mean particle size can be determined using the well-established relation between particle size and absorption onset [17]. The optical direct band gap values of the nanoparticles were determined by Tauc's relation [18], $\alpha h\upsilon=\alpha_0(h\upsilon-E_g)^{1/2}$, where $h\upsilon$, α_0 and E_g are photon energy, a constant and optical band gap of the nanoparticles, respectively. Therefore, in the plot of $(\alpha h\upsilon)^2$ versus $h\upsilon$, extrapolating the straight-line portion of the plot to zero absorption coefficient gives the corresponding E_g values. The bulk material band gap which is a characteristic of a semiconductor material becomes a size-dependent property. These particles then show a quantum confinement effect due to localization of charge carriers here after called QDs or quantum particles [19]. As the size of a semiconductor particle falls below the critical radius, the charge carriers begin to behave quantum mechanically and the charge confinement leads to a series of discrete electronic states. Free-standing nanoparticles are therefore preferred in order to understand basic quantum size effects in these materials [20]. According to the above discussion, the blue-shifted absorption edge and the increase in the band-gap energy of semiconductor are the results of decreasing the particle size and doping of nickel and copper ions. The increase in the band gap energy of a semiconductor is due to increase in the lifetime of electrons and holes; thus, it is expected that photocatalyst reactivity will increase (**Figure 3**) [21].
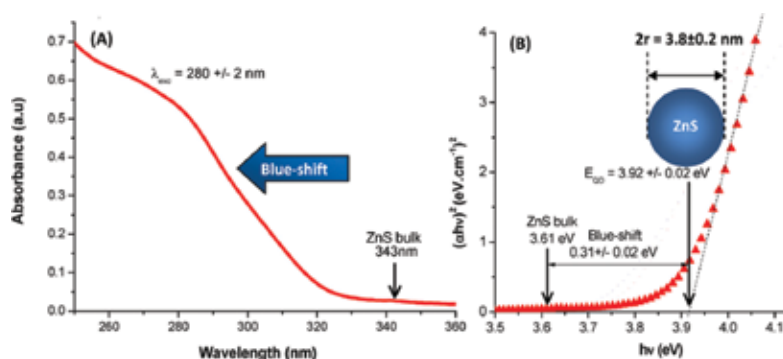
Figure 3. (A) UV-vis spectra and (B) optical band gap plot using Tauc's equation of the ZnS/chitosan conjugates [21].

In photoluminescence behavior of semiconductors, after the excitation by photons with an energy hv_e superior to its band gap, the emitted photons have an energy corresponding to the band gap of the nanocrystals; thus, the emission color can be tuned by changing the size of particle [22]. Due to spectral diffusion and the size distribution of nanocrystals, the luminescence line widths of CdSe NCs are in the range of 20–25 nm (FWHM), which the observed red-shift is usually referred to as Stokes-shift [23].

2.2. Photocatalytic activity of QDs

Up to now, many nanoscaled semiconductors have been used as nanophotocatalysts for water treatment. For example, due to some advantages such as low cost, chemical stability and abundance and suitable optical absorption in the UV region, titanium dioxide (TiO_2) has been most extensively applied for photodegradation of pollutants [24]. However, a major cause of the slow reaction kinetics in TiO_2 nanoparticle-photocatalysis systems is the fast recombination of e^- and h^+ [25]. Among the alternative cases for low-dimensional materials for photocatalytic applications, ultrasmall semiconductor nanocrystals (i.e., QDs) have recently emerged as a novel class of nanomaterials with unique physicochemical, electronic, magnetic and optical properties. Surprisingly, despite exhibiting very interesting properties, the use of QDs in environmental applications has only recently attracted attention from scientists [26–31].

QDs designed for environmental monitoring, sensing and testing would need to fulfil requirements similar to those used in biological applications, such as biocompatible fluorescent labels for diagnosis and imaging of cells, tissues and organs under physiological conditions. However, the unique properties of QDs made them as efficient semiconductor nanophotocatalysts especially for environmental applications. It has been shown to be useful and durable nanophotocatalysts for a variety of problems of environmental interest such as water and air purification. Due to higher surface area-to-volume ratio than their bulk counterparts, the recombination of the electron–hole pair within the QDs drastically reduces as particle size decreases. Therefore, QDs are expected to have higher photocatalytic activity than its bulk [32]. Moreover, QDs get more and more attention because their confinement by the excited electrons and holes leads to optical and electronic properties different from those in

bulk semiconductors. For QDs, the transportation length of electron/hole from crystal interface to the surface is short, which it helps to accelerate the migration rate of electron/hole to the QDs' surface to participate in the reaction process [33]. This pointer and increasing accessible surface of photocatalysts as nanoparticles lead to increasing photocatalytic activity of QDs.

Other advances key of QDs is the recent advances on the surface chemistry of QDs by conjugation with appropriate functional molecules [34]. The surface modification of QDs can enhance their luminescent quantum yields, their stability and prevent them from aggregating [35]. Moreover, by surface modifications of QDs, it is possible to make QDs available for interactions with target analytes [36] for various applications. However, modification of QDs by highly toxic organic reagents may restrict the application of this method [37]. Therefore, proper surface modification is a critical challenge to keep QDs colloidal and photostable under intracellular or intercellular conditions. On the other hand, surface modification of QDs can change their optical, chemical and photocatalytic properties. Being coated on any surface and capability of the band gap to be tuned by changing the size, and the shape of the particle are the potential advantages of colloidal QDs [34]. It can also cause an improvement in the photostability of QDs, the generation of new traps on the surface of the QD leading to the appearance and efficiency of light-induced reactions occurring on the surface of QDs. For the above reasons, QDs have great potential in analytical applications in aqueous media [38].

Quantum confinement effect of photogenerated electrons and holes was experimentally observed and theoretically justified. One of the most striking observations regarding the quantum confinement effect is the 'blue shift' in optical absorption spectra and enhancement of excitonic peak with reduction in particle size. The particle size below which the blue shift occurs is often termed as 'critical size' which is the Bohr radius of excitons in semiconductors [39, 40].

It is well known that the growth of a nanostructure is due to two processes namely Ostwald ripening and oriented attachment (OA). It is reported that the capping agents, as they directly modify the nanoparticle surface can largely influence the OA processes [41]. The molecular weight of the capping ligand also makes a remarkable contribution in the assembly behaviors of the capped nanoparticles on the surface of the nanoparticle restricts the growth of the nanoparticles which results in quantum confinement. The type of growth mechanism that will occur is largely based on the monomer concentration formed, the type of metal being used and the type and amount of capping agent present to induce nucleation. Monomer attachment growth typically provides the best route for single crystalline material, whereas coalescence growth often forms nanoparticles with multiple twin structures and/or high-energy facets [42]. Moreover, most of the organic capping molecules are distorted in shape and larger than a surface site. As a result, coverage of surface atoms with the organic capping molecules may be sterically hindered [43].

On the other hand, surface defects in QDs, due to the presence of capping agents, act as temporary 'traps' for the electron, hole or excitons, quenching radiative recombination and reducing the quantum yields. Surface passivation of QDs can confine the carrier inside the core and changes the size and optical properties of QDs. Therefore, capping or passivation of the surface is crucial for development of photostable QDs [44].

In the capping agent effect on the morphology of QDs, it is possible to suggest that the capping agents can cover the particles, and therefore, the particles do not coalesce to form bigger particles, even after an extensive period of time [45]. However, some aggregations between the particles may be occurring, lead to larger particles. The key point is that the capping agent must be able to suppress the growth of certain crystal facet by binding with metal cations [46]. Additionally, based on the spatial conformations of capping agents, they play an important role in controlling size and morphology of QDs (**Figure 4**) [47].
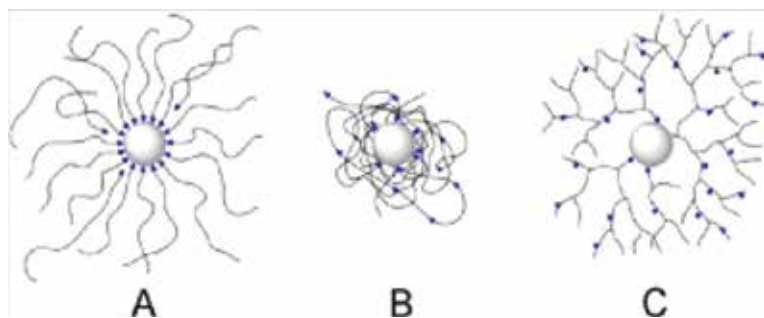
Figure 4. Spatial conformations of capping agents on nanoparticle (gray ball) surface: (A) linear long-chain hydrocarbons; (B) unbranched polymers and (C) branched polymers and dendrimers. Blue triangle represents the anchoring sites of capping agents [47].

2.3. Mechanisms of QD photocatalysis

The possible mechanism in the QD-based photocatalytic process is not yet fully understood. However, Pirkanniemi et al. [48] suggested five steps for the removal of pollutants in heterogeneous photocatalysis reaction:

(i) diffusion of reactants to the surface of photocatalyst particles,

(ii) adsorption of reactants onto the surface,

(iii) reaction on the surface,

(iv) desorption of products from the surface and

(v) diffusion of products from the surface to the bulk solution.

In homogeneous photocatalysis (for example, graphene quantum dots (GQDs)), both photocatalytic degradation and photosensitization degradation pathways may be occurring (**Scheme 1**). The light can be absorbed efficiently by both the QD and the pollutant molecule (P). According to the proposed pathway for the photocatalytic activity of the QDs, electrons in the valence band of QDs could be excited to the conduction band and electron–hole pairs are generated (Eq. (3)). Then the molecular oxygen (O_2) near the interface photocatalyst could be quickly reduced to the superoxide radical ($O_2(\bullet^-$ and hydrogen peroxide radical ($\bullet OOH$) by the photogenerated electrons (Eqs. (4)–(7)), whereas the valence band holes can directly oxidize organic pollutants adsorbed on the surface of catalyst (QDs) or mineralized them

indirectly through hydroxyl radicals•) OH) generated by the reaction of holes and water molecules (H_2O) or chemisorbed (OH^-) (Eqs. (8)–(10)) [49]. For example, in the self-photosensitization pathway for the new fuchsin dye, photodegradation in the presence of QDs under visible light irradiation as shown in **Scheme 1b**. Firstly, the large surface area of GQDs can effectively adsorb molecules. Then, under vis-light irradiation, some photogenerated electrons can transfer from excited-state of adsorbed molecules to the conduction band (CB) of QDs. Thus, it would facilitate for the photoinduced active species (e.g., $O_2•^-$, •OOH, •OH) to oxidize or degrade the surface-absorbed organic pollutants. Subsequently, $P^{•+}$ readily reacts with these oxygen radicals to finally dissociate (Eqs. (11)–(13)).

$$QDs + h\nu \rightarrow QDs\left(e^-_{CB} + h^+_{VB}\right) \tag{3}$$
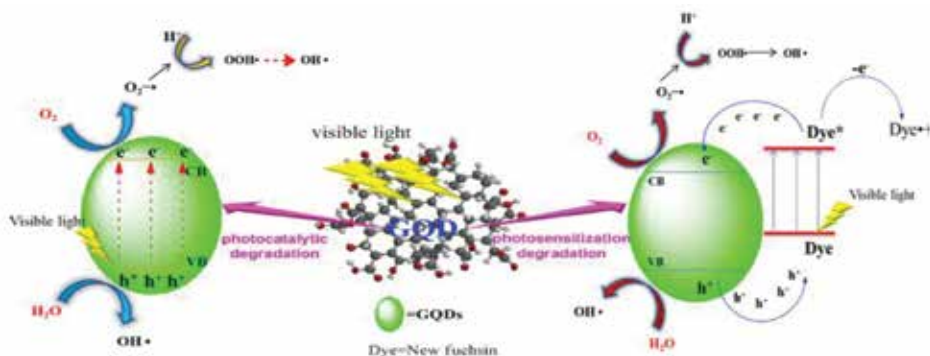
Scheme 1. Schematic representation of the proposed mechanism for degradation of New Fuchsin (NF) under visible light irradiation by (a) photocatalytic and (b) photosensitization pathways.

When the irradiation energy exceeds the energy difference between the valence and conduction bands (band gap) of a semiconductor, electron-hole pairs will be generated. This is referred to as the photoexcited state of the semiconductor [50]. The photogenerated charges (i.e., e^- and h^+ carriers) cause oxidation reactions on the particle surface, giving rise to free radicals, which in turn degrade the organic molecules. The photogenerated holes are highly oxidizing than the conventional oxidizing agents as the redox potential for the photogenerated holes is +2.53 V against the standard hydrogen electrode (SHE) in neutral (pH=7) solution.

$$QDs\left(e^-_{CB}\right) + \left(O_2\right)_{ads} \rightarrow QDs + (O_2^-•)_{ads} \tag{4}$$

$$(O_2•^-)_{ads} + H^+ \rightarrow + HO_2• \tag{5}$$

$$2HO_2• \rightarrow H_2O_2 + O_2 \tag{6}$$

$$H_2O_2 + e^- \rightarrow OH^- + OH\bullet \tag{7}$$

These holes react with water to produce hydroxyl radicals (OH•), whose redox potential is only slightly decreased [51]. Moreover, the high oxidative potential of h$^+$ in the catalyst permits direct oxidation of organic matter to reactive intermediate, or it can react with chemisorbed H_2O molecules to form reactive species such as hydroxyl radicals (OH•) [31, 33], as illustrated in the following equations:

$$QDs\left(h^+_{VB}\right) + \left(H_2O\right)_{ads} \rightarrow \quad QDs + \left(HO\bullet\right)_{ads} + \left(H^+\right)_{ads} \tag{8}$$

$$QDs\left(h^+_{VB}\right) + \left(HO^-\right)_{ads} \rightarrow \quad QDs + \left(HO\bullet\right)_{ads} \tag{9}$$

$$QDs\left(h^+_{VB}\right) + Dye_{ads} \rightarrow QDs + \left(P\bullet^+\right)_{ads} \tag{10}$$

$$P + h\upsilon \rightarrow \quad P^* \tag{11}$$

$$P^* + QDs \rightarrow P\bullet^+ + QDs\left(e^-_{CB}\right) \tag{12}$$
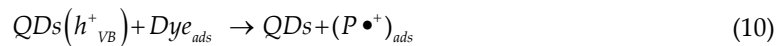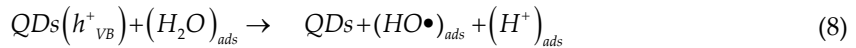
On the other hand, e$^-$ in the conduction band can reduce molecular oxygen to superoxide anion, then the superoxide anion can react with H_2O to form other active radicals [52]. Depending upon the exact experimental conditions, the holes, electrons, hydroxyl radicals, super oxide radicals and oxygen itself can play an important role in the photocatalytic reaction mechanism [53]. Therefore, the produced hydroxyl radicals can cause organic matter mineralization:

$$\left[OH^\bullet / O_2^{\bullet-} + dye \rightarrow CO_2 + H_2O + small / less toxic species\right] \tag{13}$$

$$QDs(h^+_{VB}, \bullet OH, \bullet OOH \, or \, O_2(^-\bullet P \rightarrow \cdots \rightarrow CO_2 + H_2O + small \, molecule \, byproducts \tag{14}$$
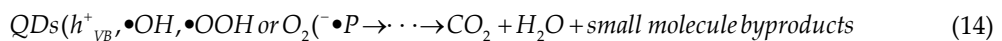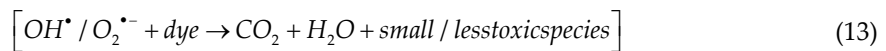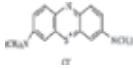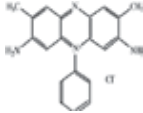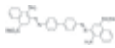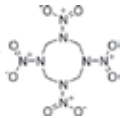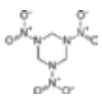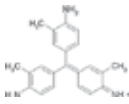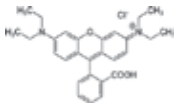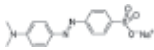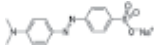
In doped QDs with proper elements, the energy from absorbed photons can be efficiently transferred to the impurity, quickly localizing the excitation and suppressing undesirable reactions on the nanocrystal surface [26]. For example, incorporation of ZnS with other transition metals such as manganese, nickel and copper can have a beneficial effect on the photoreactivity of photocatalysts. These doped ZnS semiconductor materials have a wide range of applications in electroluminescence devices, phosphors, light emitting displays and optical sensors. As mentioned, the number and the lifetime of free carriers (electrons/holes)
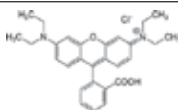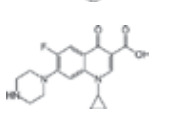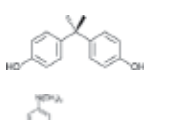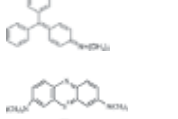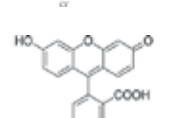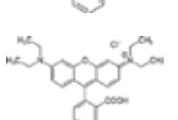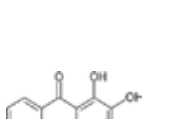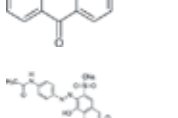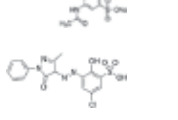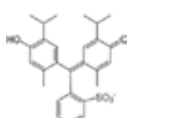
are particle size- and dopant-dependent. Doping of ZnS with other transition metal ions offers a way to trap charge carriers and extend the lifetime of one or both of the charge carriers (Scheme 2) [54]. **Table 1** illustrates the application of some prepared QDs by different methods in the photocatalytic degradation of pollutants [55–69].
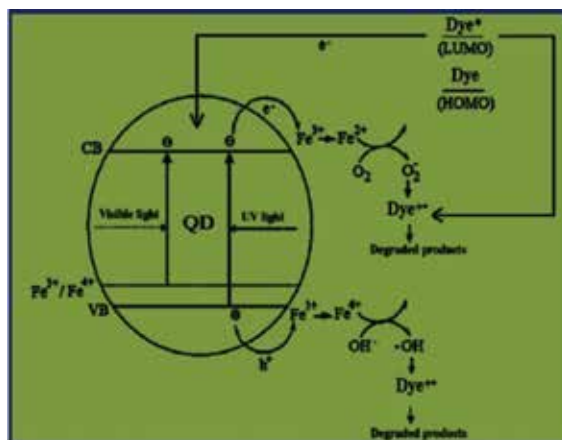
Scheme 2. Proposed mechanism for dye degradation under UV or visible light irradiations in the presence of doped QDs, such as iron-doped ZnS QDs [7].

Type of QDs	Synthesis method	Characterization methods	Name of the tested pollutant	Chemical structure	References
ZnS QDs, as pure and doped with different metal ions such as Cu, Mn, Ni, Co and Fe	Chemical precipitation	XRD, TEM, SEM, colorimetry, UV -vis absorption spectroscopy, fluorescence and atomic absorption spectroscopy	Methyl violet		[31]
			Victoria blue		[6, 28, 30]
			Malachite green		
			Thymol blue		
			Congo red		[55]

Type of QDs	Synthesis method	Characterization methods	Name of the tested pollutant	Chemical structure	References
			Methylene blue		[54]
			Safranin		
			Congo red		[32, 56, 57]
			HMX (octahydro-1,3,5,7-tetranitro-1,3,5,7-tetrazocine)		[58]
			RDX (hexahydro-1,3,5-trinitro-1,3,5-triazine)		
Graphene QDs	Pyrolyzing	Colorimetry, UV-vis absorption spectroscopy, Raman and fluorescence spectroscopy andzeta potential measurements	New fuchsin		[5]
	Chemical exfoliation of multi wall carbon nanotubes	TEM, XRF, UV-vis spectro photometry and thermal gravimetry	Rhodamine B		[59]
			Methyl orange		
Graphene quantum dots (GQDs) -polyvinyl pyrrolidone (PVP)-CdS nano composite	One-step hydro thermal method	XRD, TEM FT-IR, Raman spectroscopy, X-ray photoelectron spectroscopy and UV-vis spectroscopy	Methyl orange		[60]

Type of QDs	Synthesis method	Characterization methods	Name of the tested pollutant	Chemical structure	References
Carbon quantum dots/BiOX (X = Br, Cl) hybrid nano sheets	Ionic liquid-induced strategy	SEM, TEM and XRD	Phenol rhodamine B (RhB)		[61]
			Ciprofloxacin		
			Bisphenol A (BPA)		
Carbon quantum dots/N-doped zinc oxide (CQD/N-ZnO)	One-step chemical method	Raman and X-ray photo electron spectroscopy	Malachite green		[62]
			Methylene blue		
			Fluorescein		
Graphitic carbon nitride quantum dots decorated self-organized TiO$_2$ nanotube arrays	Electro chemical anodiza tion technique followed by a facile organic molecular linkage	SEM, TEM, XPS and UV–vis spectrophoto metry	Rhodamine B		[63]
CdS QDs	Chemical precipi tation	TEM, XRD and absorption and fluorescence spectroscopy techniques	Alizarin		[64]
			Acid violet		
			Mordant red		
			Thymol blue		
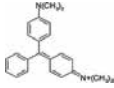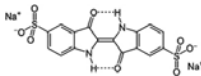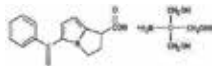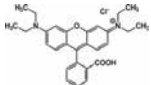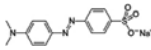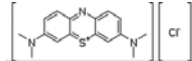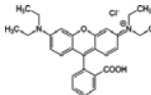
Type of QDs	Synthesis method	Characterization methods	Name of the tested pollutant	Chemical structure	References
CdSe/ZnS quantum dots	Chemical synthesis based on Schlenk reaction	UV/vis spectroscopy	Methyl green		[65]
TiO₂ quantum dots	Simple sol-gel, template free	UV-light irradiation, TEM and XRD images	Indigo carmine		[66]
	Facile ultrasonic-assisted hydro thermal process	FTIR spectrum, TEM and XRD images	Ketorolac tromethamine		[67]
ZnO foam /carbon quantum dots	Combus tion method	TEM, XRD EDAX, UV-vis spectrophoto metry and fluorescence	Rhodamine B		[68]
			Methyl orange		
			Methylene blue		
Ag@AgCl QDs sensitized Bi2WO6	Oil-in -water self-assembly method	XRD, TEM, SEM, DRS and XRF	Rhodamine B		[69]

Table 1. Characteristics of some prepared QDs by different methods in the photocatalytic degradation of pollutants.

2.4. Toxicity of QDs

Although QDs offer potentially invaluable societal benefits such as in vivo biomedical imaging and detection, they may also pose risks to human health and the environment under certain conditions. Generally, there are at least three different pathways by which QDs can interfere with organism function and lead to metabolic disability or death. First and most important is the composition of QDs. Upon corrosion inside the organism, toxic ions could be released from QDs and poison the cells. Compared with the bulk material, nanoparticles are more likely to have partial decomposition and release of ions due to their high surface-to-volume ratio. Another possible negative effect of QDs results from their small size, regardless of the

composition of material. Particles can stick onto the surface of cell membranes, or can be ingested and retained inside cells, causing the impairing effects. The shape of particles may cause some adverse problems as well [70]. To date, most commercial QDs contain toxic elements, such as Cd, Pb, Hg and As. It was reported that the Cd-core QDs were indeed cytotoxic, especially when surface oxidation through exposure to air or UV irradiation led to the formation of reduced Cd on particle surface and the release of free Cd^{2+} ions. The cells cultured with CdSe QDs for 7 days were damaged with poorly defined cell boundaries and diffused nuclei. It was also shown that CdTe QDs exerted deleterious effects on cellular processes, and the smaller ones with green emission were more harmful than the larger red-emitting ones [71].

Meanwhile, studies suggest that the QD toxicity depends on multiple factors such as size and charge of particles, initial concentration of used QDs and type, structure and shape of the outer coating bioactivity (capping material and functional groups). To alleviate the toxicity of QDs, a variety of synthesis, storage and coating strategies have been proposed. Surface coatings such as ZnS, bovine serum albumin and vitamin E were shown to reduce, but not eliminate the cytotoxicity. With different surface modifications including mercaptopropionic acid, silanization and polymer coating, there were always quantitative concentration limits of QDs for the onset of cytotoxic effects to occur. Therefore, QDs with toxic elements will eventually induce cell death due to their inherent chemical composition. They can never be considered as 100% biocompatible or safe, but depending on the experimental conditions under which the toxicity can be tolerated [72, 73]. Another potential disadvantage arises from the possible toxicity of the II–VI semiconductors that are commonly used to prepare QDs (e.g., CdS, CdSe, PbS and PbSe). There are concerns that the toxicity of these materials may, for example, hinder in vivo applications of QDs [13].

Biography

Dr. Hamid Reza Rajabi is currently associate professor of analytical chemistry, Chemistry Department, Faculty of Science, Yasouj University, Yasouj, Iran. He obtained his PhD in 2011 (Razi University, Kermanshah). He started his career as a researcher at Yasouj University in 2011. His research work is on synthesis, characterization and application of nanostructured imprinted polymers, magnetic nanoparticles and quantum dots.

Author details

Hamid Reza Rajabi

Address all correspondence to: h.rajabi@mail.yu.ac.ir

Chemistry Department, Yasouj University, Yasouj, Iran

References

[1]   A. P. Alivisatos, Science, 271 (1996) 933.

[2]   L. E. Brus, J. Chem. Phys., 80 (1984) 4403.

[3]   M. Roushani, M. Shamsipur, H. R. Rajabi, J. Electroanal. Chem., 712 (2014) 19.

[4]   B. Hemmateenejad, M. Shamsipur, F. Samari, H. R. Rajabi, J. Iran. Chem. Soc., 12 (2015) 1729.

[5]   M. Roushani, M. Mavaei, H. R. Rajabi, J. Mol. Catal. A: Chem., 409 (2015) 102.

[6]   H. R. Rajabi, M. Farsi, Mater. Sci. Semicon. Proc., 31 (2015) 478.

[7]   H. R. Rajabi, O. Khani, M. Shamsipur, V. Vatanpour, J. Hazard. Mater., 250–251 (2013) 370.

[8]   M. Shamsipur, H. R. Rajabi, Mater. Sci. Eng. C, 36 (2014) 139.

[9]   W. C. W. Chan, D. J. Maxwell, X. H. Gao, R. E. Bailey, M. Y. Han, S. M. Nie, Curr. Opin. Biotechnol., 13 (2002) 40.

[10]   T. Jamieson, R. Bakhshi, D. Petrova, R. Pocock, M. Imani, A. M. Seifalian, Biomaterials, 28 (2007) 4717.

[11]   J. Liab, J. J. Zhu, Analyst, 138 (2013) 2506.

[12]   C. Klingshirn, Semiconductor Optics, Springer-Verlag, Berlin, 2005.

[13]   L. J. Brus, Phys. Chem., 90 (1986) 2555.

[14]   F. Wang, W. B. Tan, Y. Zhang, X. P. Fan, M. Q. Wang. Nanotechnology, 17 (2006) R1.

[15]   A. E. Saunders, B. A. Korgel, J. Phys. Chem. B, 108 (2004) 16732.

[16]   B. D. Rabideau, R. T. Bonnecaze, Langmuir, 21 (2005) 10856.

[17]   T. Vossmeyer, L. Katsikas, M. Giersig, I. G. Popovic, K. Diesner, A. Chemseddine, A. Eychmuller, H. Weller, J. Phys. Chem., 98 (1994) 7665.

[18]   J. Tauc, Optical Properties of Solids, Academic Press Inc., New York, 1966.

[19]   A. A. Khosravi, M. Kundu, L. Jatwa, S. K. Deshpande, Appl. Phys. Lett., 67 (1995) 2702.

[20]   C. Vatankhah, M. H. Yuosefi, A. A. Khosravi, M. Savarian, Eur. Phys. J. Appl. Phys., 48 (2009) 20601.

[21]   A. A. P. Mansur, H. S. Mansur, F. P. Ramanery, L. C. Oliveira, P. P. Souz, Appl. Catal. B, 158–159 (2014) 269.

[22]   A. I. Ekimov, F. Hache, M. C. S. Klein, D. Ricard, C. Flytzanis, I. A. Kudryavtsev, T. V. Yazeva, A. V. Rodina, A. L. Efros, J. Optic. Soc. Am. B-Optic. Phys., 10 (1993) 100.

[23] M. Nirmal, D. J. Norris, M. Kuno, M. G. Bawendi, A. L. Efros, M. Rosen, Phys. Rev. Lett., 75 (1995) 3728.

[24] X. Qu, P. J. J. Alvarez, Q. Li, Water Res., 47 (2013) 3931.

[25] Z. B. Zhang, C. C. Wang, R. Zakaria, J. Y. Ying, J. Phys. Chem. B, 102 (1998) 10871.

[26] D. J. Norris, A. L. Efros, S. C. Erwin, Science, 319 (2008) 1776.

[27] M. T. Swihart, Curr. Opin. Colloid Interface Sci., 8 (2003) 127.

[28] H. R. Rajabi, M. Farsi, J. Mol. Catal. A: Chem., 399 (2015) 53.

[29] O. Khani, H. R. Rajabi, M. H. Yousefi, A. A. Khosravi, M. Jannesari, Spectrochim. Acta, Part A, 79 (2011) 361.

[30] M. Shamsipur, H. R. Rajabi, O. Khani, Mat. Sci. Semicon. Proc., 16 (2013) 1154.

[31] M. Shamsipur, H. R. Rajabi, Spectrochim. Acta Part A, 22 (2014) 260.

[32] H. R. Pouretedal, S. Narimany, M. H. Keshavarz, Int. J. Mat. Res., 101 (2010) 1046.

[33] D. Beydoun, R. Amal, G. Low, S. McEvoy, J. Nanoparticle Res., 1 (1999) 439.

[34] X. Peng, M. C. Schlamp, A. V. Kadavanich, A. P. Alivisatos, J. Am. Chem. Soc., 119 (1997) 7019.

[35] A. R. Kortan, R. Hull, R. L. Opila, M. G. Bawendi, M. L. Steigerwald, P. J. Carroll, L. E. Brus, J. Am. Chem. Soc., 112 (1990) 1327.

[36] C. J. Murphy, Anal. Chem., 74 (2002) 520A.

[37] H. Kuang, Y. Zhao, W. Ma, Liguang Xu, Libing Wang, Chuanlai Xu, Trends Anal. Chem., 30 (2011) 1620–1636.

[38] S. Jin, Y. Hu, Z. Gu, L. Liu, H. C. Wu, J. Nanomater., 2011 (2011) 13.

[39] M. R. Hoffmann, S. T. Martin, W. Choi, D. W. Bahnemannt, Chem. Rev., 95 (1995) 69.

[40] P. H. Borse, N. Deshmukh, R. F. Shinde, S. K. Date, S. K. Kulkarni, J. Mater. Sci., 34 (1999) 6087.

[41] T. Hemalatha, S. Akilandeswari, Int. J. Recent Sci. Res., 6 (2015) 7502.

[42] H. M. Zheng, R. K. Smith, Y. W. Jun, C. Kisielowski, U. Dahmen, A. P. Alivisatos, Science, 324 (2009) 1309.

[43] V. L. Colvin, A. N. Goldstein, A. P. Alivisatos, J. Am. Chem. Soc., 114 (1992) 5221.

[44] D. Bera, L. Qian, T. K. Tseng, P. H. Holloway, Materials, 3 (2010) 2260.

[45] H. R. Rajabi, M. Shamsipur, A. A. Khosravi, O. Khani, M. H. Yousefi, Spectrochim. Acta Part A, 107 (2013) 256.

[46] K. Liu, Z. R. Shen, Y. Li, S. D. Han, T. L. Hu, D. S. Zhang, X. H. Bu, W. J. Ruan, Sci. Rep., 4 (2014) 7.

[47] Z. Niu, Y. Li, Chem. Mater., 26 (2014) 72.

[48] K. Pirkanniemi, M. Sillanpaa, Chemosphere, 48 (2002) 1047.

[49] J. Wang, Y. Guo, B. Liu, X. Jin, L. Liu, R. Xu, Y. Kong, B. Wang, Ultrason. Sonochem., 18 (2011) 177.

[50] S. H. S. Chan, T. Y. Wu, J. C. Juan, C. Y. Teh, J. Chem. Technol. Biotechnol., 86 (2011) 1130.

[51] V. V. Jadhav, R. S. Dhabbe, S. R. Sabale, G. H. Nikam, B. V. Tamhankar, Universal J. Environ. Res. Technol., 3 (2013) 667.

[52] K. Kumar, M. Chitkara, I. S. Sandhua, D. Mehta, S. Kumar, Mat. Sci. Semicon. Proc., 30 (2015) 142.

[53] A. Fujishima, X. Zhang, CR Chimie, 9 (2006) 750.

[54] H. R. Pouretedal, A. Norozi, M. H. Keshavarza, A. Semnani, J. Hazard. Mater., 162 (2009) 674.

[55] H. R. Pouretedal, M. H. Keshavarz, Int. J. Phys. Sci., 6 (2011) 6268.

[56] H. R. Pouretedal, H. Beigy, M. H. Keshavarz, Environ. Technol., 31 (2010) 1183.

[57] H. R. Pouretedal, M. H. Keshavarz, J. Alloys Comp., 501 (2010) 130.

[58] H. R. Pouretedal, M. H. Keshavarz, M. H. Yosefi, A. Shokrollahi, A. Zali, Iran. J. Chem. Chem. Eng., 28 (2009) 13.

[59] S. Wei, R. Zhang, Y. Liu, H. Ding, Y. L. Zhang, Catal. Comm. 74 (2016) 104.

[60] T. Fan, Y. Li, J. Shen, M. Ye, Appl. Surf. Sci., 367 (2016) 518.

[61] J. Xia, J. Di, H. Li, H. Xu, H. Li, S. Guo, Appl. Catal. B, 181 (2016) 260.

[62] S. Muthulingam, I. H. Lee, P. Uthirakumar, J. Colloid Interf. Sci., 455 (2015) 101.

[63] J. Su, L. Zhu, G. Chen, Appl. Catal. B, 186 (2016) 127.

[64] A. Samadi-Maybodi, M. R. Sadeghi-Maleki, Spectrochim. Acta Part A, 152 (2016) 156.

[65] L. Y. Sheng, S. Z. Yong, Q. J. Tao, H. H. Tao, H. Yan, Chin. J. Anal. Chem., 44 (2016) 61.

[66] S. Sood, S. Kumar, A. Umar, A. Kaur, S. K. Mehta, S. K. Kansal, J. Alloys Compd., 650 (2015) 193.

[67] A. Kaur, A. Umar, S. K. Kansal, J. Colloid Interf. Sci., 459 (2015) 257.

[68] D. Ding, W. Lan, Z. Yang, X. Zhao, Y. Chen, J. Wang, X. Zhang, Y. Zhang, Q. Su, E. Xi, Mat. Sci. Semicond. Proc., 47 (2016) 25.

[69] Y. Liang, S. Lin, L. Liu, J. Hu, W. Cui, Appl. Catal. B, 164 (2015) 192.

[70] L. B. Stolle, S. Hussain, J. J. Schlager, M. C. Hofmann, Toxicol. Sci., 88 (2005) 412.

[71] J. Lovric, H. S. Bazzi, Y. Cuie, G. R. A. Fortin, F. M. Winnik, D. Maysinger, J. Mol. Med., 83 (2005) 377.

[72] G. N. Guo, W. Liu, J. G. Liang, Z. K. He, H. B. Xu, X. L. Yang, Mater. Lett., 61 (2007) 1641.

[73] H. R. Rajabi, M. Farsi, Mat. Sci. Semicon. Proc., 48 (2016) 14.

Graphene Materials to Remove Organic Pollutants and Heavy Metals from Water: Photocatalysis and Adsorption

Eduardo E. Pérez-Ramírez,
Miguel de la Luz-Asunción,
Ana L. Martínez-Hernández and
Carlos Velasco-Santos

Additional information is available at the end of the chapter

http://dx.doi.org/10.5772/62777

Abstract

Since graphene was isolated from graphite, different researches have been developed around it. The versatility of graphene properties and their derivates, such as graphene oxide or doped and functionalized graphene materials have expanded the possible applications of these nanostructures. The areas studied of graphene include the following: nanocomposites, drug delivery, transistors, quantum dots, optoelectronic, storage energy, sensors, catalyst support, supercapacitors, among others. However, other important field of these materials is their applications in environment, mainly in the removal of pollutants in water. In this context, there are two possible alternatives to use graphene materials in water purification: photocatalysis and adsorption. In the first case, the key is related to the bandgap and semiconductors properties of these materials, also the versatility of different graphene structures after the oxidation or functionalization, play an important role to get different arrangements useful in photocatalysis and avoid recombination, one of the problems of typical semiconductors photocatalysts. In the second case, surface area and useful chemical groups in carbon material give different options to produce efficient adsorbents depending on different synthesis conditions. Thus, this book chapter covers a review of the photocatalytic activity of graphene materials with emphasis in the removal of organic pollutants and heavy metals from water, in the next topics: graphene-based semiconductor photocatalyst and graphene oxide as photocatalyst. On the other hand, the chapter also discusses the research related to the removal of organic compounds and heavy metals using graphene materials as adsorbents, the topics in this second part are as follows: graphene and graphene oxide as adsorbent of heavy metals from water, graphene, and graphene oxide as adsorbent of organic pollutants from water,

functionalized graphene materials as adsorbent of water pollutants, carbon nanomaterials vs. graphene as adsorbents. Therefore, the book chapter presents a review and the discussion of the keys that play an important role in the advances in the research of graphene materials as photocatalysts. In addition, the isotherms and kinetic that produce these materials as adsorbents are also reviewed and discussed, because adsorption process in these materials is important to remove pollutants from water, but also for adsorption is a first step to achieve photocatalyst. The future of this topic in graphene materials is also analyzed.

Keywords: Graphene, Graphene oxide, Photocatalysis, Adsorption, Water pollution

1. Introduction

Water demand has increased as a consequence of different human activities and industrial growth. Water resources are contaminated due to the discharge of wastewater. The discharge of industrial effluents uncontrolled, containing large amounts of contaminants, represents a danger for human beings and aquatic life. By the aforementioned, the water pollution is a worldwide problem, which represents a serious risk to the environment and water quality. Therefore, it is necessary to develop new methods and materials for removing contaminants from wastewater.

Several conventional methods have been reported in the literature to remove contaminants from water and wastewater; however, these methods have large disadvantages. Photocatalytic degradation has shown great potential in the treatment of water. It has many advantages over conventional methods. Semiconductor-based photocatalysis has received great attention due to its use in water purification. Some researchers have reported water splitting using semiconductor photocatalyst, and it has attracted a lot of attention in different fields of science.

Adsorption is also widely used to remove contaminants from industrial wastewaters. When compared to conventional methods, adsorption offers significant economic and environmental advantages such as low cost, ease of operation, and high removal efficiency.

At present, the application of nanomaterials in water treatment has attracted significant attentions for the advantages of large surface areas and activated functionalized sites. Nanomaterials are very attractive in different fields of the science and have gained great interest due to their adsorption, catalytic, optical, and thermal properties among others. Researchers in science and engineering show an increased interest in the use of nanoparticles due to their unique physical and chemical properties.

Research on graphene (GE) has experienced strong growth in recent years. Graphene materials have already made great impacts in many fields ever since its discovery in 2004. Graphene oxide (GO) is one of the most important graphene materials.

This kind of nanomaterials represents a new type of photocatalyst/adsorbent offering an alternative to remove specific contaminants from water. Due to this, in this chapter, we present

a review of investigation studies where graphene and graphene based materials have been used as photocatalysts and adsorbents for the removal of heavy metals and organic compounds from water. The effect of some parameters affecting the process of photocatalysis and adsorption is analyzed.

2. Photocatalysis of graphene materials to remove pollutants from water

Heterogeneous photocatalysis is an advanced oxidation process (AOP) that offers an important potential for the decomposition of recalcitrant organic pollutants of water. In this process, the photon energy is converted into chemical energy which is able for the decomposition of these contaminants. One of the challenges in the heterogeneous photocatalysis is to improve the charge separation for make more efficient the process. In this regard, graphene materials are very promising for solve the recombination process. The structures of graphene materials with sp^2 hybridization of carbon atoms can allow a fast electron transfer improving the charge separation. Therefore, in this section, we present a review of investigations about of the use of graphene materials and graphene-based materials for the organic pollutants removal of water through of photocatalysis process.

2.1. Graphene-based semiconductor photocatalysts

With the aim to improve the performance of photocatalytic semiconductors materials, some strategies have been employed. One of the combinations of these semiconductors materials are with graphene. This nanomaterial can serve as an electron acceptor and therefore to improve the charge separation.

Although titanium supported over graphene materials is the most studied semiconductor on the removal of organic pollutants from water [1–4], exist other semiconductors that have been incorporated to graphene layers, in order to observe the modification of its effect on the removal of organic pollutants of water. This chapter section will be focused on making a review of semiconductors of oxides and sulfides which have had important impact when these are incorporated to the graphene materials.

Cuprous oxide (Cu_2O) is one of the more important semiconductors that have been combined with graphene materials. Han [5] investigated the performance of nanocomposite of Cu_2O–reduced GO (Cu_2O–RGO) on the photodegradation of methylene blue under visible light. The results showed an important increase of the photocatalytic activity of the Cu_2O–RGO nanocomposites respect to Cu_2O nanoparticles. This enhancement of the nanocomposites was attributed to the enhanced light absorbance, the extended light absorption range and a more easy transfer of photogenerated electrons of Cu_2O to RGO getting better charge separation which was corroborated by photoluminescence. Similar results have been found by Zhigang [6] and Sun [7] on the rhodamine B degradation where the enhanced photocatalytic activity was attributed to the strong interaction between Cu_2O and RGO nanosheets. Zou [8] synthesized Cu_2O–RGO composites for the methylene blue degradation under visible light finding that the photocatalytic activity of the composites was influenced by the Cu_2O crystal facet,

being the {111} facet that exhibited the enhanced visible light absorption and faster charge-transfer rate. Besides, the catalytic activity of the Cu$_2$O–RGO composites was related to the interfacial interactions and electronic structures.

Other semiconductor that has been combined with graphene materials is zinc oxide (ZnO). Tayyebi [9] decorated GO with zinc oxide quantum dots (QDs) by a chemical method for degradation of methyl orange in water. Strong interaction between ZnO and GO were found through C–O–Zn and C–Zn bridges. Besides, the adsorption range of visible light was increasing. The bandgap decreased of 3.1 eV in ZnO QDs to 2.8 and 2.9 eV in ZnO-10% graphene and ZnO-5% graphene, respectively. These hybrids of ZnO–graphene showed a better performance on the degradation of methyl orange that ZnO QDs. The increasing of the photocatalytic activity of the hybrids was attributed to the reduction of electron–hole recombination rate, the extended absorption of visible light, and the high surface area of graphene. Similar behavior was found by Rabieh [10]. The ZnO–RGO composites achieved a 99% of efficiency on the azure B dye degradation after of 20 min of reaction. The photocatalytic activity of ZnO–RGO composites was increased with the increasing of graphene. Other composites of graphene–ZnO with different morphologies have been synthesized by different methods showing good results on the organic pollutants degradation in water [11,12]. **Figure 1** shows a schema of the transfer of photogenerated electrons from a metallic oxide to graphene.
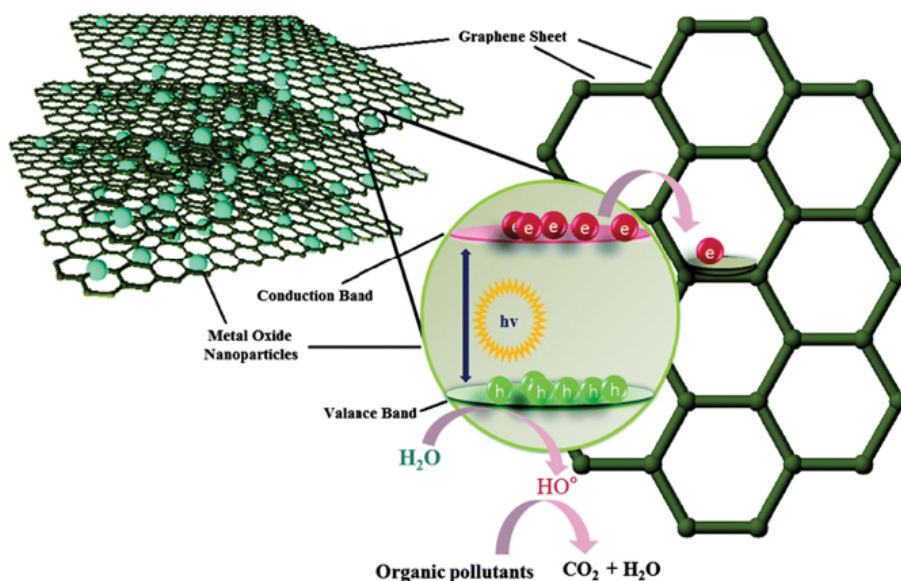
Figure 1. Schema of the mechanism of electron transfer from conduction band of metal oxide to graphene sheets. Reproduced with permission from Upadhyay et al. [13]. Copyright ©2014, The Royal Society of Chemistry.

In addition to metallic oxides, metal sulfides have also been combined with graphene searching photocatalysts with a higher photocatalytic activity for the organic contaminants degrada-

tion in water. Chakraborty [14] reported the synthesis of RGO–ZnS composites for optoelec-tronic device. The photocatalytic activity of the composite was proved on the rhodamine B under UV light irradiation for 4 h, getting a degradation efficiency of 84, 34% more than ZnS nanorods. The same composite was used for four cycles showing a constant degradation efficiency of rhodamine B. Composites of CdS and RGO were synthesized by Zou [15]. The photocatalytic activity of the RGO–CdS composites on the Congo red dye degradation improved the efficiency obtained with CdS, reaching a efficiency of 90% which was attribut-ed to the RGO performance as an effective acceptor electron.

Ternary systems such as RGO–TiO$_2$–ZnO [16] and RGO–TiO$_2$–Cu$_2$O [17] have been synthe-sized and employed successfully as photocatalysts for the degradation of organic pollutants of water. Other compounds with graphene that have been used are GO–Ag$_2$CO$_3$ [18], GO–Ag$_3$PO$_4$ [19,20], and RGO–BiPO$_4$ [21].

2.2. Graphene oxide as photocatalyst

GO is a functional form of graphene containing oxygenated groups. The basal plane of GO is covalently surrounded by the hydroxyl and epoxy groups, while carboxyl groups are found in the edges of the sheets [22]. These oxygenated groups make of the GO a hydrophilic material, improving the dispersion in water. Its bandgap can be adjusted modifying the level oxida-tion [23]. The easy dispersion in water and its tunable bandgap motivate to explore this material for applications in the photocatalysis area [24].

The photocatalytic activity of GO has been reported in some investigations. Krishnamoorthy [24] reported the photocatalytic properties of GO nanostructures. The photocatalytic activity was evaluated through of the resazurin (RZ) reduction as a function of irradiation time under UV light of 350 nm. The bandgap of GO was calculated to be 3.26 eV. In the photocatalytic experiments were used 10 mL of resazurin solution at a concentration of 1.5 mg/L and different concentrations of GO (0.5, 0.75, and 1 mg). Results showed the reduction of RZ into resoru-fin (RF) which was corroborated by the color change from blue into pink and the change in the bands adsorption of the adsorption spectra (**Figure 2**). The reduction of resazurin into resorufin was well fitted to pseudo-order reaction. The reduction of resazurin was attributed to the photoexcited electrons from the surface state of GO caused by the UV irradiation.

Aromatic compounds as phenol and 4-chlorophenol have been removed of water using GO as photocatalyst [25]. In the experiments for the removal of phenol were employed 100 mL of phenol solution at a concentration of 100 mg/L. The concentrations of GO were 100 and 200 mg/L and was used an UV lamp of 254 nm. The maximum removal achieved was 38%. The photocatalytic activity was influenced by the deggasing units used in the preparation of GO samples [26]. A major photocatalytic activity of GO was found on the degradation of 4-chlorophenol in water. 30 mL of 4-chlorophenol solution at a concentration of 30 mg/L were used in the experiments. The concentration of GO was 0.8 g/L. 97% of the 4-clorophenol was eliminated after of 120 min of reaction. The chemical oxygen demand (COD) results showed that up to 97% of organic matter was removed.
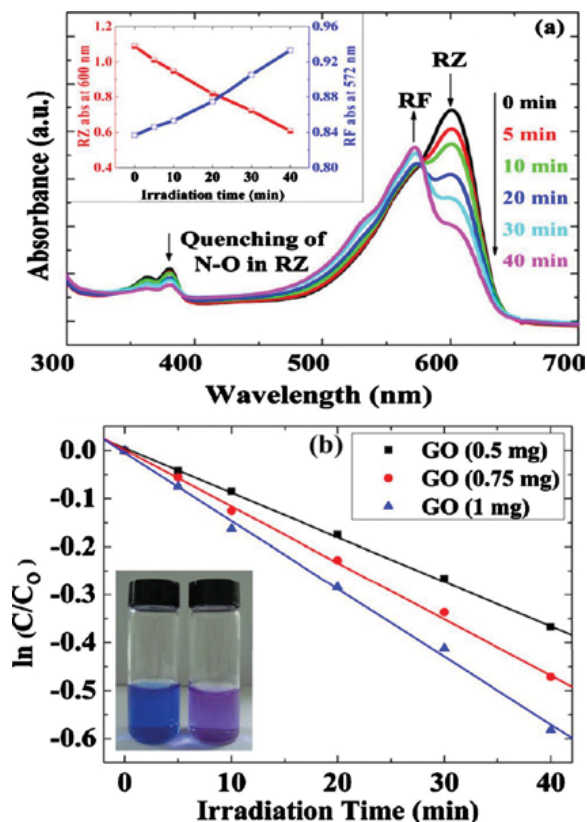
Figure 2. (a) Reduction of RZ into RF catalyzed by 1 mg of GO with respect to time. (b) Influence of the catalyst concentration (GO) on the reduction process of RZ into RF. Inset: Image of the GO–RZ solution before (left) and after (right) UV exposure. Reprinted with permission from Krishnamoorthy et al. [24]. Copyright ©2011, AIP Publishing LLC.

In addition to decontamination of water, GO promises good results as photocatalyst for hydrogen production from water and for CO_2 to methanol conversion. Yeh [23] confirmed the photocatalytic activity of GO through the generation of H_2 from water. For the experiments was used a glas-closed circulation system with inner irradiation. The mercury lamp used consists of both UV and visible light. The reactions were conducted in pure water and 20% volume aqueous methanol. The methanol in the solution reduced the recombination increasing the amount of H_2 produced. The high dispersion in water of GO induced that the carbon atoms on the sheets were accessible to protons that could be transformed to H_2.

The CO_2 to methanol conversion was studied by Hsu [22]. The experiments of photocatalytic reduction of CO_2 in gas phase were carried out under ambient conditions using a halogen lamp as irradiation source. Modified Hummers method was employed for the synthesis of three GO samples. The samples GO-1, GO-2, and GO-3 corresponding to the traditional form, excess of $KMnO_4$ and excess of H_3PO_4, respectively. The results obtained with this three samples of GO were compared with the results obtained with the commercial TiO_2. The order of methanol

formation was found to be as follows GO-3 > GO-1 > GO-2 > TiO_2 (P-25). The good perform‐ ance of GO-3 was attributed to the excess of H_3PO_4 which improved the protection of the GO basal plane. The modulation of oxygenated functional groups is an important control parameter. In addition to the CO_2 reduction, GO can be simultaneously used for the solar energy harvesting.

3. Graphene materials as adsorbents

In this section, graphene, graphene oxide and reduced graphene oxide were analyzed as adsorbent to study the adsorption characteristics of heavy metal compounds and organic from aqueous solutions. Some concepts about the kinetics and isotherms adsorption are provided. Otherwise, some researchers have suggested carbon nanotubes (CNT) and oxidized carbon nanotubes (OCNT) as adsorbents with good adsorption capacity. Thereby, subsequently, we include a discussion about the comparison between CNT and graphene materials.

The main emphasis is on the description relevant experiments and important results as well as some of the novel applications of graphene materials as adsorbents. We include a summa‐ ry of current experimental work that has been done in the area of graphene materials on adsorption process. In the end of the chapter is presented a comparison of adsorbents derived from graphene materials versus others carbon nanomaterials (CNM).

At present, carbon-based porous materials assembled by two dimensional (2D) such as GE, GO, and RGO have attracted a great attention as effective pollutant adsorbents owing to their high adsorption capacities and rapid adsorption rates [27]. However, search for novel and efficient adsorbents for the removal of contaminants from wastewater is imperative.

Researchers have tested many different types of developed adsorbents such as activated carbon (AC), zeolite and polymer, nanoparticles and nanocomposites, and other adsorbents are used for the removal of impurities from the aqueous solution. However, these adsorb‐ ents have been suffering from either low adsorption capacities or low efficiencies. Therefore, great effort has been made in recent years to seek new adsorbents and develop new techni‐ ques [28]. Many papers have been published in the past few decades, confirming that the carbonaceous materials are effective adsorbents for decontamination from wastewater. Their high sorption capacities are associated with the large specific surface area and the existence of a wide spectrum of surface functional groups [29]. Nanomaterials have been studied for the absorption of metal ions and organic compounds. Although it was discovered just a few years ago, GE and its derivates have attracted tremendous research interests not only in electron‐ ics and energy fields, but also in environmental applications [30]. The inherent advantages of the nano-structured adsorbent, such as adsorption capacity, easy and rapid extraction, handy operation, and regeneration, may pave a new, efficient, and sustainable way toward highly-efficient pollutant removal in water and wastewater treatment [31].

CNT, as member of the carbon family, have attracted special attentions to many researchers after their discovery in 1991, because they possess unique morphologies and have showed excellent properties and great potential for engineering applications. CNT are also good anion

and cation adsorption materials for wastewater treatment, as they exhibit exceptionally large specific surface areas [32]. Their layered nanosized structures make them a good candidate as absorbers [33].

Similarly, GE consisting of 2D hexagonal lattices of sp^2 carbon atoms covalently bonded has been theorized to have a huge specific surface area (over 2600 $m^2 g^{-1}$), leading to its potential in the environmental field as an effective choice for pollutant elimination or environmental remediation [34]. Graphene is hydrophobic and, consequently, stable dispersions in polar solvents can only be obtained with addition of proper surfactants. GO is similar to GE, but presents oxygen-containing functional groups such as hydroxyl and epoxide (mostly located on the top and bottom surfaces), and carboxyl and carbonyl (mostly at the sheet edges), randomly distributed in the graphene structure [28,34]. These functional groups markedly increase the hydrophilicity of GO, making it easily dispersible in aqueous solution and stable under common environmental conditions [35]. These functional groups can interact with positively charged species such as metal ions, polymers, and biomolecules [36].

CNT, GE, and GO are newly emerged carbonaceous nanomaterials, their characteristic structures and electronic properties make them interact strongly with organic molecules, via non-covalent forces, such as hydrogen bonding, π–π stacking, electrostatic forces, van der Waals forces, and hydrophobic interactions. Their nanosized structures also endow them some advantages such as rapid equilibrium rates, high adsorption capacity, and effectiveness over a broad pH range [37]. All these advantages suggest that CNM are promising adsorbents for environmental protection applications [38].

Parameters such as pH, adsorbate concentration, type of chemical specie, and agitation among others influence in the adsorbent–adsorbate interaction. Some properties of the adsorbents that affect the adsorption process are specific surface area, pore size, and surface functional groups.

The pH is the most important factor affecting the adsorption process. The solution pH can affect the surface charge of the sorbent and the dissociation of functional groups on the active sites of the adsorbent as well as the adsorbate speciation [31]. The pH at which the positive and negative charges are balanced, and no net charge is available on nanomaterials surfaces, is called point of zero charge (PZC) [39]. The adsorbent surface is positively charged at pH values below the pH_{PZC} and negatively charged at pH values above the pH_{PZC} [29].

3.1. Kinetics of adsorption

Adsorption process generally involves four different steps. They are (a) external mass transfer in bulk liquid phase, (b) boundary layer diffusion, (c) intraparticle mass transfer within particle, and (d) sorption on active sites. However, out of the four steps, the effect of boundary layer diffusion and sorption on active sites on the adsorption kinetics is negligible whereas external mass transfer and intraparticle mass transfer affect the kinetics considerably [36].

Many models have been extensively applied in batch reactors to describe the transport of adsorbates inside the adsorbent particles, such as the pseudo-first order and the pseudo-second order equation, the Elovich and Intraparticle diffusion equation [40] (**Table 1**).

Kinetic model	Equation	Nomenclature	References
Pseudo-first order	$\log\left(q_e - q_t\right) = \log q_e - \frac{k_1}{2.303}t$	Where q_e and q_t (mg/g) are the amounts of adsorbate adsorbed at equilibrium and at time t, respectively, and k_1 (min^{-1}) is rate constant of pseudo-first order	[41]
Pseudo-second order	$\frac{t}{q_t} = \frac{1}{k_2 q_e^2} + \frac{1}{q_e}t$	Where, q_e and q_t have the same meaning as before, and k_2 is the pseudo-second order rate constant [g/(mg min)]	[27]
Elovich	$q_t = \frac{1}{\beta}\ln\left(\alpha\beta\right) + \frac{1}{\beta}\ln t$	Where q_t is the adsorbed phenol (mg/g) at time t (min), α is the initial adsorption rate [mg/(g min)] and β is related to the activation energy for chemisorption (g/mg)	[42]
Intraparticle diffusion	$q_t = k_{id}t^{1/2} + \theta$	Where k_{id} is the intraparticle diffusion rate constant (mg/g min$^{1/2}$), and θ represents the value of the thickness of the boundary layer (mg/g)	[43]

Table 1. Kinetic models reported in the literature.

Isotherm model	Equation	Nomenclature	References
Langmuir	$q_e = \frac{q_{max}K_L C_e}{1 + K_L C_e}$	Where q_e is the adsorption capacity of the adsorbate per unit weight of adsorbent (mg/g), q_{max} is the maximum adsorption capacity (mg/g) and K_L is the constant related to the free energy of adsorption (L/mg), C_e the equilibrium concentration of the adsorbate (mg/L)	[44]
Freundlich	$q_e = K_F C_e^{1/n}$	Where q_e is the equilibrium amount of the adsorbate per unit mass of adsorbent (mg/g), C_e the equilibrium concentration of the adsorbate (mg/L), K_F the constant indicative of the relative adsorption capacity of the adsorbent (mg/g (L/mg)$^{1/n}$), $1/n$ the constant indicative of the intensity of the adsorption	[45]

Table 2. Langmuir and Freundlich isotherm models.

3.2. Adsorption isotherm

Adsorption isotherm is the relationship between adsorption capacity and concentration of the remaining adsorbate at constant temperature [37]. That is, it indicates the relationship between the absorbent and the adsorbate when the adsorption process reaches an equilibrium state [39]. The adsorption process may be generally modeled by Langmuir and Freundlich isotherms.

However, other models, such as BET, Tempkin, and Toth, are also used. The Langmuir model assumes that the adsorption occurs on a homogenous surface and no interaction between adsorbates in the plane of the surface. The Freundlich equation is an empirical equation based on adsorption on a heterogeneous surface [40]. The parameters obtained from the models provide important information on the sorption mechanism and the surface property and affinity of the adsorbent [37] (**Table 2**).

3.3. Graphene and graphene oxide as adsorbent of heavy metals from water

The discharge of effluents has increased due to industrialization. Heavy metals in the water pose risks to health and cause harmful effects to living organisms in aquatic life. In contrast to organic compounds, heavy metals are not biodegradable. Effluents from industrial wastewater include chromium, arsenic, zinc, cobalt, mercury, cadmium, lead, and so on. Even at low concentrations, these metals can be toxic and carcinogenic to organisms. Several physical and chemical methods have been used to remove metals and organic compounds, such as filtration, chemical precipitation, coagulation, solvent extraction, biological systems, electrolytic processes, reverse osmosis, oxidation, and ion exchange [38]. However, these methods present low removal efficiency. Adsorption process is the most widely used method for water treatment due to its low cost, ease of operation, efficiency in treatment [46], environmentally friendly [47], and adsorbents can be regenerated through a desorption process. Besides, adsorption does not generate the formation of harmful substances [48].

Ren [29] presented a comparative study of Cu(II) decontamination by three different carbonaceous materials, such as GO, multiwalled CNT (MWCNT), and AC. Cu(II) adsorption on the carbonaceous materials as a function of pH and Cu(II) ion concentration was investigated. The PZC values of carbonaceous materials decrease in the order of PZC(GO) < PZC(AC) < PZC(MWCNT). The carbonaceous surface is positively charged at pH values below the PZC and negatively charged at pH values above the PZC. GO has the lowest PZC value and the maximum adsorption efficiency, followed by AC, and then MWCNT, suggesting that GO is a promising material for the removal of Cu(II) ions from aqueous solutions in acidic wastewater treatment.

GO was prepared via modified Hummers' method by Wang [49] to remove Zn(II) ions from aqueous solutions. Results indicated that the optimum pH for Zn(II) removal was about 7.0. The Fourier Transform Infrared analysis indicated the presence of oxygen-containing functional groups on the surface of GO. The q_e values, calculated by pseudo-second order model, represent a fine agreement with the detected values in experiment. Adsorption isotherm can provide the most important parameter for designing a desired adsorption system. The values of 'n', obtained from Freundlich isotherm, are larger than 1 and decrease as the temperature increases. These values indicate the favorable nature of adsorption at lower temperature. Langmuir isotherms fit better with experimental data than Freundlich isotherms. This result suggests that Zn(II) adsorption on GO may be monolayer. The adsorption–desorption experiments were performed to investigate the possibility of recycling of GO and recovery of Zn(II) ions. The desorption percentages of Zn(II) from GO are 91.6, 73.4, and 53.2% employing 0.1 M HCl, 0.1 M HNO_3, and H_2O, respectively.

Recently, Tan [50] synthesized GO membranes and were used as adsorbents for the removal of Cu(II), Cd(II), and Ni(II). The maximum adsorption capacities for Cu(II), Cd(II), and Ni(II) were 72.6, 83.8, and 62.3 mg/g, respectively. The adsorption reached an equilibrium state in a short time (10–15 min) owing to a larger interlayer spacing of the GO membranes, which is favorable for facilitating the interstitial diffusion of heavy metal ions to active sites. The GO membranes were regenerated more than six times, with a slight loss in the adsorption capacity.

The adsorption kinetics and isotherms of Cr(III) on GO has been studied by Yang [51]. According to thermodynamic parameters calculated, the adsorption of Cr(III) on GO was spontaneous and endothermic. The maximum adsorption capacity of Cr(III) on GO at pH 5.0 and T = 296 K was 92.65 mg/g, which was higher than other reported adsorbents. The number of negatively charged sites increased on the surface of GO with increasing pH, whereby the adsorption of Cr(III) was favorable. In this study, oxygen-containing functional groups on GO played an important role in the adsorption of Cr(III). Results suggest that GO was a suitable material for the removal of Cr(III) from water.

GO was used by Madadrang [52] to investigate the adsorption and desorption behavior on Pb(II) removal. Boehm's titration method was used to determine the amount of functional groups on the GO surface. Pb(II) reacts with these functional groups on GO surface to form a complex. The BET surface area of GO was determined to be 430 m^2/g. The time required to reach the equilibrium state with a sonication treatment was 5–15 min. This time is much shorter than AC and other carbon-based adsorbents, these results show the GO as an available product for the waste treatment.

GO was utilized as adsorbent by Yari [53] for the removal of Pb(II). In this work, the equilibrium time adsorption on GO surface was 60 min. This time is greater than the work reported by Madadrang [52], which was carried out at different conditions. In this study, adsorption capacity of Pb(II) on GO surface increased with increase in the temperature of surrounding, the adsorption capacity increases from 15.9 to 19.7 mg/g when the temperature increased from 288 to 308 K. This result shows the endothermic nature of Pb(II) adsorption on GO. Therefore, higher temperatures favor adsorption. The value of ΔH° was 22.70 (kJ/mol) from GO. Thus, this result indicate that adsorption Pb(II) on GO surface was a physisorption. A thermodynamic study was carried out, the results indicate that the adsorption of Pb(II) ion on GO surface was spontaneous and endothermic. A review about of heavy metals removal by graphene materials is shown in **Table 3**.

Adsorbent	Adsorbate	T (°C)	pH	Model used	References
GO	Zn	20, 30, 45	2–10	Langmuir Pseudo-second order	[49]
GO	Cu, Cd, Ni	30	2–7	Langmuir Pseudo-second order	[50]
RGO	Cd	25, 45, 65	2–9	Langmuir Pseudo-second order	[54]

Adsorbent	Adsorbate	T (°C)	pH	Model used	References
GO	Cr	23, 33, 43	3–8	Langmuir	[51]
				Pseudo-second order	
GO	Cu	30	3–10	Langmuir	[29]
GO	Pb	25	2–8	Langmuir	[52]
GO	Pb	15, 25, 35, 45	2–9	Langmuir	[53]
				Type I	

Cd, Cadmium; Cr, Chromium; Cu, Copper; Ni, Nickel; Pb, Lead; Zn, Zinc.

Table 3. Graphene materials as adsorbents for removal of heavy metals.

3.4. Graphene and graphene oxide as adsorbent of organic pollutants from water

The organic compounds have been widely employed in a large number of industries, such as paper making, coating, chemical, pharmaceutical, petroleum refining, leather, and textiles, among others. Discharges of these compounds on effluents have caused serious problems in water bodies. Dyes and phenolic compounds are two of the most important contaminants of water. These are harmful to aquatic organisms and human beings [31,55]. The complex aromatic structures of dyes make them more difficult to remove [40]. Phenols and their derivatives are well known for their biorecalcitrant and acute toxicity [56]. The removal of organic contaminants in water resources not only protects the environment itself, but can also stop the toxic contaminant transfer in food chains. Due to these harmful effects, they must be removed from wastewater discharge before releasing into the environment [28]. The necessity of remove the organic contaminants of water has generated the search of effective alternatives for solve this problem. The use of graphene materials as adsorbent for decontamination of water promises to generate good results. Different investigations of adsorption of organic contaminants onto graphene materials have been reported.

GO, RGO, and GE have been developed and investigated for their use on the removal of organic pollutants in aqueous solution. Kim [27] reported adsorption behavior of acid red 1 (AC1) and methylene blue (MB) dyes on RGO. The equilibrium adsorption time of MB onto RGO was around 10 min, while the equilibrium adsorption of AC1 was reached to a time of 800 min. The surface charge of RGO and the structure of dye molecules had an important influence in the adsorption capacities and the equilibrium adsorption times. The adsorption of MB onto RGO was due to electrostatic interactions and $\pi-\pi$ interactions. On the other hand, $\pi-\pi$ interactions and hydrogen bonding were responsible for the adsorption of AC1 onto RGO. **Figure 3** shows the interactions presents in RGO-MB (a) and RGO-AC1 (b) systems. The negative charge of the surface oxygenated groups of GO favored the fast adsorption of MB cationic dye through of electrostatic interactions. A similar behavior of MB adsorption onto GO was found in other works [30,37,39]. In other investigation on the MB removal by RGO, Liu [40] found that with increasing RGO dose the removal of MB increased but the MB adsorption capacity decreased. This decrease in the MB adsorption capacity is because only a part of the active sites of RGO are available for the adsorption of MB when the RGO dose

increased. The pH solution had no significant impact on the removal of MB. At pH = 3, the removal of MB was 85.95%; while at pH = 10, the removal reached 99.68%. When the temperature was increased from 293 to 333 K, the adsorption capacity of MB increased from 153.85 to 204.08 mg/g. The equilibrium data were better fitted to the Langmuir isotherm model than the Freundlich model which is agreed with the reported by other authors [27,37,39]. The oxidation degree of GO can increases greatly the adsorption capacity of MB and adsorption behavior would change from Freundlich-type to Langmuir-type [57].

Figure 3. Scheme of interactions between RGO and AC1 dye molecules (up) and RGO and MB dyes molecules (down). Adapted with permission from Kim et al. [27].

The feasibility of using GE and GO as adsorbents for the removal of two toxic cationic dye basic red 12 (BR 12) and basic red 46 (BR 46) from aqueous solution was explored by Moradi [28]. The adsorption capacity of BR 12 and BR 46 increased with increasing of pH from 2 to 9. The major changes were observed in the adsorption of dyes onto GO. The changes on removal of dyes were very light when GE was used as adsorbent. This same behavior was found when was studied the effect of contact time. The order of removal of MB was as follows: GO-BR12 > GO-BR46 > GE-BR12 ≈ GE-BR46. The removal percentage of dye increased with increasing in the initial dye concentration. The adsorption of BR 12 onto RGO and GO indicate that the adsorption process was endothermic while the adsorption of BR 46 onto RGO and GO was an exothermic process. The results of adsorption of both cationic dyes indicated that the removal was more effective using GO as adsorbent, which was attributed to the surface oxygenated groups. Similar behavior of results had the experiment reported by Elsagh [46] on the removal of BR 46 onto GE and GO. In the adsorption process, the physisorption was found to be the main adsorption mechanism. The equilibrium adsorption data were best fitted to the Langmuir model and the adsorption kinetic data were well fitted to pseudo-second-order model.

The ability of RGO and GO to adsorb dyes such as methylene blue, methyl violet (MV), rhodamine B (RB), and orange G (OG) from aqueous solutions was studied by Ramesha [36]. GO showed an important affinity for the cationic dyes (MV and MB) reached the removal efficiencies up to 95%, while the adsorption of anionic dyes (RB and OG) was very low. On the other hand, RGO had better removal efficiency on anionic dyes than anionic dyes. The

removal efficiencies of RGO for anionic dyes were about of 95% while it were of 50% for cationic dyes. In the GO–MV and GO–MB systems, the adsorption was attributed to the electrostatic interactions, while the GO–OG system was mainly favored by the van der Waals interactions. In the GO–RB system, the interactions present are probably both electrostatic and van der Waals type. The adsorption process was found to follow pseudo-second-order kinetics in all the cases.

The removal of phenol from aqueous solution by RGO was studied by Li [55]. The adsorption of phenol onto RGO was studied in the pH range from 2.3 to 11.5. The best results of adsorption capacity were found in the pH range from 4 to 6.6. This was attributed to the surface functional groups which increased their surface complexation capability and π–π interactions between the aromatic ring of phenol and the aromatic structure of RGO. The percent removal of phenol was increased with increasing of the RGO dosage from 0.5 to 1.7 g/L but the adsorption capacity decreased. The pseudo-second-order equation was well fitted to the adsorption data. The adsorption isotherm data were well fitted by both Freundlich and Langmuir models. Thermodynamic study showed that adsorption of phenol onto RGO was endothermic and spontaneous process. In other work, the removal of 4-Chloro-2-nitrophenol (4C2NP) from aqueous solutions was performed using graphene as adsorbent [58]. Effect of the pH solution, contact time, initial concentration and temperature on the adsorption of 4C2NP onto GE was studied. The adsorption capacity of GE decreased with increasing dosage, but in all cases, the adsorption of 4C2NP by GE increased in the first 10 min and then achieved equilibrium at about 60 min. The higher adsorption of 4C2NP by GE was achieved in the pH range from 3 to 7. When the pH > 7 the adsorption of 4C2NP decreased. The adsorption of 4C2NP onto GE was increased with increasing the initial 4C2NP concentration from 2 to 10 mg/L. The opposite effect on the adsorption of 4C2NP was found when the temperature was increasing from 298 to 328 K. The adsorption kinetic data were best fitted to pseudo-second-order model, and the isotherm data were well described by the Freundlich isotherm model. Thermodynamic study indicated that the adsorption of 4C2NP onto GE was feasible, spontaneous, and exothermic in the temperature range from 298 to 328 K.

In addition to the dyes and phenols, others organic contaminants have been removed of water using GO as adsorbent. Pavagadhi [59] investigated the removal of two algal toxins, microcystin-LR (MC-LR) and microcystin-RR (MC-RR) from water. The adsorption kinetic of MC-LR and MC-RR onto GO was reached within 5 min with a removal major than 90% at the doses of 500, 700, and 900 μg/L. The adsorption capacity of GO was higher than AC. Due to their fast adsorption which is a very important parameter for design of water and wastewater treatment system, GO is a promising adsorbent for effective removal of MC-LR and MC-RR.

The adsorption of diclofenac (DCF) and sulfamethoxazole (SMX) onto GO in aqueous solution was reported by Nam [60]. Hydrophobic interactions and π–π electron donor acceptor were found to be the main adsorption mechanism of DCF and SMX onto GO. Both compounds reached the equilibrium within 24 h. The removal of DCF and SMX at equilibrium states were 50 and 12%, respectively, at a GO concentration of 100 mg/L. The sonication process had an important role on the removal of DCF and SMX. The removal percentage increased from 34 to 75% for DCF and from 12 to 30% for SMX. This was attributed to the reduction of

oxygenated groups on the surface of GO due to the increase in the sonication time which reduce the negative surface charge of GO and reduce the repulsion with the anionic compounds. The adsorption equilibrium data of DCF and SMX onto GO were fitted by the Freundlich isotherm. **Table 4** shows a summary of the results of adsorption of contaminant organics in water onto graphene materials.

Adsorbent	Adsorbate	T (°C)	pH	Model used	References
RGO	AC1	–	7	(MB) Langmuir	[27]
	MB			(AC1)Freundlich	
				Pseudo-second order	
G	MB	20, 40, 60	3–10	Langmuir	[40]
G	BR 12	20–40	2–9	Pseudo-second order	[28]
GO	BR 46				
GO	MB	20	2–9	Langmuir	[37]
				Pseudo-second order	
G	BR 46	20–40	2–9	Langmuir	[46]
GO				Pseudo-second order	
RGO	MB	ambient	2–10	(RB) Freundlich	[36]
GO	MV			Langmuir	
	OG			Pseudo-second order	
	RB				

AC1, acid red 1; BR 12, basic red 12; BR 46, basic red 46; MB, methylene blue; MV, methyl violet; OG, orange G; RB, rhodamine B.

Table 4. Comparison of graphene materials as adsorbents for removal of organic compounds.

3.5. Functionalized graphene materials as adsorbent of water pollutants

In an effort to improve the graphene and GO efficiency and overcome the limitations of these on the removal of the different pollutants in water, these materials have been functionalized with different organic groups. Some limitations for the use of GO are the high water absorption and the poor performance of the solid–liquid separation [61]. It will cause a risk of exposure to humans, animals, and aquatic organisms if GO remains in the filtered water [62,63]. Also, the functionalization of graphene materials can facilitate its dispersion and stabilization to prevent agglomeration [64]. Different functional groups such as carboxyl groups [65], hydroxyl groups [66], sulfhydryl groups, and amine groups [67] tend to have affinity by organic and inorganic pollutants as dyes and metals ions which are very important to achieve good removal efficiency. Different studies of heavy metal ion and dyes adsorption have been reported using as adsorbent functionalized graphene materials.

Wu [61] reported the removal of methylene blue employing a rhamnolipid-functionalized GO (RL–GO) hybrid which was prepared by one-step ultrasonication. The results showed that

the removal efficiency of RL–GO is superior to GO when used dosages of adsorbent of 5–15 mg under the experiment conditions. When the pH of the MB solution was increasing from 3 to 11, the amount of dye adsorbed increased from 287.98 to 499.64 mg/g, indicating a strong influence of this parameter on the MB removal with this adsorbent. The adsorption capacity was increased with the increasing temperature, indicating that the adsorption was due to an endothermic process. The main mechanism of adsorption was considered to be the electro-static interaction between the MB cations, and the negatively charged sites on surface of RL–GO which was corroborated by FTIR spectroscopy. The kinetic data showed an excellent fit to pseudo-second-order model, while the equilibrium data were best fitted to the Freundlich isotherm. The adsorption of MB onto RL–GO was favorable at all temperatures studied.

In their investigation, Madadrang [52] functionalized GO and RGO with N-(trimethoxysilyl-propyl) ethylenediamine triacetic acid (EDTA) for use both EDTA-GO and EDTA-RGO as adsorbent on the removal of Pb(II). It was found a good affinity between the Pb(II) ions and EDTA-GO. The adsorption capacity of Pb(II) was increasing of 328 ± 39 mg/g in GO to 479 ± 46 mg/g in EDTA-GO at an equilibrium concentration of 208 ± 17 mg/L. EDTA-RGO had a higher surface area (730 m^2/g) respect to GO (430 m^2/g) and EDTA-GO (623 m^2/g); however, their adsorption capacity of Pb(II) was the lowest which was attributed to their low amount of acid groups. The adsorption capacity was dependent of the pH of the solution and the total of acidity groups present in the adsorbent. The adsorption process involved on the removal of Pb(II) with EDTA-GO were the ion-exchange reaction between Pb(II) and –COOH or –OH groups and surface complexation and a complex of Pb(II) with EDTA. The equilibrium data of the adsorption of Pb(II) on EDTA-GO were best fitted to the Langmuir equation. **Figure 4** shows EDTA-GO structure before and after of the interaction with Pb(II) and other heavy metal cations.
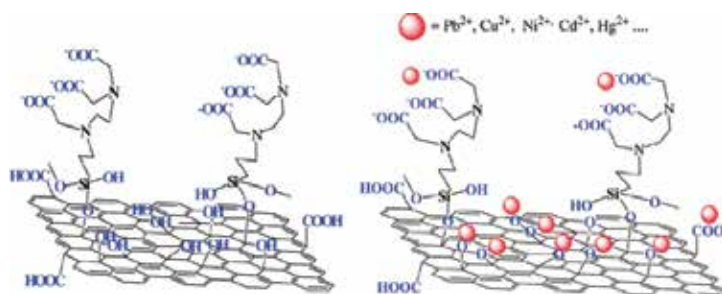
Figure 4. Chemical structure of EDTA-GO before (left) and after of its interaction with heavy metal cations (right). Reprinted with permission from Madadrang et al. [52]. Copyright ©2014, American Chemical Society.

The removal efficiency of Pb(II) using a thiol-functionalized GO (GO-SH) as adsorbent was investigated by Yari [53]. Three different amounts of cysteamine were used as follows 60, 80, and 100 mg which corresponding to GO-SH$_1$, GO-SH$_2$, and GO-SH$_3$ nanocomposites, respectively. The adsorption capacities at equilibrium were 18, 19.8, 20.8, and 21.7 (mg/g) for GO, GO-SH$_1$, GO-SH$_2$, and GO-SH$_3$, respectively. This indicate that the adsorption capacity of Pb(II) onto GO-SHs was increased with the increase in the cysteamine concentration which is due to

a increases in the number of functional groups (S–H) and (N–H) on the adsorbent surfaces. The Pb(II) adsorption increased for all adsorbents with the increase in the pH of the solution from 2 to 7 and when the temperature increased from 288 to 308 K. The results of kinetic experiments suggested that the adsorption of Pb(II) onto the different adsorbents was first due to a surface adsorption and after by possible slow intracellular diffusion in the interior of the adsorbents. On the other hand, the experimental data of equilibrium were well fitted to the Langmuir isotherm model (Type I) for all adsorbents. The negative values of the Gibbs free-energy change of adsorption ($\Delta G°$) and the positive values of enthalpy ($\Delta H°$) indicated that the adsorption process of Pb(II) ion on the GO and GO-SHs were spontaneous and endothermic in nature, respectively.

In another study, Wu [54] prepared a novel adsorbent 3D sulfonated reduced GO (3D-SRGO) aerogel with porous structure, large surface area, excellent hydrophilicity, and high adsorption capacity was prepared, characterized and applied in the Cd(II) ions removal from contaminated water. Filtration experiments revealed that the membranes fabricated by 3D-SRGO could quickly remove Cd(II) ions from the aqueous solutions. Regeneration tests showed that HNO_3 solution can desorb 97.23% cadmium, suggesting that the prepared 3D-SRGO can be repeatedly reused. The SRGO structure shows that there are a number of suspended hydroxyl, carboxylic, and sulfonic groups on the surface; therefore, the adsorption of Cd(II) ions on SRGO is governed by the cation exchange reaction of Cd(II) ions on the SRGO surface. Equilibrium adsorption isotherms are usually used to determine the capacities of adsorbents. The calculated adsorption capacity of the adsorbent for cadmium at pH 6.0 was 234.8 mg/g from Langmuir model, which is higher than many reported adsorbent for cadmium removal.

Li [68] synthesized and used a Chitosan/Sulfydryl-functionalized GO composite (CS/GO-SH) as adsorbent for the adsorption of Pb(II), Cd(II), and Cu(II) in single- and multi-metal ions systems. The adsorption capacities of CS/GO-SH on the individual removal of Pb(II), Cu(II), and Cd(II) were of 447, 425, and 177 mg/g, respectively, at a metal ion concentration of 500 mg/L, pH 5, and 293 K. However, the adsorption capacity of CS/GO-SH for individual metal ion decreased and changed when was used a ternary metal ion system. At each metal ion concentration of 250 mg/L, the adsorption ability of metal ion in mono-component solution followed the order Cu(II) > Pb(II) > Cd(II), while the competitive ability of metal ion in tri-component solution followed the order Cd(II) > Cu(II) > Pb(II). The kinetic experimental data were best fitted to the pseudo-second-order model and the equilibrium experimental data were best fitted to the Freundlich equation for CS/GO-SH. According to the thermodynamic study, the adsorption process of Pb(II), Cu(II), and Cd(II) onto the CS/GO-SH was spontaneous and endothermic.

The elimination of Ni(II) from the aqueous solutions by GO and glycine funcionalized GO (GO-G) was reported by Nafaji [69]. The adsorption capacity of Ni(II) on the two materials increased with the increasing the initial concentration of Ni(II) from 10 to 25 mg/L. The equilibrium data of Ni(II) on GO showed that the adsorption was best fitted of the Langmuir isotherm model (Type II), while the experimental data of the adsorption of Ni(II) on GO-G were best fitted to the Freundlich isotherm model. Both GO and GO-G showed to have a

better adsorption capacity of Ni(II) than some other adsorbents reported in the literature. In this study, the adsorption capacity of Ni(II) by GO-G was only slightly better than the adsorption capacity of GO and this was attributed to the functional groups of the glycine. The removal of Ni(II) by GO decreased when the temperature was increased from 283 to 308 K, while the adsorption of Ni(II) by GO-G decreased until 298 K and after that it was increased. Better results on the removal of Ni(II) were obtained by Wu [61]. In their experimental work, was prepared and used an effective and low-cost porous GO/sawdust composite (GOCC) as adsorbent for the removal of Ni(II) in aqueous solutions. The composite exhibited a strong ability to adsorb nickel ions. The equilibrium data were best fitted to Freundlich isotherm model while the kinetic data showed a better fit to the pseudo-second order kinetic model. The adsorption capacity of Ni(II) was increased considerably from 67.95 mg/g in GO to 98.06 mg/g in GO-G, indicating in this case, that the functionalization of GO improved the removal of Ni(II). This increase in the adsorption capacity of GOCC is attributed to the hydroxyl and carboxyl groups on the GO sheets that increase the ability of the porous GO-G composite to adsorb nickel ions.

As can be seen, GO has a better functionality in the removal of pollutants of water than reduced GO or also called graphene. This difference between GO and reduced GO is attributed to the major amount of oxygenated groups presents on the surface of GO which confer it a hydrophilic character and also interact whit the pollutants as cationic dyes and cationic metal ions. These surface oxygenated groups improve the interaction of GO with other organic molecules with the purpose of to improve the efficiency on the removal of pollutants of water. In general, the functionalization of graphene or GO with other organic molecules improved the adsorption capacity with respect to the individual materials. This increase on the removal of pollutants of water was largely dependent of the acid groups on the surface of GO or reduced GO and present in the organic molecule. Factors as pH of the solution and temperature play an important role on the removal of pollutants with these adsorbents. The removal times of pollutants are very short which indicate that these materials have an important adsorption capacity. The kinetic experimental data of the adsorption of MB and some cationic ions by some functionalized graphene materials showed a well fitted to the pseudo-second-order kinetic model. The equilibrium data of the adsorption of dyes and metal ions on the different functionalized graphene materials were well fitted to the Langmuir and Freundlich isotherm models, but do not showed a tendency by one in special, indicating that the surface homogeneity and heterogeneity of the adsorbents is dependent of the organic molecule nature, the surface of the graphene material and the interaction among them.

3.6. Carbon nanomaterials vs. graphene as adsorbents

As already mentioned above, graphene and GO have demonstrated an important adsorption capacity in the removal of some pollutans of water so they have a promising future in this area. However, these carbonaceous nanomaterials are not the unique that have been used in the decontamination of water. The effectiveness of CNT in the removal of various contaminants of water has been demonstrated in different studies [70–72]. The structural characateristics and electronic properties of graphene, GO, and CNT make them interact with organic

molecules, via non-covalent forces [37]. Furthermore, their nanosized structure also endows them some advantages such as rapid equilibrium rates, high adsorption capacity, and effectiveness over a broad pH range [73]. The exceptional high specific surface area available for adsorption of these nanomaterials makes them will be promising replacement for other adsorbents like AC [74]. Since the emergence of graphene in 2004, comparisons between graphene and CNT for different applications have been investigated.

Despite of be carbonaceous materials, graphene and CNT have different topology. Graphene is the hypothetical infinite aromatic sheet with sp^2 hybridization of the carbon atoms [75]. On the other hand, the structure of MWCNT can be rationalized as resulting from the folding of several graphene sheets (sp^2-hybridized carbon) aligned in a concentric manner [76]. This topological variation can result in different interactions between the carbon adsorbent and the contaminant molecule which has direct influence in the adsorption capacity [29]. Besides topology, the content of surface oxygenated groups play an important role on the adsorption capacity of CNM. Some investigations have compared the performance of graphene and CNT as adsorbents of pollutants molecules present in aqueous solutions at the same conditions in order to determinate which nanomaterial is more efficient in the decontamination of water by adsorption.

The removal of methylene blue by GO and CNT was reported by Li [37]. Both nanomaterials were modified by nitric acid. The surface oxygenated groups were identified by infrared spectroscopy. The removal efficiencies reached were 94.8–98.8% for GO and 72.4–82.7% for CNT in the pH range from 2 to 9, where both nanomaterials showed be negatively charged which enhanced the adsorption of the positively charged MB. The adsorption capacities for GO and CNT were 240.65 and 176.02 mg/g, respectively, at initial concentration of 120 mg/L. The experimental adsorption data for both nanomaterials were well fitted to the Langmuir equation model. The kinetic study of the adsorption of MB onto GO and CNT showed that the experimental data were best fitted to the pseudo-second-order kinetic model. The initial adsorption stage of GO is faster than CNT. This was attributed to the single-atom-layered structure of GO which benefited the attraction of dye molecules speedy. The highest normalized adsorption capacity of GO was due to the largest surface area accessibility which was attributed to its unique single-atom-layered structure. Electron donor acceptor interactions, π–π electron coupling and electrostatic interactions are the mechanisms that favored the adsorption of MB onto GO and CNT.

Elsagh [46] investigated the elimination of cationic dye Basic Red 46 (BR46) from aqueous solutions using as adsorbents GO, graphene, single-walled CNT (SWCNT), carboxylate group functionalized SWCNT (SWCNT-COOH). The adsorption kinetic data of GE and GO were well fitted to the pseudo-second-order model, while the experimental data of SWCNT and SWCTN-COOH were best fitted to the pseudo-first-order model. The adsorption capacity order of the different CNM used was SWCNT-COOH > SWCNT > GO > GE. The adsorption capacity was increased with increasing of the initial dye concentration and with increasing the pH of the dye solution and reached a maximum level at the pH of 9. The equilibrium experimental data of adsorption of BR46 on the four adsorbents were well fitted to the Langmuir

equation model. The physisorption was found to be the main adsorption mechanism and the rate-limiting step was mainly surface adsorption.

The adsorption of reactive red 2 (RR2) using RGO, GO, MWCNT, and oxidized multiwalled CNT (O-MWCNT) was investigated by Pérez-Ramírez [77]. The influence of the dosage of adsorbent and the dimension of the CNM on the removal of RR2 was studied. The adsorption of RR2 increased with increasing the loading of adsorbent. The better performance on the removal of RR2 was reached by MWCNT and O-MWCNT, which removed almost the total color of the solution. The order of the adsorption of RR2 was MWCNT = O-MWCNT > GO > RGO at adsorbent loading of 0.75 g/L. The effect of the contact time can be seen in **Figure 5**. Factors such as surface area, surface-oxygenated groups, the shape of the carbon structures, and the nature of the dye played an important role in this adsorption process. The main adsorption mechanism for the removal of RR2 was via π–π interactions between the aromatic rings. The kinetic adsorption data were better fitted to the pseudo-second-order model. The results suggested that the RR2 adsorption onto RGO, GO, MWCNT, and O-MWCNT was through a physisorption process but with strong interactions. The removal of RR2 was strongly influenced by the dimension of the CNM. One dimension of MWCNT and O-MWCNT allow them to have an arrangement (entangled) which produce different available sites for adsorption [78] unlike of 2D nanomaterials as RGO and GO where the available sites for adsorption are found on the external surface and maybe in the interplanar space.

The Cu(II) removal from aqueous solutions by GO and CNT was studied and reported by Ren [29]. Infrared spectroscopy showed the presence of oxygen-containing functional groups on the surface of all carbon materials, which provide chemical adsorption sites for heavy metal ions. The effect of pH and Cu(II) initial concentration were investigated. At the low acidic pH medium, the oxygenated groups on the surface of the GO and MWCNT were positively
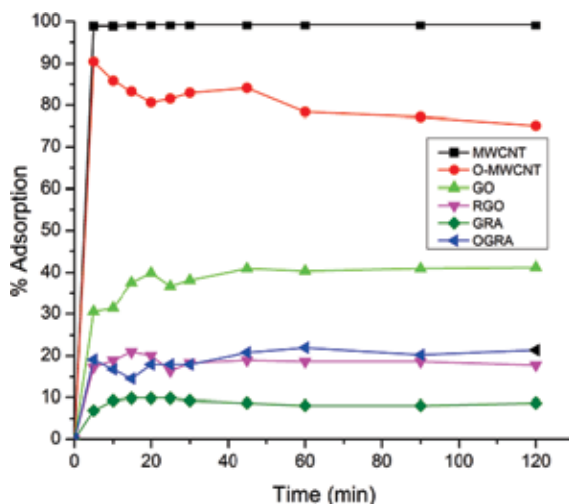
Figure 5. Effect of contact time on removal of RR2 by MWCNT, O-MWCNT, GO, RGO, graphite (GRA), and graphite oxide (OGRA). Adapted with permission from Pérez-Ramírez et al. [77]. Copyright ©2015, Mary Ann Liebert, Inc.

charged generating electrostatic repulsion with the free metal ions which leaded to a low adsorption percentage. At alkaline pH medium, these oxygenated groups were negatively charged generating attraction for the free metal ions and metal ions can form precipitates as their hydroxides. Therefore, the increase in the adsorption at alkaline pH was attributed to the electrostatic attraction, inner-sphere surface complexation, and surface precipitation. At pH range from 7 to 10, the adsorption percentage of Cu by GO and MWCNT was very similar; however, at pH 5, the adsorption percentage obtained by GO was around of 75%, while for MWCNT was minor to 20%. The adsorption experimental data were better fitted to Langmuir model. The maximum adsorption capacities of Cu(II) according to Langmuir were 1.18 × 10^{-3} and 3.19 × 10^{-5} mol g^{-1} for GO and MWCNT, respectively. The more important factors controlling the adsorption of Cu(II) on GO and MWCNT were the speciation in solution and adsorbate–adsorbent interaction across all the pH values.

Smith [79] investigated the removal of Lisozyme protein in water by graphene, GO, and SWCNT. Protein adsorption capacity of the CNM was evaluated to different initial concentrations of Lisozyme in aqueous solutions. The capacities adsorption order were GO > SWCNT > GE. GO exhibited an adsorption capacity of 500 mg/g with an initial Lysozyme concentration of 0.4 mg/mL, while SWCNT and GE obtained an adsorption capacity minor to 100 mg/g at the same conditions. The abundance of carboxylic acid groups on the surface of GO can cause an attractive electrostatic force with the positively charged Lisozyme being the cause of the high adsorption performance of this nanomaterial. Furthermore, the hydrophilic character of GO could facilitate the interaction with the protein. The adsorption of the Lisozyme onto SWNT and GE could be attributed to the van der Waals forces and some electrostatic interactions. In the equilibrium study, the nanomaterial with the highest adsorption capacity at all initial concentration was GO. The Langmuir, Freundlich, and Temkin models were used to model the adsorption experimental data of the protein onto GO, GE, and SWCNT. The adsorption data of Lysozyme onto SWCNT and GE were better fitted to the Langmuir equation model (R^2 = 0.94 and 0.98, respectively), while the values of R^2 in Langmuir, Freundlich, and Temkin models for GO were 0.656, 0.616, and 0.741, respectively. However, the high value of adsorption capacity of GO in Langmuir model (1428.57 mg/g) indicated a high adsorption. Further, the high value of K$_T$ (198.97) suggested the electrostatic interactions as possible mechanism of the Lysosyme protein adsorption onto GO. According to results, GO, GE, and SWCNT were more efficient on the removal of organic fouling agents than AC.

Adsorption of phenanthrene (PNT) and biphenyl (BP) by graphene nanosheets A and B (GNS-A and GNS-B), GO, SWCNT and MWCNT was investigated by Apul [80]. Phenanthrene and biphenyl solutions were prepared with distilled and deionized water and in the presence of natural organic matter (NOM). The surface area of the different CNM was GNS-A > GO > GNS-B > SWCNT > MWCNT. Adsorption capacities for PNT in distillate and deionized water at C$_e$ = 1 mg/L were higher than BP for all adsorbent nanomaterials. The order of the adsorption capacities of PNT was SWCNT > GNS-A > GNS-B ~ GO > MWCNT, while the order for BP adsorption capacities was SWCNT > GNS-A ~ GNS-B > GO > MWCNT. The adsorption was depending on the surface area, pore size, and oxygen content of CNM as well as hydropho-

bicity and molecular structure of adsorbates. The adsorption capacities of PNT and BP under NOM preloading followed a similar order than the obtained in distillate and deionized water but it decreased. The influence of NOM on the PNT and BP adsorption was smaller on GNS-A and GNS-B than SWCNT and MWCNT which was attributed to a lower compact bundle structure for graphenes than SWCNT or MWCNT aggregates.

A comparative study on removal of phenol with respect to the dimension of the nanomaterial (1D and 2D nanomaterials in their unoxidized and oxidized forms) was carried out by de la Luz-Asunción [45]. Six adsorbents such as SWCNT, MWCNT, oxidized SWCNT (O-SWCNT), O-MWCNT, GO, and RGO were employed. The adsorption kinetics indicate that most of phenol removal takes place during the first 50 min. It is implied that CNM possess very strong adsorption ability for phenol. The pseudo-second-order model provides the best correlation for the adsorption data ($R^2 > 0.99$). The results indicate that Freundlich isotherm provides the best fit for the equilibrium data ($R^2 > 0.94$). Differences in adsorption capacity between 1D and 2D nanomaterials are shown by the parameter, K_F, obtained from Freundlich isotherm. K_F, decreases in the following order: GO (7.456) > MWCNT (6.162) > O-MWCNT (4.777) > RGO (4.338). R_L values are between 0 and 1; this represents favorable adsorption between CNM and phenol. The adsorption process occurs by hydrogen bonding (**Figure 6**a) and mainly by $\pi-\pi$ interactions (**Figure 6**b) and not by electrostatic interactions. The mechanism of interaction between RGO and GO with phenol is similar to CNT and OCNT.
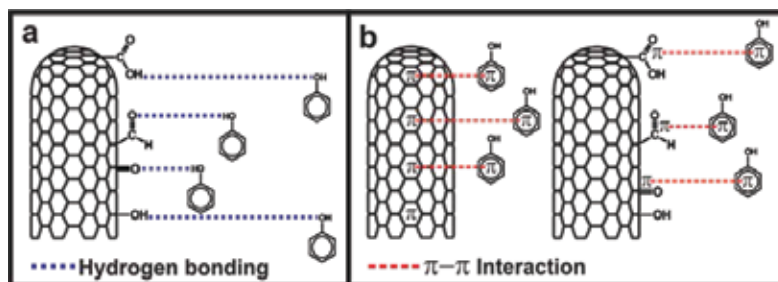
Figure 6. Proposed mechanisms of interaction between carbon nanotubes in their unoxidized and oxidized forms with phenol. Reprinted with permission from de la Luz-Asunción et al. [45]copyright 2015 Hindawi Publishing Corporation.

In an interesting study, Balamurugan [81] investigated the adsorption of chlorobenzenes (CBs) onto (5, 5) armchair SWCNT and graphene sheet through of density functional theory-based calculations. The interaction between the SWCNT and GE with CBs was studied with the Bader's theory of atoms. The interaction energy of the CBs increased according to the chlorine content was increasing from one to six atoms for both SWCNT and GE. The values of interaction energy were higher for G-CBs than those of SWCNT-CBs, and the variation of the interaction energy between both systems was found in the range from 2.30 to 3.42 Kcal/mol. On the other hand, GE presented a better adsorption capacity of CBs than SWCNT. This was attributed to the planar geometry of graphene which facilities the adsorption surface of pollutants. With the increasing of the chlorine content, the solubility of the CBs decreased while

their toxicity increased. The electrostatic interactions play an important role in the adsorption process of CBs onto SWCNT and GE. A summary with the different systems of adsorption and the kinetic models and Isotherms which were best fitted to the adsorption data are found in **Table 5**.

Adsorbent	Adsorbate	Kinetic model	Isotherm	References
GO	MB	Pseudo-second-order	Langmuir	[37]
CNTs	MB	Pseudo-second-order	Langmuir	[37]
GO	BR46	Pseudo-second-order	Langmuir	[46]
G	BR46	Pseudo-second order	Langmuir	[46]
SWCNT	BR46	Pseudo-first order	Langmuir	[46]
SWCNT-COOH	BR46	Pseudo-first order	Langmuir	[46]
GO	RR2	Pseudo-first order		[77]
rGO	RR2	Pseudo-first order		[77]
MWCNT	RR2	Pseudo-first order		[77]
OMWCNT	RR2	Pseudo-first order		[77]
G	PNT		Freundlich	[80]
G	PNT		Freundlich	[80]
GO	PNT		Freundlich	[80]
SWCNT	PNT		Freundlich	[80]
MWCNT	PNT		Freundlich	[80]
G	BP		Freundlich	[80]
G	BP		Freundlich	[80]
GO	BP		Freundlich	[80]
SWCNT	BP		Freundlich	[80]
MWCNT	BP		Freundlich	[80]
GO	Cu(II)		Langmuir	[29]
MWCNT	Cu(II)		Langmuir	[29]
G	Lysozime		Langmuir	[79]
GO	Lysozime		Temkin	[79]
SWNT	Lysozime		Langmuir	[79]

BP, biphenyl; BR 46, basic red 46; Cu, copper; MB, methylene blue; PNT, phenanthrene ; RR2, reactive red 2..

Table 5. Adsorption results of different pollutants from water onto carbon nanomaterials.

It is difficult to say whether graphene is better than CNT or vice versa. Results of the different investigations where these nanomaterials were compared indicated that there are some factors such as surface area, surface oxygenated groups, and pH solution which have strong influence on the adsorption of pollutants in water onto graphene and CNT. In both materials, the equilibrium adsorption time is short. The planar and tubular structure of graphene and CNT, respectively, and the contaminant molecule structure play an important role on the adsorption process and therefore the efficiency of this.

4. Concluding remarks

The results of graphene materials and graphene-based materials in photocatalysis and adsorption indicate that these materials have a great future in the decontamination of water. GO has shown photocatalytic activity when has been used of individual form on the removal of contaminants from water. Besides, the combination of graphene materials with different semiconductor nanoparticles has shown good results on the removal pollutans, increasing the efficiency of the photocatalytic process due to a charge separation more efficient. On the other hand, the removal of pollutant from water by adsorption using graphene materials as adsorbents shows a favorable panorama. The efficiency of these materials on the removal of heavy metals and organic compounds from water will be depending on factors such as surface area, pH, temperature, surface charge, content of functional groups, among others. Surface oxygenated groups in the graphene sheets improve the interaction with cationic dyes and cationic metal ions. The functionalization of graphene with different functional groups can be used to obtain a better affinity for the contaminant, thus improving the efficiency of adsorption process. Definitely, graphene materials are promising to play an important role in the photocatalysis and adsorption processes for environmental remediation.

Author details

Eduardo E. Pérez-Ramírez, Miguel de la Luz-Asunción, Ana L. Martínez-Hernández and Carlos Velasco-Santos[*]

*Address all correspondence to: cylaura@gmail.com

Division of Graduate Studies and Research, The Technological Institute of Querétaro, Santiago de Querétaro, Querétaro, México

References

[1] Nguyen-Phan T-D, Pham VH, Shin EW, Pham H-D, Kim S, Chung J S, Kim EJ, Hur S H. The role of graphene oxide content on the adsorption-enhanced photocatalysis of titanium dioxide/graphene oxide composites. Chemical Engineering Journal. 2011; 170:226–232. doi:10.1016/j.cej.2011.03.060

[2] Min Y, Zhang K, Zhao W, Zheng F, Chen Y, Zhang Y. Enhanced chemical interaction between TiO_2 and graphene oxide for photocatalytic decolorization of methylene blue. Chemical Engineering Journal. 2012; 193–194:203–210. doi:10.1016/j.cej.2012.04.047

[3] Rong X, Qiu F, Zhang C, Fu L, Wang Y, Yang D. Preparation, characterization and photocatalytic application of TiO_2–graphene photocatalyst under visible light irradiation. Ceramics International. 2014; 41:2502–2511. doi:10.1016/j.ceramint.2014.10.072

[4] Gao P, Li A, Sun D D, Ng W. Effects of various TiO_2 nanostructures and graphene oxide on photocatalytic activity of TiO_2. Journal of Hazardous Materials. 2014; 279:96–104. doi:10.1016/j.jhazmat.2014.06.061

[5] Han F, Li F, Yang J, Cai X, Fu L. One-pot synthesis of coprous oxide-reduced graphene oxide nanocomposite wit enhanced photocatalytic and electrocatalytic performance. Physica E: Low Dimensional Systems and Nanostructures. 2016; 77:122–126. doi:10.1016/j.physe.2015.11.020

[6] Zhigang N. Reduced graphene oxide-cuprous oxide hybrid nanopowders: Hydrothermal synthesis and enhanced photocatalytic performance under visible light irradiation. Materials Science in Semiconductor Processing. 2014; 23:78–84. doi:10.1016/j.mssp.2014.02.026

[7] Sun L, Wang G, Hao R, Han D, Cao S. Solvothermal fabrication and enhanced visible light photocatalytic activity of Cu_2O-reduced graphene oxide composite microspheres for photodegradation of rhodamine B. Applied Surface Science. 2015; 358:91–99. doi:10.1016/j.apsusc.2015.08.128

[8] Zou W, Zhang L, Liu L, Wang X, Sun J, Wu S, Deng Y, Tang C, Gao F, Dong L. Engineering the Cu_2-reduced graphene oxide interface to enhance photocatalytic degradation of organic pollutants under visible light. Applied Catalysis B, Environmental. 2015; 181:495–503. doi:10.1016/j.apcatb.2015.08.017

[9] Tayyebi A, Outokesh M, Tayebi M, Shafikhani A, Şengör S S. ZnO quantum dots-graphene composites: Formation mechanism and enhanced photocatalytic activity for degradation of methyl orange dye. Journal of Alloys and Compound. 2016; 663:738–749. doi:10.1016/j.jallcom.2015.12.169.

[10] Rabieh S, Nassimi K, Bagheri M. Synthesis of hierarchical ZnO-reduced graphene oxide nanocomposites with enhanced adsorption-photocatalytic performance. Materials Letters. 2016; 162:28–31. doi:10.1016/j.matlet.2015.09.111

[11] Huang K, Li Y H, Lin S, Liang C, Wang H, Ye C X, Wang Y J, Zhang R, Fan D Y, Yang H J, Wang Y G, Lei M. A facile route to reduced graphene oxide–zinc oxide nanorod composites with enhanced photocatalytic activity. Powder Technology. 2014; 257:113–119. doi:10.1016/j.powtec.2014.02.047

[12] Zhang C, Zhang J, Su Y, Xu M, Yang Z, Zhang Y. ZnO nanowire/reduced graphene oxide nanocomposites for significantly enhanced photocatalytic degradation of Rhodamine 6G. Physica E. 2014; 56:251–255. doi:10.1016/j.physe.2013.09.020

[13] Upadhyay R K, Soin N, Roy S S. Role of graphene/metal oxide composites as photocatalysts, adsorbents and disinfectants in water treatment: A review. RSC Advances. 2014; 4: 3823–3851. doi:10.1039/c3ra45013a

[14] Chakraborty K, Chakrabarty S, Das P, Ghosh S, Pal T. UV-assisted synthesis of reduced graphene oxide zinc sulfide composite with enhanced photocatalytic activity. Materials Science and Engineering B. 2016; 204:8–14. doi:10.1016/j.mseb.2015.11.001

[15] Zou L, Wang X, Xu X, Wang H. Reduced graphene oxide wrapped CdS composites with enhanced photocatalytic performance and high stability. Ceramics International. 2016; 42:372–378. doi:10.1016/j.ceramint.2015.08.119

[16] Raghavan N, Thangavel S, Venugopal G. Enhanced photocatalytic degradation of methylene blue by reduced graphene-oxide/titanium dioxide/zinc oxide ternary nanocomposites. Materials Science in Semiconductor Processing. 2015; 30:321–329. doi:10.1016/j.mssp.2014.09.019

[17] Almeida B M, Jr Melo A M, Bettini J, Benedetti J E, Nogueira A F. A novel nanocomposite based on TiO_2/Cu_2O/reduced graphene oxide with enhanced solar-light-driven photocatalytic activity. Applied Surface Science. 2015; 324:419–431. doi:10.1016/j.apsusc.2014.10.105

[18] Li J, Wei L, Yu C, Fang W, Xie Y, Zhou W, Zhu L. Preparation and characterization of graphene oxide/Ag_2CO_3 photocatalyst and its visible light photocatalytic activity. Applied Surface Science. 2015; 358:168–174. doi:10.1016/j.apsusc.2015.07.007

[19] Wang C, Zhu J, Wu X, Xu H, Song Y, Yan J, Song Y, Ji H, Wang K, Li H. Photocatalytic degradation of bisphenol A and dye by graphene-oxide/ Ag_3PO_4 composite under visible light irradiation. Ceramics International. 2014; 40:8061–8070. doi:10.1016/j.ceramint.2013.12.159

[20] Chen X-J, Dai Y-Z, Wang X-Y, Guo J, Liu T-H, Li F-F. Synthesis and characterization of Ag_3PO_4 immobilized with graphene oxide (GO) for enhanced photocatalytic activity and stability over 2,4-dichlorophenol under visible light irradiation. Journal of Hazardous Materials. 2015; 292:9–18. doi:10.1016/j.jhazmat.2015.01.032

[21] Zhang Y, Shen B, Huang H, He Y, Fei B, Lv F. $BiPO_4$/reduced graphene oxide composites photocatalyst with highphotocatalytic activity. Applied Surface Science. 2014; 319:272–277. doi:10.1016/j.apsusc.2014.07.052

[22] Hsu H-C, Shown I, Wei H-Y, Chang Y-C, Du H-Y, Lin Y-G, Tseng C-A, Wang C-H, Chen L-C, Lin Y-C, Chen K-H. Graphene oxide as a promising photocatalyst for CO_2 to methanol conversion. Nanoscale. 2013; 5:262–268. doi:10.1039/c2nr31718d

[23] Yeh T-F, Syu J-M, Cheng C, Chang T-H, Teng H. Graphite oxide as a photocatalyst for hydrogen production from water. Advanced Functional Materials. 2010; 20:2255–2262. doi:10.1002/adfm.201000274

[24] Krishnamoorthy K, Mohan R, Kim S-J. Graphene oxide as a fotocatalytic material. Applied Physics Letters. 2011; 98:244101 (1–3). doi:10.1063/1.3599453

[25] Bustos-Ramirez K, Barrera-Diaz CE, De Icaza M, Martínez-Hernández AL, Velasco-Santos C. Photocatalytic activity in phenol removal of water from graphite and graphene oxides: Effect of degassing and chemical oxidation in the synthesis process. Journal of Chemistry. 2015; 2015; 1–10. doi:10.1155/2015/254631

[26] Bustos-Ramirez K, Barrera-Diaz C E, De Icaza M, Martínez-Hernández A L, Velasco-Santos C. 4-chlorophenol removal from water using graphite and graphene oxides as photocatalysts. Journal of Environmental Health Science & Engineering. 2015; 13. 1-10. doi:10.1186/s40201-015-0184-0.

[27] Kim H, Kang S O, Park S, Park H S. Adsorption isotherms and kinetics of cationic and anionic dyes on three-dimensional reduced graphene oxide macrostructure. Journal of Industrial and Engineering Chemistry. 2015; 21:1191–1196. doi:10.1016/j.jiec.2014.05.033.

[28] Moradi O, Gupta V K, Agarwal S, Tyagi I, Asif M, Makhlouf A S H, et al. Characteristics and electrical conductivity of graphene and graphene oxide for adsorption of cationic dyes from liquids: Kinetic and thermodynamic study. Journal of Industrial and Engineering Chemistry. 2015; 28:294–301. doi:10.1016/j.jiec.2015.03.005.

[29] Ren X, Li J, Tan X, Wang X. Comparative study of graphene oxide, activated carbon and carbon nanotubes as adsorbents for copper decontamination. Dalton Transactions. 2013; 42(15):5266–5274. doi:10.1039/c3dt32969k.

[30] Yang S-T, Chen S, Chang Y, Cao A, Liu Y, Wang H. Removal of methylene blue from aqueous solution by graphene oxide. Journal of Colloid and Interface Science. 2011; 359:24–29. doi:10.1016/j.jcis.2011.02.064.

[31] Fan L, Luo C, Sun M, Qiu H, Li X. Synthesis of magnetic β-cyclodextrin-chitosan/graphene oxide as nanoadsorbent and its application in dye adsorption and removal. Colloids Surfaces B Biointerfaces. 2013; 103:601–607. doi:10.1016/j.colsurfb.2012.11.023.

[32] Li Y H, Di Z, Ding J, Wu D, Luan Z, Zhu Y. Adsorption thermodynamic, kinetic and desorption studies of Pb2+ on carbon nanotubes. Water Research. 2005; 39(4):605–609. doi:10.1016/j.watres.2004.11.004.

[33] Kabbashi N A, Atieh M A, Al-Mamun A, Mirghami M E, Alam M D Z, Yahya N. Kinetic adsorption of application of carbon nanotubes for Pb(II) removal from aqueous

solution. Journal of Environmental Sciences. 2009; 21(4):539–544. doi:10.1016/s1001-0742(08)62305-0.

[34] Sun L, Yu H, Fugetsu B. Graphene oxide adsorption enhanced by in situ reduction with sodium hydrosulfite to remove acridine orange from aqueous solution. Journal of Hazardous Materials. 2012; 203–204:101–110. doi:10.1016/j.jhazmat.2011.11.097.

[35] Wang F, Haftka J J H, Sinnige T L, Hermens J L M, Chen W. Adsorption of polar, nonpolar, and substituted aromatics to colloidal graphene oxide nanoparticles. Environmental Pollution. 2014; 186:226–233. doi:10.1016/j.envpol.2013.12.010.

[36] Ramesha G K, Vijaya Kumara A, Muralidhara H B, Sampath S. Graphene and graphene oxide as effective adsorbents toward anionic and cationic dyes. Journal of Colloid Interface Science. 2011; 361(1):270–277. doi:10.1016/j.jcis.2011.05.050.

[37] Li Y, Du Q, Liu T, Peng X, Wang J, Sun J. Comparative study of methylene blue dye adsorption onto activated carbon, graphene oxide, and carbon nanotubes. Chemical Engineering Research and Design. 2013; 91(2):361–368. doi:10.1016/j.cherd.2012.07.007.

[38] Wang H J, Zhou A L, Peng F, Yu H, Chen LF. Adsorption characteristic of acidified carbon nanotubes for heavy metal Pb(II) in aqueous solution. Materials Science and Engineering A. 2007; 466(1–2):201–206. doi:10.1016/j.msea.2007.02.097.

[39] Zhang W, Zhou C, Zhou W, Lei A, Zhang Q, Wan Q. Fast and considerable adsorption of methylene blue dye onto graphene oxide. Bulletin of Environmental Contamination and Toxicology. 2011; 87(1):86–90. doi:10.1007/s00128-011-0304-1.

[40] Liu T, Li Y, Du Q, Sun J, Jiao Y, Yang G. Adsorption of methylene blue from aqueous solution by graphene. Colloids Surfaces B Biointerfaces. 2012; 90(1):197–203. doi:10.1016/j.colsurfb.2011.10.019.

[41] Arasteh R, Masoumi M, Rashidi A M, Moradi L, Samimi V, Mostafavi S T. Adsorption of 2-nitrophenol by multi-wall carbon nanotubes from aqueous solutions. Applied Surface Science. 2010; 256(14):4447–4455. doi:10.1016/j.apsusc.2010.01.057.

[42] Zhao G, Li J, Wang X. Kinetic and thermodynamic study of 1-naphthol adsorption from aqueous solution to sulfonated graphene nanosheets. Chemical Engineering Journal. 2011; 173(1):185–190. doi:10.1016/j.cej.2011.07.072.

[43] Kuo CY. Comparison with as-grown and microwave modified carbon nanotubes to removal aqueous bisphenol A. Desalination. 2009; 249(3):976–982. doi:10.1016/j.desal.2009.06.058.

[44] Hu X-J, Liu Y-G, Wang H, Zeng G-M, Hu X, Guo Y-M, Li T-T, Chen A-W, Jiang L-H, Guo F-Y. Adsorption of copper by magnetic graphene oxide-supported β-cyclodextrin: Effects of pH, ionic strength, background electrolytes, and citric acid. Chemical Engineering Research and Design. 2015; 93: 675–683. doi:10.1016/j.cherd.2014.06.002

[45] de la Luz-Asunción M, Sánchez-Mendieta V, Martínez-Hernández A L, Castaño, V M, Velasco-Santos C. Adsorption of phenol from aqueous solutions by carbon nanomate-

rials of one and two dimensions: Kinetic and equilibrium studies. Journal of Nanom-aterials. 2015; 2015:1–15. doi:10.1155/2015/405036.

[46] Elsagh A, Moradi O, Fakhri A, Najafi F, Alizadeh R, Haddadi V. Evaluation of the potential cationic dye removal using adsorption by graphene and carbon nanotubes as adsorbents surfaces. Arabian Journal of Chemistry. 2014; 1–8 doi:10.1016/j.arabjc.2013.11.013.

[47] Yu X, Luo T, Zhang Y, Jia Y, Zhu B, Fu X. Adsorption of Lead (II) on O_2-plasma-oxidized multiwalled carbon nanotubes®: Thermodynamics , kinetics , and desorption. Applied Materials and Interfaces. 2011; 3(7):2585–2593. doi:10.1021/am2004202.

[48] Ahmaruzzaman M. Industrial wastes as low-cost potential adsorbents for the treat-ment of wastewater laden with heavy metals. Advances in Colloid and Interface Science. 2011; 166(1–2):36–59. doi:10.1016/j.cis.2011.04.005.

[49] Wang H, Yuan X, Wu Y, Huang H, Zeng G, Liu Y. Adsorption characteristics and behaviors of graphene oxide for Zn(II) removal from aqueous solution. Applied Surface Science. 2013; 279:432–440. doi:10.1016/j.apsusc.2013.04.133.

[50] Tan P, Sun J, Hu Y, Fang Z, Bi Q, Chen Y. Adsorption of Cu2+, Cd2+ and Ni2+ from aqueous single metal solutions on graphene oxide membranes. Journal of Hazardous Materials. 2015; 297:251–260. doi:10.1016/j.jhazmat.2015.04.068.

[51] Yang S, Li L, Pei Z, Li C, Lv J, Xie J. Adsorption kinetics, isotherms and thermodynam-ics of Cr(III) on graphene oxide. Colloids and Surfaces A: Physicochemical and Engineering Aspects. 2014; 457(1):100-106. doi:10.1016/j.colsurfa.2014.05.062.

[52] Madadrang C J, Kim H Y, Gao G, Wang N, Zhu J, Feng H. Adsorption behavior of EDTA-graphene oxide for Pb(II) removal. ACS Applied Materials and Interfaces. 2012; 4(3):1186-1193. doi:10.1021/am201645g.

[53] Yari M, Norouzi M, Mahvi A H, Rajabi M, Yari A, Moradi O. Removal of Pb(II) ion from aqueous solution by graphene oxide and functionalized graphene oxide-thiol: Effect of cysteamine concentration on the bonding constant. Desalination and Water Treatment. 2015; 1-16. doi:10.1080/19443994.2015.1043953.

[54] Wu S, Zhang K, Wang X, Jia Y, Sun B, Luo T, Meng F, Jin Z, Lin D, Shen W, Kong L, Liu J. Enhanced adsorption of cadmium ions by 3D sulfonated reduced graphene oxide. Chemical Engineering Journal. 2015; 57. 262:1292-1302. doi:10.1016/j.cej.2014.10.092.

[55] Li Y, Du Q, Liu T, Sun J, Jiao Y, Xia Y. Equilibrium, kinetic and thermodynamic studies on the adsorption of phenol onto graphene. Materials Research Bulletin. 2012; 47(8): 1898–1904. doi:10.1016/j.materresbull.2012.04.021.

[56] Ahmed S, Rasul M G, Martens W N, Brown R J, Hashib M A. Heterogeneous photoca-talytic degradation of phenols in waste water: A review on current status and devel-opments. Desalination. 2010; 261(1–2):3–18. doi:10.1016/j.desal.2010.04.062.

[57] Yan H, Tao X, Yang Z, Li K, Yang H, Li A. Effects of the oxidation degree on the adsorption of methylene blue. Journal of Hazardous Materials. 2014; 268:191–198. doi:10.1016/j.jhazmat.2014.01.015.

[58] Mehrizad A, Gharbani P. Decontamination of 4-chloro-2-nitrophenol from aqueous solution by graphene adsorption: Equilibrium, kinetic, and thermodynamic studies. Polish Journal of Environmental Studies. 2014; 23(6):2111–2116. doi:10.15244/pjoes/26779.

[59] Pavagadhi S, Tang A L L, Sathishkumar M, Loh K P, Balasubramanian R. Removal of microcystin-LR and microcystin-RR by graphene oxide: Adsorption and kinetic experiments. Water Research. 2013; 47(13):4621–4629. doi:10.1016/j.watres.2013.04.033.

[60] Nam S-W, Jung C, Li H, Yu M, Flora J R V, Boateng L K. Adsorption characteristics of diclofenac and sulfamethoxazole to graphene oxide in aqueous solution. Chemosphere. 2015; 136:20–26. doi:10.1016/j.chemosphere.2015.03.061.

[61] Wu Z, Zhong H, Yuan X, Wang H, Wang L, Chen X, Zeng G, Wu Y. Adsorptive removal of methylene blue by rhamnolipid-functionalized graphene oxide from wastewater. Water Research. 2014; 67:330–344. doi:10.1016/j.watres.2014.09.026

[62] Bianco A. Graphene: safe or toxic? The two faces of the medal. Angewandte Chemie International Edition. 2013; 52:4986–4997. doi:10.1002/anie.201209099

[63] Chen L, Hu P, Zhang L, Huang S, Luo L, Huang C. Toxicity of graphene oxide and multi-walled carbon nanotubes against human cells and zebrafish. Science China Chemistry. 2012; 55:2209–2216. doi:10.1007/s11426-012-4620-z

[64] Kuilla T, Bhadrab S, Yaoa D, Hoon Kimc N, Bosed S, HeeLee J. Recent advances in graphene based polymer composites. Progress in Polymer Science. 2010; 35:1350–1375. doi:10.1016/j.progpolymsci.2010.07.005

[65] Anirudhan T, Sreekumari S. Adsorptive removal of heavy metal ions from industrial effluents using activated carbon derived from waste coconut buttons. Journal of Environmental Sciences. 2011; 23:1989–1998. doi:10.1016/s1001-0742(10)60515–3

[66] Zhao M, Liu P. Adsorption of methylene blue from aqueous solutions by modified expanded graphite powder. Desalination. 2009; 249:331–336. doi:10.1016/j.desal.2009.01.037

[67] Aguado J, Arsuaga J M, Arencibia A, Lindo M, Gascón V. Aqueous heavy metals removal by adsorption on amine-functionalized mesoporous silica. Journal of Hazardous Materials. 2009; 163:213–221. doi:10.1016/j.jhazmat.2008.06.080

[68] Li X, Zhou H, Wu W, Wei S, Xu Y, Kuang Y. Studies of heavy metal ion adsorption on Chitosan/Sulfydryl functionalized graphene oxide composites. Journal of Colloid and Interface Science. 2015; 448:389–397. doi:10.1016/j.jcis.2015.02.039

[69] Najafi F, Moradi O, Rajabi M, Asif M, Tyagi I. Agarwa S, Gupta V K. Thermodynamics of the adsorption of nickel ions from aqueous phase using graphene oxide and

glycine functionalized graphene oxide. Journal of Molecular Liquids. 2015; 208:106–113. doi:10.1016/j.molliq.2015.04.033

[70] Prola LDT, Machado FM, Bergmann CP, de Souza FE, Gally CR, Lima E C, Adebayo MA, Dias SLP, Calvete T. Adsorption of Direct Blue 53 dye from aqueous solutions by multi-walled carbon nanotubes and activated carbon. Journal of Environmental Management. 2013; 130:166–175. doi:10.1016/j.jenvman.2013.09.003

[71] Xu D, Tan X, Chen C, Wang X. Removal of Pb(II) from aqueous solution by oxidized multiwalled carbon nanotubes. Journal of Hazardous Materials. 2008; 154:407–416. doi:10.1016/j.jhazmat.2007.10.059

[72] Kragulj M, Trickovic J, Kukovecz A, Jovic B, Molnar J, Roncevic S, Kónya Z, Dalmaci-ja B. Adsorption of chlorinated phenols on multiwalled carbon nanotubes. Royal Society of Chemistry Advances. 2015; 5, 24920–24929. doi:10.1039/c5ra03395k

[73] Mauter M S, Elimelech M. Environmental applications of carbon-based nanomateri-als. Environmental Science Technology. 2008; 42:5843–5859. doi:10.1021/es8006904

[74] Zhang X, Cheng C, Zhao J, Ma L, Sun S, Zhao C. Polyethersulfone enwrapped graphene oxide porous particles for water treatment. Chemical Engineering Journal. 2013; 215–216:72–81. doi:10.1016/J.CEJ.2012.11.009

[75] Niyogi S, Bekyarova E, Itkis M E, Mc Williams J L, Hamon M A, Haddon R C. Solution properties of graphite and graphene. Journal American Chemical Society. 2006; 128:7720–7721. doi:10.1021/ja060680r

[76] Esteves IAAC, Cruz FJAL, Müller EA, Agnihotri S, Mota JPB. Determination of the surface area and porosity of carbon nanotube bundles from a Langmuirian analysis of sub- and supercritical adsorption data. Carbon. 2009; 47:948–956. doi:10.1016/j.carbon. 2008.11.044.

[77] Pérez-Ramírez EE, de la Rosa-Álvarez G, Salas P, Velasco-Santos C, Martínez-Hernández A L. Comparison as effective photocatalyst or adsorbent of carbon materials of one, two, and three dimensions for the removal of reactive red 2 in water. Environ-mental Engineering Science. 2015; 32:872–880. doi:10.1089/ees.2015.0083.

[78] Ren X, Chen C, Nagatsu M, Wang X. Carbon nanotubes as adsorbents in environmen-tal pollution management: A review. Chemical Enginering Journal. 2011; 170:395–410. doi:10.1016/j.cej.2010.08.045.

[79] Smith SC, Ahmed F, Gutierrez KM, Rodrigues DF. A comparative study of lysozyme adsorption with graphene, graphene oxide, and single-walled carbon nanotubes: Potential environmental applications. Chemical Engineering Journal. 2014; 240:147–154.

[80] Apul OG, Wang Q, Zhou Y, Karanfil T. Adsorption of aromatic organic contaminants by graphene nanosheets: Comparison with carbon nanotubes and activated carbon. Water Research. 2013; 47:1648–1654. doi:10.1016/j.watres.2012.12.031

[81] Balamurugan K, Subramanian V. Adsorption of chlorobenzene onto (5,5) armchair single-walled carbon nanotube and graphene sheet: Toxicity versus adsorption strength. Journal Physical Chemistry C. 2013; 117:21217–21227. doi:10.1021/jp403646h

Photocatalytic Membranes for Efficient Water Treatment

Alex T Kuvarega and Bhekie B Mamba

Additional information is available at the end of the chapter

Abstract

Membrane processes which combine the physical separation through filtration and pollutant degradation or antibacterial properties achieved by photocatalysis in a single unit are gaining popularity as wastewater treatment alternatives. There has been considerable progress in the development of photocatalytic membranes through incorporation of metal-oxide photocatalysts to enhance the performance of the membranes. An optimum amount of the photocatalyst should be incorporated into the membrane in order to realise reasonable photocatalytic activity with minimal consequences on water flux. Besides TiO_2 loading, membrane performance is also affected by light intensity and irradiation time. This chapter highlights some of the recent progresses in photocatalytic membrane fabrication, reactor configuration and membrane application in disinfection and pollutant removal from wastewater.

Keywords: titanium dioxide, photocatalytic membrane, photodegradation, membrane fouling, water treatment

1. Introduction

The past few decades have seen membrane-based technologies gaining global popularity largely due to the high separation efficiencies, relatively low costs, small footprint and ease of operation. A membrane is a physical porous barrier between two phases that allows substances to be selectively transported through it. The efficiency and effectiveness of a

membrane as a separation barrier depends on a number of factors, including the type of membrane, the pore structure and sizes, polarity, roughness, hydrophilicity as well as its mechanical properties [1].

In the water sector, membranes have found applications as physical barriers to specific size ranges of water contaminants. They act as filters or selective sieves, removing contaminants that are larger than the membrane pore size and allowing smaller contaminants and water molecules to pass through [2]. However, the use of membranes is without drawbacks. Membrane separation efficiency is compromised mainly due to two effects: concentration polarisation and membrane fouling. Concentration polarisation is a result of increase in concentration of the rejected suspended or dissolved solids near the membrane surface. Membrane fouling is a result of irreversible deposition of suspended or dissolved solids on the external membrane surface or membrane pores compromising the overall performance of the membrane. Once fouled, complex and often expensive cleaning procedures that affect the continuous operation of the membrane filtration process, such as forward and reverse flushing, backwashing, air scouring and back permeation, need to be performed. Although membrane systems may incur higher capital or operational costs than conventional processes (such as evaporation, use of activated carbon, deep-bed filtration, coagulation, sedimentation or chemical treatment), they are generally able to achieve superior quality water, while imposing a smaller footprint at the plant level. Fouling remediation is currently receiving much research attention in an effort to mitigate these challenges through modification of traditional membranes to improve their antifouling properties. Recently, a whole new field of study focused on membrane modification has emerged. One such innovation is the modification of membrane characteristics with nanomaterials to fine-tune performance for specific pollutant types or improve resistance to fouling.

2. Classification of membranes

Membrane technology has developed to a point where there are a variety of membranes tailored for specific contaminants and even different membrane configurations and technologies designed for specific industries such as milk production, beer production, desalination, solvent separation and material regeneration. Depending on their pore sizes, which determine their selectivity, membranes can be classified as microfiltration (MF), ultrafiltration (UF), nanofiltration (NF) and reverse osmosis (RO) membranes [3] (**Table 1**). The so-called nanoporous membranes consist of a film in which molecules are transported through solution-diffusion mechanism. Transport through such membranes is driven by pressure, concentration or potential gradient across the membrane. Nanoporous membranes are typically used for processes such as reverse osmosis (RO) and, more recently, forward osmosis (FO). Nanofiltration (NF) membranes have very small pores (0.1–1 nm). Microporous membranes are used for other pressure-driven processes such as microfiltration (MF) and ultrafiltration (UF). MF membranes can separate particles between 0.1 and 10 μm, whereas UF membranes can remove particles of size range 1–100 nm [1,4].

Filtration mode	Particle capture size	Typical contaminant removed	Typical operating pressure ranges
Microfiltration (MF)	0.1 to −10 μm	Suspended solids, bacteria, protozoa	0.1–2 bar
Ultrafiltration (UF)	0.001–0.1 μm	Colloids, proteins, polysaccharides, most bacteria, viruses (partially)	1–5 bar (cross-flow) 0.2–0.3 bar (dead-end and submerged)
Nanofiltration (NF)	0.0001–0.001 μm	Viruses, natural organic matter, multivalent ions (including water hardness)	5–20 bar
Reverse osmosis (RO)	<0.0001 μm	Almost all impurities (including monovalent ions)	10–100 bar

Table 1. Operational characteristics of membranes.

3. Photocatalytic membranes

Materials in which one or more phases with nanoscale dimensions are embedded in another matrix phase are called nanocomposites. The motive behind fabricating such materials is to create synergies between the various phase constituents to result in smart materials capable of meeting or even exceeding the intended design expectations [5]. Membranes have been functionalised through incorporation of engineered nanoparticles deposited on their surfaces or embedded into their matrices to result in tailored properties such as capability to bind specific contaminants or catalyse degradation reactions. The resulting mixed matrix membranes (MMMs) play a multifunctional role in water treatment. Variables such as the nanomaterial loading, the matrix material, degree of particle dispersion, size, shape and orientation of the nanoscale phase as well as interactions between the phases have a bearing on the overall properties of the hybrid material. In photocatalytic membranes, nanoscale inorganic photocatalysts are embedded in a membrane matrix to enhance the properties of the resultant polymer.

The first attempts at combining photocatalysis with membrane technology were aimed at achieving the separation and reuse of the photocatalyst nanoparticles from the reactor slurry. However, the approach faced the usual problems of membrane fouling, photocatalyst deactivation and nanoparticle agglomeration. This stirred interest in the development of stand-alone hybrid photocatalysis/filtration water treatment processes exhibiting both photocatalytic and separation efficiency. The advantages of such innovations include the absence of any requirement for post- or pre-treatment stage, an attractive feature for upscaling the technology in membrane wastewater treatment applications [6].

Among various photocatalysts, TiO$_2$ has been proven to be an attractive and promising semiconductor catalyst in heterogeneous photocatalysis and in advanced oxidation processes owing to its stability, low cost, availability, non-toxicity, unique photocatalytic efficiency and its promise for applications in water and wastewater treatment [7]. Several methods have recently been developed and optimised for the fabrication of TiO$_2$-based photocatalytic membranes. Among them are dip-coating or spin-coating of porous supports using TiO$_2$ precursor sols, filtration of TiO$_2$ nanofibers through glass filters followed by hot pressing or liquid phase pressurisation, hydrothermal growth of free-standing TiO$_2$ nanowire membranes, anodisation of titanium films sputtered on to stainless steel substrates, embedding TiO$_2$ nanoparticles into the polymeric membranes matrix, electrospinning TiO$_2$ fibres or flat membranes by recasting, development of TiO$_2$ layers with rapid atmospheric plasma spray coating and the fabrication of free-standing and flow-through TiO$_2$ nanotube membranes among others [6].

Photocatalytic membranes can be broadly classified into four categories, based on the location of the nanoparticles on the membrane [8] (**Figure 1**):

1. Conventional nanocomposites

2. Thin-film nanocomposites (TFC)

3. Thin film nanocomposite with nanocomposite substrate

4. Surface-located nanocomposites
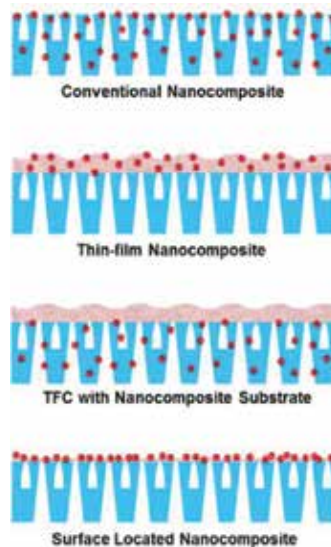
Figure 1. Typical type of nanocomposite membranes (The red spheres represent photocatalyst nanoparticles) (Adapted from [8], with permission from Elsevier. Copyright © 2014 Elsevier B.V.).

3.1. TiO$_2$—polymer membranes

Polymer membranes have gained popularity for use in wastewater treatment and water purification. A number of polymers have successfully been used as supports for photocatalysts, and these include polymers such as polyamide, polyvinylidene fluoride (PVDF), polysulfone (PSf), polyethersulfone (PES), sulfonated polyethersulfone (SPES), polyurethane (PU), polyethylene terephthalate (PET), polyester, polyacrylonitrile (PAN) and polytetrafluoroethylene (PTFE) [4,9].

The photocatalyst nanoparticles can either be deposited onto the membrane surface or dispersed in the polymer dope solution prior to membrane casting. Several other methods have been proposed and tried for the fabrication of polymeric and ceramic photocatalytic membranes (**Figure 2**). The overall objective is to incorporate the photocatalyst onto the membrane to impart some photocatalytic activity to the membrane.
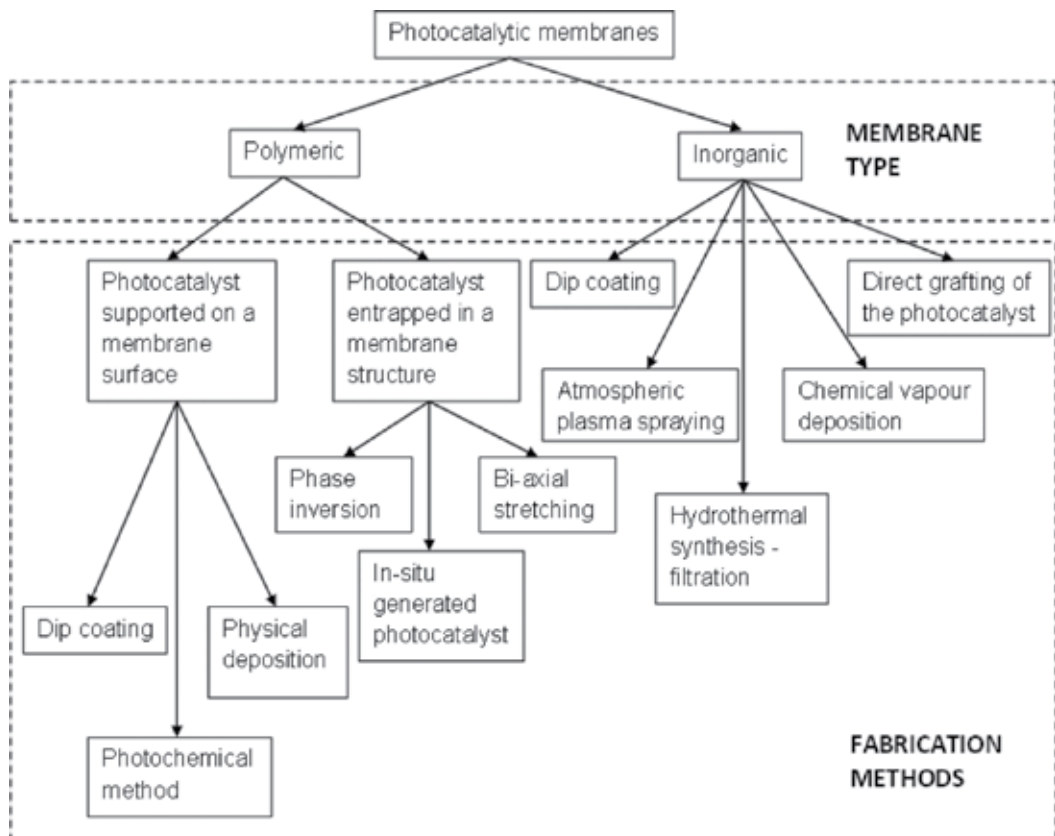
Figure 2. Methods for the preparation of photocatalytic membranes.

3.1.1. Surface-located TiO₂ polymer membranes

3.1.1.1. Dip-coating or self-assembly

Surface-located TiO_2 polymer membranes are prepared through dip-coating or self-assembly [10], chemical or photochemical processes based on chemical grafting and photopolymerisation [11] and physical deposition of a TiO_2 layer via ultrafiltration of a TiO_2 suspension through a polymer membrane [12]. In the dip-coating or self-assembly method, a layer of TiO_2 is coated on the surface of a membrane through dipping the membrane into a sol–gel TiO_2 slurry solution, followed by drying and pressing with a compressed gas. The TiO_2 particles tend to self-assemble on the membrane due to the anchoring effect of the functional groups (e.g. carbonyl, sulfone) located on the membrane surface or through hydrogen bonding of the membrane surface groups and TiO_2. Kim et al. prepared a hybrid thin-film composite (TFC) membrane by self-assembly of TiO_2 nanoparticles through coordination and H-bonding interaction with the COOH functional group of aromatic polyamide thin-film layer. The TFC membrane with self-assembled TiO_2 nanoparticles showed photocatalytic activity towards the destruction of microorganisms. Such membranes can be used to reduce membrane biofouling [13]. In another study, reverse osmosis (RO) membranes composed of aromatic polyamide thin films underneath titanium dioxide (TiO_2) nanosized particles were fabricated by a self-assembly process. Sol–gel colloidal TiO_2 were self-assembled on a TFC aromatic polyamide membrane containing COOH groups along its surface. The TiO_2 hybrid membrane was examined for its photocatalytic efficiency for the destruction of *Escherichia coli* (*E. coli*) as a model bacterium under UV light illumination. The photocatalytic bactericidal destruction was remarkably higher for the TiO_2 hybrid membrane under UV illumination [14]. Bae and Tak anchored sol–gel synthesised nanosized TiO_2 on commercial polyethersulfone microfiltration (MF) membranes with sulfonic acid ($SO^{3-}H^+$) groups generated on the membrane surfaces through sulfonation. The fouling mitigation effects of the membrane were investigated over a mixed liquor membrane bioreactor (MBR) system. Results showed that membrane fouling could be considerably reduced by the introduction of TiO_2 nanoparticles on the surface of the membranes. This can be attributed to the higher hydrophilicity of these membranes, which facilitated easy dislodging of adsorbed foulants by shear force than those on neat membranes [15]. One major challenge with the dip-coating technique is the risk of nanoparticle leaching during continuous operation or use of high pressure. The membrane performance thus deteriorates with time.

3.1.1.2. Chemical grafting and photopolymerisation

In this method, appropriate monomers containing the photocatalyst to be immobilised and an initiator are photo-irradiated on a support. In a study by Razmjou et al., commercial TiO_2 nanoparticles were functionalised by aminopropyltriethoxysilane (APTES) to initiate coupling with PES in the dope solution, prior to casting and precipitation, to form hollow fibre membranes. Initial pure water flux was significantly enhanced while there was a small improvement in the fouling performance in comparison with the control. The modified hollow fibre membrane showed increased glass transition temperature, membrane porosity and pore

size, stiffness and hydrophilicity, whereas tensile strength and elongation at break decreased [16].

In a chemical grafting and photopolymerisation study, TiO_2 was added to a suitable acrylic acid monomer and sonicated for about 20 min to facilitate the interaction between TiO_2 and acrylic acid. Ethylene glycol was then added as a cross-linker, and potassium persulfate (1 wt.%) as an initiator. The PVDF support membrane was then dipped in the polymerisation solution for 2 min and placed on a glass plate. The grafted membranes were irradiated with UV light (160 W) for 15 min. The covalent attachment of TiO_2 to PAA network in the membrane composite resulted in improved fouling resistance due to the hydrophilic functional groups of PAA and the photocatalytic effect of TiO_2 that reduced the hydrophobic adsorption between the whey protein and the modified membrane surface [17].

3.1.1.3. Physical deposition

In this method, the photocatalyst is physically deposited on the membrane surface through pressure-driven filtration of the photocatalyst suspension slurry. A photocatalyst cake builds on the surface of the membrane, the thickness of which can be controlled by varying the filtration time and operational pressure [18]. Bai et al. synthesised TiO_2 nanothorn spheres and assembled them on a piece of cellulose acetate polymer membrane through compression on a dead-end filtration set-up. The resulting TiO_2 nanothorn membrane was reported to exhibit a hierarchical porous structure, which gave a high water flux and a multifunctional TiO_2 surface for mitigation of membrane fouling [12].

3.1.2. TiO$_2$-entrapped polymer membranes

3.1.2.1. Phase inversion

Phase inversion is by far the most common and popular method for synthesising nanoparticle-entrapped membranes. In this method, the preformed photocatalyst is added to the polymer dope solution to form a homogenous solution. The solution is then cast on a glass plate and immersed in a coagulation bath to effect gelation. In the dry method, the solvent is allowed to evaporate until gelation is complete after casting [8]. Phase inversion membranes may be fabricated in different forms, such as hollow fibres or flat sheets, which can be incorporated modules designed to produce optimal hydrodynamic conditions for separation (**Figure 3**). TiO_2-embedded membranes have been reported to show improved membrane properties such as porosity, wettability, permeability and antifouling propensity. Application of photocatalytic membranes requires irradiation of the membrane to activate the photocatalyst. However, sulfone group containing membranes (PES and PSf) are generally sensitive to UV radiation, and irradiation may lead to destruction of some membrane bonds. The least affected membranes are PTFE and PVDF [19].
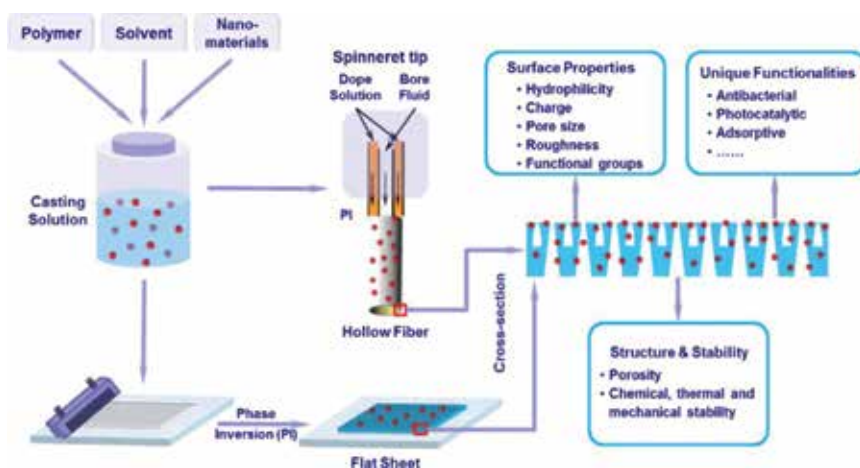
Figure 3. Fabrication of conventional nanocomposite membranes through the PI process and the main effects of nano-fillers on final products. (Adapted from [8], with permission from Elsevier. Copyright © 2014 Elsevier B.V.).

Although embedding nanoparticles onto membranes eliminate the need for post-treatment removal of the nanoparticles, one major limitation of immobilising nanoparticles onto membrane supports is the reduction in the available surface area of the nanoparticles due to coverage by the polymer phase material.

3.1.2.2. Biaxial stretching

Biaxial stretching is a physical method where membranes are stretched to modify their properties in an effort to improve overall membrane performance. This modification indu-ces significant and permanent membrane pore deformation, which may result in improved porosity [20]. In a typical study, catalytic membranes were fabricated via biaxial stretching of a polytetrafluoroethylene (PTFE) extrusion containing 2 wt.% of anatase TiO_2. The catalyst particles were uniformly distributed throughout the membrane. The photocatalytic mem-brane could degrade organic solutes in ultra-pure water [21].

3.1.2.3. In-situ generated photocatalyts

The formation of mixed matrix membranes through in-situ generation of the desired nano-materials is a relatively new innovation in membrane technology. The main advantages of in-situ generation of nanoparticles include control over nanoparticle–membrane matrix compatibility, nanomaterial loading capacity, water flux as well as selectivity [22].

Luisa Di Vona et al. successfully synthesised a sulfonated poly(ether ether ketone) (SPEEK) nanocomposite membrane via an in situ mixed sol–gel process in which titanium butoxide/2,4-pentanedione in DMAc was added to a SPEEK solution and the solvents allowed to evaporate at 120°C. The resulting composite membranes were flexible and transparent, and showed improved mechanical and thermal properties as well as hydrolytic stability [23]. In another study, a mixed matrix membrane was fabricated through in situ polymerisation of

titanium isopropoxide in polyvinyl acetate, PVAc. The titanium alkoxide can cross-link with PVAc through a transesterification reaction. The strong chemical interaction prevents phase separation and improves TiO_2 dispersion within the PVAc matrix. One major drawback is that the Ti-based clusters contain some residual isopropyl groups and the TiO_2 phase may show limited crystallinity [24].

3.2. TiO_2-based ceramic membranes

Ceramic membranes are currently receiving significant attention as candidates for water decontamination because of their various properties, including sufficiently high mechanical strength, thermal stability, high flux, lower life cycle cost and resistance to corrosive environments. Depending on their pore diameters, they can be classified as MF, UF, NF, RO, pervaporation (PV), gas separation (GS) or ceramic membrane reactors (CMR). Oxides such as Al_2O_3, TiO_2, ZrO_2, SiO_2 and combinations thereof are some of the common ceramic membrane fabrication materials [25].

Ceramic membranes are fabricated through methods such as dip-coating, where a photocatalyst is deposited on a porous ceramic support (e.g. SiO_2, Al_2O_3, ZrO_2, $Al_2O_3/SiO_2/ZrO_2$, SiN/SiC, Al_2O_3/SiC), and hydrothermal synthesis followed by filtration and calcination, where a suspension of hydrothermally synthesised TiO_2 is filtered through a glass fibre filter, dried and calcined at high temperature. Another method is grafting of TiO_2 onto ceramic membranes, where TiO_2 nanotubes are grafted onto channels of ceramic membranes such as alumina (Al_2O_3) [26]. Other methods such as chemical vapour deposition (CVD) and atmospheric plasma spraying (APS) have also been used to fabricate ceramic membranes [27,28].

3.3. Polymeric versus ceramic photocatalytic membranes

Ceramic membranes generally have many advantages compared to polymeric membranes from an application point of view, mainly because of their superior thermal properties and resistance to corrosion by harsh chemicals. With polymeric membranes, there are some risks associated with membrane degradation under extreme chemical conditions. Ceramic membranes are also less prone to membrane fouling because of their hydrophilic surfaces. Ceramic membranes generally have relatively uniform pore structures and thus significantly higher flux and lower membrane resistance compared to polymeric membranes. Unlike polymeric membranes which are soft and rather difficult to analyse by most physicochemical characterisation techniques, the composition of ceramic membranes can be well-characterised. Ceramic membranes have a lower membrane resistance and therefore require a lower pressure to produce the same volume of water as the polymeric ones. They also have a longer lifespan. However, the capital costs are huge [10].

Anchoring photocatalytic nanoparticles on commercially available ceramic membranes requires appropriate anchor sites on the membrane in order to form bonds between the nanoparticles and the ceramic support. This is currently a big hindrance to ceramic membrane modification attempts.

4. Photocatalytic membrane reactor configurations

A number of engineering designs and configurations have been proposed for possible scaling up of the photocatalytic membrane technology. The photocatalytic membrane reactors can be classified into four different configurations based on the stage at which the membrane will be used in the water treatment train (**Figure 4**):

a. Slurry photocatalytic reactor followed by a membrane filtration unit,

b. Ceramic or polymeric membrane submerged in a slurry photocatalytic reactor,

c. Membrane placed inside a photocatalyst-coated (TiO_2) photoreactor,

d. Photocatalytic membranes (pure TiO_2 or TiO_2-mixed matrix membranes).
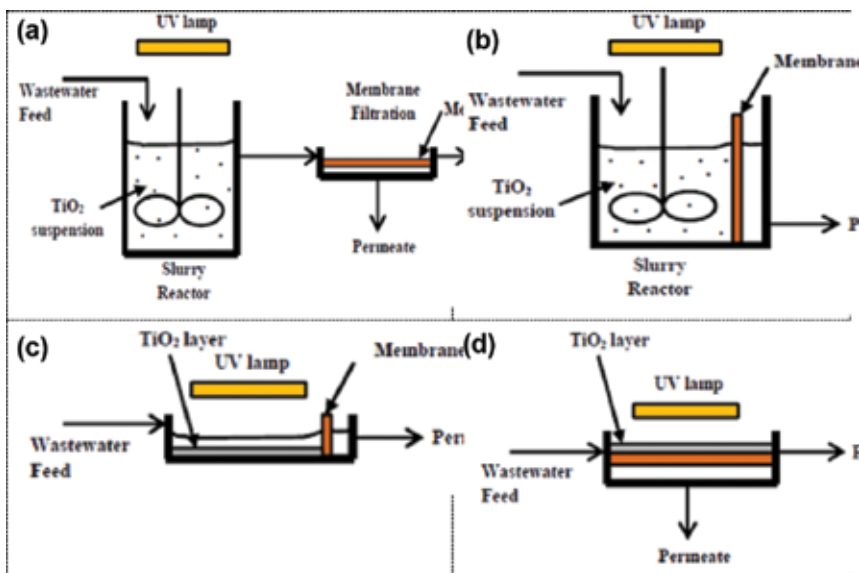
Figure 4. Photocatalytic membrane reactor configurations. (a) Slurry reactor followed by a membrane filtration unit; (b) Submerged membrane in a slurry reactor; (c) Submerged membrane in TiO_2-coated reactor; (d) Photocatalytic membrane. (Adapted from [9], with permission from Elsevier. Copyright © 2014 Elsevier B.V.).

While a number of these configurations have been put to test, the photocatalytic membrane is currently receiving immense research focus because of its potential advantages over the other configurations. Some of its advantages include the duality of physical separation during membrane filtration, and degradation of organics and bacteria, all achieved in a single unit. Generally, photocatalytic membranes tend to outperform conventional membranes in terms of reducing membrane fouling and improving permeate quality [6,18].

Despite the potential advantages using these different reactor configurations, the research on a combined use of photocatalysis and membranes is still not sufficiently developed.

5. Application of TiO$_2$ photocatalytic membranes

Photocatalytic membranes have evolved as promising innovations for providing sustainable quality water to end users. The use of multimembrane systems or coupling membrane separation with other biological, chemical or physical treatments is envisaged to have a huge positive impact on the provision of quality water at low cost and lower energy consumption. TiO$_2$-based catalytic membranes have found applications in a wide range of wastewater and water treatment applications.

5.1. Disinfection

Membrane biofouling is the deposition of microorganisms and microbial products on the surface of a membrane. Incorporation of TiO$_2$ into polymeric or ceramic membranes has been reported to mitigate membrane biofouling. In a study on self-assembly of TiO$_2$ nanoparticles on hybrid thin-film composite (TFC) membrane, dramatic photoactivity for bactericidal degradation of *E. coli* under UV light illumination was observed [13]. Ma et al. prepared Ag–TiO$_2$/hydroxyapatite bioceramic composite membrane for membrane separation and photocatalytic bacterial inactivation (*E. coli*) using a sol–gel method followed by calcination. *E. coli* inactivation was evaluated under UV illumination, and a higher inactivation performance was achieved compared to dark conditions. The permeate flux decline pattern of membrane however remained the same under UV irradiation and in the dark [29]. Liu et al. deposited Ag nanoparticles on electrospun TiO$_2$ nanofibers to form a membrane. The group reported irreversible bacterial cell damage under UV light irradiation. A 99.9% bacteria inactivation and 80.0% dye degradation under solar irradiation was reported within 30 min [30]. In another application study, Damodar et al. embedded TiO$_2$ on PVDF membranes through the phase inversion method and tested the membrane for its antibacterial property by using *E. coli*, photocatalytic activity using Reactive Black 5 (RB5) dye and antifouling properties using 1% BSA solution. The membrane showed enhanced flux and permeability properties. Almost 100% of *E. coli* was degraded by 4% TiO$_2$/PVDF membrane after 1 min of UV irradiation. A faster RB5 colour removal rate was also reported, while the self-cleaning study showed a lower fouling resistance for the 2% TiO$_2$/PVDF membrane [31]. Rahimpour et al. loaded 4% TiO$_2$ on PVDF/Sulfonated PES blend membrane through a phase inversion method and observed dramatic antibacterial (*E. coli*) effect under 1 h of UV irradiation, which the inhibition rings on the composite membrane as evidence of the antibacterial effect against *E. coli*. The photocatalytic bactericidal effect was attributed to the presence of reactive oxygen species like O$_2$ radicals, H$_2$O$_2$ and OH radicals generated by the entrapped TiO$_2$ upon UV illumination [32].

5.2. Removal of pollutants

By and large, removal of pollutants in water is the widely used application of photocatalytic membranes. A number of studies have recently emerged on batch and reactor scale application of photocatalytic membranes for fouling mitigation through photodegradation of foulants. A PVDF/TiO$_2$ mixed matrix UF membrane was reported to show enhanced performance for the removal of methylene blue (MB) due to the extra adsorption sites provided by the

embedded TiO_2 nanoparticles [33]. In a similar study, Hua et al. fabricated a PVDF membrane with self-assembled TiO_2 nanoparticles, and the permeability and antifouling ability of self-assembled membranes were significantly improved [34]. A multifunctional polyurethane (PU)/TiO_2/fly ash composite membrane fabricated through electrospinning showed enhanced adsorption of heavy metals (Pb, Hg), enhanced MB dye removal, superior water flux and antibacterial properties attributed to the photocatalytic properties of TiO_2 as well as the adsorptive property of fly ash [35]. Bae and Tak observed a positive effect of the presence of dip-coated and entrapped TiO_2 on membrane antifouling in a membrane bioreactor (MBR) [36]. Cao et al. observed remarkable improvement in the antifouling property of PVDF membrane with different sizes of nanosized TiO_2 particles, with smaller particles having greater effect than the larger ones [37]. Kim et al. self-assembled TiO_2 nanoparticles on carboxylic acid groups on the surface of a thin-film composite (TFC) polymer membrane. The membrane was observed to mitigate biofouling through photodegradation effect under UV radiation [13].

A ceramic TiO_2/Al_2O_3 composite membrane was prepared using a sol–gel technique and applied in a filtration/photodegradation membrane reactor under UV radiation. UV irradiation enhanced the wettability of the ceramic membrane, and a stable water flux was rapidly archived. 25% of Acid Orange dye was degraded within several milliseconds. The membrane could easily be cleaned by irradiating the membrane surface under static conditions [38]. Syafei et al. observed greater flux decline with TiO_2-coated alumina/titania/zirconia (ATZ) ultrafiltration ceramic membrane disk under UV irradiation than with uncoated membrane in the treatment of natural organic matter (NOM). It was postulated that UV irradiation alters the molecular weight distribution of humic materials to below1 kDa, which facilitates their attachment to TiO_2 nanoparticles [39]. In a similar approach, TiO_2 nanoparticles were coated on Al_2O_3 nanoparticles through solid-state sintering method. The resulting membrane was reported to show enhanced photocatalytic properties and reduced membrane fouling in oil emulsion wastewater treatment [40]. The effect of UV irradiation on membrane performance was evaluated on TiO_2-entrapped and self-assembled PES membranes. The TiO_2-coated membranes showed a uniform distribution of the TiO_2 nanoparticles on the membrane surface. The non-irradiated membranes showed a flux decline while the irradiated membranes exhibited higher fluxes and superior antifouling properties. It was then concluded that dip-coating TiO_2 on PES membrane surface is a superior technique to minimise membrane fouling than entrapping the TiO_2 [41]. Similar observations were reported by other researchers on TiO_2/PES, TiO_2/poly(styrene-alt-maleic anhydride)/poly(vinylidene fluoride) (TiO_2/SMA/PVDF) and TiO_2/PES/polyimide (PI) composite membranes, using polyethylene glycol-5000 [42] and Bovine serum albumin (BSA) [34,43]. In a study by Lin et al., it was concluded that the effectiveness of photodegradation of 1,2-dichlorobenzene was higher with TiO_2 immobilised on low-density polyethylene (LDPE) support than on quartz support using four UV lamps of 15 W each [44].

Inasmuch as progress has been realised in the application of photocatalytic membranes for water decontamination, further research is needed to investigate the combined effects of water

chemistry, nature of nanoparticles, loading capacity and the photocatalyst incorporation conditions on membrane performance.

6. Conclusions and perspectives

As engineering technology innovation continues to grow, new opportunities and prospects to solve the ever-increasing environmental challenges continue to emerge. Innovative techniques for the integration of photocatalyst in both polymeric and ceramic membranes need to be continuously developed in order to open new insights into the development of functional membranes capable of mitigating fouling with minimal consequences on water flux. Polymer and ceramic membranes have both been used as TiO_2 supports, though the stability of polymeric membranes under UV irradiation still requires further investigation. Commercialisation of photocatalytic membranes will depend on the design of the membrane reactors as well as optimisation of the radiant flux on the membrane surface during the short time frame that the polluted water filters through the membrane. The use of solar light as an energy source instead of UV light could reduce the cost of the filtration process. This requires band-tuning of the TiO_2 through doping with non-metals or metals to shift the absorption edge to the visible region. Currently, the membrane fouling mechanisms are not fully understood. Another challenge is possible leaching of the entrapped photocatalyst particles into the permeate solution during the filtration process. Given the present knowledge gaps regarding possible health and ecological hazards of nanoparticles' aquatic environment, caution should be exercised to avoid discharge of the particles into the water stream.

Author details

Alex T Kuvarega[*] and Bhekie B Mamba

*Address all correspondence to: kuvarat@unisa.ac.za

University of South Africa, Nanotechnology and Water Sustainability Research Unit, College of Science, Engineering and Technology, Florida Science Campus, Johannesburg, South Africa

References

[1] Ahmed FE, Lalia BS, Hashaikeh R. A review on electrospinning for membrane fabrication: challenges and applications. Desalination. 2015; 356: 15–30. DOI:10.1016/j.desal.2014.09.033

[2] Meng S, Greenlee LF, Shen YR, Wang EG. Basic science of water: challenges and current status, towards a molecular picture. Nano Res. DOI: 10.1007/s12274-015-0822-y

[3] UnionEuropean. Membrane technologies for water applications: highlights from a selection of European research projects. European Union. 2010; DOI: 10.2777/25163

[4] Bet-moushoul E, Mansourpanah Y, Farhadi KH, Tabatabaei M. TiO$_2$ nanocomposite based polymeric membranes: a review on performance improvement for various applications in chemical engineering processes. Chem Eng J. 2016; 283: 29–46. DOI: 10.1016/j.cej.2015.06.124

[5] Sealy C. Cleaning up water on the nanoscale. Nano Today. 2013; 8: 337–338. DOI: 10.1016/j.nantod.2013.06.004

[6] Romanos GE, Athanasekou CP, Likodimos V, Aloupogiannis P, Falaras P. Hybrid ultrafiltration/photocatalytic membranes for efficient water treatment. Ind Eng Chem Res. 2013; 52: 13938–13947. DOI: 10.1021/ie303475b

[7] Shi F, Ma Y, Ma J, Wang P, Sun W. Preparation and characterization of PVDF/TiO2 hybrid membranes with different dosage of nano-TiO$_2$. J Membr Sci. 2012; 389: 522–531. DOI: 10.1016/j.memsci.2011.11.022

[8] Yin J, Deng B. Polymer-matrix nanocomposite membranes for water treatment. J Membr Sci. 2015; 479: 256–275. DOI: 10.1016/j.memsci.2014.11.019

[9] Leong S, Razmjou A, Wang K, Hapgood K, Zhang X, Wang H. TiO$_2$ based photocatalytic membranes: a review. J Membr Sci. 2014; 472; 167–184. DOI: 10.1016/j.memsci.2014.08.016

[10] Kim J, Van der Bruggen B. The use of nanoparticles in polymeric and ceramic membrane structures: review. Environ. Poll. 2010; 158: 2335–2349. DOI: 10.1016/j.envpol.2010.03.024

[11] Barni B, Cavicchioli A, Riva E, Zanoni L, Bignoli F, Bellobono IR, Gianturco F, De Giorgi A, Muntau H, Montanarella L, Facchetti S, Castellano L. Pilot-plant-scale photodegradation of phenol in aqueous solution by photocatalytic membranes immobilizing titanium dioxide (PHOTOPERM® process). Chemosphere. 1995; 30: 1861–1874. DOI: 10.1016/0045-6535(95)00067-I

[12] Bai H, Liu Z, Sun DD. Hierarchically multifunctional TiO$_2$ nano-thorn membrane for water purification. Chem Commun. 2010; 46: 6542–6544. DOI: 10.1039/C0CC01143F

[13] Kim SH, Kwak SY, Sohn BH, Park TH. Design of TiO$_2$ nanoparticle self-assembled aromatic polyamide thin-film-composition (TFC) membrane as an approach to solve biofouling problem. J Membr Sci. 2003; 211: 157–165. DOI: 10.1016/S0376-7388(02)00418-0

[14] Kwak SY, Kim SH. Hybrid organic/inorganic reverse osmosis (RO) membrane for bactericidal anti-fouling 1. Preparation and characterization of TiO$_2$ nanoparticle self-assembled aromatic polyamide thin-film-composite (TFC) membrane. Environ. Sci Technol. 2001; 35: 2388–2394. DOI: 10.1021/es0017099

[15] Bae TH, Tak TM. Preparation of the TiO_2 self-assembled polymeric nanocomposite membranes and examination of their fouling mitigation effects in a membrane bioreactor system. J Membr Sci. 2005; 266: 1–5. DOI: 10.1016/j.memsci.2005.08.014

[16] Razmjou A, Holmes ARL, Li H, Mansouri J, Chen V. The effect of modified $Ti\,O_2$ nanoparticles on polyethersulfone ultrafiltration hollow fiber membranes. Desalination. 2012; 287: 271–280. DOI: 10.1016/j.desal.2011.11.025

[17] Madaeni SS, Zinadini S, Vatanpour V. A new approach to improve antifouling property of PVDF membrane using in situ polymerization of PAA functionalized TiO_2 nanoparticles. J Membr Sci. 2011; 380: 155–162. DOI: 10.1016/j.memsci.2011.07.006

[18] Molinari R, Palmisano L, Drioli E, Schiavello M. Studies on various reactor configurations for coupling photocatalysis and membrane processes in water purification. J Membr Sci. 2002; 206: 399–415. DOI: 10.1016/S0376-7388(01)00785-2

[19] Chin SS, Chiang K, Fane AG. The stability of polymeric membranes in a TiO_2 photocatalysis process. J Membr Sci. 2006; 275: 202–211. DOI: 10.1016/j.memsci.2005.09.033

[20] Morehouse JA, Taylor DL, Lloyd DR, Lawler DF, Freeman BD, Worrel LS. The effect of uni-axial stretching on the roughness of microfiltration membranes. J Membr Sci. 2006; 280: 712–719. DOI: 10.1016/j.memsci.2006.02.027

[21] Morris RE, Krikanova E, Shadman F. Photocatalytic membrane for removal of organic contaminants during ultra-purification of water. Clean Technol Environ Policy. 2004; 6: 96–104. DOI: 10.1007/s10098-003-0198-7

[22] Kotte MR, Choi M, Diallo MS. A facile route to the preparation of mixed matrix polyvinylidene fluoride membranes with in-situ generated polyethyleneimine particles. J Membr Sci. 2014; 450: 93–102. DOI: 10.1016/j.memsci.2013.08.025

[23] Luisa Di Vona M, Ahmed Z, Bellitto S, Lenci A, Traversa E, Licoccia S. SPEEK-TiO_2 nanocomposite hybrid proton conductive membranes via in situ mixed sol–gel process. J Membr Sci. 2007; 296: 156–161. DOI: 10.1016/j.memsci.2007.03.037

[24] Lantelme B, Dumon M, Mai C, Pascault JP. In situ polymerization of titanium alkoxides in polyvinylacetate. J Non-Cryst Solids. 1996; 194: 63–71. DOI: 10.1016/0022-3093(95)00498-X

[25] Xing W, Fan Y, Jin W. Application of ceramic membranes in the treatment of water. In Duke M, Zhao D, Semiat R (eds), Functional Nanostructured Materials and Membranes for Water Treatment. Wiley-VCH Verlag GmbH & Co. KGaA, 2013. ISBN: 978-3-527-32987-8

[26] Basile A. (Ed). Handbook of membrane reactors: Volume 2 Reactor types and industrial applications. Woodhead Publishing, Cambridge, 2013. ISBN: 978-0-85709-415-5

[27] Athanasekou CP, Romanos GE, Katsaros FK, Kordatosb K, Likodimos V, Falaras P. Very efficient composite titania membranes in hybrid ultrafiltration/photocatalysis

water treatment processes. J Membr Sci. 2012; 392–393: 192–203. DOI: 10.1016/j.memsci. 2011.12.028

[28]   Lin Y-F, Tung K-L, Tzeng Y-S, Chen J-H, Chang K-S, Rapid atmospheric plasma spray coating preparation and photocatalytic activity of macroporous titania nanocrystalline membranes. J Membr Sci. 2012; 389: 83–90. DOI: 10.1016/j.memsci.2011.10.018

[29]   Ma N, Fan X, Quan X, Zhang Y. Ag-TiO$_2$/HAP/Al$_2$O$_3$ bioceramic composite membrane: fabrication, characterization and bactericidal activity. J Membr Sci. 2009; 336: 109–117. DOI: 10.1016/j.memsci.2009.03.018

[30]   Liu L, Liu Z, Bai H, Sun DD. Concurrent filtration and solar photocatalytic disinfection/degradation using high-performance Ag/TiO$_2$ nanofiber membrane. Water Res. 2012; 46: 1101–1112. DOI: 10.1016/j.watres.2011.12.009

[31]   Damodar RA, You SJ, Chou HH. Study the self-cleaning, antibacterial and photocatalytic properties of TiO$_2$ entrapped PVDF membranes. J Hazard Mater. 2009; 172: 1321–1328. DOI: 10.1016/j.jhazmat.2009.07.139

[32]   Rahimpour A, Jahanshahi M, Rajaeian B, Rahimnejad M. TiO$_2$ entrapped nanocomposite PVDF/SPES membranes: preparation, characterization, antifouling and antibacterial properties. Desalination. 2011; 278: 343–353. DOI: 10.1016/j.desal. 2011.05.04

[33]   Ngang HP, Ooi BS, Ahmad AL, Lai SO. Preparation of PVDF-TiO$_2$ mixed-matrix membrane and its evaluation on dye adsorption and UV-cleaning properties. Chem Eng J. 2012; 197: 359–367. DOI: 10.1016/j.cej.2012.05.050

[34]   Li JH, Xu YY, Zhu LP, Wang JH, Du CH. Fabrication and characterization of a novel TiO$_2$ nanoparticle self-assembly membrane with improved fouling resistance. J Membr Sci. 2009; 326: 659–666. DOI: 10.1016/j.memsci.2008.10.049

[35]   Kim HJ, Pant HR, Kim JH, Choi NJ, Kim CS. Fabrication of multifunctional TiO$_2$–fly ash/polyurethane nanocomposite membrane via electrospinning. Ceram Int. 2014; 40: 3023–3029. DOI: 10.1016/j.ceramint.2013.10.005

[36]   Bae TH, Tak TM. Effect of TiO$_2$ nanoparticles on fouling mitigation of ultrafiltration membranes for activated sludge filtration. J Membr Sci. 2005; 249: 1–8. DOI: 10.1016/ j.memsci.2004.09.008

[37]   Cao XH, Ma J, Shi XH, Ren ZJ. Effect of TiO$_2$ nanoparticle size on the performance of PVDF membrane. Appl Surf Sci. 2006; 253: 2003–2010. DOI: 10.1016/j.apsusc. 2006.03.090

[38]   Mendret J, Hatat-Fraile M, Rivallin M, Brosillon S. Hydrophilic composite membranes for simultaneous separation and photocatalytic degradation of organic pollutants. Sep. Purif Technol. 2013; 111: 9–19. DOI: 10.1016/j.seppur.2013.03.030

[39] Syafei AD, Lin CF, Wu CF. Removal of natural organic matter by ultrafiltration with TiO$_2$-coated membrane under UV irradiation. J Colloid Interface Sci. 2008; 323: 112–119. DOI: 10.1016/j.jcis.2008.03.037

[40] Qi Z, Fan Y. Xu N. Effect of the surface properties on filtration performance of Al$_2$O$_3$-TiO$_2$ composite membrane. Sep Purif Technol. 2009; 66: 306–312. DOI: 10.1016/j.seppur.2008.12.010

[41] Rahimpour A, Madaeni SS, Taheri AH, Mansourpanah Y. Coupling TiO$_2$ nanoparticles with UV irradiation for modification of polyethersulfone ultrafiltration membranes. J Membr Sci. 2008; 313: 158–169. DOI: 10.1016/j.memsci.2007.12.075

[42] Luo M-J, Zhao J-Q, Tang W, Pu CS. Hydrophilic modification of poly (ether sulfone) ultrafiltration membrane surface by self-assembly of TiO$_2$ nanoparticles. Appl Surf Sci. 2005; 249: 76–84. DOI: 10.1016/j.apsusc.2004.11.054

[43] Mansourpanah Y, Madaeni SS, Rahimpour A, Farhadian A, Taheri AH. Formation of appropriate sites on nanofiltration membrane surface for binding TiO$_2$ photo-catalyst: performance, characterization and fouling-resistant capability. J Membr Sci. 2009; 330: 297–306. DOI: 10.1016/j.memsci.2009.01.001

[44] Lin HF, Ravikrishna R, Valsaraj KT. Reusable adsorbents for dilute solution separation 6. Batch and continuous reactors for the adsorption and degradation of 1,2-dichlorobenzene from dilute wastewater streams using titania as a photocatalyst. Sep Purif Technol. 2002; 28: 87–102. DOI: 10.1016/S1383-5866(02)00017-5

Degradation of Lignin Derivatives by Photocatalysts

Colin Awungacha Lekelefac and Peter Czermak

Additional information is available at the end of the chapter

Abstract

Photocatalytic degradation experiments were done with lignin sulfonate in a circulating reactor. Catalysts (TiO_2-P25-SiO_2 + Pt, TiO_2-P25-SiO_2, $TiOSO_4$_30.6 wt%, ZnO + TiO_2-P25-SiO_2), synthesized via the sol–gel method, were immobilized on porous glass support material. A comparative study was done regarding morphology of coatings, degradation rates, reaction rates, dissolved carbon (DC), formation of peaks, and fluorescence of products formed from the photocatalytic degradation of lignin sulfonate obtained from a local paper plant. Through simultaneous reaction–extraction pathways applying dialysis filtration and highly porous polystyrene divinylbenzene adsorbent resin (HR-P) for solid-phase extraction (SPE), an attempt was been made to isolate smaller molecules produced from photocatalytic degradation. Moreover, relatively high lignin sulfonate (0.5 g/L) concentrations are used in the reactions. UV–Vis spectroscopy revealed a faster reduction in the concentration values for the aliphatic moiety compared to the aromatic moiety. Peaks were observed by both fluorescence spectroscopy and high-performance liquid chromotography (HPLC), suggesting the production of new substances and fluorophores.

Keywords: photocatalysis, lignin degradation, coatings, sintered glass, lignin fluorescence

1. Introduction

There is a growing awareness of the rapid depletion of fossil materials which makes it imperative to think of the development of commercial viable "green products" based on alternatives for fossil fuels. Commercial lignin is a byproduct of the pulp and paper industries, wood hydrolysis industries, and pre-treatment technologies to obtain cellulosic ethanol and biodiesel. More than 70 million tons of various types of lignin are produced as a waste material by the paper industry yearly [1, 2]. Coupled to that, lignin and its degradation products cannot be

completely decomposed by sludge processes and are the source of chemical oxygen demand (COD) of waste water from pulp and paper mills [3]. Lignin is primarily a structural material to add strength and rigidity to cell walls and constitutes between 15 and 40 wt% of the dry matter of woody plants. After cellulose, it is the most abundant renewable carbon source on earth. Lignin can be available through various sources and biomass transformation technologies [4].

Photocatalysis, belonging to the so-called advanced oxidation processes (AOPs) [5], is a potential new transformation technology for lignin to value-added products, for example, phenol, benzene, toluene, and xylene [6]. One of such transforming methods is the heterogeneous procedure in which a photocatalytically active layer is immobilized on a support material. In such a system, both adsorption and photocatalysis take place which have major advantages such as reuse of catalyst; minimization of catalyst leaching or resistance to extreme physical and chemical conditions is exploited. Most publications treating lignin photocatalysis describe suspension systems [7] with the disadvantage that catalyst particles have to be recovered after reaction through downstream processes such as ultrafiltration, which bring along additional process steps and higher cost. Besides photocatalyis, lignin can be degraded by other ways such as biochemical degradation through microbial/enzymatic attack [8–10], thermal degradation [11, 12], and electrochemical oxidation [13].

For a good catalytic efficiency in an immobilized catalytic system, a good hydrodynamic design of the system and modifications involving the utilization of the visible light spectrum by catalyst doping can be of great importance. The selection and design of the supporting material influences both the fluidic design as well as the available catalyst surface. The photocatalytic efficiency increases with an increase in active surface. This means that the carrier material has to provide a high surface to volume ratio. Also, the materials used as supports for photocatalytic purposes must also fulfill stringent optical properties such as transparency to UV-A light, in order to achieve high photonic efficiencies and to minimize the energy consumption required for the illumination.

Stable catalytic coatings produced on porous glass material and their photocatalytic activity studied by degradation experiments of lignin under UV light illumination is described by Awungacha et al [2, 14]. Sintered glass particles were coated to exploit the advantages of a heterogeneous system, and a good fluidic design was assumed by the porosity of the glass particles. Moreover, parameters such as flow characterization and irradiance which are required for the rigorous design and scaling-up of a photocatalytic reactor in order to accomplish a commercial application were reported. Additionally, a simultaneous reaction–extraction pathway, applying dialysis filtration, and highly porous polystyrene divinylbenzene adsorbent resin (HR-P) were applied. Awungacha et al. [2] used a relatively high concentration of lignin sulfonate (0.5 g/L) obtained from a local paper company.

The reaction design introduces a method which can remediate the pollution problem in waste water discharged from pulp and paper mills on the one hand, and on the other hand, it gives room to further exploit the degradation of lignin as an alternative chemical source. Peaks observed by both high-performance liquid (HPLC) and fluorescence chromatograms suggest the production of new substances and fluorophores [2].

1.1. Degradation and mineralization of lignin

Lignin degradation is generally in the range of lower energy (between 300 and 400 nm) because of its multifunctional character [15–17]. For a better illustration, **Figure 1** shows the structure of a softwood lignin fragment containing all prominent linkage types. During the photodegradation process of lignin, radical sites and excited α-carbonyl are involved. Excited α-carbonyl groups are able to abstract hydrogen from some lignin units, preferably phenolic hydrogen, initiating an oxidative chain reaction with the participation of ground-state oxygen, leading to the fragmentation and the formation of new chromophores, dimers, and sometimes oligomers as major products [18]. The action of hydroxyl radicals can induce the formation of radical sites on a substrate, thus inducing further oxidation or disproportionation reactions. The process can be accelerated by oxygen [19]. Machado et al. [20] report a rapid initial decrease of phenolic hydroxyl groups followed by a clear tendency of increasing explained as an effect of incorporation of hydroxyl groups on aromatic rings, occurring by hydroxylation and/or demethoxylation [19]. **Figure 2** summarizes the formation of radicals under photocatalytic conditions [21, 22]. S stands for the lignin substrate, while TiO_2 (h^+) and TiO_2 (e^-) represent the electron deficient and electron-rich parts in the structure of TiO_2, respectively [7].
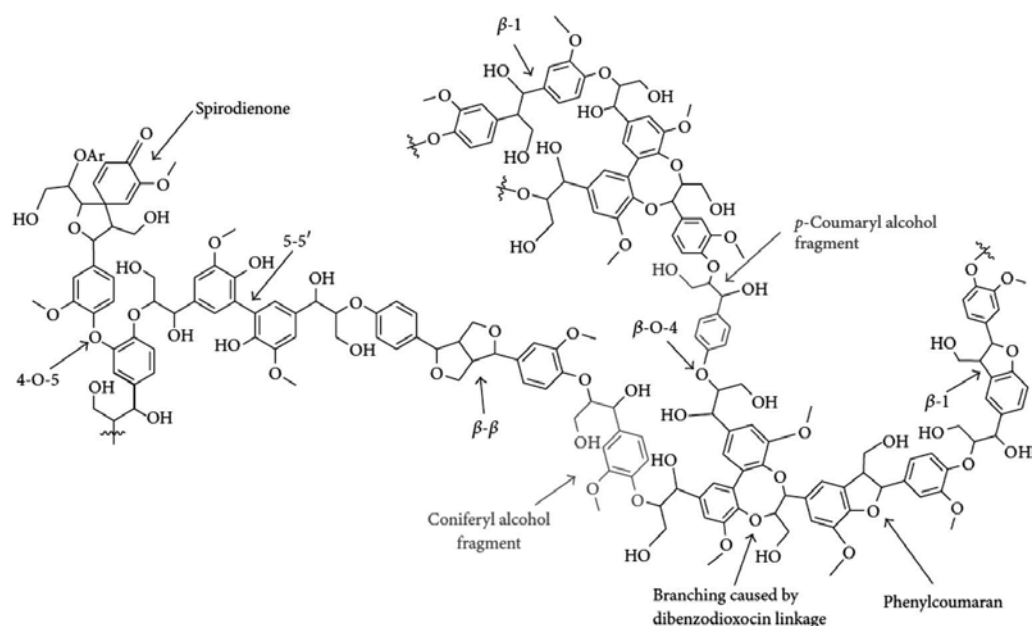
Figure 1. Structure of a softwood lignin molecule showing the prominent linkage types. Reproduced with the permission from Awungacha Lekelefac et al [7].
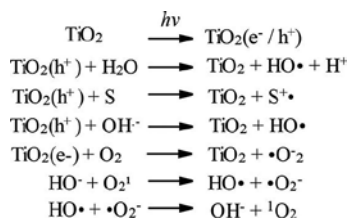
Figure 2. Formation of singlet oxygen, hydroxyl, and superoxide radicals as principal reactive species in a photocatalytic process [21, 22].

From investigations carried out by Mazelier et al. [18], (photochemistry of 2,6-dimethylphenol), it was postulated that hydrogen can be abstracted by α-carbonyl groups. In the same context, lignin derivatives having similar functionality can follow a similar pathway. In addition, oxidative chain reactions with the participation of ground-state oxygen can be initiated leading to fragmentation and combination reactions, thus forming of new dimers or oligomers (**Figure 3**) [7, 18].
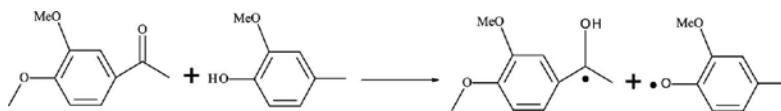
Figure 3. Formation of phenoxyl radicals by intermolecular abstraction of phenolic hydrogen by carbonyl groups [7, 18].
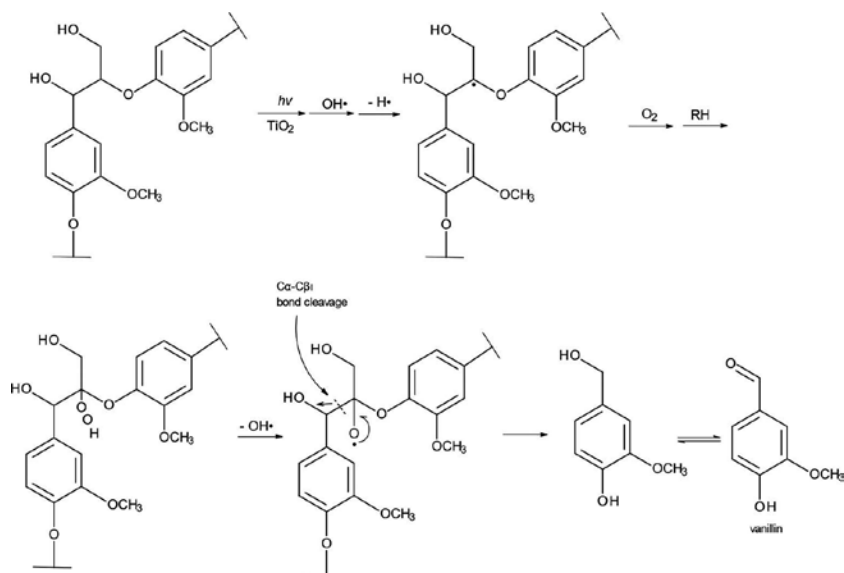
Figure 4. Supposed lignin degradation scheme by auto-oxidation induced by TiO$_2$/Poly (ethylene oxide) [23].

Miyata et al. [23] proposed a cleavage mechanism for the Cα–Cβ bonds which lead to the formation of small fragments such as vanillin as shown in **Figure 4**.
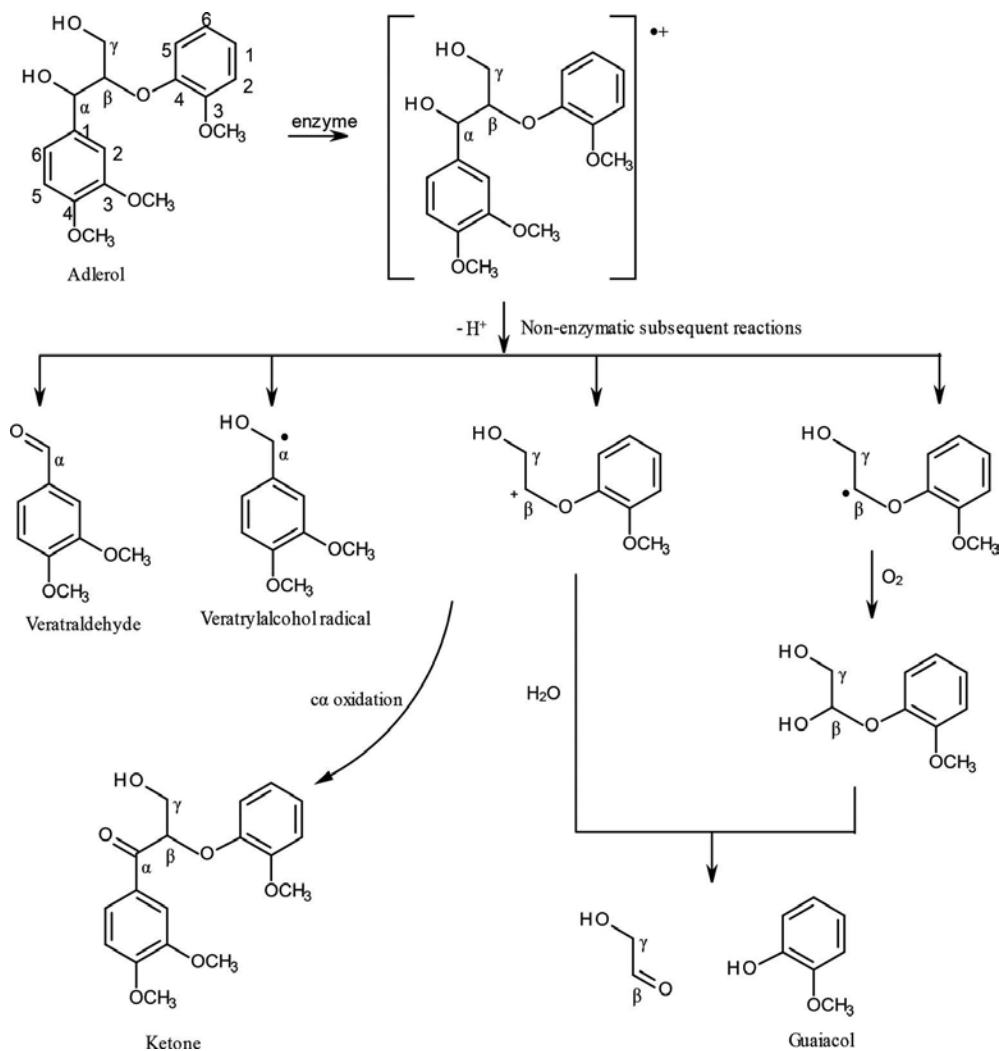
Figure 5. Proposed radical reaction scheme initiated by enzyme (Lignolitic Heme Peroxidase) for the conversion of adlerol possessing Cβ-O-4 bonds into smaller units, summarized by Busse et al. [7, 10], Abstracted from Tien and Kirk [24], Kirk et al. [25], Lundell et al. [26], Schoemaker et al. [27], and Palmer et al. [28].

Figure 5 illustrates the formation of a radical cation formed as a result of enzyme (lipase)-mediated reaction of adlerol. Adlerol is characterized by a Cβ-O-4 bond and considered to be a lignin model compound. With the formation of the radical species, subsequent non-enzymatic reactions such as radical reactions can take place, generating a wide variety of products and complex compounds.

Reporting on the degradation pathway of lignin derivatives and even that of lignin model compounds is still a major challenge. This is probably due to the complex nature and variety of possible degradation products. Indeed, the mechanism is far more complex, considering other factors such as type of lignin, type of catalyst, pH, illumination source, and additives [7]. It is widely assumed that the photocatalytic degradation of lignin follows a radical reaction pathway which is similar to that considered in thermal, electrochemical, and biochemical processes [7].

2. Experimental

2.1. Photocatalytic experiments

The degradation experiments of lignin sulfonate were carried out with a starting concentration of 0.5 g/L in 200 mL deionized water. The reaction design consisted of TiO_2 coatings on sintered glass (150–250 μm nominal pore size), packed in a borosilicate tube 26 cm long, 1 cm outer diameter, and 6 mm internal diameter. Glass particle grain size was between 200 and 400 μm. The following catalysts were synthesized as follows: TiO_2-P25-SiO_2 + Pt, TiO_2-P25-SiO_2, ZnO + TiO_2-P25-SiO_2, and $TiOSO_4$_30.6 wt%. A detail description of the catalysts synthesis and coating has been described elsewhere [14].

The tube was placed between two planar dielectric barrier discharge lamps. The broad surface of the light source insured incident light to be well distributed all over the surface of the glass tubes. **Figure 6** depicts the reaction setup, while **Figure 7** illustrates the reactor used for the experiments.

Figure 6. Experimental setup for the photocatalytic degradation of lignin.
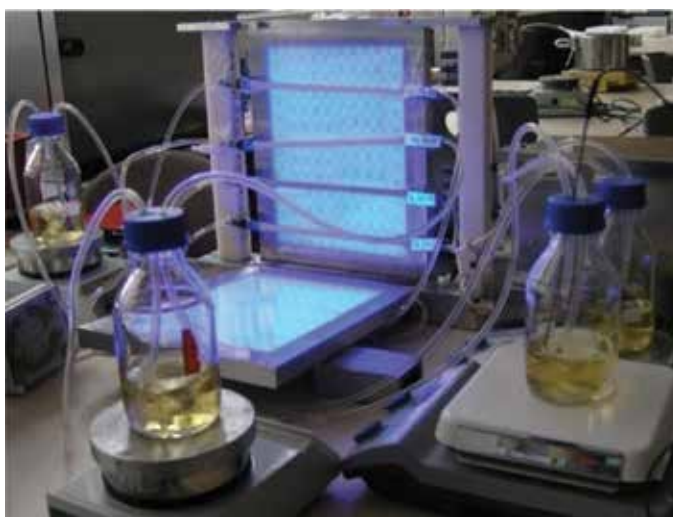
Figure 7. Photocatalytic reactor.
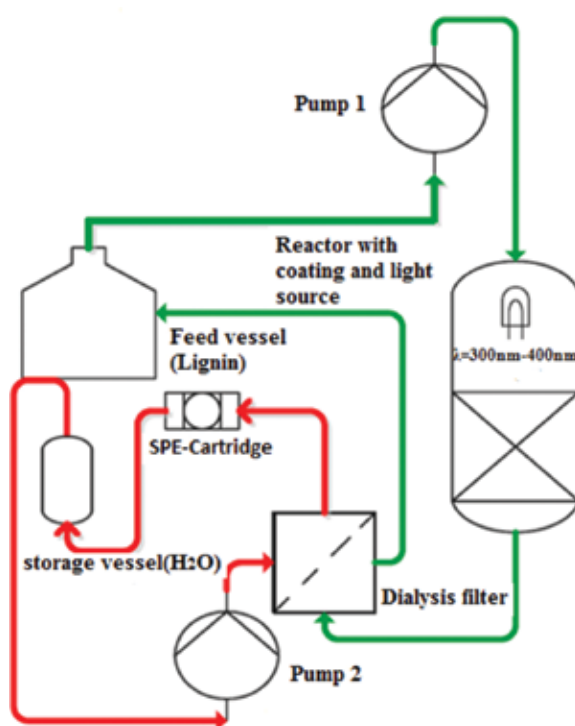
Figure 8. Photocatalytic cycle process with integrated solid-phase extraction and dialysis membrane.

The reaction procedure involved 03 pathways. In the first one, lignin sulfonate solution was pumped through the reactor using roller pumps in a continuous manner with a flow rate of 22.5 mL/min. Samples were collected at intervals up to a period of 20 h reaction time. Reactions were carried out at roo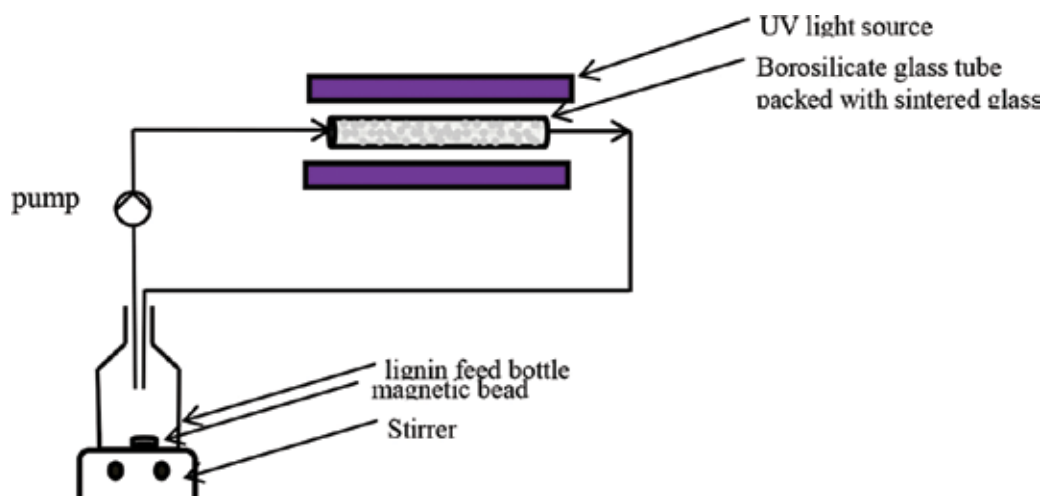m temperature. Blank experiments were performed in the absence of UV light illumination as well as with uncoated sintered glass tubes. For all experiments, lignin was recirculated through the reactor for 60 min before UV light was put on. This was to ensure uniform wettability within the packed bed and same starting reaction conditions for all experiments. The second procedure involved a reaction–extraction pathway in which extraction followed after reaction with the use of highly porous polystyrene divinylbenzene adsorbent resin (HR-P). In the third procedure, the reactor was connected to a dialysis filter fitted with a HRP extraction column operating in a cycle process, and this is depicted in **Figure 8**. Its aim was to directly extract smaller molecules produced and preferably aromatic and phenol like compounds from aqueous the medium.

3. Results and discussion

3.1. Degradation experiments

Figure 9 shows time-dependent UV–Vis spectra of lignin sulfonate. Absorption peaks were observed at 203 and 280 nm, while a shoulder at around 230 nm was observed. Lignin absorbs UV light with high molar extinction coefficients because of the several methoxylated phenyl-propane units of which they are composed of [29]. The absorption peaks decrease gradually, indicating the decomposition of lignin sulfonate and hence deterioration of the chromophor groups present. Peaks around 203 nm correspond to portions of unsaturated chains [29, 30], while those around 280 nm correspond to unconjugated phenolic hydroxyl groups [31] and aromatic rings [30] of lignin sulfonate [2]. Ohnishi et al. [30] report the absorption tailing arising from the color of lignin.

Preliminary reactions carried out involved in lignin sulfonate degradation experiments performed on uncoated glass in the presence of UV light as well as on coated glass particles in the absence of UV light. Results obtained revealed no significant change in absorbance over a 20 h period, indicating no major degradation and adsorption. Houas et al. [32] note that at catalytic surfaces experiencing unfavorable conditions such as repellent interactions, there may be no adsorption. It can further be argued that because of the nature of lignin used in this work (lignin sulfonate), the sulfonate groups attached to lignin render it anionic. Likewise, because of the basic nature of the reaction medium (pH 9) and the negatively charged hydroxyl (OH^-) ions generated from photochemical reactions, adsorption conditions do not prevail [2].
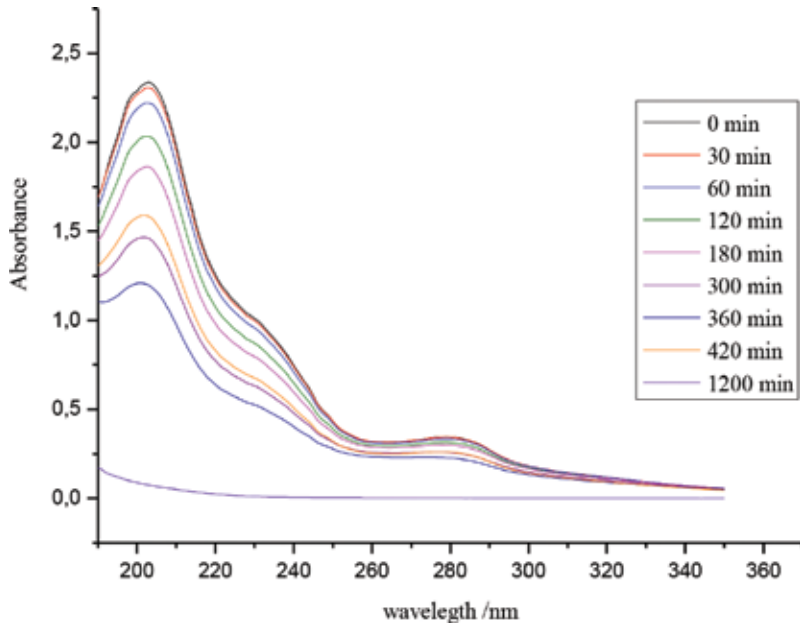
Figure 9. Time-dependent UV–Vis absorption spectra of aqueous lignin sulfonate solution. Concentration: 0.5 g/L in 200 mL, reaction time: 20 h, catalyst: sol–gel derived TiO_2-P25-SiO_2, reaction at room temperature, UV radiation (280–420 nm) [2].
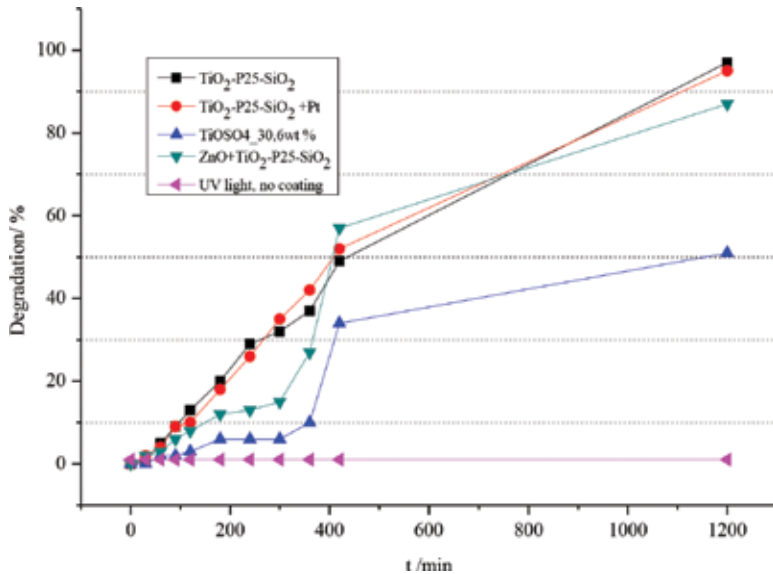
Figure 10. Effect of different catalyst on percentage degradation of lignin sulfonate under UV light at wavelength 203 nm (lignin sulfonate concentration: 0.5 g/L in 200 mL, reaction time: 20 h, reaction at room temperature, UV radiation (280–420 nm) [2].
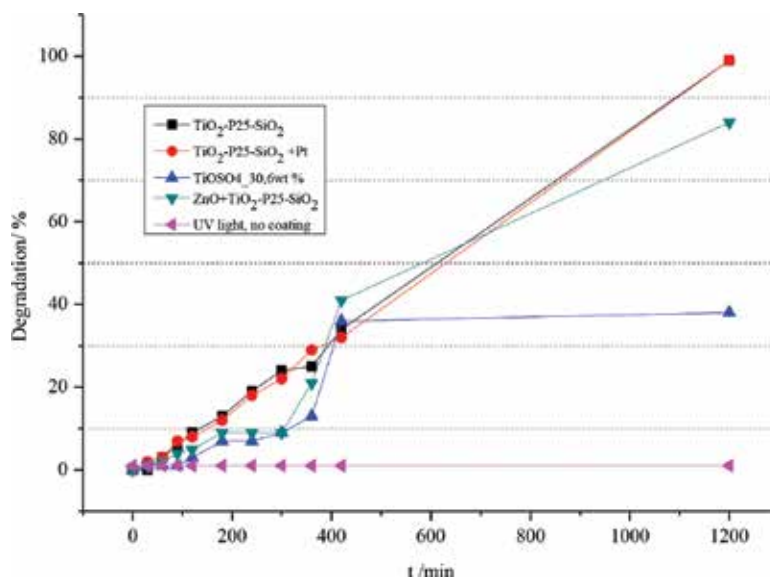
Figure 11. Effect of different catalyst on percentage degradation of lignin sulfonate under UV light at wavelength 280 nm (lignin sulfonate concentration: 0.5 g/L in 200 mL, reaction time: 20 h, reaction at room temperature, UV radiation (280–420 nm) [2].

Figure 10 depicts the degradation of lignin sulfonate by different catalyst at wavelength 203 and 280 nm, respectively. Degradation of lignin sulfonate prevailed in the presence of a catalyst. An abrupt degradation increase was observed for $TiOSO_4$_30.6 wt% and $ZnO + TiO_2$-P25-SiO_2 catalysts between 240 and 300 min. Here, the slow reaction at the beginning is the rate-determining step [33]. In this step, processes such as absorption of photons of light by catalyst, production of electrons, and other oxidizing species among other take place before a faster reaction takes place [34]. An almost linear degradation pattern was noted for TiO_2-P25-SiO_2 + Pt and TiO_2-P25-SiO_2 throughout the complete reaction time. Degradation rates of 97, 95, 87, and 51% were attained by coatings TiO_2-P25-SiO_2 + Pt, TiO_2-P25-SiO_2, $ZnO + TiO_2$-P25-SiO_2, and $TiOSO_4$_30.6 wt%, respectively, after 20 h reaction time for the straight chain lignin sulfonate moiety (**Figure 11**). Similar degradation values are also observed for the aromatic moiety after 20 h (Figure 11). $TiOSO_4$_30.6 wt% catalyst was less reactive compared with the others because of the relatively low degradation values it produced. Less than 40% degradation was achieved after 420 min for both the aromatic and aliphatic moiety. Comparing the degradation rates of the aromatic moiety against that of the straight chain moiety after 420 min, it was observed that higher degradation values were attained by the aliphatic moiety. In detail, for the aliphatic moiety, degradation rates of 49, 52, 57, and 34% were noted, while for the aromatic moiety, degradation rates of 34, 32, 41, and 36% were observed for TiO_2-P25-SiO_2 + Pt, TiO_2-P25-SiO_2, $ZnO + TiO_2$-P25-SiO_2, and $TiOSO_4$_30.6 wt%, respectively. This suggests a faster transformation of the aliphatic side chains as compared to the aromatic species. A similar conclusion was arrived at by Tanaka et al. [35], whereby FTIR measurements were applied.

Comparing the degradation values of lignin sulfonate by using plain TiO_2-P25-SiO_2 and that of the combination between ZnO andTiO_2-P25-SiO_2, a higher degradation rate was observed for ZnO and TiO_2-P25-SiO_2 after 420 min, both for the straight chain moiety and aromatic moiety. However, after 20 h reaction time, TiO_2-P25-SiO_2 had a higher degradation value, both for the straight chain moiety and aromatic moiety. Degradation rates of 49 and 57% were observed after 420 min for TiO_2-P25-SiO_2 and ZnO + TiO_2-P25-SiO_2 catalysts, respectively. Meanwhile, after 20 h reaction time, values of 97 and 87% are attained byTiO_2-P25-SiO_2 and ZnO + TiO_2-P25-SiO_2 catalyst, respectively. This means that ZnO + TiO_2-P25-SiO_2 catalyst was more active during the first 420 min and its activity decreased in the proceeding time.

Adding (doping) Pt as metal ion to TiO_2-P25-SiO_2 slightly improved the degradation values compared with that of plain TiO_2-P25-SiO_2 catalyst. Values of 49 and 52% are attained after 420 min reaction time for TiO_2-P25-SiO_2 andTiO_2-P25-SiO_2 + Pt catalyst, respectively, whereas after 20 h reaction time, values of 97 and 95% are attained byTiO_2-P25-SiO_2 andTiO_2-P25-SiO_2 + Pt catalyst, respectively. These results indicate that Pt contributed little or no change in degradation rate which is contradictory to some published results on the effect of doping [36, 37]. However, for reactions in which doping enhances degradation, a threshold dosage has to be considered [37].
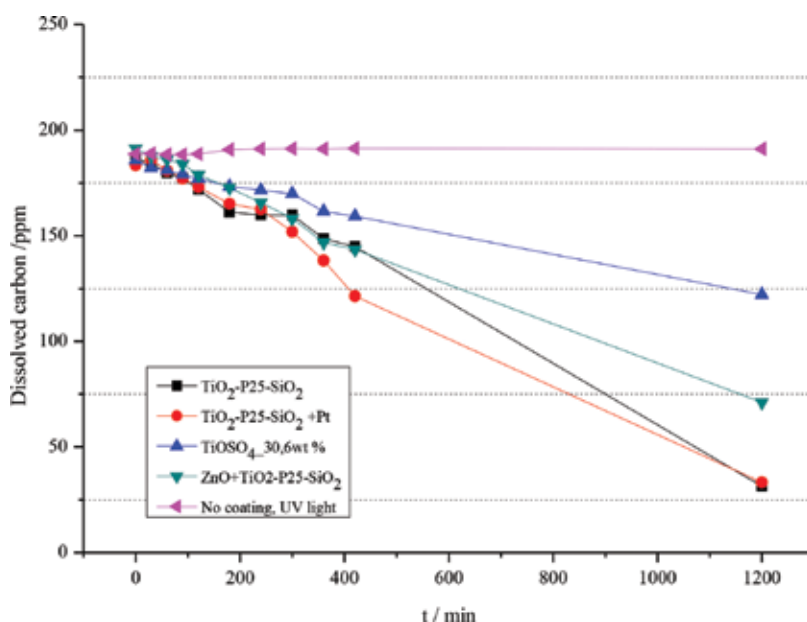
Figure 12. Removal of dissolved carbon in lignin sulfonate. Concentration: 0.5 g/L in 200 mL, reaction time: 20 h, reaction at room temperature, UV radiation (280–420 nm) [2].

In order to effectively quantify lignin degradation, dissolved carbon (DC) measurements were done (**Figure 12**). DC describes the amount of carbon bound in a compound. DC in lignin sulfonate of initial concentration 500 mg/L decreased from 185 to 144 ppm, 121, 159, and

143 ppm after 420 min for the catalyst TiO$_2$-P25-SiO$_2$, TiO$_2$-P25-SiO$_2$ + Pt, ZnO + TiO$_2$-P25-SiO$_2$ and TiOSO$_4$_30.6 wt%, respectively. This value further decreased to 31, 33, 122, and 71 ppm making a DC removal of 84, 82, 61, and 34% for TiO$_2$-P25-SiO$_2$, TiO$_2$-P25-SiO$_2$ + Pt, ZnO + TiO$_2$-P25-SiO$_2$, and TiOSO$_4$_30.6 wt% respectively. Hence, TC removal was in the order: TiO$_2$-P25-SiO$_2$ + Pt ~ TiO$_2$-P25-SiO$_2$ > ZnO + TiO$_2$-P25-SiO$_2$ > TiOSO$_4$_30.6 wt%. Decrease in DC has been reported to generate carbon dioxide and a small amount of carbon monoxide as the main gaseous products [2, 30].
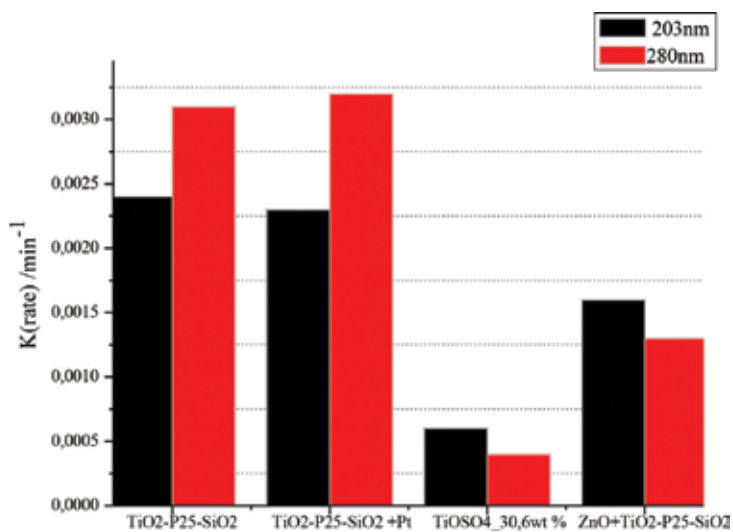
Figure 13. Reaction rates of the photocatalytic degradation of lignin sulfonate (500 mg/L) under UV light on immobilized catalysts. Concentration: 0.5 g/L in 200 mL, reaction time: 20 h, reaction at room temperature, UV radiation (280–420 nm) [2].

The rate constant values for the different catalyst are shown in **Figure 13**. Reaction rate was in the order: TiO2-P25-SiO2 + Pt ~ TiO2-P25-SiO2 > ZnO + TiO$_2$-P25-SiO$_2$ > TiOSO$_4$_30.6 wt% for both the aromatic and aliphatic side chain wavelength regions.

Comparing ZnO + TiO$_2$-P25-SiO$_2$ and TiO$_2$-P25-SiO$_2$, adding ZnO to TiO$_2$-P25-SiO$_2$ had an adverse effect to reaction rate probably because ZnO occupies some of the active sites on the catalyst support and it does not optimally absorb UV light in the domain of the wavelengths transmitted by the photo reactor (280 < λ < 420 nm), and as a consequence, limitations in electron transfer between the band gap [2, 38].

3.2. Fluorescence and HPLC results

Fluorescence spectroscopy was used as a means to identify non-aliphatic component in the complex mixture of lignin degradation products. Fluorescence emission in lignin is attributed to aromatic structures such as conjugated carbonyl, biphenyl, phenylcoumarone, and stilbene groups [39, 40]. New fluorophores were detected in the time ranging from 10 min to around 40 min (Figure 14) with application of TiOSO$_4$_30.6 wt% catalyst. With the use of TiO$_2$-

P25-SiO$_2$ catalyst, new fluorophores were detected as soon as 5 min to around 55 min (**Figure 14**) [2].
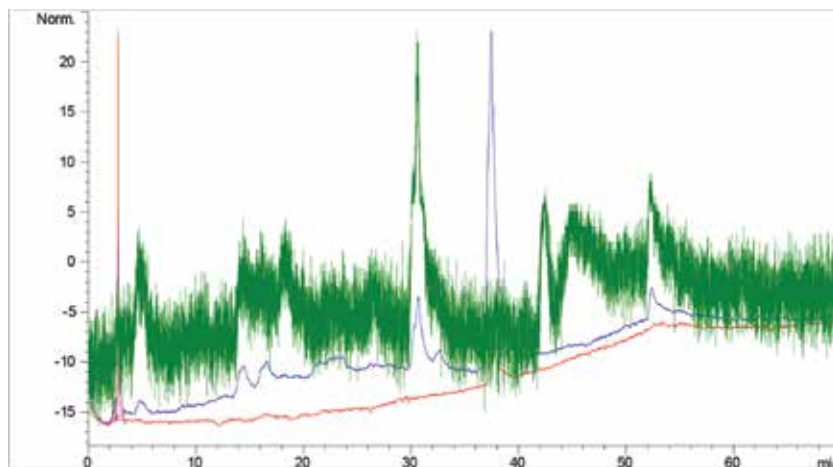
Figure 14. HPLC chromatogram and fluorescence peaks of lignin sulfonate solution. Concentration: 200 mL of 0.5 g/L, reaction time: 4 h, catalyst: TiO$_2$-P25-SiO$_2$, reaction at room temperature, presence of UV radiation, simultaneous reaction, dialysis filter, and SPE with HP-R cartridge during reaction [2].
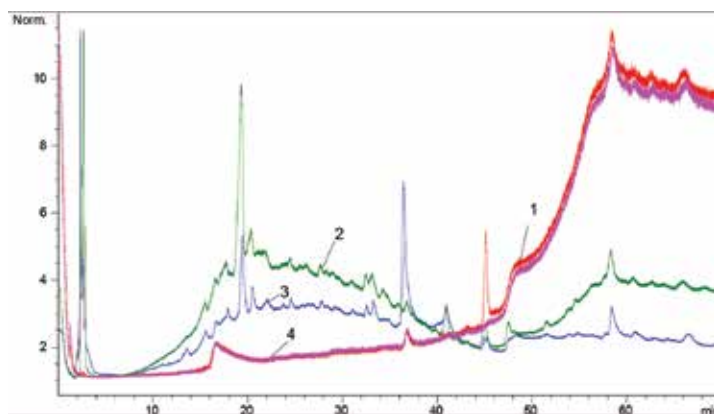
Figure 15. Fluorescence chromatogram of lignin sulfonate degradation product. Emission spectrum, λ_{em}: 240 nm, λ_{ex}: 330 nm, concentration: 100 mL 0.5 g/L, reaction time: 20 h, catalyst: TiOSO$_4$_30.6 wt%, reaction at room temperature.

(1): absence of UV radiation, SPE with HP-R cartridge after reaction suspended in methanol. (2): presence of UV radiation, SPE with HP-R cartridge after reaction suspended in methanol. (3): presence of UV radiation, simultaneous SPE with HP-R cartridge during reaction. (4): presence of UV radiation, aqueous raffinate from continuous extraction.

Comparing pathway (2) and pathway (3) from **Figure 15**, it was observed that the fluorophores produced had similar retention times and similar peak areas. This indicates that it did

not matter whether the extraction was done after the reaction or during the reaction. No peaks were observed for (1) reinforcing the necessity of UV light for lignin sulfonate degradation. The absence of peaks for (4) suggests that the degradation was complete and the all-produced substances were adsorbed on the SPE cartridge. Moreover, tailing was observed for samples (1) and (4) that did not contain degradation products dissolved in it [2].

Figure 14 depicts an HPLC and fluorescence chromatogram in which both measuring apparatus were coupled. The peak at around 2 min retention time arises from methanol used as eluting agent during SPE. Peaks were observed on both chromatograms, suggesting the production of new substances in which some generated fluorescence peaks. However, some fluorescence peaks appear only on the fluorescence chromatogram. Also broad peaks were found on the both HPLC and fluorescence chromatograms. During measurements, diode array detector (DAD) wavelength was set at 240 nm and not all degradation products could be detected at this particular wavelength. In fact, one of the challenges to analyze lignin through HPLC is to set the DAD wavelength for maximum detection. An analogous scenario was observed during fluorescence in which emission wavelength was set at 240 nm and excitation wavelength set at 330 nm. These difficulties arise because of the vast range of possible products arising from lignin degradation. Because of that, distinct emission decay peaks cannot be produced due to superimposition of the different fluorophores [2].

4. Conclusion

It is widely assumed that the photocatalytic degradation of lignin follows a radical reaction pathway which is similar to that considered in thermal, electrochemical, and biochemical processes. Indeed, the mechanism is far more complex considering other factors such as type of lignin, type of catalyst, pH, illumination source, and additives [7].

Despite developed analytical technologies, analyzing lignin degradation products from photocatalysis remains challenging. Proofs such as mass spectroscopy (MS), HPLC, ^{13}C, or ^{1}H-NMR spectra from photocatalytic lignin degradations are not yet established. This is probably due to the complex nature and variety of possible degradation products [7].

The reactor design reported here effectively degraded relatively high concentration of lignin sulfonate solutions (500 mg/L) from paper waste water. UV–Vis spectroscopy revealed a faster transformation of the aliphatic side chains as compared to the aromatic species. Adding Pt as metal ion to TiO_2-P25-SiO_2 catalyst showed a negligible effect on degradation rates. The reaction rate of the catalytic systems was in the order: TiO_2-P25-SiO_2 + Pt ~ TiO_2-P25-SiO_2 > ZnO + TiO_2-P25-SiO_2 > $TiOSO_4$_30.6 wt% [2].

Peaks were observed on HPLC and fluorescence chromatograms, suggesting the production of new substances and fluorophores. Through simultaneous reaction–extraction pathways applying dialysis filtration and highly porous polystyrene divinylbenzene adsorbent resin (HR-P), an attempt has been made to isolate smaller molecules produced from photocatalytic degradation [2].

Acknowledgements

Author details

Colin Awungacha Lekelefac[1,2,3] and Peter Czermak[1,2,3*]

*Address all correspondence to: peter.czermak@kmub.thm.de

1 University of Applied Sciences Mittelhessen, Institute of Bioprocess Engineering and Pharmaceutical Technology, Giessen, Germany

2 Department of Chemical Engineering, Faculty of Engineering, Kansas State University, Manhattan, NY, USA

3 Faculty of Biology and Chemistry, Justus-Liebig-University, Giessen, Germany

References

[1] Kumar MNS, Mohanty AK, Erickson L, Misra M. Lignin and its applications with polymers. *Journal of Biobased Materials and Bioenergy*. 2009, 3 (1), 1–24.

[2] Awungacha Lekelefac C, Czermak P, Hild J, Herrenbauer M. Photocatalytic active coatings for lignin degradation in a continuous packed bed reactor. *International Journal of Photoenergy*. 2014, Article ID 502326.

[3] Tantemsapya N, Wirojanagud W, SakolchaiS.. Removal of color, COD and lignin of pulp and paper wastewater using wood ash. *Journal of Science and Technology*. 2004, 26, 1–12.

[4] Hill, C *Wood Modification. Chemical, Thermal, and Other Processes*. Chichester, UK: John Wiley & Sons, 2006.

[5] Mantzavinos D, Psillakis E Enhancement of biodegradability of industrial wastewaters by chemical oxidation pre-treatment. *Journal of Chemical Technology and Biotechnology*. 2004, 79(5), 431–454.

[6] Zakzeski J, Bruijnincx PC, Jongerius AL, Weckhuysen BM The catalytic valorization of lignin for the production of renewable chemicals. *Chemical Review*. 2010, 110, 3552–3599.

[7]   Awungacha Lekelefac C, Busse N, Herrenbauer M, Czermak P Photocatalytic based degradation processes of lignin derivatives. *International Journal of Photoenergy*. 2014, Article ID 137634.

[8]   Masai E, Katayama Y, Fukuda M Genetic and biochemical investigations on bacterial catabolic pathways for lignin-derived aromatic compounds. *Bioscience Biotechnology Biochemistry*. 2007, 71(1), 1–15.

[9]   Meux E, Prosper P, Masai E, Mulliert G, Dumarçay S, Morel M, Didierjean C, Gelhaye E, Favier F *Sphingobium* sp.SYK-6 LigG involved in lignin degradation is structurally and biochemically related to the glutathione transferase omega class. *FEBS Letters*. 2012, 586(22), 3944–3950.

[10] Busse N, Wagner D, Kraume M, Czermak P Reaction kinetics of versatile peroxidase for the degradation of lignin compounds. *American Journal of Biochemistry and Biotechnology*. 2013, 9(4), 365–394.

[11] Rodrigues J, Graça J, Pereira H Influence of tree eccentric growth on syringyl/guaiacyl ratio in *Eucalyptus globulus* wood lignin assessed by analytical pyrolysis. *Journal of Analytical and Applied Pyrolysis*. 2001, 58–59, 481–489.

[12] Alén R, Kuoppala E, Oesch P Formation of the main degradation compound groups from wood and its components during pyrolysis. *Journal of Analytical and Applied Pyrolysis*. 1996, 36(2), 137–148.

[13] Pana K, Tiana M, Jianga Z-H, Kjartansonb B, Chena A Electrochemical oxidation of lignin at lead dioxide nanoparticles photoelectrodeposited on TiO2 nanotube arrays. *Electrochimica Acta*. 2012, 60, 147–153.

[14] Awungacha Lekelefac C, Czermak P, Herrenbauer M Evaluation of photocatalytic active coatings on sintered glass tubes by methylene blue. *International Journal of Photoenergy*. 2013, Article ID 614567.

[15] Neumann MG, De Groote RAMC, Machado AEH Flash photolysis of lignin, Part 1. Deaerated solutions of dioxane-lignin. *Polymer Photochemistry*. 1986, 7(5), 401–406.

[16] Kringstad KP, Lin SY Mechanism in the yellowing of high yield pulps by light. Structure and reactivity of free radical intermediates in the photodegradation of lignin. *Tappi Journal*. 1970, 53, 2269–2301.

[17] Castellan A, Colombo N, Vanucci C, Fornier de Violet P, Bouas-Laurent H Photodegradation of lignin. A photochemical study of an O-methylated α-carbonyl β-1 lignin model dimer: 1,2-di(3′4′-dimethoxyphenyl) ethanone (deoxyveratroin). *Journal of Photochemistry and Photobiology A*. 1990, 51, 451–467.

[18] Mazelier P, Sarakha M, Rossi A, Bolte M The aqueous photochemistry of 2,6-dimethylphenol. Evidence for the fragmentation of the Alpha C-C bond. *Journal of Photochemistry and Photobiology A*. 1998, 115, 117–121.

[19] Gierer,J Formation and involvement of superoxide (O_2^-:/H_2O_2) and hydroxyl (OH.) radicals in TCF bleaching processes: A review. *Holzforschung*. 1997, 51, 34–46.

[20] Machado A, Furuyama AM, Falone SZ, Ruggiero R, Perez DD, Castellan A Photocatalytic degradation of lignin and lignin models, using titanium dioxide: the role of the hydroxyl radical. *Chemosphere*. 2000, 40, 115–124.

[21] Serpone N Relative photonic efficiencies and quantum yields in heterogeneous photocatalysis. *Journal of Photochemistry and Photobiology A*. 1997, 104, 1–12.

[22] Hoffman M, Martin S, Choi W, Bahnemann D Environmental applications of semiconductor photocatalysis. *Chemical REviews*. 1995, 95, 69–96.

[23] Miyata Y, Miyazaki K, Miura M, Shimotori Y, Aoyama M, Nakatani H Solventless Delignification of wood flour with TiO_2/poly(ethylene oxide) photocatalyst system. *Journal of Polymers and Environment*. 2012, 21(1), 115–121.

[24] Tien M, Kirk TK Lignin-degrading enzyme from phanerochaete chrysosporium: Purification, characterization, and catalytic properties of a unique H(2)O(2)-requiring oxygenase. *Proceedings of the National Academy of Sciences* (*PNAS*). 1984, 81, 2280–2284.

[25] Kirk TK, Tien M, Kersten PJ, Mozuch MD, Kalyanaraman B Ligninase of Phanerochaete chrysosporium. Mechanism of its degradation of the non-phenolic arylglycerol beta-aryl ether substructure of lignin. *Biochemical Journal*. 1986, 236 (1), 279–287.

[26] Lundell T, Wever R, Floris R, Harvey P, Hatakka A Lignin peroxidase L3 from Phlebia radiata. Pre-steadystate and steady-state studies with veratryl alcohol and a non-phenolic lignin model compound 1-(3,4-dimethoxyphenyl)-2-(2-methoxyphenoxy)propane-1,3-diol. *European Journal of Biochemistry*. 1993b, 211, 391–402.

[27] Schoemaker H E, Lundell TK, Hatakka AI, PiontekK.. The oxidation of veratryl alcohol, dimeric lignin models and lignin by lignin peroxidase: The redox cycle revisited. *FEMS Microbiology Reviews*. 1994b, 13,321–331.

[28] Palmer JM, Harvey PJ, Schoemaker HE The role of peroxidases, radical cations and oxygen in the degradation of lignin [and discussion]. *Philosophical Transactions of the Royal Society London A*. 1987, 321 (1561), 495–505.

[29] Tonucci L, Coccia F, Bressan M, N d'Alessandro Mild photocatalysed and catalysed green oxidation of lignin: A useful pathway to low-molecular-weight derivatives. *Waste and Biomass Valorization*. 2012, 3, 165–174.

[30] Ohnishi H, Matsumura M, Tsubomura H, Iwasaki M Bleaching of lignin solution by a photocatalyzed reaction on semiconductor photocatalysts. *Industrial & Engineering Chemistry Research*. 1989, 28, 719–724.

[31] Shende A, Jaswal R, Harder-Heinz D, Menan A, Shende R Intergrated photocatalytic and microbial degradation of kraft lignin. *Cleantech*. 2012, 91,120–123.

[32] Houas A, Lachheb H, Ksibi M, Elaloui E, Guillard C, Herrmann JM Photocatalytic degradation pathway of methylene blue in water. *Applied Catalysis B*: *Environmental*. 2001, 31, 145–157.

[33] Laidler KJ *Chemical Kinetics*, 3rd edition. Harper & Row, New York, 1987.

[34] PSA Ciemat, Platforma Solar de Almeria. Solar Photocatalysis. http://www.psa.es/webesp/areas/tsa/docs/solar_photocatalysis.pdf. [Online]

[35] Tanaka K, Calanag RCR, Hisanaga T Photocatalyzed degradation of lignin on TiO2. *Journal of Molecular Catalysis A*: *Chemical*. 1999, 138, 287–294.

[36] Ohnishi H, Matsumura M, Tsubomura H, Iwasaki M Bleaching of lignin solution by a photocatalyzed reaction on semiconductor photocatalysts. *Industrial and Engineering Chemistry Research*. 1989, 28, 719–724.

[37] Portjanskaja E, Preis S Aqueous photocatalytic oxidation of lignin: The Influence of mineral admixtures. *International Journal of Photoenergy*. 2007, 1–7. Article ID 73760.

[38] Kansal SK, Singh M, Sud D Studies on TiO2/ZnO photocatalysed degradation of lignin. *Journal of Hazardous Materials*. 2008, 153, 412–417.

[39] Castellan A, Choudhury H, Davidson RS, Grelier S Comparative study of stone-ground wood pulp and native wood 3. Application of fluorescence spectroscopy to a study of the weathering of stone-ground pulp and native wood. *Journal of Photochemistry and Photobiology A*. 1994, 81, 123.

[40] Albinsson B, Li S, Lundquist K, Stomberg R The origin of lignin fluorescence. *Journal of Molecular Structure*. 1999, 508, 19–27.

Photocatalytic Removal of Organics over BiVO$_4$-Based Photocatalysts

Kunfeng Zhang, Jiguang Deng, Yuxi Liu,
Shaohua Xie and Hongxing Dai

Additional information is available at the end of the chapter

Abstract

Organic compounds, such as organic dyes and phenols, are the main pollutants in wastewater. In the past years, a large number of studies on the fabrication and photocatalytic organics degradation of BiVO$_4$ and its related materials have been reported in the literature. In this chapter, we shall focus on the advancements in the synthesis and photocatalytic applications of several kinds of BiVO$_4$-based photocatalysts: (i) well-defined morphological BiVO$_4$ photocatalysts, (ii) porous BiVO$_4$ photocatalysts, (iii) heteroatom-doped BiVO$_4$ photocatalysts, (iv) BiVO$_4$-based heterojunction photocatalysts, and (v) supported BiVO$_4$ photocatalysts. We shall discuss the structure–photocatalytic performance relationship of the materials and the involved photocatalytic degradation mechanisms. In addition, we also propose the research trends and technologies for practical applications of the BiVO$_4$-based photocatalytic materials.

Keywords: well-defined morphology, porous BiVO$_4$ photocatalyst, heteroatom-doped BiVO$_4$, BiVO$_4$-based heterojunction, supported BiVO$_4$

1. Introduction

With the unceasingly expanding industrial development, environmental pollution caused by industrial effluents has nowadays become the most urgent issue to be solved [1]. In particular, various industrial processes and human activities contaminate the global water supply, which is a serious problem for living beings. During the past decades, great efforts have been made on the degradation of organic wastewater pollutants. The visible-light-driven photocatalysis attracts much attention, since such a photocatalytic process can directly convert organic

pollutants (e.g., methylene blue (MB), methyl orange (MO), rhodamine B (RhB), phenol, and etc.) to harmless products (CO_2 and H_2O) under sunlight irradiation.

The organic dye models (MB, MO, and RhB) in textile and other industrial effluents have become one series of the major environmental contaminants, which have serious implications on the environment and human health [2]. Meanwhile, phenol is a widely used chemical and present in a great variety of emitted waste effluents. Organic dyes and phenol degrade slowly in the environment and are extremely toxic, carcinogenic, teratogenic, and refractory in nature [3]. Therefore, tremendous efforts have been made to fabricate high-efficiency photocatalysts for the control of wastewater pollution.

As one of the earliest studied *n*-type semiconductor photocatalysts, TiO_2 has been widely used in environmental purification owing to its appropriate band position, high chemical stability, low cost, and nontoxicity [4]. However, TiO_2 is only responsive to ultraviolet (UV) light owing to its wide bandgap energy (3.2 eV), which occupies no more than 4% of the solar spectrum, hence greatly restricting its practical applications [5]. Among the developed catalysts, $BiVO_4$ is one of the most attractive photocatalysts due to its unique properties, such as ferroelasticity, photochromic effect, ionic conductivity, and visible-light responsibility [6]. It is nontoxic and has a relatively narrow bandgap energy (2.4 eV) when it is monoclinic in crystal structure. Many publications on $BiVO_4$ describing phase structures, synthesis methods, physicochemical properties, applications, and so on have emerged since its inaugural work by Kudo et al. as a photocatalyst for O_2 evolution in 1999 [7]. As a promising material, $BiVO_4$ is extensively applied in various fields, such as gas sensors, batteries, electrolytes, water splitting, and other applications [8].

Semiconductor is a kind of materials with electrical conductivity between conductor (such as metals) and insulator (such as ceramics). The unique electronic property of a semiconductor is characterized by its valence band (VB) and conduction band (CB). The VB of a semiconductor is formed by the interaction of the highest occupied molecular orbital (HOMO), while the CB is formed by the interaction of the lowest unoccupied molecular orbital (LUMO). There is no electron state between the top of the VB and the bottom of CB. The energy range between CB and VB is called forbidden bandgap (also called bandgap energy), which is usually denoted as E_g. The band structure, including the bandgap and the positions of VB and CB, is one of the important properties for a semiconductor photocatalyst, because it determines the light absorption property as well as the redox capability of a semiconductor [9].

As shown in reaction 1, the photocatalytic reaction initiates from the generation of electron −hole pairs upon light irradiation. When a semiconductor photocatalyst absorbs photons with energy equal to or greater than its E_g, the electrons in the VB will be excited to the CB, leaving the holes in the VB. The electron-hole pairs generation process in $BiVO_4$ can be expressed as follows:

$$BiVO_4 + h\nu \rightarrow e^- \left(BiVO_4\right) + h^+ \left(BiVO_4\right)$$

(1)

These photogenerated electron–hole pairs may further be involved in the following three possible processes [9]: (i) successfully migrating to the surface of semiconductor, (ii) being captured by the defect sites in bulk and/or on the surface region of semiconductor, and (iii) recombining and releasing the energy in the form of heat or photon. The last two processes are generally viewed as deactivation processes because the photogenerated electrons and holes do not contribute to the photocatalytic reactions. Only the photogenerated charges that reach to the surface of semiconductor can be available for photocatalytic reactions. The defect sites in the bulk and on the surface of semiconductor may serve as the recombination centers for the photogenerated electrons and holes, which would decrease the efficiency of the photocatalytic reaction.

It is well known that the photocatalytic activity of a semiconductor depends strongly upon three factors: adsorption behavior, photoresponsive region, and separation efficiency of electron–hole pairs [10]. The adsorption behavior can usually be enhanced by improving the surface areas of catalysts. In this aspect, how to extend the photoresponsive region and improve the separation efficiency of electron–hole pairs are important factors on the photocatalytic performance of a semiconductor [11]. The way to extend the photoresponsive region of a semiconductor photocatalyst is mainly the doping of nonmetals or transition metals, which can also improve the separation efficiency of electron–hole pairs and increase the oxidation power of photogenerated carriers [12, 13]. In general, noble metals (e.g., Ag, Pt, Au, and Pd) have been used as electron acceptors to separate the photoinduced hole–electron pairs and promote the interfacial charge transfer processes [14].

Generally speaking, physicochemical properties of a material may be quite different depending on its crystal phase structure. The phase structure of BiVO$_4$ is one of the important factors determining its photocatalytic performance [15]. BiVO$_4$ has mainly three polymorphs in nature, including zircon–tetragonal, scheelite–tetragonal, and scheelite–monoclinic. The zircon–tetragonal phase can be formed via a low-temperature (100°C) synthesis route, whereas the scheelite-monoclinic phase can be generated using a high-temperature (400–600°C) synthesis method [16]. Moreover, the phase transformation between the scheelite monoclinic and the scheelite tetragonal can occur reversibly at 255°C [17]. It has been confirmed that the sheelite monoclinic structure of BiVO$_4$ is the most photocatalytically active under visible-light irradiation. The greater reactivity can be associated with the energy band structure since monoclinic and tetragonal BiVO$_4$ have bandgap energies of 2.4 and 2.9 eV, respectively. [8, 18, 19] Though BiVO$_4$ has better photocatalytic performance, various strategies have been proposed to further improve its activity. In addition to the crystal structure, the photocatalytic property also strongly depends upon the morphology of BiVO$_4$ [20]. Different morphological semiconductor photocatalysts have been prepared by many researchers. Efficient charge separation is the most important factor that determines the photocatalytic performance [9]. Furthermore, creation of heterjunction [21] and porous structure [22] as well as doping of element(s) [23] and using of support [24] are also effective strategies for improving charge separation efficiency.

2. Well-defined morphological BiVO$_4$ photocatalysts

As one of new photocatalysts, monoclinic BiVO$_4$ (*m*-BiVO$_4$) with a bandgap energy of 2.4 eV has drawn great attention for its excellent performance under visible-light illumination [7, 25]. Therefore, many strategies, such as solid-state reaction, hydrothermal or solvothermal, chemical bath deposition, and solution combustion methods, are employed for the synthesis of monoclinic BiVO$_4$. The morphology of a crystal plays a crucial role in determining its physicochemical property [26]. In recent years, scientists have been devoted to developing various synthetic routes to realize the tailored fabrication of *m*-BiVO$_4$ with different morphologies that show distinct photocatalytic properties [27]. For example, the hydrothermal method is widely used to prepare *m*-BiVO$_4$ with different morphologies because the morphology of the final product obtained via such a process can be easily controlled by changing the reaction conditions, such as reaction temperature, reaction time, solution pH, and concentration [6]. Recently, different morphologies (such as nanospheres, nanorods, nanoflowers, nanosheets, nanotubes, hyperbrached) of monoclinically structured BiVO$_4$ crystallites have been synthesized by the hydrothermal method with the assistance of surfactants and pH-controlling additives [28]. **Table 1** summarizes the physical properties and photocatalytic activities of the typical BiVO$_4$ reported in the literature.

Photocatalyst	Crystal structure	Surface area (m^2/g)	E_g (eV)	Reaction condition	Degradation efficiency and light illumination time	References
Sphere-like BiVO$_4$	Monoclinic	1.75	–	Visible light, 80 mL RhB (0.01 mmol/L), 0.1 g sample	100% and 20 min	[2]
	Monoclinic	–	–	UV light, RhB	84.1% and 2.5 h	[6]
	Monoclinic	8.4	2.45	Visible light, 200 mL MO (0.01 mmol/L), 0.1 g sample	84% and 2 h	[22]
	Monoclinic	10	2.37	Sunlight, 50 mL phenol (25 mg/L), 0.3 mL H$_2$O$_2$, 0.1 g sample	100% and 1.5 h	[29]
	Monoclinic	2.62	2.48	Visible light, 100 mL RhB (0.01 mmol/L), 0.08 g sample	97.7% and 6 h	[30]
	Monoclinic	–	2.5	Visible light, 100 mL RhB, 0.01 g sample	80% and 50 min	[31]
	Tetragonal	–	2.81	Sunlight, 100 mL MB (5 mg/L), 0.1 g sample	90% and 5 h	[32]
	Monoclinic	24.4	2.50	Blue light, 50 mL MB (0.01 mmol/L), 0.005 g sample	100% and 5 h	[33]
	Monoclinic	85.4	2.38	Visible light, 20 mL MB (20 mg/L), 0.02 g sample	63% and 2 h	[34]

Photocatalyst	Crystal structure	Surface area (m^2/g)	E_g (eV)	Reaction condition	Degradation efficiency and light illumination time	References
	Monoclinic	0.7	2.42	Visible light, 100 mL MB (0.01 mmol/L), 0.01 g sample	90% and 3 h	[35]
Flower-like BiVO$_4$	Monoclinic	0.9	2.3	Visible light, MB (10 mg/L), 1 g/L sample	60% and 2 h	[28]
	Monoclinic	61.6	2.14	Visible light, 20 mL MB (20 mg/L), 0.02 g sample	75% and 2 h	[34]
	Monoclinic	–	2.46	Sunlight, 100 mL MO (10 mg/L), 0.5 g sample	58% and 4 h	[36]
	Monoclinic	1.6	2.45	Sunlight, 200 mL RhB (5 mg/L), 0.1 g sample	62% and 10 h	[37]
	Monoclinic	2.1	2.52	Visible light, 100 mL MO (0.01 mmol/L), 0.1 g sample	60% and 4 h	[38]
Rod-like BiVO$_4$	Monoclinic	3.5	2.46	Sunlight, 200 mL RhB (10 mg/L), 0.2 g sample	98.3% and 8 h	[27]
	Monoclinic	4.3	2.26	Visible light, 100 mL MB (0.01 mmol/L), 0.01 g sample	90% and 2 h	[35]
	Monoclinic	3.8	2.47	Visible light, 100 mL MO (0.01 mmol/L), 0.1 g sample	87% and 4 h	[38]
	Monoclinic/ tetragonal	–	2.46	Visible light, 100 mL RhB (10 mg/L), 0.04 g sample	39.5% and 2.5 h	[39]
	Monoclinic	–	2.45	Visible light, 100 mL RhB (0.01 mmol/L), 0.2 g sample	96% and 50 min	[40]
Peanut-like BiVO$_4$	Monoclinic	10.3	2.4	Sunlight, 200 mL RhB (5 mg/L), 0.1 g sample	61% and 10 h	[37]
	Monoclinic	0.54	2.4	Solar light, 100 mL crystalviolet (0.02 mmol/L), 0.05 g sample	98% and 1 h	[41]
	Monoclinic	33.9	2.44	Visible light, 100 mL MB (10 mg/L), 0.1 g sample	95% and 225 min	[42]
	Monoclinic	5.4	2.35	UV–Vis light, 100 mL MB (10 ppm), 1 g/L sample	40% and 2 h	[43]
Polyhedron-like BiVO$_4$	Monoclinic	0.9	2.34	Visible light, 100 mL MB (0.01 mmol/L), 0.01 g sample	90% and 2 h	[35]
	Monoclinic	3.97	2.25	Visible light, 50 mL RhB (0.015 mmol/L), 0.1 g sample	60% and 10 h	[44]
	Monoclinic	–	2.35	Visible light, 30 mL MB (5 mg/L), 0.1 g sample	81.6% and 160 min	[45]

Photocatalyst	Crystal structure	Surface area (m²/g)	E_g (eV)	Reaction condition	Degradation efficiency and light illumination time	References
	Monoclinic	0.4	2.35	Visible light, alachlor (50 mg/L), 1 g/L sample	97% and 6 h	[46]
Olive-like BiVO$_4$	Monoclinic	0.91	2.40	Sunlight, 50 mL MB (10 mg/L), 0.1 g sample	18% and 3.5 h	[26]
	Monoclinic	4.6	2.40	Sunlight, 200 mL RhB (5 mg/L), 0.1 g sample	97% and 10 h	[37]
	Monoclinic	–	2.50	Visible light, 100 mL RhB (10 mg/L), 0.04 g sample	50.5% and 2.5 h	[39]
	Monoclinic	–	2.45	Visible light, 100 mL MB (10 mg/L), 0.1 g sample	67% and 225 min	[42]
Microtube-like BiVO$_4$	Monoclinic	6.6	2.33	Visible light, 100 mL MB (0.01 mmol/L), 0.01 g sample	90% and 3 h	[35]
	Monoclinic	–	2.36	Visible light, 100 mL RhB (0.01 mmol/L), 0.5 mmol sample	96% and 3 h	[47]
	Monoclinic	0.3	2.36	Visible light, MO (20 mg/L), 0.01 g sample	95% and 3 h	[48]
	Monoclinic	3.46	2.48	Visible light, 100 mL RhB (0.01 mmol/L), 0.2 g sample	100% and 5 h	[49]
Dumbbell-like BiVO$_4$	Monoclinic	4.6	2.43	Visible light, 200 mL RhB (5 mg/L), 0.1 g sample	89% and 10 h	[37]
	Monoclinic	–	2.51	Visible light, 600 mL RhB (0.01 mmol/L), 0.3 g sample	90% and 4.5 h	[50]
	Monoclinic	9.87	2.25	Sunlight, 100 mL ofloxacin (20 mg/L), 0.1 g sample	80.8% and 1 h	[51]
	Monoclinic	53.6	2.42	Visible light, 100 mL RhB (0.01 mmol/L), 0.1 g sample	100% and 1 h	[52]
Needle-like BiVO$_4$	Monoclinic	–	–	Sunlight, 200 mL RhB (5 mg/L), 0.1 g sample	40% and 10 h	[37]
	Monoclinic	2.0	2.41	UV–Vis light, MB (10 ppm), 1 g/L sample	60% and 2 h	[43]
	Monoclinic	17.63	2.42	Visible light, 100 mL MB (10 mg/L), 0.005 g sample	81% and 200 min	[53]
	Monoclinic	1.6	2.38	UV–Vis light, MB (10 ppm), 1 g/L sample	66% and 3 h	[54]
Dendrite-like BiVO$_4$	Monoclinic/ tetragonal	1.88	2.52	Visible light, 100 mL MB (20 mg/L), 0.1 g sample	95% and 3 h	[16]

Photocatalyst	Crystal structure	Surface area (m^2/g)	E_g (eV)	Reaction condition	Degradation efficiency and light illumination time	References
Butterfly-like BiVO$_4$	Monoclinic	1.22	2.34	Sunlight, 50 mL MB (10 mg/L), 0.1 g sample	74.8% and 3.5 h	[26]
Nanosheet-like BiVO$_4$	Monoclinic	–	3.3	Visible light, 100 mL RhB, 0.01 g sample	50% and 50 min	[31]
Leaf-like BiVO$_4$	Monoclinic	3.0	2.34	Visible light, 100 mL MB (0.01 mmol/L), 0.01 g sample	100% and 3 h	[35]
Cuboid-like BiVO$_4$	Monoclinic	–	2.39	Sunlight, 100 mL MO (10 mg/L), 0.5 g sample	36% and 4 h	[36]
Star-like BiVO$_4$	Monoclinic	–	2.44	Visible light, 100 mL MB (10 mg/L), 0.1 g sample	76% and 225 min	[42]
Bone-like BiVO$_4$	Monoclinic	10.32	2.36	Visible light, 100 mL MB (0.01 mmol/L), 0.005 g sample	61% and 200 min	[53]

Table 1. Physical properties and photocatalytic activities of the well-defined morphological BiVO$_4$ photocatalysts.

2.1. Sphere-like BiVO$_4$

Among different morphologies of BiVO$_4$, microspherical or nanospherical BiVO$_4$ particles are mostly reported. For example, Kunduz et al. [29] reported the preparation of monoclinic bismuth vanadate catalysts by hydrothermal method at different pH values and the removal of phenol from wastewater under natural sunlight illumination. Homogenous and spherical BiVO$_4$ (particle size = 40–90 nm) was formed at pH = 2 (**Figure 1d**), the bandgap energy of the BiVO$_4$ sample calculated from the absorption edge was 2.37 eV. This BiVO$_4$ sample showed a high phenol conversion (100%) within 90 min of natural sunlight illumination, which was related to the morphology of BiVO$_4$ (surface area = 10 m^2/g).
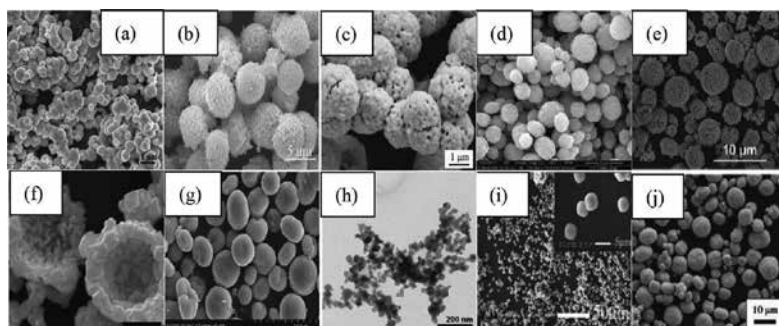

Figure 1. (a–g, i, j) SEM and (h) TEM images of sphere-like BiVO$_4$: (a) [2], (b) [6], (c) [22], (d) [29], (e) [30], (f) [31], (g) [32], (h) [33], (i) [34], and (j) [35].

An one-pot template-free hydrothermal method was developed for the fabrication of $BiVO_4$ microspheres with a tetragonal–monoclinic heterophasic structure [30]. The average diameter, bandgap energy, and BET surface area of the as-prepared $BiVO_4$ microspheres were 4–6 µm, 2.48 eV, and 2.62 m^2/g, respectively. The $BiVO_4$ microspheres exhibited the highest photocatalytic activity with ca. Ninety-eight percentage degradation of RhB, remarkably superior to the pure monoclinic–scheelite $BiVO_4$ and tetragonal–zircon $BiVO_4$. The enhanced photocatalytic performance was attributed to the more effective separation of photogenerated carriers generated in the heterophasic $BiVO_4$. Based on free radical scavenging and N_2/O_2-purging experiments, the degradation of RhB was believed to be driven mainly by the participation of $^\bullet O_2^-$ and a lesser extent by the participation of holes and $^\bullet OH$.

Sun et al. [31] prepared monoclinic scheelite $BiVO_4$ hollow spheres (diameter = 3000–4000 nm) using a simple hydrothermal method with urea as guiding surfactant. It is observed that the RhB removal efficiency of $BiVO_4$ hollow spheres was more than 80% after 50 min of visible-light irradiation without adding any H_2O_2. The superior activity of the m-$BiVO_4$ sample was attributed to two reasons: (i) the BET surface area of the hierarchical hollow spheres was 10.6 m^2/g, the higher surface area provided not only more surface reached by the visible light but also more active sites, which would result in good photocatalytic performance and (ii) the large hollow space inside the microspheres greatly decreased the density of m-$BiVO_4$, thus rendering them to be easily suspended in water.

Monoclinic $BiVO_4$ crystals with a particle size of 400–700 nm and a surface area of 1.75 m^2/g were synthesized with the assistance of cetyltrimethylammonium bromide (CTAB) [2]. The given RhB solution (100 mL, 10^{-5} M) was completely degraded within 20 min of visible-light irradiation, which was due to the addition of CTAB during the catalyst fabrication process.

Many other researchers also reported various kinds of spherical $BiVO_4$ crystallites (Table 1). For example, Ma et al. [32] prepared $BiVO_4$ microspheres by a hydrothermal method in the presence of ethylenediamine tetraacetic acid (EDTA) for the removal of MB under sunlight illumination. Jiang et al. [22] reported porous spherical $BiVO_4$ using urea as pH adjustor and polyvinyl pyrrolidone (PVP) as surfactant for MO degradation. Castillo et al. [33] studied flame-assisted synthesis of nanoscale spherical $BiVO_4$ for the degradation of MB under visible-light illumination. These spherical $BiVO_4$ samples exhibited good photocatalytic activities for the degradation of organic dyes under visible-light irradiation.

2.2. Flower-like $BiVO_4$

A flower-like morphology is usually composed of nanorods or nanosheets. Flower-like particles not only look beautiful, but also show good photocatalytic performance. Fan et al. [34] prepared monoclinic $BiVO_4$ with a flower-like morphology via a simple hydrothermal route by adjusting the amount of surfactant (PVP K30). The photocatalytic efficiency for the decolorization of MB aqueous solution could reach 75% in 2 h of visible-light irradiation. The UV-visible diffuse reflectance absorption spectra reveal that this $BiVO_4$ sample showed excellent absorption of visible light in the region of up to 600 nm, and the E_g was 2.14 eV. The flower-like sample was composed of numerous $BiVO_4$ sub-nanoparticles (400–500 nm) (**Figure 2**). The

BiVO$_4$ possessed a small size, a narrow bandgap energy, and a high BET surface area (61.6 m^2/g), which facilitated the enhancement of photocatalytic activity.
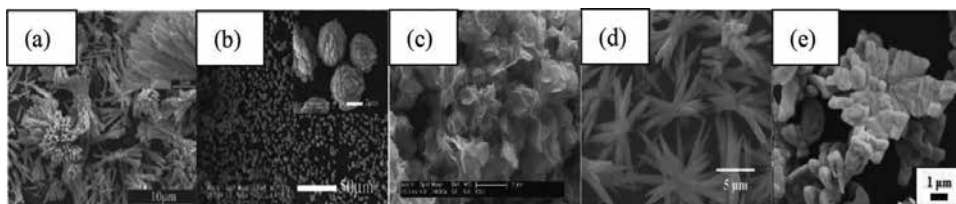
Figure 2. SEM images of flower-like BiVO$_4$: (a) [28], (b) [34], (c) [36], (d) [37], and (e) [38].

An *m*-BiVO$_4$ sample with a regular morphology was prepared using a facile hydrothermal method with Bi$_2$O$_3$ and NH$_4$VO$_3$ as starting material [36]. The as-synthesized sample had a flower-like structure with a diameter of 1–2 μm and a bandgap energy of 2.46 eV. About 58% of MO in the aqueous solution was degraded after sunlight irradiation for 4 h. Photocatalytic performance of the as-prepared BiVO$_4$ sample was much better than that of P25 under the same reaction conditions, which might be ascribable to the flower structure and the larger surface area of the nanosheet-like BiVO$_4$ sample. Larger surface area can facilitate the harvesting of light, whereas the thinness of the nanosheets can cause a bigger distortion of the unit cell induced by the large surface strain. All of those factors might contribute to the improvement in photocatalytic activity of BiVO$_4$.

2.3. Rod-like BiVO$_4$

Figure 3 shows the scanning electron microscopic (SEM) images of the rod-like BiVO$_4$ samples. Hu et al. [27] reported the controlled fabrication of monoclinic BiVO$_4$ with a rod-like structure and investigated the effect of calcination temperature on the sunlight-driven photocatalytic degradation of RhB. It is found that the sample calcined at 300°C exhibited a superior photocatalytic activity: RhB at an initial concentration of RhB lower than 10 mg/L could be completely decolorized after 6 h of sunlight irradiation. The bandgap energy and BET surface area of the rod-like BiVO$_4$ photocatalyst were 2.46 eV and 3.5 m^2/g, respectively. It can be observed from the SEM images (Figure 3) that the sample obtained after calcination at 300°C was composed of dispersive and short rod-like nanocrystals, thus displaying higher BET surface area, which would enhance the adsorption ability and hence improve the photocatalytic performance. Dai and coworkers [35] prepared monoclinic BiVO$_4$ single crystallites with different morphologies using the triblock copolymer P123-assisted hydrothermal strategy with bismuth nitrate and ammonium metavanadate as metal source and various bases as pH adjustor. The rod-like BiVO$_4$ sample was obtained at pH = 6 using NH$_3$–H$_2$O as pH adjustor. This sample displayed a higher surface area (3.2 m^2/g) and a lower bandgap energy (2.26 eV). The rod-like BiVO$_4$ sample showed excellent visible-light-driven photocatalytic activity for MB degradation in an aqueous solution under visible light irradiation: 90% degradation was achieved within 2 h of reaction. The unusually high visible-light-driven catalytic performance of monoclinically

crystallized rod-like $BiVO_4$ single crystallite was associated with its higher surface area and surface oxygen defect concentrations as well as the unique particle morphology.
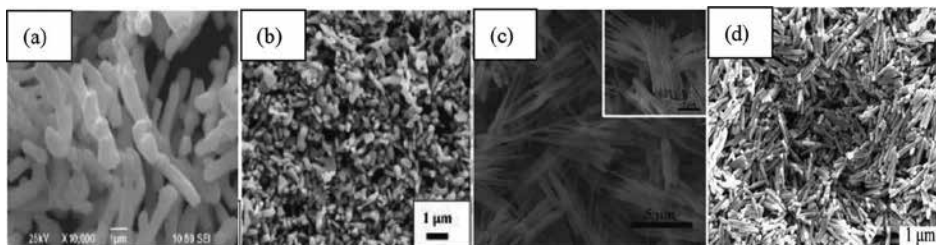
Figure 3. SEM images of rod-like $BiVO_4$: (a) [27], (b) [35], (c) [39], and (d) [40].

2.4. Peanut-like $BiVO_4$

Chen et al. [41] synthesized m-$BiVO_4$ with a hollow peanut-like morphology (**Figure 4b**) using L-lysine as surfactant, and studied its photocatalytic activity for the degradation of crystal violet under solar light irradiation. The best performance was observed over the sample crystallized at 160°C in the presence of L-lysine and after calcination at 550°C. Ninety-eight percentage of the crystal violet could be removed after exposure for 1 h. Although the surface area decreased with the rise in calcination temperature [2.0 m²/g (at 350°C), 0.86 m²/g (at 450°C), and 0.54 m²/g (at 550°C)], their bandgap energies were about 2.4 eV, and the sample calcined at 550°C performed better than the one calcined at 450 or 350°C. The authors assigned the good photocatalytic activity of m-$BiVO_4$ to its unique hollow peanut-like morphology and pure monoclinic phase of high crystallinity, rather than to the bandgap energy and surface area. The physical properties and photocatalytic activities of several kinds of peanut-like $BiVO_4$ samples reported in the literature are listed in **Table 1**.
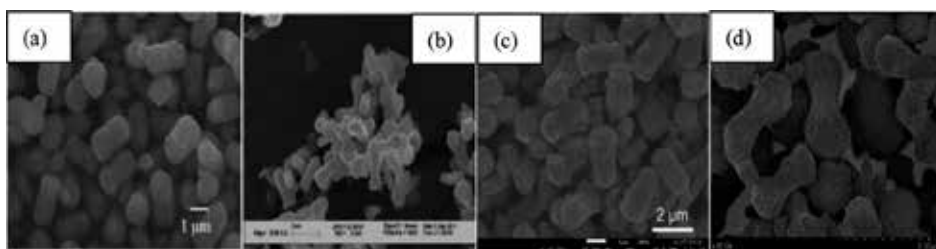
Figure 4. SEM images of peanut-like $BiVO_4$: (a) [37], (b) [41], (c) [42], and (d) [43].

2.5. Polyhedron-like $BiVO_4$

The physical properties and photocatalytic activities of the related polyhedral $BiVO_4$ samples are summarized in **Table 1**. For example, Han et al. [44] reported the synthesis of monodis-

persed octahedral *m*-BiVO$_4$ nanocrystals via a simple hydrothermal route in the presence of sodium dodecyl benzene sulfonate (SDBS). The octahedral *m*-BiVO$_4$ nanocrystal with a size of 200–300 nm (**Figure 5b**) exhibited the highest photocatalytic activity (RhB was completely degraded within 10 h of visible-light irradiation). The octahedral crystals displayed higher surface area (3.97 m^2/g) and narrower bandgap energy (2.25 eV). Such a good photocatalytic activity was attributed to the good crystallization with fewer structural defects and preferred crystal facets for surface-controlled photocatalysis as well as the better optical absorption property and higher surface area. Zhu et al. [45] has successfully synthesized monoclinic decahedral BiVO$_4$ by the microwave-assisted hydrothermal method with Tween-80 as template. The photocatalytic efficiency of decahedral BiVO$_4$ obtained hydrothermally at 160°C showed the highest photocatalytic MB degradation efficiency (ca. 82% MB was degraded after 160 min of visible-light irradiation). The bandgap energy of the sample derived hydrother-mally at 160°C was 2.35 eV. The authors concluded that the good photocatalytic performance of the decahedral BiVO$_4$ sample was related to the imperfect crystal and small size, which resulted in the efficient separation of the electron–hole pairs.
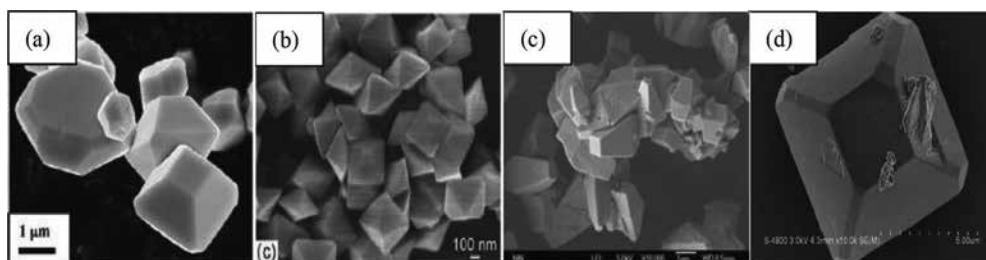
Figure 5. SEM images of polyhedron-like BiVO$_4$: (a) [35], (b) [44], (c) [45], and (d) [46].

2.6. Olive-like BiVO$_4$

The physical properties and photocatalytic activities of several kinds of olive-like BiVO$_4$ samples are listed in Table 1. Adopting the facile pH-dictated solvothermal route with the aid of either NH$_3$–H$_2$O or NaOH, Dong et al. [37] controllably synthesized the uniform monoclinic scheelite BiVO$_4$ with hierarchical structures. As the pH value was adjusted to 6.26 using NaOH as the pH controller, the olive-like BiVO$_4$ crystallites (bandgap energy = 2.40 eV) was generated. The olive-like BiVO$_4$ sample showed a RhB degradation efficiency of 97% after 10 h of sunlight irradiation. It should be noted that this sample did not have a high surface area (4.6 m^2/g) in comparison with other samples (surface area = 6.3–11.1 m^2/g) obtained at different pH values. Apparently, the enhanced photocatalytic performance was not related to the surface area and aspect ratios of the fabricated photocatalysts, but to the unique morphological configurations. Lei et al. [39] synthesized olive-like BiVO$_4$ using a hydrothermal strategy at pH = 3.0. As seen from the SEM images (**Figure 6c**), the sizes of the BiVO$_4$ particles were predominantly 1.8–2.9 μm in length and 1.1–1.8 μm in diameter. The olive-like BiVO$_4$ photocatalyst with a bandgap energy of 2.5 eV showed the highest photocatalytic activity, which could photocatalytically

degrade 50.5% RhB after 150 min of visible-light illumination. The synergic effect of monoclinic phase and particle size contributed to the high photocatalytic efficiency of the olive-like BiVO$_4$ photocatalyst.
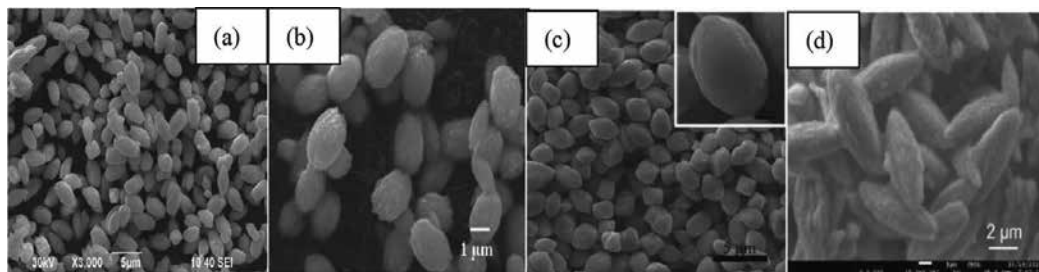
Figure 6. SEM images of olive-like BiVO$_4$: (a) [26], (b) [37], (c) [39], and (d) [42].

Dai and coworkers [38] fabricated the BiVO$_4$ samples with a monoclinic scheelite-type structure and various morphologies via an alcoho-hydrothermal route with Bi(NO$_3$)$_3$ and NH$_4$VO$_3$ as precursor and sodium hdroxide as pH adjustor in the absence or presence of triblock copolymer P123. It is realized that the pH of the precursor solution and the surfactant greatly affected the particle shape and architecture of BiVO$_4$. Porous BiVO$_4$ particles with spherical, flower-like, and sheet-like shapes were obtained in the presence of P123 at a reaction temperature of 180°C and a pH of 2, 7, or 10, respectively. A rod-like BiVO$_4$ was generated at reaction temperature = 180°C and pH = 2. The four BiVO$_4$ samples possessed a surface area of 1.4–3.8 m^2/g and a bandgap energy of 2.47–2.54 eV. The difference in morphology of the BiVO$_4$ particles gave rise to discrepancies in surface area, surface oxygen deficiency density, and (040) crystal face exposure. The rod-like BiVO$_4$ sample that possessed the largest surface area, the highest surface oxygen deficiency density, the highest (040) crystal face exposure, and the lowest bandgap energy performed the best for MO degradation under visible-light irradiation. It is concluded that the particle morphology could influence the photocatalytic activity of BiVO$_4$ and the rod-like shape was favorable for the improvement in photocatalytic activity.

2.7. Microtube-like BiVO$_4$

The physical properties and photocatalytic activities of tubular BiVO$_4$ samples reported in the literature are summarized in **Table 1**. Single-crystalline monoclinic BiVO$_4$ microtubes with a side length of 800 nm and a wall thickness of 100 nm (**Figure 7b**) were synthesized by a facile reflux method at 80°C [47]. The results of optical absorption experiments reveal that in addition to the UV light region, the BiVO$_4$ microtubes also had a strong absorption in the visible-light region and the bandgap energy was estimated to be 2.36 eV. The RhB photodegradation over the BiVO$_4$ microtubes was up to 96% after 3 h of visible-light irradiation, which could be associated with its distinctive morphology.
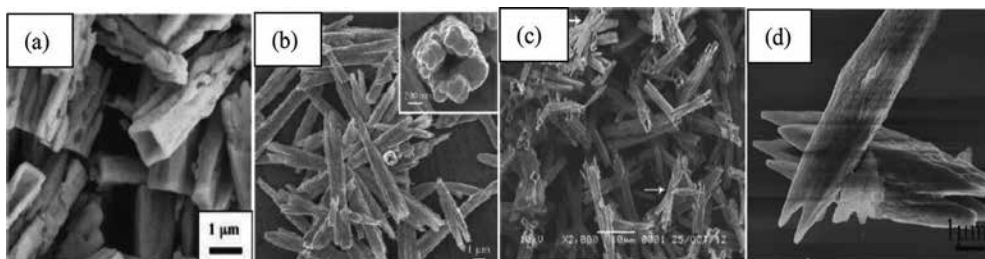
Figure 7. SEM images of microtube-like BiVO$_4$: (a) [35], (b) [47], (c) [48], and (d) [49].

2.8. Dumbbell-like BiVO$_4$

Lu et al. [50] reported the controllable synthesis of dumbbell-like BiVO$_4$ with a hierarchical nanostructure (**Figure 8b**) and a bandgap energy of 2.51 eV by employing a simple hydro-thermal process. The photocatalytic degradation of RhB over the dumbbell-like BiVO$_4$ sample was up to 90% within 4.5 h of visible-light irradiation, which was much higher than the P25 sample under the same reaction conditions. The good visible-light-driven photocatalytic efficiency was related to the exposed crystal planes, which could not only provide more active sites for the photocatalytic reaction but also effectively promote the separation efficiency of the electron–hole pairs. The physical properties and photocatalytic activities of several kinds of dumbbell-like BiVO$_4$ samples reported in the literature are summarized in **Table 1**.
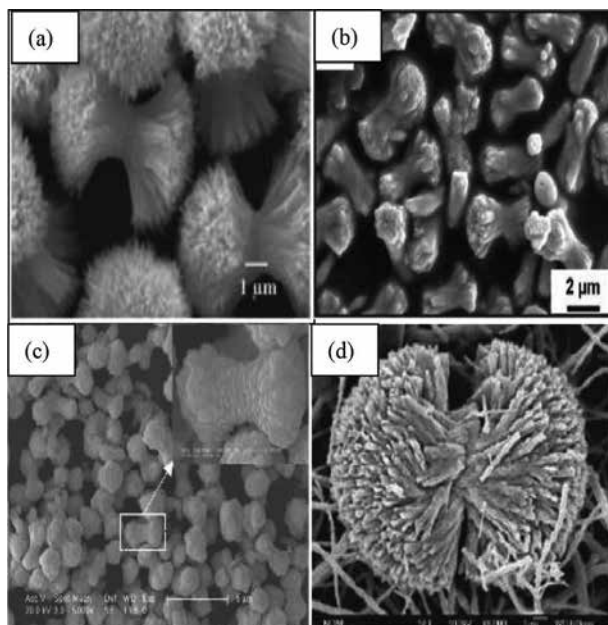
Figure 8. SEM images of dumbbell-like BiVO$_4$: (a) [37], (b) [50], (c) [51], and (d) [52].

2.9. Needle-like BiVO$_4$

The physical properties and photocatalytic activities of the typical needle-like BiVO$_4$ samples are summarized in **Table 1**. For example, Obregón et al. [43] prepared monoclinic BiVO$_4$ with different morphologies by a surfactant-free hydrothermal method through adjusting the pH value, precipitating agent type, hydrothermal temperature, and treatment time. The needle-like particles (**Figure 9b**) obtained with hydrothermal treatment at 100°C and NH$_4$OH as pH controlling agent showed the best efficiency (50–60% after 2 h of UV-visible-light irradiation) for MB photodegradation. The surface areas of the samples obtained with hydrothermal treatment time of 2, 8, and 20 h were 30.2, 2.7, and 1.6 m^2/g, respectively. It should be noted that the slight diminution in surface area had no clear effect on the photocatalytic performance of the sample. Therefore, the best performance was not associated with the surface area, but strongly affected by the crystallite size and morphology.
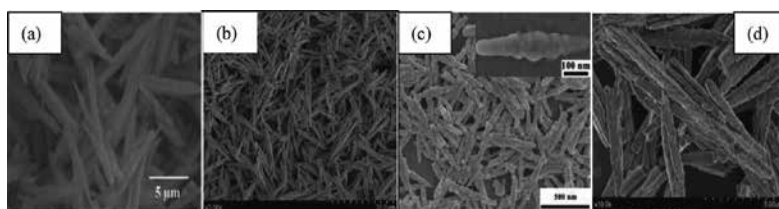
Figure 9. SEM images of needle-like BiVO$_4$: (a) [37], (b) [43], (c) [53], and (d) [54].

2.10. BiVO$_4$ with other morphologies

In addition to the well-morphological BiVO$_4$ samples described above, there are some kinds of BiVO$_4$ samples with other morphologies (**Figure 10**) that have been prepared. Most of them perform well in the photocatalytic degradation of organic dyes (**Table 1**).
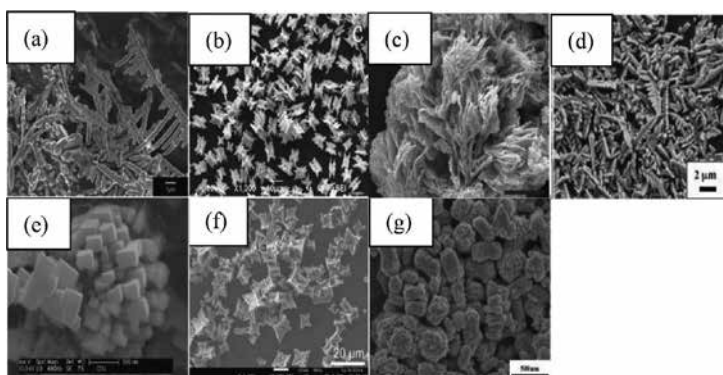
Figure 10. SEM images of BiVO$_4$ with various morphologies: (a) [16], (b) [26], (c) [31], (d) [35], (e) [36], (f) [42], and (g) [53].

3. Porous BiVO$_4$ photocatalysts

Most of the monoclinic BiVO$_4$ samples obtained using the above methods are bulk materials and are low in surface area (<4 m^2/g) [55, 56], which is unfavorable for photocatalytic applications. The reasons are as follows: (i) the amount of surface active sites is intimately related to the surface area [57, 58] and (ii) a porous architecture can increase the ability to capture incident light and the transfer of reactant and product molecules [59]. Therefore, it is of significance to controllably prepare BiVO$_4$ photocatalysts that are porous in structure and high in surface area. The physical properties and photocatalytic activities of typical porous BiVO$_4$ samples are summarized in **Table 2**.

Photocatalyst	Crystal structure	Crystallite size (nm)	Surface area (m^2/g)	E_g (eV)	Reaction condition	Degradation efficiency and light illumination time	References
3DOM BiVO$_4$	Monoclinic	185	23.6	2.50	Visible light, 200 mL phenol (0.1 mmol/L), 0.2 g sample	94% and 3 h	[3]
Mesoporous BiVO$_4$	Monoclinic	–	8.4	2.45	Visible light, 200 mL MO (0.01 mmol/L), 0.1 g sample	84% and 2 h	[22]
Ordered mesoporous BiVO$_4$	Monoclinic	3.5	59	2.20	Visible light, 80 mL MB (10 ppm), 0.08 g sample	85% and 3h	[57]
Mesoporous BiVO$_4$	Monoclinic	–	11.8	2.38	Visible light, 200 mL phenol (0.2 mmol/L), 0.2 g sample	91% and 4 h	[60]
Mesoporous BiVO$_4$	Monoclinic	2.2	7.2	2.38	Sunlight, 200 mL RhB (0.02 mmol/L), 0.2 g sample	100% and 1 h	[61]
3DOM InVO$_4$	Monoclinic	130–140	52.3	2.50	Visible light, 100 mL MB (10 mg/L), 0.1 g sample	98% and 1 h	[62]
15 wt% CrO$_x$/InVO$_4$	Monoclinic	155–165	45	2.10	Visible light, 100 mL RhB (15 mg/L), 0.1 g sample	99% and 200 min	[63]
0.08 wt% Au/3DOM InVO$_4$–BiVO$_4$	Monoclinic	22.3	25.1	2.54	Visible light, 100 mL RhB (15 mg/L), 0.1 g sample	100% and 50 min	[64]
0.08 wt% Au/3DOM InVO$_4$–BiVO$_4$	Monoclinic	22.3	25.1	2.54	Visible light, 100 mL MB (20 mg/L), 0.1 g sample	100% and 90 min	[64]
0.08 wt% Au/3DOM InVO$_4$–BiVO$_4$	Monoclinic	22.3	25.1	2.54	Visible light, 100 mL RhB (15 mg/L) + MB (20 mg/L), 0.1 g sample	100% and 120 min	[64]
0.17 wt% Pd/10 wt % AgBr/BiVO$_4$	Monoclinic	29.8	12.9	2.49	Visible light, 100 mL 4-chlorophenol (15 mg/L), 0.05 g sample	100% and 2.5 h	[65]

Table 2. Physical properties and photocatalytic activities of the porous BiVO$_4$ photocatalysts.

By adopting an alcoho-hydrothermal method with $Bi(NO_3)_3$ and NH_4VO_3 as precursor, sodium hydroxide as pH adjustor, ethanol and ethylene glycol as solvent, and dodecylamine, oleylamine, or oleic acid as surfactant, Dai and coworkers [59] prepared the $BiVO_4$ materials with various shapes and/or mesoporous architectures. Photocatalytic activities of the as-derived samples were measured for phenol degradation in the presence of H_2O_2 under visible-light illumination, and effect of phenol concentration on photocatalytic performance was also probed. The authors pointed out that the surfactant and pH exerted a significant impact on particle morphology and crystal phase structure of $BiVO_4$. Monoclinic $BiVO_4$ samples with a porous olive-like shape could be fabricated with dodecylamine, oleylamine, or oleic acid as surfactant at a pH of 1.5 or 3.0 and a reaction temperature of 100°C. Short-rod-like monoclinic $BiVO_4$ and porous sheet-layered spherical orthorhombic $Bi_4V_2O_{11}$ were generated with dodecylamine as surfactant at reaction temperature = 100°C and pH = 7.0 and 11.0, respectively. Among all of the as-prepared $BiVO_4$ samples, the porous sample with an olive-like morphology and a surface area of 12.7 m^2/g (derived with dodecylamine and at pH = 1.5) exhibited the best visible-light-driven photocatalytic performance for phenol degradation (96% phenol was removed within 4 h of visible-light illumination).

Jiang et al. [60] prepared monoclinic $BiVO_4$ single crystallites with a porous octapod-like morphology using the P123-assisted hydrothermal method with bismuth nitrate and ammonium metavanadate as metal source and various bases as pH adjustor. The $BiVO_4$ with a surface area of 11.8 m^2/g and a bandgap energy of 2.38 eV showed excellent photocatalytic activities for the degradation of MB and phenol. Near 100 and 91% degradation of MB and phenol were achieved within 2 and 4 h of visible-light irradiation, respectively. The authors concluded that the high visible-light-driven catalytic performance of the porous octapod-like $BiVO_4$ single crystallites was associated with the higher surface area, porous structure, and lower bandgap energy.

Peanut-shaped porous monoclinic $BiVO_4$ with high yield was prepared using a simple template-free solvothermal method [61]. The pore size of the sample was 2.2 nm. Compared to the $BiVO_4$ sample obtained hydrothermally, the porous $BiVO_4$ sample exhibited a higher photocatalytic activity for the degradation of RhB and maintained high catalytic efficiency in the repeated recycles of the H_2O_2-containing system. Nearly, complete degradation of RhB was observed after 1 h of sunlight irradiation. It is noteworthy that the bandgap energy (2.38 eV) of the porous $BiVO_4$ sample was higher than that (2.28 eV) of the nonporous $BiVO_4$ sample, but the surface area (7.3 m^2/g) of the former was considerably higher than that (2.1 m^2/g) of the latter.

Li et al. [57] prepared ordered mesoporous monoclinic $BiVO_4$ using mesoporous silica (KIT-6) as template. The mesoporous $BiVO_4$ sample had a surface area of 59 m^2/g and a pore size of 3.5 nm. The mesoporous $BiVO_4$ exhibited a superior visible-light-driven photocatalytic activity for the degradation of MB. The degradation rate over the mesoporous $BiVO_4$ sample was twice as active as the conventional $BiVO_4$ sample, and 85% MB could be degraded after 3 h of visible-light illumination. The mesoporous $BiVO_4$ sample possessed a large surface area, an ordered structure, and a small crystal size, thus resulting in excellent visible-light photocatalytic

activity. The most attractive feature of the mesoporous BiVO$_4$ semiconductor with a bandgap energy of 2.20 eV was its excellent visible-light response ability.

Liu et al. [3] prepared three-dimensionally ordered macroporous (3DOM) bismuth vanadates with a monoclinic crystal structure and high surface areas (18–24 m^2/g) using ascorbic acid-assisted poly(methyl methacrylate) (PMMA)-templating strategy. The average macropore size and wall thicknesses of the BiVO$_4$ samples were in the ranges of 160–185 and 24–70 nm, respectively. The photocatalytic performance of the porous BiVO$_4$ samples was evaluated for the degradation of phenol in the presence of a small amount of H$_2$O$_2$ under visible-light illumination. The results showed that the conversion of phenol could reach 94% at an initial phenol concentration of 0.1 mmol/L after 3 h of visible-light irradiation. However, only 51% phenol was degraded over the bulk BiVO$_4$ sample. The authors concluded that the excellent photocatalytic activity of 3DOM BiVO$_4$ was associated with the high-quality 3DOM-structured BiVO$_4$ that has a high surface area and a surface oxygen vacancy density.

Wang et al. [62] reported the 3DOM-structured monoclinic InVO$_4$ with high surface areas (35–52 m^2/g) using the citric acid-, tartaric acid-, or ascorbic acid-assisted PMMA-templating strategy. From the SEM images, among the as-obtained samples, the InVO$_4$ sample derived with PMMA in the presence of ascorbic acid showed the best quality in 3DOM architecture and a bandgap energy of 2.50 eV, with the macropore and nanovoid (on the skeletons) sizes being in the ranges of 130–160 and of 2–10 nm, respectively. Ninety-eight percentage MB was removed over the ascorbic acid-derived sample within 1 h of visible-light illumination. It is concluded that the excellent photocatalytic activity of this sample was related to its higher surface area and surface oxygen vacancy density and lower bandgap energy as well as the better quality of 3DOM structure.

Dai and coworker [63] loaded certain amounts of chromia on the surface of 3DOM InVO$_4$ to obtain the yCrO$_x$/3DOM InVO$_4$ (y = 5, 10, 15, and 20 wt%) photocatalysts. They investigated the photocatalytic degradation of RhB in the presence of H$_2$O$_2$ under visible-light illumination and found that (i) chromia in the yCrO$_x$/3DOM InVO$_4$ samples were highly dispersed on the surface of 3DOM InVO$_4$; (ii) after loading of CrO$_x$, the surface areas of the yCrO$_x$/3DOM InVO$_4$ samples decreased; (iii) after visible-light illumination for 200 min, the RhB conversion was 47% over 3DOM InVO$_4$, 90% over 5CrO$_x$/3DOM InVO$_4$, 96% over 10CrO$_x$/3DOM InVO$_4$, 97% over 20CrO$_x$/3DOM InVO$_4$, and 99% over 15CrO$_x$/3DOM InVO$_4$; (iii) the yCrO$_x$/3DOM InVO$_4$ samples exhibited stronger absorption in the UV- and visible-light than the 3DOM InVO$_4$; (iv) the yCrO$_x$/3DOM InVO$_4$ samples possessed higher amounts of surface oxygen vacancies than the 3DOM InVO$_4$ sample. These authors concluded that the good visible-light-driven catalytic activity of 15CrO$_x$/3DOM InVO$_4$ was associated with its CrO$_x$ loading, higher surface area and surface oxygen vacancy density, and lower bandgap energy as well as the better quality of 3DOM structure.

Ji et al. [64] prepared the 3DOM InVO$_4$–BiVO$_4$ (InBi-3D) and its supported noble metal (M) nanoparticles (0.17 wt% M/InBi-3D, M = Au, Ag, Pd, Pt) using the PMMA-templating and polyvinyl alcohol (PVA)- or PVP-assisted reduction methods, respectively. There was co-presence of orthorhombic InVO$_4$ and monoclinic BiVO$_4$ in the InBi-3D or M/InBi-3D samples. The as-fabricated samples displayed a surface area of 17–30 m^2/g, a M particle size of 2.5–3.8

nm, and a bandgap energy of 2.50–2.56 eV. The 0.08 wt% Au/InBi-3D sample exhibited the best photocatalytic activity: The complete degradation of RhB, MB, and RhB + MB could be achieved within 50, 90, and 120 min of visible-light illumination. The authors believe that the 3DOM hierarchical architecture, $InVO_4$–$BiVO_4$ composite, and high dispersion of plasmonic gold nanoparticles were the main factors responsible for excellent photocatalytic efficiency of the InBi-3D-supported Au sample.

Dai and coworkers [65] prepared 3DOM $BiVO_4$ (3D-BiV), AgBr/3D-BiV, and M/AgBr/3D-BiV (M = Au, Pt, and Pd) photocatalysts using the PMMA-templating, low-temperature deposition, and PVA-protected reduction methods, respectively. The AgBr and noble metals were uniformly distributed on the surface of 3D-BiV. The 3DOM $BiVO_4$ sample performed better than the commercial TiO_2 sample. The 10 wt% AgBr/3D-BiV sample exhibited a reduced performance, which might be caused by the shielding effect of excessive AgBr in visible-light spectrum on the 3DOM $BiVO_4$ support. When noble metal was deposited on the surface of 10 wt% AgBr/3D-BiV, the photocatalytic performance was much improved, and the 0.17 wt% Pd/AgBr/3D-BiV sample performed the best: Almost complete degradation of 4-chlorophenol was achieved within 150 min of visible-light illumination. The authors assigned the excellent photocatalytic performance of 0.17 wt% Pd/AgBr/3D-BiV to the good 3DOM structure, high surface oxygen adspecies concentration, easy transfer and separation of photogenerated carriers, and synergistic effect between AgBr or Pd nanoclusters and $BiVO_4$.

4. Heteroatom-doped $BiVO_4$ photocatalysts

Up to now, many investigations have been made to improve the photocatalytic performance of visible-light-responsive $BiVO_4$ by doping heteroatoms that can efficiently avoid the charge recombination via trapping both electrons and holes. The co-doping with both cations and anions can also extend the visible-light absorption spectrum of $BiVO_4$.

4.1. Doping with anions

Yin et al. [66] reported the one-step fabrication of high-performance C-doped $BiVO_4$ photocatalyst with hierarchical structures under visible-light irradiation. The sample calcined at 400°C with a carbon content of 1.5 wt% showed the best photocatalytic MB degradation efficiency (100% degradation after 1 h of visible-light irradiation), which was 6.3 times higher than that over the pure $BiVO_4$ sample (18% degradation after 1 h of visible-light irradiation). The XRD result showed that 1.5 wt% C-$BiVO_4$ had a smaller crystalline size (18.7 nm) in comparison with pure $BiVO_4$ (28.5 nm). Moreover, the bandgap energy of 1.5 wt% C-$BiVO_4$ was about 2.39 eV, which was smaller than that (2.46 eV) of pure $BiVO_4$. The photocatalytic performance was enhanced by C-doping because it improved the efficient separation and transfer of the photogenerated electrons and holes, as evidenced by the results of electron paramagnetic resonance (EPR) measurements.

Tan et al. [67] fabricated a N-doped monoclinic BiVO$_4$ photocatalyst via a facile microwave hydrothermal route using NaN$_3$ as nitrogen source. The photocatalytic performance of the samples was evaluated by the decolorization of RhB under the simulated sunlight irradiation. After 4 h of the simulated sunlight irradiation, the degradation efficiencies over the pure BiVO$_4$ and N-doped BiVO$_4$ samples were 48 and 97%, respectively, indicating that N-doped BiVO$_4$ was twice as active as pure BiVO$_4$. The bandgap energy (2.0 eV) of N-doped BiVO$_4$ was narrower than that (2.2 eV) of pure BiVO$_4$, whereas the surface area (1.34 m^2/g) of the former was close to that (0.21 m^2/g) of the latter. The enhancement in photocatalytic activity could be attributable to the small particle size, narrow bandgap, and most importantly, the existence of multi-atomic BiVO$_4$ centers and surface oxygen vacancies, which improved the mobility of charge carriers and inhibited the recombination of charge carriers.

F-doped BiVO$_4$ particles were synthesized through a simple two-step hydrothermal process [68]. The XRD results demonstrated that the presence of F$^-$ ions did not change the phase structure of monoclinic BiVO$_4$. F-doped BiVO$_4$ was consisted of relatively uniform spheres with a diameter of 2–4 μm, and the bandgap energy was 2.39 eV. When the BiVO$_4$/NaF molar ratio was 1: 0.9, the derived F-doped BiVO$_4$ sample exhibited the highest photocatalytic MB degradation activity (99% MB was degraded after 3 h of visible-light irradiation). The appropriate amount of F$^-$ ions introduced into the BiVO$_4$ crystal lattice might effectively restrain the recombination of photogenerated electron–hole pairs, thus facilitating the improvement in photocatalytic activity.

Jiang et al. [69] prepared fluoride-doped BiVO$_4$ with the different F/Bi molar ratios using the hydrothermal strategy with the hydrothermally derived BiVO$_4$ as precursor and NH$_4$F as fluoride source. All of the samples were of single-phase monoclinic scheelite structure. The doping of fluorine did not induce any alteration in crystal structure but changed the morphology of the sample particles. Compared to the undoped BiVO$_4$ sample, the fluoride-doped BiVO$_4$ samples showed higher oxygen adspecies concentration. When the F/Bi molar ratio was 0.29, the BiVO$_4$ sample with a surface area of 14.6 m^2/g and a bandgap energy of 2.42 eV performed the best for the degradation of phenol, giving a 97% phenol degradation efficiency within 2 h of visible-light irradiation. The authors concluded that the excellent photocatalytic performance of fluoride-doped BiVO$_4$ was associated with its higher surface area and adsorbed oxygen species concentration, stronger optical absorbance performance, and lower bandgap energy.

Other anions (e.g., S and B) were also doped into the BiVO$_4$ lattice (**Table 3**). For example, Guo et al. [70] found that S-doped BiVO$_4$ was superior to pure BiVO$_4$ in photocatalyzing the degradation of MB under visible-light irradiation, since an appropriate amount of S^{2-} ions could improve the separation efficiency of photogenerated electron–hole pairs and hinder their recombination.

Photocatalyst	Crystal structure	Crystallite size (nm)	Surface area (m²/g)	E_g (eV)	Reaction condition	Degradation efficiency and light illumination time	References
0.5 wt% C–BiVO$_4$	Monoclinic	35.7	1.18	–	Visible light, 200 mL phenol (5 mg/L), 0.2 g sample	88.7% and 5 h	[79]
4 mol% B–BiVO$_4$	Monoclinic	23.0	4.17	2.34	Visible light, 50 mL MO (15 mg/L), 0.01 g sample	96% and 50 min	[80]
F–BiVO$_4$ (F/Bi molar ratio = 0.29)	Monoclinic	–	14.6	2.42	Visible light, 200 mL phenol (0.2 mmol/L), 0.2 g sample	97% and 2 h	[69]
0.17 wt% S–BiVO$_4$	Monoclinic	29.01	3.18	2.44	Visible light, 100 mL MB (10 mg/L), 0.1 g sample	100% and 25 min	[70]
0.08 wt% S–BiVO$_4$	Monoclinic	–	9.9	2.40	Visible light, 100 mL MB (0.005 mmol/L), 0.01 g sample	95% and 2 h	[71]
1.40 wt% FeO$_x$/BiVO$_{4-\delta}$S$_{0.08}$	Monoclinic	–	5.1	2.39	Visible light, 100 mL MB (0.01 mmol/L), 0.01 g sample	100% and 90 min	[72]
N–BiVO$_4$ (N : Bi molar ratio = 0.2)	Monoclinic	49.8	3.03	2.23	Visible light, 50 mL MO (10 mg/L), 0.01 g sample	85% and 50 min	[81]
1% wt% Cu-BiVO$_4$	Monoclinic	39.78	15.37	1.90	UV light, 90 mL MB (50 mg/L), 0.15 g sample	96% and 2 h	[82]
2 mol% Mo-BiVO$_4$	Monoclinic	–	0.1	2.39	Visible light, MB (16 ppm), 0.1 g sample	100% and 1.5 h	[78]
1.08 wt% Er-BiVO$_4$	Monoclinic	–	4.39	2.11	Visible light, 100 mL MO (10 mg/L), 0.2 g sample	99.4% and 3 h	[83]
8 mol% Yb-BiVO$_4$	Tetragonal	–	11.02	2.9	Sunlight, 50 mL RhB (5 mg/L), 0.05 g sample	98% and 2 h	[84]
3 mol% Yb/0.75 mol% Er-BiVO$_4$	Monoclinic/tetragonal	–	4	2.35/2.68	UV–vis–NIR light, 150 mL MB (10 ppm), 1 g/L sample	100% and 1 h	[77]
0.8 wt% Eu/4 wt% B-BiVO$_4$	Monoclinic	44.89	4.61	2.28	Visible light, 50 mL MO (15 mg/L), 0.015 g sample	90% and 50 min	[76]

Table 3. Physical properties and photocatalytic activities of the heteroatom-doped BiVO$_4$ photocatalysts.

Employing a dodecylamine-assisted alcohol-hydrothermal method in the absence and presence of thiourea or Na$_2$S, Zhao et al. [71] synthesized the sulfur-doped BiVO$_4$ samples. The S-doped samples possessed a monoclinic scheelite structure and a surface area of 8.4–9.9 m^2/g, and the bandgap energies of the S-doped BiVO$_4$ samples were narrower than that of pure BiVO$_4$. The S-doped BiVO$_4$ sample with a S content of 0.78 wt% showed the best photocatalytic performance for the degradation of MB and formaldehyde. The photodegradation efficiency of MB was 92% within 2.5 h of visible-light illumination, but only 45% MB was degraded over pure BiVO$_4$ under the same conditions. It is believed that a higher adsorbed oxygen species concentration and a lower bandgap energy were responsible for the excellent photocatalytic activity of the 0.78 wt% S-BiVO$_4$ sample. These authors also investigated the porous olive-like morphological S-doped bismuth vanadate-supported iron oxide (yFeO$_x$/BiVO$_{4\delta}$S$_{0.08}$, y = 0.06–1.40 wt%) photocatalysts derived from the dodecylamine-assisted alcohol-hydrothermal and incipient wetness impregnation methods [72]. It is shown that the yFeO$_x$/BiVO$_{4\delta}$S$_{0.08}$ photocatalysts possessed a monoclinic scheetlite BiVO$_4$ phase, a porous olive-like shape, a surface area of 8.8–9.2 m^2/g, and a bandgap energy of 2.38–2.42 eV. Bi^{5+}, Bi^{3+}, V^{5+}, V^{3+}, Fe^{3+}, and Fe^{2+} species were concurrently present on the surface of yFeO$_x$/BiVO$_{4\delta}$S$_{0.08}$. Among all of the as-fabricated samples, the 1.40 wt% FeO$_x$/BiVO$_{4;\delta}$S$_{0.08}$ sample showed the highest photocatalytic activity for MB degradation under visible-light irradiation. It is concluded that the sulfur and FeO$_x$ co-doping, higher adsorbed oxygen species concentration, and lower bandgap energy were responsible for the excellent visible-light-driven catalytic activity of 1.40 wt% FeO$_x$/BiVO$_{4\delta}$S$_{0.08}$.

4.2. Doping with cations

Cation doping is another approach to enhance the photocatalytic degradation efficiency of BiVO$_4$, including transition metal doping and rare-earth doping (**Table 3**). For example, Li et al. [73] prepared Cu-doped monoclinic BiVO$_4$ by a facile hydrothermal method and used the degradation of RhB to evaluate their photocatalytic activities. 1 wt% Cu-BiVO$_4$ showed the best degradation performance: 95% of RhB was degraded within 80 min of visible-light irradiation, whereas pure BiVO$_4$ can only degrade 60% of RhB within the same time. The bandgap energy of 1 wt% Cu-BiVO$_4$ was 2.55 eV, resulting in the photoabsorption ability of the 1 wt% Cu-BiVO$_4$ sample slightly stronger than undoped BiVO$_4$ (bandgap energy = 2.57 eV). The amount of oxygen vacancies increased in the copper-doped samples. Possible factors that significantly enhance photocatalytic performance could be as follows: (i) Cu^{2+} substituted partial V^{5+} ions with lower oxidation state, generating a certain amount of oxygen vacancies; (ii) the generated oxygen vacancies can capture the electrons to suppress recombination of the photoinduced carriers; and (iii) the photoinduced carriers freely diffuse to the active sites on the surface of the photocatalyst where oxidation of organic species takes place.

Zhou et al. [74] prepared a series of visible-light-sensitive monoclinic Co-BiVO$_4$ photocatalysts by the heteronuclear complexing method with diethylenetriamine pentaacetic acid (DTPA) as chelating agent. The bandgap was narrowed by doping cobalt. The bandgap energies of the Co-doped BiVO$_4$ samples at cobalt molar content of 0 and 1–10 wt% were 2.44 and 2.39–2.43 eV, respectively. The photocatalytic activity of Co-BiVO$_4$ was studied by the decolorization of MB. The 5 wt% Co-BiVO$_4$ sample exhibited the highest photocatalytic activity with a 85% of

MB removal (65% of MB removal by pure $BiVO_4$) within 5 h of visible-light irradiation. There was no significant loss of photocatalytic activity in three successive runs (each lasted for 6 h). Therefore, Co-$BiVO_4$ was photocatalytically stable and resistant to photocorrosion during the photocatalytic degradation of organic dyes.

Obregón et al. [75] synthesized Er-$BiVO_4$ by means of a microwave-assisted hydrothermal method and examined the photodegradation of MB under sunlike excitation. The Er-doped $BiVO_4$ sample showed a mixed phase of monoclinic and tetragonal structures. The optimal MB conversion was achieved over the sample with 0.75 atom% of erbium, over which the complete MB degradation was reached after 40 min of light illumination. The reaction rate obtained over this photocatalyst was 20 times higher than that over the undoped $BiVO_4$ sample. Two clear absorption edges in the diffuse reflectance spectra of the sample appeared, and the corresponding bandgap energies were ca. 2.4 and 2.8 eV, which were associated with the monoclinic and tetragonal phases, respectively. In order to understand the role of erbium doping in the luminescent properties of the sample, the photoluminescence spectra upon 523 and 655 nm excitations were studied. Upon 655 nm excitation, the up-converted emission of the 0.75 atom % Er-$BiVO_4$ sample was almost suppressed in the 400–600 nm range. Therefore, the dramatic improvement in photocatalytic activity induced by Er^{3+} doping could correlate to a cooperative process involving the electronic and luminescence mechanism. This sensitization mechanism could improve the photon efficiency of the photocatalytic process, and the formation of a monoclinic–tetragonal heterostructure could also be responsible for a more effective charge separation.

Co-doping with two different elements can exhibit better photocatalytic activity than the doping of single element. Wang et al. [76] reported that photodegradation of MO over $BiVO_4$ doped with B species showed a higher MO degradation rate than the pure $BiVO_4$ sample under visible-light irradiation. With the doping of europium, the photocatalytic MO degradation rate over Eu–B co-doped $BiVO_4$ increased with the rise in europium content, and then decreased when the amount of europium was high enough. Co-doping of two different elements can further increase the photocatalytic activity due to the synergistic effects of a number of factors (such as higher specific area, smaller E_g, and more oxygen vacancies) induced by the co-doping of Eu and B.

Obregón et al. [77] also reported a highly active monoclinic–tetragonal $BiVO_4$ by doping with Yb^{3+} and Er^{3+}, which can completely photodegrade MB within 1 h of sunlike excitation. According to the results of structural and morphological characterization, one can deduce that the presence of Yb^{3+} and Er^{3+} induced the stabilization of the tetragonal phase probably due to its partial incorporation into the $BiVO_4$ lattice. The improved photocatalytic efficiency was ascribed to two reasons: (i) the doping of lanthanide ions favored the co-existence of a monoclinic-tetragonal heterostructure, and such a structural configuration could optimize the charge separation and (ii) Yb^{3+} and Er^{3+} luminescence tandem led to a supportive photoluminescence up-conversion process, which could render the energy transfer process from erbium ions to the monoclinic $BiVO_4$ phase.

It should be noted that not all of the photocatalytic activity enhancement can be ascribed to the higher specific area, small crystallite sizes, smaller E_g, and more oxygen vacancies of the

heteroatom-doped BiVO$_4$ samples. For example, Yao et al. [78] reported that the doping of Mo ions could significantly enhance the photocatalytic activity of BiVO$_4$ for MB photodegradation, which was due to its strong acidity on the surface instead of the reasons mentioned above. Moreover, many other researchers also studied the effect of heteroatom-doping on photocatalytic activity of BiVO$_4$, as been summarized in Table 3.

5. BiVO$_4$-based heterojunction photocatalysts

In comparison with single-component photocatalyst, the heterostructure photocatalyst usually exhibits a higher photocatalytic performance for the degradation of various organic contaminants since it can facilitate the effective separation of photoinduced carriers and suppress the recombination of the electron–hole pairs, leaving more charge carriers to form reactive species [85].

Absorption of photons by a semiconductor photocatalyst induces the photogenerated electrons and holes. The photogenerated charge carriers are separated or recombined on the way to the surface reaction sites. The charge separation is a crucial factor determining the light to conversion efficiency [9]. Therefore, much attention has been paid on increasing the charge separation efficiency. Fabrication of a heterojunction structure has been recognized as a useful strategy to avoid charge recombination in a semiconductor catalyst.

5.1. Co$_3$O$_4$/BiVO$_4$ heterojunction

Co$_3$O$_4$ is a *p*-type semiconductor with interesting electronic and magnetic properties, thus various kinds of Co$_3$O$_4$/BiVO$_4$ composite structures have been studied [86]. The enhancement in photocatalytic activity of the Co$_3$O$_4$/BiVO$_4$ composite is attributed to the efficient charge transfer and separation between Co$_3$O$_4$ and BiVO$_4$ driven by the internal electric field or potential difference created by the heterojunction.

Long et al. [86] prepared the Co$_3$O$_4$/BiVO$_4$ composite photocatalyst with a *p–n* heterojunction semiconductor structure using the impregnation method. These authors observed that the Co$_3$O$_4$/BiVO$_4$ composite sample (0.8 wt% cobalt content) obtained after calcination at 300°C showed a much better photocatalytic activity than pure BiVO$_4$ for phenol degradation under visible-light irradiation. The decrease of phenol concentration over pure BiVO$_4$ was only about 6% within 3 h of visible-light irradiation, but phenol concentration dropped by 85% after Co$_3$O$_4$ was loaded on the surface of BiVO$_4$ under the same conditions. The enhanced activity was attributed to the formation of a *p–n* heterojunction structure and the decrease of recombination of photogenerated hole–electron pairs.

Yu and coworkers [87] also investigated the BiVO$_4$ decorated with Co$_3$O$_4$, which showed a much higher photocatalytic activity than pure BiVO$_4$. The authors believed that the high crystallinity of BiVO$_4$ and the formed *p–n* heterojunction of Co$_3$O$_4$/BiVO$_4$ improved the photocatalytic performance. The physical properties and photocatalytic activities of the Co$_3$O$_4$/BiVO$_4$ heterojunction samples reported in the literature are summarized in **Table 4**.

Photocatalyst	Surface area (m²/g)	E_g (eV)	Reaction condition	Degradation efficiency and light illumination time	References
0.8 wt% Co_3O_4/$BiVO_4$	1.38	–	Visible light, phenol (18 mg/L), 3 g/L sample	96% and 3 h	[86]
3 wt% Co_3O_4/$BiVO_4$	8.03	2.34	Visible light, 80 mL acid orange II (20 mg/L), 0.05 g sample	78% and 5 h	[87]
9 wt% $BiVO_4$/TiO_2	107.7	–	Visible light, 80 mL RhB (0.01 mmol/L), 0.08 g sample	79% and 6 h	[119]
8 mol% $BiVO_4$/TiO_2	17	2.4	Visible light, 50 mL RhB (1 mmol/L), 0.02 g sample	95% and 2 h	[120]
40 mol% CeO_2/$BiVO_4$	–	2.40	Visible light, 100 mL RhB (5 mg/L), 0.15 g sample	73% and 4 h	[121]
40 mol% CeO_2/$BiVO_4$	–	2.46	Visible light, 50 mL MB (0.02 mmol/L), 0.05 g sample	80% and 30 min	[89]
30 mol% $BiVO_4$/C_3N_4	4.52	2.45	Visible light, 50 mL RhB (0.01 mmol/L), 0.05 g sample	85% and 5 h	[97]
16.7 mol% $BiVO_4$/C_3N_4	12.99	2.25	Visible light, 100 mL MB (10 mg/L), 0.05 g sample	96% and 1 h	[98]
1 wt% GR/$BiVO_4$	10	2.38	Visible light, 100 mL RhB (10 mg/L), 0.02 g sample	94% and 140 min	[122]
3 wt% GR/$BiVO_4$	44.2	1.94	Visible light, 100 mL RhB (0.01 mmol/L), 0.6 mmol sample	100% and 10 min	[123]
5 wt% RGO/$BiVO_4$	15.73	2.41	Visible light, 50 mL RhB (10 mg/L), 0.1 g sample	89% and 3 h	[100]
3 wt% RGO/$BiVO_4$	4.84	2.32	Sunlight, 200 mL RhB (7.5 mg/L), 0.15 g sample	96.5% and 6 h	[124]
50 mol% Bi_2WO_6/$BiVO_4$	2.69	2.08	Visible light, 100 mL RhB (0.01 mmol/L), 0.1 g sample	100% and 0.5 h	[105]
3 wt% Bi_2WO_6/$BiVO_4$	–	2.50	Visible light, 50 mL phenol (10 mg/L), 0.15 g sample	81% and 6 h	[125]
2.5 wt% Cu_2O/$BiVO_4$	–	2.4	Visible light, 50 mL MB (0.02 mmol/L), 0.05 g sample	100% and 75 min	[126]
33 wt% Cu_2O/$BiVO_4$	–	2.45	Visible light, 100 mL phenol (100 mg/L), 0.2 g sample	41% and 6 h	[109]
8 wt% CuO/$BiVO_4$	–	2.12	Visible light, 30 mL MO (5 mg/L), 0.03 g sample	90.4% and 3 h	[127]
1 wt% CuO/$BiVO_4$	2	2.28	Visible light, 100 mL acid orange 7 (0.05 mmol/L), 0.05 g sample	95% and 3 h	[128]

Photocatalyst	Surface area (m²/g)	E_g (eV)	Reaction condition	Degradation efficiency and light illumination time	References
Bi$_2$O$_3$/BiVO$_4$ (Bi/V molar ratio = 1.1)	2.3	2.40	Sunlight, 100 mL MB (0.02 mmol/L), 0.05 g sample	100% and 40 min	[129]
Bi$_2$O$_3$/BiVO$_4$	1.48	2.52	Visible light, 100 mL RhB (0.01 mmol/L), 0.1 g sample	88% and 4 h	[113]
43 mol% BiOBr/BiVO$_4$	–	2.38	Visible light, 50 mL MB (10 mg/L), 0.05 g sample	97.2% and 4 h	[130]
13 mol% BiOCl/BiVO$_4$	2.80	2.38	Visible light, 100 mL MO (0.0263 mmol/L), 0.1 g sample	85% and 11 h	[118]
15 mol% BiIO$_4$/BiVO$_4$	–	2.40	Visible light, 50 mL RhB (0.01 mmol/L), 0.05 g sample	75% and 5 h	[131]
MoS$_2$/BiVO$_4$	–	–	Visible light, 100 mL MB (40 mg/L), 0.1 g sample	95% and 2 h	[132]
80 mol% InVO$_4$/BiVO$_4$	25.45	2.52	Visible light, 100 mL MB (0.02 mmol/L), 0.1 g sample	87% and 2 h	[133]
16.7 wt% Ag$_2$O/BiVO$_4$	–	2.06	Visible light, 30 mL MO (5 mg/L), 0.03 g sample	91% and 160 min	[134]
22.47 wt% AgBr/BiVO$_4$	–	–	Visible light, 75 mL MB (10 mg/L), 0.075 g sample	83.1% and 2.5 h	[135]
10 mol% Ag$_3$PO$_4$/BiVO$_4$	–	2.46	Visible light, 100 mL MB (10 mg/L), 0.05 g sample	92% and 10 min	[136]

Table 4. Physical properties and photocatalytic activities of the BiVO$_4$-based heterojunction photocatalysts.

5.2. TiO$_2$/BiVO$_4$ heterojunction

As we know, TiO$_2$ has been widely used in environmental purification, H$_2$ production, photosynthesis, CO$_2$ reduction, etc. TiO$_2$ is cheap, stable, nontoxic, and environmentally friendly, and hence an ideal model for investigations of semiconductor photocatalysts [9]. However, a major drawback of TiO$_2$ is that only UV in the solar spectrum (about 3–5%) can be utilized to initiate the photocatalytic redox processes.

Table 4 summarizes the physical properties and photocatalytic activities of the TiO$_2$/BiVO$_4$ heterojunction samples reported in the literature. Xie et al. [88] prepared TiO$_2$/BiVO$_4$ nano-composites with different molar ratios by impregnating BiVO$_4$ particles into a TiO$_2$ sol and after a thermal treatment at 450°C. The phenol degradation efficiency (74% after 1 h of visible-light illumination) over the TiO$_2$/BiVO$_4$ nanocomposites was as 4 times as that over pure BiVO$_4$. The results of the transient-state surface photovoltage responses and atmosphere-controlled steady-state surface photovoltage spectra demonstrated that the lifetime of photo-generated charge carriers over the nanosized BiVO$_4$ sample could be prolonged by

approximately millisecond timescale after a proper molar ratio of nanocrystalline TiO_2 was coupled. The promoted charge separation was responsible for the unexpected high photocatalytic activity for phenol degradation under visible-light irradiation.

5.3. CeO$_x$/BiVO$_4$ heterojunction

Apart from the most commonly used TiO_2 catalyst, cubic fluorite cerium dioxide (CeO_2), a semiconductor with a bandgap energy similar to that of TiO_2 [89], shows a promising photocatalytic activity for the degradation of various organic dye pollutants [90]. CeO_2 has been used in the splitting of water for H_2 evolution and the degradation of phenol or chlorinated phenol under UV irradiation [91, 92]. However, the broad bandgap energy of CeO_2 limits its applications in visible-light illumination [92]. As we know, the heterojunction structure in composite photocatalysts can dominate photoinduced charges in the direction of transport, distance of separation, and rate of recombination, leading to the efficient separation of photogenerated charges and thus greatly improving the photocatalytic activity of the heterojunction-structured sample. If $BiVO_4$ is coupled with CeO_2 to form a heterojunction structure, it is possible to generate visible-light-driven catalysts that show excellent photocatalytic performance.

Wetchakun et al. [89] prepared the $BiVO_4$/CeO_2 nanocomposites by coupling a homogeneous precipitation method with a hydrothermal process. Photocatalytic activities of the as-prepared samples were examined for the degradation of MB, MO, and a mixture of MB and MO aqueous solutions under visible-light irradiation. The XRD patterns reveal that the $BiVO_4$/CeO_2 nanocomposite was composed of $BiVO_4$ and CeO_2, and $BiVO_4$ in the composite sample was present in two crystalline phases. The sample with a $BiVO_4$/CeO_2 molar ratio of 0.6: 0.4 showed the highest photocatalytic activity (the highest MB degradation of 80% was achieved within 30 min of light irradiation). The absorption of $BiVO_4$/CeO_2 nanocomposites increased in the visible-light region (485–505 nm). Moreover, the low bandgap energy (2.46 eV) of $BiVO_4$/CeO_2 nanocomposites also influenced the dyes degradation.

The physical properties and photocatalytic activities of the CeO_2/$BiVO_4$ heterojunction samples reported in the literature are summarized in **Table 4**.

5.4. g-C$_3$N$_4$/BiVO$_4$ heterojunction

As a promising photocatalyst candidate for organic pollutant removal, graphite-like carbon nitride (g-C_3N_4) exhibits a relatively high photocatalytic activity under visible-light illumination due to its rapid separation of photoinduced charge carriers [93, 94]. The very negative CB (−1.13 eV) of g-C_3N_4 enables a strong reduction power of electrons (e$^-$) in the CB. Nevertheless, there are still some shortcomings (e.g., the limited visible-light absorption below 450 nm and the low surface area) for the utilization of g-C_3N_4 in photocatalysis [95, 96]. Recently, continuous efforts have been made to improve the photocatalytic performance of g-C_3N_4. Among these, combining g-C_3N_4 with other semiconductors to construct heterostructures can effectively promote the separation rate of photoexcited charge carriers [97]. $BiVO_4$ and g-C_3N_4 are selected to construct heterojunction photocatalysts according to the following considerations: (i) both $BiVO_4$ and g-C_3N_4 have been proved to be promising visible-light photocatalysts with

desirable chemical stability and (ii) their suitable energy band alignments are beneficial for the separation of light-induced electron–hole pairs in the as-formed heterojunction photocatalysts. More importantly, the g-C$_3$N$_4$/BiVO$_4$ heterojunction structures can be easily modified to achieve a controllable coverage of g-C$_3$N$_4$ on BiVO$_4$ via a thermal annealing process, during which the g-C$_3$N$_4$ phase can be thermally etched by oxidation in air [7, 98].

Li et al. [98] prepared an efficient g-C$_3$N$_4$/BiVO$_4$ heterojunction photocatalyst with BiVO$_4$ networks decorated by discrete g-C$_3$N$_4$ nanoislands for highly efficient photocatalytic degradation of MB. There was the co-existence of BiVO$_4$ and g-C$_3$N$_4$ phase in the composite samples. Among these heterojunction photocatalysts, the g-C$_3$N$_4$/BiVO$_4$ heterojunction sample with a g-C$_3$N$_4$/BiVO$_4$ ratio of 15: 3 performed the best photocatalytically in the degradation of MB. In this sample, the g-C$_3$N$_4$ phase displayed a discrete nanoisland morphology (5–10 nm in diameter), which was attached tightly to the surface of BiVO$_4$. The as-synthesized g-C$_3$N$_4$/BiVO$_4$ photocatalyst showed a superior visible-light photocatalytic activity, which was about 4.5 and 6.9 times as high as that over pure BiVO$_4$ and g-C$_3$N$_4$, respectively. The enhanced photocatalytic activity can be ascribed to the increased charge separation efficiency, fully exposed reactive sites, and separated redox reaction sites as well as excellent visible-light response in the network composites. The physical properties and photocatalytic activities of the g-C$_3$N$_4$/BiVO$_4$ heterojunction samples are summarized in **Table 4**.

5.5. rGO/BiVO$_4$ heterojunction

Reduced graphene oxide (rGO) with excellent electrical conductivity and high carrier mobility has been proved to be an excellent media for electron transfer. The widely accepted mechanism for the enhancement in photocatalytic performance is that chemical bonding between rGO and semiconductor could accelerate the transfer of photogenerated electrons in semiconductor to rGO, thus effectively suppressing the recombination of photogenerated carriers [99]. The rGO/BiVO$_4$ composites have attracted much attention and significant research progress has been achieved.

Wang et al. [100] fabricated the rGO/BiVO$_4$ nanocomposite photocatalysts with excellent visible-light photocatalytic activities through electrostatic self-assembly via a simple surface charge modification on amorphous BiVO$_4$ powders with silane coupling agent. The surface areas of rGO/BiVO$_4$ and BiVO$_4$ were 23.57 and 2.62 m^2/g, respectively, and their corresponding bandgap energies were 2.41 and 2.47 eV. The photocatalytic MB degradation efficiency over rGO/BiVO$_4$ was 94.1%, whereas that over bare BiVO$_4$ was just 24.1% after 30 min of visible-light irradiation. The smaller particle size with a high surface area and an increased interfacial interaction in rGO/BiVO$_4$ gave rise to increased photocatalytic reaction sites, extended photoresponding range, and enhanced photogenerated charge separation and transportation efficiency.

The physical properties and photocatalytic activities of the rGO/BiVO$_4$ heterojunction samples reported in the literature are summarized in **Table 4**.

5.6. Bi$_2$WO$_6$/BiVO$_4$ heterojunction

As one of the typical Aurivillius oxides with a layered structure, Bi$_2$WO$_6$ has attracted increasing attention in many research fields due to its excellent intrinsic physicochemical properties [101], including ferroelectric piezoelectricity, pyroelectricity, catalytic activity, non-linear dielectric susceptibility, and luminescence. Besides, Bi$_2$WO$_6$ is a typical *n*-type semiconductor with a direct bandgap energy of 2.8 eV and exhibits good photocatalytic performance in the degradation of organic pollutants and the splitting of water under visible-light irradiation [102]. However, pure Bi$_2$WO$_6$ can only respond to the light with a wavelength of less than 450 nm, which accounts for a small part of solar light [103]. In addition, fast recombination of the photoinduced electron–hole pairs in Bi$_2$WO$_6$ restricts photocatalytic performance considerably [104]. Hence, to extend the range of light absorption and accelerate separation of the photogenerated charge carriers in Bi$_2$WO$_6$, a semiconductor with a low bandgap energy could be doped with Bi$_2$WO$_6$ to generate a heterojunction architecture [105]. For example, Ju et al. [105] prepared the Bi$_2$WO$_6$/BiVO$_4$ (C-Bi$_2$WO$_6$/BiVO$_4$) heterojunction photocatalyst via a hydrothermal process and after calcination at 600°C. There were co-presence of monoclinic BiVO$_4$ and orthorhombic Bi$_2$WO$_6$ phases, and no obvious changes in XRD peak shape and position in the calcined (C-Bi$_2$WO$_6$, C-BiVO$_4$, and C-Bi$_2$WO$_6$/BiVO$_4$) and uncalcined (Bi$_2$WO$_6$/BiVO$_4$) samples. The C-Bi$_2$WO$_6$/BiVO$_4$ sample possessed a better crystallinity than the uncalcined Bi$_2$WO$_6$/BiVO$_4$. The surface areas of the C-Bi$_2$WO$_6$, C-BiVO$_4$, Bi$_2$WO$_6$/BiVO$_4$, and C-Bi$_2$WO$_6$/BiVO$_4$ samples were 7.67, 3.62, 20.78, and 2.69 m^2/g, respectively, indicating that calcination at a high temperature led to a decrease in surface area. The C-Bi$_2$WO$_6$/BiVO$_4$ sample exhibited a higher photocatalytic activity (RhB degradation efficiency reached 100% within 30 min of visible-light illumination) than the C-Bi$_2$WO$_6$, C-BiVO$_4$, or Bi$_2$WO$_6$/BiVO$_4$ sample. A high surface area did not give rise to a good photocatalytic activity, suggesting that there were other factors influencing the photocatalytic activity of the sample. The bandgap energies of C-Bi$_2$WO$_6$, C-BiVO$_4$, Bi$_2$WO$_6$/BiVO$_4$, and C-Bi$_2$WO$_6$/BiVO$_4$ were 2.69, 2.30, 2.18, and 2.08 eV, respectively. The results indicate that the C-Bi$_2$WO$_6$/BiVO$_4$ photocatalyst had a wider light absorption range and a more suitable bandgap energy. Based on the calculated energy bands and trapping experiment results, the authors proposed that the difference of band potentials in the two semiconductors could induce an inner electric field at the interface between Bi$_2$WO$_6$ and BiVO$_4$, resulting in the efficient separation of photoinduced electrons and holes on the *n*–*n* heterojunction and a great reduction in recombination of the photoinduced charge carriers. Therefore, the enhanced photocatalytic activity of C-Bi$_2$WO$_6$/BiVO$_4$ could be mainly ascribed to the effective separation of photoinduced electron–hole pairs at the heterojunction interface as well as the wider photoabsorption range and better crystallinity.

5.7. Cu$_2$O/BiVO$_4$ heterojunction

Cu$_2$O is a *p*-type semiconductor with a direct bandgap energy of 2.0 eV and has a noticeable light absorption capability in the visible-light region [106]. The physical properties and photocatalytic activities of the Cu$_2$O/BiVO$_4$ and CuO/BiVO$_4$ heterojunction samples reported in the literature are summarized in **Table 4**. For example, Yang et al. [107] reported that the Cu$_2$O/TiO$_2$ network sample showed a much higher photocatalytic activity than the pure

TiO$_2$ sample under the irradiation of artificial solar light, and the enhanced activity of the former could be attributed to the extended absorption in the visible-light region and the effective separation of photogenerated carriers at the *p–n* junction interface formed between Cu$_2$O and TiO$_2$. Since the CB edge of Cu$_2$O is much higher than that of BiVO$_4$ [108], the Cu$_2$O/BiVO$_4$ composite may be an ideal system to form the *p–n* junction, consequently enhancing the separation of charge carriers and promoting the photocatalytic activity of BiVO$_4$.

Wang et al. [109] prepared the Cu$_2$O/BiVO$_4$ photocatalysts with a heterogeneous nanostructure and a *p–n* junction by coupling a hydrothermal process with a polyol strategy. The XRD pattern of the Cu$_2$O/BiVO$_4$ sample was quite similar to that of the pure BiVO$_4$ nanocrystals, and no obvious peaks due to the Cu$_2$O phase were detected. It can be seen from the SEM image of the Cu$_2$O/BiVO$_4$ sample that a large number of Cu$_2$O nanoparticles (5–20 nm in size) were assembled on the surface of the BiVO$_4$ nanocrystals. Under the irradiation of visible light, the photocatalytic phenol degradation efficiency (41.0%) over the Cu$_2$O/BiVO$_4$ sample was more than two times higher than that (20%) of pure BiVO$_4$ nanocrystals. The bandgap energies of BiVO$_4$ and Cu$_2$O/BiVO$_4$ were 2.48 and 2.45 eV, respectively. Therefore, the enhanced photo-catalytic activity of the Cu$_2$O/BiVO$_4$ sample could be ascribed to formation of the *p–n* junction between *p*-type Cu$_2$O and *n*-type BiVO$_4$. The photogenerated electrons and holes were effectively separated and the recombination of electron–hole pairs was substantially sup-pressed. Thus, the separated electrons and holes were then free to initiate reactions with the reactants adsorbed on the photocatalyst surface, leading to an enhanced photocatalytic activity.

5.8. Bi$_2$O$_3$/BiVO$_4$ heterojunction

Bi$_2$O$_3$ is an active *p*-type semiconductor with an E_g of 2.7–2.8 eV [110]. **Table 4** summarizes the physical properties and photocatalytic activities of the Bi$_2$O$_3$/BiVO$_4$ heterojunction samples. Bessekhouad et al. [111] applied the Bi$_2$O$_3$ semiconductor to degrade orange II in water under visible-light illumination. There are few studies in the literature on the use of Bi$_2$O$_3$ as photo-catalyst in the degradation of organic dyes [112]. Coupling *m*-BiVO$_4$ with Bi$_2$O$_3$ to form a heterojunction is an effective approach to enhance the separation of generated electron–hole pairs.

Guan et al. [113] synthesized the BiVO$_4$ and BiVO$_4$@Bi$_2$O$_3$ microspheres with a hollow olive-like morphology and a *n–p* core-shell structure by a sodium bis(2-ethylhexyl) sulfosuccinate (AOT)-assisted mixed solvothermal method and a NaOH etching process under hydrothermal conditions. The degradation of RhB was employed to evaluate the photocatalytic activity of the BiVO$_4$@Bi$_2$O$_3$ samples. The BiVO$_4$@Bi$_2$O$_3$ sample was composed of two phases: monoclinic scheelite BiVO$_4$ and cubic Bi$_2$O$_3$. Surface areas of BiVO$_4$ and BiVO$_4$@Bi$_2$O$_3$ were 1.45 and 1.48 m^2/g, respectively, and their corresponding photocatalytic RhB degradation efficiencies were 42 and 88%. The results indicate that the photocatalytic activity of the sample did not depend on the surface area. The estimated bandgap energies of the BiVO$_4$ and BiVO$_4$@Bi$_2$O$_3$ were 2.43 and 2.52 eV, respectively. In order to probe the reason of enhanced photocatalytic performance, the band-edge positions of the two semiconductors were calculated. The CB-edge potential of Bi$_2$O$_3$ (0.03 eV) was more active than that of BiVO$_4$ (0.32 eV). Therefore, photoinduced electrons

on the surface of Bi_2O_3 would easily transfer to $BiVO_4$ under the inducement action of the internal *p–n* electric field, leaving holes on the Bi_2O_3 VB. In such a way, the photoinduced electrons and holes could be effectively separated. Therefore, the enhanced activity of core-shell $BiVO_4@Bi_2O_3$ microspheres can be mostly attributed to the *p–n* heterojunction structure, thus the reducing the recombination probability of photogenerated hole–electron carriers.

5.9. BiOCl/ BiVO$_4$ heterojunction

In recent years, much attention has been paid on the bismuth oxyhalides (BiOX, X = Cl, Br, I) [114] and their composites in heterogeneous photocatalysis because of their characteristic hierarchical structures and unique optical properties [115]. Among them, BiOCl has drawn considerable attention as a novel photocatalyst due to their unique layered structure and high photocorrosion property [116]. However, BiOCl is similar to TiO_2, which is semiconductor with a wide bandgap E_g of 3.5 eV [117] and can only absorb UV light (less than 5% of solar energy), leading to poor photocatalytic activity under visible-light illumination.

A visible-light-active BiOCl/BiVO$_4$ photocatalyst with a *p-n* heterojunction structure was prepared using a hydrothermal method [118]. There were co-presence of two phases: mono-clinic BiVO$_4$ and tetragonal BiOCl. The highest photocatalytic activity (85% MO was degraded after 11 h of visible-light irradiation) was obtained over the BiOCl/BiVO$_4$ heterojunction catalyst (BiOCl/BiVO$_4$ molar ratio = 13: 87). The surface area (2.802 m^2/g) of this sample was medium in comparison with those of pure BiVO$_4$ (0.950 m^2/g), Degussa P25 (56.000 m^2/g), and other heterojunction catalysts (2.512–5.315 m^2/g). The absorption edges of pure BiOCl and BiVO$_4$ were 360 and 520 nm, respectively. The BiOCl/BiVO$_4$ composites exhibited dual absorption edges at 360 and 520 nm, indicating the co-presence of BiOCl and BiVO$_4$. Moreover, the absorbance in the 360−520 nm range gradually decreased with increasing the BiOCl content in the BiOCl/BiVO$_4$ samples. Because BiOCl had negligible activity for MO degradation under visible-light irradiation, the enhanced photocatalytic activity after addition of BiOCl was due to formation of the heterojunction structure. The physical properties and photocatalytic activities of the BiOX (X = Cl, Br, I)/BiVO$_4$ heterojunction and other BiVO$_4$-based heterojunction samples are listed in **Table 4**.

6. Supported BiVO$_4$ photocatalyst

Due to fast recombination of photogenerated electrons and holes or lack of appropriate reaction sites, single semiconductor-based photocatalysts usually do not show high efficiency in photocatalysis [9]. To improve the photocatalytic performance, it is necessary to fabricate composite photocatalysts by loading proper oxidation or reduction cocatalyst(s) on a semi-conductor. In such a composite photocatalyst, the role of the cocatalyst(s) is as follows [9]: (i) providing trapping sites for the photogenerated charges and promoting the charge separation, thus enhancing the quantum efficiency; (ii) improving the photostability of the catalyst by timely consuming the photogenerated electrons and holes; and (iii) catalyzing the reactions by lowering the activation energy. Various kinds of cocatalysts have been applied to BiVO$_4$ to

improve the photocatalytic removal of organics, including metal cocatalysts, metal oxide cocatalysts, and metal sulfide cocatalysts. As early in 2005, Kohtani et al. [137] prepared silver particles loaded on BiVO$_4$ by an impregnation method for the degradation of 4-*n*-alkylphenols. Since then, noble metal-loaded BiVO$_4$ has been widely investigated. Because the work function of a noble metal is usually larger than that of most semiconductors, electron transfer from CB of semiconductor to metal happens readily.

Chen et al. [138] prepared the Ag/BiVO$_4$ composites using a one-step method with ethylene glycol and water as solvent and L-lysine as surfactant. The photocatalytic performance of the composites was evaluated for the degradation of MB in an aqueous solution under visible-light irradiation. Based on the XRD and XPS results, only a small part of the Ag presented as metallic Ag (Ag^0) dispersed on the surface of BiVO$_4$, whereas most of Ag was present in oxidized Ag (Ag$^+$). The Ag particles with a size of about 5 nm were in close contact with BiVO$_4$. More than 98% of MB could be degraded over 6.5 wt% Ag/BiVO$_4$ within 100 min of visible-light illumination. The 6.5 wt% Ag/BiVO$_4$ sample had a surface area of 4.84 m^2/g and a bandgap energy of 2.4 eV. The results demonstrate that a proper amount of Ag in the composite could promote the separation of photogenerated electrons and holes.

Au/BiVO$_4$ heterogeneous nanostructures were synthesized using a cysteine-linking strategy through the *in situ* growth of gold nanoparticles on the BiVO$_4$ microtubes and nanosheets [139]. Many small gold nanoparticles with an average size of 7.2 nm were dispersed on the surface of BiVO$_4$ microtubes or nanosheets. The bandgap energies of BiVO$_4$ microtubes, Au-BiVO$_4$ microtubes, BiVO$_4$ nanosheets, and Au-BiVO$_4$ nanosheets were 2.52, 2.51, 2.55, and 2.54 eV, respectively. The MO degradation efficiencies over the Au-BiVO$_4$ microtubes and nanosheets were 36 and 100% after 50 min of visible-light irradiation, respectively. However, the pure BiVO$_4$ microtubes and nanosheets exhibited almost no activities for MO degradation. The enhanced photocatalytic efficiency of the Au-loaded sample was attributed to two aspects: (i) the conjugated gold nanoparticles on the BiVO$_4$ surface might act as electron sinks to retard the recombination of the photogenerated electrons and holes in BiVO$_4$ so as to improve the charge separation on its surface and (ii) the surface plasmon resonance (SPR) of gold nano-particles attached on the BiVO$_4$ surface can also enhance the visible-light photocatalytic efficiency.

Table 5 summarizes the physical properties and photocatalytic activities of BiVO$_4$-supported reduction cocatalysts reported in the literature.

Li et al. [140] prepared the CuO/BiVO$_4$ photocatalysts by an impregnation method. The highest MB photodegradation efficiency was obtained over the sample with a 5 atom% Cu content and after calcination at 300°C. MB could be completely degraded after 2 h of light irradiation. The bandgap energies of pure BiVO$_4$ and 5 atom% CuO/BiVO$_4$ were 2.40 and 2.34 eV, respectively. Moreover, the surface area (5.62 m^2/g) of 5 atom% CuO/BiVO$_4$ was higher than that (1.89 m^2/g) of pure BiVO$_4$. Therefore, the authors concluded that a proper Cu loading could effectively improve the photocatalytic activity.

Photocatalyst	Crystal structure	Crystallite size (nm)	Surface area (m²/g)	E_g (eV)	Reaction condition	Degradation efficiency and light illumination time	References
6.5 wt% Ag/BiVO₄	Monoclinic	5	4.83	2.40	Visible light, 100 mL MB (0.02 mmol/L), 0.05 g sample	98% and 100 min	[138]
1.5 wt% Ag/BiVO₄	Monoclinic	10–30	–	2.10	Visible light, MB (10 mg/L), 1 g/L sample	98% and 2 h	[144]
3.5 wt% Au/BiVO₄	Monoclinic	5		2.54	Visible light, 10 mL MO (5 mg/L), 0.01 g sample	100% and 50 min	[139]
1 wt% Au/BiVO₄	Monoclinic	8–10		2.0	Visible light, 50 mL phenol (10 mg/L), 3 g/L sample	99% and 2.5 h	[145]
1 mol% CuO/BiVO₄	Monoclinic	32.7	5.62	2.34	UV light, 200 mL MB (10 mg/L), 0.2 g sample	100% and 2 h	[140]
5.0 mol% Fe₂O₃/ BiVO₄	Monoclinic	20.38	15.27	2.38	Visible light, 50 mL MB (0.05 mmol/L), 0.05 g sample	81% and 0.5 h	[141]
0.1 wt% Pt/0.1 wt% MnOₓ/BiVO₄	Monoclinic	–	–	–	Visible light, 100 mL MO (10 mg/L), 0.05 g sample	100% and 1.5 h	[142]
0.03 wt% Pt/0.01 wt% RuO₂/BiVO₄	Monoclinic	–	–	2.3	Visible light, 30 mL thiophene (600 ppm), 0.05 g sample	78% and 3 h	[143]
1 mol% Ag₂O/BiVO₄	Monoclinic	100	2.70	2.31	Visible light, 50 mL ibuprofen (10 mg/L), 0.04 g sample	96% and 4 h	[146]
1 wt% PdO/BiVO₄	Monoclinic	–	–	1.63	Visible light, 30 mL MO (10 mg/L), 0.2 g sample	100% and 15 h	[147]

Table 5. Physical properties and photocatalytic activities of the BiVO₄-supported photocatalysts.

Chala et al. [141] prepared the pure BiVO₄ and Fe-loaded BiVO₄ samples by a hydrothermal method. Photocatalytic activities of the samples were examined using the degradation of MB under visible-light irradiation. The Fe/BiVO₄ sample with an optimal iron loading of 5.0 mol % showed the best photodegradation performance (81%) within 30 min of visible-light illumination. The iron loading did not affect the crystal structure of BiVO₄, and the iron oxides (mainly Fe₂O₃) might be loaded merely on the surface of BiVO₄. The bandgap energies of BiVO₄ and 5.0 mol% Fe/BiVO₄ were 2.51 and 2.38 eV, respectively. Loading with Fe₂O₃ creates subband states in the bandgap of BiVO₄ which could then be easily excited to produce more electron–hole pairs under visible-light irradiation, hence resulting in higher photocatalytic

performance. Surface areas of the pure BiVO$_4$ and 5.0 mol% Fe/BiVO$_4$ samples were 6.44 and 15.27 m^2/g, respectively, indicating that loading of BiVO$_4$ with iron oxides led to an increase in surface area. The higher surface area could possibly provide more active sites on the catalyst surface, which gave rise to an enhancement in photocatalytic activity. The physical properties and photocatalytic activities of BiVO$_4$-supported oxidation cocatalysts and dual cocatalysts reported in the literature are summarized in **Table 5**.

In comparison with single cocatalyst-loaded BiVO$_4$ photocatalysts stated above, Li et al. [142] prepared two types of photocatalysts (M/MnO$_x$/BiVO$_4$ and M/Co$_3$O$_4$/BiVO$_4$, where M stands for noble metals) with reduction and oxidation cocatalysts by a photodeposition method for the photocatalytic degradation of MO and RhB. The photocatalytic activity of Pt/MnO$_x$/BiVO$_4$ was remarkably enhanced when Pt and MnO$_x$ were selectively deposited on the electron-rich and hole-rich facets, which was mainly due to the synergetic effect of dual cocatalysts. Moreover, Lin et al. [143] also studied Pt-RuO$_2$/BiVO$_4$ for photocatalytic oxidation of thiophene under visible-light irradiation. The considerable enhancement in photocatalytic activity also confirmed the simultaneous presence of the reduction and oxidation cocatalysts, which was beneficial for the efficient separation and transfer of the photogenerated electrons and holes.

7. Photocatalytic degradation mechanism

7.1. Organic dyes photodegradation mechanisms

According to the literature, the main factors influencing the degradation rate of organic dyes are hydroxyl radicals ($^\bullet$OH), superoxide radical ($^\bullet$O$_2^-$), dissolved oxygen (O$_2$), and holes (h$^+$). The mechanisms for degradation of organic dyes (such as MB, MO, and RhB) are similar. Taking an example, the photocatalytic degradation mechanism over the BiVO$_4$ quantum tubes–graphene composite sample for the degradation of RhB under visible-light illumination is illustrated in **Figure 11**.

It is well known that a complete photocatalytic process is generally divided into three stages: light harvesting, separation of photogenerated charges, and interfacial reactions [148]. In the photocatalytic reaction of converting dyes to CO$_2$ and H$_2$O over the BiVO$_4$–graphene composite material, the electrons (e$^-$) are provided by photoexcitation of BiVO$_4$ (CB electrons). In this regard, BiVO$_4$ can absorb visible light to generate electron–hole pairs (reaction (1)). In fact, the photogenerated electrons instantly transfer from the CB of BiVO$_4$ to the carbon atoms of graphene (reaction (2)). Simultaneously, these electrons on the surface of graphene can be captured by the adsorbed O$_2$ molecules to produce $^\bullet$O$_2^-$ (reaction (3)). Meanwhile, the holes on the surface of BiVO$_4$ can be scavenged by the ubiquitous H$_2$O molecules or OH$^-$ to yield $^\bullet$OH radicals (reaction (4)). In this case, the RhB molecules can be subsequently destroyed into CO$_2$ and H$_2$O (reaction (5)) by the generated $^\bullet$O$_2^-$ and $^\bullet$OH radicals due to their high activities [123].
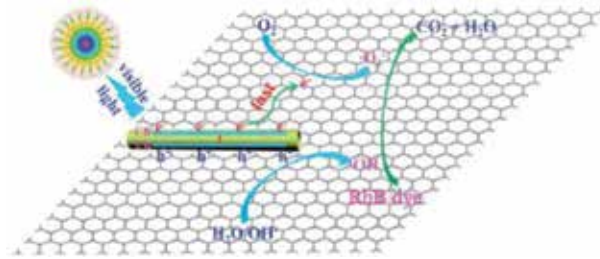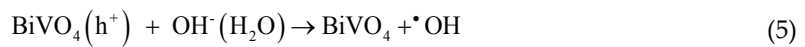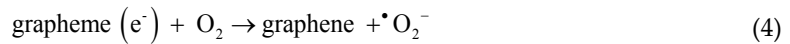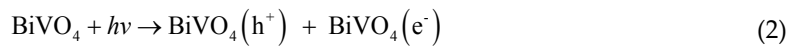
Figure 11. A schematic reaction mechanism illustrating the visible light-driven photodegradation of RhB over the *m*-BiVO$_4$ quantum tubes–graphene nanocomposite catalyst [123].

$$BiVO_4 + hv \rightarrow BiVO_4\left(h^+\right) \; + \; BiVO_4\left(e^-\right) \tag{2}$$

$$BiVO_4\left(e^-\right) \; + \; graphene \rightarrow BiVO_4 + \; graphene\left(e^-\right) \tag{3}$$

$$grapheme\left(e^-\right) \; + \; O_2 \rightarrow graphene \; +^{\bullet}O_2^{\;-} \tag{4}$$

$$BiVO_4\left(h^+\right) \; + \; OH^-\left(H_2O\right) \rightarrow BiVO_4 \; +^{\bullet}OH \tag{5}$$

$$^{\bullet}O_2^{\;-} \; +^{\bullet}OH \; + \; RhB \rightarrow CO_2 \; + \; H_2O \tag{6}$$

$$h^+ \; + \; RhB \rightarrow CO_2 \; + \; H_2O \tag{7}$$

$$H_2O_2 \; + \; e^- \rightarrow^{\bullet}OH \tag{8}$$

It is noteworthy that holes (h$^+$) can directly react with RhB molecules to generate CO$_2$ and H$_2$O (reaction (6)). Moreover, in order to improve the photocatalytic performance, H$_2$O$_2$ is often added to the dye solution as electronic sacrificial agent. It has been reported that a small amount of H$_2$O$_2$ in the initial dye solution was beneficial for trapping e$^-$ to form $^{\bullet}$OH radicals (reaction (7)) and also inhibiting the recombination of e$^-$/h$^+$ pairs.

7.2. Phenol and its derivatives photodegradation mechanisms

The difference of degradation of phenol and its derivatives from that of degradation of organic dyes is that the intermediate products are usually generated, which are difficult to be completely degraded to CO$_2$ and H$_2$O.

$$\cdot O_2^- + \cdot OH + phenol \rightarrow by-products \tag{9}$$
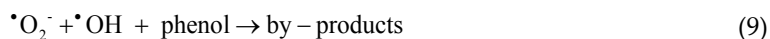
There are at least 20 intermediates (see **Figure 12**) of phenol photodegradation [149], the photodegradation process of phenol is hence very complicated. Furthermore, the routes of phenol photodegradation are different under different experimental conditions. Although the active species for phenol degradation are also the $\cdot OH$, $\cdot O_2^-$, O_2, and h^+, phenol is difficult to be completely destroyed to CO_2 and H_2O.
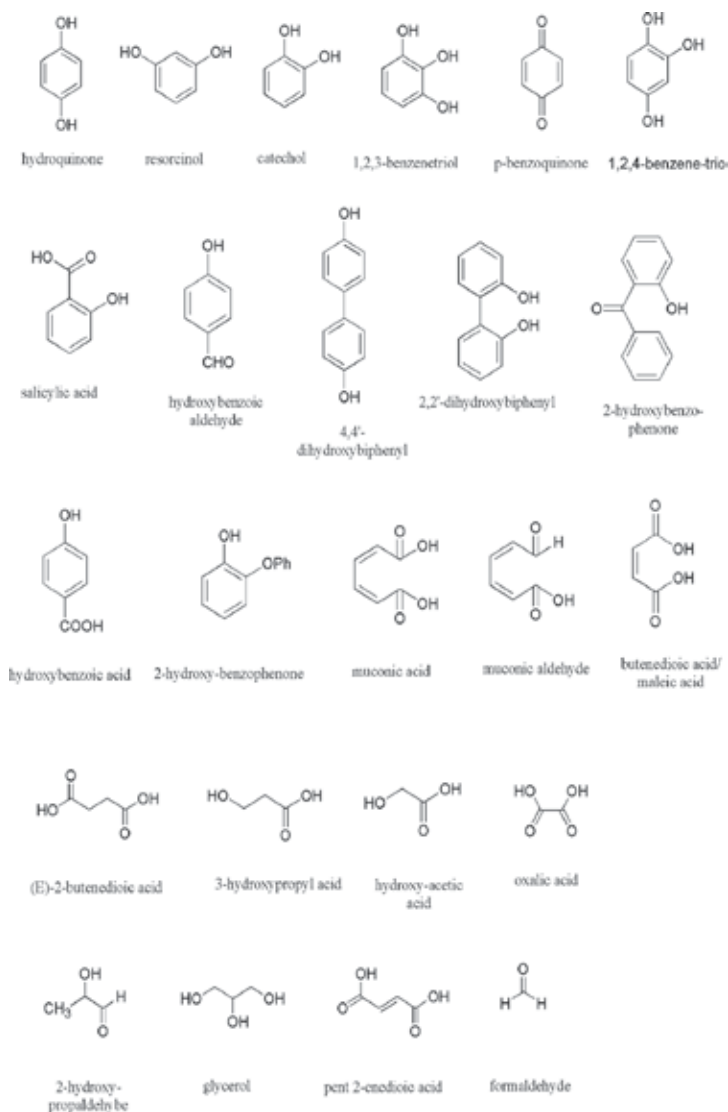

Figure 12. Chemical structures of the by-products derived from phenol photocatalytic degradation [149].

For example, Guo et al. [150] studied degradation of phenol (C_0 = 100 mg/L) over TiO_2 under UV light irradiation. Intermediates were analyzed with gas chromatography/mass spectrometry (GC–MS). The reaction routes were proposed, as shown in **Figure 13**. The $^\bullet$OH radicals attack the phenyl ring, yielding catechol, resorcinol, and hydroquinone, then the phenyl rings in these compounds break up to give malonic acid, the formed short-chain organic acids (such as maleic, oxalic, acetic, formic) are finally converted to CO_2 and H_2O.
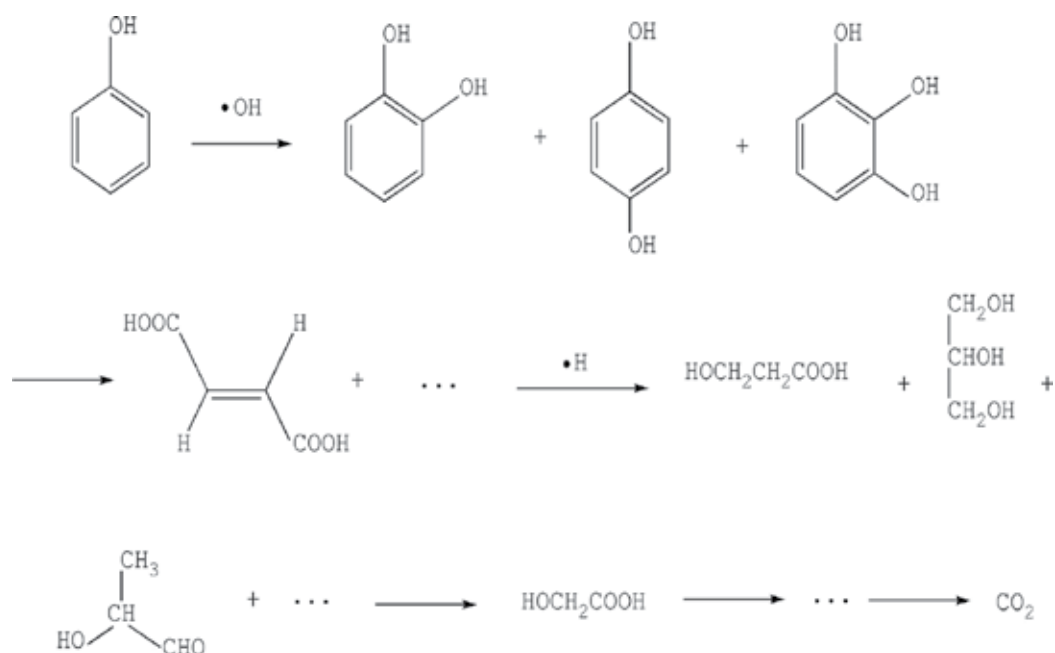

Figure 13. Phenol photodegradation route [150].

Moreover, Devi and Rajashekhar [151] also proposed a possible phenol degradation mechanism over TiO_2 under the conditions of UV light, catalyst dosage = 400 mg/L, phenol concentration = 20 mg/L, and ammonium persulfate (APS) = 100 mg/L), as shown in **Figure 14**.

Based on a plenty of literature, many possible phenol degradation mechanisms have been proposed. Unfortunately and inevitably, the by-products are always generated. It is noted that the toxicity of the by-products generated in phenol degradation processes may be stronger than phenol itself. Therefore, how to directly convert phenol into harmless products is still a big challenge.
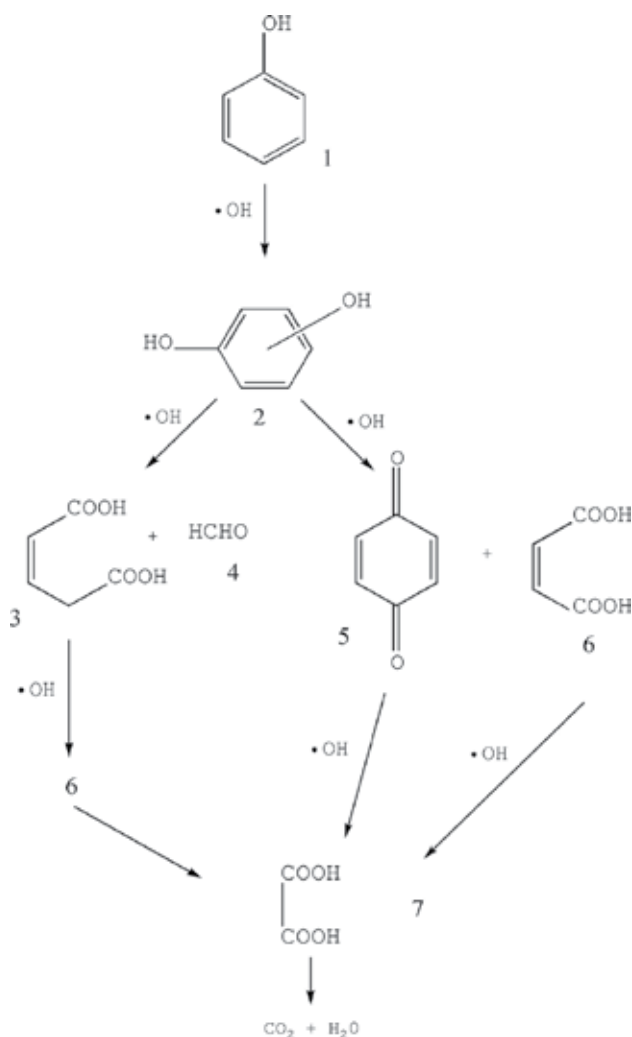
Figure 14. Phenol photodegradation mechanism [151].

8. Conclusive remarks and prospect

A large number of BiVO$_4$ and its related materials with different morphologies and various structures, such as well-defined morphological BiVO$_4$, porous BiVO$_4$, heteroatom-doped BiVO$_4$, BiVO$_4$-based heterojunction, and supported BiVO$_4$, have been successfully synthesized in the literature. Most of them show good or even excellent photocatalytic performance for the degradation of organic dyes, phenol or its derivatives under the illumination of visible light. The structure–photocatalytic performance relationship of these materials has been established, and the involved photocatalytic degradation mechanisms have been proposed.

Due to severe situations in water contamination, researchers have devoted themselves to resolve these problems. In particular, the photocatalytic technology has attracted more and more attention because of its unique advantages. However, it has still a long way to make photocatalytic technology widely practicable. Therefore, three strategies are suggested to further improve the photocatalytic performance: (i) It is greatly desired to design and fabricate novel and highly efficient photocatalytic materials; (ii) although photocatalytic reaction mechanisms have been studied for many years, it is still difficult to identify the elementary reaction steps, therefore *in situ* characterization techniques are used to disclose the reaction mechanisms in essence; and (iii) since the photocatalytic performance can be improved significantly if light, heating, plasmon, electric or magnetic field is coupled, the synergetic effects of these energy coupling would be expected to improve the photocatalytic performance of a photocatalyst.

Author details

Kunfeng Zhang[1,2], Jiguang Deng[1,2], Yuxi Liu[1,2], Shaohua Xie[1,2] and Hongxing Dai[1,2*]

*Address all correspondence to: hxdai@bjut.edu.cn

1 Beijing Key Laboratory for Green Catalysis and Separation, Key Laboratory of Beijing on Regional Air Pollution Control, Key Laboratory of Advanced Functional Materials, Education Ministry of China, Beijing, China

2 Laboratory of Catalysis Chemistry and Nanoscience, Department of Chemistry and Chemical Engineering, College of Environmental and Energy Engineering, Beijing University of Technology, Beijing, China

References

[1] Li HY, Sun YJ, Cai B, Gan SY, Han DX, Niu L, et al. Hierarchically Z-scheme photocatalyst of Ag@AgCl decorated on $BiVO_4$ (040) with enhancing photoelectrochemical and photocatalytic performance. Applied Catalysis B: Environmental. 2015;170–171:206–214. doi:10.1016/j.apcatb.2015.01.043

[2] Yin WZ, Wang WZ, Zhou L, Sun SM, Zhang L. CTAB-assisted synthesis of monoclinic $BiVO_4$ photocatalyst and its highly efficient degradation of organic dye under visible-light irradiation. Journal of Hazardous Materials. 2010;173:194–199. doi:10.1016/j.jhazmat.2009.08.068

[3] Liu YX, Dai HX, Deng JG, Zhang L, Au CT. Three-dimensional ordered macroporous bismuth vanadates: PMMA-templating fabrication and excellent visible light-driven

photocatalytic performance for phenol degradation. Nanoscale. 2012;4:2317–2325. doi: 10.1039/c2nr12046a

[4]   Ni M, Leung MKH, Leung DYC, Sumathy K. A review and recent developments in photocatalytic water-splitting using TiO$_2$ for hydrogen production. Renewable and Sustainable Energy Reviews. 2007;11:401–425. doi: 10.1016/j.rser.2005.01.009

[5]   Wu Q, Han RB, Chen PF, Qi XM, Yao WF. Novel synthesis and photocatalytic performance of BiVO$_4$ with tunable morphologies and macroscopic structures. Materials Science in Semiconductor Processing. 2015;38:271–277. doi:10.1016/j.mssp.2015.04.040

[6]   Li F, Yang CY, Li QG, Cao W, Li TH. The pH-controlled morphology transition of BiVO$_4$ photocatalysts from microparticles to hollow microspheres. Materials Letters. 2015;145:52–55. doi:10.1016/j.matlet.2015.01.043

[7]   Kudo A, Omori K, Kato H. A novel aqueous process for preparation of crystal form-controlled and highly crystalline BiVO$_4$ powder from layered vanadates at room temperature and its photocatalytic and photophysical properties. Journal of the American Chemical Society. 1999;121:11459–11467. doi:10.1021/ja992541y

[8]   Nalbandian MJ, Zhang ML, Sanchez J, Choa YH, Cwiertny DM, Myung NV. Synthesis and optimization of BiVO$_4$ and co-catalyzed BiVO$_4$ nanofibers for visible light-activated photocatalytic degradation of aquatic micropollutants. Journal of Molecular Catalysis A. 2015;404–405:18–26. doi:10.1016/j.molcata.2015.04.003

[9]   Ma Y, Wang XL, Jia YS, Chen XB, Han HX, Li C. Titanium dioxide-based nanomaterials for photocatalytic fuel generations. Chemical Reviews. 2014;114:9987–10043. doi: 10.1021/cr500008u

[10] Gao XM, Wang ZH, Fu F, Li WH. Effects of pH on the hierarchical structures and photocatalytic performance of Cu-doped BiVO$_4$ prepared via the hydrothermal method. Materials Science in Semiconductor Processing. 2015;35:197–206. doi:10.1016/j.mssp.2015.03.012

[11] Jiang RB, Li BX, Fang CH, Wang JF. Metal/semiconductor hybrid nanostructures for plasmon-enhanced applications. Advanced Materials. 2014;26:5274–5309. doi:10.1002/adma.201400203

[12] Tang JT, Song BB, Deng Q, Xin HC. Facile hydrothermal-carbonization approach to carbon-modified BiVO$_4$ composites with enhanced photocatalytic activity. Materials Science in Semiconductor Processing. 2015;35:90–95. doi: 10.1016/j.mssp.2015.01.053

[13] Zhou B, Zhao X, Liu HJ, Qu JH, Huang CP. Synthesis of visible-light sensitive M–BiVO$_4$ (M = Ag, Co, and Ni) for the photocatalytic degradation of organic pollutants. Separation and Purification Technology. 2011;77:275–282. doi:10.1016/j.seppur.2010.12.017

[14] Shiraishi Y, Tsukamoto D, Sugano Y, Shiro A, Ichikawa S, Tanaka S, et al. Platinum nanoparticles supported on anatase titanium dioxide as highly active catalysts for

aerobic oxidation under visible light irradiation. ACS Catalysis. 2012;2:1984–1992. doi: 10.1021/cs300407e

[15] Zhang LL, Long JX, Pan WW, Zhou SY, Zhu JW, Zhao YJ, . Efficient removal of methylene blue over composite-phase $BiVO_4$ fabricated by hydrothermal control synthesis. Materials Chemistry and Physics. 2012;136:897–902. doi:10.1016/j.matchemphys.2012.08.016

[16] Zhang X, Ai ZH, Jia FL, Zhang LZ, Fan XX, Zou ZG. Selective synthesis and visible-light photocatalytic activities of $BiVO_4$ with different crystalline phases. Materials Chemistry and Physics. 2007;103:162–167. doi:10.1016/j.matchemphys.2007.02.008

[17] Fan HM, Jiang TF, Li HY, Wang DJ, Wang LL, Zhai JL, . Effect of $BiVO_4$ crystalline phases on the photoinduced carriers behavior and photocatalytic activity. The Journal of Physical Chemistry B. 2012;116:2425–2430. doi:10.1021/jp206798d

[18] Walsh A, Yan Y, Huda MN, Al-Jassim MM, Wei SH. Band edge electronic structure of $BiVO_4$: Elucidating the role of the Bi s and V d orbitals. Chemistry of Materials. 2009;21:547–551. doi:10.1021/cm802894z

[19] Park Y, McDonald KJ, Choi KS. Progress in bismuth vanadate photoanodes for use in solar water oxidation. Chemical Society Reviews. 2013;42:2321–2337. doi:10.1039/c2cs35260e

[20] Ying YQ, Tao FF, Hong TJ, Wang LX. Controlled fabrication of bismuth vanadium oxide hierarchical microtubes with enhanced visible light photocatalytic activity. Materials Science in Semiconductor Processing. 2015;32:82–89. doi:10.1016/j.mssp.2015.01.009

[21] Wetchakun N, Chaiwichain S, Inceesungvorn B, Pingmuang K, Phanichphant S, Minett AI, . $BiVO_4$/CeO_2 nanocomposites with high visible-light-induced photocatalytic activity. ACS Applied Materials & Interfaces. 2012;4:3718–3723. doi:10.1021/am300812n

[22] Jiang HY, Dai HX, Meng X, Zhang L, Deng JG, Liu YX, . Hydrothermal fabrication and visible-light-driven photocatalytic properties of bismuth vanadate with multiple morphologies and/or porous structures for methyl orange degradation. Journal of Environmental Sciences. 2012;24:449–457. doi:10.1016/S1001-0742(11)60793-6

[23] Thalluri SM, Hernándeza S, Bensaid S, Saracco G, Russo N. Green-synthesized W- and Mo-doped $BiVO_4$ oriented along the {040} facet with enhanced activity for the sun-driven water oxidation. Applied Catalysis B: Environmental. 2016;180:630–636. doi: 10.1016/j.apcatb.2015.07.029

[24] Ge L. Novel Pd/$BiVO_4$ composite photocatalysts for efficient degradation of methyl orange under visible light irradiation. Materials Chemistry and Physics. 2008;107:465–470. doi:10.1016/j.matchemphys.2007.08.016

[25] Luo HM, Mueller AH, McCleskey TM, Burrell AK, Bauer E, Jia QX. Structural and photoelectron chemical properties of $BiVO_4$ thin films. The Journal of Physical Chemistry C. 2008;112:6099–6102. doi:10.1021/jp7113187

[26] Wang XJ, Liu HL, Wang JR, Chang LL, Song NN, Yan ZZ, . Additive-free solvothermal preparation, characterization, and photocatalytic activity of 3D butterfly-like BiVO$_4$. Research on Chemical Intermediates. 2015;41:2465–2477. doi:10.1007/s11164–013-1360-4

[27] Hu LM, Dong SY, Li YK, Pi YQ, Wang JQ, Wang YK, . Controlled fabrication of monoclinic BiVO$_4$ rod-like structures for natural-sunlight-driven photocatalytic dye degradation. Journal of the Taiwan Institute of Chemical Engineers. 2014;45:2462–2468. doi:10.1016/j.jtice.2014.04.022

[28] Xu C, Zhu GQ, Wu JL, Liang J. Template-free hydrothermal synthesis different morphologies of visible-light-driven BiVO$_4$ photocatalysts. Journal of Nanoscience and Nanotechnology. 2014;14:4475–4480. doi:10.1166/jnn.2014.8039

[29] Kunduz S, Soylu GSP. Highly active BiVO$_4$ nanoparticles: The enhanced photocatalytic properties under natural sunlight for removal of phenol from wastewater. Separation and Purification Technology. 2015;141:221–228. doi:10.1016/j.seppur.2014.11.036

[30] Hu Y, Li DZ, Sun FQ, Wang HB, Weng YQ, Xiong W, . One-pot template-free synthesis of heterophase BiVO$_4$ microspheres with enhanced photocatalytic activity. RSC Advances. 2015;5:54882–54889. doi:10.1039/c5ra09785a

[31] Sun JX, Chen G, Wu JZ, Dong HJ, Xiong GH. Bismuth vanadate hollow spheres: Bubble template synthesis and enhanced photocatalytic properties for photodegradation. Applied Catalysis B: Environmental. 2013;132–133:304–314. doi:10.1016/j.apcatb.2012.12.002

[32] Ma WQ, Li ZL, Liu W. Hydrothermal preparation of BiVO$_4$ photocatalyst with perforated hollow morphology and its performance on methylene blue degradation. Ceramics International. 2015;41:4340–4347. doi:10.1016/j.ceramint.2014.11.123

[33] Castillo NC, Heel A, Graule T, Pulgarin C. Flame-assisted synthesis of nanoscale, amorphous and crystalline, spherical BiVO$_4$ with visible-light photocatalytic activity. Applied Catalysis B: Environmental. 2010;95:335–347. doi:10.1016/j.apcatb.2010.01.012

[34] Fan HM, Wang DJ, Wang LL, Li HY, Wang P, Jiang TF, . Hydrothermal synthesis and photoelectric properties of BiVO$_4$ with different morphologies: an efficient visible-light photocatalyst. Applied Surface Science. 2011;257:7758–7762. doi:10.1016/j.apsusc.2011.04.025

[35] Meng X, Zhang L, Dai HX, Zhao ZX, Zhang RZ, Liu YX. Surfactant-assisted hydrothermal fabrication and visible-light-driven photocatalytic degradation of methylene blue over multiple morphological BiVO$_4$ single-crystallites. Materials Chemistry and Physics. 2011;125:59–65. doi:10.1016/j.matchemphys.2010.08.071

[36] Li HB, Liu GC, Duan XC. Monoclinic BiVO$_4$ with regular morphologies: Hydrothermal synthesis, characterization and photocatalytic properties. Materials Chemistry and Physics. 2009;115:9–13. doi:10.1016/j.matchemphys.2009.01.014

[37] Dong SY, Feng JL, Li YK, Hu LM, Liu ML, Wang YF, . Shape-controlled synthesis of BiVO$_4$ hierarchical structures with unique natural-sunlight-driven photocatalytic activity. Applied Catalysis B: Environmental. 2014;152–153:413–424. doi:10.1016/j.apcatb.2014.01.059

[38] Jiang HY, Dai HX, Meng X, Zhang L, Deng JG, Ji KM. Morphology-dependent photocatalytic performance of monoclinic BiVO$_4$ for methyl orange degradation under visible-light irradiation. Chinese Journal of Catalysis. 2011;32:939–949. doi:10.1016/S1872-2067(10)60215-X

[39] Lei BX, Zeng LL, Zhang P, Sun ZF, Sun W, Zhang XX. Hydrothermal synthesis and photocatalytic properties of visible-light induced BiVO$_4$ with different morphologies. Advanced Powder Technology. 2014;25:946–951. doi:10.1016/j.apt.2014.01.014

[40] Wang XK, Li GC, Ding J, Peng HR, Chen KZ. Facile synthesis and photocatalytic activity of monoclinic BiVO$_4$ micro/nanostructures with controllable morphologies. Materials Research Bulletin. 2012;47:3814–3818. doi:10.1016/j.materresbull.2012.04.082

[41] Chen L, Yin SF, Huang R, Zhang Q, Luo SL, Au CT. Hollow peanut-like m-BiVO$_4$: facile synthesis and solar-light-induced photocatalytic property. CrystEngComm. 2012;14:4217–4222. doi:10.1039/c2ce06684j

[42] Lu YJ, Shang HS, Shi FJ, Chao C, Zhang X, Zhang B. Preparation and efficient visible light-induced photocatalytic activity of m-BiVO$_4$ with different morphologies. Journal of Physics and Chemistry of Solids. 2015;85:44–50. doi:10.1016/j.jpcs.2015.04.016

[43] Obregón S, Caballero A, Colón G. Hydrothermal synthesis of BiVO$_4$: Structural and morphological influence on the photocatalytic activity. Applied Catalysis B. 2012;117–118:59–66. doi:10.1016/j.apcatb.2011.12.037

[44] Han MD, Chen XF, Sun T, Tan O, Tse M. Synthesis of mono-dispersed m-BiVO$_4$ octahedral nano-crystals with enhanced visible light photocatalytic properties. CrystEngComm. 2011;13:6674–6679. doi:10.1039/c1ce05539a

[45] Zhu ZF, Zhang L, Li JQ, Du J, Zhang YB, Zhou JQ. Synthesis and photocatalytic behavior of BiVO$_4$ with decahedral structure. Ceramics International. 2013;39:7461–7465. doi:10.1016/j.ceramint.2013.02.093

[46] Chang YK, Wu YS, Lu CS, Lin PF, Wu TY. Photodegradation of alachlor using BiVO$_4$ photocatalyst under visible light irradiation. Water, Air & Soil Pollution. 2015;226:194–205. doi:10.1007/s11270-015-2452-0

[47] Zhou L, Wang WZ, Zhang LS, Xu HL, Zhu W. Single-crystalline BiVO$_4$ microtubes with square cross-sections: Microstructure, growth mechanism, and photocatalytic property. The Journal of Physical Chemistry C. 2007;111:13659–13664. doi:10.1021/jp065155t

[48] Ying YQ, Tao FF, Hong TJ, Wang LX. Controlled fabrication of bismuth vanadium oxide hierarchical microtubes with enhanced visible light photocatalytic activity. Materials Science in Semiconductor Processing. 2015;32:82–89. doi:10.1016/j.mssp.2015.01.009

[49] Liu W, Yu YQ, Cao LX, Su G, Liu XY, Zhang L, . Synthesis of monoclinic structured BiVO$_4$ spindly microtubes in deep eutectic solvent and their application for dye degradation. Journal of Hazardous Materials. 2010;181:1102–1108. doi:10.1016/j.jhazmat.2010.05.128

[50] Lu Y, Luo YS, Kong DZ, Zhang DY, Jia YL, Zhang XW. Large-scale controllable synthesis of dumbbell-like BiVO$_4$ photocatalysts with enhanced visible-light photocatalytic activity. Journal of Solid State Chemistry. 2012;186:255–260. doi:10.1016/j.jssc.2011.12.003

[51] Dong L, Guo S, Zhu SY, Xu DF, Zhang LL, Huo MX, . Sunlight responsive BiVO$_4$ photocatalyst: Effects of pH on L-cysteine-assisted hydrothermal treatment and enhanced degradation of ofloxacin. Catalysis Communications. 2011;16:250–254. doi:10.1016/j.catcom.2011.05.005

[52] Shang M, Wang WZ, Ren J, Sun SM, Zhang L. A novel BiVO$_4$ hierarchical nanostructure: Controllable synthesis, growth mechanism, and application in photocatalysis. CrystEngComm. 2010;12:1754–1758. doi:10.1039/b923115c

[53] Ma YF, Jiang HQ, Zhang XC, Xing JB, Guan YS. Synthesis of hierarchical m-BiVO$_4$ particles via hydro-solvothermal method and their photocatalytic properties. Ceramics International. 2014;40:16485–16493. doi:10.1016/j.ceramint.2014.07.158

[54] Obregón S, Colón G. On the different photocatalytic performance of BiVO$_4$ catalysts for methylene blue and rhodamine B degradation. Journal of Molecular Catalysis A. 2013;376:40–47. doi:10.1016/j.molcata.2013.04.012

[55] Ke DN, Peng TY, Ma L, Cai P, Dai K. Effects of hydrothermal temperature on the microstructures of BiVO$_4$ and its photocatalytic O$_2$ evolution activity under visible light. Inorganic Chemistry. 2009;48:4685–4691. doi:10.1021/ic900064m

[56] Shen Y, Huang ML, Huang Y, Lin JM, Wu JH. The synthesis of bismuth vanadate powders and their photocatalytic properties under visible light irradiation. Journal of Alloys and Compounds. 2010;496:287–292. doi:10.1016/j.jallcom.2010.01.144

[57] Li GS, Zhang DQ, Yu JC. Ordered mesoporous BiVO$_4$ through nanocasting: A superior visible light-driven photocatalyst. Journal of Materials Chemistry. 2008;20:3983–3992. doi:10.1021/cm800236z

[58] Zhou Y, Vuille K, Heel A, Probst B, Kontic R, Patzke GR. An inorganic hydrothermal route to photocatalytically active bismuth vanadate. Applied Catalysis A. 2010;375:140–148. doi:10.1016/j.apcata.2009.12.031

[59] Jiang HY, Dai HX, Meng X, Ji KM, Zhang L, Deng JG. Porous olive-like BiVO$_4$: Alcoho-hydrothermal preparation and excellent visible-light-driven photocatalytic performance for the degradation of phenol. Applied Catalysis B: Environmental. 2011;105:326–334. doi:10.1016/j.apcatb.2011.04.026

[60] Jiang HY, Meng X, Dai HX, Deng JG, Liu YX, Zhang L, . High-performance porous spherical or octapod-like single-crystalline BiVO$_4$ photocatalysts for the removal of

phenol and methylene blue under visible-light illumination. Journal of Hazardous Materials. 2012;217–218:92–99. doi:10.1016/j.jhazmat.2012.02.073

[61] Ge M, Liu L, Chen W, Zhou Z. Sunlight-driven degradation of rhodamine B by peanut-shaped porous $BiVO_4$ nanostructures in the H_2O_2-containing system. CrystEngComm. 2012;14:1038–1044. doi:10.1039/c1ce06264f

[62] Wang Y, Dai HX, Deng JG, Liu YX, Zhao ZX, Li XW, . Three-dimensionally ordered macroporous $InVO_4$: Fabrication and excellent visible-light-driven photocatalytic performance for methylene blue degradation. Chemical Engineering Journal. 2013;226:87–94. doi:10.1016/j.cej.2013.04.032

[63] Wang Y, Dai HX, Deng JG, Liu YX, Arandiyan H, Li XW. 3DOM $InVO_4$-supported chromia with good performance for the visible-light-driven photodegradation of rhodamine B. Solid State Sciences. 2013;24:62–70. doi:10.1016/j.solidstatesciences.2013.07.007

[64] Ji KM, Deng JG, Zang HJ, Han JH, Arandiyand H, Dai HX. Fabrication and high photocatalytic performance of noble metal nanoparticles supported on 3DOM $InVO_4$–$BiVO_4$ for the visible-light-driven degradation of rhodamine B and methylene blue. Applied Catalysis B. 2015;165:285–295. doi:10.1016/j.apcatb.2014.10.005

[65] Ji KM, Dai HX, Deng JG, Zang HJ, Arandiyan H, Xie SH, . 3DOM $BiVO_4$ supported silver bromide and noble metals: High-performance photocatalysts for the visible-light-driven degradation of 4-chlorophenol. Applied Catalysis B: Environmental. 2015;168–169:274–282. doi:10.1016/j.apcatb.2014.12.045

[66] Yin C, Zhu SM, Chen ZX, Zhang W, Gu JJ, Zhang D. One step fabrication of C-doped $BiVO_4$ with hierarchical structures for a high-performance photocatalyst under visible light irradiation. Journal of Materials Chemistry A. 2013;1:8367–8378. doi:10.1039/c3ta11833a

[67] Tan GQ, Zhang LL, Ren HJ, Huang J, Yang W, Xia A. Microwave hydrothermal synthesis of N-doped $BiVO_4$ nanoplates with exposed (040) facets and enhanced visible-light photocatalytic properties. Ceramics International. 2014;40:9541–9547. doi:10.1016/j.ceramint.2014.02.028

[68] Li JQ, Guo ZY, Liu H, Du J, Zhu ZF. Two-step hydrothermal process for synthesis of F-doped $BiVO_4$ spheres with enhanced photocatalytic activity. Journal of Alloys and Compounds. 2013;581:40–45. doi:10.1016/j.jallcom.2013.06.141

[69] Jiang HY, Dai HX, Deng JG, Liu YX, Zhang L, Ji KM. Porous F-doped $BiVO_4$: Synthesis and enhanced photocatalytic performance for the degradation of phenol under visible-light illumination. Solid State Sciences. 2013;17:21–27. doi:10.1016/j.solidstatesciences.2012.12.009

[70] Guo MN, Wang Y, He QL, Wang WJ, Wang WM, Fu ZY, . Enhanced photocatalytic activity of S-doped BiVO$_4$ photocatalysts. RSC Advances. 2015;5:58633–58639. doi: 10.1039/c5ra07603j

[71] Zhao ZX, Dai HX, Deng JG, Liu YX, Au CT. Effect of sulfur doping on the photocatalytic performance of BiVO$_4$ under visible light illumination. Chinese Journal of Catalysis. 2013;34:1617–1626. doi:10.1016/S1872-2067(12)60632-9

[72] Zhao ZX, Dai HX, Deng JG, Liu YX, Wang Y, Li XW, . Porous FeO$_x$/BiVO$_4$·$_·$S$_{0.08}$: Highly efficient photocatalysts for the degradation of methylene blue under visible-light illumination. Journal of Environmental Sciences. 2013;25:2138–2149. doi:10.1016/S1001-0742(12)60279-4

[73] Li DZ, Wang WZ, Jiang D, Zheng YL, Li XM. Surfactant-free hydrothermal fabrication of monoclinic BiVO$_4$ photocatalyst with oxygen vacancies by copper doping. RSC Advances. 2015;5:14374–14381. doi:10.1039/C4RA14318C

[74] Zhou B, Zhao X, Liu HJ, Qu JH, Huang CP. Visible-light sensitive cobalt-doped BiVO$_4$ (Co-BiVO$_4$) photocatalytic composites for the degradation of methylene blue dye in dilute aqueous solutions. Applied Catalysis B: Environmental. 2010;99:214–221. doi: 10.1016/j.apcatb.2010.06.022

[75] Obregón S, Colón G. Heterostructured Er^{3+} doped BiVO$_4$ with exceptional photocatalytic performance by cooperative electronic and luminescence sensitization mechanism. Applied Catalysis B: Environmental. 2014;158–159:242–249. doi:10.1016/j.apcatb.2014.04.029

[76] Wang M, Che YS, Niu C, Dang MY, Dong D. Effective visible light-active boron and europium co-doped BiVO$_4$ synthesized by sol–gel method for photodegradion of methyl orange. Journal of Hazardous Materials. 2013;262:447–455. doi:10.1016/j.jhazmat.2013.08.063

[77] Obregón S, Colón G. Excellent photocatalytic activity of Yb^{3+}, Er^{3+} co-doped BiVO$_4$ photocatalyst. Applied Catalysis B: Environmental. 2014;152–153:328–334. doi:10.1016/j.apcatb.2014.01.054

[78] Yao WF, Iwai H, Ye JH. Effects of molybdenum substitution on the photocatalytic behavior of BiVO$_4$. Dalton Transactions. 2008;11:1426–1430. doi:10.1039/b713338c

[79] Niu ML, Zhu RS, Tian F, Song K, Cao G, Ouyang F. The effects of precursors and loading of carbon on the photocatalytic activity of C–BiVO$_4$ for the degradation of high concentrations of phenol under visible light irradiation. Catalysis Today. 2015;258:585–594. doi:10.1016/j.cattod.2015.04.005

[80] Wang M, Zheng HY, Liu J, Dong D, Che YS, Yang CX. Enhanced visible-light-driven photocatalytic activity of B-doped BiVO$_4$ synthesized using a corn stem template. Materials Science in Semiconductor Processing. 2015;30:307–313. doi:10.1016/j.mssp.2014.09.031

[81] Wang M, Liu Q, Che YS, Zhang LF, Zhang D. Characterization and photocatalytic properties of N-doped BiVO$_4$ synthesized via a sol-gel method. Journal of Alloys and Compounds. 2013;548:70–76. doi:10.1016/j.jallcom.2012.08.140

[82] Chen X, Li L, Yi TT, Zhang WZ, Zhang XL, Wang LL. Microwave assisted synthesis of sheet-like Cu/BiVO$_4$ and its activities of various photocatalytic conditions. Journal of Solid State Chemistry. 2015;229:141–149. doi:10.1016/j.jssc.2015.05.026

[83] Zhang AP, Zhang JZ. Visible-light activities of erbium doped BiVO$_4$ photocatalysts. Chinese Journal of Chemical Physics. 2010;23:73–78. doi:10.1088/1674-0068/23/01/73-78

[84] Huang J, Tan GQ, Zhang LL, Ren HJ, Xia A, Zhao CC. Enhanced photocatalytic activity of tetragonal BiVO$_4$: Influenced by rare earth ionYb^{3+}. Materials Letters. 2014;133:20–23. doi:10.1016/j.matlet.2014.06.123

[85] Li HY, Sun YJ, Cai B, Gan SY, Han DX, Niu L, . Hierarchically Z-scheme photocatalyst of Ag@AgCl decorated on BiVO$_4$ (040) with enhancing photoelectrochemical and photocatalytic performance. Applied Catalysis B: Environmental. 2015;170–171:206–214. doi:10.1016/j.apcatb.2015.01.043

[86] Long M, Cai WM, Cai J, Zhou BX, Chai XY, Wu YH. Efficient photocatalytic degradation of phenol over Co$_3$O$_4$/BiVO$_4$ composite under visible light irradiation. The Journal of Physical Chemistry B. 2006;110:20211–20216. doi:10.1021/jp063441z

[87] Yu CL, Yang K, Yu JC, Cao FF, Li X, Zhou XC. Fast fabrication of Co$_3$O$_4$ and CuO/BiVO$_4$ composite photocatalysts with high crystallinity and enhanced photocatalytic activity via ultrasound irradiation. Journal of Alloys and Compounds. 2011;509:4547–4552. doi:10.1016/j.jallcom.2011.01.100

[88] Xie MZ, Fu XD, Jing LQ, Luan P, Feng YJ, Fu HG. Long-lived, visible-light-excited charge carriers of TiO$_2$/BiVO$_4$ nanocomposites and their unexpected photoactivity for water splitting. Advanced Energy Materials. 2014;4:1–6. doi:10.1002/aenm.201300995

[89] Wetchakun N, Chaiwichain S, Inceesungvorn B, Pingmuang K, Phanichphant S, Minett AI, . BiVO$_4$/CeO$_2$ nanocomposites with high visible-light-induced photocatalytic activity. ACS Applied Materials & Interfaces. 2012;4:3718–3723. doi:10.1021/am300812n

[90] Song S, Xu LJ, He ZQ, Chen JM. Mechanism of the photocatalytic degradation of C.I. reactive black 5 at pH 12.0 using SrTiO$_3$/CeO$_2$ as the catalyst. Environmental Science & Technology. 2007;41:5846–5853. doi: 10.1021/es070224i

[91] Chug KH, Park DC. Water photolysis reaction on cerium oxide photocatalysts. Catalysis Today. 1996;30:157–162. doi:10.1016/0920-5861(96)00006-5

[92] Valente JS, Tzompantzi F, Prince J. Highly efficient photocatalytic elimination of phenol and chlorinated phenols by CeO$_2$/MgAl layered double hydroxides. Applied Catalysis B: Environmental. 2011;102:276–285. doi:10.1016/j.apcatb.2010.12.009

[93] Ge L, Han CC, Liu J. In situ synthesis and enhanced visible light photocatalytic activities of novel PANI–g-C$_3$N$_4$ composite photocatalysts. Journal of Materials Chemistry. 2012;22:11843–11850. doi:10.1039/c2jm16241e

[94] Han CC, Ge L, Chen CF, Li YJ, Xiao XL, Zhang YN, . Novel visible light induced Co$_3$O$_4$-g-C$_3$N$_4$ heterojunction photocatalysts for efficient degradation of methyl orange. Applied Catalysis B: Environmental. 2014;147:546–553. doi:10.1016/j.apcatb. 2013.09.038

[95] Dong F, Wang ZY, Li YH, Ho WK, Lee SC. Immobilization of polymeric g-C$_3$N$_4$ on structured ceramic foam for efficient visible light photocatalytic air purification with real indoor illumination. Environmental Science & Technology. 2014;48:10345–10353. doi:10.1021/es502290f

[96] Liu G, Niu P, Sun CH, Smith SC, Chen ZG, Lu GQ, . Unique electronic structure induced high photoreactivity of sulfur-doped graphitic C$_3$N$_4$. Journal of the American Chemical Society. 2010;132:11642–11648. doi:10.1021/ja103798k

[97] Tian N, Huang HW, He Y, Guo YX, Zhang TR, Zhang YH. Mediator-free direct Z-scheme photocatalytic system: BiVO$_4$/g-C$_3$N$_4$ organic–inorganic hybrid photocatalyst with highly efficient visible-light induced photocatalytic activity. Dalton Transactions. 2015;44:4297–4307. doi:10.1039/c4dt03905j

[98] Li CJ, Wang SP, Wang T, Wei YJ, Zhang P, Gong JL. Monoclinic porous BiVO$_4$ networks decorated by discrete g-C$_3$N$_4$ nano-Islands with tunable coverage for highly efficient photocatalysis. Small. 2014;10:2783–2790. doi:10.1002/smll.201400506

[99] Liu BQ, Liu ZF, Zhang XY, Yang LY, Zhang N, Pan GL. Polymer photovoltaic cells based on solution-processable graphene and P3HT. Advanced Functional Materials. 2009;19:894–904. doi:10.1002/adfm.200800954

[100] Wang YZ, Wang W, Mao HY, Lu YH, Lu JG, Huang JY, . Electrostatic self-assembly of BiVO$_4$-reduced graphene oxide nanocomposites for highly efficient visible light photocatalytic activities. ACS Applied Materials & Interfaces. 2014;6:12698–12706. doi: 10.1021/am502700p

[101] Zhang LS, Wang HL, Chen ZG, Wong PK, Liu JS. Bi$_2$WO$_6$ micro/nano-structures: Synthesis, modifications and visible-light-driven photocatalytic applications. Applied Catalysis B: Environmental. 2011;106:1–13. doi:10.1016/j.apcatb.2011.05.008

[102] Cao XF, Zhang L, Chen XT, Xue ZL. Microwave-assisted solution-phase preparation of flower-like Bi$_2$WO$_6$ and its visible-light-driven photocatalytic properties. CrystEng-Comm. 2011;13:306–311. doi:10.1039/c0ce00031k

[103] Zhang ZJ, Wang WZ, Wang L, Sun SM. Enhancement of visible-light photocatalysis by coupling with narrow-band-gap semiconductor: A case study on Bi$_2$S$_3$/Bi$_2$WO$_6$. ACS Applied Materials & Interfaces. 2012;4:593–597. doi:10.1021/am2017199

[104] Gui MS, Zhang WD, Chang YQ, Yu YX. One-step hydrothermal preparation strategy for nanostructured WO_3/Bi_2WO_6 heterojunction with high visible light photocatalytic activity. Chemical Engineering Journal. 2012;197:283–288. doi:10.1016/j.cej.2012.05.032

[105] Ju P, Wang P, Li B, Fan H, Ai SY, Zhang D, . A novel calcined $Bi_2WO_6/BiVO_4$ heterojunction photocatalyst with highly enhanced photocatalytic activity. Chemical Engineering Journal. 2014;236:430–437. doi:10.1016/j.cej.2013.10.001

[106] Fernando CAN, de Silva PHC, Wethasinha SK, Dharmadasa IM, Delsol T, Simmonds MC. Investigation of n-type Cu_2O layers prepared by a low cost chemical method for use in photovoltaic thin film solar cells. Renewable Energy. 2002;26:521–529. doi: 10.1016/S0960-1481(01)00157-4

[107] Yang LX, Luo SL, Li Y, Xiao Y, Kang Q, Cai QY. High efficient photocatalytic degradation of p-nitrophenol on a unique Cu_2O/TiO_2 p–n heterojunction network catalyst. Environmental Science & Technology. 2010;44:7641–7646. doi:10.1021/es101711k

[108] Abdulkarem AM, Aref AA, Abdulhabeeb A, Li YF, Yu Y. Synthesis of Bi_2O_3/Cu_2O nanoflowers by hydrothermal method and its photocatalytic activity enhancement under simulated sunlight. Journal of Alloys and Compounds. 2013;560:132–141. doi: 10.1016/j.jallcom.2013.01.134

[109] Wang WZ, Huang XW, Wu S, Zhou YX, Wang LJ, Shi HL, . Preparation of p–n junction $Cu_2O/BiVO_4$ heterogeneous nanostructures with enhanced visible-light photocatalytic activity. Applied Catalysis B: Environmental. 2013;134–135:293–301. doi:10.1016/j.apcatb.2013.01.013

[110] Paola AD, García-López E, Marcì G, Palmisano L. A survey of photocatalytic materials for environmental remediation. Journal of Hazardous Materials. 2012;211–212:3–29. doi:10.1016/j.jhazmat.2011.11.050.

[111] Bessekhouad Y, Robert D, Weber JV. Photocatalytic activity of Cu_2O/TiO_2, Bi_2O_3/TiO_2 and $ZnMn_2O_4/TiO_2$ heterojunctions. Catalysis Today. 2005;101:315–321. doi:10.1016/j.cattod.2005.03.038

[112] Sánchez-Martínezn D, Juárez-Ramírez I, Torres-Martínez LM, León-Abarte I. Photocatalytic properties of Bi_2O_3 powders obtained by an ultrasound-assisted precipitation method. Ceramics International. 2016;42:2013–2020. doi:10.1016/j.ceramint.2015.10.007

[113] Guan ML, Ma DK, Hu SW, Chen YJ, Huang SM. From hollow olive-shaped $BiVO_4$ to n-p core-shell $BiVO_4@Bi_2O_3$ microspheres: Controlled synthesis and enhanced visible-light-responsive photocatalytic properties. Inorganic Chemistry. 2011;50:800–805. doi: 10.1021/ic101961z

[114] Wang CH, Shao CL, Liu YC, Zhang LN. Photocatalytic properties BiOCl and Bi_2O_3 nanofibers prepared by electrospinning. Scripta Materialia. 2008;59:332–335. doi: 10.1016/j.scriptamat.2008.03.038

[115] Zhao LJ, Zhang XC, Fan CM, Liang ZH, Han PD. First-principles study on the structural, electronic and optical properties of BiOX (X = Cl, Br, I) crystals. Physica B. 2012;407:3364–3370. doi:10.1016/j.physb.2012.04.039

[116] Shenawi-Khalil S, Uvarov V, Menes E, Popov I, Sasson Y. New efficient visible light photocatalyst based on heterojunction of BiOCl–bismuth oxyhydrate. Applied Catalysis A: General. 2012;413–414:1–9. doi:10.1016/j.apcata.2011.10.029

[117] Chai SY, Kim YJ, Jung MH, Chakraborty AK, Jung D, Lee WI. Heterojunctioned BiOCl/Bi$_2$O$_3$, a new visible light photocatalyst. Journal of Catalysis. 2009;262:144–149. doi:10.1016/j.jcat.2008.12.020

[118] He ZQ, Shi YQ, Gao C, Wen LN, Chen JM, Song S. BiOCl/BiVO$_4$ p-n heterojunction with enhanced photocatalytic activity under visible-light irradiation. The Journal of Physical Chemistry C. 2014;118:389–398. doi:10.1021/jp409598s

[119] Hu Y, Li DZ, Wang HB, Zeng GP, Li XH, Shao Y. Role of active oxygen species in the liquid-phase photocatalytic degradation of RhB using BiVO$_4$/TiO$_2$ heterostructure under visible light irradiation. Journal of Molecular Catalysis A: Chemical. 2015;408:172–178. doi:10.1016/j.molcata.2015.07.025

[120] Zalfani M, Schueren B, Hu ZY, Rooke JC, Bourguiga R, Wu M, . Novel 3DOM BiVO$_4$/TiO$_2$ nanocomposites for highly enhanced photocatalytic activity. Journal of Materials Chemistry A. 2015;3:21244–21256. doi:10.1039/c5ta00783f

[121] Xu J, Wang WZ, Wang J, Liang YJ. Controlled fabrication and enhanced photocatalystic performance of BiVO$_4$@CeO$_2$ hollow microspheres for the visible-light-driven degradation of rhodamine B. Applied Surface Science. 2015;349:529–537. doi:10.1016/j.apsusc.2015.04.195

[122] Yu QQ, Tang ZR, Xu YJ. Synthesis of BiVO$_4$ nanosheets-graphene composites toward improved visible light photoactivity. Journal of Energy Chemistry. 2014;23:564–574. doi:10.1016/S2095-4956(14)60186-8

[123] Sun YF, Qu BY, Liu Q, Gao S, Yan ZX, Yan WS, . Highly efficient visible-light-driven photocatalytic activities in synthetic ordered monoclinic BiVO$_4$ quantum tubes-graphene nanocomposites. Nanoscale. 2012;4:3761–3767. doi:10.1039/c2nr30371j

[124] Li YK, Dong SY, Wang YF, Sun JY, Li YF, Pi YQ, . Reduced graphene oxide on a dumbbell-shaped BiVO$_4$ photocatalyst for an augmented natural sunlight photocatalytic activity. Journal of Molecular Catalysis A: Chemical. 2014;387:138–146. doi:10.1016/j.molcata.2014.02.027

[125] Zhang XF, Gong Y, Dong XL, Zhang XX, Ma C, Shi F. Fabrication and efficient visible light-induced photocatalytic activity of Bi$_2$WO$_6$/BiVO$_4$ heterojunction. Materials Chemistry and Physics. 2012;136:472–476. doi:10.1016/j.matchemphys.2012.07.013

[126] Yuan Q, Chen L, Xiong M, He J, Luo SL, Au CT, . Cu$_2$O/BiVO$_4$ heterostructures: synthesis and application in simultaneous photocatalytic oxidation of organic dyes and

reduction of Cr(VI) under visible light. Chemical Engineering Journal. 2014;255:394–402. doi:10.1016/j.cej.2014.06.031

[127]   Li JQ, Cui MM, Guo ZY, Liu ZX, Zhu ZF. Synthesis of dumbbell-like CuO-BiVO$_4$ heterogeneous nanostructures with enhanced visible-light photocatalytic activity. Materials Letters. 2014;130:36–39. doi:10.1016/j.matlet.2014.05.084

[128]   Jang JS, Kim HG, Lee SH. Efficient photocatalytic degradation of acid orange 7 on metal oxide p–n junction composites under visible light. Journal of Physics and Chemistry of Solids. 2012;73:1372–1377. doi:10.1016/j.jpcs.2012.07.009

[129]   Chen L, Zhang Q, Huang R, Yin SF, Luo SL, Au CT. Porous peanut-like Bi$_2$O$_3$–BiVO$_4$ composites with heterojunctions: one-step synthesis and their photocatalytic properties. Dalton Transactions. 2012;41:9513–9518. doi:10.1039/c2dt30543g

[130]   Wu XB, Zhou HL, Gu SN, Wang FZ, Liu J, Li WJ. In situ preparation of novel heterojunction BiOBr/BiVO$_4$ photocatalysts with enhanced visible light photocatalytic activity. RSC Advances. 2015;5:92769–92777. doi:10.1039/c5ra17552f

[131]   Huang HW, Liu LY, Zhang YH, Tian N. Novel BiIO$_4$/BiVO$_4$ composite photocatalyst with highly improved visible-light-induced photocatalytic performance for rhodamine B degradation and photocurrent generation. RSC Advances. 2015;5:1161–1167. doi: 10.1039/c4ra12916d

[132]   Li HL, Yu K, Lei X, Guo BJ, Fu H, Zhu ZQ. Hydrothermal synthesis of novel MoS$_2$/BiVO$_4$ hetero-nanoflowers with enhanced photocatalytic activity and a mechanism investigation. The Journal of Physical Chemistry C. 2015;119:22681–22689. doi:10.1021/acs.jpcc.5b06729

[133]   Lamdab U, Wetchakun K, Phanichphant S, Kangwansupamonkon W, Wetchakun N. Highly efficient visible light-induced photocatalytic degradation of methylene blue over InVO$_4$/BiVO$_4$ composite photocatalyst. Journal of Materials Science. 2015;50:5788–5798. doi:10.1007/s10853-015-9126-6

[134]   Li JQ, Cui MM, Guo ZY, Liu ZX, Zhu ZF. Preparation of p–n junction BiVO$_4$/Ag$_2$O heterogeneous nanostructures with enhanced visible-light photocatalytic activity. Materials Letters. 2015;151:75–78. doi:10.1016/j.matlet.2015.03.078

[135]   Song YH, Xu H, Yan J, Wang C, Cai GB, Li HM, . Preparation, characterization and photocatalytic activity of AgBr/BiVO$_4$ composite photocatalyst. Journal of Nanoscience and Nanotechnology. 2014;14:6816–6823. doi:10.1166/jnn.2014.8978

[136]   Li CJ, Zhang P, Lv R, Lu JW, Wang T, Wang SP, . Selective deposition of Ag$_3$PO$_4$ on monoclinic BiVO$_4$ (040) for highly efficient photocatalysis. Small. 2013;9:3951–3956. doi: 10.1002/smll.201301276

[137]   Kohtani S, Hiro J, Yamamoto N, Kudo A, Tokumura K, Nakagaki R. Adsorptive and photocatalytic properties of Ag-loaded BiVO$_4$ on the degradation of 4-n-alkylphenols

under visible light irradiation. Catalysis Communications. 2005;6:185–189. doi:10.1016/j.catcom.2004.12.006

[138] Chen L, Huang R, Ma YJ, Luo SL, Au CT, Yin SF. Controllable synthesis of hollow and porous Ag/BiVO$_4$ composites with enhanced visible-light photocatalytic performance. RSC Advances. 2013;3:24354–24361. doi:10.1039/c3ra43691h

[139] Cao SW, Yin Z, Barber J, Boey FYC, Loo SCJ, Xue C. Preparation of Au-BiVO$_4$ heterogeneous nanostructures as highly efficient visible-light photocatalysts. ACS Applied Materials & Interfaces. 2012;4:418–423. doi:10.1021/am201481b

[140] Xu H, Li HM, Wu CD, Chu JY, Yan YS, Shu HM, . Preparation, characterization and photocatalytic properties of Cu-loaded BiVO$_4$. Journal of Hazardous Materials. 2008;153:877–884. doi:10.1016/j.jhazmat.2007.09.039

[141] Chala S, Wetchakun K, Phanichphant S, Inceesungvorn B, Wetchakun N. Enhanced visible-light-response photocatalytic degradation of methylene blue on Fe-loaded BiVO$_4$ photocatalyst. Journal of Alloys and Compounds. 2014;597:129–135. doi:10.1016/j.jallcom.2014.01.130

[142] Li RG, Han HX, Zhang FX, Wang DE, Li C. Highly efficient photocatalysts constructed by rational assembly of dual-cocatalysts separately on different facets of BiVO$_4$. Energy & Environmental Science. 2014;7:1369–1376. doi:10.1039/c3ee43304h

[143] Lin F, Wang DE, Jiang ZX, Ma Y, Li J, Li R, . Photocatalytic oxidation of thiophene on BiVO$_4$ with dual co-catalysts Pt and RuO$_2$ under visible light irradiation using molecular oxygen as oxidant. Energy & Environmental Science. 2012;5:6400–6406. doi: 10.1039/c1ee02880d

[144] Zhu GQ, Que WX. Hydrothermal synthesis and characterization of visible-light-driven dumbbell-like BiVO$_4$ and Ag/BiVO$_4$ photocatalysts. Journal of Cluster Science. 2013;24:531–547. doi:10.1007/s10876-012-0531-6

[145] Long M, Jiang JJ, Li Y, Cao RQ, Zhang LY, Cai WM. Effect of gold nanoparticles on the photocatalytic and photoelectrochemical performance of Au modified BiVO$_4$. Nano-Micro Letters. 2011;3:171–177. doi:10.3786/nml.v3i3.p171-177

[146] Bian ZY, Zhu YQ, Zhang JX, Ding AZ, Wang H. Visible-light driven degradation of ibuprofen using abundant metal-loaded BiVO$_4$ photocatalysts. Chemosphere. 2014;117:527–531. doi:10.1016/j.chemosphere.2014.09.017

[147] Ge L. Novel Pd/BiVO$_4$ composite photocatalysts for efficient degradation of methyl orange under visible light irradiation. Materials Chemistry and Physics. 2008;107:465–470. doi:10.1016/j.matchemphys.2007.08.016

[148] Liao GZ, Chen S, Quan X, Zhang YB, Zhao HM. Remarkable improvement of visible light photocatalysis with PANI modified core-shell mesoporous TiO$_2$ microspheres. Applied Catalysis B: Environmental. 2011;102:126–131. doi:10.1016/j.apcatb. 2010.11.033

[149] Grabowska E, Reszczynska J, Zaleska A. Mechanism of phenol photodegradation in the presence of pure and modified-TiO_2: A review. Water Research. 2012;46:5453–5471. doi:10.1016/j.watres.2012.07.048

[150] Guo ZF, Ma RX, Li GJ. Degradation of phenol by nanomaterial TiO_2 in wastewater. Chemical Engineering Journal. 2006;119:55–59. doi:10.1016/j.cej.2006.01.017

[151] Devi LG, Rajashekhar KE. A kinetic model based on non-linear regression analysis is proposed for the degradation of phenol under UV/solar light using nitrogen doped TiO_2. Journal of Molecular Catalysis A: Chemical. 2011;334:65–76. doi:10.1016/j.molcata.2010.10.025

Photocatalytic Properties of Commercially Available TiO$_2$ Powders for Pollution Control

Manuel Nuño, Richard J. Ball and Chris R. Bowen

Additional information is available at the end of the chapter

Abstract

The photocatalytic properties of titanium dioxide have been widely studied over recent decades since the discovery of water photolysis by TiO$_2$ electrodes in 1972. Titanium dioxide has three main crystal polymorphs; anatase, rutile and brookite and rutile is the most common as the metastable polymorph. Each polymorph has different band gap positions. Anatase's band gap is 3.2 eV, higher than rutile's which is 3.0 eV. This difference in the band gap will determine their optimum UV wavelength range to promote a photocatalytic process. There are different methods to assess the photocatalytic activity of a material. The most commonly used method is the degradation of a dye in aqueous solution under UV light, due to its simplicity. Under these conditions the decomposition rate of a suitable organic dye is used as a measure of activity. Physical properties such as particle size and surface area will determine the effective area that will interact and absorb the dye prior to degradation. The physical mechanisms involved in such aqueous based methods differ from gas phase reactions. More advanced techniques use mass spectrometers to evaluate photocatalytic activity of titanium dioxide in the gas phase. An effective photocatalyst for heterogeneous reactions in the gas phase is one which is efficient at creating radicals as a result of an absorbed photon.

Keywords: photocatalysis, UV irradiation, nitrogen dioxide, methylene blue reduction, mass spectrometer

1. Introduction

The increase in the worldwide population demands resources and a constant energy supply, leading to an increment of pollutants, as reported by the Intergovernmental Panel on Climate Change released in March 2014 [1]. The report indicated actions must be taken immediately for

the mitigation of climate change. Anthropogenic greenhouse gases such as carbon dioxide, sulphur and nitrous oxides contribute significantly to global warming. Governments and international organizations such as The European Union and the United States of America set maximum levels for emissions of NO_2 and SO_2 amongst others [2].

Since 1972, when Fujishima and Honda discovered the photocatalytic properties of titanium dioxide (TiO_2), the research has been driven by the potential applications of photocatalysis for pollution remediation. Under UV radiation, TiO_2 can create free radicals on its surface by promoting electrons to the conduction band. The available hole which is very reactive and the electron can react with adsorbed water or oxygen to create free radicals and singlet oxygen. The process is illustrated by equations 1–6 [3–6]:

$$TiO_2 \xrightarrow{h\nu} e^- + h^+ \tag{1}$$

$$h^+ + H_2O \rightarrow {}^\bullet OH + H^+ \tag{2}$$

$$e^- + H^+ \rightarrow {}^\bullet H \tag{3}$$

$$H^+ + O_2^{\bullet -} \rightarrow HO_2^\bullet \tag{4}$$

$$e^- + O_2 \rightarrow O_2^{\bullet -} \tag{5}$$

$$h^+ + O_2^{\bullet -} \rightarrow {}^1 O_2 \tag{6}$$

One of the most promising applications is the development of novel coatings for both indoor and outdoor urban areas [7–10]. Available commercial photocatalytic coatings cover a range of products, from ceramic tiles with a photocatalytic coating, photocatalytic paints and pigments, antifogging windows to cementitious materials with TiO_2 in its formulation. The application of TiO_2 usually relies on its hydrophilic properties, an excellent advantage for self-cleaning surfaces. To accomplish this, a reliable analytical technique is required to assess the photoactivity of TiO_2 against gaseous pollutants. The photocatalytic activity of various materials is routinely studied for powders whilst in the form of an aqueous suspension. Under these conditions the decomposition rate of a suitable organic dye, such as methylene blue, is used as a measure of activity. This simple method was subsequently standardized in ISO (International Organization for Standardization) 10678. A problem associated with the use of dyes is related to their molecular structure which is not equivalent to typical pollutants. This is the reason that it is difficult to correlate results obtained from methylene blue and an air

pollutant. However, the physical mechanisms involved in such aqueous based methods can be significantly different compared to those of gas-phase reactions, thereby making comparison of relative performance problematic. There are currently a further three published ISO methods related to air purification, each one being specific to a single pollutant:

i.   Nitric oxide (NO) ISO 22197–1

ii.   Acetaldehyde (CH$_3$CHO) ISO 222197–2

iii.   Toluene (CH$_3$C$_6$H$_5$) ISO 22197–3

The aim of this chapter is to assess the photocatalytic activity of commercially available materials by two different techniques (in the aqueous phase as well as the gas phase). Pure TiO$_2$ and photocatalytic coatings specifically developed for use on construction materials were fully characterised and analysed by using X-ray photoelectron spectroscopy (XPS) and X-ray diffraction (XRD), UV-Visible diffusive spectroscopy, Raman spectroscopy, scanning electron microscope (SEM), field emission SEM (FE-SEM) and transmission electron microscopy (TEM).

2. Materials and methods

Four commercially available TiO$_2$ powders were studied. Anatase was supplied by three different companies:

i.   Anatase in the form of Kronos vlp 7000 manufactured by Kronos Titan GmbH [referred to as **7000**]

ii.   Anatase in the form of CristalACTiV™ PC500 manufactured by Crystal Global (85 wt % TiO$_2$, 100% anatase) [referred to as **PC500**]

iii.   Anatase in the form of Aeroxide® P25 manufactured by EVONIK Degussa Industries [referred to as **P25**]

iv.   Rutile in the form of TiPure® R-960 supplied by DuPont (TiO$_2$ > 89 wt %; Al$_2$O$_3$ ~3.3 wt % and amorphous SiO$_2$ ~5.5 wt %) [referred to as **rutile**]

2.1. Characterization of TiO$_2$ powders

Raman Spectroscopy, XPS and XRD were used to characterise the phase composition on the powders. The evaluation of the crystalline phases of the samples were analysed using a Renishaw inVia2012 Raman microscope equipped with diode excitation sources of wavelengths 532 nm and 785 nm.

The XPS equipment used was a Thermo Scientific Theta Probe with a micro-focussed monochromatic Al K$_a$ (1486.6 eV) X-ray source (Thermo Fisher Scientific Inc., Waltham, MA.), with an operating voltage of 12 kV and 3 mA of current. The default spot size was 400 × 800 μm using a flood gun, with a 180° double focussing hemspherical analyser with two-dimension-

al PARXPS detector in an operating vacuum of 10^{-8} mbar. The software CASAXPS 2.3.16 RP 1.6 (Casa Software Ltd., Teingmouth, Devon, UK) was used for data analysis and peak fitting. The adventitious hydrocarbon C 1s peak at 284.8 eV was used to correct for the shift in binding energy attributed to surface charging of the specimen. The XRD equipment used was a Bruker D8 ADVANCE X-ray diffractometer with CuK$_\alpha$ radiation (at 40 kV and 40 mA emission current) equipped with a graphite monochromator and a NaI scintillation detector. 2θ scans were recorded within the range of 20° to 60° with a step of 0.016° and a step time of 269 s.

The bandgap of the photocatalysts was calculated from their reflectance. A PerkinElmer 750 S UV/Vis Spectrometer with a 60 mm Integrating Sphere in a wavelength range between 240 nm and 800 nm was used to measure the reflectance of the TiO_2 powders. The reflectance data was converted into the absorption energy using the Kubelka-Munk equation alongside the Tauc's plot, allowed conversion of the reflectance into absorption energy which corresponds to the band gap [11–13].

The surface morphology and particle size of nanostructured of TiO_2 powders was characterised using FESEM and TEM as together they cover a suitable range of magnifications. A JEOL FESEM6301F equipped with a motorised stage, allowing low accelerating voltages from 1kV to 10kV and TEM (JEOL JEM 1200 EXII with a tungsten filament equipped with a motorised stage, and a Gatan Dual View camera) with working accelerating voltages of 120 kV.

2.2. Evaluation of photocatalytic performance

The photocatalytic activity of the commercial powders was tested by following the degradation of a dye in the aqueous phase and the degradation of NO_2 and CO_2 in the gas phase. Specimens were irradiated under two different UV sources comprising 4×4 arrays of 16 individual GaN UV-LED's. LEDs of wavelength 376–387 nm provided a maximum intensity at 380 nm with a total intensity at the specimen surface of 4.7 W/m^2.

2.2.1. Photocatalytic degradation of methylene blue

Three tests were undertaken for each TiO_2 powder; one in the dark, to evaluate the amount of dye which was absorbed by the powders; and two tests under UV light. Photocatalytic activity of TiO_2 in solution was studied by following the decrease in the solution's absorption using a Jenway 6300 UV-Visible spectrophotometer. The organic dye methylene blue was used as an indicator.

2.2.2. Photocatalytic degradation of gaseous pollutants

To assess the photocatalytic activity of TiO_2 powders in the gas phase, a mass spectrometer was employed due to its ability to monitor a range of species simultaneously. The system has been reported previously in detail [14–16], including the ionic species and corresponding masses commonly formed in the gas phase [15]. A schematic diagram of the system is shown in **Figure 1**.
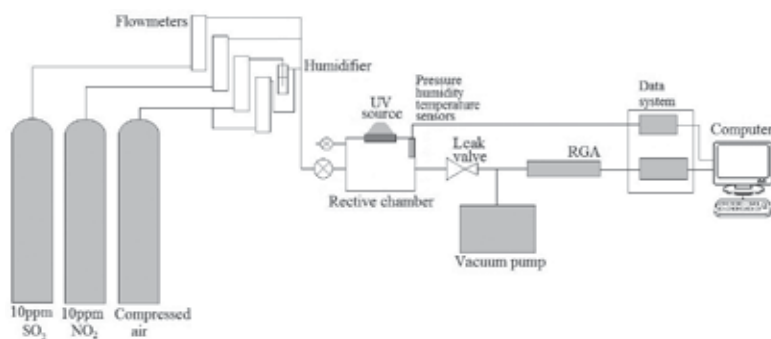
Figure 1. Diagram of the mass analyser. Gas cylinders are connected via flowmeters to the reactive chamber. One output is connected to the detector [15].

TiO$_2$ powders were compressed into 13 mm diameter pellets using a uniaxial press at 500 MPa. The experiments were carried out at 25°C and atmospheric pressure for 150 min inside the chamber. The LED's intensity was 30 W/m^2. Air was mixed with 203 ppm of NO$_2$ diluted in N$_2$ to provide enough O$_2$ and H$_2$O for TiO$_2$ to initiate photocatalytic reactions, leading an initial concentration of 190 ppm of NO$_2$.

3. Results and discussion

3.1. Electron microscopy

Calculated particle sizes, specific surface area, bandgap and crystallite size are given in **Table 3**.

			7000	PC500	P25	Rutile TiPure
Binding energy (eV) /	**C 1s**	**C-N**	**286.7**/3.7	**286.4**/5.4	**287.1**/5.6	–
Relative concentration (at. %)		**CO$_3$** $^{2-}$	**288.7**/1.8	**289.6**/4.5	–	**288.9**/5.2
	O 1s	**TiO$_2$**	**529.6**/57.1	**529.5**/37	**529.1**/59.9	**529.8**/71.3
		CO$_3$ $^{2-}$	**531.0**/11.5	**531.4**/18.9	**531.3**/7.8	–
		SiO$_2$	–	**533.2**/1.7	–	**533.2**/9.1
	Ca 2p	**Ca**	–	**347.4**/2.6	–	–
	(CaCO$_3$)	**2p$_{3/2}$**				
		Ca 2p$_{1/2}$	–	**350.8**/1.3	–	–
	Si 2p (SiO$_2$)	**Si 2p**	–	**103.2**/2.2	–	**102.8**/12.3
	Ti 2p (TiO$_2$)	**Ti 2p$_{3/2}$**	**458.4**/17.4	**458.5**/17.6	**458.4**/17.9	**458.1**/1.3
	Ti 2p (TiO$_2$)	**Ti 2p$_{1/2}$**	**464.1**/8.5	**464.2**/8.8	**464.1**/8.8	**463.8**/0.7

Table 1. Element ratios and chemical state derived from XPS analysis.

	Lattice plane	7000 (Å)	PC500 (Å)	P25 (Å)	Rutile (Å)
Anatase	(101)	3502	3496	3518	–
	(004)	2375	2384	2377	–
	(112)	–	–	2486	–
	(200)	1896	1889	1891	–
	(105)	1684	1675	1699	–
	(211)	–	–	2,33113	–
	(118)	1485	1483	1480	–
	(116)	–	–	1668	–
Rutile	(110)	–	–	3245	3200
	(101)	–	–	–	2460
	(200)	–	–	–	2276
	(111)	–	–	–	2166
	(210)	–	–	–	2037
	(211)	–	–	1687	1677
	(220)	–	–	–	1614
	(002)	–	–	–	1472
	(310)	–	–	–	1445
	(301)	–	–	–	1354

Table 2. d spacing Calculated from the X-ray diffraction data of rutile and anatase powders.

	Particle size (nm)*	Average particle size (nm)	Crystallite size(nm)	BET (m²/g)*	BET (m²/g)	Band gap (eV)
7000	15	<10	10.1	>250	225	3.37
PC500	5–10	20.8	9.5	350	312	3.35
P25	21	29.8	22.6	35–65	13	3.25
Rutile	500	402	50	-	3.3	3.00

*From producer's datasheet.

Table 3. Particle size, BET and optical band gap for TiO$_2$ powders.

	Absorbed dye (%) in the dark	Degraded dye (%) under λ=376–387 nm	Degraded dye (%) under λ=381–392 nm
7000	18.2	94.7	39.9
PC500	14.8	98.8	95.23
P25	18.2	99.8	92.8
Rutile	16.3	26.3	16.6

Table 4. Percentage of absorbed and degraded dye after 60 min under two different UV LED and in the dark.

3.1.1. 7000

Anatase 7000 presented a distribution of micro and nanoparticles as shown in **Figure 2**. TEM revealed an agglomeration of nanoparticles (>10 nm), being unable to determine an average particle size.
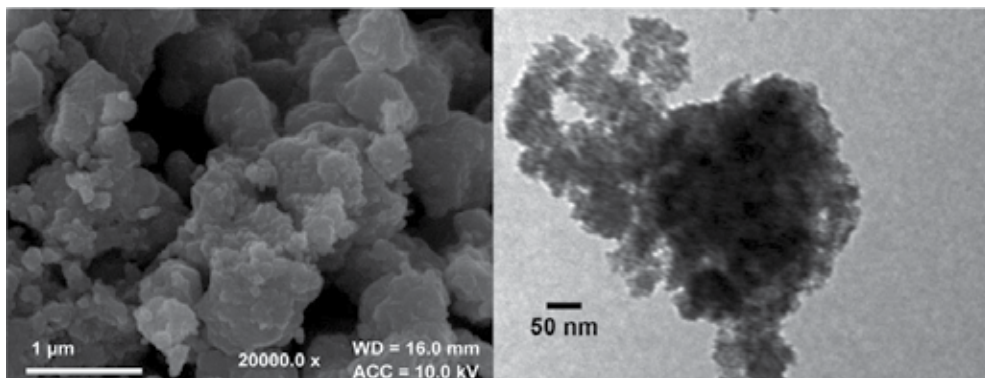
Figure 2. FESEM (left) and TEM (right) images of anatase 7000.

3.1.2. PC500

FESEM revealed a large number of particles of ~ 600 nm, whereas TEM showed particles in the range of 20 nm (**Figure 3**).
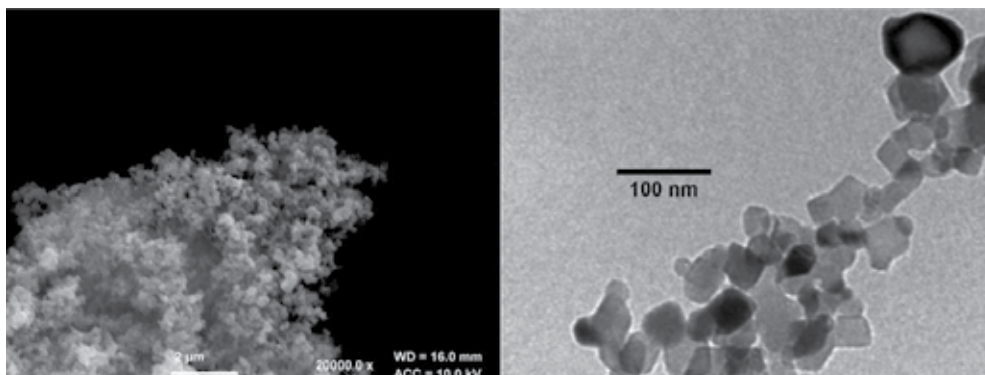
Figure 3. FESEM (left) and TEM (right) images of anatase PC500.

3.1.3. P25

Anatase P25 showed the most homogeneous particle size distribution in FESEM as well as in TEM, held in the range of 30 nm (**Figure 4**).
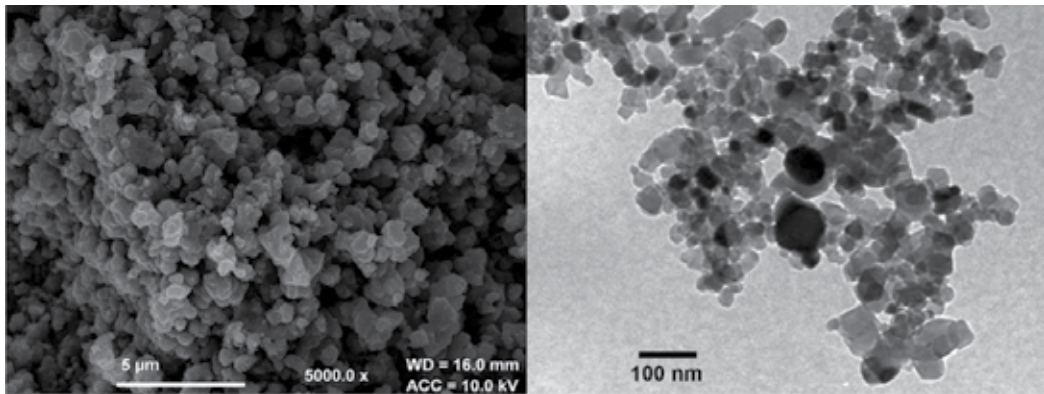
Figure 4. FESEM (left) and TEM (right) images of anatase P25.

3.1.4. Rutile

Rutile TiPure shows a narrow particle size distribution with 400 μm of average particle size. This average particle size was corroborated with sizes estimated from TEM images, as **Figure 5** shows.
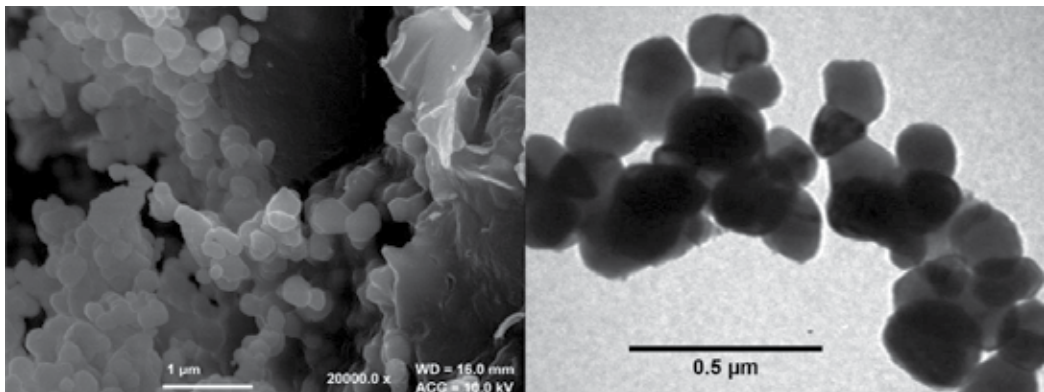
Figure 5. FESEM (left) and TEM (right) images of rutile TiPure.

3.2. Raman spectroscopy

Raman spectroscopy was conducted on the samples before exposure to reactive gases over the range 0–1000 cm^{-1} where the main vibrational modes can be observed. **Figure 6** shows complied Raman spectra form the four TiO$_2$ powders.
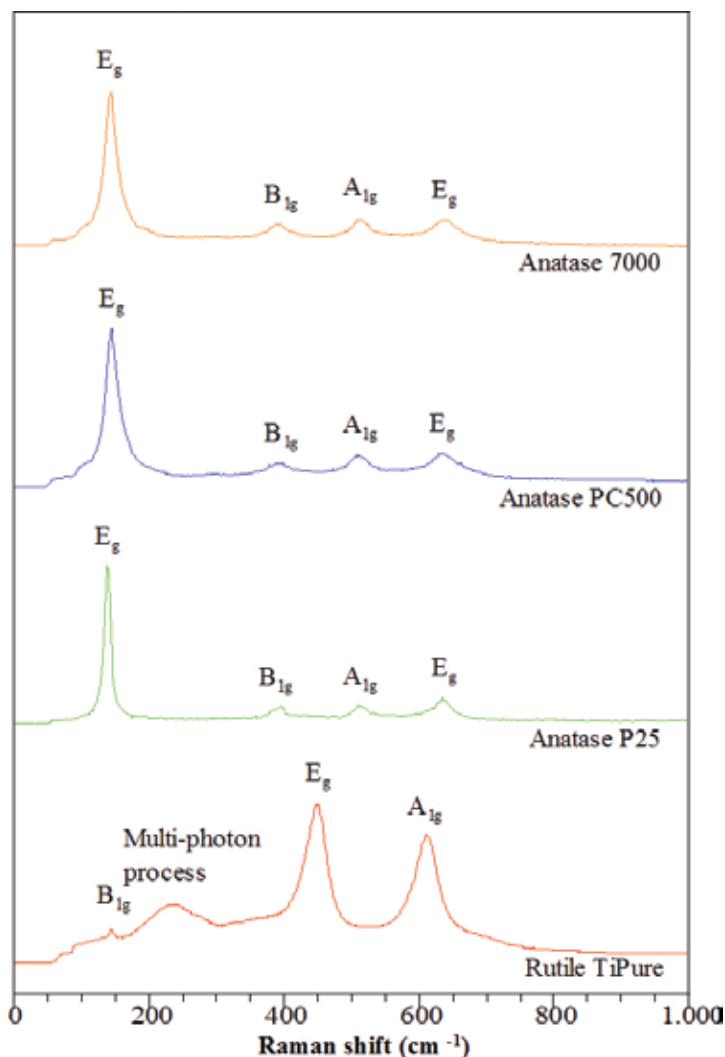
Figure 6. Raman spectra from 0 to 1000 cm^{-1} of four different TiO$_2$ powders.

There are four lattice displacements for rutile which are active in Raman, B$_{1g}$ (145 cm^{-1}) and E$_g$ (445 cm^{-1}, most intense), where O^{2-} anions move relative to the stationary Ti^{4+}; A$_{1g}$ (610 cm^{-1}) which is an asymmetric bending vibration of O-Ti-O, and a multi-phonon process (240 cm^{-1}) [17–20].

For anatase, there are six lattice displacements which are active in Raman, A$_{1g}$ (513 cm^{-1}), B$_{1g}$ (399 and 519 cm^{-1}) and E$_g$ (144, 197 and 639 cm^{-1}) caused by Ti-O bond stretching and bending of the O-Ti-O bond [21, 22]. The peak at 197 cm^{-1} assigned to the E$_g$ mode is very weak and is not listed in **Figure 6** due to its low intensity (0.05%). The peak B$_{1g}$ at 519 cm^{-1} was reported at 73 K and it is not visible at room temperature.

3.3. X-ray photoelectron spectroscopy

Figure 7 shows a typical survey spectra of TiO_2 (P25) and **Table 1** shows the binding energies and elemental ratios for carbon, oxygen, calcium, silicon and titanium, calculated from higher resolution spectra in specific regions for the commercial powders.
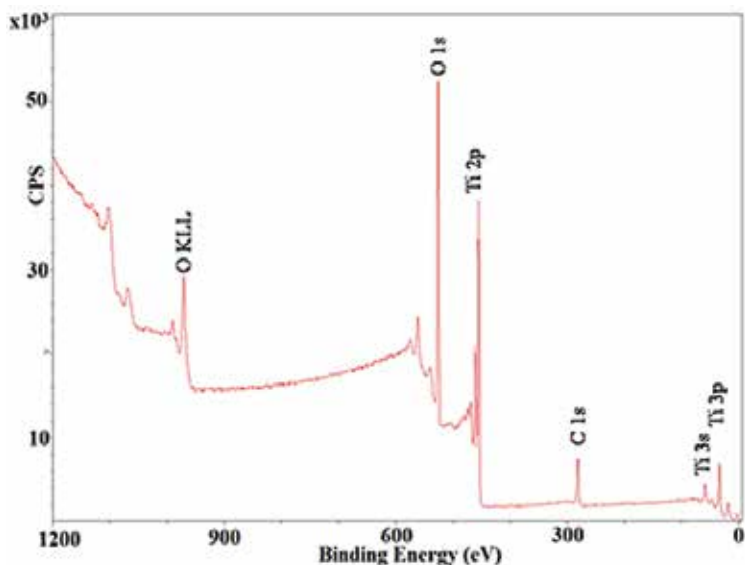
Figure 7. XPS spectra of anatase P25.

As **Table 1** shows, KRONOS vlp 7000 and Aeroxide® P25 are the purest TiO_2 powders, whereas PC500 and Rutile TiPure® contain $CaCO_3$ and SiO_2 impurities.

Binding energies for TiO_2 related to Ti 2p peaks varied between 458.1 and 458.5 eV in accordance with previous studies [23, 24], and for O 1s the observed peaks are within the range of 528.8–529.8 eV. These results agreed with studies carried by Dementjev [23] and Erdem [24], where the Ti 2p binding energies ranged from 458.0 to 459.4 eV and for O 1s ranged from 529.4 to 530.6 eV.

Peaks corresponding to C 1s were assigned to adventitious carbon with a binding energy of 284.8 eV and were used to calibrate the spectrum for charging and a second peak corresponding to CO_3^{2-} in 7000, PC500 and rutile TiO_2 powders. The binding energy of this peak in the different powders ranged between 288.7 and 289.6 eV which is in agreement with studies by Kang et al. [25] and Demri and Muster [26] who report $CaCO_3$ binding energies of 288.6 and 289.2eV. The binding energy for the Ca 2p peak identified at 347.4 eV was in agreement with previous studies by Stipp [27] who reported a $CaCO_3$ binding energy of 347.7 eV. For SiO_2, the reported values for the O 1s peak at 533.2 eV and ~103 eV is also in agreement with previous studies [28].

3.4. X-ray diffraction

XRD was undertaken to characterise the crystal phase of the powders. **Figure 8** compares the normalised diffractograms for anatase (PC500, 7000 and P25) and rutile crystals. Previous studies were used to identify and label peaks from different crystal phases [20, 21, 29–32] and **Table 2** compares the lattice d spacing for those peaks.
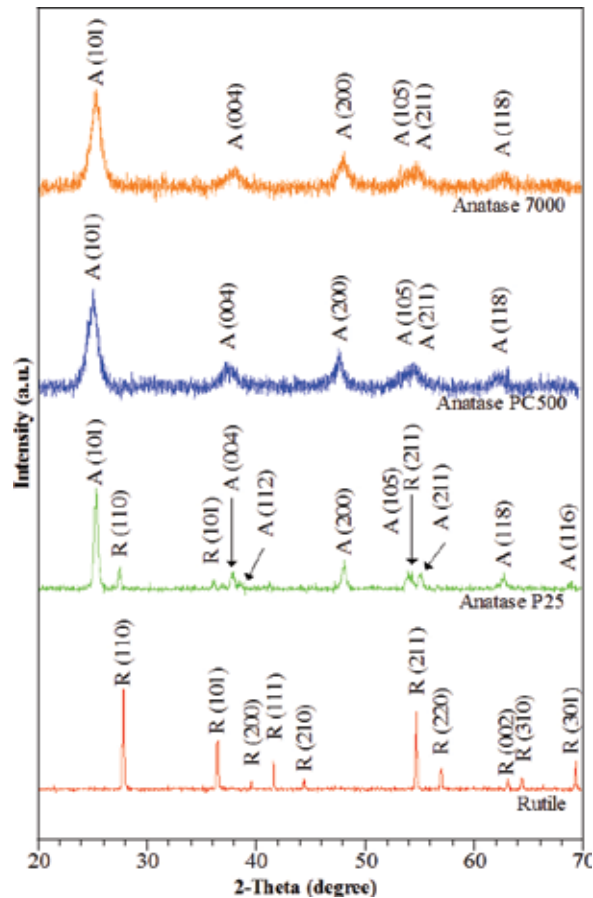

Figure 8. X-ray diffractogram of rutile and anatase powders.

In the case of anatase, the P25 diffractogram is sharper than the PC500 and 7000, revealing more peaks that correspond to anatase. It also shows 12% rutile (by comparing the maximum intensity of anatase crystallographic plane (101) with the maximum of rutile's (110)). For PC500 and 7000, fewer peaks are observed compared to the P25. This is attributed to internal strains within the crystals and lattice defects broadening the peaks causing subsequent overlap.

From Scherrer's equation, the crystallite size was calculated from the most intense peaks for each powder. The values are presented in **Table 3** which compiles other results.

3.5. UV–vis diffusive spectroscopy

UV-Visible reflectance of powders was measured from 250 to 800 nm for all the commercial powders. **Figure 9** shows the reflectance of TiO_2 particles over a wavelength range on the abscissa. The plot shows that, PC500 has a drop in the reflectance at 405 nm, 7000 at 377 nm, P25 at 381 and rutile at 371 nm.
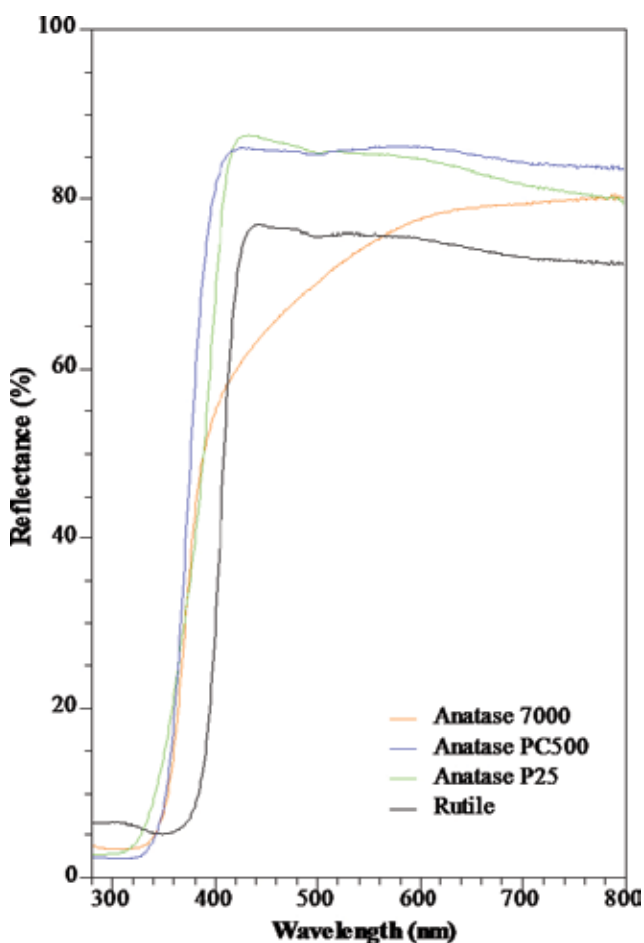
Figure 9. Graphical representation of reflectance against wavelength for rutile and anatase powders.

Table 3 compiles the calculated optical band gap, BET surface area, average crystallite size (from XRD diffractogram using Scherrer's equation) and average particle size calculated from TEM images. It also contains particle size and BET from the material safety data sheets.

Particle size and BET results agreed with the information in the technical data sheets of anatase nanoparticles, and also with reported values in the literature [13, 33, 34]. As the 7000 consisted of aggregates of nanoparticles, it was not possible to report an average particle size, as

shown in **Figure 2**. From the TEM images the size of the individual nanoparticles forming the agglomerates was less than 10 nm. Scherrer equation's estimations are close to the calculated values from TEM and FE-SEM. For the case of rutile, the estimated crystallite size was 50 nm. A possible explanation for the difference of an order of magnitude is that particles are formed from different grains; where the crystallite size is the size of those grains.

The estimated band gaps for anatase powders range from 3.37 eV (for 7000) to 3.25 eV (for P25). Although these results show a small discrepancy in the band gap determination, previous researchers reported different values for P25 (3.10–3.15 eV) [13, 34]; as well as for 7000, carbon doped, which has band gap higher than 3.2 eV [35, 36]. PC500 also exhibits a wider band gap than reported previously. For the PC500 and 7000 band gaps, the optimum wavelength was 370 nm. Rutile's band gaps agree with the reported values for M. Kete, D. Reyes-Coronado and K. Madhusudan Reddy [33, 37, 38].

3.6. Photocatalytic performance

3.6.1. Photocatalytic degradation of methylene blue

Figure 10 shows the degradation of methylene blue for sixty minutes, and **Table 4** collates the dye removed per specimen under irradiation at different wavelengths.
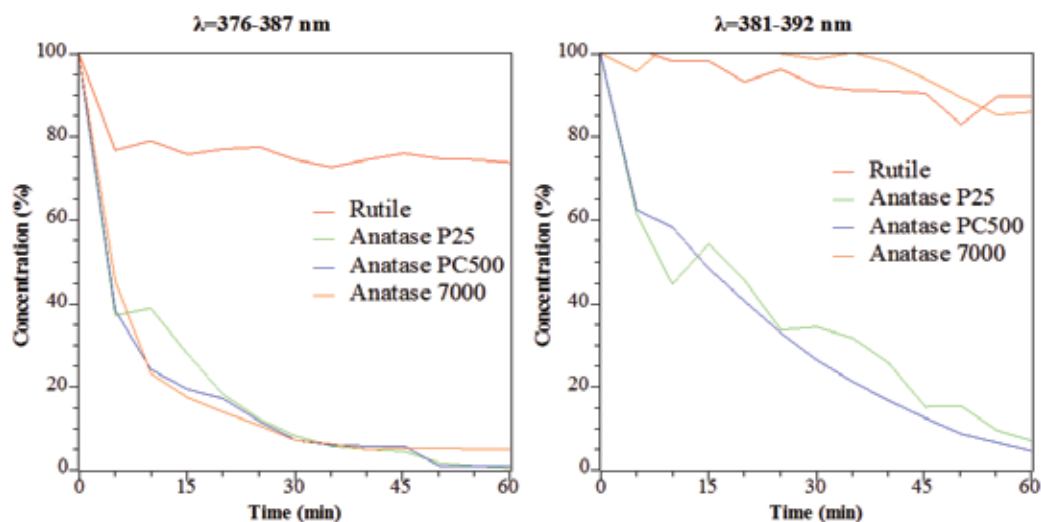
Figure 10. Photo-oxidation of an aqueous solution of methylene blue under different UV LED (I=4.7 W/m²) for TiO₂ powders.

Anatase P25 and PC500 successfully degraded more than 90% of methylene blue under different UV light. In the case of 7000, the difference in its photoreactivity under different wavelengths is remarkable. Whereas P25 band gaps are in the 387 nm wavelength region, PC500 and 700 band gaps are in the 370 nm region. This is the reason why under a wavelength range 381–392 nm, 7000 was not able to degrade more than 40% of dye; whereas

under 376–387 nm, 95% of methylene blue was degraded. Under the irradiation of the UV LED of 376–387 nm, 7000 received more photons with the required energy to initiate the photocatalytic process.

For rutile, if the percentage of absorbed dye is considered, it only worked as a photocatalyst under the UV LED with a wavelength of 381–392 nm, near to its band gap (413 nm) degrading less than 26%.

3.6.2. Photocatalytic degradation of gaseous pollutants

Figures 11–14 show the fractional change of CO_2, NO_2, H_2O and O_2 related to Ar.
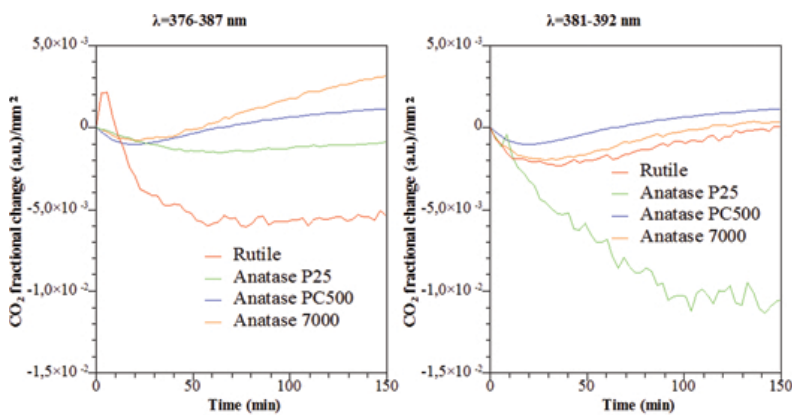
Figure 11. Fractional reduction of CO_2 related to Ar over time under different conditions.
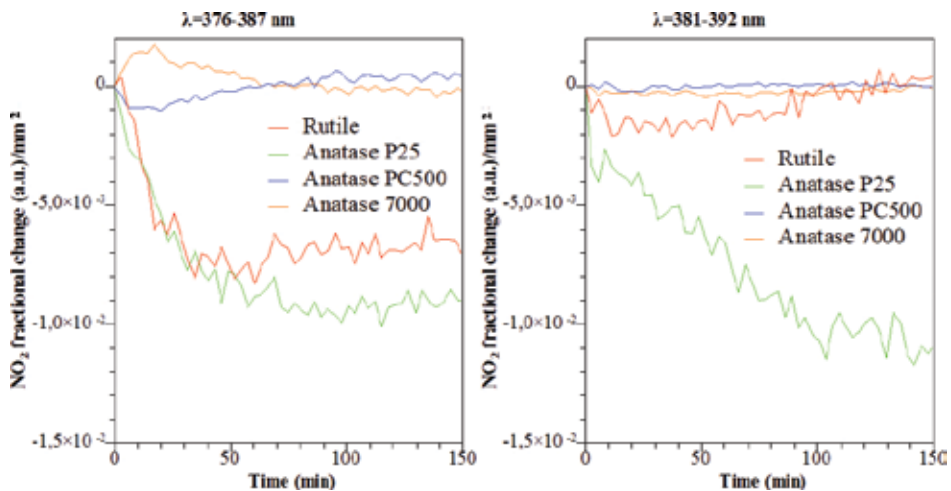
Figure 12. Fractional reduction of NO_2 related to Ar over time under different conditions.
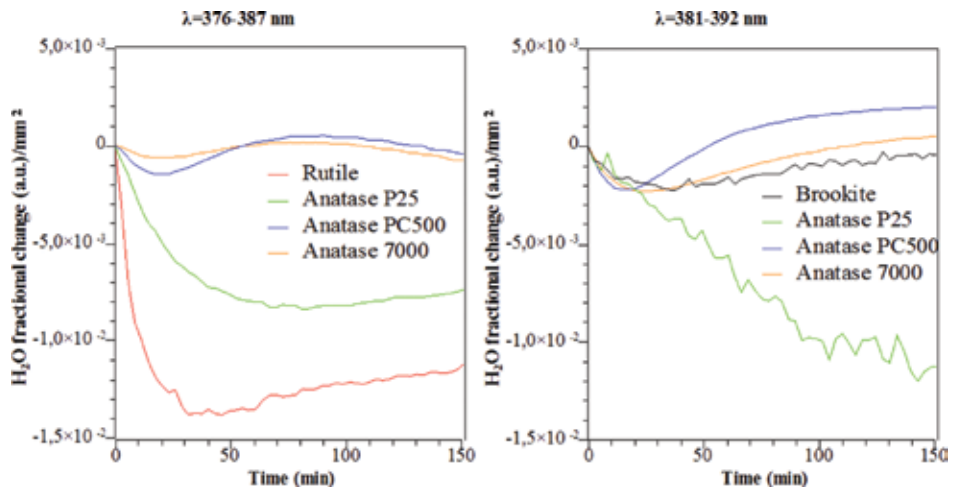
Figure 13. Fractional reduction of H_2O related to Ar over time under different conditions.
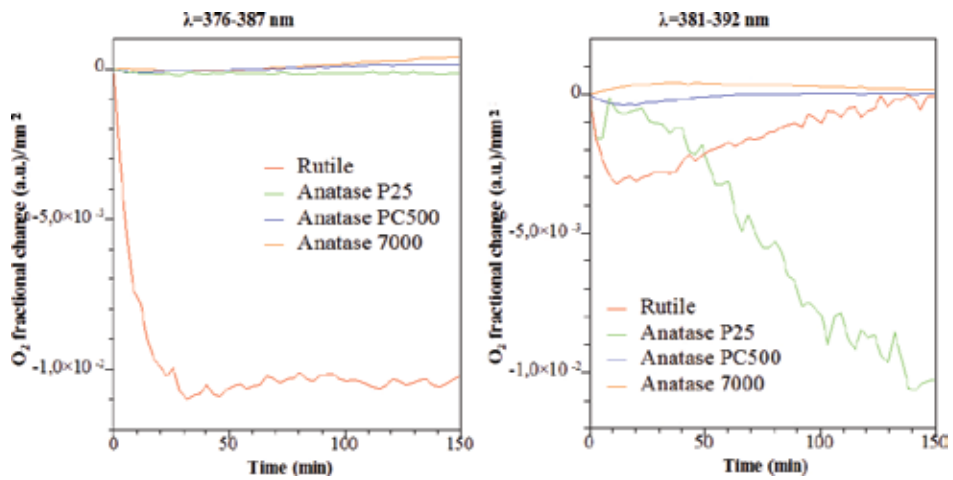
Figure 14. Fractional reduction of O_2 related to Ar over time under different conditions.
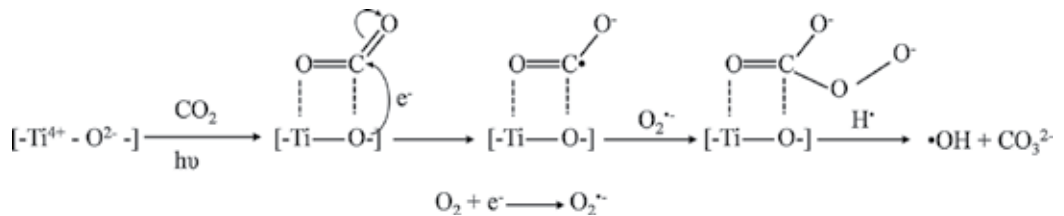

Figure 15. Proposed mechanism of photo-oxidation of CO_2.

The high photoreactivity TiO_2 powders show degradation of methylene blue in the aqueous phase, however their reactivity in the gas phase was different. Not all the commercial anatase powders were able to degrade NO_2 and CO_2, only P25 removed those molecules successfully. Rutile, which was not effective in aqueous solution, was able to remove CO_2 and NO_2 under UV irradiation. Rutile's band gap is 370 nm, which made it more photoactive under the UV LED of wavelength of 376–387 nm, as its band gap is held.

When evaluating the photocatalytic TiO_2 powders, it is noteworthy that their sizes and physical properties differ from each other. Anatase 7000 has the smallest particle size and highest specific surface area whereas rutile exhibits the largest particle size and smallest specific surface area.

The phase (liquid or gas) in which the particles are evaluated has important influences upon the performance observed. In the gas phase, probabilities of direct contact of TiO_2 surface with the molecules of interest (H_2O and O_2 to create radicals) and thereafter the collision of those radicals with NO_2 and CO_2 is much smaller than in the aqueous phase.

For anatase PC500 and 7000, the high efficiency in the photodegradation of methylene blue is due to the low particle size and high specific surface area, which increase the contact of the exposed surface to H_2O and UV light. When analysed in gas phase, they showed a lower photon/e^--h^+ conversion yield, and were unable to promote a photocatalytic reaction under UV exposure at both the wavelength ranges tested.

Figures 13 and 14 show the fractional change of H_2O and O_2 with time, which are required in the photocatalytic process to generate radicals. The figures illustrate that the decay of O_2 corresponds to the decomposition of CO_2 and H_2O, as with NO_2.

The reaction of NO_2 and H_2O promoted by TiO_2 under UV light has been previously reported, forming HNO_3 as the reaction product [39–42]. Under wavelength 376–387 nm in the gas phase removal of NO_2 was observed alongside that of H_2O. Whereas when irradiating under 381–392 nm, not only were NO_2 and H_2O were removed from the atmosphere, but also O_2 and CO_2 were consumed in the same ratio.

This can be explained by anatase's bandgap reported value 3.2 eV [38, 42], which is held in the range of the UV LED of wavelength 381–392 nm, as **Figure 11** shows. This difference in energy would be sufficient to promote the radicalisation of O_2 and, subsequently the reaction with CO_2.

The proposed mechanisms for CO_2 removal suggest that the molecule anchors to the photocatalyst's surface, reducing CO_2 into CO and finally into C, desorbing CO and O [43, 44]. This mechanism would not explain the consumption of O_2. Nonetheless, if CO_2 anchors as shown in **Figure 15** the oxidation of CO_2 in the presence of TiO_2 surface absorbed $O_2^{\bullet-}$ could be feasible.

4. Conclusions

The following conclusions can be drawn from the analysis of commercial TiO_2 powders:

- Photocatalytic degradation of methylene blue in aqueous solution is influenced by factors such as particle size and surface area which can influence the measured activity relative to the gas phase reaction.

- Mass spectrometry has been demonstrated as a powerful technique for the assessment of photocatalytic properties in the gas phase.

- From the three commercial available anatase powders, Aeroxide P25 proved to be the most efficient photocatalyst, in the aqueous phase as well as gas phase. Rutile, the most stable polymorph also showed photocatalytic activity.

- The removal of NO_2 in the presence of H_2O, with HNO_3 as the product was observed. The capability of TiO_2 to decompose CO_2 in the presence of O_2 was also noted and a new mechanism proposed.

Acknowledgements

Author details

Manuel Nuño[1*], Richard J. Ball[1] and Chris R. Bowen[2]

*Address all correspondence to: manuelnunotutor@hotmail.com

1 BRE Centre for Innovative Construction Materials, Department of Architecture and Civil Engineering, University of Bath, BA2 7AY, Bath, England

2 Department of Mechanical Engineering, University of Bath, BA2 7AY, Bath, England

References

[1] Contribution of Working Groups I, II and III to the Fifth Assessment Report of the Intergovernmental Panel on Climate Change [Core Writing Team, R.K. Pachauri and L.A. Meyer (eds.)], "IPCC 2014: Climate Change 2014: Synthesis report," Geneva, Switzerland, 2014.

[2] "Directive 2008/50/EC of the European Parliament and of the Council of 21 May 2008 on ambient air quality and cleaner air for Europe."

[3] M. R. Hoffmann, S. T. Martin, W. Choi, and D. W. Bahnemann, "Environmental applications of semiconductor photocatalysis," Chem. Rev., vol. 95, no. 1, pp. 69–96, 1995.

[4] A. Heller, "Chemistry and applications of photocatalytic oxidation of thin organic films," Acc. Chem. Res., vol. 28, no. 12, pp. 503–508, 1995.

[5] D. A. Tryk, A. Fujishima, and K. Honda, "Recent topics in photoelectrochemistry: achievements and future prospects," Electrochim. Acta, vol. 45, no. 15–16, pp. 2363–2376, 2000.

[6] M. Serratos and A. Bronson, "The effect of oxygen partial pressure on the stability of Magneli phases in high temperature corrosive wear," Wear, vol. 198, no. 1–2, pp. 267–270, 1996.

[7] B. Tryba, P. Homa, R. J. Wróbel, and A. W. Morawski, "Photocatalytic decomposition of benzo-[a]-pyrene on the surface of acrylic, latex and mineral paints. Influence of paint composition," J. Photochem. Photobiol. A Chem., vol. 286, pp. 10–15, 2014.

[8] T. Maggos, J. G. Bartzis, M. Liakou, and C. Gobin, "Photocatalytic degradation of NO_x gases using TiO_2-containing paint: A real scale study," J. Hazard. Mater., vol. 146, no. 3, pp. 668–673, 2007.

[9] L. Hochmannova and J. Vytrasova, "Photocatalytic and antimicrobial effects of interior paints," Prog. Org. Coatings, vol. 67, no. 1, pp. 1–5, 2010.

[10] M. Baudys, J. Krýsa, M. Zlámal, and A. Mills, "Weathering tests of photocatalytic facade paints containing ZnO and TiO_2," Chem. Eng. J., vol. 261, pp. 83–87, Feb. 2015.

[11] P. Kubelka, "New contributions to the optics of intensely light-scattering materials part I," J. Opt. Soc. Am., vol. 38, no. 5, p. 448, 1948.

[12] A. Murphy, "Band-gap determination from diffuse reflectance measurements of semiconductor films, and application to photoelectrochemical water-splitting," Sol. Energy Mater. Sol. Cells, vol. 91, no. 14, pp. 1326–1337, 2007.

[13] R. López and R. Gómez, "Band-gap energy estimation from diffuse reflectance measurements on sol–gel and commercial TiO_2: a comparative study," J. Sol–gel Sci. Technol., vol. 61, no. 1, pp. 1–7, 2012.

[14] M. Nuño, R. J. Ball, C. R. Bowen, R. Kurchania, and G. D. Sharma, "Photocatalytic activity of electrophoretically deposited (EPD) TiO_2 coatings," J. Mater. Sci., vol. 50, no. 14, pp. 4822–4835, 2015.

[15] M. Nuño, R. J. Ball, and C. R. Bowen, "Study of solid/gas phase photocatalytic reactions by electron ionization mass spectrometry," J. Mass Spectrom., vol. 49, no. 8, pp. 716–726, 2014.

[16] M. Nuño, G. L. Pesce, C. R. Bowen, P. Xenophontos, and R. J. Ball, "Environmental performance of nano-structured Ca(OH)₂/TiO₂ photocatalytic coatings for buildings," Build. Environ., vol. in press, 92, pp. 734–742, 2015.

[17] Y. Zhang, C. X. Harris, P. Wallenmeyer, J. Murowchick, and X. Chen, "Asymmetric Lattice Vibrational Characteristics of Rutile TiO₂ as Revealed by Laser Power Dependent Raman Spectroscopy," J. Phys. Chem. C, vol. 117, no. 45, pp. 24015–24022, 2013.

[18] T. Lan, X. Tang, and B. Fultz, "Phonon anharmonicity of rutile TiO₂ studied by Raman spectrometry and molecular dynamics simulations," Phys. Rev. B, vol. 85, no. 9, p. 094305, 2012.

[19] G. A. Samara and P. S. Peercy, "Pressure and Temperature Dependence of the Static Dielectric Constants and Raman Spectra of TiO₂ (Rutile)," Phys. Rev. B, vol. 7, no. 3, pp. 1131–1148, 1973.

[20] M. Rezaee, S. M. Mousavi Khoie, and K. H. Liu, "The role of brookite in mechanical activation of anatase-to-rutile transformation of nanocrystalline TiO₂: An XRD and Raman spectroscopy investigation," CrystEngComm, vol. 13, no. 16, p. 5055, 2011.

[21] W. F. Zhang, Y. L. He, M. S. Zhang, Z. Yin, and Q. Chen, "Raman scattering study on anatase TiO₂ nanocrystals," J. Phys. D. Appl. Phys., vol. 33, no. 8, p. 912, 2000.

[22] T. Ohsaka, F. Izumi, and Y. Fujiki, "Raman spectrum of anatase, TiO₂," J. Raman Spectrosc., vol. 7, no. 6, pp. 321–324, 1978.

[23] A. P. Dementjev, "Altered layer as sensitive initial chemical state indicator∗," J. Vac. Sci. Technol. A Vacuum, Surfaces, Film., vol. 12, no. 2, p. 423, 1994.

[24] B. Erdem, R. A. Hunsicker, G. W. Simmons, E. D. Sudol, V. L. Dimonie, and M. S. El-Aasser, "XPS and FTIR Surface Characterization of TiO₂ Particles Used in Polymer Encapsulation," Langmuir, vol. 17, no. 9, pp. 2664–2669, 2001.

[25] I.-C. Kang, Q. Zhang, S. Yin, T. Sato, and F. Saito, "Preparation of a visible sensitive carbon doped TiO₂ photo-catalyst by grinding TiO₂ with ethanol and heating treatment," Appl. Catal. B Environ., vol. 80, no. 1–2, pp. 81–87, 2008.

[26] B. Demri and D. Muster, "XPS study of some calcium compounds," J. Mater. Process. Technol., vol. 55, no. 3–4, pp. 311–314, 1995.

[27] S. L. Stipp and M. F. Hochella, "Structure and bonding environments at the calcite surface as observed with X-ray photoelectron spectroscopy (XPS) and low energy electron diffraction (LEED)," Geochim. Cosmochim. Acta, vol. 55, no. 6, pp. 1723–1736, 1991.

[28] T. Gross, M. Ramm, H. Sonntag, W. Unger, H. M. Weijers, and E. H. Adem, "An XPS analysis of different SiO₂ modifications employing a C 1s as well as an Au 4f7/2 static charge reference," Surf. Interface Anal., vol. 18, no. 1, pp. 59–64, 1992.

[29]   R. J. T. and P. K. S. and R. G. K. and R. V Jasra, "Photocatalytic degradation of dyes and organic contaminants in water using nanocrystalline anatase and rutile TiO_2," Sci. Technol. Adv. Mater., vol. 8, no. 6, p. 455, 2007.

[30]   Y. F. You, C. H. Xu, S. S. Xu, S. Cao, J. P. Wang, Y. B. Huang, and S. Q. Shi, "Structural characterization and optical property of TiO_2 powders prepared by the sol–gel method," Ceram. Int., vol. 40, no. 6, pp. 8659–8666, 2014.

[31]   B. K. Mutuma, G. N. Shao, W. D. Kim, and H. T. Kim, "Sol–gel synthesis of mesoporous anatase-brookite and anatase-brookite-rutile TiO_2 nanoparticles and their photocatalytic properties.," J. Colloid Interface Sci., vol. 442, pp. 1–7, 2015.

[32]   D. M. Tobaldi, M. P. Seabra, G. Otero-Irurueta, Y. R. de Miguel, R. J. Ball, M. K. Singh, R. C. Pullar, and J. A. Labrincha, "Quantitative XRD characterisation and gas-phase photocatalytic activity testing for visible-light (indoor applications) of KRONOClean 7000[registered sign]," RSC Adv., vol. 5, no. 124, pp. 102911–102918, 2015.

[33]   M. Kete, E. Pavlica, F. Fresno, G. Bratina, and U. Štangar, "Highly active photocatalytic coatings prepared by a low-temperature method," Environ. Sci. Pollut. Res., vol. 21, no. 19, pp. 11238–11249, 2014.

[34]   K. Nagaveni, M. S. Hegde, N. Ravishankar, G. N. Subbanna, and G. Madras, "Synthesis and structure of nanocrystalline TiO_2 with lower band gap showing high photocatalytic activity," Langmuir, vol. 20, no. 7, pp. 2900–2907, 2004.

[35]   T. M. Triantis, T. Fotiou, T. Kaloudis, A. G. Kontos, P. Falaras, D. D. Dionysiou, M. Pelaez, and A. Hiskia, "Photocatalytic degradation and mineralization of microcystin-LR under UV-A, solar and visible light using nanostructured nitrogen doped TiO_2," J. Hazard. Mater., vol. 211–212, pp. 196–202, 2012.

[36]   A. Manassero, M. L. Satuf, and O. M. Alfano, "Evaluation of UV and visible light activity of TiO_2 catalysts for water remediation," Chem. Eng. J., vol. 225, pp. 378–386, 2013.

[37]   D. Reyes-Coronado, G. Rodríguez-Gattorno, M. E. Espinosa-Pesqueira, C. Cab, R. de Coss, and G. Oskam, "Phase-pure TiO_2 nanoparticles: anatase, brookite and rutile," Nanotechnology, vol. 19, no. 14, p. 145605, 2008.

[38]   K. Madhusudan Reddy, S. V Manorama, and A. Ramachandra Reddy, "Bandgap studies on anatase titanium dioxide nanoparticles," Mater. Chem. Phys., vol. 78, no. 1, pp. 239–245, 2003.

[39]   S. Daito, T. Watanabe, and F. Tochikubo, "NO x Removal Process in Pulsed Corona Discharge Combined with TiO_2 Photocatalyst," Jpn. J. Appl. Phys., vol. 40, no. 4R, p. 2475, 2001.

[40]   N. Negishi, K. Takeuchi, and T. Ibusuki, "Surface structure of the TiO_2 thin film photocatalyst," J. Mater. Sci., vol. 33, no. 24, pp. 5789–5794, 1998.

[41] Y. Bedjanian and A. El Zein, "Interaction of NO$_2$ with TiO$_2$ surface under UV irradiation: products study," J. Phys. Chem. A, vol. 116, no. 7, pp. 1758–1764, 2012.

[42] Y.-M. Lin, Y.-H. Tseng, J.-H. Huang, C. C. Chao, C.-C. Chen, and I. Wang, "Photocatalytic activity for degradation of nitrogen oxides over visible light responsive titania-based photocatalysts," Environ. Sci. Technol., vol. 40, no. 5, pp. 1616–1621, 2006.

[43] M. Anpo, H. Yamashita, Y. Ichihashi, and S. Ehara, "Photocatalytic reduction of CO$_2$ with H$_2$O on various titanium oxide catalysts," J. Electroanal. Chem., vol. 396, no. 1–2, pp. 21–26, 1995.

[44] M. Anpo, H. Yamashita, K. Ikeue, Y. Fujii, S. G. Zhang, Y. Ichihashi, D. R. Park, Y. Suzuki, K. Koyano, and T. Tatsumi, "Photocatalytic reduction of CO$_2$ with H$_2$O on Ti-MCM-41 and Ti-MCM-48 mesoporous zeolite catalysts," Catal. Today, vol. 44, no. 1–4, pp. 327–332, 1998.

A New Frontier of Photocatalysis Employing Micro-Sized TiO$_2$: Air/Water Pollution Abatement and Self-Cleaning/ Antibacterial Applications

Claudia L. Bianchi, Carlo Pirola, Marta Stucchi,
Benedetta Sacchi, Giuseppina Cerrato,
Sara Morandi, Alessandro Di Michele,
Alessandra Carletti and Valentino Capucci

Additional information is available at the end of the chapter

http://dx.doi.org/10.5772/62892

Abstract

This chapter presents the use of a commercial micro-sized TiO$_2$ powder as an alternative to the traditional nano-powders as semiconductors in photocatalytic processes. Results of the photocatalytic efficiency towards the photodegradation of the traditional pollutant molecules both in gas phase (nitrogen oxides (NO$_x$) and volatile organic compounds (VOCs)) and in water phase (phenol) are presented and compared to the results obtained with two nano-sized reference powders. Micro-sized TiO$_2$ is also industrially coated at the surfaces of porcelain grés tiles (Active Clean Air and Antibacterial Ceramic™). The possibility to have a photocatalytic material, strongly stuck at the surface of a vitrified tile, increases the use of photocatalysis in real conditions: no problem of filtration of the semiconductor from the liquid medium after use and no risks of leakage of nanoparticles in the atmosphere. Tests were performed using reactors equipped with UV-A lamps and with suitable analytical systems, depending on the final purpose. Characterization data from both powders and coated tiles are put in correlation with the photocatalytic results to understand the semiconductor action during the photocatalytic process. Polluting molecules were chosen in order to cover all the common aspects of environmental pollution: NO$_x$ and some VOCs represent the model molecules to test the efficiency of the micro-sized TiO$_2$ (degradation from the pristine molecule to CO$_2$ or inorganic salts) in gas phase. As for the water pollution, phenol was chosen as common pollutant in worldwide rivers. Moreover, tests on self-cleaning and antibacterial properties are also report‐ ed. The positive results of micro-sized TiO$_2$ both in powder and coated onto the surface of porcelain grés tiles open the way to new photocatalytic products that do

not make use of nanoscale powders avoiding problems to human safety caused by the inherent toxicity of the nanoparticles.

1. Introduction

The importance of photocatalysis is related to the increase of the environmental problems regarding climate changes, scarcity of energy and greenhouse gases emissions, which increase the need of new environmentally beneficial technologies. Photocatalysis can also be used for water purification: many references are already present in literature on the degradation of dyes or drugs in aqueous solutions simulating the real pollution of rivers and lakes.

TiO_2 is very stable and very suitable for applications in environmental improvement and protection. Other than the antipollution properties, TiO_2, always in the anatase phase, is capable of conferring both self-cleaning and antibacterial properties to the surfaces [1].

Titanium dioxide is a semiconductor widely used in nanotechnology [2]. Since Fujishima and Honda discovered the phenomenon of photocatalytic water splitting [3], effort has been devoted to the research of TiO_2 materials, with potential applications in several fields, from biomaterials to self-cleaning processes and from sensing to photovoltaic applications, as well as in photocatalysis [4–6]. Indeed, it has been broadly studied for environmental applications, such as pollutant abatement both in liquid and in gas phase, and it has many advantages compared to other photocatalysts in particular because of low production cost and high chemical stability [7].

It is possible to find TiO_2 in three different crystallographic phases: anatase, rutile and brookite. Anatase is the most photocatalytically active; it has a bipyramid tetragonal symmetry, with four units per elementary cell (**Figure 1a**), and its structure consists in elongated octahedra. On the contrary, rutile is largely used as pigment and in the coating industry, precisely because of its chemical inertness; it is tetragonal, with two formula units per elementary cell (**Figure 1c**). Brookite is a metastable phase, and apart from a limited range of temperature and pressure, it easily turns in the other two forms; it has got an orthorhombic symmetry, with eight formula units per elementary cell (**Figure 1b**) [8].

Powdered TiO_2 is used as a common white pigment and effective opacifier thanks to its brightness and very high refractive index. More than 5 million tons of pigmentary TiO_2 are produced annually worldwide, and this amount is expected to increase as consumption continues to rise [9]. It is often used to provide whiteness and opacity in commercial products such as paints, coatings, plastics, papers, inks, foods, medicines (i.e. pills and tablets) as well as most toothpastes [10].
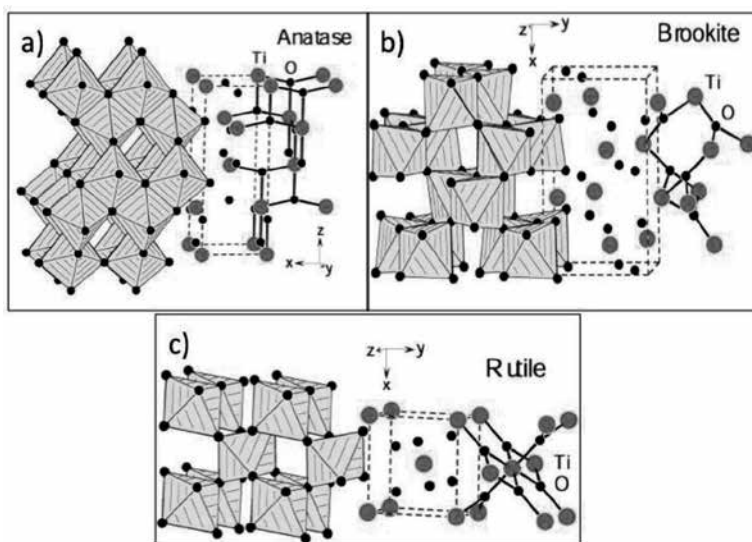
Figure 1. TiO$_2$ crystallographic phases: (a) anatase; (b) brookite; (c) rutile.

The use of nanomaterials (NMs) such as titanium dioxide in the production of cosmetics, sunscreens, surface coatings and some food products is widespread and successfully applied [11], as well as the most part of NMs has been used in products for health and fitness, including both medical/pharmaceutical and personal care products [12].

New physical and chemical properties emerge when the size of the material reaches the nanoscale. Firstly, the specific surface area increases dramatically as the size of a material decreases [13], and the high surface area brought about by small particle size is beneficial to many TiO$_2$-based devices, as it facilitates the interaction between the devices and the surrounding environment.

For this reason, in recent years nanotechnology has spread through all sectors of science and technology including engineering, medical, pharmaceutical, agriculture, environment and many more.

However, nanoparticles exhibit potential risks in terms of: (i) dispersibility, that is, the ability to disperse in the environment including potential long range transport; (ii) ecotoxicity, i.e. the ability to cause adverse effects to organisms in the environment; (iii) persistency, that is the ability to remain in the environment; (iv) bioaccumulation, that is the ability to either bioaccumulate or bioconcentrate in higher order organisms; (v) reversibility, i.e. the ability for removal or to reverse their original introduction from environment.

Human health risks associated with nanotechnology include both inhalation and/or exposure of/to nanoparticles or the ingestion of water or food and dermal contact [14]. The exposure to nanoparticles leads to a number of effects including oxidative stress, lipid peroxidation, genotoxicity, lung diseases, inflammation or pulmonary pathological changes [15–18].

In literature, there are many references that describe and present information on titanium dioxide health risks [19]. The International Agency for Research on Cancer (IARC) classified ultrafine TiO_2 as possible carcinogenic to humans [20]. The USA National Institute for Occupational Safety and Health reported that the exposure to ultrafine TiO_2 should be considered potentially carcinogenic [21] and the Federal Institute for Occupational Safety and Health showed some results of toxicokinetic analysis in lungs and in organs like liver and brain, finding a small solubility effect under physiological conditions, as well as lung tissue inflammation for exposures to high dose of TiO_2.

Moreover, TiO_2 inhalation studies prove to be injurious on rodents as well [15], as higher incidence of lung tumours was detected after exposure to ultrafine TiO_2 for 2 years in rats [22].

Thus, despite the good properties and the high efficiency of nano-sized TiO_2, these concerns over safety may limit its applications, and it is very important to find a replacement.

For this reason, the use of micrometric TiO_2 becomes more and more interesting and few years ago some investigations demonstrated the possibility to use this material for the photodegradation of pollutant molecules, such as volatile organic compounds (VOCs), nitrogen oxides (NO_x) or organic molecules that mainly pollute the water systems [23, 24]. It has also been successfully used in building materials to exploit self-cleaning and antibacterial effects [25].

Generally, micro-TiO_2 is usually used as a pigment but never in photocatalysis; however, as already mentioned, testing it for the photodegradation of different kinds of pollutants, both in gas and in aqueous phase, the efficiency of this material was confirmed at this point [1, 10, 24]. Furthermore, application of micro-TiO_2 in different materials, such as building materials and paintings, may bring many benefits, because when compared with nanometric TiO_2, it is easier to handle, cheaper as well, and shows a good photoefficiency [10].

The coating of TiO_2 allows conferring the material surfaces all the properties of TiO_2 as semiconductor [26]. It is already widely used on different materials, for different applications: on exterior construction materials [27, 28] for water [3] and air purification [29], for the preparation of self-cleaning and antibacterial cements [30], on tiles [23, 31], on glass [32], and, recently, for the protection of the cultural heritage [33]. Most of these materials are currently prepared with nanometric titanium dioxide, with all the ensuing problems described above.

Different techniques can be used to prepare and coat TiO_2 on solid supports, such as glass, metals or ceramics; to improve both adhesion and hydrophilicity of coating, silica can be added as a suspension, while several coating techniques, such as dipcoating, spincoating and spraycoating, can be used to spread the TiO_2 mixture over the support.

Among the several kinds of supports to obtain TiO_2-coated materials, with interesting photocatalytic properties that can be used in both outdoor and indoor environments, porcelain grés tiles are very attractive. When the industrial production began in the 1970s, porcelain grés tiles were aesthetically not very attractive and considered as just a technical material characterized by lack of porosity and strong resistance to both abrasion and acid attack. However, in the last decades, porcelain grés tiles underwent significant transformations in terms of appearance, mainly in size. Currently, thanks to advanced and innovative industri-

al production methods, both properties and appearances of these materials are improved and completely fit the market requests. In particular, the possibility to prepare slabs of large sizes (such as 300×150 cm) is the new frontier of building materials [23]. Porcelain grés tiles are manufactured under high pressure by dry-pressing fine processed ceramic raw materials with large proportions of quartz, feldspar and other fluxes and are characterized by a very low water absorption rate (less than 0.5%). In fact, these materials are fired at very high temperatures (1200–1300°C) in kilns [34]. A complete frost resistance due to the lack of porosity, complete waterproofing, durability, hardness and wear resistance properties thus characterizes the final ceramic product.

Besides these noteworthy architectural features, the deposition of anatase TiO$_2$ form converts the traditional ceramic into a photocatalytic eco-active material with the ability to reduce polluting molecules present in both air and water, to eliminate bacteria and to reduce the surface dirt thanks to the self-cleaning properties [35].

Self-cleaning refers to the pollutant degradation and dirt removal from surfaces, by their different behaviour towards water, relating to their hydrophobicity or hydrophilicity [36]. The main characteristic of superhydrophobic surfaces is high roughness, which implies low adhesion forces between contaminating particles and the surface, so water droplets roll off very quickly [37], and dirt can be very efficiently removed. On the contrary, TiO$_2$ confers the superhydrophilicity feature to the surfaces, under light irradiation, and water dropped onto titanium dioxide forms low contact angle. The Research Institute of Toto Ltd discovered the effect for a photocatalytic surface irradiated by sunlight in 1995.

There are two different ways to exploit the TiO$_2$ features for self-cleaning: (i) in the first case, TiO$_2$ nanoparticles are introduced inside a polymeric matrix in order to create nano-roughness on the surfaces and make them hydrophobic and superhydrophobic [38, 39]; (ii) secondly, the hydrophilicity of TiO$_2$ is the key property. Indeed, under UV exposure, titanium dioxide becomes super hydrophilic, and the decrease of the water contact angle creates a uniform water film on the treated surfaces, preventing contact between external dirt and surfaces themselves [40]. The main application is on building coverings because it decreases the periodicity of cleaning or renovation of the surfaces, maintaining their aspect as constant as possible [41].

The antibacterial properties are also important and interesting. They allow destroying the bacteria present at the photocatalytic material surfaces with the only action of light and humidity present in the air without using specific detergents, source of pollution for rivers and seas [42, 43]. Many bacteria have been investigated, and the photocatalytic antibacterial activity is always confirmed even with the most dangerous MRSA species, resistant to antibiotics [44].

In this chapter, we show two new frontiers in photocatalysis. Firstly, the real possibility to use a commercial micro-sized TiO$_2$ in powder form (K1077 by Kronos) as a photocatalyst is reported, with results compared with two traditional nanometric powdered samples (P25 by Evonik and PC105 by Cristal). Secondly, we report the industrial preparation of a photoactive porcelain grés tile, coated by spray method with the micro-sized TiO$_2$ (White Ground Active sample). In both cases, characterization results of both powders and tiles will be put in correlation with all the photocatalytic properties: antipollution in water (phenol) and air

(NO$_x$ and VOCs), self-cleaning (oleic acid as reported in the standard ISO 27448 rule) and antibacterial investigating the degradation of *Escherichia coli* and *Staphylococcus aureus MRSA*.

The possibility to use micro-sized TiO$_2$ in a commercially manufactured product opens the way to a new generation of intrinsically safer materials than the traditional photocatalytic products for both workers in the factories and public safety.

2. Material and methods

Three commercial TiO$_2$ samples were selected without further treatment: two nano-sized by Evonik (P25) and by Cristal (PC105) and one micro-sized by Kronos (K1077).

Staring from the traditional porcelain grés tiles fired at 1200°C with a vitrified surface, photoactive porcelain grés tiles by GranitiFiandre S.p.A were prepared covering the surface with an aqueous mixture of pure anatase micro-TiO$_2$ in powder form (K1077) and a commercial SiO$_2$-based compound by spray method in airless cabins. To ensure the semiconductor strong adherence and the complete surface vitrification, given by the presence of SiO$_2$, tiles were heated at 680°C for 80 min in an industrial kiln and then brushed to remove TiO$_2$ particles present at the ceramic surface and not completely stuck (sample name: White Ground Active, i.e. WGA) [21; Patent n. EP2443076].

2.1. Sample characterization

We used the following equipments to characterize the powdered samples. N$_2$ adsorption/desorption measurements at 77 K Brunauer–Emmett–Teller method (BET) using Sorptometer instrument (Costech Mod. 1042) to investigate specific surface area (SSA) of all samples.

X-ray diffraction (XRD) with a PW3830/3020 X'Pert diffractometer from PANalytical working in Bragg-Brentano geometry (Cu Kα1 radiation; k = 1.5406 Å) was chosen to inspect the crystalline nature of the samples.

High-resolution transmission electron microscopy (HR-TEM) using a JEOL 3010-UHR instrument (acceleration potential: 300 kV; LaB6 filament) was used to detect the fine morphology of the materials (powder form). Samples were always 'dry' dispersed on lacey carbon Cu grids.

X-ray photoelectron spectra (XPS) were obtained in an M-probe apparatus (surface science instruments) using a monochromatic source of Al Kα radiation (1486.6 eV).

For the band-gap determinations, diffuse reflectance spectra of the materials in powder form were recorded employing a UV-Vis scanning spectrophotometer (PerkinElmer, Lambda 35 model), equipped with a diffuse reflectance accessory. The Kubelka-Munk function was used to elaborate data to determine the band gap values by performing the first derivative of the Kubelka-Munk equation.

In situ FTIR spectroscopy was used to detect the surface functionalities, mainly surface hydroxyl species. Absorption/transmission IR spectra were collected at room temperature (RT)

on the samples outgassed in vacuo at RT by means of a Perkin-Elmer FT-IR System 2000 spectrophotometer equipped with a Hg-Cd-Te cryo-detector. Spectra were collected in the 7200– 580 cm^{-1} range at 2 cm^{-1} resolution. For this analysis, the powdered photocatalyst was pressed in self-supporting pellet (~10 mg cm^{-2}), placed in a homemade quartz cell, equipped with KBr windows, connected to a conventional vacuum line.

High-resolution SEM-EDX investigations were performed on ceramic tiles using a field emission gun electron scanning microscopy LEO 1525, while the elemental composition was obtained using Bruker Quantax EDS.

2.2. Photocatalytic tests

2.2.1. VOCs (volatile organic compounds)

The photodegradation of some VOCs (i.e. acetone, acetaldehyde, ethanol and toluene) was monitored conducting the degradation in a Pyrex glass cylindrical reactor with diameter of 200 mm and effective volume of 5 L [25]. For each test, 0.05 g of photocatalyst (in powder form deposited on flat glass disk from a 2-propanol slurry) was used. Hot chromatographic air, humidified at 40%, and a fixed amount of the volatilized VOC were mixed to obtain the requested gaseous mixture in the reactor. The actual concentration of the organic molecule in the reactor was determined directly by micro-GC sampling as shown in **Figure 2**. Photon sources were provided by a 500 W iron halogenide lamp (Jelosil, model HG 500) emitting in the 315–400 nm wavelength range (UV-A) at 30 Wm^{-2}. The duration of each test was selected by considering the difficulty in degrading a molecule, in a time between 2 and 6 hours. The intermediate oxidation products were determined directly by investigating the sample surface after the kinetic run by FTIR spectroscopy and the determination of CO$_2$ was performed by gas chromatography as well.
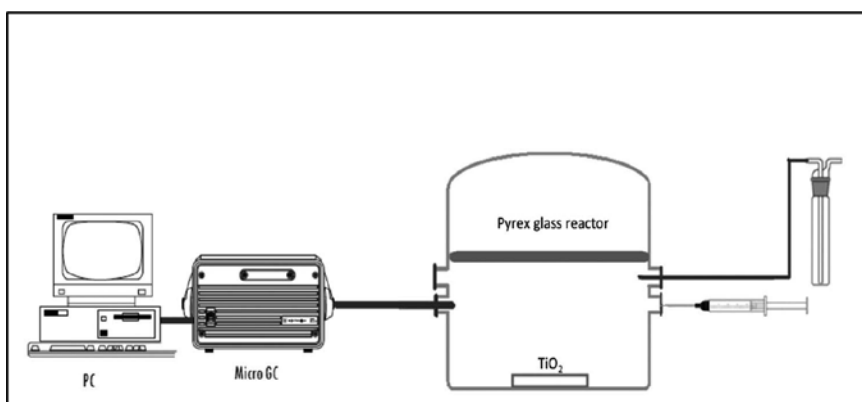

Figure 2. VOC photodegradation—set-up.

2.2.2. NO$_x$

• *Static condition*

The photocatalytic activity of both powder samples was tested in NO$_x$ degradation, operating in static conditions in a Pyrex glass cylindrical reactor with an effective volume of 25 L [10]. The amount of catalyst used in the tests in this case was 0.05 g.

NO$_2$ (0.6% in nitrogen) was mixed with air humidified at 40% to obtain the gaseous mixture in the reactor. It is important to underline that we start from an inlet gas of pure NO$_2$ pulsed into the reactor that, as soon as it comes into contact with the air present inside the vessel, reaches the chemical equilibrium between NO and NO$_2$ so as to naturally obtain the NO and NO$_2$ mixture in air. Different concentrations of NO$_x$ in the reactor were chosen: i) 1000 ppb in order to follow the same pollutant concentration requested by the ISO 22197-1 rule; ii) 200 ppb that is very close to the alert threshold set by the EU Directive 2008/50/CE for NO$_2$. Photon sources were provided by a 500 W iron halogenide lamp (Jelosil, model HG 500) emitting in the 320–400 nm wavelength range (UV-A), but with a specific UV power on the surface of the samples set at 10 Wm^{-2}. The NO$_x$ photocatalytic tests were performed at 30°C and lasted for 4 or 6 hours. The actual concentration of pollutants (NO, NO$_2$ and consequently their sum, i.e. NO$_x$) in the reactor was determined in this case directly by a chemiluminescence (Teledyne, Mod. 200E).

• *Continuous flow reactor*

The photoefficiency towards the NO$_x$ degradation of tiles of 600×600 mm was confirmed using a purpose-built reactor [45]. The continuous flow reactor (**Figure 3**) has walls of 10 mm of thickness and an internal size of 625×625×115 mm with four inlets and one opposite outlet and can house a sample of 600×600×10 mm. This configuration assures a good homogeneity of the reactants in the gas phase and a contact between reactant and photocatalytic tiles that well reproduces the real working conditions.
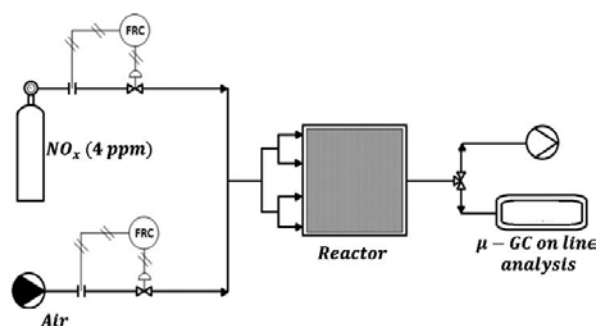

Figure 3. Scheme of the experimental continuous NO$_x$ set-up.

Reactor is equipped with a thermo-hygrometer model HT-3006A to measure both temperature and humidity during the tests. Humidity inside the reactor is maintained constant

between 40–50% through bubbling the gas flow into a gas bubbler (containing water and saturated aqueous vapour). The irradiation was emitted by two iron halogenide lamps (Jelosil, model HG 500) positioned at 770 mm centre-to-centre distance. The light intensity incident on the sample surface in the UV-A region was measured with a Delta Ohm radiometer and regulated at 20 Wm^{-2} by adjusting the distance of the lamp from the reactor. The degradation was performed at different initial NO$_x$ concentrations, obtained by diluting the stream of NO$_x$ from the cylinder with air, at RT and working with a total gas flow of 140 and 180 NL h^{-1}. The concentration values were chosen to work closely to the limit values reported on the Directive 2008/50/EC, in particular, 106 ppb (equal to 200 μg m^{-3}, value not to be exceeded more than 18 times in a calendar year) and 213 ppb (400 μg m^{-3}, alert threshold).

2.2.3. Liquid phase

Regarding photocatalytic tests in liquid phase, the experimental set-ups are different depending on whether we use powders or tiles.

• *Photocatalytic test using powdered nano- and micro-TiO$_2$ catalysts*

Dye degradation in water media was performed in a slurry reactor, equipped by an internal refrigerating serpentine system (**Figure 4a**) of 0.5 L volume [44]. Irradiation was allowed by the use of an external UV-A lamp (500W, Jelosil®, HG500, halide lamp), emitting in the range 315–400 nm and with a power evaluated by a radiometer instrument (Delta OHM, model HD2102.2) of 75 Wm^{-2}. A UV-Vis spectrophotometer analyzer (T60 UV-Vis PG LTD instrument) has been used to measure the concentration of dyes or organic molecules as a function of time.
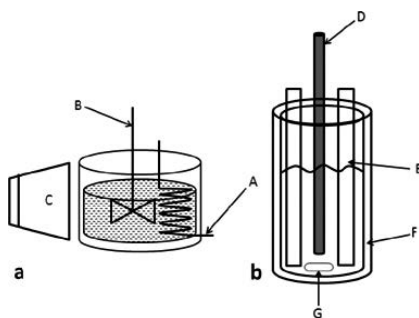

Figure 4. Liquid phase reactors: a) Continuous stirred slurry reactor. A: refrigerating serpentine system; B: Stirrer; C: UV lamp. B) Cylindrical batch reactor used for photocatalytic experiments. D: UV lamp; E: photocatalytic tiles; F: cooling jacket; G: magnetic stirrer.

• *Photocatalytic test using photoactive TiO$_2$ tiles*

A cylindrical batch reactor of 1 L volume, refrigerated with a cooling jacket, was used for dye degradation tests in the presence of 10 photoactive tiles (0.03 m^2 total surface photoactive area)

immersed into the liquid solution, as schematically shown in **Figure 4b** [46]. In this case, two different lamps directly immersed into the aqueous solution were used: a typical germicidal W UV lamp (Philips TUV BL-S, model AEPL-7913 mercury vapour low pressure), with an UV-A illuminance at the tile surface of 1 Wm^{-2} and a 125 W UV-A lamp (Jelosil, mercury vapour low pressure), with an illuminance of 65 Wm^{-2}.

2.2.4. Self-cleaning

The ISO 27448 rule was precisely followed to perform the measurements on tiles. The *self-cleaning* action is assessed by measuring the contact angle generated by the film of pure oleic acid and by monitoring the changes in the angle due to any degradation of the deposited acid due to the UV irradiation. Only if the surface has photocatalytic properties, the changes of the contact angle value occur.

The contact angle was measured (Kruss instrument equipped with high resolution TV camera) after the cleaning pre-treatment by UV irradiation, after contact with the oleic acid (zero time) and after irradiation with UV lamp at 20 Wm^{-2} at 2, 4, 6, 24, 48, 72, 74 and 76 hours. At each time, the measurement is repeated on five random points on the surface of the tested material.

Samples of WGA (size 100×100 mm), randomly taken from an industrial production batch, were placed in a suitably prepared solution containing 0.5 vol% of oleic acid (Fluka reagent, purity >80%) in n-eptane (Fluka reagent, purity >99%), in order to obtain a uniform coating of oleic acid at the surface. The amount of oleic acid thus applied resulted to be 2.0 ± 0.2 mg, (value measured by means of a Gibertini Elettronica precision balance). An additional sample of WGA was pre-treated and then coated with the oleic acid using the same method. At the end of this procedure, the additional sample was then placed in a vessel in the dark with controlled air and humidity, throughout the duration of the whole test (76 hours).

2.2.5. Antibacterial efficiency

The measure was performed on photocatalytic tiles following the ISO 27447:2009 rule (film adhesion method) (rif. ISO 27447:2009 Fine Ceramics (Advanced Ceramics, Advanced Technical Ceramics)—Test Method for Antibacterial Activity of Semiconducting Photocatalytic Materials, 2009).

The test used *E. coli* ATCC 8739 and *S. aureus* ATCC 43300 methicillin-resistant MRSA. Each strain was inoculated into a nutrient agar slant, incubated for 16–24 hours at 37°C ± 1°C and subsequently transferred in a new nutrient agar slant and again incubated at 37°C ± 1°C for 16–20 hours. An adequate quantity of bacteria was dispersed in 1/500 NB (nutrient broth) to obtain a count of 6.7×10^5 to 2.6×10^6 cells/ml. Samples of 50×50 mm square was rinsed with distilled water and autoclaved at 121°C for 30 minutes before the test to remove any organic residue present at the ceramic surface. For each bacterium strain were tested specimens without antibacterial treatment and six specimens with antibacterial treatment; 0.15 ml of bacterium suspension was put onto each specimen and covered with a 40×40 mm square inert and non-water adsorbent film with a transparency rate over 85% for the 340–380 nm range. Each specimen was placed in a 100 mm diameter Petri dish containing moistened paper filter

to prevent drying out of the suspension covered with a 1 mm thickness borosilicate glass with a transparency rate over 85% for the 340–380 nm range.

The samples were irradiated with a fluorescent UV lamp (18W Philips PL-L) with an intensity of 0.25 mWcm^{-2} for 8 hours. A similar sample was treated with the same procedure but left in the dark for the whole test. A viability count was performed by dilution and plating on nutrient agar (NA) incubated at 37°C for 48 hours [45].

The bacterium concentration of the washout liquid is obtained by Eq. 1 and expressed to two significant digits:

$$P = Z \times R \tag{1}$$

where P is the bacteria concentration (cells/ml); Z is the average number of colonies in two Petri dishes; R is the dilution factor. When the number of viable bacteria is less than 30 in the Petri dishes with 1 ml of washout solution, the cell number is used to calculate the average number.

The bacteria concentration obtained in Eq. (1) is applied in Eq. (2) to calculate the number of viable bacteria.

$$N = P \times V \tag{2}$$

where N is the number of cells of viable bacteria; P is the bacteria concentration obtained in Eq. (1) (cells/ml); V is the volume of Soybean-casein digest broth with lecithin and polysorbate (SCDLP) medium for washout (ml).

Equations (3) and (4) are necessary to calculate the photocatalyst antibacterial activity value after the test is completed.

$$R_L = \left(\log\left(B_L/A\right) - \log\left(C_L/A\right)\right) = \log\left(B_L/C_L\right) \tag{3}$$

where R_L is the photocatalyst antibacterial activity value, after UV irradiation of intensity L; L is the UV irradiation intensity (mWcm^{-2}); A is the average number of viable bacteria of non-treated specimens, just after inoculation; B_L is the average number of viable bacteria of non-treated specimens, after UV irradiation of intensity L; C_L is the average number of viable bacteria of photocatalytic treated specimens, after UV irradiation of intensity L.

$$\begin{aligned} \Delta R &= \log\left(B_L/C_L\right) - \left(\log\left(B_D/A\right) - \log\left(C_D/A\right)\right) \\ &= \log\left(B_L/C_L\right) - \log\left(B_D/C_D\right) \end{aligned} \tag{4}$$

where ΔR is the photocatalyst antibacterial activity value with UV irradiation; B_D is the average number of viable bacteria of non-treated specimens, after being kept in a dark place; C_D is the average number of viable bacteria of photocatalytic treated specimens, after being kept in a dark place.

3. Results and discussion

3.1. Characterization

3.1.1. Commercial powders of TiO_2

The XRD patterns relative to the three selected samples are reported in **Figure 5**. Anatase is the unique polymorph present for all samples, except for the well-known P25 material, which exhibits the 80:20 anatase/rutile ratio phase composition. The crystallographic reflexes (1 0 1), (2 0 0) and (2 1 1) have been used to calculate the average crystallite size of the various titania particles (**Table 1**, third column). P25 and P105 possess comparable crystallite size centred at around 25 nm, while the sample K1077 exhibit a value of 130 nm. These features are reflected in the BET surface area of the micro-sized sample (K1077), which is much lower compared to the nano-sized ones (**Table 1**, second column).
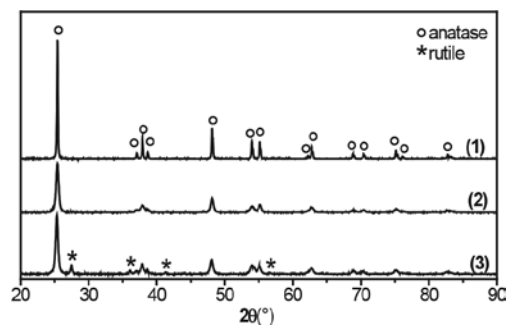

Figure 5. XRD patterns of K1077 (1), PC105 (2) and P25 (3).

Sample	BET surface area (m²g⁻¹)	Average crystallite size (nm)	XPS Ti 2p$_{3/2}$ (eV)	XPS OH/O$_{tot}$	Band gap (eV)
P25	50	26	458.4 ± 0.1	0.14	3.21
PC105	80	23	458.4 ± 0.2	0.85	3.19
K1077	12	130	458.3 ± 0.1	0.32	3.15

Table 1. Main features of commercial TiO_2 samples.

A comparison between the morphological features exhibited by the nano-sized powders, respectively known as P25 and PC105, and the micro-sized K1077, was carried out by TEM.

TEM images (**Figure 6**) confirm the above average crystallite size extrapolated by XRD analysis also excluding the presence of ultra-fine particles in K1077. It can also be evidenced that the nano-sized materials perfectly fall within the 'nano' definition: in fact, both nano-samples are characterized by average particles size of 15–30 nm; they exhibit a closely packed nature and almost roundish contours. However, the highly crystalline nature of these powders is confirmed by the high incidence of fringe patterns, which are generated by the superimposition of crystals almost all belonging to the TiO_2 anatase polymorph. In both cases, the prevalently observed planes ($d = 0.357$ nm) are ascribable to the (1 0 1) family (ICDD anatase file no. 21-1272).
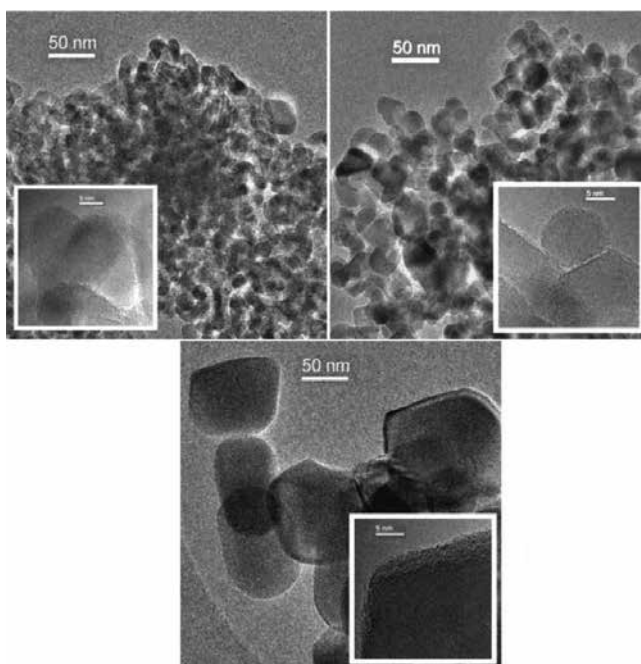
Figure 6. Top left-hand image refers to PC105, top right-hand image refers to P25 and bottom image refers to K1077.

As far as the micro-sized sample is concerned, much larger average dimensions of the particles (**Figure 6**) are observed. This feature is in total agreement with the indications obtained by means of XRD analysis, evidencing the average dimensions in the 120–200-nm range for the K1077 sample. Moreover, also in this case the most frequently observed crystal planes are those belonging to the (1 0 1) family of the TiO_2 anatase polymorph, thus exhibiting a much less defective nature of the particles.

XPS was used to detect the surface state of the TiO_2 particles by (**Figure 7**). No significant differences can be appreciated among all the investigated samples in the Ti 2p region concerning both binding energies (BE) and full width at half-maximum (FWHM) values. The Ti $2p_{3/2}$ peak is always present as a single doublet and the BE (forth column in Table 1) compares

well with the data for Ti(IV) in TiO_2 [48]. The analysis of the oxygen peaks exhibits the presence of two different components, which can be attributed to lattice oxygen in TiO_2 (529.9 eV) and to surface OH species (>531.5 eV), respectively [49]. For PC105, a particular O1s shape was observed (**Figure 7b**): in fact, the OH component is very intense probably due to a particular industrial synthesis in order to enhance the photocatalytic efficiency of the sample.
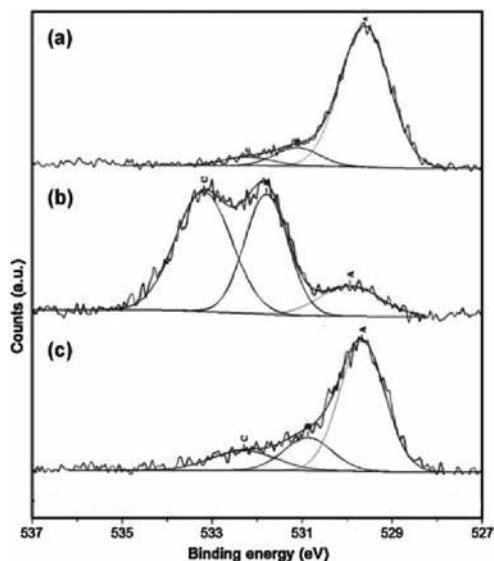

Figure 7. O1s XPS spectra for (a) P25; (b) PC105; (c) K1077.

The hydrophilicity/hydrophobicity character of photocatalyst surface plays a crucial role in determining the adsorption step and thus the photocatalytic activity in the degradation of pollutants [50]. The OH/O_{tot} surface ratio, reported in the fifth column of **Table 1**, is a quantitative measure of the hydrophilicity/hydrophobicity of the TiO_2 surface, estimated using the XPS-determined surface OH atomic concentrations normalized by the total oxygen atomic concentrations (O_{tot}) [51]. PC105 exhibits the highest concentration of OH that represents the 85% of the oxygen at the surface as previously underlined. It is noteworthy that the micro-sized sample presents a higher atomic concentration of OH groups in comparison with P25, pointing out the higher hydrophilic character of its surface.

From XPS spectra, we can obtain both the information on the BE of a specific element and the total density of states (DOS) of the valence band (VB) [52]. This measurement is useful to unravel the effect of TiO_2 structural modifications on the electronic properties of the material. Comparing semiconductor nanoparticles/microparticles, the quantum size effect could also play a role, giving band-gap narrowing in the bigger-sized particles in respect to the smaller ones. **Figure 8** reports the VB XPS spectra of both nano-sized samples and the micro-sized one. The VB maximum position was determined through linear extrapolation and the same values around −2.6 eV were measured for all samples, which is a typical value for TiO_2 [53].
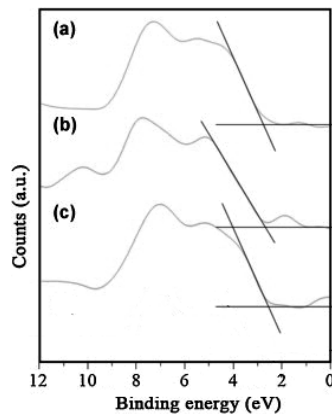
Figure 8. VB XPS spectra along with VB maximum determining by the linear extrapolation method for (a) P25; (b) PC105; (c) K1077.

Experimental data of diffuse reflectance were elaborated to absorption coefficient values F(R) according to the Kubelka-Munk equation (Eq. 5),

$$f(R_\infty) = \frac{(1-R_\infty)^2}{2R_\infty}$$

(5)

where R is the reflectance.

The corresponding band gap values obtained by this procedure for all samples are reported in **Table 1** (sixth column). The obtained band gap values do not exhibit large differences among the various samples and fall in the range expected for the TiO₂ material.

3.1.2. Photocatalytic active tiles

Basic features of the porcelain grés tiles were determined after the coverage with the photo-catalytic mixture to verify that the coating procedure does not alter the ceramic body. Lack of porosity, resistance to surface abrasion and durability were measured by water absorption [54], rotation of an abrasive load on the tile surface [55] and determination of frost resistance [56], respectively. The frost resistance determination is an intrinsic measurement of the product durability.

The coating with the SiO₂-based compounds and the following calcination step preserve the pure anatase form verified by XRD measurements [35]. The presence of SiO₂, together with TiO₂, enhances the formation of hydroxyl radical •OH, which would be achieved via strong Brønsted acid sites at the TiO₂/SiO₂ interface region [57]. This incorporation inhibits the crystal growth of TiO₂ allowing the preservation of the anatase structure at 680°C [58].

SEM images of WGA show a homogeneous distribution of the micro-sized TiO₂ crystallites without ultrafine particles (**Figure 9**), on the porcelain tile surface. If measurement is carried

out at higher magnification (**Figure 9**, at the bottom), it is possible to observe that the particle dimension falls in the 100–125 nm range, while at lower magnification it is possible to evidence larger particles of SiO_2.
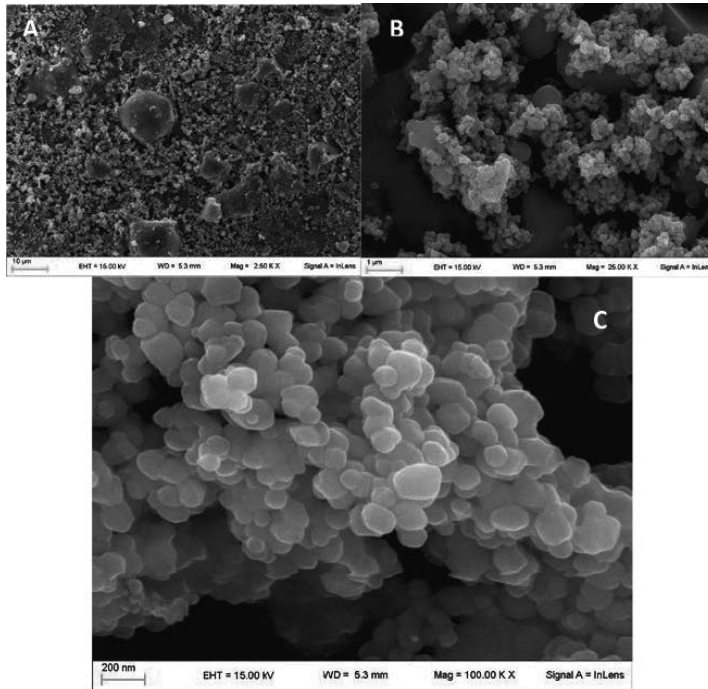

Figure 9. SEM images of photocatalytic active tiles (WGA at different magnifications: (a) 2.50 K X; (b) 25.00 K X; (c) 100.00 K X).

Wettability measurements were performed on both a grés tile and a photocatalytic active tile (**Figure 10**), exhibiting a completely different surface; in fact, the photocatalytic WGA tile presents very hydrophilic surface features with an average angle of 23.0°, which can be explained by the super hydrophilic property of TiO_2 photocatalyst [59].
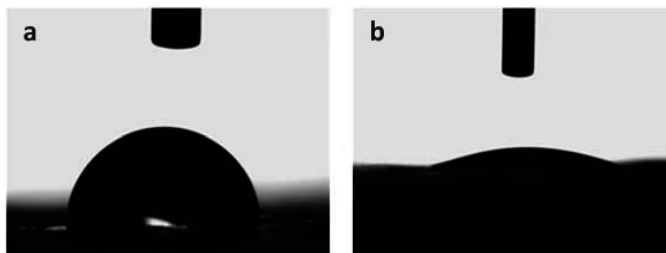

Figure 10. Contact angle: (a) traditional porcelain grés tile; (b) photocatalytic WGA tile.

3.2. Photocatalytic tests

3.2.1. Nano- and Micro-TiO$_2$ commercial samples

The results obtained with the commercial catalysts starting from 1000 ppb of NO$_x$ are reported in **Figure 11**, and it is well evident that all samples show good photocatalytic performances. In particular, after 60 minutes of reaction, the NO$_x$ conversion is almost complete. From this point, the actual difference between the nano-powder and the micro-one is evident, because while P25 reaches a complete degradation of NO$_x$, K1077 is not able to degrade the entire NO$_x$ amount, even if it is able to convert more than 90% of the pollutant approximately. Thus, even if the nano-sized material exhibits the best performances, the photocatalytic activity of the pigmentary sample is very good, in agreement with the presence of appreciable amount of surface hydroxyls.
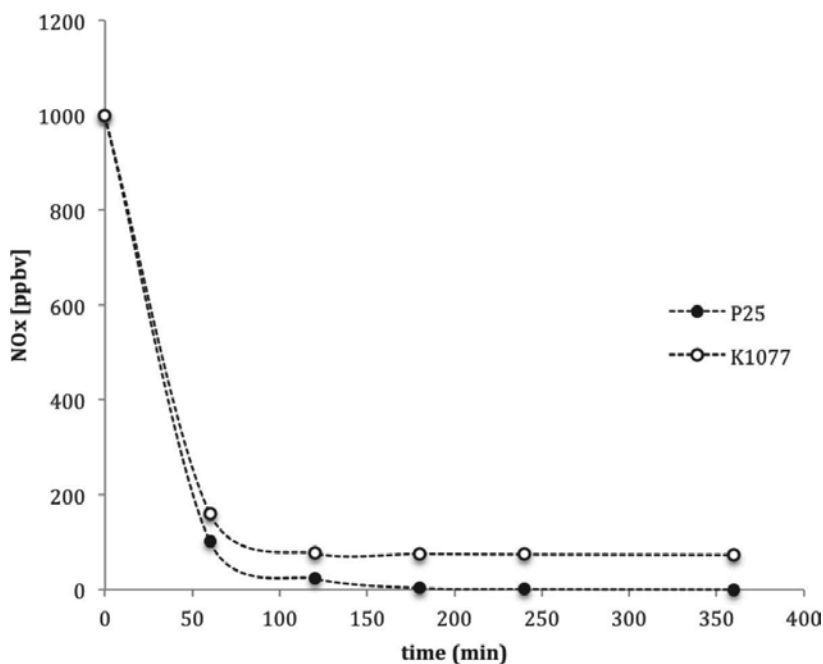

Figure 11. Comparison between nano-TiO$_2$ (P25; full dots) and micro-TiO$_2$ (K1077; empty dots).

Moreover, the results obtained using lower NO$_x$ concentration show that nano-sized and micro-sized powders have a similar photocatalytic activity. Both samples reach the complete NO$_x$ degradation within 50 minutes. Testing the materials in more diluted initial concentrations, the difference between micro and nano-samples is highly limited, and this means that the amount of surface OH species on the K1077 is enough to guarantee performances similar to that of P25, as also evident in **Figure 12**, relative to the FTIR features typical of OH species present at the surface of the three TiO$_2$ systems, after evacuation at RT.
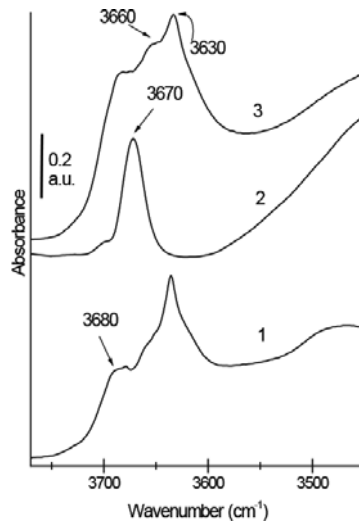
Figure 12. IR. Absorbance IR spectra relative to the OH stretching spectral region of samples outgassed at RT for 60 min: (a) P25; (b) K1077; (c) PC105.

Nano- and micro-sized commercial sample photoactivity has been studied also for the degradation of different VOCs (acetone, acetaldehyde, toluene and ethanol), as shown in **Figure 13** for the K1077 sample. VOC molecules are very interesting to study because they are mainly responsible for both outdoor and, even more, indoor pollution [60, 61].
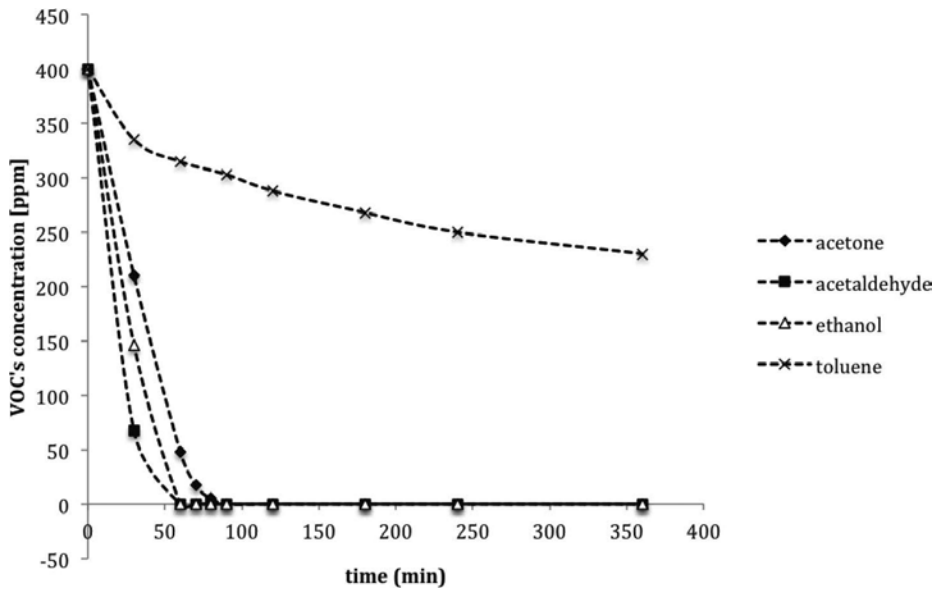

Figure 13. K1077 in the photodegradation of some VOCs.

Acetone reaction pathway passes through the formation of acetaldehyde as a by-product (**Figure 14a**) as reported by Stengl et al., while toluene is a less polar and less hydrophilic VOC, with a degradation that is more difficult because of the presence of the aromatic ring. Moreover, the degradation pathway of toluene passes through many by-products, which are not so easy to degrade and that in most cases are adsorbed on the TiO$_2$ surface (**Figure 14b**).
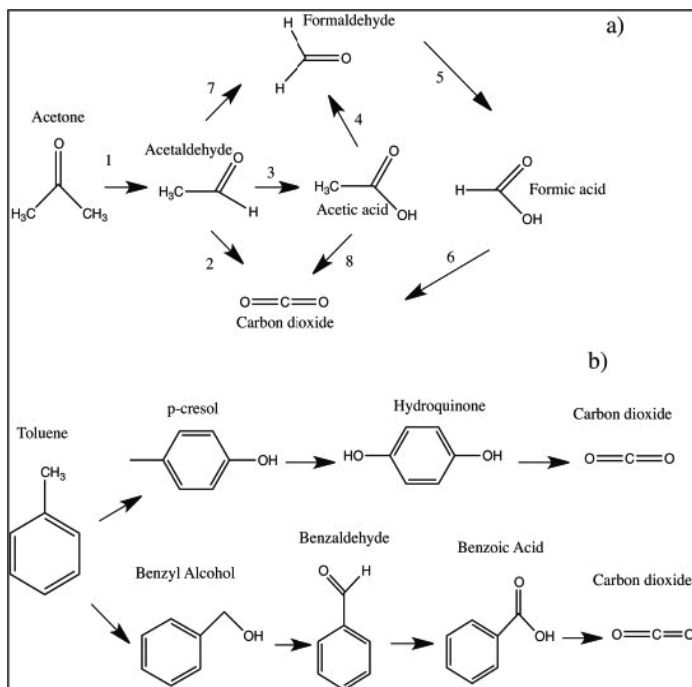

Figure 14. Reaction pathways of photocatalytic: (a) acetone oxidation; (b) toluene oxidation.

The nano-sized samples exhibit higher photocatalytic efficiency, leading to the complete pollutant degradation within a shorter reaction time, than the micro-sized K1077 sample. For acetone, acetaldehyde and ethanol, using both nano- and micro-sized powders, CO$_2$ is the only final product of the reaction, confirming the complete degradation without the formation of by-products adsorbed on the sample surface (verified by FTIR measurements on the sample surface after the kinetic runs). The case of toluene is different: for all samples, the pristine pollutant is not completely degraded even after 6 hours of reaction, and most of the by-products are not completely degraded, as well.

Considering surface area and particle size, the VOC photodegradation kinetic is faster when the particle crystallite size is smaller. The nature of the reactive sites is influenced by the morphological features of crystallites, thus inducing different type of exposed OH reactive sites onto the surface of nano- and micro-sized TiO$_2$ samples. Despite the low surface area, K1077 presents an abundant OH radicals' population, thus it shows to be able to photo-degrade

several VOCs, with not excessive differences in terms of performance compared to nano-TiO_2 powders.

3.2.2. Photocatalytic active tiles

Micrometric titanium dioxide can be used with very good results for the photocatalytic abatement of pollutants, such as NO_x or VOCs. Thus it has been industrially applied on porcelain grés tiles with many advantages in terms of (i) ease of manipulating micrometre powders instead of nano-powders, (ii) cost, because pigmentary TiO_2 is cheaper and (iii) safety, because of the toxicity of TiO_2 nanoparticles that can be inhaled.

The photocatalytic active tiles, obtained after the TiO_2 coating as described above, have been tested in the photodegradation of both gas and liquid pollutants, in particular studying their photocatalytic performances for the photodegradation of NO_x in gas phase, and for the photodegradation of phenol in liquid phase. Particularly, nitrogen oxides are the worldwide air pollution reference.

When tested for the NO_x abatement, photocatalytic active tiles show very good results. The pollutants are successfully degraded and the maximum conversion is reached just after about 40 minutes. The experiments of this run were performed at 140 NL h^{-1} and with a starting concentration of 100 ppb of NO_x (**Figure 16**). These experiments were conducted changing the parameters, in particular the NO_x starting concentration, as well as the duration of the reaction, obtaining in all cases good results [10].
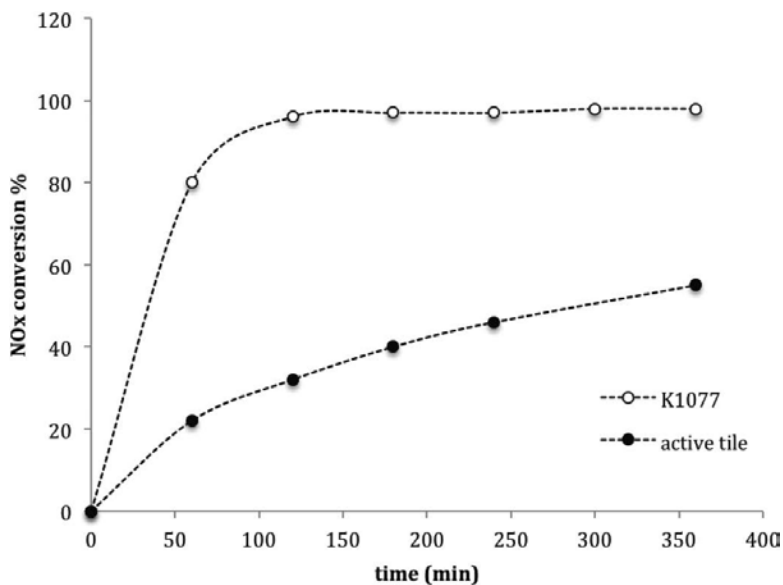

Figure 15. NO_x conversion % vs. time; comparison between K1077 (empty dots) and WGA (full dots).
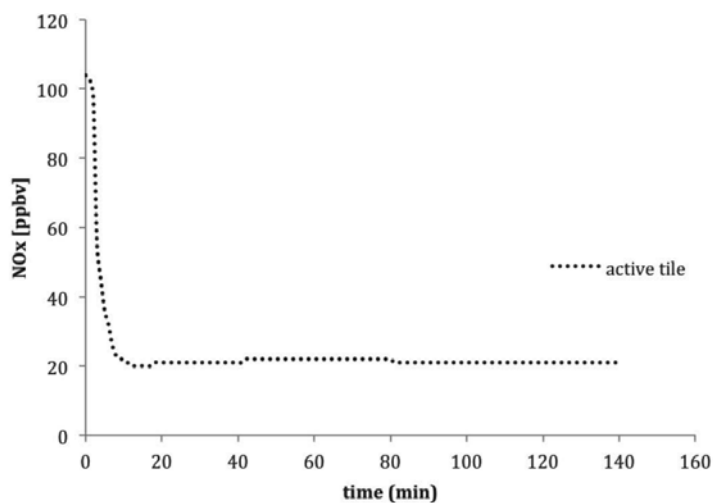
Figure 16. NO$_x$ photodegradation using a WGA tile (3600 cm^2)—continuous flow reactor.

Investigating the phenol removal in water in the presence of WGA, it was observed that the trend of the degradation processes depends on the pollutant starting concentration. After 6 hours of exposure, the phenol photodegradation percentage is almost the same at 15 and 25 ppm (78 and 73%, respectively), and much lower at 50 ppm (46%), as shown in **Figure 17**.
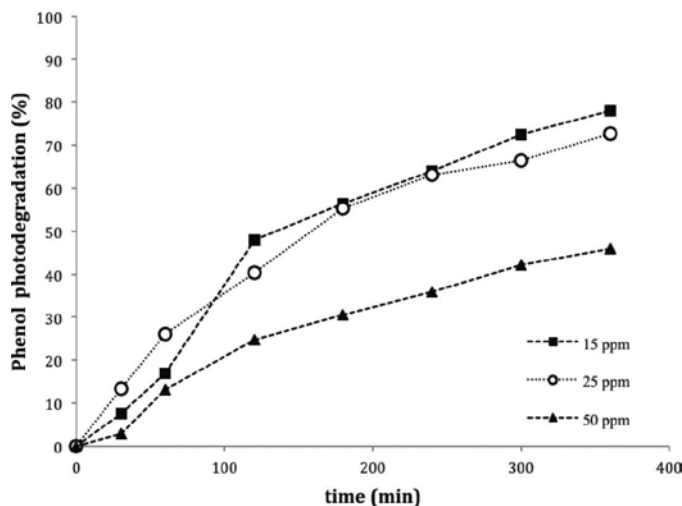

Figure 17. Photocatalytic degradation of phenol in the presence of WGA at different starting concentrations (15, 25 and 50 ppm, respectively)—influence of the starting phenol concentration on the reaction rate.

The mineralization data show that at the lowest concentrations, the pollutant adsorption is followed immediately by its degradation and mineralization; on the contrary, at higher

concentrations, the mineralization process starts later, and it is related to the hydroquinone formation, that is the main by-product (see **Figure 18**).
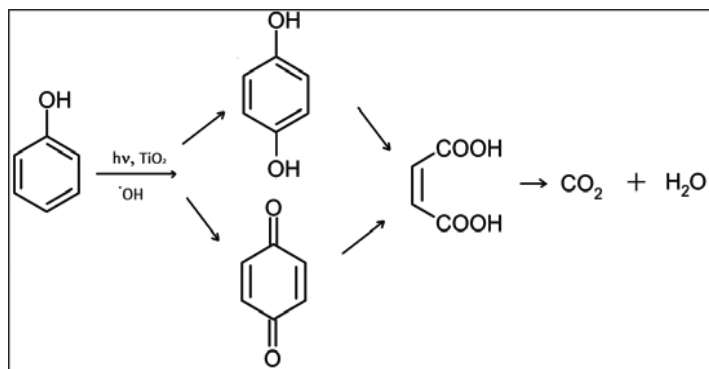

Figure 18. Degradation pathway of phenol photodegradation.

Therefore, the photocatalytic tile performances strongly depend on the starting pollutant concentration; anyway, photocatalytic tiles are able to degrade also the organic molecule, and they are effective in liquid phase.

These tests were carried out under UV-A light, but the real frontier will have to transform these materials active and efficient to sunlight and artificial light. The artificial lighting in the most part of the indoor environments is achieved with LED lamps, without any contribution of UV irradiation. Concerning this, many studies on the commercial micro-sized powders show that, modifying TiO_2, it is possible to make it photoactive even to the visible wavelengths [62, 63]. This is very promising for a future application on porcelain grés tiles and for their application in the indoor environments lit by LED lights.

3.3. Self-cleaning tests

The surface of the WGA sample is coated with a film of oleic acid (**Figure 19**), following the method described in the experimental section. In the presence of UV irradiation, this substance is completely degraded, proving that the substrate has photocatalytic properties. Measurement was carried out according to the mentioned ISO Standard, by monitoring the change of the contact angle of a drop of water that fell onto the sample surface, which was illuminated by a UV-A source at known wavelength and power.
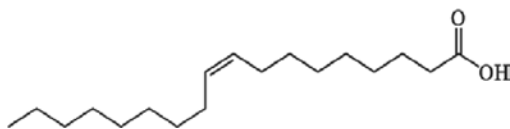

Figure 19. Oleic acid structure.

When between the beginning and the end of the test (76 hours), there is a variation in the contact angle, a photocatalytic material can be defined as *self-cleaning*.

The results of the measurements on WGA tiles are summarized in **Figure 20** that shows two pictures taken and processed by the instrument used for the contact angle measurements.
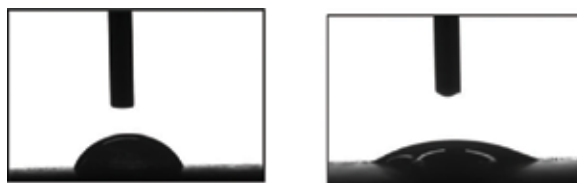

Figure 20. Profile of the water drops at time 0 (image on the left) and at 76 hours (image on the right) on a WGA slab.

Contact angle value of the WGA sample stored in the dark was also examined, but only at the end of the 76 hours. The comparison between the two tested slabs is listed in **Table 2**:

Sample	UV	Original slab contact angle	Contact angle t_0	Contact angle t_{48}	Contact angle t_{76}
WGA	Yes	31.3° ± 0.9°	68.5° ± 1.0°	41.0° ± 2.9°	30.1° ± 2.8°
WG A	No	31.3° ± 0.9°	67.8° ± 0.9°	—	68.2° ± 1.1°

Table 2. Summarizing data from self-cleaning test.

As shown in the table, the value of the contact angle gradually decreases from time t_0 to t_{76}, achieving the original value measured before the application of oleic acid onto the tile surface. This is due to the photocatalytic efficiency of the material, which is then able to degrade the oleic acid under UV irradiation [64].

The contact angle value at 72, 74 and 76 hours is constant, and it has returned to the value of the pristine ceramic surface at the beginning of the test, demonstrating that the oleic acid molecule has been completely degraded. On the contrary, there were no changes in the value of the contact angle of the sample of WGA treated with oleic acid but kept in the dark, confirming that natural degradation is not effective and that the photocatalytic process is needed to activate the photodegradation of the organic contaminant.

3.4. Test on antibacterial properties

Antibacterial tests performed on WGA samples confirmed the efficiency of the material to destroy bacteria present at the ceramic surface. Test results are reported in **Table 3**:

Experimental conditions of the test such as bacterial strains, temperature, humidity, irradiation, exposure time etc. are similar to the common condition of applications on the WGA. To evaluate the antibacterial activity of WGA, *E. coli* (Gram negative), as common inhabitant of human and animal intestine and therefore a suitable indicator of drinking water and quality

food, and *S. aureus* (Gram positive) as human pathogen bacteria in particular the MRSA strain, characterized by some antibiotic-resistance to beta-lactam, have been chosen.

Test	Unit Measurement	Results	
Antibacterial activity of photocatalytic materials—materials		*E. coli* **ATCC 8739**	*Staphylococcus aureus* **MRSA ATCC 43300**
No. of bacteria inoculated	Cells /ml	1,100,000	1,500,000
A—Average number of bacteria Non-treated specimens after inoculation	cells /ml	160,000	230,000
B_L—Average number of bacteria non -treated specimens after UV irradiation	cells /ml	170,000	108,000
C_L—Average number of bacteria photocatalytic treated specimens after UV irradiation	cells /ml	10	10
R_L—Photocatalytic antibacterial activity value after UV irradiation	Log10	4.2	4.0
Reductions of bacteria from non-treated specimens after UV irradiation	%	99,994	99,991
B_D—Average number of bacteria non-treated specimens after being kept in a dark place	cells /ml	600,000	400,000
C_D—Average number of bacteria photocatalytic treated specimens after being kept in a dark place	cells /ml	130,000	37,000
ΔR—Photocatalytic antibacterial activity value with UV irradiation	Log10	3.6	3.0

Table 3. Summary of the antibacterial results on WGA.

Test was performed at 25°C ± 1°C, temperature in the range of activity of the photocatalytic process and vitality of the microorganism tested both mesophilic. Test was conducted at pH 7.0 ± 0.2 (1/500 Nutrient broth), pH is an influential parameter for organism viability and a neutral pH near 7 is optimal for many biological processes. Test was performed in aerobic conditions (oxygen presence) to favour *E. coli* and *S. aureus* viability (aerobe/anaerobe facultative) at 0.25 mWcm^{-2} as normally indoor exposure beside the window in the daytime, for 8 hours of exposure time.

The antibacterial tests in this work passed all the evaluation conditions as:

1. The logarithmic value of the number of viable bacteria of non-treated specimens after inoculation derived from the equation: $(L_{max} - L_{min})/(L_{mean}) \leq 0.2$, where L_{max} is the maximum logarithmic value of viable bacteria, L_{min} is the minimum logarithmic value of viable bacteria, L_{mean} is the average logarithmic value of viable bacteria for three specimens;

2. The logarithmic value of viable bacteria of non-treated specimens after inoculation shall be within the 1.0×10^5 to 4.0×10^5 cell range;

3. The viable bacteria of non-treated specimens after light exposure shall be more than 1.0×10^3 cells for all three specimens;

4. After being kept in a dark place, the viable bacteria of non-treated specimens shall be more than 1.0×10^3 cells for all three specimens.

In the first test, the average logarithmic value of *E. coli* for three non-treated specimens after inoculation is 160,000 cells/ml, and this value increases to 600,000 cells/ml after being kept in a dark place, and a 170,000 cells/ml after 8 hours of UV irradiation. The average logarithmic value of *E. coli* for three treated specimens decreases to 130,000 cells/ml after being kept in a dark place, and a 10 cells/ml after 8 hours of UV irradiation.

In the second test, the average logarithmic value of *S. aureus* for three non-treated specimens after inoculation is 230,000 cells/ml, and this value increases to 400,000 cells/ml after being kept in a dark place, and 108,000 cells/ml after 8 hours of UV irradiation. The average logarithmic value of irradiation.

For both bacterial strains, an increase after being kept in a dark place on non-treated specimens is observed, but greater for *E. coli* than *S. aureus*, and a decrease was observed for treated specimens, but greater for *S. aureus* than *E. coli*. These differences may be due to the different structures of the cell wall of the two bacterial strains, and bacterial reduction is imputable to non-photocatalytic antibacterial activity which can be present in different intensities in ceramic tiles. Both microorganisms tested same decrease after UV irradiation is detected and WGA showed a photocatalyst antibacterial activity *R* greater than 2 (reduction greater than 99.99%); the antibacterial activity is similar for both Gram negative and Gram positive bacteria, including strains with methicillin resistance.

These results indicate that the action of reactive oxygen species (ROS), generated during the photocatalysis, on cell wall, cell membrane and internal cellular components, is very effective, and it does not seem to be affected by methicillin-resistant mechanisms. The same trend is observed for *ΔR* (photocatalyst antibacterial activity value with UV irradiation); the values obtained for *E. coli* and *S. aureus* (3.6 and 3.0) indicate a good photoefficiency on the WGA tiles.

4. Conclusions

Micro-sized TiO$_2$ can successfully replace the nanometric powders for photocatalytic applications, as well as for the removal of dirt or bacteria from surfaces. The use of micrometric powders of TiO$_2$ brings several advantages in terms of health safety, limitation of the problems related to the use of nano-powders in industries and cost.

From a chemical point of view, the commercial and micro-sized sample K1077 consists completely of anatase, which is the most photoactive crystallographic phase, as well as it exhibits a rather high population of hydroxyl radicals at the surface that confer an improve-

ment of the performances in terms of pollutant oxidation. From an economic point of view, micro-TiO$_2$ is much cheaper than the commercial nano-powders. In particular for high amount of powder, the replacement of the nano-powder by micro-powder leads to an extremely high cost saving. Moreover, micrometric TiO$_2$ is overall efficient against all the different pollutants, with a not so high difference in performance compared to nano-TiO$_2$, especially in pollution levels closest to the actual values.

The application of micro-TiO$_2$ on porcelain grés tiles paves the way to a new scenario of products to improve the quality of life. Indeed, when TiO$_2$ is coated on the porcelain grés tiles, all its properties can be fully exploited. Not only the photocatalytic tiles show self-cleaning features and antibacterial properties, but also they are able to degrade both organic and inorganic pollutants in gas and liquid phases. Particularly, the possibility to exploit the photocatalytic properties of tiles even in aqueous phase is a real innovation compared with most of the photocatalytic building materials, already available in the market.

To conclude, the use of micro-TiO$_2$ is an actionable and necessary road, as well as the photocatalytic tiles coated with micro-powders are actually effective for a real improvement of our indoor and outdoor environments.

Acknowledgements

Author details

Claudia L. Bianchi[1*], Carlo Pirola[1], Marta Stucchi[1], Benedetta Sacchi[1], Giuseppina Cerrato[2], Sara Morandi[2], Alessandro Di Michele[3], Alessandra Carletti[4] and Valentino Capucci[5]

*Address all correspondence to: claudia.bianchi@unimi.it

1 University of Milan – Department of Chemistry, Milan, Italy

2 University of Turin – Department of Chemistry, Turin, Italy

3 University of Perugia – Department of Physics and Geology, Perugia, Italy

4 Artest SpA, Modena, Italy

5 GranitiFiandre Group, Castellarano, Italy

References

[1] Macwan D.P., Dave P.N., Chaturvedi S. (2011). A review on nano-TiO$_2$ sol–gel tyspe syntheses and its applications. *Material Science*, Vol. 46, pp. 3669–3686.

[2] Ismail A.A., Bahnemann D.W. (2011). Mesoporous titania photocatalysts: preparation, characterization and reaction mechanisms. *Journal of Materials Chemistry*, Vol. 21, pp. 11686.

[3] Fujishima A., Honda K. (1972). Electrochemical photolysis of water at a semiconductor electrode. *Nature*, Vol. 238, pp. 37–38.

[4] Rios P.F., Dodiuk H., Kenig S., McCarthy S., Dotan A. (2007). The effect of polymer surface on the wetting and adhesion of liquid systems. *Adhesion Science Technology*, Vol. 21, pp. 227–241.

[5] Kaune G., Memesa M., Meier R., Ruderer M.A., Diethert A., Roth S.V., D'Acunzi M., Gutmann J.S., Mueller-Buschbaum P. (2009). Hierarchically structured titania films prepared by polymer/colloidal templating. *ACS Applied Materials & Interfaces*, Vol. 1, pp. 2862–2869.

[6] Morris, A.J., Meyer, G.J. (2008). TiO$_2$ surface functionalization to control the density of states. *Journal of Physical Chemistry C*, Vol. 112, pp. 18224–18231.

[7] Kumar S.G., Devi L.G. (2011). Review on modified TiO$_2$ photocatalysis under UV/visible light: selected results and related mechanisms on interfacial charge carrier transfer dynamics. *The Journal of physical chemistry A*, Vol. 115 No. 46, pp. 13211–13241.

[8] Lawless D., Serpone N., Meisel D. (1991). Role of OH radicals and trapped holes in photocatalysis. A pulse radiolysls study. *Journal of Physical Chemistry*, Vol. 95, pp. 5166–5170.

[9] Mineral Commodity Summaries (2011). Titanium and titanium dioxide. U.S. *Geological Survey*, Retrieved from http://minerals.usgs.gov/minerals/pubs/mcs/2011/mcs2011.pdf

[10] Bianchi C.L., Pirola C., Galli F., Cerrato G., Morandi S., Capucci V. (2014). Pigmentary TiO$_2$: a challenge for its use as photocatalyst in NOx air purification. *Chemical Engineering Journal*, Vol. 261, pp. 76–82.

[11] Patil S.S., Shedbalkar U.U., Truskewycz A., Chopaded B.A., Ball A.S. (2016). Nanoparticles for environmental clean-up: a review of potential risks and emerging solutions. *Environmental Technology & Innovation*, Vol. 5, pp. 10–21.

[12] Wang J., Gerlach J.D., Savage N., Cobb G.P. (2013). Necessity and approach to integrated nanomaterial legislation and governance. *Science of the Total Environment*, Vol. 442, pp. 56–62.

[13] Alivisatos A. P. (1996). Perspectives on the physical chemistry of semiconductor nanocrystals. *Journal of Physical Chemistry*, Vol. 100, pp. 13226.

[14] Vishwakarma V., Samal S.S., Manoharan N. (2010). Safety and risk associated with nanoparticles - a review. *Journal of Minerals & Materials Characterization & Engineering*, Vol. 9, No. 5, pp. 455–459.

[15] Bermudez E., Mangum J., Wong B., Asgharian B., Hext P., Warheit D., et al. (2004). Pulmonary responses of mice, rats, and hamsters to subchronic inhalation of ultra-fine titanium dioxide particles. *Toxicological Sciences*, Vol. 77, pp. 347–357.

[16] Oberdörster G., Oberdörster E., Oberdörster J. (2005). Nanotoxicology: an emerging discipline evolving from studies of ultrafine particles. *Environmental Health Perspectives*, Vol. 113, No.7, pp. 823–839.

[17] Sharma N., Kalra K.L., Oberoi H.S., Bansal S. (2007). Optimization of fermentation parameters for production of ethanol from kinnow waste and banana peels by simultaneous saccharification and fermentation. *Indian Journal of Microbiology*, Vol. 47, No.4, pp. 310–316.

[18] Sayes C.M., Gobin A.M., Ausman K.D., Mendez J., West J.L., Colvin V.L. (2005). Nano-C60 cytotoxicity is due to lipid peroxidation. *Biomaterials*, Vol. 26, No. 36, pp. 7587–7595.

[19] Silva F., Arezes P., Swuste P. (2015). Risk assessment in a research laboratory during sol–gel synthesis of nano-TiO$_2$. *Safety Science*, Vol. 80, pp. 201–212.

[20] Review of Human Carcinogens. IARC Monographs, vol. 100, Retrieved from http://monographs.iarc.fr

[21] NIOSH, The national institute for occupational safety and health, Retrieved from www.cdc.gov/niosh

[22] Heinrich U., Fuhst R., Rittinghausen S., Creutzenberg O., Bellmann B., Koch W., Levsen K. (1995). Chronic inhalation exposure of Wistar rats and two different strains of mice to diesel engine exhaust, carbon black, and titanium dioxide. *Inhalation Toxicology: International Forum for Respiratory*, Vol. 7, No. 4, pp. 533–556.

[23] Bianchi C.L., Pirola C., Gatto S., Nucci S., Minguzzi A., Cerrato G., Biella S., Capucci V. (2012). New surface properties in porcelain grés tiles with a look to human and environmental safety. *Advances in Materials Science and Engineering*, Vol. 2012, 8 p.

[24] Bianchi C.L., Gatto S., Pirola C., Scavini M., Vitali S., Capucci V. (2013). Micro-TiO$_2$ as a starting material for new photocatalytic tiles. *Cement and Concrete Composites*, Vol. 36, pp. 116–120.

[25] Bianchi C.L., Gatto S., Pirola C., Naldoni A., Di Michele A., Cerrato G., Crocellà V., Capucci V. (2014). Photocatalytic degradation of acetone, acetaldehyde and toluene in gas-phase: comparison between nano and micro-sized TiO$_2$. *Applied Catalysis B: Environmental*, Vol. 146, pp. 123–130.

[26] Taurino R., Barbieri L., Bondioli F. (2016). Surface properties of new green building material after TiO$_2$–SiO$_2$ coatings deposition. *Ceramics International*, Vol. 42, pp. 4866–4874.

[27] Graziani L., Quagliarini E., Bondioli F., D'Orazio M. (2014). Durability of self-cleaning TiO$_2$ coatings on fired clay brick facades: effects of UV exposure and wet & dry cycles. *Building and Environment*, Vol. 71, pp. 193–203.

[28] Chen J., Poon C.S. (2009). Photocatalytic construction and building materials: from fundamentals to applications. *Building and Environment*, Vol. 44, pp. 1899–1906.

[29] Zhao J., Yang X.D. (2003). Photocatalytic oxidation for indoor air purification: a literature review. *Building Environment*, Vol. 38, pp. 645–654.

[30] Diamanti M.V., Del Curto B., Ormellese M., Pedeferri M.P. (2013). Photo-catalytic and self-cleaning activity of colored mortars containing TiO$_2$. *Construction and Building Materials*, Vol.46, pp. 167–174.

[31] Sciancalepore C., Bondioli F. (2015). Durability of SiO$_2$–TiO$_2$ photocatalytic coatings on ceramic tiles. *International Journal of Applied Ceramic Technology*, Vol. 12, pp. 679–684.

[32] Zhao X.J., Zhao Q.N., Yu J.G., Liu B.S. (2008). Development of multifunctional photoactive self-cleaning glasses. *Journal of Non-Crystal Solids*, Vol. 354, pp. 1424–1430.

[33] Quagliarini E., Bondioli F., Goffredo G.B., Licciulli A., Munafo P. (2012). Smart surfaces for architectural heritage: preliminary results about the application of TiO$_2$-based coatings on travertine. *Journal of Cultural Heritage*, Vol. 13, pp. 204–209.

[34] Casasola R., Rinco'n J. M., Romero M. (2012). Glass-ceramic glazes for ceramic tiles: a review. *Journal of Materials Science*, Vol. 47, No. 2, pp. 553–582.

[35] Bianchi C.L., Gatto S., Nucci S., Cerrato G., Capucci V. (2013). Self-cleaning measurements on tiles manufactured with micro-sized photoactive TiO$_2$. *Advances in Materials Research, An Interntional Journal*, Vol. 2, No. 1, pp. 65–75.

[36] Ragesh P., Ganesh V.A., Naira S.V. (2014). A review on self-cleaning and multifunctional materials. *Materials Chemistry A*, Vol. 2, pp. 14773.

[37] Furstner R., Barthlott W., Neinhuis C., Walzel P. (2005). Wetting and self-cleaning properties of artificial superhydrophobic surfaces. *Langmuir*, Vol. 21, pp. 956–961.

[38] Cappelletti G., Fermo P., Camiloni M. (2015). Smart hybrid coatings for natural stones conservation. *Progress in Organic Coatings*, Vol. 78, pp. 511–516.

[39] La Russa M.F., Ruffolo S.A., Rovella N., Belfiore C.M., Palermo A.M., Guzzi M.T., Crisci G.M. (2012). Multifunctional TiO$_2$ coatings for cultural heritage. *Progress in Organic Coatings*, Vol. 74, pp. 186–191.

[40] Quagliarini E., Bondioli F., Goffredo G.B., Cordoni C., Munafò P. (2012). Self-clean‐
ing and de-polluting stone surfaces: TiO$_2$ nanoparticles for limestone. *Construction and Building Materials*, Vol. 37, pp. 51–57.

[41] Manoudis P.N., Tsakalof A., Karapanagiotis I., Zuburtikudis I., Panayiotou C. (2009). Fabrication of super-hydrophobic surfaces for enhanced stone protection. *Surface and Coatings Technology*, Vol. 203, pp. 1322–1328.

[42] Matsunaga T., Tomoda T., Nakajima T., Wake H. (1985). Photoelectrochemical sterilization of microbial cells by semiconductor powders. *FEMS Microbiology Letters*, Vol. 29, pp. 211–214.

[43] Scuderi V., Buccheri M.A., Impellizzeri G., Di Mauro A., Rappazzo G., Bergum K., Svensson B.G., Privitera V. (2016). Photocatalytic and antibacterial properties of titanium dioxide flat film. *Materials Science in Semiconductor Processing*, Vol. 42, pp. 32–35.

[44] Fostera H.A., Sheel D.W., Sheel P., Evans P., Varghese S., Rutschke N., Yates H.M. (2010). Antimicrobial activity of titania/silver and titania/copper films prepared by CVD. *Journal of Photochemistry and Photobiology A: Chemistry*, Vol. 216, No. 2-3, pp. 283–289.

[45] Bianchi C.L., Pirola C., Galli F., Vitali S., Minguzzi A., Stucchi M., Manenti F., Capucci V. (2016). NO$_x$ degradation in a continuous large-scale reactor using full-size industri‐
al photocatalytic tiles. *Catalysis Science & Technology*, DOI: 10.1039/C5CY01627D.

[46] Bianchi C.L., Colombo E., Gatto S., Stucchi M., Cerrato G., Morandi S., Capucci V. (2014). Photocatalytic degradation of dyes in water with micro-sized TiO$_2$ as powder or coated on porcelain-grès tiles. *Journal of Photochemistry and Photobiology A: Chemis‐
try*, Vol. 280, pp. 27–31.

[47] Foster G., Annan J.D., Jones P.D., Mann M.E., Mullan B., Renwick J., Salinger J., Schmidt G.A., Trenberth K.E. (2010). Comment on Influence of the Southern Oscillation on tropospheric temperature by J.D. McLean, C.R. de Freitas, and R.M. Carter. *Journal of Geophysical Research*, Vol. 115, pp. 1-4.

[48] Ardizzone S., Bianchi C.L., Cappelletti G. (2006). Growth of TiO$_2$ nanocrystals in the presence of alkylpyridinium salts: the interplay between hydrophobic and hydrophil‐
ic interactions. *Surface and Interface Analysis*, Vol. 38, No. 4, pp. 452–457.

[49] Ardizzone S., Bianchi C.L., Cappelletti G., Gialanella S., Pirola C., Ragaini V. (2007). Tailored anatase/brookite nanocrystalline TiO$_2$. The optimal particle features for liquid and gas-phase photocatalytic reactions. *Journal of Physical Chemistry C*, Vol. 111, No. 35, pp. 13222–13231.

[50] Ardizzone S., Bianchi C.L., Cappelletti G., Naldoni A., Pirola C. (2008). Photocatalytic degradation of toluene in the gas phase: relationship between surface species and catalyst features. *Environmental Science & Technology*, Vol. 42, No.17, pp. 6671–6676.

[51] Naldoni A., Bianchi C.L., Pirola C., Suslick K.S. (2013). TiO$_2$ porous microsphere with tunable properties for air purification. *Ultrasonics Sonochemistry*, Vol. 20, pp. 445–451.

[52] Naldoni A., Allieta M., Santangelo S., Marelli M., Fabbri F., Cappelli S., Bianchi C.L., Psaro R., Dal Santo V. (2012). Effect of nature and location of defects on bandgap narrowing in black TiO$_2$ nanoparticles. *Journal of the American Chemical Society*, Vol. 134, pp. 7600–7603.

[53] Chen X., Burda C. (2008). The electronic origin of the visible-light absorption properties of C-, N-and S-doped TiO$_2$ nanomaterials. *Journal of the American Chemical Society*, Vol. 130, pp. 5018–5019.

[54] ASTM C373-88 (2006). Standard test method for water absorption, bulk density, apparent porosity, and apparent specific gravity of fired whiteware products. *ASTM International*, Retrieved from http://www.astm.org/DATABASE.CART/HISTORICAL/C373-88R06.htm.

[55] ISO 10545-7 (1996). Ceramic tiles, Part 7: determination of resistance to surface abrasion for glazed tiles. Retrieved from http://www.iso.org/iso/catalogue_detail.htm

[56] ISO 10545-12 (1995). Ceramic tiles, Part 12: determination of frost resistance. Retrieved from http://www.iso.org/iso/iso_catalogue/catalogue_tc/catalogue_detail.htm

[57] Anderson C., Bard A.J. (1997). Improved photocatalytic activity and characterization of mixed TiO$_2$ /SiO$_2$ and TiO$_2$/Al$_2$O3 materials. *Journal of Physical Chemistry B*, Vol. 101, No. 14, pp. 2611–2616.

[58] Xie T.H., Lin J. (2007). Origin of photocatalytic deactivation of TiO2 film coated on ceramic substrate. *Journal of Physical Chemistry C*, Vol. 111, No. 27, pp. 9968–9974.

[59] Wang R., Hashimoto K., Fujishima A. (1997). Light-induced amphiphilic surfaces. *Nature*, Vol. 388, No. 6641, pp. 431–432.

[60] Cerrato G., Bianchi C.L., Morandi S., Pirola C., Stucchi M., Diamanti M.V., Pedeferri M.P., Capucci V. (2015). The role of nano/microstructure in the case of the photodegradation of two model VOC pollutants using commericial TiO$_2$. *Energy and Environment Focus*, Vol. 4, pp. 226–231.

[61] Bianchi C.L., Pirola C., Galli F., Stucchi M., Morandi S., Cerrato G., Capucci V. (2015). Nano or micro- TiO$_2$ for the photodegradation of ethanol: experimental data and kinetic modeling. *RSC Advances*, Vol. 5, pp. 53419–53425.

[62] Stucchi M., Bianchi C.L., Pirola C., Vitali S., Cerrato G., Morandi S., Argirusis C., Sourkouni G., Sakkas P.M., Capucci V. (2015). Surface decoration of commercial microsized TiO$_2$ by means of high energy ultrasound: a way to enhance its photocatalytic activity under visible light. *Applied Catalysis B, Environmental*, Vol. 178, pp. 124–132.

[63] Stucchi M., Bianchi C.L., Pirola C., Cerrato G., Morandi S., Argirusis C., Sourkouni G., Naldoni A., Capucci V. (2016). Copper NPs decorated titania: a novel synthesis by high

energy US with a study of the photocatalytic activity under visible light. *Ultrasonics Sonochemistry*, Vol. 31, pp. 295–301.

[64] Watanabe T., Fukayama S., Miyauchi M., Fujishima A., Hashimoto K. (2000). Photocatalytic activity and photo-induced wettability conversion of TiO_2 thin film prepared by sol-gel process on a soda-lime glass. *Journal of Sol-Gel Science and Technology*, Vol. 19, No. 1–3, pp. 71–76.

Edited by Wenbin Cao

Photocatalysis is a hot topic because it is an environmentally friendly approach toward the conversion of light energy into chemical energy at mild reaction environments. Also, it is well applied in several major areas such as water splitting, bacterial inactivation, and pollutants elimination, which is a possible solution to energy shortage and environmental issues. The fundamental knowledge and the frontier research progress in typical photocatalytic materials, such as TiO2-based and non-TiO2-based photocatalysts, are included in this book. Methods to improve the photocatalytic efficiency and to provide a hint for the rational design of the new photocatalysts are covered.

IntechOpen